Astrophysics and Space Science Library 388

Gregory D. Fleishman
Igor N. Toptygin

Cosmic Electrodynamics

Electrodynamics and Magnetic Hydrodynamics of Cosmic Plasmas

ASSL

Springer

Cosmic Electrodynamics

Astrophysics and Space Science Library

EDITORIAL BOARD

For further volumes:
http://www.springer.com/series/5664

Gregory D. Fleishman • Igor N. Toptygin

Cosmic Electrodynamics

Electrodynamics and Magnetic Hydrodynamics of Cosmic Plasmas

Springer

Gregory D. Fleishman
Center for Solar-Terrestrial Research
New Jersey Institute of Technology
Newark, New Jersey, USA

Igor N. Toptygin
Department of Theoretical Physics
St. Petersburg State Polytechnical University
St. Petersburg, Russia

ISSN 0067-0057
ISBN 978-1-4614-5781-7 ISBN 978-1-4614-5782-4 (ebook)
DOI 10.1007/978-1-4614-5782-4
Springer New York Heidelberg Dordrecht London

Library of Congress Control Number: 2012951419

Printed on acid-free paper

Springer is part of Springer Science+Business Media (www.springer.com)

Preface

Astrophysics is a highly important part of the modern vision of the world around us. Over the past century, it has transformed the very foundation and basic philosophical concepts on the fundamental laws of nature controlling the structure and evolution of the Universe. One can recall such fascinating astrophysical discoveries as the expansion of the Universe and more recently the accelerated expansion; dark matter and dark energy and so on. This is why astrophysics is studied in hundreds of universities throughout the world; astrophysical courses are taken by students with highly diverse backgrounds, often concentrating on disciplines lacking a direct connection to astrophysics.

This textbook considers primarily those astrophysical and space plasma phenomena, in which electromagnetic interactions play a primary or at least essential role. This textbook has been written based on graduate and undergraduate courses and seminars on "cosmic electrodynamics," "magnetohydrodynamics," "plasma astrophysics," and "radiative processes in astrophysics" that the authors have taught to many generations of students at State Polytechnic University (St. Petersburg, Russia) and New Jersey Institute of Technology (Newark, New Jersey, USA), cumulatively, over more than half a century, in conjunction with the authors' astrophysical studies in the field of theoretical astrophysics, including plasma astrophysics, cosmic rays, solar wind, solar flares, supernova remnants, performed mainly at the above universities, Ioffe Institute (St. Petersburg, Russia), and National Radio Astronomy Observatory (Charlottesville, Virginia, USA). Jointly, we have a long history of teaching these sciences in Russia and the USA, and at some point we felt more and more strongly a deficit of appropriate textbooks to teach our students, which led us to substitute journal papers for use in teaching. We know that many of our colleagues teaching these courses experience similar feelings, so we decided to convert our research and teaching experience to a modern, concise textbook on cosmic electrodynamics and magnetohydrodynamics.

A driver of the textbook writing was, therefore, our willingness to share our teaching experience with our peers and supply them with a textbook representing a core, self-contained reading source, much needed to facilitate delivering undergraduate and graduate courses to students concentrating in

the field of astrophysics, solar/stellar Physics, and space physics. The field of cosmic electrodynamics is exceptionally broad, which implies that there is no hope to describe this science field fully and comprehensively within a single textbook. Therefore, it is highly important to clearly formulate the concept of material selection and the approach to depth of presentation.

First of all, we are going to make the case that modern cosmic electrodynamics is a science dealing with a highly nonlinear, nonstationary, turbulent conducting fluid (plasma) in conditions of strong energy release manifesting itself in fast fluid motions, strong magnetic field amplification, and energetic particle generation. We made an attempt to sort out and include only a "fundamental" theory, although not necessarily the "old" one: in many cases we include relatively recent discoveries and developments if we had a good reason to believe that they are reliable and potentially broadly applicable or science transforming.

Furthermore, in application of the theory we restricted ourselves in most cases to analytical solutions of the specific problems discussed: it is the analytical solutions and order-of-magnitude estimates made with them that develop our understanding of sophisticated natural phenomena. Even though we fully appreciate numerical methods and corresponding results and widely use them in our everyday research, we believe that analytical study (solutions and estimates) is the key in developing students' physical understanding and intuition, which is needed to create the science vision, to dig up what is hidden behind observations, and, in particular, to set up sophisticated numerical simulations as well as sort out and interpret their results.

The textbook presents fundamental concepts of the science illustrated by numerous examples of astrophysical applications of the theory. In doing so we try to combine classical concepts with their new developments and clearly demarcate what is well established and what is still under debate. We attempt to present the live science and illustrate how apparently complicated phenomena can be addressed and understood both qualitatively and quantitatively using well-known physics principles and equations applied under appropriate approximations and simplifications. For this purpose a limited number of astrophysical examples are considered in greater detail than it might be expected for most textbooks. In many cases we specifically address the points of agreement or disagreement between the theory and astrophysical observations, employing the latest observational data and modern theory.

The textbook delivers the most essential equations, ideas, and models widely used in modern astrophysics (see the chapter titles as a guide) in the order of increasing complexity of the material: it begins with basic concepts and linear processes including linear eigenmodes (Chaps. 1–3), then considers instabilities, weak and strong nonlinearity, and turbulence (Chaps. 4–6), and finally addresses key astrophysical problems of particle acceleration and transport, magnetic field generation, and electromagnetic radiation including self-consistent nonlinear models (Chaps. 7–12). Later chapters extensively use

the material given in earlier chapters. We tried to avoid the opposite cross-referencing of later chapters, but it was not always possible, which once again illustrates that various astrophysical phenomena are tightly connected. Many topics are presented with a full theoretical completeness, although in other cases derivations are truncated or fully omitted depending on the availability of the required theory in complementary reading on the subject (Melrose 1980; Kulsrud 2005; Somov 2006, 2007). For example, the highly important topic of magnetic reconnection is described very briefly, given that it is very well described by Kulsrud (2005) and Somov (2006, 2007).

One of the main focuses of the textbook is detailed application of the theory to astrophysical phenomena. Obviously, we cannot apply all the presented theory to all astrophysical objects and phenomena; thus, we apply some of the theory to some objects/phenomena in such a way to eventually touch upon most (if not all) of the diverse astrophysical objects including stellar interior and atmosphere, solar/stellar flares and winds, interstellar medium, supernova explosions, neutron stars, superbubbles, supernova remnants, pulsar wind nebulae, active galactic nuclei, and gamma-ray burst sources. It may seem that having so many diverse objects implies necessarily that they can be described only superficially given a limited book volume. Nevertheless, this is not the case: many phenomena are presented in all essential detail and a number of cutting-edge examples of comprehensive data analysis and interpretation are given. Complementarily, in most of the cases the derived equations and equation sets are general enough to be immediately used in scientific research work without further consulting original journal papers. This implies that the textbook will be highly useful well beyond the target audience (undergraduate and graduate students)—for active researches in astrophysics, space physics, and, perhaps, geophysics.

To easily learn the textbook, the basic knowledge obtained in general mathematics and physics courses is desirable along with a general astrophysics course. However, understanding of our book does not require any special knowledge beyond that; e.g., the most essential information from plasma physics is given in the textbook itself, although a more specialized and detailed information can be learned from Melrose (1980) and Kulsrud (2005). The book has a long list of recommended bibliography, which can be helpful for both students and researchers as a guideline for deeper study of a topic. The reference list, however, is incomplete: in most cases we included the monographs, textbooks, and review articles, which we actually used in our work on the topic. Not surprisingly, the reader can notice many sources published in Russian, given that this is the main language of both co-authors of the book. Citation of original papers is limited to the cases when we explicitly use the corresponding paper in devising a topic or in case of a few “classical” science-transforming papers. No paper has been ignored intentionally.

Finally, the authors are happy to sincerely thank our colleagues and collaborators V. Abramenko, A. Altyntsev, T. Bastian, M. Bietenholz, A. Bykov, D. Gary, P. Goode, E. Kontar, A. Kuznetsov, V. Melnikov, G. Nita, K. Platonov, J. Stone, A. Tsygan, D. Yakovlev, and V. Yurchishin for their help, highly important discussions, or sharing their observational data, as well as funding agencies NSF, NASA, Russian Ministry of Education and Science, and RFBR, which have partly been supporting our research in the areas closely related to this textbook. We are highly grateful to Professor B. Somov, who reviewed the entire textbook and came up with a number of highly valuable comments, which helped to significantly improve the final manuscript.

Newark, NJ G.D. Fleishman
St. Petersburg, Russia I.N. Toptygin

Contents

Notations (Conventions)

c_s	Sound speed
$v_{\rm A}$	Alfvén velocity
e	Elementary charge; charge of the electron
m_a	Mass of the particle (of sort a)
χ	Coefficient of heat conductivity
κ	Coefficient of thermal diffusivity; diffusion coefficient of accelerated particles
R	Reynolds number
Ra	Rayleigh number
Pr	Prandtl number
$Pe = uL/\kappa$	Pécklet number
$R_\odot$	Radius of solar photosphere
c	Speed of light
h	Plank constant
m_e	Mass of the electron
$k_{\rm B}$	Boltzman constant
ω	Cyclic frequency
ω_B (ω_{Bi})	Gyrofrequency (cyclotron frequency) of a particle (of sort i)
$\mathbf{r}$	Radius-vector of a particle
t	Time
$\mathbf{v}$, $\mathbf{u}$, $\mathbf{V}$, $\mathbf{U}$	Velocities
f, F	Distribution functions
$\mathbf{F}$, $\boldsymbol{\mathcal{F}}$	Forces
T	Temperature
ρ	Mass density or charge density
ρ_e	Charge density (if interfere with the mass density ρ)
σ	Electric conductivity or effective cross-section (typically, with subscripts)
η	Dynamic viscosity
$\nu = \eta/\rho$	Kinematic viscosity
ν_m	Collisional magnetic diffusivity (magnetic viscosity)
$\nu^{\rm eff}$ $\parallel, \perp$	Effective magnetic diffusivities (viscosities)

$\mathbf{A} \cdot \mathbf{B}$	Dot product
$\mathbf{A} \times \mathbf{B}$	Cross product
$\nabla \times \mathbf{B}$	Curl
$\nabla \cdot \mathbf{B}$	Divergence
$\nabla f \equiv \frac{\partial f}{\partial \mathbf{r}}$	Gradient
$\mathbf{B}$, $\boldsymbol{\mathcal{B}}$, $\mathbf{b}$	Magnetic field
$\mathcal{R} = 1.49 \times 10^{13}\,\mathrm{cm}$	Sun to Earth distance (1 AU)
$\mathbf{E}$, $\boldsymbol{\mathcal{E}}$, $\boldsymbol{E}$	Electric field

Physical units in equations are given in [], e.g., [erg]

$P_{\alpha\beta}$	Tensor of the momentum flux density
$\Pi_{\alpha\beta}$	Viscous tension tensor
$\ln \Lambda_{\mathrm{C}}$	Coulomb logarithm
O-mode	Electromagnetic ordinary mode
X-mode	Electromagnetic (fast) extraordinary mode
Z-mode	Electromagnetic (slow) extraordinary mode

Acronyms

AR	Active region
AU	Astronomical unit; 1 AU $= 1.49 \times 10^{13}$ cm
BGK	Bhatnagar–Gross–Krook
CMB	Cosmic microwave background
CME	Coronal mass ejection
CR	Cosmic ray
DM	Dispersion measure
DSR	Diffusive synchrotron radiation
EM	Emission measure
Eq	Equation
FASR	Frequency agile solar radiotelescope (project)
FFF	Force Free Field
GRB	Gamma-ray burst
GS	Gyrosynchrotron
GSR	Gyrosynchrotron radiation
GUI	Graphical user interface
HD	Hydrodynamics
HXR	Hard X-ray
IPM	Interplanetary medium
ISM	Interstellar medium
LCP	Left circular polarization
lhs	Left hand side
MDI	Michelson Doppler Imager
MERLIN	Multi-element radio-linked interferometer network
mfp	Mean free path
MHD	Magnetohydrodynamics
MRI	Magneto-rotational instability
NLFFF	NonLinear force free field
NoRH	Nobeyama radioheliograph
NoRP	Nobeyama radio polarimeters
NST	New solar telescope (Big Bear Solar Observatory, California, USA)

OVSA	Owens Valley Solar Array (Owens Valley Radio Observatory, California, USA)
PIC	Particle-in-cell
PWN	Pulsar wind nebula
RCP	Right circular polarization
rhs	Right hand side
RM	Rotation measure
rms	Root mean square
RHESSI	Reuven Ramaty high energy solar spectroscopic imager
RTR	Resonant transition radiation
SEP	Solar energetic particle(s)
sfu	Solar flux unit
SHH	Soft-hard-harder
SHS	Soft-hard-soft
SN	Supernova
SNR	Supernova remnant
SOHO	Solar and heliospheric observatory
SSRT	Siberian solar radio telescope
SST	Solar sub-THz telescope (Andes, Argentina)
STR	Stochasic theory of radiation
SXR	Soft X-ray
SXT	Soft X-ray telescope
TRACE	Transition region and coronal explorer is a mission of the Stanford-Lockheed institute for space research, and part of the NASA small Explorer program
UT	Universal time
VCR	Vavilov–Cherenkov radiation
WR	Wolf–Rayet (star)

Chapter 1

General Information About Cosmic Media and Approaches to Their Analysis

The main scope of this textbook includes those physical phenomena, where electromagnetic interactions, occurring in various astrophysical objects, play a dominant or at least essential role. The emphasis is given to relatively tenuous collisionless plasmas such as solar and stellar atmospheres, interplanetary medium, various phases of the interstellar medium (ISM) and extended galactic objects, and intergalactic plasma, while we do not specifically address dense, collisionally dominated, plasmas such as stellar interiors and other compact objects, although effect of collisions such as collisional dissipation or viscosity is widely considered throughout the book.

Even with this constraint, relevant plasma parameters, such as the number densities of the neutral atoms n_a, ions n_i, and electrons n_e [cm^{-3}], the temperature T [K], and the magnetic field B [G], vary within very broad ranges. The characteristic orders of magnitudes of the involved parameters can be taken from Table 1.1.[1] We have to note, however, that most of the astrophysical parameters are not well defined and known typically to an order of magnitude, rather than precisely measured. In addition, many of the plasma parameters vary in space and time. Thus, the parameters given in the Table can only be used for ballpark estimates, which, nevertheless, is a very important first step in studying any given phenomenon.

1.1 Terrestrial, Solar, and Astrophysical Plasmas

Parameters of cosmic and astrophysical objects are known to vary within very broad limits, which makes it difficult to formulate any universal

[1] For more data see monographs (Pikel'ner 1966; Akasofu and Chapman 1974, 1975; Allen 1976; Kaplan and Pikel'ner 1979; Spitzer 1981; Marochnik and Suchkov 1984) and numerous modern papers.

G.D. Fleishman and I.N. Toptygin, *Cosmic Electrodynamics*, Astrophysics and Space Science Library 388, DOI 10.1007/978-1-4614-5782-4_1,

Table 1.1: Some typical parameters of space plasmas

Object	B_0, G	n_a, cm^{-3}	n_i, cm^{-3}	T, K	Note
Galaxy	1.5×10^{-5}	20	0.05	100	Neutral clouds (HI)
Galaxy	3×10^{-6}	0.2	0.03	10^4	Intercloud warm gas
Galaxy	3×10^{-6}	–	2×10^{-3}	10^6	Hot coronal gas
Sun	1.0–4000	10^{16}	10^{13}	5.8×10^3	Photosphere
Sun	1.0–2000	10^{12}	10^{10}	$(4.3–20)\times10^3$	Chromosphere
Sun	1.0–1000	–	10^8–10^{11}	$(0.5–50)\times10^6$	Low corona
Solar wind	5×10^{-5}	–	5	3×10^4	At the Earth orbit
Intergalactic plasma	10^{-9}	5×10^{-9}	4×10^{-5}	10^4	$z < 1$
Earth ionosphere	$\lesssim 0.5$	2×10^8	10^6	10^3	

characteristics and properties applicable throughout all the astrophysical objects. We, nevertheless, can note some typical properties valid for many astrophysical objects. They are large spatial scales, relatively low densities, and strong energy release. The strong energy release, in particular, leads to ionization of individual atoms via numerous ionization processes, while the recombination is then very slow because of low densities in the objects. Even though the density can be very low, the mean free paths of the particles are frequently much smaller than the source size; therefore, the charged particles behave collectively, rather than follow individual independent trajectories, as they would in the vacuum.

Therefore, the astrophysical media are typically in the state of plasma—a collective of interacting charged particles. Moreover, we will see that even in many dense and compact objects, this is also the case. This is because more ionization processes, compared with typical laboratory conditions, are involved. In an equilibrium gas with temperature T the degree of thermal (collisional) ionization α is given by approximate Saha (1920) equation

$$\frac{\alpha^2}{1-\alpha^2} = \frac{2g_i}{g_a}\frac{(2\pi m_e)^{3/2}}{h^3}\frac{(k_B T)^{5/2}}{P}\exp(-I/k_B T), \tag{1.1}$$

where $\alpha = n_i/(n_i + n_a)$ is the ratio of ionized atoms to the total number of atoms, P is the total gas pressure, I is the energy of ionization, g_a is the statistical weight of the atom's ground state ($g_a = 2$ for hydrogen), and g_i is the statistical weight of the ion (=1 for proton). In this form the formula is valid for a three-component gas consisting of neutral atoms, singly ionized ions, and electrons—in particular, for partly ionized hydrogen. Note that because of large pre-exponential factor in Eq. (1.1) the gas becomes noticeably ionized at a temperature $k_B T$ much smaller than I. In astrophysical media other mechanisms driven by powerful short-wave electromagnetic radiation and energetic charged particles (cosmic rays, CRs) make a major contribution to ionization rate of the astrophysical plasmas.

Astrophysical plasmas are different from each other provided by variation of their parameters within exceptionally broad limits (Zasov and Postnov 2006). For example, the number density varies within more than 40 orders of magnitude, from $10^{-8}\,\mathrm{cm}^{-3}$ in the intergalactic medium to more than $10^{38}\,\mathrm{cm}^{-3}$ in the neutron stars; the characteristic energy of individual charged particles varies within more than 20 orders of magnitude, from less than $10^{-2}\,\mathrm{eV}$ (100 K) in relatively cool objects to about $10^{20}\,\mathrm{eV}$ in highest energy CRs; the magnetic field varies within more than 20 orders of magnitude, from $10^{-7}\,\mathrm{G}$ in extended objects to $10^{15}\,\mathrm{G}$ in the neutron stars.

Accordingly, depending on the given parameter regime, the plasma can be a classical Maxwellian one—equilibrium nongenerate and nonrelativistic, although it can be highly non-equilibrium, degenerate, relativistic, or even ultrarelativistic, as can be seen from the diagram shown in Fig. 1.1, as well as it can be weakly or strongly magnetized.

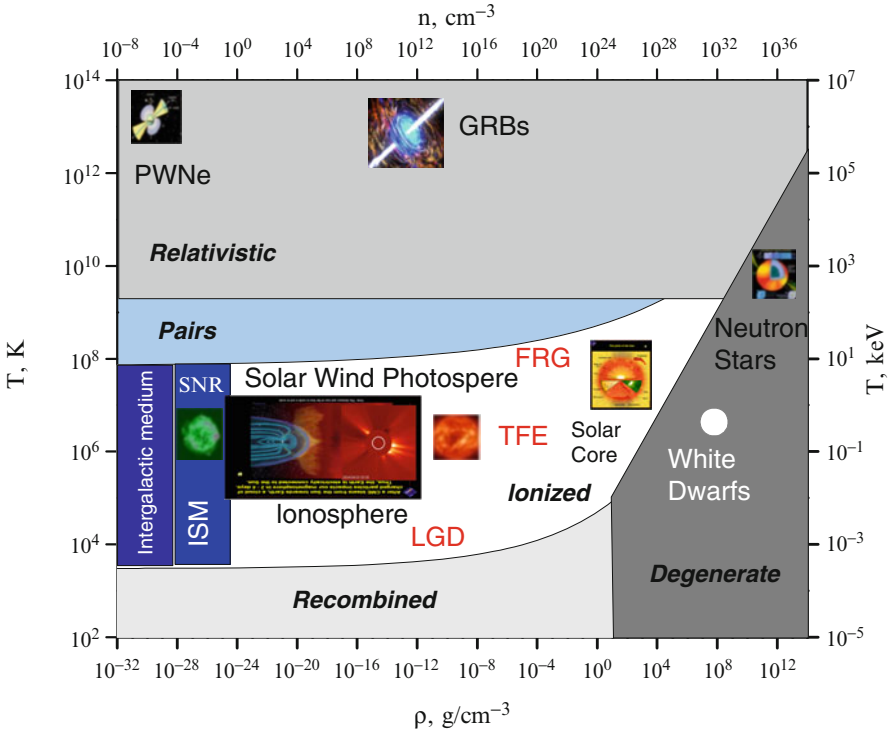

Figure 1.1: Plasma parameter diagram shows parameter regions, where the astrophysical gas is mainly neutral, ionized, relativistic, or quantum degenerate. A few types of astrophysical sources are placed in their corresponding parameter regions. For comparison, typical laboratory devices are shown by *red* abbreviations: LGD for laboratory glow discharge; TFE for today fusion experiment; and FRG for the fusion reactor goal.

As a vivid example, we touch upon structure of the Sun depicted in Fig. 1.2. The inner part of the Sun consists of the core, where nuclear fusion supplies the Sun (and the solar system including the Earth) with energy, and the radiative and convective zones, where this energy is transferred to the solar surface, the photosphere, and then radiated away into interplanetary space. The solar atmosphere above the photosphere consists of relatively cool chromosphere and hot and highly inhomogeneous corona. It is the corona that generates and drives numerous powerful phenomena including solar flares and coronal mass ejections (see Fig. 1.3), having major effects on the interplanetary space (space weather) and the Earth (e.g., spectacular polar lights produced as a result of solar charged particle penetration into the Earth's atmosphere; see Fig. 1.4), which accelerate plasma to produce solar wind, etc. The complexity of the corona is primarily related to the magnetic field, which, being produced by subphotospheric motions, forms numerous loops in the corona, filled by multitemperature plasmas and so detectable

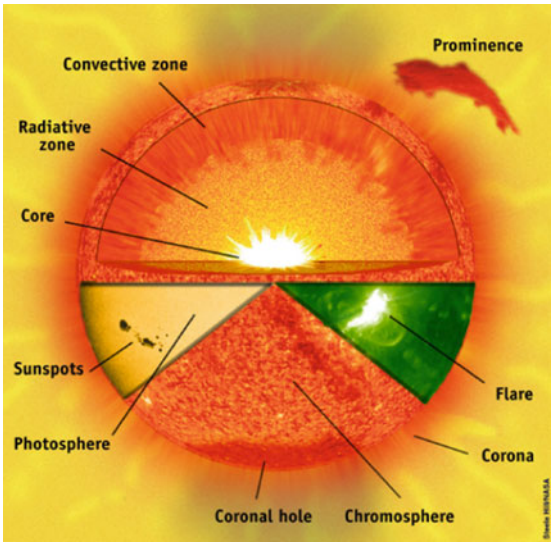

Figure 1.2: The structure of the Sun (courtesy of SOHO/synthetic artist view consortium. SOHO is a project of international cooperation between ESA and NASA).

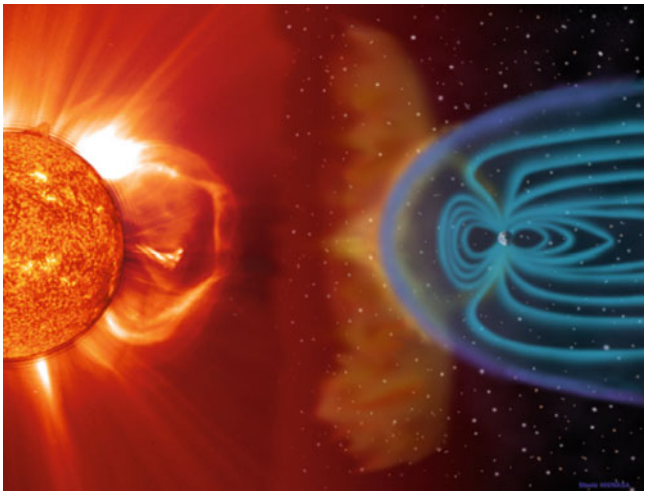

Figure 1.3: CME and its interaction with the Earth's magnetic field (courtesy of SOHO/synthetic artist view consortium. SOHO is a project of international cooperation between ESA and NASA).

due to emission at certain atomic lines (sensitive to a given narrow temperature range) as narrow arch-like structures, Fig. 1.5.

The plasma complexity and nonuniformity is typical for astrophysical sources. As a further example we can point to highly inhomogeneous images of supernova remnants (SNRs); see Fig. 1.6. In addition to the complex spatial structure, some SNRs also display high temporal variability due to activity of the compact central object—neutron star or black hole; see Fig. 1.7.

Before going to a more detailed analysis of the astrophysical plasma properties we introduce a few the most basic parameters characterizing the most general properties of the plasma. The first of them are the plasma temperature, T, which can be different for different plasma particles, e.g., electrons, T_e, and protons, T_p, and the plasma density, n (n_e and n_p). Because of very different masses, the electrons and protons with the same temperature have very different thermal velocities

$$v_{Ti} = \left(\frac{3k_B T_i}{m_i}\right)^{1/2}, \tag{1.2}$$

where i is the sort of the particle ($i = e$ for the electrons and $i = p$ for protons) with $v_{Te} = 6.74 \times 10^5 \sqrt{T_e[K]}$ [cm/s] and $v_{Tp} = 1.57 \times 10^4 \sqrt{T_p[K]}$ [cm/s].

Then, we introduce a so-called electron plasma frequency,

$$\omega_{\rm pe} = \left(\frac{4\pi e^2 n_e}{m_e}\right)^{1/2}, \tag{1.3}$$

Figure 1.4: The polar lights after a large solar flare (courtesy of Dr. V.F. Melnikov).

which is a resonant frequency of the electron component of the plasma; similarly, other plasma frequencies can be introduced for other plasma species.

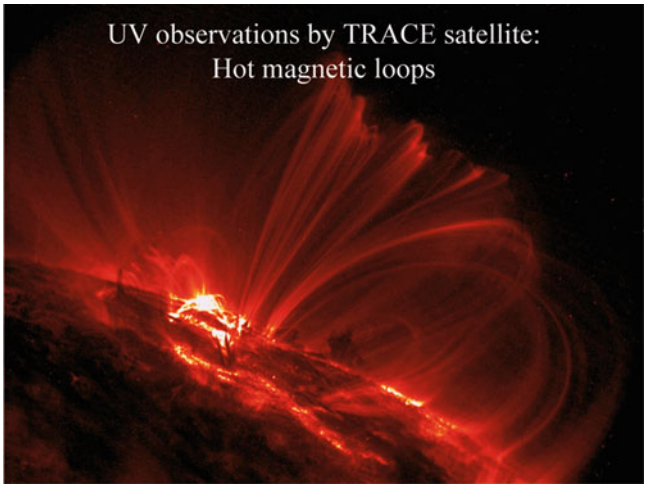

Figure 1.5: Coronal loops observed in UV range of the spectrum by the TRACE instrument (credit: TRACE team).

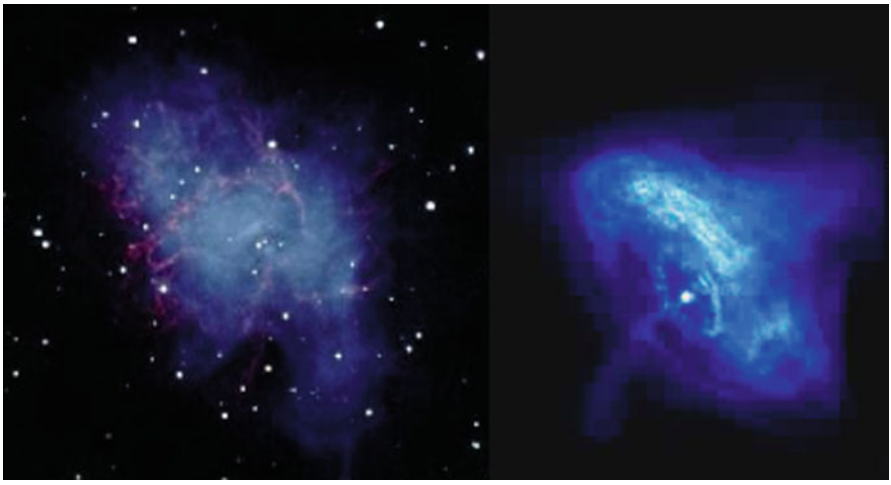

Figure 1.6: Images of crab nebula in optical (credit: STScI hubble space telescope) and X-ray (credit: Chandra team) ranges.

Having defined the plasma frequency and thermal velocity, one can introduce a parameter $v_{Te}/\omega_{\mathrm{pe}}$ with the dimension of scale; the corresponding parameter defined as $r_{\mathrm{De}} = \left(\frac{k_B T_e}{4\pi e^2 n_e}\right)^{1/2}$ is called the Debye radius, which plays a fundamental role in many plasma properties. In particular, the dimensionless **plasma parameter**, $\zeta_e = n_e r_{\mathrm{De}}^3$, shows how many electrons reside in a sphere with the Debye radius, which is a measure of the plasma ideality.

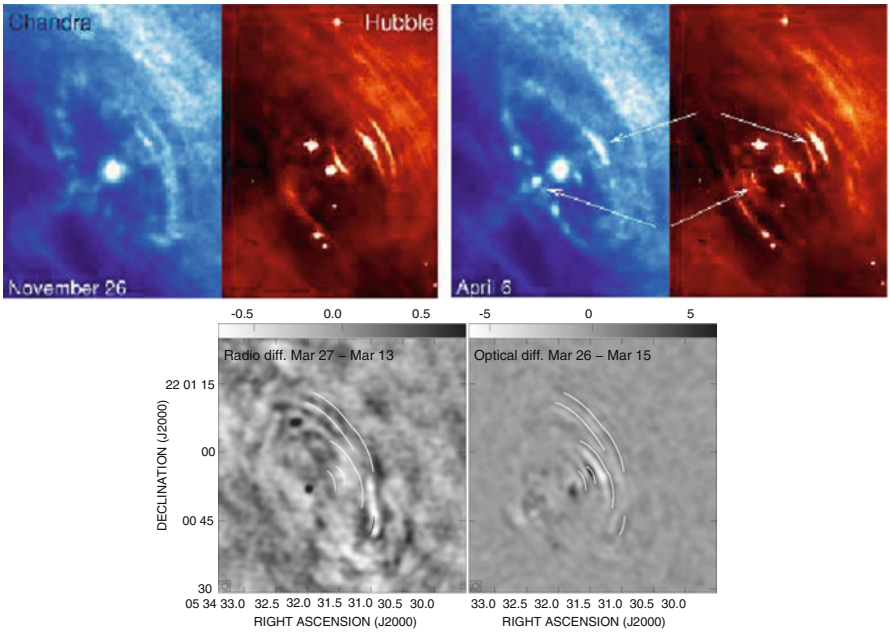

Figure 1.7: Quickly moving structures (wisps) in the crab nebula (credit: STScI hubble team. Bietenholz et al. (2004); reproduced by permission of the AAS).

Finally, we introduce some parameters related to the magnetic field, which is frequently present in the plasma volume. The cyclotron frequency (or gyrofrequency) is defined as

$$\omega_{\mathrm{Bi}} = \frac{e_i B}{m_i c}, \tag{1.4}$$

which depends on the particle mass m_i and charge e_i. Accordingly, this frequency is different for electrons $\omega_{\mathrm{Be}} = 1.76 \times 10^7 (B\ [G])$ [rad/s] and protons $\omega_{\mathrm{Bp}} = 9.58 \times 10^3 (B\ [G])$ [rad/s], although it does not depend on the particle velocity. The radius of particle rotation in the magnetic field, called the Larmor radius, does depend on the particle momentum as $r_L = cp_\perp/(e_i B)$. Now we remind some properties of the single-particle motion in external fields, and then proceed to description of the plasma properties within the MHD and kinetic theories.

1.2 Single-Particle Motion, Drifts, and Adiabatic Invariants

The force $\boldsymbol{\mathcal{F}}$ acting on a particle with a charge e (positive or negative), which is moving with a velocity $\boldsymbol{v}$ in an electromagnetic field $\boldsymbol{E}, \boldsymbol{B}$, is given by the

Lorentz formula

$$\boldsymbol{\mathcal{F}} = e\boldsymbol{E} + \frac{e}{c}\boldsymbol{v} \times \boldsymbol{B}. \tag{1.5}$$

The changes of the momentum

$$\boldsymbol{p} = m\gamma\boldsymbol{v}, \qquad \gamma = \frac{1}{\sqrt{1 - v^2/c^2}} \tag{1.6}$$

and the energy

$$\mathcal{E} = m\gamma c^2 = \sqrt{m^2c^4 + c^2p^2} \tag{1.7}$$

of the particle per unit time are given by

$$\frac{\mathrm{d}\boldsymbol{p}}{\mathrm{d}t} = e\boldsymbol{E} + \frac{e}{c}\boldsymbol{v} \times \boldsymbol{B}, \qquad \frac{\mathrm{d}\mathcal{E}}{\mathrm{d}t} = \boldsymbol{v} \cdot \boldsymbol{\mathcal{F}} = e\boldsymbol{v} \cdot \boldsymbol{E}. \tag{1.8}$$

Here c is the speed of light (in vacuum), and the particle energy includes the rest energy. The magnetic field produces no work on the particle, since the force associated with it is always perpendicular to the particle velocity.

1.2.1 Particle in Constant Uniform Magnetic and Electric Fields

Motion in Uniform Magnetic Field

We consider here a simple case $\boldsymbol{B} = \text{const}$, while $\boldsymbol{E} = 0$. The second of equations (1.8) shows that the particle energy and the absolute value of its momentum does not change given that the electric field $\boldsymbol{E}$ is absent: $\mathcal{E} = \mathcal{E}_0 = \text{const}$, $p = p_0 = \text{const}$. We introduce a new independent variable $\tau = t/\gamma = mc^2t/\mathcal{E}_0$ (the proper time of the moving particle) so that $\mathrm{d}\tau = \mathrm{d}t/\gamma$ and obtain the following equations for the transverse and parallel components of $\boldsymbol{p}$:

$$\frac{\mathrm{d}\boldsymbol{p}_\perp}{\mathrm{d}\tau} = \omega_B\boldsymbol{p}_\perp \times \boldsymbol{e}_\parallel, \qquad \frac{\mathrm{d}\boldsymbol{p}_\parallel}{\mathrm{d}\tau} = 0, \qquad \omega_B = \frac{eB}{mc}, \tag{1.9}$$

where $\boldsymbol{e}_\parallel = \boldsymbol{B}/B$ is the unit vector and ω_B is the cyclotron frequency. We find $p_\parallel = p_{\parallel 0} = \text{const}$ and search for solution of the first equation in the form

$$\boldsymbol{p}_\perp(\tau) = \boldsymbol{p}_{\perp 0}\cos\omega_B\tau + C\boldsymbol{p}_{\perp 0} \times \boldsymbol{e}_\parallel \sin\omega_B\tau \tag{1.10}$$

with initial condition $\boldsymbol{p}_\perp(0) = \boldsymbol{p}_{\perp 0}$ and indefinite constant C. Substitution of (1.10) in (1.9) yields $C = 1$. Particle trajectory is defined from the equation $\mathrm{d}\boldsymbol{r}/\mathrm{d}\tau = \boldsymbol{p}/m$ and has the form

$$\boldsymbol{r}(\tau) = \frac{\boldsymbol{p}_{\perp 0}}{m\omega_B}\sin\omega_B\tau + \frac{\boldsymbol{p}_{\perp 0} \times \boldsymbol{e}_\parallel}{m\omega_B}(1 - \cos\omega_B\tau) + \frac{\boldsymbol{p}_{\parallel 0}}{m}\tau + \boldsymbol{r}_0. \tag{1.11}$$

From expressions (1.9) to (1.11) it follows that the vector of particle momentum rotates around the direction of the magnetic field, remaining

constant in absolute value. Angular velocity is ω_B (if we use the proper time) and has smaller (energy-dependent) value

$$\Omega = \frac{\omega_B mc^2}{\mathcal{E}_0} = \frac{\omega_B}{\gamma}, \tag{1.12}$$

if the laboratory time is used. The particle moves along spiral trajectory with the step $H = 2\pi v_{\|0}/|\Omega|$ and radius

$$r_{g\perp} = \frac{cp_\perp}{|e|B}, \tag{1.13}$$

which is called Larmor radius or gyroradius.

Motion in Uniform Electric Field

We consider now motion of a charged particle with an initial momentum $\boldsymbol{p}_0$ belonging the xy-plane in an electric field $\boldsymbol{E}$ (or, more generally, in the presence of a force $\boldsymbol{\mathcal{F}} = e\boldsymbol{E}$) directed along y-axes, while no magnetic field is present. Equation of motion (1.8) receives the form for the momentum components:

$$\frac{\mathrm{d}p_x}{\mathrm{d}t} = 0, \qquad \frac{\mathrm{d}p_y}{\mathrm{d}t} = eE, \tag{1.14}$$

which can be explicitly integrated to yield

$$p_x = p_{0x}, \;\; p_y = eEt + p_{0y}, \;\; p^2 = p_0^2 + 2eEtp_{0y} + (eEt)^2 = p_{0x}^2 + (eE)^2(t-t_0)^2, \tag{1.15}$$

where $t_0 = -p_{0y}/(eE)$.

Now we apply relativistic relation $\mathcal{E}^2/c^2 = m^2c^2 + p^2$ to find the particle energy $\mathcal{E}$. One can see that a charged particle experiences an infinite acceleration (unlimited gain of energy) as it moves in a uniform constant electric field

$$\gamma^2 = \gamma_0^2 + (eE/mc)^2(t-t_0)^2, \tag{1.16}$$

where $\gamma = \mathcal{E}/mc^2$ is the particle Lorentz factor and γ_0 is the Lorentz factor at $t = t_0$.

Then to find the particle trajectory we note that from Eq. (1.6) the particle velocity is expressed via particle momentum and Lorentz factor, $\boldsymbol{v} \equiv \mathrm{d}\boldsymbol{r}/\mathrm{d}t = \boldsymbol{p}/(m\gamma)$, so equations of the trajectory components receive the form

$$\begin{aligned} \frac{\mathrm{d}x}{\mathrm{d}t} &= \frac{p_x}{m\gamma} = \frac{p_x}{m\sqrt{\gamma_0^2 + (eE/mc)^2(t-t_0)^2}}, \\ \frac{\mathrm{d}y}{\mathrm{d}t} &= \frac{p_y}{m\gamma} = \frac{eE(t-t_0)}{m\sqrt{\gamma_0^2 + (eE/mc)^2(t-t_0)^2}}, \end{aligned} \tag{1.17}$$

which are explicitly integrated to yield the trajectory in the parametric form

$$x = \frac{p_{0x}c}{eE}\operatorname{arcsinh}\frac{eE(t-t_0)}{mc\gamma} + x_0,$$
$$y = \frac{mc^2}{eE}\sqrt{\gamma_0^2 + (eE/mc)^2(t-t_0)^2} + y_0, \tag{1.18}$$

where $(x_0;\ y_0)$ represent the particle coordinates at $t = t_0$. Expressing the time from the first equation and substituting it into the second equation in (1.18) give rise to the following (catenary) equation of the particle trajectory:

$$y - y_0 = \frac{mc^2\gamma_0}{eE}\left[\cosh\left(\frac{eE(x-x_0)}{p_0c}\right) - 1\right]. \tag{1.19}$$

The nonrelativistic asymptote of this equation is, apparently, a parabolic trajectory:

$$y - y_0 = \frac{eE(x-x_0)^2}{2mv_0^2}. \tag{1.20}$$

For arbitrary constant non-electric force the obtained solutions apply after substitution $eE \to \mathcal{F}$.

Motion in Crossed Fields

We consider now the crossed uniform fields, $\boldsymbol{E} \neq 0$, $\boldsymbol{E} \perp \boldsymbol{B}$, and $E < B$. The last condition is fulfilled in most astrophysical objects owing to shielding of electric field by free plasma charges. Curiously, it is possible to describe the particle motion in the crossed fields by the above solution obtained for the motion in the uniform magnetic field. To do so we transit from the laboratory reference frame S to a moving one S', in which the electric field $\boldsymbol{E'} = 0$ and only magnetic field $\boldsymbol{B'} \neq 0$ remains. Such reference frame does exist because the field Lorentz invariants

$$B^2 - E^2 = \text{inv}, \qquad \boldsymbol{E}\cdot\boldsymbol{B} = \text{inv} \tag{1.21}$$

can be fulfilled as long as $E < B$. If $E > B$, a system S'' exists, in which $B' = 0$, $E' \neq 0$. The particle is accelerated unlimitedly, while when $E = B$, the system with $E = 0$ or $B = 0$ is absent.

Denote the velocity of S' relative to S as $\boldsymbol{v}_E$ and use the Lorentz transformations for electromagnetic field components:

$$E'_\parallel = E_\parallel, \quad \boldsymbol{E}'_\perp = \gamma_E(\boldsymbol{E}_\perp + \boldsymbol{v}_E \times \boldsymbol{B}/c), \quad \gamma_E = (1 - v_E^2/c^2)^{-1/2}; \tag{1.22}$$
$$B'_\parallel = B_\parallel, \quad \boldsymbol{B}'_\perp = \gamma_E(\boldsymbol{B}_\perp - \boldsymbol{v}_E \times \boldsymbol{E}/c). \tag{1.23}$$

Indices $\parallel$, $\perp$ denote here components relative to the velocity $\boldsymbol{v}_E$ (in contrast to previous usage of the subscripts).

We see from (1.22) that condition $\boldsymbol{E}' = 0$ can be satisfied, if $\boldsymbol{E} \cdot \boldsymbol{v}_E = 0$, while $\boldsymbol{B} \times \boldsymbol{v}_E \neq 0$. The component of $\boldsymbol{v}_E$ along $\boldsymbol{B}$ may be arbitrary. We choose the condition $\boldsymbol{B} \cdot \boldsymbol{v}_E = 0$ and then find from (1.22)

$$\boldsymbol{v}_E = \frac{c}{B^2} \boldsymbol{E} \times \boldsymbol{B}. \tag{1.24}$$

Lorentz transformation gives electromagnetic vectors in S' reference frame:

$$\boldsymbol{E}' = 0, \qquad \boldsymbol{B}' = \gamma_E \left(1 - \frac{E^2}{B^2}\right) \boldsymbol{B} = \sqrt{B^2 - E^2} \frac{\boldsymbol{B}}{B}. \tag{1.25}$$

We can now use the above solution, Eq. (1.10), in S' system:

$$\boldsymbol{p}'(\tau) = \boldsymbol{p}'_{\perp 0} \cos \omega'_c \tau + \boldsymbol{p}'_{\perp 0} \times \boldsymbol{e}_{\parallel} \sin \omega'_c \tau + \boldsymbol{p}'_{\parallel 0}, \ \mathcal{E}' = \mathcal{E}_0, \ \omega'_c = eB'/mc = e\sqrt{B^2 - E^2}/mc. \tag{1.26}$$

Here the indices $\parallel$, $\perp$ are again used relative to the common direction of $\boldsymbol{B}$ and $\boldsymbol{B}'$. The values τ and ω'_c are relativistic invariants. The solution in the laboratory system S may be obtained by Lorentz transformation (we use here transformation formulae in terms of 3D vectors) of momentum $\boldsymbol{p}'$ and energy $\mathcal{E}$ from S' back to S:

$$\mathcal{E} = \gamma_E(\mathcal{E}' + \boldsymbol{p}' \cdot \boldsymbol{v}_E), \qquad \boldsymbol{p} = \boldsymbol{p}' + \frac{\gamma_E \mathcal{E}'}{c^2} \boldsymbol{v}_E + \frac{(\gamma_E - 1)\boldsymbol{p}' \cdot \boldsymbol{v}_E}{v_E^2} \boldsymbol{v}_E. \tag{1.27}$$

We note that the dependence of the particle energy and momentum on the proper time is rather complicated even for a particle moving in the homogeneous fields. If fields are inhomogeneous and/or nonsteady, then the problem has typically no exact solution and so approximate methods are needed.

1.2.2 Averaging over the Fast Motions: Drifts

Generally, the picture of charged particle motion in inhomogeneous and varying in time electromagnetic fields is extremely complicated because of nonlinearity of the equations of motion. However, this picture can be significantly simplified if the magnetic field is strong and varies slowly in space and time, while the electric field is weak. In this case the effects of the electric field, the spatial inhomogeneity, and temporal variability of the magnetic field can be taken into account with the perturbation theory. Indeed, motion of the particle can be described as a superposition of fast and slow components. The first one is fast rotation of the particle around direction of local magnetic field lines with the cyclotron frequency $ceB/\mathcal{E}$, while the second one contains a slow displacement of the quasi-circular particle orbit. The center

around which the particle gyrates (the guiding center) travels along the magnetic field line and is also slowly drifting across it under the influence of the electric field and inhomogeneity of the magnetic field. The transverse and longitudinal momenta of the particle change their absolute magnitude slowly.

The approximation corresponding to this picture of the particle motion is called the guiding center or drift approximation, and the motion of the guiding center transverse to the magnetic field lines is called **drift**. Equation of motion in the drift approximation can be derived by averaging the exact equations of motion over the fast rotation of particles around the magnetic field line.

We start from averaging of exact solution (1.27) over the period $T = 2\pi/\omega_c'$ of the proper time. From (1.26) we find

$$\overline{\boldsymbol{p}}'_\perp = \frac{1}{T}\int_{\tau_0}^{\tau_0+T} \boldsymbol{p}'_\perp(\tau)\mathrm{d}\tau = 0, \qquad \overline{p}'_\parallel = p'_{\parallel 0}$$

and obtain from (1.27) and (1.24) averaged values of the particle energy and momentum in the laboratory system:

$$\overline{\mathcal{E}} = \gamma_E \mathcal{E}', \qquad \overline{p}_\parallel = p'_{\parallel 0} = p_{\parallel 0}, \qquad \overline{p}_\perp = \frac{\gamma_E \mathcal{E}'}{c^2}\boldsymbol{v}_E. \tag{1.28}$$

We then can express the smoothed velocity $\boldsymbol{v}_c$ of particle guiding center in terms of the averaged values:

$$\boldsymbol{v}_c = \frac{c^2\overline{\boldsymbol{p}}_\perp}{\overline{\mathcal{E}}} + \frac{c^2\overline{\boldsymbol{p}}_\parallel}{\overline{\mathcal{E}}} = \boldsymbol{v}_E + \boldsymbol{v}_\parallel. \tag{1.29}$$

It consists of the velocity $\boldsymbol{v}_\parallel$ along the magnetic field and **electric drift** velocity $\boldsymbol{v}_E$ (1.24) across the magnetic and electric fields. Electric drift velocity (1.24) does not depend on the charge, mass, and energy of the particle. Nevertheless, expression (1.29) cannot be applied to neutral particles since they do not participate in Larmor rotation so the averaging over rotation has no sense for such particles. In cosmic media $E \ll B$ typically, so the electric drift velocity is nonrelativistic, $v_E \ll c$, $\gamma_E \approx 1$; the guiding center velocity along magnetic field $v_{\parallel c} \approx v_{\parallel 0}$ coincides with the particle velocity.

The drift across the magnetic field can be caused by force $\boldsymbol{\mathcal{F}}$ of any nature acting to the particle. We introduce an effective electric field, equivalent to a given force $\boldsymbol{E}_{\mathrm{eff}} = \boldsymbol{\mathcal{F}}/e$, which will enable us to extend the solutions obtained for the electric field to other, non-electric, forces. Specifically, using expression (1.24), we find the drift velocity corresponding to the given force $\boldsymbol{\mathcal{F}}$:

$$\boldsymbol{v}_d = \frac{c}{eB^2}\boldsymbol{\mathcal{F}} \times \boldsymbol{B}. \tag{1.30}$$

If $\boldsymbol{\mathcal{F}} = m\boldsymbol{g}$ is the gravitation force, we obtain the **gravitation drift** velocity

$$\boldsymbol{v}_g = \frac{mc}{eB^2}\boldsymbol{g} \times \boldsymbol{B}. \tag{1.31}$$

Here $\boldsymbol{g}$ is the acceleration due to gravity. Gravitation drift depends on the particle charge and mass unlike the electric drift.

Let us consider a few more examples of the particle drift. Adopt that electric and gravitation fields are absent, the absolute value of magnetic field $B = \text{const}$, but its force lines are slightly curved, $\boldsymbol{e}_\parallel \neq \text{const}$. The curvature radius R of the force lines is large in comparison with the particle Larmor radius r_g, $R \gg r_g$. In zeroth approximation the particle moves along a curved force line with velocity $v_\parallel$ and so experiences action of the centripetal force

$$\boldsymbol{\mathcal{F}}_c = -\frac{\mathcal{E} v_\parallel^2}{c^2 R}\boldsymbol{n}, \tag{1.32}$$

needed to link the particle to the curved field line, where $\boldsymbol{n}$ is the orth of main normal. We use equation $\boldsymbol{n}/R = (\boldsymbol{e}_\parallel \cdot \nabla)\boldsymbol{e}_\parallel$ known from differential geometry, where $\boldsymbol{e}_\parallel$ is the tangent orth. From expression (1.30) and the above equation we find the **centrifugal drift** velocity

$$v_{\mathrm{dc}} = v_\parallel r_{g\parallel} \boldsymbol{e}_\parallel \times (\boldsymbol{e}_\parallel \cdot \nabla)\boldsymbol{e}_\parallel. \tag{1.33}$$

It is the first-order effect relative to the small parameter r_g/R:

$$v_{\mathrm{dc}} \approx v_\parallel r_{g\parallel}/R \ll v_\parallel. \tag{1.34}$$

A similar effect is the transverse (gradient) drift, related to a change of the magnetic field absolute value. Let us adopt $\boldsymbol{B} = B\boldsymbol{e}_\parallel$, $\boldsymbol{e}_\parallel = \text{const}$, while B depends weakly on transverse coordinates only. The particle energy is conserved; the motion transverse to the magnetic field is described by equation

$$\dot{\boldsymbol{v}}_\perp = \boldsymbol{\Omega} \times \boldsymbol{v}_\perp, \qquad \boldsymbol{\Omega} = -\frac{ec}{\mathcal{E}}\boldsymbol{B}. \tag{1.35}$$

Here $\boldsymbol{B}$ is the magnetic field at the point, in which the particle is instantly located. We represent radius-vector of this point as a sum $\boldsymbol{r}_c + \boldsymbol{r}$ of guiding center radius-vector $\boldsymbol{r}_c$ and running particle radius-vector $\boldsymbol{r}$ relative to the guiding center.

With the accuracy of the first order we have $B(\boldsymbol{r}_c + \boldsymbol{r}) \approx B(\boldsymbol{r}_c) + (\boldsymbol{r}_\perp \cdot \nabla) B(\boldsymbol{r}_c)$, which we substitute into Eq. (1.35) to obtain the following approximate equation of motion

$$\dot{\boldsymbol{v}}_\perp = \boldsymbol{\Omega} \times \boldsymbol{v}_\perp \left(1 + \frac{(\boldsymbol{r}_\perp \cdot \nabla)B}{B}\right). \tag{1.36}$$

Magnetic field B is everywhere taken at the guiding center point. The smallness parameter is the ratio of the gyroradius to inhomogeneity scale L of the magnetic field, $r_g/L \ll 1$.

We then represent the particle velocity as the sum $\boldsymbol{v}_\perp = \boldsymbol{v}_{\perp 0} + \boldsymbol{v}'_\perp$, where $\boldsymbol{v}_{\perp 0} = \dot{\boldsymbol{r}}_{\perp 0}$ is the velocity in homogeneous field $\boldsymbol{B}(\boldsymbol{r}_c)$ and $\boldsymbol{v}'_\perp$ is the small

correction, caused by field inhomogeneity. In the second parenthetical term in (1.36) we substitute nonperturbed values $\boldsymbol{v}_{\perp 0}$ and $\boldsymbol{r}_{\perp 0}$ for $\boldsymbol{v}_\perp$ and $\boldsymbol{r}_\perp$, use expression $\dot{\boldsymbol{v}}_{\perp 0} = \boldsymbol{\Omega} \times \boldsymbol{v}_{\perp 0}$, and find

$$\dot{\boldsymbol{v}}'_\perp = \boldsymbol{\Omega} \times [\boldsymbol{v}'_\perp + \boldsymbol{v}_{\perp 0}(\boldsymbol{r}_{\perp 0} \cdot \nabla B)/B].$$

After averaging over the cyclotron period we have $\overline{\dot{\boldsymbol{v}}}'_\perp = \frac{1}{T}[\boldsymbol{v}'_\perp(t+T) - \boldsymbol{v}'_\perp(t)] \approx 0$ to the first-order accuracy and, thus, obtain the transverse drift velocity

$$\boldsymbol{v}_{\mathrm{dt}} = \overline{\boldsymbol{v}_{\perp 0}} + \overline{\boldsymbol{v}'_\perp} = -\overline{(\boldsymbol{v}_{\perp 0}(\boldsymbol{r}_{\perp 0} \cdot \nabla B))}/B. \tag{1.37}$$

Here $\boldsymbol{r}_{\perp 0} = r_{g\perp}(\boldsymbol{e}_1 \sin \Omega t + \boldsymbol{e}_2 \cos \Omega t)$ is the particle radius-vector in the homogeneous magnetic field, $r_{g0} = cp_\perp/eB$. After the averaging over time we find the **gradient drift** velocity

$$\boldsymbol{v}_{\mathrm{dt}} = \frac{v_\perp r_{g\perp}}{2B} \boldsymbol{e}_\parallel \times \nabla B, \tag{1.38}$$

which depends on the particle charge and energy.

The full velocity of the particle guiding center (1.29) to the first order of accuracy is determined simply by adding up the obtained values of (1.24), (1.31), (1.33), and (1.38):

$$\boldsymbol{v}_c = \dot{\boldsymbol{r}}_c = v_\parallel \boldsymbol{e}_\parallel + \frac{c}{B^2}\boldsymbol{E} \times \boldsymbol{B} + \frac{mc}{eB^2}\boldsymbol{g} \times \boldsymbol{B} + v_\parallel r_{g\parallel} \boldsymbol{e}_\parallel \times (\boldsymbol{e}_\parallel \cdot \nabla)\boldsymbol{e}_\parallel + \frac{v_\perp r_{g\perp}}{2B}\boldsymbol{e}_\parallel \times \nabla B. \tag{1.39}$$

1.2.3 Adiabatic Invariants. The Particle Energy Change in Drift Approximation

The adiabatic invariants are the approximate integrals of particle motion. They exist, if the electromagnetic field changes smoothly in space and slowly in time during particle cyclotron rotation period T (Landau and Lifshitz 1969; Sagdeev et al. 1988), which, for $E \ll B$, requires the following inequalities $\omega T \ll 1$ and $r_g \ll R$ to be fulfilled, where ω is the frequency of the magnetic field $\boldsymbol{B}$ variation in time and R is the scale of the magnetic field change in space.

Adiabatic invariant I is defined as

$$I = \frac{1}{2\pi} \oint p \mathrm{d}q, \tag{1.40}$$

where p, q are canonic variables (Landau and Lifshitz 1969). The integration is over the quasiperiod of Larmor rotation (in weakly inhomogeneous and variable field the particle motion is not strictly periodic, but almost periodic). Adiabatic invariant (1.40), calculated with exact p, q, experiences small oscillations. But the averaging over the oscillation period leads to a

constant value, which conserves with high, often exponential, accuracy during many periods. For actual calculation of integral (1.40) we have to use zeroth approximation, assuming the field is constant, and then, after finding explicit dependence $I(B)$, insert actual field having weak coordinate and time dependence.

Let us assume the magnetic field $\boldsymbol{B}(\boldsymbol{r},t)$ to change weakly in time and space and the electric field to be small, $E \ll B$, and calculate the adiabatic invariant in S' system of the particle guiding center. The canonical variables p' and q' are taken in zeroth approximation. For the canonic coordinate q we consider the azimuthal angle, $q' = \alpha'$, which determines the particle position at the Larmor orbit. The particle velocity has only azimuthal component $\boldsymbol{v}' = v'\boldsymbol{e}'_\alpha$, $v'_\alpha = r'_{g\perp}\dot{\alpha}'$. The generalized momentum can be determined by means of the Lagrange function, $p'_\alpha = \partial L/\partial\dot{\alpha}'$, where

$$L = -mc^2\sqrt{1-\frac{v'^2}{c^2}} + \frac{e}{c}\boldsymbol{v}'\cdot\boldsymbol{A}' - e\varphi' = -mc^2\sqrt{1-\frac{r'^2_{g\perp}\dot{\alpha}'^2}{c^2}} + \frac{e}{c}A'_\alpha r'_{g\perp}\dot{\alpha}' - e\varphi'. \tag{1.41}$$

The differentiation gives

$$p'_\alpha = \mathcal{E}' r'^2_{g\perp}\dot{\alpha}' + (e/c)A'_\alpha r'_{g\perp}, \qquad \dot{\alpha}' = \frac{ceB'}{\mathcal{E}'}. \tag{1.42}$$

Integral (1.40) contains, therefore, two terms:

$$\int_0^{2\pi} \mathcal{E}' r'^2_{g\perp}\dot{\alpha}'\mathrm{d}\alpha' = \frac{2\pi e}{c} r'^2_{g\perp}B' \tag{1.43}$$

and

$$\int_0^{2\pi} A'_\alpha r'_{g\perp}\mathrm{d}\alpha' = \oint \boldsymbol{A}'\cdot\mathrm{d}\boldsymbol{l}' = \int(\nabla\times\boldsymbol{A})\cdot\boldsymbol{n}\mathrm{d}S = \pi r'^2_{g\perp}B', \tag{1.44}$$

where the Stokes theorem has been used.

From Eqs. (1.40), (1.43), and (1.44) we find the adiabatic invariant in the guiding center system:

$$I' = \frac{3e}{2c} r'^2_{g\perp}B' = \frac{3ep'^2_\perp}{2cB'}. \tag{1.45}$$

The observer system S moves along the field $\boldsymbol{B}'$ with velocity $v_\parallel$ (recall that in this calculation the field is constant so no drift is present), and we have $B = B'$, $p_\perp = p'_\perp$. Thus, we find the adiabatic invariant in the observer system:

$$I = \frac{p_\perp^2}{B} = \text{inv}. \tag{1.46}$$

It is possible to find more particle adiabatic invariants in electromagnetic field; see problems to this chapter.

If the field is homogeneous, but slowly changing in time, we have $p_\parallel =$ const and from (1.46) $p_\perp(t) = p_\perp(0)\sqrt{B(t)/B(0)}$, particle energy changes in time according to the $B(t)$ change $\mathcal{E}^2(t) = c^2 p_\perp^2(t) + c^2 p_\parallel^2 + m^2c^4$. The fact that the particle energy changes during its motion in the magnetic field seems to be in apparent contradiction with a statement made earlier that the magnetic field produces no work on charged particles. The solution of this "paradox" is that the evolving magnetic field induces an electric field, which, in its turn, produces the work on the particle, so the particle energy changes as described.

If the field does not depend on time, but is nonuniform in space, we have $\mathcal{E} =$ const in agreement with the fact that constant magnetic field produces no work. The angle ϑ between field direction and particle momentum (pitch angle) changes during the particle motion: $\sin\vartheta = \sqrt{B(r)/B(0)}\sin\vartheta_0$; this effect leads to mirroring of the particle from regions with strong magnetic field.

Finally we calculate increase of particle energy in the drift approximation. The full particle velocity is the sum of guiding center velocity (1.39) and the rotation velocity $\dot{\boldsymbol{r}}_\perp$ around the guiding center. The instantaneous rate of particle energy change $\dot{\tilde{\mathcal{E}}}$ is described by the following equation:

$$\dot{\tilde{\mathcal{E}}} = e\boldsymbol{E}\cdot(\boldsymbol{v}_c + \dot{\boldsymbol{r}}_\perp). \tag{1.47}$$

This equation should be averaged over the cyclotron period $T = 2\pi\mathcal{E}/ecB$: $\dot{\mathcal{E}} = T^{-1}\oint \dot{\tilde{\mathcal{E}}}\mathrm{d}t$. The first term, $e\boldsymbol{E}\cdot\boldsymbol{v}_c$, contains only smooth values and is not affected by the averaging. The second term gives

$$T^{-1}\oint e\boldsymbol{E}\cdot\dot{\boldsymbol{r}}_\perp \mathrm{d}t = eT^{-1}\oint e\boldsymbol{E}\cdot\mathrm{d}\boldsymbol{r}_\perp = -(e/2)v_\perp r_{g\perp}\boldsymbol{e}_\perp\cdot(\nabla\times\boldsymbol{E}). \tag{1.48}$$

The final result is

$$\dot{\mathcal{E}} = e\boldsymbol{E}\cdot\boldsymbol{v}_c - \frac{1}{2}ev_\perp r_{g\perp}\boldsymbol{e}_\perp\cdot(\nabla\times\boldsymbol{E}). \tag{1.49}$$

The particle energy change includes effects of the first and second orders relative to small parameters E/B and r_g/L. All values in right-hand side of the latter equation are taken in guiding center point. Equations (1.39), (1.46), and (1.49) form a complete set for describing particle motion in the drift approximation. For more details about the drift theory we refer to the article by Sivukhin (1965) and to the book by Somov (2006).

1.3 Kinetic Theory and MHD Approximation

We have considered motions of single particles in external fields, but the real plasmas contain huge numbers of interacting charged and neutral particles;

thus, our treatment has to be accordingly generalized to account these huge numbers. A straightforward way of doing so is just to solve that big number of equations of each particle motion complemented by Maxwell equations for the accompanying fields.

Until recently such approach seemed to be entirely impractical, because there was no way to solve this system of equations analytically either exactly or approximately. Nowadays, however, rapid development of fast powerful computers has started to allow approaching such solution through so-called particle-in-cell (PIC) simulations, which compute solutions of a large number (of the order of a million) of the microscopic equations of motion.

Although the PIC simulations have already provided a number of interesting and important results about microscopic behavior of the charge particle ensembles, the parameter space, which can be consistently included in the PIC simulations, is highly restricted (small volumes, short time scales, and limited number of particles). Therefore, to apply the PIC results to real astrophysical plasmas requires scaling of the simulation parameters by many orders of magnitude—a highly nontrivial task, which can easily overlook important physical effects. Below we concentrate on "classical" statistical treatment of the plasma.

1.3.1 Microscopic Description of Plasma

A consistent description of charged particles in classical kinetic theory may be achieved by using a *microscopic* distribution function of particles—the phase density of the particles. The state of a system of charged particles is completely described by their generalized coordinates and momenta $(\boldsymbol{r},\ \boldsymbol{p})$ and by the electromagnetic field in the considered volume. We introduce the phase density for each kind a of the involved particles as

$$F_a(\boldsymbol{r},\ \boldsymbol{p},\ t) = \sum_{i=1}^{N_a} \delta[\boldsymbol{r} - \boldsymbol{r}_i(t)]\delta[\boldsymbol{p} - \boldsymbol{p}_i(t)], \tag{1.50}$$

where N_a is the total number of these particles and $\boldsymbol{r}_i(t)$ and $\boldsymbol{p}_i(t)$ are the coordinates and momenta of the ith particle. The microscopic distribution function determined in this way satisfies the continuity equation in the six-dimensional phase space defined by the particle coordinates and momenta:

$$\frac{\partial F_a}{\partial t} + \boldsymbol{v} \cdot \frac{\partial F_a}{\partial \boldsymbol{r}} + \boldsymbol{\mathcal{F}}_a \cdot \frac{\partial F_a}{\partial \boldsymbol{p}} = 0, \tag{1.51}$$

where $\boldsymbol{\mathcal{F}} = \dot{\boldsymbol{p}}$ is the force acting on the particle. The force consists of both electromagnetic Lorentz force and any non-electromagnetic forces $(\boldsymbol{f})$ such as gravity and short-acting forces between neutral atoms:

$$\dot{\boldsymbol{p}} = e_a \boldsymbol{E}(\boldsymbol{r}, t) + \frac{e_a}{c} \boldsymbol{v} \times \boldsymbol{B}(\boldsymbol{r}, t) + \boldsymbol{f}. \tag{1.52}$$

We assume for now that the type of the particle a, with electric charge e_a, does not change during interaction. Inelastic processes of ionization, atomic and ionic excitation, and so on require quantum theoretical calculations and may be included later in the scheme developed below. Electromagnetic field in Eq. (1.52) is described by the Maxwell equations:

$$\nabla \times \boldsymbol{E} = -\frac{1}{c}\frac{\partial \boldsymbol{B}}{\partial t}, \tag{1.53a}$$

$$\nabla \times \boldsymbol{B} = \frac{4\pi}{c}(\boldsymbol{j} + \boldsymbol{j}^{\text{ext}}) + \frac{1}{c}\frac{\partial \boldsymbol{E}}{\partial t}, \tag{1.53b}$$

$$\nabla \cdot \boldsymbol{E} = 4\pi(\rho + \rho^{\text{ext}}), \tag{1.53c}$$

$$\nabla \cdot \boldsymbol{B} = 0. \tag{1.53d}$$

The sources of the self-consistent microscopic electromagnetic field in Eq. (1.53), the charge and current densities, are defined by the phase density as follows:

$$\rho(\boldsymbol{r}, t) = \sum_a e_a \int F_a(\boldsymbol{r}, \boldsymbol{p}, t)\mathrm{d}^3 p, \tag{1.54a}$$

$$\boldsymbol{j}(\boldsymbol{r}, t) = \sum_a e_a \int \boldsymbol{v} F_a(\boldsymbol{r}, \boldsymbol{p}, t)\mathrm{d}^3 p. \tag{1.54b}$$

The charge density $\rho^{\text{ext}}(\boldsymbol{r}, t)$ and current density $\boldsymbol{j}^{\text{ext}}(\boldsymbol{r}, t)$ that are external to the system under consideration must be defined separately, along with the non-self-consistent part of the force $\boldsymbol{f}$.

Hence, provided that the external forces and external sources are known, the evolution of particle systems can be fully described by the system of equations for the microscopic distribution function and the electromagnetic field strengths. This description of charged particles is equivalent to the exact solution of the dynamical problem, and so it depends on huge body of data on the initial coordinates and momenta of all N_a particles, as well as on the initial field state. For problems in cosmic electrodynamics, as well as for macroscopic problems in general, the data on the initial conditions is, as a rule, unavailable, and a statistical representation is frequently used in place of the excessive dynamic treatment.

1.3.2 Statistical Representation of Plasmas

For a proper statistical treatment one has to average phase density (1.50) and the electromagnetic fields over an ensemble of macroscopically equivalent systems having different initial conditions. However, this function is inconvenient for full statistical description of the particle system. Straightforward averaging of function (1.50) over the statistical ensemble yields statistical

one-particle distribution function (1.58) derived below. The one-particle distribution function allows calculating macroscopic charge and current densities (1.54), but it is insufficient to calculate, e.g., the mean energy of particle pair interaction in physical system. Such values must be calculated from two-particle statistical distribution function (1.59), which, of course, can also be obtained from microscopic phase density (1.50) but less straightforwardly than the one-particle statistical distribution function. Below we introduce a microscopically equivalent but more convenient N-particle distribution function $F^{(N)}$:

$$F^{(N)}(\boldsymbol{r}_1, \boldsymbol{p}_1; \ldots \boldsymbol{r}_N, \boldsymbol{p}_N; t) = \frac{1}{N_1! \ldots N_a! \ldots} \sum_P \delta[\boldsymbol{r}_1 - \boldsymbol{r}_1(t)]\delta[\boldsymbol{p}_1 - \boldsymbol{p}_1(t)] \ldots \delta[\boldsymbol{r}_N - \boldsymbol{r}_N(t)]\delta[\boldsymbol{p}_N - \boldsymbol{p}_N(t)]. \tag{1.55}$$

Here the summation includes all transpositions of identical particles, and the number of vectors $(\boldsymbol{r}, \boldsymbol{p})$ is equal to the total number of particles $N = \sum_a N_a$ in the system where a denotes sort of the plasma particles. Averaging of this N-particle distribution function over the ensemble of initial conditions, which we denote by the angle brackets, results in N-particle *statistical* distribution function

$$D(\boldsymbol{r}_1, \boldsymbol{p}_1; \ldots \boldsymbol{r}_N, \boldsymbol{p}_N; t) = \langle F^{(N)}(\boldsymbol{r}_1, \boldsymbol{p}_1; \ldots \boldsymbol{r}_N, \boldsymbol{p}_N; t) \rangle, \tag{1.56}$$

giving rise to a most complete statistical treatment of the problem.

The statistical distribution function D is a microscopic one, and it provides the most detailed information in a probabilistic sense. The probability of each particle to reside in their own element $\mathrm{d}^3 r \mathrm{d}^3 p$ of the phase space at a time t is given by

$$\mathrm{d}W = D(\boldsymbol{r}_1, \boldsymbol{p}_1; \ldots \boldsymbol{r}_N, \boldsymbol{p}_N; t) \mathrm{d}^3 r_1 \mathrm{d}^3 p_1 \ldots \mathrm{d}^3 r_N \mathrm{d}^3 p_N. \tag{1.57}$$

The statistical distribution function D satisfies the continuity equation in the $6N$-dimensional phase space of the entire system, and it takes into account all possible correlations among particles and fields. For many problems, however, it is sufficient to use a simpler and less detailed representation of the system, which is achieved by introducing the one-particle distribution function

$$f_a^{(1)}(\boldsymbol{r}_1, \boldsymbol{p}_1, t) = N_a \int D(\boldsymbol{r}_1, \boldsymbol{p}_1; \ldots \boldsymbol{r}_N, \boldsymbol{p}_N; t) \mathrm{d}^3 r_2 \mathrm{d}^3 p_2 \ldots \mathrm{d}^3 r_N \mathrm{d}^3 p_N = \langle F_a(\boldsymbol{r}_1, \boldsymbol{p}_1, t) \rangle, \tag{1.58}$$

the two-particle distribution function

$$\begin{aligned} f_a^{(2)}(\boldsymbol{r}_1, \boldsymbol{p}_1; \boldsymbol{r}_2, \boldsymbol{p}_2; t) &= N_a(N_a - 1) \int D(\boldsymbol{r}_1, \boldsymbol{p}_1; \ldots \boldsymbol{r}_N, \boldsymbol{p}_N; t) \mathrm{d}^3 r_3 \mathrm{d}^3 p_3 \ldots \mathrm{d}^3 r_N \mathrm{d}^3 p_N \\ &= \langle F_a(\boldsymbol{r}_1, \boldsymbol{p}_1, t) F_a(\boldsymbol{r}_2, \boldsymbol{p}_2, t) \rangle, \end{aligned} \tag{1.59}$$

and all higher-order many-particle distribution functions. But in this case the correlation of separate particles is partially or entirely neglected.

The one-particle and two-particle functions $f_a^{(1)}$ and $f_a^{(2)}$ are the most frequently used. In particular, one-particle distribution function provides information on practically all of the macroscopic parameters of the system. A self-consistent recipe for obtaining the chain of coupled equations for the many-particle distribution functions derived from the continuity equation for the function $D(\boldsymbol{r}_1, \boldsymbol{p}_1; \ldots; t)$ was proposed by Bogoliubov (1946). Derivation of the kinetic equation for the one-particle distribution function is frequently based on truncating the chain of coupled equations for the many-particle functions, that is, on system closure. This closure depends essentially on the type of interaction between particles, on the degree of deviation of the system from equilibrium, on the particle density, etc.

In plasmas that are only weakly out of equilibrium, characterized by the temperature T and the density of charged particles n, the correlation effects are small provided that the interaction energy of the particles is small compared with the kinetic energy

$$e^2 n^{1/3}/T \approx (n r_{\mathrm{D}}^3)^{-2/3} \ll 1, \tag{1.60}$$

where $r_{\mathrm{D}} = (T/4\pi n e^2)^{1/2}$ is the *Debye radius*. Plasmas of this kind can be described by the self-consistent field approximation. Including the lowest-order correlation effects, we get the kinetic equation

$$\frac{\partial f_a^{(1)}}{\partial t} + \boldsymbol{v} \cdot \frac{\partial f_a^{(1)}}{\partial \boldsymbol{r}} + \boldsymbol{\mathcal{F}}_a \cdot \frac{\partial f_a^{(1)}}{\partial \boldsymbol{p}} = \sum_b St(f_a^{(1)}, f_b^{(1)}). \tag{1.61}$$

The collision operator St is discussed below. The force $\boldsymbol{\mathcal{F}}_a$ given by Eq. (1.52) is determined for this equation by the mean self-consistent fields, which satisfy Maxwell equations (1.53). These equations become macroscopic and describe the mean self-consistent field if the microscopic phase density is replaced by the one-particle statistical distribution function $f_a^{(1)}$ for the field sources in Eq. (1.54):

$$\rho(\boldsymbol{r}, t) = \sum_a e_a \int f_a^{(1)}(\boldsymbol{r}, \boldsymbol{p}, t) \mathrm{d}^3 p, \tag{1.62a}$$

$$\boldsymbol{j}(\boldsymbol{r}, t) = \sum_a e_a \int \boldsymbol{v} f_a^{(1)}(\boldsymbol{r}, \boldsymbol{p}, t) \mathrm{d}^3 p. \tag{1.62b}$$

The collision operator at the right-hand side of Eq. (1.61) changes the distribution functions for interactions occurring inside the Debye sphere. The collision integrals are most often used in the form given by Landau or by Balescu–Lenard (Silin 1971; Klimontovich 1972; Akhiezer et al. 1975). We will not consider the explicit structure of this operator here. A detailed discussion of its properties and the corresponding transfer coefficients in a plasma can be found in Somov (2006).

1.3.3 Magnetohydrodynamic Description of Collisional Plasmas

Electromagnetic processes in a plasma are called *collisional*, if their characteristic frequencies ω are small compared with collisional frequencies ν_{ab} of the plasma particles. By analogy with this condition, the spatial scales λ of processes under consideration must be large compared with the mean free paths Λ_{ab} of the plasma particles:

$$\omega \ll \nu_{ab}, \qquad \lambda \gg \Lambda_{ab}. \tag{1.63}$$

Processes with the opposite inequalities are called *collisionless*. Most often, one simply refers to a collisional and collisionless plasma.

In collisional plasmas, such as the interior regions and atmosphere of stars and Sun, the solar chromosphere, and the ionosphere of the Earth, the macroscopic parameters vary slowly both during the intervals between Coulomb collisions and over distances exceeding the mean free path of the particles, so that the solution of the kinetic equation (1.61) is close to a local Maxwellian distribution

$$f_a^{(1)}(\boldsymbol{r},\boldsymbol{p},t) = n_a(\boldsymbol{r},t)[2\pi m_a T_a(\boldsymbol{r},t)]^{-3/2} \exp\left\{-\frac{[\boldsymbol{p}-m_a\boldsymbol{u}^{(a)}(\boldsymbol{r},t)]^2}{2m_a T_a(\boldsymbol{r},t)}\right\} + \delta f_a^{(1)}. \tag{1.64}$$

Here the macroscopic parameters n_a, T_a, and $\boldsymbol{u}^{(a)}$ (particle number density, temperature in energy units, and macroscopic velocity of the a-component of the plasma) vary in space and time. The deviation $\delta f_a^{(1)}$ is small compared with the Maxwell term in Eq. (1.64) and is expressed using the gradients of macroscopic parameters: its calculation with the use of Eq. (1.61) enables one to determine the kinetic transfer coefficients for a collisional plasma (Braginskii 1965).

The macroscopic (equilibrium) plasma parameters are connected with the distribution function $f_a^{(1)}$ by the following expressions:

$$n_a(\boldsymbol{r},t) = \int f_a^{(1)}(\boldsymbol{r},\boldsymbol{p},t)\mathrm{d}^3p, \tag{1.65a}$$

$$\boldsymbol{u}^{(a)}(\boldsymbol{r},t) = \frac{1}{n_a}\int \boldsymbol{v} f_a^{(1)}(\boldsymbol{r},\boldsymbol{p},t)\mathrm{d}^3p, \tag{1.65b}$$

$$T_a(\boldsymbol{r},t) = \frac{m_a}{3n_a}\int (\boldsymbol{v}-\boldsymbol{u}^{(a)})^2 f_a^{(1)}(\boldsymbol{r},\boldsymbol{p},t)\mathrm{d}^3p, \qquad P_a(\boldsymbol{r},t) = n_a(\boldsymbol{r},t)T_a(\boldsymbol{r},t), \tag{1.65c}$$

$$\Pi_{\alpha\beta}^{(a)}(\boldsymbol{r},t) = m_a\int (\boldsymbol{v}-\boldsymbol{u}^{(a)})_\alpha (\boldsymbol{v}-\boldsymbol{u}^{(a)})_\beta f_a^{(1)}(\boldsymbol{r},\boldsymbol{p},t)\mathrm{d}^3p - P_a(\boldsymbol{r},t)\delta_{\alpha\beta}, \tag{1.65d}$$

$$\boldsymbol{q}^{(a)}(\boldsymbol{r},t)=\frac{1}{2}m_a\int(\boldsymbol{v}-\boldsymbol{u}^{(a)})(\boldsymbol{v}-\boldsymbol{u}^{(a)})^2 f_a^{(1)}(\boldsymbol{r},\boldsymbol{p},t)\mathrm{d}^3p. \tag{1.65e}$$

Here P_a is scalar partial **pressure** of a-component, $\delta_{\alpha\beta}$ is the **Kronecker tensor**, and $\Pi^{(a)}_{\alpha\beta}$ is the **viscous stress tensor**. The vector $\boldsymbol{q}^{(a)}$ is the **heat flux density** carried by particles of type a.

We note, that in the equilibrium equations (1.65) require the conditions

$$\int\delta f_a^{(1)}(\boldsymbol{r},\boldsymbol{p},t)\mathrm{d}^3p=0,\quad \int\boldsymbol{v}\delta f_a^{(1)}(\boldsymbol{r},\boldsymbol{p},t)\mathrm{d}^3p=0,\quad \int(\boldsymbol{v}-\boldsymbol{u}^{(a)})^2\delta f_a^{(1)}(\boldsymbol{r},\boldsymbol{p},t)\mathrm{d}^3p=0 \tag{1.66}$$

for the perturbation function $\delta f_a^{(1)}$ to be fulfilled. As they must hold in any spatial place at any time, conditions (1.66) are equivalent to the requirement $\delta f_a^{(1)}=0$. However, the dissipative processes (e.g., viscosity and heat conduction[2]) driving the system toward the equilibrium come into play only when the distribution function differs from the local Maxwellian function, i.e., $\delta f_a^{(1)}\neq 0$ giving rise to $n_a(\boldsymbol{r},t)=\overline{n}_a(\boldsymbol{r},t)+\delta n_a(\boldsymbol{r},t)$, $\boldsymbol{u}^{(a)}(\boldsymbol{r},t)=\overline{\boldsymbol{u}}^{(a)}(\boldsymbol{r},t)+\delta\boldsymbol{u}^{(a)}(\boldsymbol{r},t)$, and $T_a(\boldsymbol{r},t)=\overline{T}_a(\boldsymbol{r},t)+\delta T_a(\boldsymbol{r},t)$; see in Kogan (1967) and Silin (1971) for greater detail.

The set of equations for macroscopic parameters can be obtained from kinetic equation (1.61). However, microscopically derived and so more precise collision integrals in the forms of Landau or Balescu–Lenard are very complicated. For the sake of simplicity, we use model Bhatnagar–Gross–Krook (BGK) collision integral (Bhatnagar et al. 1954; Gross and Krook 1956; Ginzburg and Rukhadze 1975):

$$St(f_a^{(1)},f_b^{(1)})=-\nu_{ab}(f_a^{(1)}-n_a\Phi_{ab}). \tag{1.67}$$

Here $\nu_{ab}=\tau_{ab}^{-1}$ are phenomenological parameters (effective collision frequencies), $T=T_a=T_b=\cdots$ is the temperature, which we suppose common for all plasma components, and

$$\Phi_{ab}(\boldsymbol{r},\boldsymbol{p},t)=[2\pi m_aT(\boldsymbol{r},t)]^{-3/2}\exp\left\{-\frac{[\boldsymbol{p}-m_a\boldsymbol{u}^{(b)}(\boldsymbol{r},t)]^2}{2m_aT(\boldsymbol{r},t)}\right\}. \tag{1.68}$$

In the model BGK integral, the collision frequencies are not consistently derived; instead, they are estimated to an order of magnitude from a qualitative

[2]Hereafter we define the *dissipative* processes as those leading to the entropy increase; see Eq. (1.129). From this perspective the heat conduction is classified as a dissipative process even though no energy transformation process into the thermal energy is apparent during the heat conduction. In fact, however, it is a potential work, which could have been done as a result, e.g., of a Carnot cycle applied to the system, that is transferred to the thermal energy. Another example of a similar irreversible dissipative process is mixing up of two different gases.

physical consideration. It is within the required accuracy, because in the majority of astrophysical problems plasma parameters are known only to an order of magnitude; thus, this simplification of the collision integral is well justified.

We use collision integral (1.67) in Eq. (1.61) to obtain the equations describing balance of particles, momentum, and energy. We multiply left-hand and right-hand sides of Eq. (1.61) sequentially by 1, $m_a(\boldsymbol{v}-\boldsymbol{u}^{(a)})$, and $m_a(\boldsymbol{v}-\boldsymbol{u}^{(a)})^2$ and integrate over d^3p. As a result we obtain the set of equations in quasi-hydrodynamic approximation:

$$\frac{\partial n_a}{\partial t}+\nabla\cdot n_\alpha \boldsymbol{u}^{(a)}=0 \tag{1.69}$$

—continuity equations;

$$\begin{aligned} n_a m_a\left[\frac{\partial \boldsymbol{u}^{(a)}}{\partial t}+(\boldsymbol{u}^{(a)}\cdot\nabla)\boldsymbol{u}^{(a)}\right]_\alpha &= e_a n_a\left(\boldsymbol{E}+\frac{1}{c}\boldsymbol{u}^{(a)}\times\boldsymbol{B}\right)_\alpha \\ -\nabla_\alpha P_a-\nabla_\beta\Pi^{(a)}_{\alpha\beta}-n_a m_a\sum_b\frac{(\boldsymbol{u}^{(a)}-\boldsymbol{u}^{(b)})_\alpha}{\tau_{ab}} & \end{aligned} \tag{1.70}$$

—equations of medium motion

$$\frac{3}{2}n_a\left(\frac{\partial T}{\partial t}+\boldsymbol{u}^{(a)}\cdot\nabla T\right)+P_a\nabla\cdot\boldsymbol{u}^{(a)}+\nabla\cdot\boldsymbol{q}^{(a)}+\Pi^{(a)}_{\alpha\beta}\nabla_\beta u^{(a)}_\alpha=\frac{1}{2}n_a m_a\sum_b\frac{(\boldsymbol{u}^{(a)}-\boldsymbol{u}^{(b)})^2}{\tau_{ab}} \tag{1.71}$$

— equations of heat transfer. Here

$$\begin{aligned} \Pi^{(a)}_{\alpha\beta} \;=\; & -\frac{P_a}{\sum_b\nu_{ab}}\left(\nabla_\beta u^{(a)}_\alpha+\nabla_\alpha u^{(a)}_\beta-\frac{2}{3}\delta_{\alpha\beta}\nabla\cdot\boldsymbol{u}^{(a)}\right) \\ & +\frac{n_a m_a}{\sum_b\nu_{ab}}\sum_b\nu_{ab}\left((\boldsymbol{u}^{(a)}-\boldsymbol{u}^{(b)})_\alpha(\boldsymbol{u}^{(a)}-\boldsymbol{u}^{(b)})_\beta-\frac{1}{3}\delta_{\alpha\beta}(\boldsymbol{u}^{(a)}-\boldsymbol{u}^{(b)})^2\right) \end{aligned} \tag{1.72}$$

— viscous stress tensor;

$$\boldsymbol{q}=-\frac{5P_a}{2m_a\sum_b\nu_{ab}}\nabla T+\frac{n_a m_a}{2\sum_b\nu_{ab}}\sum_b\nu_{ab}(\boldsymbol{u}^{(a)}-\boldsymbol{u}^{(b)})^2(\boldsymbol{u}^{(a)}-\boldsymbol{u}^{(b)}) \tag{1.73}$$

— heat flux density.

Calculations of collision frequencies have been made by Spitzer (1962), Braginskii (1965), Alfven and Fälthammar (1963) and Baranov and Krasnobaev (1977) etc. We list below (see Sect. 1.3.7) the necessary kinetic coefficients for MHD equations.

Equation of motion (1.70) contains electric $\boldsymbol{E}$ and magnetic $\boldsymbol{B}$ fields. Thus, we must complement Eqs. (1.69)–(1.73) by Maxwell equations neglecting the displacement current, $c^{-1}\partial \boldsymbol{E}/\partial t$. This term is small compared with the conductivity current $\boldsymbol{j}$ if the frequency ω of the electromagnetic field is small such as $\omega E \ll j$. This condition is fulfilled for relatively slow MHD processes. We, thus, have the following set of the Maxwell equations:

$$\nabla \cdot \boldsymbol{B} = 0, \qquad \nabla \times \boldsymbol{B} = \frac{4\pi}{c}(\boldsymbol{j} + \boldsymbol{j}^{\,\mathrm{ext}}), \qquad \nabla \times \boldsymbol{E} = -\frac{1}{c}\frac{\partial \boldsymbol{B}}{\partial t}. \tag{1.74}$$

Here $\boldsymbol{j}$ is the electric current produced by the plasma particles ($e > 0$ is adopted),

$$\boldsymbol{j} = e(n_i \boldsymbol{u}^{(i)} - n_e \boldsymbol{u}^{(e)}), \tag{1.75}$$

$\boldsymbol{j}^{\mathrm{ext}}$ is the external current. Since a plasma is supposed to consist of collectively interacting charged and neutral particles, the inclusion of an external current needs some more clarification. Although, as a model of this current, one can always imagine well-isolated current-carrying wires embedded by a plasma; this example has little practical importance, while a current composed of free particles identical to the plasma particles is indistinguishable of the internal plasma current and so must not be treated as an external current. A practically important situation, when the concept of the external current makes sense, is when the current is formed by a particle population distinct from the plasma particles, e.g., distinct nuclei or ions (including different ionization state) or higher-energy (nonthermal) population of the same particles. In some cases, the population forming the external current cannot itself be described within the MHD approximation (as is often true for nonthermal particles), and requires a more general kinetic treatment, while its effect on the main plasma can still be accounted within the MHD approach. Maxwell equations then allow calculating-the magnetic field, if we have specified the dependence between current $\boldsymbol{j}$ and electromagnetic field, i.e., generalized Ohm's law.

1.3.4 Ohm's Law in a Partially Ionized Collisional Plasma

In this section we examine partly ionized collisional plasmas, following Pikel'ner 1966; Bykov and Toptygin 2007. We consider the three-component medium (electrons e, ions i, neutral atoms a) and use Eqs. (1.69)–(1.70). The momentum conservation law leads to the relationship between the collision frequencies:

$$m_b n_b \nu_{bc} = m_c n_c \nu_{cb}. \tag{1.76}$$

In the subsequent discussion we adopt a single-fluid model and consider the conditions when in zeroth approximation all three components move as

an aggregate continuum medium. We therefore introduce the bulk velocity $\boldsymbol{u}$ of the medium

$$\boldsymbol{u} = \frac{n_i m_i \boldsymbol{u}^{(i)} + n_a m_a \boldsymbol{u}^{(a)} + n_e m_e \boldsymbol{u}^{(e)}}{n_i m_i + n_a m_a + n_e m_e}\,, \qquad \boldsymbol{u}^{(i,a,e)} = \boldsymbol{u} + \boldsymbol{v}^{(i,a,e)} \tag{1.77}$$

and take into account the equality

$$n_i m_i \boldsymbol{v}^{(i)} + n_a m_a \boldsymbol{v}^{(a)} + n_e m_e \boldsymbol{v}^{(e)} = 0 \tag{1.78}$$

and the inequalities $m_e \ll m_i,\ v^{(i,a)} \ll u,\ v^{(e)} \sim u$.

Substituting expression (1.78) in Eqs. (1.69) and (1.70) and neglecting the terms of the second-order smallness allows writing down equations of motion for three components of the medium. Equations for the heavy components are

$$\begin{aligned} n_i m_i \left[\frac{\partial \boldsymbol{u}}{\partial t} + (\boldsymbol{u}\cdot\nabla)\boldsymbol{u}\right] + n_i m_i \left[\frac{\partial \boldsymbol{v}^{(i)}}{\partial t} + (\boldsymbol{u}\cdot\nabla)\boldsymbol{v}^{(i)} + (\boldsymbol{v}^{(i)}\cdot\nabla)\boldsymbol{u}\right] \\ = e n_i \left(\boldsymbol{E} + \frac{1}{c}\boldsymbol{u}\times\boldsymbol{B}\right) + \frac{e n_i}{c}\boldsymbol{v}^{(i)}\times\boldsymbol{B} - \nabla P_i + \eta_i\left(\Delta\boldsymbol{u} + \frac{1}{3}\nabla(\nabla\cdot\boldsymbol{u})\right) \\ - n_i m_i\ \frac{\boldsymbol{v}^{(i)} - \boldsymbol{v}^{(e)}}{\tau_{ie}} - n_i m_i\ \frac{\boldsymbol{v}^{(i)} - \boldsymbol{v}^{(a)}}{\tau_{ia}}, \end{aligned} \tag{1.79}$$

$$\begin{aligned} n_a m_a \left[\frac{\partial \boldsymbol{u}}{\partial t} + (\boldsymbol{u}\cdot\nabla)\boldsymbol{u}\right] + n_a m_a \left[\frac{\partial \boldsymbol{v}^{(a)}}{\partial t} + (\boldsymbol{u}\cdot\nabla)\boldsymbol{v}^{(a)} + (\boldsymbol{v}^{(a)}\cdot\nabla)\boldsymbol{u}\right] \\ = -\nabla P_a + \eta_a\left(\Delta\boldsymbol{u} + \frac{1}{3}\nabla(\nabla\cdot\boldsymbol{u})\right) - n_a m_a\ \frac{\boldsymbol{v}^{(a)} - \boldsymbol{v}^{(e)}}{\tau_{ae}} - n_a m_a\ \frac{\boldsymbol{v}^{(a)} - \boldsymbol{v}^{(i)}}{\tau_{ai}}. \end{aligned} \tag{1.80}$$

The equation for electrons is simplified using the inequality $m_e \ll m_i$:

$$\begin{aligned} 0 = -e n_e \left(\boldsymbol{E} + \frac{1}{c}\boldsymbol{u}\times\boldsymbol{B}\right) - \frac{e n_e}{c}\boldsymbol{v}^{(e)}\times\boldsymbol{B} - \nabla P_e + \eta_e\left(\Delta\boldsymbol{u} + \frac{1}{3}\nabla(\nabla\cdot\boldsymbol{u})\right) \\ - n_e m_e\ \frac{\boldsymbol{v}^{(e)} - \boldsymbol{v}^{(i)}}{\tau_{ei}} - n_e m_e\ \frac{\boldsymbol{v}^{(e)} - \boldsymbol{v}^{(a)}}{\tau_{ea}}. \end{aligned} \tag{1.81}$$

Here everywhere $e > 0$. We omit viscosity term in the last equation, because ions and neutral atoms dominate in the momentum transfer. The terms of order $v^{(i,a)}/u$ also neglected in dissipative terms containing the dynamic viscosity $\eta_{i,a}$ in Eqs. (1.79) and (1.80).

We next take into account the quasineutrality of the medium and introduce the total mass density

$$\rho = n_i m_i + n_a m_a \tag{1.82}$$

and the electric current density (1.75)

$$\boldsymbol{j} = en_i(\boldsymbol{v}^{(i)} - \boldsymbol{v}^{(e)}), \tag{1.83}$$

as well as the total pressure $P = P_e + P_i + P_a$ and the total viscosity $\eta = \eta_e + \eta_i + \eta_a$. Term-by-term summation of Eqs. (1.79)–(1.81) yields the equation of motion of the medium as a whole:

$$\rho\left[\frac{\partial \boldsymbol{u}}{\partial t} + (\boldsymbol{u}\cdot\nabla)\boldsymbol{u}\right] = \frac{1}{c}\boldsymbol{j}\times\boldsymbol{B} - \nabla P + \eta\left(\Delta\boldsymbol{u} + \frac{1}{3}\nabla(\nabla\cdot\boldsymbol{u})\right). \tag{1.84}$$

From Eq. (1.69) we obtain the continuity equation

$$\frac{\partial \rho}{\partial t} + \nabla\cdot\rho\boldsymbol{u} = 0. \tag{1.85}$$

The friction forces between plasma components do not enter Eq. (1.84) by virtue of conditions (1.76).

We specify now the conditions when a multicomponent fluid can be described by means of the one-fluid model. The characteristic frequencies ω of processes under consideration must be small compared with the reverse times τ_{ab}^{-1} between collisions of all distinct components. The lengths λ of waves must be large compared with the mean free paths Λ_{ab} between collisions

$$\omega \ll \tau_{ab}^{-1}, \qquad \lambda = 2\pi/k \gg \Lambda_{ab} \tag{1.86}$$

for both $a = b$ and $a \neq b$. The meaning of this conditions for $a \neq b$ is that collisions between different particles are numerous over the time interval $2\pi/\omega$, which ensures that motions of all plasma components are identical. In particular, the neutral component adjusts itself to motion of the charged components, if $2\pi/\omega \gg \tau_{ia}, \tau_{ea}$. In the opposite case the neutral particles do not have sufficient time of interaction with charges to respond to rapid changes of the electromagnetic field. Neutral and charged particles move independently in this case, so, the one-fluid description is inapplicable to such "fast" processes. Conditions (1.86) also ensure smallness of deviations from the local equilibrium in every component.

Let us derive a generalized Ohm law from the above equations. To do so we neglect the last dissipative term on the right-hand side of Eq. (1.84), which is assumed to be small. The combination $\partial\boldsymbol{u}/\partial t + (\boldsymbol{u}\cdot\nabla)\boldsymbol{u}$ is then expressed from Eq. (1.84), where the terms of the form $\partial\boldsymbol{v}^{(i,a)}/\partial t + (\boldsymbol{u}\cdot\nabla)\boldsymbol{v}^{(i,a)}$ have already been discarded. For these approximations to be valid it is essential that the frequencies ω of the involved oscillations are low compared with collisional frequencies τ_{ab}^{-1}, and the wavelengths are long compared with the particle transport mean free paths $\Lambda_b = v_{Tb}/\sum_c \tau_{bc}^{-1}$, where v_{Tb} are the thermal velocities. Then, we introduce the mass fraction of the neutral component

$$F = \frac{n_a m_a}{n_a m_a + n_i m_i} \approx \frac{n_a}{n_a + n_i}, \tag{1.87}$$

assuming only one sort of singly ionized atoms in the plasma, so that $m_a \approx m_i$. We also assume that the ratio between the number densities of ions and neutral atoms persists in the collisional plasma in the presence of low-frequency oscillations, i.e., $n'_a/n'_i = n_a/n_i$ and $F = \text{const}$, where $n'_{i,a}$ are perturbed number densities.

Then, from Eqs. (1.78) and (1.83), we express the electron and neutral component velocities, $\boldsymbol{v}^{(e)}$ and $\boldsymbol{v}^{(a)}$, in terms of the current density and the ion velocity $\boldsymbol{v}^{(i)}$ using the smallness of the mass ratio $m_e/m_i \ll 1$:

$$\boldsymbol{v}^{(e)} = \boldsymbol{v}^{(i)} - \frac{\boldsymbol{j}}{en_i}, \qquad \boldsymbol{v}^{(e)} - \boldsymbol{v}^{(a)} \approx \frac{\boldsymbol{v}^{(i)}}{F} - \frac{\boldsymbol{j}}{en_i}, \qquad \boldsymbol{v}^{(i)} - \boldsymbol{v}^{(a)} \approx \frac{\boldsymbol{v}^{(i)}}{F}. \tag{1.88}$$

Term-by-term summation of Eqs. (1.79) and (1.81), with the above simplifications, yields the relation between the ion velocity and electric current:

$$\boldsymbol{v}^{(i)} \approx \frac{F^2\tau_{ia}}{n_i m_i c}\,\boldsymbol{j} \times \boldsymbol{B} + \frac{Fm_e\tau_{ia}}{en_i m_i \tau_{ea}}\,\boldsymbol{j}. \tag{1.89}$$

In what follows, in addition to $m_e/m_i \ll 1$, we discard the small terms of the order of $(m_e/m_i)^{1/2} \ll 1$. The ratio $m_e\tau_{ia}/m_i\tau_{ea} = m_e v_{Te}\Lambda_{ia}/m_i v_{Ti}\Lambda_{ea} = (m_e/m_i)^{1/2}\sigma_{ea}/\sigma_{ia} \approx (m_e/m_i)^{1/2}$, where $\sigma_{ia,ea}$ denote the cross sections for collisions between charged and neutral particles, has the same order of magnitude and the corresponding terms are safely discarded as well. By eliminating the velocity $\boldsymbol{v}^{(i)}$ from Eq. (1.79) with account of relations (1.88), we arrive at generalized Ohm's law—the relationship between the electromagnetic field, the current, and the hydrodynamic parameters of the medium:

$$\boldsymbol{E} + \frac{1}{c}\boldsymbol{u} \times \boldsymbol{B} + \frac{1}{en_i}\nabla[(1-F)P - P_i] = \frac{\boldsymbol{j}}{\sigma} + \frac{1}{n_i ec}\boldsymbol{j} \times \boldsymbol{B} + \frac{F^2\tau_{ia}}{n_i m_i c^2}\boldsymbol{B} \times (\boldsymbol{j} \times \boldsymbol{B}). \tag{1.90}$$

The pressure gradient also enters this relationship and so produces an additional effective electric field. The quantity

$$\sigma = \frac{e^2 n_i \tau_e}{m_e}, \qquad \text{where} \qquad \tau_e = \frac{\tau_{ei}\tau_{ea}}{\tau_{ei} + \tau_{ea}} \tag{1.91}$$

is the plasma conductivity with the account of neutral atoms in the absence of an external magnetic field, which can be called the **classical Drude conductivity**, as it is analogous to arbitrary conducting medium (Drude 1900a,b).

In a "cold" plasma, wherein the pressure P can be neglected, Ohm's law takes the form

$$\boldsymbol{E} + \frac{1}{c}\boldsymbol{u} \times \boldsymbol{B} = \frac{\boldsymbol{j}}{\sigma} + \frac{1}{n_i ec}\boldsymbol{j} \times \boldsymbol{B} + \frac{F^2\tau_{ia}}{n_i m_i c^2}\boldsymbol{B} \times (\boldsymbol{j} \times \boldsymbol{B}). \tag{1.92}$$

If the electric current $\boldsymbol{j} = \boldsymbol{j}_{\parallel} + \boldsymbol{j}_{\perp}$ is separated into two components parallel and perpendicular to the magnetic field $\boldsymbol{B}$, Ohm's law can be presented as

$$\boldsymbol{E} + \frac{1}{c}\boldsymbol{u} \times \boldsymbol{B} = \frac{\boldsymbol{j}_{\parallel}}{\sigma} + \frac{B}{n_i e c}\boldsymbol{j} \times \boldsymbol{e}_{\parallel} + \frac{\boldsymbol{j}_{\perp}}{\sigma_{\perp}^{\text{eff}}}, \tag{1.93}$$

where $\boldsymbol{e}_{\parallel} = \boldsymbol{B}/B$, and

$$\frac{1}{\sigma_{\perp}^{\text{eff}}} = \frac{1}{\sigma} + \frac{1}{\sigma_C}, \qquad \sigma_C = \frac{n_i m_i c^2}{F^2 B^2 \tau_{ia}}, \tag{1.94}$$

where the second term, specified by the ion contribution, σ_C, is called the **Cowling conductivity**.

Hence, it follows that the quantities σ, $\sigma_{\perp}^{\text{eff}}$ play the roles of the effective longitudinal and transverse conductivities of a partially ionized magnetized plasma. The relationships inverse to Eq. (1.93) have the form

$$\boldsymbol{j}_{\parallel} = \sigma \boldsymbol{E}_{\parallel}, \quad \boldsymbol{j}_{\perp} = \sigma_{\perp}\left(\boldsymbol{E}_{\perp} + \frac{1}{c}\boldsymbol{u} \times \boldsymbol{B}\right) - \sigma_{\perp}\frac{B\sigma_{\perp}^{\text{eff}}}{ecn_i}\left(\boldsymbol{E} \times \boldsymbol{e}_{\parallel} - \frac{B}{c}\boldsymbol{u}_{\perp}\right), \tag{1.95}$$

where

$$\frac{1}{\sigma_{\perp}} = \frac{1}{\sigma_{\perp}^{\text{eff}}}\left[1 + \left(\frac{B\sigma_{\perp}^{\text{eff}}}{ecn_i}\right)^2\right]. \tag{1.96}$$

Note that

$$\boldsymbol{E} + \frac{1}{c}\boldsymbol{u} \times \boldsymbol{B} = \boldsymbol{E}' \tag{1.97}$$

is the electric field in co-moving system; thus, we can transform Eq. (1.95) to the form

$$\boldsymbol{j} = \widehat{\sigma}'\boldsymbol{E}' - \boldsymbol{E}' \times \boldsymbol{G}, \tag{1.98}$$

where $\widehat{\sigma}' = (\sigma_{\perp},\ \sigma_{\parallel})$ is the diagonal tensor, while vector $\boldsymbol{G}$ is determined by

$$\boldsymbol{G} = \frac{\sigma_{\perp}\sigma_{\perp}^{\text{eff}}}{ecn_i}\boldsymbol{B} \tag{1.99}$$

and describes gyrotropy of the medium. The sum $\sigma'_{\alpha\beta} - e_{\alpha\beta\gamma}G_{\gamma} = \sigma_{\alpha\beta}$ is the electroconductivity tensor of partly ionized plasma and so the sum $\delta_{\alpha\beta} + i(4\pi/\omega)\sigma_{\alpha\beta} = \varepsilon_{\alpha\beta}$ is the electric permeability tensor, which determines the electric induction vector $\boldsymbol{D}'$, if the electric field depends on time as $\boldsymbol{E}'(t) = \boldsymbol{E}'e^{-i\omega t}$ and the frequency ω is small, $\omega \ll \sigma_{\perp},\ \sigma_{\parallel}$:

$$D'_{\alpha} = \varepsilon_{\alpha\beta}E'_{\beta}. \tag{1.100}$$

In the absence of the neutral component,

$$F^2\tau_{ia}=0,\ \sigma_\perp^{\rm eff}=\sigma=\sigma_{\rm S}=e^2n_i\tau_{ei}/m_e,\ \sigma_\perp^{-1}=\sigma^{-1}(1+\omega_{\rm Be}^2\tau_{ei}^2),\quad(1.101)$$

where $\sigma_{\rm S}$ is the **Spitzer conductivity** calculated in Sect. 1.3.7, Eq. (1.149), $\sigma_\perp$ is the **Pedersen conductivity**, and $\sigma_{\rm H}=\sigma_\perp\omega_{\rm Be}\tau_{ei}$ is the corresponding **Hall conductivity**, so we have a well-known relation for the electric current

$$\boldsymbol{j}=\sigma\boldsymbol{E}'_\parallel+\frac{\sigma}{1+\omega_{\rm Be}^2\tau_{ei}^2}\boldsymbol{E}'_\perp-\frac{\sigma\omega_{\rm Be}\tau_{ei}}{1+\omega_{\rm Be}^2\tau_{ei}^2}\boldsymbol{E}'\times\boldsymbol{e}_\parallel,\qquad(1.102)$$

where $\omega_{\rm Be}=eB/m_ec$ is the electron cyclotron frequency. An estimate of characteristic time τ_{ei} of e-i collisions, entering here, is given below by expression (1.148).

Electric current (1.102) in fully ionized hydrogen plasma is almost solely produced by the electron plasma component $\boldsymbol{j}\approx\boldsymbol{j}^e$. When $n_a=0$, the ion current $\boldsymbol{j}^i=en_i\boldsymbol{v}^{(i)}$, according to Eq. (1.78), is linked to the electron current by

$$\boldsymbol{j}^i=-\frac{m_e}{m_i}en_i\boldsymbol{v}^{(e)}=\frac{m_e}{m_i}\boldsymbol{j}^e=\frac{m_e}{m_i}\boldsymbol{j},\qquad(1.103)$$

i.e., it contains a very small factor m_e/m_i and so does not enter the total current produced by both charged components.

It is curious to consider another limiting case of a weakly ionized plasma:

$$1-F\ll F,\quad n_i=n_e\ll n_a.\qquad(1.104)$$

Adopt that the number densities of the charged components are sufficiently small to ensure

$$\tau_{ei}\gg\tau_{ea},\ \tau_{ia}\qquad(1.105)$$

that means that the collisions between electrons and ions are inessential. The collision times of the electrons and ions with neutrals can be estimated as

$$\tau_{ea}\approx(v_{Te}n_a\sigma_{ea})^{-1},\ \tau_{ia}\approx(v_{Ti}n_a\sigma_{ia})^{-1},\ \text{and}\ \tau_{ea}/\tau_{ia}\approx(m_e/m_i)^{1/2},\qquad(1.106)$$

if the cross sections of the charged particle collisions with neutrals are comparable, $\sigma_{ea}\approx\sigma_{ia}$. Assume also that the charged particles are strongly magnetized:

$$\omega_{\rm Be}\tau_{ea}\gg1,\quad\omega_{\rm Bi}\tau_{ia}\gg1.\qquad(1.107)$$

In our case of weak ionization, equalities (1.88) yield $\boldsymbol{v}^{(a)}\approx0$. This means that the neutral component moves with the bulk velocity $\boldsymbol{u}$, while electrons and ions, whose contributions to the total momentum of the fluid are inessential under condition (1.104), have some mean velocities $\boldsymbol{v}^{(e)}$ and

$\boldsymbol{v}^{(i)}$ relative to this neutral background. Equation (1.91) with account of Eq. (1.105) yields the longitudinal electron conductivity

$$\sigma^e = \frac{e^2 n_e \tau_{ea}}{m_e} \equiv \sigma^e_{\parallel}. \tag{1.108}$$

The corresponding ion conductivity has, apparently, the form

$$\sigma^i_{\parallel} = \frac{e^2 n_i \tau_{ia}}{m_i} \tag{1.109}$$

and, accordingly,

$$\sigma^e_{\parallel}/\sigma^i_{\parallel} \approx (m_e/m_i)^{1/2} \gg 1. \tag{1.110}$$

The ion current makes, therefore, a small contribution to total longitudinal current (1.95) because of $\sigma^i_{\parallel}$ smallness. However, in the case of weakly ionized plasma this smallness is much weaker $\sim (m_e/m_i)^{1/2}$ than in the case of fully ionized plasma, where it is $\sim (m_e/m_i)$.

Let us transform Eq. (1.94) with account of Eqs. (1.108) and (1.107):

$$\frac{1}{\sigma^{\text{eff}}_{\perp}} = \frac{1}{\sigma^e_{\parallel}}(1 + \omega_{\text{Be}}\tau_{ea}\omega_{\text{Bi}}\tau_{ia}) \approx \frac{(\omega_{\text{Bi}}\tau_{ia})^2}{\sigma^i_{\parallel}} \approx \frac{1}{\sigma^i_{\perp}}. \tag{1.111}$$

Here $\sigma^{\text{eff}}_{\perp} \approx \sigma^i_{\perp}$ [cf. transverse conductivity in Eq. (1.102)]. Remarkably, in this case, the transverse current is specified by ions (Cowling conductivity), not by electrons. Electron conductivity is described by $\sigma^e_{\perp} = \sigma^e_{\parallel}/(\omega_{\text{Be}}\tau_{ea})^2$, so $\sigma^e_{\perp}/\sigma^i_{\perp} \approx (m_e/m_i)^{1/2} \ll 1$ and, thus, the electron transverse current is small compared with the ion transverse current.

The gyration vector in the Hall current [see Eqs. (1.98) and (1.99)] can here be transformed as follows:

$$\boldsymbol{G} \approx \boldsymbol{G}^i \approx -\frac{\sigma^i_{\perp}}{\omega_{\text{Bi}}\tau_{ia}}\boldsymbol{e}_{\parallel}. \tag{1.112}$$

Again, the ion contribution dominates over the electron one; their ratio is $G^i/G^e \approx (m_i/m_e)^{1/2}$. Therefore, the relative roles of the electrons and ions in creation of the electric current is essentially dependent on the plasma ionization an composition as well as on the direction and value of the external magnetic field.

1.3.5 Plasma in a Weak Magnetic Field

Relationships (1.90)–(1.102) show that the inclusion of both the magnetic anisotropy of conductivity and neutral particles substantially complicates the electric current-to-electromagnetic field coupling and enhances its nonlinearity. We therefore derive here the system of equations in simplified forms,

but with inclusion of an external current $\boldsymbol{j}^{\rm ext}$, which is typically ignored in standard MHD (Alfvén 1942; Elsasser 1950; Syrovatskii 1958).[3]

Consider highly collisional case, $\omega_{\rm Be}\tau_{ei} \ll 1$, where no neutral particles are present, $F = 0$. Ohm's law takes then the following simple form:

$$\boldsymbol{j} = \sigma\left(\boldsymbol{E} + \frac{1}{c}\boldsymbol{u}\times\boldsymbol{B}\right). \tag{1.113}$$

Assuming σ = const, Eq. (1.53a) with Eq. (1.53b) yields the induction equation

$$\frac{\partial \boldsymbol{B}}{\partial t} = \nabla\times(\boldsymbol{u}\times\boldsymbol{B}) + \nu_m\Delta\boldsymbol{B} - \frac{4\pi\nu_m}{c}\nabla\times\boldsymbol{j}^{\rm ext}. \tag{1.114}$$

Here

$$\nu_m = \frac{c^2}{4\pi\sigma} \tag{1.115}$$

is the collisional **magnetic diffusivity** (called also the magnetic viscosity). Then, Eq. (1.114) must be complemented by the continuity equation

$$\frac{\partial\rho}{\partial t} + \nabla\cdot\rho\boldsymbol{u} = 0, \tag{1.116}$$

equation of motion

$$\rho\left[\frac{\partial\boldsymbol{u}}{\partial t} + (\boldsymbol{u}\cdot\nabla)\boldsymbol{u}\right] = \frac{1}{c}(\boldsymbol{j}+\boldsymbol{j}^{\rm ext})\times\boldsymbol{B} - \nabla P + \eta\left(\Delta\boldsymbol{u} + \frac{1}{3}\nabla(\nabla\cdot\boldsymbol{u})\right) \tag{1.117}$$

and the heat transfer equation, which is obtained below in this section.

The first term in the rhs of Eq. (1.117) represents Ampère's force

$$\boldsymbol{f}_{\rm A} = \frac{1}{c}(\boldsymbol{j}+\boldsymbol{j}^{\rm ext})\times\boldsymbol{B} \tag{1.118}$$

applied to both internal plasma current $\boldsymbol{j}$ and external current $\boldsymbol{j}^{\rm ext}$. Inclusion of the latter one into the equation assumes that there is a strong coupling between this external current and the plasma. This coupling may generally be provided by either frequent Coulomb collisions of external particles with thermal ones or their interactions via macroscopic (self-consistent) and turbulent electromagnetic fields. Consequently, strong coupling may happen in both collisional and collisionless plasma. Turbulent fields are discussed in

[3] For various aspects of MHD, the reader can also consult classical textbooks and monographs by Alfven (1950), Cowling (1957), Alfven and Fälthammar (1963), Pikel'ner (1966), Landau and Lifshits (1982), as well as from the most recent, modern textbook by Somov (2006, 2007).

greater detail in Chap. 4. In such a case Ampère's force is determined by the full current $\boldsymbol{j} + \boldsymbol{j}^{\text{ext}}$ and using Eq. (1.53b) can be represented as

$$\boldsymbol{f}_{\text{A}} = \frac{1}{4\pi}(\nabla \times \boldsymbol{B}) \times \boldsymbol{B}. \tag{1.119}$$

In the case of weak coupling, however, the external current has no direct effect on the plasma, so the corresponding term must be excluded from Ampère's force:

$$\boldsymbol{f}_{\text{A}} = \frac{1}{4\pi}(\nabla \times \boldsymbol{B}) \times \boldsymbol{B} - \frac{1}{c}\boldsymbol{j}^{\text{ext}} \times \boldsymbol{B}. \tag{1.120}$$

Let us derive now the heat transfer equation from Eqs. (1.71) to (1.73). Taking into account condition (1.60) (the energy of particle interaction is small compared with the kinetic energy), we designate

$$\frac{3}{2}(n_i + n_e)T = \rho\epsilon, \quad w = \epsilon + \frac{P}{\rho}, \quad P = (n_i + n_e)T, \tag{1.121}$$

where ϵ is the specific (per the mass unit) internal energy and w is the specific **enthalpy** (the heat function). In the one-fluid model of fully ionized plasma considered here, we use the approximations

$$|\boldsymbol{u}^{(i)} - \boldsymbol{u}^{(e)}| \ll u, \quad (m_e/m_i)^{1/2} \ll 1, \quad \tau_{ei}|\partial u_\alpha/\partial x_\beta| \ll (m_e/m_i)^{1/2}. \tag{1.122}$$

Here, the first of inequalities (1.122) is the condition of the one-fluid description. The second one has been used for simplification of generalized Ohm's law (1.90). The third inequality allows simplifying Eq. (1.71) and discarding the last terms in the rhs of expressions (1.72) and (1.73) compared with rhs of Eq. (1.71). The relaxation time τ_{ei} is estimated in Sect. 1.3.7. After the indicated approximations we obtain the heat flux density in the form

$$\boldsymbol{q} = \boldsymbol{q}_e + \boldsymbol{q}_i \approx \boldsymbol{q}_e \approx -\chi\nabla T, \quad \chi = \frac{5P\tau_{ei}}{8m_e} = \frac{5Pk_B\tau_{ei}}{8m_e}, \tag{1.123}$$

and viscous stress tensor

$$\Pi_{\alpha\beta} = \Pi^{(i)}_{\alpha\beta} + \Pi^{(e)}_{\alpha\beta} \approx \Pi^{(i)}_{\alpha\beta} \approx -\rho\nu\left(\frac{\partial u_\alpha}{\partial x_\beta} + \frac{\partial u_\beta}{\partial x_\alpha} - \frac{2}{3}(\nabla \cdot \boldsymbol{u})\delta_{\alpha\beta}\right), \quad \nu = \frac{P\tau_{ei}}{2\rho}. \tag{1.124}$$

Here χ is the **heat conductivity**, which is derived from Eq. (1.73) using obvious relations $P_e = P/2$ and $\nu_{ee} + \nu_{ei} \approx 2\nu_{ei} = 2/\tau_{ei}$. First equality for χ in Eq. (1.123) is written for the temperature measured in energy units [erg], while the second for the temperature measured in [K]. The first of Eqs. (1.123) expresses the **Fourier law** of heat conductivity.

After adding equations (1.71) for electrons and ions term by term, use of continuity equations (1.69) and relation between the electric current density and component velocities $\boldsymbol{j} = en_i(\boldsymbol{u}^{(i)} - \boldsymbol{u}^{(e)})$, we obtain the energy balance equation:

$$\frac{\partial(\rho\epsilon)}{\partial t}+\nabla\cdot(\rho w\boldsymbol{u})-\boldsymbol{u}\cdot\nabla P=\nabla\cdot(\chi\nabla T)+\rho\nu\left(\frac{\partial u_\alpha}{\partial x_\beta}+\frac{\partial u_\beta}{\partial x_\alpha}-\frac{2}{3}(\nabla\cdot\boldsymbol{u})\delta_{\alpha\beta}\right)\frac{\partial u_\alpha}{\partial x_\beta}+\frac{j^2}{\sigma}. \tag{1.125}$$

Let us reformulate now the previous equation in terms of specific entropy s (per the mass unit). From the thermodynamic relations

$$\mathrm{d}w = T\mathrm{d}s + \frac{\mathrm{d}P}{\rho}, \qquad \mathrm{d}\epsilon = T\mathrm{d}s + \frac{P\mathrm{d}\rho}{\rho^2}, \tag{1.126}$$

we obtain

$$\mathrm{d}P = \rho\mathrm{d}w - \rho T\mathrm{d}s, \qquad \nabla P = \rho\nabla w - \rho T\nabla s, \qquad \frac{\partial\epsilon}{\partial t} = T\frac{\partial s}{\partial t} - \frac{P}{\rho^2}\nabla\cdot\rho\boldsymbol{u}$$

and find

$$\frac{\partial(\rho\epsilon)}{\partial t} + \nabla\cdot(\rho w\boldsymbol{u}) - \boldsymbol{u}\cdot\nabla P = \rho\frac{\partial\epsilon}{\partial t} + \frac{P}{\rho}\nabla\cdot\rho\boldsymbol{u} + \rho T\boldsymbol{u}\cdot\nabla s$$

$$= \rho T\left(\frac{\partial s}{\partial t} + \boldsymbol{u}\cdot\nabla s\right) = T\left(\frac{\partial(\rho s)}{\partial t} + \nabla\cdot(\rho s\boldsymbol{u})\right).$$

Finally we obtain the heat transfer equation in terms of entropy:

$$\rho T\left(\frac{\partial s}{\partial t} + \boldsymbol{u}\cdot\nabla s\right) = \nabla\cdot(\chi\nabla T) + \rho\nu\left(\frac{\partial u_\alpha}{\partial x_\beta} + \frac{\partial u_\beta}{\partial x_\alpha} - \frac{2}{3}(\nabla\cdot\boldsymbol{u})\delta_{\alpha\beta}\right)\frac{\partial u_\alpha}{\partial x_\beta} + \frac{j^2}{\sigma} \tag{1.127}$$

or in equivalent form

$$\frac{\partial(\rho s)}{\partial t} + \nabla\cdot\rho s\boldsymbol{u} = \dot{\tilde{S}}, \tag{1.128}$$

where $\dot{\tilde{S}}$ is the density of entropy sources:

$$\dot{\tilde{S}} = \nabla\cdot\frac{\chi\nabla T}{T} + \frac{\chi(\nabla T)^2}{T^2} + \frac{\rho\,\nu}{2T}\left(\frac{\partial u_\alpha}{\partial x_\beta} + \frac{\partial u_\beta}{\partial x_\alpha} - \frac{2}{3}(\nabla\cdot\boldsymbol{u})\delta_{\alpha\beta}\right)^2 + \frac{\nu_m}{4\pi T}\left(\nabla\times\boldsymbol{B} - \frac{4\pi}{c}\boldsymbol{j}^{\,\mathrm{ext}}\right)^2. \tag{1.129}$$

The first two terms in the rhs describe the entropy variation due to thermal conduction. It must be noted that these two terms are essentially different from each other. Indeed, the first one is sign alternating and, thus, can provide either increase or decrease of the entropy at the given location due to heat redistribution driven by the thermal conduction. The second one is positively defined and so results in the entropy *increase* only indicative that the heat conduction is essentially irreversible process. The next term describes the entropy increase due to the viscosity, while the last term describes the Joule heating of medium. In Eq. (1.129) only the "direct" Joule entropy increase is included, which is related to the plasma current $\boldsymbol{j}$, while the contribution of external current $\boldsymbol{j}^{\,\mathrm{ext}}$ is supposed to be small, so the term $4\pi\boldsymbol{j}^{\,\mathrm{ext}}/c$ is subtracted. This requires that the conductivity of the external current is much larger than for the internal plasma current. For example, one can imagine a highly conducting well-isolated current-carrying wire in a plasma as a vivid model of such external current. A more practical astrophysical example, however, is a current produced by highly nonthermal (e.g., relativistic) particle population. The Coulomb losses of ultrarelativistic particles are small, so the plasma heating by this external current is extremely low, although their contribution to plasma dynamics (including generation of magnetic field or return currents (see Sect. 7.1.3) whose Joule dissipation is essential) can be significant or even dominant. In many cases in astrophysics, however, the nonthermal particle population can, nevertheless, participate in energy dissipation via the Coulomb losses, ionization, radiative losses, and wave–particle interactions. In particular, solar flares represent a vivid example where Coulomb losses of nonthermal particles are significant. Indeed, most of the nonthermal flare energy resides in nonrelativistic and mildly relativistic particles, whose Coulomb losses in dense coronal loops or in the chromosphere result in strong plasma heating, which is routinely observed via flare-stimulated evaporation of the chromospheric plasma and via thermal SXR emission from the flare-heated coronal plasma.

The system of equations (1.113)–(1.120) is still complicated, and it allows some further simplifications in special cases. For example, in the "cold" plasma, $T \to 0,\ P \to 0,\ \nu \to 0$, the system of equations contains Eqs. (1.114) and (1.116) and simplified equation of the plasma motion

$$\rho\left[\frac{\partial \boldsymbol{u}}{\partial t} + (\boldsymbol{u}\cdot\nabla)\boldsymbol{u}\right] = \frac{1}{4\pi}(\nabla\times\boldsymbol{B})\times\boldsymbol{B}. \tag{1.130}$$

Then, in non-dissipative ("ideal") plasma $\nu \to 0,\ \nu_m \to 0,\ \chi \to 0,\ T = \mathrm{const}$; local thermodynamic equilibrium approximation yields

$$\nabla P = \frac{\partial P(\rho, s)}{\partial \rho}\nabla\rho' = c_s^2\nabla\rho', \qquad s = \mathrm{const}, \tag{1.131}$$

here s is the specific medium entropy and $c_s = (\partial P/\partial\rho)_s^{1/2}$ is the sound velocity. The system of equations reads

$$\frac{\partial \boldsymbol{B}}{\partial t} = \nabla \times (\boldsymbol{u} \times \boldsymbol{B}), \tag{1.132a}$$

$$\rho\left[\frac{\partial \boldsymbol{u}}{\partial t} + (\boldsymbol{u}\cdot\nabla)\boldsymbol{u}\right] = \frac{1}{4\pi}(\nabla \times \boldsymbol{B}) \times \boldsymbol{B} - \nabla P, \tag{1.132b}$$

$$P = P(\rho, s), \qquad s = \text{const} \tag{1.132c}$$

and Eq. (1.116).

External current drops out from the induction equation in the last case. This phenomenon is explained by shielding of electric charges in a plasma. Indeed, the shielding is perfect in the ideal plasma with infinite conductivity, so the external current is entirely neutralized by free plasma charges. This neutralization is only partial, however, if the conductivity is finite.

1.3.6 Plasma in a Strong Magnetic Field

Let us consider now the case of rare collisions and strong magnetic field, $\omega_{\mathrm{Be}}\tau_{ei} \gg 1$. Since the nonlinearity and complexity of the equations are very high, analytical methods can only be used for a limited class of problems including linearized equations. In what follows we use the notations $\boldsymbol{U} = \boldsymbol{U}_0 + \boldsymbol{u}$ for the velocity, $\boldsymbol{B} = \boldsymbol{B}_0 + \boldsymbol{b}$ for the magnetic field, and $\rho = \rho_0 + \rho'$ for the plasma density and suppose $\boldsymbol{u}$, $\boldsymbol{b}$, and ρ' are the values of the first order of smallness. Zero-order values are constant: $\boldsymbol{U}_0 = \text{const}$, $\boldsymbol{B}_0 = \text{const}$, and $\rho_0 = \text{const}$. In the first order we have

$$\boldsymbol{e}_\parallel = \frac{\boldsymbol{B}}{B} \approx \boldsymbol{e}_0 + \frac{\boldsymbol{b}_\perp}{B_0}, \qquad \boldsymbol{e}_0 = \frac{\boldsymbol{B}_0}{B_0}. \tag{1.133}$$

After linearization of Eqs. (1.84), (1.85), and (1.90) we obtain the following set of equations:

$$\begin{aligned}\frac{\partial \boldsymbol{b}}{\partial t} + (\boldsymbol{U}_0\cdot\nabla)\boldsymbol{b} - B_0[(\boldsymbol{e}_0\cdot\nabla)\boldsymbol{u} - \boldsymbol{e}_0\nabla\cdot\boldsymbol{u}] &= \nu_m\Delta\boldsymbol{b} - (\nu_{\mathrm{eff}} - \nu_m)\nabla\times(\nabla\times\boldsymbol{b})_\perp \\ - \frac{cB_0}{4\pi e n_i}(\boldsymbol{e}_0\cdot\nabla)(\nabla\times\boldsymbol{b}) + \frac{4\pi\nu_m}{c}\nabla\times\boldsymbol{j}^{\,\mathrm{ext}} + \frac{4\pi}{c}(\nu_{\mathrm{eff}} - \nu_m)\nabla& \\ \times\left[\boldsymbol{j}_\perp^{\,\mathrm{ext}} - \frac{j_\parallel^{\,\mathrm{ext}}}{B_0}\boldsymbol{b}_\perp\right] + \frac{B_0}{n_i e}((\boldsymbol{e}_0\cdot\nabla)\boldsymbol{j}^{\,\mathrm{ext}} - \boldsymbol{e}_0\nabla\cdot\boldsymbol{j}^{\,\mathrm{ext}}).&\end{aligned} \tag{1.134}$$

$$\frac{\partial \boldsymbol{u}}{\partial t} + (\boldsymbol{U}_0\cdot\nabla)\boldsymbol{u} = -\frac{1}{\rho_0}\nabla P + \frac{B_0}{4\pi\rho_0}(\nabla\times\boldsymbol{b})\times\boldsymbol{e}_\parallel, \tag{1.135}$$

$$\frac{\partial \rho'}{\partial t} + \boldsymbol{U}_0\cdot\nabla\rho' + \rho_0\nabla\cdot\boldsymbol{u} = 0. \tag{1.136}$$

Here the subscript $\perp$ denotes a direction, perpendicular to vector $\boldsymbol{B}_0$;

$$\nu_m = \frac{c^2}{4\pi\sigma}, \qquad \nu_{\text{eff}} = \frac{c^2}{4\pi\sigma_\perp^{\text{eff}}} \tag{1.137}$$

are the Coulomb magnetic diffusivity and the effective magnetic diffusivity, respectively, with the account of the neutral component. The quantity $\sigma_\perp^{\text{eff}}$ is given by (1.94), in which $B = B_0$. Note that the terms proportional to $(\nu_{\text{eff}} - \nu_m)$ can play a role of additional sources of the magnetic field due to the neutrals forming ν_{eff}. This apparently unexpected conclusion turns to be evident if we recall that the neutrals reduce the plasma conductivity and so the neutralization of an external current becomes less perfect and the residual electric current produces additional magnetic field; the mentioned terms drop out from Eq. (1.134) when the neutral component makes little contribution and so $\nu_{\text{eff}} = \nu_m$.

To make more lucid the complicated structure of Eq. (1.134), we rewrite it for a special case of an incompressible medium in a simplified geometry, when the plasma current $\boldsymbol{j}$ and the external current $\boldsymbol{j}^{\text{ext}}$ are directed transversely to the field $\boldsymbol{B}_0$:

$$\frac{\partial \boldsymbol{b}}{\partial t} + (\boldsymbol{U}_0 \cdot \nabla)\boldsymbol{b} = (\boldsymbol{B}_0 \cdot \nabla)\boldsymbol{u} + \nu_{\text{eff}}\Delta\boldsymbol{b} - \frac{c}{4\pi e n_i}(\boldsymbol{B}_0 \cdot \nabla)(\nabla \times \boldsymbol{b}) + \frac{4\pi\nu_{\text{eff}}}{c}\nabla \times \boldsymbol{j}^{\text{ext}} + \frac{1}{e n_i}(\boldsymbol{B}_0 \cdot \nabla)\boldsymbol{j}^{\text{ext}}. \tag{1.138}$$

This equation has the same form as that describing the magnetic field in fully ionized plasma, differing from it only by the value of effective magnetic diffusivity in place of Coulomb one. The ratio

$$\frac{\nu_{\text{eff}}}{\nu_m} = \frac{\sigma}{\sigma_\perp^{\text{eff}}} = 1 + \frac{F^2 B_0^2 \tau_{ia}\sigma}{n_i m_i c^2} = 1 + F^2(\omega_{\text{Bi}}\tau_{ia})(\omega_{\text{Be}}\tau_{ei}), \tag{1.139}$$

where $\omega_{\text{Bi},\,e} = eB_0/m_{i,\,e}c$ are the cyclotron frequencies, can be very large in many important cases (see Table 1.2), even when the number density of the neutrals is small. If $\nu_{\text{eff}}/\nu_m \gg 1$, the contribution of neutral component is highly significant.

The contribution of the Hall terms (i.e., the third and the fifth in the rhs of Eq. (1.138)) to Eq. (1.138) is defined by the ratio

$$\frac{cB_0}{4\pi e n_i \nu_{\text{eff}}} \approx \frac{1}{F^2\omega_{\text{Bi}}\tau_{ia}}. \tag{1.140}$$

For $F^2\omega_{\text{Bi}}\tau_{ia} \gg 1$ the Hall term plays a minor role. However, it prevails over all the remaining terms within the parameter regime defined by inequalities $\nu_{\text{eff}}/\nu_m \gg 1$ and $F^2\omega_{\text{Bi}}\tau_{ia} \ll 1$.

Dissipative processes lead to damping of mechanical motion and magnetic field and so increase the entropy. The damping may be characterized by the quantity Q, the power density of heat release, that is the dissipation of energy per unit volume over unit time. The dissipation consists of hydrodynamic and electromagnetic components. We consider here the latter one—the Joule's heat Q_{J}. If no external current is present, the change of the magnetic field energy, which can be explicitly derived from the Maxwell equations (with the use of differential equality $\nabla \cdot (\boldsymbol{E} \times \boldsymbol{B}) = \boldsymbol{B} \cdot (\nabla \times \boldsymbol{E}) - \boldsymbol{E} \cdot (\nabla \times \boldsymbol{B})$), has the form

$$\frac{\partial}{\partial t}\frac{B^2}{8\pi} = \frac{1}{4\pi}\boldsymbol{B} \cdot \frac{\partial \boldsymbol{B}}{\partial t} = -\frac{c}{4\pi}\boldsymbol{B} \cdot (\nabla \times \boldsymbol{E}) = -\nabla \cdot \boldsymbol{\gamma} - \boldsymbol{E} \cdot \boldsymbol{j}, \tag{1.141}$$

where $\boldsymbol{\gamma} = (c/4\pi)\boldsymbol{E} \times \boldsymbol{B}$ is the flux density of the electromagnetic energy. The heating of the medium is described by the last term, from which we have yet to subtract the mechanical work of Ampère's force:

$$Q_{\mathrm{J}} = \boldsymbol{E} \cdot \boldsymbol{j} - \frac{1}{c}(\boldsymbol{j} \times \boldsymbol{B}) \cdot \boldsymbol{u} = \boldsymbol{E}' \cdot \boldsymbol{j}, \qquad \boldsymbol{E}' = \boldsymbol{E} + \frac{1}{c}\boldsymbol{u} \times \boldsymbol{B}. \tag{1.142}$$

This result shows that the medium heating is determined by electric field $\boldsymbol{E}'$ and electric current $\boldsymbol{j}' \approx \boldsymbol{j}$ in the co-moving system. We, thus, obtain from (1.93)

$$Q_{\mathrm{J}} = \left(\frac{\boldsymbol{j}_{\parallel}}{\sigma} + \frac{B}{n_i e c}\boldsymbol{j} \times \boldsymbol{e}_{\parallel} + \frac{\boldsymbol{j}_{\perp}}{\sigma_{\perp}^{\mathrm{eff}}}\right) \cdot \boldsymbol{j} = \frac{j_{\parallel}^2}{\sigma} + \frac{j_{\perp}^2}{\sigma_{\perp}^{\mathrm{eff}}}. \tag{1.143}$$

If $\sigma_{\perp}^{\mathrm{eff}} \ll \sigma$, the dissipation of perpendicular current is very strong in comparison with parallel one. This effect is caused by ion collisions with neutral atoms. But if neutral atoms are absent, we have from (1.101) $\sigma_{\perp}^{\mathrm{eff}} = \sigma$ and in fully ionized plasma

$$Q_{\mathrm{J}} = \frac{j^2}{\sigma}. \tag{1.144}$$

We obtain an apparently unexpected result: the Joule's heat does not depend on the strong magnetic field. The trick is that the dissipation is caused by e-i collisions, whose rate depends on the particle number density and temperature but does not depend on the external magnetic field.

Another approach to describing a tenuous plasma in a strong magnetic field has been proposed by Chew et al. (1956): the **CGL approximation**. Specifically, they entirely neglect the Coulomb collisions and use the ion gyroradius for the particle mfp, which must be small compared with other available scales to render the hydrodynamic approximation valid. However, the gyromotion bounds the particle motion transverse to the magnetic field only, while not in the longitudinal direction. Thus, for the CGL approximation to

be valid, an extra condition is required that would reduce the third moment of the distribution function over velocity and bound pressure transfer along the magnetic field. If this is fulfilled, then the MHD set of equations receives the form (Chew et al. 1956):

$$\rho\frac{\mathrm{d}\boldsymbol{u}}{\mathrm{d}t} = \nabla\widehat{P} + \frac{1}{4\pi}(\nabla\times\boldsymbol{B})\times\boldsymbol{B} + \frac{1}{4\pi c^2}\left[\frac{\partial}{\partial t}(\boldsymbol{u}\times\boldsymbol{B})\times\boldsymbol{B}\right] + \frac{1}{4\pi c^2}(\boldsymbol{u}\times\boldsymbol{B})\nabla\cdot(\boldsymbol{u}\times\boldsymbol{B}), \tag{1.145a}$$

$$(\nabla\widehat{P})_\alpha = \nabla_\beta P_{\alpha\beta} = \nabla_\beta[P_\parallel e_\alpha^\parallel e_\beta^\parallel + P_\perp(\delta_{\alpha\beta} - e_\alpha^\parallel e_\beta^\parallel)], \tag{1.145b}$$

$$\frac{\partial\rho}{\partial t} + \nabla\cdot(\rho\boldsymbol{u}) = 0, \qquad \frac{\partial\boldsymbol{B}}{\partial t} = \nabla\times(\boldsymbol{u}\times\boldsymbol{B}), \tag{1.145c}$$

$$\frac{\mathrm{d}}{\mathrm{d}t}\left(\frac{P_\parallel B^2}{\rho^3}\right) = 0, \qquad \frac{\mathrm{d}}{\mathrm{d}t}\left(\frac{P_\perp}{\rho B}\right) = 0, \qquad \frac{\mathrm{d}}{\mathrm{d}t} = \frac{\partial}{\partial t} + (\boldsymbol{u}\cdot\nabla). \tag{1.145d}$$

No dissipative process is included, thus, the total energy W of the physical system considered is conserved:

$$W = \frac{1}{2}\int\left\{\rho u^2 + (2P_\perp + P_\parallel) + \frac{B^2}{4\pi} + \frac{1}{4\pi c^2}(\boldsymbol{u}\times\boldsymbol{B})\right\}\mathrm{d}^3 r = \text{const}. \tag{1.146}$$

Noteworthy, this approach allows an anisotropy of the kinetic pressure due to overall system anisotropy driven by the strong magnetic field.

1.3.7 Dissipative Kinetic Coefficients

We make now approximate analytical estimates and evaluations of basic kinetic coefficients in the set of above equations following mainly the reviews by Brandenburg and Subramanian (2005) and Bykov and Toptygin (2007).

Consider the Coulomb magnetic diffusivity formed by electron–ion collisions. For single-charged ions considered here the Coulomb cross section can be approximated by

$$\sigma_{ei} \approx \pi\left(\frac{e^2}{m_e v_e^2}\right)^2 \ln\Lambda_\mathrm{C}, \tag{1.147}$$

where $\ln\Lambda_\mathrm{C} = 5 - 20 = \text{const}$ is the Coulomb logarithm. This quantity defines relative role of "distant" collisions (with small angles of deflections). For thermal particles $m_e v_e^2 \approx T$.

Characteristic time between collisions is estimated as

$$\tau_{ei} \approx \frac{1}{n_i\sigma_{ei}v_{Te}} \approx \frac{T^{3/2}m_e^{1/2}}{\pi e^4 n_i \ln\Lambda_\mathrm{C}}; \tag{1.148}$$

thus, Eq. (1.91) applied to the case of the Coulomb collisions between electrons and ions yields a so-called **Spitzer conductivity**

$$\sigma = \sigma_\mathrm{S} = \frac{e^2 n_e \tau_{ei}}{m_e} \approx \frac{T^{3/2}}{\pi e^2 m_e^{1/2}\ln\Lambda_\mathrm{C}}, \tag{1.149}$$

which depends on the particle number density very weakly—only via $\ln \Lambda_C$. More exact calculation (Lifshitz and Pitaevskii 1981) leads to a numeric coefficient 0.6 instead of $1/\pi$ in Eq. (1.149). It is easy now to find the magnetic diffusivity, $\nu_m = c^2/4\pi\sigma$. For astrophysical applications it is often convenient to present such formulae in "natural" units, which gives an immediate idea about the order of magnitude of the involved measure. Substitution of the required constants and typical parameters into (1.149) then yields (Brandenburg and Subramanian 2005)

$$\nu_m \approx 10^4 \left(\frac{T}{10^6\mathrm{K}}\right)^{-3/2} \frac{\ln \Lambda_C}{20}\ \mathrm{cm^2 s^{-1}}. \tag{1.150}$$

The kinematic viscosity is caused by the momentum transfer, where ions (and neutral atoms, if present) play an important role. Therefore, the coefficient ν, related to the Coulomb collisions, may be estimated as

$$\nu \approx v_{Ti} l_{ii} \approx \frac{v_{Ti}}{n_i \sigma_{ii}} \approx \frac{T^{5/2}}{\pi n_i m_i^{1/2} e^4 \ln \Lambda_C}. \tag{1.151}$$

Here $l_{ii} \approx 1/n_i\sigma_{ii}$ is the mean free path between ion collisions and σ_{ii} is given by expression (1.147) with change of $m_e v_{Te}^2 \approx T$ by $m_i v_{Ti}^2 \approx T$.

Lifshitz and Pitaevskii (1981) perform more precise calculations and find a slightly different numerical coefficient of 0.4 instead of $1/\pi$ in Eq. (1.151); Brandenburg and Subramanian (2005) present this expression in the following convenient "astrophysical" form:

$$\nu \approx 6.5 \times 10^{22} \left(\frac{T}{10^6\mathrm{K}}\right)^{5/2} \left(\frac{n_i}{1\ \mathrm{cm^{-3}}}\right)^{-1} \frac{20}{\ln \Lambda_C}\ \mathrm{cm^2 s^{-1}}. \tag{1.152}$$

For completeness, using Eqs. (1.73), (1.123), and (1.148), let us present in a similar form the thermal (heat) conductivity coefficient χ

$$\chi \approx 9 \times 10^8 \left(\frac{T}{10^6\mathrm{K}}\right)^{5/2} \frac{20}{\ln \Lambda_C}\ \mathrm{erg\ cm^{-1} s^{-1}\ K^{-1}} \tag{1.153}$$

and, taking into account that for the fully ionized hydrogen ideal gas $c_p\rho = 5k_B n_e$, where $c_p = 2\gamma k_B/[(\gamma-1)m_p]$ erg/g·K is the specific heat and ρ is the mass density, the thermal diffusivity coefficient $\kappa = \chi/(c_p\rho)$

$$\kappa \approx 1.3 \times 10^{24} \left(\frac{T}{10^6\mathrm{K}}\right)^{5/2} \left(\frac{n_e}{1\ \mathrm{cm^{-3}}}\right)^{-1} \frac{20}{\ln \Lambda_C}\ \mathrm{cm^2 s^{-1}}. \tag{1.154}$$

The mean collision time of charged particles with the neutrals can be estimated as

$$\tau_{ia} \approx \frac{1}{n_a \sigma_{ia} v_{Ti}}, \qquad \tau_{ea} \approx \frac{1}{n_a \sigma_{ea} v_{Te}}, \tag{1.155}$$

where $\sigma_{ia} \approx \sigma_{ea} \lesssim 10^{-14}$ cm^2. The results of calculation for some typical cases are given in Table 1.2.

As is clear from Table 1.2, in all the cases considered, except for the solar photosphere, the contribution of the neutral component is quite significant even when the fraction of neutral atoms is smaller than that indicated in the table. This is highly significant for many applications including particle acceleration processes near the shock fronts, where the degree of ionization may be enhanced due to heating of the medium. Important role of neutral component in many electromagnetic processes in Galaxy was noted by Piddington (1954), Cowling (1957) and Pikel'ner (1966).

1.3.8 Collisionless Plasma

A plasma can be consistently considered as collisionless if frequency ω of analyzed processes is large compared with the collision frequencies ν_{ab} of plasma particles, while wavelength λ is small compared with the mean free paths Λ_{ab} of the plasma particles:

$$\omega \gg \nu_{ab}, \qquad \lambda \ll \Lambda_{ab}, \tag{1.156}$$

which is opposite to inequalities (1.63). Under conditions (1.156) we can discard the collision integral $St(f_a, f_b)$ in Eq. (1.61) and use the collisionless kinetic equation:

$$\frac{\partial f_a}{\partial t} + \boldsymbol{v} \cdot \frac{\partial f_a}{\partial \boldsymbol{r}} + \boldsymbol{\mathcal{F}}_a \cdot \frac{\partial f_a}{\partial \boldsymbol{p}} = 0 \tag{1.157}$$

(superscript (1) of the function $f_a^{(1)}$ is omitted here for brevity). This equation in application to fully ionized plasma is called the Vlasov equation. Along with Maxwell equations (1.53) it allows describing the electromagnetic phenomena in collisionless plasma in approximation of *self-consistent electromagnetic field*. Macroscopic parameters can, thus, be calculated with the distribution function and expressions (1.65).

Equilibrium Distribution Function of Collisionless Plasmas

Apparently, to apply those equations we have to specify the steady-state distribution function of the collisionless plasma. Recall, that in the collisional case, we obtain the **Maxwellian distribution** function from requirement of vanishing the binary Boltzmann collision integral in the equilibrium. In the collisionless case, however, this consideration does not necessarily apply because no collision integral enters the rhs of Eq. (1.157). Thus, there is no unique solution for the steady-state distribution function of the collisionless plasma.

Table 1.2: Plasma parameters and dissipative kinetic coefficients

Object	B_0 G	n_a cm^{-3}	n_i cm^{-3}	F	T K	Λ_{ia} cm	ν_m $\mathrm{cm}^2\mathrm{s}^{-1}$	ν_{eff} $\mathrm{cm}^2\mathrm{s}^{-1}$	ν $\mathrm{cm}^2\mathrm{s}^{-1}$
Neutral clouds	1.5×10^{-5}	20	0.05	≈ 1	100	5×10^{12}	5×10^{9}	10^{21}	6.5×10^{18}
Intercloud warm medium	2×10^{-6}	0.2	0.03	0.85	10^4	5×10^{14}	5×10^{6}	2.5×10^{20}	6.5×10^{11}
Solar photosphere	1.0	10^{16}	10^{13}	≈ 1	6×10^3	1×10^{-2}	$\times 10^7$	10^7	4×10^4
Cosmological medium ($z<1$)	10^{-9}	5×10^{-9}	4×10^{-5}	10^{-4}	10^4	2×10^{22}	5×10^{6}	5×10^{15}	3×10^{22}
Terrestrial ionosphere	1.0	2×10^8	10^6	≈ 1	10^3	5×10^5	10^8	5×10^{15}	4×10^9

One possibility is a plasma, which is only slightly collisionless, or collisionless for a given high-frequency process, while collisional for other essential processes (typically—lower frequency phenomena). Clearly, for such cases, the equilibrium distribution is still Maxwellian to which the plasma returns over a corresponding relaxation time after a perturbation.

But what if the plasma is "truly" collisionless—i.e., the collisional relaxation time is much longer than *any* competing characteristic time of interests, including, perhaps, the system lifetime? Will the Maxwellian distribution still remain relevant to this plasma? A general answer to this question is "NO" since the Maxwellian distribution does not represent a unique steady-state solution of the collisionless kinetic equation (although it is still a solution).

Another approach to derive the steady-state distribution is a maximization of the system entropy based on the second law of thermodynamics. Classical statistics tells us that the entropy

$$S_1 = -k_{\mathrm{B}} \sum_i p_i \ln p_i, \tag{1.158}$$

where p_i is a probability for a system to occupy a state i, k_{B} is the Boltzmann constant, is an extensive measure, i.e., the entropy of the whole system adds up of the entropies of its macroscopic constituents:

$$S_1(A+B) = S_1(A) + S_1(B). \tag{1.159}$$

Maximizing the classical entropy leads again to the Maxwellian distribution.

However, the extensivity of the entropy is based on the idea that the energy dissipation is a local process involving binary interaction of neighboring particles, but no distant interaction or correlation is involved. In collisionless plasma the situation can be essentially different: since the true collisions between particles are negligible, all the interactions are mediated by electromagnetic waves excited in the plasma self-consistently. Thus, long-distance and collective interactions and correlations may become crucial, leading to the necessity of a *non-extensive* statistics for the collisionless plasma.

One version of the non-extensive statistics is based on the Tsallis entropy concept (Hasegawa et al. 1985; Tsallis 1999; Leubner 2004; Hasegawa 2006; Treumann and Jaroschek 2008; Tsallis 2009). In place of classical entropy (1.159), a modified non-extensive expression

$$S_q(A+B) = S_q(A) + S_q(B) + (1-q) S_q(A) S_q(B) \tag{1.160}$$

is introduced leading to a generalized Tsallis entropy

$$S_q = k_B \frac{1 - \sum_i p_i^q}{1-q}, \tag{1.161}$$

where q is a measure of the system non-extensivity; a special case of $q = 1$ yields the classical entropy S_1.

It can be demonstrated (see Problem 1.12) that maximization of the Tsallis entropy leads to a so-called *kappa* distribution (which is given below in a form applicable for both nonrelativistic and relativistic plasmas)

$$N(\gamma)\mathrm{d}\gamma = A_{\mathrm{norm}} \frac{\gamma\sqrt{\gamma^2-1}}{\theta^{3/2}\left(1+\frac{\gamma-1}{(\kappa-3/2)\theta}\right)^{\kappa+1}}\mathrm{d}\gamma; \quad \gamma = \frac{\mathcal{E}}{mc^2}; \quad \int N(\gamma)\mathrm{d}\gamma = n_{\mathrm{tot}}, \tag{1.162}$$

where $\kappa = 1/(1-q)$, A_{norm} is the normalization factor providing that n_{tot} is the number density of a given sort of the particles, in place of the Maxwellian distribution. When $\kappa \to \infty$, the kappa distribution transforms to the Maxwellian distribution with temperature $k_B T = mc^2\theta$, while for small κ the distribution consists of a quasi-Maxwellian core smoothly merged to a quasi-power-law tail, whose hardness is determined by the κ value.

Although no full understanding of the status of the non-extensive statistics in general and non-Maxwellian steady-state distributions in particular has yet been established, we emphasize that this problem is highly important for modern astrophysics and has potentially far-reaching consequences, e.g., for theories of particle acceleration, transport, and electromagnetic emission.

In particular, routine in situ measurements of the distribution functions in the solar wind (see Sect. 2.5.1) reveal the kappa distributions even during the most quiet periods of the solar wind state. The measured index κ is not unique and different for the regions of the slow and fast wind, which raises a fundamental question of what plasma processes and parameters control the shape of the steady-state distribution in collisionless plasmas.

Furthermore, in the presence of an external magnetic field, the steady-state distribution can be anisotropic, so Eq. (1.65c) requires a correction. As a result of the anisotropy, the temperature and the pressure of collisionless plasma become anisotropic relative to the magnetic field: $T_\parallel \neq T_\perp$, $P_\parallel \neq P_\perp$. In this case the pressure tensor $P_{\alpha\beta}$ has the form

$$P_{\alpha\beta} = P_\perp \delta_{\alpha\beta} + (P_\parallel - P_\perp) e_\alpha e_\beta, \tag{1.163}$$

where $\boldsymbol{e} = \boldsymbol{B}/B$.

If the magnetic field is strong enough for the gyrofrequency $\omega_{Ba} = eB/m_a c$ to be much larger than the frequency of the process under consideration and for the Larmor radius $r_{ga} = cp_a/eB$ of the particle to be small compared with the typical scale over which the magnetic field changes, then the equations can be averaged over the particle's fast rotation in the magnetic field in a way similar to that applied to a single-particle motion in Sect. 1.2.2. This averaging yields the guiding center approximation (drift approximation), which is described in more detail, e.g., in Sect. 7.5 and by Sivukhin (1965) and Kulsrud (1983).

Transfer Processes Mediated by Turbulence (Anomalous Processes)

It is necessary to bear in mind that numerous sources of energy are present in cosmic medium. They excite plasma instabilities and generate stochastic (turbulent) electromagnetic fields of different scales. Macroscopic random electromagnetic fields may scatter charged particles and lead to their random wandering. In such a case Eq. (1.157) cannot be used directly, if stochastic fields are present, because the force $\boldsymbol{\mathcal{F}}$ becomes a stochastic quantity, so only statistical measures make sense. Therefore, Eq. (1.157) must be averaged over the realizations of the turbulent fields. As a result of averaging, Eq. (1.157) receives a form with an effective nonbinary "collision integral" which is eventually provided by the stochastic electromagnetic fluctuations in place of true collisions.

Such statistical approach is especially important and valuable for the description of superthermal, including relativistic, cosmic plasma component (cosmic rays). The motion of fast charged particles in a cosmic plasma depends strongly on the magnetic and electric fields. The energy of cosmic ray particles considerably exceeds that of thermal particles, so that Coulomb collisions with a thermal plasma can be neglected as we have already pointed out in Sect. 1.3.3. The interaction of cosmic rays with magnetic fields depends essentially on the relation between the energy densities of the cosmic rays and the thermal plasma. If the energy density of the cosmic rays is small then the back reaction of the cosmic rays on the plasma can be neglected in the first approximation, and one can consider the diffusion of fast particles in specified regular and stochastic fields. The evolution of cosmic rays can be described by a one-particle distribution function $f(\boldsymbol{r}, \boldsymbol{p}, t)$, satisfying (1.157).

In some cases (e.g., when the particles are accelerated by strong shocks), the energy density of cosmic rays can reach the energy density of hydromagnetic motion and thermal plasmas. In this situation, one should take into account the back-reaction of the cosmic rays on the thermal plasma, which is usually done by means of the hydrodynamic approximation. It is often necessary to take into account the gradient of energetic particles pressure and the Ampère force, created by electric current produced by the energetic particles as well as numerous kinetic and MHD instabilities giving rise to ensembles of the plasma eigen-waves, which in their turn can affect the distribution of the charged particles via anomalous (i.e., non-collisional) transfer processes.

Problems

1.1 Plot trajectories of relativistic charged particle moving in uniform electric, magnetic, and crossed fields; see Sect. 1.2.1. Consider various initial conditions.

1.2 A charged particle moves in a uniform magnetic field $\boldsymbol{B}$. Plot projections of its trajectory onto the planes $(\boldsymbol{p}_{0\perp}, \boldsymbol{e}_{\parallel})$, $(\boldsymbol{p}_{0\perp} \times \boldsymbol{e}_{\parallel}), \boldsymbol{e}_{\parallel}$, and $(\boldsymbol{p}_{0\perp}, \boldsymbol{p}_{0\perp} \times \boldsymbol{e}_{\parallel})$.

1.3 Make similar plots of trajectory projections for a particle moving in crossed uniform fields $\boldsymbol{E} \perp \boldsymbol{B}$, $E \ll B$. Consider various ratios between the initial particle velocity $\boldsymbol{v}_0 = c^2 \boldsymbol{p}_0 / \mathcal{E}_0$ and its drift velocity $\boldsymbol{v}_E$.

1.4 Analyze cases of charged particle motion in presence of $\boldsymbol{E} \perp \boldsymbol{B}$ and $E \geq B$. Show that the relation $E = B$ is carried out in all inertial reference frames. Show that if $E > B$, the particle is accelerated unlimitedly and its velocity approaches the velocity of light c.

1.5 Show by direct calculation that the quantity $p_\perp^2 / B$ is an adiabatic invariant for the case of a magnetic field $B(t)$ which is uniform and constant in direction, but with a magnitude that varies slowly. To do so evaluate the electric field and integrate the equation describing variation of the transverse particle momentum $p_\perp$ with time, assuming that during a single cyclotron period the particle trajectory can be considered to be a circle coinciding with the electric field lines.

1.6 A system of identical noninteracting particles is in a uniform magnetic field B and has an isotropic momentum distribution. All particles have the same energy $\mathcal{E}_0$. Afterwards the magnetic field increases adiabatically to a magnitude nB. Find the angular distribution $\mathrm{d}w(\vartheta)$ and the mean square of the particle energy $\overline{\mathcal{E}^2}$ in the final state.

1.7 Use the fact that the quantity $I = p_\perp^2 / B$ is invariant to prove that in drift approximation the magnetic flux through the orbit of the cyclotron rotation of the particle as well as the magnetic moment of a *nonrelativistic* particle that is produced by its cyclotron rotation are conserved. What additional conditions are necessary for the magnetic moment of a *relativistic* particle to be conserved?

1.8 A particle moves in a weakly nonuniform constant magnetic field. By using the fact that the quantity $I = p_\perp^2 / B$ is invariant and the energy conservation law, show that in the drift approximation a force $\boldsymbol{\mathcal{F}}$ acts upon the particle in the direction of the magnetic field lines, and find the magnitude of the force. Express it in terms of the magnetic moment of the cyclotron rotation of the particle.

1.9 The Earth's magnetic field in a certain volume around the Earth (in which the solar wind effect is negligible) can be approximated by the field of a point dipole with magnetic moment $\mu = 8.1 \times 10^{15}$ [T m^3]$= 8.1 \times 10^{25}$ [G cm^3]. A proton with kinetic energy $K = 50\,\mathrm{MeV}$ moves at a given time through the plane of the magnetic equator at a distance of two Earth radii from the

center of the Earth at right angles to the magnetic lines of force. Find the motion of the guiding center of the proton in the drift approximation. After what time τ will it perform a full turn around the Earth? What is the Larmor radius r_g of the proton? The Earth's radius is $r_* = 6,380\,\mathrm{km}$ and its mass $M = 6 \times 10^{24}\,\mathrm{kg}$.

1.10 A proton is in the plane of the geomagnetic equator (see the previous problem) at a distance r from the center of the Earth and its momentum makes an angle α with the direction of the magnetic field lines.

(a) Neglecting the gravitational field show that the guiding center of the proton will not only move along the magnetic lines of force but will also undergo an azimuthal drift. Find the angular drift velocity ω_d, and express it in terms of r and the geomagnetic latitude λ.

(b) Find the value of geomagnetic latitude λ_m corresponding to the mirror points where the particles are reflected in the Earth's magnetic field.

(c) Find conditions under which the proton can precipitate on the Earth's surface.

1.11 Obtain Maxwellian distribution for collisional plasma from kinetic equation with the collisional integral in the Boltzmann form.

1.12 Obtain kappa distribution for collisionless plasma from maximizing the Tsallis entropy.

1.13 Runaway Electrons. Electrons in a fully ionized plasma participate in the random thermal motion and have a regular flow velocity due to external uniform electric field $\boldsymbol{E}$. Using approximate approach employed in Sect. 1.3.7 evaluate dependence of the mean drag force $\overline{\boldsymbol{\mathcal{F}}}$ on the flow velocity $\boldsymbol{u}$ assuming that the friction is produced by electron collisions with immobile ions. Demonstrate that the force $\overline{\boldsymbol{\mathcal{F}}}$ has a maximum as a function of u and estimate this maximum $\overline{\boldsymbol{\mathcal{F}}}_{\max}$. How the electron gas behaves in electric field E depending on either $E < \overline{\boldsymbol{\mathcal{F}}}_{\max}/e$ or $E > \overline{\boldsymbol{\mathcal{F}}}_{\max}/e$?

Answers and Solutions

1.4 If $E = B$, the equality $E' = B'$ follows from relativistic invariants (1.21). If $E > B$, a reference frame exist, in which $B' = 0$, $E' \neq 0$. This system moves with velocity $\boldsymbol{V} = \boldsymbol{E} \times \boldsymbol{B}/cE^2$. The particle is accelerated unlimitedly in this system. According to (1.27), unlimited acceleration takes also place in the initial (laboratory) system.

1.6 $\mathrm{d}w(\vartheta) = \dfrac{n^{1/2}\sin\vartheta \mathrm{d}\vartheta}{2[1+(n-1)\cos^2\vartheta]^{3/2}}, \qquad \overline{\mathcal{E}^2} = \dfrac{2n+1}{3}\mathcal{E}_0^2 - \dfrac{2(n-1)}{3}m^2c^4.$
In the nonrelativistic case for the average kinetic energy $\overline{T}$ in the final state we have $\overline{T} = (2n+1)T_0/3, \qquad T_0 = p_0^2/2m.$

1.7 The quantity $\gamma\mu$ is the adiabatic invariant for a relativistic particle, where $\gamma = \sqrt{1-v^2/c^2}$ and $\mu = p_\perp v_\perp/2B$ is the magnetic moment. If the kinetic energy of the particle is conserved, we have $\gamma = \text{const}$ and so $\mu = \text{const}$. The later relation is satisfied for a nonrelativistic particle, for which $\gamma \approx 1$, even when its energy is not conserved.

1.8 $\mathcal{F} = -(\boldsymbol{\mu}\cdot\nabla B)$, where $\boldsymbol{\mu} = \boldsymbol{e}_\parallel p_\perp v_\perp/2B$ is the magnetic moment produced by the rotation of the particle.

1.9 Only gradient and gravitational drifts exist under conditions considered. Gravitational drift is very small: $GmM/3Kr < 10^{-8}$. The guiding center of a proton moves uniformly along a circle of radius $r = 2r_*$ which lies in the equatorial plane. The angular velocity is

$$\omega_d = \frac{3cKr}{e\mu} - \frac{GmMc}{e\mu},$$

where G is the gravitational constant; $\omega_d \approx 0.24\,\text{rad/s}$, $r_g \approx 260\,\text{km}$, and $T \approx 26\,\text{s}$.

1.10 (a) If we evaluate the products $\boldsymbol{e}_\parallel \times \nabla B$ and $\boldsymbol{e}_\parallel \times (\boldsymbol{e}_\parallel\cdot\nabla)\boldsymbol{e}_\parallel$ for the field of a magnetic dipole, we find from Eq. (1.39) that motion across the magnetic field lines reduces to azimuthal drift for which the distance from the Earth's center and the latitudinal angle are specified by the guiding center motion along the line of force, the equation of which is $r = r_0\cos^2\lambda$, where r_0 is the distance in the equatorial plane of the line of force to the center. As we neglect the gravitational field the particle energy remains constant.

On using the well-known expressions for the field strength of a magnetic dipole and also Eqs. (1.39) and (1.46) we find the angular velocity of the azimuthal drift:

$$\omega_d = \frac{(\boldsymbol{v}_d)_\phi}{r} = -\frac{3cpvr_0\sin^2\phi(1+\sin^2\lambda)}{2e\mu\cos^2\lambda(1+3\sin^2\lambda)} - \frac{cpvr_0\cos^3\lambda(3\sin^2\lambda-1)}{e\mu(1+3\sin^2\lambda)},$$

where p and v are the proton momentum and velocity.
(b) By using Eq. (1.46), we find the condition determining $\lambda_m > 0$:

$$\frac{\cos^6\lambda_m}{(1+3\sin^2\lambda_m)^{1/2}} = \sin^2\alpha.$$

The particles move in the region $-\lambda_m \le \lambda \le \lambda_m$.
(c) The proton will reach the Earth's surface provided $r_0\cos^2\lambda_m \le r_*$, where r_* is the radius of the Earth's sphere.

1.11 If the equilibrium state is achieved due to binary collisions between gas particles, the kinetic equation can be written in the Boltzmann form $\mathrm{d}f/\mathrm{d}t = St\, f$, where $\mathrm{d}f/\mathrm{d}t$ is the full derivative over time and $St\, f = \int w(f(\boldsymbol{p}')f(\boldsymbol{p}_1') - f(\boldsymbol{p})f_1(\boldsymbol{p}_1))\mathrm{d}\boldsymbol{p}_1\mathrm{d}\boldsymbol{p}'\mathrm{d}\boldsymbol{p}_1'$ is the binary collisional Boltzmann integral, where w is the corresponding collision probability. In the equilibrium $\mathrm{d}f/\mathrm{d}t = 0$, so the collisional integral must also vanish, i.e., we require $f(\boldsymbol{p}')f(\boldsymbol{p}_1') = f(\boldsymbol{p})f_1(\boldsymbol{p}_1)$, i.e., $\ln f(\boldsymbol{p}') + \ln f(\boldsymbol{p}_1') = \ln f(\boldsymbol{p}) + \ln f_1(\boldsymbol{p}_1)$. Combining this condition with the energy conservation at a collision, $\mathcal{E}' + \mathcal{E}_1' = \mathcal{E} + \mathcal{E}_1$, we conclude that $\ln f(\boldsymbol{p}) \propto \mathcal{E}$ and, thus, $f(\boldsymbol{p}) \propto \exp(-\mathcal{E}(\boldsymbol{p})/\mathcal{E}_0)$. The minus sign is needed to avoid divergence at the infinity. The constant $\mathcal{E}_0$ is a characteristic energy of the considered gas, which is proportional to its temperature; the pre-exponential coefficient can be determined from normalization.

1.12 Study papers (Leubner 2004; Hasegawa 2006; Treumann and Jaroschek 2008; Tsallis 2009).

1.13 The mean collision time τ_{ei} is the mean time of the electron flow momentum loss due to collisions with ions; thus, the mean friction force can be estimated as

$$\overline{\mathcal{F}} = \frac{m_e v_e}{\tau_{ei}}, \qquad \tau_{ei} = \frac{1}{n_i \sigma_{ei} v_e} \tag{1}$$

Using Eq. (1.147) for the Coulomb cross section σ_{ei} we find (the minus sign reflects the braking nature of this force)

$$\boldsymbol{\mathcal{F}} = -\frac{\pi e^4 n_i \Lambda_\mathrm{C}}{m_e} \frac{\boldsymbol{v}_e}{v_e^3}. \tag{2}$$

A remarkable property of this Coulomb friction is its decrease with the velocity increase (decreasing friction).

Let us average Eq. (2) over all possible electron velocities. To do so we adopt $\boldsymbol{v}_e = \boldsymbol{u} + \boldsymbol{v}_T$, where $\boldsymbol{v}_T$ is the thermal (random) speed, while $\boldsymbol{u}$ is a flow velocity acquired due to the electric field. If $u \ll v_T$ we can adopt $v_e^3 \approx v_T^3$ in the denominator of Eq. (2). In the numerator, however, we cannot discard $\boldsymbol{u}$ compared with $\overline{\boldsymbol{v}}_T = 0$. Thus, we obtain

$$\overline{\boldsymbol{\mathcal{F}}} = -\frac{\pi e^4 n_i \Lambda_\mathrm{C}}{m_e} \frac{\boldsymbol{u}}{v_T^3} \sim \boldsymbol{u}, \tag{3}$$

where the thermal speed is $v_T^2 \approx T/m_e$.

For $u \gg v_T$ we can discard the thermal velocity everywhere so $v_e \approx u$ to obtain

$$\overline{\boldsymbol{\mathcal{F}}} = -\frac{\pi e^4 n_i \Lambda_\mathrm{C}}{m_e} \frac{\boldsymbol{u}}{u^3}, \qquad \overline{\mathcal{F}} \sim 1/u^2. \tag{4}$$

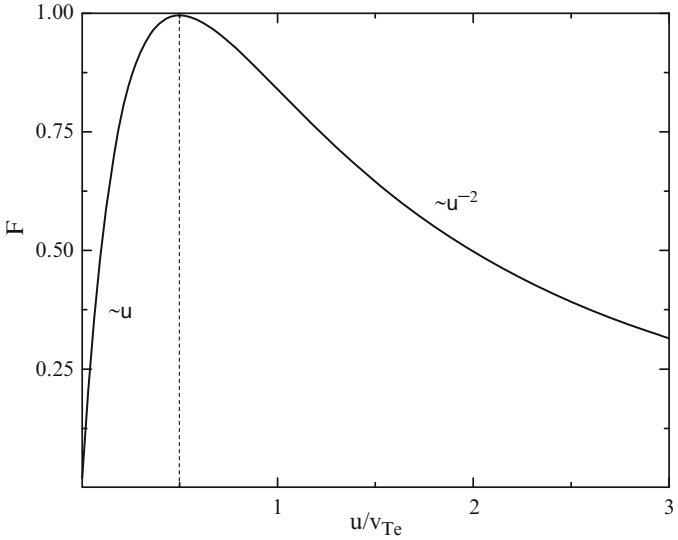

Figure 1.8: Dependence of the Coulomb friction force $F = \mathcal{F}/\mathcal{F}_{\max}$ on the charged particle flow velocity u/v_{Te} illustrating the phenomenon of runaway electrons.

Therefore, the force reaches a maximum at $u \approx v_T$, where both Eqs. (3) and (4) give an estimate of the same order of magnitude:

$$\overline{\mathcal{F}}_{\max} \approx \frac{\pi e^4 n_i \Lambda_C}{m_e v_T^2}. \tag{5}$$

Approximate shape of the function $\overline{\mathcal{F}}(u)$ is given in Fig. 1.8.

If the electric field applied to the plasma is somewhat small, $E < E_D = \overline{\mathcal{F}}_{\max}/e$, then the drag force exceeds the accelerating electric force eE at some u so no further acceleration will happen and standard Ohm's law will be valid. In the opposite case, $E > E_D$, the accelerating electric force exceeds the drag force all the way; thus, the electrons can be infinitely accelerated. This phenomenon is commonly called the **runaway electrons**. Estimate of the critical electric field (**Dreicer field**) demarcating the regimes of Ohm's law and runaway electrons can be written in the form

$$E_D \approx \frac{e\Lambda_C}{4r_D^2}, \qquad \text{where} \quad r_D = \sqrt{\frac{T}{4\pi n_i e^2}} \tag{6}$$

is the Debye radius. It should be noted that even for a "sub-Dreicer" field $E < E_D$ some fraction of electrons from a distribution tail having velocity higher than the thermal velocity, $v > v_T\sqrt{E_D/E}$, can be accelerated and form a runaway population. It should be noted, however, that a strong

electric current implied by presence of a significant runaway population is almost certainly unstable (see Chap. 4 and Sect. 7.1); it generates various waves and oscillations, which form "anomalous resistivity" quenching this regular electron acceleration at some stage.

Chapter 2

Magnetohydrodynamics of the Cosmic Plasma

2.1 Hydrodynamic Equations of the Neutral Gas

Table 1.1 shows that the cosmic media can have very different properties as their parameters vary within exceptionally broad ranges. In particular, the gas ionization can vary from almost zero (neutral media, e.g., clouds of cold neutral hydrogen) to almost unity (fully ionized plasma). It is worthwhile, therefore, to start with a simpler case of equation set for the neutral gas. We assume that the reader is familiar with the hydrodynamics (HD) fundamentals, so we just remind the equations and briefly discuss the meaning of the terms entering them without going into the detail too deeply. The relation of HD to the kinetic theory has been outlined in Sect. 1.3.

Two basic HD equations (see Sect. 1.3.3) are the continuity equation

$$\frac{\partial \rho}{\partial t} + \nabla \cdot \rho \boldsymbol{u} = 0 \tag{2.1}$$

and equation of motion

$$\rho \left(\frac{\partial \boldsymbol{u}}{\partial t} + (\boldsymbol{u} \cdot \nabla) \boldsymbol{u} \right) = -\nabla p + \boldsymbol{f} + \eta \Delta \boldsymbol{u} + \frac{\eta}{3} \nabla (\nabla \cdot \boldsymbol{u}), \tag{2.2}$$

where $\rho(\boldsymbol{r}, t)$ is the *mass density*, $\boldsymbol{u}(\boldsymbol{r}, t)$ is the macroscopic *velocity*, $\boldsymbol{f}$ is the *volume force* applied to the medium (e.g., gravitation force), and p is the gas pressure. Everywhere below we will consider "simple" media, which can be correctly described by a single viscosity coefficient, η. In case of "complex" media composed of the particles with essential role of the internal degrees of freedom, e.g., dust particles, a so-called second viscosity (Landau and Lifshitz 1966) may come into play; very few papers consider this effect in the astrophysics context, so we entirely neglect the second viscosity in this book. If the usual (first) viscosity is also neglected, Eq. (2.2) reduces to **Euler**

G.D. Fleishman and I.N. Toptygin, *Cosmic Electrodynamics*, Astrophysics and Space Science Library 388, DOI 10.1007/978-1-4614-5782-4_2,

equation (2.7b); see below. If the liquid is incompressible, $\rho = \text{const}$, and so $\nabla{\cdot}\boldsymbol{u} = 0$, then the last term in Eq. (2.2) drops out from the equation and it reduces to the **Navier–Stokes equation**. These equations must be complemented by the equation of state

$$p = p(\rho, s), \tag{2.3}$$

where s is the **specific entropy** (entropy per unit mass); hereafter we call it **entropy** for brevity.

When energy dissipation occurs in the gas studied, the entropy increases, which is described by the equation

$$\rho T \left(\frac{\partial s}{\partial t} + (\boldsymbol{u}{\cdot}\nabla) s \right) = \Pi_{\alpha\beta} \nabla_\beta u_\alpha + \nabla \cdot (\chi \nabla T), \tag{2.4}$$

where

$$\Pi_{\alpha\beta} = \eta \left(\frac{\partial u_\alpha}{\partial x_\beta} + \frac{\partial u_\beta}{\partial x_\alpha} - \frac{2}{3} (\nabla{\cdot}\boldsymbol{u}) \delta_{\alpha\beta} \right) \tag{2.5}$$

is the **tensor of viscous tensions** [cf. Eq. (1.72)] and T is the **temperature** in energy units. The specific entropy s has the dimension of reverse mass; thus, the full entropy of the entire physical system $S = \int \rho s \, \mathrm{d}V$ is dimensionless. If the temperature is measured in Kelvin [K], the full entropy must be multiplied by Boltzmann constant $k_\mathrm{B} \approx 1.38 \times 10^{-23}\,\mathrm{J/K} \approx 1.38 \times 10^{-16}\,\mathrm{erg/K}$. Here the coefficient of the **dynamic viscosity** η and coefficient of the **heat conductivity** χ are assumed to be known. In principle, these coefficients can be calculated within the physics kinetics; see Sect. 1.3.7, where these coefficients are estimated for a collisional plasma.

For closure of equation set (2.1)–(2.5) we must either express the temperature $T(\rho, s)$ via the density and the entropy or express the entropy $s(\rho, T)$ via the density and the temperature by using thermodynamic relations and the equation of state, then the number of equations becomes equal to the number of unknowns. In practice, however, the thermodynamic relations are unknown for an arbitrary medium. Nevertheless, for the tenuous gas considered here, the approximation of rarefied ("ideal") gas is sufficient for most of the practical applications.

2.1.1 General Properties

Let us discuss some global properties of the HD equations. Set of equations (2.1)–(2.5) is nonlinear in a general case and so very complicated. To obtain an analytical solution of the equations requires some simplifying assumptions and approximations to be made. One of the approximations frequently used in the astrophysical studies is the approximation of *ideal HD*, when the dissipative processes can be discarded. The applicability of this approximation

is not guarantied and so must be justified in each given case. A necessary condition for the ideal HD to work is the inequality

$$R = \frac{ul}{\nu} \gg 1, \tag{2.6}$$

where u is the typical velocity value, l is the characteristic scale of the velocity variation, and $\nu \equiv \eta/\rho$ is the kinematic viscosity. The dimensionless parameter R is called the **Reynolds number**; it plays a very important role in HD.

If inequality (2.6) is fulfilled and the temperature gradient is small or evanescent, then we can completely neglect the dissipative terms in Eqs. (2.1)–(2.5). Apparently, the entropy is constant in this case, while the set of HD equations simplifies to the form:

$$\frac{\partial \rho}{\partial t} + \nabla(\rho \boldsymbol{u}) = 0, \tag{2.7a}$$

$$\frac{\partial \boldsymbol{u}}{\partial t} + (\boldsymbol{u}\cdot\nabla)\boldsymbol{u} = -\frac{1}{\rho}\nabla p + \frac{1}{\rho}\boldsymbol{f}, \tag{2.7b}$$

$$\frac{\mathrm{d}s}{\mathrm{d}t} \equiv \frac{\partial s}{\partial t} + (\boldsymbol{u}\cdot\nabla)s = 0, \quad p = p\,(\tau, s). \tag{2.7c}$$

Equation (2.7c) for the entropy describes its constancy in every moving macroscopic element of the medium; the derivative $\mathrm{d}/\mathrm{d}t = \partial/\partial t + (\boldsymbol{u}\cdot\nabla)$ is called the **material derivative**. If the medium is uniform in the beginning, Eq. (2.7c) can be replaced by the condition of the global constancy of the entropy:

$$s = \text{const}. \tag{2.8}$$

It is worthwhile to keep in mind that the HD (or, more appropriately, the *gas dynamics, GD*)[1] can only be applied to the substances in the state of the *local thermodynamic equilibrium*. Stated another way, this means that one can define small macroscopic volume elements (with a linear scale l) in each of which the particles have *equilibrium* (e.g., *Maxwellian*) distribution with almost constant density, velocity, and temperature within each element. The gradients of these measures as well as their time variations must be small, i.e., the following inequalities must hold:

$$\left|\frac{\Lambda}{f}\frac{\partial f}{\partial x}\right| \ll 1, \qquad \left|\frac{\tau}{f}\frac{\partial f}{\partial t}\right| \ll 1, \qquad \text{or} \qquad l \gg \Lambda, \qquad \Delta t \gg \tau, \tag{2.9}$$

where f is any of the ρ, T, and $\boldsymbol{u}$ values; Λ is the mean free path of the particles between collisions; τ is the mean time between the collisions; and Δt and l are the macroscopically small intervals. Even with these simplifications, the HD equations remain nonlinear and, thus, highly sophisticated.

[1] The term GD is more appropriate in our case because the astrophysical media represent typically a gas (neutral or ionized) phase rather than a fluid, which would imply use of the term "hydro" (water).

2.2 MHD Equations

The phenomena in the gas phase and the set of equations describing them are even more complicated if the medium possesses electric conductivity σ and contains the magnetic field $\boldsymbol{B}$. The magnetic field can be generated by both external sources and by the electric current $\boldsymbol{j}$ of the medium. Unlike the magnetic field, significant large-scale electric field in the conducting medium is absent in most cases (although not always) because of its shielding by the free electric charges.

The presence of the electric current and the magnetic field requires to modify the set of equations (2.1)–(2.5) in several ways, which converts it to a set of the **MHD equations**. The MHD is well suited for description of quasistationary electromagnetic phenomena in moving conducting plasma, either fully or partially ionized. It is worthwhile to emphasize that various plasma components (i.e., ions, electrons, neutrals, dust particles) must move together, composing a single "fluid". Apparently, there are plenty natural phenomena when the electron and the ion components behave differently. Moreover, the plasma can contain many components, like ions of various elements in different ionization states, neutrals (atoms and molecules), relativistic particles and antiparticles, and the dust particles. To highlight this the classical MHD is frequently called the *one-fluid MHD*, in contrast to *two-fluid* or *multi-fluid* MHD, which consider the electrons, ions, and other available components as distinct fluids interacting with each other. The general multi-fluid approach is described in Sect. 1.3.3. Below we will return to considering corresponding generalizations of the one-fluid MHD as needed in appropriate chapters of this book. We start, however, from the phenomena allowing correct treatment within the standard one-fluid MHD.

As mentioned (see Sect. 1.3.3) the MHD description is an approximation to a more precise kinetic treatment of the plasma. Complementary, the MHD theory represents a generalization of the standard HD to the case of the conducting fluid; here we discuss how this generalization can be performed. To convert the HD into MHD equations, we first have to add the volume *Ampère force*

$$\boldsymbol{f}_{\mathrm{A}} = \frac{1}{c}\,\boldsymbol{j} \times \boldsymbol{B}, \tag{2.10}$$

to equation of motion (2.2) and the Joule losses

$$Q = \frac{j^2}{\sigma} \tag{2.11}$$

to equation of the entropy balance (2.4). Second, we have to add the entire set of the Maxwell equations in the form

$$\nabla \times \boldsymbol{B} = \frac{4\pi}{c}\boldsymbol{j}, \qquad \nabla \cdot \boldsymbol{B} = 0, \qquad \frac{\partial \boldsymbol{B}}{\partial t} = -c\nabla \times \boldsymbol{E}, \tag{2.12}$$

where, unlike Sect. 1.3.3, we do not consider the external current $\boldsymbol{j}^{\text{ext}}$. We have already taken into account inequalities (2.9), which must hold for the magnetic field like for the standard HD variables in Sect. 2.1, i.e., we discarded the displacement current from the first equation in set (2.12) since it is small compared with the conductivity current in the slow phenomena described within the MHD approach.

Eliminating electric current $\boldsymbol{j}$ from Eq. (2.10) with the use of the first of equations (2.12), we obtain MHD equations containing the magnetic field:

$$\rho\left(\frac{\partial \boldsymbol{u}}{\partial t}+(\boldsymbol{u}\cdot\nabla)\boldsymbol{u}\right) = -\nabla p+\boldsymbol{f}+\frac{1}{4\pi}[\nabla\times\boldsymbol{B}]\times\boldsymbol{B}+\eta\Delta\boldsymbol{u}+\frac{\eta}{3}\nabla(\nabla\cdot\boldsymbol{u}), \tag{2.13a}$$

$$\rho T\left(\frac{\partial s}{\partial t}+(\boldsymbol{u}\cdot\nabla)s\right) = \eta\left(\frac{\partial u_\alpha}{\partial x_\beta}+\frac{\partial u_\beta}{\partial x_\alpha}-\frac{2}{3}(\nabla\cdot\boldsymbol{u})\delta_{\alpha\beta}\right)\nabla_\beta u_\alpha+\nabla\cdot(\chi\nabla T) +\frac{\nu_m}{4\pi}[\nabla\times\boldsymbol{B}]^2 \tag{2.13b}$$

from original HD equations (2.2) and (2.4) complemented by Eqs. (2.10) and (2.11). Note that the first term in the rhs of Eq. (2.13b) can be expressed via viscous stress tensor $\Pi_{\alpha\beta}$ (2.5). Remaining equations (2.1), (2.3), and (2.5) keep the original form and so we just add them to Eq. (2.13) toward the closed MHD equation set.

The equations obtained so far do not compose the closed system yet, since the magnetic field is still undefined within it. To calculate the magnetic field we have to eliminate the electric field from Maxwell equations (2.12) with the use of Ohm's law—the relation between electric current and electromagnetic field. In a general case this law is very complicated (so-called generalized Ohm's law; see Sect. 1.3.4); we first consider the simplest case of Ohm's law. The motion of a conductor with a nonrelativistic speed $u \ll c$ in the presence of magnetic field $\boldsymbol{B}$ gives rise to an additional electric field $\boldsymbol{u}\times\boldsymbol{B}/c$ in the conductor (see the Lorentz transformation, Landau and Lifshitz 1960). Thus, Ohm's law takes the form

$$\boldsymbol{j} = \sigma\left(\boldsymbol{E}+\frac{1}{c}\boldsymbol{u}\times\boldsymbol{B}\right), \tag{2.14}$$

where σ is the electric conductivity. This expression is valid when the magnetic field is relatively weak; otherwise the conductivity becomes essentially anisotropic [i.e., σ is a tensor rather than a scalar; see expressions (1.102)] and when there are no currents produced by the conductor nonuniformity (related to gradients of temperature or density). Current density (2.14) is the same in both the conductor (moving) and laboratory (rest) reference systems to the first order over u/c.

Let us make further transformations required to derive the equation for the magnetic field. First, express the electric field $\boldsymbol{E}$ from Eq. (2.14),

$\boldsymbol{E} = \boldsymbol{j}/\sigma - \boldsymbol{u} \times \boldsymbol{B}/c$, and substitute it into the third equation of set (2.12), the **induction equation**. Then, the use of the relation

$$\Delta \boldsymbol{B} = -\frac{c}{4\pi} \nabla \times \boldsymbol{j}, \tag{2.15}$$

which follows from the first two equations of set (2.12), gives rise to equation linking the magnetic field with the motion of the medium:

$$\nabla \cdot \boldsymbol{B} = 0, \qquad \frac{\partial \boldsymbol{B}}{\partial t} = \nabla \times [\boldsymbol{u} \times \boldsymbol{B}] + \nu_m \Delta \boldsymbol{B}, \qquad \nu_m = \frac{c^2}{4\pi\sigma} = \text{const.} \tag{2.16}$$

The quantity ν_m is called the **magnetic diffusivity** or magnetic viscosity. Thus, finite conductivity gives rise to a dissipative process—the Joule dissipation of the magnetic field.

2.2.1 Magnetic Pressure and Magnetic Tensions

Consider now a few concepts and ideas, which follow from the full MHD system and so are the most widely applicable. First, we note that the magnetic Ampère force entering (2.13a) can be equivalently expanded onto two terms $[\nabla \times \boldsymbol{B}] \times \boldsymbol{B} = -\nabla B^2/2 + (\boldsymbol{B} \cdot \nabla)\boldsymbol{B}$ with the use of the corresponding equivalence of the vector analysis. As a result, part of the magnetic force reveals itself as the gradient of a **magnetic pressure** $p_m = B^2/8\pi$, which adds up to the kinematic gas pressure p:

$$\begin{aligned} \frac{\partial \boldsymbol{u}}{\partial t} + (\boldsymbol{u} \cdot \nabla)\boldsymbol{u} \quad = \quad & -\frac{1}{\rho}\nabla\left(p + \frac{B^2}{8\pi}\right) + \frac{1}{4\pi\rho}(\boldsymbol{B} \cdot \nabla)\boldsymbol{B} \\ & + \nu \Delta \boldsymbol{u} + \frac{\nu}{3}\nabla(\nabla \cdot \boldsymbol{u}) + \frac{1}{\rho}\boldsymbol{f}, \end{aligned} \tag{2.17}$$

while the other part forms the **magnetic tensions** $(\boldsymbol{B} \cdot \nabla)\boldsymbol{B}/4\pi\rho$, which have a nonzero value only when the magnetic field lines have a curved shape. Direct comparison of Eqs. (2.16) and (2.17) shows that the magnetic diffusivity ν_m plays the same role for the magnetic field as the kinematic viscosity ν plays for the hydrodynamic velocity $\boldsymbol{u}$.

2.2.2 Ideal MHD Equations

Ideal MHD equation set similar to set (2.7a) in the standard HD can be derived by neglecting the dissipative terms throughout the MHD equation system:

$$\frac{\partial \rho}{\partial t} + \nabla(\rho \boldsymbol{u}) = 0, \tag{2.18a}$$

$$\frac{\partial \boldsymbol{u}}{\partial t} + (\boldsymbol{u} \cdot \nabla)\boldsymbol{u} = -\frac{1}{\rho}\nabla\left(p + \frac{B^2}{8\pi}\right) + \frac{1}{4\pi\rho}(\boldsymbol{B} \cdot \nabla)\boldsymbol{B} + \frac{1}{\rho}\boldsymbol{f}, \tag{2.18b}$$

$$\frac{\partial s}{\partial t} + (\boldsymbol{u}\cdot\nabla)s = 0, \qquad p = p\,(\rho, s), \tag{2.18c}$$

$$\frac{\partial \boldsymbol{B}}{\partial t} = \nabla \times [\boldsymbol{u} \times \boldsymbol{B}], \qquad \nabla\cdot\boldsymbol{B} \;=\; 0. \tag{2.18d}$$

Apparently, this system is valid if the MHD parameters vary slowly in space and time and when the dissipation is weak. The electric field in this case can be expressed via the magnetic field and the medium velocity. Indeed, adopting $\sigma \to \infty$ in Eq. (2.14) and assuming the current density $\boldsymbol{j}$ to remain finite we immediately obtain

$$\boldsymbol{E} = -\frac{1}{c}\boldsymbol{u} \times \boldsymbol{B}. \tag{2.19}$$

2.2.3 Quiescent Prominence Model

Figure 1.2 offers an idea of a prominence often observed in the solar corona. In fact, prominences represent relatively cool, $T \sim 10^4$ K, and dense $n \sim 10^{10}$–$10^{11}\,\mathrm{cm}^{-3}$ partly ionized condensations (filaments) with the size exceeding 10^{10} cm, which can live high in the corona remarkably long, up to a few months, without immediate falling onto the photosphere, although the gravitational force would imply so. Kippenhahn and Schlüter (1957) noted that in certain magnetic configurations the gravitational force can be entirely compensated by the magnetic forces considered above. Let us consider a simple one-dimensional model of a quiescent prominence proposed by Kippenhahn and Schlüter (1957).

Specifically, we adopt that all relevant variables depend only on coordinate x: $\rho(x)$, $p(x)$, and $B_z(x)$, while other magnetic field components, B_x and

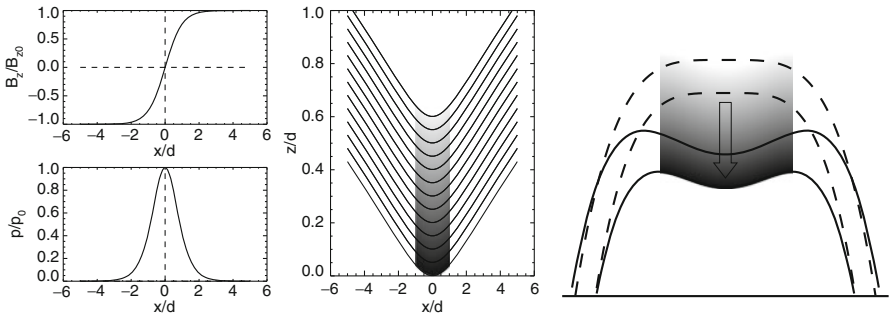

Figure 2.1: *Left*: Kippenhahn–Shclüter solution for the vertical magnetic field, pressure, and the field line structure. *Right*: a cartoon of the prominence/filament formation due to coronal condensation and corresponding magnetic field line distortion; see Aschwanden (2005) for more detail.

B_y and temperature T, are constant. In a steady state the lhs of Eq. (2.18b) is, apparently, zero; thus, projections of the rhs onto x and z axes yield

$$\frac{\partial}{\partial x}\left(p + \tfrac{B^2}{8\pi}\right) = 0, \tag{2.20a}$$

$$\tfrac{B_x}{4\pi}\frac{\partial B_z(x)}{\partial x} - \rho g = 0, \tag{2.20b}$$

where g is the free-fall acceleration. To solve the first of these equation we have yet to specify boundary conditions at the infinities, for which we adopt

$$p|_{x\to\pm\infty} = 0; \quad B_z|_{x\to\pm\infty} = \pm B_{z0}, \tag{2.21}$$

then, integration of Eq. (2.20aa) yields

$$p(x) = \frac{B_{z0}^2 - B_z^2(x)}{8\pi}. \tag{2.22}$$

Now we have to express the mass density ρ entering Eq. (2.20ab) via the gas pressure using the ideal gas equation of state:

$$p = 2n_e k_\mathrm{B} T_e; \quad n_e = \rho/m_\mathrm{eff}, \tag{2.23}$$

where m_eff is the mean mass of the coronal ions; thus, $\rho = pm_\mathrm{eff}/(2k_\mathrm{B}T_e)$.

Substituting this density into Eq. (2.20), then using solution (2.22) for the pressure, and noting that the constant combination $2k_\mathrm{B}T_e/(gm_\mathrm{eff})$ has a dimension of length (which is, in fact, the pressure scale height of a steady atmosphere, $\lambda_p = 2k_\mathrm{B}T_e/(gm_\mathrm{eff}) = 4.6\times10^9(T_e/1\ \mathrm{MK})\,\mathrm{cm}$), we obtain a closed form of equation for the magnetic field component $B_z(x)$:

$$\frac{B_{z0}^2 - B_z^2(x)}{2\lambda_p} - B_x\frac{\partial B_z(x)}{\partial x} = 0, \tag{2.24}$$

whose solution has an analytical form:

$$B_z(x) = B_{z0}\tanh\left(\frac{xB_{z0}}{2\lambda_p B_x}\right); \tag{2.25}$$

accordingly, the pressure distribution receives the form:

$$p(x) = \frac{B_{z0}^2}{8\pi}\cosh^{-2}\left(\frac{xB_{z0}}{2\lambda_p B_x}\right). \tag{2.26}$$

This solution illustrated by Fig. 2.1 implies that the magnetic pressure and the magnetic tensions are capable of compensating the gravitation force acting from the Sun to the coronal material. In particular, it can support some overdense coronal condensations observed in the form of bright prominences above the limb or as dark, compared with the photosphere, elongated filaments on the solar disk. Some of the observed filaments are indeed quiescent and can be approximately described using the presented Kippenhahn–Schlüter solution, while others are unstable eruptive structures, which are, apparently, not steady-state objects, so their description requires a dynamical approach; see Aschwanden (2005) for greater detail.

2.3 Diffusion, Reconnection, and Freezing-in of the Magnetic Field

Consider the equations for the magnetic field in more detail. First of all we note that two terms in the rhs of induction equation (2.16) have different structure and so describe different physical phenomena. First of them describes transport of the magnetic field by the plasma motion, while the second one describes the Joule dissipation of the field. The order of magnitude estimate of the first to the second term ratio yields the dimensionless parameter:

$$R_m = \frac{ul}{\nu_m}, \tag{2.27}$$

having the same structure as Reynolds number (2.6) and called the **magnetic Reynolds number**. This estimate assumes that the characteristic scales of magnetic field and velocity are the same and equal l.

2.3.1 Diffusion of the Magnetic Field

The type of solution of Eq. (2.16) depends essentially on the magnetic Reynolds number. If $R_m \ll 1$ we can neglect any motion of the plasma and so neglect the first term in the rhs of Eq. (2.16). Assume $R_m \ll 1$ and consider the problem of the magnetic field evolution in the infinite uniform conducting medium. Adopt that at $t = 0$ there is a magnetic field $\boldsymbol{B}(\boldsymbol{r}, 0) = \boldsymbol{B}_0(\boldsymbol{r})$ in the medium and find its evolution afterward for $t > 0$.

To solve the equation let us include the initial condition in the equation itself:

$$\frac{\partial \boldsymbol{B}}{\partial t} - \nu_m \Delta \boldsymbol{B} = \boldsymbol{B}_0(\boldsymbol{r})\delta(t), \qquad \boldsymbol{B} = 0 \qquad \text{at} \qquad t < 0. \tag{2.28}$$

To make sure that Eq. (2.28) is equivalent to the original equation with the initial condition, we integrate both sides of it over a small time interval, $(-\tau, +\tau)$. If $\tau \to 0$ then $\boldsymbol{B}(\boldsymbol{r}, 0) = \boldsymbol{B}_0(\boldsymbol{r})$, because $\tau \Delta \boldsymbol{B} \to 0$ and so the second term in the lhs vanishes. Unlike Eq. (2.16), equation (2.28) is inhomogeneous and thus it can be solved using the Green function method:

$$\boldsymbol{B}(\boldsymbol{r}, t) = \int G(\boldsymbol{r} - \boldsymbol{r'}, t - t')\boldsymbol{B}_0(\boldsymbol{r'})\delta(t')\mathrm{d}^3 r' \mathrm{d}t' = \int G(\boldsymbol{r} - \boldsymbol{r'}, t)\boldsymbol{B}_0(\boldsymbol{r'})\mathrm{d}^3 r', \tag{2.29}$$

where the **Green function** $G(\boldsymbol{r} - \boldsymbol{r'}, t - t')$ satisfies the equation

$$\frac{\partial G}{\partial t} - \nu_m \Delta G = \delta(\boldsymbol{r} - \boldsymbol{r'})\delta(t - t'), \qquad G = 0 \qquad \text{at} \qquad t - t' < 0. \tag{2.30}$$

Equation (2.30) can easily be solved by expansion of the Green function into Fourier integral over spatial variable $\boldsymbol{r} - \boldsymbol{r'}$. Apparently, its Fourier

transform G_k satisfies the equation

$$\frac{\partial G_k}{\partial t} + \nu_m k^2 G_k = \delta(t - t'), \tag{2.31}$$

which has the solution $G_k(t-t') = \Theta(t-t')e^{-\nu_m(t-t')k^2}$. The inverse Fourier transform yields the Green function in the spatial and temporal domain:

$$G(\boldsymbol{r} - \boldsymbol{r'}, t - t') = \int G_k(t-t')e^{i\mathbf{k}\cdot(\mathbf{r}-\mathbf{r}')}\frac{\mathrm{d}^3 k}{(2\pi)^3} = \frac{\Theta(t-t')}{[4\pi\nu_m(t-t')]^{3/2}} \exp\left\{-\frac{(\boldsymbol{r}-\boldsymbol{r'})^2}{4\nu_m(t-t')}\right\}, \tag{2.32}$$

where $\Theta(t-t')$ is the *step function*.

The structure of the exponent in Green function (2.32) shows explicitly that in the MHD (quasistationary) approximation, the magnetic field in a conducting medium propagates distance l over time $\Delta t \approx l^2/4\nu_m$. This is the very same law which describes the heat propagation or particle diffusion in a classical medium at rest. Accordingly, we can interpret the obtained solution as *diffusion of the magnetic field*; this is why the coefficient ν_m is called "magnetic diffusivity". Considering an AC field with frequency ω, we take $\Delta t \approx T/2 = \pi/\omega$, which gives rise to a characteristic scale $L \approx c/\sqrt{\sigma\omega}$, providing an order of magnitude estimate of the skin depth of a conductor into which an external AC field can penetrate.

2.3.2 Freezing-in of the Magnetic Field and Magnetic Reconnection

Consider now the case of large Reynolds number, $R_m \gg 1$, when we can safely discard the Joule dissipation term:

$$\frac{\partial \boldsymbol{B}}{\partial t} = \nabla \times [\boldsymbol{u} \times \boldsymbol{B}], \qquad \nabla \cdot \boldsymbol{B} = 0. \tag{2.33}$$

Let us show that under this condition the magnetic field has a remarkable property of *freezing-in* in the well-conducting fluid, i.e., any field line remains strictly linked with those macroscopic volume elements of the plasma, which contained it originally. Stated another way, the magnetic field is transferred along with the plasma motions; the magnetic field lines can change the length and shape, but cannot intersect and move through each other.

To see this explicitly, consider two *fluid particles* (i.e., two macroscopically small-volume elements of the plasma), which are located in nearby positions with the coordinates $\boldsymbol{r}$ and $\boldsymbol{r} + \delta\boldsymbol{l}$ with the velocities $\boldsymbol{u}$ and $\boldsymbol{u} + (\delta\boldsymbol{l}\cdot\nabla)\boldsymbol{u}$, respectively. Apparently, over the time interval $\mathrm{d}t$, the distance between the particles changes by $(\delta\boldsymbol{l}\cdot\nabla)\boldsymbol{u}\mathrm{d}t$; thus, this variation obeys the equation:

$$\frac{\mathrm{d}}{\mathrm{d}t}\,\delta\boldsymbol{l} = (\delta\boldsymbol{l}\cdot\nabla)\boldsymbol{u}. \tag{2.34}$$

The lhs contains the material derivative as it describes variation of the distance between two moving particles.

Complementary, calculate the material derivative of the $\boldsymbol{B}/\rho$ ratio. This derivative reads:

$$\frac{\mathrm{d}}{\mathrm{d}t}\frac{\boldsymbol{B}}{\rho} = \frac{1}{\rho}\frac{\mathrm{d}\boldsymbol{B}}{\mathrm{d}t} - \frac{\boldsymbol{B}}{\rho^2}\frac{\mathrm{d}\rho}{\mathrm{d}t}. \tag{2.35}$$

The material derivative of the field $\boldsymbol{B}$ is obtained from Eq. (2.33) taking into account the following transformation $\nabla \times [\boldsymbol{u} \times \boldsymbol{B}] = \boldsymbol{u}(\nabla \cdot \boldsymbol{B}) - \boldsymbol{B}(\nabla \cdot \boldsymbol{u}) - (\boldsymbol{u} \cdot \nabla)\boldsymbol{B} + (\boldsymbol{B} \cdot \nabla)\boldsymbol{u} = -(\boldsymbol{u} \cdot \nabla)\boldsymbol{B} + (\boldsymbol{B} \cdot \nabla)\boldsymbol{u} - \boldsymbol{B}(\nabla \cdot \boldsymbol{u})$:

$$\frac{\mathrm{d}\boldsymbol{B}}{\mathrm{d}t} = (\boldsymbol{B}\cdot\nabla)\boldsymbol{u} - \boldsymbol{B}(\nabla\cdot\boldsymbol{u}). \tag{2.36}$$

The material derivative of the density is obtained from continuity equation (2.1):

$$\frac{\mathrm{d}\rho}{\mathrm{d}t} = -\rho(\nabla\cdot\boldsymbol{u}). \tag{2.37}$$

Combining equations (2.35)–(2.37), we find

$$\frac{\mathrm{d}}{\mathrm{d}t}\frac{\boldsymbol{B}}{\rho} = \left(\frac{\boldsymbol{B}}{\rho}\cdot\nabla\right)\boldsymbol{u}. \tag{2.38}$$

Equations (2.34) and (2.38) for the variables $\delta\boldsymbol{l}$ and $\boldsymbol{B}/\rho$ are identical. Therefore, if these two fluid particles were originally connected by a field line, i.e., the vectors $\delta\boldsymbol{l}$ and $\boldsymbol{B}/\rho$ were parallel to each other, they remain parallel at all later times; thus, the particles remain linked to the same field line. During the plasma motion, the magnitude $\boldsymbol{B}/\rho$ is changing proportionally to the distance between the particles. In particular, the freezing-in property guaranties conservation of the magnetic flux through arbitrary closed moving contour composed of the fluid elements of the medium.

It is important to emphasize that the flux conservation holds for *arbitrary* macroscopic motions and deformations of the contour *compatible* with the condition $R_m \gg 1$. This means that if in a fluid with overall large Reynolds number there are inhomogeneous regions where the spatial gradients are extraordinary large, the freezing-in condition can break down there allowing the magnetic field to diffuse locally. Given that the field is freezing in the fluid in the most of the volume, while diffuses only in some locally inhomogeneous regions, this magnetic field dissipation process will macroscopically look like a reconnection of magnetic field lines. Stated another way, dissipation of magnetic energy in a highly conducting fluid with large Reynolds numbers can only occur in the form of **magnetic reconnection**, which requires some strong local inhomogeneities to be present in the fluid.

2.3.3 Stationary Configurations

Let us discuss briefly what requirements must be fulfilled to allow a stationary MHD configuration—stationary plasma motion or stationary magnetic field configuration. Stationary solution implies $\partial/\partial t = 0$ in Eq. (2.13), so neglecting the dissipative terms, one easily finds $s = \text{const}$ from Eq. (2.13b), while Eq. (2.13a) describes the force balance

$$\rho(\boldsymbol{u}\cdot\nabla)\boldsymbol{u} = -\nabla p - \frac{1}{4\pi}\boldsymbol{B}\times[\nabla\times\boldsymbol{B}], \tag{2.39}$$

i.e., the inertia force, $\rho(\boldsymbol{u}\cdot\nabla)\boldsymbol{u}$, must be balanced by the pressure gradient ∇p and the Ampère force $\boldsymbol{f}_{\mathrm{A}} = -\boldsymbol{B}\times[\nabla\times\boldsymbol{B}]/(4\pi)$; we do not consider a gravitational force here for simplicity. The order of magnitude of each term can be estimated if we introduce a characteristic scale of the spatial variation of the involved parameters, $\nabla \sim l^{-1}$:

$$\frac{\rho u^2}{l} \approx \frac{p}{l} + \frac{B^2}{4\pi l}, \qquad \text{or} \qquad \rho u^2 \approx p + \frac{B^2}{4\pi}. \tag{2.40}$$

Consider the case of strong pressure, $p \gg B^2/(4\pi)$. Here one can neglect the Ampère force in Eq. (2.39) in the first approximation, so the inertia force of the plasma flow $\boldsymbol{u}(\boldsymbol{r})$ is balanced by the pressure gradient. Stated another way, in a high-pressure plasma, the effect of the magnetic field on the stationary plasma flow is minor and solutions of usual HD apply. The magnetic field configuration then can be determined within the perturbation theory for a given HD flow. In particular, the magnetic field, being frozen in the plasma, is simply transferred with the predefined plasma motion. As we will show, however, in Chaps. 6 and 8, such a weak magnetic field might be kinematically amplified by plasma motions, so the stationary flows with weak magnetic field are not necessarily stable.

The opposite case of strong magnetic field, $B^2/(4\pi) \gg p$, is more complicated. Indeed, if we neglect the pressure gradient in Eq. (2.39), we arrive at two options: either the plasma flow is highly supersonic, $\rho u^2 \gg p$, or the magnetic field creates relatively small Ampère's force, $\left|\boldsymbol{B}\times[\nabla\times\boldsymbol{B}]\right| \ll B^2/l$; ultimately, this condition requires that the electric current $\boldsymbol{j} = c[\nabla\times\boldsymbol{B}]/(4\pi)$ is almost parallel to the magnetic field $\boldsymbol{B}$.

The former case is thought to be realized in so-called Poynting-dominated jets. Collimated supersonic (often relativistic) jets are widely detected or implied in astrophysical sources including active galactic nuclei, quasars and microquasars, and the gamma-ray burst sources; see Sect. 12.4. It is yet unclear, however, if those jets are pressure-dominated or Poynting-dominated.

The latter case, which is called the force-free field, because in the first approximation the Ampère force must be zero here, seems to be relevant to coronae of accretion disks and normal stars including the solar corona. For the solar corona, for example, the sources of the coronal magnetic field

are located at and beneath the photosphere, and so the magnetic pressure can strongly dominate the kinetic pressure at the active regions above the sunspots, where the photospheric field is highly enhanced compared with the mean photospheric magnetic field. The corresponding magnetic configurations are indeed routinely observed in the solar corona to be stationary and to survive over a few solar rotations with very little evolution.

Currently, there is no reliable routine method to measure coronal magnetic fields. For this reason, different force-free extrapolations of the photospheric magnetic fields, which are widely measured with the use of Zeeman effect, are developed and used to deduce some information on the coronal fields. Although the extrapolation techniques are very useful to get some idea on the coronal fields, the extrapolated magnetic structures often do not match any observed coronal structure. One of possible reason for those mismatches is that the magnetic field is in fact only approximately the force-free field.

To quantify the accuracy of the force-free approximation, assume that the plasma obeys the ideal gas equation of state, Eq. (2.23), $p = 2nT$, where temperature T is measured in energy units ($T = k_{\rm B}T$ [K]), and introduce the *plasma beta* parameter

$$\beta = \frac{4\pi p}{B^2} = \frac{8\pi nT}{B^2} = \frac{w_T}{w_B}, \tag{2.41}$$

where $w_T = nT$ and $w_B = B^2/(8\pi)$ are the densities of the thermal and magnetic energies, respectively. Thus, for the magnetic-dominated (low beta) plasma, the Ampère force equals zero not equivalently but to the accuracy of β only: $\left|\boldsymbol{B} \times [\nabla \times \boldsymbol{B}]\right| \sim \beta B^2/l$, which may have noticeable effect on the accuracy of the force-free photospheric extrapolations. To get a better feeling about the numbers involved, let us estimate the plasma beta in the solar corona—in and outside an active region. Outside active regions we can adopt the typical values $B \sim 1\,\mathrm{G}$, $n \sim 10^8\,\mathrm{cm}^{-3}$, and $T \sim 1\,\mathrm{MK}$, which yields an estimate about one: $\beta \sim 0.4$. In an active region above a sunspot, the magnetic field can be much larger, $B \sim 100\,\mathrm{G}$ or higher, and the plasma can be denser, $n \sim 10^{10}\,\mathrm{cm}^{-3}$, and hotter, $T \sim 3$–$10\,\mathrm{MK}$, so a small $\beta \lesssim 10^{-2}$ is typically expected.

Overall, we conclude that the magnetic configurations and plasma flows can be essentially different in the pressure-dominated ($\beta \gg 1$) and the magnetic-dominated ($\beta \ll 1$) plasmas—this is, in fact, relevant to both stationary and nonstationary cases.

2.4 Linear Modes in MHD

An arbitrary perturbation in a plasma can be expanded over any full system of orthogonal functions. The most convenient set of such functions, however, is the set of linear eigenmodes of the medium. Indeed, for a small-amplitude

perturbation, the amplitudes of the individual eigenmodes composing it are also small; thus, the superposition principle valid for the linear systems applies and so the individual eigenmodes do not interact with each other. Even for larger-amplitude perturbations the representation over the eigenmode superposition is frequently very useful, since, for a small nonlinearity, the nonlinear interactions of the linear eigenmodes can be taken into account by the perturbation theory. The role of the linear modes is also very important to study plasma instabilities. Therefore, we discuss now the MHD eigenmodes of the plasma.

2.4.1 Basic Equations and MHD Dispersion Relation

To study small-amplitude MHD waves in a fully ionized plasma (low-frequency plasma eigenmodes, $\boldsymbol{j}^{\,\mathrm{ext}} = 0$), we have to analyze the corresponding linearized set of equations. We start with a non-dissipative case ($\nu_m = \nu_{\mathrm{eff}} = 0,\ \dot{\tilde{S}} = 0$) and use Eqs. (1.134)–(1.136) keeping the Hall term in Eq. (1.134). We represent the macroscopic plasma parameters in the form $\boldsymbol{U} = \boldsymbol{U}_0 + \boldsymbol{u},\ s = s_0 + s',$ etc., where the index 0 designates the unperturbed values of quantities which do not depend on coordinates and time; small perturbations will be considered in the linear approximation only. Linearizing the system of MHD equations with these notations yields

$$\frac{\partial s'}{\partial t} + \boldsymbol{U_0} \cdot \nabla s' = 0, \qquad \frac{\partial \rho'}{\partial t} + \boldsymbol{U_0} \cdot \nabla \rho' + \rho_0 \nabla \cdot \boldsymbol{u} = 0, \tag{2.42a}$$

$$\frac{\partial \boldsymbol{u}}{\partial t} + (\boldsymbol{U}_0 \cdot \nabla)\boldsymbol{u} + \frac{1}{\rho_0}\nabla p + \frac{1}{4\pi\rho_0}\boldsymbol{B}_0 \times (\nabla \times \boldsymbol{b}) = 0, \qquad P = P_0 + p(s', \rho'), \tag{2.42b}$$

$$\frac{\partial \boldsymbol{b}}{\partial t} + (\boldsymbol{U}_0 \cdot \nabla)\boldsymbol{b} + \boldsymbol{B}_0(\nabla \cdot \boldsymbol{u}) - (\boldsymbol{B}_0 \cdot \nabla)\boldsymbol{u} + \frac{c}{4\pi e n_i}(\boldsymbol{B}_0 \cdot \nabla)(\nabla \times \boldsymbol{b}) = 0, \qquad \nabla \cdot \boldsymbol{b} = 0. \tag{2.42c}$$

We search for solutions of this system having the form of plane monochromatic waves $s' \propto \exp(i\boldsymbol{k} \cdot \boldsymbol{r} - i\omega t)$ and obtain the set of algebraic equations:

$$\omega' s' = 0, \qquad \omega' \rho' - \rho_0 \boldsymbol{k} \cdot \boldsymbol{u} = 0, \tag{2.43a}$$

$$\omega' \boldsymbol{u} - \frac{\boldsymbol{k}}{\rho_0}\left(p + \frac{\boldsymbol{b} \cdot \boldsymbol{B}_0}{4\pi}\right) + \frac{\boldsymbol{k} \cdot \boldsymbol{B}_0}{4\pi\rho_0}\,\boldsymbol{b} = 0, \qquad p = c_s^2 \rho' + \left(\frac{\partial P}{\partial s}\right)_{\rho_0} s', \tag{2.43b}$$

$$\omega' \boldsymbol{b} + (\boldsymbol{k} \cdot \boldsymbol{B}_0)\boldsymbol{u} - \boldsymbol{B}_0(\boldsymbol{k} \cdot \boldsymbol{u}) - i\frac{c\boldsymbol{k} \cdot \boldsymbol{B}_0}{4\pi e n_i}\,\boldsymbol{k} \times \boldsymbol{b} = 0, \qquad \boldsymbol{k} \cdot \boldsymbol{b} = 0, \tag{2.43c}$$

where $c_s^2 = (\partial P/\partial \rho)_0$ is the square of the unperturbed sound velocity; $\omega' = \omega - \boldsymbol{k} \cdot \boldsymbol{U}_0$ is the frequency in the co-moving system, which experiences a Doppler shift relative to its frequency in the laboratory reference frame. System (2.43) is a set of linear homogeneous equations and so it has a nontrivial

solution only when the determinant of the system is zero. Neglecting the Hall term, the determinant is derived, e.g., in Somov (2006):

$$\omega'^2[\omega'^2 - (\boldsymbol{k}\boldsymbol{v}_\mathrm{A})^2][\omega'^4 - k^2(c_s^2 + v_\mathrm{A}^2)\omega'^2 + k^2c_s^2(\boldsymbol{k}\boldsymbol{v}_\mathrm{A})^2] = 0,$$

where $v_\mathrm{A} = B_0/\sqrt{4\pi\rho_0}$ is the **Alfvén speed**. This equation can have four nonnegative roots, describing four linear MHD modes, which we consider below in more detail. In what follows, complementary to Somov (2006) analysis, we derive properties of the small-amplitude waves directly from the full system (with the Hall term) without explicit use of the determinant.

2.4.2 Dispersion and Polarization of Linear Modes

Hydrodynamics Case: $B_0 = 0$

Let us start from a simpler case, when no magnetic field is present in the plasma; $v_\mathrm{A} = 0$. Then, the terms containing v_A drop out from the dispersion relation, which reduces to

$$\omega'^6(\omega'^2 - k^2c_s^2) = 0.$$

Evidently, this dispersion equation describes two distinct eigenmodes, corresponding to two its different solutions: $\omega' = 0$ and $\omega'^2 = k^2c_s^2$.

Entropy and Vortex Perturbations If we suppose in Eq. (2.43) that $\boldsymbol{B}_0 = 0$ and $s' \neq 0$, we obtain $\omega' = 0$, i.e., $\omega = \boldsymbol{k} \cdot \boldsymbol{U}_0$. This means that entropy perturbations are motionless relative to the plasma and propagate with the velocity of the medium motion, $\boldsymbol{U}_0$. Also, $\boldsymbol{k} \cdot \boldsymbol{u} = 0$, $\boldsymbol{k} \cdot \boldsymbol{b} = 0$, and $p = 0$, but the density perturbation $\rho' \neq 0$ and it is defined by s'.

Note that the root $\omega' = 0$ is triple degenerate, since it originates from equation $\omega'^6 = 0$. Therefore, two more eigenmodes must be present. Indeed, for $\omega' = 0$, the system (2.43) allows having nonzero values of the components $\boldsymbol{u}_\perp$ and $\boldsymbol{b}_\perp$ transverse to $\boldsymbol{k}$. Thus, in the general case $\boldsymbol{k} \times \boldsymbol{b} \neq 0$ and $\boldsymbol{k} \times \boldsymbol{u} \neq 0$, so, in addition to the entropy perturbation, there are two more vortex perturbations traveling with the plasma velocity, namely $\nabla \times \boldsymbol{b}$ and $\nabla \times \boldsymbol{u}$. In the absence of $\boldsymbol{B}_0$, they are independent from each other and from the perturbation of s'. It is interesting that even though no regular magnetic field is present in this case, the small perturbations of the magnetic field still can exist in the form of eddies ($\nabla \times \boldsymbol{b}$), which is a direct consequence of the fact that our linearized equations were obtained from more general MHD equations rather than from standard HD equations; in the latter case no magnetic perturbation would enter the linearized equations at all.

Sound Waves For $s' = 0$, perturbations oscillate with $\omega' \neq 0$. If, as before, $B_0 = 0$ then for $\omega' \neq 0$, it follows from Eq. (2.43) that $\boldsymbol{b} = 0$ and $\boldsymbol{u}_\perp = 0$,

but the perturbations $u_\parallel$ and ρ' satisfy

$$\omega'\rho' - \rho_0 k u_\parallel = 0, \qquad c_s^2 k\rho' - \rho_0\omega' u_\parallel = 0, \tag{2.44}$$

which describes sound waves with the dispersion law

$$\omega'^2 = (c_s k)^2, \quad \omega = \pm c_s k + \boldsymbol{k}\cdot\boldsymbol{U}_0. \tag{2.45}$$

MHD Case: $B_0 \neq 0$

Entropy Perturbations in a Magnetic Field For $s' \neq 0$ and $\boldsymbol{k}\cdot\boldsymbol{B_0} \neq 0$ we find from Eq. (2.43) that $\omega = \boldsymbol{k}\cdot\boldsymbol{U}_0$ and thus

$$\left(p + \frac{\boldsymbol{b}\cdot\boldsymbol{B}_0}{4\pi}\right)\boldsymbol{k} - \frac{\boldsymbol{k}\cdot\boldsymbol{B}_0}{4\pi}\,\boldsymbol{b} = 0. \tag{2.46}$$

Vector $\boldsymbol{k}$ is orthogonal to $\boldsymbol{b}$, so Eq. (2.46) is equivalent to two equations:

$$(\boldsymbol{k}\cdot\boldsymbol{B_0})\boldsymbol{b} = 0, \qquad p + \frac{\boldsymbol{b}\cdot\boldsymbol{B}_0}{4\pi} = 0. \tag{2.47}$$

If $\boldsymbol{b} = 0$, $(\boldsymbol{k}\cdot\boldsymbol{B_0}) \neq 0$, we have from Eqs. (2.47) and (2.43) $\boldsymbol{u} = 0$, $p = 0$. Perturbations of the density and entropy are connected to each other by the condition $p = 0$.

If $\boldsymbol{b} \neq 0$, $(\boldsymbol{k}\cdot\boldsymbol{B_0}) = 0$, we obtain from Eq. (2.47) that perturbations of the full pressure are zero:

$$p + \frac{\boldsymbol{b}\cdot\boldsymbol{B}_0}{4\pi} = 0,$$

but in the general case $\rho' \neq 0$ and $p \neq 0$. It is easy to check that the vortex perturbations, $\nabla\times\boldsymbol{b}$ and $\nabla\times\boldsymbol{u}$, can exist now independently from s' and from each other. The simplest example of the entropy's perturbation is the transfer of heated cloud by medium motion.

Alfvén Waves Now we consider perturbations in which $s' = 0$ and $\rho' = 0$ but $\omega' \neq 0$. Constancy of mass density is the main generic attribute of the Alfvén waves. It follows from Eq. (2.43) that $\boldsymbol{b}\cdot\boldsymbol{B}_0 = 0$; i.e., $\boldsymbol{b} \perp \boldsymbol{B}_0$. Since $\boldsymbol{b} \perp \boldsymbol{k}$ as well, the perturbations are polarized, in the sense that $\boldsymbol{b}$ is perpendicular to the plane $(\boldsymbol{k}, \boldsymbol{B}_0)$. The amplitudes $\boldsymbol{u}$ and $\boldsymbol{b}$ satisfy

$$\boldsymbol{u} = -\frac{\boldsymbol{k}\cdot\boldsymbol{B}_0}{4\pi\rho_0\omega'}\boldsymbol{b}, \qquad \boldsymbol{k}\cdot\boldsymbol{u} = 0, \tag{2.48a}$$

$$\omega'\boldsymbol{b} + (\boldsymbol{k}\cdot\boldsymbol{B}_0)\boldsymbol{u} - i\frac{c\,(\boldsymbol{k}\cdot\boldsymbol{B}_0)}{4\pi e n_i}\,\boldsymbol{k}\times\boldsymbol{b} = 0, \qquad \boldsymbol{k}\cdot\boldsymbol{b} = 0. \tag{2.48b}$$

Excluding the velocity $\boldsymbol{u}$ from Eq. (2.48b), we obtain

$$\left[\omega'^2 - \frac{(\boldsymbol{k}\cdot\boldsymbol{B}_0)^2}{4\pi\rho_0}\right]\boldsymbol{b} - i\frac{c\,\omega'(\boldsymbol{k}\cdot\boldsymbol{B}_0)}{4\pi e n_i}\,\boldsymbol{k}\times\boldsymbol{b} = 0 \tag{2.49}$$

and further

$$\boldsymbol{k}\times\boldsymbol{b} = -i\frac{c\,\omega' k^2(\boldsymbol{k}\cdot\boldsymbol{B}_0)}{4\pi e n_i(\omega'^2 - \omega_{\rm A}^2)}\,\boldsymbol{b}, \qquad \omega_{\rm A}^2 = \frac{(\boldsymbol{k}\cdot\boldsymbol{B}_0)^2}{4\pi\rho_0}. \tag{2.50}$$

From last two equalities we find dispersion equation

$$\omega'^2 - \omega'\frac{\omega_{\rm A}^2 k}{\omega_{\rm Bi}k_\parallel} - \omega_{\rm A}^2 = 0, \tag{2.51}$$

where $\rho_0 \approx m_i n_i$ and $\omega_{\rm Bi} = eB_0/m_i c$ is the ion cyclotron frequency.

The solution of Eq. (2.51) is

$$\omega' = \omega_{\rm A}[\xi \pm \sqrt{1+\xi^2}], \quad \text{where} \quad \xi = \frac{\omega_A k}{2\omega_{\rm Bi}k_\parallel} = \frac{(\boldsymbol{k}\cdot\boldsymbol{v}_{\rm A})k}{2\omega_{\rm Bi}k_\parallel}. \tag{2.52}$$

Here the parameter $\xi = v_{\rm A}k/2\omega_{\rm Bi}$ is expressed via the Alfvén velocity:

$$\boldsymbol{v}_{\rm A} = \frac{\boldsymbol{B}_0}{\sqrt{4\pi\rho_0}}. \tag{2.53}$$

It is small, $\xi \ll 1$, if $k \ll 2\omega_{\rm Bi}/v_{\rm A}$ and $\lambda = 2\pi/k \gg v_{\rm A}/\pi\omega_{\rm Bi} = \lambda_c$. Note that parameter ξ is a result of accounting of the Hall current in the MHD equations. The scale λ_c is often small compared with other characteristic scales in astrophysics, which allows neglecting the corresponding Hall term. For example, in the "warm" phase of galactic disk $\lambda_c \approx 3\times10^7$ cm is even smaller than the gyroradius of thermal protons, $\approx 10^8$ cm, for $T \approx 1$ eV, $B_0 \approx 3$ μG; thus for certain plasmas the Hall term can be safely neglected in the entire range of the MHD applicability (recall that the MHD treatment is only correct if the wavelength is larger than the proton gyroradius).

Neglecting the small parameter ξ in Eq. (2.52) for $k \ll 2\omega_{\rm Bi}/v_{\rm A}$ we obtain simpler dispersion law for the Alfvén waves:

$$\omega' = \pm\frac{|\boldsymbol{k}\cdot\boldsymbol{B}_0|}{\sqrt{4\pi\rho_0}} = \pm|\boldsymbol{k}\cdot\boldsymbol{v}_g|, \tag{2.54}$$

where $\boldsymbol{v}_g = \pm\boldsymbol{v}_{\rm A}$ is the group velocity of the Alfvén waves. Its phase velocity is

$$\boldsymbol{v}_{\rm ph} = \pm\frac{B_0|\cos\theta|\boldsymbol{k}}{\sqrt{4\pi\rho_0}k}, \tag{2.55}$$

where θ is the angle between $\boldsymbol{k}$ and $\boldsymbol{B}_0$. According to Eqs. (2.48a) and (2.54), the velocity $\boldsymbol{u}$ and the magnetic field $\boldsymbol{b}$ in the Alfvén wave are connected by a simple dependence:

$$\boldsymbol{u} = \mp \frac{\boldsymbol{b}}{\sqrt{4\pi\rho_0}}. \tag{2.56}$$

The minus sign in this formula refers to the same sign for ω' and $\boldsymbol{k}\cdot\boldsymbol{v}_\mathrm{A}$, and the plus sign refers to different signs for their values. In Alfvén waves the curls $\nabla\times\boldsymbol{u}$ and $\nabla\times\boldsymbol{b}$ are not independent and both propagate with the Alfvén velocity relative to the plasma.

If the medium contains a significant portion of neutral atoms, the Alfvén velocity depends on the entire mass density $\rho \approx n_i m_i + n_a m_a$ only for the wavelengths $\lambda > \Lambda_{ia}$, where Λ_{ia} is the mean free path of the ions relative to collisions with the neutrals. In the case $\lambda < \Lambda_{ia}$ the motion of charged component is only weakly coupled with the motion of neutral atoms, so the true one-fluid description of the medium is not possible. The Alfvén waves with

$$\lambda \ll \Lambda_{ia}$$

may exist in the charged subsystem only, and the Alfvén velocity will be determined by the ion mass density alone, $\rho \approx n_i m_i$.

Magnetic Sound For $s' = 0$ but $\rho' \neq 0$ we find from Eq. (2.43) that

$$\omega'\rho' - \rho_0 \boldsymbol{k}\cdot\boldsymbol{u} = 0, \qquad \boldsymbol{k}\cdot\boldsymbol{b} = 0, \tag{2.57a}$$

$$c_s^2 \boldsymbol{k}\rho' - \rho_0\omega'\boldsymbol{u} + \frac{\boldsymbol{k}(\boldsymbol{B}_0\cdot\boldsymbol{b})}{4\pi} - \frac{(\boldsymbol{k}\cdot\boldsymbol{B}_0)\boldsymbol{b}}{4\pi} = 0, \tag{2.57b}$$

$$(\boldsymbol{k}\cdot\boldsymbol{B}_0)\boldsymbol{u} - \boldsymbol{B}_0(\boldsymbol{k}\cdot\boldsymbol{u}) + \omega'\boldsymbol{b} = 0. \tag{2.57c}$$

We again neglect here the Hall current, which is valid at low frequencies. Excluding the perturbation ρ' and multiplying Eqs. (2.57b) and (2.57c) by $\boldsymbol{e}_0 = \boldsymbol{B}_0/B_0$, we obtain two equations for the parallel components $u_\parallel$ and $b_\parallel$:

$$\frac{c_s^2 k^2 B_0 k_\parallel}{4\pi\rho_0(\omega'^2 - c_s^2 k^2)}\, b_\parallel - \omega' u_\parallel = 0, \tag{2.58a}$$

$$\frac{\omega'^2 - c_s^2 k^2 - v_\mathrm{A}^2 k^2}{\omega'^2 - c_s^2 k^2}\,\omega' b_\parallel + B_0 k_\parallel u_\parallel = 0. \tag{2.58b}$$

Exclusion of $u_\parallel$ leads to dispersion equation

$$\omega'^4 - \omega'^2(c_s^2 + v_\mathrm{A}^2)k^2 + c_s^2 v_\mathrm{A}^2 k^4 \cos^2\theta = 0, \tag{2.59}$$

where θ is the angle between $\boldsymbol{B}_0$ and $\boldsymbol{k}$. We find phase velocities $v = \omega'/k$ of the fast and slow magnetosonic modes from biquadratic Eq. (2.59):

$$v_{f,s}^2 = \frac{1}{2}\left[c_s^2 + v_\mathrm{A}^2 \pm \sqrt{(c_s^2 + v_\mathrm{A}^2)^2 - 4c_s^2 v_\mathrm{A}^2\cos^2\theta}\right]. \tag{2.60}$$

Directions of the vectors $\boldsymbol{b}$ and $\boldsymbol{u}$ can easily be found from the above equations: $\boldsymbol{b}$ belongs to the plane $(\boldsymbol{k}, \boldsymbol{B}_0)$ and perpendicular to the vector $\boldsymbol{k}$. The vector $\boldsymbol{u}$ belongs to the same plane, but in general it has both components parallel and perpendicular to $\boldsymbol{k}$.

Transverse Propagation For $\boldsymbol{B}_0 \neq 0$ and $\boldsymbol{k} \perp \boldsymbol{B}_0$, Eq. (2.43) allows both entropy perturbations ($s' \neq 0$), considered above, and perturbations of the MHD parameters independent of the entropy variations. For $s' = 0$, the only nonzero component of $\boldsymbol{u}$ is that parallel to $\boldsymbol{k}$, as for normal sound waves. As follows from Eq. (2.43), the magnitudes ρ' and $\boldsymbol{k} \cdot \boldsymbol{u}$ satisfy

$$\omega' \rho' - \rho_0 \boldsymbol{k} \cdot \boldsymbol{u} = 0, \quad -\frac{c_s^2 k^2 \rho'}{\rho_0} + \left(\omega' - \frac{v_\mathrm{A}^2 k^2}{\omega'} \right) \boldsymbol{k} \cdot \boldsymbol{u} = 0. \tag{2.61}$$

From this, we determine the dispersion law for the transverse sound:

$$\omega' = \pm k (c_s^2 + v_\mathrm{A}^2)^{1/2}. \tag{2.62}$$

The perturbations of the magnetic field are parallel to $\boldsymbol{B}_0$ and proportional to the density perturbations:

$$\boldsymbol{b} = \boldsymbol{B}_0 \frac{\rho'}{\rho_0}. \tag{2.63}$$

Thus, for transverse propagation, besides the entropy perturbations, it is possible to have only waves of the usual sound type, in which the velocity of the plasma is parallel to the direction of propagation. The sound velocity c_s is replaced by $(c_s^2 + v_\mathrm{A}^2)^{1/2}$, i.e., it is renormalized by the magnetic field.

Longitudinal Propagation For $\boldsymbol{k} \parallel \boldsymbol{B}_0$ the system yields two types of wave in addition to the entropy perturbations: usual sound wave, described by Eqs. (2.46) and (2.47), on which the magnetic field has no influence, and MHD waves with $\boldsymbol{u}$ and $\boldsymbol{b}$ perpendicular to both directions $\boldsymbol{k} \parallel \boldsymbol{B}_0$. Excluding velocity

$$\boldsymbol{u}_\perp = \frac{(\boldsymbol{k}\boldsymbol{B}_0)}{4\pi\rho_0\omega'} \boldsymbol{b}$$

from vector equations (2.43), we obtain

$$(\omega'^2 - \omega_\mathrm{A}^2) \boldsymbol{e}_0 \times \boldsymbol{b} + i \frac{(\boldsymbol{k}\boldsymbol{B}_0)\, ck\, \omega'}{4\pi e n_i} \boldsymbol{b} = 0, \tag{2.64}$$

where ω_A is given by Eq. (2.50). Equation (2.64) can be written for the magnetic field components (b_x, b_y), $\boldsymbol{b} = \boldsymbol{e}_x b_x + i \boldsymbol{e}_y b_y$ in the form

$$C_1 b_x - C_2 b_y = 0, \quad C_2 b_x - C_1 b_y = 0, \quad C_1 = \omega'^2 - \omega_\mathrm{A}^2, \quad C_2 = \frac{(\boldsymbol{k}\boldsymbol{B}_0)\, ck\, \omega'}{4\pi e n_i}. \tag{2.65}$$

The determinant of this set of linear equations equals zero if $C_2^2 = C_1^2$, i.e., $b_y = \pm b_x$. This means that two MHD waves have the circular polarizations with opposite directions of rotation. The dispersion equation for MHD waves has the form

$$(\omega'^2 - \omega_{\rm A}^2)^2 = \omega'^2 \omega_{\rm A}^2 \left(\frac{ck}{\omega_{\rm pi}}\right)^2, \qquad \omega_{\rm pi}^2 = \frac{4\pi e^2 n_i}{m_i}. \tag{2.66}$$

The waves have the frequencies $\omega' \approx \omega_{\rm A} = \pm kB_0/\sqrt{4\pi\rho_0}$, if contribution of the Hall current is small: $(ck/\omega_{\rm pi})^2 \ll 1$.

The Full Set of Linear Modes With the account of the condition $\boldsymbol{k} \cdot \boldsymbol{b} = 0$, the last of equations (2.43) yields two equations when projected on the axes perpendicular to $\boldsymbol{k}$. The projection along $\boldsymbol{k}$ gives the identity $0 = 0$. Together with the expression of p in terms of ρ' and s', Eqs. (2.43) allow determining the following seven quantities: s', ρ', $\boldsymbol{u}$, and two components of $\boldsymbol{b}$. In the general case, as we have seen, there are seven different (and linearly independent) solutions: (1) entropy, (2) two Alfvén, (3) two fast, and (4) two slow magnetosonic waves, where the solutions differing in the sign of ω' are considered as different solutions. These solutions comprise the full system of linear eigenmodes over which any small perturbation can be expanded (Akhiezer et al. 1975).

Any perturbation of the MHD parameters leads to generation of one or another MHD mode, and therefore the excitation of modes in cosmic conditions may be highly diverse depending on the object. Sources of the MHD waves can include mechanical motions of the plasma, rapid transformations of energy (outbursts), hydrodynamic instabilities (convection), heating (solar and stellar winds), rotations, and so on. Secondary MHD modes are often generated by nonlinear interactions of MHD waves with each other or with different kinds of nonlinear perturbations (e.g., with shock waves). MHD modes may also be excited by external currents in the plasma, induced by external sources. Finally, there are purely kinetic mechanisms for excitation of MHD waves connected with the nonequilibrium distribution function of a plasma component. For example, strong nonequilibrium relativistic component (cosmic rays) is capable of generating MHD waves in the cosmic medium.

2.4.3 Damping of MHD Waves

We consider the most important conditions, when the MHD modes are long living, i.e., $\gamma \ll \omega'$, where γ is the wave damping rate. To investigate the MHD wave damping we use Eq. (1.129). The first term on the right-hand side of Eq. (1.129) is sign alternating and, therefore, goes to zero when averaged over the volume larger than $\lambda^3 = (2\pi/k)^3$. Systematic thermal dissipation Q

per unit volume is described by the positive quadratic terms in Eq. (1.129):

$$Q = T\dot{S} = \frac{\chi(\nabla T)^2}{T} + \frac{1}{2}\rho_0\nu\left(\frac{\partial u_\alpha}{\partial x_\beta} + \frac{\partial u_\beta}{\partial x_\alpha} - \frac{2}{3}(\nabla\cdot\boldsymbol{u})\delta_{\alpha\beta}\right)^2 + \frac{\nu_m}{4\pi}(\nabla\times\boldsymbol{b})_\parallel^2 + \frac{\nu_{\rm eff}}{4\pi}(\nabla\times\boldsymbol{b})_\perp^2 . \tag{2.67}$$

The thermal dissipation includes three distinct dissipative processes: heat conductivity, viscosity, and Joule heating.

The damping rate γ, which describes a weak damping of the plane monochromatic waves in stationary plasma, can be calculated from

$$\gamma = \overline{Q}/2\overline{w}, \tag{2.68}$$

where w is the density of the wave energy; the bar over it indicates the mean amplitude over the period. The magnitude of γ describes exponential damping of MHD parameters when all the wave sources are off, e.g., $\boldsymbol{u} = \boldsymbol{u}_0\exp(-\gamma t)$ or $\overline{w}\propto\exp(-2\gamma t)$ for quadratic measures like the energy density.

Another kind of damping measures is the absorption coefficient per unit path length of the wave propagation:

$$\alpha = \overline{Q}/\overline{q}, \tag{2.69}$$

where $\overline{q}$ is the mean absolute value of the wave energy flux. This value characterizes exponential decrease of the wave amplitude in space, $\boldsymbol{u} = \boldsymbol{u}_0\exp(-\alpha z)$, as the wave propagates from the source. Here, we select the z-axes along the direction of the energy flux $\overline{\boldsymbol{q}}$. The general expressions for energy density and energy flux density are well known (Landau and Lifshitz 1966; see also Sect. 1.3.3):

$$w = \rho\left(\frac{1}{2}u^2 + \epsilon\right) + \frac{B^2}{8\pi}, \tag{2.70a}$$

$$\boldsymbol{q} = \rho\boldsymbol{u}\left(\frac{1}{2}u^2 + \epsilon + \frac{P}{\rho}\right) + \frac{1}{4\pi}\boldsymbol{B}\times(\boldsymbol{u}\times\boldsymbol{B}), \tag{2.70b}$$

where ϵ is the internal energy per unit mass and $\epsilon + P/\rho$ is the enthalpy. This energy flux does not include the dissipative terms.

It is now easy to apply these general formulae to derive the damping rates of the MHD waves; we list the final results only for the sake of brevity.

Sound Waves: $\boldsymbol{B}_0 = 0$

$$\gamma_s = \frac{1}{2}k^2\left[\frac{4}{3}\nu + \frac{\chi}{\rho}(c_{\rm V}^{-1} - c_{\rm P}^{-1})\right], \tag{2.71}$$

where $c_{\rm V}$ and $c_{\rm P}$ are the specific heats at constant volume and pressure, respectively. The absorption coefficient per unit path length is $\alpha_s = \gamma_s/c_s$, where c_s is the group velocity of the sound wave.

Alfvén Waves

$$\gamma_{\rm A} = \frac{1}{2}(\nu k^2 + \nu_m k_\perp^2 + \nu_{\rm eff} k_\parallel^2). \tag{2.72}$$

If neutral atoms are present, the damping is primarily accounted for by the high effective collisional viscosity. This takes place for $k_\parallel^2/k_\perp^2 \gg \nu_m/\nu_{\rm eff}$. In the absence of the neutral component ($\nu_m = \nu_{\rm eff}$) we obtain standard expression $\gamma_{\rm A} = (\nu + \nu_m)k^2/2$.

Magnetosonic Waves For simplicity we suppose $c_s^2 \ll v_{\rm A}^2$, omit the kinematic viscosity and the heat conductivity, while take into account the magnetic diffusivity, which yields

$$\gamma_f = \frac{1}{2}\nu_{\rm eff} k^2, \quad \gamma_{\rm slow} = \frac{c_s^2}{2v_{\rm A}^2}\nu_{\rm eff} k_\perp^2. \tag{2.73}$$

If $k_\perp \to 0$, expression (2.73) gives $\gamma_{\rm slow} \to 0$ in this approximations. In fact, the slow magnetosonic wave converts here to the usual sound wave and so damping rate Eq. (2.71) applies.

2.5 Solar and Stellar Winds

Plasma motions allowing the MHD description are highly typical for the astrophysics context. Many objects (typically, those with fast rotation) form accretion disks and produce collimated flows of the plasma—astrophysical jets; others produce more isotropic winds. We emphasize that both these kinds of the plasma outflows are very common. The jets are observed or implied in galactic microquasars, in active galactic nuclei, quasars, blazars, and gamma-ray burst sources; see Sect. 12.4. In many cases the plasma moves with relativistic or even ultrarelativistic speed in these jets.

More isotropic winds are typical for galaxies and normal stars (e.g., Fig. 1.3), although neutron stars produce ultrarelativistic "pulsar winds" in some cases, resulting in a phenomenon of pulsar wind nebulae (e.g., Figs. 1.6 and 1.7 and Sect. 12.3). As a simpler example, we consider here nonrelativistic winds of the normal stars.

The idea of stellar/solar wind had been around well before the space era; however, it was not clear if the corpuscular flows from stars are sporadic or persistent. Direct measurement of the persistent corpuscular flow from the Sun was performed in Greenhouse's experiment on board Sputnik "Luna-2" in 1959 and then confirmed by satellite Mariner-2 measurements. Soon after this fundamental discovery, the stellar winds were detected (indirectly) from stars of spectral types O and B during the 1960s of the twentieth century. It was established that many (most of the) hot massive ($M \gtrsim 10 M_\odot$) high-luminosity stars produce their winds with a very large mass loss rate (Lozinskaya 1992). For example, for the Wolf–Rayet (WR) and Of stars the

mass loss rate is about $\dot{M} \approx (10^{-5}\text{–}10^{-4})\ M_\odot$/year; thus, the star can lose a considerable fraction of its mass over time of the order of 10^6 years that is very modest time compared with other astronomic timescales. For example, the Earth are known to exist about 4.5×10^9 years, while the Sun has been shining even longer. The stellar wind speeds were found to range within $u \approx (1\text{–}4) \times 10^3$ km/s. This implies a major deposition of the wind energy into the interstellar medium: with the above values one can easily estimate that the stellar wind energy deposition over the star lifetime, $\sim 10^6$ years, is around $(0.1\text{–}10) \times 10^{51}$ erg, which is comparable with the energy released during the supernova explosion occurring at the end of the massive star evolution.

Thus, the stellar wind is not a minor effect; rather it can have numerous dynamical and evolutionary implications. For example, the rapid mass loss, $(10^{-5}\text{–}10^{-6})M_\odot$/year, affects the star evolution itself including the end of its evolution—supernova explosion, and the supernova remnant expansion—which occurs in a "preprocessed" circumstellar cavity filled by the stellar wind rather than in an average interstellar medium. That strong stellar winds affect the interstellar medium by the deposition of energy and chemical elements and disturbing its dynamics parameters, including the ISM magnetic field. Given that the massive stars are not randomly distributed in the Galaxy, but correlated within so-called OB associations, the stellar winds from different stars can interact with each other and merge into a powerful velocity field additionally enhanced by supernova explosions within the association. These interacting winds form a bubble (also called "superbubble") with a linear scale up to a few hundred pc, which is bounded by a cooler supershell expanding as a single object due to cumulative pressure produced by the winds and explosions. We will be returning to these phenomena below in the book.

Although hundreds of stars with high luminosity L within $(5 \times 10^2\text{–}5 \times 10^7)L_\odot$ were observed to produce the winds with the mass rate within $\dot{M} \approx 10^{-9} M_\odot$/year and $\dot{M} \approx 10^{-4} M_\odot$/year, the mass losses in the form of the wind are also typical for stars with much weaker luminosity. For example, observations favor winds from much less luminous stars, e.g., cool massive red giants ($\dot{M} \approx 10^{-6} M_\odot$/year, $u \approx 10$ km/s), from nuclei of planetary nebulae with the speed $(2\text{–}3) \times 10^3$ km/s (which is 3–4 times larger than the gravitation runaway velocity) and the mass loss rate $\dot{M} \approx (4 \times 10^{-9}\text{–}7 \times 10^{-7})M_\odot$/year, and, finally, from the closest to the Earth star, the Sun.

2.5.1 Basic Observational Data About the Solar Wind

The solar wind is one of the main constituents which, along with eruptive phenomena and electromagnetic radiation from the Sun and planets, determines physical conditions in the circumsolar space (Fig. 1.3). The solar wind is a more or less stationary and isotropic plasma flow, which is launched in the upper corona of the Sun and transfers magnetic fields of solar origin. The first

indications of some corpuscular flow outward the Sun in interplanetary space were obtained in the nineteenth century (e.g., see Brandt 1970 for a review). The persistent character of the solar wind was experimentally established by Biermann (1951, 1952) via investigation of the behavior of comet tails. This result was further confirmed indirectly by observations of modulation of the galactic cosmic rays and by data on geomagnetic activity and auroras.

Direct measurements of the interplanetary plasma parameters became possible in the space era by Earth-orbiting satellites and also by interplanetary spacecraft missions. They provide quasi-continuous measurements of the interplanetary plasma physical parameters in various locations of the space. Remarkably, the parameters of the solar wind, the particle number density, abundances, velocity, and temperature experience significant temporal and spatial variations. Nowadays, the running combination of the involved IPM parameters and their drivers are collectively called the "space weather" (Gary and Keller 2004).

The measurements at the Earth orbit give the solar wind velocity (mass velocity) u between ≈ 300 and $\approx 700\,\mathrm{km/s}$ (the mean value is $\approx 400\,\mathrm{km/s}$; the highest values of $\approx 2{,}000\,\mathrm{km/s}$ are measured in association with sequences of largest solar flares, e.g., in November 2003); the ion number density $\approx 5\,\mathrm{cm}^{-3}$; the flux density of positive ions $2\times10^8\,\mathrm{cm}^{-2}\mathrm{s}^{-1}$ and the temperature $T_p \approx 3\times10^4$–6×10^5 K (the mean value is $1.5\times10^5\,\mathrm{K}$) for protons and $T_e \approx 1.5\times10^5$ for electrons. The number density of He^{++} ions (the α-particles) is usually around 4–5 % of the proton number density. The number of neutral atoms is insignificant. The magnetic field is measured to be highly variable and typically to belong the range $(1\text{–}10)\times10^{-5}\,\mathrm{G}$ with the mean value of $B \approx 5\times10^{-5}\,\mathrm{G}$. Solar wind is a supersonic flow, whose Mach numbers $M = u/v_{Ti}$ and $M_A = u/v_\mathrm{A}$ have values 8–10.

The numbers allow estimating typical values of the solar wind kinetic energy density $n_i m_i u^2/2 \approx 10^{-9}\,\mathrm{erg\,cm}^{-3}$ and the magnetic energy density $B^2/8\pi \approx 10^{-10}\,\mathrm{erg\,cm}^{-3}$ near the Earth orbit, so the kinetic energy of the hydrodynamic flow exceeds the magnetic energy by a factor of ten. This allows neglecting the electromagnetic forces and considering the solar wind as a purely hydrodynamic flow to the first approximation. But before applying the HD we have to check if condition (2.9) $\Lambda_{ii} \ll r$ is fulfilled, where r is heliocentric distance and Λ_{ii} is the ion mean free path. We have $\Lambda_{ii} = 1/n_i\sigma_{ii}$ and use the Coulomb cross section $\sigma_{ii} \approx \pi(e^2/m_i v_{Ti}^2)^2 \ln\Lambda_\mathrm{C} \approx \pi(e^2/T_i)^2 \ln\Lambda_\mathrm{C}$ obtained for the thermal plasma (see Sect. 1.3.7). It is then convenient to express the mean free path Λ_{ii} in astronomical units ($1\,\mathrm{AU} \approx 1.49\times10^{13}\,\mathrm{cm}$):

$$\Lambda_{ii} \approx 0.7\times10^{-9} T_i^2/n_i, \tag{2.74}$$

where the temperature and the number density are in Kelvin and cm^{-3}, respectively.

Adopting the coronal values $n_i = 2\times10^8\,\mathrm{cm}^{-3}$ and $T_i = 2\times10^6\,\mathrm{K}$ for the height at which the solar wind is launched, we obtain $\Lambda_{ii} \approx 2\times10^8\,\mathrm{cm}$

$\ll R_\odot \approx 7 \times 10^{10}$ cm; thus, the hydrodynamic description is applicable here. However, at the Earth orbit, we have $T_i \approx 10^5$ K and $n_i \approx 5\,\mathrm{cm}^{-3}$. Formula (2.74) gives $\Lambda_{ii} \approx 1$ AU in this case, i.e., $\Lambda_{ii} \approx r$, so the space plasma is collisionless and the hydrodynamic approach seems to fail. Nevertheless, as we have discussed in Sect. 1.3.8, the anomalous processes can strongly reduce the particle mean free path in the collisionless plasma compared with that determined by the Coulomb scattering only. Fluctuations of interplanetary magnetic field and plasma waves developed due to different plasma instabilities make the particle trajectories tangled and the velocities more isotropic, and so reduce their mean free paths, which ensures broader applicability of the HD/MHD approach than it could be anticipated. Complementary, the effective mean free path of solar wind protons was measured from experimental data about its distribution function (see, e.g., the first data reported by Brandt et al. 1973; Marsch et al. 1982a,b). The anomalous mean free path varies depending on the IPM state and was found to be well below 0.1 AU in many cases. This remarkable finding justifies approximate applicability of the standard HD equations to describe the solar wind at 1 AU and farther away from the Sun.

It should be emphasized, however, that for the number densities and temperatures typical for the interplanetary plasma, the mean free path of particles with respect to Coulomb collisions is rather large and often exceeds 1 AU. Thus, the particle distributions are not necessarily isotropic, and particle distribution functions are not necessarily Maxwellian (see Sect. 1.3.8). In agreement with this expectation, the measured steady-state distribution function of the solar wind particles is typically well described by a *kappa* distribution, rather than a Maxwellian. The thermal energies of electrons and ions (i.e., the electron and ion effective temperatures) are often different. This means that the solar wind is seldom (never) in a state of a true thermodynamic equilibrium.

We note that the Sun loses an extremely small part of its mass in the form of the solar wind. The discussed parameters of the solar wind allow estimating the entire mass flow from the Sun: $J_M = 4\pi r_0^2 u m_i n_i \approx 10^{19}$ g/year $\approx 10^{-14} M_\odot$/year, where $r_0 = 1$ AU, $M_\odot \approx 2 \times 10^{33}$ g is the solar mass. During the Sun lifetime ($<10^{10}$ years) the solar wind has taken out total of only $10^{-4} M_\odot$ if we adopt that the flow parameters are more or less constant over this time.

2.5.2 Parker's Model of the Solar Corona Expansion

Let us apply, following Parker (1963), the HD equations to understand the phenomenon of the solar wind. We start with analysis of the *hydrostatic* ($\partial/\partial t = 0$ and $\boldsymbol{u} = 0$) equilibrium of a spherically symmetric fully ionized hydrogen atmosphere to which the equation of state, Eq. (2.23),

$P(r) = 2n_i(r)T(r)$ of a tenuous gas applies. Neglecting electromagnetic forces, Eq. (2.2) requires that the pressure gradient is balanced by the gravitation force:

$$\frac{\mathrm{d}}{\mathrm{d}r}\,2n_iT + \frac{GM_\odot m_i n_i}{r^2} = 0, \tag{2.75}$$

where $G \approx 6.67 \times 10^{-8}\,\mathrm{cm^3 g^{-1} s^2}$=$6.67 \times 10^{-11}\,\mathrm{m^3 kg^{-1} s^2}$ is the gravitational constant. Integration of this equation yields

$$n_i(r)T(r) = n_i(r_0)T(r_0)\exp\left[-\frac{GM_\odot m_i}{2}\int_{r_0}^{r}\frac{\mathrm{d}s}{s^2T(s)}\right]. \tag{2.76}$$

Remarkable conclusions about the hydrostatic equilibrium can be derived from analysis of the rhs of the equation. Indeed, if the temperature $T(r)$ decreases with r faster than r^{-1} then the exponent index decreases infinitely at $r \to \infty$ and, thus, $n_i(r)T(r) \to 0$ at the infinity. Stated another way, this tells us that the stellar atmosphere has a finite size and a hydrostatic equilibrium is achievable.[2] The only way of the atmosphere dissipation here is gravitation runaway of higher-energy particles from a "tail" of the steady-state distribution, which is beyond the HD applicability region.

However, if the temperature decreases slower than r^{-1} then the exponent index in Eq. (2.76) has a finite value at arbitrarily large r, which implies a finite pressure at the infinity. Since a finite gas amount (stellar atmosphere) cannot be distributed over an infinite volume with a finite density, we arrive at a conclusion that no hydrostatic equilibrium is possible in this case; thus, a HD expansion with some $u(r) \neq 0$ must appear.

Let us consider this expansion assuming the motion to be stationary ($\partial/\partial t = 0$ as before). We use the equation of mass conservation

$$n_i(r)u(r)r^2 = n_i(r_0)u(r_0)r_0^2, \tag{2.77}$$

where r_0 is the stellar radius at the base of corona, and the equation of motion

$$m_i n_i u\frac{\mathrm{d}u}{\mathrm{d}r} + \frac{\mathrm{d}}{\mathrm{d}r}2n_iT + \frac{GM_\odot m_i n_i}{r^2} = 0. \tag{2.78}$$

Full solution of the problem requires also an energy transfer equation. However, the fundamental science question of the mechanisms of the solar wind heating (and, more generally, of the corona heating) is highly sophisticated and has not yet been fully understood, which will be discussed in greater detail later. Now, to make a qualitative progress, we adopt a simple power law for the temperature dependence on r without assuming a specific mechanism of the corona heating.

[2] It must be noted that such hydrostatic equilibrium is not necessarily stable: for example, it can be convectively unstable if the temperature gradient is large; see Chap. 6.

It is convenient to introduce two characteristic proton velocities, the thermal speed (which is also the "isothermal" speed of sound)

$$v_T(r) = [2T(r)/m_i]^{1/2} \tag{2.79}$$

and the runaway velocity from r_0

$$v_e = (GM_\odot/r_0)^{1/2} = \text{const}. \tag{2.80}$$

With this notations Eq. (2.78) receives the form

$$u\frac{\mathrm{d}u}{\mathrm{d}r}\left(1 - \frac{v_T^2}{u^2}\right) = R(r), \tag{2.81}$$

where

$$R(r) = -r^2\frac{\mathrm{d}}{\mathrm{d}r}\frac{v_T^2}{r^2} - \frac{v_e^2 r_0}{r^2}. \tag{2.82}$$

We consider the case when the atmosphere is strongly coupled with the star $v_e^2 \gg v_T^2(r_0) \gg u^2(r_0)$ at the level $r = r_0$, while the temperature T monotonously decreases with r slower than r^{-1}, i.e., $T(r) = T_0(r/r_0)^{\varepsilon-1}$, $0 < \varepsilon < 1$, $T(\infty) \to 0$. For $r \to r_0$ we have $R(r) < 0$ because $v_e^2 \gg v_T^2$. Nevertheless, the first term in the rhs of Eq. (2.82) is positive and decreases slower than r^{-2}. Therefore, a "critical layer" $r = r_c$ exists, where $R(r_c) = 0$, with $R(r) > 0$ at $r > r_c$ and $R(r) < 0$ at $r < r_c$. Since at the corona base, $r = r_0$, the expansion is weak, $u^2 \ll v_T^2$, then both values entering Eq. (2.81), $1 - v_T^2/u^2$ and $R(r)$, are negative, so $\mathrm{d}u/\mathrm{d}r > 0$ is positive, i.e., the gas is being accelerated by the pressure gradient.

Consider what can happen to the flow farther away from the star. If, (1) during the gas acceleration, the flow velocity u reaches the value of v_T somewhere at $r < r_c$ then $\mathrm{d}u/\mathrm{d}r \to \infty$ at $v_T = u$ according to Eq. (2.81), while the flow velocity is directed toward the star at larger r (see curve 1 in Fig. 2.2). Such solutions seem to be inconsistent with the adopted stationarity of the flow and so require account of the time derivative in Eq. (2.2). If (2) the equality $v_T = u$ is not achieved at $r < r_c$, then the derivative $\mathrm{d}u/\mathrm{d}r$ becomes negative at $r > r_c$, and the gas motion remains subsonic at the entire space decaying gradually at large distance from the star. Such solutions (see curve 2 in Fig. 2.2) are called the *stellar breeze* to distinguish from supersonic solar *wind*. Finally, (3) if the expansion velocity u reaches the thermal velocity v_T at the very same layer r_c, where $R(r_c) = 0$ (curve 3 in Fig. 2.2), then the stellar wind becomes supersonic at $r > r_c$, where it keeps accelerating. This solution does correspond (qualitatively) to the solar wind actually observed in the IPM. For any given temperature profile, one can plot dependences of u and other relevant parameters on r numerically.

We must emphasize, however, that even though the model considered uncovers the fundamentals behind the solar wind phenomenon, it remains

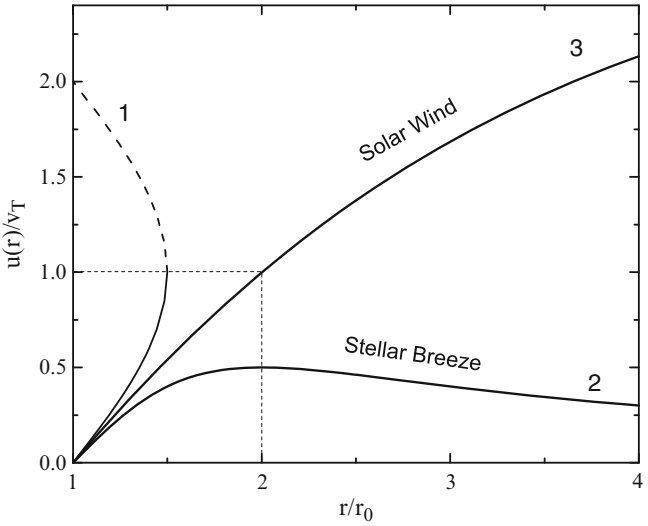

Figure 2.2: Solutions for the plasma outflow from a star: (1) double valued and so unphysical flow; (2) subsonic stellar breeze; and (3) supersonic stellar wind. In this example the critical radius $r_c = 2r_0$.

highly idealized and incomplete. In particular, it ignores the magnetic field, the star rotation, the difference between electron and ion temperatures, departure from the thermodynamic equilibrium, all kinds of inhomogeneity, nonstationarity, and heating mechanisms, all of which can have major effect on the solar wind properties. For example, eruptive processes in the solar corona often give rise to ejections of large massive plasma clouds (so-called coronal mass ejections, CMEs), which have huge effect on the space weather at the Earth orbit.

A fundamental question of an additional plasma heating, which is vital for the solar wind phenomenon, deserves more discussion. We have already noticed that to allow for the solar wind acceleration, the plasma temperature must not decrease too rapidly with r. In fact, as we are going to show below, an additional energy deposition is critically needed for the gas to overcome the gravitation force and acquire a supersonic speed.

To make this clear we note that according to Eq. (2.77) the density of expanding plasma obeys the law:

$$n_i(r) = n_i(r_0)\frac{u(r_0)r_0^2}{u(r)r^2}. \tag{2.83}$$

If no energy deposition is present, the gas expands adiabatically:

$$T = T_0(n_i/n_{i0})^{\gamma-1}, \tag{2.84}$$

with the ratio of specific heats $\gamma = 5/3$ for a single-atom gas. Thus, the

temperature decreases as

$$T \sim u^{-(\gamma-1)} r^{-2(\gamma-1)}, \tag{2.85}$$

i.e., $\propto r^{-4/3}$ for a constant expansion velocity and even faster for an accelerated expansion, which is in all the cases faster than a limiting temperature profile $\propto r^{-1}$ obtained from Eq. (2.76).

Let us estimate the required heat deposition based on the energy balance consideration (Parker 1979). The gravitation energy density per unit volume is

$$\Phi(r) = -\frac{GM_\odot m_i n_i}{r}. \tag{2.86}$$

The energy, which is spent for the gas to overcome the gravitation field and to accelerate the gas, is the enthalpy, which accounts the work of the pressure force:

$$w = \epsilon + P = \frac{2\gamma}{\gamma - 1} n_i T. \tag{2.87}$$

Here $\epsilon = n_i T/(\gamma - 1)$ is the internal energy density. The ratio

$$\frac{w}{|\Phi(r_0)|} = \frac{5 T r_0}{G M_\odot m_i} \approx 0.43 \tag{2.88}$$

is less than one for $r = r_0 \approx 0.7 \times 10^{11}$ cm and $T \approx 2 \times 10^6$ K and so is insufficient to produce the wind. Therefore, to overcome the gravitation and to accelerate then gas up to 400 km/s an additional energy Q must indeed be deposited. In place of explicit account of the energy sources, we describe this energy deposition by using the polytropic equation instead the adiabatic one:

$$T = T_0 (n_i / n_{0i})^{\alpha - 1}, \tag{2.89}$$

where α is the polytropic index. For $\alpha < \gamma$ comparison of Eq. (2.89) with adiabatic equation (2.84) reveals that for the same gas expansion n_i/n_{0i}, the temperature is larger for polytropic process than for the adiabatic process. Therefore, this does account for an additional heat deposition into the gas, with the heat efficiency defined by the polytropic index; apparently, no information on the physical mechanisms of the plasma heating is available in Eq. (2.89) within this treatment.

We can now introduce an effective enthalpy w_{eff} accounting for the additional heat deposition in the form of Eq. (2.87) with the polytropic index α in place of the adiabatic index: γ

$$w_{\text{eff}} = \frac{2\alpha}{\alpha - 1} n_i T. \tag{2.90}$$

The required polytropic index then can easily be estimated from the energy conservation per particle at the corona base and far away from the Sun in a region of the supersonic wind:

$$\frac{2\alpha}{\alpha-1}T_0 - \frac{GM_\odot m_i n_i}{r_0} = \frac{m_i u^2(r)}{2}. \tag{2.91}$$

Here we neglected the expansion velocity at the corona base and neglected thermal energy and gravitation potential far away from the Sun. Substitution of the mean solar wind speed $u(r) = 400$ km/s and typical coronal parameters yields $\alpha \approx 1.14$; Parker (1979) proposed $1.0 < \alpha < 1.3$ as the most plausible range for the polytropic indices. Equation (2.91) also tells us that for low coronal temperature

$$T_0 < \frac{(\alpha-1)Gm_i M_\odot}{2\alpha r_0}, \tag{2.92}$$

the expansion is impossible and the corona remains static.

Let us touch upon possible mechanisms of the additional heat deposition into the expanding plasma. Generally, there are absorption of the solar radiation flux, standard heat conductivity, losses of nonthermal particle population, and dissipation of various plasma/MHD waves, which are efficiently generated in the convective zone of the Sun and then transferred outward to the corona. First three mechanisms are easy to take into account; it turns that all they are insufficient to provide the required plasma heating. We, therefore, forced to conclude that the primary source of the heat is the wave dissipation. However, it is extremely difficult to quantitatively check this conclusion because the theory of wave generation, propagation, and damping is very complicated and in addition depends on poorly known details of the solar atmosphere structure and relevant physical conditions. We will consider some of the related processes and phenomena below in this book; however, the current state of the science is yet unable to fully describe the phenomenon of the solar wind and in particular—reliably identify the sources and mechanisms of the additional corona heating.

The discussed simplest model of the uniform corona expansion suggests that the solar wind overcomes the sound speed and becomes supersonic at around $r_c \approx 10 r_\odot$. Accordingly, at the Earth orbit, the plasma flow is highly supersonic and superalfvenic. We note that a very interesting physics takes place at those regions where such a supersonic flow interacts with an obstacle. A practically important and actively studied example of this is the interaction of the solar wind with the Earth's magnetosphere (Fig. 1.3), which results in a variety of observable manifestations including the polar lights (Fig. 1.4).

Then, as the wind propagates farther away from the Sun, the ISM surrounding the solar system starts to affect and modify the solar wind (see, e.g., Hundhausen 1972; Baranov and Krasnobaev 1977). Indeed, if the interstellar medium pressure were absent, the solar wind speed would remain

approximately constant, of the order of $400\,\mathrm{km\,s^{-1}}$; its number density would fall with distance as r^{-2}, and the temperature would also decrease as described. Hence, the solar wind would become more and more supersonic. However, in the real situation, the solar wind is slowed down by the interstellar medium and, therefore, the supersonic regime should give a way to a subsonic one at some distance from the Sun, which is accompanied by the appearance of a termination shock.

A rough estimate of the shock position r_{sh} may be obtained from the requirement of balance between the solar wind dynamic pressure and interstellar medium pressure:

$$n_i m_i u^2 \approx (n_a + 2n_e)T + \frac{B^2}{8\pi} + P_{\mathrm{CR}}, \tag{2.93}$$

where P_{CR} is the cosmic ray (relativistic particles) pressure, n_a is the number density of neutral atoms in interstellar medium, n_e is the electron number density in interstellar medium, and T is its temperature. Substituting $n_i = n_{iE} r^{-2}$, where $n_{iE} \approx 5\,\mathrm{cm^{-3}}$ and r_{Tsh} is the distance in AU, and other parameters adopted above, we obtain $r_{Tsh} \approx 100\,\mathrm{AU}$.

A number of space missions have been launched toward the anticipated bounds of the solar system years ago to determine where those bounds are and what are the physical conditions there. The first reliable detection of the termination shock occurred on December 14, 2004, by a spacecraft Voyager 1 at the distance 94 AU from the Sun. It took around 30 years for the spacecraft, launched on 1977, to path through the solar system. Later, Voyager 2 having a different trajectory detected the termination shock at the distance 84 AU on August 30, 2007. In fact, Voyager 2 detected the termination shock a few times: this is because the position of the termination shock is changing in time in response to short-term variations of the solar activity. It is supposed that the shock position also experiences systematic changes back and forth following the 11 years cycle of the solar activity. According to the measurements made by Voyagers 1 and 2, the solar wind velocity near the heliospheric shock wave was approximately 380 km/s, and the ratio $u_1/u_2 = \rho_2/\rho_1 \approx 3$ at the front.

2.5.3 Magnetic Field in a Cavity Filled by a Stellar Wind

Consider now another important constituent of the solar wind, the mean magnetic field. Specifically, let us apply dissipation-free induction equations (2.33) to calculate the magnetic field structure in a volume filled by solar or stellar wind within a simple model. Here, we adopt that the plasma is launched isotropically from a spherical surface of the radius a, rotating around a central axes with constant angular velocity Ω. The stellar wind speed u is constant and has radial direction. At the spherical surface there is a magnetic field,

which is described by the function $\boldsymbol{B}(a,\vartheta,\alpha) = \boldsymbol{B}_0(\vartheta,\alpha)$ in the reference frame rotating together with the star, where α is the azimuth angle in the plane transverse to the rotation axes. The energy density of the plasma motion exceeds significantly the energy density of the magnetic field; thus, we can neglect the magnetic field effect on the plasma motion. Using the freezing-in condition we find here the magnetic field distribution (dependence of the magnetic field on the coordinates and time) in the region $r > a$ in the laboratory (rest frame) system.[3]

To solve this problem we first project vector equation (2.38) to the axes r and substitute $\boldsymbol{u} = u\boldsymbol{r}/r$, $u = \text{const}$, which yields the equation for B_r:

$$\frac{\partial B_r}{\partial t} = -\frac{2u}{r}B_r - u\frac{\partial B_r}{\partial r}. \tag{2.94}$$

Solution of this equation is an arbitrary function of independent variables $r - ut$, ϑ, and α divided by r^2:

$$B_r(r,\vartheta,\alpha,t) = \frac{1}{r^2}F(r-ut,\vartheta,\alpha). \tag{2.95}$$

The boundary condition has evidently the form

$$B_r\big|_{r=a} = B_{0r}(\vartheta,\alpha+\Omega t) = \frac{1}{a^2}F(a-ut,\vartheta,\alpha), \tag{2.96}$$

where the argument $\alpha + \Omega t$ in B_{0r} originates from the transition from the rotating frame to the laboratory rest frame; therefore

$$F(a-ut,\vartheta,\alpha) = a^2 B_{0r}(\vartheta,\alpha+\Omega t)$$

and solution (2.95) reads

$$B_r(r,\vartheta,\alpha,t) = \left(\frac{a}{r}\right)^2 B_{0r}\left(\vartheta,\alpha - \frac{(r-a)\Omega}{u} + \Omega t\right). \tag{2.97}$$

In a similar way, we find two remaining components of the magnetic field:

$$B_\vartheta = \frac{a}{r}B_{0\vartheta}\left(\vartheta,\alpha - \frac{(r-a)\Omega}{u} + \Omega t\right), \tag{2.98a}$$

$$B_\alpha = \frac{a}{r}B_{0\alpha}\left(\vartheta,\alpha - \frac{(r-a)\Omega}{u} + \Omega t\right). \tag{2.98b}$$

[3]The model considered here was proposed by Parker (1959) to describe the interplanetary magnetic field produced by the solar plasma flows composing the solar wind.

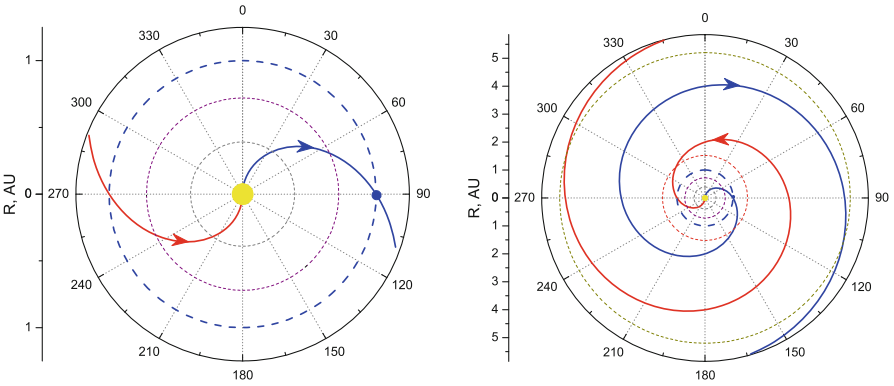

Figure 2.3: Two oppositely directed magnetic field lines illustrating the Parker model of the IPM magnetic field at the scale of the Earth (*left*) and Jupiter (*right*) orbits. The planet orbits are shown by *dashed color circles* (the orbit eccentricities are neglected) for Mercury (*grey*), Venus (*violet*), Earth (*bold blue*; the planet itself is shown by *blue circle*; not in scale), Mars (*red*), and Jupiter (*brown*).

Using Maxwell equation $\nabla \cdot \boldsymbol{B} = 0$ and Eq. (2.97) gives rise to the following useful relationship between components of the vector $\boldsymbol{B}_0$:

$$-\frac{a\Omega}{u}\frac{\partial B_{0r}}{\partial \alpha}\sin\vartheta + \frac{\partial}{\partial \vartheta}(B_{0\vartheta}\sin\vartheta) + \frac{\partial B_{0\alpha}}{\partial \alpha} = 0.$$

For example, if $B_{0\vartheta} = 0$ then $B_\vartheta = 0$ during the entire field evolution, and

$$B_{0\alpha} = \frac{a\Omega}{u}B_{0r}\sin\vartheta + f(\vartheta).$$

If we further adopt $f(\vartheta) = 0$, we then obtain

$$B_\alpha(r,\vartheta,\alpha,t) = \frac{a^2\Omega}{ur}B_{0r}\left(\vartheta, \alpha - \frac{(r-a)\Omega}{u} + \Omega t\right)\sin\vartheta. \tag{2.99}$$

Equations (2.97) and (2.99) show that the azimuth component of the magnetic field decreases with r much slower, as $\propto r^{-1}$, than the radial component does, as $\propto r^{-2}$. Thus, even if the radial component of the magnetic field dominates at the star surface, the azimuth component dominates farther away from the star, which gives rise to the spiral shape of the mean interplanetary magnetic field.

Parker applied this model to describe the interplanetary magnetic field of the solar wind (Fig. 2.3). The original Parker's model adopts $B_\vartheta = 0$, while B_r and B_α are described by Eqs. (2.97) and (2.99). Measurements of the interplanetary magnetic field indicate the presence of a slowly varying

component, which indeed has an approximately spiral structure and intersects the Earth orbit at an angle of 45°. The average magnetic field near the Earth orbit is close to 5×10^{-5} G, though the measured values are scattered very strongly. At low heliographic latitudes the spiral field consists of several sectors with mutually opposite magnetic field directions. The radial component varies with distance as r^{-2}, in good agreement with the Parker model. However, the agreement is much poorer for the azimuthal component, which displays the dependences from $B_\alpha \sim r^{-1.23}$ to $\sim r^{-1.1}$ between 1 and 5 AU. The component $B_\vartheta < 10^{-5}$ G was also observed near the Earth orbit.

The magnetic field structure unlike the solar wind itself is not spherically symmetric. Given that the magnetic energy density is one–two orders of magnitude smaller than the kinetic energy of the solar wind, thus, a relatively weak deviation of the solar wind from the spherically symmetric flow can have major effect on the magnetic field structure. Even though observations do often reveal significant departure of the measured magnetic field from the Parker's one, the overall agreement is, nevertheless, remarkably good especially if one takes into account the number of the simplifications adopted.

Problems

2.1 Using the Faraday induction law and dissipation-free equations (2.28), prove that the magnetic flux through arbitrary closed contour remains constant regardless contour motions and deformations.

2.2 Adopt stationary equilibrium of the conducting fluid in a magnetic field. Demonstrate that the vectors of the magnetic field $\boldsymbol{B}$ and the current density $\boldsymbol{j}$ are tangent to the surfaces $p(\boldsymbol{r}) = \text{const}$.

2.3 Adopt that electric current J flows along a hot plasma cylinder with radius a and a nonuniform current density $j(r)$ (z-pinch). Find stationary solution $P(r)$ for the plasma pressure under the condition that this pressure is compensated by the magnetic pressure produced by this electric current itself. Write down a relation linking the total electric current of the pinch and the pinch pressure integrated over pinch cross section.

Adopt then that the plasma is isothermal and obeys the ideal gas equation of state [Eq. (2.23)]. Express current J via the plasma temperature T and the total number of the plasma electrons (or ions) N per unit length of the cylinder. Calculate the current assuming $N \approx 10^{15}$ ions/cm and $T \approx 10^8$ K—the parameters typical for the nuclear fusion studies; see Fig. 1.1.

2.4 Determine equilibrium condition for the plasma cylinder with radius a, in which the electric current has only azimuth component $j_\alpha(r)$ (so-called theta pinch). The outside pressure is small and can be discarded compared with the pinch pressure. Is it possible to ensure equilibrium using some distribution of the magnetic field produced by external sources?

2.5 The magnetic field is called the *force-free field* (Sect. 2.3.3) if the density of Ampère's force is zero everywhere: $\boldsymbol{j} \times \boldsymbol{B}/c = 0$. To ensure this, it is apparently necessary and sufficient that the electric current is directed along the field lines everywhere.

(a) Show that the force-free field $\boldsymbol{B}$ satisfies the equation set:

$$\nabla \times \boldsymbol{B} = \alpha_{FFF}\boldsymbol{B}, \quad \boldsymbol{B}\cdot\nabla\alpha_{FFF} = 0,$$

where $\alpha_{FFF}(\boldsymbol{r})$ is arbitrary differentiable scalar function (including constant).

(b) Derive a force-free field dependent on r only in cylindrical coordinates for $\alpha_{FFF} = \text{const}$.

(c) Is it possible to have a finite energy of the force-free field for $\alpha_{FFF} = \text{const}$?

(d) Prove that $\alpha_{FFF} = \text{const}$ for any force-free field along any field line.

2.6 Consider modification of MHD eigenmodes in a plasma permitted by a nonpotential force-free magnetic field and calculate the corresponding kinetic helicity density defined as $h_k = \langle \boldsymbol{u}(\boldsymbol{r},t) \cdot \nabla \times \boldsymbol{u}(\boldsymbol{r},t) \rangle$.

2.7 Adopt that a stationary velocity field $\boldsymbol{u} = (u_x(y,z), 0, 0)$ holds in a conducting fluid (shear motion). The initial condition at $t = 0$ for the magnetic field is $\boldsymbol{B}_0 = (0, B_{0y}(y,z), B_{0z}(y,z))$. Apply dissipation-free approximation ($\nu_m \to \infty$) to derive the field at $t > 0$.

2.8 A stationary differential rotation (i.e., various fluid layer rotate with different velocities) with an angular velocity $\boldsymbol{\Omega} = \boldsymbol{e}_z\Omega(r,\vartheta)$, where r, ϑ are the spherical coordinates, holds in a conducting fluid. Originally, the magnetic field is poloidal, i.e., it belongs to meridian planes: at $t = 0$, $\boldsymbol{B} = (B_{0r}(r,\vartheta), B_{0\vartheta}(r,\vartheta), 0)$. Calculate the magnetic field at $t > 0$ neglecting the dissipation in the plasma.

2.9 Derive equation (2.98).

2.10 Plot dependences of u and other relevant parameters of the Parker's stellar wind on r numerically for different temperature profiles.

2.11 Find the form of interplanetary magnetic field force lines in Parker's model (see Sect. 2.5.3). Calculate magnetic field value and the angle θ between force line and radial direction at the Earth orbit. The solar radius is $a = 0.7 \times 10^6$ km; the mean magnetic field at the solar surface $B_0 \approx 1$ G; the radius of Earth orbit $r_0 \approx 1.5 \times 10^8$ km; the angular velocity of solar rotation $\Omega = 2.7 \times 10^{-6}$ rad/s; solar wind velocity $u = 300$ km/s (slow solar wind).

2.12 Demonstrate that the solution for the magnetic field in stationary radial stellar wind (see Sect. 2.5.3) has the form

$$\begin{aligned} B_r(r,\vartheta,\alpha,t) &= F\left(\alpha - \frac{(r-a)\Omega}{u} + \Omega t\right)\left(\frac{a}{r}\right)^2 2\cos\vartheta, \\ B_\vartheta(r,\vartheta,\alpha,t) &= p\,\frac{\partial}{\partial\alpha}F\left(\alpha - \frac{(r-a)\Omega}{u} + \Omega t\right)\frac{a^2\Omega}{ur}\,\sin\vartheta, \\ B_\alpha(r,\vartheta,\alpha,t) &= q\,F\left(\alpha - \frac{(r-a)\Omega}{u} + \Omega t\right)\frac{a^2\Omega}{ur}\,2\sin\vartheta\cos\vartheta. \end{aligned}$$

Here p and q are constants, which satisfy the condition $p+q=1$, and F is an arbitrary function, specified by the boundary conditions at the solar surface.

Answers and Solutions

2.2 In the static equilibrium ($\boldsymbol{u}=0$) and in the absence of non- electromagnetic, forces the equilibrium condition reads $\nabla p = \boldsymbol{j}\times\boldsymbol{B}/c$. Thus the vectors $\boldsymbol{B}$ and $\boldsymbol{j}$ are transverse to the pressure gradient and so tangent to the isobaric surfaces.

2.3 The magnetic field has one component:

$$B_\varphi \equiv B(r) = \frac{4\pi}{cr}\int_0^r rj(r)\,\mathrm{d}r.$$

Integrating the equilibrium condition, which follows from Eq. (2.13a) for $u=0$ with the boundary condition $p\big|_{r\geq a}=0$, we obtain

$$p\,(r) = \frac{1}{8\pi}\int_r^a \frac{1}{r^2}\frac{\mathrm{d}}{\mathrm{d}r}(r^2B^2)\,\mathrm{d}r, \tag{1}$$

where $B = (4\pi/cr)\int_0^r rj(r)\,\mathrm{d}r$ at $r<a$ and $B=2J/cr$ at $r>a$. To link the total current with the pressure we integrate Eq. (1) over full transverse section and apply the relation $aB(a)=2J/c$, which yields

$$\int_0^a p\,(r)2\pi r\,\mathrm{d}r = \frac{J^2}{2c^2}. \tag{2}$$

Assuming that the plasma is an equilibrium ideal gas with a given temperature T (in units of energy), we adopt $p=2n(r)T$ and then Eq. (2) yields

$$J = 2c\sqrt{NT}. \tag{3}$$

Substitution of required numbers into (3) results in $J = 7.5 \times 10^4$ A. In practice the plasma is often non-isothermal, with the electron temperature exceeding the ion temperature. To maintain the equilibrium the current must grow in time, because the current results in the increase of both temperature and pressure. In addition, the pinch can become unstable relative to kink or sausage mode instabilities.

2.4 The magnetic field inside the cylinder has one component $B_z(r) \equiv B(r) = (4\pi/c)\int_r^a j_\varphi(r)\mathrm{d}r$. The equilibrium inside the cylinder requires constancy of the full pressure:

$$p\,(r) + \frac{B^2(r)}{8\pi} \;=\; \text{const.}$$

Outside the cylinder without any medium we have $p = 0$ and the magnetic field generated by the azimuth current is zero, $B = 0$; thus, the internal pressure can only be balanced by a magnetic pressure produced by a field directed along the cylinder axes, whose value at the side surface of the cylinder is $B_0 = \sqrt{8\pi p\,(a)}$. The magnetic field inside the cylinder is always smaller than the external field:

$$\frac{B^2}{8\pi} = \frac{B_0^2}{8\pi} - p;$$

thus, the plasma is a diamagnetic.

2.5 (b) $\boldsymbol{B}(\boldsymbol{r}) = B_0 \cdot (0,\, J_1(\alpha_{FFF} r),\, J_0(\alpha_{FFF} r))$, where $J_n(x)$ is the Bessel function.

2.6 To investigate properties of weakly damping linear modes we neglect the dissipative terms entirely in MHD Eqs. (2.13) and (2.16). Then, for simplicity, we only consider the helicity originating from the magnetic field twist (the corresponding pseudoscalar is formed by the dot product of the polar vector $\boldsymbol{j}$ and the axial vector $\boldsymbol{B}$: $\boldsymbol{j} \cdot \boldsymbol{B}$, while no other polar vectors are explicitly considered) and so we neglect the kinetic pressure and the external force assuming that their contribution to the helicity is smaller; so the equations read

$$\nabla{\cdot}\boldsymbol{B} \;=\; 0, \qquad \frac{\partial \boldsymbol{B}}{\partial t} = \nabla \times [\boldsymbol{u} \times \boldsymbol{B}], \tag{2.100a}$$

$$\rho\left(\frac{\partial \boldsymbol{u}}{\partial t} + (\boldsymbol{u}{\cdot}\nabla)\boldsymbol{u}\right) \;=\; \frac{1}{4\pi}[\nabla \times \boldsymbol{B}] \times \boldsymbol{B}. \tag{2.100b}$$

Now, to describe the small-amplitude linear modes satisfying these equations, we have to linearize them adopting $\boldsymbol{B} = \boldsymbol{B}_0 + \boldsymbol{b}$ for the magnetic field and adopting $\boldsymbol{b}$ and $\boldsymbol{u}$ to be the first-order oscillating values of an MHD mode. Importantly, that upon substitution of $\boldsymbol{B} = \boldsymbol{B}_0 + \boldsymbol{b}$ into Eq. (2.100b) we have to take into account that in the nonpotential force-free field $\nabla \times \boldsymbol{B}_0 = \alpha_{FFF}\boldsymbol{B}_0 \neq 0$ unlike cases of a uniform field or nonuniform potential field, which yields

$$\frac{\partial \boldsymbol{b}}{\partial t} = (\boldsymbol{B}_0 \cdot \nabla)\boldsymbol{u} - (\boldsymbol{u} \cdot \nabla)\boldsymbol{B}_0, \ \frac{\partial \boldsymbol{u}}{\partial t} = \frac{\alpha_{FFF}}{4\pi\rho}\boldsymbol{B}_0 \times \boldsymbol{b} + \frac{1}{4\pi\rho}(\nabla \times \boldsymbol{b}) \times \boldsymbol{B}_0. \tag{2.101}$$

Within the eikonal approximation (i.e., adopting the wavelengths of the eigenmodes to be small compared with the source inhomogeneity scale) we can write $\boldsymbol{b} = \boldsymbol{b}_\omega e^{i\psi(\mathbf{r})-i\omega t}$ and a similar for $\boldsymbol{u}$, which yields equations for the corresponding complex amplitudes:

$$\boldsymbol{b} = (i/\omega)[i(\boldsymbol{B}_0 \cdot \nabla\psi)\boldsymbol{u} - (\boldsymbol{u} \cdot \nabla)\boldsymbol{B}_0], \tag{2.102a}$$

$$\boldsymbol{u} = \frac{i\alpha_{FFF}}{4\pi\rho\omega}\boldsymbol{B}_0 \times \boldsymbol{b} - \frac{1}{4\pi\rho\omega}[(\boldsymbol{b} \cdot \boldsymbol{B}_0)\nabla\psi - (\boldsymbol{B}_0 \cdot \nabla\psi)\boldsymbol{b}]. \tag{2.102b}$$

Let us solve these equations to the first-order accuracy over the small parameter $\alpha_{FFF}/|\nabla\psi| \ll 1$. In the zeroth-order approximation we have

$$\boldsymbol{b} = -\frac{1}{\omega}(\boldsymbol{B}_0 \cdot \nabla\psi)\boldsymbol{u}, \quad \boldsymbol{u} = -\frac{1}{4\pi\rho\omega}(\boldsymbol{B}_0 \cdot \nabla\psi)\boldsymbol{b}, \tag{2.103}$$

which yields the eikonal

$$\nabla_\parallel \psi = \pm\omega/v_\mathrm{A}, \quad v_\mathrm{A} = B_0/\sqrt{4\pi\rho}. \tag{2.104}$$

It is easy to see that in the zeroth approximation these perturbations are identical to the purely alfvénic modes for which the conditions $\boldsymbol{b} \cdot \nabla\psi = 0$, $\boldsymbol{u} \cdot \nabla\psi = 0$, $\boldsymbol{b} \cdot \boldsymbol{B}_0 = 0$, and $\boldsymbol{u} \times \boldsymbol{b} = 0$ are satisfied.

Since we use the complex amplitudes, the bilinear terms like ab must be computed as $(1/2)\Re\langle ab^*\rangle$, where in addition to averaging over the period $T = 2\pi/\omega$ we also average over the random phases of Fourier harmonics:

$$\langle b_\mu b_\nu^*\rangle = (1/2)\langle b_\omega^2\rangle(\delta_{\mu\nu} - e_\mu^\parallel e_\nu^\parallel). \tag{2.105}$$

In the zeroth over α_{FFF} approximation, the kinetic helicity parameter is zero: $\langle \boldsymbol{u} \cdot (\nabla \times \boldsymbol{u}^*)\rangle = 0$.

Now, taking into account the first order over $|\alpha_{FFF}/\nabla\psi|$ terms, Eq. (2.102b) yields

$$\boldsymbol{u} = -\frac{1}{4\pi\rho\omega}(\boldsymbol{B}_0 \cdot \nabla\psi)\boldsymbol{b} + \frac{1}{4\pi\rho\omega}[i\alpha_{FFF}\boldsymbol{B}_0 \times \boldsymbol{b} + (\boldsymbol{b} \cdot \boldsymbol{B}_0)\nabla\psi], \tag{2.106}$$

where $\boldsymbol{b} \cdot \boldsymbol{B}_0 \neq 0$ and

$$\nabla \times \boldsymbol{u} = -\frac{i}{4\pi\rho\omega}(\boldsymbol{B}_0 \cdot \nabla\psi)(\nabla\psi \times \boldsymbol{b}) + \frac{i}{4\pi\rho\omega}[-\nabla\psi \times (\boldsymbol{b} \cdot \nabla)\boldsymbol{B}_0 + \boldsymbol{b} \times (\boldsymbol{B}_0 \cdot \nabla)\nabla\psi + \boldsymbol{b} \times (\nabla\psi \cdot \nabla)\boldsymbol{B}_0]. \tag{2.107}$$

These two expressions allow calculating the kinetic helicity density:

$$\frac{1}{2}\Re\langle \boldsymbol{u}\cdot(\nabla\times\boldsymbol{u}^*)\rangle = \frac{1}{4}\alpha_{FFF}v_{\mathrm{A}}^2\frac{\langle b_\omega^2\rangle}{B_0^2}, \tag{2.108}$$

which is nonzero any longer; it is proportional to the magnetic field force-free parameter α_{FFF} and the wave intensity $\langle b_\omega^2\rangle$.

2.7

$$B_x(y,z,t) = \left(B_{0y}\frac{\partial u_x}{\partial y} + B_{0z}\frac{\partial u_x}{\partial z}\right)t,\ B_y = B_{0y},\ B_z = B_{0z}.$$

2.8

$$B_\alpha(r,\vartheta,t) = \sin\vartheta\left(rB_{0r}(r,\vartheta)\frac{\partial\Omega}{\partial r} + B_{0\vartheta}\frac{\partial\Omega}{\partial\vartheta}\right)t,\ B_\vartheta = B_{0\vartheta},\ B_r = B_{0r}.$$

2.11 The field lines have a Archimedean spiral shape:

$$r = \frac{u}{\Omega}(\alpha-\alpha_0), \qquad \alpha_0 = \text{const},$$
$$\theta = \arctan\frac{r_0\Omega}{u} \approx 56^\circ; \qquad B \approx 4.5\times10^{-5}\ \text{G}.$$

Chapter 3

Plasma Dispersion: Linear Modes in the Plasma

Dispersion of a medium is provided by a response of the particles composing the medium to an external electromagnetic field applied to the medium. To study the dispersion quantitatively we have to derive macroscopic equations describing averaged electromagnetic fields in the medium. To do so we start from microscopic Maxwell equations (1.53) complemented by electric charge density (1.54a) in the form

$$\rho = e \int (Z f_i - f_e) d^3 p, \tag{3.1}$$

explicitly accounting only electrons and one sort of ions with charge Z and electric current (1.54b) in the corresponding form

$$\boldsymbol{j} = e \int (Z f_i - f_e) \boldsymbol{v} d^3 p, \tag{3.2}$$

where f_i and f_e are the distribution function of the ions and electrons, respectively and e is the (positive) charge of proton. These electric charge and current densities represent the mentioned plasma response to the external field. To describe this response macroscopically it is sufficient to introduce a **polarization vector** $\boldsymbol{P}$ such as

$$\boldsymbol{j} = \frac{\partial \boldsymbol{P}}{\partial t}; \qquad \rho = -\nabla \cdot \boldsymbol{P}. \tag{3.3}$$

These relations ensure that the continuity equation

$$\frac{\partial \rho}{\partial t} + \nabla \cdot \boldsymbol{j} = 0 \tag{3.4}$$

is fulfilled equivalently.

G.D. Fleishman and I.N. Toptygin, *Cosmic Electrodynamics*, Astrophysics and Space Science Library 388, DOI 10.1007/978-1-4614-5782-4_3,

Substitution of ρ and $\boldsymbol{j}$ into Eq. (1.53) yields set of the macroscopic Maxwell equations:

$$\nabla \times \boldsymbol{B} = \frac{1}{c}\frac{\partial \boldsymbol{D}}{\partial t} + \frac{4\pi}{c}\boldsymbol{j}^{ext}, \tag{3.5a}$$

$$\nabla \cdot \boldsymbol{D} = 4\pi\rho^{ext}, \tag{3.5b}$$

$$\nabla \times \boldsymbol{E} = -\frac{1}{c}\frac{\partial \boldsymbol{B}}{\partial t}, \tag{3.5c}$$

$$\nabla \cdot \boldsymbol{B} = 0, \tag{3.5d}$$

where

$$\boldsymbol{D} = \boldsymbol{E} + 4\pi\boldsymbol{P} \tag{3.6}$$

is the **displacement vector** that could be more consistently called the **electric induction** in analogy with magnetic induction. Note that this new displacement vector enters only two first (inhomogeneous) Maxwell equations, while two homogeneous equations remain unchanged compared with the vacuum case. In what follows we assume that there is a linear relation between vectors $\boldsymbol{E}$ and $\boldsymbol{D}$; any nonlinear terms (if present) are assumed to be added to the external charge and current densities.

It is then convenient to apply a Fourier transform to the Maxwell equations, which yields for the Fourier components:

$$i\boldsymbol{k} \times \boldsymbol{B}_{\omega,\mathbf{k}} = -\frac{i\omega}{c}\boldsymbol{D}_{\omega,\mathbf{k}} + \frac{4\pi}{c}\boldsymbol{j}^{ext}_{\omega,\mathbf{k}}, \tag{3.7a}$$

$$i\boldsymbol{k} \cdot \boldsymbol{D}_{\omega,\mathbf{k}} = 4\pi\rho^{ext}_{\omega,\mathbf{k}}, \tag{3.7b}$$

$$\boldsymbol{k} \times \boldsymbol{E}_{\omega,\mathbf{k}} = \frac{\omega}{c}\boldsymbol{B}_{\omega,\mathbf{k}}, \tag{3.7c}$$

$$\boldsymbol{k} \cdot \boldsymbol{B}_{\omega,\mathbf{k}} = 0. \tag{3.7d}$$

Let us obtain an equation for the electric field. First, we write down a general linear relation between the electric and displacement vectors:

$$D_\alpha(\omega,\boldsymbol{k}) = \varepsilon_{\alpha\beta}(\omega,\boldsymbol{k})E_\beta(\omega,\boldsymbol{k}), \tag{3.8}$$

which is equivalent to

$$j_\alpha(\omega,\boldsymbol{k}) = \sigma_{\alpha\beta}(\omega,\boldsymbol{k})E_\beta(\omega,\boldsymbol{k}) \quad \text{with} \quad \varepsilon_{\alpha\beta} = \delta_{\alpha\beta} + \frac{4\pi i}{\omega}\sigma_{\alpha\beta}. \tag{3.9}$$

Then, we eliminate the magnetic field vector from Eq. (3.7a). To do so we apply the cross product $\boldsymbol{k}\times$ to Eq. (3.7c) and expand the double cross product containing the electric field $\boldsymbol{k} \times [\boldsymbol{k} \times \boldsymbol{E}] = \boldsymbol{k}(\boldsymbol{k} \cdot \boldsymbol{E}) - \boldsymbol{E}k^2$, which yields

$$\frac{c^2}{\omega^2}(k_\alpha k_\beta - k^2\delta_{\alpha\beta} + \varepsilon_{\alpha\beta})E_\beta = -\frac{4\pi i}{\omega}j^{ext}_\alpha. \tag{3.10}$$

This equation is convenient to rewrite in a compact form

$$T_{\alpha\beta}E_\beta = -\frac{4\pi i}{\omega} j_\alpha^{ext}, \tag{3.11}$$

where we introduced a so-called **Maxwellian tensor**:

$$T_{\alpha\beta} = \varepsilon_{\alpha\beta} - \frac{c^2k^2}{\omega^2}\left(\delta_{\alpha\beta} - \frac{k_\alpha k_\beta}{k^2}\right). \tag{3.12}$$

Now we can proceed to the analysis of the plasma dispersion and properties of the linear eigenmodes of the medium.

3.1 Eigenmodes of Anisotropic and Gyrotropic Media: General Case

3.1.1 Principal Values and Eigenvectors of the Maxwellian Tensor

In many cases electromagnetic phenomena are convenient to consider in the system of orthogonal unit vectors, in which the Maxwellian tensor is diagonal in form. In particular, this allows a consistent inclusion of spatial dispersion in the generation of quasitransverse modes and enables investigating the polarization of these modes. It is noteworthy that a dispersive medium, in principle, always exhibits absorption proportional to the anti-Hermitian part of the complex dielectric tensor. This fact follows explicitly from the Kramers–Kronig dispersion relations. However, absorption may be rather weak in certain frequency ranges. It is precisely these "transparency windows" that we have in mind below adopting a Hermitian dielectric tensor.

Let us define a natural reference frame in which the Maxwellian tensor is diagonal. We take into consideration that the Hermitian property of the permittivity tensor $\varepsilon_{\alpha\beta}(\omega, \boldsymbol{k})$ implies that the tensor $T_{\alpha\beta}(\omega, \boldsymbol{k})$ is also Hermitian. As is known from linear algebra, the principal values $\lambda^{(m)}(\omega, \boldsymbol{k})$ $(m = 1, 2, 3)$ of a Hermitian tensor are real, while its eigenvectors $\boldsymbol{b}^{(m)}(\omega, \boldsymbol{k})$ are generally complex and mutually orthogonal:

$$\boldsymbol{b}^{(m)*}(\omega, \boldsymbol{k}) \cdot \boldsymbol{b}^{(m)}(\omega, \boldsymbol{k}) = 1, \quad \boldsymbol{b}^{(m)*}(\omega, \boldsymbol{k}) \cdot \boldsymbol{b}^{(n)}(\omega, \boldsymbol{k}) = 0 \quad \text{if} \quad m \neq n. \tag{3.13}$$

Both principal values and eigenvectors should be calculated from the system of algebraic equations

$$T_{\alpha\beta}b_\beta = \lambda b_\alpha, \quad \alpha = 1, 2, 3. \tag{3.14}$$

The principal values must obey a cubic algebraic equation, which is obtained by setting the determinant of system (3.14) to zero:

$$|T_{\alpha\beta} - \lambda\delta_{\alpha\beta}| = 0. \tag{3.15}$$

Once Eqs. (3.14) and (3.15) are solved, the tensor $T_{\alpha\beta}$ obtained from the Maxwell equations and its inverse tensor can be expressed in terms of the real principal values and the complex eigenvectors:

$$T_{\alpha\beta}(\omega,\boldsymbol{k}) = \sum_{m=1}^{3} \lambda^{(m)}(\omega,\boldsymbol{k}) b_{\alpha}^{(m)}(\omega,\boldsymbol{k}) b_{\beta}^{(m)*}(\omega,\boldsymbol{k}), \tag{3.16}$$

$$(\widehat{T}^{-1})_{\alpha\beta} = \sum_{m=1}^{3} \frac{1}{\lambda^{(m)}(\omega,\boldsymbol{k})} b_{\alpha}^{(m)}(\omega,\boldsymbol{k}) b_{\beta}^{(m)*}(\omega,\boldsymbol{k}). \tag{3.17}$$

On multiplying these tensors we explicitly make sure that these two tensors are inverse to each other:

$$T_{\alpha\beta}(\omega,\boldsymbol{k})(\widehat{T}^{-1})_{\beta\nu}(\omega,\boldsymbol{k}) = b_{\alpha}^{(1)} b_{\nu}^{(1)*} + b_{\alpha}^{(2)} b_{\nu}^{(2)*} + b_{\alpha}^{(3)} b_{\nu}^{(3)*} = \delta_{\alpha\nu}.$$

The last equality follows from the completeness property of the Hermitian tensor eigenvectors.

It is important that the eigenvectors $\boldsymbol{b}^{(m)}(\omega,\boldsymbol{k})$ in an anisotropic medium are essentially dependent on the frequency and the wave vector, implying this case to be essentially different from the cases of vacuum or isotropic media. In an isotropic medium, polarization degeneracy takes place, enabling one to arbitrarily select the electromagnetic wave polarization vectors in the plane perpendicular to the wave vector. Thus, the same eigenvector basis can be selected for perturbations with any frequencies for a given direction $\boldsymbol{k}$. As a result, eigenvectors with different frequencies and wave numbers, not only with equal ones, turn out to be mutually orthogonal in an isotropic medium:

$$\boldsymbol{b}^{(m)}(\omega,k,\boldsymbol{\kappa}) \cdot \boldsymbol{b}^{(n)*}(\omega',k',\boldsymbol{\kappa}) = 0 \quad \text{for} \quad m \neq n, \tag{3.18}$$

where $\boldsymbol{\kappa} = \boldsymbol{k}/k$ is a unit vector in the direction of wave propagation. Polarization degeneracy arises from the symmetry of an isotropic medium about rotations by any angle in the plane perpendicular to the vector $\boldsymbol{\kappa}$. In an anisotropic medium, this symmetry is nonexistent in the general case (although it may take place relative to preferred directions), and the orthogonality of the eigenvectors of the Maxwellian tensor is ensured only for coinciding sets of ω and $\boldsymbol{k}$ [see expressions (3.13)].

Let us now express the eigenvector components in terms of the real basis vectors of a Cartesian coordinate system. Consider for definiteness the eigenvector which corresponds to the first principal number $\lambda = \lambda^{(1)}$. Then, by multiplying tensor (3.16) by $b_{\beta}^{(1)}$, we obtain, in view of expressions (3.13), the equation

$$T_{\alpha\beta} b_{\beta}^{(1)} = \lambda^{(1)} b_{\alpha}^{(1)}, \tag{3.19}$$

which is conveniently rewritten as

$$\tilde{T}_{\alpha\beta} b_{\beta}^{(1)} \equiv (T_{\alpha\beta} - \lambda^{(1)} \delta_{\alpha\beta}) b_{\beta}^{(1)} = 0. \tag{3.20}$$

Equation (3.20) always has a solution, because by definition of the principal value the determinant $\tilde{\Delta}$ of the tensor $\tilde{T}_{\alpha\beta}$ is always equal to zero. Writing equation (3.20) so as to solve it for the components we arrive at

$$\tilde{T}_{11}b_1^{(1)} + \tilde{T}_{12}b_2^{(1)} + \tilde{T}_{13}b_3^{(1)} = 0, \tag{3.21a}$$

$$\tilde{T}_{21}b_1^{(1)} + \tilde{T}_{22}b_2^{(1)} + \tilde{T}_{23}b_3^{(1)} = 0. \tag{3.21b}$$

We do not give the third equation, because it is a linear combination of these two owing to the zero value of the determinant $\tilde{\Delta}$. In these equations we express the y- and z-components of vector $\boldsymbol{b}^{(1)}$ in terms of the x-component $b_1^{(1)}$ to obtain

$$b_2^{(1)} = \frac{\tilde{T}_{21}\tilde{T}_{13} - \tilde{T}_{23}\tilde{T}_{11}}{\tilde{T}_{12}\tilde{T}_{23} - \tilde{T}_{13}\tilde{T}_{22}}b_1^{(1)}, \tag{3.22a}$$

$$b_3^{(1)} = \frac{\tilde{T}_{12}\tilde{T}_{21} - \tilde{T}_{11}\tilde{T}_{22}}{\tilde{T}_{12}\tilde{T}_{23} - \tilde{T}_{13}\tilde{T}_{22}}b_1^{(1)}. \tag{3.22b}$$

Noting that the combinations of the $\tilde{T}_{\alpha\beta}$ tensor components in the numerator and denominator of Eq. (3.22) are the algebraic adjuncts of the elements of the third row of tensor $\tilde{T}_{\alpha\beta}$: $\tilde{\Delta}_{31} = \tilde{T}_{12}\tilde{T}_{23} - \tilde{T}_{13}\tilde{T}_{22}$, $\tilde{\Delta}_{32} = \tilde{T}_{21}\tilde{T}_{13} - \tilde{T}_{23}\tilde{T}_{11}$, and $\tilde{\Delta}_{33} = \tilde{T}_{11}\tilde{T}_{22} - \tilde{T}_{12}\tilde{T}_{21}$, we represent Eqs. (3.22) in a compact form:

$$b_2^{(1)} = \frac{\tilde{\Delta}_{32}}{\tilde{\Delta}_{31}}b_1^{(1)}, \qquad b_3^{(1)} = \frac{-\tilde{\Delta}_{33}}{\tilde{\Delta}_{31}}b_1^{(1)}. \tag{3.23}$$

This allows writing the vector $\boldsymbol{b}^{(1)}$ in the form of a decomposition into the real unit vectors of the initial Cartesian coordinate system:

$$\boldsymbol{b}^{(1)} = C(\tilde{\Delta}_{31}\boldsymbol{e}_x + \tilde{\Delta}_{32}\boldsymbol{e}_y - \tilde{\Delta}_{33}\boldsymbol{e}_z), \tag{3.24}$$

where the constant C is determined from the condition that the vector $\boldsymbol{b}^{(1)}$ is normalized to unity, so that

$$\boldsymbol{b}^{(1)} = \frac{(\tilde{\Delta}_{31}\boldsymbol{e}_x + \tilde{\Delta}_{32}\boldsymbol{e}_y - \tilde{\Delta}_{33}\boldsymbol{e}_z)}{\sqrt{|\tilde{\Delta}_{31}|^2 + |\tilde{\Delta}_{32}|^2 + |\tilde{\Delta}_{33}|^2}}. \tag{3.25}$$

The two other eigenvectors, $\boldsymbol{b}^{(2)}$ and $\boldsymbol{b}^{(3)}$, are expressed in a similar manner, but the tensor $\tilde{T}_{\alpha\beta}$ should, in place of $\lambda^{(1)}$, contain the principal values $\lambda^{(2)}$ and $\lambda^{(3)}$, respectively.

3.1.2 Dispersion Relations for the Eigenmodes of an Anisotropic and Gyrotropic Medium

The dispersion relations and polarization vectors $e_\beta(\omega, \boldsymbol{k})$ of the eigenmodes should be calculated from the system of homogeneous equations

$$T_{\alpha\beta}(\omega, \boldsymbol{k}) e_\beta(\omega, \boldsymbol{k}) = 0, \quad \alpha = 1, 2, 3. \tag{3.26}$$

The solvability condition for this system of equations requires its determinant to vanish:

$$\Delta(\omega, \boldsymbol{k}) = |T_{\alpha\beta}(\omega, \boldsymbol{k})| = 0. \tag{3.27}$$

The Hermitian tensor $\varepsilon_{\alpha\beta} = \varepsilon'_{\alpha\beta} + i\varepsilon''_{\alpha\beta}$ has a symmetric, $\varepsilon'_{\alpha\beta} = \varepsilon'_{\beta\alpha}$, real part and an antisymmetric, $\varepsilon''_{\alpha\beta} = -\varepsilon''_{\beta\alpha}$, imaginary part. The latter may be written in terms of the gyration pseudovector g_α:

$$\varepsilon_{\alpha\beta} = \varepsilon'_{\alpha\beta} + ie_{\alpha\beta\gamma} g_\gamma. \tag{3.28}$$

We take into consideration that the tensor determinant is invariant under spatial rotations and select the coordinate axes along the mutually perpendicular principal axes of the symmetric tensor $\varepsilon'_{\alpha\beta}$; we denote the tensor $\varepsilon'_{\alpha\beta}$ principal values as ε_1, ε_2, and ε_3. With the axes selected, the tensor $T_{\alpha\beta}$ takes the form

$$\widehat{T} = \begin{pmatrix} \varepsilon_1 - n^2(1-\kappa_1^2) & ig_3 + n^2\kappa_1\kappa_2 & -ig_2 + n^2\kappa_1\kappa_3 \\ -ig_3 + n^2\kappa_1\kappa_2 & \varepsilon_2 - n^2(1-\kappa_2^2) & ig_1 + n^2\kappa_2\kappa_3 \\ ig_2 + n^2\kappa_1\kappa_3 & -ig_1 + n^2\kappa_2\kappa_3 & \varepsilon_3 - n^2(1-\kappa_3^2) \end{pmatrix}, \tag{3.29}$$

where $n = ck/\omega$ is the refractive index.

By equating the determinant Δ to zero we find the refractive indices for the eigenmodes of the medium under consideration. Upon the determinant expansion the terms proportional to n^6 cancel out and the equation in n^2 takes on the form

$$\begin{aligned} an^4 - [\varepsilon_1(\varepsilon_2+\varepsilon_3)\kappa_1^2 + \varepsilon_2(\varepsilon_1+\varepsilon_3)\kappa_2^2 + \varepsilon_3(\varepsilon_1+\varepsilon_2)\kappa_3^2 + (\boldsymbol{\kappa}\cdot\boldsymbol{g})^2 - \boldsymbol{g}^2]n^2 \\ + \varepsilon_1\varepsilon_2\varepsilon_3 - \varepsilon_1 g_1^2 - \varepsilon_2 g_2^2 - \varepsilon_3 g_3^2 = 0, \\ a(\omega, \boldsymbol{k}) = \varepsilon_1\kappa_1^2 + \varepsilon_2\kappa_2^2 + \varepsilon_3\kappa_3^2. \end{aligned} \tag{3.30}$$

Equation (3.30) is a generalization of the **Fresnel equation**, well known in crystal optics, to the case of a gyrotropic medium (see Born and Wolf 1999). The quantity $a(\omega, \boldsymbol{k}) = \varepsilon_{\alpha\beta}\kappa_\alpha\kappa_\beta$ is the permittivity longitudinal relative to the vector $\boldsymbol{k}$: $a = \varepsilon^l(\omega, \boldsymbol{k})$.

If Eq. (3.30) is treated as a quadratic equation in the explicitly appearing quantity n^2, it is easy to find two roots n_1^2 and n_2^2 of this equation. This enables writing the Maxwellian tensor determinant (3.27) as a product of three factors:

$$\Delta = a(n^2 - n_1^2)(n^2 - n_2^2) = 0; \tag{3.31}$$

setting any of these factors to zero leads to correct dispersion relations for possible eigenmodes.

The convenience of writing the determinant in the form of expression (3.31) manifests itself when the spatial dispersion is nonexistent, i.e., when the quantities ε_1, ε_2, ε_3, and g depend on ω only, while not on the absolute value $|\boldsymbol{k}|$. Then, the relationships $n^2 = n_{1,2}^2$ turn out to be *solutions* of the dispersion equation, so that in each direction (for a given $\boldsymbol{\kappa}$) two waves can propagate through the medium with two, generally different, phase velocities $v_{1,2} = c/n_{1,2}$. Here, $n_{1,2}(\omega, \boldsymbol{\kappa})$ are the positive solutions of the biquadratic equation (3.30), which depend only on the frequency and the propagation direction of the corresponding wave. The roots n_i^2 may be negative in some frequency ranges. For a Hermitian permittivity tensor, this signifies damping without dissipation, i.e., the absence of the corresponding mode. The solution $a = 0$ corresponds to the oscillating modes of the medium, whose properties are independent of the magnitude of the wave vector (as long as the spatial dispersion is discarded); the electric vector in these modes is directed along the vector $\boldsymbol{\kappa}$, i.e., the oscillations are longitudinal.

In the presence of spatial dispersion, the relations $a = 0$ and $n^2 = n_{1,2}^2$ are *equations* for determining the refractive indices rather than solutions of the dispersion equation, because a and $n_{1,2}$ are themselves functions of n. That is why, in principle, there is nothing to limit the number of eigenmodes, which are solutions of these equations. To determine the refractive indices in this case requires specifying the explicit dependence of the dielectric tensor on ω and $\boldsymbol{k}$.

3.1.3 Principal Values and Eigenvectors of the Maxwellian Tensor and Their Relation to the Eigenmodes of the Medium

Let us determine the link between the quantities introduced in the foregoing and the electromagnetic eigenmodes of an anisotropic medium. We will use the tensor expressed via its principal values (3.16) to find the determinant in the form

$$\Delta(\omega, \boldsymbol{k}) = \lambda^{(1)}(\omega, \boldsymbol{k})\lambda^{(2)}(\omega, \boldsymbol{k})\lambda^{(3)}(\omega, \boldsymbol{k}). \tag{3.32}$$

Condition (3.27) that the determinant is equal to zero implies that at least one of the principal values of the tensor should vanish:

$$\lambda^{(m)}(\omega, \boldsymbol{k}) = 0, \qquad m = 1, 2, 3. \tag{3.33}$$

Equations (3.33) give the dispersion relations $\omega^\sigma(\boldsymbol{k})$ for the eigenmodes of the medium. The number of these modes in the presence of spatial dispersion is unlimited in the general case.

Both forms of the determinant $\Delta(\omega, \boldsymbol{k})$—expressions (3.31) and (3.32)—represent it in the form of three factors. This leads to a temptation to identify the principal values $\lambda^{(m)}$ of the Maxwellian tensor with the factors a, $(n^2 - n_1^2)$, and $(n^2 - n_2^2)$. But this identification would be incorrect, because two other requisite relations

$$\begin{aligned} \lambda^{(1)} + \lambda^{(2)} + \lambda^{(3)} &= T_{11} + T_{22} + T_{33}, \\ \lambda^{(1)}\lambda^{(2)} + \lambda^{(1)}\lambda^{(3)} + \lambda^{(2)}\lambda^{(3)} &= \Delta_{11} + \Delta_{22} + \Delta_{33} \equiv \Delta_{ii}, \end{aligned} \tag{3.34}$$

would be violated in this case, which becomes evident when determinant (3.15) is expanded. We return to the determination of the principal values $\lambda^{(m)}$ in Chap. 9.

Now let us determine the relation between the polarization vector $\boldsymbol{e}^{\sigma}(\omega, \boldsymbol{k})$ of a given eigenmode and the eigenvectors $\boldsymbol{b}^{(m)}(\omega, \boldsymbol{k})$ of the Maxwellian tensor. By substituting expression (3.16) for $T_{\alpha\beta}(\omega, \boldsymbol{k})$ in the homogeneous equation (3.26), we arrive at

$$\lambda^{(1)} b_{\alpha}^{(1)} (\boldsymbol{b}^{(1)} \cdot \boldsymbol{e}^{\sigma}) + \lambda^{(2)} b_{\alpha}^{(2)} (\boldsymbol{b}^{(2)} \cdot \boldsymbol{e}^{\sigma}) + \lambda^{(3)} b_{\alpha}^{(3)} (\boldsymbol{b}^{(3)} \cdot \boldsymbol{e}^{\sigma}) = 0, \tag{3.35}$$

where the arguments $(\omega, \boldsymbol{k})$ of variables $\lambda^{(m)}$, $\boldsymbol{b}^{(m)}$, and $\boldsymbol{e}^{\sigma}$ were omitted for brevity.

Consider for definiteness the mode which corresponds to the condition $\lambda^{(1)}(\omega, \boldsymbol{k}) = 0$ (there may be several such modes). In this case, $\omega = \omega^{\sigma}(\boldsymbol{k})$, $\lambda^{(2)}(\omega^{\sigma}, \boldsymbol{k}) \neq 0$, and $\lambda^{(3)}(\omega^{\sigma}, \boldsymbol{k}) \neq 0$ (note that if two eigenvalues vanish together, e.g., $\lambda^{(1)} = 0$ and $\lambda^{(2)} = 0$ then there is no unique choice for the polarization vectors $\boldsymbol{e}^{(1)}$ and $\boldsymbol{e}^{(2)}$ indicative of polarization degeneracy). Then, equality (3.35) will be fulfilled only provided the polarization vector $\boldsymbol{e}^{\sigma}(\omega^{\sigma}, \boldsymbol{k})$ is orthogonal to the eigenvectors $\boldsymbol{b}^{(2)}(\omega^{\sigma}, \boldsymbol{k})$ and $\boldsymbol{b}^{(3)}(\omega^{\sigma}, \boldsymbol{k})$. This means that the polarization vector $\boldsymbol{e}^{\sigma}(\omega^{\sigma}, \boldsymbol{k})$ simply coincides (as long as both are normalized to unity) with the eigenvector $\boldsymbol{b}^{(1)}(\omega^{\sigma}, \boldsymbol{k})$ of the Maxwellian tensor $T_{\alpha\beta}(\omega, \boldsymbol{k})$. Attention must be drawn to the fact that the other two eigenvectors, $\boldsymbol{b}^{(2)}(\omega^{\sigma}, \boldsymbol{k})$ and $\boldsymbol{b}^{(3)}(\omega^{\sigma}, \boldsymbol{k})$, *do not* represent polarization vectors of any eigenmodes of the medium. They would turn into polarization vectors only under the conditions $\lambda^{(2)}(\omega, \boldsymbol{k}) = 0$ or $\lambda^{(3)}(\omega, \boldsymbol{k}) = 0$, respectively, i.e., when the dispersion law for the eigenmode with the same number is fulfilled, while not in an arbitrary case. In particular, the polarization vectors of the ordinary and extraordinary modes (see Sect. 3.2) with the *same* frequency propagating through an anisotropic medium in the *same* direction are *nonorthogonal*, because they differ in wave vector magnitude (due to the difference in the refractive indices).

Eventually, we showed that the polarization vectors of the eigenmodes of a medium are constructed from three eigenvectors $\boldsymbol{b}^{(m)}(\omega^{\sigma}, \boldsymbol{k})$, $m = 1, 2, 3$ of the Maxwellian tensor by assigning their arguments ω and $\boldsymbol{k}$ the values corresponding to the dispersion relation $\omega = \omega^{\sigma}(\boldsymbol{k})$ for the corresponding eigenmode.

Finally, let us obtain the explicit form of the polarization vectors of the electromagnetic eigenmodes in a given anisotropic medium. For an eigenmode, say, with number 1, we have $\lambda^{(1)} = 0$, and therefore the tensor $\tilde{T}_{\alpha\beta}$ reduces merely to the Maxwellian tensor $T_{\alpha\beta}$. Therefore, the polarization vector $\boldsymbol{e}^{(1)}$ is expressed similarly to $\boldsymbol{b}^{(1)}$ in terms of the algebraic adjuncts of the Maxwellian tensor (i.e., in terms of the quantities Δ_{ab} without a tilde):

$$\boldsymbol{e}^{(1)} = \frac{\Delta_{31}\boldsymbol{e}_x + \Delta_{32}\boldsymbol{e}_y - \Delta_{33}\boldsymbol{e}_z}{\sqrt{|\Delta_{31}|^2 + |\Delta_{32}|^2 + |\Delta_{33}|^2}}, \tag{3.36}$$

which follows from formula (3.25) on substituting into it $\lambda^{(1)} = 0$ and taking into account in the remaining terms the dispersion law corresponding to this condition. The polarization vector $\boldsymbol{e}^{(2)}$ of the second eigenmode is expressed similarly to expression (3.36) but under the condition $\lambda^{(2)} = 0$ and with the dispersion law corresponding to this condition. It may turn out that the polarization vectors are more convenient to decompose over other sets of algebraic adjuncts, for instance

$$\boldsymbol{e}^{(1)} = \frac{-\Delta_{11}\boldsymbol{e}_x + \Delta_{12}\boldsymbol{e}_y + \Delta_{13}\boldsymbol{e}_z}{\sqrt{|\Delta_{11}|^2 + |\Delta_{12}|^2 + |\Delta_{13}|^2}} = \frac{\Delta_{21}\boldsymbol{e}_x - \Delta_{22}\boldsymbol{e}_y + \Delta_{23}\boldsymbol{e}_z}{\sqrt{|\Delta_{21}|^2 + |\Delta_{22}|^2 + |\Delta_{23}|^2}}. \tag{3.37}$$

3.2 Cold Plasma Approximation

3.2.1 General Case

Having the general formalism describing dispersion of arbitrary anisotropic and gyrotropic medium developed, let us proceed to the treatment of the cosmic plasma. A typical ingredient of the astrophysical plasma is a magnetic field, so we consider the dispersion of the magnetized plasma at the first place. We start with a simple cold plasma approximation within which we adopt that each plasma component a (e.g., electrons and any kind of available ions) can be described by a single velocity $\boldsymbol{v}^a$ defined by the equation of motion

$$\frac{\partial \boldsymbol{v}^a}{\partial t} = \frac{e_a}{m_a}\boldsymbol{E} + \frac{e_a}{m_a c}[\boldsymbol{v}^a \times (\boldsymbol{B}_0 + \boldsymbol{b})], \tag{3.38}$$

where $\boldsymbol{v}^a$, e_a, and m_a are the velocity, charge (positive or negative), and mass of the particles of the sort a, $\boldsymbol{E}$ and $\boldsymbol{b}$ are small perturbations of the external electromagnetic field, and $\boldsymbol{B}_0$ is an external uniform magnetic field. These single-particle equations are explicitly derived from fluid motion equation (1.70) by discarding the temperature dependent and collisional terms at the rhs and nonlinear (inertial) term $(\boldsymbol{v}^a \cdot \nabla)\boldsymbol{v}^a$ at the lhs. To work consistently in the linear approximation we must also discard the second-order term $e_a \boldsymbol{v}^a \times \boldsymbol{b}/m_a c$. The adopted approximation implies $b \ll B_0$ and $v^a \ll v_{ph}$, where v_{ph} are the typical phase velocities of the relevant waves; the particle thermal speeds must be small compared with all other involved velocities.

Fourier transform of this equation yields:

$$i\omega v_\alpha^a + \frac{e_a}{m_a c} e_{\alpha\beta\gamma} v_\beta^a B_{0\gamma} = -\frac{e_a}{m_a} E_\alpha. \tag{3.39}$$

Assuming that $\boldsymbol{B}_0$ is directed along the z-axes (apparently, the gyration vector introduced by Eq. (3.28) has only one z-component in this case, $\boldsymbol{g} = g_3 \boldsymbol{e}_z \equiv g\boldsymbol{e}_z$) and solving Eq. (3.39) for the velocity components we find

$$v_x^a = \frac{e_a(i\omega E_x - \omega_{Ba} E_y)}{m_a(\omega^2 - \omega_{Ba}^2)}, \tag{3.40a}$$

$$v_y^a = \frac{e_a(i\omega E_y + \omega_{Ba} E_x)}{m_a(\omega^2 - \omega_{Ba}^2)}, \tag{3.40b}$$

$$v_z^a = \frac{ie_a}{m_a \omega} E_z, \tag{3.40c}$$

where $\omega_{Ba} = e_a B_0/(m_a c)$ is the gyrofrequency of the a particles.

Now, to obtain the dielectric permeability tensor, we take into account the Fourier component of Eq. (3.3), i.e., $P_\alpha = ij_\alpha/\omega$, where the electric current j_α is defined by the particle velocities

$$j_\alpha = \sum_a e_a n_a v_\alpha^a. \tag{3.41}$$

Then, combining Eqs. (3.6) and (3.8), we find for the dielectric tensor components:

$$\varepsilon_{11} = \varepsilon_{22} = \varepsilon_1, \quad \varepsilon_1 = 1 - \sum_a \frac{\omega_{pa}^2}{\omega^2 - \omega_{Ba}^2}, \tag{3.42a}$$

$$\varepsilon_{12} = -\varepsilon_{21} = ig; \quad g = -\sum_a \frac{\omega_{pa}^2 \omega_{Ba}}{\omega(\omega^2 - \omega_{Ba}^2)}, \tag{3.42b}$$

$$\varepsilon_{33} = \varepsilon_3, \quad \varepsilon_3 = 1 - \sum_a \frac{\omega_{pa}^2}{\omega^2}, \tag{3.42c}$$

where $\omega_{pa}^2 = 4\pi e_a^2 n_a/m_a$ is the plasma frequency of the ath plasma species, while all other components of the dielectric tensor are zeros.

Because the system is symmetric around the z-axes, we can adopt that the wave vector of a wave under study belongs to the xz plane without any loss of generality with $\kappa_1 = \sin\theta$, $\kappa_2 = 0$, and $\kappa_3 = \cos\theta$, where θ is the angle between the wave vector and the magnetic field. Within the adopted geometry and notations, general dispersion relation (3.30) simplifies for the cold plasma case to have the form

$$a(\omega)n^4 + b(\omega)n^2 + c(\omega) = 0, \tag{3.43}$$

$$a(\omega) = \varepsilon_1 \sin^2\theta + \varepsilon_3 \cos^2\theta, \tag{3.44a}$$

$$b(\omega) = -[\varepsilon_1\varepsilon_3(1 + \cos^2\theta) + (\varepsilon_1^2 - g^2)\sin^2\theta], \tag{3.44b}$$

$$c(\omega) = \varepsilon_3(\varepsilon_1^2 - g^2). \tag{3.44c}$$

Here, the dielectric tensor components depend only on ω, while not on k; accordingly, the coefficients a, b, and c do not depend on the absolute value of the wave vector. Therefore, for the cold plasma, the spatial dispersion plays no role and Eq. (3.31) represents solutions for the possible plasma modes, i.e.,

$$n_{1,2}^2 = \frac{-b(\omega) \pm \sqrt{b^2(\omega) - 4a(\omega)c(\omega)}}{2a(\omega)}. \tag{3.45}$$

The third root, $a(\omega) = 0$, represents a cold plasma approximation of a longitudinal plasma wave dispersion, whose correct treatment requires taking the spatial dispersion (i.e., the thermal plasma motion) into account.

3.2.2 Hydrogen Plasma

Let us consider the fully ionized electron–proton plasma as a simplest, while practical, example. Keeping explicitly the electron and proton contributions to dielectric tensor components (3.42) we obtain

$$\begin{aligned} \varepsilon_1 &= 1 - \frac{\omega_{\mathrm{pe}}^2}{\omega^2 - \omega_{\mathrm{Be}}^2} - \frac{\omega_{\mathrm{pp}}^2}{\omega^2 - \omega_{\mathrm{Bp}}^2},\ g = -\frac{\omega_{\mathrm{pe}}^2\omega_{\mathrm{Be}}}{\omega(\omega^2 - \omega_{\mathrm{Be}}^2)} - \frac{\omega_{\mathrm{pp}}^2\omega_{\mathrm{Bp}}}{\omega(\omega^2 - \omega_{\mathrm{Bp}}^2)}, \\ \varepsilon_3 &= 1 - \frac{\omega_{\mathrm{pe}}^2 + \omega_{\mathrm{pp}}^2}{\omega^2} \end{aligned} \tag{3.46}$$

where $\omega_{\mathrm{pe}}^2 = 4\pi e^2 n_e/m_e$ and $\omega_{\mathrm{pp}}^2 = 4\pi e^2 n_p/m_p$ are the squares of the electron and proton plasma frequencies, $\omega_{\mathrm{Be}} = eB_0/(m_e c)$ and $\omega_{\mathrm{Bp}} = e_p B_0/(m_p c)$ are the electron and proton gyrofrequencies. Note that when $e_p = -e$, the electron charge is negative and so two terms in g have opposite signs. In particular, this implies that if a plasma is composed from positive and negative charges with the same mass (e.g., electron–positron plasma), then the gyration vector vanishes and so no gyrotropy is present in such a plasma. In the electron–proton plasma there is a strong gyrotropy because the masses of the electron and proton differ by three orders of magnitude. However, at low frequencies, $\omega \ll \omega_{\mathrm{Bp}}$, these two contributions to g almost cancel each other out, because $\omega_{\mathrm{pp}}^2/\omega_{\mathrm{Bp}} \equiv -\omega_{\mathrm{pe}}^2/\omega_{\mathrm{Be}}$ for the neutral plasma $n_e = n_p$; in a charged plasma with $n_e \neq n_p$ this compensation does not take place and the gyrotropy of the charged plasma increases at very low frequencies where the neutral plasma is not at all gyrotropic.

To get an idea of the plasma dispersion we first consider asymptotic behavior of the dielectric components and indices of refraction at small and

large frequencies as well as zeros and discontinuity points. Clearly, as $\omega \to \infty$, $\varepsilon_1 \approx \varepsilon_3 \to 1$, and $g \to 0$; while as $\omega \to 0$, $\varepsilon_1 \approx \omega_{\rm pp}^2/\omega_{\rm Bp}^2$, $\varepsilon_3 = -\omega_{\rm pe}^2/\omega^2$, and $g \approx \omega_{\rm pp}^2\omega/\omega_{\rm Bp}^3$, so that $g \ll \varepsilon_1 \ll |\varepsilon_3|$. As we will see below, the high-frequency behavior of the dielectric tensor is primarily specified by the electron contribution, while the proton contribution is dominant at low frequencies, where two of three dielectric tensor components are specified by the protons. Then, the dielectric tensor components have discontinuities at both electron and proton gyrofrequencies. However, the refractive index is continuous there because the resonance factors in the numerator and denominator cancel out. In place, it can have discontinuities at the points, where $a = 0$, because it enters the denominator of Eq. (3.45). As has been said, equation $a = 0$ defines the plasma eigenfrequencies, i.e., those frequencies at which electrostatic oscillations (or electrostatic waves if the spatial dispersion is included) can exist. Thus, the refractive indices can have a discontinuity at the frequencies of plasma resonances. It is easy to see that the equation $a = 0$, being a cubic equation over ω^2 for the electron–proton plasma, has three positive roots; see Problem 3.1. Solving Eq. (3.45) for $n_{1,2}^2$ when $a \to 0$, we find $n_1^2 \approx -b/a \to \infty$ and $n_2^2 \to -c/b$, i.e., only one of the two roots is discontinuous when $a \to 0$. Then, zeros of the refractive indices are defined by equation $c(\omega) = \varepsilon_3(\varepsilon_1^2 - g^2) = 0$, which, neglecting the ion contribution, yields

$$\begin{aligned} \omega_0^{(1)} &= \sqrt{\omega_{\rm pe}^2 + \omega_{\rm Be}^2/4} + |\omega_{\rm Be}|/2, \\ \omega_0^{(2)} &= \omega_{\rm pe}, \\ \omega_0^{(3)} &= \sqrt{\omega_{\rm pe}^2 + \omega_{\rm Be}^2/4} - |\omega_{\rm Be}|/2. \end{aligned} \tag{3.47}$$

The quantitative shape of the dispersion curves is given in Fig. 3.1. Three resonances at the corresponding discontinuity points can easily be identified in the $n_2(\omega)$ plots; two of them are not resolved in the overall plot, although are better seen at the zoom-in panels. The right column shows the dispersion curves for five wave modes of this plasma. The lowest-frequency modes, the Alfvén mode and the fast mode, have linear dispersion laws (constant phase speed) at the low frequencies, while deviate from these laws at higher frequencies. When $\omega \to \omega_{\rm Bp}$, the Alfvén mode becomes almost electrostatic ion-cyclotron mode (where the frequency has almost no dependence on the wave number), while for the fast mode the dispersion changes first to a parabolic ($\omega \propto k^2$, this part of the fast mode is frequently called the whistler mode) and then to a constant at another, lower-hybrid, resonance frequency; the fast/whistler mode is called the lower-hybrid mode here. At the higher frequencies the role of protons is minor and the dispersion of the higher frequency modes is entirely specified by the electron contribution, the bottom panel of Fig. 3.1. There are three modes: Z-mode, which becomes the upper-hybrid mode at large k, and two "free-space" modes, the ordinary (O)-mode

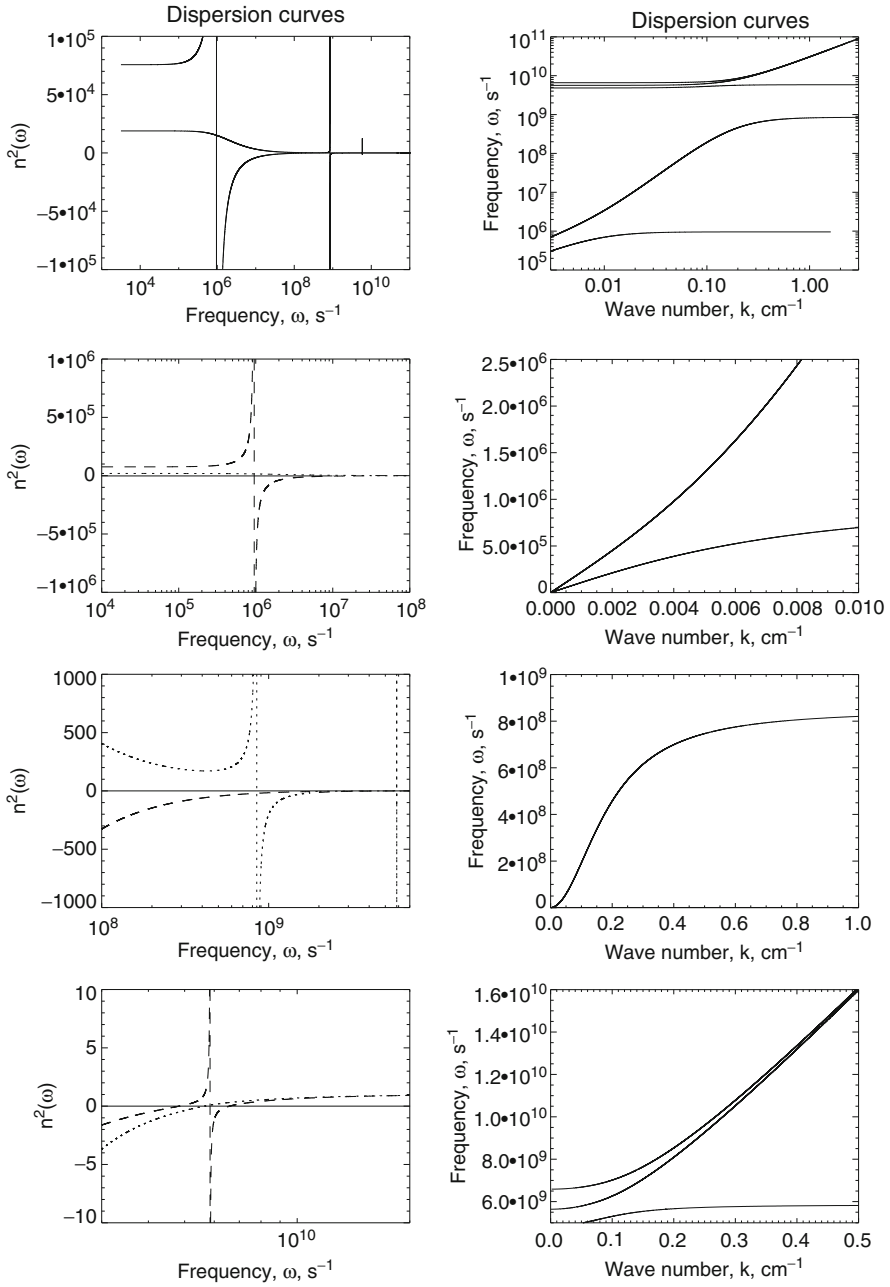

Figure 3.1: Dispersion of the electrically neutral electron–proton plasma: refractive indices *(left)* and frequency vs wave number *(right)*. Overall view is given in two *top panels*, with three zoom-ins below. The accepted parameters are the number density $n_p = n_e = 10^{10}\,\mathrm{cm}^{-3}$, $B = 100\,\mathrm{G}$, and $\theta = 60^o$.

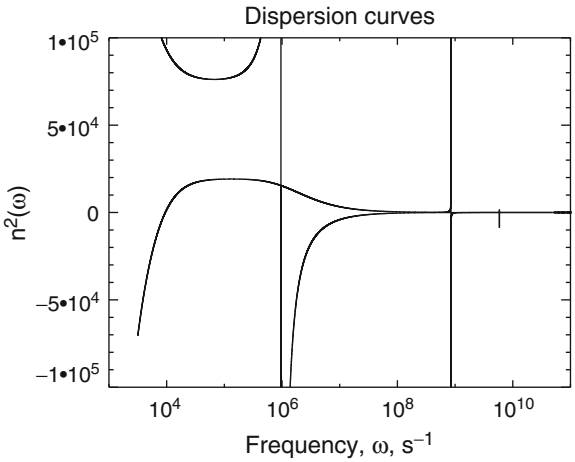

Figure 3.2: Dispersion of the electrically charged electron–proton plasma. The accepted parameters are the same as in Fig. 3.1 but $n_e = 1.01 \cdot n_p$.

with the low-k cutoff frequency $\omega_0^{(2)} = \omega_{\rm pe}$ and the extraordinary mode with the cutoff frequency $\omega_0^{(3)}$. The free-space modes are the only wave modes that can escape from the plasma and be detected by a remote observer (e.g., at the Earth or at the free space). All other wave modes, although play an important role for the plasma dynamics, can only be implied indirectly, by numerous effects they produce in the source or along the radiation path.

There are not more than two wave modes at the same frequency; some frequency ranges allow only one or no modes. It is interesting to see how the low-frequency plasma dispersion changes for electrically charged plasma. Figure 3.2 displays that if the electron to proton density mismatch is only one percent, the low-frequency behavior of the dispersion curves changes drastically: no fast mode is possible at the low frequencies; the Alfvén mode is available but the phase speed of the Alfvén mode increases as the frequency decreases. In most of the cases, however, the plasma neutrality is held with very high precision and the mentioned effects of the plasma non-neutrality play typically no role.

3.2.3 Asymptotic Behavior of the Eigenmodes

Although full equation (3.45) for the refractive indices is easy to analyze, it is often convenient to make estimates with simplified expressions, which can be obtained under certain conditions in certain frequency ranges. First, at

high frequencies, one can safely discard the proton contribution and retain only the electron contribution, which yields

$$n_\sigma^2 = 1 - \frac{2v(1-v)}{2(1-v) - u\sin^2\theta + \sigma\sqrt{\mathcal{D}}}, \tag{3.48}$$

where

$$\mathcal{D} = u^2\sin^4\theta + 4u(1-v)^2\cos^2\theta, \quad u = \left(\frac{\omega_{\rm Be}}{\omega}\right)^2, \quad v = \left(\frac{\omega_{\rm pe}}{\omega}\right)^2, \tag{3.49}$$

$\sigma = -1$ for X-mode and $\sigma = +1$ for O-mode. At the asymptotically high frequencies both refractive indices approach the free-space value one, resulting in the free-space wave dispersion $\omega = kc$.

The polarization vectors of the waves in the reference frame with z-axes along the magnetic field and the wave vector $\boldsymbol{k}$ in the (xz)-plane have the form

$$\boldsymbol{e}_\sigma = (e_x, e_y, e_z) = \frac{(T_\sigma\cos\theta + L_\sigma\sin\theta, i, -T_\sigma\sin\theta + L_\sigma\cos\theta)}{\sqrt{1 + T_\sigma^2 + L_\sigma^2}} \tag{3.50}$$

with the parameters T_σ and L_σ defined as

$$T_\sigma = \frac{2\sqrt{u}(1-v)\cos\theta}{u\sin^2\theta - \sigma\sqrt{\mathcal{D}}}, \tag{3.51}$$

$$L_\sigma = \frac{v\sqrt{u}\sin\theta + T_\sigma uv\sin\theta\cos\theta}{1 - u - v + uv\cos^2\theta}. \tag{3.52}$$

Electromagnetic waves can propagate in a plasma if their frequency exceeds the cut-off frequency, $\omega > \omega_{{\rm c}\sigma}$, where

$$\omega_{\rm cO} = \omega_{\rm pe}, \quad \omega_{\rm cX} = \frac{\omega_{\rm Be}}{2} + \sqrt{\omega_{\rm pe}^2 + \frac{\omega_{\rm Be}^2}{4}}. \tag{3.53}$$

More simplified cases for dispersion of X-, O-, Z-, and whistler modes are considered in problems to this chapter, while here we touch upon the low-frequency case. Within the previous chapters we often used MHD approximation and fluid dynamics equations. Here we are going to demonstrate that the linear MHD modes can be derived from the considered here plasma dielectric tensor. Specifically, we consider low frequencies $\omega \ll \omega_{\rm Bp}$, $v_A \ll c$,

and $c_s \ll v_A$, where v_A and c_s are the Alfvén and sound speeds. From Eq. (3.42) we find

$$\varepsilon_1 \approx \frac{c^2}{v_A^2}, \quad \varepsilon_3 \approx -\frac{\omega_{\rm pe}^2}{\omega^2}, \quad g \approx \frac{c^2\omega}{v_A^2\omega_{\rm Bp}} \ll \varepsilon_1, \quad |\varepsilon_3| \gg \varepsilon_1. \tag{3.54}$$

Discarding the terms $g^2/\varepsilon_1^2 \ll 1$ in Eq. (3.44) we obtain the refraction indices of two MHD modes:

$$n_{1,2}^2 = \pm\frac{c^2}{2v_A^2}\left(\frac{1}{\cos^2\theta} - 1\right) + \frac{c^2}{2v_A^2}\left(\frac{1}{\cos^2\theta} + 1\right) = \begin{cases} c^2/(v_A^2\cos^2\theta) \\ c^2/v_A^2 \end{cases}.$$

To identify these two modes with familiar MHD modes we note that $n = ck/\omega = c/v_{ph}$, where v_{ph} is the phase speed of the mode; thus, the upper solution corresponds to the Alfvén waves, whose phase velocity (2.55) has the absolute value of $v_A|\cos\theta|$. The Alfvén wave is nonexistent for the transverse propagation $\theta \to \pi/2$. The second (lower) solution corresponds to the fast mode since $v_f = v_A$ when $c_s \to 0$ (provided that $T_e \to 0$ in the cold plasma), cf. Eq. (2.60). The polarization vectors can easily be obtained based on Sect. 3.1. The slow mode is apparently nonexistent in the cold plasma.

3.2.4 Multi-component Plasma

We have found that at low frequencies the properties of the plasma wave modes are primarily specified by the ion contribution to the plasma dispersion, which are the protons in case of the electron–proton plasma. In a reality the astrophysical plasma consists of many different ions according to their abundances and, on top of that, there can be various ionization states of the same isotope. Even though the number density of a given ion can be low, it can give a dominant contribution around its own gyrofrequency, because it is different for different ions. Consider, as a vivid example, a plasma containing helium ions in addition to the hydrogen ions (protons).

In this case Eq. (3.42) will contain additional terms describing helium contribution to the dielectric tensor components. To quantify this contribution we have to make assumptions about the helium isotopic abundance and ionization state. To be specific, we assume the number density of He^4 to be 8.3%[1] of the hydrogen density. Figure 3.3, top, displays the case when the helium is singly ionized (HeII), no twice-ionized HeIII ions are present. We see that one more resonance appears related to the HeII gyrofrequency,

[1] This solar helium abundance is somewhat higher than the primordial abundances produced at the Big Bang nucleosynthesis, namely 76% of proton and 24% of helium by mass (roughly 7% by the number density) with only traces of heavier elements (e.g., Rowan-Robinson 2004). We note that even higher abundance of helium and heavier elements can be produced by the nucleosynthesis in star interior or due to electromagnetic separation in nonstationary processes (e.g., solar flares).

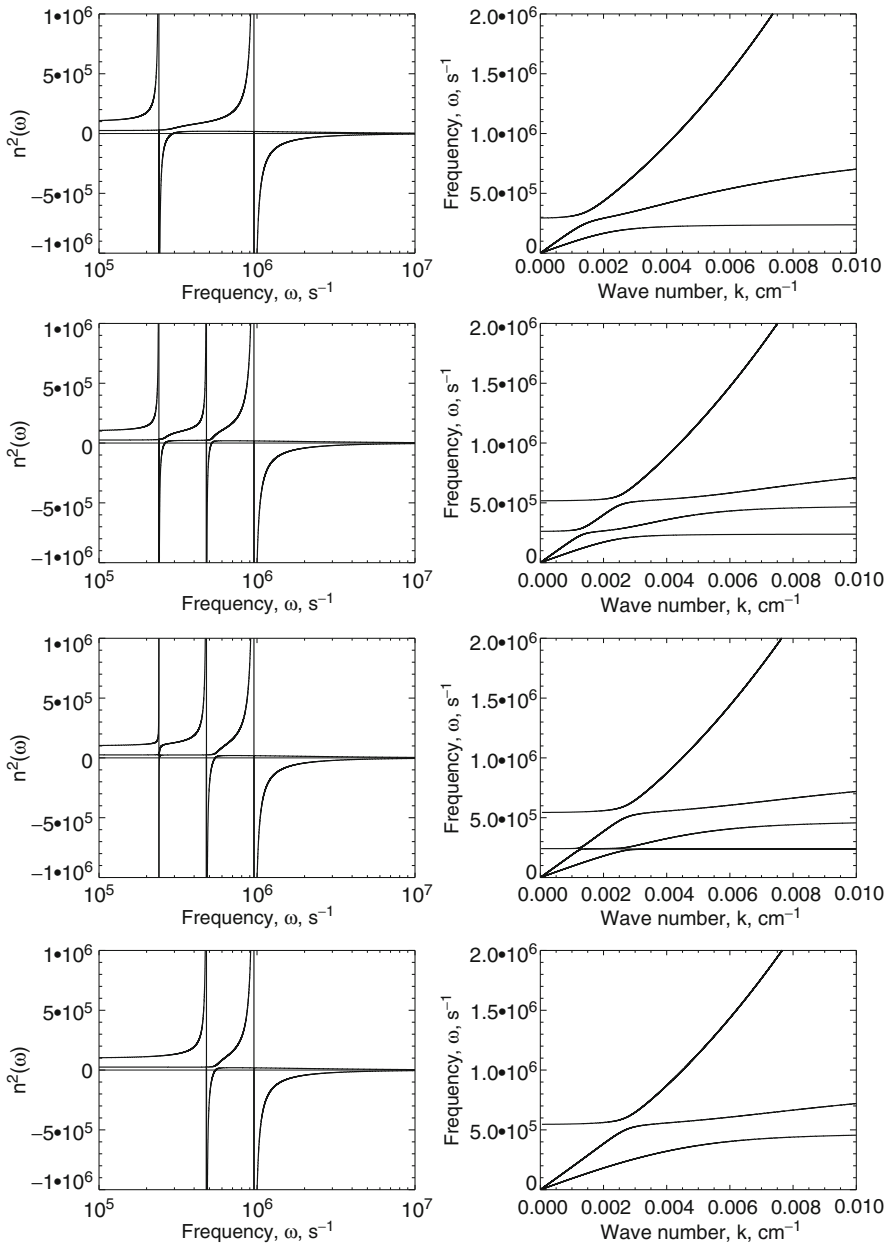

Figure 3.3: Dispersion of the electrically neutral $e - p - \mathrm{He}^4$ plasma: refractive indices (*left*) and frequency vs wave number (*right*) for various ionization states: 100% single-ionized HeII (*top row*), 50% single-ionized HeII and 50% double-ionized HeIII (*second row*), 95% double-ionized HeIII (*third row*), and 100% double-ionized HeIII (*bottom row*). Solar abundance $n_{\mathrm{He}} = 0.083 n_p$ is assumed, other parameters are as in Fig. 3.1.

which is $\omega_{\mathrm{Bp}}/4$. The second row in this figure displays the dispersion in the case when there are equal proportions of both helium ionization states,[2] HeII and HeIII. Now, a third resonance appears corresponding to the HeIII gyrofrequency, $\omega_{\mathrm{Bp}}/2$, the widths of both resonances are comparable to each other. The next row displays the case when 95% of the helium is fully ionized (HeIII) and only 5% is singly ionized (HeII). Positions of the resonances are the same as before; however, the width of the HeII resonance is much narrower now, and eventually, it is not present at all at the bottom plot, where all helium is HeIII.

The right column displays how the dispersion curves $\omega(k)$ change between these cases. It must be noted that the behavior of these curves is qualitatively different from the case of one-component electron–proton plasma. First, the number of the modes is different: we have now either four or three modes (in place of two) depending on the helium ionization state. Two of them have linear dispersion $\omega \propto k$ for $k \to 0$ and so can still be called the Alfvén and fast modes at these small k; other modes have a finite cutoff frequency when $k \to 0$. However, the Alfvén and fast modes have a different behavior at large k, where they smoothly transit to helium ion-cyclotron modes (almost flat regions of the dispersion curves). The highest frequency wave mode (that which becomes the whistler mode at even higher frequencies) is now not the fast mode at the low frequency; in place, it approaches the proton ion-cyclotron frequency as $k \to 0$. Stated another way, the presence of helium (or other ions) makes the very long-wavelength proton–cyclotron waves possible in contrast to the one-component plasma.

The number of the wave modes increases and the whole picture becomes even more complicated if we take into account presence of He^3 along with typically more abundant He^4. There are, for example, He^3-rich solar flares in which the He^3 abundance is greatly enhanced (see Sect. 11.2.2 for greater detail), so this example can be of practical importance. Now, because of noticeably smaller mass of He^3 compared with He^4, their ion gyrofrequencies ($\omega_{\mathrm{Bp}}/3$ and $2\omega_{\mathrm{Bp}}/3$) are distinctly different from those for He^4. Here the total number of the resonances can be as large as five, which yields the total of up to six wave modes, see Fig. 3.4. A few of them can be called hybrid He–He or He–p modes because their frequencies are about one ion gyrofrequency at $k \to 0$, while about another ion gyrofrequency at $k \to \infty$ with more or less sharp transition from one to another in between. The narrower the resonance in the left panel the flatter the corresponding dispersion curve in the right panel. The width of each resonance is determined by the abundance of the corresponding ion. For the ideal case of the cold plasma considered here, any small admixture of an ion results in its own resonance and in an additional wave mode. In practice, the thermal motion of the plasma particles and

[2] As is adopted in astronomy we use Roman numbers to indicate the atom ionization state—I for neutral atom, II for singly ionized ion, III for twice-ionized ion, etc.

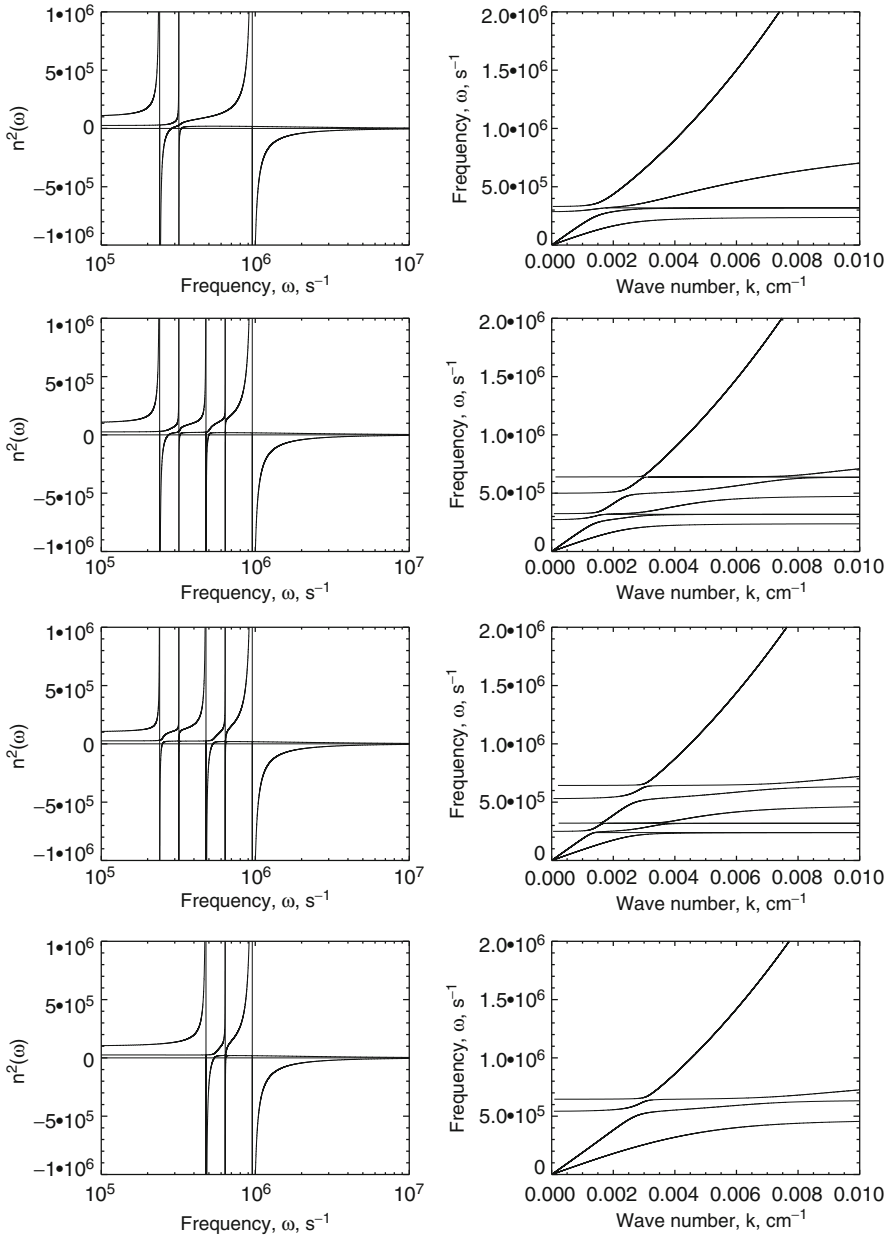

Figure 3.4: Dispersion of the electrically neutral $e - p - \mathrm{He}^4 - \mathrm{He}^3$ plasma. Refractive indices *(left)* and frequency vs wave number *(right)* for various ionization states: 100 % single-ionized HeII *(top row)*, 75 % single-ionized HeII and 25 % double-ionized HeIII *(second row)*, 25 % single-ionized HeII and 75 % double-ionized HeIII *(third row)*, and 100 % double-ionized HeIII *(bottom row)*. The number density of He^3 is assumed to be one tenth of that of He^4, other parameters are as in Fig. 3.3.

Coulomb collisions lead to broadening of the resonances, so less pronounced resonances produced by less abundant ions disappear and make no noticeable contribution to the plasma dispersion. The question of a particular ion importance must, therefore, be addressed with a more complete kinetic approach, than the simplified cold plasma approximation. It is worthwhile to note that other (than H and He) ions can provide more cyclotron resonances and, thus, produce even more wave modes at the low-frequency range, while they have no effect on the high-frequency range, which is primarily defined by the electron contribution.

3.3 Kinetic Approach to Collisionless Plasma

3.3.1 Dielectric Tensor and Resonant Particles

The cold plasma approximation considered above ignores entirely the thermal motion of the plasma particles. A more complete, kinetic treatment relies on the particle distribution functions f_i and f_e, entering Eqs. (3.1) and (3.2), determined from corresponding kinetic equations, which for a nonrelativistic case can be written as[3]

$$\frac{\partial f}{\partial t} + \boldsymbol{v} \cdot \frac{\partial f}{\partial \boldsymbol{r}} + \frac{e}{m}\boldsymbol{E} \cdot \frac{\partial f}{\partial \boldsymbol{v}} + \frac{e}{mc}[\boldsymbol{v} \times (\boldsymbol{b} + \boldsymbol{B}_0)] \cdot \frac{\partial f}{\partial \boldsymbol{v}} = \left(\frac{\partial f}{\partial t}\right)_{col}. \tag{3.55}$$

Here, as in Sect. 3.2, $\boldsymbol{E}$ and $\boldsymbol{b}$ are small electromagnetic perturbations dependent on coordinates and time, $\boldsymbol{B}_0$ is the external uniform magnetic field, and the rhs account for collisions between particles. If characteristic energies of the chaotic particle motion are large then Coulomb cross sections are accordingly small because they are reciprocal to the kinetic energy square (see Sect. 1.3.7) so the relaxation time τ_{rel} needed to approach to the plasma steady state can be remarkably large. Specifically, if the period $2\pi/\omega$ of the field variation is small compared with τ_{rel}, the collisions between the plasma particles can be discarded by setting the rhs of Eq. (3.55) to zero, which is the case of *collisionless* plasma; see Sect. 1.3.8. Moreover, even without any external field perturbation ($\boldsymbol{E} = \boldsymbol{b} = 0$), the particle collisions will play only a minor role over time periods much shorter than τ_{rel}, so the time variation of the distribution function due to collisions can be discarded by setting $\partial f_0/\partial t \approx 0$. The subscript "0" is used for the distribution function without external perturbations. For spatially uniform plasma we have additionally $\partial f_0/\partial \boldsymbol{r} = 0$; thus, the steady-state distribution function obeys the equation

$$\frac{e}{mc}[\boldsymbol{v} \times \boldsymbol{B}]\frac{\partial f_0}{\partial \boldsymbol{v}} = -\omega_B \frac{\partial f_0}{\partial \phi} = 0, \tag{3.56}$$

[3]Here, unlike Chap. 1, we use velocity $\boldsymbol{v}$ as an argument of distribution function f, with normalization condition $n_0 = \int f d^3 v$.

whose solution is an arbitrary function of two variables, $v_\parallel$ and $v_\perp$, the longitudinal and transverse to the magnetic field components of the particle velocity:

$$f_0 = f_0(v_\parallel, v_\perp). \tag{3.57}$$

This is a quasi-steady-state function but not necessarily the Maxwellian one. Approaching the full equilibrium can only happen over time $\Delta t > \tau_{rel}$ when the distribution function approaches the Maxwellian with a temperature T:

$$f_0 = n_0 \left(\frac{m}{2\pi T}\right)^{3/2} \exp\left(-\frac{mv^2}{2T}\right), \tag{3.58}$$

where n_0 is a mean density of the given particles. It must be noted that energy exchange between electrons and ions is a slow process because of big difference in their masses. Therefore, at some stage of the relaxation, both electrons and ions can become Maxwellians but with different temperatures $T_i \neq T_e$, which can become equal much later.

The dielectric tensor $\varepsilon_{\alpha\beta}$ is convenient to express via the conductivity tensor $\sigma_{\alpha\beta}$ taking into account Ohm's law (3.9). Consider a monochromatic plane wave in the form $\boldsymbol{E}$, $\boldsymbol{b} \propto \exp(i\boldsymbol{k}\cdot\boldsymbol{r} - i\omega t)$. Then, the current density stimulated by this external field can be expressed via correction to the distribution function

$$\delta f(\boldsymbol{r}, \boldsymbol{v}, t) = f(\boldsymbol{r}, \boldsymbol{v}, t) - f_0(v_\parallel, v_\perp) = \delta f(\boldsymbol{v}) \exp(i\boldsymbol{k}\cdot\boldsymbol{r} - i\omega t),$$

proportional to the external field: $\boldsymbol{j} = \sum \int e\boldsymbol{v}\delta f d^3v$, where the summation is performed over all plasma components, i.e., the electrons and all available ions.

This function δf is determined from the linearized equation (3.55):

$$-i(\omega - \boldsymbol{k}\cdot\boldsymbol{v})\delta f + \frac{e}{mc}[\boldsymbol{v}\times\boldsymbol{B}_0]\cdot\frac{\partial \delta f}{\partial \boldsymbol{v}} = -\frac{e}{m}\boldsymbol{E}\cdot\frac{\partial f_0}{\partial \boldsymbol{v}} - \frac{e}{mc}[\boldsymbol{v}\times\boldsymbol{b}]\cdot\frac{\partial f_0}{\partial \boldsymbol{v}}, \tag{3.59}$$

from which the magnetic field $\boldsymbol{b}$ can be removed using the Maxwell's equation $\boldsymbol{b} = (c/\omega)\boldsymbol{k}\times\boldsymbol{E}$. Eventually, we will obtain linear relation (3.9) between the electric current and the electric field, whose coefficients do represent the components of the conductivity tensor (and, accordingly, the dielectric tensor).

The actual analytical implementation of the outlined calculations is very cumbersome and labor consuming, but there is no simpler way to achieve this goal. The full kinetic treatment of the plasma dispersion is available in many textbooks (e.g., Akhiezer et al. 1975; Aleksandrov et al. 1984; Lifshitz and Pitaevskii 1981; Melrose 1980). Here, we only mention main milestones of full derivation following mainly Akhiezer et al. (1975) and discuss some of the relevant physical effects.

The dielectric permeability tensor may be described in the form

$$\varepsilon_{\alpha\beta} = \delta_{\alpha\beta} + \sum_{s=-\infty}^{s=\infty} \sum_a \frac{4\pi e_a^2}{m_a\omega^2} \left\{ \int \mathrm{d}^3 v \left(\frac{\omega - k_\parallel v_\parallel}{v_\perp} \frac{\partial f_a}{\partial v_\perp} + k_\parallel \frac{\partial f_a}{\partial v_\parallel} \right) \right.$$
$$\left. \frac{\Pi_{\alpha\beta}^{(s)}(\boldsymbol{v})}{\omega - s\omega_{Ba} - k_\parallel v_\parallel + i\gamma} - b_\alpha^0 b_\beta^0 \int \left(f_a + \frac{v_\parallel^2}{v_\perp} \frac{\partial f_a}{\partial v_\perp} \right) \mathrm{d}^3 v \right\}, \quad (3.60)$$

where

$$\Pi_{\alpha\beta}^{(s)}(\boldsymbol{v}) = \begin{pmatrix} \frac{s^2\omega_{Ba}^2}{k_x^2} J_s^2 & iv_\perp \frac{s\omega_{Ba}}{k_x} J_s J_s' & v_\parallel \frac{s\omega_{Ba}}{k_x} J_s^2 \\ -iv_\perp \frac{s\omega_{Ba}}{k_x} J_s J_s' & v_\perp^2 J_s'^2 & -iv_\parallel v_\perp J_s J_s' \\ v_\parallel \frac{s\omega_{Ba}}{k_x} J_s^2 & iv_\parallel v_\perp J_s J_s' & v_\parallel^2 J_s^2 \end{pmatrix}, \quad (3.61)$$

$J_s(\lambda)$ and $J_s'(\lambda) = \mathrm{d}J_s/\mathrm{d}\lambda$ are the Bessel function and its derivative over the argument $\lambda = k_x v_\perp/\omega_{Ba}$ and $\boldsymbol{b}^0$ is the unit vector along the magnetic field $\boldsymbol{B}_0$.

The imaginary part $i\gamma$ ($\gamma \to 0$) in the denominator (3.60), even though (infinitely) small, is highly important. Indeed, expanding the fraction according to **Sokhotsky rule**

$$\frac{1}{\omega - s\omega_{Ba} - k_\parallel v_\parallel + i\gamma} \to \frac{\mathcal{P}}{\omega - s\omega_{Ba} - k_\parallel v_\parallel} - i\pi\delta(\omega - s\omega_{Ba} - k_\parallel v_\parallel), \quad (3.62)$$

we find that the dielectric tensor $\varepsilon_{\alpha\beta} = \varepsilon'_{\alpha\beta} + \varepsilon''_{\alpha\beta}$ is not Hermitian any longer but contains an anti-Hermitian part

$$\varepsilon''_{\alpha\beta} = -i \sum_a \sum_{s=-\infty}^{\infty} \frac{4\pi e_a^2}{m_a\omega^2} \int \mathrm{d}^3 v \left(\frac{\omega - k_\parallel v_\parallel}{v_\perp} \frac{\partial f_a}{\partial v_\perp} + k_\parallel \frac{\partial f_a}{\partial v_\parallel} \right)$$
$$\Pi_{\alpha\beta}^{(s)}(\boldsymbol{v}) \delta(\omega - k_\parallel v_\parallel - s\omega_{Ba}), \quad (3.63)$$

whose property is $\varepsilon''^*_{\alpha\beta} = -\varepsilon''_{\beta\alpha}$, in contrast to the Hermitian part originating from the integral principal value, which is symmetric $\varepsilon'^*_{\alpha\beta} = \varepsilon''_{\beta\alpha}$. It is the anti-Hermitian part that is responsible for energy exchange between electromagnetic field and plasma. The energy density Q absorbed by the plasma (or transmitted from the plasma to the field) per unit time, averaged over the field period, has the form

$$Q = -\frac{i\omega}{8\pi} \varepsilon''_{\alpha\beta} E_\alpha^* E_\beta \quad (3.64)$$

(Toptygin 2005). Positive Q means the absorption of the energy by the plasma, while negative Q means the energy is transferred from the plasma

and so amplifies the electromagnetic field. The delta-function entering (3.63) indicates that this energy exchange is mediated by resonance particles whose longitudinal velocity obeys the equation

$$v_{\parallel} = \frac{\omega - s\omega_{Ba}}{k_{\parallel}}, \qquad s = 0, \pm 1, \pm 2 \ldots \tag{3.65}$$

The resonance with $s = 0$ is called the Cherenkov resonance because it is analogous to the Vavilov–Cherenkov effect of wave emission (or absorption) by fast particles in media. Other resonances $s \neq 0$ are called cyclotron or gyroresonances because they take place at multiples of the gyrofrequency corrected by the Doppler shift produced by the longitudinal motion of the particle:

$$\omega = s\omega_{Ba} + k_{\parallel} v_{\parallel}. \tag{3.66}$$

The equations given above are valid for arbitrary distribution function of the form (3.57), in particular, to the kappa distributions presented in Sect. 1.3.8. For distributions which do not strongly depart from equilibrium ones, electromagnetic waves are absorbed by the collisionless plasma. This phenomenon was discovered by Lev Landau for Langmuir oscillations in 1946 (so-called Landau damping, see Problem 3.5). However, nonequilibrium plasma distributions can and do amplify electromagnetic waves, which we will consider later (Chap. 10) in more detail.

In addition to the wave dispersion, the Hermitian part $\varepsilon'_{\alpha\beta}$ of the dielectric tensor also specifies the energy density w and the flux of energy density $\boldsymbol{\gamma}$ of the electromagnetic waves in the dispersive media:

$$w = \frac{1}{16\pi}\left(\frac{\partial}{\partial\omega}(\omega\varepsilon'_{\alpha\beta})E^*_{\alpha}E_{\beta} + \boldsymbol{B}^* \cdot \boldsymbol{B}\right), \tag{3.67}$$

$$\boldsymbol{\gamma} = \frac{c}{16\pi}\left(\boldsymbol{E} \times \boldsymbol{B}^* + \boldsymbol{E}^* \times \boldsymbol{B} - \frac{\omega}{c}\frac{\partial\varepsilon'_{\alpha\beta}}{\partial \boldsymbol{k}}E^*_{\alpha}E_{\beta}\right). \tag{3.68}$$

Both values are written for a monochromatic wave and averaged over its period $2\pi/\omega$. Apparently, it was assumed that wave dissipation is weak, $|\varepsilon''_{\alpha\beta}| \ll |\varepsilon'_{\alpha\beta}|$. Note that "generalized" Poynting vector (3.68) takes into account spatial dispersion; the last term in Eq. (3.68) accounts for energy flux related to the plasma waves with $\boldsymbol{B} = 0$.

3.3.2 Maxwellian Plasma

In some cases the integration of Eq. (3.60) [including Eq. (3.63)] can only be made numerically; other cases allow approximate or exact analytical integration. One of the important practical cases, where the analytical integration is possible, is the case of the Maxwellian plasma (Akhiezer et al. 1975):

$$\varepsilon_{\alpha\beta} = \delta_{\alpha\beta} + \sum_a \frac{\omega_{pa}^2}{\omega^2} \left\{ i\sqrt{\pi} z_0^a \sum_{s=-\infty}^{\infty} w(z_s^a) M_{\alpha\beta}^{(s)} + 2 z_0^{a2} b_\alpha b_\beta \right\}, \qquad (3.69)$$

where

$$M_{\alpha\beta}^{(s)} = \begin{pmatrix} \frac{s^2}{x_a} A_s(x_a) & isA_s'(x_a) & \sqrt{2/x_a} s z_s^a A_s(x_a) \\ -isA_s'(x_a) & \frac{s^2}{x_a} A_s(x_a) - 2x_a A_s'(x_a) & -i\sqrt{2x_a} z_s^a A_s'(x_a) \\ \sqrt{2/x_a} s z_s^a A_s(x_a) & i\sqrt{2x_a} z_s^a A_s'(x_a) & 2 z_s^{a2} A_s(x_a) \end{pmatrix}, \qquad (3.70)$$

$$w(z_s^a) = \exp(-z_s^{a2}) \left(\frac{k_\parallel}{|k_\parallel|} + \frac{2i}{\sqrt{\pi}} \int_0^{z_s^a} \exp(t^2) \mathrm{d}t \right) \approx \begin{cases} 1 + \frac{2iz_s^a}{\sqrt{\pi}}, & z_s^a \ll 1 \\ \exp(-z_s^{a2}) + \frac{i}{\sqrt{\pi} z_s^a} (1 + \frac{1}{2z_s^{a2}}), & z_s^a \gg 1, \end{cases} \qquad (3.71)$$

$$A_s(x_a) = \mathrm{e}^{-x_a} I_s(x_a) \approx \begin{cases} \frac{1-x_a}{s!} \left(\frac{x_a}{2} \right)^s, & x_a \ll 1 \\ \\ \frac{1}{\sqrt{2\pi x_a}} (1 + \frac{1-4s^2}{8x_a}), & x_a \gg |s^2 - 1/4|, \end{cases} \qquad (3.72)$$

$I_s(x_a)$ is the modified Bessel function, $A_s'(x_a) = \mathrm{d}A_s(x_a)/\mathrm{d}x_a$,

$$z_s^a = (\omega - s\omega_{Ba})/(\sqrt{2} k_\parallel v_a), \quad v_a = \sqrt{T_a/m_a}, \quad \sqrt{x_a} = k_x v_a/\omega_{Ba}. \qquad (3.73)$$

Now we can analyze dispersion of the Maxwellian plasma. Generally, the account of the particle thermal motion results in three different physical effects: modification of the cold plasma modes, damping of these modes, and appearance of new modes, which were not possible in the cold plasma (i.e., in a plasma without spatial dispersion). In a normal (nonrelativistic) plasma, modification of the cold plasma modes is typically important only where the corresponding refractive index is large compared with unity. As an example we consider how the wave dispersion changes around high-frequency plasma resonances (i.e., lower- and upper-hybrid frequencies). We start from the case when the dissipation in unimportant, which requires the following inequalities:

$$(k\rho_a \sin\theta)^2 \ll 1, \quad |z_s^a| \gg 1, \quad \text{for } s = 0, \pm 1, \pm 2 \ldots \qquad (3.74)$$

to be fulfilled, where $\rho_a = v_a/|\omega_{Ba}|$ is the thermal Larmor radius of particles a. Making appropriate expansions of the Bessel functions and the error function w and entirely neglecting all the dissipative terms, we find

the dielectric tensor components in the form

$$\varepsilon_{11} = \varepsilon_1 - \sum_a \frac{\omega_{pa}^2 k^2 v_a^2}{\omega^2 - \omega_{Ba}^2} \left[\frac{\omega^2 + 3\omega_{Ba}^2}{(\omega^2 - \omega_{Ba}^2)^2} \cos^2\theta + \frac{3\sin^2\theta}{\omega^2 - 4\omega_{Ba}^2} \right], \tag{3.75a}$$

$$\varepsilon_{22} = \varepsilon_1 - \sum_a \frac{\omega_{pa}^2 k^2 v_a^2}{\omega^2 - \omega_{Ba}^2} \left[\frac{\omega^2 + 3\omega_{Ba}^2}{(\omega^2 - \omega_{Ba}^2)^2} \cos^2\theta + \frac{\omega^2 + 8\omega_{Ba}^2}{\omega^2(\omega^2 - 4\omega_{Ba}^2)} \sin^2\theta \right], \tag{3.75b}$$

$$\varepsilon_{33} = \varepsilon_3 - \sum_a \frac{\omega_{pa}^2 k^2 v_a^2}{\omega^4} \left[3\cos^2\theta + \frac{\omega^2 \sin^2\theta}{\omega^2 - \omega_{Ba}^2} \right], \tag{3.75c}$$

$$\varepsilon_{13} = -\sum_a \frac{2\omega_{pa}^2 k^2 v_a^2}{(\omega^2 - \omega_{Ba}^2)^2} \sin\theta\cos\theta, \tag{3.75d}$$

$$\varepsilon_{23} = i\sum_a \frac{\omega_{pa}^2 \omega_{Ba} k^2 v_a^2 (3\omega^2 - \omega_{Ba}^2)}{\omega^3(\omega^2 - \omega_{Ba}^2)^2} \sin\theta\cos\theta, \tag{3.75e}$$

$$\varepsilon_{12} = ig - i\sum_a \frac{\omega_{pa}^2 \omega_{Ba} k^2 v_a^2}{\omega(\omega^2 - \omega_{Ba}^2)} \left[\frac{3\omega^2 + \omega_{Ba}^2}{(\omega^2 - \omega_{Ba}^2)^2} \cos^2\theta + \frac{6\sin^2\theta}{\omega^2 - 4\omega_{Ba}^2} \right], \tag{3.75f}$$

where ε_1, g, and ε_3 are the corresponding cold plasma components (3.42). Note that the dielectric tensor remains Hermitian because we entirely neglected all dissipative contributions.

When ω is around one of the hybrid frequencies, the correction to the coefficient $a(\omega)$ in dispersion equation (3.43) is the most important compared with the corrections to $b(\omega)$ and $c(\omega)$; with this correction it reads

$$(a(\omega) - \beta_e^2 n^2 a_1(\omega))n^4 + b(\omega)n^2 + c(\omega) = 0, \tag{3.76}$$

where $\beta_e = v_e/c$,

$$a_1(\omega) = \frac{\omega_{\mathrm{pe}}^2}{\omega^2} \left[3\cos^4\theta + \frac{6\omega^6 - 3\omega^4\omega_{\mathrm{Be}}^2 + \omega^2\omega_{\mathrm{Be}}^4}{(\omega^2 - \omega_{\mathrm{Be}}^2)^3} \cos^2\theta \sin^2\theta + \frac{3\omega^4 \sin^4\theta}{(\omega^2 - \omega_{\mathrm{Be}}^2)(\omega^2 - 4\omega_{\mathrm{Be}}^2)} \right], \tag{3.77}$$

with other coefficients defined by Eq. (3.44).

Now dispersion equation is the cubic one [rather than quadratic Eq. (3.43)] over n^2, which means that there can be three (rather than two) different roots and, thus, three different waves. However, those three roots are not necessarily all real positive numbers, so the number of propagating modes can be smaller than three. To estimate the refractive indices we note that one of them is about unity by the absolute value, $n^2 \approx -c(\omega)/b(\omega)$, and the spatial dispersion has a minor effect on it. Two other roots are large, so they can be estimated by neglecting the term $c(\omega)$, which is of the order of unity:

$$n^2 = \frac{a(\omega) \pm \sqrt{a^2(\omega) + 4a_1(\omega)b(\omega)\beta_e^2}}{a_1(\omega)\beta_e^2}. \tag{3.78}$$

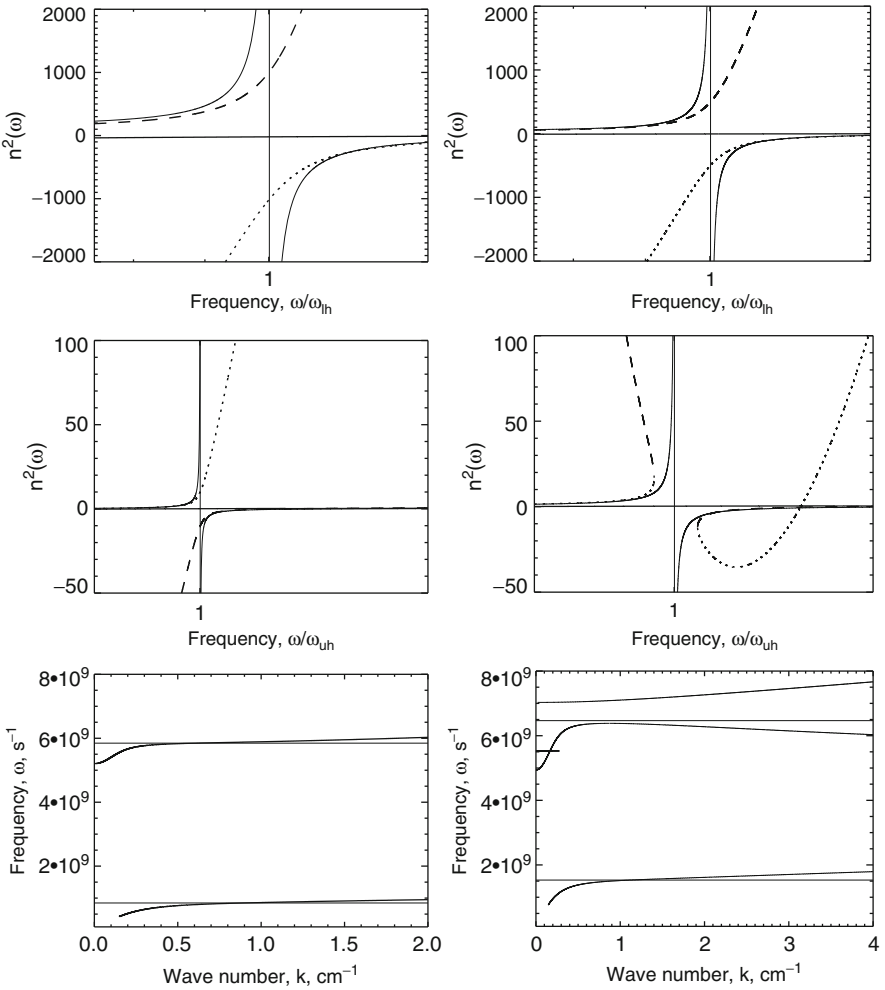

Figure 3.5: Dispersion of the waves around lower- and upper-hybrid resonances, two different cases. Parameters adopted: plasma density $n_e = 10^{10}\,\mathrm{cm}^{-3}$, plasma temperature $T = 1\,\mathrm{MK}$, $\theta = 60°$, and magnetic field either $B = 100\,\mathrm{G}$ *(left column)* or $B = 200\,\mathrm{G}$ *(right column)*. *Horizontal lines* in *bottom panels* show the level of hybrid frequencies.

Two different cases are possible depending on the parameter combinations: there can be or not be a solution exactly at a hybrid frequency. The first case, which happens when $a_1(\omega) > 0$, is shown in the left column of Fig. 3.5. Here, one of solutions (3.78) is positive, while the other is negative for both lower- and upper-hybrid resonances. The positive refractive index remains finite (although rather large compared with unity) in contrast to cold plasma

approximation, where it goes to infinity at the hybrid frequencies. Now the frequency slowly increases with k, crossing the hybrid frequency level at some point; in the cold plasma case it approached the hybrid frequency from below asymptotically remaining always smaller than it. The second case, right column of Fig. 3.5, is only possible when the frequency of the wave is between gyro- and double gyrofrequency, which can only happen for the upper-hybrid wave (middle panel). Here, both roots contain two discontinuous branches; no wave is possible at $\omega = \omega_{uh}$. There is a frequency range at $\omega < \omega_{uh}$, where two waves with the same frequency are possible. In terms of frequency dependence on k this means that initially the frequency increases with k (normal dispersion) and then it decreases with k (abnormal dispersion). At $\omega > \omega_{uh}$ there can be only one positive root, which results in the third wave mode at the bottom right panel above the upper-hybrid frequency.

3.3.3 Wave Damping in Equilibrium Plasma

The modes presented can propagate in the plasma only if their damping is small, which requires that the wavelength is large compared with the Debye radius and Larmor radius. In a collisionless plasma, the fundamental reason for the wave dissipation (and, accordingly, of the nonzero anti-Hermitian part of the dielectric tensor) is their interaction with resonant particles, whose velocity coincides with the wave phase velocity.

Consider damping of high-frequency modes in a plasma. Assuming $x_e \ll 1$ and $|z_s^e| \gg 1$ for $s = 0, \pm 1 \ldots$ we get the dielectric tensor components in the form:

$$\varepsilon_{11} = \varepsilon_{22} = \varepsilon_1 + \sum_{s\neq 0} 2i\sigma_s, \quad \varepsilon_{12} = ig - \sum_{s\neq 0} 2\sigma_s, \quad \varepsilon_{33} = \varepsilon_3 + 2i\sigma_0, \quad \varepsilon_{13} = \varepsilon_{23} = 0, \tag{3.79}$$

where

$$\sigma_s = \sqrt{\frac{\pi}{8}} \frac{\omega_{\mathrm{pe}}^2}{\omega k_\parallel v_e} \frac{n^2 x_e^{|s|-1}}{2^{|s|}|s|!} \exp(-z_s^2), \quad \sigma_0 = \sqrt{\pi} \frac{\omega_{\mathrm{pe}}^2}{\omega^2} z_0^3 \exp(-z_s^2) \tag{3.80}$$

with $z_s \equiv z_s^e$ and $x_e \equiv x_a(v^e)$ defined by Eq. (3.73), where relation $k = \omega n/c$ can be substituted, while ε_1, g, and ε_3 are the cold plasma components of the dielectric tensor.

When the wave damping is small, we can find the damping coefficients by iterations, neglecting the dissipation entirely in the zeroth approximation, which yields the real cold plasma refractive indices. Next iteration yields the **absorption index** (the imaginary part of the refraction index)

$$\gamma = \sum_{s=-\infty}^{\infty} \gamma_s, \tag{3.81}$$

where

$$\gamma_0 = \sigma_0 \frac{n^4 \cos^2\theta - \varepsilon_1(1+\cos^2\theta)n^2 + \varepsilon_1^2 - \varepsilon_2^2}{2c(\omega) + b(\omega)n^2}, \tag{3.82a}$$

$$\gamma_s = \sigma_s \frac{n^4 \sin^2\theta - \varepsilon_3(1+\cos^2\theta)n^2 + 2(\varepsilon_1 - \varepsilon_2)(\varepsilon_3 - n^2\sin^2\theta)}{2c(\omega) + b(\omega)n^2}, \tag{3.82b}$$

where dielectric tensor components (3.42) and coefficients b and c (3.44) are defined in the cold plasma approximation (only electron contribution is important).

We see that for the free-space (O and X) modes the damping coefficients at the cyclotron harmonics (so-called gyroabsorption) are small compared with unity, $\gamma_s \propto \beta_e^{2s-3}$, and exponentially small beyond the absorption contour defined by the factor $\exp(-z_s^2)$. Nevertheless, in the astrophysical condition, the gyroabsorption can be important because the wave absorption is proportional to the ray path length through the source, which can be very large. Let us make an estimate of the gyroabsorption in the case of solar corona. The absorption coefficient can be estimated as the product of γ_s and the wave number $k \sim \omega/c$. Taking $T = 10^7$ K, we find $\beta_e \approx 0.04$, so $\gamma_2 \sim 0.04$, $\gamma_3 \sim 3 \times 10^{-5}$, and $\gamma_4 \sim 3 \times 10^{-8}$; then adopting $\omega \sim 3 \times 10^{10}$ s^{-1} we obtain $k \sim 1$ cm; thus the absorption length, $L_{ga,s} \sim 1/(k\gamma_s)$, is about 25 cm, 3×10^4 cm, and 3×10^7 cm for the second, third, and fourth gyroharmonics, respectively. This means that in the solar corona the gyroabsorption is always important at the second harmonics, typically important at the third harmonics, and can even be important at the fourth harmonics.

The wave damping around lower- and upper-hybrid resonances requires additional consideration. First, as the frequency approaches the hybrid frequency, the refractive index increases, so the highest order over n^2 terms in the numerator and denominator makes the dominant contribution to the damping coefficients (3.82):

$$\gamma_0 = \sigma_0 \frac{n^2 \cos^2\theta}{b(\omega)}, \tag{3.83a}$$

$$\gamma_s = \sigma_s \frac{n^2 \sin^2\theta}{b(\omega)}, \quad (s \neq 0). \tag{3.83b}$$

These expressions are only valid until $n^2 \ll \beta_e^{-1}$, otherwise, the refraction index must be determined based on the kinetic treatment (3.78). The corresponding damping coefficients are easy to derive, taking into account that for $n^2 \gg 1$ anti-Hermitian contribution to coefficient $a(\omega)$ only is important:

$$a(\omega) \to \tilde{a}(\omega) = a(\omega) - \beta_e^2 n^2 a_1(\omega) + 2i\sigma_0 \cos^2\theta + \sum_{s\neq 0} 2i\sigma_s \sin^2\theta, \tag{3.84}$$

where $a_1(\omega)$ is defined by Eq. (3.77); other coefficients are taken in the cold plasma approximation. Eventually, the damping coefficients receive the form

$$\gamma_0 = \sigma_0 \frac{\cos^2\theta}{2\beta_e^2 a_1(\omega) n^2 - a(\omega)}, \tag{3.85a}$$

$$\gamma_s = \sigma_s \frac{\sin^2\theta}{2\beta_e^2 a_1(\omega) n^2 - a(\omega)}, \quad (s \neq 0). \tag{3.85b}$$

When $n^2\beta_e^2$ is small, we can neglect the term $2\beta_e^2 a_1(\omega)n^2$, so Eq. (3.85) reduces back to Eq. (3.83) if one takes into account that $n^2 \approx -b(\omega)/a(\omega)$. For larger $k \sim 1/r_d$ the Cherenkov damping (3.85a) of the electrostatic waves becomes very strong, so the wave is being damped on the length of the order of the Debye length; a comparably strong gyro-damping (3.85b) occurs when the wavelength approaches the Larmor radius of the thermal electrons.

3.3.4 Bernstein Modes

Let us, finally, consider new wave modes, which are only possible in the hot plasma, but were entirely not possible in the case of cold plasma. In fact, now the full dispersion equation is a transcendental one, which allows generally an infinite number of different solutions. Even though some of these solutions can be strongly damped, the number of remaining (propagating) wave modes remains infinite. We have already seen that the thermal motion of the plasma particles affects primarily the wave dispersion around the plasma resonant frequencies, so, not surprisingly, the new waves also appear close to electron and ion cyclotron or hybrid frequencies; there are both quasitransverse (electromagnetic) and longitudinal (electrostatic) waves. Although many kinds of these waves can be important in the astrophysics context, we consider here only one example of the electron cyclotron waves propagating transverse to the magnetic field, $\theta = \pi/2$, (Gross 1951; Bernstein 1958) commonly called the electron Bernstein modes.

For the case of $\theta = \pi/2$ the dispersion equation for the longitudinal electrostatic waves $a(\omega) = 0$ receives the form

$$a(\omega) = \varepsilon_{11} = 1 - \frac{\omega_{\rm pe}^2}{\omega} \sum_{s=-\infty}^{\infty} \frac{s^2}{x_e} A_s(x_e) \frac{1}{\omega - s|\omega_{\rm Be}|} = 0, \tag{3.86}$$

which does not contain any imaginary part, so there is no collisionless damping of these waves irrespectively on their wave number value.

The wave dispersion cannot be given in the closed form $\omega = \omega(k)$, because Eq. (3.86) has no explicit solution. However, asymptotic solution for small or large x_e can be obtained by expansion of the function $A(x_e)$ at small and large x_e, respectively. Straightforward analysis reveals that at small x_e the Bernstein mode frequency is close to either $s|\omega_{\rm Be}|$, $s \geq 2$, or $\omega_{uh} = \sqrt{\omega_{\rm pe}^2 + \omega_{\rm Be}^2}$, while at large x_e, it is close to $s|\omega_{\rm Be}|$, $s \geq 1$. The overall shape of the dispersion curves obtained numerically from Eq. (3.86) is shown in Fig. 3.6. The mode dispersion differs depending on whether the wave frequency is larger or smaller than the upper-hybrid frequency at small x_e.

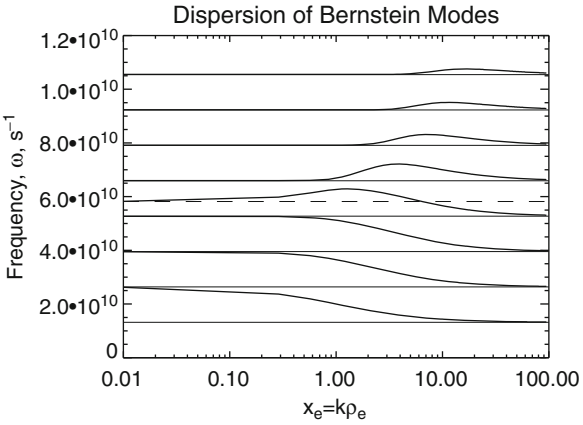

Figure 3.6: Dispersion of the electron Bernstein modes. The accepted parameters are: $n_e = 10^{10}\,\mathrm{cm}^{-3}$, $B = 75\,\mathrm{G}$. Levels of the first to eights gyro harmonics are shown by *thin solid lines*; the level of the upper-hybrid frequency is shown by the *dashed line*.

For the case of small frequencies, the frequency decreases all the way from $l|\omega_{\mathrm{Be}}|$ to $(l-1)|\omega_{\mathrm{Be}}|$ with the x_e increase, while for the case of large frequencies it behaves non-monotonically increasing from $l|\omega_{\mathrm{Be}}|$ and then decreasing back to the same $l|\omega_{\mathrm{Be}}|$. In a special case when the frequency is equal to ω_{uh} it goes up and then decreases to the closest gyroharmonics; see Fig. 3.6. More wave modes of the hot plasma can be obtained from the analysis of the full dispersion equation, see Akhiezer et al. (1975); in some cases relativistic corrections close to the resonance frequencies can be highly important to correctly describe the wave dispersion and/or excitation.

3.4 Collisional Plasma

So far, in this chapter, we only considered dispersion of a plasma entirely neglecting the true dissipation, i.e., a *collisionless plasma*. In the collisionless plasma the anti-Hermitian part of the dielectric tensor is defined by kinetic interaction between the waves and resonant particles, which is typically only important at a close proximity of the plasma resonance frequency while getting very small (frequently, exponentially small) otherwise. Collisional damping, being determined by the true dissipation, behaves differently: it maintains a finite value at any frequency, although can become anomalously large at the resonance frequencies.

3.4.1 General Case

A self-consistent way of Coulomb collisions inclusion into the plasma dispersion is taking into account the collisional integrals in kinetic equations (1.61) for different plasma species, contributing to the induced plasma

currents of the interest. This way is highly complicated and not needed given the limited accuracy of the input parameters in astrophysical conditions. A practical way is to describe the collisional integrals in BGK approximation ["lifetime" approximation; see Eq. (1.67)]:

$$St(f_a, f_b) \approx \nu_{ab}\delta f_a = \delta f_a/\tau_{ab}, \tag{3.87}$$

where δf_a is the departure of the distribution function from the steady-state one, Eq. (1.68), $\tau_{ab} = 1/\nu_{ab}$ is the relaxation time (lifetime); and ν_{ab} is the effective collision frequency of the particles a with particles b. This form of the collision integral, while relatively simple, retains fundamental properties of the true collision integral such as conservation of the particle number, momentum, and energy. In particular, this ensures that collisions with particles of the same kind (i.e., electron–electron or proton–proton) do not contribute to the momentum variation, thus, make no contribution to the plasma current; and, accordingly, the dielectric tensor.

In the elementary phenomenological theory, this is equivalent to inclusion of the corresponding friction forces $-\nu_{ab}(\boldsymbol{v}_a - \boldsymbol{v}_b)$ (with the condition $b \neq a$, which ensures that the momentum exchange only happens between distinct plasma components) into equation of motion (3.38). For a two-component hydrogen plasma, Eq. (3.38), thus, receives the form

$$-i\omega m_e \boldsymbol{v}^e = -e\boldsymbol{E} - m_e\omega_{\mathrm{Be}}\boldsymbol{v}^e \times \boldsymbol{e}_0 - m_e\nu_e(\boldsymbol{v}^e - \boldsymbol{v}^i), \tag{3.88a}$$

$$-i\omega m_i \boldsymbol{v}^i = +e\boldsymbol{E} + m_i\omega_{\mathrm{Bi}}\boldsymbol{v}^i \times \boldsymbol{e}_0 + m_e\nu_e(\boldsymbol{v}^e - \boldsymbol{v}^i). \tag{3.88b}$$

Here $\nu_e \equiv \nu_{ei}$ is a phenomenological parameter describing the rate of electron–proton collisions, which are to be determined based on kinetic theory (see, e.g., Sect. 1.3.7). Note that the form of these two collisional terms ensures the total momentum conservation of the plasma. In what follows we use Eq. (3.88) to calculate the electric current density assuming the plasma to be quasineutral:

$$\boldsymbol{j} = -en\boldsymbol{v}^e + en\boldsymbol{v}^i = en\boldsymbol{v}, \qquad \boldsymbol{v} = \boldsymbol{v}^i - \boldsymbol{v}^e, \tag{3.89}$$

where $n = n_e = n_i$ is the electron and ion number density. Adding two Eq. (3.88) up we obtain

$$-i\omega[(m_i + m_e)\boldsymbol{v}^i + m_e\boldsymbol{v}] = m_i\omega_{\mathrm{Bi}}\boldsymbol{v} \times \boldsymbol{e}_0, \tag{3.90}$$

where the term $m_e\boldsymbol{v}^i$, which is second order small over m_e/m_i, can safely be discarded. Thus, Eqs. (3.89) and (3.90) yield a relation between the ion velocity $\boldsymbol{v}^i$ and the current velocity $\boldsymbol{v}$:

$$\boldsymbol{v}^i = \frac{m_e}{m_i}\boldsymbol{v} + i\frac{\omega_{\mathrm{Bi}}}{\omega}\boldsymbol{v} \times \boldsymbol{e}_0. \tag{3.91}$$

Now, let us divide Eq. (3.88a) by m_e, Eq. (3.88b) by m_i, and subtract one from the other. Discarding all terms which are always small by m_e/m_i compared with the retained terms, and multiplying by en we obtain

$$(-i\omega+\nu_e)\boldsymbol{j}+\omega_{\mathrm{Be}}\boldsymbol{j}\times\boldsymbol{e}_0-\omega_{\mathrm{Be}}ne\boldsymbol{v}^i\times\boldsymbol{e}_0=\frac{e^2n}{m_e}\boldsymbol{E}, \tag{3.92}$$

where we have yet to eliminate the ion velocity $\boldsymbol{v}^i$ using Eq. (3.91) to obtain the link between the electric current and electric field:

$$(-i\omega+\nu_e)\boldsymbol{j}+\omega_{\mathrm{Be}}\boldsymbol{j}\times\boldsymbol{e}_0+i\frac{\omega_{\mathrm{Be}}\omega_{\mathrm{Bi}}}{\omega}\boldsymbol{j}_\perp=\frac{e^2n}{m_e}\boldsymbol{E}. \tag{3.93}$$

Projecting this equation onto Cartesian axes x, y, and z and solving for the components j_x, j_y, and j_z, we apply Eq. (3.9) to calculate the dielectric tensor components:

$$\varepsilon_{xx}=\varepsilon_{yy}=\varepsilon_1,\quad \varepsilon_1=1-\frac{\omega_{\mathrm{pe}}^2(\omega^2-\omega_{\mathrm{Be}}\omega_{\mathrm{Bi}}+i\omega\nu_e)}{(\omega^2-\omega_{\mathrm{Be}}\omega_{\mathrm{Bi}}+i\omega\nu_e)^2-\omega^2\omega_{\mathrm{Be}}^2}, \tag{3.94a}$$

$$\varepsilon_{xy}=-\varepsilon_{yx}=ig;\quad g=\frac{\omega_{\mathrm{pe}}^2\omega_{\mathrm{Be}}\omega}{(\omega^2-\omega_{\mathrm{Be}}\omega_{\mathrm{Bi}}+i\omega\nu_e)^2-\omega^2\omega_{\mathrm{Be}}^2}, \tag{3.94b}$$

$$\varepsilon_{zz}=\varepsilon_3,\quad \varepsilon_3=1-\frac{\omega_{\mathrm{pe}}^2}{\omega(\omega+i\nu_e)}. \tag{3.94c}$$

It is remarkable to note that unlike Eq. (3.42), the dielectric tensor components described by Eq. (3.94) do not represent sums of independent plasma components even in a limiting case of $\nu_e\to 0$. This apparent discrepancy originates from the total momentum conservation (always resulting in a nonzero ion velocity) taken into account here, while ignored in Sect. 3.2.1. Nevertheless, as we will see below, the main terms of the dielectric component expansion at any frequency range are consistent within both approaches. Note also that, here, unlike Sect. 3.2.1, we adopted $e>0$ and, accordingly, $\omega_{\mathrm{Be}}>0$.

3.4.2 High-Frequency Case

At high frequencies, $\omega^2\gg\omega_{\mathrm{Be}}\omega_{\mathrm{Bi}}$, we can entirely neglect the ion contribution to obtain:

$$\varepsilon_1=1-\frac{\omega_{\mathrm{pe}}^2(\omega+i\nu_e)}{\omega[(\omega+i\nu_e)^2-\omega_{\mathrm{Be}}^2]}, \tag{3.95a}$$

$$g=\frac{\omega_{\mathrm{pe}}^2\omega_{\mathrm{Be}}}{\omega[(\omega+i\nu_e)^2-\omega_{\mathrm{Be}}^2]}, \tag{3.95b}$$

which allows to straightforwardly compute dispersion of high-frequency plasma modes; see Problem 3.9.

The collisional damping coefficients can easily be found at the wave transparency windows, i.e., where the wave damping is small. In this case, the imaginary part of the refractive index can be found by iterations; see Problem 3.9. To make those expressions practical we have to specify the effective collision frequency; specifically, for the electron-ion collisions (see Sect. 1.3.7) we have:

$$\nu_e \approx \nu_{ei} \approx \frac{\pi e^4 n_e \ln \Lambda_C}{T_e^{3/2} m_e^{1/2}}, \tag{3.96}$$

where $\ln \Lambda_C$ is the Coulomb logarithm. In particular, for the free-space modes, the absorption coefficient (damping per unit wave path) reads

$$\kappa \approx 9.8 \cdot 10^{-3} \frac{n_e^2}{n T_e^{3/2} f^2} (24.6 + \ln(T_e/f)), \quad \text{cm}^{-1} \tag{3.97}$$

where $f = \omega/2\pi$ in Hz, n_e in cm^{-3}, T_e in K (here $T_e > 2 \cdot 10^5$ K), and n is the refractive index of the wave, (Dulk 1985). Even in the case of small damping coefficient compared with the corresponding refractive index, $\text{Im}n \ll \text{Re}n$, this absorption can be highly important because its effect is proportional to the wave path length in the astrophysical object, which can be very large. For example, in the solar corona for $T \sim 3 \cdot 10^6$ K, $n_e \sim 10^{10}\,\text{cm}^{-3}$, and $\omega \sim 2\omega_{\text{pe}}$, we find $l_d = 1/\kappa \sim 10^9$ cm comparable with typical scale of the solar coronal loops.

3.4.3 Ion Cyclotron Resonances

At lower frequencies, $\omega^2 \ll \omega_{\text{Be}}\omega_{\text{Bi}}$, we can apparently neglect the frequency compared with the electron gyrofrequency. Then, neglecting the term $\propto \nu_e^2$ in the denominator and taking into account $\omega_{\text{pe}}^2/\omega_{\text{Be}} = \omega_{\text{pi}}^2/\omega_{\text{Bi}}$, we find:

$$\varepsilon_1 = 1 - \frac{\omega_{\text{pi}}^2(\omega_{\text{Bi}}^2 - i\frac{\omega_{\text{Bi}}}{\omega_{\text{Be}}}\omega\nu_e)}{\omega_{\text{Bi}}^2(\omega^2 - \omega_{\text{Bi}}^2 + 2i\frac{\omega_{\text{Bi}}}{\omega_{\text{Be}}}\omega\nu_e)}, \tag{3.98a}$$

$$g = -\frac{\omega_{\text{pi}}^2\omega}{\omega_{\text{Bi}}(\omega^2 - \omega_{\text{Bi}}^2 + 2i\frac{\omega_{\text{Bi}}}{\omega_{\text{Be}}}\omega\nu_e)}. \tag{3.98b}$$

If we neglect the collisions entirely here, we obtain the ion contributions of the collisionless plasma described by Eq. (3.42), although in the presence of collisions the dielectric tensor components still contain the electron gyrofrequency in the imaginary contributions. In fact, the ratio of the gyrofrequencies is simply m_e/m_i; noting that the ion-electron collision rate $\nu_{ie} = \nu_{ei}m_e/m_i$, we express the dielectric tensor component via ion parameters only:

$$\varepsilon_1 = 1 - \frac{\omega_{\text{pi}}^2(\omega_{\text{Bi}}^2 - i\omega\nu_{ie})}{\omega_{\text{Bi}}^2(\omega^2 - \omega_{\text{Bi}}^2 + 2i\omega\nu_{ie})}, \tag{3.99a}$$

$$g = -\frac{\omega_{\text{pi}}^2\omega}{\omega_{\text{Bi}}(\omega^2 - \omega_{\text{Bi}}^2 + 2i\omega\nu_{ie})}. \tag{3.99b}$$

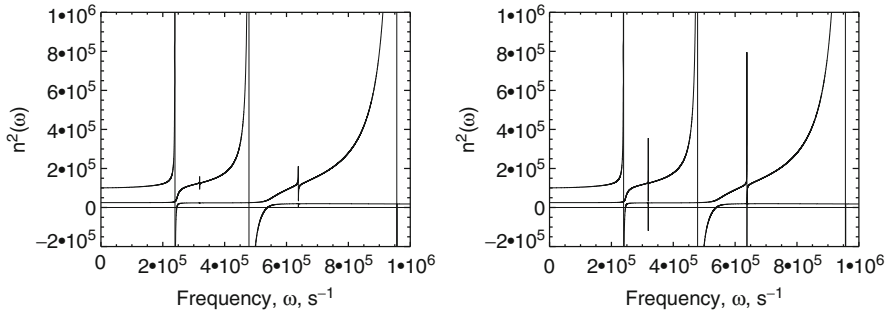

Figure 3.7: Dispersion of the collisional $p-\mathrm{He}$ plasma. The accepted parameters are: $n_p = 10^{10}\,\mathrm{cm}^{-3}$, $B = 100\,\mathrm{G}$, $n_{\mathrm{He}4} = 0.083 n_p$, $n_{\mathrm{He}3} = 5\cdot 10^{-4} n_p$, 15% of He is single ionized, and 85% of He is twice ionized; $T_e = 5\cdot 10^5\,\mathrm{K}$ *(left panel)* and $T_e = 2\cdot 10^6\,\mathrm{K}$ *(right panel)*. Significant temperature- and abundance-dependent suppression of the resonances related to He^3 is seen clearly, while those related to protons and He^4 are almost unaffected.

So far, we adopted that we have only one sort of ions, the protons. In the presence of other, less abundant, ions, estimating the proton effective collision rate needs further attention. Indeed, as we see [this consideration agrees with Eq. (1.76)], the effective rate of the proton–electron collisions $\nu_{pe} = m_e \nu_{ep}/m_p \ll \nu_{ep}$ is very small because of large mismatch in the masses of the involved particles. This means that collisions of the protons with other ions, primarily Helium, even less abundant than electrons while much heavier, can make a dominant or comparable contribution to the proton effective scattering rate

$$\nu_{p\mathrm{He}} \approx \frac{4\pi (e e_{\mathrm{He}4II})^2 n_{\mathrm{He}4II} \ln\Lambda_{Cp}}{T_p^{3/2} m_p^{1/2}} + \frac{4\pi (e e_{\mathrm{He}4III})^2 n_{\mathrm{He}4III} \ln\Lambda_{Cp}}{T_p^{3/2} m_p^{1/2}}, \quad (3.100)$$

where $n_{\mathrm{He}4II}$, $n_{\mathrm{He}4III}$, $e_{\mathrm{He}4II}$, and $e_{\mathrm{He}4III}$ are the number densities and charges of the single- and twice-ionized ions of He^4

$$\ln\Lambda_{Ca} = \begin{cases} \ln(r_d T_a/ze^2), & ze^2/\hbar v_a \gg 1 \\ \ln(r_d\sqrt{m_a T_a}/\hbar), & ze^2/\hbar v_a \ll 1. \end{cases} \quad (3.101)$$

For the typical astrophysics abundances of He^4 the proton collisions with electrons are only responsible for $\sim 10-20\%$ of the $\nu_p \approx \nu_{pe} + \nu_{p\mathrm{He}}$ depending on the Helium ionization state. In particular, the proton effective collision rate is not always a decreasing function of temperature: indeed, in the temperature range where almost all $\mathrm{He}II$ experiences the second ionization and becomes $\mathrm{He}III$, the collision rate increases with temperature, because the number of higher charged $\mathrm{He}III$ ions increases rapidly with the temperature.

In a multicomponent plasma the effect of Coulomb collisions can also be important at low frequencies at the regions of He (or other minor component) resonances. Specifically, the collisions can suppress some of the ion cyclotron modes related to less abundant ions, like the ions of He^3, although the He^4 ion cyclotron modes survive in the presence of collisions in most practical cases; see Fig. 3.7. For other (than protons) ions the main contribution to the effective collision rates comes from the collisions with other ions, primarily the most abundant protons. The corresponding collision rates are easy to calculate from the proton collision rate on a particular ion, e.g.,

$$\nu_{p\mathrm{He}III} \approx \frac{4\pi(ee_{\mathrm{He}4III})^2 n_{\mathrm{He}4III} \ln\Lambda_{Cp}}{T_p^{3/2} m_p^{1/2}}, \tag{3.102}$$

and using Eq. (1.76), which yields:

$$\nu_{\mathrm{He}IIIi} \approx \frac{4\pi(ee_{\mathrm{He}4III})^2 n_p \ln\Lambda_{Cp}}{T_p^{3/2} m_p^{1/2}} \frac{m_p}{m_{\mathrm{He}4}}, \tag{3.103}$$

which is by factor $z^2 m_p/m_{\mathrm{He}4}$ different from $\nu_{p\mathrm{He}III}$; to roughly account other ions' contribution one can use $n_e - z n_{\mathrm{He}4III}$ instead of n_p; however the corresponding corrections are typically beyond the current accuracy in the astrophysics.

3.4.4 Low-Frequency Case

Now consider the low-frequency range, $\omega \ll \omega_{\mathrm{Bi}}$, where the MHD waves (Sects. 2.4 and 3.2.3) can exist under certain conditions. Neglecting all small terms with ω we find the dielectric tensor components:

$$\varepsilon_1 = 1 - \frac{\omega_{\mathrm{pe}}^2}{i\omega\nu_e - \omega_{\mathrm{Be}}\omega_{\mathrm{Bi}}}, \tag{3.104a}$$

$$g = \frac{\omega_{\mathrm{pe}}^2 \omega_{\mathrm{Be}} \omega}{(i\omega\nu_e - \omega_{\mathrm{Be}}\omega_{\mathrm{Bi}})^2}, \tag{3.104b}$$

whose behavior is highly dependent on which, real or imaginary, term dominates in the denominators. If $\omega\nu_e \ll \omega_{\mathrm{Be}}\omega_{\mathrm{Bi}}$ the real parts dominate and neglecting the imaginary contributions we have $\varepsilon_1 \approx 1 + \omega_{\mathrm{pe}}^2/(\omega_{\mathrm{Be}}\omega_{\mathrm{Bi}}) = 1 + c^2/v_A^2$, where v_A is the Alfvén speed as usual; $g \approx c^2\omega/(v_A^2\omega_{\mathrm{Bi}}) \ll \varepsilon_1$ in full agreement with Eq. (3.54), Sect. 3.2.3. Here propagating MHD Alfvén and fast modes exit, whose relatively weak damping is controlled by the anti-Hermitian part (dependent on ν_e) of the dielectric tensor.

In the opposite case, $\omega\nu_e \gg \omega_{\mathrm{Be}}\omega_{\mathrm{Bi}}$, the external magnetic field drops out of the dielectric tensor making the Alfvén velocity irrelevant to electromagnetic phenomena in the plasma with strong Coulomb dissipation. No alternating electromagnetic field can propagate through such fluid; if a wave with

frequency ω falls onto a plasma boundary it can only enter there into a narrow layer with thickness of the order of the plasma skin scale $\delta \approx c/\sqrt{2\pi\sigma\omega}$, where σ is the Drude conductivity, Eq. (1.91). A critical Alfvén velocity below which the Alfvén waves cannot exist due to strong collisional dissipation is estimated from the equality $\omega\nu_e = \omega_{\rm Be}\omega_{\rm Bi}$ as (Alfven and Fälthammar 1963)

$$v_{A\,cr}^2 \approx c^2 \frac{\omega}{4\pi\sigma}. \tag{3.105}$$

At these low frequencies, $\omega \ll \omega_{\rm Bi}$, the plasma conductivity is often used along with (instead of) the dielectric tensor. Projecting Eq. (3.93) onto Oz we find

$$j_z = \sigma_0(\omega)E_z, \quad \sigma_0 = \frac{e^2 n}{m_e(\nu_e - i\omega)}, \tag{3.106}$$

which transforms to the Drude formula, Eq. (1.91), as $\omega \to 0$. As long as $\omega \ll \nu_e$ the electric current obeys Ohm's law with the constant Drude conductivity, while at $\omega \gg \nu_e$ (but still $\omega < \omega_{\rm pe}$) the real part of the dielectric permeability that reduces for a scalar ε_0 (provided that $v_A < v_{A\,cr}$)

$$\varepsilon_0 = 1 + i\frac{4\pi\sigma_0}{\omega} = 1 - \frac{\omega_{\rm pe}^2}{\omega^2 + i\omega\nu_e} \tag{3.107}$$

turns negative and the plasma response interferes with the external wave and efficiently quenches it.

Problems

3.1 Calculate frequencies of plasma resonances from equation $a = 0$. This is a cubic over ω^2 equation for the electron–proton plasma; thus, it has three positive roots. Consider different asymptotic forms of these frequencies.

3.2 Analyze dispersion and polarization of high-frequency (magneto-ionic) O- and X-modes in various special cases: (a) longitudinal propagation, $\theta = 0$; (b) transverse propagation, $\theta = \pi/2$; (c) arbitrary propagation, $\omega_{\rm Be} \ll \omega_{\rm pe}$; (d) arbitrary propagation, $\omega_{\rm Be} \gg \omega_{\rm pe}$; (e) arbitrary propagation, $\omega \gg \omega_{\rm Be},\ \omega_{\rm pe}$.

3.3 Analyze dispersion and polarization of Z-mode in various special cases: (a) longitudinal propagation, $\theta = 0$; (b) transverse propagation, $\theta = \pi/2$; (c) arbitrary propagation, $\omega_{\rm Be} \ll \omega_{\rm pe}$; (d) arbitrary propagation, $\omega_{\rm Be} \gg \omega_{\rm pe}$.

3.4 Analyze dispersion and polarization of the whistler mode in the same special cases.

3.5 Calculate complex dielectric tensor of fully ionized, uniform, unmagnetized isotropic collisionless Maxwellian plasma with temperature T and number densities $n_e = n_i = n$.

3.6 ⋆ Determine the frequency ω_l of longitudinal oscillations of the collisionless plasma using the dielectric tensor (including the imaginary part) found in Problem 3.5 adopting $kv_{Te} \ll \omega$. Calculate the density w of electromagnetic energy, its dissipation rate Q, and the density $\boldsymbol{\gamma}$ of the energy flux.

3.7 Consider quasi-equilibrium state when both electrons and ions are Maxwellian but with different temperatures $T_i \neq T_e$ (which can stay relatively long because of slow energy exchange between electrons and ions provided by large difference in their masses). Use the outcome of Problem 3.5 to find the longitudinal dielectric permeability for an "intermediate" case when $s_i = \omega/kv_{Ti} \gg 1$, while $s_e = \omega/kv_{Te} \ll 1$. Find frequency and damping rate of the longitudinal oscillations of these non-isothermal plasma. Specify the conditions where the damping is weak.

3.8 Calculate dielectric tensor in a magnetized plasma with account of the electron-ion collisions (see Sect. 3.4) in the basis of "cyclic" unit vectors

$$\boldsymbol{e}_{\pm 1} = \mp\frac{1}{\sqrt{2}}(\boldsymbol{e}_x \pm i\boldsymbol{e}_y) \equiv \mp\frac{1}{\sqrt{2}}(\boldsymbol{e}_1 \pm i\boldsymbol{e}_2), \qquad \boldsymbol{e}_0 = \boldsymbol{e}_z = \boldsymbol{e}_3. \tag{3.108}$$

Find transformation rule between the tensors in the standard Cartesian and cyclic coordinate basis.

3.9 Calculate high-frequency dispersion relation in a magnetized plasma with account of the electron-ion collisions; see Sect. 3.4.2.

3.10 Calculate absorption index and damping rate of Alfvén waves in a magnetized plasma with account of the electron-ion collisions; see Sect. 3.4.4. Compare the results obtained with those derived from MHD approach, Sect. 2.4.3. If the results are different, explain origin of this difference.

3.11 Calculate dielectric permittivity tensor and dispersion relations of low-frequency (ion-cyclotron/hybrid) modes in a magnetized multicomponent plasma (Sect. 3.2.4) with account of the electron-ion and proton-ion collisions.

Answers and Solutions

3.1 Let us sort the solution ω_i^2 such as $\omega_1 > \omega_2 > \omega_3$. The two highest frequencies are primarily specified by the electron contribution and called the upper- and lower-hybrid frequencies, $\omega_{UH} = \omega_1$ and $\omega_{lh} = \omega_2$. Neglecting

the ion contribution in equation $a = 0$ and solving for ω_i^2, we find (Akhiezer et al. 1975)

$$\omega_{1,2}^2 = \frac{\omega_{\rm pe}^2 + \omega_{\rm Be}^2}{2} \pm \frac{\sqrt{(\omega_{\rm pe}^2 + \omega_{\rm Be}^2)^2 - 4\omega_{\rm pe}^2\omega_{\rm Be}^2\cos^2\theta}}{2}.$$

At $\theta \to 0$ we have $\omega_{UH} = \max(\omega_{\rm pe}, |\omega_{\rm Be}|)$ and $\omega_{lh} = \min(\omega_{\rm pe}, |\omega_{\rm Be}|)$, while at $\theta \to \pi/2$: $\omega_{UH} = \sqrt{\omega_{\rm pe}^2 + \omega_{\rm Be}^2}$ and $\omega_{lh} = \omega_{\rm pe}|\omega_{\rm Be}|\cos\theta/\sqrt{\omega_{\rm pe}^2 + \omega_{\rm Be}^2}$; the latter is valid when $\cos^2\theta \gg m_e/m_i$.

In the dense plasma case, $\omega_{\rm pe} \gg \omega_{\rm Be}$ the above expressions simplify to

$$\omega_{UH}^2 \approx \omega_{\rm pe}^2 + \omega_{\rm Be}^2\sin^2\theta; \qquad \omega_{lh} = |\omega_{\rm Be}|\cos\theta, \tag{3.109}$$

while in the strong magnetic field case, $\omega_{\rm pe} \ll \omega_{\rm Be}$

$$\omega_{UH}^2 \approx \omega_{\rm Be}^2 + \omega_{\rm pe}^2\sin^2\theta; \qquad \omega_{lh} = \omega_{\rm pe}\cos\theta. \tag{3.110}$$

The third frequency is about the ion cyclotron frequency, $\omega_3 \approx \omega_{\rm Bi}(1 - m_e\tan^2\theta/(2m_i))$ if $\cos^2\theta \gg m_e/m_i$. If this condition is not fulfilled, the frequencies $\omega_{2,3} \ll \omega_{\rm Be}$; discarding the correspondingly small terms, we find

$$\omega_{2,3}^2 = \frac{\omega_{\rm pe}^2\cos^2\theta + \omega_{\rm pi}^2 + \omega_{\rm Bi}^2 \pm \sqrt{(\omega_{\rm pe}^2\cos^2\theta + \omega_{\rm pi}^2 + \omega_{\rm Bi}^2)^2 - 4(1+Y^2)\omega_{\rm pi}^2\omega_{\rm Bi}^2\cos^2\theta}}{(2+2Y^2)},$$

where $Y = \omega_{\rm pe}/\omega_{\rm Be}$, which implies that ω_{lh} remains finite at $\theta \to \pi/2$, while ω_3 goes to zero. One can further simplify the general expression for $\omega_{2,3}^2$ in various asymptotic parameter regimes (Akhiezer et al. 1975).

3.2 All asymptotic forms of the refractive indices at high frequencies are derived from Eq. (3.48).

(a) $\theta = 0$: $n_\sigma^2 = 1 - \omega_{\rm pe}^2/[\omega(\omega + \sigma|\omega_{\rm Be}|)]$; from Eq. (3.50) it is easy to find that the waves are circularly polarized.

(b) $\theta = \pi/2$: $n_O^2 = 1 - \omega_{\rm pe}^2/\omega^2$ and $n_X^2 = 1 - \omega_{\rm pe}^2(\omega^2 - \omega_{\rm pe}^2)/[\omega^2(\omega^2 - \omega_{\rm pe}^2 - \omega_{\rm Be}^2)]$. O-mode is linearly polarized along the external magnetic field; X-mode is elliptically polarized in the plane transverse to the external magnetic field; recall, there is an electric field component along the wave vector.

(c) $\omega_{\rm Be} \ll \omega_{\rm pe}$: here a quasilongitudinal approximation, $u\sin^4\theta \ll 4(1-v)^2\cos^2\theta$, can be used for most propagation directions: $n_\sigma^2 = 1 - \frac{\omega_{\rm pe}^2}{\omega^2}\left(1 - \sigma\frac{|\omega_{\rm Be}|}{\omega}\cos\theta\right)$. The polarization is almost circular.

(d) $\omega_{\rm Be} \gg \omega_{\rm pe}$: $n_\sigma^2 = 1 - \frac{2\omega_{\rm pe}^2}{2\omega^2 - \omega_{\rm Be}^2 \sin^2\theta + \sigma\sqrt{\omega_{\rm Be}^4 \sin^4\theta + \omega_{\rm Be}^2 \omega^2 \cos^2\theta}} \approx 1.$

(e) $\omega \gg \omega_{\rm Be},\ \omega_{\rm pe}$. Case (c) applies here, so depending on the accuracy requirement we obtain: $n_\sigma^2 \approx 1 - \frac{\omega_{\rm pe}^2}{\omega^2}\left(1 - \sigma\frac{|\omega_{\rm Be}|}{\omega}\cos\theta\right) \approx 1 - \frac{\omega_{\rm pe}^2}{\omega^2} \approx 1.$

3.3 Z-mode is a lower-frequency extension of the X-mode. Thus, equations from the previous solution for $\sigma = -1$ apply here in the corresponding available parameter regimes, for example, case (e) is not possible here.

3.4 The whistler mode is the high-frequency continuation of the fast magnetoacoustic mode at $\omega \gg \omega_{\rm Bi}$ (while $\omega < |\omega_{\rm Be}|$). If $\omega \ll \omega_{cr} \equiv 4\omega_{\rm pe}^2 \cos^2\theta/(\omega_{\rm Be}\sin^4\theta)$, then (for $\sigma = 1$)

$$n_w^2 = 1 + \frac{\omega_{\rm pe}^2}{\omega(|\omega_{\rm Be}|\cos\theta - \omega)}.$$

Solving this dispersion relation for ω, we find

$$\omega = \frac{|\omega_{\rm Be}| c^2 k^2 \cos\theta}{\omega_{\rm pe}^2 + c^2 k^2}.$$

Note that if $\omega_{\rm pe} \gg \omega_{\rm Be}$ then $\omega \ll \omega_{cr}$ is valid everywhere in the quasilongitudinal range of the angles. Thus, at high frequencies, $\omega \to \omega_{lh} \approx |\omega_{\rm Be}|\cos\theta$ and the whistler mode becomes the lower-hybrid quasilongitudinal mode. If $\omega_{\rm pe} \ll \omega_{\rm Be}$ then there is a frequency region $\omega \gg \omega_{cr}$, where $n_w^2 = (\omega^2 - \omega_{\rm pe}^2)/(\omega^2 - \omega_{\rm pe}^2\cos^2\theta)$; thus, the whistler wave becomes the lower-hybrid wave anyway; see Solution 3.1. At lower frequencies, $\omega \ll |\omega_{\rm Be}|$ these expressions simplify to

$$n_w^2 \approx \frac{\omega_{\rm pe}^2}{\omega|\omega_{\rm Be}|\cos\theta}, \qquad \omega = \frac{|\omega_{\rm Be}| c^2 k^2 \cos\theta}{\omega_{\rm pe}^2}.$$

3.5 Let us calculate the plasma current

$$\boldsymbol{j} = \sum \int e\boldsymbol{v}\delta f\, d^3p, \tag{1}$$

stimulated by a weak external field with given $\boldsymbol{k}$ and ω, where δf is a nonstationary part of the distribution function proportional to the external field; the summation is performed over all available kinds of charges (although we only consider explicitly electrons and singly ionized ions). The perturbation δf is determined from Eq. (3.59) with $B_0 = 0$. The collisionless plasma is convenient to be considered as a limiting case of a collisional one (with

seldom collisions); therefore, we include in Eq. (3.59) the collisional integral in a simple form $St[f] = -\nu\delta f$, where ν is a small rate of collisions between the given particles and all other kinds of particles, cf. Sect. 3.4; here, in the collisionless case, its form is unimportant since it will anyway be adopted to vanish at a final stage of manipulations. Thus, we obtain

$$(-i\omega + i\boldsymbol{k}\cdot\boldsymbol{v} + \nu)\delta f = -\frac{e}{m}\boldsymbol{E}\cdot\frac{\partial f_0}{\partial \boldsymbol{v}} - \frac{e}{mc}[\boldsymbol{v}\times\boldsymbol{b}]\cdot\frac{\partial f_0}{\partial \boldsymbol{v}}. \tag{2}$$

For Maxwellian distribution (3.58) the derivative over velocity is straightforwardly calculated

$$\frac{\partial f_0}{\partial \boldsymbol{v}} = -\frac{m\boldsymbol{v}}{T}f_0, \quad [\boldsymbol{v}\times\boldsymbol{b}]\cdot\frac{\partial f_0}{\partial \boldsymbol{v}} = 0. \tag{3}$$

Substitution of all these into Eq. (2) yields

$$\delta f(\boldsymbol{v}) = \frac{me(\boldsymbol{E}\cdot\boldsymbol{v})f_0(v)}{T(\nu + i\boldsymbol{k}\cdot\boldsymbol{v} - i\omega)}. \tag{4}$$

It must become transparent now, why retaining the small collision frequency $\nu > 0$ is convenient even in the fully collisionless case: the denominator of the above expression never reaches zero for any real (physically meaningful) values of $\boldsymbol{k}$, $\boldsymbol{v}$, and ω; thus Eq. (4) and everything derived from it are mathematically correct. Substitution of Eq. (4) into Eq. (1) yields the linear relation in the form of Ohm's law:

$$j_\alpha = \sigma_{\alpha\beta}(\boldsymbol{k},\omega)E_\beta, \tag{5}$$

where the tensor of complex conductivity has the form

$$\sigma_{\alpha\beta}(\boldsymbol{k},\omega) = \sum\frac{e^2}{T}\int\frac{v_\alpha v_\beta f_0(v)}{\nu + i\boldsymbol{k}\cdot\boldsymbol{v} - i\omega}d^3v. \tag{6}$$

According to Eq. (3.9) this tensor is linearly linked with the dielectric tensor by

$$\varepsilon_{\alpha\beta}(\boldsymbol{k},\omega) = \delta_{\alpha\beta} + i\frac{4\pi\sigma_{\alpha\beta}(\boldsymbol{k},\omega)}{\omega}. \tag{7}$$

Now, we take into account the isotropy of the analyzed plasma, which implies that only the wave vector $\boldsymbol{k}$ can enter the dielectric tensor $\varepsilon_{\alpha\beta}$. Thus, the most general tensor form of the dielectric tensor $\varepsilon_{\alpha\beta}$ is

$$\varepsilon_{\alpha\beta}(\boldsymbol{k},\omega) = \varepsilon_l(k,\omega)\frac{k_\alpha k_\beta}{k^2} + \varepsilon_t(k,\omega)\left(\delta_{\alpha\beta} - \frac{k_\alpha k_\beta}{k^2}\right), \tag{8}$$

where ε_l and ε_t are two scalar functions, which can be called the longitudinal and transverse permeability, respectively.

Let us isolate these two invariant values ε_l and ε_t from the tensor $\epsilon_{\alpha\beta}$:

$$\varepsilon_l = 1 + i \sum \frac{4\pi e^2}{\omega T} \int \frac{v_\parallel^2 f_0(v)}{\nu + ikv_\parallel - i\omega}\, d^3v, \tag{9}$$

$$\varepsilon_t = 1 + i \sum \frac{2\pi e^2}{\omega T} \int \frac{v_\perp^2 f_0(v)}{\nu + ikv_\parallel - i\omega}\, d^3v. \tag{10}$$

Here, the velocity components parallel and transverse to vector $\boldsymbol{k}$ are explicitly defined.

The forthcoming integration over transverse velocity components in Eqs. (9) and (10) is easy to perform using the explicit form of the Maxwellian distribution, which results in

$$\varepsilon_l(k,\omega) = 1 + i \sum \frac{4\pi n e^2}{m} \frac{1}{\sqrt{2\pi} k v_T \omega} \int \frac{\mathrm{e}^{-x^2/2} x^2 \mathrm{d}x}{x - s - i\nu'}, \tag{11}$$

$$\varepsilon_t(k,\omega) = 1 + i \sum \frac{4\pi n e^2}{m} \frac{1}{\sqrt{2\pi} k v_T \omega} \int \frac{\mathrm{e}^{-x^2/2} \mathrm{d}x}{x - s - i\nu'}, \tag{12}$$

where $v_T = \sqrt{T/m}$ is the thermal speed, $s = \omega/kv_T > 0$, and $\nu' = \nu/kv_T > 0$ are dimensionless frequencies. Use of Sokhotsky rules yields

$$\frac{x^2}{x - s - i\nu'} = x \left[1 + \frac{s}{x - s - i\nu'}\right] = x + s + \frac{s^2}{x - s - i\nu'}. \tag{13}$$

The integration with $x+s$ is tabular. Then, the latter integration is performed using the equivalence

$$\frac{1}{\nu' + i(x - s)} = \int_0^\infty \mathrm{e}^{-(\nu' - is + ix)t}\, \mathrm{d}t,$$

which takes place owing to $\nu' > 0$. We further have

$$\begin{aligned} \int_{-\infty}^{\infty} \frac{\mathrm{e}^{-x^2/2} \mathrm{d}x}{x - s - i\nu'} &= i \int_0^\infty \mathrm{d}t\, \mathrm{e}^{-(\nu' - is)t} \int_{-\infty}^{\infty} \mathrm{e}^{-(x^2 + 2xit)/2} \mathrm{d}x \\ &= i\sqrt{2\pi} \mathrm{e}^{-s^2/2} \left\{ \sqrt{\frac{\pi}{2}} + i \int_0^s \mathrm{e}^{u^2/2} \mathrm{d}u \right\}. \end{aligned}$$

The following notations are convenient:

$$Z(s) = X(s) - iY(s), \text{ where } X(s) = s\mathrm{e}^{-s^2/2}\int_0^s \mathrm{e}^{u^2/2}\mathrm{d}u, \; Y(s) = \sqrt{\frac{\pi}{2}}\, s\,\mathrm{e}^{-s^2/2}, \tag{14}$$

whose real part is expressed via the error integral (Abramowitz and Stegun 1964).

Using notations (14) along with plasma frequency definition, we obtain final expressions for the longitudinal and transverse dielectric permeability for any ω and k:

$$\varepsilon_l(k,\omega) = 1 - \sum \frac{\omega_p^2}{(kv_T)^2}\,[Z(s) - 1], \tag{3.111a}$$

$$\varepsilon_t(k,\omega) = 1 - \sum \frac{\omega_p^2}{\omega^2}\, Z(s). \tag{3.111b}$$

The summation is performed over electrons and all available ion species. It is worthwhile to recall that the plasma frequencies ω_{pe} and ω_{pi} and the thermal velocities v_{Te} and v_{Ti} are different for the electrons and ions because of mass (and, perhaps, temperature) difference.

Note that both ε_l and ε_t have [according to Eq. (14)] the imaginary parts proportional to $Y(s)$. Those imaginary parts determine the dissipation of electromagnetic energy in the collisionless plasma (**Landau damping**).

3.6 Consider $\varepsilon_l(k,\omega)$ when $s = \omega/kv_T \gg 1$:

$$\varepsilon_l \approx 1 - \frac{\omega_{\mathrm{pe}}^2}{\omega^2}\left(1 + \frac{3k^2v_{Te}^2}{\omega^2}\right) + i\sqrt{\frac{\pi}{2}}\,\frac{\omega\omega_{\mathrm{pe}}^2}{k^3v_{Te}^3}\,\mathrm{e}^{-\omega^2/2k^2v_{Te}^2}, \tag{1}$$

where the ion contribution is discarded since $\omega_{\mathrm{pi}}^2 = (m_e/m_i)\omega_{\mathrm{pe}}^2 \ll \omega_{\mathrm{pe}}^2$ and $s_i \gg s_e$. Note, that even though the imaginary part is exponentially small, it results in qualitatively new effect, the electromagnetic energy dissipation.

First, neglect the imaginary part entirely by adopting $\varepsilon_l''(k,\omega) \approx 0$, then

$$\omega_l^2(k) \approx \omega_{\mathrm{pe}}^2 + 3(kv_{Te})^2, \;\; w = \frac{1}{8\pi}|E|^2 = \frac{1}{4\pi}\overline{E^2(t)}, \;\; \boldsymbol{\gamma} = \frac{3v_{Te}}{8\pi}\,\frac{kv_{Te}}{\omega_l}\,\frac{\boldsymbol{k}}{k}|E|^2. \tag{2}$$

Here, the electron plasma component oscillates relative to ions holding at rest. The total energy density of these Langmuir oscillations is twice of the electric energy density; the second half of the energy density comes from potential energy of Coulomb interaction between electrons and ions. The energy flux is nonzero due to the account of spatial dispersion in spite of nonexistence of the magnetic field and, thus, absence of the standard Poynting vector. The energy is transferred here by the thermal electron motion.

At the second stage, let us include the imaginary part $\varepsilon_l''(k,\omega)$, which gives rise to a small imaginary part of the oscillation frequency $\omega_l(k)$ describing the Landau damping. Adopting $\omega_l = \omega_l' + i\gamma,\ |\gamma| \ll \omega_l'$, we find ω_l' from the equation $\varepsilon_l'(k,\omega) = 0$ which yields familiar result (2). Then, the small imaginary part is obtained from the equation

$$\varepsilon_l(k,\omega_l) \approx \varepsilon_l(k,\omega_l') + i\varepsilon_l''(k,\omega_l') + \left.\frac{\partial\varepsilon_l'(k,\omega)}{\partial\omega}\right|_{\omega=\omega_l'} i\gamma = 0, \tag{3}$$

with the imaginary part ε_l'' from Eq. (1). We obtain

$$\gamma(k) = -\frac{\varepsilon_l''(k,\omega_l')}{\partial\varepsilon_l'(k,\omega)/\partial\omega|_{\omega=\omega_l'}} = -\frac{\sqrt{\pi}}{8}\frac{\omega_{\rm pe}}{(kr_D)^2}\mathrm{e}^{-1/4(kr_D)^2-3/2}, \tag{4}$$

where $r_D = \sqrt{T/8\pi ne^2}$. If $\omega_l'/kv_{Te} = 1/\sqrt{\pi}kr_D \gg 1$ the Langmuir wave damping is exponentially small. This is apparently related to proportionally small number of electrons in the Maxwellian tail having the velocities comparable with the phase velocity $v_{ph} = \omega/k$ of the longitudinal wave. The dissipation power of the energy density is given by Eq. (3.64), which here receives the form

$$Q = \frac{\omega_l'}{8\pi}\varepsilon_l''(k,\omega_l')|E(t)|^2. \tag{5}$$

Now $|E(t)|^2 = E_0^2\mathrm{e}^{-2\gamma t}$ with the initial value of the electric field E_0. The quantities w and $\boldsymbol{\gamma}$ with account of the wave dissipation are given by same expressions (2) with ω_l substituted by ω_l'. The mean square of the electric field $|E|^2$ entering (2) decays with time accordingly.

3.7 In the specified parameter regime we have

$$\varepsilon_l'(k,\omega) \approx 1 + \frac{\omega_{\rm pe}^2}{k^2v_{Te}^2} - \frac{\omega_{\rm pi}^2}{\omega^2}\left(1 + \frac{3k^2v_{Ti}^2}{\omega^2}\right),$$

$$\varepsilon_l''(k,\omega) \approx \sqrt{\frac{\pi}{2}}\left(\frac{\omega\omega_{\rm pe}^2}{k^3v_{Te}^3} + \frac{\omega\omega_{\rm pi}^2}{k^3v_{Ti}^3}\mathrm{e}^{-\omega^2/2k^2v_{Ti}^2}\right). \tag{1}$$

Assuming the imaginary part ε_l'' to be small, obtain the real and imaginary parts of the frequency like in the previous problem:

$$\omega_l'^2(k) \approx \omega_{\rm pi}^2\left[1 + 3k^2r_{Di}^2\left(1 + \frac{1}{k^2r_{De}^2}\right)\right]\left(1 + \frac{1}{k^2r_{De}^2}\right)^{-1}, \tag{2}$$

$$\gamma(k) \approx -\sqrt{\frac{\pi}{8}}\cdot\frac{m_i}{m_e}\cdot\frac{\omega_l'^4(k)}{k^3v_{Te}^3}\left\{1 + \sqrt{\frac{m_i}{m_e}}\left(\frac{T_e}{T_i}\right)^{3/2}\exp\left[-\frac{\omega_l'^2(k)}{2k^2v_{Ti}^2}\right]\right\}. \tag{3}$$

Here we introduced the electron and ion Debye radii $r_{De,\,i} = \sqrt{T_{e,\,i}/4\pi ne^2}$ and assume the plasma to be strongly non-isothermal: $T_e \gg T_i$. Under this condition along with inequalities prescribed in the statement of the problem, Eqs. (2) and (3) yield $|\gamma| \ll \omega_l'$.

For the long waves, i.e., $kr_{De} \ll 1$ and $kr_{Di} \ll 1$, the formulae simplify to

$$\omega_l'(k) \approx v_s k, \qquad v_s = \sqrt{\frac{T_e}{m_i}\left(1 + \frac{3T_i}{T_e}\right)},$$

$$\gamma \approx -kv_s\sqrt{\frac{\pi m_e}{8m_i}}\left\{1 + \sqrt{\frac{m_i}{m_e}}\left(\frac{T_e}{T_i}\right)^{3/2}\exp\left(-\frac{3}{2} - \frac{T_e}{2T_i}\right)\right\}. \tag{4}$$

These longitudinal (potential) waves are called the **ion-sound waves**, because their dispersion law is similar to that for the sound waves in a gas. The velocity of the ion-sound waves v_s is specified primarily by the electron temperature, while the ion mass.

In the opposite short-wave case ($kr_{De} \gg 1$, but still $kr_{Di} \ll 1$,) we obtain weakly damped ion plasma oscillations (similar to the electron plasma or Langmuir oscillations):

$$\omega_l'(k) \approx \omega_{\rm pi},$$

$$\gamma \approx -\sqrt{\frac{\pi m_e}{8m_i}} \cdot \frac{\omega_{\rm pi}}{k^3 r_{De}^3}\left\{1 + \sqrt{\frac{m_i}{m_e}}\left(\frac{T_e}{T_i}\right)^{3/2}\exp\left(-\frac{3}{2} - \frac{1}{2k^2 r_{Di}^2}\right)\right\}. \tag{5}$$

3.8 Equation (3.91) in cyclic basis reads

$$v_{\pm 1}^i = \left(\frac{m_e}{m_i} \pm \frac{\omega_{\rm Bi}}{\omega}\right) v_{\pm 1}. \tag{1}$$

Accordingly, the conductivity has the form

$$\sigma_\pm = \frac{e^2 n}{m_e[\nu_e - i(\omega \pm \omega_{\rm Be}) + i\omega_{\rm Be}\omega_{\rm Bi}/\omega]}, \tag{2}$$

where the term containing the ion cyclotron frequency in the denominator accounts for ion motion. When $\omega \gg \omega_{\rm Bi}$, this term can be discarded. The dielectric tensor components have the form

$$\varepsilon_{\pm 1} = 1 - \frac{\omega_{\rm pe}^2}{\omega^2 + i\omega\nu_e \pm \omega\omega_{\rm Be} - \omega_{\rm Be}\omega_{\rm Bi}}. \tag{3}$$

When $\omega \ll \omega_{\rm Bi}$, we have

$$\varepsilon_{\pm 1} = 1 - \frac{\omega_{\rm pe}^2}{i\omega\nu_e - \omega_{\rm Be}\omega_{\rm Bi}}. \tag{4}$$

The same results can be obtained from the solution in usual Cartesian basis obtained in Sect. 3.4. To do so the vectors and tensors obtained there must be transformed from one frame to the other. This transformation of the Cartesian basis vectors into cyclic ones is performed using the unitary matrix

$$\widehat{U} = \begin{pmatrix} -1/\sqrt{2} & 0 & -i/\sqrt{2} \\ 0 & 1 & 0 \\ 1/\sqrt{2} & 0 & -i/\sqrt{2} \end{pmatrix}, \qquad \begin{pmatrix} \boldsymbol{e}_{+1} \\ \boldsymbol{e}_0 \\ \boldsymbol{e}_{-1} \end{pmatrix} = \widehat{U} \begin{pmatrix} \boldsymbol{e}_x \\ \boldsymbol{e}_z \\ \boldsymbol{e}_y \end{pmatrix}, \tag{5}$$

where standard matrix multiplication rules (row by column) must be applied. The matrix $\widehat{U}$ is a unitary one since it satisfies the required condition $\widehat{U}^{-1} = \widehat{U}^{\dagger}$, where $\widehat{U}^{\dagger}$ is the Hermit conjugate matrix. Transformation of the Cartesian dielectric tensor $\widehat{\varepsilon}$ to the cyclic basis is performed using the formula $\widehat{\varepsilon}^c = \widehat{U}\widehat{\varepsilon}\widehat{U}^{\dagger}$, where the Cartesian axes are numbered according to Eq. (5). Note that in the cyclic basis the dielectric tensor has a diagonal form, where only nonzero components are ε_{+1}, ε_0, and ε_{-1}.

3.9 In the presence of dissipation the refraction index is a complex number, $\tilde{n}_\sigma = n_\sigma + i\eta_\sigma$, where n_σ is the real part, which we will still call the refractive index, while η_σ is the imaginary part called the **absorption index**. To find $\tilde{n}_\sigma$ we have to solve characteristic equation (3.43) whose coefficients a, b, and c Eq. (3.44) must be calculated using the dielectric tensor components of collisional plasma, Eqs. (3.95) and (3.94c), which yields [cf. Eq. (3.48)]

$$\tilde{n}_\sigma^2 = (n_\sigma + i\eta_\sigma)^2 = 1 - \frac{2v(1 - v + i\nu)}{2(1 + i\nu)(1 - v + i\nu) - u\sin^2\theta + \sigma\sqrt{\widetilde{\mathcal{D}}}}, \tag{3.112}$$

where

$$\widetilde{\mathcal{D}} = u^2\sin^4\theta + 4u(1-v+i\nu)^2\cos^2\theta, \quad u = \left(\frac{\omega_{\mathrm{Be}}}{\omega}\right)^2, \quad v = \left(\frac{\omega_{\mathrm{pe}}}{\omega}\right)^2, \tag{3.113}$$

$\nu = \nu_e/\omega$. In a practically important case, when the dissipation is small, $\nu \ll 1$, we can expand Eq. (3.112) over ν powers, which yields Eq. (3.48) for the refraction index and

$$\eta_\sigma = \frac{\nu v}{n_\sigma} \frac{u^2\sin^4\theta - \sigma\sqrt{\mathcal{D}}\left[u\sin^2\theta + 2(1-v)^2\right]}{\sigma\sqrt{\mathcal{D}}\left[2(1-v) - u\sin^2\theta + \sigma\sqrt{\mathcal{D}}\right]^2}, \tag{3.114}$$

where the determinant $\mathcal{D} = \widetilde{\mathcal{D}}|_{\nu=0}$ is defined by Eq. (3.49). In particular, at high frequencies in the quasilongitudinal approximation, we have

$$\eta_\sigma = \frac{\nu v}{n_\sigma(1 + \sigma|\sqrt{u}\cos\theta|)^2}. \tag{3.115}$$

3.10 Hint: Use the same approach as in the previous solution to find the absorption index of the Alfvén waves. Then find the damping rate and compare the results with Eq. (2.72).

3.11 Hint: Complement the set of Eqs. (3.88) by a third equation for ions of a given sort, say He,

$$\begin{aligned} -i\omega m_{\mathrm{He}}\boldsymbol{v}^{\mathrm{He}} &= +ze\boldsymbol{E} + m_{\mathrm{He}}\omega_{B\mathrm{He}}\boldsymbol{v}^{\mathrm{He}} \times \boldsymbol{e}_0 + m_e\nu_e(\boldsymbol{v}^e - \boldsymbol{v}^{\mathrm{He}}) \\ &\quad + m_{p\mathrm{He}}\nu_{\mathrm{He}}(\boldsymbol{v}^i - \boldsymbol{v}^{\mathrm{He}}), \end{aligned}$$

add corresponding friction forces between electrons and helium and between protons and helium in the rhs of Eqs. (3.88). Then, take into account plasma neutrality, $n_e = n_p + zn_{\mathrm{He}}$ and momentum conservation of these three plasma components, compose the current velocity analogous to Eq. (3.89) and electric current and express it via electric field. Then, solve for the electric current components and find the required conductivity and permittivity tensors.

Chapter 4

Wave–Particle and Wave–Wave Interactions

In Chap. 3 we have discussed how plasma responds to an external (weak) electromagnetic perturbation, which results in a specific wave dispersion and damping. This damping is linear, i.e., proportional to the wave amplitude and there is no change in the plasma distribution function other than small oscillations proportional to the wave amplitude. Apparently, this treatment has a limited applicability: it can only be valid until the wave amplitude is small enough to keep all nonlinear effects negligible. In contrast, a large-amplitude wave will definitely affect the plasma distribution, while in an ensemble of waves different waves will interact with each other nonlinearly, resulting, e.g., in wave spectrum modification and new mode generation. Processes of the first kind are called wave–particle interactions, while of the second kind—wave–wave interactions. Below we consider some essentials of these interactions most relevant within the context considered in this textbook.

4.1 Two-Stream Instabilities

A key condition for a nonlinearity to come into play is the presence of large-amplitude waves in the plasma. In some cases such waves can arrive at a considered plasma volume from outside, which is often the case in laboratory experiments with interaction of high-power laser signals with a substance. In contrast, in the astrophysical sources, such powerful electromagnetic waves are produced within the source due to one or another instability, when the free energy required to generate a powerful electromagnetic field comes from an excessive energy of unstable nonstationary plasma particle distributions. In practice, most of the relevant instabilities can be classified as either streaming

G.D. Fleishman and I.N. Toptygin, *Cosmic Electrodynamics*, Astrophysics and Space Science Library 388, DOI 10.1007/978-1-4614-5782-4_4,

(two-stream, beam) instability, when a nonzero particle flow is involved, or loss-cone instabilities when particle anisotropy plays a dominant role while the presence of particle flow is not essential.

4.1.1 Excitation of Plasma Waves by Electron Beams

Here we start from a simple example of a beaming instability driven by a unidirectional monoenergetic beam of electrons (Akhiezer and Fainberg 1949; Bohm and Gross 1949a,b; Akhiezer and Fainberg 1951; Buneman 1958). Likewise examples of multi-component plasmas discussed in Sect. 3.2.4, here the beam electrons represent a distinct component in addition to the background electrons and ions. Therefore, the corresponding contribution must be added to the plasma dielectric permeability, which normally results in appearance of new wave modes; see Sect. 3.2.4.

For simplicity, we neglect the magnetic field and consider a cold plasma at high frequencies with the dielectric permeability obeying Eq. (3.42c), where the ion contribution can be discarded. To find a contribution from the electron beam with the number density n' streaming with a velocity $\boldsymbol{u}$ in z direction, we can use Eq. (3.38) but with an extra term, $u\partial v_a/\partial z$, related to the beam streaming (and neglecting the magnetic field contribution). Dispersion relation for the Langmuir waves reads $\varepsilon^l(\omega, k) = 0$; thus, taking into account both beam and background electron contributions, we can write

$$\varepsilon^l = 1 - \frac{\omega_{\rm pe}^2}{\omega^2} - \frac{\omega_{\rm pe}'^2}{(\omega - k_z u)^2} = 0, \tag{4.1}$$

where $\omega_{\rm pe}'^2 = 4\pi n' e^2/m_e$ is the plasma frequency related to only beam electrons.

This dispersion relation is an equation of fourth power over frequency; so it specifies four different (longitudinal) wave modes. Assuming the beam is tenuous, $n' \ll n_e$, we first look for "resonant" wave modes, $k_z \approx \omega_{\rm pe}/u$, i.e., search waves with the dispersion $\omega^j = k_z u + \eta^j$, where j is the number of the mode and $|\eta^j| \ll |k_z u|$, which yields equation for η:

$$\eta^3 + (1 - \omega_{\rm pe}/k_z u)\omega_{\rm pe}\eta^2 - \omega_{\rm pe}\omega_{\rm pe}'^2/2 = 0. \tag{4.2}$$

At the resonance, until $|\eta| \gg |\omega_{\rm pe} - k_z u|$, we can neglect the second term in Eq. (4.2), so it takes a simple form $\eta^3 = \omega_{\rm pe}\omega_{\rm pe}'^2/2$, which has three solutions:

$$\eta = \xi(\omega_{\rm pe}\omega_{\rm pe}'^2/2)^{1/3}; \qquad \xi = \sqrt[3]{1} = \left(1; \frac{-1 + i\sqrt{3}}{2}; \frac{-1 - i\sqrt{3}}{2}\right). \tag{4.3}$$

Remarkably, that one of these modes grows exponentially (since $E \propto \exp[-i\omega t]$) with the growth rate

$$\gamma = \frac{\sqrt{3}}{2^{4/3}} \left(\frac{n'}{n_e}\right)^{1/3} \omega_{\rm pe}, \tag{4.4}$$

which is very large even for a relatively tenuous beam because it is proportional to $(n'/n_e)^{1/3}$. This means that all the beam electrons contribute to the wave amplification coherently; otherwise one would expect a linear proportionality, $\gamma \sim n'/n_e$.

Farther from the resonance, while still $|\eta| \gtrsim |\omega_{\rm pe} - k_z u|$, two wave modes defined by Eq. (4.1) represent slightly modified Langmiur waves with $\omega^{1,2} = \pm\omega_{\rm pe}[1+\omega'^2_{\rm pe}/(2(k_z u \mp \omega_{\rm pe}))]$, while two other modes have frequencies around $k_z u$; using again $\omega^j = k_z u + \eta^j$, $|\eta^j| \ll |k_z u|$, we find

$$\eta = \pm \frac{\omega'_{\rm pe}}{\sqrt{1-(\omega_{\rm pe}/k_z u)^2}}. \tag{4.5}$$

Apparently, the short-length waves with $k_z > \omega_{\rm pe}/u$ are stable, while the long waves with $k_z < \omega_{\rm pe}/u$ are unstable because in this case η contains a square root of a negative value; the corresponding growth rate is

$$\gamma = \frac{\omega'_{\rm pe}}{\sqrt{(\omega_{\rm pe}/k_z u)^2 - 1}} \sim \omega'_{\rm pe} = \left(\frac{n'}{n_e}\right)^{1/2} \omega_{\rm pe}. \tag{4.6}$$

Again, the growth rate is relatively large being proportional to $(n'/n_e)^{1/2}$ (not to $(n'/n_e)^1$), although it is smaller than the growth rate of the resonant waves described by Eq. (4.4).

This strong (coherent) amplification of plasma waves by an electron beam is primarily related to the assumption of monoenergetic (cold) beam, whose thermal velocity scatter is negligible. To evaluate applicability of this assumption we have to use the dielectric permeability components calculated with the account of electron temperature, which is done, for the background plasma particles, in Problem 3.5; a similar contribution with $\omega \to \omega' = (\omega - \boldsymbol{ku})$ comes from a "hot" beam with the streaming velocity $\boldsymbol{u}$ and some thermal velocity $v' = \sqrt{T'/m_e}$. It is straightforward to show (see Problem 4.1) that the hot beam dispersion reduces to the cold beam dispersion if $\omega'/(kv') \sim |\eta|/(kv') \gg 1$, which requires $v' \ll (n_e/n')^{1/3} u$ for the resonant case with growth rate (4.4) and $v' \ll (n_e/n')^{1/2} u$ for the nonresonant case with growth rate (4.6). Otherwise, the kinetic approach, described in Sect. 3.3 in the linear approximation, is needed.

In the kinetic case there is no need to separate the beam and background electrons; we can assume that both components are described by a single distribution function $f(\boldsymbol{p})$. The dielectric tensor $\varepsilon_{\alpha\beta}$ is linked with this distribution function by Eq. (3.60), which according to Eq. (3.62) contains both real and imaginary parts, see Eq. (3.63). Use of the mentioned equations allows considering instabilities for any wave mode of the magnetized plasma; general dispersion relation (3.27) receives now the form

$$\Delta(\omega + i\gamma, \boldsymbol{k}) = \Delta' + i\Delta'' = 0, \tag{4.7}$$

which determines both the dispersion and damping/growth of the given waves.

Consider again the beaming instability of longitudinal waves. Dispersion relation for the longitudinal waves reads

$$\varepsilon^l \equiv \kappa_\alpha \kappa_\beta \varepsilon_{\alpha\beta} = \varepsilon'^l + i\varepsilon''^l = 0. \tag{4.8}$$

Assuming the wave growth/damping rate to be small compared with the wave frequency, we can solve Eq. (4.8) by iterations, which yields

$$\varepsilon'^l = 0; \qquad \gamma = -\varepsilon''^l / (\partial \varepsilon'^l / \partial \omega). \tag{4.9}$$

Then, consider for simplicity a plasma without magnetic field. In this case instead of Eq. (3.60) we obtain[1]

$$\varepsilon_{\alpha\beta} = \delta_{\alpha\beta} + \frac{4\pi e^2}{\omega} \int \frac{v_\alpha}{\omega - \boldsymbol{k}\boldsymbol{v} + i\gamma} \frac{\partial f(\boldsymbol{p})}{\partial p_\beta} d^3p, \tag{4.10}$$

which yields the imaginary part of the longitudinal dielectric permeability in the form

$$\varepsilon''^l = -\frac{4\pi^2 e^2}{\omega} \int v_\parallel \frac{\partial f(\boldsymbol{p})}{\partial p_\parallel} \delta(\omega - k_\parallel v_\parallel) d^3p. \tag{4.11}$$

Now, neglect the effect of spatial dispersion and unstable part of electron distribution on the real part of dielectric permeability, i.e., $\varepsilon'^l = 1 - \omega_{\rm pe}^2/\omega^2$, and taking into account that in the Langmuir waves $\omega \approx \omega_{\rm pe}$, we can find the damping (growth) rate of the Langmuir waves:

$$\gamma = \frac{\omega_{\rm pe}}{2} \varepsilon''^l = -2\pi^2 e^2 \int v_\parallel \frac{\partial f(\boldsymbol{p})}{\partial p_\parallel} \delta(\omega - k_\parallel v_\parallel) d^3p. \tag{4.12}$$

The presence of δ-function in Eq. (4.12) indicates that the wave decay or growth is provided by resonant particles with $v_\parallel = \omega/k_\parallel$. The direction of the energy transfer (from waves to particles or from particles to waves) is solely determined by the distribution function derivative at the resonant region. For stationary distributions, including the Maxwellian one, this derivative is negative everywhere; thus, all waves experience damping and no wave amplification occurs. This damping (called the **Landau damping**) is not related to collisions between particles, i.e., it is invertible in time.

Indeed, if there is a region where the distribution function increases as the parallel momentum increases (which is only possible for non-isotropic distributions, see Lifshitz and Pitaevskii 1981, Sect. 30), the corresponding resonant waves become amplified and their energy increases at the expense of the resonant electrons' free energy. Formally, within the linear theory, this energy amplification will take place infinitely long. Therefore, very soon, in a few e-folding times, the wave energy will exceed the free energy of unstable

[1] Equation (4.10) can be obtained as a limiting case $B \to 0$ of Eq. (3.60), which is a complicated task. Straightforward derivation based on the kinetic equation of a free plasma is much easier.

electrons amplifying the waves, which cannot happen in reality. This apparent contradiction implies that large energy of the growing waves becomes dynamically important very soon and, thus, starts to modify the originally unstable electron distribution toward a more stable one to eventually quench the instability. On top of that, in case of large-amplitude waves, nonlinear wave–wave interactions can further complicate the whole picture. We will consider some of these processes below in this chapter.

4.1.2 Weibel Instability

The considered above two-stream instability represents only one example of many possible instabilities driven by particle beams. In 3D geometry, both longitudinal and transverse waves can be amplified by beams, in particular, random magnetic field can be generated due to filamentation (Weibel) instability. To understand the origin of this instability imagine that a fluctuation magnetic wave is superimposed on a beam transverse to its motion. Then, the Lorentz force acting from this wave on the beam particles will displace some of them towards others, thus, forming filaments of the beam particles. These small-scale current filaments can, in certain conditions, e.g., for a relativistic beam, amplify this fluctuating field, which results in the corresponding instability.

Let us consider a simple model illustrating the essence of this "transverse" instability, which requires an anisotropy of the particle distribution but not necessarily a net particle flow. Specifically, following Fried (1959), we adopt a very simple, anisotropic monoenergetic electron distribution function describing two identical counter-streaming electron beams propagating along y axes (e.g., in case of interaction of two identical shock waves):

$$f_0(\boldsymbol{v}) \propto \delta(v_x)\delta(v_y^2 - a^2)\delta(v_z) \tag{4.13}$$

and analyze how an initial small fluctuation of magnetic field taken in the form

$$\boldsymbol{B} = (0, 0, B_z), \qquad B_z = B_0 \mathrm{e}^{ikx} \tag{4.14}$$

will evolve. The adopted magnetic field produces the Lorentz force in x direction resulting in x component of the electron velocity $\delta v_x = -a\omega_{\mathrm{Be}}\delta t$ for $v_y = \pm a$, where ω_{Be} is the positive electron gyrofrequency. To the first-order accuracy over B_0 we can write

$$\frac{\partial \langle v_x v_y \rangle}{\partial t} = -a^2 \frac{eB_z}{mc}, \tag{4.15}$$

where the angular brackets $< v_x v_y >$ denote averaging over particle distribution (4.13).

The electric current associated with the magnetic field B_0 is specified by Ampère's law (2.12), $j_y = -(ikc/4\pi)B_z$. On the other hand, $j_y = -en_e v_y$, so taking the time derivatives yields

$$\frac{\partial B_z}{\partial t} = -\frac{4\pi ie}{kc}\frac{\partial (n_e v_y)}{\partial t}. \tag{4.16}$$

The time derivative in the rhs of Eq. (4.16) can be expressed via x-derivative of $\partial(n_e v_x v_y)/\partial x$ using equation of motion (1.70) together with discontinuity equation (1.69):

$$\frac{\partial (n_e v_y)}{\partial t} = -\frac{\partial (n_e v_x v_y)}{\partial x}. \tag{4.17}$$

Now, substituting Eq. (4.17) into Eq. (4.16) and taking into account that $\partial^2(n_e v_x v_y)/\partial x \partial t \approx n_e \partial^2 (v_x v_y)/\partial x \partial t$ to the first-order approximation, we obtain the second derivative over time

$$\frac{\partial^2 B_z}{\partial t^2} = -\frac{4\pi i e n_e}{kc}\frac{\partial^2 (v_x v_y)}{\partial x \partial t}, \tag{4.18}$$

where we use the time derivative specified by Eq. (4.15) and then take x derivative of the magnetic field, which yields

$$\frac{\partial^2 B_z}{\partial t^2} = \frac{\omega_{\mathrm{pe}}^2 a^2}{c^2} B_z. \tag{4.19}$$

Thus, we obtain that any perturbation of the considered type will grow with time indicating a corresponding instability of these quasistationary transverse perturbations. This independence on the wave vector of the perturbation is, of course, an artifact of our oversimplified treatment. In particular, the growing magnetic field implies an associated electric field. Furthermore, in the reality, the electron distribution is supposed to be more complicated than has been adopted above. For example, allowing some motion along x and z axes, e.g., $f_0(\boldsymbol{v}) \propto \delta(v_x^2 - b^2)\delta(v_y^2 - a^2)\delta(v_z^2 - b^2)$, and taking into account the electric field, we can find the dispersion relation

$$\omega^4 - (k^2 c^2 + \omega_{\mathrm{pe}}^2)\omega^2 - k^2(a^2 - b^2)\omega_{\mathrm{pe}}^2 = 0, \tag{4.20}$$

which has one unstable solution for

$$k < \frac{\omega_{\mathrm{pe}}}{a}\sqrt{(a/b)^2 - 1}. \tag{4.21}$$

Apparently, during the instability development, the magnetic field increases along the lines, where $kx = m\pi/2$; the associated electric current density will apparently concentrate along these same lines so forming current

filaments, so this instability is also called a **filamentation instability**. Estimate (4.19) implies that the filamentation instability can become especially strong for relativistically moving electrons when $(a/c)^2 \approx 1$, which is, in particular, the case of collimated relativistic jets observed from active galactic nuclei and implied in the sources of cosmological gamma ray bursts.

The considered Buneman and Weibel instabilities represent two extremes of strictly longitudinal or strictly transverse instabilities. In many cases there are also oblique mixed-mode instabilities where the wave vector does not coincide with the beam velocity vector, so both electric and magnetic fields are generated. Interestingly, that the final picture of the unstable modes and their evolution is highly dependent on details of the source structure and physical conditions. Currently, essential information of the streaming instabilities is obtained from sophisticated computer modelings including particle-in-cell (PIC) simulations.

4.2 Quasilinear Approximation

As we have seen, the linear solution describing exponential growth of unstable waves is intrinsically limited; apparently that fast growth must be somehow saturated to avoid unphysical conclusions like infinitely large energy accumulated by the growing waves. An upper bound of this energy is set up by available free energy of the resonant electrons. However, the solution will in fact strongly deviate from the linear one much earlier than the wave energy approaches the particle free energy. In this section we consider the lowest-order nonlinear effects in the wave–particle interactions. Specifically, we adopt that the main effect is modification of the particle distribution function by the growing wave spectrum, while discarding any nonlinear wave–wave interactions. This approach is commonly called quasilinear approximation or **quasilinear theory**.

4.2.1 General Treatment

Let us consider effect of plasma waves on the mean distribution function of electrons. To more transparently demonstrate the key physics behind the quasilinear theory we analyze here a relatively simple case of a free (unmagnetized) plasma and take into account only one wave mode, the longitudinal Langmuir waves. The distribution function of the plasma electrons satisfies standard collisionless kinetic equation

$$\frac{\partial f}{\partial t} + \boldsymbol{v}\frac{\partial f}{\partial \boldsymbol{r}} + e\boldsymbol{E}_L\frac{\partial f}{\partial \boldsymbol{p}} = 0, \tag{4.22}$$

where $\boldsymbol{E}_L(\boldsymbol{r}, t)$ is the electric field in Langmuir waves. Then, adopt that the electron distribution function consists of two terms—averaged f_0 and fluctuating δf components, $f = f_0 + \delta f$; recall, we already used this presentation

in Chap. 3 to calculate the linear plasma response δf needed to determine the plasma dielectric tensor. In the linear theory, however, we considered the averaged component to be a given fixed function. In contrast, here we are going to account the effect of the waves on this averaged distribution function unlike the linear theory. To do so, we substitute the adopted form of the distribution function (the subscript '0' is omitted below for brevity) into Eq. (4.22), which yields

$$\frac{\partial f}{\partial t} + \boldsymbol{v}\frac{\partial f}{\partial \boldsymbol{r}} + e\boldsymbol{E}_L\frac{\partial \delta f}{\partial \boldsymbol{p}} + \frac{\partial \delta f}{\partial t} + \boldsymbol{v}\frac{\partial \delta f}{\partial \boldsymbol{r}} + e\boldsymbol{E}_L\frac{\partial f}{\partial \boldsymbol{p}} = 0. \tag{4.23}$$

Averaging of this equation over the wave ensemble yields

$$\frac{\partial f}{\partial t} + \boldsymbol{v}\frac{\partial f}{\partial \boldsymbol{r}} = -e\left\langle \boldsymbol{E}_L\frac{\partial \delta f}{\partial \boldsymbol{p}}\right\rangle. \tag{4.24}$$

Here, unlike the linear treatment, there appears a rhs dependent on the wave electric field; discarding this term leads to a constant and uniform solution for the mean distribution function. Therefore, a new effect is related to this new term in the rhs. To explicitly determine this term we subtract the averaged equation from the exact one:

$$\frac{\partial \delta f}{\partial t} + \boldsymbol{v}\frac{\partial \delta f}{\partial \boldsymbol{r}} = -e\boldsymbol{E}_L\frac{\partial f}{\partial \boldsymbol{p}} - \left[e\boldsymbol{E}_L\frac{\partial \delta f}{\partial \boldsymbol{p}} - \left\langle e\boldsymbol{E}_L\frac{\partial \delta f}{\partial \boldsymbol{p}}\right\rangle\right]. \tag{4.25}$$

The difference between the exact and averaged second-order terms in the square brackets describes nonlinearity of the plasma response, which we neglect within the quasilinear approach. After discarding these terms this equation receives a simple form:

$$\frac{\partial \delta f}{\partial t} + \boldsymbol{v}\frac{\partial \delta f}{\partial \boldsymbol{r}} = -e\boldsymbol{E}_L\frac{\partial f}{\partial \boldsymbol{p}}, \tag{4.26}$$

whose solution is convenient to find using the Green function method. Equation for the Green function $G(\boldsymbol{r}, \boldsymbol{p}, t; \boldsymbol{r}', \boldsymbol{p}', t')$ accounting the initial condition included in the rhs reads

$$\frac{\partial G}{\partial t} + \boldsymbol{v}\frac{\partial G}{\partial \boldsymbol{r}} = \delta(\boldsymbol{r} - \boldsymbol{r}')\delta(\boldsymbol{p} - \boldsymbol{p}')\delta(t - t'). \tag{4.27}$$

The rhs simply shows that at $t = t'$ we have $\boldsymbol{r} = \boldsymbol{r}'$ and $\boldsymbol{p} = \boldsymbol{p}'$; the Θ-function is related to the casuality principle. Finding the Green function is trivial:

$$G(\boldsymbol{r}, \boldsymbol{p}, t; \boldsymbol{r}', \boldsymbol{p}', t') = \delta(\boldsymbol{r} - \boldsymbol{v}(t - t') - \boldsymbol{r}')\delta(\boldsymbol{p} - \boldsymbol{p}')\Theta(t - t'). \tag{4.28}$$

Then, solution of inhomogeneous equation (4.26) for δf is straightforwardly expressed via the Green function:

$$\delta f(\boldsymbol{r}, \boldsymbol{p}, t) = -\int \mathrm{d}\boldsymbol{r}'\mathrm{d}\boldsymbol{p}'\mathrm{d}t' G(\boldsymbol{r}, \boldsymbol{p}, t; \boldsymbol{r}', \boldsymbol{p}', t')e\boldsymbol{E}_L\frac{\partial f(\boldsymbol{r}', \boldsymbol{p}', t')}{\partial \boldsymbol{p}'}. \tag{4.29}$$

Now, substituting this solution into Eq. (4.24) for the averaged distribution function f, we obtain a closed form of equation for f, which does not include the fluctuating component δf any longer:

$$\frac{\partial f}{\partial t}+\boldsymbol{v}\frac{\partial f}{\partial \boldsymbol{r}} = -e^2 \left\langle E_{L,\alpha}\frac{\partial}{\partial p_\alpha}\int E_{L,\beta}\right\rangle G(\boldsymbol{r},\boldsymbol{p},t;\boldsymbol{r}',\boldsymbol{p}',t')\frac{\partial f(\boldsymbol{r}',\boldsymbol{p}',t')}{\partial p'_\beta}\mathrm{d}\boldsymbol{r}'\mathrm{d}\boldsymbol{p}'\mathrm{d}t'. \tag{4.30}$$

Averaging over the wave ensemble denoted in Eq. (4.30) by the angular brackets gives rise to appearance of the corresponding correlator of the Langmuir wave electric field. Integrating over the space and momentum with the use of the corresponding δ-functions and changing variables $t - t' = \tau$, we obtain

$$\frac{\partial f}{\partial t} + \boldsymbol{v}\frac{\partial f}{\partial \boldsymbol{r}} = e^2\frac{\partial}{\partial p_\alpha}\int\limits_0^\infty \mathrm{d}\tau K_{\alpha\beta}(\boldsymbol{v}\tau,\tau)\frac{\partial}{\partial p_\beta}f(\boldsymbol{r}-\boldsymbol{v}\tau,\boldsymbol{p},t-\tau), \tag{4.31a}$$

$$K_{\alpha\beta}(\boldsymbol{r},\tau) = \langle E_{L,\alpha}(\boldsymbol{r}_1,t_1)E_{L,\beta}(\boldsymbol{r}_2,t_2)\rangle\,, \qquad \boldsymbol{r}=\boldsymbol{r}_1-\boldsymbol{r}_2, \quad \tau = t_1 - t_2. \tag{4.31b}$$

To further simplify Eq. (4.31a) we note that the time variable τ is related to the periods of the corresponding Langmuir waves, while we are interested in the electron distribution evolution over much longer time, when the Langmuir wave energy density changes noticeably due to a relatively weak amplification, $\gamma \ll \omega$. Thus, in the regime of weak amplification, we can neglect this dependence of f on τ and, in addition, adopt that the mean distribution function is spatially uniform; then we find

$$\frac{\partial f(\boldsymbol{p},t)}{\partial t} = \frac{\partial}{\partial p_\alpha}D_{\alpha\beta}\frac{\partial}{\partial p_\beta}f(\boldsymbol{p},t), \tag{4.32}$$

where

$$D_{\alpha\beta} = e^2\int\limits_0^\infty \mathrm{d}\tau K_{\alpha\beta}(\boldsymbol{v}\tau,\tau) \tag{4.33}$$

is the electron diffusion coefficient in the momentum space.

Equation (4.12) for the wave growth rate contains a wave–particle resonant condition described by the δ-function, which means that only a certain fraction of electrons satisfying the resonant condition contributes to the wave amplification. From this perspective it would be reasonable to anticipate that the amplified waves affect primarily the same resonant electrons, which, however, is not evident from the diffusion coefficient in form (4.33). To show the resonant nature of the electron momentum diffusion explicitly, let us use the Fourier representation of the electric field correlation tensor:

$$K_{\alpha\beta}(\boldsymbol{r},\tau) = \int \mathrm{d}\boldsymbol{k}\mathrm{d}\omega e^{-i(\omega\tau-\mathbf{kr})}K_{\alpha\beta}(\boldsymbol{k},\omega), \tag{4.34}$$

where

$$K_{\alpha\beta}(\boldsymbol{k},\omega) = \frac{k_\alpha k_\beta}{k^2}|E|^2_{\mathbf{k}}\delta(\omega-\omega(\boldsymbol{k})) \tag{4.35}$$

is a longitudinal (along $\boldsymbol{k}$) tensor, $|E|^2_{\mathbf{k}}$ is the spectral density of the Langmuir wave electric field, and $\omega(\boldsymbol{k}) \approx \omega_{\rm pe}$ for the Langmuir waves. Substitution of Eqs. (4.34) and (4.35) into Eq. (4.33) and integration over $d\tau$ and $d\omega$ give rise to

$$D_{\alpha\beta} = \pi e^2 \int \mathrm{d}\boldsymbol{k}\frac{k_\alpha k_\beta}{k^2}|E|^2_{\mathbf{k}}\delta(\omega(\boldsymbol{k})-\boldsymbol{k}\boldsymbol{v}) = 4\pi^2 e^2 \int \mathrm{d}\boldsymbol{k}\frac{k_\alpha k_\beta}{k^2}W_L(\boldsymbol{k})\delta(\omega(\boldsymbol{k})-\boldsymbol{k}\boldsymbol{v}), \tag{4.36}$$

which explicitly contains the same resonant δ-function as Eq. (4.12) for the growth rate confirming the resonant nature of the considered wave–particle interaction. The second equality replaces the electric field spectral density by the Langmuir wave energy density $W_L(\boldsymbol{k}) = \partial(\omega\varepsilon'^l/\partial\omega)|E|^2_{\mathbf{k}}/8\pi \approx |E|^2_{\mathbf{k}}/4\pi$.

Apparently, Eq. (4.32) with constant momentum-space diffusion coefficient (4.36) is valid for the case of a fixed, constant spectrum of the Langmuir turbulence. However, if the Langmuir waves are generated by the unstable electron population, then the turbulence energy is a function of time, $W_L(\boldsymbol{k},t)$ defined by

$$\frac{\mathrm{d}W_L(\boldsymbol{k},t)}{\mathrm{d}t} = -2\gamma W_L(\boldsymbol{k},t), \tag{4.37}$$

where the growth rate γ is supposed to be determined from Eq. (4.12) where a time-dependent electron distribution function $f(\boldsymbol{p},t)$ must be used instead of the constant one $f(\boldsymbol{p})$. Thus, the system composed of two coupled equations (4.32) and (4.37) represents a closed set of equations specifying consistent evolution of electrons and waves driven by the resonant wave–particle interactions.

In a more general case of the magnetized plasma and an arbitrary (i.e., not necessarily longitudinal) mode the derivation is fundamentally similar, although lengthy (Akhiezer et al. 1975; Melrose 1980). It results in the same set of coupled equations (4.32) and (4.37), whose coefficients, however, are different as they depend on the magnetic field and a given wave mode. It is often convenient to use the cylindrical coordinate system with the z-axes along the uniform magnetic field, given that only two components of the particle momentum, $p_\parallel$ and $p_\perp$, enter the equation because the distribution function does not depend on the azimuth angle φ. In this coordinate system the momentum diffusion equation receives the form

$$\frac{\partial f(\boldsymbol{p},t)}{\partial t} = \pi Q^2 \sum_{\sigma} \sum_{s=-\infty}^{\infty} \int d^3k \frac{1}{p_\perp} \hat{R} \left[p_\perp |E^\sigma|^2_{\mathbf{k}} \left| \frac{e^\sigma_x s}{|\lambda|} J_s(|\lambda|) + i\eta_\alpha e^\sigma_y J'_s(|\lambda|) \right.\right.$$
$$\left.\left. + \frac{e^\sigma_z p_\parallel}{p_\perp} J_s(|\lambda|) \right|^2 (\hat{R} f(\boldsymbol{p},t)) \right] \delta(\omega^\sigma(\boldsymbol{k}) - s|\omega_{B\alpha}| - k_\parallel v_\parallel), \qquad (4.38)$$

where Q is the charge of considered particles, e^σ_α is α component of the polarization vector of the wave σ, $\eta_\alpha = Q/|Q|$ is either -1 or 1 depending on the sign of the electric charge Q, $\omega_{B\alpha} = QB/(Mc\gamma_Q)$ is the relativistic gyrofrequency of the particle, γ_Q is the Lorentz-factor of the particle Q,

$$\hat{R} = \left[\left(1 - \frac{k_\parallel v_\parallel}{\omega^\sigma(\boldsymbol{k})} \right) \frac{\partial}{\partial p_\perp} + \frac{k_\parallel v_\perp}{\omega^\sigma(\boldsymbol{k})} \frac{\partial}{\partial p_\perp} \right], \qquad (4.39)$$

and summation over σ implies account of all available modes of the magnetized plasma. Accordingly, Eq. (4.38) must be supplied by equations for all involved wave modes

$$\frac{\mathrm{d}W^\sigma(\boldsymbol{k},t)}{\mathrm{d}t} = -2\gamma^\sigma W^\sigma(\boldsymbol{k},t), \quad \text{or, equivalently,} \quad \frac{\mathrm{d}|E|^2_\sigma(\boldsymbol{k},t)}{\mathrm{d}t} = -2\gamma^\sigma |E|^2_\sigma(\boldsymbol{k},t), \qquad (4.40)$$

whose frequencies and growth rates can be straightforwardly found by iterations from general dispersion relation (3.27) written in the form of Eq. (4.7) and assuming $\gamma^\sigma \ll \omega^\sigma$:

$$\Delta' = 0; \qquad \gamma^\sigma = -\Delta''/(\partial\Delta'/\partial\omega)|_{\omega=\omega^\sigma}. \qquad (4.41)$$

In principle, the presented set of equations allows calculating evolution of the particle distribution functions and wave energy densities in the quasilinear approximation, which often requires numerical computations. These quasilinear equations represent a foundation for analysis of electromagnetic instability saturation, e.g., for saturation of the electron cyclotron maser emission responsible for many kinds of coherent radio emission from astrophysical sources including solar radio spikes considered below in Sect. 10.3.

4.2.2 Saturation of Instabilities due to Wave–Particle Interactions

Let us consider now main properties of the quasilinear evolution qualitatively. For simplicity, start with the Langmuir wave instability driven in a free plasma by a 1D electron beam. As we have seen, for the beam instability to develop, the 1D electron distribution function must contain a region raising with $p_\parallel$, which is often called "bump-on-tail" and this instability is called "bump-on-tail" instability; see Sect. 4.1.1.

First, we address a stationary solution of the quasilinear system by analyzing corresponding stationary equations (4.32) and (4.37) with $\mathrm{d}/\mathrm{d}t = 0$. The latter implies that either $\gamma = 0$ or $W_L(\boldsymbol{k}, t) = 0$, i.e., either the growth rate or the wave energy density vanishes at the stationary case. Then the stationary solution $W_L(\boldsymbol{k}, t) = 0$ implies that all the waves are absorbed by the electrons, so there is no instability at the final stage, which means that $\partial f/\partial p_\parallel < 0$ everywhere. The other solution, $\gamma = 0$, is different. Now the wave energy can have finite (large) level; the condition $\gamma = 0$ ensures that this level does not change in time. Apparently, see Eq. (4.12), this can only happen when $\partial f/\partial p_\parallel \equiv 0$ in the region of the original bump-on-tail, where initially $\partial f/\partial p_\parallel > 0$, which is commonly called the *plateau formation*.

Note that these two possible stationary solutions for the wave energy represent also stationary solutions for the electron distribution function. Indeed, if $W_L(\boldsymbol{k}, t) = 0$, then $D_{\alpha\beta}(\boldsymbol{p}, t) = 0$ as well resulting in $\mathrm{d}f/\mathrm{d}t = 0$. For the other solution $W_L(\boldsymbol{k}, t) \neq 0$ and, thus, $D_{\alpha\beta}(\boldsymbol{p}, t) \neq 0$; however, $\partial f/\partial p_\parallel \equiv 0$ in the resonant region, implying again $\mathrm{d}f/\mathrm{d}t = 0$.

In the case of magnetized plasma there are two similar stationary solutions; however, instead of 1D plateau, a so-called generalized plateau can develop, when the condition $\hat{R}f = 0$ is fulfilled. Microscopically, however, the situation here is much more complicated: there are more wave modes and more resonances (Cherenkov and cyclotron). In particular, the saturation process now can have a few stages, corresponding to quasilinear evolution of these different wave modes excited due to different resonances. The detailed time evolution of the quasilinear relaxation process is highly dependent on the initial conditions, e.g., initial distribution function of the unstable particles and plasma parameters, and will differ substantially for the beam, loss cone, ring, etc. particle distributions, as well as on particle source, loss, and wave escape (Treumann 2006; Kuznetsov and Vlasov 2012).

4.3 Plasma Nonlinearity and Wave–Wave Interactions

In addition to the quasilinear wave–particle interactions the waves can interact with each other due to plasma nonlinearity. There are generally two kinds of nonlinear processes: wave coalescence or decay and stimulated wave scattering on the plasma particles. To understand the idea of the wave–wave interactions it is convenient to use quantum language and introduce the number of quasiparticles or *plasmons* as

$$N^\sigma(\boldsymbol{k}) = \frac{W^\sigma(\boldsymbol{k})}{\hbar\omega^\sigma(\boldsymbol{k})}, \tag{4.42}$$

where $\hbar\omega^\sigma(\boldsymbol{k})$ is energy of a single plasmon. Using this language it is simple to evaluate if a given three-wave process of the wave coalescence or decay

$$\sigma' \leftrightarrow \sigma'' \pm \sigma, \tag{4.43}$$

where σ'', σ', and σ are three different waves, is possible at all. Indeed, conservation of the energy and momentum requires that

$$\boldsymbol{k}' = \boldsymbol{k}'' \pm \boldsymbol{k}; \qquad \omega^{\sigma'}(\boldsymbol{k}') = \omega^{\sigma''}(\boldsymbol{k}'') \pm \omega^{\sigma}(\boldsymbol{k}), \tag{4.44}$$

where the dispersion laws, e.g., $\omega = \omega^{\sigma}(\boldsymbol{k})$, are taken into account.

4.3.1 Three-Wave Interactions and Nonlinear Scattering on Particles

Linear plasma dispersion relation (3.8) used earlier is apparently the first term of a more exact nonlinear dispersion relation

$$D_\alpha(\omega, \boldsymbol{k}) = \varepsilon_{\alpha\beta}(\omega, \boldsymbol{k}) E_\beta(\omega, \boldsymbol{k}) + \delta D_\alpha(\omega, \boldsymbol{k}), \tag{4.45}$$

where $\varepsilon_{\alpha\beta}$ is the standard dielectric permeability tensor, while

$$\begin{aligned}\delta D_\alpha(\omega, \boldsymbol{k}) = &\int \mathrm{d}\omega_1 \mathrm{d}\boldsymbol{k}_1 \varepsilon_{\alpha\beta\gamma}(\omega, \boldsymbol{k}; \omega_1, \boldsymbol{k}_1) E_\beta(\omega - \omega_1, \boldsymbol{k} - \boldsymbol{k}_1) E_\gamma(\omega_1, \boldsymbol{k}_1) \\ &+ \int \mathrm{d}\omega_1 \mathrm{d}\boldsymbol{k}_1 \mathrm{d}\omega_2 \mathrm{d}\boldsymbol{k}_2 \varepsilon_{\alpha\beta\gamma\delta}(\omega, \boldsymbol{k}; \omega_1, \boldsymbol{k}_1; \omega_2, \boldsymbol{k}_2) E_\beta(\omega - \omega_1, \boldsymbol{k} - \boldsymbol{k}_1) \\ &E_\gamma(\omega_1 - \omega_2, \boldsymbol{k}_1 - \boldsymbol{k}_2) E_\delta(\omega_2, \boldsymbol{k}_2) + \ldots\end{aligned} \tag{4.46}$$

Substituting nonlinear material equation (4.45) into Maxwell equations likewise in Chap. 3, we obtain

$$T_{\alpha\beta} E_\beta = -\delta D_\alpha, \tag{4.47}$$

where, compared with Eq. (3.11), the nonlinear plasma response vector δD_α enters instead of external electric current, $(4\pi i/\omega) j_\alpha^{ext}$.

It is easy to write a formal solution of Eq. (4.47), which is similar to Eq. (3.11),

$$E_\beta(\omega, \boldsymbol{k}) = -A_{\beta\nu}(\omega, \boldsymbol{k}) \delta D_\nu(\omega, \boldsymbol{k}), \tag{4.48}$$

where $A_{\alpha\beta}(\omega, \boldsymbol{k}) = (\widehat{T}(\omega, \boldsymbol{k})^{-1})_{\alpha\beta}$ is a tensor inverse to the Maxwellian one (the inverse tensor for short), Eqs. (3.16) and (3.17); see Chap. 9 for more detail. To derive equations for energy densities, we multiply Eq. (4.48) by $E_\alpha^*(\omega', \boldsymbol{k}')$ and average the obtained equation over periods and random phases of waves. The random phase approximation is valid when the instability spectral bandwidth $\Delta\omega$ is much larger than the linear growth rate of this unstable wave γ^σ, $\Delta\omega \gg \gamma^\sigma$, which is typically the case in astrophysics conditions; opposite relation holds in laboratory laser experiments with coherent signals.

In the rhs of Eq. (4.48) there are combinations of up to four amplitudes of electric field. To perform the averaging we use the following evident expressions for the first and second correlators:

$$\langle E_\alpha(\omega, \boldsymbol{k}) \rangle = 0; \qquad \langle E_\beta(\omega, \boldsymbol{k}) E_\alpha^*(\omega', \boldsymbol{k}') \rangle = K_{\alpha\beta}(\omega, \boldsymbol{k}) \delta(\omega - \omega') \delta(\boldsymbol{k} - \boldsymbol{k}'), \tag{4.49}$$

$K_{\alpha\beta}(\omega,\boldsymbol{k}) = \overline{(E_\beta E_\alpha^*)}_{\omega,\mathbf{k}}$ is the spectrum of the wave electric field, e.g., Eq. (4.35) in case of Langmuir waves. The third-order correlator, as any other odd-order amplitude combination, vanishes for zero-order amplitudes of the electric field, $\langle E_\alpha^0(\omega,\boldsymbol{k})E_\beta^0(\omega',\boldsymbol{k}')E_\gamma^0(\omega'',\boldsymbol{k}'')\rangle = 0$. However, since we take into account terms up to the fourth order over the field amplitude, we have to write down the amplitudes more accurately, taking into account the plasma nonlinearity; in the first order from Eq. (4.48) we find

$$E_\alpha(\omega,\boldsymbol{k}) = E_\alpha^0(\omega,\boldsymbol{k}) - A_{\alpha\nu}(\omega,\boldsymbol{k})\int \mathrm{d}\omega_1 \mathrm{d}\boldsymbol{k}_1 \varepsilon_{\nu\beta\gamma}(\omega,\boldsymbol{k};\omega_1,\boldsymbol{k}_1) \times E_\beta(\omega-\omega_1,\boldsymbol{k}-\boldsymbol{k}_1)E_\gamma(\omega_1,\boldsymbol{k}_1). \tag{4.50}$$

Therefore, the third-order correlator gives a contribution of the same order over the field amplitude as the fourth-order correlator. Then, straightforward but somewhat lengthy manipulations yield the nonlinear equation for the wave spectrum:

$$\begin{aligned}
&\frac{\partial}{\partial t}\frac{\partial \omega T_{\alpha\beta}^h}{\partial \omega}K_{\alpha\beta}(\omega,\boldsymbol{k}) - \frac{\partial}{\partial \boldsymbol{r}}\frac{\partial \omega T_{\alpha\beta}^h}{\partial \boldsymbol{k}}K_{\alpha\beta}(\omega,\boldsymbol{k}) = 2i\omega\varepsilon_{\alpha\beta}^a(\omega,\boldsymbol{k})K_{\alpha\beta}(\omega,\boldsymbol{k}) \\
+\omega Im\int \mathrm{d}\omega'\mathrm{d}\boldsymbol{k}' \big[&A_{\alpha\beta}^*(\omega,\boldsymbol{k})S_{\alpha\nu\mu}(\omega,\boldsymbol{k};\omega',\boldsymbol{k}')S_{\beta\delta\pi}^*(\omega,\boldsymbol{k};\omega',\boldsymbol{k}')K_{\mu\pi}(\omega',\boldsymbol{k}')K_{\nu\delta}(\omega'',\boldsymbol{k}'') \\
&+2A_{\nu\delta}(\omega'',\boldsymbol{k}'')S_{\alpha\nu\mu}(\omega,\boldsymbol{k};\omega',\boldsymbol{k}')S_{\delta\beta\pi}^*(\omega'',\boldsymbol{k}'';\omega,\boldsymbol{k})K_{\mu\beta}(\omega',\boldsymbol{k}')K_{\alpha\pi}(\omega,\boldsymbol{k}) \\
&-2V_{\alpha\beta\gamma\delta}(\omega,\boldsymbol{k};\omega',\boldsymbol{k}')K_{\beta\delta}(\omega',\boldsymbol{k}')K_{\alpha\gamma}(\omega,\boldsymbol{k})\big],
\end{aligned} \tag{4.51}$$

where the superscripts h and a denote the hermitian and antihermitian components of a tensor, respectively, $\omega'' = \omega - \omega'$, $\boldsymbol{k}'' = \boldsymbol{k} - \boldsymbol{k}'$, the nonlinear response tensors $S_{\alpha\beta\gamma}$ and $V_{\alpha\beta\gamma\delta}$ are defined by nonlinear permittivities as follows:

$$S_{\alpha\beta\gamma} = \varepsilon_{\alpha\beta\gamma}(\omega,\boldsymbol{k};\omega',\boldsymbol{k}') + \varepsilon_{\alpha\gamma\beta}(\omega,\boldsymbol{k};\omega'',\boldsymbol{k}''), \tag{4.52a}$$

$$V_{\alpha\beta\gamma\delta} = \varepsilon_{\alpha\beta\gamma\delta}(\omega,\boldsymbol{k};\omega+\omega',\boldsymbol{k}+\boldsymbol{k};\omega',\boldsymbol{k}') + \varepsilon_{\alpha\beta\delta\gamma}(\omega,\boldsymbol{k};\omega+\omega',\boldsymbol{k}+\boldsymbol{k};\omega,\boldsymbol{k}), \tag{4.52b}$$

Typically, a main contribution to the wave–wave interactions comes from the first nonlinear response tensor, $S_{\alpha\beta\gamma}$, while the second one, $V_{\alpha\beta\gamma\delta}$, is less important and is not discussed further in any detail.

Now it is convenient to express the electric field spectrum $K_{\alpha\beta}(\omega,\boldsymbol{k})$ via the energy density of the given wave mode, $W^\sigma(\boldsymbol{k})$, which contains both electromagnetic energy and kinetic energy of the plasma particle oscillations involved:

$$K_{\alpha\beta}(\omega,\boldsymbol{k}) = \sum_\sigma K_{\alpha\beta}^\sigma(\omega,\boldsymbol{k}) = 4\pi\sum_\sigma W^\sigma(\boldsymbol{k})R_\sigma e_\alpha^{\sigma*}e_\beta^\sigma\delta(\omega-\omega^\sigma(\boldsymbol{k})), \tag{4.53}$$

where e_α^σ is the polarization vector component of a given wave mode σ, $\omega^\sigma(\boldsymbol{k})$ is the corresponding eigen-frequency,

$$R_\sigma = \left(\frac{\partial\omega\varepsilon^l}{\partial\omega}\right)^{-1}_{\omega=\omega^l} \quad \text{or} \quad R_\sigma = \left(2n_\sigma\frac{\partial n_\sigma\varepsilon^l}{\partial\omega}\right)^{-1}_{\omega=\omega_\sigma}, \tag{4.54}$$

for the longitudinal (originating from dispersion relation $\varepsilon^l = 0$) and all other waves, respectively. The presentation in terms of the wave-mode energy density $W^\sigma(\boldsymbol{k})$ instead of $K^\sigma_{\alpha\beta}(\omega, \boldsymbol{k})$ is especially helpful when the electric field energy density constitutes only a minor fraction of the entire wave energy density, e.g., for the MHD modes.

Substitution of expression (4.53) into Eq. (4.51) shows that, in contrast to the linear theory, the wave modes are not independent any longer; instead, evolution of a given wave mode is defined by evolution and wave–wave interactions of all other wave modes. To obtain meaningful equations for the energy density evolution of a given wave mode, we have yet to specify the nonlinear response tensors and the explicit form of inverse tensor. The full derivation can be found elsewhere, see Tsytovich (1970), Pustovalov and Silin (1972), Melrose (1980) and other books on plasma physics or plasma astrophysics; here we give the results for some simple cases, which will be considered below in more detail. For example, in a cold magnetized plasma for a process satisfying $\omega/k \gg v_{Te}$, $\omega'/k' \gg v_{Te}$, and $\omega''/k'' \gg v_{Te}$, the nonlinear response tensor is

$$\begin{aligned} S_{\alpha\beta\gamma} \;=\; & i\frac{e}{m}\frac{\omega_{\rm pe}^2}{\omega\omega'\omega''}\Big[\frac{k'_\nu}{\omega''}\chi_{\alpha\gamma}(\omega)\chi_{\nu\beta}(\omega'')+\frac{k''_\nu}{\omega'}\chi_{\alpha\beta}(\omega)\chi_{\nu\gamma}(\omega')-\frac{k_\nu}{\omega'}\chi_{\alpha\beta}(\omega'')\chi_{\nu\gamma}(\omega') \\ & -\frac{k_\nu}{\omega''}\chi_{\alpha\gamma}(\omega')\chi_{\nu\beta}(\omega'')-\frac{k'_\nu}{\omega}\chi_{\gamma\beta}(\omega'')\chi_{\alpha\nu}(\omega)-\frac{k''_\nu}{\omega}\chi_{\beta\gamma}(\omega')\chi_{\alpha\nu}(\omega)\Big], \end{aligned} \tag{4.55}$$

where, as usual, e and m are the electron charge and mass,

$$\chi_{11}=\chi_{22}=\frac{1}{1-u};\quad \chi_{12}=\chi^*_{21}=\frac{-i\sqrt{u}}{1-u};\quad \chi_{33}=1;\quad \chi_{\alpha 3}=\chi_{3\alpha}=0;\quad u=\frac{\omega_{\rm Be}^2}{\omega^2}. \tag{4.56}$$

If, in addition, the frequency ω'' is small, $\omega'' \ll \omega', \omega$, which is, e.g., the case of a high-frequency wave scattering on a low-frequency wave with a small change of the (high) frequency, we can neglect all terms having ω or ω' in denominators in the square brackets, which yields

$$S_{\alpha\beta\gamma} = -i\frac{e}{m}\frac{\omega_{\rm pe}^2}{\omega^2\omega''^2}\chi_{\alpha\gamma}(\omega)k''_\nu\chi_{\nu\beta}(\omega''). \tag{4.57}$$

In another important parameter regime, $\omega''/k'' \ll v_{Te}$, while still $\omega/k, \omega'/k' \gg v_{Te}$, we have:

$$S_{\alpha\beta\gamma} = i\frac{ek''}{m\omega^2}\frac{\delta\varepsilon^e_{\beta\nu}(\omega'', k'')k''_\nu}{k''}\chi_{\alpha\gamma}(\omega), \tag{4.58}$$

where $\delta\varepsilon^e_{\beta\nu}(\omega'', k'') = (\varepsilon^e_{\beta\nu} - \delta_{\beta\nu})$ is the partial electron dielectric permeability accounting for the spatial dispersion (thermal motion of the plasma electrons).

The wave–wave processes imply a raise or decay of the wave energies involved and so arise due to antihermitian part of the inverse tensor $A_{\alpha\beta}(\omega, \mathbf{k})$. As we saw in Chap. 3, in the absence of dissipation, both Maxwellian and inverse tensors are hermitian; thus the only antihermitian contribution to the inverse tensor can come from zeros of the Maxwellian tensor, which represent poles of the inverse tensor, Eqs. (3.17), (3.32) and (3.33). These poles (resonances), as has been explained in Chap. 3, correspond to various plasma eigenmodes; therefore, the nonlinear processes originating from this resonant part of the inverse tensor describe nonlinear interactions between various wave modes, i.e., wave–wave interactions. However, if we take onto account the collisionless dissipation of the wave on the thermal particles (Landau damping), another, nonresonant contribution component of the inverse tensor, proportional to the antihermitian part of the dielectric tensor, can come into play. In this case only two waves are involved into the interaction, the original one and the final (scattered) one and the background particles, whose role is to absorb the initial wave and then to produce the final wave. For this reason, this kind of process is called stimulated scattering of waves on particles. The main nonresonant term of the inverse tensor expansion has the form

$$A_{\alpha\beta}(\omega, \boldsymbol{k}) = i\frac{k_\alpha k_\beta}{k^2}\frac{\delta\varepsilon_i''(\omega, \boldsymbol{k})}{|\varepsilon^l(\omega, \boldsymbol{k})|^2}, \tag{4.59}$$

where $\delta\varepsilon_i''(\omega, k)$ is the imaginary part of the ion dielectric permeability and $\varepsilon^l(\omega, k)$ is the longitudinal permeability. Substitution of Eqs. (4.53) and (4.59) along with the nonlinear response tensor into Eq. (4.51) allows finding variation of the wave energy density due to the stimulated scattering on ions:

$$\frac{\mathrm{d}^{(s)}}{\mathrm{d}t}W(\boldsymbol{k}) = 8\pi W(\boldsymbol{k})R(\boldsymbol{k})\int \mathrm{d}\boldsymbol{k}' W(\boldsymbol{k}')R(\boldsymbol{k}')$$
$$S_{\alpha\beta\gamma}(\omega, \boldsymbol{k}; \omega', \boldsymbol{k}')S_{\nu\mu\pi}(\omega'', \boldsymbol{k}''; \omega', \boldsymbol{k}')e_\pi(\omega, \boldsymbol{k})e^*_\alpha(\omega, \boldsymbol{k})e_\gamma(\omega', \boldsymbol{k}')e^*_\mu(\omega', \boldsymbol{k}')A^*_{\beta\nu}(\omega'', \boldsymbol{k}''), \tag{4.60}$$

where the superscript (s) stands for "scattering"; $\mathrm{d}/\mathrm{d}t = \partial/\partial t + \boldsymbol{v}_g\partial/\partial\boldsymbol{r}$, $\boldsymbol{v}_g$ is the wave group velocity.

Account of the resonant part of the inverse tensor describes various wave coalescence and decay processes:

$$\begin{aligned}\frac{\mathrm{d}^{(c)}}{\mathrm{d}t}W(\boldsymbol{k}) \;=\; & -4\pi^2\omega(\boldsymbol{k})\int \mathrm{d}\boldsymbol{k}'\int_{-\infty}^{\infty}\mathrm{d}\omega' Q\left[\omega(\boldsymbol{k})sign\gamma(\omega, \boldsymbol{k})W(\boldsymbol{k}')W(\boldsymbol{k}'')\right.\\ & \left.-\omega''sign\gamma(\omega'', \boldsymbol{k}'')W(\boldsymbol{k})W(\boldsymbol{k}') - \omega' sign\gamma(\omega', \boldsymbol{k}')W(\boldsymbol{k})W(\boldsymbol{k}'')\right]\\ & \times\left[\delta(\omega' - \omega'(\boldsymbol{k}'))\delta(\omega'' - \omega''(\boldsymbol{k}'')) + \delta(\omega' + \omega'(-\boldsymbol{k}'))\delta(\omega'' + \omega''(-\boldsymbol{k}''))\right.\\ & \left.+\delta(\omega' - \omega'(\boldsymbol{k}'))\delta(\omega'' + \omega''(\boldsymbol{k}'')) + \delta(\omega' + \omega'(-\boldsymbol{k}'))\delta(\omega'' - \omega''(-\boldsymbol{k}''))\right],\end{aligned} \tag{4.61}$$

where $\gamma(\omega, \boldsymbol{k})$ is the imaginary part of the corresponding wave, and the core Q has the form:

$$Q \equiv |S_{\alpha\beta\gamma}(\omega, \boldsymbol{k}; \omega', \boldsymbol{k}')e^*_\alpha(\omega, \boldsymbol{k})e^*_\beta(\omega'', \boldsymbol{k}'')e_\gamma(\omega', \boldsymbol{k}')|^2 R(\boldsymbol{k})|_{\omega=\omega(\mathbf{k})} R(\boldsymbol{k}')R(\boldsymbol{k}''). \tag{4.62}$$

Note, that in many cases, the plasma dielectric tensor derived within the cold plasma approximation, $\varepsilon_{\alpha\beta} = \delta_{\alpha\beta} - (\omega^2_{\mathrm{pe}}/\omega^2)\chi_{\alpha\beta}$, applies; for corresponding wave modes it is convenient to use Maxwell equation in the form of Eq. (3.12) to obtain

$$\chi_{\alpha\beta}k_\beta = \frac{\omega^2}{\omega^2_{\mathrm{pe}}}k_\alpha \tag{4.63}$$

and

$$\chi_{\alpha\beta}e_\beta = \frac{\omega^2}{\omega^2_{\mathrm{pe}}}\left[(1 - n^2_\sigma)e_\alpha + n^2_\sigma \frac{(\boldsymbol{k}\cdot\boldsymbol{e})k_\alpha}{k^2}\right]. \tag{4.64}$$

We will be returning to the wave coalescence and scattering in astrophysical conditions below.

4.3.2 Wave Turbulence in a Plasma

Consider longitudinal plasma waves, i.e., the Langmuir waves in the case of free plasma, upper- or lower-hybrid waves in case of cold magnetized plasma, or other potential waves (e.g., Bernstein modes) in case of hot plasma. Although all kinds of resonant and nonresonant processes are possible for these waves, the stimulated scattering of the plasma waves on thermal ions dominates in most of the cases, so the equation for the plasma wave energy density receives the form

$$\frac{\mathrm{d}W_l(\boldsymbol{k}, t)}{\mathrm{d}t} = -2\gamma_l W_l(\boldsymbol{k}, t) + 2\gamma_s W_l(\boldsymbol{k}, t), \tag{4.65}$$

where γ_l is the quasilinear growth/damping rate and

$$\gamma_s = -\frac{4\pi e^2 \omega^l(\boldsymbol{k})}{m^2\omega^4_{\mathrm{pe}}} R_l(\boldsymbol{k}) \int k''^2 \mathrm{d}\boldsymbol{k}' W_l(\boldsymbol{k}', t) R_l(\boldsymbol{k}')(\boldsymbol{\kappa}\cdot\boldsymbol{\kappa}')^2 \frac{\delta\varepsilon'^2_e(\omega'', \boldsymbol{k}'')\delta\varepsilon''_i(\omega'', \boldsymbol{k}'')}{|\varepsilon^l(\omega'', \boldsymbol{k}'')|^2}, \tag{4.66}$$

where $\boldsymbol{\kappa} = \boldsymbol{k}/k$, is the stimulated scattering contribution derived for the plasma waves from Eq. (4.60).

Although the nonlinear term is rather complicated we can make a number of general conclusions based on it. First of all, we note that sign of this term is primarily specified by a convolution of $W_l(\boldsymbol{k}')$ and $\delta\varepsilon''_i(\omega'', \boldsymbol{k}'')$, which is proportional to $\omega'' = \omega - \omega'$, see Problems 3.5 and 3.6. This means that the process of the stimulated scattering of waves on thermal ions results in

a decrease of the wave frequency. Therefore, an elementary process of the stimulated scattering on thermal ions can be understood as absorption of an initial wave at a given frequency ω' followed by an immediate emission of another wave with a frequency $\omega = \omega' - \omega'' < \omega'$, i.e., the wave energy decreases by a small value $\hbar\omega''$ after any single scattering episode, which implies the corresponding energy loss of the wave. Note, that this damping is different from a more usual collisional or collisionless (Landau) damping, which remains exponentially small for the plasma waves with the wavelength much larger than the Debye shielding radius. Here, the two waves, with frequencies ω and ω', produce a "beat" oscillation due to plasma nonlinearity at a much lower frequency ω'' and this beating wave is absorbed (via the collisionless Landau damping) by the thermal ions. The corresponding process is sometimes called the **nonlinear Landau damping**.

Although in terms of spectral evolution the stimulated scattering is always directed toward lower frequencies, this spectral "drift" can have various implications for the spectral energy density evolution in the $\boldsymbol{k}$-space depending on the specific dispersion of the given wave mode. Indeed, for the Langmuir waves in a free plasma, the dispersion relation does not depend on $\boldsymbol{k}$ direction; therefore, the scattering results in a corresponding decrease of the absolute k value, whose directions isotropize, so a more or less isotropic Langmuir turbulence can be expected.

The situation is qualitatively different in a magnetized plasma, where a large number of longitudinal wave mode is possible, although we consider two modes only, the lower- and upper-hybrid waves, which is sufficient for illustration. For a lower-hybrid (lh) wave in a plasma with $\omega_{\mathrm{Be}} \ll \omega_{\mathrm{pe}}$ we have $\omega_{lh} \approx \omega_{\mathrm{Be}} \cos\theta$, Eq. (3.109), where θ is the angle between the magnetic field and the wave vector. Apparently, the condition $\omega(\boldsymbol{k}) < \omega'(\boldsymbol{k}')$ translates here to $\cos\theta < \cos\theta'$, which implies a drift of the lower-hybrid waves toward transverse to the magnetic field direction, i.e., without other competing processes, the lower-hybrid turbulence would accumulate around $\pi/2$ and form a highly anisotropic narrow pancake distribution.

In contrast, the upper-hybrid waves obey the dispersion $\omega_{uh} \approx \sqrt{\omega_{\mathrm{pe}}^2 + \omega_{\mathrm{Be}}^2 \sin^2\theta}$, Eq. (3.109), i.e., the same condition $\omega(\boldsymbol{k}) < \omega'(\boldsymbol{k}')$ translates here to $\sin^2\theta < \sin^2\theta'$, which now implies an opposite drift of the upper-hybrid waves toward the magnetic field direction. This means that the upper-hybrid waves tend to form a 1D distribution of the wave vectors along the magnetic field direction. Apparently, account of the spatial dispersion results in corresponding terms in the wave dispersion containing the absolute value of the wave vector, so the exact path of the wave spectrum evolution will include both drifts—the angular and along the k value, whose relative importance depends on a given parameter combination.

Let us consider a stationary solution of Eq. (4.65), which is set up by $\mathrm{d}/\mathrm{d}t = 0$ implying that the quasilinear damping/growth rate is compensated by the nonlinear scattering rate,

$$\gamma_l = \gamma_s. \tag{4.67}$$

It is clear that the set of coupled equations, Eqs. (4.38) and (4.65), cannot have a stationary solution other than $W = 0$. Indeed, any other solution for the wave energy density would imply a plateau formation in the distribution function thus, $\gamma_l = 0$ and then $\gamma_s = 0$, which requires $W = 0$. However, for a given fixed particle distribution function [e.g., when the distribution function variation due to the quasilinear diffusion, Eq. (4.38), is compensated by an unspecified build up process, which means that a term for a particle source must be added in that equation], a stationary solution of Eq. (4.65) defined by Eq. (4.67) is possible.

Nevertheless, as we show below, such a stationary solution is not of practical use because it cannot be stable. Adopt that $W = W_0(\boldsymbol{k})$ is a stationary solution defined by Eq. (4.67). Then, adopt that a small perturbation $\delta W_0(\boldsymbol{k}, t)$ is superimposed on this stationary solution, $W(\boldsymbol{k}, t) = W_0(\boldsymbol{k}) + \delta W_0(\boldsymbol{k}, t)$, which also implies $\gamma_s = \gamma_{s0} + \delta\gamma_s = \gamma_l + \delta\gamma_s(\boldsymbol{k}, t)$. Substitution of this spectral energy density and the nonlinear growth rate into Eq. (4.65) and cancelation of equal terms with the account of Eq. (4.67) yields

$$\frac{\mathrm{d}\delta W(\boldsymbol{k}, t)}{\mathrm{d}t} = 2\delta\gamma_s(\boldsymbol{k}, t)W_0, \tag{4.68}$$

where the second-order term is discarded. Here the nonlinear scattering rate $\delta\gamma_s$ is specified by δW via integration (4.66). As we have discussed, Eq. (4.66) is sign alternating because it contains a first power of ω''; thus, some of possible perturbations δW will result in a positive growth rate at a region of k-space occupied by $W_0(\boldsymbol{k})$, which means that the stationary spectral density of the waves $W_0(\boldsymbol{k})$ is unstable. Therefore, all stable solutions of Eq. (4.65) are nonstationary.

Let us now consider what kind of nonstationary solution we can expect. To do so we assume that the waves are generated by resonant particles in a limited region of the k-space, where γ_l is negative, the resonant region, and introduce the wave energy density in this *resonant region*, $w(t) = \int_{res} W(\boldsymbol{k}, t)\mathrm{d}\boldsymbol{k}$. Initially, while the nonlinear term is small, this wave energy density experiences an exponential growth. After some time, the nonlinear term becomes important and the nonlinear scattering of the waves starts to transfer the wave energy toward smaller frequencies, which implies a decay of $w(t)$. Sooner or later the wave energy leaves the resonant region, i.e., the nonlinear term starts to enhance the energy density outside the resonant region, which we call a *nonresonant region* and introduce the corresponding nonresonant energy density $w^*(t) = \int_{nonres} W(\boldsymbol{k}, t)\mathrm{d}\boldsymbol{k}$. Integrating Eq. (4.65) over the resonant and nonresonant regions respectively, we obtain

two approximate equations for $w(t)$ and $w^*(t)$ (Zaitsev and Stepanov 1975; Stepanov 1980; Zaitsev and Stepanov 1983):

$$\frac{\mathrm{d}w}{\mathrm{d}\tau} = \bar{\gamma}w - \zeta w w^* \qquad \frac{\mathrm{d}w^*}{\mathrm{d}\tau} = -\tilde{\gamma}w^* + \zeta w w^* \tag{4.69}$$

where $\bar{\gamma}$ is a characteristic (positive) growth rate in the resonant region, $\bar{\gamma} = -2\langle\gamma_l\rangle_{res} > 0$, $\tilde{\gamma} = 2\langle\gamma_l\rangle_{nonres} > 0$ is the effective damping rate in the nonresonant region, ζ is the characteristic absolute value of the core of nonlinear term (4.66). Order of magnitude estimate of the core accounting the explicit form of dielectric permittivity components entering Eq. (4.66) yields

$$\zeta \sim 0.1\frac{\omega_{\mathrm{pe}}}{n_e k_B T}, \tag{4.70}$$

where $n_e k_B T$ is the plasma thermal energy density. Equation (4.69) represents a set of the **Lotka–Volterra equations**, known originally from a "predator–prey" interaction problem, whose properties are well studied. It is known, in particular, that this system allows periodic solutions, which can be visualized by closed trajectories around a singular stationary center-like point $w_0 = \tilde{\gamma}/\zeta$ and $w_0^* = \bar{\gamma}/\zeta$ at the plane w vs w^*, see Fig. 4.1. Small-amplitude (sinusoidal) oscillations arise when the departure of the energy densities from the stationary solution is small, the oscillation period is

$$\tau = \frac{2\pi}{\sqrt{\bar{\gamma}\tilde{\gamma}}}. \tag{4.71}$$

For large-amplitude oscillations the period depends on the wave energy

$$\tau = \frac{1}{\tilde{\gamma}} \ln \frac{w}{n_e k_B T} \sim \frac{1}{\tilde{\gamma}} \ln \frac{\bar{\gamma}}{\zeta w^*(t=0)}. \tag{4.72}$$

Although the approximation used to reduce the original integro-differential nonlinear equation to the Lotka–Volterra set of two coupled differential equation seems to be too crude, it, nevertheless, correctly describes qualitative behavior of the wave energy density. To show this, Fig. 4.2 presents two examples of numerical solutions of original integro-differential equation (4.65) with nonlinear scattering rate (4.66) for two different nonstationary initial distribution functions of fast electrons (Korsakov and Fleishman 1998).

The type of solution depends substantially on the resonant region, i.e., eventually, on the initial particle distribution. The first of them provides a relatively narrow resonant region, Fig. 4.2a, which results in oscillatory solution for the plasma wave energy density W (Fig. 4.2b) in qualitative agreement with simplified Lotka–Volterra description of the nonlinear evolution of the wave energy density. Most of the plasma wave energy density is concentrated in the narrow frequency range $\Delta\omega/\omega_{\mathrm{pe}} \approx 2.5\,\%$ and the bandwidth becomes even smaller, $\approx 1\,\%$, after transition to oscillatory part in Fig. 4.2b. Figure 4.2c displays logarithmic derivative of W over the time; flat regions of this curve correspond to exponential growth or decay of W.

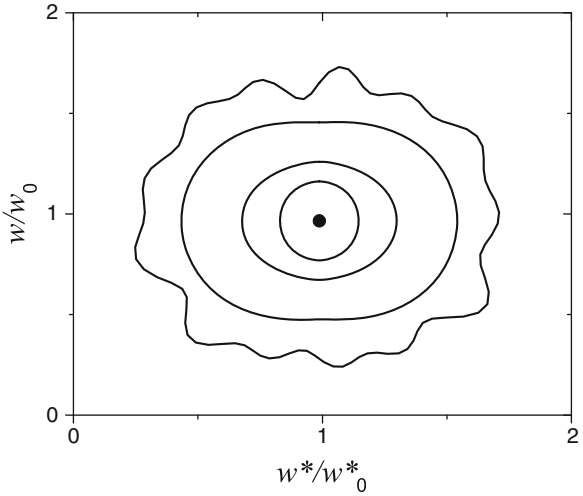

Figure 4.1: Phase portrait representation of solutions of the Lotka–Volterra equations. For small deviations of the resonant and nonresonant energy densities from their steady-state values w and $w*$ the phase trajectory is circular indicative of small-amplitude sinusoidal oscillations of the energy densities. As the deviations increase (bigger distance from the center to the curve), the phase portrait deviates from the circular one stronger and stronger, so the oscillations become highly nonlinear with time profile strongly different from the sinusoidal one. The regime of irregular pulsations (obtained from the integro-differential equation) can be represented by the outmost wavy curve.

Let us quantitatively compare the numerical results with the predictions of the simplified Lotka–Volterra approach discussed above. The numerical period, determined directly from the plot, equals to

$$\tau = 365\gamma_0^{-1}. \tag{4.73}$$

Apparently, here we deal with a large modulation regime, so the corresponding Lotka–Volterra oscillation period is defined by Eq. (4.72), i.e., it is reciprocal to the effective damping rate of the waves in the nonresonant region. Note that the effective damping rate is supposed to deviate from the maximum damping rate in the nonresonant region because only a limited spectral range marked by numbers 1–4 in Fig. 4.2a takes part in the nonlinear wave transformation. In contrast, the effective growth rate, $\bar{\gamma}$, is well defined by the maximum growth rate, $\gamma_{\max} = 4.3 \cdot 10^{-2}\gamma_0$ for this run. Now, to estimate the effective damping rate, we consider the logarithmic derivative shown in Fig. 4.2c, where the positive and negative flat regions of the logarithmic derivatives have comparable absolute values, which implies $\tilde{\gamma} \approx \bar{\gamma}$. Substituting the maximum growth rate $\gamma_{\max}$ for $\tilde{\gamma}$ in Eq. (4.72) we obtain

$$\tau \sim \tilde{\gamma}^{-1} \ln 10^7 \sim 20\gamma_{\max}^{-1} = 375\gamma_0^{-1}, \tag{4.74}$$

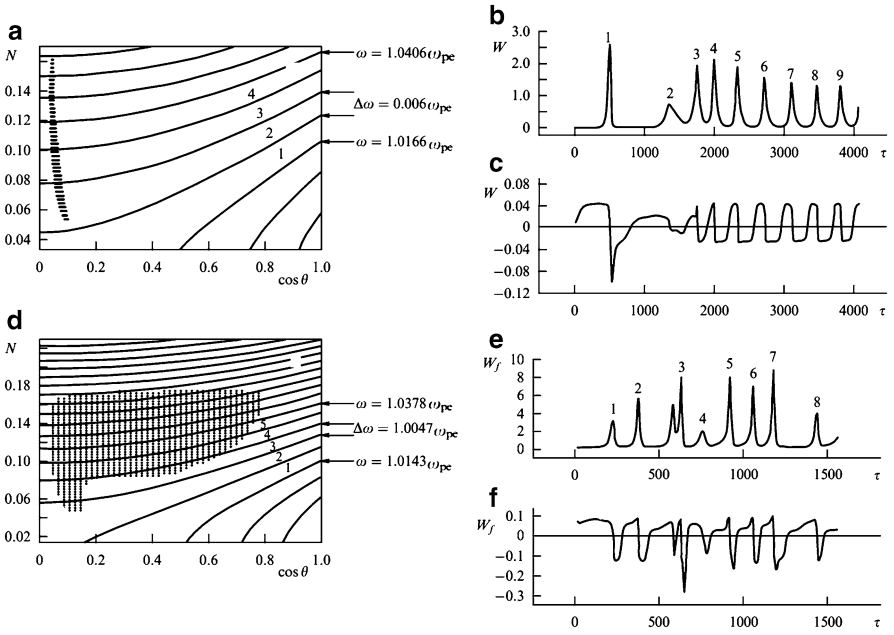

Figure 4.2: **(a)** k-plane with the region of positive growth rate (*thick hatching*) for a first particle distribution, curves of constant frequency are shown by solid lines; nonlinear wave transformation mainly occurs in regions 1–4; the following dimensionless variables $N = kd_e$, $\tau = \gamma_0 t$, $\gamma_0 = \pi\omega_{\rm pe}\frac{n_b}{n_0}$ are used, W is normalized to $W_0 = \sqrt{2}\pi^{5/2}\frac{m_e^2 v_{Te}^2}{e^2\omega_{\rm pe}}\frac{n_b}{n_0}$, $\frac{\omega_{\rm pe}}{\omega_{\rm Be}} = 5$, so the isotropic expression (see Problem 3.5) for imaginary part of ion dielectric permeability can be used; **(b)** Time dependence of the plasma wave energy density, **(c)** The logarithmic derivative; **(d–f)** The same for the second particle distribution; nonlinear wave transformation mainly occurs in regions 1–5; (Korsakov and Fleishman 1998).

in remarkable agreement with numerical result (4.73). Thus, we can correct a poorly defined expression for the oscillation period, Eq. (4.72), to a well-defined one

$$\tau = \frac{1}{\gamma_{\max}} \ln \frac{\gamma_{\max}}{\zeta w^*(t=0)}. \tag{4.75}$$

In the second case, Fig. 4.2d, there is a much broader instability region, so the nonlinear wave interaction becomes more complicated. As a result the plasma wave energy density does not oscillate periodically, while displays irregular pulsations, Fig. 4.2e. Figure 4.2f shows the corresponding logarithmic derivative with a rather complicated (nonexponential) shape of each peak containing overexponential growth phase. This irregular regime is qualitatively different from oscillating one; it cannot be obtained from the

simplified Lotka–Volterra system. However, one can still use Eq. (4.75) to roughly estimate average time between the neighboring peaks in Fig. 4.2e.

The real plasma turbulence composed of high-frequency potential modes in a magnetized plasma can be even more complicated as it includes various wave modes such as upper- and lower-hybrid waves, Bernstein modes, and lower-frequency ion-sound waves if the ion temperature is much lower than the electron temperature. In this case a number of coalescence processes can become essential, in particular, scattering of Langmuir waves on ion-sound waves. Since the ion-sound wave frequency is much lower than that of the Langmuir waves, this process is somewhat similar to the stimulated scattering on thermal ions, although its nonlinear scattering rate can strongly exceed that for the stimulated scattering. Nevertheless, the discussed above regimes of periodic or irregular oscillations are highly typical for plasma wave turbulence and widely employed for interpretation of solar and stellar coherent radio bursts, see examples in Chap. 10 below.

Problems

4.1 Consider the beam instability for a "hot" beam, with account of the thermal scatter of the beam electrons (v'_{Te}). Determine conditions when the thermal scatter can be discarded. Find the wave growth rate for a "warm" beam, when resonant and nonresonant contribution of the beam to the dielectric permittivity are comparable to each other.

4.2 Use Eq. (4.42) and derive equation for the three-wave processes in terms of plasmon numbers $N^{\sigma}(\boldsymbol{k})$ from Eq. (4.61) for the energy density. Prove that the total number of the involved plasmons is conserved.

Answers and Solutions

4.1 Use longitudinal dielectric permittivity described by Eq. (3.111a) with the account of functions $Z(s)$ for the main plasma and $Z(s')$ for the beam electrons (where $s' = (\omega - \boldsymbol{ku})/kv'_{Te}$) given by Eq. (14) from Problem 3.5. For a hot beam the imaginary contribution (function $Y(s')$) will dominate. In this case, assuming the growth rate is small compared with the frequency, one finds $\gamma_{res} = \sqrt{\pi/8}(\omega'_{\rm pe}/kv'_{Te})^2\omega_{\rm pe}$. Comparison of the resonant and nonresonant beam contributions to the dielectric permittivity suggests that the resonant contribution dominates only for rather weak (tenuous) beams until $\gamma_{\max} \ll kv'_{Te}$; otherwise, when $\gamma_{\max} \gg kv'_{Te}$ the resonant contribution can be discarded and "HD" approximation of cold monoenergetic beam performed in Sect. 4.1.1 applies. For a warm beam we, thus, have $\gamma_{\max} \sim kv'_{Te}$. To obtain a more accurate answer one has to retain both resonant and nonresonant beam contributions to the dielectric permittivity and solve for γ. Note that the nonresonant instability appears to be much stronger than the resonant one.

Chapter 5

Nonlinear MHD Waves and Discontinuities

Linear waves considered in Chap. 2 describe perturbations with small amplitudes. In the astrophysical conditions, however, a strong energy release gives often rise to large-amplitude perturbations, which cannot be fully accommodated by the linear theory and so require non-linear treatment. In this chapter we consider a number of important examples of the nonlinear waves—simple waves, solitons, and discontinuities—with the use of exact or approximate analytical methods.

5.1 Simple MHD Waves

Here we obtain a family of exact MHD solutions, called the *simple waves*, under the following simplifying assumptions:

1. The dissipation can be neglected entirely: $\nu = 0$, $\nu_m = 0$, and $\chi = 0$.

2. One-dimensional geometry, all dependent variables depend on x and t only.

3. All macroscopic parameters $\boldsymbol{u}(\varphi)$, $\boldsymbol{B}(\varphi)$, $\rho(\varphi)\ldots$ are single-valued functions of a combination $\varphi(x,t)$ of the coordinate and time. Equivalently, all but one macroscopic parameters can be treated as functions of this last parameter. If the functions become multivalued at some point, the solution becomes invalid. As an example, linear plane monochromatic waves represent a special case of the simple waves with $\varphi(x,t) = kx - \omega t$.

G.D. Fleishman and I.N. Toptygin, *Cosmic Electrodynamics*, Astrophysics and Space Science Library 388, DOI 10.1007/978-1-4614-5782-4_5,

The adopted conditions ensure the simple waves to satisfy a system of ordinary nonlinear differential equations with a single independent variable. In some cases, this equation set can be integrated analytically. The first mathematician who studied similar solution within standard HD was Bernhard Riemann.

From equation $\nabla \cdot \boldsymbol{B} = 0$ and assumption that the solution depends on x coordinate only, we deduce

$$B_x = \text{const.} \tag{5.1}$$

Let us transform the equations using the prime ($'$) mark for the derivative over φ (e.g., u_x' denotes derivative of u_x, the x-component of the velocity $\boldsymbol{u}$, over φ). For example, for the continuity equation, we have

$$\frac{\partial \rho}{\partial t} + u_x \frac{\partial \rho}{\partial x} + \rho \frac{\partial u_x}{\partial x} = \rho' \left(\frac{\partial \varphi}{\partial t} + u_x \frac{\partial \varphi}{\partial x} \right) + u_x' \rho \frac{\partial \varphi}{\partial x} = 0.$$

We note that any macroscopic variable is constant (at a given time) at surfaces $x = \text{const}$, at which, in particular,

$$\varphi(x, t) = \text{const}, \tag{5.2}$$

and which moves along axes Ox. The velocity of the planes $\mathrm{d}x/\mathrm{d}t = (\partial x/\partial t)_\varphi = v_{\mathrm{ph}}$ can apparently be called the phase velocity, as it is analogous to the phase velocity of the plane monochromatic waves. Taking the derivative of Eq. (5.2), we obtain

$$\frac{\partial \varphi}{\partial t} = -v_{\mathrm{ph}} \frac{\partial \varphi}{\partial x}, \tag{5.3}$$

which reduces the continuity equation to the form

$$\rho' v - u_x' \rho = 0, \tag{5.4}$$

where $v = v_{\mathrm{ph}} - u_x$ is the propagation speed of the simple wave in the comoving reference frame. Other equations can be transformed in a similar way, which in projection to the axes yields

$$u_x' v - p'/\rho - (B_y B_y' + B_z B_z')/4\pi\rho = 0, \tag{5.5a}$$

$$u_y' v + B_x B_y'/4\pi\rho = 0, \tag{5.5b}$$

$$u_z' v + B_x B_z'/4\pi\rho = 0, \tag{5.5c}$$

$$B_y' v - u_x' B_y + u_y' B_x = 0, \tag{5.5d}$$

$$B_z' v - u_x' B_z + u_z' B_x = 0, \tag{5.5e}$$

$$s'v = 0, \tag{5.5f}$$

$$p = p(s, \rho). \tag{5.5g}$$

Condition (5.1) and nonlinear equations (5.4) and (5.5) compose a closed set of equations for the problem considered. We proceed now to analysis of various kinds of the simple MHD waves.

Note that if $v \neq 0$ then Eq. (5.5f) yields $s' = 0$, i.e., $s = \text{const}$; thus, the simple waves with nonzero phase velocity represent motions with constant entropy. This allows to introduce the **sound speed**

$$c_s = \sqrt{\left(\frac{\partial p}{\partial \rho}\right)_s} \tag{5.6}$$

and substitute $p' = c_s^2 \rho'$ into Eq. (5.5a). Equation (5.6) describes a local sound speed value in the plasma without magnetic field. Note that the sound speed depends on local density and so varies within a simple wave in a general case.

5.1.1 Entropy Simple Waves

Let us start from the waves with a variation of the entropy, $s' \neq 0$. In this case Eq. (5.5f) yields

$$v \equiv v_e = 0, \tag{5.7}$$

which means that the entropy wave is at rest in respect to the fluid and can only be transferred by the fluid motions.

Within the Hall MHD there are two kinds of the entropy waves; see Sect. 2.4.2. In the first kind of the entropy simple waves $B_x \neq 0$, and so the equations consequently give rise to the equalities $u'_x = 0$, $B'_y = B'_z = 0$, $u'_y = u'_z = 0$, and $p' = 0$; therefore, the corresponding parameters are constant in this wave. The plasma density experiences variations linked with the entropy variations by Eq. (5.5g) and constrained by the condition $p = \text{const}$. Thus, when the dissipative processes are negligible, the shape of the entropy wave does not change, while the wave itself represents a heated or cooled region moving together with the plasma. In the real conditions, the heat conduction (diffusion of the heated particles) gives rise to a slow dissipation of the entropy excitation.

The second kind of the entropy wave takes place for $B_x = 0$; in this case Eqs. (5.4) and (5.5a) require constancy of the longitudinal speed and the total pressure

$$u_x = \text{const}, \qquad p + \frac{B^2}{8\pi} = \text{const}; \tag{5.8}$$

the derivatives u'_y and u'_z can be arbitrary.

Two described cases are closely connected with the corresponding linear entropy perturbations [see Eqs. (2.46) and (2.47)]. The first case, $B_x \neq 0$, leads to $\boldsymbol{b} = 0$, $\boldsymbol{u} = 0$, and $p = 0$ in the linear theory and to $B_y = B_{0y}$

and $B_z = B_{0z}$ in the considered here nonlinear theory, so this two cases are entirely coincident with each other. In the second case, $B_x = 0$, in linear approximation, we have $\boldsymbol{B} = \boldsymbol{B_0} + \boldsymbol{b}$; thus, Eq. (5.8) yields $B^2 \approx B_0^2 + 2\boldsymbol{b}\cdot\boldsymbol{B}_0$, and so $p + \boldsymbol{b}\cdot\boldsymbol{B}_0/4\pi = \text{const} - B_0^2/8\pi = \text{const}'$ in full agreement with Eq. (2.47).

5.1.2 Alfvén Simple Waves

The Alfvén simple waves include those plasma motions in which both the entropy and the density are constant:

$$\rho = \text{const}. \tag{5.9}$$

Now, Eqs. (5.4)–(5.5a) yield

$$u_x = \text{const}, \qquad B_y^2 + B_z^2 \equiv B_\perp^2 = \text{const}, \tag{5.10}$$

while Eqs. (5.5b)–(5.5e) split into two identical pairs

$$u_y' v + \frac{B_x B_y'}{4\pi\rho} = 0, \qquad u_y' B_x + B_y' v = 0 \tag{5.11}$$

and similar equations for u_z' and B_z'. Equation (5.11) specify the Alfvén speed of this simple wave relative to the plasma

$$v \equiv v_{\mathrm{A}x} = \pm\frac{|B_x|}{\sqrt{4\pi\rho}}. \tag{5.12}$$

This velocity is constant, which follows from Eqs. (5.1) and (5.9). The Alfvén simple wave is evanescent for $B_x = 0$, because this condition is compatible only with uniform solution of the equations $\boldsymbol{u} = \text{const}$ and $\boldsymbol{B} = \text{const}$. Equation set (5.11) and the identical set for u_z', B_z' give rise to the relationship between the velocity $\boldsymbol{u}$ of the medium and the magnetic field in the simple Alfvén wave:

$$\boldsymbol{u} = \mp\frac{\boldsymbol{B}}{\sqrt{4\pi\rho}}. \tag{5.13}$$

The integration constant is selected in such a way to provide $\boldsymbol{u} = 0$ for $\boldsymbol{B} = 0$. The minus sign must be selected if the signs of B_x and $v_{\mathrm{A}x}$ are the same, while the plus sign corresponds to the case when their signs are opposite.

An exact partial solution for the Alfvén simple wave has the form of the plane, circularly polarized, monochromatic wave propagating along the uniform magnetic field:

$$B_y = B_\perp \cos k[x - (v_{\mathrm{A}x} + u_x)t], \qquad B_z = B_\perp \sin k[x - (v_{\mathrm{A}x} + u_x)t]. \tag{5.14}$$

For arbitrary propagation angle of the simple Alfvén wave to the uniform magnetic field $\boldsymbol{B}_0$, however, no exact analytical solution is known. Approximate solution, valid for the small amplitude wave (see Sect. 2.4.2 for greater detail), is linearly polarized and has the form

$$\boldsymbol{b}(\boldsymbol{r},t) \;=\; \boldsymbol{b}_0 \cos(\boldsymbol{k}\cdot\boldsymbol{r} - \omega_{\mathrm{A}} t), \tag{5.15}$$

where $\boldsymbol{k}$ is the wave vector,

$$\omega_{\mathrm{A}} \;=\; \pm\frac{|\boldsymbol{k}\cdot\boldsymbol{B}|}{\sqrt{4\pi\rho}} \tag{5.16}$$

is the Alfvén wave frequency, and the amplitude $\boldsymbol{b}_0$ is transverse to the external field $\boldsymbol{B}_0$. Condition (5.10) requiring constancy of the absolute value of the magnetic field is fulfilled in this case to the first order over the small value b_0/B_0. The amplitude $\boldsymbol{b}_0$ is transverse to the wave vector $\boldsymbol{k}$ as well. Since the phase velocity of the Alfvén wave is constant (because both the magnetic field and the plasma density are constant), the shape of this wave does not change during propagation.

5.1.3 Fast and Slow Simple Waves

Consider now those solutions of Eqs. (5.4)–(5.5g), which have $s = \mathrm{const}$, $\rho' \neq 0$, and $v \neq v_e, v_{\mathrm{A}x}$. The corresponding small-amplitude waves are called the *magnetosonic waves*. Note that selecting the reference frame in which $u_z = 0$ and $B_z = 0$ simplifies the equation set by transforming equations (5.5c) and (5.5e) into equivalences. The remaining set of four equations (5.4)–(5.5b) and (5.5d) has a nontrivial solution when the phase velocity has the form

$$v^2 \equiv v_{f,\,s}^2 = \frac{1}{2}\left\{c_s^2 + v_{\mathrm{A}}^2 \pm \sqrt{(c_s^2 + v_{\mathrm{A}}^2)^2 - 4c_s^2 v_{\mathrm{A}x}^2}\right\}, \tag{5.17}$$

where

$$\boldsymbol{v}_{\mathrm{A}} \;=\; \frac{\boldsymbol{B}}{\sqrt{4\pi\rho}} \tag{5.18}$$

is the pseudovector of the **Alfvén speed**.

Comparison of formulae (5.17) and (5.12) shows that for any value of the magnetic field and the sound speed, the following inequalities are fulfilled:

$$0 \le v_s^2 \le v_{\mathrm{A}x}^2 \le v_f^2, \qquad v_s^2 \le c_s^2 \le v_f^2, \tag{5.19}$$

$|v_{\mathrm{A}x}| = \omega_{\mathrm{A}}/k = |\boldsymbol{k}\cdot\boldsymbol{v}_{\mathrm{A}}|/k$. The last two inequalities clarify the names of the waves considered—fast or slow compared with the ordinary sound waves in the medium without magnetic field.

Substitution of v_f or v_s into the equation set allows to integrate it. The integration is rather complicated in the general case; therefore, we consider

a simpler case of the transverse to the magnetic field propagation of the simple wave, i.e., $B_x = 0$, $B_y^2 = B^2$. In this case only the fast wave survives: $v_f = \pm(c_s^2 + v_\mathrm{A}^2)^{1/2}$, $v_s = 0$. It is convenient to take the density as the independent variable φ, then Eqs. (5.4)–(5.5b) yield

$$u_y = \text{const}, \qquad \frac{\mathrm{d}u_x}{\mathrm{d}\rho} = \frac{v_f}{\rho}, \qquad \frac{\mathrm{d}B^2}{\mathrm{d}\rho} = 8\pi v_\mathrm{A}^2. \tag{5.20}$$

Taking into account definition (5.18) of the Alfvén speed, integration of the last equation gives rise to

$$B = B_0 \frac{\rho}{\rho_0}, \tag{5.21}$$

where B_0 is the magnetic field value at $\rho = \rho_0$ (i.e., in the unperturbed region of the plasma). Equation (5.21) means in fact the freezing-in of the field into the fluid. Applying it along with equation of state (5.5g), we find dependence of v_f on ρ, which allows to integrate the second equation in Eq. (5.20):

$$u_x(\rho) = \int_{\rho_0}^{\rho} \frac{v_f(\rho)}{\rho} \mathrm{d}\rho, \tag{5.22}$$

where we adopt $u_x(\rho_0) = 0$. Taking into account $(\partial x/\partial t)_\rho = v_f(\rho) + u_x(\rho)$ we obtain the solution

$$x = [v_f(\rho) + u_x(\rho)]t + f(\rho), \tag{5.23}$$

which implicitly specifies the dependence $\rho(x, t)$. The function $f(\rho)$ can then be determined from the initial condition $\rho(x, 0) = F(x)$.

5.1.4 Turnover of the Simple Wave

Relation (5.22) is remarkable as it tells us that the velocity of the fluid in the simple wave depends on the density. Consider the outcome of this dependence in more detail. For the tenuous gas at constant entropy we have $p = p_0(\rho/\rho_0)^\gamma$, where γ is the ratio of specific heats (or the index of the Poisson adiabat, e.g., $\gamma = 5/3$ for a single-atom gas); thus

$$c_s^2 = \left(\frac{\partial p}{\partial \rho}\right)_s = c_{s0}^2 \left(\frac{\rho}{\rho_0}\right)^{\gamma-1} \tag{5.24}$$

and then using Eq. (5.21), we obtain

$$\frac{\mathrm{d}|u_x|}{\mathrm{d}\rho} = \frac{1}{\rho}\left[v_{\mathrm{A}0}^2 \frac{\rho}{\rho_0} + c_{s0}^2 \left(\frac{\rho}{\rho_0}\right)^{\gamma-1}\right] > 0.$$

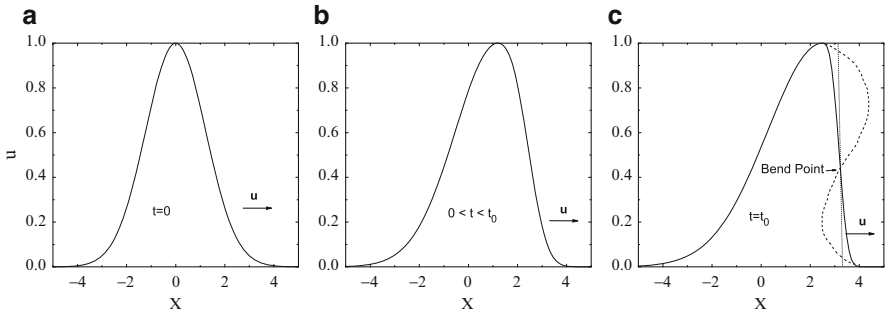

Figure 5.1: Stages of simple wave turnover and shock front formation. The wave front steepens with time and a very sharp front is formed at $t = t_0$. Afterwards, the solution becomes multi-valued (*dashed curve* in *panel c*) and so unphysical.

This inequality tells us that the absolute velocity value increases as the density increases. Therefore, the profile $u_x(x)$ changes its shape as the wave propagates; specifically, the leading edge sharpens, while the trailing edge smoothes. This process is well described by the solution obtained until a nearly vertical region is formed at the leading edge (Fig. 5.1), since then the simple wave solution becomes inapplicable any longer. The reason for that is large gradient of the velocity, which calls for account of formerly neglected dissipative processes: the viscosity, the heat conduction, and the Joule dissipation. This dissipative processes give rise to formation of a *shock front*—a narrow region with strong dissipation and large gradients ("jumps") of the macroscopic parameters—at the leading edge of the strong simple wave. The formal simple wave solution becomes multiply defined after the turnover. Note that the wave turnover is a property of the fast and slow waves; in contrast, the Alfvén and entropy waves cannot overturn because in the Alfvén wave the density is constant, while the entropy wave does not propagate relative to the fluid.

5.2 Dissipation and Dispersion Effects: Solitons

The performed analysis of the one-dimensional simple waves does not take into account any kind of dissipation in the fluid. Nevertheless, the dissipation can have major effect on the fluid motion especially when and where strong spatial gradients of the plasma parameters develop; for example, as has been mentioned in Sect. 5.1.4, the dissipation can prevent the simple wave front overturn. In many cases both nonlinearity and dissipation can be treated as small effects, which often enables quantitative treatment of these effects. Frequently, HD or MHD equations can be reduced, for a specific problem, to one or another classical nonlinear equation; in such cases well-developed theory of those equations can be successfully used.

5.2.1 Burgers Equation

We start with considering the HD equations (see Sect. 2.1) and derive an approximate equation describing the spreading of a weak nonlinear one-dimensional wave propagating along the Ox axis, taking into account the energy dissipation (dissipative kinetic coefficients are adopted constant for simplicity):

$$\frac{\partial \rho}{\partial t} + u\frac{\partial \rho}{\partial x} + \rho\frac{\partial u}{\partial x} = 0, \tag{5.25a}$$

$$\frac{\partial u}{\partial t} + u\frac{\partial u}{\partial x} = -\frac{1}{\rho}\frac{\partial p}{\partial x} + \frac{4\nu}{3}\frac{\partial^2 u}{\partial x^2}, \tag{5.25b}$$

$$\frac{\partial s}{\partial t} + u\frac{\partial s}{\partial x} = \frac{\chi}{\rho T}\frac{\partial^2 T}{\partial x^2}. \tag{5.25c}$$

Since both the nonlinearity and the dissipation are considered to be small effects, we neglect the term containing the viscous tension tensor in the rhs of Eq. (2.4), proportional to $(\partial u/\partial x)^2$, that is, of the third order of smallness, to obtain Eq. (5.25c). Transforming Eq. (5.25a) using the equation of state $\rho = \rho(p, s)$, we find

$$\frac{\partial \rho}{\partial t} + u\frac{\partial \rho}{\partial x} = \left(\frac{\partial \rho}{\partial p}\right)_s \left(\frac{\partial p}{\partial t} + u\frac{\partial p}{\partial x}\right) + \left(\frac{\partial \rho}{\partial s}\right)_p \left(\frac{\partial s}{\partial t} + u\frac{\partial s}{\partial x}\right). \tag{5.26}$$

Substituting Eq. (5.26) into Eq. (5.25a) and taking into account Eq. (5.25c) and $(\partial\rho/\partial p)_s = 1/(\partial p/\partial\rho)_s$, we get

$$\frac{\partial p}{\partial t} + u\frac{\partial p}{\partial x} + \rho\left(\frac{\partial p}{\partial \rho}\right)_s \frac{\partial u}{\partial x} = -\frac{\chi}{\rho T}\left(\frac{\partial p}{\partial \rho}\right)_s \left(\frac{\partial \rho}{\partial s}\right)_p \frac{\partial^2 T}{\partial x^2}. \tag{5.27}$$

The right-hand side of Eq. (5.27) has the first order of smallness over dissipative value (5.25c), when the second derivative is calculated in dissipativeless ($s = \text{const}$) linear approximation

$$\frac{\partial^2 T(s,p)}{\partial x^2} = \left(\frac{\partial T}{\partial p}\right)_s \frac{\partial^2 p}{\partial x^2}.$$

We then use the thermodynamic identity[1]

[1] This is derived as follows:

$$Tc_V^{-1} = (\partial_s T)_{V=1/\rho} = (\partial_s T)_\rho = \frac{\partial(s,p)}{\partial(s,\rho)}\frac{\partial(T,\rho)}{\partial(s,p)} = (\partial_\rho p)_s[(\partial_s T)_p(\partial_p \rho)_s - (\partial_p T)_s(\partial_s \rho)_p]$$

$$= Tc_P^{-1} - (\partial_\rho p)_s(\partial_p T)_s(\partial_s \rho)_p.$$

$$T\left(\frac{1}{c_V}-\frac{1}{c_P}\right)=-\left(\frac{\partial\rho}{\partial s}\right)_p\left(\frac{\partial p}{\partial\rho}\right)_s\left(\frac{\partial T}{\partial p}\right)_s,$$

where c_V and c_P are the corresponding specific heats. Using these equations we bring Eq. (5.27) to the form

$$\frac{\partial u}{\partial x}+\frac{1}{\rho}\left(\frac{\partial\rho}{\partial p}\right)_s\left(\frac{\partial p}{\partial t}+u\frac{\partial p}{\partial x}\right)=\frac{\chi}{\rho_0^2c_s^2}\left(\frac{1}{c_V}-\frac{1}{c_P}\right)\frac{\partial^2 p}{\partial x^2} \tag{5.28}$$

with the unperturbed values ρ_0 and $c_s^2=(\partial p/\partial\rho)_s$ on the rhs.

We now eliminate the variables u and ρ from Eqs. (5.25b) and (5.28) and obtain one equation. It will contain only the variable part of the pressure $p'=p-p_0$ and the unperturbed values. On the lhs of this equation, we have to take into account only the terms up to the second order of smallness, as has already been done on the rhs.

We seek a solution that changes slowly in the co-moving reference frame, which allows simplifying the equations. To explore this we adopt the following dependence of the solution on spatial and temporal variables: $p'(x-c_st,\varepsilon x)$, where ε is a small parameter (provided the nonlinearity and dissipation are small). Thus, the operator $(\partial/\partial x+c_s^{-1}\partial/\partial t)$ is of the order of ε and therefore

$$\partial/\partial t\approx-c_s\partial/\partial x,\quad(\partial/\partial x-c_s^{-1}\partial/\partial t)\approx 2\partial/\partial x. \tag{5.29}$$

We assume in the second-order terms the same links between small perturbations as those valid in the linear theory, i.e., for small amplitude sound waves:

$$u\approx\frac{c_s\rho'}{\rho_0}\approx\frac{p'}{c_s\rho_0},\quad\rho\approx\rho_0+\frac{p'}{c_s^2},\quad\frac{1}{\rho}\left(\frac{\partial\rho}{\partial p}\right)_s=\frac{1}{c_s^2\rho_0}-\frac{p'}{c_s^4\rho_0^2}-\rho_0\left(\frac{\partial^2V}{\partial p^2}\right)_s p'.$$

Using this relations, we find

$$\begin{aligned}u\frac{\partial u}{\partial x}+\frac{1}{\rho}\frac{\partial p}{\partial x}&\approx\frac{1}{\rho_0}\frac{\partial p'}{\partial x},\\ \frac{1}{\rho}\left(\frac{\partial\rho}{\partial p}\right)_s\left(\frac{\partial p}{\partial t}+u\frac{\partial p}{\partial x}\right)&\approx\frac{1}{c_s^2\rho_0}\frac{\partial p}{\partial t}+c_s\rho_0\left(\frac{\partial^2V}{\partial p^2}\right)_s p'\frac{\partial p'}{\partial x}.\end{aligned}$$

We then write Eqs. (5.25b) and (5.28) in the form

$$\frac{\partial u}{\partial t}+\frac{1}{\rho_0}\frac{\partial p'}{\partial x}=\frac{4\nu}{3c_s\rho_0}\frac{\partial^2p'}{\partial x^2},$$

$$\frac{\partial u}{\partial x}+\frac{1}{c_s^2\rho_0}\frac{\partial p'}{\partial t}=-c_s\rho_0\left(\frac{\partial^2V}{\partial p^2}\right)_s p'\frac{\partial p'}{\partial x}+\frac{\chi}{c_s^2\rho_0^2}\left(\frac{1}{c_V}-\frac{1}{c_P}\right)\frac{\partial^2p'}{\partial x^2}.$$

Differentiating the first of these equations over x and the second over t and then subtracting the results with account approximations (5.29) we get

$$\left(\frac{\partial}{\partial x}-\frac{1}{c_s}\frac{\partial}{\partial t}\right)\left(\frac{\partial}{\partial x}+\frac{1}{c_s}\frac{\partial}{\partial t}\right)p' \approx 2\frac{\partial}{\partial x}\left(ac_s^2\frac{\partial^2 p'}{\partial x^2}-\frac{b}{c_s}p'\frac{\partial p'}{\partial x}\right), \tag{5.30}$$

where a and b are constant coefficients, which account for the dissipation (both viscosity and thermal conductivity) and nonlinearity:

$$a=2^{-1}c_s^{-3}[4\nu/3+\chi V(c_V^{-1}-c_P^{-1})], \quad b=\frac{c_s^2}{2V^2}\left(\frac{\partial^2 V}{\partial p^2}\right)_s. \tag{5.31}$$

Therefore, we see that Eq. (5.30) turns to an equivalence if the following equation is satisfied:

$$\frac{\partial p'}{\partial t}+c_s\frac{\partial p'}{\partial x}+bp'\frac{\partial p'}{\partial x},= ac_s^3\frac{\partial^2 p'}{\partial x^2}. \tag{5.32}$$

Finally, we demonstrate that this equation can be reduced to a well-known canonic Burgers equation. To do so we introduce new independent variables t and $\xi = x - c_s t$ and a new unknown function $P(\xi, t) = bp'(x, t)$. Then Eq. (5.32) is transformed to

$$\frac{\partial P}{\partial t}+P\frac{\partial P}{\partial \xi}=\kappa\frac{\partial^2 P}{\partial \xi^2}, \quad \kappa = ac_s^3, \tag{5.33}$$

which is the **Burgers equation**. It is worthwhile to note that many other phenomena can be described by means of the Burgers equation (Whitham 1974; Gurbatov et al. 1983), which makes the analysis of its solution much more widely applicable than the specific HD problem considered in this section.

5.2.2 The Korteweg–de Vries Equation

Besides nonlinearity and dissipation, wave propagation in a plasma may be affected by dispersion effects, i.e., the dependence of the wave phase velocity on the wavenumber. Let us consider the role that they play, taking nonlinear waves in a cold magnetized fully ionized plasma, with $\beta_{e,i} = 8\pi n_{e,i}T_{e,i}/B^2 \ll m_e/m_i$ (which implies either very strong magnetic field or very cold and/or tenuous plasma), as an example. We use the set of equations for two-fluid MHD; see Chap. 1, Eqs. (1.69) and (1.70), and Maxwell equations:

$$n_i m_i\left[\frac{\partial \boldsymbol{u}^{(i)}}{\partial t}+(\boldsymbol{u}^{(i)}\cdot\nabla)\boldsymbol{u}^{(i)}\right]=en_i\left(\boldsymbol{E}+\frac{1}{c}\boldsymbol{u}^{(i)}\times\boldsymbol{B}\right)-n_i m_i\frac{(\boldsymbol{u}^{(i)}-\boldsymbol{u}^{(e)})}{\tau_{ie}}, \tag{5.34a}$$

$$n_e m_e \left[\frac{\partial \boldsymbol{u}^{(e)}}{\partial t} + (\boldsymbol{u}^{(e)} \cdot \nabla)\boldsymbol{u}^{(e)}\right] = -e n_e \left(\boldsymbol{E} + \frac{1}{c}\boldsymbol{u}^{(e)} \times \boldsymbol{B}\right) - n_e m_e \frac{(\boldsymbol{u}^{(e)} - \boldsymbol{u}^{(i)})}{\tau_{ei}}, \tag{5.34b}$$

$$\frac{\partial n_{i,e}}{\partial t} + \nabla \cdot n_{i,e}\boldsymbol{u}^{(i,e)} = 0, \tag{5.34c}$$

$$\nabla \times \boldsymbol{B} = \frac{4\pi}{c}\boldsymbol{j}, \qquad \boldsymbol{j} = e(n_i \boldsymbol{u}^{(i)} - n_e \boldsymbol{u}^{(e)}), \tag{5.34d}$$

$$\nabla \times \boldsymbol{E} = -\frac{1}{c}\frac{\partial \boldsymbol{B}}{\partial t}, \qquad \nabla \cdot \boldsymbol{B} = 0. \tag{5.34e}$$

For processes whose frequencies satisfy the condition $\omega \ll \omega_{\mathrm{pi}}$, we may ignore the separation of charges and take $n_e = n_i = n$. Further we introduce the mass velocity $\boldsymbol{u} \approx \boldsymbol{u}^{(i)} + (m_e/m_i)\boldsymbol{u}^{(e)}$. Adding Eqs. (5.34a) and (5.34b) term by term, using Eq. (5.34d), and ignoring terms of order m_e/m_i, we obtain, like in Sect. 1.3.4, the one-fluid plasma motion equation

$$\frac{\partial \boldsymbol{u}}{\partial t} + (\boldsymbol{u} \cdot \nabla)\boldsymbol{u} = \frac{1}{4\pi n m_i}(\nabla \times \boldsymbol{B}) \times \boldsymbol{B}. \tag{5.35}$$

We then divide Eq. (5.34a) by m_i and Eq. (5.34b) by m_e, add up the equations obtained, and take into account the following approximate equalities (see Sect. 1.3.4):

$$\frac{\boldsymbol{u}^{(i)}}{m_i} + \frac{\boldsymbol{u}^{(e)}}{m_e} \approx \frac{\boldsymbol{u} - \boldsymbol{j}/en}{m_e}, \qquad \boldsymbol{u}^{(e)} \approx \boldsymbol{u} - \frac{\boldsymbol{j}}{en},$$

where $\boldsymbol{j} = en(\boldsymbol{u}^{(i)} - \boldsymbol{u}^{(e)})$ to obtain finally generalized Ohm's law in the form

$$\boldsymbol{E} + \frac{1}{c}\boldsymbol{u} \times \boldsymbol{B} = \frac{\boldsymbol{j}}{\sigma} + \frac{1}{n_i e c}\boldsymbol{j} \times \boldsymbol{B} + \frac{m_e}{e^2}\left[\frac{\partial}{\partial t}\frac{\boldsymbol{j}}{n} + (\boldsymbol{u} \cdot \nabla)\frac{\boldsymbol{j}}{n} + \frac{1}{n}(\boldsymbol{j} \cdot \nabla)\boldsymbol{u} - \frac{1}{n}(\boldsymbol{j} \cdot \nabla)\frac{\boldsymbol{j}}{n}\right]. \tag{5.36}$$

Unlike Sect. 1.3.4 we have taken into account here the small terms of the order of m_e/m_i. They lead to the dispersion corrections and are gathered in the square brackets of Eq. (5.36). But working in the cold plasma approximation, we omit all the terms containing the pressure and viscosity from ee and ii collisions of the order of m_e/m_i. Only the interaction between two different components, e and i, is taken into account. No terms of the order of $(m_e/m_i)^{1/2}$ are present here.

Using Eqs. (5.34d), (5.34e), and (5.36), we obtain an equation for the magnetic field:

$$\frac{\partial \boldsymbol{B}}{\partial t} = \nabla \times (\boldsymbol{u} \times \boldsymbol{B}) + \nu_m \Delta \boldsymbol{B} - \frac{c}{4\pi n e} \nabla \times [(\nabla \times \boldsymbol{B}) \times \boldsymbol{B}] - \frac{m_e c}{e^2} \nabla \times \left[\frac{\partial}{\partial t} \frac{\boldsymbol{j}}{n} + (\boldsymbol{u} \cdot \nabla) \frac{\boldsymbol{j}}{n} + \frac{1}{n} (\boldsymbol{j} \cdot \nabla) \boldsymbol{u} \right) - \frac{1}{en} (\boldsymbol{j} \cdot \nabla) \frac{\boldsymbol{j}}{n} \right]. \tag{5.37}$$

To study weakly nonlinear motions in a plasma, taking into account the dispersion and dissipation, we first consider the linearized set of equations. Adopting that $\boldsymbol{b} = \boldsymbol{B} - \boldsymbol{B}_0$ and $\boldsymbol{u}$ are small and proportional to $\exp(-i\omega t + i\boldsymbol{k} \cdot \boldsymbol{r})$ and selecting the Ox axis to lie along $\boldsymbol{k}$ and $\boldsymbol{B}_0$ to belong the xz plane, we obtain a set of algebraic equations for b_y and b_z, having excluded $\boldsymbol{u}$:

$$b_y \left[\omega^2 \left(1 + \frac{c^2 k^2}{\omega_{\mathrm{pe}}^2} \right) - (\boldsymbol{k} \cdot \boldsymbol{v}_{\mathrm{A}})^2 - i\nu_m k^2 \right] + b_z \frac{i\omega\, ck(\boldsymbol{k} \cdot \boldsymbol{v}_{\mathrm{A}})}{\omega_{\mathrm{pi}}} = 0, \tag{5.38a}$$

$$- b_y \frac{i\omega\, ck(\boldsymbol{k} \cdot \boldsymbol{v}_{\mathrm{A}})}{\omega_{\mathrm{pi}}} + b_z \left[\omega^2 \left(1 + \frac{c^2 k^2}{\omega_{\mathrm{pe}}^2} \right) - k^2 v^2 - i\nu_m k^2 \right] = 0. \tag{5.38b}$$

As $\omega_{\mathrm{pe}},\ \omega_{\mathrm{pi}} \to \infty$ and $\nu_m \to 0$, we get the dispersion laws $\omega = \pm v_{\mathrm{A}} k \cos\theta$ and $\omega = \pm v_{\mathrm{A}} k$ for the Alfvén and fast magnetosonic waves, respectively. Below, we consider only the nonlinear generalization of the fast magnetosonic wave. In the approximation

$$ck \ll \omega_{\mathrm{pi}}, \qquad \nu_m k^2 \ll \omega, \qquad \theta \gg ck/\omega_{\mathrm{pi}}, \tag{5.39}$$

we find the dispersion relation

$$\omega(k) = v_A k - \mu k^3 - \frac{1}{2} i\nu_m k^2, \quad \text{where} \quad \mu = v_{\mathrm{A}} \frac{c^2}{2\omega_{\mathrm{pi}}^2} \left(\frac{m_e}{m_i} - \cot^2\theta \right), \tag{5.40}$$

where μk^3 and $\nu_m k^2$ are small corrections. This means that the scales of motion are relatively large and that the longitudinal propagation is excluded.

We now obtain a closed equation for the magnetic field component b_z. Note that $b_x = 0$ owing $\nabla \cdot \boldsymbol{b} = 0$, and $b_y \ll b_z$ in a magnetosonic wave owing to the smallness of the dispersion correction according to Eq. (5.38a). Therefore, b_z represents the main component of the wave magnetic field. Multiplying Eq. (5.40) by b_z, we then write the equation obtained in the form

$$[-i\omega + v_{\mathrm{A}} ik + \mu(ik)^3] b_z = \frac{1}{2} \nu_m (ik)^2 b_z.$$

On transforming to the space–time representation, we have

$$\frac{\partial b_z}{\partial t} + v_{\mathrm{A}} \frac{\partial b_z}{\partial x} + \mu \frac{\partial^3 b_z}{\partial x^3} = \frac{1}{2} \nu_m \frac{\partial^2 b_z}{\partial x^2}. \tag{5.41}$$

This equation describes a wave propagating in a positive direction of the Ox-axes. It, however, does not include any nonlinearity yet. To account nonlinear terms of the lowest order (quadratic nonlinearity), the term $\nabla \times (\boldsymbol{u} \times \boldsymbol{B})$ must be calculated more accurately. Specifically, it will add the term $-\boldsymbol{e}_z \cdot \nabla \times (\boldsymbol{u}^{(1)} \times \boldsymbol{b} + \boldsymbol{u}^{(2)} \times \boldsymbol{B}_0)$ to lhs of Eq. (5.41), where $\boldsymbol{u}^{(1)}$ and $\boldsymbol{u}^{(2)}$ are corrections, proportional to b_z and b_z^2, respectively.

We turn to Eq. (5.35) and write it to the accuracy of the second-order terms as

$$\frac{\partial(\boldsymbol{u}^{(1)} + \boldsymbol{u}^{(2)})}{\partial t} = \frac{1}{4\pi n m_i} \left[\left(\boldsymbol{e}_x \times \frac{\partial \boldsymbol{b}}{\partial x} \right) \times \boldsymbol{B}_0 + \left(\boldsymbol{e}_x \times \frac{\partial \boldsymbol{b}}{\partial x} \right) \times \boldsymbol{b} \right] - u_x^{(1)} \frac{\partial \boldsymbol{u}^{(1)}}{\partial x}. \tag{5.42}$$

Making replacement

$$\partial/\partial t \approx -v_\mathrm{A} \partial/\partial x, \tag{5.43}$$

which follows from Eqs. (5.40) and (5.41) when the dispersion and dissipation are discarded, we find

$$\boldsymbol{u}^{(1)} = -\frac{(\boldsymbol{e}_x \times \boldsymbol{b}) \times \boldsymbol{e}_\parallel}{\sqrt{4\pi n m_i}},$$

where $\boldsymbol{e}_\parallel = \boldsymbol{B}_0/B_0$. In calculating $\boldsymbol{u}^{(2)}$, we ignore the small component b_y:

$$\boldsymbol{u}^{(2)} = [\boldsymbol{e}_x(1 + \sin^2\theta) - \boldsymbol{e}_z \sin\theta\cos\theta] \frac{b_z^2}{2B_0}.$$

Having calculated $\nabla \times (\boldsymbol{u}^{(1)} \times \boldsymbol{b} + \boldsymbol{u}^{(2)} \times \boldsymbol{B}_0)$ and adding it to the rhs of Eq. (5.42), we get a nonlinear equation instead of Eq. (5.41):

$$\frac{\partial b_z}{\partial t} + v_\mathrm{A} \frac{\partial b_z}{\partial x} + \frac{4 v_\mathrm{A} \sin\theta}{B_0} b_z \frac{\partial b_z}{\partial x} + \mu \frac{\partial^3 b_z}{\partial x^3} = \kappa \frac{\partial^2 b_z}{\partial x^2}, \tag{5.44}$$

where we have introduced $\kappa = \nu_m/2$ for simplicity. This equation can be further simplified by introducing a new independent variable $\xi = x - v_\mathrm{A} t$ and a new unknown function $w(\xi, t) = 4 v_\mathrm{A} \sin\theta b_z/B_0$:

$$\frac{\partial w}{\partial t} + w \frac{\partial w}{\partial \xi} + \mu \frac{\partial^3 w}{\partial \xi^3} = \kappa \frac{\partial^2 w}{\partial \xi^2}. \tag{5.45}$$

In the absence of dispersion ($\mu = 0$), this equation receives the form of the Burgers equation:

$$\frac{\partial w}{\partial t} + w \frac{\partial w}{\partial \xi} = \kappa \frac{\partial^2 w}{\partial \xi^2}, \tag{5.46}$$

which was obtained in previous section in the frame of the standard HD. Here, however, both w and ξ depend on magnetic field, so the meanings of w and ξ are different from those in Sect. 5.2.1.

If the dissipation is absent ($\kappa = 0$) then we obtain the **Korteweg–de Vries (KdV) equation**

$$\frac{\partial w}{\partial t} + w\frac{\partial w}{\partial \xi} + \mu\frac{\partial^3 w}{\partial \xi^3} = 0. \tag{5.47}$$

It was first obtained by Korteweg and de Vries (1895) for gravity waves in a fluid confined in a channel with finite depth. However, it has been found during the last few decades that the applicability of the KdV equation is much wider. Besides the waves in fluids, it describes nonlinear waves in plasmas under various conditions, waves in anharmonic crystal lattices, and may be applied to quantum theory as well. When both dispersion and dissipation are present, full Eq. (5.45) can be referred to as **Korteweg–de Vries–Burgers (KdVB) equation**.

The KdV equation derived above describes nonlinear waves in a cold plasma, in which $c_s^2 \ll v_\mathrm{A}^2$. If the thermal energy and magnetic energy are of the same order of magnitude, the linear and nonlinear waves damp rapidly as a result of resonant interaction with thermal ions (Landau damping) except for transverse and longitudinal (relative to magnetic field) directions of propagation. Transverse propagation is described by KdV equation as before, while the longitudinal propagation is described by another equation. It is called the nonlinear Shrödinger's equation with the derivative in cubic term:

$$\frac{\partial u}{\partial \tau} + i\frac{\partial^2 u}{\partial \xi^2} + \frac{\partial}{\partial \xi}(u|u|^2) = 0. \tag{5.48}$$

Here $\tau = \omega_{\mathrm{Bi}}t/2$, $\xi = x/r_A - \omega_{\mathrm{Bi}}t$, $u = (b_y + ib_z)/B_0(1-\beta)^{1/2}$, $\omega_{\mathrm{Bi}} = eB_0/m_i c$, $r_A = v_\mathrm{A}/\omega_{\mathrm{Bi}}$, and $\beta = c_s^2/v_\mathrm{A}^2$. The condition $u \ll 1$ must be carried out; see Vainshtein et al. (1993) for greater detail.

5.2.3 KdV Solitons

On the basis of KdV equation, we now consider a few types of nonlinear waves in a cold plasma, ignoring dissipation. We concentrate on stationary waves, i.e., perturbations depending on coordinate and time only via a combination $x - u_w t$, where $u_w = \mathrm{const}$ is the wave velocity. These waves do not change their shape during propagation, and are, thus, distinct types of nonlinear perturbations. They exist due to interplay and balance of two effects: nonlinearity, acting toward persistent deformation of the wave front and to its eventual "overturning" (see Sect. 5.1), and dispersion, which causes spreading of the wave packet. These two effects may balance each other and so result in formation of stationary wave structures.

For the mathematical analysis of stationary nonlinear waves in the absence of dissipation, we turn to Eq. (5.44), assuming $\kappa = 0$, and introduce $h(x,t) = 4v_\mathrm{A}\sin\theta\, b_z/B_0$:

$$\frac{\partial h}{\partial t} + v_\mathrm{A}\frac{\partial h}{\partial x} + h\frac{\partial h}{\partial x} + \mu\frac{\partial^3 h}{\partial x^3} = 0. \tag{5.49}$$

We seek a solution in the form $h(x - u_w t)$. Introducing a new independent variable $\xi = x - u_w t$, we transform Eq. (5.49) to the form

$$(-\Delta u\, h + \frac{1}{2}h^2 + \mu h'')' = 0, \qquad \Delta u = u_w - v_\mathrm{A}, \tag{5.50}$$

where the prime indicates the derivative over ξ. Integrating Eq. (5.50) we obtain an equation similar to one of a particle motion in the classical mechanics:

$$\mu h'' = K + \Delta u\, h - \frac{1}{2}h^2 = -\frac{\partial W}{\partial h}, \tag{5.51}$$

where K is the constant of integration and

$$W(h) = \frac{1}{6}h^3 - \frac{1}{2}\Delta u\, h^2 - Kh \tag{5.52}$$

is the "potential energy" of the "particle," which depends on its "generalized coordinate" h, while ξ plays the role of time. The constant K may easily be taken equal to zero by the replacement $h \to h + h_0$. This replacement in Eq. (5.49) means a transition to the reference system moving with a speed $v_\mathrm{A} + h_0$. In what follows we take $K = 0$.

Exploring the mechanical analogy, it is easy to perform the integration. Using the integral of the "energy" $\mu h'^2/2 + W(h) = E = \mathrm{const}$, we write a solution of Eq. (5.51) in the quadrature:

$$\int [P(h)]^{-1/2} \mathrm{d}h = \pm \frac{\xi}{(3\mu)^{1/2}}, \tag{5.53}$$

where

$$P(h) = 6E + 3\Delta u\, h^2 - h^3 \tag{5.54}$$

is a cubic polynomial. Solution (5.53) makes physical sense only for $P(h) \geq 0$ and finite h; moreover, the condition based on KdV equation applicability is even more stringent: it correctly describes nonlinear waves in a cold plasma only when $|h| \ll v_\mathrm{A}$. Then, in Eq. (5.53), we ignore the integration constant, which can always be done by appropriate choice of the origin of the coordinate ξ. The solution is written for $\mu > 0$, which, in accordance with Eq. (5.40), corresponds to a negative correction to the linear dispersion law.

We consider here the case $E = 0$ when integral (5.53) can be expressed in terms of elementary functions. If $h \geq 0$, then the condition $P(h) = h^2(3\Delta u - h) \geq 0$ requires $\Delta u > 0$ and $0 \leq h \leq 3\Delta u$. In this case,

$$\int [P(h)]^{-1/2} \mathrm{d}h = \frac{1}{\sqrt{3\Delta u}} \ln \frac{\sqrt{3\Delta u} + \sqrt{3\Delta u + h}}{\sqrt{3\Delta u} - \sqrt{3\Delta u - h}}$$

and the solution takes the form

$$h(x,t) = 3\Delta u \cosh^{-2}[(\Delta u/4\mu)^{1/2}(x - u_w t)]. \tag{5.55}$$

This solution corresponds to a solitary wave—a **soliton**. In this case, it represents a "hump" of the magnetic field, rising above the background by the value $b_z = B_z - B_0 = B_0 h/4v_\mathrm{A}\sin\theta$ and propagating with the speed $u_w = v_\mathrm{A} + \Delta u$. The perturbations in the plasma velocity and density depend on the perturbation in the magnetic field through MHD formulae (5.34c) and (5.35). The quantity Δu, which is the soliton velocity excess compared with the linear magnetoacoustic wave velocity v_A, is related to the amplitude h_0 by

$$h_0 = 3\Delta u. \tag{5.56}$$

The soliton width

$$\delta = 2\sqrt{\mu/\Delta u} = 2\sqrt{3\mu/h_0} \tag{5.57}$$

is inversely proportional to the square root of the amplitude. For a soliton propagating across the magnetic field ($\alpha = \pi/2$),

$$\delta = \frac{c}{\omega_\mathrm{pe}}\left(\frac{3B_0}{2b_0}\right)^{1/2},$$

where b_0 is the height of the magnetic "hump" and the plasma skin scale $a_D = c/\omega_\mathrm{pe}$ determines the typical length of dispersion.

For $h < 0$, the condition $P(h) \geq 0$ is satisfied when $h \leq -3|\Delta u|$. In this case,

$$\int [P(h)]^{-1/2}\mathrm{d}h = -\frac{2}{\sqrt{3\Delta u}}\arctan(|h|/3\Delta u)^{1/2}, \tag{5.58}$$

and the soliton takes the form

$$h(x,t) = -3\Delta u \tan^2[(\Delta u/4\mu)^{1/2}(x - u_w t)].$$

This solution is unbounded and so unphysical.

We now construct a soliton for a positive dispersion correction ($\mu < 0$). Returning to Eq. (5.49), we make the change $\mu = -|\mu|$ and $h = -\overline{h}$:

$$-\frac{\partial \overline{h}}{\partial t} - v_\mathrm{A}\frac{\partial \overline{h}}{\partial x} + \overline{h}\frac{\partial \overline{h}}{\partial x} + |\mu|\frac{\partial^3 \overline{h}}{\partial x^3} = 0.$$

We again seek a solution in the form $\overline{h}(x - u_w t)$ and obtain Eq. (5.50) in the form

$$\left(-\Delta u\,\overline{h} + \frac{1}{2}\overline{h}^2 + |\mu|\overline{h}''\right)' = 0, \tag{5.59}$$

where $\Delta u = v_\mathrm{A} - u_w$ now. The problem is, thus, reduced to the previous case, $\mu > 0$, and the solution is described by the function

$$h(x,t) = -3\Delta u \cosh^{-2}\left[(\Delta u/4|\mu|)^{1/2}(x - u_w t)\right], \tag{5.60}$$

where $\Delta u > 0$ and $h \leq 0$. This soliton represents a magnetic well (i.e., a rarefaction soliton), and is slow; its velocity $u_w = v_\mathrm{A} - \Delta u$ is less than that of a small-amplitude magnetoacoustic wave.

5.3 Discontinuities in the Plasma

The physical picture of the magnetosonic wave leading edge sharpening and the discontinuity formation is rather typical for many kinds of the fluid motions in astrophysical objects. In fact, the discontinuities are a natural outcome of the ideal (dissipation-free) MHD equations. The discontinuities can result from the evolution of originally smooth excitation or from singular initial or boundary conditions (recall a piston instantly starting to move, as a vivid example). In the reality, all the discontinuities have a finite nonzero width, defined by dissipative processes. This width, however, is often small compared with other characteristic scales. Thus, if one is not specifically interested in the processes inside the discontinuity, it can be treated as infinitely narrow layer.

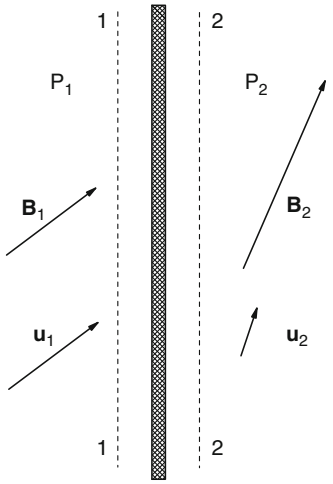

Figure 5.2: Local plane of an MHD discontinuity.

5.3.1 Local Properties and Classification

The local properties of stationary discontinuities can be investigated based on the conservation laws of basic physical measures—mass, momentum, and energy—supplemented by the boundary conditions for electromagnetic vectors. We adopt that the discontinuity is locally plane and select a reference frame with one axes directed along the normal to the plane (Fig. 5.2). Consider two additional planes, 1-1 and 2-2, located at both sides of the discontinuity at positions, where the dissipative processes and so dissipative terms in the equations can be discarded, even though they can be essential inside the transition layer (somewhere between planes 1-1 and 2-2), where MHD parameters have large gradients.

The conservation laws applied to a stationary discontinuity give rise to equations

$$\delta(i_\alpha n_\alpha) = 0, \qquad \delta(P_{\alpha\beta} n_\beta) = 0, \quad \delta(q_\alpha n_\alpha) = 0, \tag{5.61}$$

where symbol δ denotes the jump of the corresponding parameter in parentheses at the transition from plane 2-2 to 1-1, e.g., $\delta i_n = i_{n2} - i_{n1}$; $\boldsymbol{n}$ is the unit vector normal to the discontinuity surface; $\boldsymbol{i}$, $P_{\alpha\beta}$, and $\boldsymbol{q}$ are the flux densities of the mass, momentum, and energy, respectively:

$$\boldsymbol{i} = \rho \boldsymbol{u}, \qquad P_{\alpha\beta} = p\delta_{\alpha\beta} + \rho u_\alpha u_\beta - \frac{1}{4\pi} B_\alpha B_\beta + \frac{1}{8\pi} B^2 \delta_{\alpha\beta}, \tag{5.62a}$$

$$\boldsymbol{q} = \rho \boldsymbol{u} \left(\frac{u^2}{2} + \epsilon + \frac{p}{\rho} \right) + \frac{1}{4\pi} \boldsymbol{B} \times [\boldsymbol{u} \times \boldsymbol{B}]. \tag{5.62b}$$

Here, in the momentum and energy fluxes, we hold both mechanical and electromagnetic terms, although entirely neglect the dissipation. In the expression for the flux density of energy the term ϵ denotes the specific (i.e., per unit mass) internal energy of the medium, while the last term, $\boldsymbol{\gamma} = c\boldsymbol{E} \times \boldsymbol{B}/4\pi$, is the Poynting vector, where expression (2.25) for the electric field in a moving fluid without dissipation has been used. Likewise, the magnetic terms in the momentum flux density represent the magnetic part of the Maxwell tension tensor.

Along with conservation laws (5.61) boundary conditions for the field vectors must be fulfilled at the interface: continuity of the normal $\boldsymbol{B}$ component and tangential $\boldsymbol{E} = -\boldsymbol{u} \times \boldsymbol{B}/c$ component, i.e.,

$$\delta(B_\alpha n_\alpha) = 0, \qquad \delta(\boldsymbol{u} B_\alpha n_\alpha - \boldsymbol{B} u_\alpha n_\alpha) = 0. \tag{5.63}$$

Substitution of expressions (5.62) into conservation laws (5.61) and use of boundary conditions (5.63) yield four equations for the MHD parameter jumps at the interface:

$$i_n \delta \left(\epsilon + pV + \frac{i_n^2 V^2}{2} + \frac{u_\tau^2}{2} + \frac{V B_\tau^2}{4\pi} \right) - \frac{B_n}{4\pi} \delta(\boldsymbol{B}_\tau \cdot \boldsymbol{u}_\tau) = 0, \tag{5.64a}$$

$$\delta p + i_n^2 \delta V + \frac{\delta B_\tau^2}{8\pi} = 0, \tag{5.64b}$$

$$i_n \delta \boldsymbol{u}_\tau - \frac{B_n}{4\pi} \delta \boldsymbol{B}_\tau = 0, \tag{5.64c}$$

$$B_n \delta \boldsymbol{u}_\tau - i_n \delta(V \boldsymbol{B}_\tau) = 0. \tag{5.64d}$$

Here indices n and τ denote the normal and tangential components to the discontinuity plane, respectively; $V = 1/\rho$ is the specific volume. Equalities

(5.64) compose complete set of conditions at MHD discontinuities. We must note that they remain valid in collisionless plasma with isotropic pressure if local values of thermodynamic and hydrodynamic parameters can be defined consistently, and so they are more general than the set of MHD equations.

Let us consider basic properties of the MHD discontinuities based on jump conditions (5.64):

1. $i_n = 0$, $B_n \neq 0$ (**contact discontinuity**); here $\delta \boldsymbol{u} = 0$, $\delta \boldsymbol{B} = 0$, and $\delta p = 0$. Other parameters, the density, the temperature, chemical composition, and other thermodynamic parameters can have arbitrary jumps. Overall, the contact surface is a rest boundary of two fluids when they are in mechanical equilibrium.

2. $i_n \neq 0$, $\delta V = 0$ (**Alfvén or rotational discontinuity**). Equations (5.64c) and (5.64d) yield

$$i_n = \pm \frac{|B_n|}{\sqrt{4\pi V}}, \quad \delta \boldsymbol{u}_\tau = \mp \sqrt{\frac{V}{4\pi}} \delta \boldsymbol{B}_\tau. \tag{5.65}$$

   After regrouping terms in Eq. (5.64a), cancelation of nonzero factor $i_n \neq 0$ results in

$$\delta \epsilon + V \delta \left(p + \frac{B_\tau^2}{8\pi} \right) + \frac{1}{2} \left(\delta \boldsymbol{u}_\tau \pm \sqrt{\frac{V}{4\pi}} \delta \boldsymbol{B}_\tau \right)^2 = 0. \tag{5.66}$$

   The third term is zero here because of Eq. (5.65); the second one is also zero because of Eq. (5.64b) with $\delta V = 0$; thus, from Eq. (5.66) follows $\delta \epsilon = 0$. Recall that any thermodynamic parameter of the uniform fluid can be expressed as a single-valued function of two independent variables, ϵ and V. Therefore, continuity of these two parameters provides that all thermodynamic parameters, including kinematic pressure p, are continuous. Then, from Eq. (5.64b) follows $\delta B_\tau^2 = 0$, i.e., the absolute value of the magnetic field is constant through the Alfvén discontinuity like in the Alfvén simple wave. However, $\delta \boldsymbol{B}_\tau \neq 0$, which means that the magnetic field vector $\boldsymbol{B}$ rotates by arbitrary angle at the Alfvén discontinuity.

3. $i_n = 0$, $B_n = 0$ (**tangential discontinuity**); now the fluid velocity and the magnetic field both have tangential components only; they can have arbitrary jumps. Thermodynamic parameters of the fluid can also display jumps with a constraint that the full pressure is continuous at the interface:

$$\delta \left(p + \frac{B_\tau^2}{8\pi} \right) = 0. \tag{5.67}$$

If the fluid velocity is continuous through the interface, i.e., the two fluids are at rest relative to each other, then the tangential discontinuity becomes a variant of the contact discontinuity with full pressure balance (5.67) fulfilled. In the magnetically dominated plasmas ($\beta \ll 1$, see Sect. 2.3.3), e.g., in stellar coronae, the tangential discontinuities are often called the **current sheets**, where an efficient release, transformation, and dissipation of stored magnetic energy can occur via a so-called **magnetic reconnection**—a highly important process driving eruptive and flaring phenomena in the stellar/solar coronae, heliosphere, planetary magnetospheres, and other cosmic objects.

5.3.2 Magnetic Reconnection

The MHD discontinuities considered here are stationary plasma objects. However, it is necessary to keep in mind that the discontinuities and other magneto-plasma structures are often unstable relative to small perturbations, as considered in greater detail in Chap. 6. In such a case the unstable configuration evolves to different states over finite time. Moreover, these idealized discontinuities are infinitely narrow infinite planes with some properties abruptly changing at the interface between the two fluid volumes. However, it is difficult to create an infinite interface in a reality. Indeed, a discontinuity is likely to form, e.g., as a result of nonlinear evolution of a reasonably strong propagating wave or in a collision of two plasma clouds with differently oriented magnetic fields. What kind of the discontinuity is formed differs, other conditions being equal, for high- and low-β fluids. Overall, if the wave or fluid flow is kinetically dominated, while the magnetic field plays a secondary (passive) role, $\beta \gg 1$, a shock wave is likely to eventually form; see Sect. 5.4.

For a magnetically dominated fluid, $\beta \ll 1$, the available magnetic field is strong enough to stop an incident fluid flow, which can, however, bring differently oriented magnetic fields into a close contact, so a tangential discontinuity will often form in the interaction interface between the inflow and the magnetic "wall." However, since the interaction region is finite, the interface will occupy a finite area; such a finite tangential discontinuity is often called a "current sheet" or "current layer." Apparently, having a strong energy release in the low-β case requires that the magnetic energy (that is supposed to make a dominant contribution to the fluid free energy) is somehow dissipated into other kinds of the energy (kinetic, thermal, nonthermal, and electromagnetic). The magnetic energy dissipation, as we pointed out in Sect. 2.3.2, requires highly nonuniform regions to be present in the fluid such as the current sheets, which, thus, play a highly important role in the energy releases in the low-β plasmas.

Physics of current sheets and magnetic reconnection is discussed in detail in many review papers and monographs (Syrovatskii 1981; Priest and Forbes 2000; Aschwanden 2005) as well as textbooks (Benz 2002; Somov 2006, 2007); below we only give the main guidelines, definitions, and reconnection models,

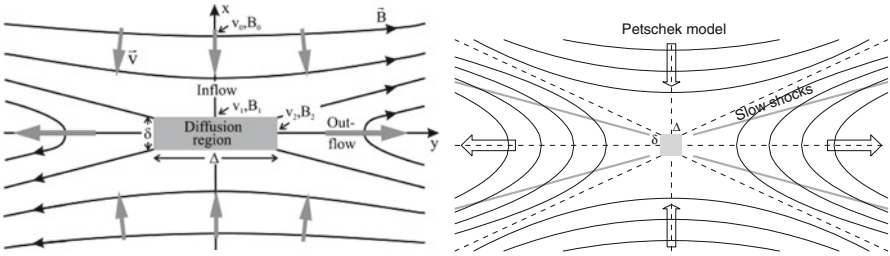

Figure 5.3: Conceptual view of a stationary (Sweet–Parker) magnetic reconnection in a current sheet, *left*. Petschek reconnection model, *right* (Aschwanden 2005).

while the reader has to consult the cited sources for a more detailed information. A classical view, Fig. 5.3, of the magnetic reconnection in a current sheet includes *fluid inflows* (driven by unspecified external source) bringing the oppositely directed magnetic field lines in a close contact. As soon as the oppositely directed field lines approach each other closer and closer, the magnetic field gradient increases accordingly and, at a certain stage, becomes strong enough for the magnetic field diffusion, see Sect. 2.3.1, to affect the field structure substantially. The plasma volume where the magnetic field diffusion plays an important role is called the **diffusion region**. In the assumed stationary conditions, the plasma inflows must be compensated by some outflows maintaining the stationary distributions of the plasma density and pressure.

Given that the magnetic field lines are oppositely directed at both sides of the current sheet, there is a *null layer* where the magnetic field is zero somewhere in the middle of the diffusion region. The pressure balance through the diffusion region requires that

$$\frac{B_1^2}{8\pi} + p_1 = p_{\rm nl} = \frac{B_2^2}{8\pi} + p_2, \tag{5.68}$$

where the magnetic fields $B_{1,2}$ and pressures $p_{1,2}$ are shown in Fig. 5.3, while $p_{\rm nl}$ is the gas pressure at the null layer. This enhanced pressure drives the outflows along the null layer. The magnetic field lines have a greatly enhanced curvature where the outflows are launched from the diffusion region, which implies an enhanced magnetic tension force; see Sect. 2.2.1. This magnetic tension acts toward relaxation of the magnetic field lines into less curved configuration suggesting an efficient mechanism of the magnetic-to-kinetic energy conversion due to **slingshot effect**. Electric field associated with the magnetic field in a moving fluid according to Eq. (2.19) is perpendicular to the plane of the picture; it produces an electric current $j_{\rm nl}$ in the null layer in the same direction according to Ohm's law:

$$E_0 = \frac{v_1 B_1}{c} = \frac{v_2 B_2}{c} = \frac{j_{\rm nl}}{\sigma}, \tag{5.69}$$

which justifies the introduced term "current sheet."

A classical Sweet–Parker reconnection model adopts that the current sheet width Δ is much larger than its thickness δ, Fig. 5.3. A number of very general conclusions can be drawn for this case. Let us start with estimating the outflow plasma velocity in a stationary case ($\partial/\partial t = 0$) from Eq. (2.13a). In the outflow region (i.e., outside the diffusion region) the plasma β is small, so we can neglect the pressure term; then, neglecting the viscosity (assuming the Reynolds number is large at the outflow region) and the external force $\boldsymbol{f}$, we reduce Eq. (2.13a) to a simplified form $\rho(\boldsymbol{v}_2\cdot\nabla)\boldsymbol{v}_2 \approx [\nabla \times \boldsymbol{B}] \times \boldsymbol{B}/(4\pi)$; for an order of magnitude estimate, we replace $\nabla \to 1/L$ at both sides of the equality, which immediately yields $v_2 \sim v_{\rm A}$.

Then, the mass flow continuity yields $\rho_1 v_1 \Delta = \rho_2 v_2 \delta$, which implies $v_1 \sim v_2 \delta/\Delta$ if $\rho_1 \sim \rho_2$. Therefore, within the adopted assumption that $\Delta \gg \delta$, the **reconnection rate** M_r defined as the inflow Mach number, i.e., the ratio of the inflow speed $v_0 \approx v_1$ to the Alfvén speed in the inflow region (outside the diffusion region)

$$M_r = \frac{v_0}{v_{\rm A}} \sim \frac{\delta}{\Delta} \ll 1, \tag{5.70}$$

is small.

The thickness of the current sheet is easy to estimate from the condition that the local Reynolds number, $v_1\delta/\nu_m$, is of the order of unity; thus, $\delta \sim \nu_m/v_1$. Using Eq. (1.150) for the magnetic diffusivity and assuming a very modest inflow speed of 10^2 cm/s, we obtain $\delta \sim 1$ m; higher inflow speed would result in a narrower current sheet. Substituting $v_1 \sim v_{\rm A}\delta/\Delta$ obtained above into $v_1\delta/\nu_m \approx 1$ and solving it for δ we find $\delta \approx \sqrt{\nu_m \Delta/v_{\rm A}}$, which yields

$$\frac{v_0}{v_{\rm A}} \sim \frac{\delta}{\Delta} \approx \sqrt{\frac{\nu_m}{v_{\rm A}\Delta}} = \frac{1}{\sqrt{\mathcal{L}}}, \tag{5.71}$$

where $\mathcal{L}$ is the **Lundquist number** defined as the magnetic Reynolds number calculated for the fluid velocity equal to the Alfvén speed. The inequality $\delta \ll \Delta$ implies that the Sweet–Parker current sheet represents a highly anisotropic structure with the thickness much smaller than the width if the corresponding Lundquist number is large.

Finally, it is easy to estimate the magnetic energy release rate $\mathrm{d}\mathcal{E}_m/\mathrm{d}t$ as the fluid kinetic energy escaping with the outflow through the side boundary of the current sheet. The kinetic energy density $\rho v_2^2/2 \approx B_2^2/(8\pi)$ is transferred through the side area $S = \Delta \cdot \delta$ with the velocity $v_2 \sim v_{\rm A}$; thus

$$\frac{\mathrm{d}\mathcal{E}_m}{\mathrm{d}t} \approx \frac{B^2}{8\pi}\Delta \cdot \delta \cdot v_{\rm A} \approx \frac{B^2}{8\pi}\Delta^2 \cdot v_1 \approx \frac{B^2}{8\pi}\frac{\Delta^2 v_{\rm A}}{\mathcal{L}}. \tag{5.72}$$

Given that the Lundquist number is large in the corona, $\mathcal{L} \sim 10^8$–10^{12}, the magnetic energy release in the Sweet–Parker model is extremely slow and in no way consistent with the required flare energy release rate.

Apparently, the origin of this magnetic energy conversion inefficiency is in uniformity of the Sweet–Parker current sheet along its width Δ. One straightforward way to get rid of this uniformity is to consider the case when $\Delta \sim \delta$, so the spatial derivatives along both directions are of the same order of magnitude and the diffusion region is much more compact and isotropic, which is the case of **Petschek reconnection model**, Fig. 5.3, right. In such a case, the reconnection rate can by much larger as it depends on the Lundquist number only logarithmically, $M_r \sim \pi/(8 \ln \mathcal{L}) \sim 10^{-2}$, implying the inflow speed of $v_0 \sim M_r v_\mathrm{A} \sim 10^6$ cm/s and roughly 3–4 orders of magnitude more efficient magnetic energy conversion mechanism.

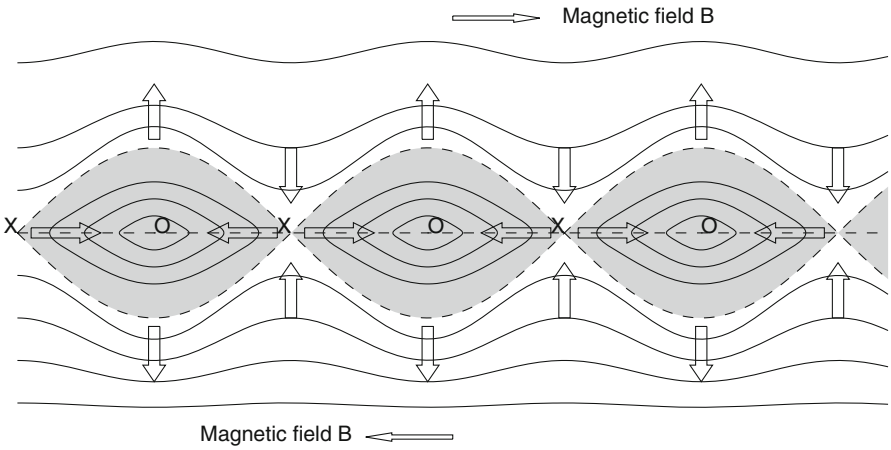

Figure 5.4: Structure of unstable current sheet: magnetic island formation due to tearing-mode instability (Aschwanden 2005).

Another possible way of breaking the spatial uniformity along the current sheet is a magnetic island formation due to tearing-mode instability (Fig. 5.4). A transverse perturbation of magnetic field lines directed along the diffusion region can grow in time with the growth rate dependent on the perturbation wavelength. The wave with the wavelength of the order of the current sheet thickness has the largest growth rate, or the shortest growth time, $\tau_\mathrm{tear} \approx \sqrt{4\delta^3/(v_\mathrm{A}\nu_m)}$, which is of the order of 1 ms for typical parameters of the solar corona; thus a current sheet may become highly fragmented over a very short time after its formation. Further evolution of such a fragmented current sheet may involve coalescence of the magnetic islands as well as creation of a highly turbulent region of the plasma driven by plasma outflows from multiple reconnection events; see the cited sources for greater detail.

5.3.3 MHD Discontinuities in IPM

A natural laboratory, where the astrophysical plasma can be studied by direct in situ measurements, is IPM. Accordingly, actual use of this laboratory

started soon after the first satellites were launched into the space. A major part of these studies is investigation of MHD discontinuities by observational methods, which has been done since 1960s of twentieth century by a variety of cosmic probes including missions of Mariners, Pioneers, and other. All discontinuities detected in the interplanetary space are collisionless. The thickness δ of the interface boundary is of order of 10^8–10^9 cm, i.e., dozens of the proton gyroradius. The Coulomb mfp Λ_i of the ions is of the order of 10^{13} cm, i.e., $\Lambda_i \gg \delta$. All types of the discontinuities predicted by the above theory (contact, tangential, rotational, and shock waves; see below) are identified in the interplanetary space, either qualitatively or quantitatively.

The detailed comparison of observational data with the theory is a very complicated task. Indeed, as mentioned above, a "discontinuity" represents, in fact, a layer of finite thickness and, therefore, is not very distinctly defined. This difficulty may even be enhanced greatly by significant fluctuations of the plasma parameters and magnetic fields in the solar wind near the discontinuity which are not related directly to the MHD properties of the discontinuity. Furthermore, identification of any observed discontinuity requires simultaneous determination of many parameters, particularly, the magnitude and direction of the magnetic field, particle number density, pressure and its anisotropy, electron and ion temperatures, and solar wind speeds on both sides of the discontinuity. Within the mentioned uncertainties, the IPM discontinuities are confidently detected in space. A review of initial stage of the interplanetary plasma study is given in monograph by Toptygin (1985). Now the explorations and monitoring of the discontinuities in interplanetary plasma represent one of the central topics within a relatively new discipline called the **space weather** (Gary and Keller 2004).

5.4 MHD Shock Waves

5.4.1 Local Properties

A discontinuity with $i_n \neq 0,\ \delta V \neq 0$ is called the **shock front**. The shock front together with related fluid inflows and outflows is called the **shock wave**.

1. Let us first prove that there is a reference frame in which vectors $\boldsymbol{u}_1,\ \boldsymbol{u}_2,\ \boldsymbol{B}_1,\ \boldsymbol{B}_2$ and the normal to the interface $\boldsymbol{n}$ all belong to one plane ("complanarity theorem").

   When $B_n \neq 0$ Eqs. (5.64c) and (5.64d) require that three vectors $\delta\boldsymbol{B}_\tau = \boldsymbol{B}_{\tau 1} - \boldsymbol{B}_{\tau 2},\ \delta(V\boldsymbol{B}_\tau) = V_1\boldsymbol{B}_{\tau 1} - V_2\boldsymbol{B}_{\tau 2}$, and $\delta\boldsymbol{u}_\tau = \boldsymbol{u}_{\tau 1} - \boldsymbol{u}_{\tau 2}$ are parallel (or antiparallel) to each other. Since $V_1 \neq V_2$, then $\boldsymbol{B}_{\tau 1}$ and $\boldsymbol{B}_{\tau 2}$ are parallel, i.e., $\boldsymbol{B}_1,\ \boldsymbol{B}_2$, and $\boldsymbol{n}$ belong to one plane. Taking into account that $\delta\boldsymbol{u}_\tau$ belongs to the same plane, we can select a reference frame (provided that $\boldsymbol{u}_1$ is in the required plane) in which both vectors $\boldsymbol{u}_1$ and $\boldsymbol{u}_2$ also belong to the same plane.

For $B_n = 0$ we derive from Eqs. (5.64c) and (5.64d)

$$\boldsymbol{u}_{\tau 1} = \boldsymbol{u}_{\tau 2}, \quad V_1 \boldsymbol{B}_{\tau 1} = V_2 \boldsymbol{B}_{\tau 2}. \tag{5.73}$$

This means that $\boldsymbol{B}_1$, $\boldsymbol{B}_2$, and $\boldsymbol{n}$ belong to one plane. Then, because the tangential velocity is continuous, we can easily select a reference frame where it is zero. Thus, both velocities will be normally directed at this reference frame, providing all considered vectors are in the same plane.

2. Equation (5.64) give rise to **Rankine–Hugoniot shock adiabat equation**

$$\epsilon_1 - \epsilon_2 + \frac{1}{2}(p_1 + p_2)(V_1 - V_2) + \frac{1}{16\pi}(V_1 - V_2)(B_{\tau 1} - B_{\tau 2})^2 = 0, \tag{5.74}$$

where the tangential field components are assumed collinear based on the complanarity theorem. Index 2 marks the downstream values, while 1 marks the upstream values.

3. MHD and thermodynamic parameters of the fluid have large gradients at the shock front region, which results in strong kinetic energy dissipation. This heats the fluid as it moves through the front and, as required by the second law of thermodynamics, the entropy increases:

$$s_2 > s_1, \tag{5.75}$$

where s_1 and s_2 are the specific entropies upstream and downstream, respectively. This condition together with thermodynamic inequalities

$$\left(\frac{\partial^2 V}{\partial p^2}\right)_s > 0, \qquad \left(\frac{\partial V}{\partial T}\right)_p > 0 \tag{5.76}$$

gives rise to the following conditions:

$$p_2 > p_1, \qquad \rho_2 > \rho_1, \tag{5.77}$$

i.e., the shock waves represent the waves of fluid contraction.

Now consider simplified cases with a special geometry.

In the *parallel shock wave* ($B_n \neq 0$, $B_{\tau 1} = B_{\tau 2} = 0$) the magnetic field is continuous and, accordingly, the tangential fluid velocity is continuous as well as follows from Eqs. (5.64c) and (5.64d). Therefore, we can select a reference frame in which the tangential velocity is zero. Then, the electric field $\boldsymbol{E} = -\boldsymbol{u} \times \boldsymbol{B}/c$ vanishes in this reference frame. As the magnetic field

does not affect the plasma motion along the field, the shock adiabat reduces to the Rankine–Hugoniot adiabat for the shock in a unmagnetized fluid:

$$\epsilon_1 - \epsilon_2 + \frac{1}{2}(p_1 + p_2)(V_1 - V_2) = 0. \tag{5.78}$$

The downstream to upstream density ratio can easily be found from this equation. For the tenuous single-atom gas the internal energy is linked with the pressure and specific volume by simple expression $\epsilon = pV/(\gamma - 1)$, $\gamma = 5/3$, which immediately yields

$$\frac{u_1}{u_2} = \frac{\rho_2}{\rho_1} = \frac{\gamma - 1 + (\gamma + 1)(p_2/p_1)}{\gamma + 1 + (\gamma - 1)(p_2/p_1)}. \tag{5.79}$$

The ratio p_2/p_1 specifies the strength of the shock wave. In a limiting case of a very strong shock, $p_2 \gg p_1(\gamma + 1)/(\gamma - 1)$, we have

$$\frac{u_1}{u_2} = \frac{\rho_2}{\rho_1} \approx \frac{\gamma + 1}{\gamma - 1} = 4 \tag{5.80}$$

for the tenuous nonrelativistic plasma; see Problem 5.8 for the relativistic case. Further relations holding at the strong shock front can also easily be found:

$$p_2 \approx \frac{2\rho_1 u_1^2}{\gamma + 1}, \quad \frac{T_2}{T_1} \approx \frac{(\gamma - 1)p_2}{(\gamma + 1)p_1} \approx \frac{2(\gamma - 1)\rho_1 u_1^2}{(\gamma + 1)^2 p_1}, \quad u_1 - u_2 \approx \frac{2u_1}{\gamma + 1}. \tag{5.81}$$

In the *perpendicular shock wave* as follows from Eq. (5.73), there exists a reference frame in which the plasma motion is normal to the shock plane at its both sides. Thus, the electric field is parallel to the front plane and so continuous:

$$\boldsymbol{E} = -\frac{1}{c}\boldsymbol{u}_1 \times \boldsymbol{B}_1 = -\frac{1}{c}\boldsymbol{u}_2 \times \boldsymbol{B}_2. \tag{5.82}$$

In this case the magnetic field is proportional to the density, $B_2/B_1 = \rho_2/\rho_1$. The shock adiabat can here also be presented in the form of the Rankine–Hugoniot adiabat (5.78), if one redefines the internal energy and pressure as follows. In place of the kinetic pressure p we use the full pressure

$$p_* = p + \frac{b^2}{8\pi V^2}, \tag{5.83}$$

while in place of ϵ we use the full density of the internal energy per unit mass:

$$\epsilon_* = \epsilon + \frac{b^2}{8\pi V}, \tag{5.84}$$

linked with p_* by relation $p_* = -(\partial\epsilon_*/\partial V)_s$. Here, $b = V_1 B_1 = V_2 B_2$ is the value continuous at the front.

For a strong perpendicular shock wave in a tenuous plasma ($\epsilon_2 \gg \epsilon_1,\ p_2 \gg p_1$) the shock adiabat takes the form

$$\frac{\rho_2}{\rho_1} = \frac{\gamma+1}{\gamma-1} - \frac{B_1^2}{4\pi p_2}\left(\frac{\rho_2}{\rho_1} - 1\right)^3. \tag{5.85}$$

The strongest compression ratio is the same (i.e., 4) as without magnetic field. However, for finite values of p_2, the compression is weaker than without magnetic field, because some part of the free energy goes here to the magnetic field increase.

The compression ratio is upper bounded by a finite value because the flow energy is converted to the thermal motion (heating) of the plasma particles downstream the front, so the increasing thermal pressure prevents stronger gas compression. However, if there is an efficient mechanism capable of reducing the internal plasma energy downstream (emission of radiation or charged particle acceleration), then the compression ratio increases given all other conditions are equal.

5.4.2 The Front Structure of a Shock Wave

In the previous section we have considered the shock front as an ideal geometric surface with zero thickness. But in fact the front is a finite transition layer with large gradients of macroscopic parameters. The analysis of the front structure in a general case is a difficult problem. We employ here the Burgers equation (see Sect. 5.2.1) to describe a weak shock wave front.

Assume the shock wave to have a stationary structure, and seek a solution of Eq. (5.32) in the form $p'(\zeta)$, where $\zeta = x - u_{\rm sh}t$ (with the shock wave velocity $u_{\rm sh}$). A stationary shock wave is an outcome of compensation of two counter-acting effects—nonlinear sharpening of the wave front and dissipation balancing the sharpening enhancement because the role of dissipative effects increases as the spatial gradients increase. Nonlinearity without dissipation causes steepening of the front and formation of a discontinuity (see Sect. 5.1.4). This leads to appearance of short-wave harmonics in the corresponding spatial spectrum. The dissipative effect suppresses harmonics with large k more efficiently, since the coefficient of wave absorption due to viscosity and thermal conductivity is proportional to k^2 (see Sect. 2.4.3). Dissipation without nonlinearity leads to diffusion spreading, i.e., unlimited expansion of the transition region. Balance between these two effects may allow the stationary nonlinear waves with a front of finite thickness in the dissipative region to exist.

Taking into account that $\partial p'/\partial t = -u_{\rm sh}\partial p'/\partial\zeta$, we write Eq. (5.32) in the form

$$\frac{\rm d}{{\rm d}\zeta}\left[(c_s - u_{\rm sh})p' + \frac{1}{2}p'^{\,2} - \kappa\frac{{\rm d}p'}{{\rm d}\zeta}\right] = 0. \tag{5.86}$$

Thus, it follows that

$$\kappa\frac{{\rm d}p'}{{\rm d}\zeta} = \frac{1}{2}p'^{\,2} + (c_s - u_{\rm sh})p' + {\rm const}. \tag{5.87}$$

The following boundary conditions for the perturbation p' to the pressure before the wave front p_1 should be fulfilled:

$$\frac{{\rm d}p'}{{\rm d}\zeta}=0, \quad p'=0 \quad \text{as} \quad \zeta\to+\infty, \quad \frac{{\rm d}p'}{{\rm d}\zeta}=0, \quad p'=\Delta p=p_2-p_1 \quad \text{as} \quad \zeta\to-\infty, \tag{5.88}$$

where p_2 is the pressure behind the front. Substituting Eq. (5.88) into Eq. (5.87), we find that the constant is zero and

$$u_{\rm sh} = c_s + \frac{1}{2}b\Delta p. \tag{5.89}$$

We rewrite Eq. (5.87) for the total pressure $p = p_1 + p'$:

$$\frac{{\rm d}p}{{\rm d}\zeta} = \frac{b}{2\kappa}(p - p_1)(p - p_2). \tag{5.90}$$

Integrating this expression we obtain

$$p(\zeta) = \frac{1}{2}(p_1 + p_2) - \frac{1}{2}(p_1 - p_2)\tanh(\zeta/\delta). \tag{5.91}$$

The pressure changes monotonically, and the thickness of the front

$$\delta = \frac{4\kappa}{b\Delta p} = \frac{2\kappa}{u_{\rm sh} - c_s} \tag{5.92}$$

decreases with increasing wave intensity, which is measured by the pressure jump Δp or by excess of the front velocity over the sound velocity $u_{\rm sh} - c_s$.

By the order of magnitude the diffusion coefficient κ equals to the sum $\nu+\nu_{\rm th}$, where ν is the kinematic viscosity and $\nu_{\rm th}$ is the coefficient of thermal diffusivity (denoted as κ in Eq. 1.154). Each of them is of the order of the product of the particle thermal velocity (or the sound velocity c_s) with the transport mfp Λ; thus, to the order of magnitude, we have

$$\delta \approx \Lambda/(M - 1), \tag{5.93}$$

where $M = u_{\rm sh}/c_s$ is the Mach number. Extrapolating Eq. (5.93) to the case $M - 1 \geq 1$, we see that the front thickness of intense shock waves is of the order of the transport mfp. This is a reasonable result, since at least a few particle collisions are required to transform the energy of the plasma flow into thermal energy behind the wave front. However, it should be kept in mind that this estimate is highly uncertain. The mfp inside the front is not a well-defined measure because of strong changes of the particle temperature and number density there.

The results obtained apply actually to a single component gas as we have not taken into account that the plasma is always a combination of several (at least two) components and that $m_e/m_i \ll 1$. This has a major effect on the shock front structure in a plasma provided the energy exchange between ions and electrons is slow. Indeed, let us consider the plasma transition through the shock front assuming the ion and electron temperatures to be equal before the wave front: $T_e^{(1)} = T_i^{(1)}$. After traveling through the front a distance of the order of the mean free path of the ion–ion collisions Λ_{ii} the ion temperature increases to $T_i^{(2)}$, since almost the entire energy of the flux at $M \gg 1$ is due to ions and a substantial part of it will be converted into the thermal energy. The electron temperature at the same distance of penetration into the front remains almost unchanged, $T_e^{(1)}$, since each electron acquires just a small portion of energy of order $(m_e/m_i)T_i^{(2)}$. Behind the wave front, the energies of electrons and ions become comparable at a distance $\Lambda_{ei} \approx \tau_{ei} v_{Te} \approx (m_i/m_e)^{1/2}\Lambda_{ii} \gg \Lambda_{ii}$. Therefore, the structure of the front will be determined by two relaxation lengths: the ion path Λ_{ii} and the scale of equalizing electron and ion temperatures, $(m_i/m_e)^{1/2}\Lambda_{ii}$. The shock-wave front becomes even more complicated in the presence of other relaxation processes,[2] e.g., radiative heat transfer, which is determined by the free path length of the photon, Λ_r.

We have considered the parallel shock wave, when the magnetic field has no effect on the HD motion of medium. The structure of the front in another special case of a purely perpendicular shock wave can also be studied using the Burgers equation. Introducing the total pressure $p_* = p + B^2/8\pi$, the transverse linear mode velocity $v_\perp = \sqrt{c_s^2 + v_{\rm A}^2}$, and the small perturbation p'_* of the total pressure, we derive Burgers equation (5.38b)

$$\frac{\partial p'_*}{\partial t} + v_\perp \frac{\partial p'_*}{\partial x} + b_* p'_* \frac{\partial p'_*}{\partial x}, = a_* v_\perp^3 \frac{\partial^2 p'_*}{\partial x^2} \tag{5.94}$$

with coefficients

[2] The structure of shock waves in a dense high-temperature plasma was studied by Imshennik and Bobrova (1997).

$$a_* = 2^{-1} v_\perp^{-3} [4\nu/3 + \nu_m v_\mathrm{A}^2/v_\perp^2 + \chi V (c_V^{-1} - c_P^{-1})/v_\perp^2], \quad b_* = \frac{v_\perp^2}{2V^2} \left(\frac{\partial^2 V}{\partial p_*^2} \right)_s \tag{5.95}$$

from MHD equations (2.1), (2.13a), (2.13b), and (2.16).

The relation between Joule dissipation and thermal conductivity depends on the relation between the sound velocity c_s and the Alfvén velocity v_A. The structure of the total pressure profile in a weak perpendicular MHD shock wave and the front thickness are described by Eqs. (5.91) and (5.92), with apparent adjustment of the notations.

We note, however, that not yet considered effect of dispersion can significantly change the front structure. To illustrate this effect we employ KdV–Burgers equation (5.44) for the analysis of the transverse shock front structure in a cold plasma. We are going to demonstrate that the monotonic structure of the shock wave (5.91) is replaced by an oscillatory structure owing to dispersion, which (depending on its sign) appears either behind or before the shock front.

Writing Eq. (5.44) for $h(x - u_\mathrm{sh} t)$, introduced in Sect. 5.2.3, we obtain (prime denotes the differentiation over $\xi = x - u_\mathrm{sh} t$)

$$\mu h'' - \kappa h' = -\frac{\partial W}{\partial h} = \Delta u \, h - \frac{1}{2} h^2, \tag{5.96}$$

which differs from Eq. (5.51) by presence of the dissipation term $-\kappa h'$. Then, $\Delta u = u_\mathrm{sh} - v_\mathrm{A} > 0$ and the integration constant $K = 0$ in the effective potential energy, Eq. (5.52). For the boundary condition we adopt that asymptotically before the front $h \to 0$ and that behind the front $h \to \Delta h = \mathrm{const}$. The parameter Δh controls strength of the shock wave. Taking $\xi \to -\infty$ in Eq. (5.96) (the region behind the front), we find the relation between the parameters Δu and Δh:

$$\Delta h = 2 \Delta u. \tag{5.97}$$

We can draw a qualitative picture of the h behavior using the mechanical analogy with oscillations of a particle in a potential well with friction (Fig. 5.5). If $\mu > 0$, the oscillations start from a state a at $\xi \to +\infty$ and asymptotically approach $h = 0$ upfront the wave. In a time t, which corresponds to ξ decrease, the oscillator reaches the state b, the peak of the first maximum of the magnetic field, much resembling a soliton, provided that dissipation is not large. Then infinite number of oscillations occurs (states c, d, etc.) accompanied by the gradual amplitude decrease, until the oscillator transits asymptotically to state f as $\xi \to -\infty$, corresponding to the constant value $h = \Delta h$ behind the wave front.

The oscillatory regime can further be quantitatively studied for the small amplitude case by the linearization of Eq. (5.96). Consider the case of $\mu > 0$. In the prefront region we have $h \to 0$ if $\xi \to +\infty$. At finite ξ we seek a

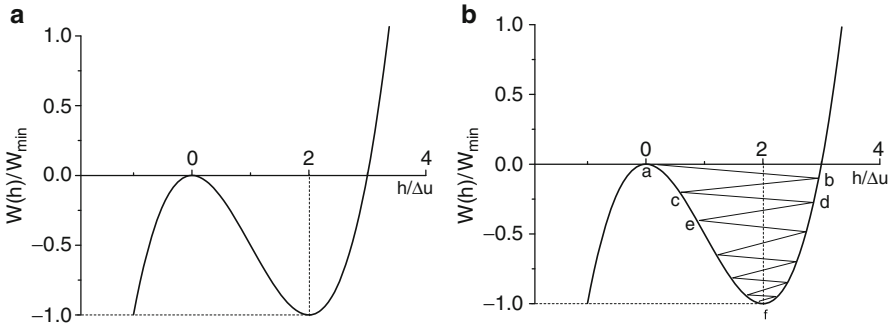

Figure 5.5: (**a**) Schematic plot of effective potential energy for KDV soliton. (**b**) Illustration to the solution of the KDV–Burgers equation. Nonlinear oscillator starts from state a and turns to state f after many oscillations. In the last state velocity is δu behind the shock front.

solution in the form of $h(\xi) = h_1(\xi) = a_1 \exp(k_1 \xi)$ and linearize Eq. (5.96), omitting quadratic term:

$$\mu h_1'' - \kappa h_1' = \Delta u \, h_1. \tag{5.98}$$

We are interested in a bounded solution with $\Re k_1 < 0$; therefore

$$k_1 = -\frac{\kappa}{2\mu}\left(\sqrt{1 + \frac{4\mu\Delta u}{\kappa^2}} - 1\right). \tag{5.99}$$

Behind the front, where $h \to \Delta h$ for $\xi \to -\infty$, we seek a solution in the form $h(\xi) = \Delta h + h_2(\xi)$ with $h_2 = a_2 \exp(k_2 \xi)$, $\Re k_2 > 0$, and $|h_2| \ll \Delta h$. Linearized equation (5.96) then reads

$$\mu h_2'' - \kappa h_2' + \Delta u \, h_2 = 0. \tag{5.100}$$

Substitution of the trial solution into Eq. (5.100) yields

$$k_2 = \frac{\kappa}{2\mu}\left(1 \pm \sqrt{\frac{4\mu\Delta u}{\kappa^2} - 1}\right). \tag{5.101}$$

Propagation constant has an imaginary part, if $\kappa < \sqrt{4\mu\Delta u}$. It is the case of oscillation structure behind the front, Fig. 5.6a. If $\kappa > \sqrt{4\mu\Delta u}$, relaxation is monotonic, with two relaxation lengths.

For $\mu < 0$ (positive dispersion), the picture reverses: before the front, there are oscillations under condition $\kappa < \sqrt{4|\mu|\Delta u}$ with the propagation constant

$$k_1 = -\frac{\kappa}{2|\mu|}\left(1 \pm \sqrt{\frac{4|\mu|\Delta u}{\kappa^2} - 1}\right). \tag{5.102}$$

Behind the front there is a smooth transition to the asymptote $h_2 = \Delta h$, and

$$k_2 = \frac{\kappa}{2|\mu|}\left(\sqrt{1 + \frac{4|\mu|\Delta u}{\kappa^2}} - 1\right). \tag{5.103}$$

The amplitudes $a_{1,2}$ may be derived from the solution of the nonlinear problem.

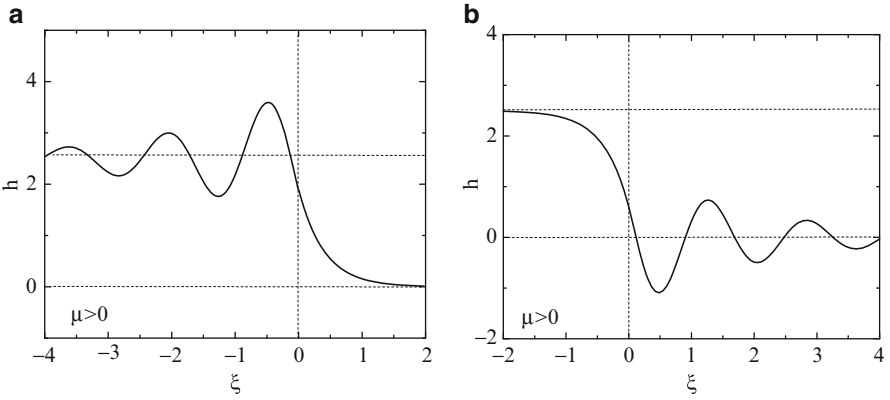

Figure 5.6: Schematic plot of shock wave's front oscillation structure. Oscillations are excited by dispersion effect. (**a**) *Negative dispersion*; oscillatory structure behind the front. (**b**) *Positive dispersion*; oscillatory structure before the front.

The width of the shock front is determined by the distance over which oscillations damp out:

$$\delta = 2\left(\frac{1}{|\Re k_1|} + \frac{1}{|\Re k_2|}\right) = \frac{4|\mu|(1 + 4|\mu|\Delta u/\kappa^2)^{1/2}}{\kappa[(1 + 4|\mu|\Delta u/\kappa^2)^{1/2} - 1]}. \tag{5.104}$$

This formula is applicable for any sign of the dispersion: $\mu < 0$ or $\mu > 0$. For $\mu \to 0$ it agrees with Eq. (5.92). For $\kappa \ll (4|\mu|\Delta u)^{1/2}$ the width of the front is independent of the shock-wave strength:

$$\delta = 4|\mu|/\kappa. \tag{5.105}$$

The oscillatory structure of the shock-wave front is shown in Fig. 5.6. An analytical solution of the KdV–Burgers equation at low damping but without linearization was obtained by Gurevich and Pitaevskii (1987).

5.4.3 Measurements of Shock Wave Parameters

The shock waves are implied or detected in many astrophysical objects, including supernovae and gamma-ray burst sources. However, direct measurements of astrophysical shocks are only possible in IPM and were repeatedly

made by space probes outside the Earth's magnetosphere. The shocks have the solar origin and moderate strengths. The typical parameters of the shocks launched by eruptive solar flares or CMEs near the Earth orbit are the following (Hundhausen 1972):

Plasma speed ahead the front	390 km/s
Plasma speed behind the front	470 km/s
Shock velocity relative to a motionless observer	500 km/s
Shock velocity relative to upstream plasma	110 km/s
Max number (acoustic or Alfvenic)	2–3
Magnetic field enhancement at front	2–3
Propagation time from the Sun	55 h.

Shock fronts are not spherical, although the shock waves are launched as bubble-like structures with significant curvature of the front; see, e.g., Fig. 1.3. The front thickness did not exceed 2,000 km in most cases, i.e., shock waves are collisionless. But in rare cases of largest events, the solar eruptions create very strong shocks. In events of 1959, 1960, 1972,. . ., 2003, and 2006 the shock fronts velocities of 1,700–2,800 km/s and Max numbers of several dozens were recorded near the Earth's orbit. Another important example of the shock wave, accessible for direct measurements, is the Earth bow shock originating as the solar wind flow collides with the terrestrial magnetic field. Finally, with a number of spacecrafts launched years ago toward outer bounds of the solar system, a termination shock demarcating the solar system and ISM becomes accessible to the direct probing as well, as discussed in more detail in Sect. 2.5.2.

5.4.4 Collisionless Shock Waves

On passing through the plasma, a soliton described by KdV equation or the nonlinear Shrödinger equation does not alter the state of the medium (or does so only in a reversible way). In fact, the collisional dissipation always exists, even though it is small when collisions are rare. A strong energy dissipation, however, is needed to form an MHD shock wave, so a shock wave may propagate in the medium when the collisions play a significant role. The state of the medium changes considerably over distances of the order of the front width (several mfp lengths of the particles). The question arises if (and how) it is possible for the shock waves to exist in a collisionless plasma? By the "shock waves" we adopt the motions that change the state of the medium irreversibly, with the change occurring over a distance much shorter than the collisional mean free path of the particles.

Observational data (see, e.g., Sect. 5.4.3) indicate that such shock waves do arise. Direct measurements of the magnetic field and the plasma parameters from IMP spacecrafts reveal that strong perturbations of shock-wave type occur rather frequently in IMP plasma. IMP shock waves near the Earth's

orbit often have the front widths of 500–1,000 km and even 100 km, while the mean free paths of electrons and ions with respect to Coulomb collisions approach 1 AU $\approx 1.5 \times 10^8$ km. Comparison of that scales shows that interplanetary shock waves are strongly collisionless and their thickness has nothing to do with the collisional dissipation of energy and momentum of the particles at the front. Hence, the question of the formation mechanism and structure of collisionless shock waves arises. This question was first raised by Roald Sagdeev, who developed the first theories of collisionless shock waves (Sagdeev 1966).

In an ordinary shock wave, the state of the medium changes owing to the dissipation of energy at the front, associated with viscosity, thermal conductivity, and Joule heat release. In the absence of collisions, the state of the medium may be changed owing to the wave oscillations excited at the front. The shock adiabate connecting the states of the medium in the two regions should incorporate the energy and momentum of both the plasma flows and the oscillations. Dissipation of regular or stochastic oscillations may occur much more efficiently through infrequent rare collisions than the dissipation of the original nonlinear large-scale motion from which they have emerged. Another possibility is the interaction of plasma particles with small-scale stochastic electric and magnetic fields of oscillations (turbulence) that may either be generated by these particles themselves or be of an external origin. This interaction leads to appearance of an anomalous transfer processes (electrical conductivity, thermal conductivity, viscosity, Sect. 1.3.8), which play the same role as processes caused by the particle collisions play in the collisional case. These qualitative considerations imply motions that can be treated as the shock waves in a collisionless plasma.

Models of quasiperpendicular and quasiparallel (relative to the regular magnetic field) shock waves differ considerably from each other. Physical considerations reveal that a sharp front is easier to form in the quasiperpendicular case: the particles cannot move freely in the direction of wave propagation because of the magnetic field. The role of the free path may be played by the Larmor radius of ions in the original regular magnetic field. With quasiparallel propagation, the background magnetic field does not prevent particles from spreading in the direction away from the front. In order to form a sharp front, the generation of additional electric and/or magnetic fields by the shock wave is necessary. These fields must create the required excess plasma density behind the front.

Gurevich and Pitaevskii (1973) considered overturning of quasiperpendicular simple wave in the absence of collisions. Dispersive effects cause the appearance of oscillations at the steep part of the front. The region of oscillations expands with time. In the collisional case, a shock wave would be formed right there, with strong energy dissipation at the front. In the case discussed, the shock wave has a laminar structure: there exist regular oscillations over the front region. This is valid, however, for rather weak shock waves only. For stronger shocks, as the Mach number grows, the amount of ions reflected

from the front grows as well. They create a multiflow current that is unstable and causes turbulence; i.e., the shock front necessarily becomes turbulent for large Mach numbers.

5.4.5 Evolutionarity of Discontinuities

As has been said some discontinuities can be unstable relative to small perturbations. This means that they evolve to a new, more stable, state over a finite time. For example, if a perturbation of the discontinuity raises as $e^{\gamma t}$, $\gamma > 0$, it remains small during the time of the order of γ^{-1}. Such discontinuities along with the stable ones are called **evolutionary** discontinuities. Unlike evolutionary discontinuities there is a different class of **non-evolutionary** discontinuities—those which disintegrate to a few other discontinuities and/or waves in such a way that the perturbation is instantly large as soon as new discontinuities are distinctly separated in space. Non-evolutionary discontinuities are often produced by an external driver, for example, by a collision of two massive plasma clouds, which results in a plane interface boundary between them. Continuity conditions (5.61) are not fulfilled at this boundary in a general case. Thus, this arbitrarily non-evolutionary discontinuity will immediately disintegrate to a few evolutionary discontinuities, contraction, and rarefaction waves, which obeys the laws, established above in Sects. 5.3 and 5.4.

To address a question of evolutionarity one has to count the number of equations derived from linearized boundary conditions at the interface and the number of parameters describing a general (initially weak) disturbance of the discontinuity: if these numbers coincide, then the equations uniquely determine further evolution of the perturbation, so the discontinuity is evolutionary. If the numbers are different, the discontinuity is non-evolutionary. As the discontinuities are the natural outcome of the ideal (dissipativeless) MHD, see Sect. 5.3, the problem of the discontinuity evolutionarity must also be considered within the ideal MHD. Within dissipative MHD, the rotational, tangential, and contact discontinuities do not represent true solutions of the MHD equations, so the question of their evolutionarity is difficult to correctly set up within the dissipative MHD.

Referring for a more detailed discussion to Landau and Lifshitz (1966) and Somov (2006), we give here the shock wave evolutionarity conditions (without derivation):

$$u_{n1} > v_{f1}, \qquad v_{f2} > u_{n2} > v_{An2} \tag{5.106}$$

and

$$v_{\mathrm{A}n1} > u_{n1} > v_{s1}, \qquad v_{s2} > u_{n2}, \tag{5.107}$$

where $v_{\mathrm{A}n} = |B_n|/\sqrt{4\pi\rho}$. The first type of the shock waves is referred to as *fast shock waves* because in the limiting case of small-amplitude jumps they propagate with the velocity $v_{f1} \approx v_{f2}$ of the fast magnetosound wave. The

second type of the shock waves is called *slow shock waves* as they transform to the slow mode in the small-amplitude limit. The tangential component of the magnetic field increases at the front in the case of fast wave, while decreases in the case of slow wave.

5.5 Supernova Explosions and Evolution of Its Remnants

Strong energy release is typical for many kinds of the astrophysical objects. Apparently, a significant fraction of the energy released is converted to the mechanical energy of the plasma outflow. Recall some typical values of the explosive energy releases in astrophysics: the solar flares can release up to 10^{32} ergs, nova explosions—up to 10^{46} ergs, and supernova explosions—up to 10^{52} ergs. It is many orders of magnitude above any energy release at the Earth, e.g., thermonuclear bomb explosion with the trotyl equivalent of 1 Mt releases about 10^{23} ergs.

5.5.1 Strong Explosion: Sedov Solution

Let us consider the perturbation of an originally motionless uniform gas with the density ρ_0, pressure p_0, and magnetic field B_0, produced by a strong energy release E in a spatially localized region (Sedov solution for the point explosion, considered by Sedov (1946), von Neumann in 1947, and Taylor in 1941; published in 1950); see Landau and Lifshitz (1966) and Sedov (1987). If the explosion is strong then a strong shock wave is formed very close to the explosion point. This isotropic (spherical) shock wave (given the energy release itself is isotropic and strongly exceeds the magnetic energy) is propagating through the originally unperturbed gas. We consider here an initial stage of this propagation while the pressure p_s downstream satisfies the condition

$$p_s \gg (\gamma + 1)(p_0 + B_0^2/8\pi)/(\gamma - 1), \tag{5.108}$$

i.e., it is much larger than the total pressure in the unperturbed gas upstream the shock. Under this assumption the shock wave is very strong, which enables us to determine the expansion law $R_s(t)$, where R_s is the radius of the shock wave, from the dimension analysis. Under condition (5.108) the external pressure is very small and so cannot affect the shock wave propagation. Thus, only three dimensional parameters, ρ_0, E, and t, remain, which can be combined in a value $R_s(t)$ having the dimension of length:

$$R_s(t) = \beta \left(\frac{Et^2}{\rho_0} \right)^{1/5}. \tag{5.109}$$

Here β is a dimensionless factor, which can be calculated by equating the explosion energy and the energy of moving media driven by the explosion.

Its value depends on the ratio of the specific heats γ: in simplest cases of $\gamma = 5/3$ and $\gamma = 7/5$ one can find $\beta = 1.148$ and $\beta = 1.033$, respectively; β will differ from those values if a substantial fraction of the explosion energy is somehow lost, e.g., spent for particle acceleration. Equation (5.109) alone yields the dependence of the front velocity u_s on time and the explosion energy:

$$u_s(t) = \dot{R}_s = \frac{2R_s}{5t} = \frac{2\beta E^{1/5}}{5\rho t^{3/5}}. \tag{5.110}$$

The problem of the gas state in the downstream (perturbed) region can then be analytically solved if we neglect the dissipation—the viscosity and the heat conduction. Taking into account the spherical symmetry of the solution, we can transform the HD equation to the form

$$\frac{\partial \rho}{\partial t} + \frac{\partial(\rho u)}{\partial r} + \frac{2\rho u}{r} = 0, \tag{5.111a}$$

$$\frac{\partial u}{\partial t} + u\frac{\partial u}{\partial r} + \frac{1}{\rho}\frac{\partial p}{\partial r} = 0, \tag{5.111b}$$

$$\frac{\partial}{\partial t}\left(\frac{1}{2}\rho u^2 + \frac{p}{\gamma - 1}\right) + \frac{1}{r^2}\frac{\partial}{\partial r} r^2 u \left(\frac{1}{2}\rho u^2 + \frac{\gamma}{\gamma - 1} p\right) = 0. \tag{5.111c}$$

Here we have used the expressions $p/(\gamma - 1)$ and $\gamma p/(\gamma - 1)$ for the internal energy and enthalpy per unit volume, respectively.

This set of equations can be simplified by introducing dimensionless functions, U, G, and Z, dependent on the "self-similar" dimensionless variable $s = r/R_s(t)$:

$$u(r,t) = \frac{2r}{5t} U(s), \qquad \rho(r,t) = \rho_0 G(s), \qquad p(r,t) = \frac{4r^2\rho_0}{25t^2\gamma} Z(s). \tag{5.112}$$

Substitution of these functions into Eq. (5.111) gives rise to cancelation of all dimensional factors and yields the set of ordinary differential equations with one independent variable $\xi = \ln s$:

$$\frac{\mathrm{d}\ln G}{\mathrm{d}\xi} = \frac{1}{1-U}\left(\frac{\mathrm{d}U}{\mathrm{d}\xi} + 3U\right), \tag{5.113a}$$

$$\frac{\mathrm{d}U}{\mathrm{d}\xi} = \frac{3UZ - 3Z/\gamma - U(1-U)(5/2 - U)}{(1-U)^2 - Z}, \tag{5.113b}$$

$$\frac{\mathrm{d}\ln Z}{\mathrm{d}\xi} = \frac{\gamma - 1}{1-U}\frac{\mathrm{d}U}{\mathrm{d}\xi} + \frac{(3\gamma - 1)U - 5}{1-U}. \tag{5.113c}$$

This set of equations must be complemented by boundary conditions at the strong shock front, which can be derived from Eqs. (5.80) to (5.81):

$$U(1) = \frac{2}{\gamma+1}, \qquad G(1) = \frac{\gamma+1}{\gamma-1}, \qquad Z(1) = \frac{2\gamma}{\gamma+1}. \tag{5.114}$$

Analytical solution of this system exists (Landau and Lifshitz 1966; Sedov 1987), but it is too cumbersome to present it here.

Figure 5.7 demonstrates the distributions of velocity, mass density, and pressure in perturbed region behind the front. The dependence of the velocity on the distance is not much different from the direct proportionality. The mass density distribution shows formation of a shell structure behind the shock front and sweeping the gas from the central part of the cavern. However, the pressure at the center of explosion remains finite. This means that the gas temperature is very high in the central region, so discarding the heat conductivity is not correct there.

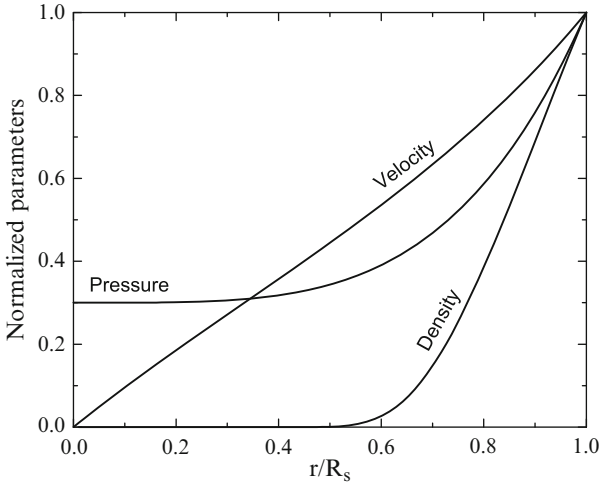

Figure 5.7: Sedov solution for the gas parameter distributions inside the sphere perturbed by a strong isotropic explosion. The gas pressure, density, and velocity are normalized by their downstream values at the front.

The opposite limiting case of isothermal gas in the cavern (i.e., very large heat conductivity) was considered by Korobeinikov (1956) and Solinger et al. (1975). The authors analyze the point burst in a medium with inhomogeneous mass density distribution specified by a single dimensional quantity $\rho_0(r) = Ar^{-\lambda}$, $0 \le \lambda < 3$. As in the uniform case, the radius of the shock front and its velocity can be found from the analysis of dimensions:

$$R_s(t) = \beta(Et^2/A)^{1/(5-\lambda)}, \qquad u_s(t) = \dot{R}_s(t). \tag{5.115}$$

The case of $\lambda = 2$ corresponds to the spherical burst in the stellar wind region.

5.5.2 Magnetic Field in Strong Explosion Region

Consider the strong explosion to occur in a homogeneous medium with a uniform magnetic field $\boldsymbol{B}_0$. Here we consider a simple approximate model of large-scale magnetic field in perturbed region behind the strong shock front (Toptygin 2004). If the magnetic field is ignored, then the self-similar solutions for an isotropic point-source explosion in a homogeneous or spherically symmetric medium are spherically symmetric, i.e., the plasma velocity is perpendicular to the front. In the presence of a magnetic field, tangential velocity components appear and obey boundary conditions in the co-moving frame of the front; see Eqs. (5.64c) and (5.64d):

$$i_n \delta \boldsymbol{u}_\tau - \frac{B_n}{4\pi} \delta \boldsymbol{B}_\tau = 0, \qquad B_n \delta \boldsymbol{u}_\tau - i_n \delta (V \boldsymbol{B}_\tau) = 0. \tag{5.116}$$

Here $i_n = \rho_0 u_s = u_s / V_0$ is the density of the mass flux through the front; u_s is the velocity of the upstream plasma, whose magnitude is equal to the velocity of the shock front relative to the stationary medium. Introducing the Alfvén velocity $\boldsymbol{v}_\mathrm{A} = \boldsymbol{B}/\sqrt{4\pi\rho_0}$ and the Alfvén Mach numbers $M_{\mathrm{A}n} = u_s / v_{\mathrm{A}n}$, $M_{\mathrm{A}\tau} = u_s / v_{\mathrm{A}\tau}$, we obtain an estimate of $u_\tau / u_s \approx (M_{\mathrm{A}n} M_{\mathrm{A}\tau})^{-1}$ from the first equation in Eq. (5.116). Thus, the deviation from spherical symmetry for a strong shock is small, $M_\mathrm{A}^{-2} \ll 1$. Neglecting this asymmetry, we find the boundary conditions at the strong shock front

$$B_n^s = B_n^0, \qquad B_\tau^s = B_\tau^0 \frac{\rho_s}{\rho_0}, \tag{5.117}$$

where the index s denotes the values of the quantities in the perturbed region inside the spherical front. For a strong shock front in a plasma $\sigma = \rho_s / \rho_0 \geq 4$. Values larger than 4 can be reached if a significant number of relativistic particles (cosmic rays or electromagnetic quants) are involved.

As has been shown in Sect. 2.3, the regime of the magnetic field evolution is controlled by the Reynolds number. The magnetic Reynolds number in supernova remnants (SNR) is very large: $R_m = ul/\nu_m \approx 10^9$, if $u \approx 3 \times 10^8$ cm/s, the scale length of the motion is $l \approx 1$ pc, and the magnetic viscosity is $\nu_m \approx 10^{18}\,\mathrm{cm}^2/\mathrm{s}$ (Ruzmaikin et al. 1988). Therefore, the dissipation-free approximation may be used to calculate the field:

$$\frac{\partial \boldsymbol{B}}{\partial t} = \nabla \times (\boldsymbol{u} \times \boldsymbol{B}), \qquad \nabla \times \boldsymbol{B} = 0. \tag{5.118}$$

Below, we assume that the velocity in the perturbed region ($r < R_s(t)$, where $R_s(t)$ is the front radius) is directed radially and does not depend on

the angles $u_r = u(r,t)$ and $u_\vartheta = u_\alpha = 0$. Equation (5.118) may be written as

$$\frac{\partial B_r}{\partial t} = -\frac{u(r,t)}{r^2}\frac{\partial}{\partial r} r^2 B_r, \quad \frac{\partial B_\vartheta}{\partial t} = -\frac{1}{r}\frac{\partial}{\partial r} r u(r,t) B_\vartheta, \quad \frac{\partial B_\alpha}{\partial t} = -\frac{1}{r}\frac{\partial}{\partial r} r u(r,t) B_\alpha. \tag{5.119}$$

The general solution of these equations can be easily found if the function $u(r,t)$ is factorized: $u(r,t) = p(r)q(t)$. Introducing new dependent variables,

$$b_r(r,t,\vartheta,\alpha) = r^2 B_r(r,t,\vartheta,\alpha),$$
$$b_\vartheta(r,t,\vartheta,\alpha) = rp(r)B_\vartheta(r,t,\vartheta,\alpha), \qquad b_\alpha(r,t,\vartheta,\alpha) = rp(r)B_\alpha(r,t,\vartheta,\alpha), \tag{5.120}$$

and new independent variables

$$\tau(t) = \int q(t)\mathrm{d}t, \qquad s(r) = \int \frac{\mathrm{d}r}{p(r)}, \tag{5.121}$$

we transform all Eqs. (5.119) to the same form

$$\frac{\partial b_i}{\partial \tau} + \frac{\partial b_i}{\partial s} = 0, \qquad i = r, \vartheta, \alpha. \tag{5.122}$$

The solutions of these equations are arbitrary differentiable functions $b_i(\varphi(r,t),\vartheta,\alpha)$ of the self-similar variable $\varphi(r,t) = s(r) - \tau(t)$. Of course, this self-similar variable differs from the Sedov self-similar variable $r/R_s(t)$. The dependence of b_i on φ can be determined from the boundary conditions if the seed field is time independent. The dependence from ϑ and α can also be determined from the boundary conditions along with the second equation of system (5.118).

In Sedov approximation we adopt the shock front to be a sphere with the radius $R_s(t)$ (5.109). The velocity field behind the front of a blast wave can be well fitted by a linear function of the radius (see Fig. 5.7):

$$u(r,t) = \dot{R}_s(t)\frac{\mu r}{R_s(t)}, \quad \mu = 1 - \sigma^{-1}, \tag{5.123}$$

which is just a simple approximation to the complicated Sedov solution. Here, σ is the compression ratio of the matter at the front introduced above. If relativistic particles are absent, then $\sigma = (\gamma+1)/(\gamma-1) = 4$ and $\gamma = 5/3$. In this case, $\mu = 2/(\gamma+1)$ and behind the front the fluid velocity $u(R_s(t),t) = \mu\dot{R}_s(t)$ is smaller than the front velocity $\dot{R}_s(t)$.

Using Eqs. (5.109) and (5.123), we obtain

$$p(r) = r, \qquad q(t) = \frac{\mu\dot{R}_s(t)}{R_s(t)}, \qquad \varphi(r,t) = \ln\left(\frac{r}{R_s^\mu(t)}\right). \tag{5.124}$$

Clearly, without loss of generality, we can take the following quantity as the self-similar variable:

$$\xi(r,t) = \exp\varphi(r,t) = \frac{r}{R_s^{\mu}(t)}. \tag{5.125}$$

We use Eqs. (5.120)–(5.125) and write the solution as

$$B_i(r,t,\vartheta,\alpha) = \frac{1}{r^2} b_i(\xi(r,t),\vartheta,\alpha). \tag{5.126}$$

In the case of the uniform external magnetic field we have boundary conditions (5.117):

$$B_r(R_s(t),t,\vartheta) = B_0\cos\vartheta, \qquad B_\vartheta(R_s(t),t,\vartheta) = -B_0\frac{\rho_s}{\rho_0}\sin\vartheta, \qquad B_\alpha = 0. \tag{5.127}$$

We then write the solution in the form

$$B_r(r,t,\vartheta) = \frac{f(r/R_s^{\mu})}{r^2} B_0\cos\vartheta, \qquad B_\vartheta(r,t,\vartheta) = -\frac{\rho_s f(r/R_s^{\mu})}{\rho_0 r^2} B_0\sin\vartheta, \tag{5.128}$$

and find the function f from boundary conditions (5.117): $f(R_s^{1-\mu}) = R_s^2$. It means that $f(x) = x^{2/(1-\mu)}$ and

$$f(r/R_s^{\mu}) = \frac{r^{2/(1-\mu)}}{R_s^{2\mu/(1-\mu)}},$$

As a final result we have

$$B_r(r,t,\vartheta) = \left(\frac{r}{R_s(t)}\right)^{2\mu/(1-\mu)} B_0\cos\vartheta, \quad B_\vartheta(r,t,\vartheta) = -\frac{\rho_s}{\rho_0}\left(\frac{r}{R_s(t)}\right)^{2\mu/(1-\mu)} B_0\sin\vartheta, \quad r \le R_s(t). \tag{5.129}$$

At $\sigma = 4$, we obtain $\mu = 3/4$, $2\mu/(1-\mu) = 6$. Thus, the radial magnetic field is swept up from the explosion region together with the plasma; attenuation factor is $(r/R_s(t))^6$. The tangential field is also swept up, but it is enhanced at the front by a factor $\sigma \ge 4$ compared with its unperturbed value. Therefore, the tangential field dominates in the cavity. Solution (5.129) is inapplicable to the central part of the cavity, because the heat conduction and the ejection of mass ΔM from the star are discarded in the Sedov solution. It appears that Eq. (5.129) correctly describes the field at the distances $r > R_0 \approx (3\Delta M/4\pi\rho_0)^{1/3}$, when the swept-up mass is of the same order of or larger than the ejected mass. We note that the performed analysis of the magnetic field is purely kinematic, and so does not take into account any mechanism of magnetic field generation (see Chap. 8).

5.5.3 Stages of the Supernova Remnant Shock Evolution

Although the described model of the spherically symmetric explosion is incomplete and simplified, it is widely used in application to explosions in the astrophysics, especially to the supernova explosions and SNRs, which are often spherically symmetric in the first approximation. SNRs are highly nonstationary hot bubbles (cavities) disturbed by a strong primary shock wave produced by a stellar explosion with a total kinetic energy release of about 3×10^{50}–10^{52} erg (Shklovskij 1976; Lozinskaya 1992). Let us outline some general properties of SNe established by both observations and theory. Overall, there are two distinct physical processes yielding the SN phenomenon.

I. Thermonuclear explosive burning of the carbon and oxygen (CO) nuclei in white dwarfs forms **thermonuclear SNe Ia type**. The nuclear synthesis produces ^{56}Ni, which then transforms to the iron through the chain of β-decay transformations $^{56}\text{Ni} \rightarrow ^{56}\text{Co} \rightarrow ^{56}\text{Fe}$. The white dwarfs do not contain the hydrogen nuclei because they entirely burned out at an earlier stage of the star evolution. Accordingly, the white dwarfs cannot have masses exceeding a so-called Chandrasekhar limit, $M \approx 1.4M_\odot$ for a nonrotating white dwarf. If the star accumulates a slightly larger mass, perhaps due to accretion from a star companion, the degenerate electron gas responsible for maintaining the hydrostatic equilibrium within the star volume cannot balance the gravitational force any longer and support the star matter against collapse. Thus, the ion number density and temperature grow, which results in the thermonuclear explosion of the star material.

   According to Nadyozhin and Imshennik (2005) explosion of a white dwarf with $M \approx 1.4M_\odot$ produces $\approx 0.6M_\odot$ of ^{56}Ni nuclei, the explosion energy $E_{\text{exp}} \approx 10^{51}$ erg is the difference between binding energies of the final products of the synthesis (primarily, ^{56}Ni) and original carbon–oxygen mixture. Full emitted electromagnetic energy is estimated to be a minor fraction of the explosion energy, $E_{\text{rad}} \approx 6 \times 10^{49}$ erg. Almost all (remaining) energy is spent to ejection of the stellar mass outward to the ISM; no compact remnant is created. The initial velocity of the outgoing plasma is $u_0 = \sqrt{2E_{\text{exp}}/M} \approx 8\times10^8$ cm/s. The SNe Ia forms a highly uniform group of objects with almost identical properties; in particular, their peak intensities (maximum absolute magnitude of about -19.3) are the same with the accuracy better than 10%, and so they are often used as "standard candles" in cosmology providing reliable measurement of the corresponding distances. In particular, careful analysis of these standard candles at various cosmological distances resulted in a remarkable discovery of accelerated expansion of the Universe (Nobel Prize in physics, 2011).

II. **Core-collapse SNe** (types Ib, Ic, and II) explode as a result of gravitational collapse of the star due to breaking of internal balance at some stage of thermonuclear burning. Such events are more diverse than the type Ia SNe and are subdivided onto a few classes depending of how much hydrogen survived until the explosion. The corresponding light curves are controlled by the plasma heating by the shock wave, the hydrogen recombination, and, at a later stage, by the β-decay $^{56}\mathrm{Ni} \rightarrow^{56}$ Co $\rightarrow^{56}$ Fe, where originally the mass of the radioactive ^{56}Ni is about $(0.02\text{–}0.2)M_\odot$. The shock wave originates at an interface between the iron core with the mass of $M_{\mathrm{Fe}} = (1.2\text{–}2)\,M_\odot$, which collapses to a neutron star, and the ejected shell carrying the remaining mass of the star progenitor. The total energy of a core-collapse SN consists of the following ingredients: (1) a main fraction of $(E_{\nu\mathrm{tot}} \approx (3-5) \times 10^{53})$ erg escapes with neutrinos and antineutrinos of all kinds (e, μ, and τ). This energy is huge; it is about 10–15 % of the neutron star rest energy, $M_{\mathrm{Fe}}c^2$. In contrast, the electromagnetic energy is "only" around 10^{49}–10^{50} erg. The mechanical energy of the explosion is about 10^{51} erg and contained originally in the kinetic energy of the shock wave.

Note that the SN explosion identified by numerous flash-like manifestations observed throughout the entire electromagnetic spectrum is infrequent phenomenon projected to human being lifetime. In our Galaxy one such event is estimated to occur once every 30–100 years; in addition, many of the explosions in the galactic disk are invisible as their optical emission is absorbed by dense gas–dust clouds concentrating to the galactic plane. The youngest SNRs (from historical SN explosions) in our Galaxy are hundreds to thousands years old. The youngest nearby SNR is SNR 1987A in a satellite galaxy—Large Magellanic Cloud. Exceptional importance of this event is evident given that it is the only nearby explosion occurred at the cosmic era and so observed by numerous modern ground- and space-based instruments via all the electromagnetic spectrum and also at the neutrino domain. Just prior to the explosion it was a blue supergiant star with the radius of $R \approx (30\text{–}60)\,R_\odot$ and mass $M \approx (10\text{–}30)\,M_\odot$. The parameter uncertainties are related to both lack of observational data and also uncertainties of internal structure evolution of massive stars (Imshennik and Nadezhin 1989; Filippenko 1997; Woosley and Bloom 2006; Smartt 2009):

To better understand the phenomenon of the SN explosion, we point out the most important effects missing from the Sedov solution.

- In addition to large energy the SN explosion ejects a large amount of stellar mass comparable with the solar mass, $\Delta M \approx (0.1\text{-}10)\,M_\odot$. The most massive stars exploding as type II SN eject a few dozens of $M_\odot$.

- Non-adiabatic processes are related to radiation of electromagnetic emission and acceleration of charged particles up to relativistic energies. This gives rise to temperature decrease downstream and, accordingly, to the compression increase ($\sigma = \rho_2/\rho_1 > 4$) there.

- There are further numerous processes affecting the SNR evolution: deviation from spherical symmetry, inhomogeneity of ISM, MHD and plasma instabilities.

According to these notes, the SNR evolution is typically categorized into four stages: (1) free expansion stage; (2) Sedov stage; (3) radiative stage, and (4) stage of dense cold shell.

1. **Free expansion stage.** The ejected stellar shell is initially much denser and hotter than the surrounding ISM; thus, the deceleration of the ejecta is initially small and so it moves out almost steadily with the initial velocity u_0, which is determined by the ejected mass ΔM and kinetic energy E of the explosion:

$$u_0 = (2E/\Delta M)^{1/2}. \tag{5.130}$$

   For the adopted above characteristic values we easily estimate $u_0 \approx (3 - 10) \times 10^8$ cm/s; in particular, $u_0 \approx (3 - 5) \times 10^8$ cm/s for SN 1987A. This stage of the evolution lasts until the swept-out ISM mass has become equal to the ejected mass: $\Delta M \approx (4\pi R_a^3 \rho_0/3)$. This estimate allows evaluating the "transition" radius (when this stage ends and gives a way to the Sedov stage) $R_a \approx 3\Delta M/4\pi\rho_0$ and typical free expansion time $t_a \approx R_a/u_0$. For $\Delta M \approx 1 \times M_\odot$, $E \approx 10^{51}$ erg we have $u_0 \approx 10^9$ cm/s, $R_a \approx 2$–10 pc, and $t_a \approx$200–1,000 years depending on the ISM number density. Overall, the estimates yield that the free expansion stage lasts around hundreds years and the expansion radius a few parsec.

2. **Sedov stage.** The larger the swept-out mass the better the Sedov's solution applicability to the actual SNR expansion: after a few t_a the SNR expansion is well described by the self-similar Sedov theory given in Sect. 5.5.1. During the first and the second stages the radiative losses are only a minor fraction of the ejecta kinetic energy [of the order of 10^{-3} for SN 1987A according to Imshennik and Nadezhin (1989)]. At the adiabatic (Sedov) stage the temperature downstream the front can be estimated according to Eq. (5.81) as

$$T_s = \frac{\gamma - 1}{(\gamma + 1)^2} m_i u_s^2. \tag{5.131}$$

   To account the actual ISM chemical composition it is typically adopted $m_i \approx 1.2 m_p$, which can be called a "standard" ISM composition.

Then, using Eqs. (5.110) and (5.111a), we obtain the downstream plasma temperature as a function of SNR radius:

$$T_s = \frac{4\beta^5(\gamma-1)}{25(\gamma+1)^2}\frac{E}{n_{0i}R_s^3}. \tag{5.132}$$

Apparently, the temperature rapidly decreases as the radius increases, i.e., the plasma cools down and the radiative losses go up, due mainly to heavy ion line emission. Detailed calculations of the plasma emissivity with a realistic radiative loss function suggest that the radiative losses become significant when $T_r \approx (5-6)\times 10^5\,\mathrm{K}$; thus, cooling down this temperature demarcates the transition to the third, radiative, stage of the SNR explosion. As long as the temperature is larger than T_r, a less efficient free–free contribution (see Chaps. 9 and 10) to the emissivity dominates making the radiative losses insignificant.

Further generalizations, including charged particle acceleration at the SNR shocks, will be considered in this book later, after the required microscopic treatment has been introduced. In some cases, at least, the role of the accelerated particle can be rather essential, which is eventually determined by the energy fraction accumulated by the relativistic particles during the acceleration. We can roughly neglect the accelerated particle effect if this energy fraction does not exceed 1%.

3. **Radiative stage.** The radius of this new transition to the radiative stage R_r can be estimated from Eq. (5.132) by substitution T_r to the lhs of the equality. For $n_{0i} = 1\,\mathrm{cm}^{-3}$, $E \approx 10^{51}\,\mathrm{erg}$, $\gamma = 5/3$, and $\beta \approx 1.15$ we obtain $R_r \approx 25\,\mathrm{pc}$. Further SNR expansion strongly deviates from the Sedov solution, since the adiabatic approximation breaks down; therefore the third stage of the SNR evolution can be studied based on model assumptions and/or computer simulations. Here we use simple semiquantitative estimates to outline some essentials of the radiative SNR stage.

4. **Stage of dense cold shell.** After the radius R_r has been reached, a thin dense cold shell surrounding the region filled with heated gas is rapidly formed. Almost the entire mass of the raked-up gas is contained in this shell. The pressure inside the shell is close to a uniform one, because the speed of sound is relatively high, but decreases with time due to the remnant expansion. The dependence of the pressure on the remnant radius can be estimated in a snowplough model (Blinnikov et al. 1982). Denoting the internal energy of the remnant as

$$E_T = \frac{4\pi R^3 p}{3(\gamma-1)}, \tag{5.133}$$

we write the condition of its adiabatic expansion in the form

$$\dot{E}_T = -4\pi R^2 p\dot{R}. \tag{5.134}$$

These equations are obtained assuming that a considerable part of the gas internal energy is lost during the radiative cooling [more than half, according to Blinnikov et al. (1982)] and subsequent radiation losses are small. But the shell continues to expand and sweep out the interstellar medium. In this approximation, from Eqs. (5.133) and (5.134) we obtain

$$E_T = E_{T0}\left(\frac{R_r}{R}\right)^{3(\gamma-1)}, \tag{5.135}$$

where E_{T0} is the internal energy of the remnant after the stage of efficient radiative cooling. To find this energy requires a numerical calculation of the radiative cooling. From Eqs. (5.133) and (5.135) we have the dependence $p \propto R^{-3\gamma} \approx R^{-5}$ after radiative cooling.

To calculate the time dependence of the remnant radius, we take into account the balance of mass and the balance of momentum of the cold shell (neglecting the small mass of the central part):

$$M = \frac{4}{3}\pi R^3 \rho_0, \qquad \frac{\mathrm{d}}{\mathrm{d}t}(M\dot{R}) = 4\pi R^2 p. \tag{5.136}$$

Combining the above equations, we can easily find the asymptote of the radiative stage of expansion of the SNR:

$$R(t) = \left(\frac{147 E_{T0} R_r^2}{8\pi\rho_0}\, t^2\right)^{1/7}, \qquad R(t) > R_r. \tag{5.137}$$

The ultimate radius of SNR—at the stage when it is completely assimilated by the ISM—is several dozens of parsecs.

5.6 Strong Explosion in an Inhomogeneous Medium, Kompaneets Solution, and Superbubble Blowouts

Another, more powerful example of rapidly expanding objects—expanding superbubbles (surrounded by a cold dense supershell) from OB associations—is congestions of stars, containing a few dozens of young hot stars capable of exploding as supernovae. To estimate a typical size of these objects we have to take into account that in place of an instant explosion, the mutual energy deposition from stellar winds and multiple supernova explosions results in roughly steady-state mechanical luminosity L_{SB} driven the expansion. Thus, we have to replace $E = L_{SB}t$ in Eq. (5.115), which yields $R_s(t) \propto t^{3/5}$ (in place of $R_s(t) \propto t^{2/5}$) for the superbubble expansion in the uniform ISM. Substitution of all required values into Eq. (5.115) yields the estimate

$$R_s(t) \approx 270[\mathrm{pc}]\left(\frac{L_{38} t_7^3}{n_0}\right)^{1/5}, \tag{5.138}$$

where $L_{38} = L_{SB}/(10^{38}\,\mathrm{erg\,s^{-1}})$ and $t_7 = t/(10^7$ year). We conclude that the superbubbles occupy a region of hundreds pc, much larger than that of a single SNR. Thus, the inhomogeneity of the Galaxy (disk–halo structure) starts to substantially affect the expansion, so one-dimensional spherically symmetric solution is insufficient to describe this more complicated physical phenomenon, which calls for more sophisticated two-dimensional treatment of the bubble expansion in the nonuniform ISM.

5.6.1 Point Explosion in a Stratified Atmosphere

Consider a spherically symmetric point explosion occurring in a plane-stratified gas with exponential density distribution

$$\rho(z) = \rho_0 \exp(-z/Z_0). \tag{5.139}$$

Here, unlike the Sedov case, the solution cannot be found based on self-similar dimension analysis because we have now three dimensional parameters involved: the midplane density ρ_0, the exponential scale height Z_0, and the explosion energy E_0. However, after Kompaneets (1960), we can find an approximate solution by adopting a number of natural simplifications: (1) bulk of the mass is concentrated in a thin expanding shell and (2) the pressure inside the bubble is uniform and equals to

$$p_{\mathrm{in}} = (\gamma - 1)\frac{\lambda E_0}{\Omega}, \tag{5.140}$$

where γ is the ratio of the specific heats, λ is a fraction of the explosion energy converted to the internal energy of the bubble gas, and Ω is the expanding bubble volume:

$$\Omega(t) = \pi \int_{z_1}^{z_2} r^2(z,t)\mathrm{d}z, \tag{5.141}$$

where $r = r(z,t)$ is the (yet to be specified) equation of the shock surface; the integration is performed between the bottom and top points of the bubble. Having in mind a strong shock, we neglect the undisturbed gas pressure, which with the Rankine–Hugoniot conditions yields the evolution of the normal (to the front) component of the expansion velocity

$$u_n(z,t) = \sqrt{\frac{(\gamma+1)p_{\mathrm{in}}(t)}{2\rho(z)}}, \tag{5.142}$$

where the ambient density is specified by Eq. (5.139).

If we define the equation of the shock surface in the form $f(r,z,t) \equiv (r - r(z,t)) = 0$ then, apparently,

$$\frac{\mathrm{d}f}{\mathrm{d}t} = \frac{\partial f}{\partial t} + u_z \frac{\partial f}{\partial z} + u_r \frac{\partial f}{\partial r}. \tag{5.143}$$

Taking into account that arbitrary vector normal to the surface can be written as

$$b_n = n_z b_z + n_r b_r = (b_r + b_z \partial r/\partial z)/|\nabla f|,$$

where

$$|\nabla f| = \sqrt{\left(\frac{\partial f}{\partial r}\right)^2 + \left(\frac{\partial f}{\partial z}\right)^2} \equiv \sqrt{1 + \left(\frac{\partial r}{\partial z}\right)^2} \tag{5.144}$$

we find

$$u_n(z,t) = -\frac{\partial f/\partial t}{|\nabla f|}. \tag{5.145}$$

Introducing a new variable

$$\tau = \int_0^t \sqrt{\frac{(\gamma^2 - 1)\lambda E_0}{2\rho_0 \Omega(t')}}\,\mathrm{d}t'. \tag{5.146}$$

in place of time t, equating two expressions (5.142) and (5.145) for the shock velocity, and using Eq. (5.144), we obtain the equation for the shock front evolution in implicit form

$$\left(\frac{\partial r}{\partial \tau}\right)^2 - \exp(z/Z_0)\left[1 + \left(\frac{\partial r}{\partial z}\right)^2\right] = 0. \tag{5.147}$$

This equation can be solved by variable separation to yield

$$\frac{\partial r}{\partial \tau} = \xi, \qquad \frac{\partial r}{\partial z} = \pm\sqrt{\xi^2 \exp(-z/Z_0) - 1}, \tag{5.148a}$$

$$r = \xi\tau \pm \int_0^z \sqrt{\xi^2 \exp(-z/Z_0) - 1}\,\mathrm{d}z + b(z), \tag{5.148b}$$

$$\frac{\partial r}{\partial \xi} = \tau \pm \int_0^z \frac{\xi \exp(-z/Z_0)}{\sqrt{\xi^2 \exp(-z/Z_0) - 1}}\,\mathrm{d}z + \frac{\partial b(z)}{\partial \xi}, \tag{5.148c}$$

where ξ is a parameter and function $b(\xi)$ is specified by initial conditions of the explosions. In particular, for the isotropic explosion considered here it is zero, $b(\xi) = 0$. Then, we can eliminate the ξ parameter to obtain the shape of the front in the form

$$r = 2Z_0 \arccos\left\{\frac{1}{2}\exp\left(\frac{z}{2Z_0}\right)\left[1 - \frac{\tau^2}{4Z_0^2} + \exp\left(-\frac{z}{Z_0}\right)\right]\right\}. \tag{5.149}$$

This Kompaneets solution can be generalized to the cases of more complicated density profiles and to a persistent (including time-dependent) mechanical luminosity in place of instant explosion considered above (see the problem section). We use the Kompaneets solution below to qualitatively understand the phenomenon of superbubble blowouts and their role in the disk–halo connections in the Galaxy.

5.6.2 Superbubble Blowout

Let us analyze the behavior of Kompaneets solution (5.149) of the point isotropic explosion in a plane-stratified gas of the galactic disk above the mid-plane. Specifically, consider first how the top and bottom points of the blast wave move after the explosion. To do this we put $r = 0$ in solution (5.149), which yields

$$\exp\left(-\frac{z_{1,2}}{2Z_0}\right) = 1 \mp \frac{\tau}{2Z_0}. \tag{5.150}$$

Apparently, this equation has a real solution only for $0 \le \tau < 2Z_0$; $\tau = 0$ corresponds to $t = 0$, while $\tau \to 2Z_0$ implying $\exp(-z_1/2Z_0) \to 0$ and, thus, $z_1 \to \infty$ corresponds to a finite t defined by Eq. (5.146). Stated another way, this means that the top end of the expanding shell reaches the infinity over a finite time, which implies an infinite shock acceleration toward decreasing

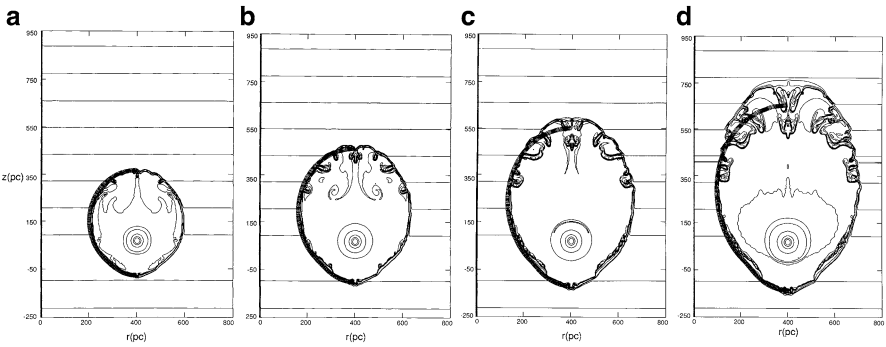

Figure 5.8: Example of numerical simulation results for a superbubble (mechanical luminosity $1.1 \times 10^{38}\,\mathrm{erg\,s^{-1}}$) blowout from the galactic disk with exponential atmosphere described by Eq. (5.139) with $\rho_0 = 2.11 \times 10^{-24}\,\mathrm{g\,cm^{-3}}$ and $Z_0 = 100\,\mathrm{pc}$ (Mac Low et al. 1989); reproduced by permission of the AAS. The point-like energy source is located 70 pc above the galactic plane. The model is presented for the time frames (**a**) 3.83 MY, (**b**) 5.02 MY, (**c**) 5.89 MY, and (**d**) 6.87 MY. The analytical Kompaneets solution described by Eq. (5.149) is shown in the *left part* of each plot by *inner part* of the *thick hatched curve*. The remarkable overall agreement between analytical and numerical results is clearly seen. At later times the numerical solution starts to deviate from the analytical one due to development of the Rayleigh–Taylor instability; see Chap. 6 for more detail.

density due to the density gradient—the atmospheric blowout. The other (bottom) end point of the shock propagates downward the distance

$$z_2 = -2Z_0 \ln 2 \tag{5.151}$$

over the same time, i.e., the shock cannot penetrate deeper than a certain depth defined by Eq. (5.151) toward the increasing density. Likewise, the shock spreading in r-direction is bounded: for $\partial r/\partial z = 0$ Eq. (5.150) yields

$$r_{\max} = 2Z_0 \arccos \frac{\tau}{2Z_0^2}. \tag{5.152}$$

Substituting $\tau = 2Z_0$ into Eq. (5.152) we find the largest accessible value $r_c = \pi Z_0$, which, likewise z_2, does not depend on the deposited energy at all. This is because whatever energy is deposited into the explosion, most of it escapes the explosion region toward direction of the largest density gradient. However, the deposited energy affects the physical time t needed for the blowout—the larger the energy deposition the faster the blowout occurs.

The considered effect of the superbubble blowouts has exceptionally strong effect on the interactions between the galactic disk and halo, in particular, on the transport of the energy and momentum to the halo; it controls the particle number density, the chemical composition, ionization state distribution, and magnetic field generation in the halo. For this reason the superbubble blowouts have been thoroughly studied numerically in 2D and 3D (including the ISM magnetic field effect) configurations. Although those advanced numerical studies reveal a lot of details about the expansion and the blowouts including a number of MHD instabilities (subject of the next chapter), the overall behavior of the expansion and the blowouts is described by the Kompaneets solution remarkably well; see Fig. 5.8.

Problems

5.1 Obtain solutions (5.10) and (5.11) for the small-amplitude Alfvén wave by linearization of the dissipation-free MHD equations (2.18).

5.2 Calculate the damping rate γ of the plane small-amplitude Alfvén wave if the kinematic viscosity ν and magnetic diffusivity ν_m of the fluid are known. Adopt that the damping rate is small compared with the wave frequency.

5.3 Consider the fast and slow simple waves in the small-amplitude approximation. Use equation set (2.18) in the linearized form. Determine orientation of vectors $\boldsymbol{k}$, $\boldsymbol{u}$, $\boldsymbol{b}$, and $\boldsymbol{B}_0$, where the last two vectors represent the magnetosonic wave amplitude and external uniform field, respectively.

5.4 ⋆ Analyze variation of the perpendicular fast simple wave shape, considered in Sect. 5.1.3, produced by the dependence of the phase velocity on the fluid density. Adopt the initial, at $t = 0$, simple wave shape to be $u_x(x,0) \equiv u(x,0) = u_0/\cosh(x/h)$, where $u_0 = c_{s0} = v_{A0}$ is equal to both sound speed c_{s0} and Alfvén speed v_{A0} in the undisturbed fluid. Apply numeric computation to derive the velocity $u(x,t)$ for $t > 0$. Plot the magnetic field $B(x,t)$ for $t = 0$ and $t > 0$. Find the time frame t_* at which the simple wave solution breaks down (i.e., the solution is single valued for $t < t_*$, while multiple valued afterwards, $t > t_*$). Adopt the adiabatic equation of state $p(\rho) = p_0(\rho/\rho_0)^\gamma$ for the fluid considered.

5.5 ⋆ Describe the general solution of Burgers equations (5.33) in homogeneous boundless medium. The initial condition is $P(\xi,0) = P_0(\xi)$, where $P_0(\xi)$ is a given function.

Hint: Reduce the nonlinear Burgers equation to the linear equation of the heat conductivity by means of the nonlinear substitution $P(\xi,t) = -2\kappa\partial_\xi \ln\varphi(\xi,t)$, where $\varphi(\xi,t)$ is a new unknown function.

5.6 Consider an initial perturbation occupying a narrow region: $P_0(\xi) = A\delta(\xi)$ (see the above problem). Here P_0 has a dimension of velocity, while A of the product of velocity and length. Dimensionless value $R = A/2\kappa$ is the Reynolds number. Find the profile of perturbation for $t > 0$ and analyze the limiting cases $R \ll 1$ and $R \gg 1$.

5.7 Derive the following relations at the front of parallel shock wave in a rarefied gas in terms of Mach number $M = u_1/c_{s1} > 1$:

$$\frac{\rho_2}{\rho_1} = \frac{u_1}{u_2} = \frac{(\gamma+1)M^2}{(\gamma-1)M^2+2}, \quad \frac{p_2}{p_1} = \frac{2\gamma M^2}{\gamma+1} - \frac{\gamma-1}{\gamma+1},$$
$$\frac{T_2}{T_1} = \frac{[2\gamma M^2-(\gamma-1)][(\gamma-1)M^2+2]}{(\gamma+1)^2M^2}.$$

5.8 Determine conditions which must be fulfilled at the ultrarelativistic shock front.

5.9 A spherical star explosion takes place in a stellar wind region with nonuniform mass density $\rho_0 \propto r^{-2}$. Magnetic field in the stellar wind region is given by Parker's model; see Problem 2.10. Calculate magnetic field after the burst, if the magnetic field does not depend on α, constants $p = 0$ and $q = 1$. The dependence $R_s(t) \propto t^{2/3}$ is given by Eq. (5.115). The velocity of ejected plasma is large compared with stellar wind velocity u_w.

5.10 Generalize the Kompaneets solution for the following cases:

1. Density profile with nonzero asymptote: $\rho(z) = \rho_0 \exp(-z/Z_0) + \alpha$.
2. Hybrid density profile: $\rho(z) = \rho_0 \exp(-z/Z_0) + \rho_1 \exp(-z^2/Z_1^2)$.
3. Off-center point explosion in a radially stratified gas.
4. Constant mechanical luminosity.

Answers and Solutions

5.5 Let us perform the substitution step by step. Making it in the first term $\partial P/\partial t$, we obtain $\partial_\xi[-2\kappa\partial_t \ln\varphi + P^2/2 - \kappa\partial_\xi P] = 0$. At the next step $\partial_\xi[\varphi^{-1}(-\partial_t\varphi + \kappa\partial_\xi^2\varphi)] = 0$. This implies that $\partial_t\varphi - \kappa\partial_\xi^2\varphi = \varphi \mathrm{d}F/\mathrm{d}t$, where $\mathrm{d}F/\mathrm{d}t$ is an arbitrary function of time. Further substitution

$$\varphi(\xi, t) = \Phi(\xi, t) \exp F(t) \tag{1}$$

transforms this equation to the form of heat transfer equation for Φ:

$$\partial_t\Phi = \kappa\partial_\xi^2\Phi. \tag{2}$$

Since $F(t)$ and $P(\xi, t)$ are independent, we can adopt $\Phi \to \varphi$ and use Eq. (2) to specify the function φ.

A general solution of Eq. (2) can be built up with the Green function method likewise in Sect. 2.3.1:

$$\varphi(\xi, t) = \frac{1}{\sqrt{4\pi\kappa t}} \int_{-\infty}^{\infty} \exp\left\{-\frac{(\xi-\eta)^2}{4\kappa t} - \frac{1}{2\kappa}\int_0^\eta P_0(\eta')\mathrm{d}\eta'\right\}\mathrm{d}\eta. \tag{3}$$

5.6 Based on Eq. (3), previous solution, we write the Burgers equation solution in the form

$$P(\xi, t) = \frac{\int_{-\infty}^{\infty}[(\xi-\eta)/t]e^{-G/2\kappa}\mathrm{d}\eta}{\int_{-\infty}^{\infty} e^{-G/2\kappa}\mathrm{d}\eta}, \tag{1}$$

where

$$G(\xi, \eta, t) = \frac{(\xi-\eta)^2}{2t} + \int_0^\eta P_0(\eta')\mathrm{d}\eta'. \tag{2}$$

The solution does not depend on lower limit of the integral, so it can be selected arbitrarily; we make the following selection:

$$\int_{+0}^{\eta} P_0(\eta')\mathrm{d}\eta' = \begin{cases} 0, & \eta > 0, \\ -A, & \eta < 0. \end{cases} \tag{3}$$

Now, the integral in the numerator of (1) can be taken, so the solution takes the form

$$P(\xi,t)=\sqrt{\frac{\kappa}{t}}\frac{(e^R-1)e^{-\xi^2/4\kappa t}}{\sqrt{\pi}+(e^R-1)\int_{\xi/\sqrt{4\kappa t}}^{\infty}e^{-\eta^2}\mathrm{d}\eta},\qquad R=\frac{A}{2\kappa}. \tag{4}$$

If $R\ll 1$, we keep only the first term in the denominator and obtain

$$P(\xi,t)=\sqrt{\frac{\kappa}{\pi t}}Re^{-\xi^2/4\kappa t}=\frac{A}{\sqrt{4\pi\kappa t}}e^{-\xi^2/4\kappa t}, \tag{5}$$

i.e., this is a typical solution of the heat transfer equation. Stated another way, the dissipation dominates the nonlinearity in the Burgers equation.

If $R\gg 1$, we introduce a new independent dimensionless variable $\zeta=\xi/\sqrt{2At}$ and write down an exact solution of (2) in the form

$$P(\xi,t)=\sqrt{\frac{2A}{t}}g(\zeta,R),\qquad g(\zeta,R)=\frac{e^R-1}{2\sqrt{R}}\frac{e^{-\zeta^2R}}{\sqrt{\pi}+(e^R-1)\int_{\zeta\sqrt{R}}^{\infty}e^{-\eta^2}\mathrm{d}\eta}. \tag{6}$$

Then, use the condition $R\gg 1$:

$$g(\zeta,R)\approx\frac{1}{2\sqrt{R}}\frac{e^{R(1-\zeta^2)}}{\sqrt{\pi}+e^R\int_{\zeta\sqrt{R}}^{\infty}e^{-\eta^2}\mathrm{d}\eta}. \tag{7}$$

For $\zeta<0$ we have

$$\int_{\zeta\sqrt{R}}^{\infty}e^{-\eta^2}\mathrm{d}\eta\approx\int_{-\infty}^{\infty}e^{-\eta^2}\mathrm{d}\eta=\sqrt{\pi},$$

i.e., $g\approx(1/2\sqrt{R})e^{-R\zeta^2}\to 0$ for $R\to\infty$.

If $\zeta>0$, then

$$\int_{\zeta\sqrt{R}}^{\infty}e^{-\eta^2}\mathrm{d}\eta\approx\frac{e^{-R\zeta^2}}{2\zeta\sqrt{R}}$$

and (7) yields

$$g(\zeta,R)\approx\frac{\zeta}{1+2\zeta\sqrt{\pi R}e^{R(\zeta^2-1)}}. \tag{8}$$

This approximation gives rise to a simple dependence $g(\zeta,R)\approx\zeta$ if $0<\zeta<1$, $R\gg 1$. Eventually, returning to initial variables, we obtain a triangle wave with a discontinuity at $\xi=\sqrt{2At}$:

$$P(\xi,t)\approx\begin{cases}\xi/t & \text{for}\quad 0<\xi<\sqrt{2At},\\ 0 & \text{for}\quad \xi<0,\ \xi>\sqrt{2At}.\end{cases} \tag{9}$$

At the vicinities of $\xi=0$ and $\xi=\sqrt{2At}$ there are narrow (for $R\gg 1$) transition regions; see Whitham (1974) for greater detail of the solution.

5.8 The jump conditions are found based on continuity of the fluxes of energy ($w\gamma^2\beta$), momentum ($w\gamma^2\beta^2+p$), and particles ($n\gamma\beta$), where the enthalpy $w = \varepsilon + p$, energy density ε, and pressure p are measured in the fluid frame; the Lorentz factor $\gamma = 1/\sqrt{1-\beta^2}$ is defined by the corresponding velocity β assuming $c = 1$. The strong shock means that $p_2/n_2 \gg p_1/n_1$; the gas pressure is related to the energy density as $p = (\hat{\gamma}-1)(\varepsilon - \rho c^2) = (\hat{\gamma}-1)(\varepsilon - \rho)$ as $c = 1$, where $4/3 \le \hat{\gamma} \le 5/3$ is the effective ratio of specific heats. Denoting the Lorentz factor of the downstream fluid measured in the "laboratory" frame where the upstream fluid is immobile as γ_2 and that of the shock front as Γ, again in the laboratory frame, we find for an arbitrary strong shock wave

$$\frac{\varepsilon_2}{n_2} = \gamma_2 \frac{w_1}{n_1}$$

$$\frac{n_2}{n_1} = \frac{\hat{\gamma}_2\gamma_2 + 1}{\hat{\gamma}_2 - 1}$$

$$\Gamma^2 = \frac{(\gamma_2+1)[\hat{\gamma}_2(\gamma_2-1)+1]^2}{\hat{\gamma}_2(2-\hat{\gamma}_2)(\gamma_2-1)+2}.$$

Now, for an ultrarelativistic shock wave, $\Gamma \gg 1$, the above jump conditions simplify to

$$p_2 = \frac{\varepsilon_2}{3} = \frac{2}{3}\Gamma^2 w_1; \qquad n_2' = 2\Gamma^2 n_1 \qquad \gamma_2^2 = \frac{1}{2}\Gamma^2,$$

where $n_2' = \gamma_2 n_2$ is the downstream density measured in the laboratory (upstream gas) frame. For a cold upstream gas $w_1 = \rho_1 c^2$, for a relativistic gas $w_1 = p_1$. Self-similar spherical and some other solutions can be obtained from a deeper analysis; see Blandford and McKee (1976).

5.9 For $r < R_s(t)$,

$$B_r(r,\vartheta,t) = \left(\frac{a}{r}\right)^2 B_{0r}(a,\vartheta), \quad B_\alpha(r,\vartheta,t) = \frac{\rho_s a^2 \Omega}{\rho_0 u_w r}\left(\frac{r}{R_s(t)}\right)^3 B_{0r}(a,\vartheta)\sin\vartheta,$$

$$B_\vartheta = 0.$$

5.10 Study papers by Mac Low and McCray (1988) and Bisnovatyi-Kogan and Silich (1995).

Chapter 6

Instability of MHD Motion and Astrophysical MHD Turbulence

Let us define *the stable states* as such medium motion or rest states, in which small random perturbations of macroscopic parameters do not increase, while they can oscillate with some damping rate and so eventually dissipate. In astrophysics, however, there are numerous examples of the states, which are not stable. Instead, an instability takes place in many cases: small random perturbations of the macroscopic parameters rise at the expense of either mechanical or magnetic energy.

Broadly speaking, instability, in most of the cases, is an attribute of the systems obeying nonlinear equations. For most of the linear systems the theorems of solution uniqueness are proved. Therefore, if the functions obeying the linear system (describing the phenomenon under study) are obtained and initial and boundary conditions are fulfilled, then the functions obtained represent the solution of the problem, and it is the only solution.

In contrast, nonlinear equations have frequently many solutions, and the theorem of solution uniqueness does not take place here in a general case. To verify if a solution can really describe the system, one must check if the solution is stable or not. *Unstable states* can only take place over a limited (frequently—rather short) time interval, then the system leaves this unstable state toward a (more) stable state, which can be strongly different compared with the initial unstable state.

Apparently, these qualitative considerations must not be overstated. In what follows (e.g., Chaps. 8 and 12) we consider many solutions of linear equations that describe unbounded rise of certain measures such as the magnetic field or an MHD wave amplitude. However, such unstable solutions just indicate that the original linear equation set is only an approximation to the reality, where some overall essential physics has reasonably been neglected for relatively small amplitudes, while it becomes significant at a later

G.D. Fleishman and I.N. Toptygin, *Cosmic Electrodynamics*, Astrophysics and Space Science Library 388, DOI 10.1007/978-1-4614-5782-4_6,

stage of the evolution, when the amplitudes become large and so use of the corresponding nonlinear theory is required. Of course, nonlinear equations are not
necessarily unstable; they often can have stationary solutions describing stable states of a given physical system.

The importance of the unstable states in astrophysics can hardly be overstated. It is the instabilities that drive the evolution of the nonstationary Universe. It is the instabilities that are giving rise to the variety of natural forms of matter including the very life, which we observe by all means of our sense organs and scientific instruments and observatories. Thus, the study of instabilities is one of the mainstreams in both theoretical and observational astrophysics.

A standard approach to the analysis of instabilities is the method of small perturbations. The idea of this method is simple and straightforward. First, we add small perturbations to the macroscopic parameters describing the obtained stationary state of the system. At the second step the nonlinear set of equations is linearized. Third, we solve the linearized equations for the small perturbations to determine imaginary parts of the frequencies of the linear oscillations. Fourth, we determine if there is any oscillation with a positive imaginary part of the frequency—those positive imaginary parts are the growth rates of the unstable perturbations. These exponentially growing solutions are valid over relatively short time intervals (order of a few inverse growth rates); thus, they cannot tell what is the final state of the system when the instability is over due to *saturation* of the instability. It is worthwhile to note here that if this analysis confirms the stability of the solution, it is not guaranteed that the solution will also be stable against finite (large) perturbations; however, this is a subject of a separate (and much more complicated) analysis.

Alternatively, an energy method is often applied to study instabilities. The core of this method is calculation of the energy variation for a small departure of the system from the given state. If this variation is negative (in the first nonzero approximation) then the system is unstable. This method is used, as an example, in solution to Problem 6.4 at the end of this chapter.

This chapter discusses only a minor fraction of the instabilities, typically those which are essentially affected by the electromagnetic field, although apparently we cannot ignore a primary force acting at astrophysics scales, the gravity force. Gravitation is the main interaction controlling the global Universe structure. The gravitation and related instabilities play a key role in global evolution of observed region of the Universe, including galaxies and galaxy clusters, stellar associations, isolated stars, and planetary systems. Thus, it seems natural to start the instability analysis from those associated with the gravity.

6.1 Gravitational Instability

Initially the idea of a gravitational instability was put forward by Isaac Newton in 1692, soon after he had discovered the gravitation law (1687). Nevertheless, the math treatment of the instability had to await the twentieth century when James Jeans (and his followers) considered this instability first within the nonrelativistic Newton theory and then within Friedman's theory of expanding Universe based on the general relativity. Below we consider simple versions of the instability, while more complete treatment can be found elsewhere (Zel'dovich and Novikov 1971; Weinberg 1972); elementary introduction into relativistic theory of gravitation is given by Beskin (2009a).

The gravitational instability is easy to qualitatively understand. Suppose there is an initially uniform distribution of the gravitating matter, characterized by a density $\rho = \text{const}$ and a pressure $p_0 = \text{const}$, in which a density enhancement $\rho + \rho'$ with a spatial scale λ randomly appears. Then, the force attracting the surrounding matter to this condensation increases approximately by $G\Delta M/\lambda^2 \approx G\rho'\lambda^3/\lambda^2 = G\rho'\lambda$ per unit mass. However, the oppositely directed force produced by the increased pressure inside the condensation also grows: neglecting the heat conductivity this force is proportional to $\rho^{-1}\partial p'/\partial r \approx c_s^2\rho'/\rho\lambda$, where c_s is the sound speed. For the instability it is essential that these two competing forces depend differently on the condensation size. This implies that for a large condensation the gravity dominates so the condensation grows, while small condensations relax to original state due to elastic force supplied by the pressure gradient. The critical condensation size $\lambda_J \approx c_s/\sqrt{G\rho}$, above which the gravitational instability can develop, is known as the **Jeans length**.

These qualitative evaluations can be confirmed and further developed quantitatively. Consider here the propagation of small perturbations in a conducting fluid taking into account the self-gravity and the magnetic field. Adopt that initially the fluid is immobile and homogeneous over the scales much larger than the perturbation under study. Neglecting all dissipative terms, the equation set reads

$$\frac{\partial \rho}{\partial t} + \nabla \cdot \rho \boldsymbol{u} = 0, \qquad \Delta\phi = -4\pi G\rho, \tag{6.1a}$$

$$\frac{\partial \boldsymbol{u}}{\partial t} + (\boldsymbol{u}\cdot\nabla)\boldsymbol{u} = -\frac{1}{\rho}\nabla p + \nabla\phi + \frac{1}{4\pi\rho}[\nabla \times \boldsymbol{B}] \times \boldsymbol{B}, \tag{6.1b}$$

$$\frac{\partial \boldsymbol{B}}{\partial t} = \nabla \times (\boldsymbol{u} \times \boldsymbol{B}), \tag{6.1c}$$

where $\phi(\boldsymbol{r}, t)$ is the gravitation potential, so the acceleration vector in the gravity force is $\boldsymbol{g} = \nabla\phi$.

Then, we discard the weak dependence of the mean values ρ_0, p_0, ϕ_0, $\boldsymbol{u}_0 = 0$ and $\boldsymbol{B}_0$ on time and spatial coordinates. The perturbations $\rho'(\boldsymbol{r}, t)$,

$p'(\boldsymbol{r},t)$, $\boldsymbol{u}'(\boldsymbol{r},t) = \boldsymbol{u}(\boldsymbol{r},t)$, and $\boldsymbol{b}(\boldsymbol{r},t)$ are assumed to be first-order small values. The linearized set of equations takes the form

$$\frac{\partial \rho'}{\partial t} + \nabla \cdot \rho_0 \boldsymbol{u} = 0, \quad \Delta\phi' = -4\pi G\rho', \tag{6.2a}$$

$$\frac{\partial \boldsymbol{u}}{\partial t} = -\frac{c_s^2}{\rho_0}\nabla\rho' + \nabla\phi' + \frac{1}{4\pi\rho_0}[\nabla \times \boldsymbol{b}] \times \boldsymbol{B}_0, \tag{6.2b}$$

$$\frac{\partial \boldsymbol{b}}{\partial t} = \nabla \times (\boldsymbol{u} \times \boldsymbol{B}_0). \tag{6.2c}$$

We seek a solution of Eq. (6.2) in the form of plane monochromatic waves, i.e., $\rho' \propto \exp(i\boldsymbol{k}\cdot\boldsymbol{r} - i\omega t)$, which yields algebraic equation set. Exclusion of the variables ρ', ϕ', and $\boldsymbol{b}$ yields

$$(\omega^2 - \Omega_\mathrm{A}^2)\boldsymbol{u} + \Omega_\mathrm{A}\boldsymbol{v}_\mathrm{A}(\boldsymbol{k}\cdot\boldsymbol{u}) - (\Omega_J^2 + v_\mathrm{A}^2k^2)\frac{\boldsymbol{k}(\boldsymbol{k}\cdot\boldsymbol{u})}{k^2} + \Omega_\mathrm{A}\boldsymbol{k}(\boldsymbol{u}\cdot\boldsymbol{v}_\mathrm{A}) = 0. \tag{6.3}$$

Here

$$\Omega_J^2 = c_s^2k^2 - 4\pi G\rho_0, \quad \Omega_\mathrm{A} = \frac{|\boldsymbol{k}\cdot\boldsymbol{B}_0|}{\sqrt{4\pi\rho_0}}, \quad \boldsymbol{v}_\mathrm{A} = \frac{\boldsymbol{B}_0}{\sqrt{4\pi\rho_0}}. \tag{6.4}$$

Investigation of the eigenmodes is reasonable to start from a simpler case of zero magnetic field, $v_\mathrm{A} = 0$ and $\Omega_\mathrm{A} = 0$; Eq. (6.3) reduces to

$$\omega^2\boldsymbol{u} - \Omega_J^2\frac{\boldsymbol{k}(\boldsymbol{k}\cdot\boldsymbol{u})}{k^2} = 0, \tag{6.5}$$

which implies that the perturbations are longitudinal along $\boldsymbol{k}$ and their frequency is

$$\omega = \pm\Omega_J = \pm\sqrt{c_s^2k^2 - 4\pi G\rho_0}. \tag{6.6}$$

For large wave numbers the negative term under the square root is negligible, so this mode corresponds to usual sound waves $\omega \approx \pm c_sk$. However, the smaller the wave number the stronger the gravitation field effect so that for

$$k < k_J = \frac{\sqrt{4\pi G\rho_0}}{c_s} \quad \text{or} \quad \lambda > \lambda_J = \frac{2\pi}{k_J} = c_s\sqrt{\frac{\pi}{G\rho_0}} \tag{6.7}$$

the gravitational (Jeans) instability appears. The growth rate $\gamma = c_s\sqrt{k_J^2 - k^2}$ is apparently upper bounded by the value $\gamma_\mathrm{max} \approx c_sk_J$.

The presence of magnetic field complicates the wave properties; however, the instability threshold stays unchanged. To see this, we collapse Eq. (6.3) onto the directions of $\boldsymbol{k}$ (axes Ox), $\boldsymbol{B}_0 \times \boldsymbol{k}$ (Oy), and $\boldsymbol{k} \times (\boldsymbol{B}_0 \times \boldsymbol{k})$ (Oz), respectively, and obtain

$$(\omega^2 - \Omega_\mathrm{A}^2)u_y = 0, \tag{6.8a}$$

$$(\omega^2 - v_{\mathrm{A}z}^2k^2 - \Omega_J^2)u_x + \Omega_\mathrm{A}kv_{\mathrm{A}z}u_z = 0, \tag{6.8b}$$

$$\Omega_\mathrm{A}kv_{\mathrm{A}z}u_x + (\omega^2 - \Omega_\mathrm{A}^2)u_z = 0. \tag{6.8c}$$

The first of them describes the Alfvén mode in which $\omega = \pm\Omega_\mathrm{A}$ and the velocity $\boldsymbol{u}$ is transverse to the plane formed by the vectors $\boldsymbol{k}$ and $\boldsymbol{B}_0$. The gravity has no effect on this mode. Two remaining equations describe magnetosonic wave modified by the gravity. They have a nontrivial solution if the determinant of these equations is zero:

$$\omega^4 - \omega^2(\Omega_J^2 + v_\mathrm{A}^2 k^2) + \Omega_\mathrm{A}^2 \Omega_J^2 = 0. \tag{6.9}$$

Solutions ω_1^2 and ω_2^2 of this biquadratic equation obey the conditions

$$\omega_1^2 + \omega_2^2 = \Omega_J^2 + v_\mathrm{A}^2 k^2, \quad \omega_1^2 \omega_2^2 = \Omega_\mathrm{A}^2 \Omega_J^2. \tag{6.10}$$

The latter one tells us that one of the frequencies, ω_1 or ω_2, becomes imaginary if the Jeans condition $\Omega_J^2 < 0$ is fulfilled. If $\boldsymbol{k} \cdot \boldsymbol{B}_0 = 0$ and, thus, $\Omega_\mathrm{A} = 0$, we have from Eq. (6.9) $\omega^2 = \Omega_J^2 + v_\mathrm{A}^2 k^2$. The Jeans instability appears for small wave numbers satisfying $k < [4\pi G\rho/(c_s^2 + v_\mathrm{A}^2)]^{1/2}$. Therefore, the magnetic field does not stabilize the gravitational instability. Furthermore, it has been proved that rotation of the object as a whole does not stabilize the instability either.

Jeans condition (6.7) has been obtained for a medium, which is at rest initially. However, the theory of expanding Universe proposed by Alexander Friedman (1922), which has been observationally confirmed by Edwin Hubble (1929) and by ample body of modern astrophysical observations, calls for investigation of the gravitational instability based on general relativity, at least at large cosmological scales where this expansion is a key property of the Universe. This is evidently beyond the scope of our textbook.

Thus, to better understand the essence of the instability at smaller scales (where we can ignore effects of the general relativity), let us estimate the Jeans scale considering the Galaxy as a uniform fluid and using typical parameters of ISM in the galactic disk: $\rho_0 \approx 10^{-24}\,\mathrm{g}$, $c_s \approx 3 \times 10^6\,\mathrm{cm/s}$, $G \approx 7 \times 10^{-8}\,\mathrm{cm^3/g\,s^2}$; we obtain $\lambda_J \approx 7\,\mathrm{kpc}$. Thus, the Jeans scale is comparable with the galactic scales and noticeably exceeds the disk thickness. This implies that the gravitational instability has no effect on the observed spatial structure of the Galaxy. Although we included the baryon mass density ρ_0 only, even for the dark matter with 10 times larger density the Jeans scale remains too large to play a role in the Galaxy.

This conclusion is only valid for initially uniform distribution of the matter. However, if some density clumps (produced by another mechanism) preexist in the matter distribution, the gravitation can enhance these inhomogeneities, which results in formation of dense self-gravitating objects including, e.g., normal stars. The gravitation instability can be enhanced by the large-scale shock waves (e.g., from SN explosions) or density waves (forming the Galaxy spiral arm structure) (see (Rohlfs 1977) for more detail).

6.2 Convective Instability

Convection, i.e., fluid mixing due to macroscopic mechanical motions of the fluid stimulated by nonuniform heating along the gravitation or/and inertia force, plays an important role in planetary (including the Earth) atmospheres, interior of the Sun and many other stars, and other astrophysical objects. In particular, the convection can efficiently transfer the heat due to macroscopic motion of the overheated fluid elements, accompanied by the mass and internal energy transfer. A more standard, microscopic heat transfer described by a Fourier law $\boldsymbol{q} = -\chi \nabla T$ in the simplest case is driven by the particle diffusion and so does not contain the macroscopic fluid transfer. Here we consider fundamentals of this phenomenon.

6.2.1 Necessary Condition of Convection: Stationary Case

Let us start from a relatively simple model of a plane region of a fluid with the height h, heated from below, so the temperatures T_1 and T_2 are held at the fluid boundaries (Fig. 6.1). The solution of this problem under the Fourier law condition is simple and well known: a linear profile of temperature is established eventually:

$$T(z) = T_1 - \beta z, \quad \text{where} \quad \beta = \frac{T_1 - T_2}{h} \tag{6.11}$$

is the temperature gradient, while the heat flux is $q_z = \beta\chi$. Gravitation does not affect noticeably the diffusion of the heated particles, so there is no macroscopic motion. However, the gravitation substantially affects the mechanical equilibrium of the fluid; the stability condition is apparently

$$\frac{\mathrm{d}p}{\mathrm{d}z} = -\rho g. \tag{6.12}$$

If the temperature gradient is large, the equilibrium can break down, which results in a macroscopic instability. Indeed, consider a small fluid element, which lifts randomly from a level z up to the level $z + \mathrm{d}z$, where the fluid temperature is lower (Fig. 6.1). If this fluid element lifts up adiabatically, its temperature change is small; thus its density appears to be smaller than the equilibrium density at the level $z + \mathrm{d}z$, so the element will hold rising up due to the Archimedes force. During this lifting the pressure in the element assimilates quickly (with the sound speed) with the external pressure, while the temperature does not assimilate, because the diffusion is a slower process. Thus, spontaneous vertical fluid flows appear that immediately give

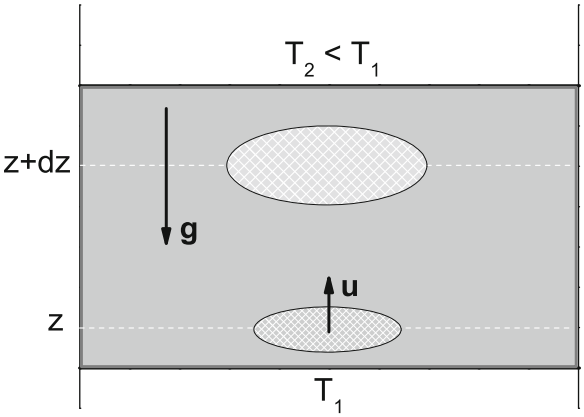

Figure 6.1: Lifting of an element of matter at convection.

rise to horizontal flows (according to continuity equation), which means the convective mixing of the nonuniformly heated fluid.

Having the phenomenon of convection clarified qualitatively, let us proceed to quantitative consideration. Adopt that the pressure and specific entropy are p and s at the level z, while p' and $s' = s + (\mathrm{d}s/\mathrm{d}z)\mathrm{d}z$ at the level $z + \mathrm{d}z$. The specific volume of the rising fluid element at the level z is $V(p, s)$, while at the level $z + \mathrm{d}z$ is $V(p', s)$. The necessary condition of the element to further lifting up is

$$V(p', s) - V(p', s') \approx -\left(\frac{\partial V}{\partial s}\right)_p \frac{\mathrm{d}s}{\mathrm{d}z}\mathrm{d}z > 0, \tag{6.13}$$

i.e., the density of the lifting element is smaller than one of surrounding fluid (its specific volume is respectively larger).

Then, a thermodynamic relation yields

$$\left(\frac{\partial V}{\partial s}\right)_p = \frac{T}{c_p}\left(\frac{\partial V}{\partial T}\right)_p = \frac{TV}{c_p}\alpha > 0$$

(the latter equality assumes that the fluid expands during heating; α is the volumetric thermal expansion coefficient), which gives rise to inequality $\mathrm{d}s/\mathrm{d}z < 0$ formulating the necessary condition of the convective instability. Let us transform this inequality considering the entropy $s(T, p)$ as a function of temperature and pressure:

$$\frac{\mathrm{d}s}{\mathrm{d}z} = \left(\frac{\partial s}{\partial T}\right)_p \frac{\mathrm{d}T}{\mathrm{d}z} + \left(\frac{\partial s}{\partial p}\right)_T \frac{\mathrm{d}p}{\mathrm{d}z} = \frac{c_p}{T}\frac{\mathrm{d}T}{\mathrm{d}z} - \left(\frac{\partial V}{\partial T}\right)_p \frac{\mathrm{d}p}{\mathrm{d}z} < 0. \tag{6.14}$$

Finally, incorporating Eq. (6.12), we obtain

$$\frac{\mathrm{d}T}{\mathrm{d}z} < -\frac{gT}{c_p V}\left(\frac{\partial V}{\partial T}\right)_p \equiv \left.\frac{\mathrm{d}T}{\mathrm{d}z}\right|_s. \tag{6.15}$$

The rhs expression is the adiabatic temperature gradient, i.e., a gradient in the element involved in the heat-isolated lifting. Thus, the convection can develop if the real gradient, produced by the heat sources, exceeds $\mathrm{d}T/\mathrm{d}z|_s$ by the absolute value.

Let us evaluate the adiabatic temperature gradient in terrestrial conditions for the air or water. For the air within the ideal gas approximation we have $(T/V)(\partial V/\partial T)_p = 1$ and $c_p \approx 10^7\,\mathrm{erg/(g\,K)}$, while for the water $\alpha \approx 2\times 10^{-4}\,\mathrm{K}^{-1}$ and $c_p \approx 4.19\times 10^7\,\mathrm{erg/(g\,K)}$. Thus, we obtain

$$\left.\frac{\mathrm{d}T}{\mathrm{d}z}\right|_{\mathrm{air}} \approx 10^{-4}\ \mathrm{K/cm} = \frac{1\ \mathrm{K}}{100\ \mathrm{m}}; \qquad \left.\frac{\mathrm{d}T}{\mathrm{d}z}\right|_{w} \approx 1.4\times 10^{-6}\ \mathrm{K/cm} \approx \frac{1\ \mathrm{K}}{7\ \mathrm{km}}.$$

In fact, condition (6.15) can underestimate the threshold value of the density gradient above at which the convection becomes possible. This happens if the adiabatic approximation breaks down (the element is not well thermally isolated from the surrounding fluid). Furthermore, the start of the uplifting can be slowed down by the fluid viscosity, which was neglected in this simplified (stationary) consideration. On top of this, in the astrophysics conditions, there is a magnetic field; atom ionization and ion recombination affect the plasma state, as well as nuclear transformations in a dense and hot plasma, e.g., in the stellar interiors. Modern astrophysical studies pay a lot of attention to account effect of all these phenomena on the convection.

6.2.2 Convection in a Weakly Compressible Fluid

We turn here to the dynamic case and start from the general MHD set of equations given in Chap. 2 (Sect. 2.2), which are gathered together below:

$$\frac{\partial \rho}{\partial t} + \nabla\cdot\rho\boldsymbol{u} = 0, \tag{6.16a}$$

$$\rho\left(\frac{\partial \boldsymbol{u}}{\partial t} + (\boldsymbol{u}\cdot\nabla)\boldsymbol{u}\right) = -\nabla p - \rho g\boldsymbol{e}_z + \frac{1}{4\pi}[\nabla\times\boldsymbol{B}]\times\boldsymbol{B} + \eta\Delta\boldsymbol{u} + \frac{\eta}{3}\nabla(\nabla\cdot\boldsymbol{u}), \tag{6.16b}$$

$$\rho T\left(\frac{\partial s}{\partial t} + (\boldsymbol{u}\cdot\nabla)s\right) = \eta\left(\frac{\partial u_\alpha}{\partial x_\beta} + \frac{\partial u_\beta}{\partial x_\alpha} - \frac{2}{3}(\nabla\cdot\boldsymbol{u})\delta_{\alpha\beta}\right)\nabla_\beta u_\alpha + \nabla\cdot(\chi\nabla T) + \frac{\nu_m}{4\pi}[\nabla\times\boldsymbol{B}]^2, \tag{6.16c}$$

$$\nabla\cdot\boldsymbol{B} = 0, \quad \frac{\partial \boldsymbol{B}}{\partial t} = \nabla\times[\boldsymbol{u}\times\boldsymbol{B}] + \nu_m\Delta\boldsymbol{B}. \tag{6.16d}$$

These equations include both gravitation and magnetic force, as well as all dissipative effects.

We now linearize these equations adopting that the velocity $\boldsymbol{u}$ and perturbations of other values p', $\boldsymbol{b} = \boldsymbol{B} - \boldsymbol{B}_0$, θ, and ρ' are small, so they can be accounted within the first-order approximation. The value $\theta(\boldsymbol{r}, t)$ is a small perturbation to the linear (with the height) temperature profile given by Eq. (6.11). The incompressibility means that the fluid density does not depend on the pressure, which itself changes only weakly throughout the system

$$\begin{aligned} \rho(p,T) &\approx \rho(p,T_1) + \left(\frac{\partial V}{\partial T}\right)_p (T + \theta - T_1) = \rho_0 + \Delta\rho + \rho', \\ \Delta\rho &= -\rho_0 \alpha (T - T_1), \quad \rho' = -\rho_0 \alpha \theta. \end{aligned} \tag{6.17}$$

Here

$$\rho_0 = \rho(p, T_1), \quad \alpha = -\frac{1}{\rho_0}\left(\frac{\partial \rho}{\partial T}\right)_p = \frac{1}{V}\left(\frac{\partial V}{\partial T}\right)_p \tag{6.18}$$

is the (already introduced in Sect. 6.2.1) volumetric thermal expansion coefficient. Then, $\Delta\rho$ is the density change associated with the temperature gradient produced by the external source. This component of the gravitation force is to be balanced by pressure gradient, Eq. (6.11), while ρ' is a small density perturbation.

In what follows we take into account dependence of the density on temperature in the Archimedes force only. In all other terms we adopt a constant density $\rho = \rho_0$ (so-called Boussinesq approximation). Although this approximation is not fully self-consistent, it is justified by the fact that the correction to the Archimedes force gives the main effect, while only a small correction for all other terms.

The linearized system then takes the form

$$\nabla \cdot \boldsymbol{u} = 0, \tag{6.19a}$$

$$\frac{\partial \boldsymbol{u}}{\partial t} = -\frac{1}{\rho_0}\nabla p' + \nu \Delta \boldsymbol{u} + \alpha g \theta \boldsymbol{e}_z + \frac{1}{4\pi\rho_0}[\nabla \times \boldsymbol{b}] \times \boldsymbol{B}_0, \tag{6.19b}$$

$$\frac{\partial \theta}{\partial t} = \beta \boldsymbol{u} \cdot \boldsymbol{e}_z + \kappa \Delta \theta, \tag{6.19c}$$

$$\frac{\partial \boldsymbol{b}}{\partial t} = \nabla \times [\boldsymbol{u} \times \boldsymbol{B}_0] + \nu_m \Delta \boldsymbol{b}. \tag{6.19d}$$

All small quadratic terms containing viscosities are discarded from Eq. (6.16c). The lhs is transformed using the fluid incompressibility:

$$\frac{\partial s(T,\rho)}{\partial t} = \left(\frac{\partial s}{\partial T}\right)_\rho \frac{\partial \theta}{\partial t}, \quad \nabla s(T,\rho) = \left(\frac{\partial s}{\partial T}\right)_\rho \nabla T = \left(\frac{\partial s}{\partial T}\right)_\rho \beta,$$

where β is again the temperature gradient. As we have assumed the constant density, the pressure change can also be discarded:

$$\left(\frac{\partial s}{\partial T}\right)_\rho \approx \left(\frac{\partial s}{\partial T}\right)_p = \frac{c_p}{T}. \tag{6.20}$$

Then, introducing the **thermal diffusivity** (a "temperature conduction coefficient") $\kappa = \chi/(c_p\rho_0)$ in place of the **thermal conductivity** (heat conductivity) χ we arrive at Eq. (6.19c).

For the boundaries at $z = 0$ and $z = h$ we use the Rayleigh boundary conditions, i.e., they are free but their shape is constant (account of the boundary deformation complicates the calculations severely; see, e.g., Sects. 6.3 and 6.4). Adopt that constant temperatures T_1 and T_2 are held at the boundaries; thus

$$\theta|_{z=0} = \theta|_{x=h} = 0. \tag{6.21}$$

The external magnetic field $\boldsymbol{B}_0 = \text{const}$ is assumed uniform and transverse to the boundaries. Inside the fluid, there can be electric currents producing additional magnetic field both inside and outside the fluid. The boundary conditions for the electromagnetic field require the continuity of the magnetic field normal component and the electric field tangential component at the boundaries, which can be written down in the form of Eq. (5.63).

Consider a two-dimensional (2D) motion in the plane (x, y). Normal components of the velocity vanish at the boundaries:

$$u_z|_{z=0} = u_z|_{z=h} = 0. \tag{6.22}$$

Conditions for the tangential components follow from vanishing of the viscous tension tensor at the free boundaries:

$$\Pi_{xz} = \eta\left(\frac{\partial u_x}{\partial z} + \frac{\partial u_z}{\partial x}\right)_{z=0,h} = 0.$$

Combining this with Eq. (6.22), we obtain

$$\left.\frac{\partial u_x}{\partial z}\right|_{z=0} = \left.\frac{\partial u_x}{\partial z}\right|_{z=h} = 0. \tag{6.23}$$

For a 2D velocity field it is convenient to transform the set of Eq. (6.19) using a flow function $\phi(x, z, t)$ (e.g., Landau and Lifshitz 1966, Sect. 10) and the vector potential $\boldsymbol{A} = A(x, z, t)\boldsymbol{e}_y$ of the magnetic field. The velocity field and the magnetic field are then expressed as follows:

$$\boldsymbol{u} = \nabla \times (\boldsymbol{e}_y\phi), \qquad \boldsymbol{b} = \nabla \times \boldsymbol{A}. \tag{6.24}$$

Now Eq. (6.19a) is satisfied equivalently; applying the operator $\nabla\times$ to Eq. (6.19b) with the velocity expressed via the flow function, Eq. (6.24), we obtain

$$\frac{\partial}{\partial t}\Delta\phi = \alpha g\frac{\partial\theta}{\partial x} + \nu\Delta\Delta\phi - \frac{B_0}{4\pi\rho_0}\frac{\partial}{\partial z}\Delta A. \tag{6.25}$$

Equation (6.19c) reduces to

$$\frac{\partial \theta}{\partial t} = \beta \frac{\partial \phi}{\partial x} + \kappa \Delta \theta. \tag{6.26}$$

Finally, the equation for the vector potential takes the form

$$\frac{\partial A}{\partial t} = B_0 \frac{\partial \phi}{\partial z} + \nu_m \Delta A. \tag{6.27}$$

Using Eq. (6.24) it is easy to check that Eq. (6.27) yields correct equations for the magnetic field $\boldsymbol{b}$ components.

Let us seek solutions of Eqs. (6.25)–(6.27) in the form of real functions satisfying the boundary conditions for the velocity and temperature:

$$\phi = \phi_0 e^{-\gamma t} \sin(\pi n z/h) \sin kx, \tag{6.28a}$$

$$\theta = \theta_0 e^{-\gamma t} \sin(\pi n z/h) \cos kx, \tag{6.28b}$$

$$A = A_0 e^{-\gamma t} \cos(\pi n z/h) \sin kx. \tag{6.28c}$$

Here k is an arbitrary wave number of standing waves in the fluid, γ is their damping rate, $n = 1, 2, \ldots$ are integer numbers, and ϕ_0, θ_0, and A_0 are unknown wave amplitudes. The very presence and efficiency of the convective instability are specified by the sign and magnitude of γ, which has to be calculated as a function of k, n, and other parameters of the problem by equating the equation set determinant to zero.

As usual, start from a simplified case of zero magnetic field, $B_0 = 0$ and $A = 0$. We introduce a dimensionless wave number $q = kh$ and substitute trial solution (6.28a) and (6.28b) into Eqs. (6.25)–(6.27), which yields algebraic equations

$$[\gamma h^2 - \kappa(\pi^2 n^2 + q^2)](\pi^2 n^2 + q^2)\phi_0 + \alpha g q h^3 \theta_0 = 0, \tag{6.29}$$

$$\beta q h \phi_0 + [\gamma h^2 - \kappa(\pi^2 n^2 + q^2)]\theta_0 = 0. \tag{6.30}$$

Then introduce two more widely used dimensionless measures—Rayleigh number and Prandtl number:

$$Ra = \frac{\alpha \beta g h^4}{\nu \kappa}, \quad Pr = \frac{\nu}{\kappa}, \tag{6.31}$$

and the dimensionless damping rate $\gamma' = \gamma h^2/\nu$.

The determinant of the equation set has the form

$$\gamma'^2 Pr - \gamma'(1 + Pr)(\pi^2 n^2 + q^2) + (\pi^2 n^2 + q^2)^2 - q^2 Ra = 0 \tag{6.32}$$

and has two solutions for the damping rate:

$$\gamma' = \frac{(1+Pr)(\pi^2 n^2 + q^2)}{2Pr} \pm \sqrt{\frac{(1-Pr)^2(\pi^2 n^2 + q^2)^2}{4Pr^2} + \frac{q^2 Ra}{(\pi^2 n^2 + q^2)Pr}}. \tag{6.33}$$

When the fluid is heated from below we have $Ra > 0$, and both roots are real. The perturbations grow if the Rayleigh number is large enough to make one of the roots negative. The critical value of the Rayleigh number Ra_c is determined from the condition $\gamma'(Ra_c) = 0$:

$$Ra_c = (\pi^2 n^2 + q^2)^3 / q^2. \tag{6.34}$$

To find the smallest Rayleigh number giving rise to the instability requires finding a minimum of Eq. (6.34) as a function of q for $n = 1$, which yields $Ra_{\min} = 27\pi^4/4 \approx 657.5$. In case of rigid (instead of free) boundaries the critical Rayleigh number increases, $Ra_{\min} \approx 1707.8$. The condition for the convective instability reads $Ra > Ra_c$.

Note that the condition obtained is substantially different from Eq. (6.15). In particular, it depends on the viscosity and heat conductivity and also strongly depends on the fluid height h, in which the convection is being developed. Stated another way, Eq. (6.15) offers a necessary condition for the convective instability, while a more complete consideration resulted in Eq. (6.34) clarifies what else (rather than the temperature gradient) and how can affect the convection. Note that this estimate remains a qualitative one, since it can be severely modified by account of discarded here effects as source nonuniformity, specific boundary conditions, and, in many cases, the external magnetic field.

Analysis of the dispersion equation in the presence of magnetic field, i.e., with account of Eq. (6.28c), has to be done numerically. However, the critical Rayleigh number has a relatively simple form:

$$Ra_c = \frac{(\pi^2 n^2 + q^2)^3}{q^2} + \frac{v_A^2 h^2 \pi^2 n^2}{\nu \nu_m}\left(1 + \frac{\pi^2 n^2}{q^2}\right). \tag{6.35}$$

As might have been expected the magnetic field acts toward stabilization of the instability that now happens at larger Rayleigh numbers than without the field. The (partial) stabilization effect is easy to understand: the conducting fluid mixing results in magnetic field line mixing, which means the magnetic energy increase.

6.2.3 Convection in the Laboratory and Astrophysics

The solution of the Rayleigh problem (1916, without magnetic field) given in the previous section explains well the Bénard experiments (1900) of the convection in a layer of mineral oil heated from below in a frying pan. Visualization of the fluid flows (achieved by adding aluminium filings into the

oil) proved that the convective Bénard cells—right hexahedrons in which the heated oil uplifts in the center of the cell and moves down on their borders—appear after reaching the critical Rayleigh number ($Ra_{\text{exp}} = 1700 \pm 51$ for a pan with a cover) (Fig. 6.2).

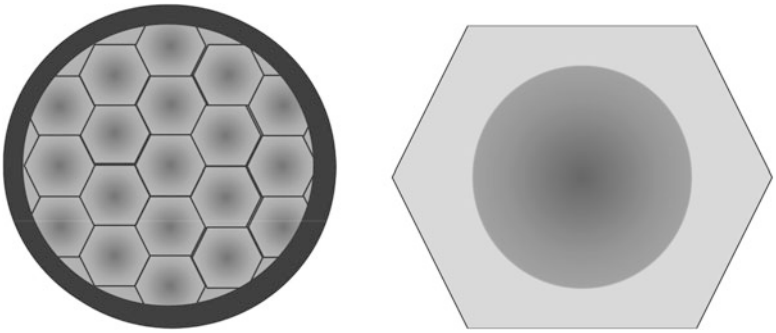

Figure 6.2: Cartoon illustrating convective cells in Bénard experiment and a single hexahedron cell with the convective upcoming flow in the central part and returning down flows at the borders.

The hexahedron structure of the convective cells was found to be controlled by the surface tension of the liquid. The importance of this experiment goes far beyond the convection problem itself: it proves that an order (a regular macroscopic motion in this instance) can originate from initially chaotic state in an open nonstationary physical system. Further increase of the Rayleigh number above the critical value results in departure of the convective cell shape from the regular one; highly above-the-threshold convection becomes turbulent (chaotic).

As has been said the convection is present at the outer layer of the sun and stars. A number of structures are observed at the photosphere and chromosphere, including granules, supergranules, giant structures, and chromospheric network, which are produced under joint action of solar convection and solar magnetic field. The largest convective speed is reached at the top of the convective zone and estimated as 2 km/s. In particular, the photospheric solar granulation as that nicely seen in Fig. 6.3 (outside the sunspot umbra) displays almost regular structure similar to the Bénard cells (although not of a perfect hexahedron shape), while the cells disappear in the sunspot umbrae because of already mentioned stabilizing effect of the magnetic field (note that the sunspot magnetic field can reach 3,000 G, while the typical photospheric field beyond active regions is about 1 G). There is fragmented structure of convective elements within the sunspot penumbrae, which indicates magnetic field inhomogeneity and so excess of the magnetic energy,

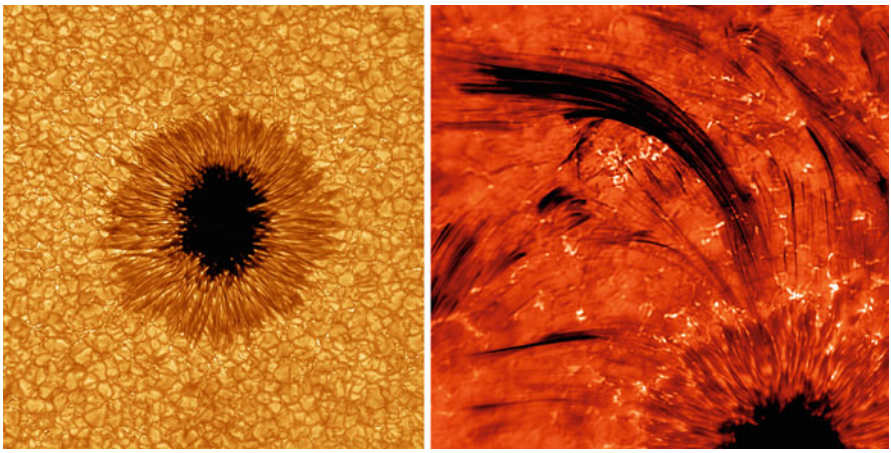

Figure 6.3: A sunspot observed with NST. *Left*: *white* light image containing dark umbra surrounded by a penumbra with elongated fibrils. The sunspot is embedded into the photosphere granulation structure indicative of the subphotospheric convection. *Right*: H_α image of the same sunspot with the field of view moved up and left to better show chromospheric "jets" (*dark narrow* arch-like structures) revealing dynamics of the low atmospheric layers (courtesy by Dr. Phil Goode and BBSO team).

which can be released in some conditions (phenomenon of solar flare). As a result of the flare the penumbra often decays implying more uniform magnetic field structure after the magnetic energy release in agreement with naive expectations.

Quantitative use of the obtained simplified solutions in the real stellar conditions requires extreme caution, since we did not consider many ingredients important for the stellar conditions. In fact, the convection in Sun and stars is much more complicated phenomenon than in the laboratory. The most essential distinctions making the quantitative treatment of the stellar convection extremely difficult are as follows: (1) the solar plasma can hardly be considered incompressible; (2) the plasma composition varies with height due to ionization and recombination of the hydrogen, helium, and other elements; eventually, the degree of ionization changes from almost 100% at the bottom of the convective zone to $\sim 10^{-3}$ in the photosphere; (3) an important role is played by the turbulent viscosity ν_t and radiative heat conductivity χ_r, which differ from the dissipative kinetic coefficients described by Eqs. (1.152) and (1.153); and (4) the star is highly nonuniform with the depth: the plasma density changes by 6–7 orders of magnitude, while the magnetic field by 3–4 orders of magnitude in the solar convection zone, which occupies roughly 30% of the solar radius. As a result, the convective zone includes many convective

layers with the cell size varying with the depth; this size decreases toward the photosphere (see Spruit et al. 1990 for greater detail). In the massive stars, the surface convective zone is rather narrow. However, they contain relatively large convective core where nuclear reactions of the carbon cycle take place, which, in their turn, affect the convection in the stellar cores. Stated another way, convection is closely tied up with stellar structure, and one cannot solve for one without the other, which does not favor finding meaningful analytic solutions. Instead, the stellar structure equations are either solved using "mixing length theory" to model convection, or convection is studied using 3D numerical simulations.

6.3 Instability of Contact Discontinuity with Magnetic Field (Rayleigh–Taylor Instability)

Consider now the stability of *contact discontinuity* separating two conducting fluids with different densities ρ_1 and ρ_2. Adopt that the fluids are in a gravitational field (with the acceleration vector $\mathbf{g}$) and in a uniform magnetic field $\mathbf{B}$; both fields are transverse to the boundary between the fluids. Consider approximation of incompressible and dissipationless medium ($\rho_1 = \text{const}$, $\rho_2 = \text{const}$, $\nu = 0$, and $\nu_m = 0$). As has been explained we apply the small perturbation method—introduce small variations $\boldsymbol{b}$, $\boldsymbol{u}$, p, and ζ to the originally unperturbed values $\boldsymbol{B}$, $\boldsymbol{u} = 0$, P, and $z = 0$. The value ζ describes shape of the perturbed boundary $z = \zeta(x, y, t)$ between these two fluids (Fig. 6.4). Now we will search the velocity perturbation in the class of potential functions.

Let us write down the linearized set of equations (as has been said, dissipation is discarded):

$$\nabla \cdot \boldsymbol{u} = 0, \quad \rho \frac{\partial \boldsymbol{u}}{\partial t} = -\nabla p - \frac{1}{4\pi} \boldsymbol{B} \times [\nabla \times \boldsymbol{b}] + \rho \boldsymbol{g}, \quad \frac{\partial \boldsymbol{b}}{\partial t} = (\boldsymbol{B} \cdot \nabla)\boldsymbol{u}. \tag{6.36}$$

Let us start from a contact discontinuity without any normal magnetic field component. Expressing the fluid velocity via scalar potential ϕ we obtain

$$\boldsymbol{u} = \nabla \phi(x, y, z, t), \quad \triangle \phi = 0, \tag{6.37}$$

so the equation of motion for u_z-component gives rise to

$$\frac{\partial p}{\partial z} = -\rho \frac{\partial}{\partial z} \left(\frac{\partial \phi}{\partial t} + gz \right), \tag{6.38}$$

whose integration is straightforward:

$$p = -\rho \left(\frac{\partial \phi}{\partial t} + gz \right) + P_0. \tag{6.39}$$

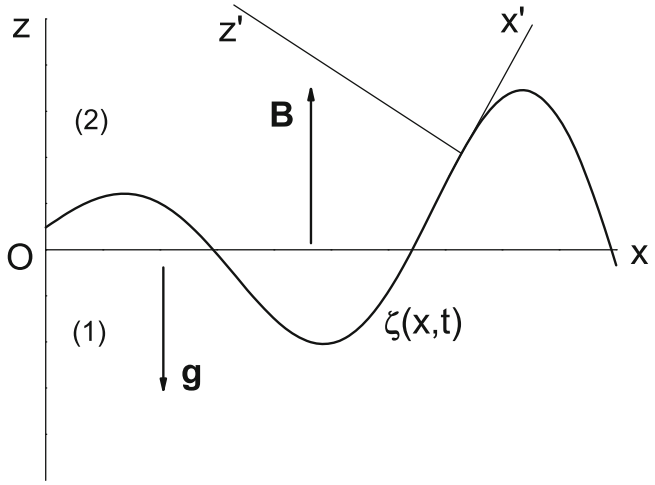

Figure 6.4: Schematic plot of disturbed surface $\zeta(x,t)$; the original undisturbed surface obeys an equations $z=0$.

Here P_0 denotes the pressure at the undisturbed boundary, which is apparently the same for both upper and lower fluids. Other parameters (except for $\boldsymbol{g}$ and $\boldsymbol{B}$) are different at these two fluids.

At the disturbed discontinuity surface $z=\zeta(x,y,t)$ boundary conditions (5.61) must be fulfilled and absence of the fluid flux through the boundary $i_{n'}=0$ must be taken into account. Then, the vertical velocities in both fluids can be rewritten using equation of the boundary surface, which is common for both fluids:

$$u_{1z}=u_{2z}=\frac{\mathrm{d}\zeta}{\mathrm{d}t}=\frac{\partial\zeta}{\partial t}+(\boldsymbol{u}\cdot\nabla)\zeta\approx\frac{\partial\zeta}{\partial t}. \tag{6.40}$$

With the accuracy to the first-order terms retained in Eq. (6.40) this condition can be applied to the undisturbed surface, $z=0$.

The second boundary condition at the distorted surface can be found by equating the pressure on both sides of the discontinuity:

$$\rho_1\left(\frac{\partial\phi_1}{\partial t}+g\zeta\right)=\rho_2\left(\frac{\partial\phi_2}{\partial t}+g\zeta\right). \tag{6.41}$$

Differentiating over the time and using Eqs. (6.37) and (6.40) we find

$$\rho_1\left(\frac{\partial^2\phi_1}{\partial t^2}+g\frac{\partial\phi_1}{\partial z}\right)=\rho_2\left(\frac{\partial^2\phi_2}{\partial t^2}+g\frac{\partial\phi_2}{\partial z}\right). \tag{6.42}$$

This equality contains only the first-order terms and can be applied to the undistorted surface $z=0$.

The scalar potential ϕ obeys Laplace equation (6.37). We search for solution in the form of plane monochromatic waves propagating along the unperturbed boundary:

$$\begin{aligned} \phi_1 &= A\exp(kz + ik_x x + ik_y y - i\omega t),\ z < 0; \\ \phi_2 &= C\exp(-kz + ik_x x + ik_y y - i\omega t),\ z > 0, k = \sqrt{k_x^2 + k_y^2}. \end{aligned} \quad (6.43)$$

Using Eq. (6.40) we find $C = -A$; then Eq. (6.42) yields the dispersion equation for the small perturbations:

$$\omega^2 = \frac{\rho_1 - \rho_2}{\rho_1 + \rho_2} gk. \quad (6.44)$$

If $\rho_1 > \rho_2$ (denser medium is located below) the contact boundary is stable against the perturbations with arbitrary k, while an instability takes place if more tenuous medium is located below ($\rho_1 < \rho_2$).

Unfortunately, the developed approach cannot be used in the presence of a vertical magnetic field, because the fluid flow becomes nonpotential in this case. Indeed, if we write down equation for the magnetic field b_z perturbation via the potential,

$$b_z = \int_{-\infty}^{t} B\frac{\partial^2 \phi}{\partial z^2} \mathrm{d}t', \quad (6.45)$$

and substitute the potential from Eq. (6.43) into the last equation, we notice that the continuity condition of b_z breaks down at the boundary, which implies inapplicability of the method.

A stabilizing effect of the vertical magnetic field on the contact discontinuity is considered by Chandrasekhar (1961), who obtained a cubic dispersion equation for small perturbations:

$$n^3 + 2k(\sqrt{\alpha_1} + \sqrt{\alpha_2})n^2 + k(2k + \alpha_1 - \alpha_2)n - 2k^2(\sqrt{\alpha_2} - \sqrt{\alpha_1}) = 0, \quad (6.46)$$

where $n = i\omega$ and $\alpha_{1,2} = \rho_{1,2}/(\rho_1 + \rho_2)$; ω and k are dimensionless frequency and wave number, measured in units (g/V_A) and (g/V_A^2), respectively; $V_\mathrm{A} = B/\sqrt{4\pi(\rho_1 + \rho_2)}$ is the modified Alfvén velocity.

The free term of Eq. (6.46) is negative if $\alpha_2 > \alpha_1$. This means that the product of three roots of Eq. (6.46) is positive and $i\omega$ has at last one positive root for any finite value of the magnetic field B. We conclude that the vertical magnetic field does not stabilize an otherwise unstable discontinuity.

The case of a magnetic field parallel to the discontinuity can be studied somewhat easier. Let us calculate components of the momentum flux tensor

using the relations for undisturbed field components in the "primed" reference frame (Fig. 6.4), whose axes are expressed via original Cartesian axes:

$$\boldsymbol{e}_{x'} = \boldsymbol{e}_x + \boldsymbol{e}_z \frac{\partial \zeta}{\partial x}, \quad \boldsymbol{e}_{y'} = \boldsymbol{e}_y + \boldsymbol{e}_z \frac{\partial \zeta}{\partial y}, \quad \boldsymbol{e}_{z'} = \boldsymbol{e}_z - \boldsymbol{e}_x \frac{\partial \zeta}{\partial x} - \boldsymbol{e}_y \frac{\partial \zeta}{\partial y}. \quad (6.47)$$

Then, we obtain for the field components

$$B_{z'} = b_z - B_x \frac{\partial \zeta}{\partial x} - B_y \frac{\partial \zeta}{\partial y}, \quad B_{x'} = B_x + b_x, \quad B_{y'} = B_y + b_y \quad (6.48)$$

and for the tensor components

$$\Pi_{z'z'} = p + \tfrac{B^2}{8\pi} + \tfrac{1}{4\pi} \boldsymbol{B} \cdot \boldsymbol{b}, \quad \Pi_{x'z'} = -\tfrac{1}{4\pi} B_x \left(b_z - B_x \tfrac{\partial \zeta}{\partial x} - B_y \tfrac{\partial \zeta}{\partial y} \right),$$
$$\Pi_{y'z'} = -\tfrac{1}{4\pi} B_y \left(b_z - B_x \tfrac{\partial \zeta}{\partial x} - B_y \tfrac{\partial \zeta}{\partial y} \right). \quad (6.49)$$

It is convenient to take time derivatives of the tensor component matching conditions $\Pi^{(1)}_{\alpha' z'} = \Pi^{(2)}_{\alpha' z'}$, $\alpha' = x', y', z'$ at $z = \zeta$,

$$\frac{\partial}{\partial t} \Pi^{(1)}_{\alpha' z'} = \frac{\partial}{\partial t} \Pi^{(2)}_{\alpha' z'}, \quad \alpha' = x', y', z', \quad (6.50)$$

to eliminate ζ using Eq. (6.40). For $\alpha' = z'$ using Eqs. (6.37), (6.39), and (6.48) we obtain

$$-\rho_2 \frac{\partial^2 \phi_2}{\partial t^2} - \rho_2 g \frac{\partial \phi_2}{\partial z} + \boldsymbol{B} \cdot (\boldsymbol{B} \cdot \nabla) \nabla \phi_2 = -\rho_2 \frac{\partial^2 \phi_2}{\partial t^2} - \rho_2 g \frac{\partial \phi_2}{\partial z} + \boldsymbol{B} \cdot (\boldsymbol{B} \cdot \nabla) \nabla \phi_2, \quad z = 0. \quad (6.51)$$

Equations with $\alpha' = x', y'$ give identities $0 = 0$. Using scalar potentials (6.43), we obtain from Eq. (6.51) the dispersion equation

$$\omega^2 = \frac{\rho_1 - \rho_2}{\rho_1 + \rho_2} gk + \frac{(\boldsymbol{B} \cdot \boldsymbol{k})^2}{2\pi(\rho_1 + \rho_2)}. \quad (6.52)$$

Again, for $\rho_2 > \rho_1$, the instability cannot be stabilized by *a uniform* magnetic field: perturbations with wave vectors transverse to the magnetic field $\boldsymbol{k} \perp \boldsymbol{B}$ will grow, because corresponding plasma displacement does not disturb the magnetic field lines.

This instability can take place in a plasma, which is supported from below by the magnetic pressure (Fig. 6.5). Adopt that the fluid density ρ_2 and kinetic pressure p_2 are larger above than below $p_2 > p_1$, but the total pressures are the same: $p_2 + B_2^2/8\pi = p_1 + B_1^2/8\pi$. The magnetic field lines are transverse to the figure plane. This equilibrium is unstable because any small random fluid contraction leads to the pressure increase and the corresponding plasma element will move further down. The magnetic lines being freezed in the plasma redistribute in the space without conjunctions and rarefactions, i.e., without the magnetic energy change. The potential energy in

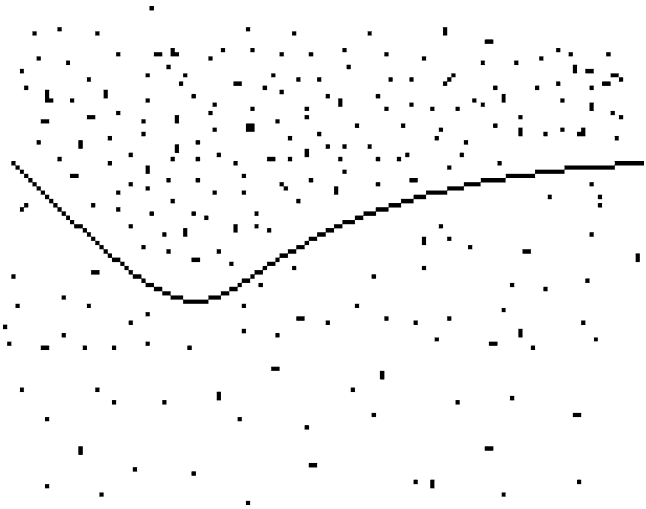

Figure 6.5: Rayleigh–Taylor instability. The dense fluid falls downwards.

the gravitation field, however, decreases, which corresponds to a more stable state. This consideration, however, relies essentially on the assumption of a uniform magnetic field, while a real nonuniform 3D magnetic field can efficiently stabilize the instability. As a vivid example, we can mention magnetic arcades supporting dense and cool prominences in the solar corona as those considered in Sect. 2.2.3.

The discussed phenomenon is known as **Rayleigh–Taylor instability**. It can also develop under inertia force if a boundary moves as a whole with acceleration and if in the reference frame (moving together with the boundary) the inertia force is directed from denser medium toward more tenuous one. For example, a complicated filamentary structure of the Crab Nebula seen in the optical range is often interpreted in terms of the Rayleigh–Taylor instability.

6.4 Instability of Tangential Discontinuity with Magnetic Field (Kelvin–Helmholtz Instability)

We investigate now stability of tangential discontinuity in incompressible conducting fluid. The fluid density, velocity, and magnetic field are all different at both sides of the boundary. Gravitation and dissipation are discarded.

Let us denote the unperturbed values as $\boldsymbol{v}$, $\boldsymbol{B}$, P, while their small perturbations as $\boldsymbol{u}$, $\boldsymbol{b}$, p, respectively. Perturbed surface of the discontinuity is described by yet unknown equation $z = \zeta(x, y, t)$. Then, introduce the

Alfven speed $\boldsymbol{v}_\mathrm{A} = \boldsymbol{B}/\sqrt{4\pi\rho}$ and a similar speed corresponding to the magnetic field perturbation $\boldsymbol{w} = \boldsymbol{b}/\sqrt{4\pi\rho}$. The linearized equations take the form

$$\nabla\cdot\boldsymbol{u} = \nabla\cdot\boldsymbol{w} = 0, \quad \frac{\partial\boldsymbol{w}}{\partial t} + (\boldsymbol{v}\cdot\nabla)\boldsymbol{w} = (\boldsymbol{v}_\mathrm{A}\cdot\nabla)\boldsymbol{u},$$
$$\frac{\partial\boldsymbol{u}}{\partial t} + (\boldsymbol{v}\cdot\nabla)\boldsymbol{u} = -\frac{1}{\rho}\nabla p - \nabla(\boldsymbol{v}_\mathrm{A}\cdot\boldsymbol{w}) + (\boldsymbol{v}_\mathrm{A}\cdot\nabla)\boldsymbol{w}. \tag{6.53}$$

Boundary conditions at tangential discontinuity $z = \zeta$ require equality of full pressures $p + (\boldsymbol{B}+\boldsymbol{b})^2_{\tau'}/8\pi$ and vanishing the normal component of the magnetic field $(\boldsymbol{B}+\boldsymbol{b})_{n'} = 0$. Linearizing these conditions and making transformation from local ("primed") reference frame to original Cartesian one, like in the previous section, we get

$$\delta(p + \rho\boldsymbol{v}_\mathrm{A}\cdot\boldsymbol{w}) = 0, \quad w_z - (\boldsymbol{v}_\mathrm{A}\cdot\nabla)\zeta = 0 \quad \text{for} \quad z = 0. \tag{6.54}$$

Taking divergence of the last equation (6.53) we find equation for the pressure perturbation:

$$\Delta(p + \rho\boldsymbol{v}_\mathrm{A}\cdot\boldsymbol{w}) = 0. \tag{6.55}$$

From this equation we can easily conclude that one can search for the small perturbation solution in the form

$$\boldsymbol{u}, \boldsymbol{w}, p \propto \exp(\pm kz + ik_x x + ik_y y - i\omega t), \quad \zeta \propto \exp(ik_x x + ik_y y - i\omega t), \tag{6.56}$$

where $k = \sqrt{k_x^2 + k_y^2}$, while the signs $\pm$ in the exponent relate to the regions $z < 0$ and $z > 0$, respectively.

Excluding the velocity $\boldsymbol{u}$ from Eq. (6.53) using Eq. (6.56), we obtain

$$[(\omega - (\boldsymbol{k}\cdot\boldsymbol{v})^2 - (\boldsymbol{k}\cdot\boldsymbol{v}_\mathrm{A})^2]\boldsymbol{w} = -\frac{1}{\rho}(\boldsymbol{k}\cdot\boldsymbol{v}_\mathrm{A})(\boldsymbol{k} \mp ik\boldsymbol{e}_z)(p + \rho\boldsymbol{v}_\mathrm{A}\cdot\boldsymbol{w}). \tag{6.57}$$

Then, consider the projection of Eq. (6.57) on axes Oz and apply boundary conditions (6.54). This yields the following dispersion relation for small perturbations:

$$\rho_1(\omega - \boldsymbol{k}\cdot\boldsymbol{v}_1)^2 + \rho_2(\omega - \boldsymbol{k}\cdot\boldsymbol{v}_2)^2 = \rho_1(\boldsymbol{k}\cdot\boldsymbol{v}_{\mathrm{A}1})^2 + \rho_2(\boldsymbol{k}\cdot\boldsymbol{v}_{\mathrm{A}2})^2, \tag{6.58}$$

which is a quadratic equation for the frequency $a\omega^2 + b\omega + c = 0$. The condition for the roots to be real is evidently the inequality $b^2 - 4ac \geq 0$, which can be written down in the form

$$T_{\alpha\beta}k_\alpha k_\beta \geq 0. \tag{6.59}$$

Here, tensor $T_{\alpha\beta}$ $(\alpha, \beta = 1, 2)$ has the form

$$T_{\alpha\beta} = \rho_1 v^{(1)}_{\mathrm{A}\alpha} v^{(1)}_{\mathrm{A}\beta} + \rho_2 v^{(2)}_{\mathrm{A}\alpha} v^{(2)}_{\mathrm{A}\beta} - \frac{\rho_1\rho_2}{\rho_1 + \rho_2} v_\alpha v_\beta. \tag{6.60}$$

Having quadratic form, Eq. (6.59), nonnegative for arbitrary real components $k_\alpha,\ k_\beta$ requires two inequalities $T_{\alpha\alpha} > 0,\ |T_{\alpha\beta}| \geq 0$ to be fulfilled (i.e., both trace and determinant of the tensor must be nonnegative). These conditions can be expressed through the magnetic field vector:

$$B_1^2 + B_2^2 \geq 2\pi\rho v^2, \quad [\boldsymbol{B}_1 \times \boldsymbol{B}_2]^2 \geq 2\pi\rho([\boldsymbol{v} \times \boldsymbol{B}_1]^2 + [\boldsymbol{v} \times \boldsymbol{B}_2]^2), \tag{6.61}$$

where $\boldsymbol{v} = \boldsymbol{v}_1 - \boldsymbol{v}_2,\ \rho = \rho_1\rho_2/(\rho_1 + \rho_2)$, which determine the conditions for the tangential discontinuity stability in the presence of magnetic field (Sergei Syrovatskii 1953). As is clear from these conditions, a sufficiently strong magnetic field stabilizes the tangential instability. This is why numerous long-living tangential discontinuities are widely observed in interplanetary medium by instruments onboard space missions.

Without magnetic field, the tangential discontinuity is unstable in incompressible fluid. Indeed, the dispersion relation for small perturbations in this case takes the form

$$\omega = kv\frac{\rho_1 \pm i\sqrt{\rho_1\rho_2}}{\rho_1 + \rho_2}, \tag{6.62}$$

where $v = |\mathbf{v}_1 - \mathbf{v}_2|$ is unperturbed shear velocity at the boundary. Clearly, a growing solution always exists. Thus, if the instability takes place, random perturbations growing at the boundary smooth it out into a turbulent region filled by random plasma motions.

6.5 Thermal Instability

In a stable uniform fluid any fluctuation of the temperature/density will be rapidly smoothed out by the heat conduction. In many cases, however, the heat conduction is slow owing to relatively low density of astrophysical plasmas and so can be inefficient to maintain the plasma uniformity. In place, the radiative heat conduction can play a dominant role instead of the molecular heat conduction, which can lead to a radiative thermal instability (Field's instability).

The physics leading to this instability is easy to understand. Consider a random contraction of a gas. The contraction implies higher density and so more frequent collisions between the particles composing the plasma (atoms, molecules, ions, and electrons). If a fraction of atoms, molecules, and partly ionized ions is significant, the enhanced collision rate will excite more of these particles onto higher quantum levels; the exited particles will then radiate the excess energy out, which implies an enhanced energy losses by

this volume element and, thus, progressive cooling and further contraction. Whether this happens or not depends eventually on how the radiative loss of the given plasma depends on temperature.

To quantify this instability, let us consider Eq. (2.13b) of the heat transfer, where initially we neglect the heat conduction, macroscopic velocity, and magnetic field but add unknown heating E_H and cooling E_R functions, so Eq. (2.13b) receives the form

$$\rho T \frac{\partial s}{\partial t} = E_H - E_R. \tag{6.63}$$

Then, we assume that pressure of the gas remains constant (its equalization occurs with the sound speed and so very fast) and using Eq. (6.20) we find $\partial s/\partial t = (\partial s/\partial T)_p \, \partial T/\partial t = (c_p/T)\partial T/\partial t$, which yields equation for temperature T:

$$c_p \rho \frac{\partial T}{\partial t} = E_H - E_R. \tag{6.64}$$

The radiative loss function E_R depends on the plasma chemical composition and ionization states and so a very complicated one in a general case. However, to clarify the essence of the instability under study, we can adopt a power-law dependence of E_R on T, which is often presented in the form

$$E_R = n_e^2 \Lambda(T) = a\rho^2 T^\alpha, \tag{6.65}$$

where $\Lambda(T)$ is a so-called **radiative loss function** (Aschwanden 2005). Apparently, the power-law parametrization can only be approximately valid in a restricted range of the temperature variation. Substituting Eq. (6.65) into Eq. (6.64) and dividing by ρ, we obtain

$$c_p \frac{\partial T}{\partial t} = h - a\rho T^\alpha, \tag{6.66}$$

where $h = E_H/\rho$. The heating function is specified by the sources of the plasma heating and so cannot be determined from the first principles. We note, however, that to have a stationary distribution of the temperature (and density) requires $\partial T/\partial t = 0$ and so $h(\boldsymbol{r}) = a\rho_0(\boldsymbol{r})T_0^\alpha(\boldsymbol{r})$, where the density is linked to the temperature by the ideal gas equation of state, i.e., $\rho = m_{\text{eff}} p_0/(k_B T)$, where m_{eff} is the mean mass of the plasma particles and $p_0 = \text{const}$ is the plasma pressure. Substituting all these values into Eq. (6.66) we obtain the equation for the temperature variation:

$$c_p \frac{\partial T}{\partial t} = a\rho_0 T_0^\alpha \left(1 - \frac{T^{\alpha-1}}{T_0^{\alpha-1}}\right), \tag{6.67}$$

whose linearization in the form $T = T_0 + \delta T$ gives for the small perturbation

$$c_p \frac{\partial \delta T}{\partial t} = -(\alpha - 1) a \rho_0 T_0^{\alpha - 1} \delta T. \tag{6.68}$$

Apparently, the condition of the thermal instability reads $\alpha < 1$; in this case the solution of Eq. (6.68) $\delta T = \delta T_0 \exp(\beta t)$, where $\beta = -(\alpha - 1) a \rho_0 T_0^{\alpha - 1} / c_p$, will grow with time.

Note that evolution of the negative and positive temperature fluctuations δT_0 can be essentially different. For definiteness, consider the case of the solar corona, where the condition $\alpha < 1$ holds roughly at $T \gtrsim 10^5$ K. This means that negative temperature fluctuations $\delta T_0 < 0$ will grow, i.e., the given volume element will cool down to roughly $T \sim 10^5$ K (Aschwanden 2005), where the condition $\alpha < 1$ is no longer valid, which implies formation of coronal condensations, perhaps, in the form of prominences and relatively cold and dense coronal loops.

In the other case, $\delta T_0 > 0$, temperature of the volume element keeps going up, while the radiative cooling becomes less and less efficient, which could imply an infinite heating of this volume element. In fact, no infinite heating happens because the thermal conduction rapidly raising with the temperature, $\chi = \chi_0 T^{5/2}$, Eq. (1.153), comes into play soon, so the temperature must be determined from a more general equation:

$$c_p \rho \frac{\partial T}{\partial t} = E_H - E_R + \nabla(\chi \nabla T), \tag{6.69}$$

where the radiative loss term can eventually be discarded for a high temperature. The relative importance of the radiative losses and the heat conduction can be estimated from the corresponding times

$$\tau_{\rm rad} = \frac{c_p}{a \rho_0 T_0^{\alpha - 1}} \tag{6.70}$$

and

$$\tau_{\rm cond} = \frac{L^2 \rho_0 c_p}{\chi_0 T_0^{5/2}} = \frac{L^2}{\kappa}, \tag{6.71}$$

where κ is the thermal diffusivity defined by Eq. (1.154); in the solar corona the heat conduction typically dominates for $T \gtrsim 1$ MK. The solar corona is magnetized and the heat conduction transverse to the magnetic field is very slow, so the scale L in the above estimate relates to the length of the loop along the magnetic field; thus, longer loops are supposed to be hotter all other conditions being equal. We conclude that a thermally stationary solar corona would consist of relatively hot loops with $T \sim$ a few MK and cold loops with $T \sim 10^5$ K as well as even cooler prominences (when the corresponding heating function is insufficient to heat the loop up to $T \gtrsim 10^5$ K). Real corona, however, is a highly dynamic, variable object.

Table 6.1: Parameters of two-phase ISM

Parameter	Cloud	Intercloud medium
Temperature T	70 K	7,000 K
Hydrogen number density n_H	$20\,\mathrm{cm}^{-3}$	$0.2\,\mathrm{cm}^{-3}$
Electron number density n_e	$0.05\,\mathrm{cm}^{-3}$	$0.02\,\mathrm{cm}^{-3}$
Gas pressure nT	$1{,}400\,\mathrm{K\,cm}^{-3}$	$1{,}400\,\mathrm{K\,cm}^{-3}$

The Field's instability takes place in various astrophysical environments. In particular, it is likely responsible for fragmentation of the ISM gas onto two phases—cold clouds and warm diffuse gas. Not surprisingly, parameters of these two phases of ISM (Kaplan and Pikel'ner 1979) (see Table 6.1) are different from those in the solar corona. Distribution of these cold clouds over their scales a has the form $N_{\rm cl}(a)\mathrm{d}a \sim a^{-2.6}\mathrm{d}a$ within $0.75\,\mathrm{pc} < a < 5\,\mathrm{pc}$ (Cowie and Songaila 1986); the clouds can be strongly nonspherical. As the clouds are formed due to contraction of the original diffuse phase volume element, the 100-fold density contrast between the clouds and the warm phase implies that the mean distance between clouds is roughly five times larger than the cloud size. In fact, the ISM structure is much more complicated than implied by the two phase model as it is a highly dynamic nonstationary system; in addition it includes various kinds of HII regions, atomic hydrogen clouds (HI regions and shells), and hot cavities. The latter are produced by correlated SN explosions (see Sect. 5.6) and fill a relatively large fraction ($\sim$50%) of the galactic disk volume by a hot ($\sim 10^6\,\mathrm{K}$) tenuous ($\sim 3\times10^{-3}\,\mathrm{cm}^{-3}$) fully ionized plasma, called the coronal phase in analogy with the comparably hot solar corona.

6.6 Turbulence and Correlation Tensor Formalism

6.6.1 Physical Picture of Turbulent Motion

In practice, almost any kind of the gas or fluid motion can become unstable when the fluid velocity is sufficiently high. A number of specific examples of MHD instabilities have been considered in previous sections of this chapter. In an unstable state of fluid motion, small random perturbations of velocity, field, and other parameters grow in time, until nonlinear and dissipative processes stabilize them at some new level, stable in given conditions. Therefore, in an unstable fluid, the velocity and other parameters behave irregularly, their magnitudes (and directions of vectors) experience chaotic fluctuations at a given spatial location, and the fluctuating velocity is not necessarily small compared with mean (regular) flow velocity. Such a complicated irregular motion is called *turbulent* motion in contrast to laminar motion, when variations of the velocity in space and time are regular.

Transition to the turbulent motion happens at sufficiently large value of dimensionless **Reynolds number** $R = ul/\nu$ introduced in Sect. 2.1. Here u is a typical fluid velocity, l is a typical scale at which it noticeably varies, and ν is the kinematic viscosity. The Reynolds number quantifies the ratio of nonlinear inertial term in the equation of motion to dissipative term. Critical value R_c of the Reynolds number, above which the laminar motion loses its stability and turbulence arises, can be rather large. For example, for the water flow in the circular pipes, $R_c \approx 10^3 - 10^4$, depending on the pipe surface quality and uniformity of the input flow.

Here we will typically consider a so-called *developed turbulence*, when many macroscopic degrees of freedom are excited in the fluid and there are motions (vortices, waves, inhomogeneities, etc.) in a broad range of scales. To achieve this state requires that the Reynolds number to be much larger than the introduced above critical value R_c, at which the laminar–turbulent transition occurs. Such very large Reynolds numbers are indeed typical for geophysics and astrophysics conditions because the characteristic scales are often large there. For example, in the Earth's atmosphere in a town with big buildings ($l \approx 100\,\mathrm{m}$), wind speed $u \approx 20\,\mathrm{m/s}$, and the air kinematic viscosity $\nu \approx 0.15\,\mathrm{cm}^2/\mathrm{s}$, we obtain $R = ul/\nu \approx 10^8$. In the molecular clouds residing in the galactic disk (Ruzmaikin et al. 1988; Vainshtein et al. 1993) observations give $u \approx 10^6\,\mathrm{cm/s}$, $l \approx 10\,\mathrm{pc} \approx 3 \times 10^{19}\,\mathrm{cm}$, the temperature around 100 K, and molecule number density around $100\,\mathrm{particles/cm}^3$. This, using Eq. (1.151), yields $\nu \approx 0.8 \times 10^{17}\,\mathrm{cm}^2/\mathrm{s}$ for $\sigma \sim 10^{-14}$ and, correspondingly, $R \approx 4 \times 10^8$.

If the gas is not ionized, then in the subsonic regime ($u \ll c_s$) eddy motions of various scales represent the main structural elements of the turbulence. For $u \gtrsim c_s$ the sound waves and the shock fronts become significant constituents of the turbulent motion. In a conducting fluid or plasma, the turbulent motion is much more complicated because in this case the turbulent pulsations can be produced by whole variety of the waves, which can exist in a given medium, including the linear and nonlinear MHD waves.

6.6.2 Averaging of Turbulent Parameters and Correlation Tensors

To describe a random field of turbulent velocities, some averaged measures characterizing the field must be specified. For equilibrium systems such averaging is typically performed over the statistical ensemble of equilibrium states (Gibbs's ensemble). However, turbulent media are highly nonequilibrium, so the macroscopic velocity probability distributions are generally unknown. In practice, the way of averaging in such media must be closely linked with the way how the corresponding parameters are measured. Frequently, instruments perform averaging of a measured parameter in time. The interval Δt of theoretical averaging must be taken in such a way to exceed all main

periods of the turbulent pulsations, which ensures that all the pulsations are smoothed out:

$$\langle \boldsymbol{u}(\boldsymbol{r},t)\rangle \equiv \frac{1}{\Delta t}\int\limits_{-\Delta t/2}^{\Delta t/2} \boldsymbol{u}(\boldsymbol{r},t+t')\mathrm{d}t' = \boldsymbol{u}_0(\boldsymbol{r},t), \tag{6.72}$$

and thus the mean velocity $\boldsymbol{u}_0(\boldsymbol{r},t)$ becomes a regular function of position and time, which varies only slowly over time Δt. Then, the difference

$$\boldsymbol{u}'(\boldsymbol{r},t) = \boldsymbol{u}(\boldsymbol{r},t) - \boldsymbol{u}_0(\boldsymbol{r},t) \tag{6.73}$$

can be called *pulsating velocity*, whose mean is zero by definition, $\langle \boldsymbol{u}'\rangle = 0$. However, a two-point correlation tensor, being a quadratic form of the random function, is evidently nonzero:

$$U_{\alpha\beta}(\boldsymbol{r}_1,t_1;\boldsymbol{r}_2,t_2) = \frac{1}{\Delta t}\int\limits_{-\Delta t/2}^{\Delta t/2} u'_\alpha(\boldsymbol{r}_1,t_1+t')u'_\beta(\boldsymbol{r}_2,t_2+t')\mathrm{d}t'. \tag{6.74}$$

A complete description of the random field of turbulent velocities requires specifying infinite sequence of multipoint correlation tensors of all higher ranks. Indeed, any functional form $\langle F[\boldsymbol{u}'(\boldsymbol{r},t)]\rangle$, which can be expanded in a power series over components $\boldsymbol{u}'(\boldsymbol{r},t)$, can exactly be expressed via such set of tensors. This complete treatment of turbulence is exceedingly complicated and impractical in most cases. Fortunately, in many cases, a good approximate treatment can be achieved by using only two measures—the averaged velocity and the second-rank correlation tensor. For example, density of kinetic energy of incompressible turbulent fluid has the form

$$w_k(\boldsymbol{r},t) = \frac{1}{2}\rho\{u_0^2 + U_{\alpha\alpha}(\boldsymbol{r},t;\boldsymbol{r},t)\}, \tag{6.75}$$

where ρ is the mass density.

We will often consider a *stationary turbulence*, whose averaged measures do not vary over time. This means, in particular, that $U_{\alpha\beta}$ can only depend on the time difference $t = t_1 - t_2$ but not on $T = (t_1 + t_2)/2$. If the random field is also uniform in space, i.e., the averaged (but not instantaneous!) measures do not depend on coordinates, then the radius vectors $\boldsymbol{r}_1$ and $\boldsymbol{r}_2$ enter to $U_{\alpha\beta}$ only in the combination $\boldsymbol{r} = \boldsymbol{r}_1 - \boldsymbol{r}_2$. Thus, correlation tensors of stationary uniform turbulence depend on the differences of the variables only:

$$U_{\alpha\beta}(\boldsymbol{r}_1,t_1;\boldsymbol{r}_2,t_2) = U_{\alpha\beta}(\boldsymbol{r}_1-\boldsymbol{r}_2,t_1-t_2). \tag{6.76}$$

For $\boldsymbol{r} = 0$ and $t = 0$ the trace $U_{\alpha\alpha}(0,0) = \langle u'^2\rangle > 0$ gives averaged square of the pulsation velocity. But for $t \to \infty$ we have

$$U_{\alpha\beta}(0,t) = \langle u'_\alpha(\boldsymbol{r},t_1)u'_\beta(\boldsymbol{r},t_2)\rangle \approx \langle u'_\alpha(\boldsymbol{r},t_1)\rangle\langle u'_\beta(\boldsymbol{r},t_2)\rangle = 0 \tag{6.77}$$

because any correlation between the pulsation components will disappear if they are separated by a sufficiently large time interval; thus, the velocities can be averaged separately, which gives zero result. A characteristic time τ_c over which the tensor $U_{\alpha\beta}$ has a noticeably nonzero value is called the *correlation time* or the *coherence time* of the velocity components. A formal definition of the correlation time (applicable for any random variables) is obviously

$$\tau_c = \frac{1}{U_{\alpha\beta}(0,0)} \int_0^\infty U_{\alpha\beta}(0,t)\mathrm{d}t, \quad U_{\alpha\beta}(0,0) \neq 0. \tag{6.78}$$

Similarly, we can define the *correlation length* or *coherence length* L_c along arbitrary unit vector $\boldsymbol{e}$ direction:

$$L_c = \frac{1}{U_{\alpha\beta}(0,0)} \int_0^\infty U_{\alpha\beta}(s\boldsymbol{e},0)\mathrm{d}s; \tag{6.79}$$

therefore

$$U_{\alpha\beta}(\boldsymbol{r}_1 - \boldsymbol{r}_2, 0) \to 0 \quad \text{for} \quad |\boldsymbol{r}_1 - \boldsymbol{r}_2| \gg L_c. \tag{6.80}$$

Here we often assume that the turbulence is *statistically isotropic* and correlation length is the same in any direction.

Although probability distributions of velocities and other macroscopic parameters are generally unknown for nonequilibrium turbulent systems, a formal averaging over *ensemble* is still possible similarly to the equilibrium case. Consider a large (ideally—infinite) number of isolated systems, which are macroscopically equivalent to an original system. Such set of equivalent systems is called *statistical ensemble* or simply *ensemble*. Since the velocity components are random, their values u'_α, $u''_\alpha, \ldots$ in equivalent points of space at the same time are generally different: $u'_\alpha(\boldsymbol{r},t) \neq u''_\alpha(\boldsymbol{r},t) \neq u'''_\alpha(\boldsymbol{r},t) \neq \ldots$. The value averaged over ensemble (statistical average) is just the arithmetic mean

$$\langle u(\boldsymbol{r}_1,t_1)u(\boldsymbol{r}_2,t_2)\rangle = \lim_{N\to\infty} \frac{u'(\boldsymbol{r}_1,t_1)u'(\boldsymbol{r}_2,t_2) + u''(\boldsymbol{r}_1,t_1)u''(\boldsymbol{r}_2,t_2) + \cdots}{N}, \tag{6.81}$$

where N is the total number of the systems in the ensemble. In many turbulent systems the values averaged over ensemble coincide with those averaged over time provided the averaging interval is large enough. Such systems are called *ergodic* systems.

For the stationary random fields the ergodicity condition (Monin and Yaglom 1965) requires that the correlation decreases relatively rapidly with time:

$$\lim_{\Delta t\to\infty} \frac{1}{\Delta t} \int_0^{\Delta t} U_{\alpha\beta}(0,t)\mathrm{d}t = 0.$$

The statistical averaging is commonly used for theoretical treatment of the random fields.

One of the key turbulence characteristics is distribution of the turbulence pulsations energy over scales λ (or over the corresponding reciprocal values, $k = 2\pi/\lambda$). In a neutral medium without any magnetic field (i.e., when the kinetic energy is the only form of the turbulence energy) this distribution is given by a Fourier transform of the second-order **velocity** correlation tensor taken at the same moments of time:

$$U_{\alpha\beta}(\boldsymbol{r}_1 - \boldsymbol{r}_2, 0) = \int \widetilde{U}_{\alpha\beta} e^{i\mathbf{k}\cdot(\mathbf{r}_1 - \mathbf{r}_2)} \frac{\mathrm{d}^3 k}{(2\pi)^3}. \tag{6.82}$$

The turbulence energy E per unit mass is given by the tensor trace

$$E = \frac{1}{2} U_{\alpha\alpha}(0,0) = \frac{1}{16\pi^3} \int \widetilde{U}_{\alpha\beta}(\boldsymbol{k}) \mathrm{d}^3 k. \tag{6.83}$$

If, in addition to spatial uniformity, the turbulence is also isotropic (i.e., there is no preferred direction in the medium), the spectral tensor $\widetilde{U}_{\alpha\beta}(\boldsymbol{k})$ can be fully composed of the components of vector k_α and invariant unit tensors $\delta_{\alpha\beta}$ and $e_{\alpha\beta\gamma}$. Let us first construct a spectral tensor from the symmetric tensors $\delta_{\alpha\beta}$ and $k_\alpha k_\beta / k^2$ only. This spectral tensor is evidently fully defined by specifying two scalar functions $A(k)$ and $B(k)$:

$$\widetilde{U}_{\alpha\beta}(\boldsymbol{k}) = A(k)\delta_{\alpha\beta} + B(k)\frac{k_\alpha k_\beta}{k^2}. \tag{6.84}$$

In incompressible medium we can apply the condition $\nabla \cdot \boldsymbol{u} = 0$ in the Fourier presentation to find $B(k) = -A(k)$; thus, Eq. (6.84) receives a simple form:

$$\widetilde{U}_{\alpha\beta}(\boldsymbol{k}) = A(k)\left(\delta_{\alpha\beta} - \frac{k_\alpha k_\beta}{k^2}\right). \tag{6.85}$$

Spectral tensors Eqs. (6.84) and (6.85) can easily be integrated over angles of vector $\boldsymbol{k}$ to express energy, Eq. (6.83), in a form of single integral over the wave vector modulus:

$$E = \int_0^\infty \frac{\mathrm{d}E}{\mathrm{d}k} \mathrm{d}k, \quad \text{where} \quad \frac{\mathrm{d}E}{\mathrm{d}k} = \frac{k^2}{4\pi^2}(3A(k) + B(k)) \tag{6.86}$$

is the spectral density of turbulence energy per unit mass and unit range of the wave numbers. If typical velocity of the turbulent pulsations u is subsonic, then effects of fluid compression are small, of the order of $u/c_s \ll 1$; therefore, the spectral density is well defined by a single scalar function, which can easily be found from Eq. (6.86) by adopting $B = -A$:

$$\frac{\mathrm{d}E}{\mathrm{d}k} = \frac{k^2}{2\pi^2} A(k). \tag{6.87}$$

Distribution of the turbulent energy over the scales (or wave numbers) often affects other phenomena, linked to the turbulence in one or another way, for example, acceleration and transport of charged particles and generation and propagation of electromagnetic emission.

6.7 The Theory of Turbulence by Kolmogorov and Obukhov

A complete quantitative theory, which would compute the turbulence correlation tensors and distributions of energy over scales, is currently unavailable. However, semiquantitative analytical and numerical models applicable to a variety of more or less simple cases do exist (Monin and Yaglom 1965; Frisch 1995; Frick 2003). We consider a number of these models starting with perhaps the most illustrative, while well-tested, model proposed by Kolmogorov (1941) and Obukhov (1941) for developed uniform, isotropic, and stationary turbulence of incompressible neutral (not ionized) fluid. The foundation of the model is as follows:

1. A turbulence-producing energy source generates motions with the spatial scales specific to this given source; a characteristic scale of these (energy-containing) motions we denote as L and call it the *external scale* of the turbulence, which is of the order of the correlation length L_c introduced above. In fact, in this range of largest scales, the turbulence is typically inhomogeneous and anisotropic. In the considered here stationary case, all the energy deposited into the medium must dissipate and transform to the fluid heating. According to Kolmogorov's hypothesis the intensity of the turbulence source can be well characterized by a single parameter—averaged over volume and time energy $\varepsilon = \text{const}$ deposited per unit mass of the fluid per unit time. It is ε that specifies intensity of turbulent pulsations [see Eq. (6.90)].

   These two values, L and ε, complemented by the third (the only dissipative) parameter, the kinematic viscosity ν, which is discussed below in more detail, compose the full set of the input parameters in the Kolmogorov–Obukhov theory. It looks unbelievable, while highly exciting, that such a small number of the input parameters allows to firmly outline the theoretical frame for that complicated physical phenomenon as the HD turbulence. This theory is capable of calculating key quantitative measures of the turbulence and has met solid experimental (in the laboratory) and observational (in geophysics and astrophysics) justifications.

2. Most of the turbulence energy is associated with eddy motions with scale of about L, which form *energy-containing* range of scales (and corresponding wave numbers around $k_0 = 2\pi/L$; see Fig. 6.6). In case of developed turbulence we have $L \gg \nu/u$, and so dissipation of the kinetic energy at the energy containing range is insignificant. Instead, the main effect evacuating the deposited energy from this energy-containing scale is breaking down of larger eddies onto smaller ones, which is possible owing to nonlinear interaction in the fluid described by the nonlinear fluid dynamic equations. These process, called the turbulence *cascading*, occurs in a broad range of spatial scales down to some small scale l (*internal scale* of

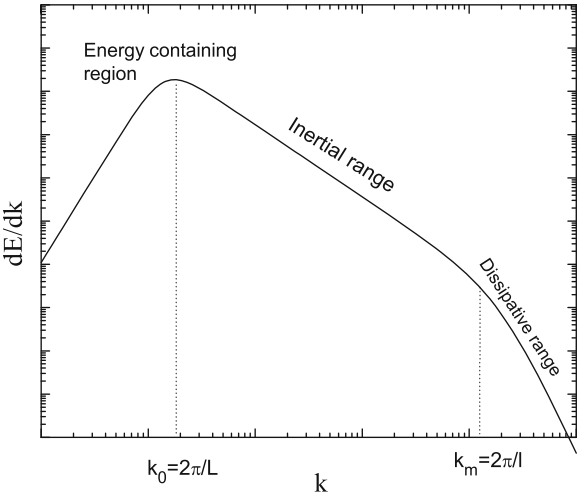

Figure 6.6: Spectrum of developed turbulence in the Kolmogorov–Obukhov theory.

the turbulence), at which the dissipation starts to play a role. Remarkably, between L and l, the main process driving the turbulence properties is the nonlinear cascade of ALL deposited energy ε received from the source from large-scale to small-scale motions. Since the main nonlinear term $(\boldsymbol{u}\cdot\nabla)\boldsymbol{u}$ responsible for the cascading is provided by the inertia force $\mathrm{d}\boldsymbol{u}/\mathrm{d}t$, the range of scales $L \gtrsim \lambda \gtrsim l$ is called the *inertial range*. The nonlinear eddy breaking ensures isotropy of the turbulent eddies; thus, at least at the scales $\lambda \ll L$ the turbulence becomes locally uniform and isotropic, even though the large-scale motions can be nonuniform and anisotropic.

3. A remarkable property of the Kolmogorov–Obukhov turbulence model is that dependence of the velocity u_λ on its scale λ at the inertial range can be found from a simple, while rather general consideration. Adopt that the eddy lifetime is of the order of its single rotation time $\tau_\lambda \approx \lambda/u_\lambda$ (so-called *strong* turbulence). Energy of a single eddy (which is $u_\lambda^2/2$ per unit mass) is transformed to smaller-scale motions over the time interval τ_λ. This process must forward down all the energy ε, deposited by the turbulence source per unit time:

$$\varepsilon \approx \frac{u_\lambda^2}{2\tau_\lambda} \approx \frac{u_\lambda^3}{\lambda}, \tag{6.88}$$

which on the order of magnitude yields the *Kolmogorov–Obukhov* law giving dependence of the velocity on scale:

$$u_\lambda \approx (\varepsilon\lambda)^{1/3} \sim \lambda^{1/3}, \tag{6.89}$$

where u_λ is in fact an rms value $u_\lambda = \langle \boldsymbol{u}_\lambda^2 \rangle^{1/2}$ (the true mean is evidently zero $\langle \boldsymbol{u}_\lambda \rangle = 0$). Dependence (6.88) is valid on the order of magnitude up to scale L; thus

$$\varepsilon \approx \frac{u^3}{L}, \tag{6.90}$$

where u is the rms value of the pulsation velocity, which is about the maximum turbulence velocity. Apparently, this estimate does not include the mean flow speed if present.

4. The internal scale l is specified by approximate balance of the inertial and dissipative terms at this scale: $l^{-1}u_l^2 \approx \nu u_l l^{-2}$, which yields $l \approx \nu/u_l$. Using Eq. (6.89) we obtain

$$l \approx \left(\frac{\nu^3}{\varepsilon}\right)^{1/4}. \tag{6.91}$$

The scales $\lambda < l$ form the *dissipative range* where the turbulence decays (Fig. 6.6).

Finally, obtain from Eq. (6.89) the spectral energy density described by Eq. (6.87). We have

$$\lambda = 2\pi/k, \qquad u_\lambda^2 = \int_k^\infty \langle u_k^2 \rangle 4\pi k^2 \mathrm{d}k \approx 4\pi \langle u_k^2 \rangle k^3, \tag{6.92}$$

which for the inertial interval yields

$$\langle u_k^2 \rangle = \frac{u_\lambda^2}{4\pi k^3} = \left(\frac{2\pi\varepsilon}{k}\right)^{2/3} \frac{1}{4\pi k^3}. \tag{6.93}$$

This gives rise to the spectral energy distribution:

$$\frac{\mathrm{d}E}{\mathrm{d}k} = \frac{\langle u_k^2 \rangle}{2} 4\pi k^2 = C\varepsilon^{2/3} k^{-5/3}, \tag{6.94}$$

which represents the *Kolmogorov–Obukhov* law for the turbulence spectral energy density in the inertial range. Note that the consideration performed here is in fact an estimate rather than a theory. In particular, it does not define the normalization constant C, which therefore must be defined from an external knowledge—more sophisticated theory, numerical modeling, or laboratory experiment. Nevertheless, in spite of apparent simplicity and numerous oversimplifications of the model, the *Kolmogorov–Obukhov* law was found to

agree with many natural phenomena—atmospheric and ocean turbulence, turbulence in galactic molecular clouds, "Big Power Law" (Sect. 6.10.2) in the Galaxy, etc.

6.8 Weak MHD Turbulence in Incompressible Conducting Fluid with Magnetic Field

In astrophysical conditions plasma moves eternally; the motion is typically irregular. Even when there is a regular motion, like a differential rotation, solar or stellar wind, and accretion, random motions superimpose on it. Thus, the velocity represents a random field; the direction and magnitude of the velocity change in a chaotic way. Nevertheless, there are various stable averaged measures of the motion capable of reasonably detailed characterizing it.

A distinctive feature of the turbulence in astrophysics is presence of random fields along with random motions. This is provided by excitation and further amplification of originally weak magnetic perturbations by turbulent fluid (dynamo-instabilities). In addition, the turbulence is always followed up by enhanced energy dissipation, which typically implies breaking down the scales of magnetic field and velocity. Eventually, the presence of charged particles and electromagnetic fields significantly complicates the picture of the astrophysical turbulence providing a remarkable diversity of its forms.

In a magnetized plasma many eigenmodes can be generated and persist, such as electrostatic Langmuir and ion-sound waves, MHD Alfvén and magnetosonic waves, and whistlers. They can be produced by a number of mechanisms involving kinetic plasma motions, particle beams, powerful radio emission, plasma currents, and numerous instabilities. Because of random way of generation along with nonlinear interactions, the waves have typically random phases and so form a random wave field. Such ensembles of weak waves with random phases are called *plasma turbulence*(accordingly, depending on the wave type forming the turbulence, we will distinguish Langmuir, Alfvén, whistler etc turbulence). The turbulence is called weak in this case because its main forming elements are linear plasma eigenmodes, weakly interacting with each other owing to nonlinear effects. For example, spacecrafts probing interplanetary medium revealed that there are MHD turbulence composed of Alfvén and fast magnetosonic waves, as well as MHD discontinuities (see Sect. 5.3.3).

Here we consider a stationary spatial spectrum of weak MHD turbulence within the ideas of the Kolmogorov–Obukhov theory and generalize it for the case of MHD turbulence. However, the result of this generalization is not unique because the magnetic field introduces anisotropy into the system and more dimensionless parameters can be composed in this case. Indeed,

in addition to $\epsilon\lambda/u^3$, there are two more dimensionless parameters—$\langle u_\lambda^2\rangle/v_\mathrm{A}^2$ and $\lambda_\parallel/\lambda$—the last one is related to the turbulence anisotropy. Thus, the analysis of dimensions alone is insufficient to uniquely derive the turbulence spectrum in the inertial range.

6.8.1 Weak MHD Turbulence Below the Diffusive Scale

We start from assumption of large Reynolds number $R = uL/\nu$ but weak large-scale magnetic field B_0, $B_0^2/8\pi\rho \ll u^2/2$, and small magnetic Reynolds number $R_m = uL/\nu_m \lesssim 1$, i.e., the *magnetic Prandtl number* is very small, $P_m = \nu/\nu_m = R_m/R \ll 1$. In these conditions the turbulence anisotropy is small, $\lambda_\parallel/\lambda \sim 1$, and effect of magnetic field on medium motion can be ignored. Thus, in the induction equation, Eq. (2.16),

$$\frac{\partial \boldsymbol{B}}{\partial t} + (\boldsymbol{U}\cdot\nabla)\boldsymbol{B} = (\boldsymbol{B}\cdot\nabla)\boldsymbol{U} + \nu_m\Delta\boldsymbol{B}; \tag{6.95}$$

the turbulent velocity $\boldsymbol{U}$ can be considered as a given stochastic function, determined by the Kolmogorov–Obukhov theory [see Eqs. (6.88) and (6.93)]. Thus, we solve the problem of small-scale ($l \ll \lambda \ll L$) and weak ($b_\lambda \ll B_0$) magnetic field generation in incompressible medium with external magnetic field B_0 by a given strong Kolmogorov–Obukhov turbulence.

To start with we obtain an approximate equation for the small-scale magnetic field $\boldsymbol{b}_\lambda$ from Eq. (6.95). In the linear terms we change $\boldsymbol{B}$ to $\boldsymbol{b}_\lambda$. The nonlinear terms are transformed according to $(\boldsymbol{B}\cdot\nabla)\boldsymbol{U} \to (\boldsymbol{B}_0\cdot\nabla)\boldsymbol{u}_\lambda + (\boldsymbol{B}_0\cdot\nabla)\boldsymbol{u}$ and $(\boldsymbol{U}\cdot\nabla)\boldsymbol{B} \to (\boldsymbol{u}\cdot\nabla)\boldsymbol{B}_0 + (\boldsymbol{u}\cdot\nabla)\boldsymbol{b}_\lambda$. Here $\boldsymbol{u}$ and $\boldsymbol{B}_0$ are the turbulent velocity and magnetic field at the largest scale L. The estimate to the order of magnitude with the account of Eqs. (6.88) and (6.89) gives $|\partial\boldsymbol{b}_\lambda/\partial t| \sim v_\mathrm{A} b_\lambda/\lambda$ and $|(\boldsymbol{u}\cdot\nabla)\boldsymbol{b}_\lambda| \sim ub_\lambda/\lambda$. These terms are small $v_\mathrm{A}\lambda/\nu_m \ll 1$, $u\lambda/\nu_m \ll 1$ relative to the term $\nu_m\Delta\boldsymbol{b}_\lambda$. The terms $|(\boldsymbol{B}_0\cdot\nabla)\boldsymbol{u}| \approx |(\boldsymbol{u}\cdot\nabla)\boldsymbol{B}_0| \sim uB_0/L$ are small by $(\lambda/L)^{2/3}$ relative to $|(\boldsymbol{B}_0\cdot\nabla)\boldsymbol{u}_\lambda| \sim B_0u_\lambda/\lambda \approx B_0(\varepsilon\lambda)^{1/3}/\lambda \approx (uB_0/L)(L/\lambda)^{2/3}$. Thus, we can keep two terms only in Eq. (6.95):

$$(\boldsymbol{B}_0\cdot\nabla)\boldsymbol{u}_\lambda + \nu_m\Delta\boldsymbol{b}_\lambda = 0. \tag{6.96}$$

Fourier transform of Eq. (6.96) has the form

$$\boldsymbol{b}_\mathbf{k} = i\frac{\boldsymbol{k}\cdot\boldsymbol{B}_0}{k^2\nu_m}\boldsymbol{u}_\mathbf{k}. \tag{6.97}$$

Squaring and averaging this equation over the angle between $\boldsymbol{k}$ and $\boldsymbol{B}_0$, we obtain the spectral density of the magnetic turbulent energy (Golitsyn 1960, 1962):

$$\frac{\mathrm{d}E_B(k)}{\mathrm{d}k} = \frac{\langle b_{\mathbf{k}}^2 \rangle}{8\pi\rho} = C_B R_m^2 \frac{v_A^2}{L^{8/3} k^{11/3}} \sim k^{-11/3}, \tag{6.98}$$

where C_B is a dimensionless constant.

Although the magnetic field just passively follows after the mechanical motions described by the Kolmogorov–Obukhov theory, the mechanism of the magnetic spectrum formation is strongly different from that of the kinetic energy spectrum. Indeed, there is no cascade of the magnetic fluctuations; instead the velocity pulsations of a given scale give rise to magnetic pulsations of the same scale, which quickly dissipate due to large magnetic viscosity; this eventually results in much steeper magnetic than kinetic spectrum. An opposite situation takes place when the magnetic Prandtl number is large (see Sect. 6.9.5).

6.8.2 Iroshnikov–Kraichnan Model of Weak Alfvénic Turbulence

We turn now to the case of large magnetic Reynolds number of a turbulent fluid with energy-containing scale L and velocity u at this scale permeated by an external magnetic field B, with the magnetic energy density comparable to the kinetic energy density:

$$\frac{B^2}{8\pi} \approx \frac{\rho u^2}{2}. \tag{6.99}$$

This, in particular, means that the fluid speed at the main scale is about the Alfvén speed, $u \approx v_\mathrm{A} = B/\sqrt{4\pi\rho}$. Note that even if the magnetic field was originally uniform, it will be randomized (with the largest scale of inhomogeneity L) at the course of time due to freezing in the random plasma motions.

Magnetic inhomogeneities, generated by turbulent motion, will then represent a superposition of the corresponding small-amplitude eigenmodes of the fluid. The eigenmodes of an incompressible magnetized fluid are the Alfvén waves; note that independently on the wavelength λ, the turbulence magnetic energy equals to the kinetic energy:

$$\frac{B_\lambda^2}{8\pi} = \frac{\rho u_\lambda^2}{2} \tag{6.100}$$

in both simple Alfvén wave and in small-amplitude Alfvén wave. Like in the Kolmogorov–Obukhov model, the spectral flux of the turbulence energy toward smaller scales occurs owing to nonlinear generation of small-scale modes. The Kolmogorov–Obukhov model can be generalized to the

considered case by taking into account that the dissipation is negligible over scales $l_m \ll \lambda \ll L$, while the small-scale velocities are small compared with the main-scale velocity ($u_\lambda^2 \ll u^2 \approx v_\mathrm{A}^2$).

In this section we adopt an assumption of the turbulence isotropy, $\lambda_\parallel/\lambda \sim 1$, and expand the spectral flux of energy ϵ over the small parameter $\langle u_\lambda^2\rangle/v_\mathrm{A}^2$:

$$\epsilon \approx a\langle u_\lambda^2\rangle/v_\mathrm{A}^2 + b(\langle u_\lambda^2\rangle/v_\mathrm{A}^2)^2 + \cdots, \tag{6.101}$$

which will result in the Iroshnikov–Kraichnan model of the weak Alfvénic turbulence. The first term here describes the Alfven wave dissipation. The dissipated energy consists of the absorbed kinetic energy $\nu\langle u_\lambda^2\rangle/\lambda^2$ per unit mass and a similar damping of the magnetic energy, $\nu_m\langle B_\lambda^2\rangle/4\pi\rho\lambda^2 \approx \nu_m\langle u_\lambda^2\rangle/\lambda^2$, which implies the following estimate for the coefficient $a \approx (\nu+\nu_m)/v_\mathrm{A}^2\lambda^2$. In the inertial range (if present) the damping is small, so the second term in expansion (6.101) must dominate there. The coefficient b, having the same dimension as ϵ, can be composed of the scale λ and the Alfvén speed v_A, which does not depend on scale $b = v_\mathrm{A}^3/\beta\lambda$, where β is a (unknown) dimensionless coefficient. We, therefore, omit the first term in the inertial range, so Eq. (6.101) reduces to

$$\epsilon \approx b\frac{\langle u_\lambda^2\rangle^2}{v_\mathrm{A}^4} \approx \frac{\langle u_\lambda^2\rangle^2}{\beta v_\mathrm{A}\lambda}, \quad \langle u_\lambda^2\rangle \approx (\beta\epsilon v_\mathrm{A}\lambda)^{1/2}, \tag{6.102}$$

which specifies dependence of the turbulent velocity on its scale. Next, this dependence can be straightforwardly used to derive distribution of the turbulence energy over spectrum in the same way as was used to obtain Eq. (6.94):

$$\frac{\mathrm{d}E}{\mathrm{d}k} \approx C(\varepsilon v_\mathrm{A})^{1/2}k^{-3/2}, \tag{6.103}$$

where C is a new dimensionless constant (different from that introduced in the previous section). According to Eq. (6.99), the spectrum of magnetic turbulence has the same form as the spectrum of kinetic energy (6.103).

Let us consider now the applicability and bounds of this inertial interval. The expansion parameter in Eq. (6.101) is $\langle u_\lambda^2\rangle/v_\mathrm{A}^2 \approx (\beta\epsilon v_\mathrm{A}\lambda)^{1/2}/v_\mathrm{A}^2 \approx (\beta\lambda/L)^{1/2}$, where expressions (6.90), (6.99), and (6.102) have been used. The ratio of the first to the second terms in Eq. (6.101) is $av_\mathrm{A}^2/b\langle u_\lambda^2\rangle^2 \approx l_m(\beta L/\lambda^3)^{1/2}$, where

$$l_m \approx \frac{\nu+\nu_m}{v_\mathrm{A}}. \tag{6.104}$$

The dissipation becomes comparable to the nonlinearity at

$$\lambda = \lambda_m \equiv (\beta l_m^2 L)^{1/3} \approx L/R_*^{2/3}. \tag{6.105}$$

Here $R_* = v_\mathrm{A}L/(\nu+\nu_m)$ is a "generalized Reynolds number" that depends on the sum of the kinematic viscosity and magnetic diffusivity.

We emphasize that the dissipation of the weak MHD turbulence is controlled by both effects, viscosity and diffusivity. Although one of them typically dominates the other, it would be incorrect to think that ν controls the velocity dissipation only, while ν_m controls the magnetic field dissipation only. In fact, energy equipartition (6.100) is fulfilled for the Alfvénic waves when the damping rate is small ($\gamma \ll \omega_\mathrm{A}$), and until it is small, kinetic and magnetic energies are strongly coupled in the Alfvén wave and they decay coherently with a single damping rate γ.

6.9 Anisotropic Turbulence: Critically Balanced Cascade

Let us now critically revise the presented weak Alfvénic turbulence model. We assumed above that the turbulence is isotropic and the corresponding nonlinear interaction leading to the turbulence cascade is weak. We now address these assumptions in more detail. Let us introduce an Alfvén time:

$$\tau_\mathrm{A} \sim 1/\omega_\mathrm{A} \sim \lambda_\parallel / v_\mathrm{A}, \tag{6.106}$$

where $\lambda_\parallel \sim 1/k_\parallel$ [see the dispersion relation for the Alfvén waves, Eq. (2.54)], $\omega_\mathrm{A} = \pm v_\mathrm{A} k_\parallel$, and the kinematic time corresponding to a certain scale λ

$$\tau_s \sim \lambda / u_\lambda. \tag{6.107}$$

Apparently, the assumption of weak interaction implies that many wave periods are needed to the wave energy to cascade further down, which requires $\tau_s \gg \tau_\mathrm{A}$. The cascading time τ_λ is τ_s/τ_A times longer than the kinematic time since each uncorrelated interaction between the wave packets occurs only a short time τ_A:

$$\tau_\lambda \sim \frac{\tau_s^2}{\tau_\mathrm{A}} \sim \frac{\lambda^2 v_\mathrm{A}}{\lambda_\parallel u_\lambda^2}. \tag{6.108}$$

If we assume the turbulence isotropy and adopt $\lambda_\parallel = \lambda$, we immediately obtain the results of Sect. 6.8. It turns, however, that the isotropy assumption is difficult to justify.

Weak nonlinear interaction between waves can be consistently described in terms of resonant three-wave and four-wave processes. For the lowest-order, three-wave processes the conservation laws imply

$$\boldsymbol{k}_1 + \boldsymbol{k}_2 = \boldsymbol{k}_3, \tag{6.109a}$$

$$\omega_1 + \omega_2 = \omega_3. \tag{6.109b}$$

It was noted (Shebalin et al. 1983; Sridhar and Goldreich 1994) that these conservation laws together with a very special (anisotropic) dispersion law of the Alfvén waves $\omega_\mathrm{A} = \pm v_\mathrm{A} k_\parallel$, where the wave frequency depends on

the longitudinal component of the wave vector only, put severe constraints on the nonlinear interaction of the Alfvén waves. Indeed, if we consider two Alfvén waves with the same propagation direction, the sum of them represents a valid solution of the exact nonlinear (non-dissipative, incompressible) MHD equations, which means no modification to the original waves and so no cascading. The only interacting Alfvén waves are those propagating in the opposite directions; for those waves the conservation laws along with the dispersion law yield

$$k_{\|1} - k_{\|2} = k_{\|3}, \quad k_{\|1} + k_{\|2} = k_{\|3}, \tag{6.110}$$

with the only solution $k_{\|2} = 0$ and $k_{\|1} = k_{\|3}$. This means that the Alfvén wave energy does not cascade along $k_{\|}$, so only transverse cascade can take place. Account of the four-wave resonant interactions does not change this conclusion (Sridhar and Goldreich 1994). We, therefore, have arrived at a conclusion that the Iroshnikov–Kraichnan model of the isotropic Alfvénic turbulence is self-contradictory and needs to be patched.

6.9.1 Developed Incompressible Turbulence

The first way of the weak turbulence model generalization is to adopt that the turbulence is "developed", i.e., other than Alfvén modes are present and can participate in the cascading. In the incompressible case, however, only static (motionless) vortex perturbations with $k_{\|} = 0$, $\nabla \times \mathbf{b}$ and $\nabla \times \mathbf{u}$, and the entropy excitations (with $k_{\|} \neq 0$) can exit besides the Alfvén waves. Since $\omega_v = 0$ for those perturbations, the resonance conditions cannot be fulfilled in the three-wave processes like those considered above, in which one of the Alfvén waves is substituted by a vortex/entropy perturbation. However, the four-wave processes, where one of the wave is the static vortex/entropy perturbation,

$$\boldsymbol{k}_1 + \boldsymbol{k}_2 + \boldsymbol{k}_v = \boldsymbol{k}_3, \tag{6.111a}$$

$$\omega_1 + \omega_2 + 0 = \omega_3, \tag{6.111b}$$

seem to be possible. Although these processes do participate in the transverse momentum cascading, they have no effect on the longitudinal momentum conservation, which again reduces to Eq. (6.109). Thus, the presence of the motionless vortex perturbations, which are also the eigenmodes of the incompressible magnetized fluid, is incapable of recovering the longitudinal cascade in the Alfvénic turbulence spectrum. It seems that this conclusion

remains valid until we take into account some corrections to the Alfvén wave dispersion law, e.g., related to the Hall current corrections considered in Sect. 2.4.2.

However, the standard entropy mode having $k_{\|} = k_2/2$ is capable of recovering the longitudinal cascade of the Alfvén turbulence according to Eq. (6.111). It does not immediately mean, however, that the cascade is isotropic in this case. We note that adding more eigenmodes implies more parameters describing the turbulence: the vortex and entropy perturbations require their own spectra to be consistently found within the same model, which depends on the model and so may not have a unique solution.

6.9.2 Weak Anisotropic Alfvénic Turbulence in Incompressible Plasma

Consider now the case of purely Alfvénic turbulence and take into account the established absence of the parallel cascade. To explicitly do this, we have to associate the longitudinal scale with the injection scale, $\lambda_{\|} \sim 1/k_{\|0}$, and, accordingly, the cascading scale with the transverse scale, $\lambda \sim \lambda_{\perp}$. Then, using Eq. (6.88), we find

$$u_{\lambda}^2 \sim (\varepsilon v_{\mathrm{A}} k_{\|0})^{1/2} \lambda_{\perp}. \tag{6.112}$$

Applying then Eq. (6.92), having $\mathrm{d}^3 k$ replaced by $\mathrm{d}^2 k_{\perp} = 2\pi k_{\perp} \mathrm{d}k_{\perp}$, we obtain the spectral energy distribution of the weak anisotropic Alfvénic turbulence:

$$\frac{\mathrm{d}E(k_{\perp})}{\mathrm{d}k} \sim (\varepsilon v_{\mathrm{A}} k_{\|0})^{1/2} k_{\perp}^{-2}, \tag{6.113}$$

which gives a solution for the weak anisotropic turbulence.

At this point we have yet to check if the solution is consistent with the assumption of weak interaction $\tau_s \gg \tau_{\mathrm{A}}$. To do so we substitute velocity Eq. (6.112) into Eq. (6.107) and form the ratio

$$\frac{\tau_{\mathrm{A}}}{\tau_s} \sim \frac{\varepsilon^{1/4}}{(v_{\mathrm{A}} k_{\|0})^{3/4} \lambda_{\perp}^{1/2}} \ll 1, \tag{6.114}$$

which must be small for the weak interaction approximation to be applicable. Solving this inequality for $\lambda_{\perp}$, we find that the weak interaction approximation is only applicable down to a critical scale:

$$\lambda_{cr} \approx \frac{\varepsilon^{1/2}}{(v_{\mathrm{A}} k_{\|0})^{3/2}}. \tag{6.115}$$

At the smaller scales, $\lambda_{\perp} < \lambda_{cr}$, which can be well within the inertial range if the Reynolds number and the magnetic Reynolds number are large, the nonlinear wave interaction is not weak any longer. Stated another way, the anisotropic weak cascade ultimately drives the turbulence toward the regime of strong cascade, which requires further analysis.

6.9.3 Critically Balanced Cascade

The idea of the critically balanced turbulence (Goldreich and Sridhar 1995) is very simple: even if the cascade started as the weak one, after some time, as the scale λ_{cr}, Eq. (6.115), has been reached and the characteristic times τ_A and τ_s have become comparable to each other, $\tau_\mathrm{A} \sim \tau_s$, this equality holds afterward. Then, using Eqs. (6.106) and (6.107) yields

$$\lambda_\parallel / \lambda_\perp \sim v_\mathrm{A} / u_\lambda; \tag{6.116}$$

this property is called the **critical balance**. As has been shown above, the cascade of the Alfvénic turbulence itself drives the system to a state in which condition (6.116) is fulfilled. In this state we have only one natural time scale, $\tau_\mathrm{A} \sim \tau_s \sim \tau_\lambda$, which, together with Eq. (6.116), uniquely defines (by applying the same consideration as in Sect. 6.7) the cascade properties including the turbulence spectrum

$$\frac{\mathrm{d}E}{\mathrm{d}k} \sim \varepsilon^{2/3} k_\perp^{-5/3} f\left(\frac{k_\parallel}{k_0^{1/3} k_\perp^{2/3}}\right), \tag{6.117}$$

which essentially recovers the Kolmogorov's scaling law but in terms of $k_\perp$ in place of k, while the factor $f(x)$ reaching a peak value at about $x_\mathrm{max} \sim 1$ and having $\int f(x)\mathrm{d}x = 1$ describes a weaker parallel cascade with effective parallel scale:

$$\lambda_\parallel \sim \frac{\lambda_\perp^{2/3}}{\lambda_{cr}^{2/3} k_{\parallel 0}}. \tag{6.118}$$

This consideration implies that the turbulence structural elements (eddies or wave packets) are essentially anisotropic and become more and more anisotropic for the respectively smaller scales. The obtained scalings must hold at all scales below the critical scale λ_{cr} and above the dissipative scales $\lambda_\nu \sim (\nu^3/\varepsilon)^{1/4}$ and $\lambda_m \sim (\nu_m^3/\varepsilon)^{1/4}$ determined by the viscosity ν and magnetic diffusivity ν_m, respectively. This inertial range does exist if the critical scale is much larger than both dissipative scales. In terms of the Reynolds numbers, this requirement implies $R,\ R_m \gg (v_\mathrm{A}/u)^3$, which is typically fulfilled in the astrophysical conditions. The model of the critically balanced turbulence is currently accepted as a standard model of astrophysical Alfvénic turbulence in place of the isotropic weak turbulence model.

6.9.4 Turbulence in Unmagnetized Plasma

The cases considered above assume that the plasma is permitted by an external magnetic field. However, we can consider a situation in which a conducting plasma is free from the external magnetic field and so initially isotropic; thus, the turbulence developing in such a fluid is also supposed to be globally statistically isotropic and the above anisotropic cascade seems to be invalid from this perspective.

One possibility is that the MHD fluctuations at the largest scale are isotropic but the cascade at smaller scales is driven by this large-scale field and so is locally anisotropic. This model assumes that the smaller-scale dynamics is dominated by larger-scale dynamics. Numerical simulations (Schekochihin and Cowley 2007) reveal that this is not always the case. Instead, the isotropic turbulence can often be dominated by a small-scale dynamo with most or significant fraction of the energy residing at the small scales. We return to the small-scale dynamo in the Chap. 8 when the magnetic field generation is considered.

6.9.5 Turbulence Below the Viscous Scale

Classical inertial range is located above both characteristic dissipative scales of the plasma—viscous λ_ν and resistive λ_m. In astrophysical objects, however, the kinematic viscosity is often much larger than the magnetic diffusivity, oppositely to the case considered in Sect. 6.8.1. Indeed, using Eqs. (1.150) and (1.152), we find the *magnetic Prandtl number* P_m:

$$P_m \approx 6.5 \times 10^{18} \left(\frac{T}{10^6\,\mathrm{K}}\right)^4 \left(\frac{n_i}{\mathrm{cm}^{-3}}\right)^{-1}; \tag{6.119}$$

thus, typically $\lambda_\nu \gg \lambda_m$. This implies that although plasma motions strongly decay below the viscous scale, the magnetic field can have much smaller-scale structure here down to the resistive scale λ_m.

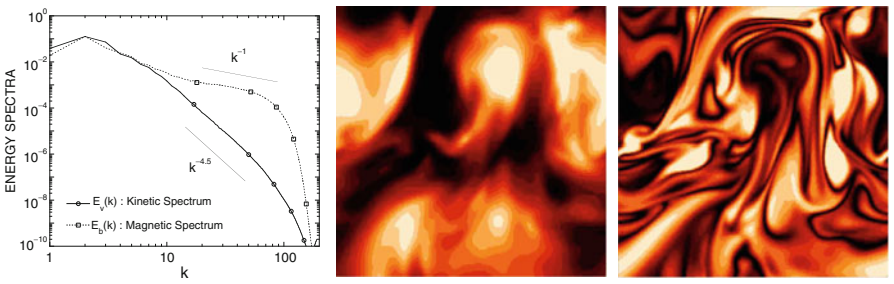

Figure 6.7: Spectrum of turbulence below the viscous scale obtained in numerical modeling by Cho et al. (2002), *left panel*. Corresponding spatial distributions of the fluid velocity (smooth image in the *middle*) and magnetic field (having prominent small-scale structure in the *right*) from Schekochihin and Cowley (2007).

Let us estimate the magnetic spectrum in this (dissipative inertial) range of the spacial scales. To do so we note that because the motions below the viscous scale are damped, we have to conclude that all the small-scale magnetic structure is mediated by the fluid motion at the viscous scale:

$$b_\lambda^2/\tau_\nu \approx \mathrm{const}, \tag{6.120}$$

where $\tau_\nu \sim \lambda_\nu^2/\nu = \text{const}$ is a cascade time at the viscous dissipative scale λ_ν. Since $\tau_\nu = \text{const}$, we immediately arrive at a conclusion that the magnetic energy is equally distributed per each decade within this dissipative range $\lambda_\nu \gg \lambda \gg \lambda_m$, i.e.,

$$\frac{\mathrm{d}E_b(k)}{\mathrm{d}k} \propto k^{-1}, \tag{6.121}$$

which implies a considerable small-scale structure of the magnetic field below the viscous dissipative scale.

Numerical modeling of the turbulence in this dissipative inertial range (Cho et al. 2002; Schekochihin and Cowley 2007) shows that the magnetic structures represent locally anisotropic elongated patterns, whose Fourier spectrum roughly obeys scaling law (6.121) (see Fig. 6.7). Moreover, the coupling between the magnetic field and plasma motion results in flattening of the kinetic energy spectrum: in place of the exponential cut-off expected for a neutral fluid below the viscous scale, the presence of the small-scale magnetic structure gives rise to a power-law spectrum of the kinetic energy, $\frac{\mathrm{d}E(k)}{\mathrm{d}k} \propto k^{-9/2}$, but with a rather steep slope. Exponential cutoff is formed only below the resistive scale.

6.9.6 Turbulence in the Compressible Conducting Fluid

Consider the case of compressible fluid, when the turbulent velocities are somewhat small, so that the characteristic Mach numbers are smaller than one. In this case, at least at initial stages of the turbulence cascading, we can adopt that the turbulence is composed of the MHD linear modes: the Alfvén waves, the fast waves, and the slow waves. In a general case, one must also take into account the static entropy modes, which are not considered here for simplicity.

It is easy to estimate that the dispersion law of the slow mode is similar to that of the Alfvén waves (the frequency is approximately proportional to the parallel component of the wave vector, so it is sometimes called a pseudo-Alfvénic mode). This results in a consideration similar to that for the incompressible case, so the spectrum of the slow mode is formed under condition of the critically balanced cascade, and the spectrum similar to Eq. (6.117) is valid for the slow mode.

$$\frac{\mathrm{d}E_s}{\mathrm{d}k} \sim k_\perp^{-5/3} f_s\left(\frac{k_\parallel}{k_0^{1/3} k_\perp^{2/3}}\right). \tag{6.122}$$

The dispersion law of the fast mode is different: the frequency is determined by the absolute value of the wave vector. This means that the Iroshnikov–Kraichnan consideration applies for the fast mode, which brings back their scaling law, but only for the fast mode:

$$\frac{\mathrm{d}E_f}{\mathrm{d}k} \sim k^{-3/2}. \tag{6.123}$$

It is worthwhile to note that the presence of the fast and slow modes results in fluctuations of the fluid density in addition to the velocity and magnetic field. Stated another way, in a developed compressible turbulence, which includes many MHD eigenmodes, the spectra of the velocity, magnetic field, and density are produced by different modes and so are not necessarily strictly correlated. Different slopes of the fast- and slow-mode spectra imply that the large-scale density fluctuations are determined by the slow mode, while the small-scale end of the density fluctuation spectrum is by the fast mode.

However, as we have discussed in Sect. 5.1.4, evolution of the finite-amplitude fast and slow modes necessarily results in the wave front steepening and formation of discontinuities. The effect of the discontinuities including the shock waves is especially pronounced in the case of the motions with strong Mach numbers, which is considered in more detail in the next section.

6.10 Turbulence Composed of Shock Waves and Discontinuities

In astrophysical conditions, main sources of the energy and momentum of the turbulence are various large-scale motions of the gas flows and stellar systems (rotation, density waves, accretion, etc.) as well as active processes in stars, galactic nuclei, stellar associations (such as stellar winds, supernova explosions, and collimated jets). If the energy release is sufficiently strong to generate turbulent fluid motions with velocities larger that typical velocity of linear modes in this fluid, i.e., the sound and Alfvén speeds, this *supersonic turbulence* rapidly evolves to an ensemble of shock fronts and rarefaction waves. Weak MHD waves (or weak sound waves and vortices if there is no magnetic field) can be present between the shock fronts. The idea of the supersonic turbulence was likely introduced by Solomon Pikelner when he analyzed an old *supernova remnant* Cygnus Loop.

In a general case, other MHD discontinuities as well as various nonlinear waves including solitons can be present in the supersonic turbulence along with the shock waves. Overall, both the turbulence composed of strongly interacting vortices at subsonic velocities (Sect. 6.7) and the supersonic turbulence composed of the shock waves and other nonlinear structures can be called *strong turbulence* in contrast to *weak turbulence* consisting of quasilinear MHD modes (Sect. 6.8).

6.10.1 Model of Turbulence Formed by Supernova Explosions

Since properties and dynamics of the strong turbulence depend significantly on the energy-release nature and the source structure, there is no unique model adequately describing the strong turbulence. We consider a relatively simple HD model of the turbulence formation by shock waves at the galactic disk. Main sources of energy are supernova explosions and cumulative

effect of the stellar winds. The most powerful stellar winds are produced by young O and B stars (concentrated in the galactic disk within so-called OB associations), which explode at the end of their evolution as a supernova. The stellar winds and supernova explosions produce primary strong shocks in the disk (see Sects. 2.5, 5.5.3, and 5.6). These primary shocks then propagate within nonuniform interstellar medium and interact with numerous clouds. The clouds with typical scale about a few pc with a density much larger than in diffuse interstellar gas can arise due to the thermal instability, discussed in Sect. 6.5.

Propagation of the primary shock waves in a cloudy medium results in efficient production of multiple secondary shock waves and accompanying large-scale motions. The secondary shock waves, in contrast to the primary ones, cannot be arbitrarily strong, e.g., within one-dimensional model with a single-atom gas, the largest Mach number of a scattered (secondary) shock is $M_{\max} = \sqrt{5}$.

Let us estimate the fluctuation spectra of the random velocity and other parameters created by the secondary shock waves, which are not spherical and have different values of the Max numbers μ. However, we consider here a simple model in which all the secondary shock waves are the same, have a spherical shape, a moderate Mach number $M = \mu$, and a radius $R(\mu)$; assume a purely random spatial distribution of the shocks without intersections. Contrary to the consideration in the previous sections, here we calculate the turbulence statistics by explicit account of its structural elements—the shock waves.

Instantaneous velocity field within this model can evidently be represented as

$$\boldsymbol{u}(\boldsymbol{r}) = v \sum_a \boldsymbol{n}_a g(|\boldsymbol{r} - \boldsymbol{r}_a|/R). \tag{6.124}$$

Here

$$v = c_s \frac{2(\mu^2 - 1)}{\mu(\gamma + 1)} \tag{6.125}$$

is the gas velocity just downstream of the shock front in a reference frame in which the center of the shock expansion is at rest, while the spherical front with radius $\boldsymbol{r}_a$ is expanding; $\boldsymbol{n}_a = (\boldsymbol{r} - \boldsymbol{r}_a)/|\boldsymbol{r} - \boldsymbol{r}_a|$ is a unit vector directed from the center of sphere number a; $g(r/R)$ is a dimensionless function describing the velocity field inside the sphere of the radius R, such as $g = 0$ for $r > R$ and $g = 1$ for $r = R$ and $g < 1$ for $r < R$; exact form of this function is generally unknown.

Taking spatial Fourier transform we obtain

$$\boldsymbol{u}_{\mathbf{k}} = i\boldsymbol{k} \frac{4\pi v R^2}{k^2} \int_0^1 \left(\cos kRy - \frac{\sin kRy}{kRy} \right) g(y) y \mathrm{d}y \sum_a e^{i\mathbf{k}\cdot\mathbf{r_a}}. \tag{6.126}$$

The turbulence energy density E per unit mass in a statistically uniform system can be calculated as

$$E = \frac{1}{2}\langle \boldsymbol{u}(\boldsymbol{r}) \cdot \boldsymbol{u}(\boldsymbol{r}) \rangle = \frac{1}{2} \int \langle \boldsymbol{u}^*_{\mathbf{k}'} \boldsymbol{u}_{\mathbf{k}} \rangle e^{i(\mathbf{k}-\mathbf{k}')\cdot\mathbf{r}} \frac{\mathrm{d}^3 k}{(2\pi)^3} \frac{\mathrm{d}^3 k'}{(2\pi)^3}, \tag{6.127}$$

where the averaging must be performed over random spatial locations of the clouds (i.e., over the centers of secondary spherical shocks):

$$\begin{aligned} \sum_{a,a'} \langle e^{i(\mathbf{k}\cdot\mathbf{r}_a - \mathbf{k}'\cdot\mathbf{r}_{a'})} \rangle &= \sum_a \int \frac{\mathrm{d}^3 r_a}{V} e^{i(\mathbf{k}-\mathbf{k}')\cdot\mathbf{r}_a} + \sum_{a\neq a'} \int \frac{\mathrm{d}^3 r_a}{V} e^{i(\mathbf{k}\cdot\mathbf{r}_a - \mathbf{k}'\cdot\mathbf{r}_{a'})} \\ &= \frac{(2\pi)^3 N}{V} \delta(\boldsymbol{k}-\boldsymbol{k}') = (2\pi)^3 n_{\mathrm{cl}} \delta(\boldsymbol{k}-\boldsymbol{k}'). \end{aligned} \tag{6.128}$$

Here V is volume of the system, N is the total number of clouds, and n_{cl} is the number density of the clouds. The term with $a \neq a'$ gives no contribution if locations of different clouds are uncorrelated; thus, the spectral density of the turbulence energy reads

$$E = \int \frac{\mathrm{d}E}{\mathrm{d}k} \mathrm{d}k, \quad \frac{\mathrm{d}E}{\mathrm{d}k} = 8 v^2 R^4 n_{\mathrm{cl}} \left[\int_0^1 \left(\cos kRy - \frac{\sin kRy}{kRy} \right) g(y) y \mathrm{d}y \right]^2. \tag{6.129}$$

To calculate the spectrum we need to know function $g(y)$, which is in fact unknown for arbitrarily strong shock wave. Nevertheless, we can determine asymptotes of the spectrum under some general assumption about analytical properties of the functions entering the integral:

$$\frac{\mathrm{d}E}{\mathrm{d}k} \approx \begin{cases} (8C/9) v^2 R^4 n_{\mathrm{cl}} (kR)^4, & kR \ll 1, \quad C = \int_0^1 g(y) y^2 \mathrm{d}y, \\ 8 v^2 R^2 n_{\mathrm{cl}} \sin^2 kR/k^2, & kR \gg 1. \end{cases} \tag{6.130}$$

This spectrum contains a fluctuating component at $kR \gg 1$. Frequently one is interested in a smooth component of this spectrum, which can be determined by averaging of Eq. (6.130) over a finite interval Δk of the wave numbers such as $\Delta k \gg R^{-1}$. Making this averaging $\overline{\sin^2 kR} = 1/2$ we obtain the smoothed spectrum in the form

$$\frac{\mathrm{d}E}{\mathrm{d}k} \approx 4 v^2 R^2 n_{\mathrm{cl}}/k^2, \quad kR \gg 1, \quad k\delta \lesssim 1. \tag{6.131}$$

Here, in the last inequality, we introduced thickness δ of a separate shock front, which is typically specified in astrophysical objects by collisionless processes (see Sect. 5.4.4). The spectral range $kR \ll 1$ in Eq. (6.130) is governed by gradual variation of the velocity at the rarefaction regions, while

the dependence $\mathrm{d}E/\mathrm{d}k \sim k^{-2}$ is produced by sharp velocity jumps at the shock fronts. The model considered is purely hydrodynamic one; however, in the presence of magnetic field the asymptotes of the magnetic energy spectrum have the same shapes as Eq. (6.130). Interestingly, in the interplanetary medium the magnetic turbulence is often observed to have the spectral index about 2. Typically such cases occur when many tangential and Alfvén discontinuities were present in the analyzed region of the interplanetary medium. According to our analysis, the spectrum $\propto k^{-2}$ is in fact a natural outcome of the magnetic field jumps at the discontinuities.

In a more realistic case the secondary shock waves can have different Mach numbers μ and various $R(\mu)$ and $v(\mu)$. This calls for additional averaging of Eq. (6.130) over all possible μ. Furthermore, interaction of the shock waves with each other and with the clouds, as well as other available sources, produces quasilinear MHD modes, which contain a considerable fraction of the turbulence energy and so affect the overall turbulence spectra. The whole problem is highly nonlinear because all these modes experience nonlinear interactions with each other and also transform at the shock fronts of different strength. If the main nonlinear transformation effect is the *linear* MHD mode conversion at sharp shock front of the shock wave ensemble, then equations for the energy density of the transverse ($w = T$), longitudinal ($w = S$), and entropy ($w = W$) modes take the form

$$\frac{\partial w_i(k,t)}{\partial t} + \frac{\partial \Pi^i_\alpha(k,t)}{\partial k_\alpha} = \sum \gamma_{ij} w_j(k,t), \tag{6.132}$$

where the transformation coefficients represent a 3×3 matrix (Vainshtein et al. 1993) such as $\gamma_{TT} > 0$, while $\gamma_{SS},\ \gamma_{WW} < 0$. Therefore, only the transverse (vortex or Alfvén) mode is directly enhanced by the shock fronts, while the longitudinal (sound or magnetosound) and entropy modes both decay at the fronts. Then, $\gamma_{ST},\ \gamma_{WT} > 0$, which implies that the transverse mode converts partly to the sound and entropy modes and so supplies their energy densities. Eventually, the set of coupled equations for the corresponding energy densities receives the form

$$\frac{\partial T(k,t)}{\partial t} + \frac{\partial \Pi^T(k,t)}{\partial k} = (\gamma_{TT} + \gamma_{ST} - \gamma_{dT})T(k,t) - \gamma_{ST}T(k,t) + \gamma_{TS}S(k,t), \tag{6.133a}$$

$$\frac{\partial S(k,t)}{\partial t} + \frac{\partial \Pi^S(k,t)}{\partial k} = (\gamma_{SS} - \gamma_{dS})S(k,t) + \gamma_{ST}T(k,t), \tag{6.133b}$$

$$\frac{\partial W(k,t)}{\partial t} = (\gamma_{WW} - \gamma_{dW})W(k,t) + \gamma_{WT}T(k,t) + \gamma_{WS}S(k,t), \tag{6.133c}$$

where only the most essential terms are retained; the terms containing γ_{dw} describe the standard dissipative damping of the waves. The nonlinear spectral

fluxes of the transverse and longitudinal modes are assumed isotropic and can be estimated as

$$\Pi^T(k,t) \approx \frac{k^{5/2}T^{3/2}(k,t)}{\rho^{1/2}}, \qquad \Pi^S(k,t) \approx c_s k \frac{k^2 S^2(k,t)}{k_{0S} S_0}, \tag{6.134}$$

where c_s is the sound speed, while the corresponding term can safely be discarded for the entropy mode (Vainshtein et al. 1993). The transformation coefficients can be estimated as

$$\gamma_{TT} \sim \frac{2\pi}{3}\frac{R_0^3 P}{(\mu_* - 1)^2}, \qquad \gamma_{ST} \sim c_s k_0, \tag{6.135}$$

where R_0 is the largest radius of available spherical shock waves, P is the rate of shock wave generation, μ_* is the Mach number of the weakest shock wave, $(\mu_* - 1) \gtrsim (1-3)\times 10^{-2}$, and $k_0 \sim 2\pi/L_{\max}$ with $L_{\max}$ being the main scale of the turbulence which is about the mean distance between the fronts.

It is worthwhile to note that the total energy density of the modes included in Eq. (6.133) is not conserved: it is supplied by the shock wave ensemble energy density implying that the shock wave ensemble decays while amplifying the turbulent modes. Accordingly, the amplification of the vortex mode at the fronts and its conversion to the sound mode there play a role of the turbulence source, which energy is then transferred along the spectrum to smaller scales due to the nonlinear spectral fluxes; eventually, the stationary spectra of these modes, neglecting the dissipation, receive the form

$$T(k) = \frac{\gamma_{TT}^2 \rho}{4k_0^3}\left[1 - \left(\frac{k_0}{k}\right)^{2/3}\right]^2 \left(\frac{k_0}{k}\right)^{5/3}, \quad k_0 \le k < k_d, \tag{6.136a}$$

$$S(k) = S_0\left(\frac{k_{0S}}{k}\right)^{3/2}, \quad S_0 \simeq \frac{\gamma_{ST}}{c_s k_0}\frac{\gamma_{TT}^2\rho}{(27)^{3/2}k_0^3}, \quad k_{0S} \simeq 4k_0/3 \le k < k_d, \tag{6.136b}$$

$$W(k) = -\frac{\gamma_{WT}}{\gamma_{WW}}T(k) - \frac{\gamma_{WS}}{\gamma_{WW}}S(k), \tag{6.136c}$$

where $|\gamma_{WT}/\gamma_{WW}| \ll 1$, $|\gamma_{WS}/\gamma_{WW}| \ll 1$, so the entropy mode produced by the linear mode conversion at the shock fronts makes a minor contribution to the turbulence spectra. In fact, the entropy mode, e.g., in the form of dense clouds, is produced by other mechanisms including the thermal instability considered in Sect. 6.5.

Thus, the resulting turbulence spectral index is not necessarily constant along the spectrum: since the large-scale spectrum related to the shock fronts is rather sharp, $\propto k^{-2}$, the smaller-scale part of the spectrum is dominated by smooth MHD perturbation resulting in a flatter spectra [Eq. (6.136)]; for more detail see Chap. 10 in (Vainshtein et al. 1993). In contrast, if no

discontinuity ensemble is present, the mode conversion occurs at the spatial gradients formed by the turbulence spatial inhomogeneity itself. Apparently, in the lowest order of the perturbation theory one expects the corresponding "cross-terms" to have a form $\gamma_{TS}S(k,t) = -\gamma_{ST}T(k,t) = \alpha S(k,t)T(k,t)$ for conversion processes with small variation of the wave number, where α is a nonlinear interaction constant, which is typically small compared with unity, $\alpha \sim (0.01 - 0.1)\omega/(nk_BT)$ (cf. Sect. 4.3.2).

6.10.2 About Interstellar Medium Turbulence

MHD turbulence represents currently an exceptionally broad interdisciplinary field of science—in the physics and chemistry laboratories, geophysics, and astrophysics. For example, origin of the turbulence in the Galaxy and in galactic objects and study of its statistical measures are of primary importance for many specific issues: for generation and transport of magnetic fields, production and propagation of high-energy particles (*cosmic rays*), emission of nonthermal electromagnetic radiation throughout the entire electromagnetic spectrum from radio waves to gamma rays, plasma mixing in the interstellar medium and transport of chemical elements synthesized inside young massive stars and deposited to the Galaxy by supernova explosions, and many more important phenomena.

Currently, there is ample observational evidence in favor of presence of the turbulence in various phases of the interstellar medium at various scales, at least between 10^8 cm and 10^{20} cm. Given this huge range of scales, the observational means with which to study the turbulence vary with the subrange of scales analyzed. For example, dispersion of gas velocities in molecular clouds favors the turbulence with a power-law spectrum with index around the Kolmogorov–Obukhov value at scales of the order of dozens of parsecs. In contrast, fluctuations of thermal electron density at relatively small scales, $\lambda \approx 10^8$ cm and above, are measured from radio scintillations, since the fluctuations of thermal electron number density and magnetic field affect dispersion of electromagnetic waves and propagation of radiation giving rise to scintillation of compact sources such as pulsars and quasars.

Strong indirect evidence in favor of turbulence with intermediate scales comes from data on energetic particles—cosmic rays. The point is that their distribution function at energies $\mathcal{E} \lesssim 10^6$ GeV has a very weak anisotropy, with the relative value $\sim 10^{-3}$. A currently adopted (and indeed the most plausible) interpretation for this small anisotropy is due to angular scattering of the particles by resonant magnetic inhomogeneities—waves with the length of the order of particle's Larmour radius $r_g = \mathcal{E}/eB$, which, given the Galactic magnetic field strength $B \sim 3 \times 10^{-6}$ G, corresponds to the scales $\lambda \lesssim 1$ pc.

Globally, the data are consistent with a single power-law spectrum of galactic turbulence with the energy density $\mathrm{d}E/\mathrm{d}k \sim k^{-\nu}$ in an exceptionally broad range of spatial scales, $10^{20} > \lambda > 10^8$ cm, with $1.4 \leq \nu \leq 1.8$ ("Big Power Law"). On the other hand, observations point to a remarkable spatial

nonuniformity of the turbulence distribution in the Galaxy. This nonuniformity is provided by both inhomogeneous distribution of the main sources of energy and differences of excitation, dispersion, and dissipation of the MHD perturbations in different phases of interstellar medium.

Turbulent fluctuations of macroscopic parameters affect substantially the astrophysical plasmas. This includes formation of stars, ISM structure, disk–halo connection, etc. In particular, the turbulence spectrum shape affects greatly the acceleration of nonthermal particles in the Galaxy. Modern data confirm a long-living hypothesis that the cosmic rays are accelerated by the galactic supernova remnants (see Sect. 12.1 for more detail). Remarkably, an efficient, consistent with observations, particle acceleration at the SNR shocks is only possible if a turbulence with a very flat and broad spectrum is created, perhaps much flatter than most of the spectra considered above (and much flatter than the observed averaged turbulence spectrum in the Galaxy). Overall, the modern cosmic electrodynamics is largely the physics of highly turbulent plasma, which is illustrated by numerous examples throughout the book.

6.11 Turbulent Magnetic Diffusivity

To illustrate importance of turbulence effect on astrophysical plasma properties, let us calculate an effective magnetic diffusivity of a turbulent fluid. We consider an incompressible fluid and adopt some given collisional diffusivity $\nu_m = c^2/4\pi\sigma$ and correlation tensor of the turbulent velocity:

$$\widetilde{U}_{\alpha\beta}(\boldsymbol{k}) = A(k)\left(\delta_{\alpha\beta} - \frac{k_\alpha k_\beta}{k^2}\right). \tag{6.137}$$

Let us define an exact (fluctuating) magnetic field as $\mathcal{H}$, whose averaged value is $\langle\mathcal{H}\rangle = \boldsymbol{B}$ and use exact MHD equations (2.16):

$$\nabla\cdot\mathcal{H} = 0, \quad \frac{\partial\mathcal{H}}{\partial t} = \nabla\times[\boldsymbol{u}\times\mathcal{H}] + \nu_m\Delta\mathcal{H}. \tag{6.138}$$

Since statistical averaging over ensemble is commutative with differentiation over coordinates and time, the averaged equations take the form

$$\nabla\cdot\boldsymbol{B} = 0, \quad \frac{\partial\boldsymbol{B}}{\partial t} = \nabla\times\langle\boldsymbol{u}\times\mathcal{H}\rangle + \nu_m\Delta\boldsymbol{B}. \tag{6.139}$$

To close the system the combination $\langle\boldsymbol{u}\times\mathcal{H}\rangle$ must be expressed via averaged values—mean magnetic field B and correlation tensor of the turbulent velocities. To do so we explicitly introduce a fluctuating (turbulent) component of the magnetic field, $\boldsymbol{b}(\boldsymbol{r},t) = \mathcal{H}(\boldsymbol{r},t) - \boldsymbol{B}(\boldsymbol{r},t)$, and use Eqs. (6.138) and (6.139) to derive equation describing this component:

$$\frac{\partial \boldsymbol{b}}{\partial t} - \nu_m \Delta \boldsymbol{b} = \nabla \times [\boldsymbol{u} \times \boldsymbol{B}] + \nabla \times [\boldsymbol{u} \times \boldsymbol{b}] - \nabla \times \langle \boldsymbol{u} \times \boldsymbol{b} \rangle, \tag{6.140}$$

where condition $\langle \boldsymbol{u} \rangle = 0$ has been applied.

This equation is nonlinear and is difficult to solve in a general case. To find a model solution of Eq. (6.140) one has to make an assumption about the difference between the true and averaged second-order terms, $\nabla \times [\boldsymbol{u} \times \boldsymbol{b}] - \nabla \times \langle \boldsymbol{u} \times \boldsymbol{b} \rangle$, which generally requires knowledge about higher-order correlation tensors than the second-order one we adopt to be known. Thus, as a simplest approximation, we adopt that even both of the second-order terms can be large, the difference between them is small and can be discarded from the equation. We emphasize that this approximation (quasi-linear approach developed in Sect. 4.2) is a more precise one than standard (naive) theory of perturbations, which assumes that any second-order form, composed of the small first-order values $\boldsymbol{u}$ and $\boldsymbol{b}$, is small by itself. Now, Eq. (6.140) is a linear equation and so can be solved by the Green function method:

$$\begin{aligned} \boldsymbol{b}(\boldsymbol{r}, t) = & \int_{-\infty}^{t} G(\boldsymbol{r} - \boldsymbol{r}', t - \tau)(\boldsymbol{B} \cdot \nabla)\boldsymbol{u}(\boldsymbol{r}', \tau) \mathrm{d}^3 x' \mathrm{d}\tau \\ & - \int_{-\infty}^{t} G(\boldsymbol{r} - \boldsymbol{r}', t - \tau) \frac{\partial \boldsymbol{B}}{\partial x'_\beta} u_\beta(\boldsymbol{r}', \tau) \mathrm{d}^3 x' \mathrm{d}\tau, \end{aligned} \tag{6.141}$$

where G is the Green function, whose explicit form is specified by Eq. (6.147). Effective regions of integration over coordinates and time here are evidently of the order of corresponding correlation scale and time, l and τ_c, of the given turbulent velocity field. The magnetic field $\boldsymbol{B}(\boldsymbol{r}, t)$ averaged over the turbulent pulsations is, by definition, a smoothly varying function at these scales and times. Therefore, factors containing the slowly varying vector $\boldsymbol{B}$ can be taken out from the integrals:

$$\begin{aligned} \boldsymbol{b}(\boldsymbol{r}, t) = & B_\beta \int_{-\infty}^{t} G(\boldsymbol{r} - \boldsymbol{r}', t - \tau) \frac{\partial \boldsymbol{u}}{\partial x'_\beta} \mathrm{d}^3 x' \mathrm{d}\tau \\ & - \frac{\partial \boldsymbol{B}}{\partial x_\beta} \int_{-\infty}^{t} G(\boldsymbol{r} - \boldsymbol{r}', t - \tau) u_\beta(\boldsymbol{r}', \tau) \mathrm{d}^3 x' \mathrm{d}\tau. \end{aligned} \tag{6.142}$$

Now, we can multiply this equation by a component of the turbulent velocity and then average it:

$$\begin{aligned} \langle u_\alpha b_\mu \rangle = & B_\beta \int_{-\infty}^{t} G(\boldsymbol{r} - \boldsymbol{r}', t - \tau) \langle u_\alpha(\boldsymbol{r}, t) \frac{\partial u_\mu(\boldsymbol{r}', \tau)}{\partial x'_\beta} \rangle \mathrm{d}^3 x' \mathrm{d}\tau \\ & - \frac{\partial B_\mu}{\partial x_\beta} \int_{-\infty}^{t} G(\boldsymbol{r} - \boldsymbol{r}', t - \tau) \langle u_\alpha(\boldsymbol{r}, t) u_\beta(\boldsymbol{r}', \tau) \rangle \mathrm{d}^3 x' \mathrm{d}\tau. \end{aligned} \tag{6.143}$$

The first integral represents a polar third-rank tensor, which does not depend on coordinates. For statistically uniform and isotropic turbulence [like that described by correlation tensor (6.137)] it is equivalent to zero, because there is no intrinsic tensor with required symmetry in such a fluid; antisymmetric pseudotensor $e_{\alpha\beta\gamma}$ could only be used for a gyrotropic turbulence, which is beyond the case under consideration, which will be thoroughly considered in Chap. 8. The second integral is a symmetric second-rank tensor, so it can be represented in the form

$$\int_{-\infty}^{t} G(\boldsymbol{r}-\boldsymbol{r}', t-\tau)\langle u_\alpha(\boldsymbol{r}, t)u_\beta(\boldsymbol{r}', \tau)\rangle \mathrm{d}^3x'\mathrm{d}\tau = \nu_t\delta_{\alpha\beta}, \tag{6.144}$$

where ν_t is a scalar, which can straightforwardly be calculated for a given correlation tensor $\langle u_\alpha(\boldsymbol{r}, t)u_\beta(\boldsymbol{r}', \tau)\rangle$; finally we obtain:

$$\langle \boldsymbol{u}(\boldsymbol{r}, t) \times \boldsymbol{b}(\boldsymbol{r}, t)\rangle = -\nu_t \nabla \times \boldsymbol{B}. \tag{6.145}$$

Substitution of Eq. (6.145) into the second of Eq. (6.139) yields closed averaged equation for the mean magnetic field:

$$\frac{\partial \boldsymbol{B}}{\partial t} = (\nu_t + \nu_m)\Delta \boldsymbol{B}, \tag{6.146}$$

where ν_t is the *turbulent magnetic diffusivity*. The derived equation has the same form as the standard equation for magnetic field in a dissipative fluid at rest. However, the presence of the turbulent motions enhances the magnetic diffusivity compared with the standard case: full magnetic diffusivity consists now from two contributions $\nu_{\mathrm{tot}} = \nu_m + \nu_t$, the standard (collisional) diffusivity ν_m and the turbulent diffusivity ν_t, which depends on ν_m via the Green function.

The microphysics of these diffusivity increase is easy to understand. Indeed, the dissipation is described by a second-order derivative $\Delta \boldsymbol{B}$; the stronger the spatial variations of B the larger the derivative and so the stronger the dissipation; thus the dissipation is the most efficient for the smallest-scale magnetic field. In our case, the turbulent motions reshape the magnetic field lines, breaking down the magnetic field onto smaller-scale regions of the order of the turbulence scales, so the magnetic field becomes a smaller-scale one. The small-scale field as explained experiences more efficient Joule dissipation, and so the small-scale magnetic energy transforms to the thermal energy faster than without the turbulent motions.

Let us now estimate the turbulent diffusivity in some simple cases. We use the Green function of a three-dimensional isotropic diffusion equation, which contains the collisional diffusivity ν_m:

$$G(\boldsymbol{r}-\boldsymbol{r}', t-\tau) = \frac{1}{[4\pi\nu_m(t-\tau)]^{3/2}} \exp\left\{-\frac{(\boldsymbol{r}-\boldsymbol{r}')^2}{4\nu_m(t-\tau)}\right\}. \tag{6.147}$$

We adopt the turbulence correlation scale l and correlation time $\tau_c \approx l/u$, where we denote $u \equiv \langle \boldsymbol{u}^2 \rangle^{1/2}$ for brevity. Thus, in integral (6.144) the characteristic scale of integration is $|\boldsymbol{r} - \boldsymbol{r}'| \approx l$, while the characteristic time of integration is $t - \tau \approx \tau_c \approx l/u$. As we will see the estimate of the turbulent diffusivity differs depending on how large or small the magnetic Reynolds number is.

1. The first case, $\nu_m \tau_c \gg l^2$, or $R_m = ul/\nu_m \ll 1$, is the case of small magnetic Reynolds number R_m. Here the exponential factor in the Green function is about unity; thus, integral (6.144) can be estimated as the integrand multiplied by effective interval of integration, which yields

$$\nu_t \approx \frac{u^2}{3} \frac{1}{[4\pi\nu_m\tau_c]^{3/2}} l^3 \tau_c = \frac{1}{3} ul \left(\frac{ul}{4\pi\nu_m} \right)^{3/2}. \tag{6.148}$$

   We see that $\nu_t/\nu_m < R_m^{5/2} \ll 1$ and the turbulent diffusivity constitutes only a small correction to the collisional magnetic diffusivity. This means that the turbulent diffusivity can be calculated within the perturbation theory in case of small magnetic Reynolds numbers.

2. The second case, $\nu_m \tau_c \ll l^2$, or $R_m \gg 1$, is the opposite to the first case. The Green function is very narrow in this case and so can be replaced by a δ-function in the r-space, $G(\boldsymbol{r} - \boldsymbol{r}', t - \tau) \approx \delta(\boldsymbol{r} - \boldsymbol{r}')$. Then, Eq. (6.144) immediately yields

$$\nu_t \approx \frac{1}{3} \langle \boldsymbol{u}^2 \rangle \tau_c. \tag{6.149}$$

   It is remarkable that now $\nu_t \gg \nu_m$ and so the formal perturbation theory is inapplicable. Nevertheless, as we argued, the approximation used is more precise than the standard perturbation theory and estimate (6.149) is often correct; we will widely use it in our analysis, although we will also consider more sophisticated approximations when this one turns out to be an oversimplification of the reality (see, e.g., Chap. 8). Furthermore, the analysis performed shows that non-helical turbulence as that described by symmetric tensor (6.137) cannot generate a large-scale magnetic field but only enhances its dissipation. As will be demonstrated later (Chap. 8) this conclusion is no longer valid for a helical (gyrotropic) turbulence, which does generate the large-scale magnetic field under certain conditions.

Problems

6.1 Calculate the critical temperature difference $\Delta T = T_1 - T_2$ in terms of layer thickness for water and air under the standard Earth's conditions.

Find the layer thickness for which the critical temperature difference is 1 K. Kinetic coefficients for air and water are $\nu_a = 0.15\,\mathrm{cm}^2/\mathrm{s}$, $\nu_w = 0.01\,\mathrm{cm}^2/\mathrm{s}$, $Pr_a = 0.733$, and $Pr_w = 6.75$. Values of thermal expansion coefficient α are given in Sect. 6.2.1.

6.2 Describe the dispersion equation for convective instability accounting the magnetic field. Investigate the dispersion dependencies by numerical methods. Calculate the dependence of the minimal Rayleigh number from the magnetic field. Use parameters of the solar photosphere.

6.3 Fulfill calculations and obtain the dispersion dependence (6.52) for contact discontinuity with the tangential magnetic field.

6.4 The planar contact discontinuity separates vacuum and conductive incompressible fluid with the mass density ρ and the surface tension coefficient α. The acceleration due to gravity force $\boldsymbol{g}$ and electric field $\boldsymbol{E}$ are directed along the normal to the discontinuity plane. Find value E, which leads to instability of discontinuity relative to small perturbations (Toncs effect). Find wave numbers of unstable modes.

Hint: Use the energy principle: compare energies of perturbed and unperturbed systems and find the conditions of minimal energy for the distorted interface.

6.5 Magneto-Rotational Instability, MRI. Consider a (accretion) disk composed of conducting plasma permitted by a magnetic field rotating around a gravity center (e.g., a star or a black hole). Find condition for the rotation to be stable.

6.6 (a) Prove that the Kolmogorov turbulence spectrum $W(k)$ can be derived from a model nonlinear equation describing energy transfer along the spectrum, using phenomenological continuity equation with a source

$$\frac{\partial W}{\partial t} + \frac{\partial \Pi}{\partial k} = \varepsilon \delta(k - k_0)$$

and with a nonlinear energy flux density along the spectrum $\Pi(k) = C^{-3/2} k^{5/2} W^{3/2}(k)$, where C is the Kolmogorov's constant (Kovasznay 1948). Obtain solution of this equation for a stationary case, using boundary condition $W(k) = 0$ for $k < k_0$. Make sure that $\Pi(k) = \varepsilon = \mathrm{const}$ at $k > k_0$. (b) Note that in fact the nonlinear energy flux density represents a vector Π_α in the k-space and its divergence $\partial \Pi_\alpha / \partial k_\alpha$ must enter Eq. (6.132) instead of $\partial \Pi / \partial k$. In the isotropic case the divergence has the form $(1/k^2)\partial(k^2 \widetilde{\Pi})/\partial k$. Find the functional form of $\widetilde{\Pi}$ yielding the correct Kolmogorov spectrum; analyze what is the difference between these two solutions.

6.7 Using model equation from the previous problem and adopting the nonlinear spectral fluxes for the fast and slow magnetosonic waves in the form $\Pi_f(k) = A_f k^3 W_f^2(k)$ and $\Pi_s(k) = A_s k^4 W_s^3(k)$, respectively, where A_f and A_s are some constants, obtain stationary spectra for these modes. Make sure that $\Pi(k) = \varepsilon = \text{const}$ at $k > k_0$. Consider various relations between A_f and A_s and plot the spectra of the composite turbulence composed of slow and fast magnetosonic waves.

6.8 Critically balanced turbulence considered in Sect. 6.9.3 is anisotropic; thus, the nonlinear spectral fluxes along $k_\parallel$ and $k_\perp$ are different from each other. Consider the divergence in cylindrical coordinates, $(1/k_\perp)\partial(k_\perp \Pi_\perp)/\partial k_\perp + \partial \Pi_\parallel / \partial k_\parallel$, and determine the spectral fluxes needed to obtain the turbulence spectrum described by Eq. (6.117). Is this combination of the spectral fluxes unique? Prove that the relation $\Pi_\parallel = (2k_\parallel/3k_\perp)\Pi_\perp$ holds.

6.9 In accordance with the result of Sect. 6.11 the turbulence of a conductive fluid increases the magnetic diffusivity, $\nu_{\text{tot}} = \nu_m + \nu_t$. This means the change of effective medium kinetic coefficients. If a motionless fluid has the electric conductivity σ and the magnetic permeability $\mu = 1$, the corresponding turbulent fluid has different values for these coefficients: σ_{eff} and $\mu_{\text{eff}} \neq 1$. Find the values of σ_{eff} and $\mu_{\text{eff}} \neq 1$ in terms of σ, ν_m, and ν_t.

Hint: Use Maxwell's equations in quasistationary approximation and boundary conditions for tangential components $\boldsymbol{E}$ and $\boldsymbol{B}$ at the boundary between motionless and turbulent media.

Answers and Solutions

6.1 $h_{\text{air}} \approx 4.9\,\text{cm}$; $h_w \approx 0.5\,\text{cm}$.

6.4 Adopt the disturbed discontinuity interface in the form

$$z = \zeta(x, y) = l \sin k_1 x \sin k_2 y, \qquad l \ll 2\pi/k_1,\ 2\pi/k_2. \tag{1}$$

The gravitation energy of a small mass element $\mathrm{d}m = \rho \mathrm{d}x\mathrm{d}y\mathrm{d}z$ is $gz\mathrm{d}m$. Integrate it over $\mathrm{d}z$ from 0 to ζ and then over the entire discontinuity surface S; we find variation ΔU_g of the gravitation energy produced by the discontinuity distortion. When integrating over the undisturbed surface of the discontinuity we adopt that the wavelengths of the perturbations $\lambda_{1,2} = 2\pi/k_{1,2}$ are small compared with its linear scales and replace all terms like $\sin^2 \alpha$ by their means, 1/2. This yields $\Delta U_g = \rho g l^2 S/8$.

Variation of the surface energy is determined by $\Delta U_s = \alpha \Delta S$, where ΔS is the surface variation:

$$\Delta S = \int \left\{ \sqrt{1 + \left(\frac{\partial \zeta}{\partial x}\right)^2 + \left(\frac{\partial \zeta}{\partial y}\right)^2} - 1 \right\} \mathrm{d}x\mathrm{d}y \approx \frac{l^2 k^2 S}{8}. \tag{2}$$

Thus, we have $\Delta U_s = \alpha l^2 k^2 S/8$, where $k^2 = k_1^2 + k_2^2$.

The variation of electrostatic energy can apparently be calculated as

$$\Delta U_e = \int \mathrm{d}x\mathrm{d}y \int_{\zeta}^{\infty} \mathrm{d}z \frac{\mathcal{E}^2 - E^2}{8\pi}, \tag{3}$$

where $\mathcal{E}$ is the electrostatic field above the distorted surface. The electrostatic potential φ satisfies to the Laplace equation and the boundary condition at a conductive surface $\varphi|_{z=\zeta} = 0$, as well as condition $\varphi|_{z\to\infty} = -Ez$ far away from the surface. For $kl \ll 1$ the equation and the boundary conditions are fulfilled for the potential $\varphi(x, y, z) = -Ez + E\zeta(x, y) \exp(-kz)$, which yields the electric field above the distorted surface $\boldsymbol{\mathcal{E}} = -\nabla\varphi$; then the energy variation reads $\Delta U_e = -E^2 l^2 S/32\pi\, k$.

The full energy variation is

$$\Delta U = \Delta U_e + \Delta U_s + \Delta U_g = \frac{l^2 S}{8} \left\{ \rho g + \alpha k^2 - \frac{E^2}{4\pi} k \right\}. \tag{4}$$

Apparently, the surface is unstable (i.e., the amplitude of the wave increases) if the wave growth gives rise to decrease of the full energy of the system, i.e., $\Delta U < 0$. The demarcation magnitude of the electric field is defined by

$$\frac{E^2}{4\pi} = \frac{\rho g}{k} + \alpha k. \tag{5}$$

Minimizing the rhs over k, we find $k_c = \sqrt{\rho g/\alpha}$ and, thus, obtain the minimum electric field value, $E_c^2 = 8\pi\sqrt{\rho g \alpha}$, for which the condition $\Delta U = 0$ is satisfied. For $E > E_c$, there is a wave number region in which the instability condition $\Delta U < 0$ is fulfilled, namely $k_1 < k < k_2$, where $k_{1,2} = E^2/8\pi\alpha \mp \sqrt{(E^2/8\pi\alpha)^2 - k_c^2}$.

6.5 Consider two fluid elements (1 and 2) located at different radial distances r_1 and $r_2 > r_1$ from the star and linked by a magnetic flux tube. Adopt that the first one rotates faster (as is the case for a Keplerian disk). Then, the magnetic flux tube will be stretched in such a way to slow down the first fluid element and accelerate the second one. Thus, the first element loses the angular momentum and pushed toward the star, while the second element increases the angular momentum and pushed away from

the star, which will act to further separate the fluid elements and enhance the magnetic tension. According to this consideration the stability condition is

$$\frac{\partial \Omega^2(r)}{\partial r} > 0,$$

where $\Omega(r)$ is the angular velocity distribution in the disk. The MRI instability plays an important role in astrophysics (Balbus and Hawley 1991; Balbus 2003; Mikhailovskii et al. 2009; Lominadze 2011), in particular, in the angular momentum transfer out from the accretion disk.

6.6 (a) $W(k) = C\varepsilon^{2/3}k^{-5/3}\Theta(k - k_0)$, where Θ is the step function. (b) $\widetilde{\Pi}(k) \propto k^{1/2}W^{3/2}(k)$.

6.7 $W_f(k) \propto k^{-3/2}$, $W_s(k) \propto k^{-4/3}$.

6.8 For example, $\Pi_\perp = Ak_\perp^{3/2}W^{3/2}(k_\parallel, k_\perp)/k_\parallel$, $\Pi_\parallel = (2A/3)k_\perp^{1/2}W^{3/2}(k_\parallel, k_\perp)$, where A is a constant.

6.9 Quasistationary electromagnetic field in motionless conductor with the magnetic ($\mu \neq 1$) properties is described by the Maxwell equations:

$$\nabla \times \boldsymbol{E} = -\frac{1}{c}\frac{\partial \boldsymbol{B}}{\partial t}, \quad \nabla \times \boldsymbol{H} = -\frac{4\pi}{c}\sigma \boldsymbol{E}, \quad \nabla \times \boldsymbol{B} = 0, \quad \boldsymbol{B} = \mu \boldsymbol{H}. \tag{1}$$

On the boundary separating two conductors, or a conductor and a dielectric, the field components must satisfy the boundary conditions

$$B_{1n} = B_{2n}, \quad \boldsymbol{H}_{1\tau} = \boldsymbol{H}_{2\tau}, \quad \boldsymbol{E}_{1\tau} = \boldsymbol{E}_{2\tau}. \tag{2}$$

From Eq. (1) in the case of a homogeneous medium we find

$$\Delta \boldsymbol{B} = \frac{4\pi\mu\sigma}{c^2}\frac{\partial \boldsymbol{B}}{\partial t}. \tag{3}$$

In the turbulent medium after the averaging of electromagnetic field over the turbulent ensemble we find Eq. (6.146):

$$\frac{\partial \boldsymbol{B}}{\partial t} = (\nu_m + \nu_t)\Delta \boldsymbol{B}, \quad \nu_m = \frac{c^2}{4\pi\sigma}. \tag{4}$$

We describe it in form (3) and substitute $\mu \to \mu_{\text{eff}}$ and $\sigma \to \sigma_{\text{eff}}$. This leads to the relation

$$\mu_{\text{eff}}\sigma_{\text{eff}} = \frac{\sigma}{1 + \nu_t/\nu_m}. \tag{5}$$

In order to determine μ_{eff} and σ_{eff} separately, we consider the boundary $z = a$ between non-turbulent motionless plasma in the layer $0 \le z \le a$ ($\mu = 1,\ \sigma$) and turbulent plasma in region $z > a$ ($\mu_{\text{eff}},\ \sigma_{\text{eff}}$). At the boundary $z = 0$ we assume an oscillating magnetic field $\boldsymbol{H}(t) = \boldsymbol{H}_0 e^{-i\omega t}$ with $\omega =$ const. The value a is large compared with the thickness of the skin layer $\delta = c/\sqrt{2\pi\mu\sigma\omega}$. In this approximation the magnetic fields have the following amplitudes:

$$H_1(z) = H_0 e^{-(1-i)z/\delta_1},\ z < a,\ \delta_1 = \frac{c}{\sqrt{2\pi\sigma\omega}},$$

$$H_2(z) = H_1(a) e^{-(1-i)(z-a)/\delta_2},\ z > a, \delta_2 = \frac{c}{\sqrt{2\pi\mu_{\text{eff}}\sigma_{\text{eff}}\omega}}. \tag{6}$$

The condition $H_1(a) = H_2(a)$ is fulfilled; the condition $E_1(a) = E_2(a)$ leads to algebraic equation

$$\frac{c}{4\pi\sigma} \left.\frac{\mathrm{d}H_1}{\mathrm{d}z}\right|_{z=a} = \frac{c}{4\pi\sigma_{\text{eff}}} \left.\frac{\mathrm{d}H_2}{\mathrm{d}z}\right|_{z=a}, \tag{7}$$

from which we find $\mu_{\text{eff}} = \sigma_{\text{eff}}/\sigma$. Using Eq. (5), we obtain

$$\mu_{\text{eff}} = \frac{1}{\sqrt{1 + \nu_t/\nu_m}}, \qquad \sigma_{\text{eff}} = \frac{\sigma}{\sqrt{1 + \nu_t/\nu_m}}. \tag{8}$$

Therefore, the turbulence strongly decreases the effective values μ_{eff} and σ_{eff} if $\nu_t \gg \nu_m$. Turbulent region has $\mu_{\text{eff}} < 1$ and so it possesses the diamagnetic properties: an external magnetic field is weaker in turbulent region.

Chapter 7

Particle Transport in Turbulent Cosmic Media

Transport of particles, either charged or neutral, either micro- or macroscopic, plays a fundamental role for many phenomena in astrophysics including distribution of heavy elements released by supernova explosions, dust particle distribution and evolution, propagation of energetic particles away from their sources, and many more. The particles under study can either be dynamically important for the entire system or play a passive role. In the latter case they form a "passive admixture," whose behavior can often be described in a "test particle" approximation.

The passive particle population can be composed either from particles different from the main plasma component (e.g., He ions in the electron–proton plasma) or the same kind (i.e., electrons and protons) if they compose a distinct group of particles away from equilibrium with the main plasma. Examples of such groups include fast electrons in Maxwellian plasma or a quasi-neutral plasma "cloud" (density concentration or rarefaction) embedded in a more uniform background plasma. Below we consider various effects related to particle transport in cosmic plasma.

7.1 Free-Streaming Particle Transport

Let us consider a question of how a test particle with a given charge, mass, and velocity propagates through a source with a linear scale L and volume $V \sim L^3$. As we will see below the answer depends essentially on the amount and sort of the test particles participating in the motion and on the background source properties. Apparently, the simplest case of the particle transport is a free streaming, when no external force affects the particle motion noticeably.

G.D. Fleishman and I.N. Toptygin, *Cosmic Electrodynamics*, Astrophysics and Space Science Library 388, DOI 10.1007/978-1-4614-5782-4_7,

7.1.1 Time of Flight

When a particle with a velocity $\boldsymbol{v}$ propagates freely through a volume with linear scale L, the time needed for the particle to cross the entire source is called the **time of flight**, $\tau_{\rm tof}$, which is apparently equal to

$$\tau_{\rm tof} = L/v. \tag{7.1}$$

In astrophysical observations we often deal with time-interval measurements; in these cases a time-of-flight distance can be introduced corresponding to the measured time as $L_{\rm tof} = v\tau$. This simple time of flight estimate is often helpful as it gives an idea of a minimum time needed for the particle to cross the source, i.e., the shortest possible escape time from (or residence time in) the source; any transport regimes imply a time longer than L/c.

Moreover, even this simple transport regime can happen in astrophysical sources. As an example, we consider HXR emission from solar flares. In a standard flare scenario, the fast electrons are produced somewhere at an acceleration region (see Chap. 11) in the corona, then propagate down to an emission site along the coronal magnetic field lines, and die in the dense chromospheric plasma producing HXR emission via Bremsstrahlung (see Chap. 9). A HXR light curve consists typically from a gradual component and fast time structure (multiple short peaks) superimposed on it; this latter fine structure could be produced by individual electron beams freely streaming from the acceleration region down to the emission site. If so, the higher-energy electrons arrive first, while lower-energy electrons will be progressively delayed relative to the higher-energy ones. Since HXR emission is produced by a non- or weakly relativistic electrons, the electron arrival delay will be translated to the energy-dependent delay of different HXR channels roughly proportional to the square root of energy E; one can see that the time-of-flight model curves in Fig. 7.1 fit nicely the measurements implying the time-of-flight transport regime of the elementary electron beams in (some) solar flares.

7.1.2 Limiting Alfvén Current

The considered above free streaming involves macroscopically large number of electrons and so implies electric current associated with the electron flow. It turns out, however, that it is extremely difficult to support a noticeably strong electric current in either vacuum or plasma for a number of reasons. First, consider an electric current in a vacuum (or very tenuous plasma). According to Ampére's law, electric current I produces a magnetic field $B \sim I/(cR)$, where R is the typical transverse scale of the particle beam forming the current. This magnetic field, in its turn, will affect the motion of the beam particles attempting to turn them around via the magnetic Lorentz force. The characteristic scale of the corresponding particle motion is apparently

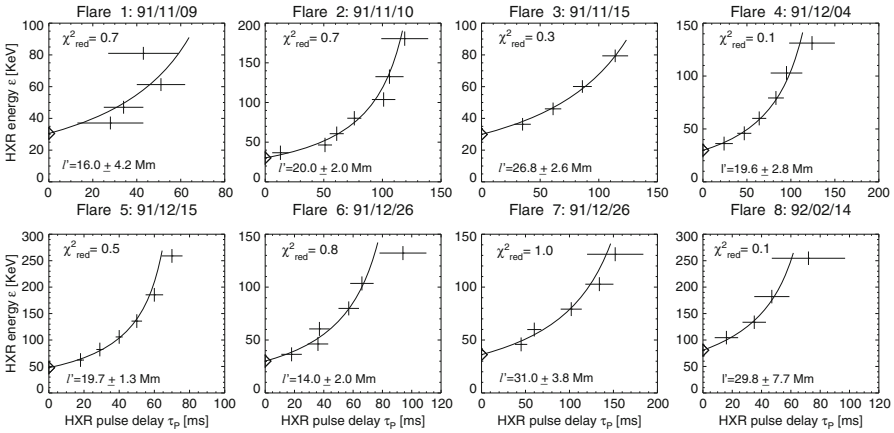

Figure 7.1: Examples of the time delays between temporal fine structures in various HXR energy channels (positive $t_d = L(1/v_0 - 1/v_i)$ means the signal at channel i arrives earlier than a reference signal in channel 0; the lowest-energy channel in this case) in a number of solar flares and fits with time-of-flight delays. The estimated time-of-flight distances and corresponding χ^2 are shown in each panel (Aschwanden 2005).

the Larmor radius in this self-generated magnetic field, $R_L = \beta\gamma(mc^2/eB)$. Obviously, the beam cannot freely propagate and will be stopped by the self-generated magnetic field at a distance equal or shorter than the beam width if $R_L \leq R$; thus, the equality, $R_L = R$ defines a **limiting Alfvén current**:

$$I_A = \beta\gamma \frac{mc^3}{e} = 5.1 \times 10^{13} \beta\gamma \text{ statA} = 17\beta\gamma \text{ kA}. \tag{7.2}$$

Note that the limiting Alfvén current is very low, many orders of magnitude lower than the implied HXR producing current in solar flares. To overcome this difficulty and allow a strong total current to propagate a large distance it must either split onto huge number of narrow current-carrying filaments (so that the current in each filament is below the Alfvén limit, but the neighboring filaments are sufficiently far away for their magnetic field to significantly decrease and have no effect on other filaments) due to filamentation instability (see Chap. 4) or drive a return current composed of the background plasma particles to significantly reduce the net current in the system. Apparently, there can be parameter regimes fully inconsistent with a streaming beam propagation; in these cases the original distribution function of the beam particles changes strongly, e.g., the isotropization of the charge particles occurs and results in diffusive regimes of their transport.

7.1.3 Return Currents

Let us now consider the mechanism and some consequences of the return current generation in response to the external beam current; for definiteness we are talking on an electron beam. Apparently, when an ensemble of moving external electrons enters a plasma volume, their charge attempts to produce an additional electric field, while their current to produce an additional magnetic field. For example, for a solar flare with volume $\sim 10^{28}\,\mathrm{cm}^3$ filled with the thermal plasma with $n_0 \sim 10^{10}\,\mathrm{cm}^{-3}$ and fast electron acceleration rate $F(> 10\,\mathrm{keV}) \sim 10^{36}$ electrons/s the implied charge separation is huge: all background electrons are being accelerated and evacuated down to the chromosphere over a couple of minutes (a very modest flare duration). This charge separation, if real, would mean a proportionally huge unrealistic electric field. The corresponding electric current would imply a strong magnetic field, up to $10^5\,\mathrm{G}$, which is 2–3 orders of magnitude larger than the original coronal magnetic field at the flare site. In the reality, however, nothing like this happens because the conducting plasma reacts almost instantly on the external beam in such a way to compensate both extra charge and current as fully as possible and so decrease generation of the fields as much as possible.

To explicitly separate the processes of the charge and current neutralization, respectively, it is convenient to represent each vector of the problem in the form $\boldsymbol{R} = \boldsymbol{R}_L + \boldsymbol{R}_T$, where $\boldsymbol{R}_L$ is a potential (irrotational), $\nabla \times \boldsymbol{R}_L = 0$, while $\boldsymbol{R}_T$ is a solenoidal, $\nabla \cdot \boldsymbol{R}_T = 0$, part of the vector $\boldsymbol{R}$; this expansion is always possible if both the source and circulation densities are zero at infinity (van den Oord 1990).

Specifically, the Maxwell equations, Eq. (1.53), take the form

$$\nabla \cdot \boldsymbol{E}_L = 4\pi e(n_i - n_b - n_e), \quad \nabla \times \boldsymbol{E}_L = 0, \tag{7.3a}$$

$$\nabla \cdot \boldsymbol{E}_T = 0, \quad \nabla \times \boldsymbol{E}_T = -\tfrac{1}{c}\tfrac{\partial \mathbf{B}_T}{\partial t}, \tag{7.3b}$$

$$\nabla \cdot \boldsymbol{B}_T = 0, \quad \nabla \times \boldsymbol{j}_T = -\nabla \times \boldsymbol{j}_{bT} + \tfrac{c}{4\pi}\left(-\Delta \boldsymbol{B}_T + \tfrac{1}{c^2}\tfrac{\partial^2 \mathbf{B}_T}{\partial t^2}\right). \tag{7.3c}$$

The equation for $\boldsymbol{j}_T$ is straightforwardly derived from Maxwell equation (1.53b) by applying operator $\nabla\times$ to it and regrouping the terms. Other conditions on the electric current density have apparently the form

$$\nabla \cdot \boldsymbol{j}_L = e\frac{\partial n_e}{\partial t}, \quad \nabla \times \boldsymbol{j}_L = 0, \quad \nabla \cdot \boldsymbol{j}_T = 0. \tag{7.4}$$

In addition, the current density satisfies generalized Ohm's law (see Sect. 1.3.4), which we derive here from the background electron equation of motion assuming the ions to be immobile:

$$\frac{\partial \boldsymbol{v}}{\partial t} + (\boldsymbol{v} \cdot \nabla)\boldsymbol{v} = -\frac{e}{m}\boldsymbol{E} - \frac{e}{mc}\boldsymbol{v} \times \boldsymbol{B} - \nu_{ei}\boldsymbol{v}, \tag{7.5}$$

which, being multiplied by $-en_e$, yields generalized Ohm's law in the form

$$\frac{\partial \boldsymbol{j}}{\partial t} + \boldsymbol{v}(\nabla \cdot \boldsymbol{j}) + (\boldsymbol{j} \cdot \nabla)\boldsymbol{v} = \frac{\omega_{\mathrm{pe}}^2}{4\pi}\boldsymbol{E} - \frac{e}{mc}\boldsymbol{j} \times \boldsymbol{B} - \nu_{ei}\boldsymbol{j}. \tag{7.6}$$

In the general nonlinear case the electrostatic (irrotational) and inductive (solenoidal) components are coupled; however, in a linearized problem, they are fully independent. Below we discuss the linear case, which is still very complicated and the corresponding manipulations are cumbersome. To further simplify generalized Ohm's law, we neglect the Hall term in the rhs (in addition to the nonlinear terms in the lhs), i.e.

$$\frac{\partial \boldsymbol{j}}{\partial t} = \frac{\omega_{\rm pe}^2}{4\pi}\boldsymbol{E} - \nu_{ei}\boldsymbol{j}. \tag{7.7}$$

Note that in a stationary case $\frac{\partial \boldsymbol{j}}{\partial t} \approx 0$, Eq. (7.7) yields standard Ohm's law, $\boldsymbol{j} = \sigma \boldsymbol{E}$ with $\sigma = \frac{\omega_{\rm pe}^2}{4\pi\nu_{ei}}$; apparently, this form of Ohm's law can only be used after a few collisional times since the beam has arrived.

Solution of the presented set of equations including Ohm's law described by Eq. (7.7) depends essentially on the properties of the fast electron beam. Consider a given 1D flow of electrons with a fixed number density and velocity in the direction of the axes z with some radial distribution. In this case the equations for the fields are convenient to replace by equations for the scalar and vector potentials and solve them in the cylindrical coordinate system (van den Oord 1990). The approximate solution (retaining, however, all essential physics) for $t > 0$, i.e., after the beam arrival, can be given in the form

$$n_e = n_i - n_b + n_b e^{-t/2\tau_{ei}} \cos\omega_{\rm pe} t, \tag{7.8a}$$

$$j_{net,z} = j_b \left[1 + e^{-t/2\tau_{ei}} \cos\omega_{\rm pe} t - e^{-t/\tau_d}\right], \tag{7.8b}$$

$$E_z = -\frac{4\pi}{\omega_{\rm pe}} j_b \left[e^{-t/2\tau_{ei}} \sin\omega_{\rm pe} t + \frac{\nu_{ei}}{\omega_{\rm pe}} e^{-t/\tau_d}\right], \tag{7.8c}$$

$$B_\phi = \frac{4\pi R}{c} j_b \left[1 - e^{-t/\tau_d}\right], \tag{7.8d}$$

where R is the transverse scale of the beam, $\tau_d = (4\pi\sigma/c^2)R^2$ is the typical time of the magnetic diffusion across the beam (cf. magnetic diffusivity introduced by Eq. (2.16), and $\tau_{ei} = 1/\nu_{ei}$. Using numerical values typical for solar coronal flux tubes, we find

$$\tau_d \approx 6.1 \times 10^{15} n_{e,10} R_9^2 \tau_{ei} \text{ s}, \tag{7.9}$$

where $n_{e,10} = n_e/(10^{10}\,\text{cm}^{-3})$ and $R_9 = R/(10^9\,\text{cm})$, which means that the magnetic field evolves on time scales much longer than the collisional time scale.

Let us discuss implications of the given solution for the plasma response to the given beam current. First, Eq. (7.8a) shows that strong Langmuir oscillations at the plasma frequency are excited upon the beam front arrival.

These oscillations, however, collisionally damp on the time scale of electron-ion collision time τ_{ei}. Therefore, the charge neutralization is established only after a few collision times; at this relatively late stage standard Ohm's law can be used, although its generalized form Eq. (7.7) must be used at the initial stage, $t \lesssim \tau_{ei}$, which is evident from Eq. (7.8c). Finally, given the magnetic diffusion time, Eq. (7.9), is huge, the net electric current is almost zero after a few collision times and remains at that level a very long time, $t \sim \tau_d$, Eq. (7.8b). Accordingly, the solenoidal magnetic field, B_ϕ, is very small during entire this stage.

We conclude that a given (weak) fast electron beam is being fully neutralized by both charge and current at a relatively short, collisional, time scale. Then, for $\tau_{ei} \ll t \ll \tau_d$, Eq. (7.8c) yields

$$\boldsymbol{E} = -\boldsymbol{j}_b/\sigma, \tag{7.10}$$

which is similar to standard Ohm's law (with the same conductivity σ) but contains the minus sign in the rhs. It is remarkable because the beam electrons have a much lower Coulomb cross section than the thermal electrons, which would imply entirely different link between their current and the electric field. However, because of the full compensation of the beam current by the background plasma return current, we have $\boldsymbol{j} = -\boldsymbol{j}_b$, which being combined with Ohm's law for the background plasma, results in Eq. (7.10). This fact has further implications for the beam dynamics. Indeed, although direct Joule losses of the beam current are very low, the Joule losses of the return plasma current are significant so the return current experiences the energy losses. To keep the net zero current, the energy must continuously be transferred from the beam to the (decaying) return current, which implies corresponding energy losses of the beam. These energy losses are not accounted by the above solution obtained within a given (unchanged) beam assumption.

Relaxing this assumption can in many cases lead to a significant modification or even qualitative change of the whole picture of the beam propagation in the plasma. In addition to the mentioned quasi-joule energy losses, the beam electrons will be decelerated by electric field (7.10) or the beam can be modified by the Langmuir oscillations it generates in the plasma, which can result in modification of the beam distribution over energy and/or pitch-angle. In particular, in case of fast isotropization, a diffusive propagation of fast electrons is expected instead of the unidirectional flow considered above. Furthermore, the turbulent magnetic diffusivity can strongly change the time scale of the magnetic field evolution and so significantly change the picture of the return current formation. Finally, in case of strong beams, the number density of available plasma electrons can turn to be too low to fully

compensate the beam current, so some of strong two-stream instabilities will come into play and affect the beam strongly over a very short time scale (see Chap. 4). Some of the mentioned effects are considered below in this chapter.

7.2 Diffusion of an Admixture in a Steady Plasma

The (test) particles of a passive component with a number density $n(\boldsymbol{r}, t)$ perform random walks relative to the medium at rest due to collisions with the main population particles; in case of small *macroscopic* test particles this random walk is commonly called the **Brown motion**. This random walk of a given particle is quantified by two parameters: rms velocity v and mfp Λ, which is the length of the particle trajectory over which direction of the particle motion changes noticeably (i.e., by an angle about 1 rad). In a general case this angle can be accumulated over many elementary collisions if each of the collisions results in a small-angle deflection of the particles (like in case of far Coulomb collisions).

In many cases, however, the problem is to describe the flow density $\boldsymbol{i}(\boldsymbol{r}, t)$, produced by a macroscopically large number of the test particles with a number density $n(\boldsymbol{r}, t)$, rather than a single particle. This flow density in an immobile isotropic medium is described by **Fick's law** for the admixture diffusion

$$\boldsymbol{i}(\boldsymbol{r}, t) = -\kappa \nabla n(\boldsymbol{r}, t), \tag{7.11}$$

where κ is the diffusion coefficient of the test particles. Fick's diffusion law is explicitly analogous to Fourier law (1.123) $\boldsymbol{q} = -\chi \nabla T$ for the heat conduction. The diffusion coefficient is connected with the test particle velocity and the mfp:

$$\kappa = \frac{1}{3} v \Lambda. \tag{7.12}$$

This relation can be derived from either elementary considerations (see Problem 7.1) or, more consistently, from kinetic or hydrodynamic equations considered in Sect. 1.3. The diffusion coefficient becomes a tensor in case of anisotropic medium. Diffusion coefficients of ions and atoms can be calculated via effective cross section of the test particles on the background particles.

Let us start from a simple case when the diffusing component (the admixture) is composed of nonrelativistic particles with charge q and mass m_r. These particles diffuse in a steady-state quasi-neutral plasma and have a temperature $T = \text{const}$ same as the main plasma. If, at a certain initial time frame, the admixture is distributed non-uniformly, $n_r(\boldsymbol{r}, t)$, this nonuniformity will yield a diffusion flow acting to smooth the nonuniformity out. Let us calculate this flow using equation similar to Eq. (1.79) but with

explicit account that the plasma is a steady state and at rest, i.e., within notations of Sect. 1.3.4, we have $\boldsymbol{u} = \boldsymbol{v}_e = \boldsymbol{v}_i = \boldsymbol{v}_a = 0$ and, accordingly,

$$n_r m_r \frac{\partial \boldsymbol{u}_r}{\partial t} = -\nabla P_r + \frac{q n_r}{c}\, \boldsymbol{u}_r \times \boldsymbol{B} - n_r m_r \nu_r \boldsymbol{u}_r, \tag{7.13}$$

where ν_r is the full frequency of collisions between the admixture particles and all the particles of the main plasma:

$$\nu_r = \nu_{ri} + \nu_{re} + \nu_{ra} = \tau_{ri}^{-1} + \tau_{re}^{-1} + \tau_{ra}^{-1} = \tau_r^{-1}. \tag{7.14}$$

These effective collision frequencies (or, equivalently, reciprocal values of the mean free times) play a role of the most important kinetic coefficients. Partial pressure of the tenuous admixture gas has the form $P_r = n(\boldsymbol{r}, t)T$ and, for $T = \text{const}$, so the pressure gradient reduces to the gradient of the number density, $\nabla P_r = T \nabla n_r(\boldsymbol{r}, t)$.

Upon a sufficiently long time Δt to fulfill $\nu_r \Delta t \gg 1$, the lhs of Eq. (7.13) becomes small compared with the last term at the rhs, so one can discard the derivative $\partial \boldsymbol{u}_r / \partial t$. This allows to approximately solve Eq. (7.13) for the admixture diffusive flow $\boldsymbol{i}_r = n_r \boldsymbol{u}_r$:

$$\boldsymbol{i}_r = -\hat{\kappa}' \nabla n_r + \boldsymbol{g} \times \nabla n_r. \tag{7.15}$$

Here

$$\hat{\kappa}' = \begin{pmatrix} \kappa_\perp & 0 & 0 \\ 0 & \kappa_\perp & 0 \\ 0 & 0 & \kappa_\parallel \end{pmatrix}, \quad \kappa_\parallel = \frac{T\tau_r}{m_r}, \quad \kappa_\perp = \frac{\kappa_\parallel}{1 + (\omega_{Br}\tau_r)^2}, \quad \omega_{Br} = \frac{qB}{m_r c} \tag{7.16}$$

is the symmetric part of the diffusion tensor, while the gyration vector

$$\boldsymbol{g} = \frac{\kappa_\parallel \omega_{Br} \tau_r}{1 + (\omega_{Br}\tau_r)^2} \frac{\boldsymbol{B}}{B} \tag{7.17}$$

describes the antisymmetric (Hall) part of the tensor.

The effective collision frequency ν_r can be expressed via the thermal speed of the test particles v_{Tr} and their full mfp Λ_r, taking into account collisions of the particles with all plasma components: $\nu_r = v_{Tr}/\Lambda_r$. Defining the characteristic speed of the test particles from $3T/2 = m_r v_{Tr}^2/2$, Eq. (7.16) yields the following diffusion coefficient:

$$\kappa_\parallel = \frac{1}{3} v_{Tr} \Lambda_r. \tag{7.18}$$

If the effective collision frequency is dominated by a single plasma component, say ions, then $\Lambda_r = \Lambda_{ri}$. The mfp Λ_{ri} for the thermal particles is estimated

Table 7.1: Coulomb particle mfps in astrophysical plasmas

Object	n_a cm^{-3}	n_i cm^{-3}	T K	Λ_{ia} cm	Λ_{ii} cm
Cosmological medium ($z < 1$)	5×10^{-9}	4×10^{-5}	10^4	2×10^{22}	5×10^{16}
Galactic neutral clouds	20	0.05	100	5×10^{12}	3×10^9
Intercloud warm medium	0.2	0.03	10^4	5×10^{14}	5×10^{13}
Hot caverns	0	2×10^{-3}	10^6	∞	10^{19}
Interplanetary medium (1 AU)	0	5	10^5	∞	10^{13}
Solar photosphere	10^{16}	10^{13}	6×10^3	10^{-2}	10^{-1}
Terrestrial ionosphere	2×10^8	10^6	10^3	5×10^5	10^4

with equations derived in Sect. 1.3.7 with the Coulomb cross section given by Eq. (1.147), which has the form

$$\sigma_{ri} \approx \pi \left(\frac{qe}{m_{ri} v_{ri}^2} \right)^2 \ln \Lambda_{\rm C}, \tag{7.19}$$

where m_{ri} and v_{ri} are the reduced mass of two particles and their relative velocity. For the thermal particles, similar to Sect. 1.3.7, $m_{ri} v_{ri}^2 \approx T$, which yields

$$\Lambda_{ri} \approx \frac{1}{n_i \sigma_{ri}} \approx \frac{T^2}{\pi n_i q^2 e^2 \ln \Lambda_{\rm C}} \propto T^2, \tag{7.20}$$

thus, the longitudinal diffusion coefficient $\kappa_\parallel \propto T^{5/2}$.

If the test particles are protons, they are primarily scattered by ions and neutrals. Collisions of ions with electrons are inefficient because of large difference in their masses, $m_e \ll m_p$. In the electron–proton plasma we have $\Lambda_{\rm pi} = \Lambda_{ii}$, while the full mfp Λ_i is

$$\frac{1}{\Lambda_i} = \frac{1}{\Lambda_{ii}} + \frac{1}{\Lambda_{ia}}. \tag{7.21}$$

On the other hand, the electrons are efficiently scattered by ions, neutrals, and electrons themselves.

The estimates of the longitudinal Coulomb mfp of the protons in various astrophysical objects are given in Table 7.1. In most of the presented cases the Coulomb collisions are more frequent than collisions with neutral with an exclusion of weakly ionized solar photosphere (cf. Table 1.1 in Sect. 1.3.7).

The diffusion coefficient transverse to the magnetic field is smaller (for magnetized particles with $\omega_{Br} \tau_r \gg 1$ is much smaller), because the transverse displacement of a particle is limited by its Larmor rotation. Diffusion of the charged particles becomes isotropic when $\omega_{Br} \tau_r \ll 1$, which is always the case for neutral particles since for them $\omega_{Br} = 0$.

We emphasize that Table 7.1 displays the mfps of the *thermal* particles. For accelerated fast particles the kinetic energy $K = m_r v^2/2 \gg T$ is much larger than the temperature, and their mfp increases as square of energy, see Eq. (7.20), which is also valid in relativistic energy range. For example, the mfp of protons accelerated up to a few MeV (still nonrelativistic) is enhanced in the photosphere by roughly ≈ 12 orders of magnitude, while in IPM by ≈ 10–12 orders of magnitude compared with numbers in the table. Therefore, for energetic particles, the Coulomb scattering becomes entirely inefficient in many cases. In such cases the particles are primarily scattered by turbulent electromagnetic fields in place of background particles. The random turbulent fields also result in the random walks of the scattered particles. This diffusion mechanism for the fast, including ultrarelativistic, particles is considered in detail in Sects. 7.4 and 7.5. For macroscopic neutral particles the diffusion coefficient can be derived via dynamical viscosity of the medium taking into account the scale and shape of the particles under study (see, e.g., Heer 1972).

Let us derive relations between the diffusion coefficients $\kappa^{e,i}_{\alpha\beta}$ related to inhomogeneity of particle spatial distribution and electroconductivity $\sigma^{e,i}_{\alpha\beta}$, i.e., in general case between tensors of diffusion and conductivity. This relation has a simpler form for a weakly ionized medium, where $\Lambda_{ii},\ \Lambda_{ei} \gg \Lambda_{ia},\ \Lambda_{ea}$. We have

$$\kappa^e_\parallel = \frac{1}{3} v_{Te} \Lambda_{ea}, \quad \sigma^e_\parallel = \frac{e^2 n_e \tau_{ea}}{m_e} \tag{7.22}$$

(see Sect. 1.3.4). This yields

$$\frac{\kappa^e_\parallel}{\sigma^e_\parallel} = \frac{m_e v^2_{Te}}{3e^2 n_e} = \frac{T}{e^2 n_e} = 4\pi r^2_D, \tag{7.23}$$

where $r_D = \sqrt{T/4\pi e^2 n_e}$ is the Debye shielding radius, one of the key plasma parameters introduced in Sect. 1.1. The same relation is valid also for transverse and Hall components (note that the Hall components for electrons and ions have opposite signs); therefore for each combination of α and β we have:

$$\frac{\kappa^{e,i}_{\alpha\beta}}{\sigma^{e,i}_{\alpha\beta}} = 4\pi r^2_D. \tag{7.24}$$

In the fully ionized plasma there is no unique relation for the tensor components. Moreover, the results depend on the chemical composition of the plasma as the collisions of the protons with other ions can be more essential than collisions of the protons with electrons (see Sect. 3.4). Using Eqs. (1.101) and (1.102), we find for the hydrogen plasma

$$\begin{aligned} \frac{\kappa^e_{\alpha\beta}}{\sigma^e_{\alpha\beta}} &= 4\pi r^2_D, \quad \text{while} \quad \frac{\kappa^i_\parallel}{\sigma^i_\parallel} = 4\pi r^2_D \left(\frac{m_i}{m_e}\right)^{1/2}, \\ \frac{\kappa^i_\perp}{\sigma^i_\perp} &= 4\pi r^2_D \left(\frac{m_i}{m_e}\right)^{3/2}, \quad \frac{g^i}{G^i} = 4\pi r^2_D \left(\frac{m_i}{m_e}\right). \end{aligned} \tag{7.25}$$

Note a fundamental difference in diffusion of the neutral and charged particles. Various kinds of passive neutral admixtures diffuse independently from each other as long as their number densities are small. The charged particles interact with each other and with plasma particles via far-acting Coulomb forces; thus, the diffusion flows of various charged particles are interdependent; this phenomenon is called the **ambipolar diffusion** (see Sect. 7.6).

7.3 Transfer of Admixture in a Turbulent Fluid

If the fluid moves, the particles of admixture are being picked up and, besides the diffusion, take part in the advection transfer with the fluid velocity $\boldsymbol{u}(\boldsymbol{r},t)$. Hereafter, we talk about transfer over a macroscopic distance, which is much larger than the mfp Λ of the test particles in the fluid. The full flux produced by the admixture particles is, therefore, composed of diffusive (7.11) and advective terms:

$$i_\alpha(\boldsymbol{r},t) = n(\boldsymbol{r},t)u_\alpha(\boldsymbol{r},t) - \kappa_{\alpha\beta}\nabla_\beta n(\boldsymbol{r},t), \tag{7.26}$$

where a general case of anisotropic fluid is assumed, although thermo- and baro-diffusions, driven by inhomogeneities of the fluid temperature or pressure (Landau and Lifshitz 1966), are not included in Eq. (7.26).

To derive equation for the number density evolution we note that if there is no creation or annihilation of the test particles the number of particles in a given volume V is only changing due to their transport in space; thus, from the particle number balance and particle flux (7.26), we find

$$-\frac{\mathrm{d}}{\mathrm{d}t}\int_V n\,\mathrm{d}V = \oint_S \boldsymbol{i}\cdot\mathrm{d}\boldsymbol{S}, \tag{7.27}$$

where the rhs is the particle flux through the closed surface enveloping this volume. Then, the Ostrogradsky–Gauss theorem yields an advection–diffusion equation:

$$\frac{\partial n}{\partial t} + \nabla\cdot n\boldsymbol{u} = \nabla_\alpha\kappa_{\alpha\beta}\nabla_\beta\, n. \tag{7.28}$$

In a hydrodynamically turbulent fluid the velocity $\boldsymbol{u}(\boldsymbol{r},t)$ is a random function of coordinates and time fluctuating on the spatial scales $l \leqslant L$ and time $\tau \leqslant \tau_c \approx L/u$ where L is the main (energy-containing) spatial scale of the turbulence. In addition, in a compressible fluid, the (microscopic) coefficient of the "molecular" diffusion κ is also a random function because of background density fluctuations. Apparently, Eq. (7.26) is only valid if the spatial scales of the turbulent pulsations l are much larger than the mfp of the test particles; this condition is required for the particles to be tightly linked to a fluid element due to the molecular diffusion, and so be transferred with it.

To describe the test particle transport over large distances $\Delta r \gg L$ we have to average Eq. (7.28) over volume elements with linear scales about L

or over statistical ensemble of the turbulent pulsations. These two ways of averaging are equivalent to each other if the correlation vanishes quickly with the distance (see Sect. 6.6). The averaging will eventually give rise to equation for the mean number density of the test particles $\langle n(\boldsymbol{r},t)\rangle$ and specify coefficients of this equation expressed via averaged measures of the turbulent velocity field.

Taylor (1921) was the first who demonstrated that for the time much longer than the turbulence velocity correlation time τ_c the transfer of the test particles is a diffusion with an effective diffusion coefficient defined by an integration of the correlation function of the **Lagrangian velocities**

$$\chi = \frac{1}{3}\int_0^\infty \langle \boldsymbol{v}(\boldsymbol{a},t)\cdot\boldsymbol{v}(\boldsymbol{a},t+\tau)\rangle \mathrm{d}\tau. \tag{7.29}$$

Here $\boldsymbol{v}(\boldsymbol{a},t)$, in contrast to Euler velocity $\boldsymbol{u}(\boldsymbol{r},t)$, is the Lagrangian velocity of the fluid element located at some initial time frame at a position $\boldsymbol{a}$. Taylor's formula (7.29) is derived neglecting the molecular diffusion. An outstanding problem, how to connect the Lagrangian and Euler correlation functions, has yet no exact solution; there are only approximate expressions linking the coefficient of the turbulent diffusion χ with the observable Euler measures of turbulence, some of which we derive below in this chapter.

7.3.1 Perturbation Theory

Let us start from analysis of incompressible motion ($\nabla\cdot\boldsymbol{u}=0$) of a fluid without any mean flow, $\langle\boldsymbol{u}\rangle = 0$. To average Eq. (7.28) over the turbulent motion ensemble, we adopt the following distribution function of the test particles:

$$n(\boldsymbol{r},t) = N(\boldsymbol{r},t) + \delta n(\boldsymbol{r},t), \quad N = \langle n\rangle, \quad |\delta n| \ll N. \tag{7.30}$$

The last inequality is a condition of the perturbation theory applicability. Tensor of local (molecular) diffusion can be assumed to be a given, fluctuation-free, value. Thus, after substitution of Eq. (7.30) into Eq. (7.28) we obtain a system of two equations:

$$\frac{\partial N}{\partial t} = \frac{\partial}{\partial x_\alpha}\kappa_{\alpha\beta}\frac{\partial N}{\partial x_\beta} - \left\langle u_\alpha \frac{\partial \delta n}{\partial x_\alpha}\right\rangle, \quad \frac{\partial \delta n}{\partial t} - \frac{\partial}{\partial x_\alpha}\kappa_{\alpha\beta}\frac{\partial \delta n}{\partial x_\beta} = -u_\alpha\frac{\partial N}{\partial x_\alpha}. \tag{7.31}$$

The latter of these equations has been linearized over fluctuating values u_α and δn. It is an inhomogeneous equation that can explicitly be solved using the Green function $G(\boldsymbol{r},\boldsymbol{r}',t,t')$, which contains the local diffusion tensor $\kappa_{\alpha\beta}$:

$$\delta n(\boldsymbol{r},t) = -\int G(\boldsymbol{r},\boldsymbol{r}',t,t')u_\alpha(\boldsymbol{r}',t')\frac{\partial N(\boldsymbol{r}',t')}{\partial x'_\alpha}\,\mathrm{d}^3r'\mathrm{d}t'. \tag{7.32}$$

Substitution of Eq. (7.32) into the first of Eq. (7.3.1) yields the averaged kinetic equation accounting for the turbulent diffusion in an incompressible fluid:

$$\frac{\partial N}{\partial t} = \frac{\partial}{\partial x_\alpha}\kappa_{\alpha\beta}\frac{\partial N}{\partial x_\beta} + \frac{\partial}{\partial x_\alpha}\int G(\boldsymbol{r},\boldsymbol{r}',t,t')\langle u_\alpha(\boldsymbol{r},t)u_\beta(\boldsymbol{r}',t')\rangle\frac{\partial N(\boldsymbol{r}',t')}{\partial x'_\beta}\,\mathrm{d}^3r'\mathrm{d}t'. \tag{7.33}$$

In case of stationary and uniform fluid the Green function and correlation tensor of Euler velocities depend only on the argument differences, so Eq. (7.33) reduces to

$$\frac{\partial N}{\partial t} = \kappa_{\alpha\beta}\frac{\partial^2 N}{\partial x_\alpha x_\beta} + \frac{\partial^2}{\partial x_\alpha x_\beta}\int G(\boldsymbol{r}-\boldsymbol{r}',t-t')\langle u_\alpha(\boldsymbol{r},t)u_\beta(\boldsymbol{r}',t')\rangle N(\boldsymbol{r}',t')\,\mathrm{d}^3r'\mathrm{d}t'. \tag{7.34}$$

We see that averaging over the turbulent pulsation ensemble gives rise to an integro-differential equation with a nonlocal interaction within the correlation length L and correlation time τ_c, specified by properties of the velocity correlation tensor $\langle u_\alpha u'_\beta\rangle$. This equation can be simplified at large time and scale, much larger than the correlation time and length, respectively. For the same conditions the ergodic theorem for uniform stationary random processes takes place (Monin and Yaglom 1965), which ensures the equivalence between averaging over ensemble from one hand and averaging over space or time on the other hand. In this case the distribution function N varies only slightly over the integration ranges, so Eq. (7.34) becomes the differential one:

$$\frac{\partial N}{\partial t} = \chi_{\alpha\beta}\frac{\partial^2 N}{\partial x_\alpha \partial x_\beta} \tag{7.35}$$

with an effective diffusion coefficient

$$\chi_{\alpha\beta} = \kappa_{\alpha\beta} + \int \mathrm{d}^3 r \int_0^\infty \mathrm{d}t\, G(\boldsymbol{r},t)\, U_{\alpha\beta}(\boldsymbol{r},t), \tag{7.36}$$

where $U_{\alpha\beta}(\boldsymbol{r}-\boldsymbol{r}',t-t')$ denotes the correlation tensor of the turbulent velocities. Thus, the overall concept of the random walks remains valid in the presence of turbulence; however, the diffusion coefficient changes.

Let us evaluate the applicability region of the perturbation theory in the problem under study. The original condition $|\delta n| \ll N$ requires the correction due to turbulence in Eq. (7.36) to be small compared with κ (for simplicity consider here the isotropic case, i.e., $\kappa_{\alpha\beta} = \kappa\delta_{\alpha\beta}$, $\chi_{\alpha\beta} = \chi\delta_{\alpha\beta}$). If $\kappa \gg L^2/\tau_c \approx uL$ then the exponential factor in the Green function

$$G(\boldsymbol{r},t) = \frac{1}{(4\pi\kappa t)^{3/2}}\exp\left[-\frac{r^2}{4\kappa t}\right] \tag{7.37}$$

is of the order of unity and estimate of the integral in Eq. (7.36) gives rise to

$$\chi \approx \kappa + \frac{1}{(4\pi\kappa\tau_c)^{3/2}}\frac{1}{3}\langle u^2\rangle L^3\tau_c = \kappa\left[1 + \frac{1}{3(4\pi)^{3/2}}\left(\frac{uL}{\kappa}\right)^{5/2}\right]. \tag{7.38}$$

The dimensionless parameter $\mathrm{Pe} = uL/\kappa$ is called the *Pécklet number*. The perturbation theory is, therefore, applicable here for the turbulent motions with small Péclet numbers, $\mathrm{Pe} < 1$, which is the case of weak and small-scale turbulence.

This estimate must be modified for a conducting fluid (plasma) in a magnetic field. Here the excitations propagate mainly in the form of Alfvén waves, so the correlation time $\tau_c \approx L/v_\mathrm{A}$ is specified by the Alfvén speed v_A rather than the fluid speed u. This effect increases the correcting factor in Eq. (7.38) by the factor $(v_\mathrm{A}/u)^{1/2}$.

The presented approach has a very limited (mainly, illustrative) applicability in astrophysics: the perturbation theory breaks down due to the presence of strong turbulence and also large spatial scales of the astrophysical objects. Nevertheless, the overall picture of the test particle diffusion via random walks often survives. Moreover, the form of averaged equation (7.35) often remains the same, although expression (7.36) for the turbulent diffusion coefficient changes. Below we consider the particle transport mediated by strong/long-wave turbulence following the renormalization approach developed by Bykov and Toptygin (1993) based on earlier methods presented by Phythian and Curtis (1978) and Moffatt (1981).

7.3.2 Renormalization of Turbulent Diffusion Coefficients

For simplicity we still consider an incompressible fluid, $\nabla\cdot\boldsymbol{u} = 0$, and $\langle\boldsymbol{u}\rangle = 0$. Let us derive the diffusion equation averaged over the large-scale turbulent pulsations in the form of Eq. (7.35) with yet unknown diffusion tensor $\chi_{\alpha\beta}$. Consider an auxiliary equation

$$\frac{\partial\widetilde{N}}{\partial t} = (\chi_{\alpha\beta} - \Delta\chi_{\alpha\beta})\,\frac{\partial^2\widetilde{N}}{\partial x_\alpha \partial x_\beta} - \delta u_\alpha \frac{\partial\widetilde{N}}{\partial x_\alpha}, \tag{7.39}$$

which is a formal result of averaging over all Fourier harmonics of the velocity field except for the harmonics belonging to a narrow-range Δk of the wave numbers, where

$$\delta\boldsymbol{u}(\boldsymbol{r},t) = \int_{-\infty}^{\infty}\frac{\mathrm{d}\omega}{2\pi}\int_{\Delta k}\frac{\mathrm{d}^3k}{(2\pi)^3}\boldsymbol{u}_{\mathbf{k}\omega}\exp(i\boldsymbol{k}\cdot\boldsymbol{r} - i\omega t) \tag{7.40}$$

is a velocity field component over which no averaging has yet been performed. Integration over d^3k must be performed over a spherical layer with thickness Δk around an arbitrary wave number k; $\widetilde{N}$ is a partly averaged distribution function needed to be further averaged over the remaining random velocity component $\delta\boldsymbol{u}$; accordingly $\chi_{\alpha\beta} - \Delta\chi_{\alpha\beta}$ is the diffusion coefficient reduced by a contribution from $\delta\boldsymbol{u}$. Averaging of Eq. (7.39) over the turbulent velocity component $\delta\boldsymbol{u}$ must compensate for $-\Delta\chi_{\alpha\beta}$ and give rise to Eq. (7.35) with the full diffusion coefficient $\chi_{\alpha\beta}$.

Note that the partly averaged auxiliary distribution function $\widetilde{N}$ depends on the k value. Nevertheless, the final renormalized kinetic coefficients, which are observable physical values, are determined by integration over the entire k-space and so do not depend on that arbitrary choice of k. Apparently, the fully averaged distribution function N does not depend on this choice either.

The final step of averaging of Eq. (7.39) can be done using the perturbation theory justified by smallness of $\delta\boldsymbol{u}$. This does not imply any constraint on the accuracy because it can be taken arbitrarily small by using $\Delta k \ll k$. However, in practice the smallness of this range is limited by requirement that the velocity Fourier harmonics from Δk do not correlate with other harmonics outside this range. Below we will always assume (until a different is explicitly stated) the turbulence to be uniform and stationary and use the common rule of the Fourier harmonics averaging:

$$\langle \boldsymbol{u}_{\mathbf{k}\omega} \cdot \boldsymbol{u}_{\mathbf{k}'\omega'} \rangle = (2\pi)^4 \langle u^2_{\mathbf{k}\omega} \rangle \delta(\omega + \omega') \delta(\boldsymbol{k} + \boldsymbol{k}'), \tag{7.41}$$

where $\langle u^2_{\mathbf{k}\omega} \rangle$ is a regular smooth function of its arguments $\boldsymbol{k}$ and ω. This definition of $\langle u^2_{\mathbf{k}\omega} \rangle$ agrees with the model concept of the Kolmogorov-type turbulence (see Sect. 6.7), which can be described by the turbulence spectral energy density.

Adopting

$$\widetilde{N} = N + \delta N, \qquad \langle \delta N \rangle = 0, \qquad \langle \widetilde{N} \rangle = N, \tag{7.42}$$

where the brackets denote averaging over the ensemble $\delta\boldsymbol{u}$, and averaging Eq. (7.39), we obtain

$$\frac{\partial N}{\partial t} = (\chi_{\alpha\beta} - \Delta\chi_{\alpha\beta}) \frac{\partial^2 N}{\partial x_\alpha \partial x_\beta} - \left\langle \delta u_\alpha \frac{\partial \delta N}{\partial x_\alpha} \right\rangle. \tag{7.43}$$

Here the correction δN to the averaged distribution function can be found from the linearized equation

$$\frac{\partial \delta N}{\partial t} - \chi_{\alpha\beta} \frac{\partial^2 \delta N}{\partial x_\alpha \partial x_\beta} = -\delta u_\alpha \frac{\partial N}{\partial x_\alpha}, \tag{7.44}$$

in which all quadratic terms over δu_α including $\Delta\chi_{\alpha\beta}$ have been discarded. Solution of this equation can be expressed via the Green function G of the corresponding homogeneous equation:

$$\frac{\partial G}{\partial t} - \chi_{\alpha\beta} \frac{\partial^2 G}{\partial x_\alpha \partial x_\beta} = \delta(\boldsymbol{r} - \boldsymbol{r}') \delta(t - t'). \tag{7.45}$$

Taking such a solution of Eq. (7.44) and substituting it into Eq. (7.43) we obtain the integro-differential equation for the averaged distribution function:

$$\frac{\partial N}{\partial t} = (\chi_{\alpha\beta} - \Delta\chi_{\alpha\beta}) \frac{\partial^2 N}{\partial x_\alpha \partial x_\beta} + \frac{\partial^2}{\partial x_\alpha \partial x_\beta} \int G(\boldsymbol{r} - \boldsymbol{r}', t - t') \, \langle \delta u_\alpha(\boldsymbol{r}, t) \delta u_\beta(\boldsymbol{r}', t') \rangle N(\boldsymbol{r}', t') \mathrm{d}^3 r' \mathrm{d}t'. \tag{7.46}$$

This equation receives a simpler form of Eq. (7.35) if the distribution function N changes only smoothly over the correlation length L and correlation time L/u. If these conditions are fulfilled one can replace $N(\boldsymbol{r}', t')$ by $N(\boldsymbol{r}, t)$ in Eq. (7.46) and, thus, determine the correction to the diffusion tensor for the velocity field component $\delta\boldsymbol{u}$:

$$\Delta\chi_{\alpha\beta} = \int G(\boldsymbol{\rho}, \tau)\langle \delta u_\alpha(\boldsymbol{r}, t)\delta u_\beta(\boldsymbol{r}', t')\rangle \mathrm{d}^3\rho \mathrm{d}\tau, \tag{7.47}$$

where $\boldsymbol{\rho} = \boldsymbol{r} - \boldsymbol{r}'$, $\tau = t - t'$. This formula, although has a form similar to Eq. (7.36), is fundamentally different from it in two major respects: in contrast to Eq. (7.36) it contains the correlator of only a minor part of the entire velocity field δu, but the Green function contains now the full, $(\chi_{\alpha\beta})$, rather than the small-scale $(\kappa_{\alpha\beta})$, yet unknown diffusion tensor, which accounts for the entire large-scale velocity field.

To determine the turbulent diffusion tensor we use the Fourier transform of the Green function of Eq. (7.45)

$$G_{\mathbf{k}\omega} = \frac{1}{-i\omega + k_\mu k_\nu \chi_{\mu\nu}}, \tag{7.48}$$

to obtain

$$\Delta\chi_{\alpha\beta} = k^2\Delta k \int \frac{\mathrm{d}\Omega_k \mathrm{d}\omega}{(2\pi)^4} \frac{\langle u_\alpha u_\beta\rangle_{\mathbf{k}\omega}}{-i\omega + k_\mu k_\nu \chi_{\alpha\beta}}, \tag{7.49}$$

where the integration is performed over the angles of $\boldsymbol{k}$ vector and over the frequency. Further integration of this expression over all wave numbers k with an obvious constraint $\chi_{\alpha\beta} = \kappa_{\alpha\beta}$ at $u = 0$ yields a self-consistent set of equations for the renormalized components of the tensor of turbulent diffusion $\chi_{\alpha\beta}$:

$$\chi_{\alpha\beta} = \kappa_{\alpha\beta} + \int \frac{\mathrm{d}^3 k \mathrm{d}\omega}{(2\pi)^4} \frac{\langle u_\alpha u_\beta\rangle_{\mathbf{k}\omega}}{-i\omega + k_\mu k_\nu \chi_{\alpha\beta}}. \tag{7.50}$$

Note that the unknowns $\chi_{\alpha\beta}$ enter here as parameters (rather than dependent variables), so Eq. (7.50) are algebraic (although transcendental) but not integral ones. The correlation tensor is assumed to be a given measure of the turbulence. For a non-gyrotropic fluid it has a form

$$\langle u_\alpha u_\beta\rangle_{\mathbf{k}\omega} = T(k, \omega)(\delta_{\alpha\beta} - k_\alpha k_\beta/k^2) + S(k, \omega)k_\alpha k_\beta/k^2. \tag{7.51}$$

For an incompressible fluid we have additionally $S(k, \omega) = 0$. For the sake of estimate consider explicit frequency dependence in a Lorentzian form with the correlation time $\tau_c(k) = \Gamma_k^{-1}$:

$$T(k, \omega) = T(k)\frac{\Gamma_k}{2}\left[\frac{1}{(\omega - \omega_0)^2 + \Gamma_k^2/4} + \frac{1}{(\omega + \omega_0)^2 + \Gamma_k^2/4}\right]. \tag{7.52}$$

The Lorentzian (dispersive) form of the spectral function is quite general while simple; the results here depend only slightly on the specific form of this function (but it can be important when particle acceleration by turbulence is considered, see Chap. 11).

For isotropic turbulence the set of equations (7.50) reduces to a single equation. Let us substitute correlation tensor (7.51) in it (with $S(k,\omega)=0$) and use the parity of the spectral function $T(k,\omega)$ over ω, as well as isotropy of the tensors $\chi_{\alpha\beta}=\chi\delta_{\alpha\beta}$ and $\kappa_{\alpha\beta}=\kappa\delta_{\alpha\beta}$. This gives rise to a single transcendental equation for χ:

$$\chi=\kappa+\frac{4\chi}{3}\int\frac{\mathrm{d}^3k}{(2\pi)^3}\int_0^\infty\frac{\mathrm{d}\omega}{2\pi}\frac{k^2T(k,\omega)}{\omega^2+k^4\chi^2}. \tag{7.53}$$

This equation cannot be solved analytically in a general case. One case allowing analytical solution is a "frozen-in" stationary turbulence $T(k,\omega)\propto\delta(\omega)$. This is a limiting case of the Lorentzian one for $\omega_0\to 0$ and $\Gamma_k\to 0$, which results in the following analytical solution:

$$\chi=\frac{1}{2}\kappa+\left[\frac{\kappa^2}{4}+\frac{2}{3\pi^2}\int_0^\infty\frac{T(k)\mathrm{d}k}{k}\right]^{1/2}. \tag{7.54}$$

A solution satisfying the natural requirement $\chi\geqslant 0$ always exists, since $T(k,\omega)>0$. Nonphysical (e.g., negative or complex) solutions would indicate either inadequacy of the method or absence of the standard diffusive mode of the particle propagation (anomalous diffusion). Although a numerical solution may be needed in a general case, an order of magnitude estimate of Eq. (7.54) for large Pécklet numbers ($\kappa\ll uL$) yields $\chi\approx uL$, which is a reasonable estimate of the turbulent diffusion coefficient.

The developed renormalization method is apparently an approximation to the reality, whose accuracy is difficult to explicitly evaluate. One of the main uncertainties introduced by the averaging performed seems to be in adoption of the diffusive particle propagation throughout all the scales including $l\leqslant L$, although this is firmly valid only for $\Delta r\gtrsim L$. This shortcoming of the theory can be consistently removed within the very renormalization method at the expense of enhanced mathematical complexity of the theory implying solving a nonlinear integral equation to calculate effective diffusion tensor describing the transport at any spatial scale (Bykov and Toptygin 1993).

A further limitation is that the renormalized diffusion tensor depends only on the pair correlation tensor of the turbulence $\langle u_\alpha u'_\beta\rangle$; thus, the particle transport can deviate from the considered here diffusive one if higher-order correlation tensors contain essential nontrivial information on the turbulence structure (intermittency of the turbulence). Comparison of the renormalized theory with results of the corresponding numerical simulations reported in the literature (see Bykov and Toptygin 1993) shows typically a quantitative agreement to better than 10 %.

7.4 Transport of Fast Particles in a Random Magnetic Field

A number of charged particle motion regimes in a regular magnetic field have been considered earlier in Sect. 1.2. Such a regular field can, at least in principle, be represented as a function of the coordinates and time. However, on top of these regular magnetic fields in the astrophysical plasma, there are also *random* inhomogeneities of the magnetic field. The drivers of this random magnetic field are numerous: macroscopic random motions of the plasma, plasma instabilities, oscillations, and wave modes excited and propagating in nonstationary plasmas. The corresponding random magnetic field, like the velocity field considered earlier, allows for many realizations; the statistical properties of these random fields can be specified (see Chap. 6) by their mean values and correlation tensors of various ranks.

Accordingly, a single-particle path has also many realizations in the random electromagnetic field, so it does not have a closed functional form of the random field. The particle, or ensemble of the particles, moving in the random fields can reasonably be characterized by distribution functions averaged over the field realizations. In a tenuous astrophysical plasma this random fields have often much stronger effect on the particle motion than seldom Coulomb collisions. Here we entirely neglect the Coulomb collisions (see the corresponding mfp estimated in Sect. 7.2) compared with the scattering by random magnetic inhomogeneities.

7.4.1 Derivation of the Kinetic Equation

Let us derive a kinetic equation for distribution function of fast, perhaps relativistic, particles propagating through a volume containing a magnetic field with a random component. We suppose that the random magnetic field component is composed of MHD modes with relatively small phase velocity v_{ph}, whose electric field is by a factor of v_{ph}/c smaller than their magnetic field, so we neglect here the effect of the electric field, which ensures conservation of the particle energy.

Adopt the magnetic field $\boldsymbol{B}$ to consist of two physically different components: a regular uniform field $\boldsymbol{B}_0 = \text{const}$ and a random field $\boldsymbol{b}(\boldsymbol{r}, t)$ with zero mean $\langle \boldsymbol{b} \rangle = 0$. This random field is assumed to be statistically uniform and isotropic, so in the (rest) reference frame linked to the plasma, we have

$$T_{\alpha\beta}(\boldsymbol{r}'_1 - \boldsymbol{r}'_2, t_1 - t_2) = \langle b_\alpha(\boldsymbol{r}'_1, t_1) b_\beta(\boldsymbol{r}'_2, t_2) \rangle. \tag{7.55}$$

The astrophysical plasma is often involved in a large-scale motion with a velocity $\boldsymbol{u}$, which is assumed to have a nonrelativistic value, $\boldsymbol{u} = \text{const}$. In such a case the radius-vectors in the laboratory and co-moving systems are related to each other as $\boldsymbol{r} = \boldsymbol{r}' + \boldsymbol{u}t$. Assume the fast particle velocity v to be much larger than any of the characteristic plasma velocities:

$$v \gg u, \qquad v \gg v_{ph} \qquad (v \gg c_s,\ v_\mathrm{A}), \tag{7.56}$$

since the velocity v_{ph} of the magnetic irregularities propagation relative to the plasma is specified by a combination of the sound c_s and Alfvén v_A velocities. Under adopted conditions, the magnetic irregularities can be consistently considered as stationary ones (in the plasma co-moving system), so the correlation tensor in the laboratory system (in which the plasma moves) receives the form

$$\langle b_\alpha(\boldsymbol{r}_1, t_1) b_\beta(\boldsymbol{r}_2, t_2)\rangle = T_{\alpha\beta}(\boldsymbol{r}_1 - \boldsymbol{r}_2 - \boldsymbol{u}(t_1 - t_2)). \tag{7.57}$$

Thus, we have neglected the phase velocities of the MHD waves and corresponding electric fields; however, the bulk velocity $\boldsymbol{u}$ can be much larger than the phase velocities, i.e., for solar and stellar winds ($u \approx$ 300–1,000 km/s), supernova explosions ($u \approx$ 3,000–30,000 km/s), and galactic and extragalactic jets (relativistic or even ultrarelativistic in case of the gamma-ray burst jets), which we will take into account. Apparently, this motion induces an electric field in the laboratory system according to Eq. (2.19).

Let us denote the exact (fluctuating) distribution function of the fast particles as $f(\boldsymbol{r}, \boldsymbol{p}, t)$; apparently, it satisfies the collisionless kinetic equation:

$$\frac{\partial f}{\partial t} + \boldsymbol{v} \cdot \frac{\partial f}{\partial \boldsymbol{r}} + \boldsymbol{\mathcal{F}} \cdot \frac{\partial f}{\partial \boldsymbol{p}} = 0. \tag{7.58}$$

The force

$$\boldsymbol{\mathcal{F}} = e\boldsymbol{E} + \frac{e}{c}\boldsymbol{v} \times \boldsymbol{B} = \frac{e}{c}(\boldsymbol{v} - \boldsymbol{u}) \times \boldsymbol{B} \tag{7.59}$$

contains both electric and magnetic components. Write down Eq. (7.58) in the form:

$$\frac{\partial f}{\partial t} + \boldsymbol{v} \cdot \frac{\partial f}{\partial \boldsymbol{r}} + \boldsymbol{B} \cdot \widehat{\boldsymbol{D}}\, f = 0, \tag{7.60}$$

where

$$\widehat{\boldsymbol{D}} = \frac{e}{c}(\boldsymbol{v} - \boldsymbol{u}) \times \frac{\partial}{\partial \boldsymbol{p}} \tag{7.61}$$

is the operator, which changes the value and direction of the particle momentum. For now we adopt the plasma velocity $\boldsymbol{u}$ to be a regular function; therefore $\widehat{\boldsymbol{D}}$ is a regular operator.

7.4.2 Small-Scale Magnetic Inhomogeneities

The distribution function describing various observable measures (including fluxes produced by numerous particles moving along unique random paths) can be found by averaging of the exact distribution function by all possible realizations of the random field:

$$F(\boldsymbol{r}, \boldsymbol{p}, t) = \langle f(\boldsymbol{r}, \boldsymbol{p}, t)\rangle. \tag{7.62}$$

Let us derive equation for this averaged function F from exact collisionless equation (7.58). We start with a simple case

$$b \lesssim B_0, \qquad R_0 = \frac{cp}{eB_0} \gg L_c, \tag{7.63}$$

where R_0 is the Larmor radius of the particle in the regular field and L_c is the correlation length of the random field. This is the case of small-scale magnetic inhomogeneities, when the particle experiences only a small Larmor rotation in the regular field and a small angular deflection due to random field over a single magnetic inhomogeneity, Fig. 7.2. On top of that we seek for the distribution function F for sufficiently long time when the particles have already interacted with many magnetic inhomogeneities.

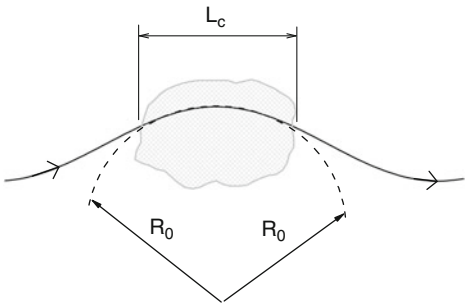

Figure 7.2: Interaction of fast particle with small-scale, $L_c \ll R_0$, magnetic inhomogeneity.

Separation of averaged and fluctuating components of the exact distribution function

$$f(\boldsymbol{r},\boldsymbol{p},t) = F(\boldsymbol{r},\boldsymbol{p},t) + \widetilde{f}(\boldsymbol{r},\boldsymbol{p},t), \qquad \langle \widetilde{f} \rangle = 0, \tag{7.64}$$

in Eq. (7.60) yields

$$\frac{\partial F}{\partial t} + \frac{\partial \widetilde{f}}{\partial t} + \boldsymbol{v}\cdot\frac{\partial F}{\partial \boldsymbol{r}} + \boldsymbol{v}\cdot\frac{\partial \widetilde{f}}{\partial \boldsymbol{r}} = \boldsymbol{B}_0\cdot\widehat{\boldsymbol{D}}\,F + \boldsymbol{B}_0\cdot\widehat{\boldsymbol{D}}\,\widetilde{f} + \boldsymbol{b}\cdot\widehat{\boldsymbol{D}}\,F + \boldsymbol{b}\cdot\widehat{\boldsymbol{D}}\,\widetilde{f}. \tag{7.65}$$

Now we are to average Eq. (7.65) over random field realizations. Using the adopted conditions $\langle \boldsymbol{b} \rangle = 0$ and $\langle \widetilde{f} \rangle = 0$ we obtain an exact equation

$$\frac{\partial F}{\partial t} + \boldsymbol{v}\cdot\frac{\partial F}{\partial \boldsymbol{r}} - \boldsymbol{B}_0\cdot\widehat{\boldsymbol{D}}\,F = \langle \boldsymbol{b}(\boldsymbol{r})\cdot\widehat{\boldsymbol{D}}\,\widetilde{f} \rangle, \tag{7.66}$$

which contains an unknown mean value of the product $\langle \boldsymbol{b}\widetilde{f} \rangle$ of two random functions ($\widehat{\boldsymbol{D}}$ is a regular operator). To close Eq. (7.66) we have yet to express

$\langle \boldsymbol{b}\cdot\widehat{\boldsymbol{D}}\,\widetilde{f}\rangle$ via the averaged function F. To do so, let us subtract Eq. (7.66) from Eq. (7.65), which yields

$$\frac{\partial\widetilde{f}}{\partial t}+\boldsymbol{v}\cdot\frac{\partial\widetilde{f}}{\partial\boldsymbol{r}}-\boldsymbol{B}_0\cdot\widehat{\boldsymbol{D}}\,\widetilde{f}=\boldsymbol{b}\cdot\widehat{\boldsymbol{D}}\,F+\boldsymbol{b}\cdot\widehat{\boldsymbol{D}}\,\widetilde{f}-\langle\boldsymbol{b}\cdot\widehat{\boldsymbol{D}}\,\widetilde{f}\rangle.$$

Assume further that the quasilinear approximation (see Sects. 4.2 and 6.11) applies, so the difference between two last terms in the rhs is small and they can be discarded from the equation. In fact, under condition (7.63), an even stronger inequality

$$|\widetilde{f}|\ll F, \tag{7.67}$$

takes place, which justifies discarding of any of these two terms independently. Therefore, the equation for the fluctuating component $\widetilde{f}$ of the distribution function reduces to the inhomogeneous equation:

$$\frac{\partial\widetilde{f}}{\partial t}+\boldsymbol{v}\cdot\frac{\partial\widetilde{f}}{\partial\boldsymbol{r}}-\boldsymbol{B}_0\cdot\widehat{\boldsymbol{D}}\,\widetilde{f}=\boldsymbol{b}\cdot\widehat{\boldsymbol{D}}\,F\equiv Q(\boldsymbol{r},\boldsymbol{p},t). \tag{7.68}$$

We have used Q for the rhs of the equation, which formally plays a role of a source for the random function $\widetilde{f}$, which has to be calculated for the scales about the correlation length L_c and time about the correlation time L_c/v needed for the particle to cross an inhomogeneity because the mean value $\langle\boldsymbol{b}\widetilde{f}\rangle$ is apparently proportional to the random field correlation tensor, which specifies the effective ranges of the integrations.

The solution of inhomogeneous equation (7.68) can be written down via the Green function of the corresponding homogeneous equation:

$$\widehat{L}G(\boldsymbol{r},\boldsymbol{p},t;\boldsymbol{r}',\boldsymbol{p}',t')=\delta(\boldsymbol{r}-\boldsymbol{r}')\delta(\boldsymbol{p}-\boldsymbol{p}')\delta(t-t'),\qquad\text{where }\widehat{L}=\frac{\partial}{\partial t}+\boldsymbol{v}\cdot\frac{\partial}{\partial\boldsymbol{r}}-\boldsymbol{B}_0\cdot\widehat{\boldsymbol{D}}. \tag{7.69}$$

At the correlation length we can discard the bulk velocity u because of $u\ll v$. Then, under conditions (7.63) a trajectory of any single particle is almost a straight line, implying constancy of the momentum vector. Therefore, a free-streaming Green function

$$G(\boldsymbol{r},\boldsymbol{p},t;\boldsymbol{r}',\boldsymbol{p}',t')=\delta(\boldsymbol{r}-\boldsymbol{r}'-\boldsymbol{v}(t-t'))\delta(\boldsymbol{p}-\boldsymbol{p}')\Theta(t-t') \tag{7.70}$$

can safely be used in this case. The fluctuating component receives the form

$$\widetilde{f}=\int_{-\infty}^{t}Q(\boldsymbol{r}-\boldsymbol{v}(t-t'),\boldsymbol{p},t')\mathrm{d}t'=\int_{-\infty}^{t}\boldsymbol{b}(\boldsymbol{r}-\boldsymbol{v}(t-t')-\boldsymbol{u}t')\cdot\widehat{\boldsymbol{D}}\,F(\boldsymbol{r}-\boldsymbol{v}(t-t'),\boldsymbol{p},t')\mathrm{d}t'. \tag{7.71}$$

Let us estimate its order of magnitude. The effective integration range over t' is about L_c/v, the operator $\widehat{\boldsymbol{D}}\sim ev/cp$; thus, $\widetilde{f}\sim(ebL_c/cp)F\approx(L_c/r_g)F$,

where $r_g \approx cp/eb$ is the Larmor radius of the particle in the random field. Inequalities (7.63) yield $L_c \ll r_g$ and so $|\widetilde{f}| \ll F$, as has already been noted.

The rhs of Eq. (7.66) contains now the averaged distribution function F itself and the correlation tensor

$$\langle \boldsymbol{b}(\boldsymbol{r}) \cdot \widehat{\boldsymbol{D}}\, \widetilde{f} \rangle = \widehat{D}_\alpha \int_{-\infty}^{t} T_{\alpha\beta}((\boldsymbol{v}-\boldsymbol{u})(t-t')) \widehat{D}_\beta F(\boldsymbol{r}-\boldsymbol{v}(t-t'), \boldsymbol{p}, t')\mathrm{d}t', \quad (7.72)$$

so Eq. (7.66) is a closed one. Let us further simplify it. Note that the tensor $T_{\alpha\beta}$ vanishes for the arguments larger than L_c; thus, at the order of magnitude, we have $v(t-t') \approx L_c$. The averaged distribution function F changes only slightly over the correlation length if the particles have already interacted with a few magnetic inhomogeneities. Likewise, it varies weakly over the time $t - t' \approx L_c/v$ needed to path through one inhomogeneity. Thus, in Eq. (7.72), the arguments of F can be replaced: $\boldsymbol{r}'$ by $\boldsymbol{r}$ and t' by t that takes it out from the integral, so only the correlation tensor has to be integrated:

$$\langle \boldsymbol{b}(\boldsymbol{r}) \cdot \widehat{\boldsymbol{D}}\, \widetilde{f} \rangle = \widehat{D}_\alpha \left(\int_0^\infty T_{\alpha\beta}((\boldsymbol{v}-\boldsymbol{u})\tau)\mathrm{d}\tau \right) \widehat{D}_\beta F(\boldsymbol{r}, \boldsymbol{p}, t). \quad (7.73)$$

The most general functional form of the correlation tensor of the statistically uniform and isotropic random field is

$$T_{\alpha\beta}((\boldsymbol{v}-\boldsymbol{u})\tau) = T((\boldsymbol{v}-\boldsymbol{u})\tau)\delta_{\alpha\beta} + P((\boldsymbol{v}-\boldsymbol{u})\tau)\frac{(\boldsymbol{v}-\boldsymbol{u})_\alpha (\boldsymbol{v}-\boldsymbol{u})_\beta}{(\boldsymbol{v}-\boldsymbol{u})^2}, \quad (7.74)$$

where $T(r)$ and $P(r)$ are two scalar function satisfying the conditions:

$$T(0) = \frac{1}{3}\langle b^2 \rangle, \qquad P(0) = 0; \quad (7.75)$$

$\langle b^2 \rangle$ is the mean square of the random field. The second term in Eq. (7.74) does not contribute to the rhs of Eq. (7.73), because $(\boldsymbol{v}-\boldsymbol{u})_\beta \widehat{\boldsymbol{D}}_\beta = 0$. Let us define the correlation length by the condition

$$\int_0^\infty T(r)\mathrm{d}r = \frac{1}{3}\langle b^2 \rangle L_c. \quad (7.76)$$

Then

$$\int_0^\infty T(|\boldsymbol{v}-\boldsymbol{u}|\tau)\mathrm{d}\tau = \frac{\langle b^2 \rangle L_c}{3|\boldsymbol{v}-\boldsymbol{u}|}$$

and kinetic equation (7.66) with account of Eqs. (7.73) and (7.76) receives the differential form

$$\frac{\partial F}{\partial t} + \boldsymbol{v} \cdot \frac{\partial F}{\partial \boldsymbol{r}} - \boldsymbol{B}_0 \cdot \widehat{\boldsymbol{D}}\, F = \frac{1}{3}\langle b^2 \rangle L_c \widehat{\boldsymbol{D}} \frac{1}{|\boldsymbol{v}-\boldsymbol{u}|} \widehat{\boldsymbol{D}}\, F. \quad (7.77)$$

The rhs of this equation, which describes interactions of the charged particles with moving magnetic inhomogeneities, plays a role of an effective collision integral. The regular functions $\boldsymbol{B}_0$, $\boldsymbol{u}$, and $\langle b^2 \rangle$ can be gradual functions of the coordinates, which are almost constant within the correlation length. Note that $u \ll v$, so the difference $|\boldsymbol{v} - \boldsymbol{u}|$ is always nonzero.

In the fluid at rest we have $\boldsymbol{u} = 0$ so the operator $\widehat{\boldsymbol{D}}$ receives the form

$$\widehat{\boldsymbol{D}} = \frac{ec}{\mathcal{E}} \widehat{\boldsymbol{\mathcal{O}}}, \qquad \text{where} \qquad \widehat{\boldsymbol{\mathcal{O}}} = \boldsymbol{p} \times \frac{\partial}{\partial \boldsymbol{p}} \tag{7.78}$$

is the operator of angular variation of the particle momentum. The absolute value of the momentum and the energy are constant in this case, so only elastic scattering takes place. Kinetic equation (7.77) simplifies to the form

$$\frac{\partial F}{\partial t} + \boldsymbol{v} \cdot \frac{\partial F}{\partial \boldsymbol{r}} - \frac{ec}{\mathcal{E}} \boldsymbol{B}_0 \cdot \widehat{\boldsymbol{\mathcal{O}}} F = \frac{v}{2\Lambda(p)} \widehat{\boldsymbol{\mathcal{O}}}^2 F. \tag{7.79}$$

Here

$$\widehat{\boldsymbol{\mathcal{O}}}^2 = \frac{1}{\sin\vartheta} \frac{\partial}{\partial \vartheta} \sin\vartheta \frac{\partial}{\partial \vartheta} + \frac{1}{\sin^2 \vartheta} \frac{\partial^2}{\partial \varphi^2}, \quad \Lambda(p) = \frac{3 r_g^2}{2 L_c}, \quad r_g^2 = \frac{c^2 p^2}{e^2 \langle b^2 \rangle}, \tag{7.80}$$

$\Lambda(p)$ is the transport mfp of the particle, i.e., the distance at which the particle is deflected by an angle of the order of 1 rad and r_g^2 is the square of the Larmor radius in the random field. As we adopted $R_0 \gg L_c$, we have accordingly $\Lambda(p) \gg r_g \gg L_c$ and $\Lambda(p) \propto p^2$, while R_0 can have arbitrary value relative to Λ. The operator $\widehat{\boldsymbol{\mathcal{O}}}^2$ in the rhs of Eq. (7.79) is the angular part of the Laplace operator in the momentum space. Note, finally, that in the considered case the mfp depends only on the correlation length and mean square of the magnetic field, while does not depend on the spatial spectrum of the magnetic irregularities, which is an attribute of the adopted here small-scale regime. The motion of the particle represents, therefore, a random walk due to small stochastic deflections by individual magnetic irregularities, i.e., angular diffusion in the momentum space.

7.4.3 Particle Diffusion in Coordinate Space

In a general case kinetic equation (7.79) can describe anisotropic particle distributions. However, if the departure from the isotropy is small, this equation can be further simplified. In practice the anisotropy significantly reduces far away $\Delta r \gg \Lambda$ from an anisotropic source. Adopt this weakly anisotropic distribution function to have the form

$$F(\boldsymbol{r}, \boldsymbol{p}, t) = \frac{1}{4\pi} \left[N(\boldsymbol{r}, p, t) + \frac{3}{v^2} \boldsymbol{v} \cdot \boldsymbol{J}(\boldsymbol{r}, p, t) \right], \tag{7.81}$$

where

$$N(\boldsymbol{r},p,t)=\int F(\boldsymbol{r},\boldsymbol{p},t)\mathrm{d}\Omega_p, \qquad \boldsymbol{J}(\boldsymbol{r},p,t)=\int \boldsymbol{v}F(\boldsymbol{r},\boldsymbol{p},t)\mathrm{d}\Omega_p \tag{7.82}$$

are, respectively, an isotropic part of the distribution function and a flux density of the particles with a given energy; weak anisotropy implies $J \ll vN$.

Let us derive a closed form of equation for $N(\boldsymbol{r},p,t)$. We substitute Eq. (7.81) into Eq. (7.79) and isolate the angle-independent terms from the terms proportional to $\boldsymbol{p}/p$, which gives rise to two equations:

$$\frac{\partial N}{\partial t}+\nabla\cdot\boldsymbol{J}=0, \tag{7.83a}$$

$$\frac{\Lambda}{v}\frac{\partial \boldsymbol{J}}{\partial t}+\boldsymbol{J}+\frac{\Lambda}{R_0}\boldsymbol{b}_0\times\boldsymbol{J}=-\frac{v\Lambda}{3}\nabla N, \qquad \boldsymbol{b}_0=\frac{\boldsymbol{B}_0}{B_0}. \tag{7.83b}$$

The first term in Eq. (7.83b) can be estimated as $(\Lambda/v)(J/t)\approx(\tau_s/t)J$, where $\Lambda/v=\tau_s$ is the particle isotropization time. The anisotropy is small at the time $t\gg\tau_s$, when this term can be discarded. So truncated equation links the flux density and the gradient of the number density:

$$J_\alpha=-\kappa_{\alpha\beta}\nabla_\beta N, \qquad \text{where}$$
$$\kappa_{11}=\kappa_{22}=\kappa_\perp=\frac{\kappa_\parallel R_0^2}{R_0^2+\Lambda^2},\ \kappa_{33}=\frac{v\Lambda}{3}=\kappa_\parallel,\ \kappa_{12}=-\kappa_{21}=\kappa_H=\frac{\kappa_\parallel\Lambda R_0}{R_0^2+\Lambda^2}. \tag{7.84}$$

Here axes 3 is directed along the field $\boldsymbol{B}_0$. The anisotropy weakness further implies $|\Lambda\nabla N/N|\ll 1$.

The anisotropy of the diffusion tensor is provided by the regular large-scale field. It has the same structure as differently obtained diffusion tensor (7.19) and (7.17) and tensor of the magnetized plasma conductivity (see Sects. 1.3.4 and 7.2). Note that the following relation takes place

$$\frac{\Lambda}{R_0}=\frac{v\tau_s eB}{cp}=\Omega\tau_s, \quad \text{where} \quad \Omega=\frac{ceB}{\mathcal{E}} \tag{7.85}$$

is the gyration frequency of a particle with an arbitrary (i.e., relativistic) energy, $\mathcal{E}$ is the full energy of the particle (including the rest energy), and $\tau_s=\Lambda/v$ is the effective isotropization time.

Off-diagonal components κ_H describe the Hall effect induced by the external magnetic field. For $B_0\to 0$ ($R_0\to\infty$) the diffusion becomes isotropic: $\kappa_{\alpha\beta}=\kappa\delta_{\alpha\beta}$, $\kappa=\kappa_\perp=\kappa_\parallel=v\Lambda/3$, and $\kappa_H=0$. For $R_0\ll\Lambda$ the tensor becomes strongly anisotropic:

$$\kappa_\parallel=v\Lambda/3, \quad \kappa_\perp\approx\kappa_\parallel\left(\frac{R_0}{\Lambda}\right)^2, \quad \kappa_H\approx\kappa_\parallel\frac{R_0}{L}, \quad \kappa_\perp\ll\kappa_H\ll\kappa_\parallel. \tag{7.86}$$

Substitution of flux density (7.84) into continuity equation (7.83a) yields for the general case of anisotropic diffusion:

$$\frac{\partial N}{\partial t} = \nabla_\alpha \kappa_{\alpha\beta} \nabla_\beta N. \tag{7.87}$$

We have to note, however, that such a strong anisotropy of the diffusion predicted by this "classical" theory of the particle transport is often in a conflict with observations. One of the most vivid examples of this conflict is almost isotropic distribution of the galactic cosmic rays (e.g., Berezinskii et al. 1990). Observations suggest for the vast majority of the cosmic rays (i.e., protons with energy about a few GeV) $\Lambda_\parallel$ is about 10^{18} cm. The proton gyroradius in the galactic magnetic field ($B \approx 3 \times 10^{-6}$ G) is about 10^{12} cm. This yields for the anisotropy factor $\kappa_\parallel/\kappa_\perp \approx (\Lambda_\parallel/R_0)^2 = (\omega_B \tau)^2$ a very big value, 10^{12}. Nevertheless, numerous direct and indirect observations favor almost isotropic diffusion in contrast to the theoretical expectations. This may imply, likewise in laboratory nuclear fusion experiments (Rechester and Rosenbluth 1978), that an "anomalous" transverse transport dominates by many orders of magnitude the "normal" classical transverse transport.

For the isotropic diffusion, $\kappa_{\alpha\beta} = \kappa\delta_{\alpha\beta}$ with $\kappa = \text{const}$, we can easily derive the diffusion equation with account of $(\Lambda/v)\partial \boldsymbol{J}/\partial t$ in Eq. (7.83b). Let us differentiate equality (7.83a) over time and substitute the derivative

$$\frac{\partial \boldsymbol{J}}{\partial t} = -\frac{v}{\Lambda}(\boldsymbol{J} + \kappa \nabla N)$$

into it. Then, to eliminate $\nabla \cdot \boldsymbol{J}$, use Eq. (7.83a) again and obtain the diffusion equation with the second derivative over time:

$$\frac{\partial N}{\partial t} + \frac{\Lambda}{v}\frac{\partial^2 N}{\partial t^2} = \kappa \Delta N. \tag{7.88}$$

Effects described by this improved diffusion equation (7.88) are discussed in Problem 7.5 to this chapter.

Energetic charged particles as they move from their sources through the turbulent magnetized astrophysical plasmas create electric current and electromagnetic perturbations in various spectral domains. Therefore, calculating the electric conductivity (which is in fact a kind of "electro-diffusivity") describing the energetic particle response to the external electric field makes sense. Here we calculate this conductivity in the considered model of the small-scale magnetic inhomogeneities.

To do so we adopt $\boldsymbol{u} = 0$ and assume a weak electric field $\boldsymbol{E}$ to be applied to the plasma; fast particle distribution is assumed to be uniform in space ($\partial F/\partial \boldsymbol{r} = 0$) and stationary in time ($\partial F/\partial t = 0$). Then, kinetic equation (7.79) receives the form

$$e\boldsymbol{E} \cdot \frac{\partial F}{\partial \boldsymbol{p}} - \frac{ec}{\mathcal{E}} \boldsymbol{B}_0 \cdot \boldsymbol{\mathcal{O}} F = \frac{1}{2\tau_s(p)} \boldsymbol{\mathcal{O}}^2 F, \tag{7.89}$$

where $\tau_s(p) = \Lambda(p)/v$ is again the isotropization time.

In a stationary regime the distribution function contains a weak anisotropy proportional to the small electric field $\boldsymbol{E}$; thus, it can be presented in a form of Eq. (7.81) but without arguments $\boldsymbol{r}$ and t. Substitution of Eq. (7.81) into Eq. (7.89) yields the equation for the particle flux density $\boldsymbol{J}(p)$ induced by the electric field:

$$\boldsymbol{J} + \Omega\tau_s \boldsymbol{e}_0 \times \boldsymbol{J} = \frac{e\tau_s v}{3}\frac{\partial N}{\partial p}\boldsymbol{E}, \qquad \boldsymbol{e}_0 = \frac{\boldsymbol{B}_0}{B_0}. \tag{7.90}$$

The current density $\boldsymbol{j}$ related to the energetic particles can be calculated as

$$\boldsymbol{j} = e\int \boldsymbol{v}F\,\mathrm{d}^3p = e\int \boldsymbol{J}(p)p^2\mathrm{d}p. \tag{7.91}$$

Solving Eq. (7.90) for the components of vector $\boldsymbol{J}$ and integrating further according to Eq. (7.91) we obtain the standard expression for the current density in a gyrotropic fluid [cf. Eq. (1.102)]:

$$\boldsymbol{j} = \sigma_\parallel \boldsymbol{E}_\parallel + \sigma_\perp \boldsymbol{E}_\perp - \sigma_H \boldsymbol{e}_0 \times \boldsymbol{E}, \tag{7.92}$$

where the conductivity components have the form

$$\sigma_\parallel = \int \sigma_\parallel(p)\mathrm{d}p, \qquad \sigma_\perp = \int \frac{\sigma_\parallel(p)}{1+\Omega_B^2\tau_s^2}\mathrm{d}p,$$

$$\sigma_H = \int \frac{\sigma_\parallel(p)\Omega_B\tau_s}{1+\Omega_B^2\tau_s^2}\mathrm{d}p, \qquad \sigma_\parallel(p) = -\frac{e^2\tau_s(p)vp^2}{3}\frac{\partial N}{\partial p}. \tag{7.93}$$

The conductivity components can be expressed via the diffusion coefficients; in the case of strongly magnetized plasma ($\Omega\tau_s \gg 1$) the corresponding relations have the form

$$\sigma_\parallel = \frac{4e^2N_0}{3}\overline{\left(\frac{\Lambda_\parallel(p)}{p}\right)}, \qquad \sigma_\perp = \frac{4e^2N_0}{3}\overline{\left(\frac{\Lambda_\perp(p)}{p}\right)}, \qquad \sigma_H = \frac{ecN_0}{B}. \tag{7.94}$$

Here $\Lambda_\parallel(p) = v\tau_s(p)$ is the longitudinal (along the field $\boldsymbol{B}_0$) mfp of an energetic particle having a given energy, $\Lambda_\perp(p) = R_0^2(p)/\Lambda_\parallel(p)$ is the transverse mfp, the overline denotes the averaging over the distribution function $N(p)$, and $N_0 = \int_0^\infty N(p)p^2\mathrm{d}p$ is the total number density of the energetic (nonthermal) particles. The mfps are linked with the diffusion coefficients by the standard relations $\kappa_{\perp,\parallel}(p) = v\Lambda_{\perp,\parallel}(p)/3$. Therefore, in the case of the strong gyrotropy, the ratios of the diffusion coefficients to the conductivities, averaged over the particle spectrum, receive the form similar to Eq. (7.24)

$$\overline{\left(\frac{\kappa_{\perp,\parallel}}{\sigma^r_{\perp,\parallel}}\right)} = \frac{\overline{pv}}{4e^2N_0} = 4\pi R_D^2, \quad \text{where} \quad R_D \approx \sqrt{\frac{\overline{K}}{8\pi e^2 N_0}} \tag{7.95}$$

plays a role similar to the classical Debye radius, but for the particles with an arbitrary energy spectrum. In this case $\overline{K}$ is the mean value of their kinetic energy (which substitutes the temperature). Given that the fast particle number density N_0 is often small compared with that of the background particles, $N_0 \ll n_0$, while their mean energy is large compared with the main plasma temperature $\overline{K} \gg T$, the effective Debye radius R_D can be larger than the classical Debye radius r_D by many orders of magnitude.

7.4.4 Resonant Scattering of Particles by Waves

Although the considered above case of the charge particle scattering by small-scale magnetic inhomogeneities is relatively simple, in a more realistic situation, there is a broad spectrum of waves composed of both small- and large-scale components of which each particle selects itself the part of the spectrum to interact the most effectively; this is the case of resonant scattering of the particles by waves (see Sect. 4.2). There is huge literature on the subject; here we consider resonant scattering of fast electrons by whistler waves (see Chap. 3) following mainly Hamilton and Petrosian (1992). In contrast to Chap. 4, where we concentrated on wave generation by charge particles, here we consider an effect of a given whistler-wave spectrum on the fast electron transport.

Having in mind application to electron transport in solar coronal magnetic flux tubes we write down the kinetic equation in terms of dimensionless electron kinetic energy $E = \gamma - 1$ taking into account Coulomb collisions of fast with background electrons and converging/diverging magnetic field effect:

$$\frac{\partial f}{\partial t} = -c\beta\cos\vartheta\frac{\partial f}{\partial s} - \frac{c\beta\sin\vartheta}{2}\frac{\mathrm{d}\ln B}{\mathrm{d}s}\frac{\partial f}{\partial\vartheta} - \frac{\partial}{\partial E}(\dot{E}_L f) + \frac{1}{\sin\vartheta}\frac{\partial}{\partial\vartheta}\sin\vartheta D_{\vartheta\vartheta}\frac{\partial f}{\partial\vartheta} + \frac{1}{p^2(E)}\frac{\partial}{\partial E}(p^2(E)D_{EE})\frac{\partial f}{\partial E} + \cdots + S(E,\vartheta,s,t), \tag{7.96}$$

where s is the coordinate along the magnetic loop, $\dot{E}_L$ is the energy loss rate (e.g., due to Coulomb collisions), $D_{\vartheta\vartheta}$ and D_{EE} are the angular and energy diffusion coefficients (s^{-1}), and $S(E,\vartheta,s,t)$ is the particle source term. Note that in the absence of the waves the fast particle still experiences angular diffusion due to Coulomb collisions with the corresponding diffusion coefficient

$$D_{\vartheta\vartheta(\mathrm{C})} = \frac{c}{\lambda_0\beta^3\gamma^2}, \tag{7.97}$$

where $\lambda_0 = 10^{24}/(n(s)\ln\Lambda_\mathrm{C})$, $n(s)$ is the local thermal plasma density, and $\ln\Lambda_\mathrm{C} \sim 20$ is the Coulomb logarithm. Apparently, the presence of the wave spectrum can only increase (but not decrease) the angular diffusion of the electrons compared with Coulomb case described by Eq. (7.97).

The resonant condition of the wave–particle interaction (Chap. 4) has the form

$$\omega - kc\beta\cos\theta\cos\vartheta - \frac{\hat{s}\omega_{\rm Be}}{\gamma} = 0, \tag{7.98}$$

where $\hat{s}$ (not to be mixed with the coordinate s) is an integer (positive or negative) order of the gyroresonance; $\hat{s} = 0$ implies Cherenkov resonance. A given particle may or may not have a resonance with a particular wave mode depending on the wave dispersion relation (e.g., Sect. 3.2.3 and Chap. 3 in general) and the particle momentum. For example, the nonrelativistic electrons do not have any gyroresonance with either Alfvén or fast mode in typical conditions of the solar corona, although they can have a Cherenkov resonance ($\beta_\parallel = \beta_{\rm A}/\cos\theta$; the transverse electron momentum is not involved) with oblique fast modes for which the refractive index is $n_f = \beta_A^{-1}$;

$$\beta_{\rm A} \equiv \frac{v_A}{c} = 7.27\times10^{-3}\left(\frac{B}{100\,{\rm G}}\right)\left(\frac{n_e}{10^{10}\,{\rm cm}^{-3}}\right)^{-1/2}. \tag{7.99}$$

In contrast, no Cherenkov resonance is possible with the Alfvén mode, for which $n_{\rm A} = \beta_{\rm A}^{-1}|\cos\theta|^{-1}$: the presence of the term $|\cos\theta|^{-1}$ in the refractive index reduces the resonant region to a single point, $\beta_\parallel = \beta_{\rm A}$ in a given magnetic field. Apparently, relativistic electrons with $\beta\gamma > (\beta\gamma)_{\rm th} \equiv (m_p/m_e)\beta_{\rm A}$, which corresponds to a few MeV in typical coronal conditions, have gyroresonances with the MHD waves.

For the whistler waves the refractive index (see Problem 3.4) can be written in the form

$$n_w^2 \approx 1 + \frac{m_e}{m_p\beta_{\rm A}^2}\frac{\omega_{\rm Be}}{\omega(\cos\theta - \omega/\omega_{\rm Be})}, \qquad \omega_{\rm pe} < \omega < \omega_{\rm Be}, \tag{7.100}$$

which has a minimum of $n_{w,\min} = [1 + (4m_e/m_p)(\beta_{\rm A}\cos\theta)^{-2}]^{1/2}$ at $\omega = \omega_{\rm Be}|\cos\theta|/2$ and increases infinitely as $\omega \to \omega_{\rm Be}|\cos\theta|$; thus, all electrons with energy up to $(\beta\gamma)_{\rm th}$ can be involved in the resonant interaction with the whistler waves. In many cases the energy change of the electrons due to resonant interaction with the wave turbulence (e.g., whistler turbulence) occurs over a longer (or much longer) time scale than the corresponding angular diffusion. For this reason, we neglect here the effect of electron acceleration by the turbulence (though return to it in Chap. 11), while we consider the transport related to the interaction with whistler turbulence.

Let us estimate the electron mfp and the electron escape time from a source with linear scale L. The mfp Λ is a distance over which the particle velocity direction changes by an angle of the order of 1 rad, which is the product of the particle velocity βc and the isotropization time $\tau_s \sim 1/\langle D_{\vartheta\vartheta}\rangle$, i.e., $\Lambda = \beta c/\langle D_{\vartheta\vartheta}\rangle$, where $\langle D_{\vartheta\vartheta}\rangle$ is the appropriately averaged angular diffusion coefficient. Accordingly, the escape time $\tau_e(E) = L^2/\kappa$ is the time needed

for a particle to diffuse the distance of the order of L with the real space diffusion coefficient $\kappa = \beta c\Lambda/3$; thus,

$$\tau_e(E) = \frac{3L^2}{\beta^2 c^2} \langle D_{\vartheta\vartheta} \rangle . \tag{7.101}$$

Specific form of the momentum space diffusion coefficients depends on the wave turbulence spectrum. We adopt a simple power-law describing the whistler-wave energy density

$$W_w(k) = \frac{q-1}{k_0} \left(\frac{k_0}{k} \right)^q W_{\rm tot}; \qquad W_{\rm tot} = \int\limits_{k_0}^{\infty} W_w(k) {\rm d}k, \tag{7.102}$$

where $W_{\rm tot}$ is the total energy density of the whistler turbulence above the minimum wave number k_0. It is reasonable to associate this minimum wave number with the threshold wave number of the whistler mode, $k_{\rm th} = \omega_{\rm Bp}/(c\beta_{\rm A})$ corresponding to $\omega = \omega_{\rm Bp}$, then the diffusion coefficients receive the form

$$\begin{pmatrix} D^w_{\vartheta\vartheta} \\ D^w_{\rm pp} \end{pmatrix} = \omega_{\rm Be} \sin^2\vartheta |\cos\vartheta|^{q-1} \left(\frac{k_{th} c}{\omega_{\rm Be}} \right)^{q-1} \frac{(\beta\gamma)^{q-1}}{\gamma} \left(\frac{8\pi W_{\rm tot}}{B^2} \right) \begin{bmatrix} I^w_{\vartheta\vartheta}(q) \\ \frac{m_p^2 c^2 \beta_{\rm A}^4 I^w_{\rm pp}}{\beta^2} \end{bmatrix}, \tag{7.103}$$

where numeric constants dependent on the turbulence spectral index q, $I^w_{\vartheta\vartheta}(q) = \pi q/[4(q+1)]$ and $I^w_{\rm pp}(q) = \pi(q-1)^2(q+2)/(2q(q-2))^2$, are introduced.

Having the momentum space diffusion coefficients specified, one can now solve numerically Eq. (7.96) to study in detail how the electron isotropization and transport occur in the presence of the whistler-wave turbulence. Here we make some estimates to illustrate how the whistler-wave-mediated electron transport can be recognized observationally compared with, e.g., collisional transport. To do so we consider the time evolution, and specifically the decay phase, of solar microwave continuum bursts, produced by accelerated electrons via GS emission mechanism (see Chaps. 9 and 10 for more detail).

In the case of the GS emission, a higher-frequency emission is produced by correspondingly higher-energy electrons. The lifetime of the electrons against the Coulomb collisions increases with electron energy; thus, the higher the radio frequency the longer the decay time of the corresponding light curve (for other equal conditions). In some solar flares this effect is prominently present, which implies a collisional transport regime. In other events, however, the decay time may not depend or can even decrease with the frequency increase.

Specifically, consider one vivid example of the observed frequency independence of the decay constants of the radio emission of the 24 October 2001 solar flare (Bastian et al. 2007). As has been said, this feature is clearly

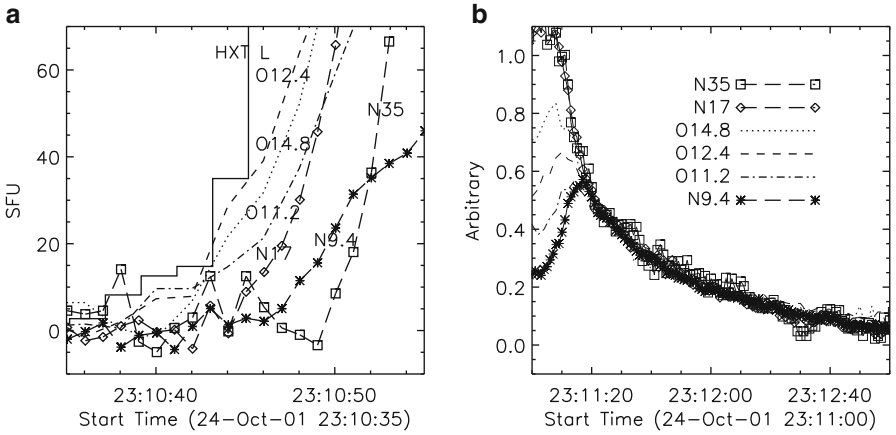

Figure 7.3: (**a**) Detail of the impulsive rise of the 24 October 2001 burst comparing the HXT Yokhoh L band and selected NoRP and OVSA frequencies. (**b**) Detail of the decay phase. The *light curves* at NoRP and OVSA frequencies labeled, respectively, by either N or O and a number indicating frequency in GHz, have been scaled to emphasize that the decay rate of each is essentially identical after 23:11:20 UT (Bastian et al. 2007). Reproduced by permission of the AAS.

at odds with flare transport models in which the weak (Coulomb) diffusion regime and magnetic trapping play a significant role: the radio decay profiles for the Oct 24 event are essentially identical (Fig. 7.3b), being of the order of 50 s for all frequencies with detectable emission for times later than approximately 23:11:20 UT. We conclude that Coulomb collisions do not appear to play a role in the transport of the 100s keV to MeV radio-emitting electrons. Instead, wave-particle interactions, as those considered above involving the whistler-mode turbulence, must mediate electron transport.

Assuming the spectral energy density of whistler-wave turbulence to be isotropic and to obey power-law dependence (7.102) we apply the developed theory to specify the energy dependence of the electron mfp $\Lambda = \beta c/\langle D_{\alpha\alpha}\rangle \propto (\beta\gamma)^{2-q}$. For a source of size L, taken here to be the observed loop length of $\approx 2 \times 10^9$ cm (Bastian et al. 2007), the electron lifetime in the source τ_e is given by $\tau_e = L^2/(\Lambda\beta c) \propto (\beta\gamma)^{q-2}/\beta$. Expressing the energy density in the turbulent spectrum relative to that in the magnetic field, $R = 8\pi W_{\rm tot}/B^2$, we find that for a given magnetic field at the source, ~ 150 G, Λ and τ_e depend on values assumed for the turbulence index q and R. For the resonant turbulent transport on the whistler waves to be relevant we must have $\Lambda \ll L$ and $\tau_e \approx 50$ s . These requirements can be met when $q \sim 2$ and $R \approx 10^{-4}$. With $\tau_e \propto (\beta\gamma)^{q-2}/\beta$ and $q \sim 2$, Λ is essentially independent of energy and τ_e depends only weakly on energy. We therefore conclude that the whistler turbulence with modest parameters can easily mediate the fast electron transport in this

solar flare and, in fact, in many other events revealing prominent departure from the collisional transport signatures (see also Sect. 7.5.3).

7.5 Diffusion in a Strong Magnetic Field with Large-Scale Turbulence

7.5.1 Longitudinal Particle Diffusion in a Strong Magnetic Field

In a reality the magnetic field often contains a very broad spectrum of the spatial scales. For example, in the Galaxy the largest turbulence scale is around 3×10^{20} cm $=100$ pc, while the minimum scale is at least 10–12 orders of magnitude smaller. This implies that the condition $R_0 \gg L_c$, employed above (other than in Sect. 7.4.4), does not in fact take place in many cases. A more likely scale hierarchy is

$$l_m \ll R_0 \ll L_c, \tag{7.104}$$

where l_m is the minimal scale of the turbulence. Here we perform an order of magnitude estimate of the diffusion coefficient assuming the turbulent field to be small to show that the most essential results of Sect. 7.4.4 have in fact much broader applicability region than those specific conditions adopted there; for more quantitative kinetic treatment, see Toptygin (1985).

If there is a broad spectrum of the turbulent pulsations in range (7.104), Fig. 7.4, then the small-scale ($l < R_0$) and the large-scale ($l > R_0$) magnetic irregularities affect the particle motion differently. Indeed, the small-scale

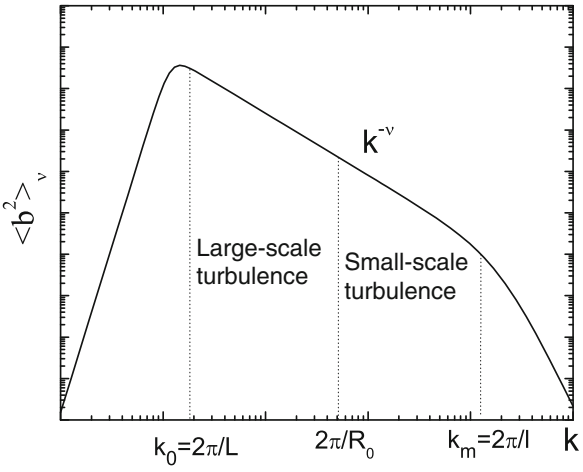

Figure 7.4: Large-scale and small-scale magnetic turbulence.

irregularities give rise to the particle scattering and so form its transport mfp along the regular field $\boldsymbol{B}_0$. An order of magnitude estimate of this mfp, $\Lambda_\parallel$, can be obtained with Eq. (7.80), but substituting R_0 for L_c and using for the turbulent field $\langle b^2\rangle$ a part of the whole turbulent field pertained to the small-scale ($R_0 \geq l \geq l_m$) region of the spectrum. Let us adopt that the turbulence spectrum can be approximated by a power-law over the wave number with an index ν:

$$\langle b^2\rangle_k = (\nu-1)\langle \widetilde{B}^2\rangle \frac{k_c^{\nu-1}\mathrm{d}k}{k^\nu}, \qquad \nu > 1, \tag{7.105}$$

where $\langle \widetilde{B}^2\rangle$ is the entire turbulent field. Integrating Eq. (7.105) from $k_0 = 2\pi/R_0$ to k_m ($k_0 \ll k_m$), we find

$$\langle b^2\rangle = \int_{k_0}^{k_m} \langle b^2\rangle_k \mathrm{d}k = \langle \widetilde{B}^2\rangle \left(\frac{R_0}{L_c}\right)^{\nu-1},$$

and then using R_0 for L_c in Eq. (7.80) we obtain

$$\Lambda_\parallel \approx \frac{B_0^2}{\langle \widetilde{B}^2\rangle}\left(\frac{R_0}{L_c}\right)^{2-\nu} L_c. \tag{7.106}$$

This estimate is correct to an unknown dimensionless factor of order of one.

A substantial difference between Eqs. (7.106) and (7.80) is that the mfp depends now on the functional shape of the magnetic irregularity spectrum. The derived dependence of the mfp on the momentum $\Lambda_\parallel \sim p^{2-\nu}$ implies that the mfp increases with the particle energy for $\nu < 2$, it is constant for $\nu = 2$, and decreases with the energy for $\nu > 2$. The longitudinal diffusion coefficient is linked to the mfp by the standard formula $\kappa_\parallel = v\Lambda_\parallel/3$. Recall that for the Kolmogorov–Obukhov turbulence $\nu = 5/3$, while for the weak isotropic MHD turbulence (Kreichnan–Iroshnikov) $\nu = 3/2$. The value of $\nu = 2$ corresponds to a turbulence composed of discontinuities (including the shock waves). Thus, for typical turbulence spectra (see Chap. 6), the particle mfp increases with its energy, although the opposite behavior might be expected in some peculiar cases. Note that this consideration is in full agreement with a more detailed analysis of the electron transport mediated by the whistler-wave turbulence, Sect. 7.4.4.

7.5.2 Transverse Particle Diffusion: Wandering of Magnetic Force Lines

Consider now what role the *large-scale inhomogeneities* play in the particle transport. The magnetic fields with $l > R_0$ affect the particles adiabatically, so the transverse adiabatic invariant $p_\perp^2/B = \mathrm{const}$ is conserved [see Eq. (1.46) in Sect. 1.2.3]. The particle-guiding center moves primarily along

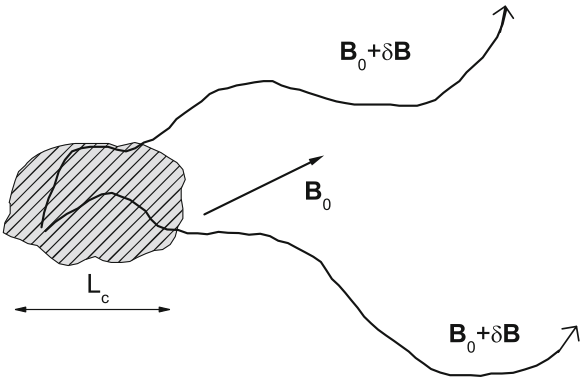

Figure 7.5: Stochastic wandering of magnetic force lines.

a field line, while participating in minor transverse drifts. However, the field line is now formed by the total large-scale field composed of both regular $\boldsymbol{B}_0$ and large-scale random $\widetilde{\boldsymbol{B}}$ fields. Thus, the magnetic field lines receive a complicated tangled shape due to the random magnetic component. In particular, two field lines crossing a given spatial region within a correlation cell can diverge substantially at a distance of a few correlation lengths (Fig. 7.5). This phenomenon is known as "a wandering of magnetic force lines." For $\widetilde{B} \ll B_0$ it has only a minor effect on the longitudinal (relative to $\boldsymbol{B}_0$) particle transport, while it can greatly enhance their transverse diffusion.

Let us estimate the corresponding coefficient of transverse diffusion for two following distinct cases.

(a) Let us first adopt that $\Lambda_\parallel \gg L_c$, i.e., the particles cross the correlation cell with a rather small angular deflection. The transverse displacement of the particle as it crosses one correlation cells $l_\perp \approx \widetilde{B}L_c/B_0$, where $\widetilde{B}(\ll B_0)$ is the rms value of the random field (in fact, only the large-scale field must be included; however, it is almost equivalent to the full one for falling with k spectra of the random field). During a given time t the particle makes $N = |v_\parallel|t/L_c$ steps (i.e., crosses N correlation cells). If the walk is truly random then the displacement $\Delta L_\perp$ in the transverse direction over this time t is proportional to the square root of the number of steps $\Delta L_\perp \approx l_\perp N^{1/2}$. Thus, $(\Delta L_\perp)^2 \approx (\langle\widetilde{B}^2\rangle/B_0^2)L_c|v_\parallel|t$. Comparing this expression with $\overline{x^2} = 4\kappa_\perp t$ (see Problem 7.4), we find $\kappa_\perp \approx (\langle\widetilde{B}^2\rangle/B_0^2)L_c|v_\parallel|$, which must yet be averaged over the pitch angle. Detailed calculations based on the kinetic equation method gives rise to

$$\kappa_\perp = \frac{1}{3}v\Lambda_\perp, \qquad \Lambda_\perp = \frac{\pi^{1/2}\Gamma(\nu/2)\langle\widetilde{B}^2\rangle}{2\Gamma(\nu/2-1/2)B_0^2}\,L_c. \tag{7.107}$$

(b) In the second case, $\Lambda_\parallel \ll L_c$, the particles move through the correlation cell diffusively, i.e., they are confined within the correlation cell and reside there some time τ_l much longer than the time of the flight, $\tau_l \gg L_c/|v_\parallel|$. No simple estimate, like one given above for the case (a), has yet been obtained for this case. To describe this regime quantitatively we apply below the renormalization method already used in Sect. 7.3.2 and the kinetic equation in the guiding center approximation.

7.5.3 Kinetic Equation in Guiding Center Approximation

We have already developed (see Sects. 1.2.2 and 1.2.3) the drift approximation to describe single particle motion. Apparently, a similar treatment is available and can be very convenient to describe ensembles of the particles moving in a large-scale inhomogeneous magnetic field with a weak electric field ($E \ll B$) superimposed on it. Averaging over fast particle rotation around the field lines allows reducing the number of independent variables in the distribution function down to six of them: $f(p_\parallel, p_\perp, \boldsymbol{r}, t)$, where $p_\parallel, p_\perp$ are the momentum components relative to the direction of the large-scale field at the guiding center location. Thus, the distribution function f describes, instead of distribution of particles, the distribution of the particles' guiding centers in the five-dimensional space.

It has widely been proved that the variables $(\boldsymbol{r}, p_\parallel, p_\perp)$ are canonical and so the Liuville theorem on the phase volume conservation is valid in terms of these variables [see, e.g., the reviews by Bogoliubov and Mitropolski (1961) and Sivukhin (1965)]. This means that the distribution function as a function of the "drift" variables satisfies the kinetic equation

$$\frac{\partial f}{\partial t} + \boldsymbol{v}_c \cdot \frac{\partial f}{\partial \boldsymbol{r}} + \dot{p}_\parallel \frac{\partial f}{\partial p_\parallel} + \dot{p}_\perp \frac{\partial f}{\partial p_\perp} = 0. \tag{7.108}$$

Here $\boldsymbol{v}_c$ is given by Eq. (1.39), while $\dot{p}_\parallel$ and $\dot{p}_\perp$ can be expressed via $p_\parallel$ and $p_\perp$ and vectors of electromagnetic fields using adiabatic invariant (1.46) and Eq. (1.49). To account the particle collisions or the small-scale turbulent fields with $l \lesssim r_g$ one has to add into the rhs of Eq. (7.108) the corresponding collisional term averaged over the fast phase: $\langle St[F]\rangle_\phi = (1/2\pi)\int St[F]\mathrm{d}\phi$. For example, for the collisional term with operator (7.80), we have

$$\langle St[F]\rangle_\phi = \frac{v}{2\Lambda}\frac{1}{\sin\vartheta}\frac{\partial}{\partial\vartheta}\sin\vartheta\frac{\partial f}{\partial\vartheta}, \tag{7.109}$$

where the function f in contrast to F does not depend on ϕ. Note that here r_g denotes the particle gyroradius defined by the entire (regular plus random) magnetic field.

Equation (7.108) with account of all terms given in Sect. 1.2.3 is very complicated. Let us consider here only linear terms over the small parameters E/B and r_g/L. Also, consider only the induced electric field driven by the fluid motions $\boldsymbol{E} = -\boldsymbol{u} \times \boldsymbol{B}/c$. In this case

$$\boldsymbol{v}_c \approx v_\parallel \boldsymbol{e}_\parallel + \frac{c}{B^2}\boldsymbol{E} \times \boldsymbol{B} = (v_\parallel - u_\parallel)\boldsymbol{e}_\parallel + \boldsymbol{u}. \tag{7.110}$$

The derivative $\dot{p}_\perp$ is calculated from adiabatic invariant (1.46)

$$\dot{p}_\perp = \frac{p_\perp}{2B}\dot{B} = \frac{p_\perp}{2B}\dot{\boldsymbol{r}}_c \cdot \nabla B = -\frac{1}{2}p_\parallel v_\perp \nabla \cdot \boldsymbol{e}_\parallel. \tag{7.111}$$

Equation (1.49) in this approximation yields $\dot{\mathcal{E}} \approx e\boldsymbol{E} \cdot \boldsymbol{v}_c = 0$, which gives $\dot{p}_\parallel = -\dot{p}_\perp(p_\perp/p_\parallel)$ or equivalently

$$\dot{p}_\parallel = \frac{1}{2}p_\perp v_\perp \nabla \cdot \boldsymbol{e}_\parallel. \tag{7.112}$$

Since collisional term (7.109) depends on the pitch-angle ϑ, we have yet to change the variables from $(p_\parallel, p_\perp)$ to $\left(p = \sqrt{p_\parallel^2 + p_\perp^2},\ \vartheta = \arctan(p_\perp/p_\parallel)\right)$ and recalculate the derivatives accordingly:

$$\dot{p}_\parallel \frac{\partial f}{\partial p_\parallel} + \dot{p}_\perp \frac{\partial f}{\partial p_\perp} = \frac{v}{2B}\frac{\partial B}{\partial s}\sin\vartheta \frac{\partial f}{\partial \vartheta}, \tag{7.113}$$

where s is the coordinate along the field line $\partial f/\partial s = (\boldsymbol{e}_\parallel \cdot \nabla)f$. The derivative $\partial/\partial p$ cancels out because of energy conservation in the approximation adopted. Finally, assuming $\boldsymbol{u} = 0$ in Eq. (7.110), we obtain the following equation:

$$\frac{\partial f}{\partial t} + v\cos\vartheta \frac{\partial f}{\partial s} + \frac{v}{2B}\frac{\partial B}{\partial s}\sin\vartheta \frac{\partial f}{\partial \vartheta} = \frac{v}{2\Lambda}\frac{1}{\sin\vartheta}\frac{\partial}{\partial \vartheta}\sin\vartheta \frac{\partial f}{\partial \vartheta}. \tag{7.114}$$

This equation discards weak transverse diffusion due to particle scattering by the small-scale fields and transverse drifts; other kinds of the transverse diffusion, e.g., due to magnetic force line wandering, are considered in Sect. 7.5.2.

Equation (7.114) supplemented by fast electron source and decay terms is often used to describe transport and evolution of electrons accelerated in solar flares. An elementary structural element of a solar flare is a coronal magnetic loop (see, e.g., Fig. 1.5), whose footpoints are buried at dense layers of the solar atmosphere—chromosphere and photosphere. The electrons reaching these dense footpoints experience rapid Coulomb losses and so they are lost from the coronal loop. In case of no angular scattering each electron moves conserving its value of the transverse adiabatic invariant, $\sin^2\vartheta_{\rm LT}/B_{\rm LT} = \text{const}$, where $\vartheta_{\rm LT}$ and $B_{\rm LT} = \min(B(s))$ are the electron pitch angle and

magnetic field values at the loop top. Thus, whether an electron reaches a footpoint (and die there) depends on its initial pitch-angle $\vartheta_{\rm LT}$: if $\vartheta_{\rm LT} > \vartheta_c$, where $\sin^2\vartheta_c = B_{\rm LT}/B_{\rm FP}$, $B_{\rm FP}$ is the magnetic field at the footpoint, this electron is trapped in this coronal loop, while if $\vartheta_{\rm LT} < \vartheta_c$, then this electron precipitates to the footpoint and so it is irreversibly lost from the coronal loop (Melrose and Brown 1976). Accordingly, an anisotropic electron distribution with a "loss-cone" is formed soon after the electron injection is off.

Let us now add a weak angular scattering described by the rhs of Eq. (7.114); in this context the term "weak" means that the electron mfp is much larger than the loop length (weak diffusion regime), i.e., a few bounce times are needed to scatter the electron by angle of the order of 1 rad. Such angular scattering will smooth out (otherwise sharp) boundary of the loss cone; accordingly, the probability of the electron to be lost at a footpoint will now depend on its pitch angle: the electrons moving transverse to the magnetic field at the loop top (and so localized there) will have longer lifetime in the loop than the electrons moving there obliquely (and so reaching lower layers of the loop at a given bounce period). Apparently, such a transport regime will result in fast electron accumulation at the loop-top region, where the magnetic field is relatively small.

To be complete, mention here two more distinct transport regimes of the fast electrons in the coronal magnetic traps—regimes of the moderate and strong angular diffusion. The moderate diffusion regime occurs when the electron mfp is comparable with the loop length. In this case the loss-cone emptying due to electron precipitation to the footpoints and the loss-cone filling due to angular diffusion occur with the same rate, which implies enhanced electron precipitation to the footpoints. The strong diffusion regime means that the electron mfp is much smaller than the loop scale, which implies that the electron distribution is almost isotropic everywhere, the electrons move diffusively and so their lifetime $\tau = L^2/\kappa \gg L/v$ is defined by the loop length L and the electron diffusion coefficient κ. We employ these transport regimes later, while discussing 3D modeling of the solar flares in Sect. 10.2.2.

7.5.4 Averaging of the Drift Kinetic Equation for the Strong Turbulence

Let us consider the "anomalous" transverse transport in case of strong turbulence, i.e., in contrast to Sect. 7.5.2 we adopt the spatial scales of the random magnetic field $\widetilde{\boldsymbol{B}}(\boldsymbol{r}, t)$ are much larger than the local mfp of the particles $\Lambda_\parallel$ formed by small-scale ($l \lesssim r_g$) electromagnetic field. On top of that, there is a quasi-uniform magnetic field $\boldsymbol{B}_0$, which varies on a scale even larger than the large-scale random field. This situation is highly typical for the astrophysics; for example, in the Galaxy there is a broad spectrum of fluctuations of both magnetic field and the fluid velocity, with $\widetilde{B} \gtrsim B_0$.

If the Larmor radius of the particles is small compared with the mfp then the local diffusion is strongly anisotropic: the particles move preferably along the local magnetic field (although with small transverse deflections due to the drifts). However, the global particle transport over distances much larger than the random field correlation length and over time much longer than the correlation time can turn to become almost isotropic due to highly tangled magnetic force lines and strong transverse fluid motions. Thus, there is an important problem of linking the local and global diffusion coefficients; especially important to determine the transverse (relative to the quasi-uniform magnetic field $\boldsymbol{B}_0$) diffusion coefficient. As has been noted in Sect. 7.4.3 the Galactic CR observations favor the isotropic global transport.

To correctly describe the particle transport in a fluid with strong turbulence one has to take into account both the turbulent velocity field and the stochastic component of the large-scale magnetic field. Below we apply the method proposed by Bykov and Toptygin (1993) and Vainshtein et al. (1993) to calculate the global diffusion tensor without any constraint on the random magnetic field magnitude, i.e., including the case when $\widetilde{B} \gtrsim B_0$, along with self-consistent account of the turbulent velocity field. This method is based on the renormalization of the drift kinetic equation, a simple version of which has been presented in Sect. 7.3.2. Likewise, the diffusion tensor components will eventually be expressed via a system of transcendental equations containing second-order correlation functions of the turbulent fields.

We adopt that the turbulence correlation lengths along and transverse to the regular field have the same order of magnitude and the turbulence is spatially and temporally smooth, so the second-order correlation function is sufficient to fully quantify the turbulence. The correlation is assumed to fall quickly outside the correlation cell: if there is a certain (even not numerous) number of long narrow flux tubes, which implies the longitudinal correlation length is much larger than the transverse correlation length, see review by Isichenko (1992), the entire transverse particle transport can be controlled by such flux tubes, which can be relevant for magnetically dominated plasmas, in particular, to the magnetic loops in the solar corona. In a complex magnetic structure of the coronal magnetic field above complicated ARs, such peculiar flux tubes can provide magnetic connectivity between otherwise well-isolated regions of the solar atmosphere; this connectivity can quickly change via magnetic reconnection during solar flares and eruptions.

Let us write down drift kinetic equation for the distribution function of magnetized particles $f(p, \theta, \boldsymbol{r}, t)$ assuming zero gyroradius ($r_g \to 0$) while taking into account medium motion, electric field $-\boldsymbol{u} \times \boldsymbol{B}/c$, and electric drift velocity $c\boldsymbol{E} \times \boldsymbol{B}/B^2 = \boldsymbol{u}_\perp$ [see Eq. (7.110)]:

$$\frac{\partial f}{\partial t} + [(\boldsymbol{v} \cdot \boldsymbol{b} - \boldsymbol{u} \cdot \boldsymbol{b})\boldsymbol{b} + \boldsymbol{u}] \cdot \nabla f = -\nu(f - \overline{f}). \tag{7.115}$$

The field $\boldsymbol{u}$ of the turbulent fluid velocity is defined via the corresponding second-order correlation tensor; $\boldsymbol{b}$ is the unit vector along the full magnetic field:

$$\boldsymbol{b} = \frac{\boldsymbol{B}_0 + \widetilde{\boldsymbol{B}}}{|\boldsymbol{B}_0 + \widetilde{\boldsymbol{B}}|}. \tag{7.116}$$

Here $\widetilde{\boldsymbol{B}}(\boldsymbol{r}, t)$ is the turbulent magnetic field with the scales l ($\Lambda_{\parallel} < l \lesssim L$), over which we then suppose to average. The same scales characterize the velocity $\boldsymbol{u}$. The field $\boldsymbol{B}_0$ is the regular one whose scale $R \gg L$ is comparable to the scale of whole object under study.

In what follows we accept the following simplifications. First, remind that all the terms containing energy variation have already been discarded from Eq. (7.115). The energy change is in fact rather small in case of incompressible fluid motion ($\nabla \cdot \boldsymbol{u} = 0$). We also neglect the turbulence gyrotropy and assume the vectors $\boldsymbol{u}$ and $\widetilde{\boldsymbol{B}}$ to be directed transverse to $\boldsymbol{B}_0$. Then, the particle interaction with the small-scale fields (with scales of the order or less than the gyroradius) is modeled by a simple "relaxation" term, $-\nu(f - \overline{f})$, where ν is the effective scattering rate of the particles by the small-scale field. The overline $\overline{f}$ denotes averaging over the pitch angle; finally, as we are going to consider a strong diffusion regime, a term describing the magnetic focusing/mirroring in the large-scale random field is discarded assuming the scattering rate ν to be much larger than the competing rate of the pitch-angle variation due to the focusing $v\nabla \cdot \boldsymbol{b}$.

Further manipulations consist of two stages. At the first stage we guess the overall structure of the final equation, which could be the result of Eq. (7.115) averaging over the ensemble of the turbulent pulsations, while the form of yet unknown diffusion tensor is just postulated, but not calculated. This tensor is derived quantitatively at the second stage by adopting small anisotropy of the distribution function and applying renormalization similar to that developed in Sect. 7.3.2. This method is justified by its ability to uniquely and self-consistently derive all auxiliary and final values including the global diffusion tensor without any constraint on the large-scale field magnitude.

Thus, the result of averaging of Eq. (7.115) is guessed in the form

$$\frac{\partial F}{\partial t} + \boldsymbol{V} \cdot \nabla F - \chi_{\alpha\beta}(\boldsymbol{p}) \nabla_\alpha \nabla_\beta F = -\nu(F - \overline{F}), \tag{7.117}$$

where $F(\boldsymbol{r}, \boldsymbol{p}, t) = \langle f(\boldsymbol{r}, p, \theta, t) \rangle$ is the averaged distribution function, while the overline $\overline{F}$ means additional averaging over momentum directions. It is important to note that the original (non-averaged) distribution function $f(\boldsymbol{r}, p, \theta, t)$ and the averaged distribution function $F(\boldsymbol{r}, p, \vartheta, \varphi, t)$ depend on *different* angular variables controlling direction of vector $\boldsymbol{p}$. Indeed, the function f depends on the local pitch-angle θ while it does not depend on the local (fast) gyration phase ϕ: Eq. (7.115) is the result of averaging over this

very phase. After averaging over the turbulent fields, however, the momentum direction is specified by the angle ϑ, between the momentum vector and the mean magnetic field $\boldsymbol{B}_0$, and new azimuth angle φ around $\boldsymbol{B}_0$. The azimuth angle φ is not a fast variable any longer: dependence of it can be introduced by either azimuth anisotropy of the turbulence or particle distribution gradient if different from the $\boldsymbol{B}_0$ direction.

Here, in Eq. (7.117),

$$\boldsymbol{V} = \langle (\boldsymbol{v}\cdot\boldsymbol{b} - \boldsymbol{u}\cdot\boldsymbol{b})\boldsymbol{b} + \boldsymbol{u}\rangle = \langle \boldsymbol{v}_c\rangle \tag{7.118}$$

is the averaged velocity of the particle-guiding center. The term with the second derivative $\chi_{\alpha\beta}\nabla_\alpha\nabla_\beta F$ is supposed to describe the result of averaging

$$\langle (\boldsymbol{v}_c - \boldsymbol{V})\cdot\nabla f\rangle = -\chi_{\alpha\beta}(\boldsymbol{p})\nabla_\alpha\nabla_\beta F. \tag{7.119}$$

Tensor $\chi_{\alpha\beta}(\boldsymbol{p})$ represents only a partial contribution to the full diffusion tensor due to large-scale turbulence, the other part is produced by the $\boldsymbol{V}\cdot\nabla F$ term. Below we calculate both contributions and the full tensor $D_{\alpha\beta}$ self-consistently, which requires some further manipulations over $\boldsymbol{V}$. Denoting

$$\epsilon = \langle \widetilde{B}^2/(B_0^2 + \widetilde{B}^2)\rangle, \tag{7.120}$$

we write down the single-point correlator of the unit vectors as

$$\langle b_\alpha b_\beta\rangle = (1-\epsilon)e_\alpha e_\beta + (\epsilon/2)\delta^\perp_{\alpha\beta}, \tag{7.121}$$

where $\boldsymbol{e}$ is the orth of the field $\boldsymbol{B}_0$. Using Eq. (7.121) we find

$$\boldsymbol{V} = (1-\epsilon)v_\parallel\boldsymbol{e} + (\epsilon/2)\boldsymbol{v}_\perp, \tag{7.122}$$

where the subscripts $\parallel$ and $\perp$ relate now to the $\boldsymbol{B}_0$ direction. The parameter ϵ varies within the limits $0 < \epsilon < 1$ and is the measure of the turbulent component in the entire magnetic field; the two-dimensional tensor $\delta^\perp_{\alpha\beta}$ is defined by $\delta^\perp_{\alpha\beta} = \delta_{\alpha\beta} - e_\alpha e_\beta$.

The full diffusion coefficient $D_{\alpha\beta}$ must be expressed via $\boldsymbol{V}$, $\chi_{\alpha\beta}(\boldsymbol{p})$, and effective scattering rate ν by transition in Eq. (7.117) to the weak anisotropy approximation. Adopting

$$F = \frac{1}{4\pi}(N(\boldsymbol{r},p,t) + \delta N(\boldsymbol{r},\boldsymbol{p},t)), \qquad \overline{\delta N(\boldsymbol{r},\boldsymbol{p},t)} = 0, \qquad |\delta N| \ll N, \tag{7.123}$$

we reduce Eq. (7.117) to the diffusion form

$$\frac{\partial N}{\partial t} = D_{\alpha\beta}(p)\nabla_\alpha\nabla_\beta N, \tag{7.124}$$

where

$$D_{\alpha\beta}(p)=\kappa_{\alpha\beta}+\overline{\chi_{\alpha\beta}(\boldsymbol{p})},\quad \kappa_{\alpha\beta}=\kappa_\perp\delta_{\alpha\beta}+\kappa_\parallel e_\alpha e_\beta,\quad \kappa_\perp=\frac{\epsilon^2 v^2}{12\nu},\quad \kappa_\parallel=(1-\epsilon)^2\frac{v^2}{3\nu}. \tag{7.125}$$

At this point we have to calculate the kinetic coefficient $\chi_{\alpha\beta}(\boldsymbol{p})$, which we perform using the approach developed in Sect. 7.3.2. Let us isolate a narrow range of the wave numbers Δk from the entire turbulence spectrum. The corresponding field components formed by the harmonics from Δk are denoted as $\delta\boldsymbol{u}$ and $\delta\widetilde{\boldsymbol{B}}$. In the linear approximation over these small values we have

$$\boldsymbol{v}_c=\boldsymbol{v}_c'+\delta\boldsymbol{v}_c, \tag{7.126}$$

where

$$\begin{aligned}\delta\boldsymbol{v}_c&=(\boldsymbol{v}\cdot\delta\boldsymbol{b}-\delta\boldsymbol{u}\cdot\boldsymbol{b}'-\boldsymbol{u}'\cdot\delta\boldsymbol{b})\boldsymbol{b}'+(\boldsymbol{v}\cdot\boldsymbol{b}'-\boldsymbol{u}'\cdot\boldsymbol{b}')\delta\boldsymbol{b}+\delta\boldsymbol{u},\\ \delta b_\alpha&=\left[\frac{B_0}{\widetilde{B}'}\delta_{\alpha\beta}-\frac{B_0}{\widetilde{B}'^3}(B_{0\alpha}+\widetilde{B}'_\alpha)\widetilde{B}'_\beta\right]\frac{\delta\widetilde{B}'_\beta}{B_0}\,.\end{aligned} \tag{7.127}$$

The primed values are those related the entire turbulence spectrum except the narrow range Δk.

Now let us average Eq. (7.115) over the entire spectrum of the turbulent pulsations except Δk. Denoting this averaging by the prime sign: $\langle f(\boldsymbol{r},p,\theta,t)\rangle'=\widetilde{F}(\boldsymbol{r},\boldsymbol{p},t)$, we obtain

$$\frac{\partial\widetilde{F}}{\partial t}+\boldsymbol{v}_c'\cdot\nabla\widetilde{F}-\chi'_{\alpha\beta}(\boldsymbol{p})\nabla_\alpha\nabla_\beta F+\nu(\widetilde{F}-\overline{\widetilde{F}})=\widehat{L}\widetilde{F}. \tag{7.128}$$

Here $\widehat{L}$ is operator of the perturbations proportional to small values $\delta\boldsymbol{u}$ and $\delta\widetilde{\boldsymbol{B}}$.

Equation (7.128) is analogous to a simpler Eq. (7.39) from Sect. 7.3.2. Further manipulations are basically similar to those given in Sect. 7.3.2 but much more cumbersome because this problem itself is much more difficult. Thus, we pass the manipulations by and give the answer in the form of the transcendental equation for the transverse diffusion coefficient $D^\perp_{\alpha\beta}=D_\perp\delta^\perp_{\alpha\beta}$

$$\begin{aligned}D^\perp_{\alpha\beta}&=\kappa_\perp\delta^\perp_{\alpha\beta}+\kappa_\parallel\frac{1-\epsilon-\varrho}{(1-\epsilon)^2}\int\frac{\langle\widetilde{B}_\alpha\widetilde{B}_\beta\rangle_{\mathbf{k},\omega}}{B_0^2}\left(1-\frac{k_\parallel^2\kappa_\parallel}{i\omega+k_\parallel^2D_\parallel+k_\perp^2D_\perp}\right)\frac{\mathrm{d}^3k\,\mathrm{d}\omega}{(2\pi)^4}\\&\quad+\left(1-\frac{\epsilon}{2}\right)^2\int\frac{\langle u_\alpha u_\beta\rangle_{\mathbf{k},\omega}}{i\omega+k_\parallel^2D_\parallel+k_\perp^2D_\perp}\frac{\mathrm{d}^3k\,\mathrm{d}\omega}{(2\pi)^4},\end{aligned} \tag{7.129a}$$

$$D_\parallel=\kappa_\parallel\left[1+\frac{\langle\widetilde{B}^2\rangle(1-\epsilon-\varrho)}{B_0^2(1-\epsilon)^2}\right],\qquad \varrho=\langle B_0^2\widetilde{B}^2/(B_0^2+\widetilde{B}^2)^2\rangle. \tag{7.129b}$$

The Hall components in the considered non-helical turbulence case are evanescent within the approximation of zero Larmor radius. Equations (7.129) do not require the turbulence to be weak: they are valid for arbitrarily strong (but smooth, i.e., without shock fronts or other discontinuities) pulsations and for arbitrary regular-to-random field ratio, $0 \le \epsilon \le 1$. The adopted above transverse orientation of the vectors $\boldsymbol{u}$ and $\widetilde{\boldsymbol{B}}$ relative to $\boldsymbol{B}_0$ provided that the turbulence correlation tensors enter only the equation for the transverse (but not the parallel) diffusion coefficient.

A shortcoming of the method is the a priori guessed classical diffusive form of the final transport equation, which, in particular, gives rise to the quadratic dependence of the particle displacement on time $\overline{x^2}(t) \propto t$. This kind of diffusion is highly frequent and widely observed. Nevertheless, we have to note that the theory of the turbulent transport allows "anomalous" transport processes described by equations with fractional derivatives leading to dependencies like $\overline{x^2}(t) \propto t^\mu$, $\mu \neq 1$ (sub-diffusion for $\mu < 1$ or super-diffusion for $\mu > 1$). Firm evidence in favor of such "peculiar" processes is very seldom in the astrophysics. One vivid example of a super-diffusive transport of bright points in solar spot penumbra with $\mu = 1.48 - 1.67$ observed with NST is given by Abramenko et al. (2011); the theory and references of this "strange" diffusion processes are available, e.g., in a review by Zelenyi and Milovanov (2004).

7.5.5 Regimes of the Transverse Diffusion

Let us apply the obtained theory to describe various possible regimes of the particle transverse diffusion in the turbulent fluid. We start from the energetic particle transport mediated by a weak Alfvénic turbulence. The Alfvén mode wave vectors are adopted to be isotropically distributed for simplicity. Assume the correlation tensors of the turbulent velocities and magnetic field to have the form

$$\langle \widetilde{B}_\alpha \widetilde{B}_\beta \rangle_{\mathbf{k},\omega} = 4\pi\rho \langle u_\alpha u_\beta \rangle_{\mathbf{k},\omega} = 4\pi\rho T(k,\omega)(\delta^\perp_{\alpha\beta} - k^\perp_\alpha k^\perp_\beta / k^2_\perp). \tag{7.130}$$

Here the sub(super)script $\perp$ means direction transverse to $\boldsymbol{B}_0$, the scalar function $T(k,\omega)$ is defined by Eq. (7.52) from Sect. 7.3.2, where $\omega_0 = \omega_A = |k_\parallel v_\mathrm{A}|$ is the Alfvén wave frequency, Γ_k is the corresponding spectral bandwidth provided, e.g., by nonlinear wave interaction. Below we use the approximation $\Gamma_k \to 0$, which yields

$$T(k,\omega) = T(k)\pi[\delta(\omega - \omega_0) + \delta(\omega + \omega_0)]. \tag{7.131}$$

The correlation tensor is normalized as follows:

$$\langle \widetilde{B}^2 \rangle = 4\pi\rho \int T(k,\omega) \frac{\mathrm{d}^3 k \mathrm{d}\omega}{(2\pi)^4} = 4\pi\rho \int_0^\infty T(k) \frac{k^2 \mathrm{d}k}{2\pi^2}, \tag{7.132}$$

and

$$\epsilon \approx \frac{\langle \widetilde{B}^2 \rangle}{B_0^2} = \frac{\langle u^2 \rangle}{v_\mathrm{A}^2} \ll 1, \qquad \varrho \ll 1. \tag{7.133}$$

The spectral function $T(k)$ is supposed to have a broad falling with k (inertial) range (see Chap. 6) and to reach a peak value at $k_0 \sim L^{-1}$, related to the main turbulence scale L.

The overall problem depends on a number of dimensionless parameters whose hierarchy demarcates different regimes of the transverse diffusion, most common of which are considered below (recall that the theory used here assumes that the local mfp is much smaller than the main scale of the turbulence, $\Lambda_\parallel \ll L$).

1. Adopt the local mfp $\Lambda_\parallel$ is small, so the following inequalities hold:

$$v_\mathrm{A} L/v\Lambda_\parallel \gg 1 \qquad \text{or} \qquad L/\Lambda_\parallel \gg v/v_\mathrm{A} \gg 1. \tag{7.134}$$

From Eqs. (7.125) and (7.129b) we have $D_\parallel \approx \kappa_\parallel \approx v\Lambda_\parallel/3$, $\kappa_\perp \ll \kappa_\parallel$. Since in a weakly turbulent fluid, Eq. (7.133), there must be $D_\perp \ll D_\parallel$; with the use of Eq. (7.134) we have $\omega_A = |k_\parallel v_A| \gg k_\parallel^2 D_\parallel + k_\perp^2 D_\perp \approx k_\parallel^2 D_\parallel$. The first integral in the rhs of Eq. (7.129a) gives

$$\approx \kappa_\parallel \int \frac{\langle \widetilde{B}_\alpha \widetilde{B}'_\beta \rangle_{\mathbf{k},\omega}}{B_0^2} \frac{\mathrm{d}^3 k \mathrm{d}\omega}{(2\pi)^4} = \frac{1}{2}\delta^\perp_{\alpha\beta} \frac{\langle \widetilde{B}^2 \rangle}{B_0^2}\kappa_\parallel = \frac{1}{2}\delta^\perp_{\alpha\beta}\epsilon\kappa_\parallel.$$

The second integral contribution is

$$\approx \int \frac{\langle u_\alpha u'_\beta \rangle_{\mathbf{k},\omega} k_\parallel^2 D_\parallel \mathrm{d}^3 k \mathrm{d}\omega}{\omega_\mathrm{A}^2 (2\pi)^4} \approx \frac{1}{2}\delta^\perp_{\alpha\beta}\frac{\langle u^2 \rangle}{v_\mathrm{A}^2}\kappa_\parallel = \frac{1}{2}\delta^\perp_{\alpha\beta}\epsilon\kappa_\parallel.$$

This eventually yields a rather simple expression:

$$D_\perp \approx \epsilon\kappa_\parallel. \tag{7.135}$$

We find that the turbulent velocity field and the turbulent magnetic field give two equal contributions to the transverse diffusion coefficient.

2. Adopt now the local mfp to be large $v\Lambda_\parallel \gg v_\mathrm{A} L$ but limited, so the inequalities

$$v_\mathrm{A} L \ll \kappa_\parallel \ll v_\mathrm{A} L \epsilon^{-1}, \qquad \epsilon,\, \varrho \ll 1 \tag{7.136}$$

are fulfilled. With correlation tensors Eq. (7.130) integration of Eq. (7.129a) over the azimuth angle of the vector $\boldsymbol{k}$ yields

$$D_\perp \approx \int_0^\infty \frac{T(k)\mathrm{d}k}{(2\pi)^2}\left[\frac{1}{\kappa_\parallel}\Re\int_0^1 \frac{\mathrm{d}x}{x^2+2i\beta x+\gamma} + \Re\int_0^1 \frac{ikx\mathrm{d}x}{v_\mathrm{A}(x^2+2i\beta x+\gamma)}\right], \tag{7.137}$$

where $\beta = v_\mathrm{A}/(D_\parallel - D_\perp) \approx v_\mathrm{A}/2k\kappa_\parallel \ll 1$, $\gamma = D_\perp/(D_\parallel - D_\perp) \approx D_\perp/\kappa_\parallel \ll 1$. Integrals over dx can be taken by the integrand expansion over the simplest fractions:

$$\frac{1}{x^2+2i\beta x+\gamma} = \frac{1}{x-x_1}\left[\frac{1}{x-x_1} - \frac{1}{x-x_2}\right], \quad x_{1,2} = -i[\beta \mp \sqrt{\beta^2+\gamma}].$$

Within the lowest (linear) approximation over ϵ the first integral in Eq. (7.137) gives no contribution, so the second one fully specifies the transverse diffusion coefficient:

$$D_\perp = \epsilon v_\mathrm{A} \overline{L}. \tag{7.138}$$

Here the scale $\overline{L}$ depends on the spectrum

$$\langle u^2 \rangle \overline{L} = \frac{1}{8\pi} \int_0^\infty T(k) k \mathrm{d}k, \qquad \langle u^2 \rangle = \frac{1}{2\pi^2} \int_0^\infty T(k) k^2 \mathrm{d}k. \tag{7.139}$$

This scale $\overline{L}$ is comparable to the main turbulence scale.

3. A further possible regime compatible with the assumption of the Alfvén turbulence weakness is defined by the inequalities:

$$v_\mathrm{A} L / \kappa_\parallel \ll \epsilon \ll 1. \tag{7.140}$$

Since in this case $D_\parallel \approx \kappa_\parallel (1 + \epsilon)$, then the terms $i\omega = \pm i\omega_\mathrm{A}$ can be discarded as they are small compared with $k_\parallel^2 D_\parallel$. After integration over the azimuth angle of the vector $\boldsymbol{k}$ and discarding some apparently small terms, Eq. (7.129a) receives the form

$$D_\perp = \kappa_\perp + \frac{\kappa_\parallel}{v_\mathrm{A}^2} \int_0^\infty \frac{T(k) k^2 \mathrm{d}k}{(2\pi)^2} \int_0^1 \left\{ 1 - \frac{\kappa_\parallel}{D_\parallel - D_\perp} \left[1 - \frac{\gamma}{x^2 + \gamma} \right] \right\} \mathrm{d}x + \frac{1}{D_\parallel - D_\perp} \int_0^\infty \frac{T(k) \mathrm{d}k}{(2\pi)^2} \int_0^1 \frac{\mathrm{d}x}{x^2 + \gamma}, \tag{7.141}$$

where $\gamma = D_\perp / (D_\parallel - D_\perp)$. Inequality (7.140) guarantees that $D_\parallel \gg D_\perp$. Now, using Eq. (7.139) and integrating over $\mathrm{d}x$, we obtain

$$D_\perp = \kappa_\perp + \frac{\kappa_\parallel \langle u^2 \rangle}{2 v_\mathrm{A}^2} \left(\epsilon + \frac{\pi}{2} \sqrt{\frac{D_\perp}{\kappa_\parallel}} \right) + \frac{\pi}{2\sqrt{D_\perp \kappa_\parallel}} \int_0^\infty \frac{T(k) \mathrm{d}k}{(2\pi)^2}. \tag{7.142}$$

The latter term in the rhs is of the order of $\langle u^2 \rangle L^2 / \sqrt{D_\perp \kappa_\parallel}$; its ratio to the second term can be evaluated as $\epsilon (\kappa_\parallel / D_\perp) (v_\mathrm{A} L / \kappa_\parallel)^2$, which, being corroborated with inequalities (7.140), gives rise to the estimate $\epsilon (\kappa_\parallel / D_\perp) (v_\mathrm{A} L / \kappa_\parallel)^2 \ll \epsilon^3 \kappa_\parallel / D_\perp \ll 1$, because $D_\perp$ is now of the order of $\epsilon^2 \kappa_\parallel$. Thus, Eq. (7.142) after discarding this small last term reduces to a simple one:

$$D_\perp = \kappa_\perp + \frac{\epsilon \kappa_\parallel}{2} \left(\epsilon + \frac{\pi}{2} \sqrt{\frac{D_\perp}{\kappa_\parallel}} \right). \tag{7.143}$$

From here it is easy to find to the first nonzero order over $\epsilon \ll 1$

$$D_\perp = g \epsilon^2 \kappa_\parallel, \qquad g \approx 1.6. \tag{7.144}$$

Thus, the transverse transport of the particles by quasi-stationary ($\omega = 0$) small-amplitude irregularities is specified by the fourth power of the random-field amplitude.

Let us discuss now the particle transport by a strong turbulence ($\epsilon \approx 1$), which in a general case requires solving corresponding transcendental algebraic Eq. (7.129). This analysis results typically in almost isotropic diffusion $D_\perp \sim D_\parallel$ due to strong turbulence. To illustrate this we make an oversimplified estimate for a one-scale strong static turbulence characterized by the magnetic correlation tensor

$$\langle \widetilde{B}_\alpha \widetilde{B}'_\beta \rangle_{\mathbf{k},\omega} = \langle \widetilde{B}^2 \rangle \frac{2\pi^3}{k_0^2} \delta(k - k_0)\delta(\omega)\delta^\perp_{\alpha\beta} \tag{7.145}$$

and neglecting the turbulent motions ($\langle u^2 \rangle = 0$). Here, as follows from Eq. (7.129b), $D_\parallel = \kappa_\parallel/(1-\epsilon)$, and the ratio $X = D_\perp/D_\parallel$ satisfies the equation derived from Eq. (7.129a) after taking the integrals:

$$X = \frac{\epsilon^2}{4(1-\epsilon)} + \frac{\epsilon}{2}\left[\frac{\epsilon - X}{1-X} + \frac{(1-\epsilon)\sqrt{X}}{(1-X)^{3/2}} \arctan\sqrt{\frac{1-X}{X}}\right]. \tag{7.146}$$

Let us consider, as an example, the transverse transport in the galactic disk. Observations (Ruzmaikin et al. 1988; Beck 2001, 2011) favor rather strong random magnetic field comparable with the regular component, which implies the strong turbulence regime. For the following ratios $\widetilde{B} \approx B_0$ ($\epsilon = 1/2$), $\widetilde{B} \approx 1.4 \times B_0$ ($\epsilon \approx 2/3$), and $\widetilde{B} \approx 1.7 \times B_0$ ($\epsilon \approx 3/4$) compatible with the observations, Eq. (7.146) yields $D_\perp/D_\parallel \approx 0.3$, $D_\perp/D_\parallel \approx 0.6$, and $D_\perp/D_\parallel \approx 0.9$, respectively. Thus, $D_\perp$ and $D_\parallel$ are indeed of the same order of magnitude. The tensor components for the Hall diffusion are negligible, because the Larmor radius of relativistic protons is too small compared with the mfp of the particles. The average diffusion tensor of the relativistic protons is diagonal in the coordinate system with the polar axis directed along the large-scale regular field.

7.6 Ambipolar Diffusion Stimulated by Energetic Particles

7.6.1 Ambipolar Diffusion in Steady Regime

Let us consider a simple model problem of how both nonthermal and thermal particles diffuse out from a point source of nonthermal particles in a uniform isotropic steady-state fluid.[1] Note that in case of neutral passive admixtures,

[1] Effective ambipolar diffusion coefficients in a weakly ionized fluid (without fast particles but with different temperatures of ions and electrons) can be found, e.g., in Alfven and Fälthammar (1963) and Chen (1984).

each kind of particles diffuse with its own diffusion coefficient that does not depend on other kinds of test particles perhaps available in the fluid. The situation differs drastically for the charged particles, because they interact with each other via far-acting Coulomb forces; thus, diffusion of each charged particle component depends generally on all other component motion.

Let us adopt an accelerating process to operate in a small region of space (point source of accelerated particles), i.e., a small fraction of the ions are converted to a nonthermal (perhaps, ultrarelativistic) component with a rate Q (ions per second). Neglecting effect of other charged particles, the fast ions would diffuse in this isotropic turbulent fluid with a diffusion coefficient κ. In the stationary case the number density of the ions obeys the equation

$$\kappa \Delta N = -Q\delta(\boldsymbol{r}), \tag{7.147}$$

which has a solution

$$N(r) = \frac{Q}{4\pi\kappa r}. \tag{7.148}$$

Apparently, the conservation of the particle number implies that generation rate Q of the accelerated ions produces the same but negative "generation" rate of the background ions $-Q$, since the accelerated particles originate from the background population. Thus, there appears a negative variation $n^i(\boldsymbol{r})$ of the background ions accompanied, due to the Coulomb interaction, by a nonstationary variation $n^e(\boldsymbol{r})$ of the background electrons. These values must be distinguished from the mean values $n_i = n_e = n_0$ of the electron and ion densities in the steady-state plasma. On top of that, these three plasma components produce an electric field and motion of charged particles, i.e., generally speaking, an electric current. Let us express all the variations of the number densities via the acceleration rate Q and diffusion coefficients κ, D^i, and D^e of the nonthermal and background particles and calculate all the partial electric current components $\boldsymbol{j}^r$, $\boldsymbol{j}^i$, and $\boldsymbol{j}^e$, where the superscript r denotes the accelerated particles.

The electric currents are defined by the particle number densities and electric field $\boldsymbol{E}$ using well-known formulae involving both diffusion and electro-conductivity:

$$j^r_\alpha = -e\kappa_{\alpha\beta}\frac{\partial N}{\partial x_\beta} + \sigma^r_{\alpha\beta}E_\beta, \tag{7.149a}$$

$$j^i_\alpha = -eD^i_{\alpha\beta}\frac{\partial n^i}{\partial x_\beta} + \sigma^i_{\alpha\beta}E_\beta, \tag{7.149b}$$

$$j^e_\alpha = eD^e_{\alpha\beta}\frac{\partial n^e}{\partial x_\beta} + \sigma^e_{\alpha\beta}E_\beta, \tag{7.149c}$$

where the plasma anisotropy due to regular magnetic field is taken into account via tensor kinetic coefficients. In what follows we will use links (7.23)–(7.25) between the kinetic coefficients to reduce their number. A similar link

is available for the nonthermal particles, which can be written in the form [see Eq. (7.95)]

$$\frac{\kappa}{\sigma^r} = 4\pi R_D^2 \approx \frac{K}{eN_0} \gg \frac{T}{en_0} = 4\pi r_D^2. \tag{7.150}$$

Here $K \gg T$ is a mean kinetic energy of nonthermal particles, $N_0 \ll n_0$ is their number density (see Sect. 7.4.3).

In the stationary case the electric currents obey the equations:

$$\nabla \cdot \boldsymbol{j}^r = eQ\delta(\boldsymbol{r}), \qquad \nabla \cdot \boldsymbol{j}^i = -eQ\delta(\boldsymbol{r}), \qquad \nabla \cdot \boldsymbol{j}^e = 0, \tag{7.151}$$

while the electric field obeys the Maxwell equation

$$\nabla \cdot \boldsymbol{E} = 4\pi e(N + n^i - n^e). \tag{7.152}$$

The Fourier transform of Eqs. (7.149)–(7.152) yields the set of algebraic equations for the Fourier amplitudes:

$$e\kappa_{\alpha\beta}k_\alpha k_\beta N_k + \sigma^r_{\alpha\beta}k_\alpha k_\beta \varphi_k = eQ, \tag{7.153a}$$

$$eD^i_{\alpha\beta}k_\alpha k_\beta n^i_k + \sigma^i_{\alpha\beta}k_\alpha k_\beta \varphi_k = -eQ, \tag{7.153b}$$

$$eD^e_{\alpha\beta}k_\alpha k_\beta n^e_k + \sigma^e_{\alpha\beta}k_\alpha k_\beta \varphi_k = 0, \tag{7.153c}$$

$$k^2\varphi_k - 4\pi e(N_k + n^i_k - n^e_k) = 0. \tag{7.153d}$$

Here we use equation for the scalar potential φ instead of electric field.

The last two equations along with Eqs. (7.24) and (7.25) give rise to

$$N_k + n^i_k - n^e_k = (kr_D)^2 n^e_k. \tag{7.154}$$

To estimate the rhs on the order of magnitude we note that the diffusive particle transport can only take place on the scales exceeding the maximum transport mfp of the plasma components, which is the longitudinal transport mfp of the accelerated ions $\Lambda^r_\parallel$. Thus, for typical wave number values, we have $k < 1/\Lambda^r_\parallel$, and, accordingly, a strong inequality

$$(kr_D)^2 \ll \left(\frac{r_D}{\Lambda^r_\parallel}\right)^2 \ll 1 \tag{7.155}$$

takes place (e.g., in the warm diffuse galactic phase $r_D/\Lambda^r_\parallel \approx 10^{-10}$ for the cosmic rays). The rhs of Eq. (7.154) is zero to this accuracy, i.e., the local electroneutrality holds here with high precision:

$$N_k + n^i_k - n^e_k = 0. \tag{7.156}$$

However, this is only true for the stationary conditions; nonstationarity can break the local electroneutrality down (see below).

Let us consider a weakly ionized plasma where relation (7.24) between the kinetic coefficients takes place. Making manipulations to the accuracy of $r_D/R_D \ll 1$, we obtain the number densities

$$N_k = \frac{Q}{\widetilde{\kappa}}, \qquad n_k^i = -\frac{Q}{2}\left(\frac{1}{\widetilde{D}^i} + \frac{1}{\widetilde{\kappa}}\right), \qquad n_k^e = -\frac{Q}{2}\left(\frac{1}{\widetilde{D}^i} - \frac{1}{\widetilde{\kappa}}\right), \quad (7.157)$$

where we introduce the notations $\widetilde{\kappa} = \kappa_{\alpha\beta}k_\alpha k_\beta$, $\widetilde{D}^i = D^i_{\alpha\beta}k_\alpha k_\beta$.

Thus, the nonthermal particles (with $K \gg T$) diffuse with their own diffusion tensor $\kappa_{\alpha\beta}$; the self-consistent electric field effect on their motion is negligible. The background ions and electrons, however, diffuse with accordingly modified diffusion coefficients (7.157); remarkably, the effective *electron* diffusion coefficient is specified by the diffusion coefficients of the accelerated and background ions. If $\widetilde{\kappa} \gg \widetilde{D}^i$ then

$$\widetilde{D}^i_{ef} \approx \widetilde{D}^e_{ef} \approx 2\widetilde{D}^i. \quad (7.158)$$

Consider now a highly ionized plasma and apply Eq. (7.25). The calculations are similar to the previous case; however, in addition to Eq. (7.150) there appears one more small parameter $(m_e/m_i)^{1/2}$. Discarding the corresponding small terms yields the effective diffusion coefficients of the background particles

$$\widetilde{D}^i_{ef} \approx \widetilde{D}^i, \qquad \widetilde{D}^e_{ef} = \frac{\widetilde{D}^i\widetilde{\kappa}}{\widetilde{\kappa} - \widetilde{D}^i} \approx \widetilde{D}^i, \quad (7.159)$$

where the last approximate equality is valid when $\widetilde{\kappa} \gg \widetilde{D}^i$.

Substitution of Eq. (7.157) into the Fourier transform of Eq. (7.149) yields the corresponding partial electric current densities:

$$j^r_{k\alpha} = -\frac{ie\kappa_{\alpha\beta}k_\beta}{\widetilde{\kappa}}Q, \qquad j^i_{k\alpha} = \frac{ieD^i_{\alpha\beta}k_\beta}{\widetilde{D}^i}Q, \qquad j^e_{k\alpha} = 0. \quad (7.160)$$

The total current stimulated by the fast particles

$$j^{\mathrm{tot}}_{k\alpha} = -ieQ\left(\frac{\kappa_{\alpha\beta}}{\widetilde{\kappa}} - \frac{D^i_{\alpha\beta}}{\widetilde{D}^i}\right)k_\beta; \quad (7.161)$$

it consists of the contributions from the fast and background ions, which enter with the opposite signs.

Electric current described by Eq. (7.161) is not equivalent to zero. Broadly speaking, the possibility of a nonzero net current driven by high-energy particles propagating out from a localized "point" source in a thermal plasma seems natural. However, in many cases, no net current appears because the

partial current driven by the fast particles can be entirely compensated by a return current driven by the background particles. In particular, this happens in 1D model of electron return currents considered in Sect. 7.1.3. Therefore, having a net electric current is not guaranteed, while it requires some additional conditions to be fulfilled. For example, Eq. (7.161) results in a zero net current in case of isotropic plasmas with isotropic diffusion tensors, $\kappa_{\alpha\beta} = \kappa\delta_{\alpha\beta}$ and $D^i_{\alpha\beta} = D^i\delta_{\alpha\beta}$. This is fully consistent with a naive expectation based on the system symmetry: the current can only be directed isotropically along a radius drawn from the point source. Thus, its nonzero value would imply a sustained nonzero charge flow from the source, which is impossible in the steady state. In an anisotropic case, however, this consideration does not work since the current components are different in different directions, which is controlled by various components of the conductivity tensor.

If the tensor structures of both diffusion tensors of fast and background particles, $\kappa_{\alpha\beta}$ and $D^i_{\alpha\beta}$, are the same (i.e., they are proportional to each other), they fully compensate each other in Eq. (7.161). To avoid this compensation, the tensor structures must differ substantially from each other. For example, if the diffusion tensor components are defined by Eq. (7.84), having such a different tensor structure requires that the Larmor radius R_0 and the mfp Λ have different energy dependence; thus the thermal and fast particles will have different transverse to parallel diffusion coefficient ratios. On the other hand, for a strong turbulent diffusion, which is almost isotropic, one cannot expect a noticeable net current as in the truly isotropic case. In real objects, e.g., in the case of galactic CRs, different components of the CR diffusion tensor are different from each other, although they have the same order of magnitude (weakly anisotropic diffusion). Diffusion of the background particles having much smaller Larmor radii is severely different from the CR diffusion so it is unlikely that the diffusion tensors $\kappa_{\alpha\beta}$ and $D^i_{\alpha\beta}$ have exactly same tensor structure, which is needed to fully compensate these two contributions to Eq. (7.161). However, to confidently conclude that there is a nonzero net current in the system under study, one has to explicitly consider the entire set of the Maxwell equations including equations for the magnetic field (cf. Sect. 7.1.3) not included in the above simplified model of the ambipolar diffusion.

We can, nevertheless, calculate the electric current arising within the considered simplified model in the explicit coordinate form. Adopt the net current to be a sum of two terms $j^{\rm tot}_{k\alpha} = j^r_{k\alpha} + j^i_{k\alpha}$ related to the two terms in the rhs of Eq. (7.161). We write the first term in the form $\widetilde{\kappa} j^r_{k\alpha} = -ieQ\kappa_{\alpha\beta}k_\beta$ and apply the inverse Fourier transform to obtain the following differential equation:

$$\nabla_\mu \kappa_{\mu\nu} \nabla_\nu j^r_\alpha(\boldsymbol{r}) = -eQ\kappa_{\alpha\beta}\nabla_\beta \delta(\boldsymbol{r}), \tag{7.162}$$

whose solution can be expressed via the Green function G^r of stationary diffusion in an anisotropic fluid:

$$\nabla_\mu \kappa_{\mu\nu} \nabla_\nu G^r(\boldsymbol{r} - \boldsymbol{r}') = -\delta(\boldsymbol{r} - \boldsymbol{r}'). \tag{7.163}$$

This Green function has a form equivalent to electrostatic potential of a unit-point charge in an anisotropic dielectric and has the form

$$G^r(\boldsymbol{r} - \boldsymbol{r}') = \frac{1}{4\pi\sqrt{\kappa_\perp}[(\boldsymbol{r}_\perp - \boldsymbol{r}'_\perp)^2\kappa_\parallel + (z - z')^2\kappa_\perp]^{1/2}}. \tag{7.164}$$

The current density is straightforwardly described via this Green function as

$$j^r_\alpha(\boldsymbol{r}) = -eQ\kappa_{\alpha\beta}\int G_r(\boldsymbol{r} - \boldsymbol{r}')\nabla'_\beta\delta(\boldsymbol{r}')\mathrm{d}^3 r' = -eQ\kappa_{\alpha\beta}\nabla_\beta G^r(\boldsymbol{r}). \tag{7.165}$$

The second term can be transformed in a similar way. Thus, the net current receives the form

$$j_\alpha(\boldsymbol{r}) = -\frac{eQ}{4\pi}\left(\frac{D^i_{\alpha\beta}}{\sqrt{D^i_\perp}}\nabla_\beta\frac{1}{R^i} - \frac{\kappa_{\alpha\beta}}{\sqrt{\kappa_\perp}}\nabla_\beta\frac{1}{R^r}\right), \quad \text{where}$$

$$R^i = \sqrt{r^2_\perp D^i_\parallel + z^2 D^i_\perp},\ R^r = \sqrt{r^2_\perp\kappa_\parallel + z^2\kappa_\perp}. \tag{7.166}$$

This current produces a large-scale perturbation of the fluid; it occupies a volume with a linear scale much exceeding the mfp of CRs (and, apparently, thermal particle mfp). This current decreases reciprocally to the R^2 at large distance.

The electric current, if present, produces additional large-scale magnetic field $\boldsymbol{b}$ that is easy to calculate from the Maxwell equations written in the form

$$\Delta\boldsymbol{b} = \frac{4\pi}{c}\nabla\times\boldsymbol{j}(\boldsymbol{r}), \qquad \nabla\cdot\boldsymbol{b} = 0. \tag{7.167}$$

Solution of the Poison equation for the magnetic field can be written in the integral form:

$$\boldsymbol{b}(\boldsymbol{r}) = \frac{1}{c}\int\frac{\boldsymbol{r}'\times\boldsymbol{j}(\boldsymbol{r}')}{|\boldsymbol{r} - \boldsymbol{r}'|^3}\mathrm{d}\boldsymbol{r}'. \tag{7.168}$$

Remember, that since no equation for the magnetic field was self-consistently included in the model, the derivation performed could only be valid for a reasonably small perturbation of the fluid. In particular, fast particle pressure must be weak and produce no noticeable fluid motion, while the generated magnetic field remain weak compared with the original magnetic field. Otherwise, the problem becomes highly nonlinear, so the fluid motion and the varying magnetic field effects on the diffusion coefficients become essential.

7.6.2 Ambipolar Diffusion in Impulsive Regime

In the astrophysics there are many impulsive, prompt processes when the energetic particles are generated over a relatively short time scale, e.g., supernova explosions, gamma-ray bursts, and solar and stellar flares, rather than stationary processes. In this case the electric current depends on time, so it has to be determined from a system of nonstationary equations:

$$\frac{\partial eN}{\partial t}+\nabla\cdot\boldsymbol{j}^{\,r}=eQ\delta(\boldsymbol{r})\delta(t-t_0),\quad \frac{\partial en^i}{\partial t}+\nabla\cdot\boldsymbol{j}^{\,i}=-eQ\delta(\boldsymbol{r})\delta(t-t_0),\quad -\frac{\partial en^e}{\partial t}+\nabla\cdot\boldsymbol{j}^{\,e}=0. \tag{7.169}$$

Here, in contrast to the previous case, Q is the *total* number (in contrast to the acceleration *rate*) of the accelerated particles produced by a point source at the initial time frame $t=t_0$. The current densities obey Eq. (7.149); the electric field is specified by Poisson equation (7.152).

Let us solve Eqs. (7.169) and (7.152) by the Laplace transformation

$$n(s)=\int_0^\infty n(t)e^{-st}\mathrm{d}t \tag{7.170}$$

over the time and Fourier transformation over the space. Poisson equation supplemented by the electron diffusion equation yields the exact relationships:

$$\varphi_k=\frac{4\pi e}{k^2}(N_k+n_k^i-n_k^e),\qquad N_k+n_k^i-n_k^e=(kr_D)^2\left(1+\frac{s}{\widetilde{D}^e}\right)n_k^e. \tag{7.171}$$

Two remaining equations of system (7.169), with the use of Eqs. (7.171), (7.95), and (7.24), for definiteness, we consider a weakly ionized plasma here; the ambipolar diffusion in the fully ionized plasma can be studied in a similar way (see, e.g., Problem 7.8), receive the form

$$(s+\widetilde{\kappa})N_k+\frac{r_D^2}{R_D^2}\left(1+\frac{s}{\widetilde{D}^e}\right)\widetilde{\kappa}n_k^e=Qe^{-st_0},\qquad (s+\widetilde{\kappa})n_k^i+\left(1+\frac{s}{\widetilde{D}^e}\right)\widetilde{\kappa}n_k^e=-Qe^{-st_0}. \tag{7.172}$$

Equations (7.171) and (7.172) contain small parameters

$$\frac{r_D^2}{R_D^2}\ll 1\quad\text{and}\quad (kr_D)^2\ll\left(\frac{r_D}{\Lambda_\parallel^r}\right)^2\ll 1. \tag{7.173}$$

In addition, the diffusion coefficients of accelerated particles often exceed the diffusion coefficients of the background particles considerably. And on top of this, the diffusion coefficients of the background electrons and ions are highly different from each other. Eventually, in most of the k-space, the following inequalities hold:

$$\widetilde{\kappa}\gg\widetilde{D}^e\gg\widetilde{D}^i. \tag{7.174}$$

The first of them is due to high energy of the accelerated particles, while the second one is due to low electron-to-ion mass ratio and valid everywhere except a minor part of the k-space, where $(k_\parallel/k_\perp)^2 \lesssim D^i_\perp/D^e_\parallel \approx (m_e/m_i)^{1/2}(\omega_{\rm Bi}\tau_i)^{-2}$, with the subscripts $\parallel$ and $\perp$ related to the regular large-scale field $\boldsymbol{B}_0$ direction and $\omega_{\rm Bi}\tau_i \gg 1$ the ion magnetization parameter. Taking into account inequalities (7.173) and (7.174) and apparent condition $s \lesssim \widetilde{\kappa}$ of the diffusion equation applicability we may obtain an approximate solution of the analyzed equation. Skipping any detailed analysis we point out some important properties of the nonstationary ambipolar diffusion.

High-energy particles diffuse with their own diffusion tensor $\kappa_{\alpha\beta}$ and create a pulse of electric current, which can be expressed via the corresponding diffusion Green function:

$$j^r_\alpha(\boldsymbol{r},t) = e\,Q\kappa_{\alpha\beta}\nabla_\beta G^r(\boldsymbol{r},t-t_0), \tag{7.175}$$

where

$$G^r(\boldsymbol{r},t) = \frac{\Theta(t)}{\kappa_\perp\kappa_\parallel^{1/2}(4\pi t)^{3/2}}\exp\left[-\frac{r_\perp^2}{4\kappa_\perp t}-\frac{z^2}{4\kappa_\parallel t}\right]. \tag{7.176}$$

The fast particle pressure has the form

$$P(\boldsymbol{r},t) = \frac{1}{3}\overline{pv}\,Q\,G^r(\boldsymbol{r},t-t_0), \tag{7.177}$$

where the overline denotes averaging over the fast particle energy spectrum. At and around the acceleration site it can be rather large and even dominate pressures of the background plasma and the magnetic field.

The Laplace and Fourier transform of the electric current $j^{ph}_{k\alpha} = j^e_{k\alpha} + j^i_{k\alpha}$ of the background particles assuming the perfect electroneutrality receives the form

$$\begin{aligned} j^{ph}_{k\alpha}(s) &= -ieD^i_{\alpha\beta}k_\beta\left[\frac{1}{s+\widetilde{\kappa}}-\frac{2}{s+2\widetilde{D}^i}\right]Qe^{-st_0} \\ &\quad +ieQ\frac{\partial}{\partial t_0}\frac{(D^e_{\alpha\beta}+D^i_{\alpha\beta})k_\beta}{\widetilde{D}^e}\left[\frac{1}{s+\widetilde{\kappa}}-\frac{1}{s+2\widetilde{D}^i}\right]Qe^{-st_0}, \end{aligned} \tag{7.178}$$

which has two poles over variable s. This implies two "waves" of the background particle current: the first of them is produced by the background particle response to the fast particle perturbation, while the second one describes the joint ambipolar diffusion of background ions and electrons with the diffusion coefficient roughly equal to the doubled ion diffusion coefficient.

To compute this current in the coordinate space it is convenient to start with inverse Laplace transformation, which turns the singular terms in

Eq. (7.178) into exponent factors. The inverse Fourier transform is performed similarly to that in the previous section. Eventually, the current density induced by an impulsive source is expressed via integrals over the real 3D space from the Green functions of the diffusion equations and their derivatives.

Thus, we can outline the following evolutionary pattern. Initially, when at a given location a fast particle current arises, a compensating (return) current formed by the background particles starts to grow. A noticeable current compensation occurs, however, only in a time of the order of $r^2/8D^i$ needed for the background particles to establish the return current (this time is relatively long as the diffusion coefficients of fast and background particles can differ by many orders of magnitude). However, the full compensation of the direct and return currents in a stationary regime of the considered here model only happens if the diffusion coefficients have the same tensor structure (i.e., if they are proportional to each other), which implies that considering the entire set of Maxwell equations (rather than only the Poison equation for the electric field) is needed to correctly solve the problem of establishing the net electric current in an anisotropic turbulent fluid.

Problems

7.1 Using the naive concept of the random walk of the test particles with a mfp Λ and velocity v, obtain Eqs. (7.11) and (7.12) for the diffusive flux of the admixture induced by weak inhomogeneity of its number density in nonmoving medium.

7.2 Adopt that a fluid participates in both turbulent motion with velocity $\boldsymbol{u}$, $\langle \boldsymbol{u} \rangle = 0$ and regular motion with a velocity $\boldsymbol{U}$ that changes only weakly over the main scale L of the turbulence. Obtain equation for the number density N of the admixture and express the effective diffusion coefficient via the turbulent velocity correlator using the perturbation theory. Accept that the fluid is incompressible and uniform.

7.3 Adopt the fast particles to be uniformly distributed in a volume with a uniform magnetic field $\boldsymbol{B}_0$ and random magnetic inhomogeneities. Their angular distribution at $t = 0$ is known: $F(\theta, \phi, 0) = F_0(\theta, \phi)$, where θ, ϕ are the polar and azimuth angles in the spherical system with the polar axes along the uniform magnetic field. Use Eq. (7.79) to calculate the angular distribution for $t > 0$. Determine the isotropization time τ_s defined as the time needed for the anisotropic part of the distribution to e fold decrease.

7.4 Find the solution of anisotropic diffusion equation (7.87) for a prompt point-like source of the particles $Q(\boldsymbol{r}, t) = \delta(\boldsymbol{r})\delta(t)$. Calculate the mean sizes of the particle cloud in the corresponding three directions for $t > 0$.

7.5 ⋆ Determine the Green function of diffusion equation (7.88) with the second derivative over time for the whole (infinite) space. Discuss the physical meaning of the solution versus the standard diffusion equation having only the first time derivative.

7.6 Adopt a fluid with magnetic inhomogeneities to move with a velocity $\boldsymbol{u}$. The fast particles are isotropically distributed $F_0 = N(p_0)/4\pi$ in the fluid reference frame. Calculate the differential flux density of the fast particles with a given p in the laboratory system.

7.7 Magnetized particles propagate along the magnetic field lines from a point stationary source toward the field decrease being scattered by magnetic inhomogeneities. Use kinetic equation (7.114) to calculate their distribution as a function of the pitch-angle ϑ and distance s along the field line. The functions $B(s)$ and $\Lambda(s)$ are known. Use small-angle scattering approximation. Compare the results with scattering in a uniform medium.

7.8 A point-like stationary source of the particles is located in a fully ionized plasma and generate Q accelerated ions per second extracting them from the background plasma. The diffusion coefficients of three involved plasma components $D^e_{\alpha\beta}$, $D^i_{\alpha\beta}$, and $\kappa_{\alpha\beta}$ are known. Calculate the electric current distribution $\boldsymbol{j}(\boldsymbol{r})$ in the anisotropic plasma. Adopt that the anisotropy is set up by a uniform magnetic field $\boldsymbol{B}_0$. Use Eq. (7.25) neglecting small terms of the order of $(r_D/R_D)^2 \ll 1$ and $(m_e/m_i)^{1/2} \ll 1$.

Answers and Solutions

7.1 Within the macroscopic theory the minimal scale is Λ and the minimal time is Λ/v. The theory can only be applied for the scales and time exceeding the minimal ones. Consider a spatial location $\boldsymbol{r}$: at a time t there arrive the particles that have experienced the previous scattering at the location $\boldsymbol{r} - \Lambda\boldsymbol{v}/v$ at $t - \Lambda/v$. These particles form the flux density $\boldsymbol{i}_v(\boldsymbol{r}, t) = \boldsymbol{v}n(\boldsymbol{r} - \Lambda\boldsymbol{v}/v, t - \Lambda/t)$ along the vector $\boldsymbol{v}$. The total flux density of the particles with a given absolute velocity value v is given by averaging the flux density over $\boldsymbol{v}$ direction:

$$\boldsymbol{i}(\boldsymbol{r}, t) = \int \boldsymbol{i}_v(\boldsymbol{r}, t)\frac{\mathrm{d}\Omega_v}{4\pi} \approx -\kappa\nabla n(\boldsymbol{r}, t), \qquad \kappa = \frac{1}{3}v\Lambda.$$

7.2

$$\frac{\partial N}{\partial t} + \boldsymbol{U}\cdot\nabla N = \chi_{\alpha\beta}\,\frac{\partial^2 N}{\partial x_\alpha, x_\beta},$$

where

$$\chi_{\alpha\beta} = \kappa\delta_{\alpha\beta} + \int \mathrm{d}^3 r \int_0^\infty \mathrm{d}\tau G(\boldsymbol{r}, \tau)K_{\alpha\beta}(\boldsymbol{r}, \tau),$$

G is the diffusion Green function, $K_{\alpha\beta}(\boldsymbol{r}, \tau)$ is the turbulent velocity correlation tensor, and κ is the "molecular" diffusion coefficient.

7.3

$$F(\theta,\phi,t)=\sum_{l,m}C^0_{lm}Y_{lm}(\theta,\varphi)\exp\left\{im\Omega t-\frac{v}{2\Lambda}\,l(l+1)t\right\},$$
$$C^0_{lm}=\int F_0(\theta,\phi)Y^*_{lm}(\theta,\phi)\mathrm{d}\Omega_p,$$
$$\Omega=\frac{ec}{\mathcal{E}}\,B_0,\quad \tau_s=\frac{\Lambda}{v}.$$

This τ_s value suggests that Λ plays a role of the isotropization length. Higher-angular harmonics isotropize faster.

7.4

$$N(\boldsymbol{r},t) = \frac{1}{(4\pi t)^{3/2}\kappa_\perp\sqrt{\kappa_\parallel}}\exp\left(-\frac{x^2+y^2}{4\kappa_\perp t}-\frac{z^2}{4\kappa_\parallel t}\right).\overline{x^2}=\overline{y^2}=4\kappa_\perp t,$$
$$\overline{z^2} = 4\kappa_\parallel t.$$

7.5 The wanted Green function obeys the equation

$$\frac{\Lambda}{v}\frac{\partial^2 G}{\partial t^2}+\frac{\partial G}{\partial t}-\kappa\Delta G=\delta(\boldsymbol{r}-\boldsymbol{r}')\delta(t-t'). \tag{1}$$

For clearer interpretation of this equation and its solution let us rewrite Eq. (1) in a different form using the notations

$$u=\frac{v}{\sqrt{3}},\qquad \varrho=\frac{1}{\kappa}=\frac{3}{v\Lambda},\qquad u^2\varrho=\frac{v}{\Lambda},\qquad \boldsymbol{R}=\boldsymbol{r}-\boldsymbol{r}',\qquad \tau=t-t': \tag{2}$$

$$\Delta_R G-\frac{1}{u^2}\frac{\partial^2 G}{\partial\tau^2}-\varrho\frac{\partial G}{\partial\tau}=-\varrho\delta(\boldsymbol{R})\delta(\tau). \tag{3}$$

This equation has a form of a wave equation with a damping: the first two terms in the lhs contain D'Alembertian operator, while the third one, containing the first time derivative, describes a dissipation process; u is the velocity of wave perturbations.

Equation (3) can be solved using a method already applied to simpler Eq. (2.30) in Sect. 2.3.1. An only complication arises in passing by a cut in the complex plane when performing the inverse Fourier transform. The result is the following Green function:

$$G(R,\tau)=\frac{u\varrho}{4\pi R}\,e^{-u^2\varrho\tau/2}\left\{\delta(u\tau-R)+\frac{u\varrho R}{2\sqrt{R^2-u^2\tau^2}}\,J_1\left[\frac{1}{2}\varrho u\sqrt{R^2-u^2\tau^2}\right]\Theta(u\tau-R)\right\}, \tag{4}$$

containing the Bessel function J_1 [for the details, see Morse and Feshbach (1953) Chap. 7].

The first term containing the δ-function is similar to the Green function of the standard wave equation: it describes propagation of a wave with a velocity u out from a point source. Its amplitude declines due to both geometry as $1/R$ and dissipation in the fluid $\exp(-u^2\varrho\tau/2)$. The second term (with the Bessel function) describes purely dissipative effect, in which, however, a step function describing a finite propagation velocity is present. Therefore, this Green function ensures the finite propagation speed of the particles, while solutions of the standard diffusion equations (see above) are nonzero arbitrarily far away from the source for $t > 0$ implying a particle population moving with arbitrarily large velocity in contradiction with the special relativity theory.

To make a transition to the standard diffusion we consider a regime when $u\tau \gg R$ and $\varrho u^2\tau \gg 1$, i.e., $v\tau \gg \Lambda$. Then, using well-known properties of the Bessel functions and their asymptotes, we find the Green function of the diffusion equation

$$G(R,\tau) = \frac{1}{(4\pi\kappa\tau)^{3/2}} \exp\left(-\frac{R^2}{4\kappa\tau}\right). \tag{5}$$

Apparently, this transport regime becomes established over the time needed for the particles to travel a distance of many mfp.

7.6 Transition from a moving system to the laboratory system requires relativistic kinematics momentum transformation:

$$\boldsymbol{p}_0 = \frac{\boldsymbol{p} - \boldsymbol{u}\mathcal{E}/c^2}{\sqrt{1-u^2/c^2}} \approx \boldsymbol{p} - \frac{\boldsymbol{u}\mathcal{E}}{c^2}. \tag{1}$$

In the laboratory system the distribution function has the form

$$F(\boldsymbol{p}) = \frac{1}{4\pi} N(|\boldsymbol{p} - \boldsymbol{u}\mathcal{E}/c^2|) \approx \frac{1}{4\pi}\left[N(p) - \frac{\mathcal{E}\boldsymbol{u}\cdot\boldsymbol{p}}{c^2 p}\frac{\partial N}{\partial p}\right]. \tag{2}$$

The electric current density is

$$\boldsymbol{J} = \frac{1}{4\pi}\int \boldsymbol{v}F(\boldsymbol{p})\mathrm{d}\Omega_p = -\frac{p}{3}\frac{\partial N}{\partial p}\boldsymbol{u}. \tag{3}$$

7.7 The small-angle approximation implies $\sin\vartheta \approx \vartheta$, $\cos\vartheta \approx 1$; thus, the transport equation with a source in a stationary case receives the form

$$\frac{\partial f}{\partial s} + \frac{1}{2B}\frac{\partial B}{\partial s}\vartheta\frac{\partial f}{\partial \vartheta} = \frac{1}{2\Lambda(s)}\frac{1}{\vartheta}\frac{\partial}{\partial\vartheta}\vartheta\frac{\partial f}{\partial\vartheta} + \frac{Q_0}{2\pi\vartheta}\delta(\vartheta)\delta(s-s_0). \tag{1}$$

Here the point source enters the rhs; Q_0 is the particle generation rate by the source. The distribution function is

$$f(s,\vartheta) = \frac{Q_0 B(s)}{\pi B(s_0)\overline{\vartheta^2}(s)} \exp\left(-\frac{\vartheta^2}{\overline{\vartheta^2}(s)}\right), \qquad \overline{\vartheta^2}(s) = 2\int_{s_0}^{s} \frac{B(s)\mathrm{d}z}{B(z)\Lambda(z)}. \tag{2}$$

If the values B and Λ do not depend on s (uniform case), then the mean square of the scattering angle increases proportionally to the particle path $s - s_0$. However, in the nonuniform case, there are particles focusing due to the regular field in addition to the particle isotropization due to the random scattering. Consider, as an example, the magnetic field nonuniformity in the form $B \propto s^{-2}$, roughly typical for the solar wind region bounded by the Earth orbit. If the random field changes with the same law then $\Lambda(s) \approx \Lambda_0(s/s_0)^{2(2-\nu)}$ [here Eq. (7.106) for the transport mfp $\Lambda \propto R_0^{2-\nu}$ has been used]. For this case, Eq. (2) yields $\overline{\vartheta^2}(s) \propto s^{2\nu-3}$ for $s \gg s_0$. In particular, for the turbulent spectrum with $\nu = 3/2$, we obtain $2\nu - 3 = 0$, i.e., the particle beam propagates with a constant angular width: the angular scattering by the turbulence is compensated by the focusing in the declining regular field. Curiously, such cases of the "coherent" propagation of the solar protons have been observed in the interplanetary space.

7.8 The Fourier transform of the electric current is

$$j_{k\alpha} = ieQ\left(\frac{D^i_{\alpha\beta}}{\widetilde{D}^i} - \frac{\kappa_{\alpha\beta}}{\widetilde{\kappa}}\right)k_\beta.$$

Accordingly, in the real space,

$$\begin{aligned}\boldsymbol{j}(\boldsymbol{r}) \;=\; & \frac{eQ}{4\pi}\left\{\boldsymbol{e}_z\frac{\partial}{\partial z}\left[\frac{D^i_\parallel}{\sqrt{D^i_\perp(D^i_\perp z^2 + D^i_\parallel r_\perp^2)}} - \frac{\kappa_\parallel}{\sqrt{\kappa_\perp(\kappa_\perp z^2 + \kappa_\parallel r_\perp^2)}}\right]\right.\\ & +\nabla_\perp\left[\frac{D^i_\perp}{\sqrt{D^i_\perp(D^i_\perp z^2 + D^i_\parallel r_\perp^2)}} - \frac{\kappa_\perp}{\sqrt{\kappa_\perp(\kappa_\perp z^2 + \kappa_\parallel r_\perp^2)}}\right]\\ & \left.+\nabla\times\left[\frac{\boldsymbol{g}^i}{\sqrt{D^i_\perp(D^i_\perp z^2 + D^i_\parallel r_\perp^2)}} - \frac{\boldsymbol{g}^r}{\sqrt{\kappa_\perp(\kappa_\perp z^2 + \kappa_\parallel r_\perp^2)}}\right]\right\},\end{aligned}$$

where $\boldsymbol{g}^i = D^i_H\boldsymbol{e}_z$, $\boldsymbol{g}^r = \kappa_H\boldsymbol{e}_z$, and the axes Oz is along the uniform magnetic field $\boldsymbol{B}_0$.

Chapter 8

Dynamo Mechanism of Large-Scale Magnetic Field Generation

8.1 Astrophysical Magnetic Fields

Magnetic field is an important constituent of almost any astrophysical object; magnetic field values typical for some galactic astrophysical objects are listed in Table 1.1. The characteristic spatial scales of these fields can be of the same order of or ever greater than the size of the object. These large-scale fields often coexist with small-scale fields varying on scales much shorter than the object size. The small-scale field is not necessarily small compared with the large-scale one. It is important to realize that the effect produced by the magnetic fields on the source dynamics and evolution depends critically on the distribution of the magnetic energy over spatial and temporal scales, not on the magnetic field energy density alone. Therefore, study of the magnetic field over all available scales is needed to deeply understand astrophysical phenomena.

Remind that the magnetic fields vary from the smallest values about 10^{-9} G in extragalactic medium or at the Moon-like planetary satellites up to the largest values 10^{13}–10^{15} G in neutron stars; normal stars poses smaller magnetic fields but the stellar magnetic fields often exceed the mean magnetic field of the Sun ($\sim$1 G). In particular, young stars with well-developed convective zones display magnetic fields of the order of 2 kG, some "magnetic" Ap stars have the fields up to tens kG.

Magnetic fields are detected in most of the galaxies. An estimate of the mean galactic magnetic field using synchrotron radio emission (see Chap. 9) from 74 spiral galaxies yields $\langle B_{tot} \rangle = 9\ \mu$G, scattered between 4 and 15 μG, which agrees with values determined for the Galaxy using different methods (including the Faraday rotation; see Chap. 10). Considerable magnetic fields are reliably detected in Galaxy clusters with scales of a few Mpc and masses of 10^{14}–$10^{15} M_{\odot}$. The detected fields are of the order of a few μG at the cluster

G.D. Fleishman and I.N. Toptygin, *Cosmic Electrodynamics*, Astrophysics and Space Science Library 388, DOI 10.1007/978-1-4614-5782-4_8,

edges and up to a few tens μG at the central regions. The typical inhomogeneity scale of the magnetic field in the clusters is about 1 pc. A detailed review of the magnetic fields in various astrophysical objects is done by (Vallée 2003, 2004).

Origin and evolution of the magnetic fields are, therefore, fundamental astrophysical questions. The simplest hypothesis, that the currently observed fields are leftovers of a primary magnetic field of the Universe, only shifts the same question back to early stages of the Universe evolution. More importantly, this hypothesis is not supported by physical considerations: the magnetic fields are subject to Joule dissipation, so they would vanish without sources capable of producing magnetic fields and compensating the Joule dissipation. In addition, turbulent motions present in many cases enhance dissipation of the large-scale magnetic fields, as was shown in Chap. 6.

As a vivid example, consider here the turbulent dissipation of the magnetic field in the disk of our Galaxy. Observations suggest that the magnetic field belongs to the disk plane and has a value of a few μG. This "magnetic" disk has a diameter about $30\,\mathrm{kpc} \approx 10^{23}\,\mathrm{cm}$ and semithickness h around $0.4\text{–}0.5\,\mathrm{kpc} \approx (1.2-1.5)\times 10^{21}\,\mathrm{cm}$. In the disk there is turbulence with the main scale of $l \approx 100\,\mathrm{pc}$ and the characteristic velocity (at this scale) of $u \approx 10\,\mathrm{km/s} \approx 10^{6}\,\mathrm{cm/s}$. Accordingly, estimate (6.149) yields for the turbulent magnetic diffusivity $\nu_t \approx 10^{26}\,\mathrm{cm^2/s}$. In addition, there is a collisional magnetic diffusivity ν_m provided mainly by collisions of electrons and ions with neutral atoms, which was calculated in Chap. 1, Sect. 1.3.7: $\nu_m \approx (0.3-1)\times 10^{21}\,\mathrm{cm^2/s}$. Thus, here the turbulent magnetic diffusivity exceeds the collisional magnetic diffusivity by 5–6 orders of magnitude. The magnetic field diffusion time transverse to the disk is evaluated with Eq. (6.147) by equating the exponent index to one:

$$\Delta t \approx \frac{h^2}{4\nu_t} \approx 5\times 10^{15}\ s \approx 5\times 10^{8}\,\mathrm{years}.$$

This time is approximately one order of magnitude shorter than the Galaxy lifetime, which proves the necessity of a magnetic field source capable of supporting/amplifying the magnetic field.

Compact sources, e.g., stars or SNRs, have smaller sizes, so their magnetic fields would decay due to the turbulent magnetic diffusivity much faster. An extreme power of the magnetic field generation mechanisms is likely needed in the neutron stars. Right after the collapse of the parent star exploding as supernova, a stage of hydrodynamic instability occurs in the compact remnant. Numerical simulations suggest that this stage lasts about one minute with the typical fluid velocity up to subliminal values of $10^9\,\mathrm{cm/s}$; the full rotation of the fluid in a single convective cell takes around 10^{-3}–$10^{-4}\,\mathrm{s}$. Depending on the star rotation rate, this strong convection results in either dissipation of the primary magnetic field or its amplification by many orders of magnitude by the turbulent dynamo mechanism (see below) up to extremely high observed values.

8.2 Dynamo Mechanism and Antidynamo Theorems

MHD dynamo is currently believed to be the most universal way of the large-scale magnetic field generation. The term "dynamo" means support and amplification of a primary field $\boldsymbol{B}_0(\boldsymbol{r})$ by mechanical motions of ionized electroconducting gas or fluid. Initially, this idea was proposed by English scientist Joseph Larmor in 1919 in the context of solar and terrestrial magnetic field origin.

The currently available dynamo models require typically some initial (seed) magnetic field. If present, this field can then be amplified by the conducting fluid motions under certain conditions. Most of the models explore a kinematic approximation, i.e., assuming a given velocity field of the fluid neglecting any back effect of the generated magnetic field on the fluid motions. However, even this simplified problem is still very complicated. Let us consider a number of simple cases clarifying the problem and its complexity.

Adopt that the fluid volume of interest ($\boldsymbol{u}(\boldsymbol{r}) \neq 0$) is spatially bounded and initial magnetic energy $W_0 = \int (B^2/8\pi)\mathrm{d}V$ is bounded as well. Then, the dynamo problem requires solving a linear set of equations (2.16) with variable coefficients:

$$\nabla\cdot\boldsymbol{B} = 0, \qquad \frac{\partial \boldsymbol{B}}{\partial t} = \nabla\times[\boldsymbol{u}\times\boldsymbol{B}] - \nabla\times\nu_m(\nabla\times\boldsymbol{B}), \qquad \nu_m = \frac{c^2}{4\pi\sigma(\boldsymbol{r})}. \quad (8.1)$$

Here the velocity field $\boldsymbol{u}(\boldsymbol{r}) \neq 0$ and the magnetic diffusivity $\nu_m(\boldsymbol{r})$ are fixed, though can depend on the coordinates, which complicate the equation compared with Eq. (2.16). The initial condition is $\boldsymbol{B}(\boldsymbol{r}, t = 0) = \boldsymbol{B}_0(\boldsymbol{r})$, while the boundary conditions require that the field is bounded everywhere and goes at the infinity to zero as r^{-3} or faster:

$$B(r)|_{r\to\infty} \lesssim Cr^{-3} \to 0. \quad (8.2)$$

The dependence $B \sim r^{-3}$ at large r implies a nonzero magnetic dipole moment produced by electric currents in the original volume; otherwise, the field decreases faster.

Let us derive now an equation for magnetic energy balance from Eq. (8.1). Multiplying the induction equation by $\boldsymbol{B}/4\pi$ and applying simple manipulations, we obtain

$$\frac{\mathrm{d}}{\mathrm{d}t}\int \frac{B^2}{8\pi}\mathrm{d}V = -\frac{1}{c}\int \boldsymbol{u}\cdot[\boldsymbol{j}\times\boldsymbol{B}]\mathrm{d}V - \int \frac{j^2}{\sigma}\mathrm{d}V, \quad (8.3)$$

where $\boldsymbol{j} = c\nabla\times\boldsymbol{B}/4\pi$. Here, we have used condition (8.2) of fast magnetic field decrease at large distance. In Eq. (8.3), the first term in the rhs describes energy exchange between the field and the fluid interacting by the Ampère law $\boldsymbol{j}\times\boldsymbol{B}/c$; this is a sign-alternating term. The second term describing the Joule dissipation of the field is positively defined. Thus, without the first

term, i.e., when $u = 0$, or when the integral goes to zero, the only remaining process is the field dissipation; the vector $\boldsymbol{B}$ and any of its component go to zero as $t \to \infty$.

Operation of a dynamo process implies that the fluid velocity field acts so as to compensate the Joule loss and maintain the magnetic energy (of the considered object) at some nonzero level over an arbitrarily long time with, perhaps, some pulsations around the mean level. Within the kinematic approximation, i.e., linear theory, the magnetic field can even grow infinitely; however, in a reality, any linear growth will end at a saturation level due to yet uncounted nonlinearity created by the dynamic effect of the growing magnetic field on the velocity field. An oscillatory (cyclic) behavior of the field is observed in stars and Sun; see below for more detail (Sects. 8.7.2 and 8.7.4).

Differential Rotation. However, an arbitrary large-scale plasma motion will not necessarily generate and support the magnetic field. Let us address this question by considering a so-called differential rotation, which is typical for many rotating objects including stars, accretion disks, and spiral galaxies (e.g., our Galaxy). This type of plasma rotation takes place when different plasma layers rotate with different angular velocities. In particular, at the Sun, the equatorial region rotates faster (around 14° per day) than the high-latitude zones ($\approx 10°$ per day). Synodic (i.e., as viewed from the Earth) rotation period of the solar equator is 26.24 days, which corresponds to sidereal (i.e., in the galactic frame) rotation period of 24.47 days, while at a latitude of 26° the so-called Carrington rotation is slower: a synodic rotation period is 27.28 days (the sidereal period is 25.38 days). Rotation curves of the spiral galaxies (i.e., dependencies $u(r)$, where u is the linear rotation speed, r is the distance to the galactic center) display a complicated shape, which often highly deviates from the direct proportionality typical for a "rigid-body" rotation with a constant angular velocity $\Omega = \text{const}$. The differential rotation results in an increase of the distance between two plasma elements rotating with different angular velocities. If they are linked by a magnetic field line, it stretches, which means the field amplification; cf. Problem 6.5.

Now perform a quantitative consideration of this effect. Consider a plasma involved in a stationary differential rotation with angular velocity $\boldsymbol{\Omega} = \boldsymbol{e}_z \Omega(r, \vartheta)$, where r and ϑ are the spherical coordinates. Adopt that initially the field belongs to the meridian planes: $\boldsymbol{B} = (B_{0r}(r, \vartheta), B_{0\vartheta}(r, \vartheta), 0)$ at $t = 0$ (a poloidal field); a dipole field is a simplest example of the poloidal field. Let us first calculate the magnetic field at $t > 0$ neglecting the dissipation, ($\nu_m \to 0$).

The field of the linear velocities $\boldsymbol{u}(\boldsymbol{r})$ in the plasma is described by a vector function $\boldsymbol{u}(\boldsymbol{r}) = \boldsymbol{e}_\alpha r \Omega(r, \vartheta) \sin\vartheta$. Induction equation (8.1) with $\nu_m \to 0$ gives the equation set for the field components

$$\frac{\partial B_r}{\partial t} = 0, \quad \frac{\partial B_\vartheta}{\partial t} = 0, \quad \frac{\partial B_\alpha}{\partial t} = \sin\vartheta \left(r B_r(r, \vartheta) \frac{\partial \Omega}{\partial r} + B_\vartheta \frac{\partial \Omega}{\partial \vartheta} \right), \tag{8.4}$$

which is easily solved to yield

$$B_\alpha(r,\vartheta,t)=\sin\vartheta\left(rB_{0r}(r,\vartheta)\frac{\partial\Omega}{\partial r}+B_{0\vartheta}\frac{\partial\Omega}{\partial\vartheta}\right)t,\ B_\vartheta=B_{0\vartheta},\ B_r=B_{0r}. \tag{8.5}$$

This solution shows that the differential rotation produces an azimuthal component of the magnetic field (a toroidal field) from the original poloidal field. This process, however, being proportional to the time, is relatively slow and cannot last arbitrarily long. Indeed, the poloidal field, and accordingly the toroidal field, will decay due to a finite magnetic diffusivity (in fact, always $\nu_m\neq 0$). This decay occurs with an exponential law, which overcomes the linear growth law at a long run; thus, eventually the field will fully disappear from the region under study. Before that, however, it does experience a significant evolution; solar active regions (ARs) (see, e.g., Fig. 6.3) offer a vivid example of such long-living changing magnetic structures, which eventually decay and disappear from the solar disk typically in a month or a few months.

Let us estimate the time interval Δt after which the magnetic diffusivity comes into play. Consider the field at some radius r_0; on the order of magnitude we have $B_\alpha(t)\approx B_0\Omega_0 t$, where B_0 is the seed poloidal field and Ω_0 is an appropriate mean value of the angular velocity (for this estimate, we adopted $\sin\vartheta\approx 1$ and $r\mathrm{d}\Omega/\mathrm{d}r\approx\Omega_0$), while estimate of the dissipative term is $(\triangle\boldsymbol{B})_\alpha\approx B_\alpha(t)/r_0^2$. Compare these two terms with each other in the rhs of induction Eq. (8.1):

$$\frac{\partial B_\alpha(t)}{\partial t}\approx B_0\Omega_0+\nu_m\frac{B_\alpha}{r_0^2}.$$

They have the same order of magnitude at $t=\Delta t\approx r_0^2/\nu_m$. By this time the toroidal field reaches $B_\alpha\approx B_0R_m$, where $R_m=r_0^2\Omega_0/\nu_m$ is the magnetic Reynolds number. Then, the field dissipates at times larger than Δt.

Now, we apply these equations to estimate the lifetime of ARs in the solar photosphere. Using the solar radius $r_0=R_\odot\approx 6.96\cdot 10^{10}$ cm and collisional magnetic diffusivity, Eq. (1.150), $\nu_m\approx 10^7\,\mathrm{cm}^2/\mathrm{s}$, we find $\Delta t\sim R_\odot^2/\nu_m\sim 5\cdot 10^{14}\,\mathrm{s}\approx 1.7\cdot 10^7$ years in a huge contradiction with the observed AR lifetime. To remedy this inconsistency we note that the magnetic Reynolds number in the solar photosphere is large, $R_m=R_\odot^2\Omega_\odot/\nu_m\sim 2\cdot 10^8$, where $\Omega_\odot\approx 4\cdot 10^{-7}\,\mathrm{s}$, which implies a dominant role of the turbulent magnetic diffusivity (Sect. 6.11) over the collisioinal one. Taking the characteristic AR size $l\sim 10^{10}$ cm and identifying the proton thermal speed with the turbulent velocity $u\sim 10^5$ cm/s we use Eq. (6.149) to estimate the turbulent magnetic diffusivity as $\nu_t\sim ul/3\sim 3\cdot 10^{14}\,\mathrm{cm}^2/\mathrm{s}$. Replacing the collisional to turbulent diffusivity in the above estimate, we find $\Delta t\sim R_\odot^2/\nu_t\sim 1.5\cdot 10^7\,\mathrm{s}\approx 0.5$ year in full qualitative agreement with observations, which confirms once again the primary role the turbulence plays in the astrophysics.

Elsasser Antidynamo Theorem. We now confirm these qualitative considerations and estimates by more solid quantitative analysis. We adopt

the vector velocity field to have the following form in the spherical coordinates $\boldsymbol{u} = \nabla \times (\boldsymbol{e}_r \psi(\boldsymbol{r}))$, where $\psi(\boldsymbol{r})$ is an arbitrary scalar function, while the electroconductivity $\sigma(r)$ depends on the radial distance only. Let us prove that the magnetic field disappears over a finite time regardless initial state of the field.

Write $\boldsymbol{u} = \nabla\psi \times \boldsymbol{e}_r$ and project induction Eq. (8.1) on the axes $\boldsymbol{e}_r$. We obtain for the dissipative term $\boldsymbol{e}_r \cdot (\nabla \times [\boldsymbol{u} \times \boldsymbol{B}]) = -(\boldsymbol{u}\cdot\nabla)B_r$:

$$-\boldsymbol{e}_r \cdot (\nabla \times \nu_m [\nabla \times \boldsymbol{B}]) = \nu_m \left(\triangle B_r + \frac{2}{r}\frac{\partial B_r}{\partial r} + \frac{2}{r^2} B_r \right). \tag{8.6}$$

We have taken into account that $\nabla\nu_m$ is directed along $\boldsymbol{e}_r$ and $\nabla\cdot\boldsymbol{B} = 0$. Thus, equation for B_r receives the form

$$\frac{\partial B_r}{\partial t} + (\boldsymbol{u}\cdot\nabla)B_r = \nu_m \left(\triangle B_r + \frac{2}{r}\frac{\partial B_r}{\partial r} + \frac{2}{r^2} B_r \right). \tag{8.7}$$

Let us multiply Eq. (8.7) by $B_r/4\pi$ and integrate both parts of the equation over the whole space. Then, transforming the term $\int B_r(\boldsymbol{u}\cdot\nabla)B_r \mathrm{d}V$ according to Ostrogradsky–Gauss theorem and using incompressibility condition $\nabla\cdot\boldsymbol{u} = 0$, we obtain zero. The energy balance equation for B_r-component,

$$\frac{\mathrm{d}}{\mathrm{d}t}\int \frac{B_r^2}{8\pi}\mathrm{d}V = \frac{1}{4\pi}\int \nu_m B_r \left(\triangle B_r + \frac{2}{r}\frac{\partial B_r}{\partial r} + \frac{2}{r^2} B_r \right) \mathrm{d}V, \tag{8.8}$$

does not contain the fluid velocity $\boldsymbol{u}$ and so describes a purely dissipative process, dissipation of B_r-component due to the magnetic diffusivity, i.e., $B_r \to 0$ at $t \to \infty$ (cf. discussion after Eq. (8.3)). Therefore, evolution of the field components transverse to $\boldsymbol{r}$ can be studied adopting $B_r = 0$.

The transverse components of the field are convenient to consider using the vector potential $\boldsymbol{B}(\boldsymbol{r}, t) = \nabla \times \boldsymbol{A}(\boldsymbol{r}, t)$, which obeys the equation

$$\frac{\partial \boldsymbol{A}}{\partial t} = \boldsymbol{u} \times [\nabla \times \boldsymbol{A}] - \nu_m \nabla \times [\nabla \times \boldsymbol{A}]. \tag{8.9}$$

To make sure that this equation is equivalent to Eq. (8.1) one can apply operator $\nabla\times$ to it. It is convenient to adopt the following form of the vector potential $\boldsymbol{A}(\boldsymbol{r}, t) = \boldsymbol{e}_r A(\boldsymbol{r}, t)$ that explicitly ensures vanishing B_r. Here $A(\boldsymbol{r}, t)$ is an arbitrary differentiable function; equation for this scalar function $A(\boldsymbol{r}, t)$ receives the form:

$$\frac{\partial A}{\partial t} + (\boldsymbol{u}\cdot\nabla)A = \nu_m \left(\triangle A - \frac{2}{r^2} A - \frac{\partial}{\partial r}\frac{1}{r^2}\frac{\partial}{\partial r} r^2 A \right). \tag{8.10}$$

Let us multiply both sides of the equality by A/ν_m; then integration over the entire space yields

$$\frac{\mathrm{d}}{\mathrm{d}t}\int \frac{A^2}{\nu_m}\mathrm{d}V = -2\int \left(\nabla A - \boldsymbol{e}_r \frac{\partial A}{\partial r} \right)^2 \mathrm{d}V \le 0. \tag{8.11}$$

This condition ensures $A = \text{const}$ everywhere in space for $t \to \infty$, because the integral $\int (A^2/\nu_m) \mathrm{d}V \geq 0$ cannot become negative; thus, the derivatives over time and coordinates must vanish, which means evanescent transverse magnetic field.

This result envisions only one example of a large number of the so-called "antidynamo theorems," which can be found in a number of books, e.g., Moffatt (1978) and Vainshtein (1983). Overall, these theorems demonstrate that too symmetric (e.g., two-dimensional) fluid motion cannot support the magnetic field for a long time; the first of these theorems was proved by Cowling (1957). See also Zeldovich's antidynamo theorem in Problem 8.1.

Nevertheless, no antidynamo theorem proves absence of the dynamo effect in principle. In fact, each such a theorem is only valid within an assumption of some specific symmetry of the velocity or magnetic field. There is no general theorem formulating a set of necessary and sufficient conditions excluding the magnetic field amplification; it is unclear if they can be formulated in a general form. On the contrary, there are many models of 3D fluid motion, which do give rise to a magnetic field amplification.

8.3 Examples of Laminar Dynamo

Efficient generation of the magnetic field, as established, requires an asymmetric 3D motion of the conducing fluid or gas. A historically first laboratory model of that kind was proposed by Herzenberg (1958). He proposed a stationary fluid velocity field $\boldsymbol{u}(\boldsymbol{r})$ in a spherical volume capable of compensating damping of initial stationary magnetic field $\boldsymbol{B}_0(\boldsymbol{r})$ and producing a nonzero dipole moment outside the sphere. The velocity field was created by two spherical rotors embedded in a conducting fluid inside the large sphere; the fluid was assumed immobile. The angular velocities of the rotors were adopted constant and generally different by both magnitude and direction; the rotor radii were small compared with the distance between their centers, while the distance small compared with the sphere radius. The toroidal field produced by each rotor played a role of a seed poloidal field for the other rotor, which, thus, mutually helped each other in amplifying their fields due to rotations.

The Herzenberg model is particularly remarkable as it received direct qualitative experimental confirmation in the laboratory experiments of Lowes and Wilkinson (1963, 1968). Their device was composed of a large cylindrical body inside which two cylindrical rotors made from the same metal rotated. The electric lubricator between the main body and the rotors was provided by a narrow layer of liquid mercury (Fig. 8.1). At some appropriate rotor orientation and reasonably high rotation velocity of 400 cycles/min (which provided the magnetic Reynolds number of $R_m \approx 200$) the dynamo effect appeared: the magnetic field measured outside the main cylinder went up. The electric currents in the cylinder kept increasing up to the point when

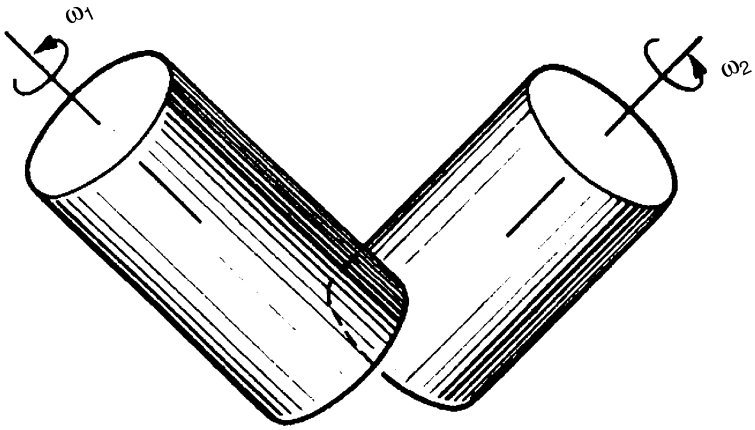

Figure 8.1: Rotor dynamo of Lowes and Wilkinson (Moffatt 1978).

the breaking angular momentum produced by the Ampère force acting on the rotors turned to be strong enough to slow the rotors' rotation down to subcritical values. Later the Herzenberg theoretical model was generalized to the case of n spheres; other models were proposed, e.g., Gailitis model, where the magnetic field is amplified by a moving pair of vortex rings; for more examples see Moffatt (1978) (Chap. 6), and Gailitis et al. (2002). The field propagated from one rotor to the other due to the field diffusion, which is a relatively slow process; thus, this kind of dynamo is relatively slow.

In contrast, there are also models of fast dynamo, e.g., stretch-twist-fold-merge dynamo proposed by Yakov Zeldovich (see, e.g., Vainshtein et al. 1980). Consider a bundle of closed lines of magnetic force frozen into a conducting fluid and so composing a ring with a finite thickness (Fig. 8.2a). Let the fluid motion stretch this ring to an ellipse (Fig. 8.2b) with twice smaller bundle cross section; then, given the magnetic flux conservation, the magnetic field B is twice enhanced at the expense of the fluid velocity energy that had produced this ring deformation. The next stage of this process is transformation of the ellipse into "Zeldovich's eight" (Fig. 8.2c), i.e., its twist. To do so, the contour must leave the original plane, i.e., the process must necessarily be 3D. The last step is to fold the eight and merge the two rings into one ring with original area while twice enhanced magnetic field (Fig. 8.2d).

Note that although initial stages of this fast dynamo can occur within the field freezing-in, the final merge requires to remove the unwanted poloidal field and thus requires a dissipative diffusion process. Repetition of this process n times results in 2^n folding field amplification, i.e., the field grows exponentially, $B(t) = B_0 \mathrm{e}^{t \ln 2/\tau}$, where τ is one cycle time.

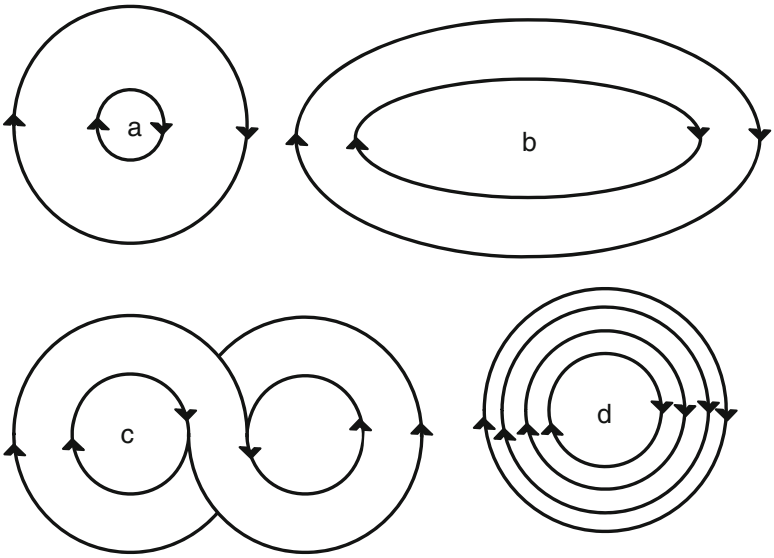

Figure 8.2: Zeldovich's "eight." Magnetic field strengthening at 3D movement of medium.

Apparently, this is a fast dynamo; its speed is defined by the fluid velocity. It is important to realize that even here the entire cycle must include a dissipative process of magnetic force line reconnection; see Sect. 2.3.2, to allow overall field enhancement. This enhancement, however, cannot last infinitely long; a finite free energy stored in the fluid velocity field will eventually saturate it; the fluid resistance to this process will increase with each cycle.

8.4 Helical Turbulence and Kinetic Helicity

8.4.1 Kinetic Helicity Parameter

Since the dynamo mechanism requires nonsymmetric three-dimensional motions to operate, it is reasonable to explore the turbulent motions—those displaying stochasticity, random variations in space and time, and lack of the order. However, even some turbulent motions, namely those described by symmetric correlation tensor (6.137), do not support large-scale magnetic field, while just break it down toward smaller scales and so enhance the magnetic field dissipation; see Sect. 6.11 where the turbulent magnetic diffusivity is calculated. Thus, even less symmetric motions are needed to support and amplify the field.

Parker, Steenbek, and Krause (see Parker 1979; Krause and Rädler 1980) discovered that the large-scale field can be produced by a turbulence without mirror symmetry (gyrotropic or helical turbulence), e.g., a turbulence with a different amount of clockwise and anticlockwise eddies. This ability to amplify the large-scale magnetic field is the main driver of studying the

helical turbulence in the astrophysical context. The correlation tensor of this turbulence contains both polar and axial vectors. Perhaps the simplest example of such structure represents the correlation tensor of statistically uniform gyrotropic incompressible fluid:

$$\widetilde{U}_{\mu\nu}(\boldsymbol{k},t) = A(k,t)\left(\delta_{\mu\nu} - \frac{k_\mu k_\nu}{k^2}\right) - iP(k,t)e_{\mu\nu\lambda}k_\lambda. \tag{8.12}$$

Importantly, the function $P(k,t)$ here must be a pseudoscalar, i.e., change the sign at the coordinate inversion. The unit antisymmetric tensor $e_{\mu\nu\lambda}$ is axial, i.e., does not change the sign at the coordinate inversion. As a result, all the terms in the rhs of Eq. (8.12) are the polar tensors as needed.

Helical turbulence can appear in a rotating body due to the Coriolis force. Let us show that the turbulence helicity can be quantified by the following integral parameter:

$$\alpha = -\frac{1}{3}\int_0^\infty \langle \boldsymbol{u}(\boldsymbol{r},t+\tau)\cdot\nabla\times\boldsymbol{u}(\boldsymbol{r},t)\rangle \mathrm{d}\tau = -\frac{\tau_c}{3}\langle \boldsymbol{u}(\boldsymbol{r},t)\cdot\nabla\times\boldsymbol{u}(\boldsymbol{r},t)\rangle. \tag{8.13}$$

The last equality is in fact the definition of the turbulence correlation time τ_c. For stationary turbulence α does not depend on time, so we can adopt $t=0$ and then write

$$\begin{aligned}\langle \boldsymbol{u}(\boldsymbol{r},0)\cdot\nabla\times\boldsymbol{u}(\boldsymbol{r},0)\rangle &= e_{\lambda\mu\nu}\frac{\partial}{\partial x_{2\mu}}\langle u_\lambda(\boldsymbol{r}_1,0)u_\nu(\boldsymbol{r}_2,0)\rangle\,|_{\boldsymbol{r}_1\to\boldsymbol{r}_2}\\ &= -i\,e_{\lambda\mu\nu}\int\frac{\mathrm{d}^3k}{(2\pi)^3}k_\mu\widetilde{U}_{\lambda\nu}(\boldsymbol{k},0).\end{aligned}$$

Substituting here Eq. (8.13) and making use of Eq. (8.12), we obtain the relation between the pseudoscalar α and the pseudoscalar function $P(k,0)$:

$$\alpha = -\frac{\tau_c}{3\pi^2}\int_0^\infty k^4 P(k,0)\mathrm{d}k. \tag{8.14}$$

This measure, α, is called the kinetic helicity parameter.

Nonzero helicity is only possible for the systems in which the pseudoscalar α can be build from the available physical parameters. For example, this is the case for a rotating body (the rotation is quantified by an axial vector of angular velocity $\boldsymbol{\Omega}$) with a nonuniform density distribution characterized by the density gradient $\nabla\rho/\rho \neq 0$. This gradient is a usual (polar) vector whose components change the sign at the coordinate inversion, while the components of the axial vector $\boldsymbol{\Omega}$ do not change the sign. Thus, the dot product of these vectors forms a pseudoscalar $\boldsymbol{\Omega}\cdot\nabla\rho/\rho = \Omega/h$, which changes the sign at the coordinate inversion and so is suitable to built the helicity parameter α. Here $h = \rho\mathrm{d}z/\mathrm{d}\rho$, if Oz axes are along $\boldsymbol{\Omega}$. The length h is the spatial scale of the density inhomogeneity; α parameter with the required dimension can then be built using the characteristic spatial scale of the turbulent motion l:

$$\alpha \approx \frac{l^2\Omega}{h}. \tag{8.15}$$

Apparently, this qualitative consideration can determine neither the sign of the expression nor the dimensionless factor.

8.4.2 Helical Turbulence in Rotating Bodies

In various objects the helicity can be estimated explicitly by accounting forces acting on the gas. Consider the galactic disk as an example; see Fig. 8.3. The disk rotates differentially around axes Oz. The gas density has a peak at the galactic plane, while decreases upward and downward. The galactic turbulence is only weakly nonuniform: the scale of the nonuniformity is large compared with the turbulence correlation scale.

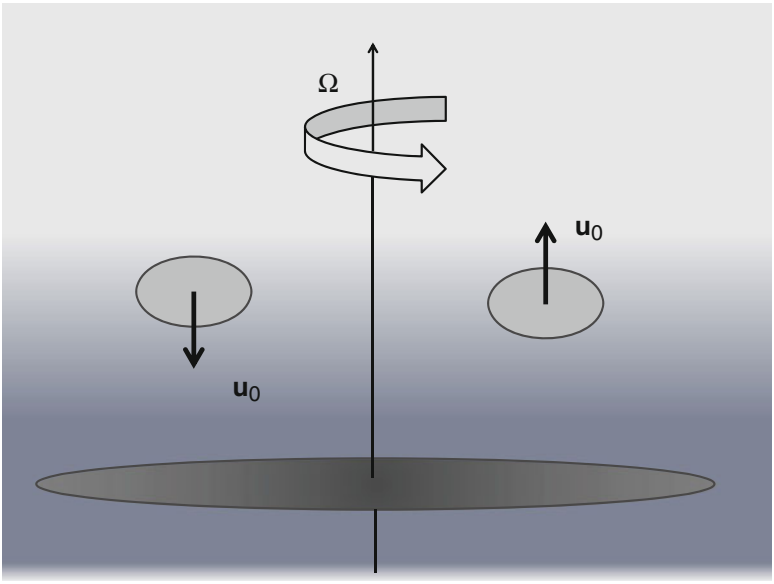

Figure 8.3: Illustration of Coriolis force origin and correlation between velocity and velocity vortex in a turbulent cell of the nonuniform medium.

Now, consider a gas cloud with a size comparable with the turbulence cell l located in the upper part of the disk and moving up with the velocity $u_z^+ \approx u_0 > 0$. In the adopted statistically uniform (along the galactic plane) turbulence there is a similar cloud moving down with the same velocity $u_z^- \approx -u_0 < 0$. However, these clouds are not perfectly the same: the cloud moving up expands, while the cloud moving down contracts because of the mentioned density gradient. Thus, radial components of the velocity $u_r^\pm$ are produced by this expansion/contraction; its value is set up by the density inhomogeneity, $u_r^\pm \approx \mp u_0 l/h$. In the non-inertial (rotating) system the radial motion produces the Coriolis force $\boldsymbol{F}_C = 2\boldsymbol{u} \times \boldsymbol{\Omega}$ per unit mass, whose magnitude is estimated as $F_C^\pm \approx -2u_r^\pm \Omega$.

This Coriolis force spins the clouds around the vertical axes: the upper cloud rotates oppositely to the disk rotation, while the lower cloud along the disk rotation. However, the net effect of these spinning clouds is nonzero: the

contribution from the larger upper cloud prevails. As a result, the upper part of the disk is dominated by the left-handed motions, while the lower part by the right-handed. Over the correlation time $\tau_c \approx l/u_0$, which is a lifetime of a distinct turbulent cell roughly equal to the time needed to complete one-fluid rotation in the cell, the azimuth components of the cloud velocities will get values of $u_\alpha^\pm \approx F_C^\pm \tau_c$ under the Coriolis force action.

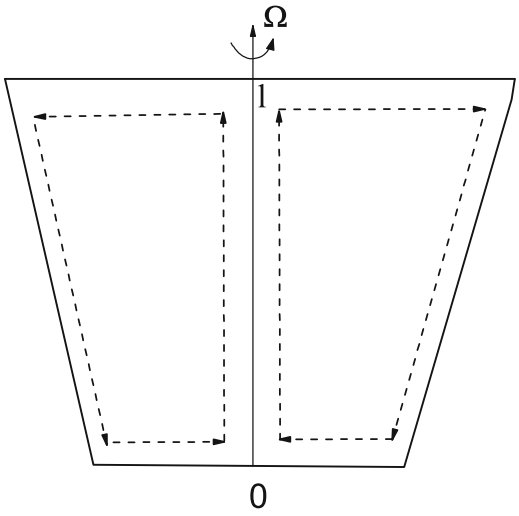

Figure 8.4: Illustration of helicity origin in a convection cell.

The azimuth components of the cloud velocities gain the value $u_\alpha^\pm \approx F_C^\pm \tau_c$ due to the Coriolis force action during the correlation time $\tau_c \approx l/u_0$ over which the clouds exist in the strong turbulence (Sect. 6.7). Finally, gathering all required factors, we again obtain order-of-magnitude estimate (8.15):

$$\alpha = -\frac{\tau_c}{3}\langle \boldsymbol{u} \cdot \nabla \times \boldsymbol{u} \rangle \approx \begin{cases} l^2\Omega/|h|, & z > 0; \\ -l^2\Omega/|h|, & z < 0. \end{cases} \tag{8.16}$$

A similar picture takes place in a rotating star with a turbulent convective zone. Parameter l can be associated here with the height of the convective cell (Fig. 8.4); arrows indicate the fluid velocity in a single convective cell. Equation (8.16) is valid (to the order of magnitude) for this case as well.

8.5 Mean Field in a Fluid with Helical Turbulence

8.5.1 Approximation of Short Correlation Time

Let us demonstrate that the helical turbulence is indeed capable of producing a magnetic field with spatial scales much larger than the turbulence

scales. It is easy to foresee that the turbulent dynamo problem is much more complicated than analysis of the laminar dynamo; thus, some approximations and simplifications are unavoidable to formulate a concise analytical consideration. First, we will consider here the large-scale field only, to make averaging over the turbulent ensemble. A similar approach, typical for macroscopic electrodynamics, has already been applied in Sect. 6.11. Second, since the large-scale magnetic field varies only slowly with time, while the realization of the statistically stationary turbulence changes over time $\tau_c \approx l/\sqrt{\langle u^2 \rangle}$, we can safely neglect the finiteness of the correlation time and set this time to zero, which yields the following form of the correlation tensor [cf. Eq. (6.84)]:

$$U_{\alpha\beta}(\boldsymbol{r}, t) = \{Q(r)\delta_{\alpha\beta} + R(r)x_\alpha x_\beta + C(r)e_{\alpha\beta\sigma}x_\sigma\} \cdot 2\tau_c\, \delta(t). \tag{8.17}$$

In contrast to Eq. (6.84), this tensor is presented in the spatial–temporal form. And third, we again use the kinematic approximation, i.e., consider a given turbulent velocity field that does not evolve in spite of the large-scale magnetic field growth.

Let us first derive equations describing the large-scale magnetic field in the presence of the helical turbulence and then investigate its solutions. Using notation of Sect. 6.11, the induction equation (before the statistical averaging) can be written in the form

$$\frac{\partial \mathcal{H}_\alpha}{\partial \tau} - \nu_m \triangle \mathcal{H}_\alpha = A^{\alpha\mu}_{\gamma\sigma} \frac{\partial}{\partial x_\mu} u_\gamma \mathcal{H}_\sigma + B_\alpha(\boldsymbol{r}, t)\delta(\tau - t), \qquad \tau \geq t, \tag{8.18}$$

where $A^{\alpha\mu}_{\gamma\sigma} = e_{\alpha\mu\nu}e_{\nu\gamma\sigma}$, u_γ is the turbulent velocity with zero mean, the collisional magnetic diffusivity $\nu_m = c^2/4\pi\sigma$ is assumed to be finite and constant, and δ-term describes the initial condition for non-averaged field $\boldsymbol{\mathcal{H}}(\boldsymbol{r}, t)$.

Integral form of Eq. (8.18) can be written as

$$\mathcal{H}_\alpha(\tau) = A^{\alpha\mu}_{\gamma\sigma} \int \mathrm{d}\tau' \int \mathrm{d}^3 x' G(\boldsymbol{r} - \boldsymbol{r}', \tau - \tau') \frac{\partial}{\partial x'_\mu} u'_\gamma \mathcal{H}'_\sigma + B^{(0)}_\alpha(\boldsymbol{r}, \tau), \tag{8.19}$$

where

$$B^{(0)}_\alpha(\boldsymbol{r}, \tau) = \int \mathrm{d}^3 x' G(\boldsymbol{r} - \boldsymbol{r}', \tau - t) B_\alpha(\boldsymbol{r}', t) \tag{8.20}$$

and G is Green function (2.32), obeying the initial condition $G(\boldsymbol{r}, \tau) \to \delta(\boldsymbol{r})$ for $\tau \to 0$.

In contrast to consideration performed in Sect. 6.11, we do not apply here the perturbation theory over the turbulence measures. Instead, we derive from Eq. (8.19) the field component $\mathcal{H}_\alpha$ at the time $\tau = t + \Delta t$ by the iteration method with the linear term Δt accuracy. Since $\mathcal{H}_\alpha(\boldsymbol{r}, t + \Delta t)$ depends explicitly on the turbulent velocities, the corresponding averaging can then be performed straightforwardly. Then, assuming Δt to be small compared with the variability scale of the mean (but not the turbulent!) field,

we obtain a differential equation for $\boldsymbol{B}(\boldsymbol{r},t)$, which will be valid for large magnetic Reynolds numbers.

Zero-order iteration over the random velocity is given by Eq. (8.20), which can be rewritten in the form

$$B_\alpha^{(0)}(\boldsymbol{r},t+\Delta t) = B_\alpha(\boldsymbol{r},t) + \Delta t\,\nu_m \triangle B_\alpha(\boldsymbol{r},t). \tag{8.21}$$

This follows from the fact that $G(\boldsymbol{r},\tau) \to \delta(\boldsymbol{r})$ for $\tau \to 0$, while the correction to the Green function for a small Δt has the form $(\partial G/\partial\tau)\Delta t = \Delta t \nu_m \triangle G(\boldsymbol{r}-\boldsymbol{r}',t)$. Integration of the corresponding term in Eq. (8.20) by parts twice yields Eq. (8.21).

In the first-order iteration we substitute the zero-order solution (8.20) or (8.21) into the integral term in Eq. (8.19):

$$\mathcal{H}_\alpha^{(1)}(\boldsymbol{r},\tau) = A_{\gamma\sigma}^{\alpha\mu}\int_t^\tau \mathrm{d}\tau' \int \mathrm{d}^3x' G(\boldsymbol{r}-\boldsymbol{r}',\tau-\tau')\frac{\partial}{\partial x'_\mu}u'_\gamma(\boldsymbol{r}',\tau')B_\sigma^{(0)}(\boldsymbol{r}',\tau') + B_\alpha^{(0)}(\boldsymbol{r},\tau). \tag{8.22}$$

Finally, the second-order iteration has the form

$$\begin{aligned}
\mathcal{H}_\alpha^{(2)}(\boldsymbol{r},\tau) &= A_{\gamma\sigma}^{\alpha\mu}\int_t^\tau \mathrm{d}\tau' \int \mathrm{d}^3x' G(\boldsymbol{r}-\boldsymbol{r}',\tau-\tau')\frac{\partial}{\partial x'_\mu}u'_\gamma(\boldsymbol{r}',\tau')\mathcal{H}_\sigma^{(1)}(\boldsymbol{r}',\tau') + B_\alpha^{(0)}(\boldsymbol{r},\tau) \\
&= A_{\gamma\sigma}^{\alpha\mu}A_{\kappa\epsilon}^{\sigma\nu}\int_t^\tau \mathrm{d}\tau_1 \int \mathrm{d}^3x_1 G(\boldsymbol{r}-\boldsymbol{r}_1,\tau-\tau_1)\frac{\partial}{\partial x_{1\mu}}u_\gamma(\boldsymbol{r}_1,\tau_1) \\
&\quad\times \int_t^{\tau_1}\mathrm{d}\tau_2 \int \mathrm{d}^3x_2 G(\boldsymbol{r}_1-\boldsymbol{r}_2,\tau_1-\tau_2)\frac{\partial}{\partial x_{1\nu}}u_\kappa(\boldsymbol{r}_2,\tau_2)B_\epsilon^{(0)}(\boldsymbol{r}_2,\tau_2) \\
&\quad + A_{\gamma\sigma}^{\alpha\mu}\int_t^\tau \mathrm{d}\tau_1 \int \mathrm{d}^3x_1 G(\boldsymbol{r}-\boldsymbol{r}_1,\tau-\tau_1)\frac{\partial}{\partial x_{1\mu}}u_\gamma(\boldsymbol{r}_1,\tau_1)B_\sigma^{(0)}(\boldsymbol{r}_1,\tau_1) + B_\alpha^{(0)}(\boldsymbol{r},\tau).
\end{aligned} \tag{8.23}$$

Averaging of Eq. (8.23) contains terms $\langle\mathcal{H}_\alpha^{(2)}(\boldsymbol{r},\tau)\rangle = B_\alpha(\boldsymbol{r},\tau)$, $\langle u_\gamma\rangle = 0$ and the correlation tensor $\langle u_\gamma(\boldsymbol{r}_1,\tau_1)u_\kappa(\boldsymbol{r}_2,\tau_2)\rangle$, which is assumed to obey Eq. (8.17). We then take the integrals over $d\tau_2$ and d^3x_2 by means of the δ-functions:

$$\begin{aligned}
&\int_t^\tau d\tau_1 \int \mathrm{d}^3x_1 G(\boldsymbol{r}-\boldsymbol{r}_1,\tau-\tau_1) \\
&\quad\times \frac{\partial}{\partial x_{1\mu}}\langle u_\gamma(\boldsymbol{r}_1,\tau_1)\int_t^{\tau_1}\mathrm{d}\tau_2 \int \mathrm{d}^3x_2 G(\boldsymbol{r}_1-\boldsymbol{r}_2,\tau_1-\tau_2)\frac{\partial}{\partial x_{1\nu}}u_\kappa(\boldsymbol{r}_2,\tau_2)\rangle B_\epsilon^{(0)}(\boldsymbol{r}_2,\tau_2) \\
&\quad = \tau_c\int_t^\tau \mathrm{d}\tau_1 \int \mathrm{d}^3x_1 G(\boldsymbol{r}-\boldsymbol{r}_1,\tau-\tau_1)\left\{Q(0)\frac{\partial^2 B_\epsilon^{(0)}}{\partial x_{1\mu}\partial x_{1\nu}}\delta_{\gamma\kappa} - C(0)\frac{\partial B_\epsilon^{(0)}}{\partial x_{1\mu}}e_{\gamma\kappa\nu}\right\}.
\end{aligned} \tag{8.24}$$

Now substitute $\tau = t+\Delta t$ into Eq. (8.24) and calculate the rhs in the linear over Δt approximation. For this purpose it is sufficient to take the Green function in zeroth approximation, i.e., $G \approx \delta(\boldsymbol{r}-\boldsymbol{r}_1)$. The magnetic field component must be taken in the same approximation $B_\epsilon^{(0)}$, i.e., discarding in

Eq. (8.21) the term proportional to Δt. Thus, the rhs of Eq. (8.24) takes the form

$$\Delta t\,\tau_c \left\{ Q(0)\frac{\partial^2 B_\epsilon(\boldsymbol{r},t)}{\partial x_\mu \partial x_\nu}\delta_{\gamma\kappa} - C(0)\frac{\partial B_\epsilon(\boldsymbol{r},t)}{\partial x_\mu} e_{\gamma\kappa\nu} \right\}. \tag{8.25}$$

To transform combination $A^{\alpha\mu}_{\gamma\sigma}A^{\sigma\nu}_{\kappa\epsilon}$ including summation over the repeating index pairs we apply the equivalence $e_{\alpha\beta\gamma}e_{\alpha\mu\nu} = \delta_{\beta\mu}\delta_{\gamma\nu} - \delta_{\beta\nu}\delta_{\gamma\mu}$. Eventually we use the obvious relation

$$\frac{B_\alpha(t+\Delta t) - B_\alpha(t)}{\Delta t} \approx \frac{\partial B_\alpha}{\partial t} \tag{8.26}$$

and obtain the following equation:

$$\frac{\partial \boldsymbol{B}}{\partial t} = \alpha\,\nabla \times \boldsymbol{B} + (\nu_t + \nu_m)\triangle \boldsymbol{B}. \tag{8.27}$$

Here $\nu_t = Q(0)\tau_c = \langle \boldsymbol{u}^2\rangle \tau_c/3$ is the turbulent magnetic diffusivity and $\alpha = -(2/3)C(0)\tau_c = -\langle \boldsymbol{u}(\boldsymbol{r})\cdot\nabla \times \boldsymbol{u}(\boldsymbol{r})\rangle \tau_c/3$ is the helicity parameter.

The Fourier transforms $\widetilde{Q}$, $\widetilde{R}$, and $\widetilde{C}$ of the functions $Q(r)$, $R(r)$, and $C(r)$ describing the correlation tensor of the turbulent velocities are linked with the spectral functions $A(k,t)$ and $P(k,t)$ entering Eq. (8.12) by the following relations:

$$\widetilde{Q}(k) = A(k), \qquad \widetilde{C}(k) = -P(k), \qquad k\frac{\mathrm{d}}{\mathrm{d}k}\frac{1}{k}\frac{\mathrm{d}\widetilde{R}(k)}{\mathrm{d}k} = -A(k).$$

Here, in contrast to Eq. (8.12), a factor $2\tau_c\delta(t)$ containing the δ-function is isolated from the spectral functions $A(k,t)$ and $P(k,t)$: $A(k,t) = A(k)2\tau_c\delta(t)$, $P(k,t) = P(k)2\tau_c\delta(t)$.

The physical meaning of Eq. (8.27) becomes more transparent if we compare it with induction equation (2.12) in the vacuum. To do so we present Eq. (8.27) in the form

$$\frac{\partial \boldsymbol{B}}{\partial t} = -c\nabla \times \boldsymbol{\mathcal{E}},$$

where

$$\boldsymbol{\mathcal{E}} = -\frac{\alpha}{c}\boldsymbol{B} + \frac{\nu_{tot}}{c}\nabla \times \boldsymbol{B} \tag{8.28}$$

can be interpreted as an effective averaged large-scale electric field. The term with the full magnetic diffusivity $\nu_{tot} = \nu_t + \nu_m$ describes only dissipation of the electromagnetic field, while the term $-(\alpha/c)\boldsymbol{B}$ represents an electric field produced by the helical turbulence and capable of amplifying the mean magnetic field. The corresponding process is conventionally called the α-effect. It is worthwhile to note that generation of an electromotive force along

external magnetic field by a helical fluid flow was confirmed experimentally by (Steenbeck et al. 1968), where the conducting fluid was represented by a liquid sodium moving in spiral channels.

If there is a regular large-scale motion with the velocity $\boldsymbol{U}$ we must add the corresponding standard term $\nabla \times (\boldsymbol{U} \times \boldsymbol{B})$ into Eq. (8.27):

$$\frac{\partial \boldsymbol{B}}{\partial t} = \nabla \times (\boldsymbol{U} \times \boldsymbol{B}) + \alpha \nabla \times \boldsymbol{B} + \nu_{tot} \triangle \boldsymbol{B}. \tag{8.29}$$

Let us note that the derivation presented is not universal as based on a number of simplifications ignoring some of essential physics of the real astrophysical sources, e.g., anisotropy and nonuniformity of the turbulence. Nevertheless, the mean magnetic field can be weakly nonuniform and slowly vary in time here. A more detailed study of the subject is available in review papers and monographs, e.g., (Vainshtein 1983; Molchanov et al. 1985; Ruzmaikin et al. 1988). Specifically, the account of a weak turbulence nonuniformity results in the following equation for the mean magnetic field:

$$\frac{\partial \boldsymbol{B}}{\partial t} = \nabla \times (\boldsymbol{U} \times \boldsymbol{B}) + \nabla \times \alpha \boldsymbol{B} - \nabla \times \nu_{tot} \left[\nabla \times \frac{\boldsymbol{B}}{\mu} \right]. \tag{8.30}$$

Here μ is the diamagnetic permittivity of the turbulent fluid (see Problem 6.9); all coefficients α, ν_{tot}, and μ can be slow functions of coordinates.

8.5.2 Renormalization of Mean Field Equation

The considered renormalization method in Chap. 7 can also be applied to describe transfer of a vector (in place of scalar) admixture by a turbulent motion. Here we develop it in a practically important case of the magnetic field averaging in the turbulent dynamo problem. We start with the induction equation

$$\frac{\partial \boldsymbol{b}}{\partial t} = \nabla \times (\boldsymbol{u} \times \boldsymbol{b}) + \nu^m_{\alpha\beta} \frac{\partial^2 \boldsymbol{b}}{\partial x_\alpha \partial x_\beta}; \tag{8.31}$$

here $\boldsymbol{u}(\boldsymbol{r}, t)$ is the turbulent velocity field specified by given statistical measures, and $\nu^m_{\alpha\beta}$ is the tensor of local (molecular) magnetic diffusivity. The turbulent magnetic diffusivity can often greatly exceed the local one, which we consider as a seed value whose exact form is inessential; we adopt a simple form $\nu^m_{\alpha\beta} = \nu_m \delta_{\alpha\beta}$, where $\nu_m = c^2/4\pi\sigma$ is defined by the electroconductivity σ of the plasma. We take into account possible anisotropy and helicity of the turbulence, but still assume its uniformity, and use the Fourier transform of the velocity correlation tensor in the following form (cf. Eqs. (8.12) and (8.17)):

$$U_{\alpha\beta}(\boldsymbol{k}, \omega) = T_{\alpha\beta}(\boldsymbol{k}, \omega) - iP_{\alpha\beta}(\boldsymbol{k}, \omega), \tag{8.32}$$

where

$$T_{\alpha\beta}(\boldsymbol{k}, \omega) = T_{\beta\alpha}(\boldsymbol{k}, \omega) = T_{\alpha\beta}(-\boldsymbol{k}, \omega) \tag{8.33}$$

is a symmetric real tensor, invariant for interchange of $\boldsymbol{k}$ and $-\boldsymbol{k}$, while

$$P_{\alpha\beta}(\boldsymbol{k},\omega) = P_{\beta\alpha}(-\boldsymbol{k},\omega) = -P_{\alpha\beta}(-\boldsymbol{k},\omega) \tag{8.34}$$

is an antisymmetric, non-invariant for the inversion, tensor describing the turbulence helicity.

Let us perform averaging of Eq. (8.31) over the ensemble of the turbulent pulsations by the developed renormalization method. Specifically, we postulate the equation for the averaged large-scale field $\boldsymbol{B} = \langle \boldsymbol{b} \rangle$ to have a form

$$\frac{\partial B_\alpha}{\partial t} = M_{\alpha\beta\mu}\frac{\partial B_\mu}{\partial x_\beta} + \nu^{tot}_{\beta\mu}\frac{\partial^2 B_\alpha}{\partial x_\mu \partial x_\beta}; \tag{8.35}$$

where $M_{\alpha\beta\mu}$ and $\nu^{tot}_{\beta\nu}$ are constant tensor coefficients in the case of a uniform turbulence; repeated pairs of indices imply summation. If the fluid does not contain any natural vector rather than $\boldsymbol{k}$, for the incompressible fluid, we have

$$T_{\alpha\beta}(\boldsymbol{k},\omega) = A(k,\omega)(\delta_{\alpha\beta} - k_\alpha k_\beta/k^2), \quad P_{\alpha\beta}(\boldsymbol{k},\omega) = P(k,\omega)e_{\alpha\beta\gamma}k_\gamma, \tag{8.36}$$

where $e_{\alpha\beta\gamma}$ is the unit antisymmetric tensor and Eq. (8.35) receives well-known form Eq. (8.27). The coefficient α describing generation of the large-scale magnetic field in Eq. (8.27) is nonzero only for a helical turbulence ($P(k,\omega) \neq 0$).

To determine coefficients in more general Eq. (8.35) we isolate, like in the previous section, a minor component $\delta\boldsymbol{u}$ composed of harmonics from a narrow range of wave numbers Δk. Performing then averaging in Eq. (8.31) over all harmonics except that narrow range and denoting that "partly averaged magnetic field" as $\widetilde{\boldsymbol{B}}$ we arrive at the equation

$$\frac{\partial \widetilde{B}_\alpha}{\partial t} = M'_{\alpha\beta\mu}\frac{\partial \widetilde{B}_\mu}{\partial x_\beta} + \nu'^{tot}_{\beta\mu}\frac{\partial^2 \widetilde{B}_\alpha}{\partial x_\mu \partial x_\beta} + (\nabla \times (\delta\boldsymbol{u} \times \widetilde{\boldsymbol{B}}))_\alpha, \tag{8.37}$$

in which $M'_{\alpha\beta\mu}$ and $\nu'^{tot}_{\beta\mu}$ only slightly depart (because of Δk smallness) from exact coefficients $M_{\alpha\beta\mu}$ and $\nu^{tot}_{\beta\mu}$.

Averaging of Eq. (8.37) over ensemble of $\delta\boldsymbol{u}$ is then performed within the perturbation theory. By adopting

$$\widetilde{\boldsymbol{B}} = \boldsymbol{B} + \delta\widetilde{\boldsymbol{B}}, \qquad \langle \delta\widetilde{\boldsymbol{B}} \rangle = 0, \tag{8.38}$$

Eq. (8.37) yields two equations:

$$\frac{\partial B_\alpha}{\partial t} = M'_{\alpha\beta\mu}\frac{\partial B_\mu}{\partial x_\beta} + \nu'^{tot}_{\beta\mu}\frac{\partial^2 B_\alpha}{\partial x_\mu \partial x_\beta} + (\nabla \times \langle(\delta\boldsymbol{u} \times \delta\widetilde{\boldsymbol{B}})\rangle)_\alpha, \tag{8.39a}$$

$$\frac{\partial \delta\widetilde{B}_\alpha}{\partial t} = M'_{\alpha\beta\mu}\frac{\partial \delta\widetilde{B}_\mu}{\partial x_\beta} + \nu'^{tot}_{\beta\mu}\frac{\partial^2 \delta\widetilde{B}_\alpha}{\partial x_\mu \partial x_\beta} + (\nabla \times (\delta\boldsymbol{u} \times \boldsymbol{B}))_\alpha. \tag{8.39b}$$

We note that a significant difference of scales of the turbulent pulsations ($l \ll L$) and regular field B ($R \gg L$) is only possible when the helical part $P_{\alpha\beta}$ of correlation tensor (8.32) is small compared with its symmetric part $T_{\alpha\beta}$. Indeed, generation of the large-scale field occurs at the scales larger than L_{crit} defined as

$$L_{crit} \approx 2\pi\nu^{tot}/\alpha \approx 2\pi\langle u^2\rangle^{1/2}/\alpha, \tag{8.40}$$

and the condition $L_{crit} \gg L$ can only take place if $\alpha \ll \langle u^2\rangle^{1/2}$.

We, therefore, will assume this smallness, which allows discarding the first term at the rhs of Eq. (8.39b) so the solution reads

$$\begin{aligned}\delta\widetilde{B}_\alpha(\boldsymbol{r},t) &= B_\beta(\boldsymbol{r},t)\int G_m(\boldsymbol{r}-\boldsymbol{r}',t-t')\frac{\partial\delta u_\alpha(\boldsymbol{r}',t')}{\partial x'_\beta}\mathrm{d}^3r'\mathrm{d}t' \\ &\quad -\frac{\partial B_\alpha}{\partial x_\beta}\int G_m(\boldsymbol{r}-\boldsymbol{r}',t-t')\delta u_\alpha(\boldsymbol{r}',t')\mathrm{d}^3r'\mathrm{d}t'. \end{aligned}\tag{8.41}$$

The Green function G_m with the account of incompressibility $\nabla\cdot\delta\boldsymbol{u} = 0$ written for the turbulent transport has the form:

$$\frac{\partial G_m}{\partial t} - \nu^{tot}_{\beta\mu}\frac{\partial^2 G_m}{\partial x_\mu \partial x_\beta} = \delta(\boldsymbol{r}-\boldsymbol{r}')\delta(t-t'). \tag{8.42}$$

Substitution of solution (8.41) in the last term in the rhs of Eq. (8.39a) yields the contributions $\Delta M_{\alpha\beta\mu}$ and $\Delta\nu^{tot}_{\beta\mu}$ to the kinetic coefficients resulting from the range Δk:

$$\Delta M_{\alpha\beta\mu} = 2\int_{\Delta k} G_m(\boldsymbol{r},t)\frac{\partial}{\partial x_\mu}\delta P_{\alpha\beta}(\boldsymbol{r},t)\mathrm{d}^3r\,\mathrm{d}t, \tag{8.43a}$$

$$\Delta\nu^{tot}_{\beta\mu} = \int_{\Delta k} G_m(\boldsymbol{r},t)\delta T_{\beta\mu}(\boldsymbol{r},t)\mathrm{d}^3r\,\mathrm{d}t. \tag{8.43b}$$

Then, integrating Eq. (8.43) over the full range of the wave numbers we obtain a set of self-consistent equations for the magnetic diffusivity $\nu^{tot}_{\beta\mu}$ and magnetic field generation $M_{\alpha\beta\mu}$, which enter into averaged Eq. (8.35):

$$\nu^{tot}_{\beta\mu} = \int \frac{T_{\beta\mu}(\boldsymbol{k},\omega)}{i\omega + k_\epsilon k_\lambda \nu^{tot}_{\epsilon\lambda}}\frac{\mathrm{d}^3k\,\mathrm{d}\omega}{(2\pi)^4} + \nu^m_{\beta\mu}, \tag{8.44a}$$

$$M_{\alpha\beta\mu} = -2\int \frac{k_\mu P_{\alpha\beta}(\boldsymbol{k},\omega)}{i\omega + k_\epsilon k_\lambda \nu^{tot}_{\epsilon\lambda}}\frac{\mathrm{d}^3k\,\mathrm{d}\omega}{(2\pi)^4}, \tag{8.44b}$$

where Fourier transforms of the integrands have been performed.

The solutions for the coefficients must be determined sequentially: first, from Eq. (8.44a), we calculate the magnetic diffusivity tensor and then, using so determined $\nu^{tot}_{\beta\mu}$, integration of Eq. (8.44b) yields the third-rank tensor $M_{\alpha\beta\mu}$, which is antisymmetric over two first indices.

For the simplest helical turbulence, Eq. (8.36), the equations can be simplified. The tensor of magnetic diffusivity reduces to a diagonal one $\nu^{tot}_{\beta\mu} = \nu^{tot}\delta_{\beta\mu}$, while the tensor of the magnetic field generation is expressed via pseudoscalar α: $M_{\alpha\beta\mu} = \alpha\, e_{\alpha\beta\mu}$. The coefficients ν^{tot} and α are calculated from the set of equations:

$$\nu^{tot} = \nu_m + \frac{2}{3}\int \frac{T(k,\omega)}{i\omega + k^2\nu^{tot}} \frac{\mathrm{d}^3k\,\mathrm{d}\omega}{(2\pi)^4}, \qquad \alpha = -\frac{2}{3}\int \frac{k^2 P(k,\omega)}{i\omega + k^2\nu^{tot}} \frac{\mathrm{d}^3k\,\mathrm{d}\omega}{(2\pi)^4}. \tag{8.45}$$

The equations derived take into account the transfer of a field at any given scale l by the turbulent flows of all other scales. Possible non-stationarity of the flow is also taken into account via integration over frequencies. The practical importance of the derived equations is very high because solution of the transcendental equations obtained is incomparably easier task than the full numeric simulations of the large-scale dynamo problem. Numeric simulations, apparently, remain important due to both their internal merit, and also as a cross-check to validate simplified theories as that developed here for the turbulent motion and magnetic field evolution in the gyrotropic fluids.

8.6 Large-Scale Magnetic Field Generation

8.6.1 Simplified Examples

Let us consider a few examples when the magnetic field is indeed being amplified by a helically turbulent fluid. Let us start with a simple case accommodated by Eq. (8.27). Assume an initial magnetic field $\boldsymbol{B}(\boldsymbol{r},t)|_{t=0} = \boldsymbol{B}^0(\boldsymbol{r})$ and apply the Fourier transform over spatial coordinates to Eq. (8.27):

$$\frac{\partial \boldsymbol{B}_k}{\partial t} = i\alpha\,\boldsymbol{k}\times\boldsymbol{B}_k - \nu_{tot}k^2\boldsymbol{B}_k, \tag{8.46}$$

which has the following solution:

$$\boldsymbol{B}_k(t) = \{\boldsymbol{B}^0_k\cosh(k\alpha t) + i[\boldsymbol{k}\times\boldsymbol{B}^0_k]k^{-1}\sinh(k\alpha t)\}\mathrm{e}^{-\nu_{tot}k^2 t}, \tag{8.47}$$

where $\boldsymbol{B}^0_k$ is the Fourier component of the initial (seed) field, satisfying the conditions $\boldsymbol{k}\cdot\boldsymbol{B}^0_k = 0$, $\boldsymbol{B}^{0*}_{\mathbf{k}} = \boldsymbol{B}^0_{-\mathbf{k}}$. Enhancement of kth component does not depend on the helicity sign, although the following conditions must be fulfilled:

$$k < k_c = \frac{|\alpha|}{\nu_{tot}} \qquad \text{or} \qquad \lambda > \lambda_c = \frac{2\pi}{k_c} = \frac{2\pi\nu_{tot}}{|\alpha|}. \tag{8.48}$$

Therefore, only quite long-wave components of the magnetic field are unstable and experience amplification; in particular, the object must have a sufficiently large scale $L > \lambda_c$, for them to exist. In addition, the correlation time τ_c

of the turbulent motions (whose value was neglected above) must be small compared with the characteristic time of the magnetic field amplification:

$$(|\alpha|k)^{-1} \gg \tau_c. \tag{8.49}$$

If all of the above conditions are fulfilled, the large-scale magnetic field increases with the growth rate

$$\gamma = |\alpha|k - \nu_{tot}k^2 > 0. \tag{8.50}$$

Apparently, the solution obtained is only valid over a finite time; at some stage of the field amplification it becomes sufficiently strong to affect the helical turbulence itself. This back reaction of the growing field results eventually in a nonlinear stabilization of the considered instability and to saturation of the field growth. It is worthwhile to remind that the considered mechanism can only amplify a "seed" field, although cannot produce it from a zero level.

The considered model of the helical turbulence in the infinite space offers only a qualitative viability of the turbulent dynamo, i.e., instability of the helically turbulent conducting fluid leading to growth of large-scale magnetic perturbations. In contrast, for practical astrophysical applications, one has to consider bounded inhomogeneous objects, e.g., spherical bodies (stars), disks (accretion disks and spiral galaxies), and cylinders (jets, including the relativistic ones).

Nevertheless, the considered simple model does make sense for applications to small regions, when the length λ_c is small compared with the scale of the object under study. For example, in the case of a star, we can identify, at a given surface point, the Cartesian axes Ox with direction of $\boldsymbol{e}_r$, Oy with $\boldsymbol{e}_\vartheta$, and Oz with $\boldsymbol{e}_\alpha$, and then adopting the seed field and the wave vector to belong to the plane xy, we obtain a growth of toroidal field from the poloidal one from solution (8.47). Likewise, a seed toroidal field will give rise to growth of the poloidal field. Therefore, α-effect gives rise to amplification of both types of the field; for this reason, the considered model is often called the α^2 model (i.e., **double α-effect**).

Then, we consider a role of differential rotation in the mean magnetic field generation, called **$\alpha\Omega$-dynamo**. To do so, in Eq. (8.29), adopt a shear fluid motion $\boldsymbol{U} = \Omega x \boldsymbol{e}_y$, where $\Omega = \text{const}$ is a constant with dimension of frequency (reciprocal to the time), which yields

$$\frac{\partial \boldsymbol{B}}{\partial t} = \Omega \boldsymbol{e}_y B_x + \alpha \nabla \times \boldsymbol{B} + \nu_{tot} \triangle \boldsymbol{B}. \tag{8.51}$$

For simplicity, we seek a solution independent on the coordinate y and write a single Fourier harmonics in the form $\boldsymbol{B}_{\mathbf{k}}(\boldsymbol{r}, t) = \boldsymbol{\mathcal{B}} \exp(i\boldsymbol{k} \cdot \boldsymbol{r} + \gamma(\boldsymbol{k})t)$, where $\boldsymbol{k} = (k_x, 0, k_z)$, $\gamma(\boldsymbol{k})$ is a complex growth rate and $\boldsymbol{\mathcal{B}}(\boldsymbol{k})$ is the amplitude obeying a vector equation explicitly derived from Eq. (8.51):

$$(\gamma + \nu_{tot}k^2)\boldsymbol{\mathcal{B}} - \Omega \mathcal{B}_x \boldsymbol{e}_y - i\alpha\, \boldsymbol{k} \times \boldsymbol{\mathcal{B}} = 0. \tag{8.52}$$

The functional form of $\gamma(\boldsymbol{k})$ is calculated from the solvability condition of the linear equation system obtained by projecting Eq. (8.52) onto the coordinate axes, i.e., from equating determinate of the system to zero:

$$\begin{vmatrix} \gamma' & i\alpha k_z & 0 \\ -(\Omega + i\alpha k_z) & \gamma' & i\alpha k_z \\ 0 & -i\alpha k_z & \gamma' \end{vmatrix} = \gamma'^3 - \gamma'[\alpha^2(k_x^2+k_y^2) - i\alpha\Omega k_z] = 0. \quad (8.53)$$

Here $\gamma' = \gamma + \nu_{tot}k^2$, $k^2 = k_x^2 + k_z^2$. The roots of this equation are:

$$\gamma'_0 = 0, \qquad \gamma'_\pm = \pm\sqrt{-i\alpha\Omega k_z + \alpha^2 k^2}. \quad (8.54)$$

The first root $\gamma'_0 = 0$ corroborated with Eq. (8.51) and the necessarily transverse character of the magnetic field Fourier components $\boldsymbol{k} \cdot \boldsymbol{B}_\mathbf{k} = k_x B_{\mathbf{k}x} + k_z B_{\mathbf{k}z} = 0$ gives rise to equalities $B_{\mathbf{k}x} = B_{\mathbf{k}y} = B_{\mathbf{k}z} = 0$ for any real values of Ω, k_x, and k_y. Consider two other roots adopting $|\alpha k_z|/\Omega \ll 1$. Then, we have $\gamma'_\pm \approx \pm\sqrt{i}|\alpha\Omega k_z|^{1/2} = \pm(1+i)|\alpha\Omega k_z/2|^{1/2}$, so growing modes can originate from the root γ'_+, so

$$\Re\gamma \equiv \gamma_B = |\alpha\Omega k_z/2|^{1/2} - \nu_{tot}k^2 \quad (8.55)$$

if $\gamma_B > 0$.

To further simplify the discussion, let us adopt $k_x = 0$ while $k = |k_z| \neq 0$. This immediately yields $B_{\mathbf{k}z} = 0$, while $B_{\mathbf{k}x} \neq 0$ and $B_{\mathbf{k}y} \neq 0$. Then, the instability giving rise to the large-scale field amplification occurs under condition

$$k < k_c = \left(\frac{|\alpha|}{4\nu_{tot}^2\Omega}\right)^{1/3}. \quad (8.56)$$

Under this condition, likewise in the case of α^2-dynamo, the magnetic field grows exponentially; thus, the equation is only applicable over a limited time until the amplifying field does not significantly affect the original helical turbulent field. The mode with $\Re\gamma_+(k_c) = 0$ propagates with a constant amplitude. The physical value of the magnetic field for a given $\boldsymbol{k}$ can be determined by the real part of the complex Fourier component $\boldsymbol{B}_\mathbf{k}$, which reads $\Re\boldsymbol{B}_\mathbf{k} = \Re\boldsymbol{\mathcal{B}}_c \exp(i\boldsymbol{k}\cdot\boldsymbol{r} + \gamma_+ t) = \boldsymbol{\mathcal{B}}_c \cos(k_c z - \omega_c t)$, where $\omega_c = -\Im\gamma_+(k_c)$. The amplitude $\boldsymbol{\mathcal{B}}_c$ is specified by initial value of the seed magnetic field, whose magnitude and origin is beyond the considered simplified model. Denoting amplitude of the component $B_{\mathbf{k}x}(z,t)$ as $\mathcal{B}_0$, we can write (adopting an appropriate phase)

$$B_{\mathbf{k}x}(z,t) = \mathcal{B}_0 \cos k_c(z - v_{\rm ph}t), \quad \text{where} \quad v_{\rm ph} = \frac{-\Im\gamma_+}{k_z} = \pm\left(\frac{|\alpha|\Omega}{2k_c}\right)^{1/2} \quad (8.57)$$

is the phase velocity. The component $B_{\mathbf{k}y}(z,t)$ is then expressed via $B_{\mathbf{k}x}(z,t)$ using Eq. (8.52):

$$B_{\mathbf{k}y}(z,t) = \sqrt{2}\left|\frac{v_{\rm ph}}{\alpha}\right| \mathcal{B}_0 \cos[k_c(z - v_{\rm ph}t) + \varphi]. \tag{8.58}$$

Here, everywhere the phase velocity $v_{\rm ph}$ and the helicity parameter α can have different signs, which affects the phase φ. Further models as well as more detailed analysis of the models considered here can be found, e.g., in the review by Brandenburg and Subramanian (2005).

8.6.2 Nonlinear Effects in the Dynamo Theory

As has been repeatedly said, the kinematic dynamo theory is intrinsically unable to bound the large-scale field amplification, which is a significant limitation of the theory as the growing magnetic field must become dynamically important rather soon after the amplification started. This dynamic effect produced by the mean field will necessarily reduce the original helical turbulence in such a way that the mean field amplification slows down and ends at some saturation level. Apparently, this follows from the energy conservation law. Indeed, adopt the turbulence is characterized by some energy density, $w_t = \rho\langle u^2\rangle/2$. Then, because the magnetic energy $w_m = B^2/8\pi$ is taken from the turbulence energy, w_m cannot exceed the originally available w_t level:

$$\frac{B^2}{8\pi} \lesssim \frac{\rho\langle u^2\rangle}{2}. \tag{8.59}$$

In the case of a "driven" turbulence when some stationary sources of the turbulent motion support it at a given state providing the mean density of the turbulence energy to be $w_t = \rho\langle u^2\rangle/2 = \text{const}$, Eq. (8.59) also looks a reasonable estimate, even though not required in this case (in principle, the energy of the external sources can path by the turbulence toward the mean magnetic field and be accumulated there). Indeed, a strong imbalance between the magnetic and turbulent energy densities looks unlikely as there are good reasons to expect that strong magnetic field will suppress the turbulent motions and, thus, anyway affect the entire system dynamically. An exception is only possible for a 2D turbulence (Landau and Lifshitz 1960), which seems unlikely in most of the astrophysical objects; so we do not consider this extreme case here.

It is also possible that in some cases inequality (8.59) can become a strong one, $\ll$, because nonlinear mechanisms of the mean field—helical turbulence interaction can saturate the mean field generation process much earlier than the equipartition level has been achieved, which was spotted, in particular, by Vainshtein and Zel'dovich (1972).

It turns that for both more reliable estimates of the field growth and developing numerical models of the turbulent dynamo, the mean field theory equations are convenient to represent in an alternative form proposed by Blackman and Field (2002). Let us rewrite the second of Eq. (6.139) as follows:

$$\frac{\partial \boldsymbol{B}}{\partial t} = \nabla \times \boldsymbol{\mathcal{E}} + \nu_m \triangle \boldsymbol{B}, \qquad \boldsymbol{\mathcal{E}} = \langle \boldsymbol{u} \times \boldsymbol{b} \rangle \tag{8.60}$$

and derive equation for the vector $\boldsymbol{\mathcal{E}}$ by differentiating it over time and using MHD equations

$$\frac{\partial \boldsymbol{\mathcal{E}}}{\partial t} = \left\langle \frac{\partial \boldsymbol{u}}{\partial t} \times \boldsymbol{b} \right\rangle + \left\langle \boldsymbol{u} \times \frac{\partial \boldsymbol{b}}{\partial t} \right\rangle. \tag{8.61}$$

We do not linearize them here as we are specifically going to analyze effect of nonlinearity, that is,

$$\frac{\partial \boldsymbol{u}}{\partial t} = \frac{1}{4\pi\rho}(\nabla \times \boldsymbol{b}) \times \boldsymbol{B} - (\boldsymbol{u} \cdot \nabla)\boldsymbol{u} + \frac{1}{4\pi\rho}(\nabla \times \boldsymbol{b}) \times \boldsymbol{b}, \tag{8.62a}$$

$$\frac{\partial \boldsymbol{b}}{\partial t} = (\boldsymbol{B} \cdot \nabla)\boldsymbol{u} - (\boldsymbol{u} \cdot \nabla)\boldsymbol{B} + (\boldsymbol{b} \cdot \nabla)\boldsymbol{u} - (\boldsymbol{u} \cdot \nabla)\boldsymbol{b} + \nu_m \triangle \boldsymbol{b}. \tag{8.62b}$$

Here $\boldsymbol{u}$ and $\boldsymbol{b}$ relate to the turbulence; the plasma is assumed cold enough to discard the pressure gradient ($p \sim T$) and the kinematic viscosity ($\nu \sim T^{5/2}$). The largest dissipative effect is the magnetic diffusivity ($\nu_m \sim T^{-3/2}$), which is retained above; nevertheless, for large magnetic Reynolds numbers typical for astrophysical objects, it can be discarded as well.

Substitution of Eq. (8.62) into Eq. (8.61) generates terms containing either second or third moments of the turbulent measures $\boldsymbol{u}$ and $\boldsymbol{b}$. The second moments $\langle \boldsymbol{u} \times [(\boldsymbol{B} \cdot \nabla)\boldsymbol{u} - (\boldsymbol{u} \cdot \nabla)\boldsymbol{B}] \rangle$ have been calculated in various ways in Sects. 6.11, 8.5.1, and 8.5.2; we use here the already familiar results, which yields

$$\begin{aligned} \frac{\partial \boldsymbol{\mathcal{E}}}{\partial t} = {} & \frac{\alpha}{\tau_c}\boldsymbol{B} - \frac{1}{3}\langle u^2 \rangle \nabla \times \boldsymbol{B} + \frac{\boldsymbol{B}}{4\pi\rho}\langle \boldsymbol{b} \cdot (\nabla \times \boldsymbol{b}) \rangle - \frac{B_\lambda}{4\pi\rho}\langle b_\lambda (\nabla \times \boldsymbol{b}) \rangle \\ & - \langle \boldsymbol{u} \cdot (\boldsymbol{u} \cdot \nabla)\boldsymbol{b} \rangle + \langle \boldsymbol{u} \times (\boldsymbol{b} \cdot \nabla)\boldsymbol{u} \rangle + \langle (\boldsymbol{u} \cdot \nabla)\boldsymbol{u} \times \boldsymbol{b} \rangle. \end{aligned} \tag{8.63}$$

The term proportional to ν_m is of the order of $R_m^{-1} \ll 1$ and has been discarded as explained above. It is worthwhile to note that the second moments like $\langle \boldsymbol{b} \cdot (\nabla \times \boldsymbol{b}) \rangle$, as well as kinetic helicity parameter α, are the pseudoscalars. As so, one can expect the magnetic pseudoscalar to be linked somehow to the kinetic pseudoscalar α. To obtain this link let us express the single-point moments $\langle b_\mu(\boldsymbol{r}, t) b_\nu(\boldsymbol{r}, t) \rangle$, entering Eq. (8.63), via the correlation tensor of the turbulence velocities using Eq. (8.41). If the averaging is performed over a large scale, $L \gg l$, then we can discard the term with the derivative of the field $\boldsymbol{B}$ in Eq. (8.41), i.e., adopt its uniformity on the $\boldsymbol{b}$

variation scales. For a small fraction of the turbulent magnetic field, we can discard nonlinear terms in Eq. (8.62b) to write

$$\delta\widetilde{B}_\alpha(\boldsymbol{r},t) = B_\beta(\boldsymbol{r},t)\int G_m(\boldsymbol{r}-\boldsymbol{r}',t-t')\frac{\partial\delta u_\alpha(\boldsymbol{r}',t')}{\partial x'_\beta}\mathrm{d}^3r'\mathrm{d}t', \tag{8.64}$$

where $\delta\widetilde{B}_\alpha(\boldsymbol{r},t)$ is a minor fraction of the field $\boldsymbol{b}$ related to a small range of the wave numbers Δk. Taking the Fourier transform of Eq. (8.64) we obtain the link between the correlation tensors within the random phase approximation ($b_{\mu\mathbf{k}\omega}b_{\nu\mathbf{k}'\omega'} = \langle b_\mu b_\nu\rangle_{\mathbf{k}\omega}\delta(\boldsymbol{k}-\boldsymbol{k}')\delta(\omega-\omega')$):

$$\langle b_\mu b_\nu\rangle_{\mathbf{k}\omega} = (\boldsymbol{k}\cdot\boldsymbol{B})^2|\widetilde{G}_m(\boldsymbol{k},\omega)|^2\langle u_\mu u_\nu\rangle_{\mathbf{k}\omega}. \tag{8.65}$$

This link between the correlation tensors is *nonlinear* because the Green function, according to Eq. (8.42), contains, via ν^{tot}, the entire velocity field and has the form

$$\widetilde{G}_m(\boldsymbol{k},\omega) = (-i\omega + k_\sigma k_\lambda \nu^{tot}_{\sigma\lambda})^{-1}. \tag{8.66}$$

To find the correlator value $\langle b_\mu(\boldsymbol{r},t)b_\nu(\boldsymbol{r},t)\rangle$ at a given time and a given point one has to integrate Eq. (8.65) over all frequencies and wave vectors. Before that, we have yet to differentiate the components of $\boldsymbol{b}$ over coordinates, Eq. (8.63), to form $\nabla\times\boldsymbol{b}$. Apparently, this gives rise to an additional $\boldsymbol{k}$ vector factor. Noting that for the $\delta(t)$-correlation model the tensor $\langle u_\mu u_\nu\rangle_{\mathbf{k}}$ does not depend on frequency and calculating some simple integrals over frequency and angles of the $\boldsymbol{k}$ vector, we obtain

$$\frac{\boldsymbol{B}}{4\pi\rho}\langle\boldsymbol{b}\cdot(\nabla\times\boldsymbol{b})\rangle - \frac{B_\lambda}{4\pi\rho}\langle b_\lambda(\nabla\times\boldsymbol{b})\rangle = -\alpha\boldsymbol{B}\frac{4v_A^2}{5\nu_t}. \tag{8.67}$$

Thus, account of the turbulent magnetic field correlators ends up with a cubic nonlinearity over the mean large-scale magnetic field $\boldsymbol{B}$. Importantly, nonlinear magnetically induced helicity (8.67) has a sign opposite to that of the kinetic helicity (see Eq. (8.63)). This reduces an "effective" helicity parameter, which, in turn, reduces the magnetic field amplification:

$$\alpha_{\mathrm{eff}} = \alpha\left(1 - \frac{12v_A^2}{5\langle u^2\rangle}\right). \tag{8.68}$$

Equation (8.63) contains also the third moments of the turbulence measures; each moment represents a polar vector. Thus, the corresponding terms are unlikely to contribute to the field amplification as they are "non-helical" ones. This implies that they are related to a field dissipation process, which can be collectively roughly described in the "lifetime" approximation by the term $-\boldsymbol{\mathcal{E}}/\tau_c$:

$$-\langle\boldsymbol{u}\cdot(\boldsymbol{u}\cdot\nabla)\boldsymbol{b}\rangle + \langle\boldsymbol{u}\times(\boldsymbol{b}\cdot\nabla)\boldsymbol{u}\rangle + \langle(\boldsymbol{u}\cdot\nabla)\boldsymbol{u}\times\boldsymbol{b}\rangle = -\frac{\boldsymbol{\mathcal{E}}}{\tau_c}. \tag{8.69}$$

This assumption, however, is mainly an intuitive guess, with some support from available numerical simulations (see, e.g., Brandenburg and Subramanian 2005; Brandenburg 2009, 2011):

$$\frac{\partial \boldsymbol{B}}{\partial t} = \nabla \times \boldsymbol{\mathcal{E}} + \nu_m \triangle \boldsymbol{B} \tag{8.70}$$

and

$$\frac{\partial \boldsymbol{\mathcal{E}}}{\partial t} = \frac{\alpha \boldsymbol{B}}{\tau_c}\left(1 - \frac{12}{5}\frac{B^2}{4\pi\rho\langle u^2\rangle}\right) - \frac{1}{3}\langle u^2\rangle \nabla \times \boldsymbol{B} - \frac{\boldsymbol{\mathcal{E}}}{\tau_c}. \tag{8.71}$$

This nonlinear system of equations, partly accounting the nonlinearity over the physical value of interest, the large-scale magnetic field $\boldsymbol{B}$, is apparently not equivalent to kinematic dynamo equations (8.27) or (8.35) obtained earlier by a simpler approach. Equations (8.70) and (8.71) are more general than Eq. (8.27); the latter can be derived from the former within some simplifications. Specifically, one has to discard the nonlinear term, which is valid for $B^2/8\pi \ll \rho\langle u^2\rangle/2$. Then, the inequality $|\partial \boldsymbol{\mathcal{E}}/\partial t| \ll |\boldsymbol{\mathcal{E}}/\tau_c|$ must be fulfilled, which implies that the turbulence-induced mean electric field changes only slowly during the characteristic turbulent pulsation time. Under these assumptions, Eq. (8.71) yields $\boldsymbol{\mathcal{E}} \approx \alpha \boldsymbol{B} - \nu_t \nabla \times \boldsymbol{B}$; substitution of this value into Eq. (8.70) yields Eq. (8.27).

Consider the saturated level of the large-scale magnetic field. Order-of-magnitude estimate (8.59) derived from the energy conservation law is confirmed by nonlinear helicity parameter (8.68): $\alpha_{\text{eff}}(B)$ decreases as B increases and the mean field generation stops when

$$B^2 \approx B_0^2 = \frac{5\pi}{3}\rho\langle u^2\rangle = \frac{10\pi}{3} w_t. \tag{8.72}$$

Similar result can be obtained from evaluation of a "stationary" level of the field from Eqs. (8.70) and (8.71) by discarding the time derivatives, while replacing the spatial derivatives by dividing by appropriate spatial scales.

The developed nonlinear treatment suffers from a lack of consistent joint account of the Coriolis and magnetic force effect on the helical turbulent motion. This problem is highly non-trivial given that the turbulence helicity is a kind of "subtle" effect, which is supposed to be efficiently suppressed by the growing mean magnetic field, thus, reducing the mean field amplification (α-quenching effect), although a nonpotentiality (twists) of the generated large-scale magnetic field can increase the kinetic helicity component as we show in Sect. 11.2.2. Then, there is no firm evidence that the dependence of the helicity on the mean field does follow the link, Eq. (8.68), derived here from a simplified consideration. In addition, we only considered unbounded fluid volume, while any real object is bounded. All this (and some other effects) can strongly affect the nonlinear dynamo process, in particular, reduce the saturated level of the mean field compared with Eq. (8.72). This concern

is confirmed in review by Brandenburg and Subramanian (2005), which discusses a number of different contradictory nonlinear models, whose predictions are different from each other by orders of magnitude.

On the other hand, observational data about the Galaxy do show that the energy densities of interstellar turbulence and large-scale magnetic field are comparable to each other, i.e., equipartition described by Eqs. (8.59) and (8.72) takes place in the Galaxy (see Sect. 8.7.1 for more detail).

In the solar case, Eq. (8.68) can help to locate the region of the Sun, where the bulk of the solar magnetic field is generated. Adopting the photospheric density of $2 \cdot 10^{-7}\,\mathrm{g/cm^3}$ and $u \sim 10^5\,\mathrm{cm/s}$, from Eq. (8.72) we obtain $B \sim 100\,\mathrm{G}$, which is apparently insufficient to create typical sunspot magnetic field of a few thousand G. In the convective zone the plasma density, with $0.2\,\mathrm{g/cm^3}$ at the base, is up to six orders of magnitude larger than the photospheric value so for the same convection velocity we estimate $w_t \sim 10^9\,\mathrm{erg/cm^3}$, which results in $B_0 \sim 10^5\,\mathrm{G}$ at the base of the convection zone; the modern helioseismology data imply the magnetic field of $50-100\,\mathrm{kG}$ there, in a remarkable agreement with the prediction of the nonlinear dynamo model developed here. In the concept of the solar magnetic field generation inside the convection zone, the surface (photospheric) magnetic field of the active regions is a result of the much stronger subphotospheric field emergence; only a minor fraction of the subphotospheric magnetic flux is, thus, needed to build an active region; see Sect. 8.7.4 for more detail.

8.6.3 Generation of Primary Field

Dynamo equations derived above are capable of amplifying an available large-scale magnetic field, while cannot produce it from nothing. Stated another way, a "seed" initial magnetic field must first be created by another mechanism. In fact, there are a number of such "non-dynamo" mechanisms capable of producing either the seed field or even a relatively large mean field; see Sect. 7.6 and a review by Dolginov (1987) for more examples. Here we consider only one classical example of such mechanisms based on generalized Ohm's law (1.90) derived in Sect. 1.3.4.

Consider a fully ionized, hot $P_e \neq 0$, plasma, i.e., $F = 0$ and $n_i = n_e$. Then Eq. (1.90) takes the form

$$\boldsymbol{E} + \frac{1}{c}\boldsymbol{u} \times \boldsymbol{B} + \frac{1}{en_e}\nabla P_e = \frac{\boldsymbol{j}}{\sigma} + \frac{1}{n_e ec}\boldsymbol{j} \times \boldsymbol{B}. \tag{8.73}$$

Let us derive from it an equation for the magnetic field using the equation of state for the electron gas $P_e = n_e T_e$, applying the $\nabla\times$ operator to Eq. (8.73), and using then the Maxwell equations

$$\frac{\partial \boldsymbol{B}}{\partial t} = \nabla \times (\boldsymbol{u} \times \boldsymbol{B}) - \nabla \times \nu_m (\nabla \times \boldsymbol{B}) - \frac{c}{en_e}\nabla n_e \times \nabla T_e. \tag{8.74}$$

Here, like in Eq. (2.16), the Hall current is discarded, while the electron pressure P_e is retained. It is the pressure that is responsible for the last term, which is nonzero if the temperature and density gradients are not parallel to each other. These nonparallel gradients interact with each other to produce a thermocurrent generating the magnetic field without any seed field. Indeed, $\partial \boldsymbol{B}/\partial t|_{t=0} \neq 0$ even when $\boldsymbol{B}|_{t=0} = 0$. This effect discovered by Ludwig Biermann is known as a **Biermann battery**. Even though the Biermann battery often produces a very weak field (if any), it can be sufficient to launch the dynamo process resulting in much larger mean field.

8.7 Magnetic Field Generation in Stars and the Galaxy

8.7.1 Dynamo in the Galactic Disk

In the galactic disk one has to take into account the differential rotation, mentioned already in Sects. 8.2 and 8.6, in addition to the helicity effect. Let us apply the locally plane $\alpha\Omega$-model (Sect. 8.6.1) to the galactic disk adopting standard physical parameters of the galactic disk pertained to $R \approx 10\,\mathrm{kpc}$ from the galactic center, which roughly corresponds to the Sun location: the linear velocity of the disk rotation $u_\varphi \approx 25\,\mathrm{km/s} \cdot R\,\mathrm{kpc} = 2.5 \times 10^7\,\mathrm{cm/s}$ for $R = 10\,\mathrm{kpc}$; a flat rotation curve with $u_\varphi = \Omega r = \mathrm{const}$ would result in the same absolute value of $\Delta\Omega = r d\Omega/dr = -\Omega$. The angular velocity is $\Omega = u_\varphi/R \approx 8 \times 10^{-15}\,\mathrm{rad/s}$, which corresponds to the time needed for one rotation of the Galaxy $T_G = 2\pi/\Omega \approx 0.8 \times 10^{15}\,\mathrm{s} \approx 2.7 \times 10^7$ years. Adopt the main turbulence scale (size of large turbulent cells) to be $l \approx 100\,\mathrm{pc}$, mean turbulent velocity to be $\overline{u} \approx 10^6\,\mathrm{cm/s}$, and disk semithickness of $h \approx 400\,\mathrm{pc}$. For the sake of the order of magnitude estimate we everywhere replace k_z by the inverse scale parameter h^{-1} because k_z came from differentiation over coordinate z, for which the natural scale is given by the disk semithickness.

Use Eq. (8.16) to estimate the helicity parameter: $\alpha \approx l^2\Omega/h \approx 6\,\mathrm{km/s}$. The growth/damping rate γ_B determined by Eq. (8.55) is

$$\gamma_B = |\alpha\Omega k_z/2|^{1/2} - \nu_{tot} k^2. \tag{8.75}$$

Its negative part (damping) γ_d is specified by the turbulent magnetic diffusivity $\nu_{tot} \approx 10^{26}\,\mathrm{cm^2/s}$ and the disk semithickness: $\gamma_d \approx \nu_{tot}/h^2 \approx 0.7 \times 10^{-15}\,\mathrm{s}$. The positive part is $\gamma_i = |l^2\Omega^2/2h^2|^{1/2} \approx 1.4 \times 10^{-15}\,\mathrm{s}$.

We conclude that with the adopted parameters the dynamo can operate in the galactic disk but only marginally with the growth rate $\gamma_B = \gamma_i - \gamma_d \approx 0.7 \times 10^{-15}\,\mathrm{s}$, the characteristic e-folding growth time of the mean field is $T_B = \gamma_B^{-1} \approx 1.4 \times 10^{15}\,\mathrm{s} \approx 5 \times 10^7$ years, roughly two Galaxy rotation times. The fact that the growth and damping of the field nearly compensate each other is a good indication that the currently observed galactic magnetic field is close to the corresponding saturation state (recall, it is in equipartition with other components of the Galaxy as turbulence and CRs). One can expect that

at some earlier stages of the Galaxy evolution the magnetic field grew faster and could reach the observed values of $(1-10)\times 10^{-6}$ G over the Galaxy lifetime even starting from a very weak seed field.

For the galaxies, one of the favorite mechanisms capable of producing the seed magnetic field is plasma ejections from early type stars in the form of strong stellar winds and supernova explosions. In this case the problem of the magnetic field generation is transferred to another class of objects, the stars, where indeed the small spatial scales and fast rotation favor the dynamo process more than in extended regions of a Galaxy; see Sect. 8.7.2.

We emphasize that the consideration given above for the galactic magnetic field amplification is highly simplified offering the orders of magnitude of the involved parameters at best, indicative that account of discarded here physical effects can significantly modify the obtained numbers. A more precise (but still idealistic) model of a narrow disk must rely on induction Eq. (8.30) for the mean field in cylindrical coordinates with the account of the galactic differential rotation and the α-effect as well as correct boundary conditions at the disk surface. Strong disk asymmetry allows discarding the derivatives over r and retains only derivatives over time and coordinate z perpendicular to the disk plane. Then, equations for the magnetic field components transverse to disk axes in the axially symmetric case have the form

$$\frac{\partial B_r}{\partial t}=-\frac{\partial}{\partial z}(\alpha B_\varphi)+\nu_{tot}\frac{\partial^2 B_r}{\partial z^2},\qquad \frac{\partial B_\varphi}{\partial t}=r\frac{\partial\Omega}{\partial r}B_r+\nu_{tot}\frac{\partial^2 B_\varphi}{\partial z^2}, \tag{8.76}$$

where the term $\partial(\alpha B_r)/\partial z$ is discarded compared with the differential rotation term in the second equation. The helicity parameter is treated as a function of z because it changes the sign at the disk central plane (see Eq. (8.16)). Although the equations look relatively simple they do not have a simple solution; see more detailed analysis and some partial solutions in Ruzmaikin et al. (1988) and Brandenburg and Subramanian (2005). Vainshtein and Zel'dovich (1972) neglected the dissipation to obtain the following estimate of the e-folding field growth time:

$$T_B\approx\left(-R\frac{\partial\Omega}{\partial r}\frac{\partial\alpha}{\partial z}\right)^{-1/2}\approx 2\times 10^8\,\text{years}, \tag{8.77}$$

which is four times longer than our simplified estimate above. This manifests a good agreement between different approaches given the nature of the simplifications made; on the other hand, it demonstrates that getting precise numbers does require quantitative accounting of many physical effects, which is extremely uneasy task.

Overall, a more precise theory of the galactic dynamo needs more detailed information on physical parameters, which are only known currently to the order of magnitude. Thus, although the galactic dynamo theory does provide a qualitative framework to understand the large-scale magnetic field origin,

it is yet long way to reliable quantitative field calculation of the level and spatial structure of the mean field.

On top of that, the dynamo is not the only mechanism capable of producing the large-scale field (see the cited references for more detail). For example, Dolginov and Toptygin (2004) pointed out that the galactic large-scale field can be generated and supported by electric current carried by the accelerated particles (cosmic rays), whose free energy looks sufficient to compensate the turbulent dissipation of the field. This model is also very far from its completion mainly because of uncertainty with the intensity of the return currents produced by the background (thermal) particles capable of reducing or even fully compensating the CR-produced electric current; see, e.g., Sects. 7.1.3 and 7.6. Perhaps, the galactic disk dynamo is coupled with formation of the galactic corona and emission of the galactic wind; see Zirakashvili et al. (1996) for more detail.

8.7.2 Dynamo in Stars

Let us evaluate the characteristic time of the field growth in a main sequence O class star with a convective core following the classical Vainshtein and Zeldovich (1972) review paper. In contrast to the core, which is convective in these stars, the outer layers are free from convection because the temperature gradient is small there owing to strong radiative thermal conductivity, so no outer convective zone is available. The star mass is $M = 30M_\odot$, the surface temperature is $T \approx 4 \times 10^4\,\mathrm{K}$, the radius is $R = 6.6R_\odot \approx 5 \times 10^{11}\,\mathrm{cm}$, and the linear velocity of the surface rotation at the equator is about 250 km/s, which corresponds to the angular velocity about $\Omega \approx 5 \times 10^{-5}\,\mathrm{rad/s}$. The convection speed is estimated as $u_0 \approx 2.5 \times 10^5\,\mathrm{cm/s}$; the vertical size of a convective cell is $l \approx 0.1R \approx 5 \times 10^{10}\,\mathrm{cm}$. For these parameters the turbulence correlation time is estimated as $\tau_c \approx l/u_0 \approx 2.5 \times 10^5\,\mathrm{s}$. Let us apply here the α^2-model fully neglecting a possible role of the differential rotation.

The large-scale ($L \approx R$) magnetic field according to Eqs. (8.49) and (8.50) is amplified over the time:

$$T_B = \frac{1}{k\alpha} \approx \frac{R}{2\pi\alpha} \approx \frac{|h|R}{2l^2\Omega} \tag{8.78}$$

(we use here the α estimate from Eq. (8.16)). The density variation scale $|h|$ in the convective stellar core is yet undefined. It is reasonable to adopt it to belong to the range $l \lesssim |h| \lesssim R$. Applicability region of Eq. (8.47) requires that Eq. (8.49) is fulfilled to the order of magnitude, $T_B > \tau_c$. For the adopted stellar parameters this translates to $|h| > 2.5\,l$ and $T_B > \tau_c \approx 2.5 \times 10^5\,\mathrm{s}$. The magnetic field generated in the convective core then can be transferred to the star surface by the meridional circulation having the same characteristic time scale. Many O and B stars display a global surface magnetic field of the order of 100 G.

The estimated time is very short compared with the O star life time (which is between half and a few million years, i.e., $\approx 5 \times 10^{13}$ s). Even for the largest value $|h| = R$ we have $T_B \approx 10^6$ s ≈ 0.1 years. These estimates imply that the dynamo mechanism can in fact efficiently work in the specified stellar conditions, and call for a comprehensive theory of the stellar dynamo, which has yet to be built.

8.7.3 Generation of Superstrong Magnetic Fields in Neutron Stars

The strongest magnetic fields in astrophysics, 10^8–10^{14} G, are observed at magnetospheres and surfaces of the neutron stars. In a subclass of the neutron stars with an enhanced magnetic field, called **magnetars**, the magnetic field is even stronger, $B > 10^{14}$ G. Measurements of the magnetic fields of neutron stars with fast rotation (radiopulsars) are performed basically by two methods: (1) from the star rotation spin down assuming that the corresponding energy losses are mainly provided by the magnetodipole radiation [see Chap. 9, Eqs. (9.66), (9.100), and Sect. 12.2.2] and (2) by cyclotron lines in the X-ray spectra of the neutron stars.

The fast rotation of the neutron stars is provided by conservation of angular momentum during the parent star collapse. The spin-down rate provides information on the global dipole field of the pulsar, while the cyclotron lines relate to surface regions contributing to the X-ray emission of the star. The magnetic fields derived by these two methods are often different from each other, which are typically ascribed to smaller-scale magnetic field (magnetic spots), whose magnitude can be 1–2 orders of magnitude larger than that of the global dipole field.

Originally, these superstrong magnetic fields of the neutron stars were ascribed to busting the initial magnetic field of the collapsing parent stars due to freezing-in of the magnetic field into the stellar plasma. However, this mechanism requires a relatively strong initial stellar magnetic field even if one entirely neglects the loss of a considerable fraction of the stellar magnetic flux with the expanding ejection shell of the supernova, whose core remnant forms the pulsar. For example, in the case of Sun contraction ($R_\odot \approx 7 \times 10^{10}$ cm) down to typical pulsar radius of ($r \approx 10^6$ cm), the magnetic field at the pulsar surface would be about $B = B_\odot (R_\odot/r)^2 \approx 5 \times 10^9$ G, if the mean field at the photosphere level were $B_\odot \approx 1$ G. Thus, to obtain the largest pulsar fields, the collapsing star must have a field of about 10^4 G. Even though there are normal stars with required field, their total number in the Galaxy is insufficient to create all known pulsars with that strong magnetic field.

On top of that, there is, perhaps, even stronger shortcoming of the concept of this relict origin of the pulsar magnetic field, which came from theoretical consideration and numerical modeling. Specifically, it has been established that the star collapse is immediately followed by a stage of strong

hydrodynamic instability lasting about 1 s. A strong shock wave heats the star interior up to 10^{11} K. Hydrostatic equilibrium is then established over a short time of 10^{-3}–10^{-2} s. Hydrodynamic instabilities develop at this stage due mainly to gradients of entropy and lepton densities (including neutrino). The corresponding motion of the matter starts at outer layers of the star and propagates toward the star center. Velocity of this convective motion is rather large, up to subluminal values of 10^9 cm/s. This strong convection gives rise to enhanced magnetic diffusivity capable of fast restructuring and destroying the original magnetic field of the star. On the other hand, the turbulent convection along with fast rotation of the star can quickly generate new magnetic field by the turbulent dynamo.

Analytical consideration and numerical models show that the instability develops unevenly in different zones of the star. An outer zone, $R > r > R_c$, where R_c is some critical radius, is unstable due to strong lepton gradients (viz., electrons and neutrino–antineutrino balance), while the inner zone, $r < R_c$, hosts a standard convection driven by gradients of temperature and density. The instability begins at a subsurface region and takes $\sim$10 ms to occupy the entire star volume; the instability fully develops over just 30–100 ms. This stage of well-developed convection is, however, rather short; in $\sim$ 20 ms the "convective" zone begins to shrink toward the star center, gradients smooth out, and the instability quenches by the end of the first minute of its development. Nevertheless, even this extremely short (for astronomical scales) episode turns to be sufficient to generate a superstrong magnetic field observed at the neutron stars.

In both outer ($r > R_c$) and inner ($r < R_c$) zones there are turbulent convective cells, star rotation, and violent fluid motion; however, the fluid velocities and turbulence properties including the helicity are different. The convective velocities in the turbulent cells are estimated as 10^9 and $(1 - 3) \times 10^6$ cm/s in the inner and outer zones, respectively, while the boundary between these zones moves toward the center over the typical star cooling time (1–10) s. The largest spatial scale of the turbulent cell is 1–3 km (recall, the star radius is only 10–15 km).

The turbulence nonuniformity is taken into account by inclusion of variable parameters in the equation for the magnetic field:

$$\frac{\partial \boldsymbol{B}}{\partial t} = \nabla \times (\boldsymbol{u} \times \boldsymbol{B} + \alpha \boldsymbol{B}) - \nabla \times (\nu_t \nabla \times \boldsymbol{B}), \tag{8.79}$$

where the velocity of large-scale motion is $\boldsymbol{u} = \boldsymbol{\Omega} \times \boldsymbol{r}$, with the angular velocity $\boldsymbol{\Omega}$ dependent on the coordinates. A possible rotation model includes a spherically symmetric component:

$$\Omega(r) = \Omega_0 + \left(\frac{r}{R}\right)^2 \Omega_1, \tag{8.80}$$

where Ω_0 and Ω_1 are some constants. The ratio $q = \Omega_1/(\Omega_0 + \Omega_1)$ quantifies the differential rotation. This parameter is positively or negatively defined depending on where the rotation is faster—at the center or surface of the star.

The turbulent parameters α and ν_t, which are distinctly different in the two considered zones, can be modeled by smooth functions with a narrow transition region:

$$\nu_t = \nu_1 + (\nu_2 - \nu_1)\{1 + erf[(r - R_c)/\Delta R]\}/2, \tag{8.81a}$$

$$\alpha(r, \theta) = \alpha_2(r)\cos\theta\{1 + erf[(r - R_c)/\Delta R]\}/2, \tag{8.81b}$$

where $\Delta R = 0.025R$ is the width of the transition layer; erf is the error function. Then, let us neglect the turbulence helicity in the inner zone, $\alpha_1 \approx 0$, while adopt $\alpha_2(r)$ to be constant, $\alpha_2 = \Omega h$, assuming that the turbulent cell and spatial scales of both density and pressure are all of the same order of magnitude.

Induction Eq. (8.79) supplemented by vacuum boundary condition at the star surface and zero toroidal field at the star center requires a numerical solution, e.g., utilizing a finite grid for the radial variation with expansion over spherical harmonics for the angular dependence (Bonanno et al. 2005). The corresponding numerical calculations show that for a "normal" neutron star the dynamo works for $P = 2\pi/\Omega < P_0$, where the critical star rotation period is $P_0 \approx 0.5$–1 s. Since young neutron stars rotate fast, $P \sim 10$–100 ms, the turbulent dynamo is likely to work for most of the neutron stars. Depending on the differential rotation parameter q, either stationary or oscillatory dynamo regime is possible. The first one, typical for $|q| \leq 1$, originates from α^2-dynamo regime, while the second one, $|q| \geq 1$, is produced by $\alpha\Omega$-dynamo. These two regimes of the magnetic field generation are noticeably different in efficiency of the poloidal B_p and toroidal B_ϕ field generation. For $|q| < 1$ their ratio is $B_\phi/B_p \approx 10$, while for $|q| > 1$ ($\alpha\Omega$-regime) $B_\phi/B_p \approx 100$–200. A typical period of the oscillating regime is 1 s.

As has been noted, this unstable stage of the neutron star evolution lasts only about 1 min. For the practical purpose, it s highly important to estimate the saturation magnetic field produced by the end of this stage, which then freezes in the star crust and then declines slowly due to the Joule dissipation. Typically, effect of the helicity suppression by the growing magnetic field is taken into account by a model expression

$$\alpha(B) = \frac{\alpha_0}{1 + B^2/B_{\rm eq}^2}, \tag{8.82}$$

where $B_{\rm eq}$ is the "equilibrium magnetic field" obeying the equality of the magnetic and turbulent energies, $B_{\rm eq}^2/8\pi = \rho\langle u^2\rangle/2$, which results in "global quenching" of the magnetic field generation.

However, we have to emphasize that nonlinear generalization (8.82) of the helicity parameter is lacking a firm theoretical justification as it was not derived consistently from the MHD equations. Furthermore, it differs from Eq. (8.68), which, even being an approximation, has been obtained by the account of the lowest-order nonlinear terms in the MHD equations. Not surprisingly, two different expressions, (8.82) and (8.68), offer different estimates for the saturation field, $B_{\rm sat}$. Equation (8.68) gives rise to the estimate $B_{\rm sat} \approx B_{\rm eq} \approx (1-3) \times 10^{13}$ for the turbulent cell size about $l_t = (1\text{–}3)\,{\rm km}$ and typical cooling time of the order of a few seconds. In contrast, Eq. (8.82) gives rise to $B_{\rm sat} = B_{\rm eq}\sqrt{P_0/P - 1}$, where $P_0 \approx 1$ is a critical (largest) period for the dynamo operation, and P is period of star rotation. The ratio P_0/P can be as high as 10^3, implying a 1,000-fold imbalance in favor of the magnetic field energy against the turbulence energy. This option is highly unlikely because the turbulence is supposed to be suppressed by the magnetic field at much earlier stage of the field growth. Nevertheless, generation of the magnetic field of the order of $10^{13}\,{\rm G}$ by the turbulent dynamo is a feasible process.

The described model implies presence of a specific neutron star subclass without the large-scale magnetic field. Such stars can appear if their rotation period right after the parent star collapse is larger than the corresponding threshold and the large-scale dynamo does not work, i.e., for $P \gtrsim 0.3\,{\rm s}$. Nevertheless, a small-scale field of the order of $B_{\rm eq} \approx 3 \times 10^{13}\,{\rm G}$ must be generated by the turbulence and then can survive at the star surface. Such stars are supposed to have the following main properties:

1. Absence of noticeable radio emission because no magnetic moment is present; in fact, such radio quiet young neutron stars have been observed, e.g., “magnificent seven” at the Gould belt.

2. Small spin down and nearly constant rotation period.

3. X-ray emission due to surface magnetic field; weak X-ray pulsations are possible due to inhomogeneities of the temperature and the magnetic field at the star surface.

4. A strong disconnect between the magnetic field values determined from the spin down and X-ray emission.

8.7.4 Solar Magnetism, Cycles, and Activity

The Sun is the only star accessible for direct observations of the magnetic fields in great detail. Role of the solar magnetic field can hardly be overstated: no doubts, all kinds of the solar activity (affecting the human life and technology) are either produced by the magnetic fields or, at least, strongly

coupled to them. By now, we well know three main components of the solar large-scale magnetic field (see numerous review papers, e.g., Bruzek and Durrant 1977; Vainshtein et al. 1980; Vitinskii 1983; Obridko 1985; Weiss and Thompson 2009; Jones et al. 2010 for greater detail).

Toroidal (azimuth) magnetic field up to a few $\times 10^3$ G is located beneath the photosphere, although it reveals itself at the photosphere at some regions, called **active regions (ARs)**, and seen as dark **sunspots** or groups of the sunspots discovered by Galilei. The sunspots (Figs. 1.2 and 6.3) have a nonuniform highly dynamic structure with a dark region, **umbra**, in the central part surrounded by a less dark filamentary region, **penumbra**. The sunspots often appear in bipolar structures consisting of two, leading and trailing (i.e., following with respect to the solar rotation), spots with opposite magnetic polarities (e.g, Fig. 10.3) ordered almost parallel to the solar equator. During a given solar cycle (see below) the polarity of the leading sunspot is the same in all ARs of the given hemisphere, while different in the north and south hemispheres, respectively; the polarities reverse each 11-year cycle. The presence of the bipolar groups can be understood as a result of emergence of the flux tubes with the toroidal magnetic field from the convective zone with formation of Ω-like loops; these loops emerging above the photosphere form a bipolar group at two regions of the fluxtube cross section with the photosphere level.

The field forming the sunspots has opposite polarities in the north and south hemispheres; it varies with a period about 22 years. A largest field over the 22-year cycle appears at latitudes around $\approx \pm 35°$, then moves over roughly 11 years toward equator, and disappears at latitudes of $\approx \pm 8°$ (Spörer's law). Then, new strong field having the opposite polarity appears at the middle latitudes; thus, the 22-year cycle consists of two 11-year (semi-) cycles differing by the magnetic field direction.

This behavior is prominently illustrated by a "butterfly diagram" (upper panel in Fig. 8.5). It shows appearance of the sunspots at the middle latitudes in the beginning of each solar (11-year) cycle, their "drift" to the equator, and disappearance at the end of the cycle. One can note that the cycles can overlap: new cycle sunspots appear at the middle latitudes along with old cycle sunspots still present almost at the equator, although some cycles (e.g., no. 24) have a delayed start and so do not overlap with the previous cycle. The lower panel of this figure displays a fraction of visible solar surface occupied by the sunspots and averaged over a few solar rotations. Both presented measures are clearly quasiperiodic. Optical observations of the sunspots lasting continuously since Galilei's invention of the telescope, i.e., over a long period from 1610 to now have demonstrated that the amplitude of the cyclic solar activity itself experiences significant variations over a longer time scale (Fig. 8.6). The largest, over the last 400 years, number of the sunspots (around 200) was observed in 1958; sometimes the number of sunspots is small or zero; in particular, during a rather long period, 1645–1715, called the Maunder minimum, there were no observed sunspots at all.

There is also a **poloidal (longitudinal)** axisymmetric dipole-like **magnetic field**. It is present at high helio latitudes (55° and up) in both hemispheres; it varies with the 22 year quasiperiod and reaches a maximum (∼10 G) during minima of the sunspot activity, i.e., it seems to be 180°-phase shifted compared with the toroidal field. Along with this dipole component (antisymmetric about the equatorial plane), there is a weaker symmetric quadruple component.

Finally, there is a so-called **"sector" magnetic field** discovered originally by first spacecrafts measuring the magnetic field outside the terrestrial magnetosphere. This component of the large-scale solar magnetic field is transferred by the solar wind to the interplanetary space and clearly observed at the Earth orbit and farther heliocentric locations (see Sect. 2.5.3). This field has a magnitude of about 1 G and varies for a remote observer with the period of solar rotation (≈27 days). It does not possess an axial symmetry; two-sector, four-sector, and six-sector structures have been observed, which might have been created by a combination of magnetic dipole and quadruple located in the solar equatorial plane. In the system rotating along with the Sun, this field is relatively stable and roughly constant over many solar rotations. The magnetic sectors in the solar photosphere are relatively

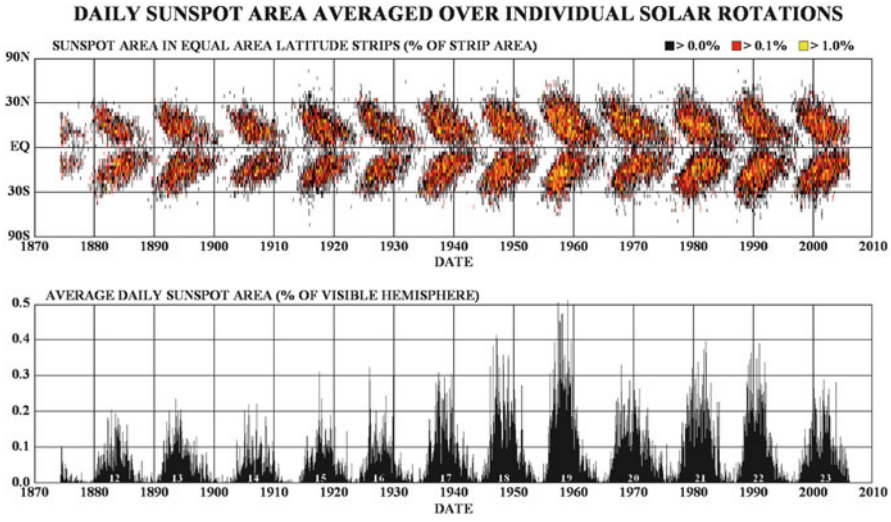

Figure 8.5: Two complementary ways of showing long-term solar-cycle activity; data from 1874 includes twelve full cycles. *Top panel*: the butterfly diagram shows evolution of the sunspot position with phase of the cycle. Specifically, it clearly illustrates that at the beginning of a new cycle, spots appear at high latitudes around of 30°. The activity zones migrate toward the equator and then gradually disappear, along with appearance of the new spots at higher latitudes manifesting the next cycle activity. *Bottom panel*: averaged daily sunspot area, i.e., fraction of the visible hemisphere covered by sunspots (Weiss and Thompson 2009).

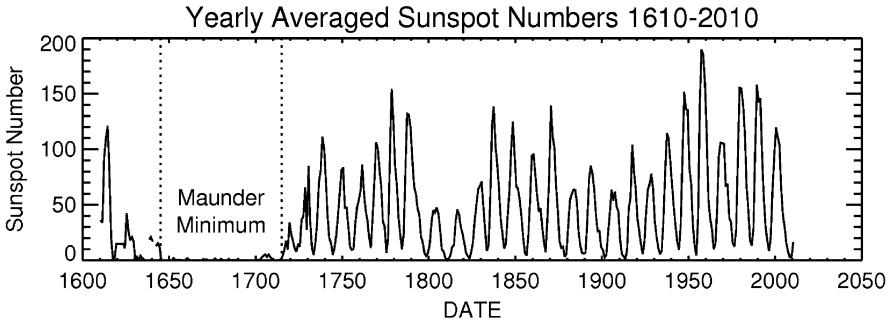

Figure 8.6: The full range of available yearly averaged sunspot numbers covering the period from 1610 to 2000. Although the variability is clearly seen, the amplitude of this activity measure varies irregularly including a prominent interval of extended inactivity in the seventeenth century—the **Maunder Minimum** (Weiss and Thompson 2009).

large regions dominated by a field with a given polarity; they occupy a photospheric area between $\approx \pm 35°$. Thus, the effective heliomagnetic equator is not a circle, while a wavy line whose shape changes with the solar cycle phase.

Understanding the solar magnetic field origin requires a detailed information on the solar differential rotation as well as on the fluid motions in the convective zone. The rotation of the solar surface is directly observed via the spectroscopic Doppler measurements as well as tracing the sunspots and other features in the photosphere. These observations yield the rotation period about 25 days at the equator and above 30 days at polar regions; see Sect. 8.2.

Highly valuable data on the internal solar rotation including dependence of the rotation on the subphotospheric depth and latitude as well as on parameters of the fluid and its turbulent motions come from **helioseismology**. It is based on investigation of global acoustic solar oscillations modified by the rotation and magnetic field. These oscillations are likely generated by convective turbulence and, because of almost spherical shape of the Sun, can be rather precisely described by spherical harmonics, whose resonant frequencies are specified by the solar fluid properties. The solar rotation gives rise to a small difference in the frequencies of the waves propagating along and opposite to the solar rotation; this splitting is sensitive to the rotation velocity distribution over the depth and latitude. Eventually, a sophisticated fine tuned technique allows deriving the differential rotation inside the Sun.

Moreover, the helioseismology quantifies the bounds of the convective zone and type of the fluid motion around those bounds. In particular, it is well established that the transport of the nuclear fusion energy released in the solar core up to the heights about $0.7R_\odot$ is provided by the radiative heat transfer. There, the temperature gradient is small and so no convection arises. Above this radiative zone, there is a convective zone, where the gradient is slightly super-adiabatic, which drives the convection. However, the

distribution of the density and pressure is rather close to the adiabatic ones. Measurements of the sound speed gradient, which changes strongly when the heat transfer regime changes from the radiative to the convective one, yielded the inner radius of the convective zone: $r/R_\odot = 0.713 \pm 0.003$, independent on latitude. The transition between the radiative and convective zones is rather sharp, less than 0.1 of the pressure scale.

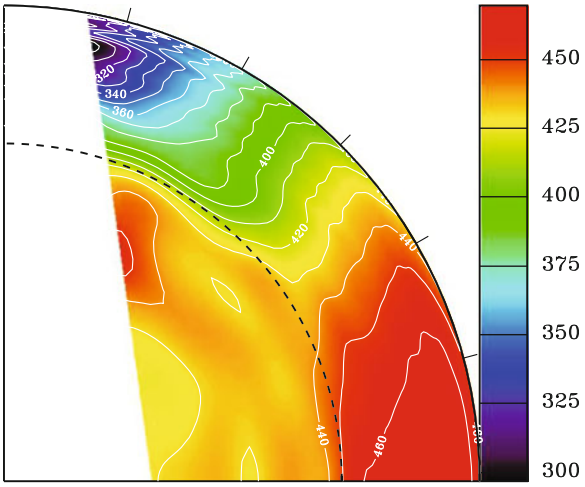

Figure 8.7: The internal rotation of the Sun, as measured with the helioseismology technique based on observations made by the MDI/SOHO instrument. X-axes (*horizontal*) shows the solar equator, z (*vertical*) is directed to the pole, the *solid circle* segment is the solar surface, and the *dashed circle* segment indicates the base of the convection zone. The differential rotation rate $\Omega/2\pi$ is shown in nHz by the contour levels and color code (Weiss and Thompson 2009).

The differential rotation profiles derived from the helioseismology are given in Fig. 8.7. Below the convective zone base (the dashed line) the rotation is almost rigid body, while it is a differential one in the convective zone, faster in the equatorial zone and slower at the polar regions. The rotation velocity of the inner radiative zone is roughly the same as in the outer zone in the middle latitudes. Above and below these latitudes, there is a region of sheared fluid flow at the base of the convective zone. This region is called the **tachocline**. It is supposed that the solar dynamo works the most efficiently in this tachocline region, which generates here the magnetic field observed then in the sunspots. There is one more sheared fluid flow region at upper bound of the convective zone.

The helioseismology measurements locate the center of the tachocline region from $r/R_\odot = 0.692 \pm 0.002$ at low latitudes up to 0.710 ± 0.002 at higher latitude, 60°. The relative depth of this region $w/R_\odot$ is 0.033 ± 0.007 and 0.076 ± 0.010, respectively. In addition, helioseismology is capable of providing temporal variations of the differential rotation profile of a few months and

years. Specifically, comparison of the running measurements on the averaged rotation profiles reveals small, while statistically significant, stripes of zonal flows migrating from middle latitudes to equator covering at least one-third of the convective zone below its upper bound. These stripes represent likely the traces of the active latitude migration, where the sunspots are localized, although no firm causal relation between the magnetic activity and these zonal flows has yet been established. If the main location of the solar dynamo is the tachocline region, then one can expect detecting the duration of the solar cycle by temporal variations of the angular velocity in the tachocline region.

One more important dynamic ingredient is a so-called north–south **meridional circulation**. The corresponding fluid flows were detected by a local helioseismology technique. These flows are poleward directed; they are steady on the scale of a few years. In the layer of roughly 2% of the solar radius these polar flows move with a velocity 20–30 m/s independent on the depth.

The presented summary of observational data, whose volume has drastically increased over the first decade of the third millennium, clearly demonstrates that all conditions necessary for the turbulent dynamo to work are available at the Sun. Indeed, there are (1) well-localized convective zone with turbulent cells, (2) general rotation and the differential rotation; and (3) regions with shear flow capable (in principle) of producing a significant helicity of the turbulence and, thus, provide operation of $\alpha\Omega$-dynamo. Attempts to reproduce the solar cycle with required properties (e.g., the butterfly diagram) yielded controversial results; in particular, the toroidal field often drifts toward poles in place of equator. An idealized illustrative example of numerical dynamo modeling, presented in Fig. 5 of Weiss and Thompson (2009), does show some general resemblance with the butterfly diagram, though, not surprisingly, lacking any detail similarity. Indeed, development of quantitative theory of the solar dynamo and solar cycles possessing a reliable predictive power is extremely complicated, which is additionally enhanced by nonexistence of closed nonlinear theory of the turbulent convection with account of the magnetic fields and Coriolis forces, as well as by a complex asymmetric geometry of the system under study. Furthermore, given a large volume of available detailed observational data on the solar interior and cycle, the theory is supposed to yield a highly detailed picture capable of consistent quantitative interpretation of this whole data volume. The target theory, thus, must disentangle local and sporadic manifestations of the solar activity from the main cycle properties, consistently accounting for both. Given this great complexity of the system complemented by the detailed observational demand to the theory, it becomes clear why no commonly accepted quantitative theory of the solar dynamo has yet been developed; see recent review papers (Weiss and Thompson 2009; Jones et al. 2010) for more discussion on the subject.

We have already mentioned that the global solar cycle is accompanied by

plenty local manifestations reviewed in many monographs and textbooks, e.g., Kaplan et al. (1977), Benz (2002) and Aschwanden (2005). Here, we briefly discuss some of them, using Fig. 1.2 as a general guideline. In the atmosphere there are **bipolar and unipolar magnetic regions** and **coronal holes**. The latter ones are characterized by a low density and temperature; they are located above unipolar photospheric regions providing open magnetic field lines merging the solar wind field lines. The coronal holes produce the high-speed solar wind flows.

Sunspots (Fig. 6.3): Dark (in visual light) regions at the photosphere with a typical scale of a few thousand km and temperature by 500–1000 K below the photosphere temperature. They only appear at a restricted region of latitudes, between 40° and 5° at both hemispheres. The magnetic field in the sunspots reaches relatively high values of 10^3 to 5×10^3 G (recall, the mean photospheric field is about 1 G). The sunspots often appear in groups and form an **active region** with a typical lifetime from weeks to months. These active regions drive most of the solar activity by different kind of their magnetic energy release.

Prominences (Sect. 2.2.3): Elongated gas filaments, hundred thousand km long, "hanged" at tens thousand km above the photospheric level. They have diverse shapes that reflected in a number of poetic names like coronal rain, hedgerow, tornado, and fountain. The prominence density is higher, while the temperature is lower than in the ambient coronal plasma, which implies that the magnetic field (a few tens G) plays an important role in maintaining the pressure balance. The prominence lifetime is from a few minutes to many months. The prominences are highly dynamic structures with a plethora of regular and chaotic motions of the prominence plasma. Some prominences, called **eruptive prominences**, can sporadically explode and produce ejections into the interplanetary space after which the prominence either experiences a restructurization or disappears entirely.

Coronal Mass Ejections, CMEs (Fig. 1.3): Excessive free magnetic energy accumulated in the corona above active regions can produce unstable twisted (due, in particular, to differential photosphere rotation) magnetic structures capable to be ejected with a velocity between 20 km/s and 3,200 km/s (the mean value is about 500 km/s). The ejected mass can exceed 10^{15} g, which corresponds to "mean" CME kinetic energy of $\sim 3 \times 10^{30}$ erg. The CMEs have strong effect on the space weather (Gary and Keller 2004) including numerous effects on the Earth magnetosphere, human life, and technology. Some of the eruptions result in a "failed CME," which falls back to the photosphere instead of propagation out of the Sun.

Solar Flares: Events of a relatively fast, impulsive, release of the free magnetic energy, perhaps, via a "**magnetic reconnection**" process (see Sect. 5.3.2), giving rise to a firework of secondary effects throughout the entire electromagnetic spectrum and particular emissions. One important solar flare property is its ability to accelerate charged particles (electrons and ions) up

to high, including ultrarelativistic, energies. These nonthermal particles propagate in the magnetized corona and produce a whole variety of nonthermal electromagnetic emissions (see Chap. 9), e.g., coherent decimeter emissions, incoherent microwave gyrosynchrotron emission, hard X-ray bremsstrahlung, gamma-ray lines, and π°-decay generated quanta (stimulated by ions). Some fraction of the accelerated particles loses its energy to collisionally heat the coronal and chromospheric plasma, and the other fraction escapes into interplanetary space and is detected in-situ by spacecrafts. These escaping particles also drive very-low-frequency emissions as they propagate in the tenuous solar wind plasma. The total flare energy is within 10^{29}–10^{32} erg. The flare duration varies from a minute to a few hours (Syrovatskii 1981; Sakai and Ohsawa 1987; Priest and Forbes 2000; Benz 2002; Aschwanden 2005).

Problems

8.1 Adopt a 2D motion with a given stationary velocity field $\boldsymbol{u} = (u_x(x, y), u_y(x, y), 0)$ in an incompressible homogeneous conducting fluid. Prove that such a motion cannot support the magnetic field so the initial field dissipates over a finite time (Zeldovich antidynamo theorem).

8.2 A star with a solar radius $R_{\odot} \approx 7 \times 10^{10}$ cm collapses to the size of a typical neutron star, $R_N \approx 10^6$ cm, conserving the shape, mass, and the angular momentum (but not the energy). How the rotation period P will change?

8.3 Calculate helicity parameter α and mean DC electric field induced by the turbulence composed of MHD waves excited on top of a nonpotential force-free magnetic field characterized by the force-free parameter α_{FFF}; see Problem 2.6.

Answers and Solutions

8.1 Use Cartesian coordinates and project the second of Eq. (8.1) onto the axes Oz:

$$\frac{\partial B_z}{\partial t} + (\boldsymbol{u}\cdot\nabla)B_z = \nu_m \triangle B_z. \tag{1}$$

Then, multiply both sides of the equality by B_z and integrate over all 2D space. The term containing velocity $\boldsymbol{u}$ vanishes for the incompressible bounded fluid ($\nabla\cdot\boldsymbol{u} = 0$). All other terms can be transformed to the form

$$\frac{\partial}{\partial t}\int B_z^2 \mathrm{d}x\mathrm{d}y = -2\nu_m \int (\nabla B_z)^2 \mathrm{d}x\mathrm{d}y. \tag{2}$$

Since the rhs of the equality is negative if the region filled by the field is bounded, then the field energy decreases monotonically and, thus, $B_z \to 0$

for $t \to \infty$. Thus, B_z-component decays, so two other components can be studied assuming $B_z = 0$.

They obey the equation

$$\frac{\partial B_{x,y}}{\partial t} + (\boldsymbol{u}\cdot\nabla)B_{x,y} = \nu_m \triangle B_{x,y} + (\boldsymbol{B}\cdot\nabla)\boldsymbol{u}_{x,y}. \tag{3}$$

These components are convenient to express in a standard way via the vector potential ($\boldsymbol{B} = \nabla \times \boldsymbol{A}$) directed along the axes Oz, so, $A_z(x, y) \equiv A(x, y)$. Both Eqs. (3) can be derived from equation

$$\frac{\partial A}{\partial t} + (\boldsymbol{u}\cdot\nabla)A = \nu_m \triangle A \tag{4}$$

(the fluid incompressibility must again be taken into account in proving this statement). Let us multiply Eq. (4) by A and then integrate over the plane (x, y) and over t to obtain

$$\int A^2(x, y, 0)\mathrm{d}x\mathrm{d}y - \int A^2(x, y, t)\mathrm{d}x\mathrm{d}y = 2\nu_m \int_0^t \mathrm{d}t \int (B_x^2 + B_y^2)\mathrm{d}x\mathrm{d}y. \tag{5}$$

The integral in the rhs of the equality is a monotonically rising function of time bounded by the value $\int A^2(x, y, 0)\mathrm{d}x\mathrm{d}y$. Thus, the integral over time converges at $t \to \infty$, which proves that $B^2 = B_x^2 + B_y^2 \to 0$ at $t \to \infty$. This finding represents one of the antidynamo theorems, proving impossibility of generating a large-scale magnetic field by certain (relatively symmetric) fluid motions.

8.2 Assuming that the star mass is uniformly distributed over its volume both before and after the collapse we obtain

$$P_N = P_\odot \left(\frac{R_N}{R_\odot}\right)^2 \approx 0.5\,\mathrm{ms}.$$

This period is roughly one order of magnitude shorter than rotation periods typically observed from young neutron stars.

8.3 Let us calculate the large-scale electric field, created by helical turbulence, taking into account the entire range of harmonics forming the random fields of $\boldsymbol{u}(\boldsymbol{r}, t)$ and $\boldsymbol{b}(\boldsymbol{r}, t)$. From the first of Eq. (2.101) we find

$$\boldsymbol{b}(\boldsymbol{r}, t) = B_{0\nu} \int_{-\infty}^{t} \frac{\partial \boldsymbol{u}(\boldsymbol{r}, \tau)}{\partial x_\nu}\mathrm{d}\tau - \frac{\partial \boldsymbol{B}_0}{\partial x_\beta} \int_{-\infty}^{t} u_\beta(\boldsymbol{r}, \tau)\mathrm{d}\tau, \tag{8.83}$$

which allows to form the required bilinear cross product $\boldsymbol{u} \times \boldsymbol{b}$ and perform the averaging

$$\boldsymbol{E}_h = -(1/c)\langle \boldsymbol{u}(\boldsymbol{r}, t) \times \boldsymbol{b}(\boldsymbol{r}, t)\rangle \tag{8.84}$$

over the turbulent ensemble according to Eqs. (8.28) and (8.60), which is convenient to express via the vector components

$$\langle u_\sigma(\boldsymbol{r},t)b_\mu(\boldsymbol{r},t)\rangle = -\frac{\partial B_{0\mu}}{\partial x_\beta}\int_{-\infty}^{t}\langle u_\sigma(\boldsymbol{r},t)u_\beta(\boldsymbol{r},\tau)\rangle \mathrm{d}\tau + B_{0\nu}\int_{-\infty}^{t}\langle u_\sigma(\boldsymbol{r},t)\frac{\partial u_\mu(\boldsymbol{r},\tau)}{\partial x_\nu}\rangle \mathrm{d}\tau. \quad (8.85)$$

The first term in the rhs describes a modification to Ohm's law due to the wave turbulence ensemble (anomalous resistivity), while the second one describes another correction to Ohm's law due to the turbulence helicity; we will see below that these two terms provide comparable contribution in the problem studied. Adopting for simplicity that the turbulence is statistically uniform and isotropic, we can express the first integral using the invariant Kronecker's tensor as

$$\int_{-\infty}^{t}\langle u_\sigma(\boldsymbol{r},t)u_\beta(\boldsymbol{r},\tau)\rangle \mathrm{d}\tau = (\langle u^2\rangle\tau_c/3)\delta_{\sigma\beta}, \quad (8.86)$$

where $\langle u^2\rangle\tau_c/3 = \nu_t$ is the magnetic turbulent diffusivity; cf. Sect. 6.11.

The second integral, which is a third-rank tensor, is apparently proportional to the Levi–Civita's permutation tensor $e_{\sigma\mu\nu}$ and the kinetic helicity pseudoscalar α

$$\int_{-\infty}^{t}\left\langle u_\sigma(\boldsymbol{r},t)\frac{\partial u_\mu(\boldsymbol{r},\tau)}{\partial x_\nu}\right\rangle \mathrm{d}\tau = \frac{1}{2}\alpha e_{\sigma\mu\nu}. \quad (8.87)$$

Now, the large-scale DC electric field can be written in the form

$$\boldsymbol{E}_h = (\nu_t/c)\nabla\times\boldsymbol{B}_0 - (\alpha/c)\boldsymbol{B}_0 = -(\alpha_{\mathrm{eff}}/c)\boldsymbol{B}_0, \quad (8.88)$$

where, according to Eqs. (2.108) and (8.13),

$$\alpha = -\frac{\tau_c}{12}\alpha_{FFF}v_A^2\frac{\langle b^2\rangle}{B_0^2}, \qquad \alpha_{\mathrm{eff}} = \alpha - (\nu_t/c)\alpha_{FFF} \quad (8.89)$$

and

$$\alpha_{\mathrm{eff}} = -\frac{5\tau_c}{12}\alpha_{FFF}v_A^2\frac{\langle b^2\rangle}{B_0^2} \quad (8.90)$$

is the total effective helicity parameter specifying the electric field in a non-potential flux tube. Although both terms in α_{eff} are comparable, the contribution from the anomalous magnetic diffusivity (anomalous resistivity) is four times larger than the direct helicity contribution. The correlation time can be estimated using the correlation scale L_c and the Alfvén velocity v_A: $\tau_c = L_c/v_A$. Finally, recalling that the magnetic field vector can be expressed via the electric current density, Eq. (8.88) can be presented in Ohm's law form $\boldsymbol{j} = \sigma_{\mathrm{eff}}\boldsymbol{E}$, where $\sigma_{\mathrm{eff}} = -(c^2/4\pi)(\alpha_{FFF}/\alpha_{\mathrm{eff}})$ is the anomalous (turbulent) electric conductivity.

Chapter 9

Emission Processes

A classical problem of calculating the electromagnetic emission produced by a charge (or a group of charges) moving in the vacuum is formulated in terms of computing the Poynting vector flux through a closed infinitely distant surface surrounding the radiation source (Melrose 1980; Rybicki and Lightman 1986; Ginzburg 1987; Nagirner 2007b). In contrast, computing the emission from a plasma, which is an anisotropic, dispersive, and absorbing matter, is distinctly different from the classical vacuum problem. In particular, unlike the vacuum case, the polarization vectors of the eigenmodes are not arbitrary any longer, while set up by the plasma dispersion (see Chap. 3). Then, the concept of the nonzero energy flux through an infinitely distant surface can only work in case of truly nonabsorbing matter, which is strictly speaking not the case for real media including astrophysical plasmas.

In fact, in the case of absorbing matter, there is no exact way of isolating the radiated energy from the total energy losses of a moving charge. Indeed, if a radiating particle moves in a finite region of the infinite space filled by an absorbing matter, the energy flux through an infinitely distant surface is always evanescent. The emission processes in the strong absorption conditions are specifically addressed in monograph (Bazylev and Zhevago 1987). Here we consider the case of weak absorption, when the characteristic length of the photon absorption is much larger than the wavelength and the length over which the emission is formed (called the coherence length or formation zone). In such a case (valid within certain spectral *transparency windows*) the absorption can be discarded while calculating the elementary emission process (e.g., volume emissivity) but can be accounted at a later stage of the radiation transfer through the plasma (see Chap. 10). In this way, the radiation flux from a volume becomes uniquely defined, although it does depend on the volume now unlike the vacuum case.

G.D. Fleishman and I.N. Toptygin, *Cosmic Electrodynamics*, Astrophysics and Space Science Library 388, DOI 10.1007/978-1-4614-5782-4_9,

9.1 Emission of Waves by a Given Electric Current

9.1.1 Energy Loss and Electromagnetic Wave Radiation in an Anisotropic Medium

Let us consider the energy loss of an electric current $\boldsymbol{j}_{\omega,\mathbf{k}}$ in an anisotropic absorbing medium (Toptygin and Fleishman 2008; Fleishman 2008):

$$W = -\int\limits_{-\infty}^{\infty}\int\limits_{V}\boldsymbol{j}(\boldsymbol{r},t)\boldsymbol{E}(\boldsymbol{r},t)\mathrm{d}\boldsymbol{r}\mathrm{d}t = -(2\pi)^4\int\limits_{-\infty}^{\infty}\int\boldsymbol{j}^*_{\omega,\mathbf{k}}\boldsymbol{E}_{\omega,\mathbf{k}}\mathrm{d}\boldsymbol{k}\mathrm{d}\omega = \int\limits_{0}^{\infty}\int W_{\mathbf{n},\omega}\mathrm{d}\Omega\mathrm{d}\omega, \tag{9.1}$$

where

$$W_{\mathbf{n},\omega} = -2(2\pi)^4\,\mathrm{Re}\int\boldsymbol{j}^*_{\omega,\mathbf{k}}\boldsymbol{E}_{\omega,\mathbf{k}}k^2\mathrm{d}k. \tag{9.2}$$

The factor of 2 and real part selector Re in Eq. (9.2) appear because in the most rhs of Eq. (9.1) we integrate over the positive frequencies only rather than over the entire infinite frequency axes. Let us calculate the electric current produced by the electric current $\boldsymbol{j}_{\omega,\mathbf{k}}$ in the anisotropic medium using Eqs. (3.11) and (3.12).

Apparently, the formal solution of Eq. (3.11) has the form, cf. Eq. (4.48),

$$E_\alpha(\omega,\boldsymbol{k}) = g_{\alpha\beta}(\omega,\boldsymbol{k})j_\beta(\omega,\boldsymbol{k}), \tag{9.3}$$

where

$$g_{\alpha\beta}(\omega,\boldsymbol{k}) = -i\frac{4\pi}{\omega}A_{\alpha\beta}(\omega,\boldsymbol{k}), \tag{9.4}$$

$A_{\alpha\beta}(\omega,\boldsymbol{k}) = (\widehat{T}(\omega,\boldsymbol{k})^{-1})_{\alpha\beta}$ is a tensor inverse to the Maxwellian one (the inverse tensor for short), such as

$$T_{\alpha\beta}(\omega,\boldsymbol{k})A_{\beta\nu}(\omega,\boldsymbol{k}) = \delta_{\alpha\nu}. \tag{9.5}$$

According to the tensor algebra for $\Delta \neq 0$ the inverse tensor reads

$$A_{\beta\nu} = (\widehat{T}^{-1})_{\beta\nu} = \frac{\Delta_{\nu\beta}}{\Delta}. \tag{9.6}$$

Here (like in Chap. 3) $\Delta = |T_{\alpha\beta}|$ is the determinant of the Maxwellian tensor $T_{\alpha\beta}$ and $\Delta_{\nu\beta}$ is its adjoint (accordingly, $\Delta_{\beta\nu}$ is its cofactor).

Equations (9.3), (9.4), and (9.6) yield the electric field in the form

$$E_\alpha = -i\frac{4\pi}{\omega\Delta}j_\nu\Delta_{\nu\alpha}. \tag{9.7}$$

Note that in anisotropic or gyrotropic medium this vector is not necessarily transverse to the wave vector $\boldsymbol{k}$. The transverse direction is only guaranteed for the electric displacement $\boldsymbol{D}$ and magnetic induction $\boldsymbol{B}$ vectors.

Substituting Eq. (9.7) into Eq. (9.2), we present the energy loss of a *given current* $\boldsymbol{j}$ *in a medium* in the form

$$W_{\mathbf{n},\omega} = 4(2\pi)^5 \Re\, i \int\limits_0^\infty \frac{j_\nu \Delta_{\nu\alpha} j_\alpha^*}{\omega \Delta(\omega, \boldsymbol{k})}\, k^2 \mathrm{d}k. \tag{9.8}$$

The necessary and sufficient condition for inverse tensor (9.6) to exist is a nonzero value of the determinant $\Delta \neq 0$. Note that for real $\boldsymbol{k}$ and ω the integration path contains poles where $\Delta = 0$; thus, we have to adopt rules of how to bypath the poles in the complex plane ensuring the generated perturbations to asymptotically represent outgoing spherical waves at large distance from the source, likewise in the vacuum case. In the medium this can easily be achieved by adopting a small damping of the waves provided by a small anti-Hermitian part of the dielectric tensor, resulting in $\omega \to \omega + i0$. Accordingly, in the vicinities of the determinant zeros, we can write

$$\Delta(\omega, \boldsymbol{k}) = \frac{\partial \Delta}{\partial \omega}(\omega - \omega(\boldsymbol{k}) + i0), \tag{9.9}$$

which for further integration can be transformed using the **Sokhotsky rule**:

$$\frac{1}{\omega - \omega(\boldsymbol{k}) + i0} = \frac{\mathcal{P}}{\omega - \omega(\boldsymbol{k})} - i\pi\delta(\omega - \omega(\boldsymbol{k})). \tag{9.10}$$

The principal value of the integral yields no real contribution, so the emission is entirely specified by the δ-function term

$$W_{\mathbf{n},\omega} = 2(2\pi)^6 \Re \int\limits_0^\infty \frac{j_\nu \Delta_{\nu\alpha} j_\alpha^*}{\omega \partial \Delta(\omega, \boldsymbol{k})/\partial \omega} \delta(\omega - \omega(\boldsymbol{k}))\, k^2 \mathrm{d}k, \tag{9.11}$$

where a summation over all possible zeros of the determinant is implied. Given that all the quantities entering Eq. (9.11) are known, this expression represents a valid formal solution to the problem.

Along with this formal solution, another variant of Eq. (9.8) employing explicit form Eq. (3.31) of determinant Δ can be convenient. Assume that the refraction coefficients $n_{1,2}(\omega, \boldsymbol{\kappa})$ are known (as they can always be found in principle from the dispersion relation $\Delta = 0$). Then, using Eq. (3.31), the denominator of the integrand in Eq. (9.8) can be transformed to the form

$$\frac{1}{\omega\Delta} = \frac{\omega}{ac^2(n_1^2 - n_2^2)} \left[\frac{1}{k^2 - \omega^2 n_1^2/c^2} - \frac{1}{k^2 - \omega^2 n_2^2/c^2} \right]. \tag{9.12}$$

Accordingly, Eq. (9.8) transforms to

$$W_{\mathbf{n},\omega} = 4(2\pi)^5 \Re\, i \int\limits_0^\infty \frac{\omega j_\alpha \Delta_{\alpha\beta} j_\beta^*}{ac^2(n_1^2 - n_2^2)} \left[\frac{1}{k^2 - \omega^2 n_1^2/c^2} - \frac{1}{k^2 - \omega^2 n_2^2/c^2} \right] k^2 \mathrm{d}k. \tag{9.13}$$

Again, to perform the integration around poles we adopt a small damping of the normal modes giving rise to small positive imaginary parts of the refractive indices $\Im\, n_\sigma^2 > 0$ for $\omega > 0$, which yields the integration rules:

$$\Re \frac{i}{k^2 - \omega^2 n_\sigma^2/c^2}\bigg|_{\Im n_\sigma^2 \to +0} \to -\frac{\pi}{2k}\delta(k - \omega n_\sigma/c), \quad \sigma = 1, 2. \tag{9.14}$$

We note next that the adjoint tensor $\Delta_{\mu\nu}$ is a Hermitian one: $\Delta_{\mu\nu} = \Delta^*_{\nu\mu}$. Thus, the tensor product $j_\mu \Delta_{\mu\nu} j^*_\nu$ is real for real ω and $\boldsymbol{k}$. Integrating Eq. (9.13) with Eq. (9.14) we obtain

$$W_{\mathbf{n},\omega} = -\frac{(2\pi)^6 \omega^2}{ac^3(n_1^2 - n_2^2)}[n_1(j_\alpha \Delta_{\alpha\beta} j^*_\beta)_1 - n_2(j_\alpha \Delta_{\alpha\beta} j^*_\beta)_2]. \tag{9.15}$$

Although the adjoints entering Eq. (9.15) can always be computed based on the Maxwellian tensor, it is convenient to express them via the polarization vectors of the corresponding eigenmodes of the medium. Let us demonstrate that a polarization vector can be written as

$$e^{(i)}_\beta = A^i \Delta^{(i)}_{\mu\beta}, \tag{9.16}$$

where i is index of the mode and A^i is a normalization constant; the index μ has arbitrary fixed value (from 1 to 3). Indeed, substitution of the refractive index $n = n_i$ and solution (9.16) into Eq. (3.26) turns them to a set of equivalences: two of the equalities (those with $\mu \neq \alpha$) are satisfied irrespectively of n, while the third one (that with $\mu = \alpha$) does only for $n = n_i$ due to vanishing of the determinant. Likewise, using Hermitian properties of the Maxwellian tensor $T_{\alpha\beta}$, it is straightforward to show that the first index of the adjoint defines the components of the complex conjugate polarization vector e^*_μ. This allows, for $n = n_i$, expressing the adjoint via the normalized polarization vectors:

$$\Delta^{(i)}_{\mu\nu} = C^{(i)} e^*_\mu e_\nu, \tag{9.17}$$

where $e^*_\mu e_\mu = 1$, so $C^{(i)} = \Delta^{(i)}_{\mu\mu}$ is a real (positive or negative) normalization constant that is equal to the adjoint trace. We have to emphasize that the adjoint can be reduced to the direct product of the polarization vectors *only when* the corresponding dispersion relation $n = n_i$ is fulfilled; otherwise, relation (9.17) does not take place.

Accordingly, the radiation spectral density is expressed via the eigenmode polarization vectors and refractive indices as

$$W_{\mathbf{n},\omega} = \frac{(2\pi)^6 \omega^2}{a(\omega, \boldsymbol{\kappa}) c^3 (n_2^2 - n_1^2)}[n_1 C^{(1)} |(e^{(1)*}_\mu j_\mu)|^2 - n_2 C^{(2)} |(e^{(2)*}_\mu j_\mu)|^2]. \tag{9.18}$$

This equation describes transformation of a given current energy to the energy of electromagnetic radiation, which, apparently, must describe emission of the transverse free-space modes in the vacuum when ($\varepsilon_{\alpha\beta} \to \delta_{\alpha\beta}$). However, this turns Eq. (9.18) to an indefiniteness of 0/0 kind, whose computation can be easier done at an earlier step of the derivation.

9.1.2 Emission in Vacuum

When $\varepsilon_{\alpha\beta} \to \delta_{\alpha\beta}$, Eq. (3.29) yields the following simplified expressions of the determinant and the adjoint tensor:

$$\Delta \to \Delta^0 = (1-n^2)^2, \qquad \Delta_{\alpha\beta} \to \Delta^0_{\alpha\beta} = (1-n^2)(\delta_{\alpha\beta} - n^2\kappa_\alpha\kappa_\beta). \quad (9.19)$$

Upon their substitution into Eq. (9.7) the common factor cancels out from numerator and denominator, so the Fourier-transform of the electric field produced by a given current in the vacuum reads

$$\boldsymbol{E} = -i\frac{4\pi}{\omega(1-n^2)}[\boldsymbol{j} - n^2(\boldsymbol{\kappa}\cdot\boldsymbol{j})\boldsymbol{\kappa}] = -i\frac{4\pi\omega}{\omega^2 - c^2k^2}\left[\boldsymbol{j} - \frac{c^2(\boldsymbol{k}\cdot\boldsymbol{j})\mathbf{k}}{\omega^2}\right]. \quad (9.20)$$

Then, Eq. (9.2) with Eq. (9.20) yields

$$W_{\mathbf{n},\omega} = 4(2\pi)^5\frac{\omega^3}{c^4}\Re(-i)\int\limits_0^\infty \frac{|\boldsymbol{j}_\perp(\omega,\boldsymbol{k})|^2 \mathrm{d}k}{k^2 - \omega^2/c^2}. \quad (9.21)$$

Selection of the retarded solution is again achieved by adding an infinitely small imaginary part to the frequency ω, which gives rise to a familiar expression

$$W_{\mathbf{n},\omega} = (2\pi)^6\frac{\omega^2}{c^3}|\boldsymbol{j}_\perp(\omega,\boldsymbol{\kappa})|^2, \quad (9.22)$$

describing emission of two free-space modes with (arbitrary orthogonal) transverse polarizations, which can also be obtained by explicit analysis of the Poynting vector:

$$\boldsymbol{S} = \frac{c}{4\pi}[\boldsymbol{E}\times\boldsymbol{H}] = c\frac{H^2}{4\pi}\boldsymbol{n} = c\frac{E^2}{4\pi}\boldsymbol{n}. \quad (9.23)$$

9.1.3 Emission of Electrostatic Modes

The considered wave modes can be called quasitransverse modes because they contain nonzero displacement $\boldsymbol{D} \neq 0$ and magnetic $\boldsymbol{B} \neq 0$ vectors, which are transverse to the wave vector. The condition $\boldsymbol{B} \neq 0$ was used to derive Eq. (3.12). In addition, there can be wave modes with $\boldsymbol{B} = 0$ (and $\boldsymbol{D} = 0$) and purely longitudinal electric vector $\boldsymbol{E}\|\boldsymbol{k}$ satisfying the following equation for the Fourier components:

$$\boldsymbol{k}\times\boldsymbol{E} = 0, \qquad k_\alpha\varepsilon_{\alpha\beta}E_\beta = -i\frac{4\pi}{\omega}k_\alpha j_\alpha(\omega,\boldsymbol{k}). \quad (9.24)$$

Seeking the electric field in the form $\boldsymbol{E} = E_\|\boldsymbol{\kappa}$ we find from Eqs. (9.24)

$$E_\| = -i\frac{4\pi\boldsymbol{\kappa}\cdot\boldsymbol{j}(\omega,\boldsymbol{k})}{\omega\varepsilon^l(\omega,\boldsymbol{k})}, \qquad \varepsilon^l(\omega,\boldsymbol{k}) \equiv a(\omega,\boldsymbol{k}) = \kappa_\alpha\kappa_\beta\varepsilon_{\alpha\beta}(\omega,\boldsymbol{k}). \quad (9.25)$$

Then, calculation of the spectral energy density of the generated longitudinal waves using Eq. (9.2) and a small imaginary part of ε^l yields

$$W^l_{\mathbf{n},\omega} = \frac{2(2\pi)^6}{\omega} \int\limits_0^\infty \mathrm{d}k |\boldsymbol{k} \cdot \boldsymbol{j}(\omega, \boldsymbol{k})|^2 \delta(\varepsilon^l(\omega, \boldsymbol{k})). \tag{9.26}$$

Here, unlike Eq. (9.18) one must take the spatial dispersion into account. Without the spatial dispersion the corresponding electric oscillations, appearing at a number of distinct single frequencies, cannot propagate and transfer the energy. Integration in Eq. (9.26) can be performed using the expression

$$\delta(\varepsilon^l(\omega, \boldsymbol{k})) = \sum_a \frac{\delta(k - k_a(\omega, \kappa))}{|\partial\varepsilon^l/\partial k|_{k=k_a(\omega)}}, \tag{9.27}$$

where the summation is made over all possible roots of the equation $\varepsilon^l(\omega, \boldsymbol{k}) = 0$, setting up the dispersion laws of the longitudinal waves in the plasma, i.e., over all possible longitudinal waves of the plasma. Generally, the number of these mode can be quite (infinitely) large.

9.1.4 Energy Loss and Electromagnetic Wave Radiation in Plasma with Spatial Dispersion

In addition to modification of the longitudinal wave dispersion, the spatial dispersion can have other diverse effects on the eigenmodes; in particular, it results in new eigenmodes and additional absorption of the eigenmodes (because anti-Hermitian part of the dielectric tensor is nonzero in this case). Let us explicitly expand our treatment to the case when the spatial dispersion is present and the wave damping is not necessarily infinitely small (Toptygin and Fleishman 2008; Fleishman 2008). To do so, we express inverse tensor (9.6) via the eigenvectors $\boldsymbol{b}^{(i)}(\omega, \boldsymbol{k})$ of the Maxwellian tensor, which results in a simple diagonal form [cf. Eq. (3.17)] of the inverse tensor:

$$A_{\alpha\beta}(\omega, \boldsymbol{k}) = \sum_{i=1}^{3} \frac{1}{\lambda^{(i)}} b^{(i)}_\alpha b^{(i)*}_\beta = \frac{b^{(1)}_\alpha(\omega, \boldsymbol{k}) b^{(1)*}_\beta(\omega, \boldsymbol{k})}{\lambda^{(1)}(\omega, \boldsymbol{k})} + \frac{b^{(2)}_\alpha(\omega, \boldsymbol{k}) b^{(2)*}_\beta(\omega, \boldsymbol{k})}{\lambda^{(2)}(\omega, \boldsymbol{k})} + \frac{b^{(3)}_\alpha(\omega, \boldsymbol{k}) b^{(3)*}_\beta(\omega, \boldsymbol{k})}{\lambda^{(3)}(\omega, \boldsymbol{k})}. \tag{9.28}$$

Thus, we can calculate the electric field produced by the current $\boldsymbol{j}_{\omega,\mathbf{k}}$ using Eqs. (9.3), (9.4), and (9.28) and substitute it into Eq. (9.2), to express energy losses of the current in the anisotropic medium via eigenvectors and eigenvalues of the Maxwellian tensor:

$$W_{\mathbf{n},\omega} = -\frac{4(2\pi)^5}{\omega} \operatorname{Im} \int k^2 \mathrm{d}k \sum_{i=1}^{3} \frac{|\ (\boldsymbol{b}^{(i)*}(\omega, \boldsymbol{k}) \cdot \boldsymbol{j}_{\omega,\mathbf{k}})\ |^2}{\lambda^{(i)}(\omega, \boldsymbol{k})}. \tag{9.29}$$

In an arbitrary absorbing medium the eigenvalues $\lambda^{(i)}(\omega, \boldsymbol{k})$ are complex and their imaginary parts are fully responsible for the energy loss of a given electric current $\boldsymbol{j}_{\omega,\mathbf{k}}$. In principle, Eq. (9.29) allows finding the loss because all entering terms can be algebraically determined. However, such calculations are highly cumbersome for the most general case of an anisotropic absorbing medium with spatial dispersion. In particular, the Cardano formulae for the roots of cubic equation (3.15) specifying the eigenvalues of the Maxwellian tensor are very complicated. Nevertheless, the problem simplifies in a number of important cases, e.g., if the medium possesses a symmetry or in the spectral transparency windows when the anti-Hermitian part of the dielectric tensor is small. In the latter case the eigenvalue of the (almost) Hermitian Maxwellian tensor is real number, so the only imaginary contribution to integral (9.29) comes from zero eigenvalues related to the eigenmodes according to condition (3.33). Thus, it is the case of generation of the eigenmodes by a given current.

Let us derive the emission of the eigenmodes from Eq. (9.29) entirely neglecting the wave damping in the medium (while keeping the spatial dispersion). Since in a nonabsorbing media the Maxwellian tensor is a Hermitian one its eigenvalues $\lambda^{(i)}(\omega, \boldsymbol{k})$ are real. This implies that for any $\lambda^{(i)}(\omega, \boldsymbol{k}) \neq 0$ the integral in Eq. (9.29) is real as well, thus, its imaginary part (and, accordingly, the energy loss) is evanescent. The only imaginary contribution comes from the poles, where the eigenvalues $\lambda^{(i)}(\omega, \boldsymbol{k})$ vanish. Recall that the condition $\lambda^{(i)}(\omega, \boldsymbol{k}) = 0$ is just the dispersion law for the eigenmode with index i. Thus, we arrive at a familiar conclusion that in nonabsorbing media the energy loss of the current $\boldsymbol{j}_{\omega,\mathbf{k}}$ is entirely formed by excitation of the eigenmodes (including but not limited to the high-frequency electromagnetic waves capable of leaving the volume).

To account for the imaginary contribution to integral (9.29), we again introduce an infinitely small wave damping by adding small imaginary part to the refractive index: $n \to n + i\epsilon,\ \epsilon \to +0$, which yields

$$\lambda^{(i)}(\omega, \boldsymbol{k}) \to \lambda^{(i)}(ck/(n + i\epsilon), \boldsymbol{k}) \approx \lambda^{(i)}(\omega - i\gamma, \boldsymbol{k}) \approx \lambda^{(i)}(\omega, \boldsymbol{k}) - i\gamma \frac{\partial \lambda^{(i)}}{\partial \omega}.$$

Then, we use the Sokhotsky rule, Eq. (9.10):

$$\Im \frac{1}{\lambda^{(i)}(\omega - i\gamma, \boldsymbol{k})}\bigg|_{\gamma \to 0} \to +\pi \mathrm{sign} \left\{ \frac{\partial \lambda^{(i)}}{\partial \omega}\bigg|_{\omega = \omega_i^{\sigma}(\mathbf{k})} \right\} \delta(\lambda^{(i)}(\omega, \boldsymbol{k})). \tag{9.30}$$

Now we can take into account that when the dispersion law $\lambda^{(i)}(\omega, \boldsymbol{k}) = 0$ is fulfilled, the eigenvectors $\boldsymbol{b}^{(i)}(\omega, \boldsymbol{k})$, coincide with the polarization vectors of the given mode $\boldsymbol{e}^{(i)}(\omega, \boldsymbol{k})$, thus the current energy loss for eigenmode generation reads

$$W_{\mathbf{n},\omega} = -\frac{2(2\pi)^6}{\omega} \int k^2 \mathrm{d}k \sum_{i=1}^{3} \mid (\boldsymbol{e}^{(i)*}(\omega, \boldsymbol{k}) \cdot \boldsymbol{j}_{\omega,\mathbf{k}}) \mid^2 \mathrm{sign} \left\{ \frac{\partial \lambda^{(i)}}{\partial \omega}\bigg|_{\omega = \omega_i^{\sigma}(\mathbf{k})} \right\} \delta(\lambda^{(i)}(\omega, \boldsymbol{k})), \tag{9.31}$$

which is approximately valid in the case of finite small damping. Thus, we explicitly express the radiated energy as a sum over all possible eigenmodes of the medium. The number of these modes is generally unlimited because each dispersion equation $\lambda^{(i)}(\omega, \boldsymbol{k}) = 0$ can have many roots if the spatial dispersion is taken into account, so the actual number of terms in the sum can be larger than three.

To make practical use of Eq. (9.29) or Eq. (9.31) we have to explicitly compute the corresponding eigenvalues. Let us expand Eq. (3.15) with the Maxwellian tensor components; using its determinant in form (3.31) we write down the characteristic equation for the eigenvalues λ:

$$\lambda^3 - [\varepsilon_1 + \varepsilon_2 + \varepsilon_3 - 2n^2]\lambda^2 + [n^4 - (\varepsilon_1 + \varepsilon_2 + \varepsilon_3 + a)n^2 + \varepsilon_1\varepsilon_2 + \varepsilon_2\varepsilon_3 + \varepsilon_1\varepsilon_3 - g^2]\lambda - a(n^2 - n_1^2)(n^2 - n_2^2) = 0. \tag{9.32}$$

Here we consider the case of interest when dispersion law (3.33) is fulfilled for an eigenmode, say, $n^2 = n_1^2$. Then, the free term in Eq. (9.32) vanishes so λ can be taken out of the brackets and the cubic equation reduces to a quadratic one:

$$\lambda\Big[\lambda^2 - \left[\varepsilon_1 + \varepsilon_2 + \varepsilon_3 - 2n_1^2\right]\lambda + \left[n_1^4 - (\varepsilon_1 + \varepsilon_2 + \varepsilon_3 + a)n_1^2 + \varepsilon_1\varepsilon_2 + \varepsilon_2\varepsilon_3 + \varepsilon_1\varepsilon_3 - g^2\right]\Big] = 0, \tag{9.33}$$

which is easy to solve:

$$\lambda^{(1)} = 0, \tag{9.34}$$

$$\lambda^{(2,3)} = \frac{\varepsilon_1 + \varepsilon_2 + \varepsilon_3 - 2n_1^2 \pm \sqrt{\varepsilon_1^2 + \varepsilon_2^2 + \varepsilon_3^2 + 4g^2 - 2(\varepsilon_1\varepsilon_2 + \varepsilon_2\varepsilon_3 + \varepsilon_1\varepsilon_3) + 4an_1^2}}{2}. \tag{9.35}$$

Since according to Eq. (9.31) the emission is only produced when $\lambda = 0$, we are interested in $\lambda^{(1)}$, which must be calculated more accurately as $n^2 \to n_1^2$. Accordingly, let us rewrite Eq. (9.32) in the form

$$\lambda\Big[\lambda^2 - \left[\varepsilon_1 + \varepsilon_2 + \varepsilon_3 - 2n^2\right]\lambda + \left[n^4 - (\varepsilon_1 + \varepsilon_2 + \varepsilon_3 + a)n^2 + \varepsilon_1\varepsilon_2 + \varepsilon_2\varepsilon_3 + \varepsilon_1\varepsilon_3 - g^2\right]\Big] = a(n^2 - n_1^2)(n^2 - n_2^2). \tag{9.36}$$

The condition $\lambda \to 0$ allows adopting $\lambda = 0$ inside the square brackets in Eq. (9.36) so the evanescent eigenvalue $\lambda^{(1)}$ receives the form:

$$\lambda^{(1)} = \frac{a(n_1^2 - n_2^2)}{[n_1^4 - (\varepsilon_1 + \varepsilon_2 + \varepsilon_3 + a)n_1^2 + \varepsilon_1\varepsilon_2 + \varepsilon_2\varepsilon_3 + \varepsilon_1\varepsilon_3 - g^2]}(n^2 - n_1^2) = \frac{a(n_1^2 - n_2^2)}{\lambda^{(2)}\lambda^{(3)}}(n^2 - n_1^2), \tag{9.37}$$

i.e., $\lambda^{(1)}$ is proportional to the difference $(n^2 - n_1^2)$ with a non-unitary coefficient in a general case; the latter equality in Eq. (9.37) is written based on the Vieta's theorem applied to Eq. (9.33):

$$\lambda^{(2)}\lambda^{(3)} = [n_1^4 - (\varepsilon_1 + \varepsilon_2 + \varepsilon_3 + a)n_1^2 + \varepsilon_1\varepsilon_2 + \varepsilon_2\varepsilon_3 + \varepsilon_1\varepsilon_3 - g^2], \quad (9.38)$$

which means that finding the evanescent eigenvalue $\lambda^{(1)}$ does not require the other two eigenvalues; one only needs their product (9.38). Using the second equality in Eq. (3.34) we can conclude that for $\lambda^{(1)} = 0$,

$$\lambda^{(2)}\lambda^{(3)} = \Delta_{ii}^{(1)} = C^{(1)} \quad (9.39)$$

in full agreement with Eqs. (9.17) and (9.18). Note that explicit forms (9.35) and (9.37) allow straightforward confirmation that all required relationships (3.34) including Eq. (9.39) for the eigenvalues are fulfilled.

The second eigenvalue has a similar form:

$$\lambda^{(2)} = \frac{a(n_2^2 - n_1^2)}{\lambda^{(1)}\lambda^{(3)}}(n^2 - n_2^2),$$
$$\lambda^{(1)}\lambda^{(3)} = n_2^4 - (\varepsilon_1 + \varepsilon_2 + \varepsilon_3 + a)n_2^2 + \varepsilon_1\varepsilon_2 + \varepsilon_2\varepsilon_3 + \varepsilon_1\varepsilon_3 - g^2 = \Delta_{ii}^{(2)} = C^{(2)}. \quad (9.40)$$

Finally, the third eigenvalue arising for $a = 0$ corresponds to generation of longitudinal modes described above. As has been noted correct treatment of the longitudinal wave generation requires account of the spatial dispersion. When the spatial dispersion is discarded, only two quasitransverse wave modes can be generated. For this case from Eqs. (9.37) and (9.40) we find

$$\Im\frac{1}{\lambda^{(1)}} = \frac{\pi\omega\lambda^{(2)}\lambda^{(3)}}{2acn_1(n_1^2 - n_2^2)}\delta(k - \omega n_1/c), \qquad \Im\frac{1}{\lambda^{(2)}} = \frac{\pi\omega\lambda^{(1)}\lambda^{(3)}}{2acn_2(n_2^2 - n_1^2)}\delta(k - \omega n_2/c). \quad (9.41)$$

Then, Eqs. (9.29)–(9.31) yield the spectral and angular density of the quasitransverse wave emission:

$$W_{\mathbf{n},\omega} = \frac{(2\pi)^6\omega^2}{a(\omega,\boldsymbol{\kappa})c^3(n_2^2 - n_1^2)}[n_2\lambda^{(1)}\lambda^{(3)}|_{n=n_2}|(e_\mu^{(2)*}j_\mu)|^2 - n_1\lambda^{(2)}\lambda^{(3)}|_{n=n_1}|(e_\mu^{(1)*}j_\mu)|^2] \quad (9.42)$$

in full agreement with earlier derived Eq. (9.18) after taking into account Eq. (9.39), i.e., $C^{(1)} = \lambda^{(2)}\lambda^{(3)}|_{n=n_1}$ and $C^{(2)} = \lambda^{(1)}\lambda^{(3)}|_{n=n_2}$. We note that if the refractive indices of the anisotropic medium are both around unity then the factors

$$F_1 = \frac{\lambda^{(2)}\lambda^{(3)}|_{n=n_1}}{a(n_2^2 - n_1^2)}, \quad F_2 = \frac{\lambda^{(1)}\lambda^{(3)}|_{n=n_2}}{a(n_1^2 - n_2^2)} \quad (9.43)$$

go to one as well. The same happens in the vacuum and isotropic media. However, in the general case of the anisotropic or gyrotropic media the departure of these factors from the unity can be significant, which results in

a strong departure of the radiation intensity and polarization from the case of the isotropic medium. Physically, departure of these factors from the vacuum value (one) is related to the fact that the energy of the eigenmodes of a medium is composed of both electromagnetic energy and the energy of the plasma particles involved in the wave motion.

Let us finally rewrite radiation intensity (9.42) in a more compact form explicitly using introduced anisotropy factors (9.43):

$$W_{\mathbf{n},\omega} = \frac{(2\pi)^6\omega^2}{c^3}\left[n_1F_1|(e_\mu^{(1)*}j_\mu)|^2 + n_2F_2|(e_\mu^{(2)*}j_\mu)|^2\right]. \tag{9.44}$$

In the general case when the spatial dispersion is included we have to add generation of the longitudinal waves (l) and all new quasitransverse waves (σ) appeared due to the spatial dispersion

$$W_{\mathbf{n},\omega} = \sum_\sigma \mathcal{E}^\sigma_{\mathbf{n},\omega} + \mathcal{E}^l_{\mathbf{n},\omega}, \tag{9.45}$$

where

$$\mathcal{E}^\sigma_{\mathbf{n},\omega} = (2\pi)^6\frac{\omega^2 n_\sigma(\omega)}{c^3}F_\sigma|(\boldsymbol{e}^*_\sigma\cdot\boldsymbol{j}_{\omega,\mathbf{k}})|^2, \tag{9.46}$$

$$\mathcal{E}^l_{\mathbf{n},\omega} = 2\frac{(2\pi)^6}{\omega}\int \mathrm{d}k \mid (\boldsymbol{k}\cdot\boldsymbol{j}_{\omega,\mathbf{k}}) \mid^2 \delta(\varepsilon^{l'}(\omega,\boldsymbol{k})), \tag{9.47}$$

$\varepsilon^{l'}(\omega,\boldsymbol{k}) = \Re\varepsilon^l(\omega,\boldsymbol{k})$ is the real part of the longitudinal dielectric permittivity. Since we have integrated over dk with the use of δ-functions in the quasitransverse terms, then ω and $\boldsymbol{k}$ are linked in Eq. (9.46), by the corresponding dispersion law $\omega = \omega_\sigma(\boldsymbol{k})$. In contrast, in longitudinal term (9.47) the δ-function is kept, although this integration can always be performed by employing relation (9.27) in which the summation is performed over all possible longitudinal waves of the medium. The number of these waves can be rather large (in particular, infinitely large in case of the hot magnetized plasma) and some of them have a very weak dependence $\omega(\boldsymbol{k})$. This is why it is typically more convenient to first integrate over the frequency, rather than over the wave number, and consider distribution of the radiated energy over k, rather than over ω.

We conclude that in an anisotropic dispersive medium with a weak wave damping, the energy radiated by a given electric current into any given eigenmode of the medium is described by Eqs. (9.46) and (9.47) with the corresponding refraction indices and polarization vectors. In the case of the magnetized plasma, the dispersion curves consist of a number of isolated branches (see Chap. 3) separated by discontinuities around the electron or ion resonances. The low frequency modes are often considered as separate modes (Alfvén, fast, whistler, Z- mode etc); emission of all those modes is described by the derived equations without limitation.

Then, we have to note that even though the anisotropic factors go to one in the isotropic medium and, accordingly, the radiation intensities of the

two normal modes are defined by two terms in Eq. (9.44) with the same refraction indices, this does not imply an unpolarized radiation. In fact, the polarization can be very strong (up to 100% as in case of Vavilov–Cherenkov radiation (VCR), see Sect. 9.2.1) depending on relative directions of the electric current vectors, wave vector, and other vectors essential for the problem under study.

At the high frequencies, where no longitudinal waves are available and any difference between the normal modes can be ignored, we can add up the two contribution using

$$\overline{e_\alpha e_\beta} = \frac{1}{2}(\delta_{\alpha\beta} - n_\alpha n_\beta) \tag{9.48}$$

to find the total (in all polarizations) radiation intensity generated by the current at a given frequency in a given direction

$$\mathcal{E}_{\mathbf{n},\omega} = (2\pi)^6 \frac{\omega^2 n(\omega)}{c^3} |(\boldsymbol{n} \times \boldsymbol{j}_{\omega,\mathbf{k}})|^2. \tag{9.49}$$

This equation resembles (being only by the factor $n(\omega) \sim 1$ different from) Eq. (9.22) for the wave radiation in the vacuum. Nevertheless, these two equations are fundamentally different from each other. Indeed, here the variables ω and $\boldsymbol{k}$, defining the Fourier component of the current $\boldsymbol{j}_{\omega,\mathbf{k}}$, are linked by the plasma dispersion law $\omega = \omega(\boldsymbol{k})$ rather than the vacuum relation $\omega = kc$, which modifies the emission in the medium compared with the corresponding emission in the vacuum. Then, the given external current stimulates a plasma current, which, in its turn, is a source of additional electromagnetic emission. As a result, the radiative processes in a medium are much more rich and diverse than in the vacuum.

We note that the equations obtained are also valid for radiation by a single charged particle. Indeed, the electric current produced by a single particle with charge Q, moving along a given path $\boldsymbol{r}(t)$, is

$$\boldsymbol{j}(\boldsymbol{r}, t) = Q\boldsymbol{v}(t)\delta(\boldsymbol{r} - \boldsymbol{r}(t)), \tag{9.50}$$

whose Fourier component has the form

$$\boldsymbol{j}_{\omega,\mathbf{k}} = Q \int \boldsymbol{v}(t) e^{i(\omega t - \mathbf{k}\boldsymbol{r}(t))} \frac{\mathrm{d}t}{(2\pi)^4}. \tag{9.51}$$

Substitution of Eq. (9.51) into equations for the radiated energy yields eventually the radiation produced by a single charged particle; see Problem 9.1.

9.2 Emission by a Rectilinearly Moving Particle

The simplest kind of the particle motion is a rectilinear trajectory with a constant velocity. Such a particle can produce electromagnetic emission if some additional conditions are met. One possibility is a particle moving strictly rectilinearly without any acceleration. The other possibility is a case of weak acceleration, when the particle velocity can be considered constant and the path is a straight line, while the nonzero acceleration can be taken into account within the perturbation theory. Remarkably, in both of these cases, a radiation can be produced and both of them allow finding general solutions applicable for any media and any kind of weak acceleration. Both cases are considered below.

9.2.1 Vavilov–Cherenkov Radiation

Let us consider radiation arising as a charged particle moves rectilinearly in a medium with the refractive index exceeding one. Adopt for simplicity the medium to be isotropic so the two refractive indices are equal to each other: $n_{\sigma=1}(\omega) = n_{\sigma=-1}(\omega) = n(\omega)$.

The electric current produced by this charge is

$$\boldsymbol{j}(\boldsymbol{r}, t) = Q\boldsymbol{v}\delta(\boldsymbol{r} - \boldsymbol{v}t), \tag{9.52}$$

whose Fourier transform is straightforward to find by direct integration:

$$\boldsymbol{j}_{\omega,\mathbf{k}} = \frac{Q\boldsymbol{v}}{(2\pi)^3}\delta(\omega - \boldsymbol{k}\boldsymbol{v}). \tag{9.53}$$

As the polarization vectors of the eigenmodes of the isotropic medium are not uniquely specified, we consider emission of two orthogonal linearly polarized modes in a given direction; in one of the modes the electric vector belongs to the plane defined by vectors $\boldsymbol{k}$ and $\boldsymbol{v}$; in the other one the electric vector is transverse to this plane. Apparently, the second wave mode will not be emitted in this direction because the dot product $(\boldsymbol{e}_\sigma \cdot \boldsymbol{v})$ entering Eq. (9.46) vanishes.

Thus, the generated emission is 100% linearly polarized with the electric vector belonging the $(\boldsymbol{k}, \boldsymbol{v})$ plane. Substitution of Eq. (9.53) into Eq. (9.46) yields the spectral and angular distribution of the VCR:

$$\mathcal{E}_{\mathbf{n},\omega} = \frac{Q^2\omega^2 n(\omega)}{c^3} v^2 \sin^2\theta\,\delta^2(\omega - \boldsymbol{k}\boldsymbol{v}). \tag{9.54}$$

The infinite radiated energy contained in Eq. (9.54) due to squared δ-function is just a math formulation of the fact that a particle forced to move rectilinearly an infinitely long time will generate proportionally infinite amount

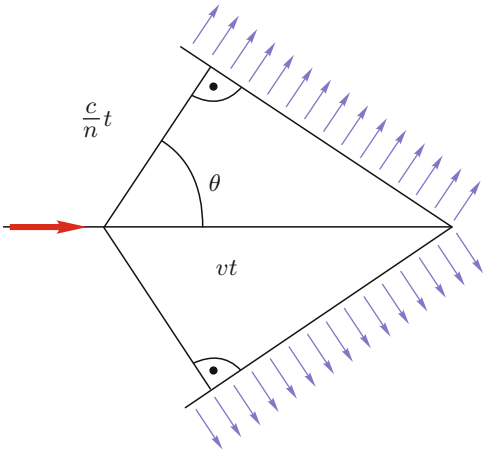

Figure 9.1: VCR kinematics.

of energy. To obtain a more meaningful measure of the energy produced *per unit time* we use the following presentation of the squared δ-function:

$$\delta^2(\omega - \boldsymbol{kv}) = \frac{T}{2\pi}\delta(\omega - \boldsymbol{kv}), \tag{9.55}$$

where T is the total time of emission. Now, we can divide Eq. (9.54) by T and take into account $\boldsymbol{kv} = \omega\frac{v}{c}n(\omega)\cos\theta$ to obtain the spectral and energy distribution of VCR per unit time:

$$I_{\mathbf{n},\omega} = \frac{Q^2\omega n(\omega)v^2}{2\pi c^3}\sin^2\theta\ \delta\left(1 - \frac{v}{c}n(\omega)\cos\theta\right). \tag{9.56}$$

Apparently, radiation (9.56) has a nonzero value for the only directions satisfying the **VCR condition**:

$$\cos\theta = \frac{c}{vn(\omega)}. \tag{9.57}$$

This means that all the existing particles that move "sub-luminally," $v < c$, can only produce the VCR at frequencies where $n(\omega) > 1$; in particular, no VCR is possible in the vacuum (though, it would be possible for hypothetical super-luminal particles). Equation (9.56) implies that the VCR directivity pattern at a given frequency is an infinitely narrow open cone whose surface is defined by Eq. (9.57) (Fig. 9.1).

Then, integrating Eq. (9.56) over full solid angle $\mathrm{d}\Omega = \mathrm{d}\cos\theta\mathrm{d}\varphi$ we find the radiation spectral intensity

$$I_\omega = \frac{Q^2\omega v}{c^2}\left(1 - \frac{c^2}{v^2n^2(\omega)}\right)\Theta\left(\frac{v}{c}n(\omega) - 1\right). \tag{9.58}$$

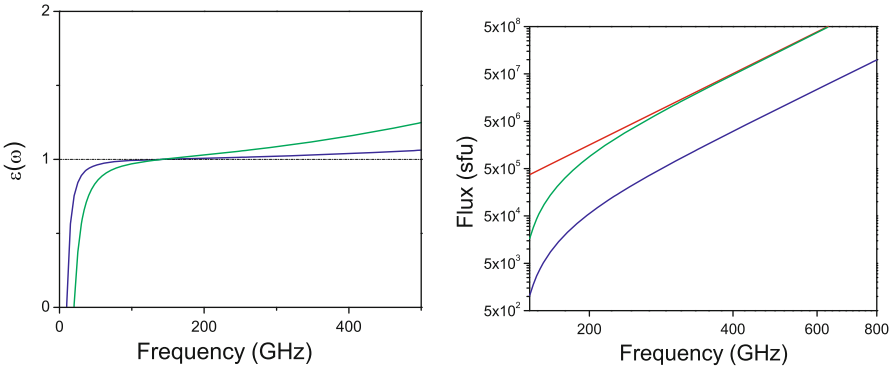

Figure 9.2: **(a)** A model of plasma dielectric permittivity with molecular line contribution included; **(b)** Vavilov–Cherenkov radiation produced by fast electrons with a power-law distribution over the velocity—*blue and green curves* corresponding to the *blue and green models* of the dielectric permittivity in the *left panel*, respectively; the *red curve* is for $\varepsilon(\omega) = 1 + \omega^2/\omega_0^2$, i.e., without standard plasma contribution (Fleishman and Kontar 2010). Reproduced by permission of the AAS.

Eventually, the full radiated VCR energy per unit time is specified by integration of Eq. (9.58) over all frequencies, which depends on the specific spectral shape of the function $n(\omega)$ in a given medium.

9.2.2 Vavilov–Cherenkov Radiation from Solar Chromosphere

We see that the VCR is produced by any charged particle moving faster than the corresponding speed of light in the medium. It, therefore, seems irrelevant to the astrophysical objects since in a fully ionized plasma the high-frequency dielectric permittivity is less than unity, $\varepsilon(\omega) \lesssim 1$. Therefore, the phase velocity of electromagnetic waves $c/\sqrt{\varepsilon(\omega)}$ is larger than the speed of light, c, and the VCR does not occur. However, there are partly or weakly ionized astrophysical plasmas (molecular clouds, stellar atmospheres, planetary ionospheres, etc.) in which contributions from neutrals can make the VCR possible in some favorable spectral windows.

One of many examples of such partly ionized plasmas is the solar chromosphere; there are numerous atoms and molecules whose quantum transitions can make positive contribution to the dielectric permittivity and, accordingly, make the VCR possible at certain frequencies. A charged particle with velocity v emits VCR in the medium, where its dielectric permittivity $\varepsilon(\omega)$ is such that $v > c/\sqrt{\varepsilon(\omega)}$. The dielectric permittivity of normal gases is only slightly more than unity in the optical range [e.g., Hydrogen gas has $(\varepsilon - 1) \sim 2 \times 10^{-4}$], so only highly relativistic particles with $\gamma > 50$ can emit. The situation is however very different in other frequency ranges, near

transition frequencies of atoms or molecules: $\varepsilon(\omega)$ goes up and down being considerably larger than one at certain frequency windows, which allows even sub-relativistic electrons to emit VCR at favorable conditions.

Each atomic or molecular quantum transition makes a contribution to the dielectric permittivity of the form of $\delta\varepsilon_{nm}(\omega) = \frac{4\pi n_e e^2}{m_e} \frac{S_{nm}}{(\omega_{nm}^2 - \omega^2) + i\Gamma_{nm}\omega}$, where S_{nm} is the oscillator strength of the transition, ω_{nm} is the transition frequency, and Γ_{nm} is the transition decay constant. The resulting dielectric permittivity accounting for plasma (free electrons) and molecular contributions is $\varepsilon(\omega) = 1 - \omega_{\rm pe}^2/\omega^2 + \sum \delta\varepsilon_{nm}$. The exact spectroscopic permittivity depends on the chemical composition of the chromosphere with the sum over all excitation states of corresponding molecules, and, so, complicated and not unique. Here, to perform an order of magnitude estimate, we assume that there are many atomic/molecular transitions capable of making a contribution to the dielectric properties of gas. Then, the energy level populations over the rotational levels of chromospheric molecules can be assumed to have a Boltzmann distribution with the gas temperature T; therefore population densities will have maxima at energy levels above the THz range increasing to about $k_{\rm B}T$. Thus, we adopt the mean molecular contribution to the dielectric permittivity to have a *model* form ω^2/ω_0^2, where ω_0 is an unknown constant, which is a parameter of the model.

To estimate the Cherenkov spectrum from an ensemble of accelerated electrons precipitating from coronal part of the flare volume onto the chromosphere (Fleishman and Kontar 2010), we adopt a spectrum of the electrons described by a power law over electron velocity $n_e(v) = AN_0 v_0^{\beta-1}/v^\beta$, $v < c$ (it is more convenient in this case than a more familiar power law over energy since the VCR intensity depends on the velocity rather than on energy), where N_0 is the total number of electrons with velocity above minimum velocity v_0, β is the spectral index, and A is a dimensionless normalization constant of order of unity, the VCR yields flux at Earth:

$$F_f = \frac{10^{19}}{4\pi\mathcal{R}^2} \frac{(2\pi)^2 A N_0 e^2 f v_0^{\beta-1}}{c^\beta} \left[\frac{2\varepsilon^{(\beta-2)/2}}{\beta(\beta-2)} + \frac{1}{\beta\varepsilon} - \frac{1}{\beta-2} \right] \text{(sfu)}. \quad (9.59)$$

We emphasize that when the flare-accelerated electrons are present, they produce VCR at all frequency windows (including IR, viz, and UV bands) where the dielectric permittivity is (even marginally) above unity, giving rise to a radiation spectrum raising with frequency for (mean) dielectric permittivity increasing with frequency and vice versa.

Fig. 9.2a displays the model dielectric permittivity rising with frequency as described, while Fig. 9.2b shows the corresponding Cherenkov spectra. One can see that the standard plasma contribution to the dielectric permittivity dominates below roughly 100 GHz; thus, the VCR is only possible at higher frequencies, $f > 100$ GHz. The spectrum shape and the flux density level allow this emission to be easily detected in observations for typical numbers

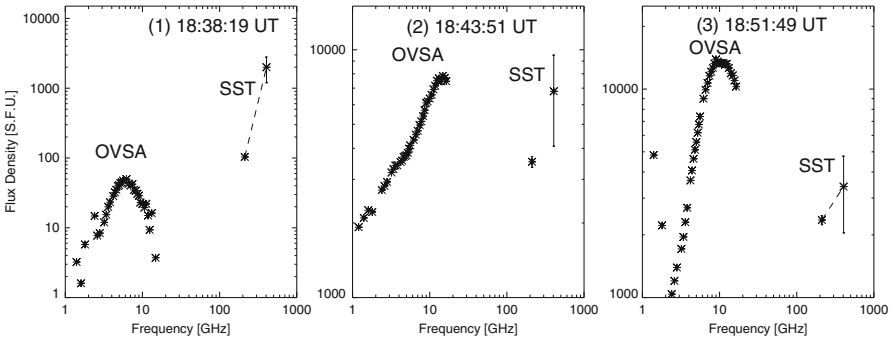

Figure 9.3: Decimeter to submillimeter spectra of a strong solar flare occurred on December 06, 2006, around 18:40 UT, at three phases: precursor, impulsive, and decay phases obtained by OVSA in the microwave range and SST at sub-THz range; from Kaufmann et al. (2009). Presence of a distinct sub-THz component, presumably produced by the VCR mechanism at solar chromosphere, is evident.

of flare-accelerated electrons. The predicted flux density, being up to $\sim 5 \times 10^7$ sfu at 400 GHz, is much larger than the strongest radio bursts recorded from flares, which is good as this allows a competing VCR even from lower number of radiating electrons, for unfavorable viewing angles, or/and when chromospheric absorption is enhanced.

The sub-THz radiation from solar flares has only recently been observed from a few large events, at a small number of frequencies. The available at the time or writing observational tools are unable to measure polarization and are clearly insufficient to provide detailed spectral and positional information about the sub-THz bursts.

The available observations suggest that, on top of quiet Sun emission, at least two kinds of sub-THz emission can be produced. The first kind looks like a natural extension of the microwave spectrum to higher frequencies and so can reasonably be interpreted as synchrotron radiation (see Sect. 9.4), from accelerated electrons, which are also responsible for microwave and hard X-ray emission. The second kind looks like a distinct spectral component rising with frequency in the sub-THz range in contrast to the microwave spectrum, which falls with frequency, Fig. 9.3. The main observational characteristics of this component are the following: relatively large radiation peak flux of the order of 10^4 sfu; radiation spectrum rising with frequency $F(f) \propto f^{\delta}$; spectral index varying with time within $\delta \sim 1$–6; sub-THz component can display a sub-second time variability with the modulation about 5%; the source size is believed to be less than $20''$.

The VCR from compact sources located at the chromospheric level, Fig. 9.2, is likely to be responsible for this distinct rising with frequency sub-THz component of large solar flares: it produces a very large radiation flux, while the spectral slope does not have any fundamental constrain, so can cover all the observed range from 1 to 6. Given that the emission is from

compact footpoints $<10''$, where energetic particles interact with the chromosphere in a typical flare, we conclude that the VCR is fully consistent with the observations of the rising sub-THz flare component. The time variability requires corresponding fluctuations of the electron distribution function, similar to sub-second variations of microwave GS or HXR radiations.

In contrast, models based on other emission mechanisms (see below this chapter) proposed so far to account for the sub-THz component, including thermal free–free emission or gyro emission from flare-accelerated electrons, suffer from a number of shortcomings; thus, none of them is readily consistent with the full list of the sub-THz component properties and/or with available context observations at other wavelength. We emphasize a high value of the VCR diagnostics potential: since its spectrum depends on the dielectric permittivity of the chromosphere in a straightforward way, the sub-THz emission represents a sensitive tool to measure the chromospheric dielectric permittivity and so chromosphere atomic and molecular composition and the corresponding excitation states.

9.2.3 Perturbation Theory for Radiation

Assuming the departure of the particle motion from the rectilinear one is somewhat small we adopt the particle velocity to be constant, while the acceleration of the particle due to an external field effect is accounted by the perturbation theory (Fleishman 2008). It is convenient here to start from well-known expression for the Fourier component of the emission field in the wave zone (Landau and Lifshitz 1971):

$$\boldsymbol{E}_{\omega}=\frac{Q}{2\pi c^2 R}\frac{e^{ikR}}{\left(1-\frac{\boldsymbol{nv}}{c}\sqrt{\varepsilon(\omega)}\right)^2}\int\limits_{-\infty}^{\infty}\left[\boldsymbol{n}\times\left[\left(\boldsymbol{n}-\frac{\boldsymbol{v}}{c}\right)\times\boldsymbol{w}(t)\right]\right]e^{i\omega t\left(1-\frac{\boldsymbol{nv}}{c}\sqrt{\varepsilon(\omega)}\right)}\mathrm{d}t, \tag{9.60}$$

where R is the distance between the source and observer, $\boldsymbol{n}$ is the unit vector along the wave vector, $\varepsilon(\omega)$ is the dielectric permittivity of the plasma (adopted here isotropic for simplicity; otherwise, one of two refractive indices must be used instead) and $\boldsymbol{w}(t)$ is the particle acceleration due to external field. Introducing a parameter with the dimension of frequency

$$\omega'=\omega\left(1-\frac{\boldsymbol{nv}}{c}\sqrt{\varepsilon(\omega)}\right) \tag{9.61}$$

and the corresponding Fourier component of the acceleration

$$\boldsymbol{w}_{\omega'}=\int\limits_{-\infty}^{\infty}\boldsymbol{w}(t)e^{i\omega' t}\frac{\mathrm{d}t}{2\pi}, \tag{9.62}$$

we obtain

$$\boldsymbol{E}_{\omega}=\frac{Q}{c^2}\frac{e^{ikR_0}}{R_0}\left(\frac{\omega}{\omega'}\right)^2\left[\boldsymbol{n}\times\left[\left(\boldsymbol{n}-\frac{\boldsymbol{v}}{c}\right)\times\boldsymbol{w}_{\omega'}\right]\right]. \tag{9.63}$$

Then, the radiation intensity in a given direction at a given frequency, i.e., the Poynting flux (9.23) via a distant closed surface in the Fourier representation

$$\mathcal{E}_{\mathbf{n},\omega} = cR_0^2 \mid \boldsymbol{E}_\omega \mid^2 \tag{9.64}$$

takes the form

$$\mathcal{E}_{\mathbf{n},\omega} = \frac{Q^2}{c^3}\left(\frac{\omega}{\omega'}\right)^4 \left|\left[\boldsymbol{n}\times\left[\left(\boldsymbol{n}-\frac{\boldsymbol{v}}{c}\right)\times\boldsymbol{w}_{\omega'}\right]\right]\right|^2. \tag{9.65}$$

Equation (9.65) is rather general; it is valid for particles with arbitrary energy, both relativistic and nonrelativistic.

In particular, for the nonrelativistic case we can take advantage of $v/c \ll 1$ and make expansion of Eq. (9.65) over this small parameter. The zeroth order term is convenient to display via the dipole moment of the system of emitting charges, $\boldsymbol{d} = \sum\limits_Q Q\boldsymbol{r}_Q$. Adopting $v/c \to 0$ and noting that in this case $\omega' \approx \omega$ and $Q\boldsymbol{w} = \ddot{\boldsymbol{d}}$, we find

$$\mathcal{E}_{\mathbf{n},\omega} = \frac{\sqrt{\varepsilon}}{c^3}\left|\left[\boldsymbol{n}\times\ddot{\boldsymbol{d}}_\omega\right]\right|^2, \tag{9.66}$$

while the first-order terms result in a quadruple and magneto-dipole radiation; the latter can be calculated by Eq. (9.66) where the electric dipole moment must be replaced by the magnetic moment $\boldsymbol{m}_\omega$.

In the ultrarelativistic case Eq. (9.65) can further be simplified by taking into account strong directivity of the emission along the particle velocity, i.e., smallness of the angle θ between the particle velocity $\boldsymbol{v}$ and the direction of the emitted waves $\boldsymbol{n}$. Let us introduce a 2D vector $\boldsymbol{\theta}$, transverse to $\boldsymbol{n}$, whose absolute value equals to the angle between $\boldsymbol{v}$ and $\boldsymbol{n}$, defined as

$$\frac{\boldsymbol{v}}{v} = \boldsymbol{n}\left(1-\frac{\theta^2}{2}\right)+\boldsymbol{\theta}. \tag{9.67}$$

Then, present the acceleration vector $\boldsymbol{w}_{\omega'}$ as a sum of two components: the parallel ($\boldsymbol{w}_{\omega'\parallel}$) and perpendicular ($\boldsymbol{w}_{\omega'\perp}$) to the velocity vector:

$$\boldsymbol{w}_{\omega'} = \boldsymbol{w}_{\omega'\parallel} + \boldsymbol{w}_{\omega'\perp} \tag{9.68}$$

Substitution of Eqs. (9.67) and (9.68) into Eq. (9.65) gives rise to the following expression for the spectral and angular distribution of the radiation intensity:

$$\mathcal{E}_{\mathbf{n},\omega} = \frac{Q^2}{c^3}\left(\frac{\omega}{\omega'}\right)^4 \left|\left[(\boldsymbol{w}_{\omega'\perp}\boldsymbol{\theta})\,\boldsymbol{\theta} - \frac{\widetilde{\omega}}{\omega}\boldsymbol{w}_{\omega'\perp} - \boldsymbol{\theta}\frac{(\boldsymbol{v}\boldsymbol{w}_{\omega'\parallel})}{c}\right]\right|^2, \tag{9.69}$$

where $\widetilde{\omega}/\omega = (1-\boldsymbol{v}\boldsymbol{n}/c) \approx (1/2)(\gamma^{-2}+\theta^2)$.

In most cases, contribution of the parallel acceleration is small (by a factor of γ^2) due to a large difference between the so-called "longitudinal" and "transverse" masses of a relativistic particle and can safely be discarded. We, however, keep this contribution, having in mind those situations when the transverse acceleration is small or evanescent.

Apparently, the contributions related to $\boldsymbol{w}_{\omega'\parallel}$ and $\boldsymbol{w}_{\omega'\perp}$ in Eq. (9.69) are coupled in a general case. Nevertheless, they decouple if the acceleration vector does not depend on the velocity direction $\boldsymbol{\theta}$. Likewise, they decouple after averaging Eq. (9.69) over the azimuth angle of the vector $\boldsymbol{\theta}$. This averaging yields:

$$\mathrm{d}\bar{\mathcal{E}}_{\mathbf{n},\omega} = \frac{1}{2\pi}\int_0^{2\pi} \mathcal{E}_{\mathbf{n},\omega}\mathrm{d}\phi = \mathcal{E}^{\perp}_{\mathbf{n},\omega} + \mathcal{E}^{\parallel}_{\mathbf{n},\omega}, \tag{9.70}$$

where

$$\mathcal{E}^{\perp}_{\mathbf{n},\omega} = \frac{Q^2}{c^3}\left(\frac{\omega}{\omega'}\right)^2 |\boldsymbol{w}_{\omega'\perp}|^2 \left[1 - \frac{\omega}{\omega'}\left(\gamma^{-2} + \frac{\omega_{\mathrm{pe}}^2}{\omega^2}\right) + \frac{\omega^2}{4\omega'^2}\left(\gamma^{-2} + \frac{\omega_{\mathrm{pe}}^2}{\omega^2}\right)^2 + \frac{\omega^2}{4\omega'^2\gamma^4}\right], \tag{9.71}$$

$$\mathcal{E}^{\parallel}_{\mathbf{n},\omega} = \frac{2Q^2}{c^3}\left(\frac{\omega}{\omega'}\right)^3 \left|\boldsymbol{w}_{\omega'\parallel}\right|^2 \left[1 - \frac{\omega}{2\omega'}\left(\gamma^{-2} + \frac{\omega_{\mathrm{pe}}^2}{\omega^2}\right)\right]. \tag{9.72}$$

Equations (9.71) and (9.72) adopt a simple plasma formula for the dielectric permittivity $\varepsilon(\omega) = 1 - \frac{\omega_{\mathrm{pe}}^2}{\omega^2}$ that is always valid at high frequencies. Thus, the derived formulae solve the problem of radiation by a rectilinearly moving particle under condition of known weak acceleration, which has yet to be determined.

To do so we write equation of relativistic particle motion for components parallel and transverse to the initial particle velocity:

$$M\gamma\boldsymbol{w}_{\parallel} + M\gamma^3(\boldsymbol{v}_{\parallel}/c^2)(\boldsymbol{v}_{\parallel}\cdot\boldsymbol{w}_{\parallel} + \boldsymbol{v}_{\perp}\cdot\boldsymbol{w}_{\perp}) = \boldsymbol{F}_{\parallel}, \tag{9.73}$$

$$M\gamma\boldsymbol{w}_{\perp} + M\gamma^3(\boldsymbol{v}_{\perp}/c^2)(\boldsymbol{v}_{\parallel}\cdot\boldsymbol{w}_{\parallel} + \boldsymbol{v}_{\perp}\cdot\boldsymbol{w}_{\perp}) = \boldsymbol{F}_{\perp}. \tag{9.74}$$

As we consider the case of constant velocity, $v_{\perp} = 0$, $v \approx v_{\parallel} \approx v_0 \approx c$, and $\gamma = \sqrt{1 - v_0^2/c^2} \gg 1$, the second term in the lhs of Eq. (9.74) vanishes; while the first term in the lhs of Eq. (9.73) can be discarded for highly relativistic particles, which yields

$$\boldsymbol{w}_{\perp} = \frac{\boldsymbol{F}_{\perp}}{M\gamma}; \qquad \boldsymbol{w}_{\parallel} = \frac{\boldsymbol{F}_{\parallel}}{M\gamma^3} \tag{9.75}$$

where $\boldsymbol{F}_{\parallel}$ and $\boldsymbol{F}_{\perp}$ are the longitudinal and transverse components of the external force acting on the particle; then for $\boldsymbol{F}_{\parallel} \sim \boldsymbol{F}_{\perp}$ at $\omega \sim \omega'\gamma^2$ we have

$$\mathcal{E}^{\parallel}_{\mathbf{n},\omega} \sim \frac{\mathcal{E}^{\perp}_{\mathbf{n},\omega}}{\gamma^2}, \tag{9.76}$$

which justifies that the contribution $\mathcal{E}^{\parallel}_{\mathbf{n},\omega}$ can in many cases be discarded. Note that the radiation related to the longitudinal acceleration is only relevant to the case of external electric field; in the magnetic field the acceleration is always transverse to the particle velocity vector.

To transform the solution obtained to a practical form we have yet to express the particle acceleration components in terms of the external electromagnetic field, supposed to be a given function of the coordinates and time. Note that in a general case the field can contain both regular and random components so the square of the acceleration modulus $|\boldsymbol{w}_{\omega'\perp}|^2$ includes both regular and random components as well. To find a stationary radiation level we have to average $|\boldsymbol{w}_{\omega'\perp}|^2$ over the random field distribution.

Let us adopt that the random Lorentz force $\boldsymbol{F}(\boldsymbol{r},t)$, composed of both electric and magnetic components, can be presented via the Fourier transform over ω and $\boldsymbol{k}$:

$$\boldsymbol{F}(\boldsymbol{r},t)=\int e^{-i(\omega t-\mathbf{kr})}\boldsymbol{F}_{\omega,\mathbf{k}}\mathrm{d}\omega\mathrm{d}\boldsymbol{k}. \tag{9.77}$$

The dependence of the magnetic Lorentz force on the particle velocity does not complicate the problem because within the perturbation theory $\boldsymbol{v}=$ const. Force (9.77) is a *global* field that varies in both space and time. In contrast, the particle acceleration is driven by a *local* value of these field present in the very place where the particle is located instantly. Finding this local force as a function of time is a highly complicated task. However, within the perturbation theory this problem simplifies greatly because the particle velocity is adopted constant and the trajectory needed to be substituted into Eq. (9.77) takes an especially simple form $\boldsymbol{r}=\boldsymbol{r}_0+\boldsymbol{v}t$; thus

$$\boldsymbol{F}(\boldsymbol{r}_0+\boldsymbol{v}t,t)=\int e^{-i(\omega t-\mathbf{kr}_0-\mathbf{kv}t)}\boldsymbol{F}_{\omega,\mathbf{k}}\mathrm{d}\omega\mathrm{d}\boldsymbol{k}. \tag{9.78}$$

This expression depends only on time (rather than on $\boldsymbol{r}$), so the Fourier component $\boldsymbol{F}_{\omega'}$ defining the acceleration $\boldsymbol{w}_{\omega'}=\boldsymbol{F}_{\omega'}/M\gamma$ is determined by a Fourier transform of Eq. (9.78) over time:

$$\boldsymbol{F}_{\omega'}=\int\frac{\mathrm{d}t}{2\pi}e^{i\omega' t}\boldsymbol{F}(\boldsymbol{r}_0+\boldsymbol{v}t,t)=\int\mathrm{d}\omega\mathrm{d}\boldsymbol{k}\delta(\omega'-\omega+\boldsymbol{kv})\boldsymbol{F}_{\omega,\mathbf{k}}e^{i\mathbf{kr}_0}. \tag{9.79}$$

Accordingly, the square modulus of the force $|\,\boldsymbol{F}_{\omega'}\,|^2$ receives the form

$$|\,\boldsymbol{F}_{\omega'}\,|^2=\int\mathrm{d}\omega\mathrm{d}\boldsymbol{k}\mathrm{d}\omega_1\mathrm{d}\boldsymbol{k}_1e^{i(\mathbf{k}-\mathbf{k}_1)\mathbf{r}_0}\delta(\omega'-\omega+\boldsymbol{kv})\delta(\omega'-\omega_1+\boldsymbol{k}_1\boldsymbol{v})\boldsymbol{F}_{\omega,\mathbf{k}}\boldsymbol{F}^*_{\omega_1,\mathbf{k}_1}. \tag{9.80}$$

The force square modulus $|\,\boldsymbol{F}_{\omega'}\,|^2$ depends according to Eq. (9.80) on the initial position of the fast particle $\boldsymbol{r}_0$; thus, value (9.80) fluctuates although its mean value is nonzero (even when the entire field $\boldsymbol{F}_{\omega,\mathbf{k}}$ is a complex function with zero mean). As has been said, the stationary emission level is specified by the averaging of the value $\langle|\,\boldsymbol{F}_{\omega'}\,|^2\rangle$ in Eq. (9.80), which is easy to perform assuming that all the initial positions of the radiating particle are equally probable. In this case noting that the exponent $\exp(i(\boldsymbol{k}-\boldsymbol{k}_1)\boldsymbol{r}_0)$ oscillates strongly for $\boldsymbol{k}\neq\boldsymbol{k}_1$, we find

$$\frac{1}{V}\int e^{i(\mathbf{k}-\mathbf{k}_1)\mathbf{r}_0}\mathrm{d}\boldsymbol{r}_0=\frac{(2\pi)^3}{V}\delta(\boldsymbol{k}-\boldsymbol{k}_1), \tag{9.81}$$

where V is the source volume. Then, for $\langle \mid \boldsymbol{F}_{\omega'} \mid^2 \rangle$, we obtain

$$\langle \mid \boldsymbol{F}_{\omega'} \mid^2 \rangle = \frac{(2\pi)^3}{V} \int \mathrm{d}\omega \mathrm{d}\boldsymbol{k} \delta(\omega' - \omega + \boldsymbol{k}\boldsymbol{v}) \mid \boldsymbol{F}_{\omega,\mathbf{k}} \mid^2 . \tag{9.82}$$

Finally, the averaged value of the square of the particle acceleration Fourier component receives the form

$$\mid \boldsymbol{w}_{\omega'\perp} \mid^2 = \frac{(2\pi)^3}{M^2\gamma^2 V} \int \mathrm{d}\omega \mathrm{d}\boldsymbol{k} \delta(\omega' - \omega + \boldsymbol{k}\boldsymbol{v}) \mid \boldsymbol{F}_{\omega,\mathbf{k}\perp} \mid^2, \tag{9.83}$$

which uniquely links the *spatiotemporal* Fourier component of the Lorentz force (rhs) and the *temporal* Fourier component of the particle acceleration (lhs). Substituting Eq. (9.83) into Eq. (9.71) and using the dummy arguments $(q_0, \boldsymbol{q})$ for $(\omega, \boldsymbol{k})$, we eventually obtain the energy emitted over the *entire time*[1] of the particle motion per unit solid angle Ω per unit frequency ω

$$\mathcal{E}^{\perp}_{\mathbf{n},\omega} = \frac{(2\pi)^3 Q^2}{M^2 c^3 \gamma^2 V} \left(\frac{\omega}{\omega'}\right)^2 \left[1 - \frac{\omega}{\omega'\gamma_*^2} + \frac{\omega^2}{2\omega'^2\gamma_{**}^4}\right] \int \mathrm{d}q_0 \mathrm{d}\boldsymbol{q} \delta(\omega' - q_0 + \boldsymbol{q}\boldsymbol{v}) \mid \boldsymbol{F}_{q_0,\mathbf{q}\perp} \mid^2, \tag{9.84}$$

where

$$\gamma_*^{-2} = \gamma^{-2} + \omega_{\mathrm{pe}}^2/\omega^2; \qquad \gamma_{**}^{-4} = \frac{1}{2}\left(\gamma^{-2} + \frac{\omega_{\mathrm{pe}}^2}{\omega^2}\right)^2 + \frac{1}{2\gamma^4}, \tag{9.85}$$

defined in a way ensuring $\gamma_{**} = \gamma_* = \gamma$ at high frequencies $\omega \gg \omega_{\mathrm{pe}}\gamma$, where the plasma dispersion (term $\omega_{\mathrm{pe}}^2/\omega^2$) can be discarded. Recall that the frequency ω' (when the emission takes place in a plasma with dielectric permittivity $\varepsilon(\omega) = 1 - \frac{\omega_{\mathrm{pe}}^2}{\omega^2}$) is

$$\omega' = \frac{\omega}{2}\left(\gamma^{-2} + \theta^2 + \frac{\omega_{\mathrm{pe}}^2}{\omega^2}\right). \tag{9.86}$$

To compute the radiation intensity into the full solid angle one has to integrate Eq. (9.84) over $\mathrm{d}\Omega = \sin\theta \mathrm{d}\theta \mathrm{d}\varphi$. Since Eq. (9.84) does not depend on φ, while the angle θ is small, $\sin\theta \mathrm{d}\theta \simeq \theta \mathrm{d}\theta = \mathrm{d}\theta^2/2 = d(\omega'/\omega)$, then

$$\mathcal{E}^{\perp}_{\omega} = \frac{(2\pi)^4 Q^2}{M^2 c^3 \gamma^2 V} \int\limits_{1/2\gamma_*^2}^{\infty} d\left(\frac{\omega'}{\omega}\right)\left(\frac{\omega}{\omega'}\right)^2 \left[1 - \frac{\omega}{\omega'\gamma_*^2} + \frac{\omega^2}{2\omega'^2\gamma_{**}^4}\right]$$
$$\times \int \mathrm{d}q_0 \mathrm{d}\boldsymbol{q} \delta(\omega' - q_0 + \boldsymbol{q}\boldsymbol{v}) \mid \boldsymbol{F}_{q_0,\mathbf{q}\perp} \mid^2 . \tag{9.87}$$

[1] Note that the adopted constancy of the particle velocity implies that the particle moves in the given field infinitely long so the entire radiated energy is proportionally infinite.

If there is a magnetic field only (no electric field), then the square of the transverse Lorentz force is $\mid \boldsymbol{F}_{q_0,\mathbf{q}\perp} \mid^2 = Q^2 \mid \boldsymbol{B}^{\perp}_{q_0,\mathbf{q}} \mid^2 = Q^2(\delta_{\alpha\beta} - v_\alpha v_\beta/v^2)B^{\alpha}_{q_0,\mathbf{q}}B^{\beta *}_{q_0,\mathbf{q}}$, and, likewise (substituting $B^{\alpha}_{q_0,\mathbf{q}} \to E^{\alpha}_{q_0,\mathbf{q}}$) for the electric field only.

To be more specific let us consider a random magnetic field, i.e., $|\boldsymbol{F}_{q_0,\mathbf{q}\perp}|^2 = e^2|\boldsymbol{B}^{\perp}_{q_0,\mathbf{q}}|^2 = e^2(\delta_{\alpha\beta} - v_\alpha v_\beta/v^2)B^{\alpha}_{q_0,\mathbf{q}}B^{\beta *}_{q_0,\mathbf{q}}$, and introduce the second-order correlation tensor of the statistically uniform random magnetic field as follows; see Sect. 7.4:

$$T_{\alpha\beta}(\boldsymbol{r},\tau) = \langle B_{st,\alpha}(\boldsymbol{R},t)B_{st,\beta}(\boldsymbol{R}+\boldsymbol{r},t+\tau)\rangle = \frac{1}{TV}\int \mathrm{d}t\mathrm{d}\boldsymbol{R}B_{st,\alpha}(\boldsymbol{R},t)B_{st,\beta}(\boldsymbol{R}+\boldsymbol{r},t+\tau). \tag{9.88}$$

Then, express $\mid \boldsymbol{B}^{\perp}_{q_0,\mathbf{q}} \mid^2$ via the Fourier spectrum $T_{\alpha\beta}(q_0,\mathbf{q})$ of this correlation tensor using the following expression:

$$B^{\alpha}_{q_0,\mathbf{q}}B^{\beta *}_{q_0,\mathbf{q}} = \frac{TV}{(2\pi)^4}T_{\alpha\beta}(q_0,\boldsymbol{q}). \tag{9.89}$$

Here we used the correlation tensor defined by Eq. (9.88), whose Fourier transform is $T_{\alpha\beta}(q_0,\boldsymbol{q}) = \int \frac{\mathrm{d}\mathbf{r}\mathrm{d}\tau}{(2\pi)^4}e^{i(q_0\tau-\mathbf{qr})}T_{\alpha\beta}(\boldsymbol{r},\tau)$. Then, multiplying this by $(\delta_{\alpha\beta} - v_\alpha v_\beta/v^2)$, we obtain

$$\mid \boldsymbol{B}^{\perp}_{q_0,\mathbf{q}} \mid^2 = \frac{TV}{(2\pi)^4}\left(\delta_{\alpha\beta} - \frac{v_\alpha v_\beta}{v^2}\right)T_{\alpha\beta}(q_0,\boldsymbol{q}) = \frac{TV}{(2\pi)^4}T_{\perp}(q_0,\boldsymbol{q}), \tag{9.90}$$

where $T_{\perp}(q_0,\boldsymbol{q}) = T_{\alpha\beta}(q_0,\boldsymbol{q})\left(\delta_{\alpha\beta} - \frac{v_\alpha v_\beta}{v^2}\right)$ is the spectrum of the random magnetic field transverse to the particle velocity. If the random field is composed of random waves with the dispersion relation $q_0 = q_0(\boldsymbol{q})$ (in the limiting case of a static random field we have $q_0(\boldsymbol{q}) \equiv 0$), the spectrum takes the form $T_{\perp}(q_0,\boldsymbol{q}) = T_{\perp}(\boldsymbol{q})\delta(q_0 - q_0(\boldsymbol{q}))$.

Substituting all required values into Eq. (9.84) and dividing it by the total duration of emission T we arrive (Fleishman 2006) at the radiation intensity (energy emitted per unit frequency per unit solid angle *per unit time*):

$$I_{\mathbf{n},\omega} = \frac{Q^4}{2\pi M^2c^3\gamma^2}\left(\frac{\omega}{\omega'}\right)^2\left[1 - \frac{\omega}{\omega'\gamma_*^2} + \frac{\omega^2}{2\omega'^2\gamma_{**}^4}\right] \times \int \mathrm{d}q_0\mathrm{d}\boldsymbol{q}\delta(\omega' - q_0 + \boldsymbol{qv})T_{\perp}(\boldsymbol{q})\delta(q_0 - q_0(\boldsymbol{q})). \tag{9.91}$$

When the particle moves in an arbitrary *potential* electric field it could be convenient to express the radiation intensity via the scalar potential $\varphi_{\omega,\mathbf{k}}$ instead of the electric field itself. Using well known expression for the electric field $\boldsymbol{E}_{\omega,\mathbf{k}}$ via the potential $\varphi_{\omega,\mathbf{k}}$, we obtain the square modulus of the Fourier component $\mid \boldsymbol{E}_{\omega'} \mid^2$ in the form:

$$\mid \boldsymbol{E}_{\omega'} \mid^2 = \frac{(2\pi)^3}{V}\int k^2\mathrm{d}\omega\mathrm{d}\boldsymbol{k}\delta(\omega' - \omega + \boldsymbol{kv}) \mid \varphi_{\omega,\mathbf{k}} \mid^2 . \tag{9.92}$$

Then, the transverse and parallel accelerations receive the forms

$$\mid \boldsymbol{w}_{\omega'\perp} \mid^2 = \frac{Q^2}{M^2\gamma^2}\frac{(2\pi)^3}{V}\int k_\perp^2 \mathrm{d}\omega \mathrm{d}\boldsymbol{k}\delta(\omega' - \omega + \boldsymbol{k}\boldsymbol{v}) \mid \varphi_{\omega,\mathbf{k}} \mid^2, \tag{9.93}$$

$$\mid \boldsymbol{w}_{\omega'\parallel} \mid^2 = \frac{Q^2}{M^2\gamma^6}\frac{(2\pi)^3}{V}\int k_\parallel^2 \mathrm{d}\omega \mathrm{d}\boldsymbol{k}\delta(\omega' - \omega + \boldsymbol{k}\boldsymbol{v}) \mid \varphi_{\omega,\mathbf{k}} \mid^2; \tag{9.94}$$

thus, the radiation intensities produced by the transverse and parallel particle accelerations, respectively, transform to

$$\mathcal{E}^\perp_{\mathbf{n},\omega} = \frac{(2\pi)^3 Q^4}{M^2c^3\gamma^2 V}\left(\frac{\omega}{\omega'}\right)^2\left[1 - \frac{\omega}{\omega'\gamma_*^2} + \frac{\omega^2}{2\omega'^2\gamma_{**}^4}\right]\int q_\perp^2 \mathrm{d}q_0 \mathrm{d}\boldsymbol{q}\delta(\omega' - q_0 + \boldsymbol{q}\boldsymbol{v}) \mid \varphi_{q_0,\mathbf{q}} \mid^2, \tag{9.95}$$

$$\mathcal{E}^\parallel_{\mathbf{n},\omega} = \frac{2(2\pi)^3 Q^4}{M^2c^3\gamma^6 V}\left(\frac{\omega}{\omega'}\right)^3\left[1 - \frac{\omega}{2\omega'\gamma_*^2}\right]\int q_\parallel^2 \mathrm{d}q_0 \mathrm{d}\boldsymbol{q}\delta(\omega' - q_0 + \boldsymbol{q}\boldsymbol{v}) \mid \varphi_{q_0,\mathbf{q}} \mid^2, \tag{9.96}$$

where we have replaced the dummy arguments $(\omega, \boldsymbol{k}) \to (q_0, \boldsymbol{q})$ in the integrands. Integrating then over all possible directions of the $\boldsymbol{n}$ vector we obtain the radiation intensity (related to the transverse acceleration) into the full solid angle:

$$\mathcal{E}^\perp_\omega = \frac{(2\pi)^4 Q^4}{M^2c^3\gamma^2 V}\int\limits_{\frac{1}{2}\left(\gamma^{-2} + \frac{\omega_{\mathrm{Pe}}^2}{\omega^2}\right)}^{\infty} \mathrm{d}\left(\frac{\omega'}{\omega}\right)\left(\frac{\omega}{\omega'}\right)^2\left[1 - \frac{\omega}{\omega'\gamma_*^2} + \frac{\omega^2}{2\omega'^2\gamma_{**}^4}\right]$$
$$\times \int q_\perp^2 \mathrm{d}q_0 \mathrm{d}\boldsymbol{q}\delta(\omega' - q_0 + \boldsymbol{q}\boldsymbol{v}) \mid \varphi_{q_0,\mathbf{q}} \mid^2; \tag{9.97}$$

a similar integration is easy to perform also for $\mathcal{E}^\parallel_\omega$.

9.2.4 Thomson Scattering

As one of the simplest examples of the electromagnetic emission by charged particles we consider a process of emission by a slow, nonrelativistic particle, whose motion is perturbed by an external electromagnetic wave. Because this original wave already represents a radiation, the process under study is commonly called **scattering of radiation**, which is convenient to characterize by the differential and total cross sections of the scattering:

$$\mathrm{d}\sigma = \frac{\mathrm{d}I(\theta,\alpha)}{\overline{\gamma}_0} \qquad \sigma = \int \mathrm{d}\sigma. \tag{9.98}$$

Here $\mathrm{d}I(\theta,\alpha) = \overline{\gamma} r^2 \mathrm{d}\Omega$ is the radiation intensity per solid angle $\mathrm{d}\Omega$ averaged over time; $\overline{\gamma}$ and $\overline{\gamma}_0$ are the mean energy flux densities defined by the Poynting vector in the scattered and incident waves, respectively.

Below we calculate the scattering cross section of a weak electromagnetic wave satisfying the condition

$$e|E_0|/m\omega c \ll 1, \tag{9.99}$$

where E_0 and ω are the amplitude and frequency of the incident wave, by a free nonrelativistic particle, which is called **Thomson scattering**. Condition (9.99) ensures that the particle remains nonrelativistic during its interaction with the wave. Equation (9.66) for the dipole radiation in the time (instead of Fourier) domain is

$$\frac{\mathrm{d}I}{\mathrm{d}\Omega} = \frac{1}{4\pi c^3}\overline{(\ddot{\boldsymbol{d}} \times \boldsymbol{n})^2}, \tag{9.100}$$

where $\boldsymbol{d} = e\boldsymbol{r}$ is the electric dipole moment, $\boldsymbol{r}$ is the radius vector of the particle, and $\boldsymbol{n}$ is the direction of scattering.

In the equation of nonrelativistic motion we can safely discard the magnetic force ($vB/c \ll E$) so we obtain

$$m\ddot{\boldsymbol{r}} = e\boldsymbol{E}(t) = e\boldsymbol{E}_0 \cos\omega t = \frac{e\boldsymbol{E}_0}{2}(e^{i\omega t} + e^{-i\omega t}), \qquad \ddot{\boldsymbol{r}} = e\boldsymbol{E}/m. \tag{9.101}$$

To the same accuracy the factor $e^{i\mathbf{k}\cdot\mathbf{r}}$ can be replaced by one since its variation over the wave period is of the order of small parameter (9.99). From here we conclude that the electron oscillates with the same frequency as the incident wave, so the scattered wave will also have the same frequency. Using the averaged wave amplitude $\overline{\boldsymbol{E}^2(t)} = |\boldsymbol{E}_0|^2/2$ we can find the differential cross sections, which differ depending on incident wave polarization.

For a wave propagating along Oz axes with linear polarization, $\boldsymbol{E}_0 = E_0\boldsymbol{e}_x$, we obtain

$$\frac{\mathrm{d}\sigma}{\mathrm{d}\Omega} = r_0^2(1-\sin^2\theta\cos^2\alpha), \quad r_0 = \frac{e^2}{mc^2}; \quad \sigma = \sigma_T = \frac{8\pi}{3}r_0^2 \approx 6.65 \times 10^{-25}\ \mathrm{cm}^{-2}, \tag{9.102}$$

where θ and α are the polar and azimuth angles of the scattered wave vector relative to Oz axes; the total cross section is found by integration of the differential one over the angles and is called **Thomson cross section**.

In the case of circular polarization, $\boldsymbol{E}_0 = E_0(\boldsymbol{e}_x \pm i\boldsymbol{e}_y)/\sqrt{2}$,

$$\frac{\mathrm{d}\sigma}{\mathrm{d}\Omega} = \frac{1}{2}r_0^2(1+\cos^2\theta), \qquad \sigma = \sigma_T, \tag{9.103}$$

for any direction of the electric vector rotation in the wave; thus the cross section of unpolarized wave is also given by Eq. (9.103). As we see from Eqs. (9.102) and (9.103), the total cross section is equal to the Thomson cross section in all the cases, so it does not depend on the wave polarization. The parameter r_0 has a dimension of size and is called **classical electron radius**.

The equations obtained show that heavy particles (ions) almost do not take part in the wave scattering because of their big masses: the ion contribution to the scattering by free charges is about $(m_e/m_i)^2 \lesssim 10^{-6}$ compared with the electron contribution.

Note that this conclusion is a consequence of ignoring the plasma dispersion and, specifically, the Debye shielding. Indeed, for scattering of waves with the length larger than the Debye radius, each electron is surrounded by an equal positive charge formed by the corresponding lack of other electrons within the Debye sphere. Thus, the electron having the negative charge and the Debye sphere around it having the same positive charge will produce radiations in opposite phases, which will effectively compensate each other. This compensation does not occur in case of ions because the compensating negative charge in the Debye sphere around the ions is mainly formed by the electrons. Thus, the oscillations of the Debye spheres around the ions will give the main contribution in this regime, which is called **Rayleigh scattering**.

The Thomson scattering, therefore, correctly describes the electromagnetic wave scattering for reasonably short waves, shorter than the Debye radius, which varies depending on the source conditions. In most cases, it is valid in the optical range, e.g., applicable to the stellar light scattering, or even down to infrared and millimeter range. In contrast, in the meter and decimeter radio domains, the collective plasma behavior is typically important, so the Rayleigh scattering is relevant.

9.2.5 Inverse Compton Effect

Thomson or Rayleigh scattering (Sect. 9.2.4) of relatively low-frequency electromagnetic waves by nonrelativistic electrons does not change the frequency of the scattered radiation. However, if the frequency of the scattered wave ω is large so that the corresponding photon energy $\hbar\omega$ is comparable to the electron rest energy mc^2 or if the scatterer is a relativistic electron, the scattering is accompanied by a change of the wave frequency: it can either increase or decrease depending on the parameters involved. To explicitly illustrate this let us consider the energy and momentum conservation laws (cf. Sect. 4.3) during a photon to electron collision.

Below we use these conservation laws in a form of conservation of a four-momentum p in a 4D space, defined as $p = (\mathcal{E}/c, \boldsymbol{p})$, for which the following statements are valid:

$$|\boldsymbol{p}| \neq p, \qquad \mathcal{E} = \sqrt{m^2c^4 + c^2|\boldsymbol{p}|^2}, \tag{9.104}$$

while the square of the four-momentum is defined as

$$p^2 = \mathcal{E}^2/c^2 - |\boldsymbol{p}|^2 = (mc)^2. \tag{9.105}$$

Square of any four-vector is invariant, whose value does not depend on the reference system. For a photon $m = 0$ so the square of its four-momentum is

zero, $\hbar^2 k^2 = 0$ and $|\boldsymbol{k}| = \omega/c$. The dot product of two four-vectors is another invariant defined as

$$pk = \frac{\mathcal{E}\omega}{c^2} - \boldsymbol{p}\cdot\boldsymbol{k} = \frac{\mathcal{E}\omega}{c^2} - \frac{|\boldsymbol{p}|\omega}{c}\cos\theta_0, \tag{9.106}$$

where θ_0 is angle between 3D vectors $\boldsymbol{p}$ and $\boldsymbol{k}$.

Consider now a collision of electron and photon with initial four-momentum vectors p and k, which transform to p' and k' after the collision. Conservation of the total four-momentum can be written in the form

$$p + k - k' = p'. \tag{9.107}$$

Then, we take squares of both sides and simplify it employing Eqs. (9.104)–(9.106), which yields

$$pk - pk' - kk' = 0. \tag{9.108}$$

Expressing the dot products via 3D angles θ_0 between initial 3D momentums of the electron and photon, θ between initial 3D momentum of the electron and final momentum of the photon, and ϑ between initial and final 3D momentums of the photon, we find

$$\hbar\omega' = \hbar\omega\frac{\mathcal{E} - c|\boldsymbol{p}|\cos\theta_0}{\mathcal{E} - c|\boldsymbol{p}|\cos\theta + \hbar\omega(1-\cos\vartheta)}. \tag{9.109}$$

This equation is applicable for arbitrary energies of the involved particles and for any scattering angles. Let us consider a few simplified cases.

1. The earlier considered Thomson scattering takes place as nonrelativistic electrons ($|\boldsymbol{p}| \ll mc$) interact with reasonably "soft" photons ($\hbar\omega$) $\ll mc^2$. Taking this inequalities into account we see that the fraction in Eq. (9.109) is about one and, thus, $\hbar\omega' \approx \hbar\omega$.

2. The photon scattering on a nonrelativistic electron can occur with a frequency change if the initial photon energy is comparable with the electron rest energy mc^2. Here, the terms with the electron momentum in Eq. (9.109) are small and can be discarded, so the energy of the final photon has the form

$$\hbar\omega' = \frac{1}{1 + \hbar\omega(1-\cos\vartheta)/mc^2}. \tag{9.110}$$

   The final photon energy decreases for any scattering angle $\vartheta > 0$, the corresponding energy defect is transferred to the electron; this is a usual **Compton effect** discovered by *Arthur Holly Compton* in 1922.

3. When photon scattering occurs on ultrarelativistic electrons the angular distribution of the final photons narrows because of relativistic kinematic effects. Equation (9.109) in this parameter range implies that the energy of the final photon is largest when $\theta_0 = \vartheta = \pi$, while $\theta = 0$, i.e., for a "head-on" collision with a soft photon and emission of a hard photon along the electron motion:

$$\hbar\omega' = \hbar\omega \frac{2\mathcal{E}}{(mc^2)^2/2\mathcal{E} + 2\hbar\omega}. \tag{9.111}$$

We see that the enhancement of the photon energy can be very large. For example, for $\hbar\omega \ll mc^2/\gamma$, where $\gamma = \mathcal{E}/mc^2$ is the Lorentz factor, Eq. (9.111) yields $\hbar\omega' \approx 4\hbar\omega\gamma^2 \gg \hbar\omega$, although $\hbar\omega' \ll \mathcal{E}$. In the other case, $\hbar\omega \gg mc^2/\gamma$, the photon energy $\hbar\omega'$ approaches the initial electron energy $\mathcal{E}$.

Such scattering of photons on ultrarelativistic electrons, which results in generation of high-energy quanta (typically, the gamma rays) is called the **inverse Compton effect**. This process can play an important role in many astrophysical phenomena because both relativistic electrons and photons are typically available; in particular, the soft CMB photons are always present. Note that the inverse Compton process can result in severe radiative losses of ultrarelativistic electrons if $\hbar\omega \gtrsim mc^2/\gamma$.

Below we calculate the intensity of the inverse Compton emission by relativistic electrons interacting with soft photons within classical electrodynamics, which yields correct results for the parameter regime where $\hbar\omega \ll \mathcal{E}$. Alternatively, when the energy of emitted photon approaches the relativistic electron energy $\mathcal{E}$, a more exact quantum consideration is needed.

Let us calculate intensity of radiation produced by an ultrarelativistic electron perturbed by a weak monochromatic linearly polarized plane electromagnetic wave:

$$\boldsymbol{E}(\boldsymbol{r}, t) = \boldsymbol{E}_0 \cos(\omega_0 t - \boldsymbol{k} \cdot \boldsymbol{r}), \qquad \boldsymbol{B}(\boldsymbol{r}, t) = \boldsymbol{n}_0 \times \boldsymbol{E}(\boldsymbol{r}, t), \tag{9.112}$$

where $\boldsymbol{n}_0 = \boldsymbol{k}_0/k_0$ is the unit wave vector; assuming the wave frequency ω to be large enough to discard any plasma effect on the wave dispersion, we adopt the vacuum dispersion relation $k_0 = \omega/c$.

Here, compared with the case adopted to derive Eq. (9.91) in Sect. 9.2.3, both electric and magnetic fields are comparably important in producing the Lorentz force

$$\boldsymbol{F} = e\left(\boldsymbol{E} + \frac{1}{c}\boldsymbol{v} \times [\boldsymbol{n}_0 \times \boldsymbol{E}]\right). \tag{9.113}$$

Note that the exact expression for this Lorentz force depends on the wave polarization. We adopt that the particle moves along the z-axes, i.e., $\boldsymbol{v} = v_0 \boldsymbol{e}_z$, while the wave vector belongs to the xz-plane. Therefore, there are two distinct linearly polarized waves; we use index 1 for the wave with the electric

vector $\boldsymbol{E}_1$ directed along the y-axes, while index 2 for the wave with the electric vector $\boldsymbol{E}_2$ belonging to the xz-plane. Accordingly, for the first wave, the Lorentz force has only y component, $\boldsymbol{F}_1 = eE_1\boldsymbol{e}_y(1-\cos\theta_0)$, while for the second one it has x and z components: $\boldsymbol{F}_2 = -eE_2(\boldsymbol{e}_x(1-\cos\theta_0)+\boldsymbol{e}_z\sin\theta_0)$. Then, to apply Eq. (9.84) for the radiation intensity, we have to calculate the squares of the Lorentz forces transverse to the particle velocity, $(\delta_{\alpha\beta} - v_\alpha v_\beta/v^2)F_\alpha F_\beta$, cf. Eqs. (9.88)–(9.90), which have similar forms for both polarizations, $i = 1,\ 2$ if we adopt $v = c$ (this is correct everywhere except a narrow angular range $\theta_0^2 \sim \gamma^{-2}$ of the head–tail collision of photon and electron):

$$|\boldsymbol{F}_{iq_0,\mathbf{q}\perp}|^2 = \left(\delta_{\alpha\beta} - \frac{v_\alpha v_\beta}{v^2}\right) F_{i\alpha}F_{i\beta} = e^2(1-\cos\theta_0)^2 E_{i\alpha}E^*_{i\alpha}$$
$$= e^2(1-\cos\theta_0)^2\frac{TV}{(2\pi)^4}K_{i\alpha\alpha}(q_0,\boldsymbol{q}), \tag{9.114}$$

where $K_{i\alpha\alpha}(q_0,\boldsymbol{q})$ is the trace of the electric field correlation tensor for the i polarizations:

$$K_{i\alpha\beta}(q_0,\boldsymbol{q}) = \overline{E_i^2}e_{i\alpha}e^*_{i\beta}f(\boldsymbol{q})\delta(q_0 - qc). \tag{9.115}$$

The correlation tensor is normalized in such a way that $\overline{E_i^2} = \int \mathrm{d}\boldsymbol{q}\mathrm{d}q_0 K_{i\alpha\alpha}(q_0,\boldsymbol{q})$; $e_{i\alpha}e^*_{i\alpha} = 1$. For a monochromatic wave we have $f(\boldsymbol{q}) = \delta(\boldsymbol{q}-\boldsymbol{k}_0)$; substituting this into Eq. (9.115), then integrating Eq. (9.87) with account of Eq. (9.114), and dividing by the total time of the electron emission T, we obtain

$$I_{\mathbf{n},\omega} = \frac{e^4(1-\cos\theta_0)^2}{2\pi m^2c^3\gamma^2}\left(\frac{\omega}{\omega'}\right)^2\left(1-\frac{\omega}{\omega'\gamma^2}+\frac{\omega^2}{2\omega'^2\gamma^4}\right)\overline{E_i^2}\delta\left(\omega'-\Omega\right), \tag{9.116}$$

where $\Omega = \omega_0\left(1-(v/c)\cos\theta_0\right)$. Since the radiation intensity does not depend on the scattered wave polarization, we can add up the contributions for i=1, 2, so $\overline{E_i^2}$ will be substituted by $\overline{E_0^2} = \overline{E_1^2} + \overline{E_2^2}$.

Argument of the delta function controls the frequency range of emitted waves. The largest frequencies are emitted along the electron velocity, $\theta = 0$. In this case, for a given initial angle θ_0, we have

$$\omega = \omega_{IC} = 2\omega_0\gamma^2\left(1-\frac{v}{c}\cos\theta_0\right). \tag{9.117}$$

This equation demonstrates that the inverse Compton scattering by relativistic particles is remarkably different from the Thomson scattering. The very largest frequency is emitted for a head-on collision between soft photon and relativistic electron, $\cos\theta_0 = -1$, which is $\omega = 4\omega_0\gamma^2$. This implies that relativistic electrons interacting with microwave or optical radiation can produce very energetic X-ray or gamma radiation; in many cases the energy of radiated photon estimated as $\hbar\omega_{IC}$ will exceed the initial electron energy; see

Eq. (9.111). In such cases, as has been said, a more exact quantum consideration of the inverse Compton process is required to correctly describe this process. On the contrary, for a head–tail collision, $\cos\theta_0 = 1$ and $\omega = \omega_0$.

Using the link between ω' and emission angle implied by definition of Eq. (9.86), we can easily calculate inverse Compton radiation into the full solid angle for a given set of parameters ω_0, θ_0, and $\boldsymbol{E}_0$, similarly to Eq. (9.87):

$$I_\omega = \frac{e^4(1-\cos\theta_0)^2}{m^2c^3\gamma^2}\frac{\omega}{\Omega^2}\left(1-\frac{\omega}{\Omega\gamma^2}+\frac{\omega^2}{2\Omega^2\gamma^4}\right)\overline{E_0^2}\Theta\left(2\Omega\gamma^2-\omega\right). \quad (9.118)$$

This radiation intensity can be expressed via the Thomson cross section defined by Eq. (9.102):

$$I_\omega = \frac{3\sigma_T cW(1-\cos\theta_0)^2}{\gamma^2}\frac{\omega}{\Omega^2}\left(1-\frac{\omega}{\Omega\gamma^2}+\frac{\omega^2}{2\Omega^2\gamma^4}\right); \qquad \omega < 2\Omega\gamma^2, \quad (9.119)$$

where $W = E_0^2/8\pi$ is the initial wave energy density averaged over the wave period.

In a real situation the background ensemble of soft photons has some angular and spectral distributions over which the obtained intensity of the inverse Compton radiation must yet be averaged. Although this averaging is straightforward to perform, one has to take into account that the original delta function present in Eq. (9.116) due to corresponding conservation laws implies some restrictions for the further integration ranges, in particular, while averaging over the angle θ_0, one must take into account the following inequalities:

$$1-\frac{2\omega}{\omega_0} \le \cos\theta_0 \le 1-\frac{\omega}{2\omega_0\gamma^2}, \qquad |\cos\theta_0| \le 1. \quad (9.120)$$

Let us estimate the characteristic energy of the inverse Compton quanta produced due to scattering of the CMB photons on the electrons of CRs. The temperature of the CMB photon gas $T \approx 3\,\mathrm{K}$ corresponds to the energy $\hbar\omega_0 \approx 3\times10^{-4}\,\mathrm{eV}$. Relativistic electrons have energies at least up to $\gamma = 10^6$ and so they can produce very hard gamma-ray emission up to $4\gamma^2\hbar\omega_0 \approx 1\,\mathrm{GeV}$. The inverse Compton radiation makes a contribution to high-energy radiation from relativistic jets, neutron stars, accretion disks, and so on; see, e.g., Nagirner (2007b); this mechanism likely dominates in the range of ultra-high-energy gamma rays (Aharonian et al. 2007) from some sources, e.g., from pulsar wind nebulae (Sect. 12.3).

Another exciting and highly practical outcome of the Compton scattering was discovered in 1969 by Zeldovich and Sunyaev (1969). They noted that clouds of hot gas, e.g., in **galaxy clusters** where the plasma temperature can be as high as $10^7\,\mathrm{K}$, must scatter the CMB radiation and thus distort its original Planck distribution: the Planck spectrum moves toward larger frequencies as a result of this scattering; which is called the **Zeldovich–Sunyaev effect**. Observations of these spectrum distortions and polarization

modifications offer a very efficient tool of measuring various cosmological parameters including the Hubble constant, peculiar velocities of the galaxy clusters, temperature, and spatial distribution of the hot plasma, which is presented in more detail in Rephaeli (1995).

9.3 Bremsstrahlung

Let us consider radiation arising as a fast particle collides with a background (immobile) particle. This emission process is called bremsstrahlung ("breaking emission") because the collisions lead eventually to slowing the particle down to the thermal velocity.

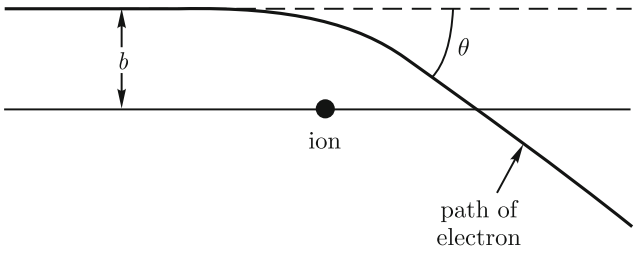

Figure 9.4: Deflection of a fast electron moving in the Coulomb electric field of a heavy positive charge (ion).

Perhaps, a simplest model allowing to calculate the emission arising from a single collision is to assume that at the collision the radiating particle velocity changes instantly by a value $\Delta \boldsymbol{v}$, so this instant acceleration drives the emission. This approach can be approximately valid when the radiation formation length is much larger than the particle path region where its velocity experiences a significant change. The corresponding Fourier transform of the electric current carried by this particle (assuming the VCR condition is not fulfilled) is

$$\boldsymbol{j}_{\omega,\mathbf{k}} = -\frac{iQ}{(2\pi)^4}\left[\frac{\boldsymbol{v}_1}{\omega - \boldsymbol{k}\boldsymbol{v}_1} - \frac{\boldsymbol{v}_2}{\omega - \boldsymbol{k}\boldsymbol{v}_2}\right], \tag{9.121}$$

where $\boldsymbol{v}_1$ and $\boldsymbol{v}_2$ are the particle velocities before and after the collision, respectively. Thus, Eq. (9.49) reads

$$\mathcal{E}_{\mathbf{n},\omega} = \frac{Q^2 n(\omega)}{(2\pi)^2 c^3}\left|\frac{[\boldsymbol{n}\boldsymbol{v}_1]}{1 - \dfrac{\boldsymbol{v}_1\boldsymbol{n}}{c}n(\omega)} - \frac{[\boldsymbol{n}\boldsymbol{v}_2]}{1 - \dfrac{\boldsymbol{v}_2\boldsymbol{n}}{c}n(\omega)}\right|^2. \tag{9.122}$$

However, this expression is not explicitly practical because even though the vector $\boldsymbol{v}_1$ can be known, the other vector $\boldsymbol{v}_2$ can be arbitrary as the collision impact parameter b (Fig. 9.4) is generally unknown. Moreover, in a media

there are many scatterers, so each fast particle experiences many collisions before it becomes fully thermalized. Thus, Eq. (9.122) has yet to be averaged over all possible $\boldsymbol{v}_2$ values, which is not unique.

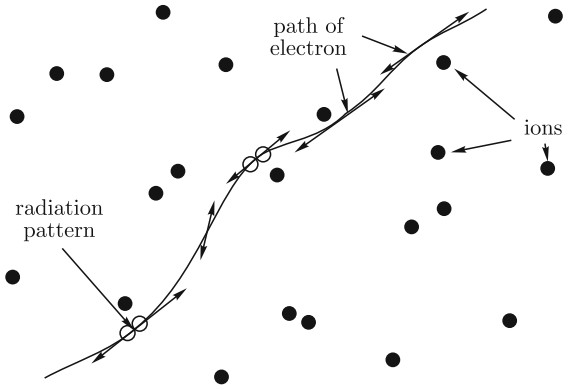

Figure 9.5: Random walk of a fast electron scattered by randomly located plasma ions.

In a medium, Fig. 9.5, using the perturbation theory results developed in Sect. 9.2.3 turn to be more convenient than averaging Eq. (9.122). To do so we start from the electric potential associated with a single background particle with the account of the Debye shielding appropriate for usual plasma:

$$\varphi(\boldsymbol{r},t)=\frac{ez}{|\boldsymbol{r}-\boldsymbol{R}_A(t)|}e^{-\frac{|\mathbf{r}-\mathbf{R}_A(t)|}{R_d}}, \tag{9.123}$$

where ez is charge of the background particle A and $\boldsymbol{R}_A(t)$ is its radius vector at the time t, whose Fourier transform is easy to find:

$$\varphi_{q_0,\mathbf{q}}=\frac{4\pi ez}{q^2+R_d^{-2}}\int\frac{\mathrm{d}t}{(2\pi)^4}e^{iq_0t-i\mathbf{q}\mathbf{R}_A(t)}. \tag{9.124}$$

Now, to apply Eq. (9.95), we have to compute the square of the electric potential modulus created by all background particles, which is straightforward to construct from Eq. (9.124):

$$|\,\varphi_{q_0,\mathbf{q}}\,|^2=\frac{(4\pi ez)^2}{(q^2+R_d^{-2})^2}\int\frac{\mathrm{d}t\mathrm{d}t'}{(2\pi)^8}e^{iq_0(t-t')}\sum_{A,B}e^{-i\mathbf{q}(\mathbf{R}_A(t)-\mathbf{R}_B(t'))}. \tag{9.125}$$

We emphasize that at this point the expression is rather general as it accounts for microscopic motion of every single background plasma particle, which is excessive and impractical. In many cases, however, it can be greatly simplified. First, in case of emission by a fast particle, to a good accuracy we can entirely neglect the slow (nonrelativistic) motion of the background

particles; thus, $\boldsymbol{R}_A$ and $\boldsymbol{R}_B$ are constants independent on time. And second, we can average the double sum over the particle locations assuming they are entirely uncorrelated (random). Under this averaging all the terms with $A \neq B$ vanish, while the contribution of the terms $A = B$ gives just the total number of particles N:

$$\left\langle \sum_{A,B} e^{-i\mathbf{q}(\mathbf{R}_A - \mathbf{R}_B)} \right\rangle = N. \tag{9.126}$$

Then, taking the integrals over $\mathrm{d}t\mathrm{d}t'$ in Eq. (9.125), we obtain

$$\mid \varphi_{q_0,\mathbf{q}} \mid^2 = \frac{TN}{(2\pi)^7} \frac{(4\pi e z)^2}{(q^2 + R_d^{-2})^2} \delta(q_0), \tag{9.127}$$

where T is the entire time of emission by the particle in the plasma.

A dominant contribution to the bremsstrahlung produced by an ultrarelativistic particle in the plasma comes from the transverse component of its acceleration, Eq. (9.93). Thus, dividing Eq. (9.95) by the total time of emission T, we obtain spectral and angular distribution of the radiation intensity:

$$I^{\perp}_{\mathbf{n},\omega} = \frac{4Q^4 z^2 e^2}{(2\pi)^2 M^2 c^3 \gamma^2} n \left(\frac{\omega}{\omega'}\right)^2 \left[1 - \frac{\omega}{\omega' \gamma_*^2} + \frac{\omega^2}{2\omega'^2 \gamma_{**}^4}\right] \int q_\perp^2 \mathrm{d}q_0 \mathrm{d}\boldsymbol{q} \frac{\delta(q_0)\delta(\omega' - q_0 + \boldsymbol{q}\boldsymbol{v})}{(q^2 + R_d^{-2})^2}, \tag{9.128}$$

where $n = N/V$ is the number density of the background plasma particles.

Integration of Eq. (9.128) over $\mathrm{d}q_0$ is trivial, while integration over $\mathrm{d}\boldsymbol{q}$ is convenient to perform in the cylindrical coordinate system, i.e., $\mathrm{d}\boldsymbol{q} = 2\pi \mathrm{d}q_\parallel q_\perp \mathrm{d}q_\perp$. This yields

$$I^{\perp}_{\mathbf{n},\omega} = \frac{Q^4 z^2 e^2}{\pi v M^2 c^3 \gamma^2} n \left(\frac{\omega}{\omega'}\right)^2 \left[1 - \frac{\omega}{\omega' \gamma_*^2} + \frac{\omega^2}{2\omega'^2 \gamma_{**}^4}\right] \int_0^{(mc/\hbar)^2} \frac{q_\perp^2 \mathrm{d}q_\perp^2}{(q_\perp^2 + \omega'^2/v^2 + R_d^{-2})^2}. \tag{9.129}$$

Then, taking the integral over $\mathrm{d}q_\perp^2$, we find

$$I^{\perp}_{\mathbf{n},\omega} = \frac{2Q^4 z^2 e^2}{\pi v M^2 c^3 \gamma^2} n \left(\frac{\omega}{\omega'}\right)^2 \left[1 - \frac{\omega}{\omega' \gamma_*^2} + \frac{\omega^2}{2\omega'^2 \gamma_{**}^4}\right] \left(\ln \frac{mc/\hbar}{\sqrt{(\frac{\omega'}{v})^2 + R_d^{-2}}} - \frac{1}{2}\right). \tag{9.130}$$

In a general case the logarithm in Eq. (9.130) depends on frequency; however, at low frequencies, $\omega \ll (c/R_d)\gamma^2$, one can discard a small (compared with R_d^{-2}) value ω'^2/v^2, so the logarithm simplifies to a frequency-independent form $\ln \frac{mcR_d}{\hbar}$.

To find the bremsstrahlung intensity into the full solid angle, $I_\omega^\perp$, Eq. (9.130) has yet to be integrated over

$$\mathrm{d}\Omega \approx 2\pi \frac{\mathrm{d}\theta^2}{2} = 2\pi d\left(\frac{\omega'}{\omega}\right), \tag{9.131}$$

where, according to definition (9.86), the lower bound of integration over $d(\omega'/\omega)$ is $\frac{1}{2}\left(\gamma^{-2} + \frac{\omega_{\mathrm{pe}}^2}{\omega^2}\right)$. When integrating, one can safely adopt $\omega' \approx \frac{\omega}{2}\left(\gamma^{-2} + \frac{\omega_{\mathrm{pe}}^2}{\omega^2}\right)$ in the logarithm argument as the logarithm is anyway a very slow function of its argument. At low frequencies, $\omega \ll (c/R_d)\gamma^2$, where the logarithm does not depend on frequency, we have

$$I_\omega^\perp = \frac{16Q^4 z^2 e^2 n}{3vM^2c^3\left(1 + \frac{\omega_{\mathrm{pe}}^2\gamma^2}{\omega^2}\right)}\left(\ln\frac{mcR_d}{\hbar} - \frac{1}{2}\right) = \frac{8Q^2\gamma^2}{3\pi c\left(1 + \frac{\omega_{\mathrm{pe}}^2\gamma^2}{\omega^2}\right)}q, \tag{9.132}$$

where

$$q = q_0\gamma^{-2} = \frac{2\pi Q^2 z^2 e^2 n}{vM^2c^2\gamma^2}\left(\ln\frac{mcR_d}{\hbar} - \frac{1}{2}\right) \tag{9.133}$$

is the effective rate of angular scattering of the radiating particle. At relatively high frequencies, $\omega_{\mathrm{pe}}\gamma \ll \omega \ll (c/R_d)\gamma^2$, the terms containing the plasma frequency can be discarded, so

$$I_\omega^\perp = \frac{16Q^4 z^2 e^2 n}{3vM^2c^3}\left(\ln\frac{mcR_d}{\hbar} - \frac{1}{2}\right) \tag{9.134}$$

depends neither on frequency nor on particle energy. At the low frequencies, $\omega \ll \omega_{\mathrm{pe}}\gamma$, the bremsstrahlung intensity decreases due to the density effect (**Ter-Mikaelian effect**):

$$I_\omega^\perp = \frac{16Q^4 z^2 e^2 n}{3vM^2c^3}\frac{\omega^2}{\omega_{\mathrm{pe}}^2\gamma^2}\left(\ln\frac{mcR_d}{\hbar} - \frac{1}{2}\right). \tag{9.135}$$

Formal integration of bremsstrahlung spectrum (9.134) over all frequencies diverges as the spectrum does not depend on frequency. The cause for that infinite radiated energy is in fact the classical treatment of the radiation process. It is clear, however, that no particle can generate more energy than it has. Energy of high-frequency $\hbar\omega \sim Mc^2\gamma$ photons is comparable with the particle energy, so the correct emission treatment requires quantum description. To roughly estimate the total radiated energy one can use $Mc^2\gamma/\hbar$ for the upper integration bound over frequencies (apparently, the full frequency dependence of the logarithm has to be included).

Let us estimate if/when the perturbation theory used is indeed applicable for the problem considered. For an ultrarelativistic particle most of

the emission is produced within a narrow cone with the characteristic angle $\theta \sim \gamma^{-1}$ around the particle velocity. The particle path can be approximated by a straight line if its velocity vector does not change by an angle larger or about that at the trajectory region equal to the radiation formation zone, $l_c \sim \lambda\gamma^2$, λ is the wavelength. The mean deflection angle due to uncorrelated scatterings accumulated over the formation time τ_ω is $\overline{\theta^2} \sim q\tau_\omega$, where q is the scattering rate defined by Eq. (9.133). The formation time is apparently $\tau_\omega \sim l_c/c \sim \gamma^2/\omega$; thus $\overline{\theta^2} \sim q\gamma^2/\omega$. The perturbation theory is valid until $\overline{\theta^2} \ll \gamma^{-2}$, i.e., at relatively high frequencies $\omega \gg q\gamma^4 = q_0\gamma^2$ only. If this condition is not fulfilled, the departure of the particle trajectory is essential and must be taken into account. An accurate account of the angular deflections due to multiple scattering gives rise to the following modification of the bremsstrahlung intensity (Migdal 1956) (Fig. 9.6):

$$I_\omega^\perp = \frac{8Q^2\gamma^2 q}{3\pi c\left(1+\frac{\omega_{\rm pe}^2\gamma^2}{\omega^2}\right)}\Phi(s), \tag{9.136}$$

where

$$\Phi(s) = 24s^2\int\limits_0^\infty {\rm d}t\exp(-2st)\sin 2st\left[\coth t - \frac{1}{t}\right] = \begin{cases} 1, & s \gg 1 \\ 6s, & s \ll 1 \end{cases}, \tag{9.137}$$

$$s = \frac{1}{8\gamma^2}\left(\frac{\omega}{q}\right)^{1/2}\left(1+\frac{\omega_{\rm pe}^2\gamma^2}{\omega^2}\right). \tag{9.138}$$

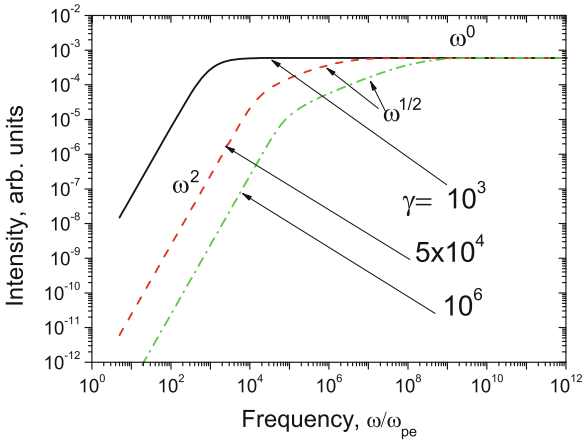

Figure 9.6: Examples of bremsstrahlung spectra for electrons with different energies; parameters are shown in the plot.

Apparently, the radiation spectrum differs for the high- and low-energy particles, respectively. For

$$\gamma \gg \gamma_{cr} = \frac{\omega_{\rm pe}}{4q_0}, \tag{9.139}$$

at the low frequencies, $\omega \ll \frac{\omega_{\rm pe}}{2}\left(\frac{\omega_{\rm pe}\gamma^2}{2q_0}\right)^{1/3}$, where $s \gg 1$, we have

$$I_\omega = \frac{8Q^2q_0}{3\pi c}\frac{\omega^2}{\omega_{\rm pe}^2\gamma^2}. \tag{9.140}$$

Here the bremsstrahlung is suppressed by the Ter-Mikaelian ("density") effect, $I_\omega \propto \omega^2$, in agreement with Eq. (9.135).

At higher frequencies, $\frac{\omega_{\rm pe}}{2}\left(\frac{\omega_{\rm pe}\gamma^2}{2q_0}\right)^{1/3} \ll \omega \ll 16q_0\gamma^2$, where $s \ll 1$, the radiation spectrum is formed by **multiple scattering** of the radiating particle by numerous background particles:

$$I_\omega = \frac{2Q^2}{\pi c\gamma}(\omega q_0)^{1/2}. \tag{9.141}$$

Here the bremsstrahlung intensity is lower than the incoherent sum of emissions on the same number of independent scatterers; this suppression, $I_\omega \propto \omega^{1/2}$, is called the **Landau–Pomeranchuck–Migdal effect**.

At even higher frequencies, $\omega \gg 16q_0\gamma^2$, the multiple scattering is inessential again, $s \gg 1$, and the radiation intensity does not depend on the frequency:

$$I_\omega = \frac{8Q^2q_0}{3\pi c}. \tag{9.142}$$

Equation (9.142) is valid up to the frequencies $\omega \sim Mc^2\gamma/\hbar$, where the impact of the emitted high-energy photon becomes kinematically important.

Note that for moderately energetic particles, such as

$$\gamma \ll \gamma_{cr} = \frac{\omega_{\rm pe}}{4q_0}, \tag{9.143}$$

the parameter s is greater than one at all frequencies, so the multiple scattering plays no role and the spectrum region $I_\omega \propto \omega^{1/2}$ is absent. Here, at low frequencies, $\omega \ll \omega_{\rm pe}\gamma$, Eq. (9.140) holds, while at high frequencies, $\omega \gg \omega_{\rm pe}\gamma$, Eq. (9.142) holds.

9.4 Gyro Emission

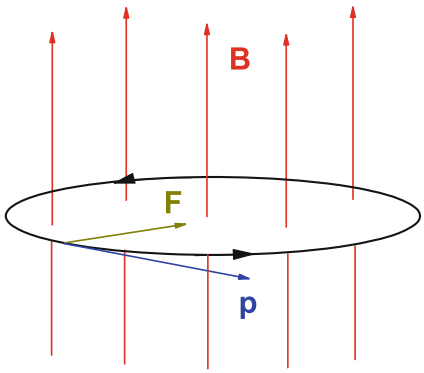

Figure 9.7: Gyration of a fast electron in a uniform magnetic field.

To address explicitly how an essentially curved particle trajectory affects emission we consider radiation produced by a particle gyrating in a constant uniform magnetic field (Fig. 9.7). It is straightforward to prove that the use of the perturbation theory yields a zero radiation intensity in this case. It does not mean, however, that there is no radiation, rather the perturbation theory is fully inapplicable here.[2] Thus, to correctly describe the radiation in the uniform magnetic field (which is called gyro emission or magnetobremsstrahlung) one has to more precisely describe the particle trajectory in the magnetic field, which greatly complicates the theory of gyro emission. Note that the gyro emission process is commonly called synchrotron, cyclotron, or gyrosynchrotron emission for the ultrarelativistic, nonrelativistic, and mildly relativistic particles, respectively.

9.4.1 Gyrosynchrotron Radiation

The general case of a particle with an arbitrary (including nonrelativistic or mildly relativistic) energy is highly complicated (Eidman 1958, 1959; Melrose 1968; Ramaty 1969) because one have to consider here exact expressions for the particle velocity and trajectory containing the sine and cosine functions to calculate electric current Eq. (9.51), where the dot product in the exponent can be written in the form

$$\boldsymbol{k} \cdot \boldsymbol{r}(t) = k_\perp R_L \sin(\phi + \Omega t) + k_z v_z t, \tag{9.144}$$

[2]Formally, the perturbation theory is applicable at high frequencies, where the radiation intensity is exponentially small; see below. But it is not helpful even there since, within the perturbation theory, the exponentially small emission is undistinguishable from zero emission level.

where ϕ is the azimuth angle of the $\boldsymbol{k}$ vector. The analysis is facilitated by using expansion of the $\exp(A\sin(\alpha t+\phi))$ term into a series over Bessel functions:

$$\exp[-ik_\perp R_L\sin(\phi+\Omega t)]=\sum_{s=-\infty}^{\infty}e^{-is(\phi+\Omega t)}J_s(k_\perp R_L). \tag{9.145}$$

Further straightforward although cumbersome manipulations (see, e.g., Melrose 1980) yield for the electric current components:

$$j^i_{\omega,\mathbf{k}}=\frac{|Q|}{2(2\pi)^3 m\gamma}\sum_{s=-\infty}^{\infty}\left(\frac{æ k_x}{k_\perp}\right)^{s+1}\Gamma^s_i\delta(\omega-s|\Omega|-k_z v_z), \tag{9.146}$$

where $æ=Q/|Q|$ is the sign of the particle charge:

$$\Gamma^s_1=2p_\perp\frac{s}{z}J_s(\lambda);\qquad \Gamma^s_2=-2iæ p_\perp J'_s(\lambda);$$
$$\Gamma^s_3=2p_z\frac{k_x}{k_\perp}J_s(\lambda);\qquad \lambda=k_\perp R_L. \tag{9.147}$$

Finally, we have to make use of the refractive indices and anisotropy factors of the magnetized plasma to apply Eq. (9.46), which yields

$$I^\sigma_{f,\mathbf{n}}=\frac{2\pi Q^2}{c}\frac{n_\sigma f^2}{1+T^2_\sigma}\times\sum_{s=-\infty}^{\infty}\left[\frac{T_\sigma(\cos\theta-n_\sigma\beta\mu)+L_\sigma\sin\theta}{n_\sigma\sin\theta}J_s(\lambda)+J'_s(\lambda)\beta\sqrt{1-\mu^2}\right]^2$$
$$\times\,\delta\left[f(1-n_\sigma\beta\mu\cos\theta)-\frac{sf_B}{\gamma}\right], \tag{9.148}$$

where the intensity is expressed in terms of practically used frequency $f=\omega/2\pi$, $f_B=QB/(2\pi Mc)$ is the particle gyrofrequency, n_σ, T_σ, and L_σ are the refraction index and transverse and longitudinal (relative to the wave vector) components of the polarization vector respectively (see Sect. 3.2.3), θ is the angle between the wave vector and the magnetic field vector, $\beta=v/c$ is the normalized (by c) particle velocity, $\mu=\cos\alpha$, α is the particle pitch angle (i.e., the angle between the particle momentum and the magnetic field vector), $\lambda=k_\perp R_L=\frac{f}{f_B}\gamma n_\sigma\beta\sin\theta\sqrt{1-\mu^2}$. We will return to this general case in Chap. 10 where we discuss a 3D modeling of radiation sources, while here we consider a much simpler although highly practical case of synchrotron radiation produced by ultrarelativistic particles.

9.4.2 Synchrotron Radiation

To consider synchrotron emission by relativistic particles we take advantage of the already used in Sects. 9.2.3 and 9.3 strong directivity of the emission

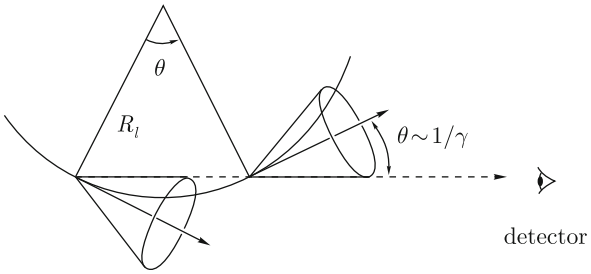

Figure 9.8: Directivity of synchrotron radiation: the spectrum recorded by a localized detector is formed from a small part of the particle path over which the particle gyrates by an angle of order $1/\gamma$.

along the relativistic particle velocity with the typical beaming angle θ of the order of

$$\theta \sim \gamma^{-1}. \tag{9.149}$$

Since the particle velocity direction varies broadly as it gyrates in the magnetic field, the presence of directivity Eq. (9.149) implies that the synchrotron radiation is formed over a small fragment of the circle orbit over which the velocity vector rotates by an angle about γ^{-1} (Fig. 9.8). Therefore, in the expressions for the trajectory and the velocity, the sine and cosine functions can be expanded into the series valid for small arguments, where the first terms describing the departure of the trajectory from the straight line must be retained:

$$\boldsymbol{v}(\tau) = \boldsymbol{v}_{\parallel} + \boldsymbol{v}_{\perp}\cos\Omega\tau + [\boldsymbol{b}\boldsymbol{v}_{\perp}]\sin\Omega\tau \approx \boldsymbol{v} + [\boldsymbol{\Omega}\boldsymbol{v}]\tau - \boldsymbol{v}_{\perp}\frac{\Omega^2\tau^2}{2}, \tag{9.150}$$

$$\boldsymbol{r}(\tau) = \boldsymbol{v}_{\parallel}\tau + \frac{\boldsymbol{v}_{\perp}}{\Omega}\sin\Omega\tau - \frac{[\boldsymbol{b}\boldsymbol{v}_{\perp}]}{\Omega}(\cos\Omega\tau - 1) \approx \boldsymbol{v}\tau + [\boldsymbol{\Omega}\boldsymbol{v}]\frac{\tau^2}{2} - \boldsymbol{v}_{\perp}\frac{\Omega^2\tau^3}{6}, \tag{9.151}$$

where $\boldsymbol{\Omega} = \frac{Q\boldsymbol{B}}{Mc\gamma}$ is the angular velocity vector of the particle with the mass M and charge Q, gyrating in the magnetic field $\boldsymbol{B}$, $\boldsymbol{b}$ is the unit vector in the $\boldsymbol{B}$ direction, and $\boldsymbol{v}_{\parallel}$ and $\boldsymbol{v}_{\perp}$ are the initial (at $\tau = 0$) parallel and transverse to the magnetic field components of the particle velocity, $\boldsymbol{v} = \boldsymbol{v}_{\parallel} + \boldsymbol{v}_{\perp}$. Substitution of Eqs. (9.150) and (9.151) into the expression for the particle current and then into Eq. (9.46) yields the spectral and angular distributions of the synchrotron emission. In particular, the polarization tensor components (for the polarization tensor definition, see Sect. 10.1.6) have the form

$$I^{(11)}_{\mathbf{n},\omega} = \frac{3Q^2\omega_B\gamma}{(2\pi)^3 c}\left(\frac{\omega}{\omega_c}\right)^2 (1+\gamma^2\theta^2)^2 K^2_{2/3}(\xi), \tag{9.152}$$

$$I^{(22)}_{\mathbf{n},\omega} = \frac{3Q^2\omega_B\gamma}{(2\pi)^3 c}\left(\frac{\omega}{\omega_c}\right)^2 \gamma^2\theta^2(1+\gamma^2\theta^2) K^2_{1/3}(\xi), \tag{9.153}$$

$$I^{(12)}_{\mathbf{n},\omega} = -I^{(21)}_{\mathbf{n},\omega} = -i\frac{3Q^2\omega_B\gamma}{(2\pi)^3 c}\left(\frac{\omega}{\omega_c}\right)^2 \gamma\theta(1+\gamma^2\theta^2)^{3/2}K_{1/3}(\xi)K_{2/3}(\xi), \tag{9.154}$$

where axes (1 and 2) of the coordinate system in the plane transverse to $\boldsymbol{k}$ are such that the unit vector $\boldsymbol{l}_2$ is along the projection $\boldsymbol{B}_\perp$ of the uniform magnetic field on this plane, while $\boldsymbol{l}_1 = [\boldsymbol{l}_2, \boldsymbol{k}]/k$, $\omega_B = \frac{Q\overline{B}}{Mc}$ is the gyrofrequency of the radiating particle, $\xi = \frac{\omega}{\omega_c}(1+\gamma^2\theta^2)^{3/2}$, $\omega_c = (3/2)\omega_{B\perp}\gamma^2$, $\omega_{B\perp} = \omega_B \sin\chi$, where χ is the angle between the particle velocity and the magnetic field and $K_\mu(\xi)$ is the MacDonald function with index μ. The radiation described by components Eq. (9.152)–(9.154) of the polarization tensor is elliptically polarized in a general case.

The spectral distribution of synchrotron radiation is obtained from Eqs. (9.152) and (9.153) by integration over the full solid angle. This integration is straightforwardly performed using the narrow directivity of the emission:

$$I^{(11)}_\omega = \frac{\sqrt{3}Q^2\omega_{B\perp}}{2\pi c}\left(\frac{\omega}{2\omega_c}\right)\left\{\int\limits_{\omega/\omega_c}^{\infty} K_{5/3}(x)\mathrm{d}x + K_{2/3}(\omega/\omega_c)\right\}, \tag{9.155}$$

$$I^{(22)}_\omega = \frac{\sqrt{3}Q^2\omega_{B\perp}}{2\pi c}\left(\frac{\omega}{2\omega_c}\right)\left\{\int\limits_{\omega/\omega_c}^{\infty} K_{5/3}(x)\mathrm{d}x - K_{2/3}(\omega/\omega_c)\right\}. \tag{9.156}$$

Alternatively, intensities (9.155) and (9.156) can be expressed via the Airy function. The total intensity of the synchrotron radiation (the Stokes I parameter, see Sect. 10.1.6) in the vacuum is the sum of these two expressions (Fig. 9.9). In the plasma we have yet to take into account the wave dispersion. Consider for simplicity an isotropic plasma with dielectric permittivity

$$\varepsilon(\omega) = 1 - \frac{\omega_{\mathrm{pe}}^2}{\omega^2}. \tag{9.157}$$

Then, in contrast to the vacuum case, we obtain

$$I_\omega = \frac{\sqrt{3}Q^2\omega_{B\perp}}{2\pi c}\left(1+\frac{\omega_{\mathrm{pe}}^2\gamma^2}{\omega^2}\right)^{-1/2} F_s\left(\frac{\omega}{\omega_{cp}}\right), \tag{9.158}$$

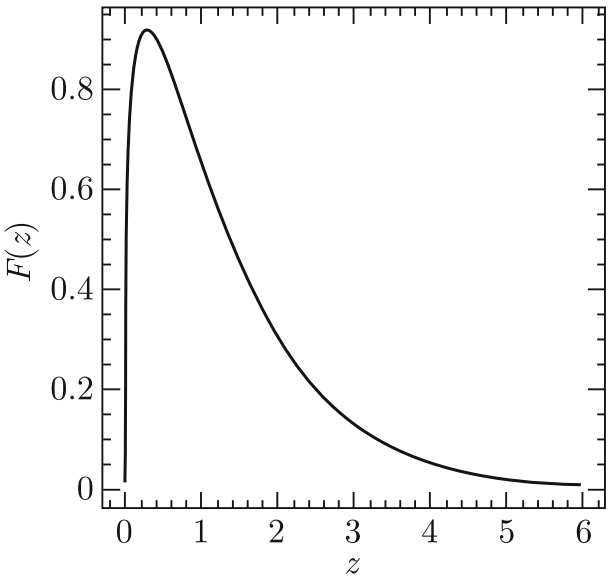

Figure 9.9: Universal function Eq. (9.159) describing the spectrum of synchrotron radiation in a uniform magnetic field.

where

$$F_s(z) = z \int_z^\infty K_{5/3}(x)\mathrm{d}x, \tag{9.159}$$

$$\omega_{cp} = \omega_c \left(1 + \frac{\omega_{\mathrm{pe}}^2 \gamma^2}{\omega^2}\right)^{-3/2}. \tag{9.160}$$

Other Stokes parameters are determined in a similar way.

The function $F_s(z)$ is a smooth function with a single peak at $z = 0.29$. For small arguments, $z \ll 1$, a power-law asymptote takes place:

$$F_s(z) = \frac{4\pi}{\sqrt{3}\Gamma(1/3)2^{1/3}} z^{1/3}, \tag{9.161}$$

where $\Gamma(a)$ is the Euler gamma function. For large arguments, $z \gg 1$, the function $F_s(z)$ decreases exponentially:

$$F_s(z) = \sqrt{\frac{\pi z}{2}} e^{-z}. \tag{9.162}$$

It is important to note that in a plasma (in contrast to the vacuum case) the value ω/ω_{cp} has a maximum at a frequency about $\omega_{\mathrm{pe}}\gamma$. Thus, for

$$\gamma \ll \omega_{\mathrm{pe}}/\omega_{B\perp}, \tag{9.163}$$

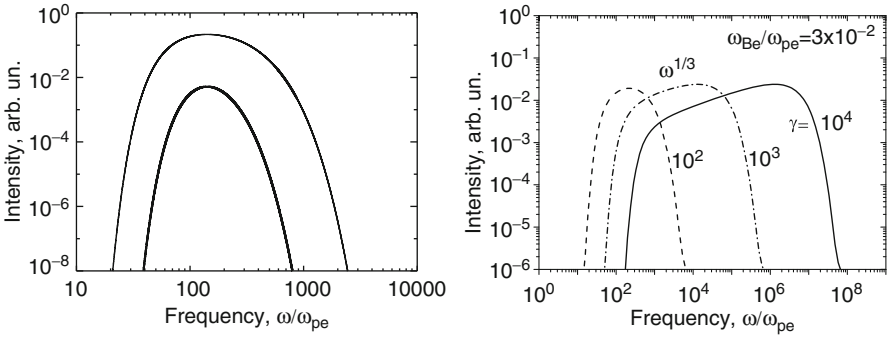

Figure 9.10: Synchrotron spectra for a low-energy [Eq. (9.163)], *left*, and high-energy, [Eq. (9.164)], *right*, radiating particle. *Left*: $\gamma = 100$, $n_e = 10^{10}\,\mathrm{cm}^{-3}$, $B = 1\,\mathrm{G}$ ($\omega_{\mathrm{pe}}/\omega_{\mathrm{Be}} \approx 320$, *thick curve*), and $B = 3\,\mathrm{G}$ ($\omega_{\mathrm{pe}}/\omega_{\mathrm{Be}} \approx 107$, *thin curve*). *Right*: $\omega_{\mathrm{pe}}/\omega_{\mathrm{Be}} \approx 33$, values of the Lorentz factor are given in the plot.

$\omega/\omega_{cp} \gg 1$ at all frequencies so Eq. (9.162) is valid everywhere and the synchrotron radiation is exponentially small at all frequencies; see Fig. 9.10, left; the peak frequency is about $\omega_{\mathrm{pe}}\gamma$ and so does not depend on the gyrofrequency here. The **density effect** revealing itself in suppression of the synchrotron radiation due to wave dispersion provided by a nonzero *plasma density* is called the **Razin effect**. Remarkably, for the relatively low-energy electrons obeying Eq. (9.163), the entire synchrotron spectrum turns out to be exponentially suppressed according to Eq. (9.162) provided that $\omega_{\mathrm{pe}} \gg \omega_{B\perp}$, in contrast to the bremsstrahlung case (the Ter-Mikaelian effect takes only place at a low-frequency part of the spectrum). For higher energy particles

$$\gamma \gg \omega_{\mathrm{pe}}/\omega_{B\perp}, \tag{9.164}$$

there is a frequency range

$$\omega_{\mathrm{pe}}\sqrt{\frac{\omega_{\mathrm{pe}}\gamma}{\omega_{B\perp}}} \ll \omega \ll \omega_c, \tag{9.165}$$

where Eq. (9.161) is valid so the synchrotron radiation intensity raises with frequency as a power-law $I_\omega \propto \omega^{1/3}$; outside this range the synchrotron radiation decreases exponentially.

The high-frequency exponential cutoff is valid for both vacuum and plasma, while the low-frequency one can only take place in a plasma. Here, for relatively high-energy particles, the Razin effect suppresses only a low-frequency part of the spectrum at $\omega \le \omega_{\mathrm{pe}}\sqrt{\frac{\omega_{\mathrm{pe}}\gamma}{\omega_{B\perp}}}$, Fig. 9.10, right, not the entire one as for the low-energy particles.

Curiously, the spectra of the synchrotron radiation and bremsstrahlung are qualitatively different from each other: the former displays a prominent

peak at the frequencies around $\omega_{B\perp}\gamma^2$ (or at $\omega_{\rm pe}\gamma$) and decreases exponentially at higher frequencies, while the latter is almost independent on the frequency up to very high frequencies around $Mc^2\gamma/\hbar$. The account of the plasma dispersion on the bremsstrahlung spectrum (Ter-Mikhaelyan 2003) gives rise [see Eq. (9.132)], to a suppression of the spectrum at the low frequencies $\omega \lesssim \omega_{\rm pe}\gamma$ according to $I_\omega \sim \omega^2$, much more gradual than exponential suppression of the synchrotron spectrum describing the Razin effect. All these dissimilarities are eventually provided by underlying dissimilarities of the radiating electron trajectories.

The polarization of synchrotron radiation depends on the angle θ between the particle velocity and the wave vector. Figure 9.11 shows that electric vector of the wave rotates along an ellipse with the axes ratio:

$$\tan\beta = \frac{\theta K_{1/3}\left[\frac{\omega}{2\omega_c}\left(1+\frac{\theta^2}{\gamma^2}\right)^{3/2}\right]}{(\gamma^{-2}+\theta^2)K_{2/3}\left[\frac{\omega}{2\omega_c}\left(1+\frac{\theta^2}{\gamma^2}\right)^{3/2}\right]}. \tag{9.166}$$

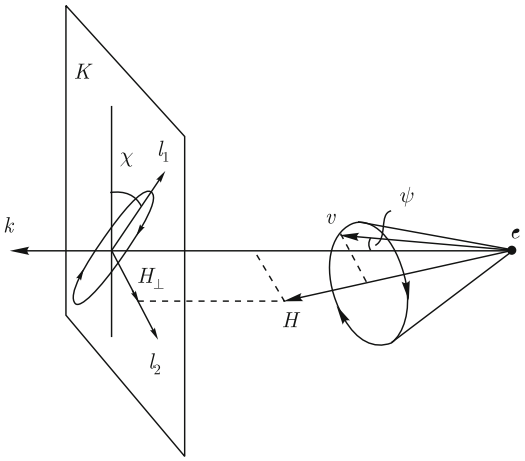

Figure 9.11: Shape of polarization ellipse and direction of the electric vector rotation produced by a positive charge gyrating in a magnetic field.

The synchrotron radiation of an isotropic ensemble of monoenergetic particles (in practice, an "isotropy" within only a small angle $\tilde{\theta} > 1/\gamma$ is required) is (partly) linearly polarized. The circular polarization vanishes because Eq. (9.166) contains θ to an odd power, which is integrated with an (even) isotropic distribution. A circular polarization, however, can recover if one takes into account the plasma gyrotropy provided by an external magnetic field (Melrose 1980; Ruzmaikin et al. 1988).

The degree of linear polarization (Ginzburg and Syrovatskii 1965)

$$P_l = \frac{K_{2/3}\left(\frac{\omega}{\omega_c}\right)}{\int\limits_{\omega/\omega_c}^{\infty} K_{5/3}(\eta)\mathrm{d}\eta} = \begin{cases} \frac{1}{2}, & \text{for } \omega \ll \omega_c \\ 1 - \frac{2\omega_c}{3\omega}, & \text{for } \omega \gg \omega_c \end{cases} \tag{9.167}$$

increases with frequency and at $\omega \gg \omega_c$ (where the intensity decreases exponentially) reaches almost 1.

In a reality, in an astrophysical source, there are many radiating electrons, described by a distribution function $f(\boldsymbol{p})$; thus, the volume emissivity is calculated by integration of the emission produced by a single particle over the particle distribution:

$$j^{\sigma}_{\mathbf{n},\omega} = \int I^{\sigma}_{\mathbf{n},\omega} f(\boldsymbol{p})\mathrm{d}\boldsymbol{p}. \tag{9.168}$$

As discussed in great detail in Chap. 11, the nonthermal fast particles are isotropically distributed in many cases and have typically rather broad distributions over energy, which can often be described by power laws with different indices, $N(E) = K_\xi/E^\xi$. This implies that the synchrotron radiation formulae have yet to be integrated over the fast electron distribution over energy according to Eq. (9.168). Adopt that this power-law distribution is valid between some bounding energies, $E_{\min} = mc^2\gamma_{\min}$ and $E_{\max} = mc^2\gamma_{\max} \gg E_{\min}$, and evanescent outside this range:

$$\mathrm{d}N_e(\gamma) = (\xi - 1)N_e\gamma_{\min}^{\xi-1}\gamma^{-\xi}\mathrm{d}\gamma, \quad \gamma_{\min} \le \gamma \le \gamma_{\max}, \tag{9.169}$$

where N_e is the number density of electrons with energies $E \ge mc^2\gamma_{\min}$, ξ is the power-law index of the distribution, and $\gamma_{\min} \gg 1$.

There can be a few different regimes of the synchrotron radiation produced by the fast electron ensemble depending on the parameters. If $\gamma_{\min} \sim 1$ and $\omega_{\mathrm{pe}} \gg \omega_{\mathrm{Be}}$, then a power-law spectrum

$$P(\omega) \propto \omega^{-\alpha}, \qquad \alpha = (\xi - 1)/2 \tag{9.170}$$

appears between $\omega_{\min} \sim \omega_{\mathrm{pe}}^2/\omega_{\mathrm{Be}}$ and $\omega_{\max} \sim \omega_{\mathrm{Be}}\gamma_{\max}^2$. This asymptote is easy to understand: the electron energy spectrum here is much broader than the synchrotron spectrum produced by a single electron. Thus, one can ignore the exact shape of this spectrum and approximate it by a narrow peak $\propto \delta(1\text{–}0.3\omega_{\mathrm{Be}}\gamma^2/\omega)$ and integrate it with electron spectrum (9.169), which immediately yields Eq. (9.170). This means, in particular, that any emission mechanism producing a spectrum peaking at a $\omega_0\gamma^2$ will produce spectrum (9.170) from electrons distributed over energy with a power law. Outside this range the synchrotron spectrum drops exponentially; the low-frequency exponential cutoff is due to the Razin effect. If $\gamma_{\min} \gg \omega_{\mathrm{pe}}/\omega_{\mathrm{Be}}$,

then the mentioned power-law part of the synchrotron spectrum, Eq. (9.170), starts at about $\omega_{\rm Be}\gamma_{\rm min}^2$, below which a single electron asymptote, $P(\omega) \propto \omega^{1/3}$, appears. At a lower frequency, $\omega \simeq \omega_{\rm pe}\sqrt{\omega_{\rm pe}\gamma_{\rm min}/\omega_{B\perp}}$, the radiation is suppressed by the Razin effect.

The degree of linear polarization of the synchrotron radiation produced by electron ensemble with the power-law distribution is (Trubnikov 1958; Westfold 1959)

$$P_l = \frac{\xi + 1}{\xi + 7/3}. \tag{9.171}$$

It is 75% for $\xi = 3$ and 69% for $\xi = 2$. These numbers are much higher than the degree of polarization typically measured in observations, which implies a major role of radiation depolarization in the astrophysical sources, in particular, due to random inhomogeneities of the magnetic field.

9.4.3 Applications of Synchrotron Radiation

Applications of synchrotron radiation in astrophysics are more than numerous. Historically, the synchrotron radiation came into astrophysical context starting from fifties of the twentieth century when a new observing window, the **radio astronomy**, appeared and started to bring unexpected new observations. A naive expectation based on the Rayleigh–Jeans regime of the thermal blackbody spectrum (see Chap. 10) was that a typical radio spectrum would increase with frequency as f^2. In contrast to this expectation the radio observations immediately revealed many compact and extended sources (including background radio emission from the Galaxy) with a radio spectrum falling with frequency roughly as $\propto f^{-\alpha}$ with positive α, which was impossible to reconcile with the thermal hypothesis of the radio emission. In contrast, as we have seen above, the synchrotron radiation generated by nonthermal relativistic particles has naturally a falling spectrum with shape (9.170) if the relativistic electrons are distributed over energy with a power law. Remarkably that Eq. (9.170) offers a nice diagnostics of the power-law index in the electron energy distribution ξ using the observed spectral index of the radio emission α:

$$\xi = 2\alpha + 1. \tag{9.172}$$

In many cases these radiation spectra extend to much higher frequencies including optical and HXR ranges indicative of the particle acceleration up to accordingly high energy. For example, for a magnetic field about 10^{-5} G, the electron energy needed to produce synchrotron X-ray emission at $f > 10^{17}$ Hz is $\gamma > 10^7$, i.e., $E \gtrsim 10^4$ GeV. Note that in case of very broadband synchrotron spectra occupying many decades from the radio to optical and/or X-ray range, the spectrum often departs from a single power law implying corresponding breaks or cutoffs in the energy spectrum of radiating electrons.

In particular, this is the case for the galactic background radiation, Fig. 9.12, left, which has a relatively flat spectrum $\propto f^{-0.4}$ at 10–300 MHz

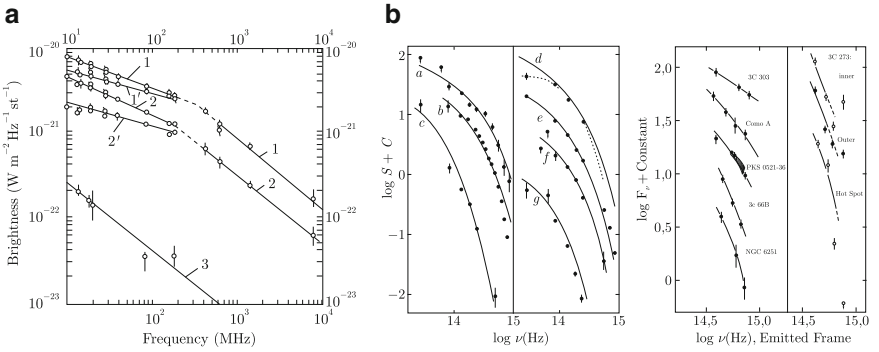

Figure 9.12: *Left panel*: spectra of background galactic radio emission for a few selected directions. Note a relatively sharp break in the spectra around 300 MHz *Right panels*: exponential cutoffs of nonthermal spectra at optical or infrared for a number of extragalactic sources including jets and radio galaxies. Credit: Rieke et al. (1982) and Keel (1988). Some of the spectra do consistent with a power law rather than the exponential cutoff.

and then experiences a break and softening to roughly f^{-1}. The latter spectrum agrees well with measured energy spectra of relativistic electrons at the IPM (e.g., at the Earth orbit) $\propto E^{-3}$ above a few GeV.

Nonthermal radiation is also observed from many kinds of extragalactic objects including jets, active galactic nuclei, quasars, and radio galaxies. Right panels in Fig. 9.12 display infrared and optical spectra of a number of extragalactic objects demonstrating a quasiexponential cutoff of the spectrum, which is a characteristic feature of the synchrotron spectrum produced by a high-energy cutoff in the electron spectrum. This spectral feature along with relatively large polarization detected in many cases is a strong evidence in favor of the synchrotron origin of the corresponding emission in this wide spectral band—from radio to optical. However, at a slightly larger frequency, these exponential cutoffs give a way to a more gradual, perhaps, a power-law decrease of the spectrum, Fig. 9.13, which is indicative of a distinct spectral component produced by either different population of relativistic particles or a different emission process or both; we return to this point later in this chapter.

Note that this nonthermal electromagnetic emission is mainly produced by electrons and so provides us with information about only the electron component of CRs, while the protons and other ions, that presumably contain more energy and, thus, more dynamically important than the electrons, cannot be directly observed via most of the spectral range (excluding gamma-ray range, where the ions do contribute via various nuclear processes, e.g., nuclear excitation and pion decay; see Sect. 12.1.8). This means that most information of the nuclear CR component in remote sources or distant regions of the Galaxy is obtained indirectly using emission produced by the relativistic electrons in combination with detailed theoretical analysis and numerical modeling.

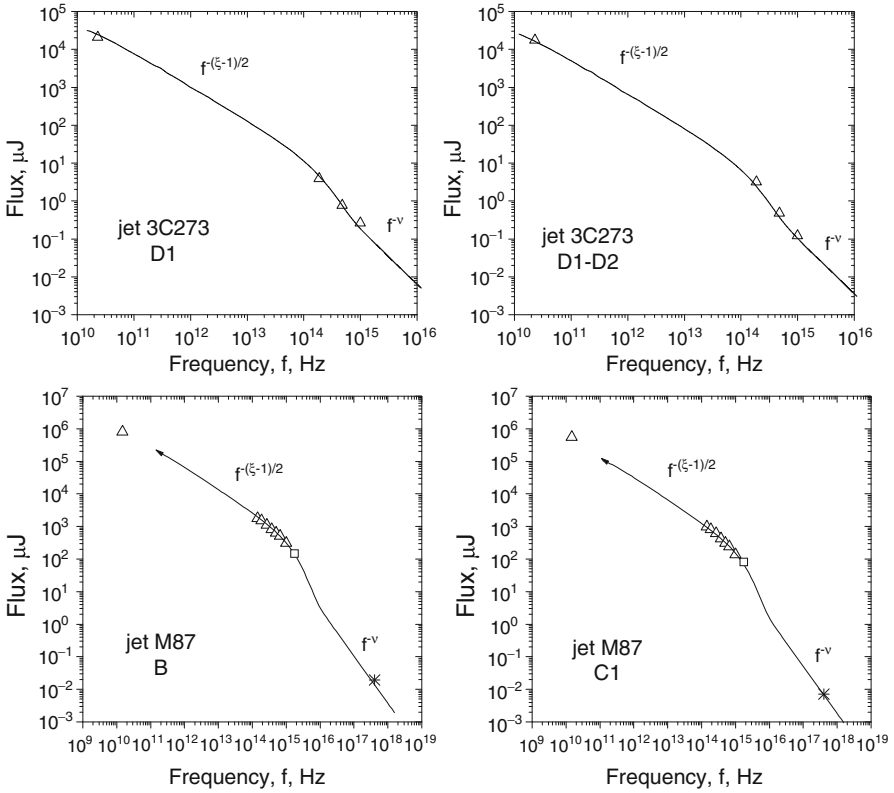

Figure 9.13: Observational broadband spectra from Jester et al. (2005) (*triangles*) and model synchrotron plus DSR spectra for a knot D1 (*upper left*) and interknot region between the knots D1 and D2 (*upper right*) for the jet in quasar 3C273. The model spectrum is plotted with equations from Sect. 9.5.3 for parameters: $B_{\rm st} = 1.2B_{\rm ls}$ and $\nu = 1.5$; the parameters of the synchrotron part of the spectrum are the same as in Jester et al. (2005). *Bottom*: Same for two knots (B, *left*, and C, *right*) of the jet in M87. Model uses the same parameters ($B_{\rm st} = 1.2B_{\rm ls}$ and $\nu = 1.5$, *solid lines*). *Data*: *triangles* from Perlman et al. (2001), *squares* at 2×10^{15} Hz from Waters and Zepf (2005), and *asterisks* from Marshall et al. (2002).

9.5 Diffusive Synchrotron Radiation

As we have discussed throughout the book, in many astrophysical magnetic fields, there is a stochastic, turbulent component, variable over a wide range of spatial and temporal scales, which can often dominate over the regular field. In order to calculate the radiation spectrum from a volume encompassing regions of varying field strength and orientation, it is apparently necessary to average the microscopic emission intensity over the different field strengths and orientations (as well as over the range of particle energies which may be present). A common approach to this problem is to simply average the

standard synchrotron formulae for a regular field over the varying magnetic field. However, in general, this approach is only correct if the field can be described as regular over the volume large compared with a typical particle orbit.

In the case of a field which has structure in a volume small compared with the average particle orbit, the particle paths deviate significantly from regular gyration around the field lines, and the standard synchrotron formulae (see Sect. 9.4.2), can lead to incorrect results. For example, if a turbulent magnetic field is composed of *random* waves, then the ensemble of these waves results in an incoherent superposition of random Lorentz forces which produces a stochastic electron trajectory quite different from the circular orbit in the regular field. To correctly calculate the emission spectrum in such a case requires not only averaging over the regions of different field strengths and orientations but also over the many possible particle paths (Toptygin and Fleishman 1987; Fleishman 2005), since the microscopic nature of the particle path strongly influences the spectrum, as we have already pointed out when compared synchrotron radiation and bremsstrahlung. This problem is highly nonlinear: in addition to the electron path affecting the nature of the emission, electrons are efficiently mirrored from regions of high magnetic field and thus spend a disproportionate time in the regions of lower field.

The radiation from electrons moving diffusively in stochastic magnetic fields is called **Diffusive Synchrotron Radiation** (DSR); it can be properly described within stochastic theory of radiation (STR) (Fleishman 2008), which attempts to calculate the average emission over the many possible particle paths. We consider here a special case of DSR where the magnetic field represents an incoherent superposition of waves with different scales and random phases and orientations and having a power-law spectrum. We note that such a field, consisting of *only* random waves and having no regular component, is almost certainly an oversimplification. Real astrophysical fields will often contain a combination of stochastic and regular magnetic fields. The case considered here, however, is an important limiting case, with the opposite limiting case being that of only regular field, Sect. 9.4.2, while a superposition of the random and regular fields is discussed in Sect. 9.5.3.

9.5.1 DSR in Weak Random Field

Assume initially that the random magnetic field is weak, so the perturbation theory is applicable. The spectrum of the radiation described by Eq. (9.87) or Eq. (9.91) depends on the statistical properties of the random force, which is convenient to describe in terms of effective scattering rate $q(\omega, \theta)$ of the particle by the magnetic inhomogeneities:

$$I_{\mathbf{n},\omega} = \frac{Q^2}{2\pi^2 c}\left(\frac{\omega}{\omega'}\right)^2 \left[1 - \frac{\omega}{\omega'\gamma_*^2} + \frac{\omega^2}{2\omega'^2\gamma_{**}^4}\right] q(\omega,\theta), \tag{9.173}$$

where

$$q(\omega,\theta)=\pi\left(\frac{Qc}{\mathcal{E}}\right)^2\int \mathrm{d}q_0\mathrm{d}\boldsymbol{q}\left(\delta_{\alpha\beta}-\frac{v_\alpha v_\beta}{v^2}\right)T_{\alpha\beta}(\boldsymbol{q},q_0)\delta(\omega-q_0-(\boldsymbol{k}-\boldsymbol{q})\boldsymbol{v}). \tag{9.174}$$

The intensity of radiation into the full solid angle is determined by integration of Eq. (9.173) over the angles, which simplifies in the relativistic case by using Eq. (9.131):

$$I_\omega=\frac{Q^2}{\pi c}\int\limits_{1/2\gamma_*^2}^{\infty} d\left(\frac{\omega'}{\omega}\right)\left(\frac{\omega}{\omega'}\right)^2\left[1-\frac{\omega}{\omega'\gamma_*^2}+\frac{\omega^2}{2\omega'^2\gamma_{**}^4}\right]q(\omega,\theta). \tag{9.175}$$

We emphasize that down to this point all consideration is valid for an arbitrarily anisotropic distribution of the random magnetic field. Below, as an example, we consider the case of an isotropic quasistationary random field in more detail. Adopting $T_{\alpha\beta}(\boldsymbol{q},q_0)=(T(\boldsymbol{q})/2)\delta(q_0)(\delta_{\alpha\beta}-q_\alpha q_\beta/q^2)$ we find the effective scattering rate $q(\omega,\theta)\equiv q(\omega')$ in the form

$$q(\omega,\theta)=\frac{\pi}{2}\left(\frac{Qc}{\mathcal{E}}\right)^2\int \mathrm{d}\boldsymbol{q}(1+\cos^2\theta)T(\boldsymbol{q})\delta(\omega-(\boldsymbol{k}-\boldsymbol{q})\boldsymbol{v}), \tag{9.176}$$

where θ is the angle between vectors $\boldsymbol{q}$ and $\boldsymbol{v}$.

Apparently, exact form of the scattering rate $q(\omega,\theta)$ depends on the distribution of random magnetic field energy over spatial scales; adopting a power-law distribution

$$T(\boldsymbol{q})=\frac{A_\nu}{q^{\nu+2}},\quad A_\nu=a_\nu k_{\min}^{\nu-1}\left\langle B_{\mathrm{st}}^2\right\rangle,\quad a_\nu=\frac{(\nu-1)}{4\pi},\quad k_{\min}<k<k_{\max}, \tag{9.177}$$

where ν is the spectral index of the random field spectrum, $T(\boldsymbol{q})$ is normalized by d^3q, so

$$\int\limits_{k_{\min}}^{k_{\max}} T(\boldsymbol{q})\mathrm{d}^3q=\left\langle B_{\mathrm{st}}^2\right\rangle,\ \text{for } k_{\min}\ll k_{\max},\ \nu>1, \tag{9.178}$$

$\left\langle B_{\mathrm{st}}^2\right\rangle$ is the mean square of the random magnetic field. For this spectrum, integration of Eq. (9.176) yields

$$q(\omega')=\frac{\pi^2 A_\nu}{v}\left(\frac{Qc}{\mathcal{E}}\right)^2\frac{(\nu+2)q_*^2+\nu\omega'^2/v^2}{\nu(\nu+2)q_*^{\nu+2}},\ q_*=\max(k_{\min},\omega'/v). \tag{9.179}$$

Substitution of $q(\omega,\theta)$ into Eq. (9.173) for the spectral and angular distribution of the emission yields the radiation spectrum in a closed analytical

form. Finding the spectral distribution into the full solid angle requires further integration over angles. For the considered here model case described by Eq. (9.179) the integration of Eq. (9.175) can be performed analytically, which yields

$$I_\omega^\perp = \frac{8Q^2\gamma_*^2}{3\pi c} q(\omega), \tag{9.180}$$

where

$$q(\omega) = \frac{\pi^2 a_\nu}{2\nu} \begin{cases} \frac{3\cdot 2^\nu(\nu^2+3\nu+4)}{(\nu+2)^2(\nu+3)} \frac{\omega_0^{\nu-1}\omega_{\rm st}^2\gamma_*^{2\nu}}{\omega^\nu\gamma^2}, & \omega > 2\omega_0\gamma_*^2 \\ \frac{\omega_{\rm st}^2}{\omega_0\gamma^2}\left[1+\frac{3\nu(\nu+1)\omega^2}{4(\nu+2)^2\gamma_*^4\omega_0^2}-\frac{\nu\omega^3}{2(\nu+3)\gamma_*^6\omega_0^3}+\frac{3\nu\omega^2}{4(\nu+2)\gamma_*^4\omega_0^2}\ln\left(\frac{\omega}{2\gamma_*^2 k_{\min}c}\right)\right], \\ \omega < 2\omega_0\gamma_*^2, \end{cases} \tag{9.181}$$

$\omega_0 = k_{\min}c, \omega_{\rm st}^2 = Q^2\left\langle B_{\rm st}^2\right\rangle/(Mc)^2$ (to make expression in the square brackets more compact we adopted $\gamma_{**} = \gamma_*$; this has only a very minor effect on $q(\omega)$). The matching condition $\omega = 2\omega_0\gamma_*^2$ can be fulfilled at two frequencies: $\omega_1 = 2\omega_0\gamma^2$ at $\omega > \omega_{\rm pe}\gamma$ and $\omega_2 = \omega_{\rm pe}^2/2\omega_0$ at $\omega < \omega_{\rm pe}\gamma$. In particular, at high frequencies $\omega' \gg k_{\min}c$, where $\gamma_* = \gamma$, we have (Nikolaev and Tsytovich 1979)

$$I_\omega = \frac{2^{\nu+2}\pi(\nu^2+3\nu+4)a_\nu}{\nu(\nu+2)^2(\nu+3)} \frac{Q^2}{c} \frac{\omega_0^{\nu-1}\omega_{\rm st}^2}{\omega^\nu}\gamma^{2\nu}. \tag{9.182}$$

It is remarkable that the spectrum of electromagnetic emission at high frequencies is described by the spectral index ν, characterizing distribution of the random magnetic field over wave numbers, which implies a way of measuring the turbulence spectrum in remote sources.

At lower frequencies, $\omega' \ll k_{\min}c$, where the effective scattering rate $q(\omega,\theta)$ does not depend on frequency, the radiation spectrum receives the form

$$I_\omega = \frac{4\pi a_\nu}{3\nu} \frac{Q^2}{c} \frac{\omega_{\rm st}^2}{\omega_0} \left(1+\frac{\omega_{\rm pe}^2\gamma^2}{\omega^2}\right)^{-1}. \tag{9.183}$$

We note that the spectrum shape is here the same as for the bremsstrahlung. In particular, at relatively high frequencies, $\omega > \omega_{\rm pe}\gamma$, the radiation intensity does not depend on frequency at all, while for $\omega < \omega_{\rm pe}\gamma$ it decreases with the frequency decrease as $\propto \omega^2$ following the Ter-Mikaelian effect. At even lower frequencies, the value $\gamma_*^2 \approx \omega^2/\omega_{\rm pe}^2$ decreases faster than ω; thus, the condition $\omega > 2\omega_0\gamma_*^2$ holds again at these low frequencies, $\omega < \omega_{\rm pe}^2/(2\omega_0)$, so the radiation intensity has the form $\propto \omega^{\nu+2}$.

It should be emphasized that the applicability of the perturbation theory developed above is itself rather limited. Indeed, even if the deflection of the particle is small during the time needed to pass through a single correlation cell of the random field, it is not necessarily small along the coherence length

of the emission, since multiple scattering of the particle by several successive magnetic inhomogeneities can easily provide large enough deflections due to angular diffusion to render perturbation theory inapplicable.

Thus, we have to explicitly consider the applicability of perturbation theory to the emission of fast particles moving in the small-scale random fields. The coherence length $l_c(\omega) \sim c\gamma_*^2/\omega$ of emission by a relativistic particle with a Lorentz-factor γ at a frequency ω decreases as frequency increases, so the approximation of the rectilinear motion is eventually valid at sufficiently high frequencies. However, at lower frequencies, the coherence length may be larger than the correlation length of the random field, and this necessarily will be the case at some low frequencies if one neglects the effect of the wave dispersion in the plasma. Thus, the particle trajectory traverses several correlation lengths of the random field to emit this low frequency and its trajectory random walks due to uncorrelated scattering by successive magnetic inhomogeneities. This angular diffusion will clearly affect the radiation spectrum if the mean angle of the particle deflection θ_c *accumulated* along the coherence length l_c exceeds the beaming angle of the emission γ^{-1}.

To estimate the deflection angle θ_c, adopt that the random field consists of cells with the characteristic scale l_0 and rms field value $\left\langle B_{st}^2 \right\rangle^{1/2}$. Inside each cell, the electron velocity rotates by the angle $\theta_0 \sim (\omega_{st}/\gamma)(l_0/c) \sim \omega_{st}/(\omega_0\gamma)$; $\theta_0 \ll 1/\gamma$ if $\omega_{st} \ll \omega_0$. Since the deflections are produced by successive *uncorrelated* cells of the random field, the mean square of the deflection angle after traversing N cells will be $\theta_c^2 \approx \theta_0^2 N$, where the number of the cells is specified by the ratio of the coherence length l_c to the correlation length l_0 of the random field, $N \approx l_c/l_0$. Therefore, when the particle passes the length $l_c(\omega)$ required to produce emission at a frequency ω, its characteristic deflection angle is $\theta_c^2 \simeq \omega_{st}^2/(\omega_0\omega)$. This angular diffusion will strongly affect the emission if $\theta_c \gtrsim 1/\gamma$, i.e., at

$$\omega \lesssim \frac{\omega_{st}^2}{\omega_0}\gamma^2, \tag{9.184}$$

which occurs in the range of the low-frequency asymptotic limit discussed above, Eq. (9.183).

9.5.2 DSR in Strong Random Field

Likewise the bremsstrahlung case, the (non-perturbative) intensity of DSR (assuming the regular magnetic field is zero) is expressed via the Migdal function, Eq. (9.137):

$$I_\omega = \frac{8Q^2 q(\omega)}{3\pi c}\gamma^2 \left(1 + \frac{\omega_{\rm pe}^2\gamma^2}{\omega^2}\right)^{-1} \Phi(s). \tag{9.185}$$

A fundamental distinction between this expression and Eq. (9.136) for the bremsstrahlung is that $q(\omega)$, according to Eq. (9.181), now depends on fre-

quency. Here the random field is not necessarily weak; the case of $\omega_{st} > \omega_0$ is also described by Eq. (9.185). Although Eq. (9.185) in general must be integrated numerically, we can analytically obtain several characteristic asymptotes, which gives a good qualitative idea of the overall shape of the DSR spectrum.

As we will see, the regime of strong random field contains a new characteristic frequency

$$\omega_{\rm lsc} = \left[\left(\frac{2\pi c}{L_0}\right)^{\nu-1} \frac{e^2\left\langle B_{\rm st}^2\right\rangle}{m^2c^2}\right]^{\frac{1}{\nu+1}} = \left(\frac{\omega_{\rm st}}{\omega_0}\right)^{\frac{2}{\nu+1}} \omega_0 = \left(\frac{\omega_0}{\omega_{\rm st}}\right)^{\frac{\nu-1}{\nu+1}} \omega_{\rm st}, \quad (9.186)$$

which plays a role similar to some extent to the role of the frequency $\omega_{B\perp}$ in the standard synchrotron theory. At high frequencies,

$$\omega \gg \omega_{\rm lsc}\gamma^2 \equiv \left(\frac{\omega_{\rm st}}{\omega_0}\right)^{\frac{2}{\nu+1}} \omega_0\gamma^2 \equiv \left(\frac{\omega_0}{\omega_{\rm st}}\right)^{\frac{\nu-1}{\nu+1}} \omega_{\rm st}\gamma^2 \quad (9.187)$$

we have $s \gg 1$, so the radiation spectrum has the standard high-frequency form

$$I_\omega = \frac{8Q^2q(\omega)}{3\pi c}\gamma^2, \quad (9.188)$$

with the spectral asymptote $I_\omega \propto \omega^{-\nu}$, typical for the high-frequency perturbative regime of DSR. Note that if the magnetic field were regular with the same strength, then the bounding frequency would be $\omega_{\rm st}\gamma^2$ in place of $\omega_{\rm lsc}\gamma^2$, Eq. (9.187), and the radiation intensity would decrease exponentially rather than as a power law, Eq. (9.188). The decrease of the bounding frequency (compared with the regular field regime) happens because the deviation of the particle trajectory from the straight line occurs more slowly in the random than in regular field; thus the region of applicability of the perturbation theory [asymptote Eq. (9.188)] broadens toward lower frequencies.

Accordingly, the amount of radiated energy in the random magnetic field is lower than in the regular magnetic field with the same energy density. Stated another way, larger random (than regular) magnetic field is required to provide the same radiative losses.

The parameter s decreases with frequency, and when it falls below unity at

$$\omega < \omega_{\rm lsc}\gamma^2, \quad (9.189)$$

the perturbation theory is no longer valid. For $s \ll 1$ we have $\Phi(s) \simeq 6s$; therefore

$$I_\omega = \frac{2Q^2}{\pi c}(\omega q(\omega))^{1/2}. \quad (9.190)$$

This expression is valid down to relatively low frequencies, where parameter s increases again under the influence of the effect of density (term $\omega_{\rm pe}^2/\omega^2$) and again reaches the unity at a sufficiently low frequency.

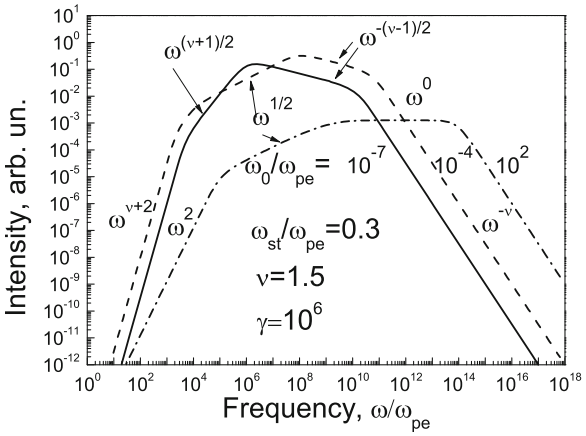

Figure 9.14: Single-particle DSR spectra for $\nu = 1.5$ and $\gamma = 10^6$. Cases of small-scale/weak ($\omega_0/\omega_{\rm pe} = 10^2$) and large-scale/strong ($\omega_0/\omega_{\rm pe} = 10^{-4}$ and 10^{-7}) random magnetic field are shown. The shape of the DSR radiation spectrum changes significantly as the largest scale of the field ($L_0 = 2\pi c/\omega_0$) changes as described in the text; in particular, the regime of large-scale magnetic field (*solid and dashed curves*) differs substantially from the regime of the small-scale field (*dash-dotted curve*).

The asymptotic regime $\Phi(s) \simeq 6s$, at $s \ll 1$, is due to multiple scattering of the fast particle by the uncorrelated long waves composing the random magnetic field at the scales $l > c/\omega_{\rm lsc}$. Even though the perturbation of the particle trajectory due to any single Fourier component of the random field is small, their cumulative effect results in significant angular diffusion of the charged particle. Accordingly, the direction of the particle's motion changes by a value exceeding the characteristic beaming angle of emission ($\vartheta \sim \gamma^{-1}$), which leads to a suppression of the emission compared with that predicted by the perturbation theory ($I_\omega \propto \omega^{-\nu}$).

Note that this essentially non-perturbative regime of DSR has no direct analogies in other emission mechanisms. In particular, it cannot be obtained by either perturbation theory or any averaging of the standard synchrotron radiation, since the real particle trajectory in the presence of the large-scale random magnetic inhomogeneities deviates strongly from both the straight line and a circle.

In the region of applicability of Eq. (9.190), the radiation spectrum is composed of two or three power-law asymptotes depending on the relation between $\omega_{\rm pe}\gamma$ and $\omega_0\gamma^2$. If $\omega_0 \ll \omega_{\rm pe}/\gamma$ then $\omega > 2\omega_0\gamma_*^2$; so the top row of Eq. (9.181) for $q(\omega)$ is valid at all frequencies. Accordingly, discarding also the term $\omega_{\rm pe}^2/\omega^2$, which is valid at $\omega \gg \omega_{\rm pe}\gamma$, we obtain

$$I_\omega \sim \frac{Q^2}{c}\omega_{\rm st}\left(\frac{\omega_0\gamma^2}{\omega}\right)^{(\nu-1)/2} \quad ; \quad \omega_{\rm pe}\gamma \ll \omega \ll \omega_{\rm lsc}\gamma^2, \tag{9.191}$$

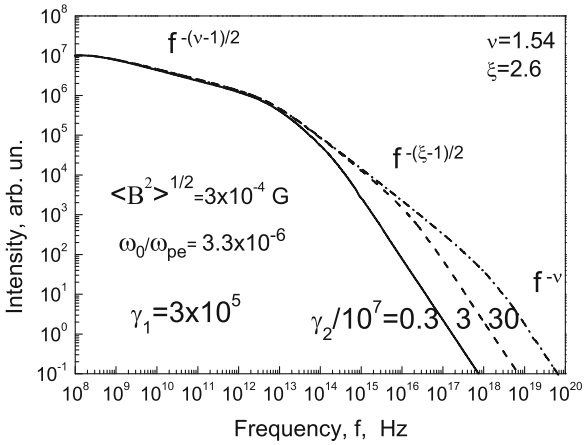

Figure 9.15: Broadband DSR spectra as produced by three different power-law distributions [Eq. (9.169)] of ultrarelativistic nebular electrons, which extend from a Lorentz factor $\gamma_1 = 0.3 \times 10^6$ to $\gamma_2 = 3 \times 10^6$, 3×10^7, and 3×10^8, respectively. The values of the model parameters were chosen so as to match the spectral energy distribution of the Crab Nebula; see Sect. 12.3. The values adopted for the spectral index of the turbulence, ν, the energy index of the power-law electron distribution, ξ, the plasma frequency, $\omega_{\rm pe}$, and the mean square of the random magnetic field, $\langle B^2_{\rm st} \rangle$, are indicated in the figure.

where we have omitted a numeric coefficient near unity for simplicity. It is important to note that for typical turbulence spectra with ν =1–2, Chap. 6, the DSR spectrum, Eq. (9.191), is relatively flat having the spectral index $\alpha = (\nu - 1)/2 = 0$–0.5.

In the other case, $\omega_0 \gg \omega_{\rm pe}/\gamma$, the lower bound of this region shifts toward larger frequencies, and the spectrum has the form given by Eq. (9.191) at $\omega_0 \gamma^2 \ll \omega \ll \omega_{\rm lsc} \gamma^2$. At low frequencies, $\omega^2_{\rm pe}/\omega_0 \ll \omega \ll \omega_0 \gamma^2$, the scattering rate does not depend on frequency, and $I_\omega \sim \omega^{1/2}$ as in the case of small-scale magnetic inhomogeneities. Then, for even lower frequencies, $\omega \ll \omega^2_{\rm pe}/\omega_0$ (or, if $\omega_0 \ll \omega_{\rm pe}/\gamma$, for $\omega \ll \omega_{\rm pe}\gamma$), the effect of density, described by the term $\omega^2_{\rm pe}/\omega^2$, dominates γ_* entering $q(\omega)$. Discarding small terms, we obtain

$$I_\omega \sim \frac{Q^2}{c} \, \frac{\omega_{\rm st}}{\gamma} \, \frac{\omega_0^{(\nu-1)/2} \omega^{(\nu+1)/2}}{\omega_{\rm pe}^{\nu}}. \tag{9.192}$$

Therefore, at these low frequencies, the spectrum falls with frequency decrease as $I_\omega \sim \omega^{(\nu+1)/2} = \omega^{1-1.5}$ for ν =1–2. Finally, at even lower frequencies, the parameter s will again be larger than unity due to effect of plasma dispersion (term $\omega^2_{\rm pe}/\omega^2$), so a standard low-frequency DSR asymptote, $I_\omega \sim \omega^{\nu+2}$, applies. In Fig. 9.14 we show the DSR spectra calculated by the numerical integration of Eq. (9.185) in the case of *large-scale* random

magnetic field, i.e., under condition

$$\omega_{\rm st} \gg \omega_0 \tag{9.193}$$

along with the DSR spectrum in a small-scale field.

We conclude that the spectrum of electromagnetic emission produced by a single relativistic particle in the presence of large-scale random magnetic field is entirely different from the standard synchrotron spectrum and also deviates significantly from that in the small-scale random magnetic field.

9.5.3 Superposition of Regular and Random Fields

The general case when both regular and random magnetic fields are present has not yet been comprehensively studied. Here, without derivation, we present expressions valid when either the random field is weaker than the regular magnetic field or the deviation of the particle trajectory from the straight line (due to effect of the *regular* magnetic field) is small over the correlation length of the random field (Toptygin and Fleishman 1987; Fleishman 2005):

$$I_\omega = \frac{8Q^2q(\omega)}{3\pi c}\gamma^2\left(1+\frac{\omega_{\rm pe}^2\gamma^2}{\omega^2}\right)^{-1}\Phi_1(s,r) \; + \frac{Q^2\omega}{4\pi c\gamma^2}\left(1+\frac{\omega_{\rm pe}^2\gamma^2}{\omega^2}\right)\Phi_2(s,r), \tag{9.194}$$

where $\Phi_1(s,r)$ and $\Phi_2(s,r)$ stand for the integrals

$$\Phi_1(s,r) = 24s^2\,{\rm Im}\int\limits_0^\infty {\rm d}t\exp(-2s_0t)\times\left[\coth t\exp\left(-2rs_0^3(\coth t-\sinh^{-1}t-t/2)\right)-\frac{1}{t}\right], \tag{9.195}$$

$$\Phi_2(s,r)=4rs^2{\rm Re}\int\limits_0^\infty {\rm d}t\frac{\cosh t-1}{\sinh t}\times\exp\left(-2s_0t-2rs_0^3(\coth t-\sinh^{-1}t-t/2)\right), \tag{9.196}$$

which depend on the dimensionless parameters s_0, s, r:

$$s_0 = (1-i)s = \frac{1-i}{8\gamma^2}\left(\frac{\omega}{q(\omega)}\right)^{1/2}\left(1+\frac{\omega_{\rm pe}^2\gamma^2}{\omega^2}\right), \tag{9.197}$$

$$r = 32\gamma^4\left(\frac{\omega_{B\perp}}{\omega}\right)^2\left(1+\frac{\omega_{\rm pe}^2\gamma^2}{\omega^2}\right)^{-3}, \tag{9.198}$$

$q(\omega)$ is the rate of scattering of the particle by magnetic inhomogeneities defined by Eq. (9.181). These expressions contain, as limiting cases, both synchrotron emission, when $q(\omega) \to 0$, and the DSR: when $r \to 0$ then $\Phi_2 \to 0$ while $\Phi_1 \to \Phi$, where Φ is the Migdal function considered above.

9.5.4 DSR from Astrophysical Sources

Relatively strong random magnetic fields, produced in particular by strong shocks generated by powerful energy release, are typical for many observed phenomena, such as supernova remnants (SNRs) and gamma-ray bursts (GRBs), and many dynamic processes, such as cosmic ray generation, turbulence production and transformation, and heating of the interstellar plasma. Thus, the DSR, describing radiation from turbulent sources, is highly relevant throughout all of astrophysics, being widely applicable to such disparate sources as extragalactic jets, pulsar wind nebulae, sub-MeV diffuse galactic emission, and solar radio bursts; see Sects. 12.3.3 and 12.4 for greater detail.

Although several different regimes of DSR are possible, depending on the value of ξ, we consider the case when

$$\nu < \xi < 2\nu + 1, \tag{9.199}$$

which is probably of the most practical importance. Indeed, the turbulence spectral index is typically $\nu < 2$ (e.g., $\nu \approx 1.7$ for the Kolmogorov turbulence), while the particle index $\xi > 2$ (e.g., $\xi \approx 2.7$ for the galactic cosmic rays). In this regime, the standard nonthermal spectrum typical also for synchrotron radiation, Eq. (9.170), $P_\omega \propto \omega^{-\alpha_{\rm nth}}$, where $\alpha_{\rm nth} = (\xi - 1)/2$, produced by the inner part $\gamma_{\rm min} \ll \gamma \ll \gamma_{\rm max}$ of distribution (9.169) is steeper than the non-perturbative DSR spectrum, $P_\omega \propto \omega^{-(\nu-1)/2}$, but shallower than the high-frequency perturbative spectrum, $P_\omega \propto \omega^{-\nu}$.

An example of the DSR spectrum (no regular field is present) generated by the power-law electron distribution is given in Fig. 9.15. We note that at some low frequencies the spectrum decreases as $P_\omega \propto \omega^{(\nu+1)/2}$ and then as $P_\omega \propto \omega^{\nu+2}$, but these regions of the spectrum may or may not be observable from the Earth depending on the source parameters; in Fig. 9.15 these regions take place at $f \lesssim 10^8$ Hz.

The account of a small-scale or weak field on top of an overall *dominant regular* magnetic field, Sect. 9.5.3, is particularly important at those frequency regions where the synchrotron emission decreases exponentially, e.g., at $\omega \gg \omega_{\rm Be}\gamma_{\rm max}^2$, where the DSR contribution decreases with frequency over a much slower, power law, Eq. (9.188). As a result, the exponential cutoff of the synchrotron spectrum gives a way to the DSR power-law $\propto \omega^{-\nu}$ at these high frequencies, which manifests itself as a secondary spectral component distinct from the standard synchrotron spectrum. A few examples of such spectra representing excellent fits to broadband imaging spectroscopy spectra from notes and internote region of extragalactic jets presented in Fig. 9.13 are indicative of the presence of a small-scale component of the jet magnetic fields.

9.6 Transition Radiation

9.6.1 General Consideration

Transition radiation is an emission formed by background particles in response to electromagnetic perturbation produced by an extraneous (fast) particle (Ginzburg and Tsytovich 1990; Platonov and Fleishman 2002). Such a radiation does not apparently require any acceleration of the fast particle; thus, it does not depend on its mass (for a given Lorentz factor γ; although for a given energy E the radiation does depend on the mass because particles with same energy while different masses have distinct Lorentz factors).

Full radiation involving both direct emission by the fast particle and background electrons is defined, according to Eq. (9.46), by the full electric current composed on the intrinsic electric current of the particle

$$\boldsymbol{j}^{Q}(\boldsymbol{r},t) = Q\boldsymbol{v}(t)\delta(\boldsymbol{r}-\boldsymbol{r}(t)) \tag{9.200}$$

and the plasma response current

$$\boldsymbol{j}^{m}(\boldsymbol{r},t) = e\int \boldsymbol{v} f_m(\boldsymbol{r},\boldsymbol{v},t)\frac{\mathrm{d}^3 p}{(2\pi)^3}, \tag{9.201}$$

formed by the plasma electrons perturbed by the fast particle field. Here, $f_m(\boldsymbol{r},\boldsymbol{v},t)$ is the electron distribution function in the turbulent plasma with the account of the plasma (random) inhomogeneity and fast particle effects. Being calculated and substituted into Eq. (9.46) it yields the transition radiation intensity.

Let us calculate the second-order correction $f_m^{(2)}(\boldsymbol{r},\boldsymbol{v},t)$ to the electron distribution function dependent on both plasma inhomogeneities and fast particle electromagnetic field. The kinetic equation for the plasma electrons has the form

$$\frac{\partial f(\boldsymbol{r},\boldsymbol{p},t)}{\partial t} + \boldsymbol{v}\frac{\partial f(\boldsymbol{r},\boldsymbol{p},t)}{\partial \boldsymbol{r}} + e\boldsymbol{F}(\boldsymbol{r},t)\frac{\partial f(\boldsymbol{r},\boldsymbol{p},t)}{\partial \boldsymbol{p}} = 0, \tag{9.202}$$

or, for the Fourier transform $f_{\omega,\mathbf{k}}(\boldsymbol{p})$,

$$f_{\omega,\mathbf{k}}(\boldsymbol{p}) = \frac{e}{i(\omega-\boldsymbol{k}\boldsymbol{v})}\int \boldsymbol{F}_{\omega-\omega',\mathbf{k}-\mathbf{k}'}\frac{\partial}{\partial \boldsymbol{p}} f_{\omega',\mathbf{k}'}(\boldsymbol{p})\mathrm{d}\omega'\mathrm{d}\boldsymbol{k}'. \tag{9.203}$$

Here

$$\boldsymbol{F}_{\omega,\mathbf{k}} = \boldsymbol{E}_{\omega,\mathbf{k}} + \frac{\boldsymbol{v}}{c}\times \boldsymbol{B}_{\omega,\mathbf{k}} \tag{9.204}$$

is the Lorentz force (per a unit charge) acting on a single plasma electron, and the electric $\boldsymbol{E}_{\omega,\mathbf{k}}$ and magnetic $\boldsymbol{B}_{\omega,\mathbf{k}}$ fields are composed of the fields produced by the plasma eigenmodes (m) and fast particle (Q):

$$\boldsymbol{E}_{\omega,\mathbf{k}} = \boldsymbol{E}^{m}_{\omega,\mathbf{k}} + \boldsymbol{E}^{Q}_{\omega,\mathbf{k}}; \qquad \boldsymbol{B}_{\omega,\mathbf{k}} = \boldsymbol{B}^{m}_{\omega,\mathbf{k}} + \boldsymbol{B}^{Q}_{\omega,\mathbf{k}}. \tag{9.205}$$

Kinetic equation (9.203) in the integral form is convenient when the corrections to the distribution function related to the fields $\boldsymbol{E}_{\omega,\mathbf{k}}$ and $\boldsymbol{B}_{\omega,\mathbf{k}}$ can be consistently taken into account within the perturbation theory. Note that Eq. (9.203) is rather general; e.g., it is valid for a relativistic background plasma.

In the zeroth approximation (for an unperturbed plasma) we have

$$f^{(0)}_{\omega,\mathbf{k}}(\boldsymbol{p}) = f(\boldsymbol{p})\delta(\omega)\delta(\boldsymbol{k}), \tag{9.206}$$

where $f(\boldsymbol{p})$ is a standard plasma distribution function over momentum. The first-order correction can be written in the form

$$f^{(1)}_{\omega,\mathbf{k}}(\boldsymbol{p}) = \frac{e\boldsymbol{E}^{(0)}_{\omega,\mathbf{k}}}{i(\omega - \boldsymbol{kv})}\frac{\partial f(\boldsymbol{p})}{\partial \boldsymbol{p}} + \delta f_{\omega,\mathbf{k}}(\boldsymbol{p}), \tag{9.207}$$

where we explicitly isolated a component $\delta f_{\omega,\mathbf{k}}(\boldsymbol{p})$ to describe possible spatial and temporal inhomogeneity of the plasma electron distribution $\delta N_{\omega,\mathbf{k}}$. The functions $f(\boldsymbol{p})$ and $\delta f_{\omega,\mathbf{k}}(\boldsymbol{p})$ are normalized to the plasma electron number density N_0 and its variation $\delta N_{\omega,\mathbf{k}}$, respectively:

$$\int f(\boldsymbol{p})\frac{\mathrm{d}\boldsymbol{p}}{(2\pi)^3} = N_0, \qquad \int \delta f_{\omega,\mathbf{k}}(\boldsymbol{p})\frac{\mathrm{d}\boldsymbol{p}}{(2\pi)^3} = \delta N_{\omega,\mathbf{k}}. \tag{9.208}$$

This form of $f^{(1)}_{\omega,\mathbf{k}}(\boldsymbol{p})$ with an arbitrary variation $\delta f_{\omega,\mathbf{k}}(\boldsymbol{p})$ is convenient because the inhomogeneities of the plasma electron number density can be coupled with the ion inhomogeneities so the overall charge variation can be highly reduced or evanescent; alternative (and much more complicated) way of inclusion of such inhomogeneities into our treatment is via an additional equation for the ions. Then, the second-order correction receives the form:

$$\begin{aligned} f^{m(2)}_{\omega,\mathbf{k}} = {} & \frac{e^2}{i(\omega - \boldsymbol{kv})}\int \boldsymbol{F}_{\omega-\omega',\mathbf{k}-\mathbf{k}'}\frac{\partial}{\partial \boldsymbol{p}}\left[\frac{\boldsymbol{F}_{\omega',\mathbf{k}'}}{i(\omega' - \boldsymbol{k}'\boldsymbol{v})}\frac{\partial}{\partial \boldsymbol{p}}f(\boldsymbol{p})\right]\mathrm{d}\omega'\mathrm{d}\boldsymbol{k}' \\ & + \frac{e}{i(\omega - \boldsymbol{kv})}\int \boldsymbol{F}_{\omega-\omega',\mathbf{k}-\mathbf{k}'}\frac{\partial}{\partial \boldsymbol{p}}\delta f_{\omega',\mathbf{k}'}(\boldsymbol{p})\mathrm{d}\omega'\mathrm{d}\boldsymbol{k}'. \end{aligned} \tag{9.209}$$

In case of relativistic background plasma the term $\boldsymbol{kv}$ in the denominator is of the same order of magnitude as ω; thus, the difference $(\omega - \boldsymbol{kv})$ is a small value compared with ω. Then, the magnetic field of the fast particle has an effect comparable to its electric field because $v_T/c \sim 1$. This gives rise to a great complication of (not yet available) transition radiation theory in relativistic plasmas compared with usual nonrelativistic plasma. Therefore, for the sake of simplicity, from this point we consider a nonrelativistic plasma and note that further results should not be applied to relativistic plasmas.

We do not include any large-scale magnetic field B_0 into Eq. (9.209) because its effect on the plasma dielectric tensor (see Chap. 3) is small for

$\omega_{\rm Be} \ll \omega_{\rm pe}$ and can be discarded at $\omega \gg \omega_{\rm pe}$ in the zeroth order approximation. Calculating the Fourier transform of the current using Eqs. (9.201), (9.209), and (9.208), we obtain

$$\boldsymbol{j}^{m(1)}_{\omega,\mathbf{k}} = \frac{ie^2}{m\omega}\int \boldsymbol{E}^{Q}_{\omega-\omega',\mathbf{k}-\mathbf{k}'}\delta N_{\omega',\mathbf{k}'}\mathrm{d}^3k'\mathrm{d}\omega' - \frac{e^3N}{m^2c\omega}\int \mathrm{d}^3k'\frac{\mathrm{d}\omega'}{\omega-\omega'}[\boldsymbol{E}^{Q}_{\omega-\omega',\mathbf{k}-\mathbf{k}'}\times\boldsymbol{B}^{m}_{\omega',\mathbf{k}'}]. \tag{9.210}$$

To obtain Eq. (9.210) we adopted a few natural simplifications: small terms of the order of v_T/c and u/c, where u is a fluid plasma velocity, were discarded as well as electric component of the eigenmodes composing the turbulence. The latter is correct because the potential part of the electric field is taken into account via $\delta N_{\omega',\mathbf{k}'}$, while the inductive electric fields of the MHD waves are small compared with the magnetic fields of these waves.

9.6.2 Transition Radiation on Random Density Inhomogeneities

As is apparent from Eq. (9.210) there are two main ways generating the transition radiation: by inhomogeneities of the background electron density or the random magnetic fields. Let us consider the first of them related to $\delta N_{\omega',\mathbf{k}'}$ in greater detail, for which we write the radiated energy in the form

$$\mathcal{E}^{m}_{\mathbf{n},\omega} = \frac{(2\pi)^6e^4}{m^2c^3}\int [\boldsymbol{n}\times\boldsymbol{E}^{Q}_{\omega-\omega',\mathbf{k}-\mathbf{k}'}][\boldsymbol{n}\times\boldsymbol{E}^{Q*}_{\omega-\omega'',\mathbf{k}-\mathbf{k}''}] \times\left\langle\delta N_{\omega',\mathbf{k}'}\delta N^{*}_{\omega'',\mathbf{k}''}\right\rangle\mathrm{d}^3k'\mathrm{d}\omega'\mathrm{d}^3k''\mathrm{d}\omega''. \tag{9.211}$$

In case of an ultrarelativistic radiating particle it is sufficient to include into Eq. (9.211) only the transverse electric field of the particle, that is much larger than its longitudinal field at $\omega \gg \omega_{\rm pe}$. The transverse electric field is expressed via its electric current:

$$E^{Q,\mathrm{tr}}_{i,\omega,\mathbf{k}} = G^{\mathrm{tr}}_{ij}(\omega,\boldsymbol{k})j^{Q}_{j,\omega,\mathbf{k}}, \tag{9.212}$$

where $G^{\mathrm{tr}}_{ij}(\omega,\boldsymbol{k})$ is the corresponding transverse Green's function:

$$G^{\mathrm{tr}}_{ij}(\omega,\boldsymbol{k}) = \left(\delta_{ij}-\frac{k_ik_j}{k^2}\right)\frac{4\pi i\omega}{c^2\left(k^2-\frac{\omega^2\varepsilon(\omega)}{c^2}\right)}, \tag{9.213}$$

while the electric current of the relativistic particle is specified by its path $\boldsymbol{r}(t)$ and velocity $\boldsymbol{v}(t)$ according to Eq. (9.200); thus, for the steady rectilinear motion of the particle the current is described by Eqs. (9.52) and (9.53).

Substituting Eqs. (9.212) and (9.213) into Eq. (9.211), and then averaging over the random phases using the relation

$$\left\langle \delta N_{\omega',\mathbf{k}'} \delta N^*_{\omega'',\mathbf{k}''} \right\rangle = |\delta N|^2_{\mathbf{k}'} \delta(\omega') \delta(\omega' - \omega'') \delta(\boldsymbol{k}' - \boldsymbol{k}''), \tag{9.214}$$

we find for the radiation intensity per unit time:

$$I^m_{\mathbf{n},\omega} = \frac{8\pi Q^2 e^4}{m^2 c^3 \omega^2 \varepsilon^2(\omega)} \int \mathrm{d}^3 k' \frac{|\delta N|^2_{\mathbf{k}'} \delta(\omega - (\boldsymbol{k} - \boldsymbol{k}')\boldsymbol{v})[\boldsymbol{n} \times \boldsymbol{v}_*]^2}{\left(1 - \frac{(\mathbf{k}-\mathbf{k}')^2 c^2}{\omega^2 \varepsilon(\omega)}\right)^2}, \tag{9.215}$$

where $\boldsymbol{v}_* = \boldsymbol{v} - (\boldsymbol{k} - \boldsymbol{k}')((\boldsymbol{k} - \boldsymbol{k}')\boldsymbol{v})/(\boldsymbol{k} - \boldsymbol{k}')^2$, $\delta(\omega - (\boldsymbol{k} - \boldsymbol{k}')\boldsymbol{v}) \simeq \delta(\omega(\frac{1}{2\gamma^2} + \frac{\omega_{\mathrm{pe}}^2}{2\omega^2} + \frac{\theta^2}{2} + \frac{\boldsymbol{k}'\boldsymbol{v}}{\omega}))$, $\theta \approx |\boldsymbol{v}/v - \boldsymbol{n}|$ is the viewing angle relative to the particle velocity vector.

To simplify integration of Eq. (9.215) over angles of the vector $\boldsymbol{k}'$ using δ-function we adopt that the angle between $\boldsymbol{k}'$ and $\boldsymbol{k}$ is the same as between $\boldsymbol{k}'$ and $\boldsymbol{v}$, which is justified by a strong directivity of emission along the particle velocity. To the same accuracy, in $\boldsymbol{v}_*$ we can use $\boldsymbol{k}^2$ for $(\boldsymbol{k} - \boldsymbol{k}')^2$ because $k'/k \ll 1$, while the vectors are almost transverse to each other; this yields:

$$I^m_{\mathbf{n},\omega} = \frac{16\pi^2 Q^2 e^4}{m^2 c^2 \omega^2} \int\limits_{k'_{\min}(\theta)}^{\infty} \frac{\theta^2 |\delta N|^2_{\mathbf{k}'} k' \mathrm{d}k'}{\left(\theta^2 + \gamma^{-2} + \frac{\omega_{\mathrm{pe}}^2}{\omega^2}\right)^2}. \tag{9.216}$$

We made here an expansion over the small angle θ between $\boldsymbol{n}$ and $\boldsymbol{v}$ using Eq. (9.67). The lower bound of the integration is set up by the δ-function argument:

$$k'_{\min}(\theta) = \frac{\omega}{2c}\left(\theta^2 + \gamma^{-2} + \frac{\omega_{\mathrm{pe}}^2}{\omega^2}\right). \tag{9.217}$$

The radiation intensity into the full solid angle is specified by integration of Eq. (9.216) over all possible directions of the vector $\boldsymbol{k}$. Changing the order of integration over $\mathrm{d}\theta$ and $\mathrm{d}k'$, we obtain the spectral density of the transition radiation in the form

$$I^m_{\omega} = \frac{16\pi^3 Q^2 e^4}{m^2 c^2 \omega^2} \int\limits_{k'_{\min}}^{\infty} |\delta N|^2_{\mathbf{k}'} k' \mathrm{d}k' \int\limits_0^{\theta^2_{\max}} \frac{\theta^2 \mathrm{d}\theta^2}{\left(\theta^2 + \gamma^{-2} + \frac{\omega_{\mathrm{pe}}^2}{\omega^2}\right)^2}, \tag{9.218}$$

where

$$\theta^2_{\max} = \frac{2ck'}{\omega}\left(1 - \frac{k'_{\min}}{k'}\right), \qquad k'_{\min} = \frac{\omega}{2c}\left(\gamma^{-2} + \frac{\omega_{\mathrm{pe}}^2}{\omega^2}\right). \tag{9.219}$$

Integration of Eq. (9.218) over $\mathrm{d}\theta^2$ yields the spectrum

$$I_\omega^m = \frac{16\pi^3 Q^2 e^4}{m^2 c^2 \omega^2} \int\limits_{k'_{\min}}^{\infty} |\delta N|^2_{\mathbf{k}'} \Phi\left(\frac{k'_{\min}}{k'}\right) k' \mathrm{d}k', \tag{9.220}$$

where

$$\Phi(x) = x - \ln x - 1. \tag{9.221}$$

Adopt the density inhomogeneity spectrum to have the power-law form of Eq. (9.177) with $\langle B_{\mathrm{st}}^2 \rangle \to \langle \Delta N^2 \rangle$,

$$| \delta N |^2_{\mathbf{k}} = \frac{\nu - 1}{4\pi} \frac{k_{\min}^{\nu-1} \langle \Delta N^2 \rangle}{k^{\nu+2}}, \tag{9.222}$$

where $\langle \Delta N^2 \rangle$ is the mean square of the electron density irregularities at the scales $l \le L_0 = 2\pi/k_{\min}$. Integrating Eq. (9.220) with spectrum (9.222) we find

$$I_\omega^m = \frac{4\pi^2(\nu-1)}{\nu^2(\nu+1)} \frac{Q^2 e^4 \langle \Delta N^2 \rangle k_{\min}^{\nu-1}}{m^2 c^2 \omega^2} \left(\frac{2c}{\omega}\right)^\nu \left(\gamma^{-2} + \frac{\omega_{\mathrm{pe}}^2}{\omega^2}\right)^{-\nu}. \tag{9.223}$$

Thus, the transition radiation spectrum produced by an ultrarelativistic particle moving rectilinearly through a nonrelativistic plasma with random inhomogeneities of the electron density consists of two smoothly linked power-law regions: at $\omega_{\mathrm{pe}} \ll \omega \ll \omega_{\mathrm{pe}}\gamma$ there is a flat spectral asymptote $I_\omega^m \propto \omega^{\nu-2}$, while at $\omega \gg \omega_{\mathrm{pe}}\gamma$ the spectrum falls as $I_\omega^m \propto \omega^{-\nu-2}$. In particular, this means that for $\nu > 1$ bulk of the transition radiation energy is generated around the frequencies $\sim \omega_{\mathrm{pe}}\gamma$. Integration of Eq. (9.223) around this frequency, $\omega_{\mathrm{pe}}\gamma$, yields the total radiated energy per unit time:

$$I_{\mathrm{tot}}^{\mathrm{tr}} \approx \frac{16\pi^2}{\nu(\nu+1)^2} \frac{Q^2 e^4 \langle \Delta N^2 \rangle}{\mathrm{cm}^2 \omega_{\mathrm{pe}}^2} \left(\frac{2k_0 c}{\omega_{\mathrm{pe}}}\gamma\right)^{\nu-1} \propto \gamma^{\nu-1}. \tag{9.224}$$

For the purpose of further references, we present below the transition radiation intensity valid for arbitrary particle energy, including the nonrelativistic case without emission directivity along the particle velocity (Platonov and Fleishman 2002):

$$I_\omega = \frac{4\pi^2(\nu-1)}{\nu^2(\nu+1)} \frac{e^4 Q^2 \langle \Delta N^2 \rangle k_0^{\nu-1}}{m^2 c^3} \frac{v}{k^\nu \omega^2} \frac{n(\omega)}{\varepsilon^2(\omega)} \left\{ \left(\frac{\omega}{kv} - 1\right)^{-\nu} + \frac{8\nu^3 + 8\nu^2 - 3\nu - 6}{3(\nu+2)} \left(\frac{kv}{\omega}\right)^\nu \right.$$
$$\left. - \frac{400(1.18\nu^2 - 2.17\nu + 1.18)}{3(\nu+2)} \left(\frac{kv}{\omega}\right)^{3.03\nu+1.14} \right\}. \tag{9.225}$$

It should be noted that Eqs. (9.223) and (9.225) are valid for transition radiation by the particle interacting with an ensemble of weak shock waves and/or other discontinuities. For this case we must adopt $\nu = 2$ (see Sect. 6.10), i.e., the radiation loss according to Eq. (9.224) is proportional to the fast particle energy. Then, at $\omega \ll \omega_{\rm pe}\gamma$ the radiation spectral density is constant, while at $\omega \gg \omega_{\rm pe}\gamma$, it decreases as ω^{-4}. In case of strong shocks the spectrum shape does not change much; however, the numeric factors do change.

9.6.3 Resonant Transition Radiation

Equation (9.215) diverges when $\omega \to \omega_{\rm pe}$ because $\varepsilon(\omega) \to 0$ in the denominator. The corresponding peak in the transition radiation spectrum, we call the **resonant transition radiation** (RTR) since it happens around the resonance plasma frequency. In this frequency region, however, we cannot use the ultrarelativistic approximation. Indeed, since the phase velocity of the transverse waves around $\omega_{\rm pe}$ is much larger than the speed of light so $v/v_{\rm ph} \ll 1$ for any $v < c$, then to calculate the transition radiation to the accuracy of $(v/v_{\rm ph})^2$, we can safely consider only the longitudinal electric field of the fast particles (nonrelativistic, dipole approximation) specified by the **longitudinal Green function**:

$$G^l_{ij}(\omega, \boldsymbol{k}) = -\frac{4\pi i k_i k_j}{\omega k^2 \varepsilon(\omega, \boldsymbol{k})}. \tag{9.226}$$

However, the dielectric permittivity entering the expression for this field must be treated more accurately—with the account of the spatial dispersion, $\varepsilon(\omega, \boldsymbol{k}) = \varepsilon(\omega) - 3k^2 d^2 + i\varepsilon''$. The RTR intensity then receives the form

$$I^R_{\mathbf{n},\omega} = \frac{8\pi e^4 Q^2 \varepsilon^{1/2}}{m^2 c^3} \int k'^2 {\rm d}k' \frac{[\boldsymbol{n}\boldsymbol{k}']^2 \delta[\omega - (\boldsymbol{k} - \boldsymbol{k}')\boldsymbol{v}] \mid \delta N \mid^2_{\mathbf{k}'} {\rm d}\varphi {\rm d}\cos\vartheta}{(\boldsymbol{k} - \boldsymbol{k}')^4 [(\varepsilon(\omega) - 3(\boldsymbol{k} - \boldsymbol{k}')^2 d^2)^2 + \varepsilon''^2]}, \tag{9.227}$$

where $d = v_T/\omega_{\rm pe}$ is the Debye length, while the imaginary part of the dielectric permittivity ε'' is kept to avoid divergence of the integral in Eq. (9.227). At this frequency region $\varepsilon(\omega) \ll 1$ and $k \ll k'$; thus we can discard $\boldsymbol{k}$ compared with $\boldsymbol{k}'$ everywhere except the resonant denominator. Then, it is convenient to integrate Eq. (9.227) over angles of $\boldsymbol{n}$, which yields the radiation intensity into the full solid angle (the directivity pattern approximately corresponds to a dipole):

$$I^R_\omega = \frac{32\pi^3 e^4 Q^2 \varepsilon^{1/2}}{v m^2 c^3} \int_{\omega/v}^{\infty} \frac{{\rm d}k'}{k'} \mid \delta N \mid^2_{\mathbf{k}'} \int_{-1}^{1} \frac{\sin^2\vartheta {\rm d}\cos\vartheta}{(\varepsilon(\omega) + 6kk'd^2\cos\vartheta - 3k'^2 d^2)^2 + \varepsilon''^2}, \tag{9.228}$$

where ϑ is the angle between the wave vector $\boldsymbol{k}'$ and particle velocity $\boldsymbol{v}$. To obtain Eq. (9.228) we also performed a trivial integration over the azimuth angle $\int \mathrm{d}\varphi \ldots = 2\pi$. Expansion of the integrand onto partial fractions and integration over ϑ yields

$$I_\omega^R = \frac{32\pi^3 e^4 Q^2 \varepsilon^{1/2}}{vm^2c^3} \int_{\omega/v}^{\infty} \frac{\mathrm{d}k'}{k'} \mid \delta N \mid_{\mathbf{k}'}^2 \frac{J_\vartheta}{36k^2k'^2d^4}, \tag{9.229}$$

where

$$J_\vartheta = a \ln \frac{(a+1)^2+b^2}{(a-1)^2+b^2} - 2 + \frac{1+b^2-a^2}{b} \left(\pi\Theta(1-a^2-b^2) + \arctan \frac{2b}{a^2+b^2-1} \right), \tag{9.230}$$

$$a = \frac{3k'^2d^2 - \varepsilon(\omega)}{6kk'd^2}, b = \frac{\varepsilon''}{6kk'd^2}.$$

Let us consider J_ϑ in greater detail. A nonabsorbing medium corresponds to the case of $b \to 0$. Then at $a^2 \leq 1$ the value $J_\vartheta \to \infty$ as π/b. This divergence has a simple origin: when $a^2 \leq 1$ then the condition for VCR of the plasma waves is fulfilled, so the electric field with corresponding combination of ω, $\boldsymbol{k}$, and $\boldsymbol{k}'$ is a propagating wave rather than a quasistationary field linked to the fast particle, which implies an infinitely large formation zone and, thus, is in a contradiction with the small damping approximation for any small while finite wave absorption. The transition radiation is a conversion of the *quasistationary* electric field into propagating waves; thus, the region $a^2 \leq 1$ must be removed from integration over $\mathrm{d}k'$.

In this case the function J_ϑ can be simplified by discarding $\pi\Theta(1-a^2-b^2)$ and expanding $\arctan x$ into a series for small argument at $a^2 > 1$:

$$J_\vartheta = \left\{ a \ln \frac{(a+1)^2+b^2}{(a-1)^2+b^2} - 4 \right\} \Theta(a^2-1). \tag{9.231}$$

J_ϑ still has a singularity at $b \to 0$, $a^2 \to 1$; however, this singularity is integrable. This can easily be shown if we expand J_ϑ in powers of $1/a$, which converges within $1/|a| < 1$. Retaining only the first nonvanishing term of this expansion

$$J_\vartheta \simeq \frac{4}{3a^2} \Theta(a^2-1) \tag{9.232}$$

ensures the accuracy with an error less than 30%. Substituting Eq. (9.232) into Eq. (9.229) and introducing a dimensionless variable $\mu = k'v/\omega$, we obtain the RTR spectrum in the form

$$I_\omega^R = \frac{32\pi^2(\nu-1)}{27} \frac{e^4 Q^2 \varepsilon^{1/2}}{vm^2c^3} k_0^{\nu-1} \langle \Delta N^2 \rangle \left(\frac{v}{\omega} \right)^{\nu+2} \left(\frac{v}{\omega d} \right)^4 \int_1^\infty \frac{\mathrm{d}\mu \Theta(a^2-1)}{\mu^{\nu+3}(\mu^2-\alpha)^2}, \tag{9.233}$$

where

$$\alpha = \frac{\varepsilon}{3}\left(\frac{v}{\omega d}\right)^2 \approx \frac{\varepsilon}{3}\left(\frac{v}{v_T}\right)^2, \tag{9.234}$$

v_T is the thermal velocity of the plasma electrons. For an arbitrary spectral index value ν the integral in Eq. (9.233) is taken via a hypergeometric function. In fact, the dependence of the spectrum of the spectral index is minor in this restricted range of the frequencies; thus, one can use a result of analytical integration of Eq. (9.233) available for ν=2 in the class of elementary functions.

Introducing a function $F(\alpha)$ as

$$F(\alpha) \equiv \frac{(\nu+2)\varepsilon^{1/2}}{9}\left(\frac{v}{\omega d}\right)^4 \int_1^\infty \frac{\mathrm{d}\mu\Theta(a^2-1)}{\mu^{\nu+3}(\mu^2-\alpha)^2}, \tag{9.235}$$

and taking the integral for ν=2, we obtain

$$\begin{aligned} F(\alpha) \;=\; & 2\varepsilon^{-3/2}\Bigg\{\frac{1}{\alpha}\left[\frac{1}{1-\alpha}+2+\frac{\alpha}{2}+\frac{3}{\alpha}\ln(1-\alpha)\right]\Theta(\omega_1-\omega) \\ & +\frac{1}{\alpha^2}\frac{c}{2\cdot 3^{0.5}v_T}\left[1-\frac{6\cdot 3^{0.5}v_T}{c}\ln\frac{c}{2\cdot 3^{0.5}v_T}+\frac{5\cdot 3^{1/2}v_T}{c}\right]\Theta(\omega-\omega_1)\Theta(\omega_2-\omega) \\ & +\left\{\frac{1}{\alpha^2}\frac{c}{3^{0.5}v_T}+\frac{1}{\alpha}\left[\frac{1}{1-\alpha}+2+\frac{\alpha}{2}+\frac{3}{\alpha}\ln(\alpha-1)\right]\right\}\Theta(\omega-\omega_2)\Bigg\}. \end{aligned} \tag{9.236}$$

where

$$\omega_{1,2} = \omega_{\mathrm{pe}}\left[1+\frac{3}{2}\left(\frac{v_T}{v}\right)^2\left(1\mp\frac{2\cdot 3^{0.5}v_T}{c}\right)\right]. \tag{9.237}$$

At high frequencies $\omega \gg \omega_{\mathrm{pe}}$, $\alpha \gg 1$ we have $F(\alpha) \approx \varepsilon^{-3/2}(\omega)$ so Eq. (9.236) merges smoothly to the higher-frequency spectrum of transition radiation, Eq. (9.225). Therefore, the transition radiation spectrum valid at all frequencies, $\omega \geq \omega_{\mathrm{pe}}$, is obtained by replacing $\varepsilon^{-3/2} \to F(\alpha)$ in Eq. (9.225), which yields around the spectrum peak:

$$I_\omega^{\mathrm{RTR}} = \frac{32\pi^2(\nu-1)}{3(\nu+2)}\frac{e^4Q^2\left\langle\Delta N^2\right\rangle k_0^{\nu-1}}{c^3m^2\omega^{\nu+2}}F(\alpha)v^{\nu+1}. \tag{9.238}$$

Apparently, at high frequencies, $\omega \gg \omega_{\mathrm{pe}}$, the spatial dispersion plays no role and so $F(\alpha) \approx \varepsilon^{-3/2} \approx 1$, at low frequencies, $\alpha \ll 1, F(\alpha) \approx (\varepsilon^{1/2}/18)(v/v_T)^4 \propto (\omega-\omega_{\mathrm{pe}})^{1/2}$, while at the spectrum peak region $\alpha \approx 1$ and $F(\alpha) \sim v^3c/v_T^4$.

Figure 9.16 displays the function $F(\alpha)$, specifying the RTR spectrum plotted by analytical formulae (9.236) for $\nu = 2$ and by a numeric integration of Eq. (9.235) for various ν. One can note that the peak of the analytical

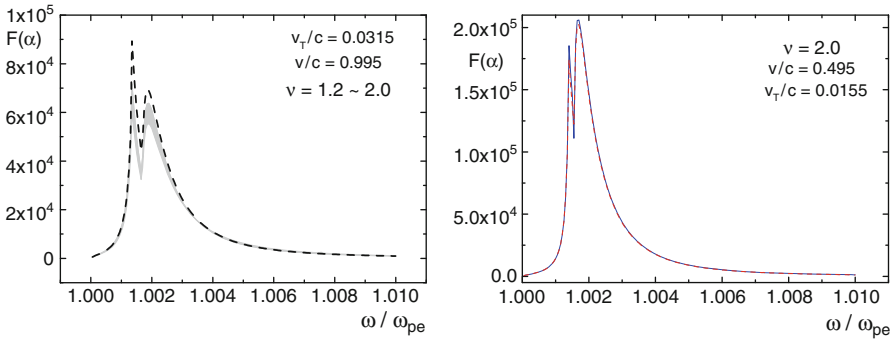

Figure 9.16: *Left*: function $F(\alpha)$ plotted using analytical formula at $\nu = 2$ (*dashed curve*) and numerical integration for various values $\nu = 1.2 - 2$ (*grey region*). The bottom bound of this region corresponds to $\nu = 1.2$, while the upper bound—to $\nu = 2$. The numerically obtained curves are systematically lower than the analytical curve. *Right*: $F(\alpha)$, analytically (*thin solid curve*) and numerically (*thick dashed curve*) computed for $\nu = 2$ in a cold plasma with $v_T/c = 0.0155$. Apparently, the departure between the analytical and numerical curves decreases for smaller v_T/c.

function always exceeds those of the numerical curves. The deviation between the numerical and analytical curves plotted for $\nu = 2$ in Fig. 9.16 is related to the assumption $v_T/c \ll 1$, made to derive Eq. (9.236). Since v_T/c enters together with numeric factors of $(2-6) \times \sqrt{3}$, then, for adopted $v_T/c \approx 0.03$ in Fig. 9.16, the corresponding error is about 20–30%. For smaller v_T/c the curves match each other very well, Fig. 9.16, right.

Let us calculate now the full power generated by the resonant transition mechanism. Integrating spectrum (9.238), valid around $\omega_{\rm pe}$ for particles with arbitrary energy, over frequency, we obtain

$$I^R_{\rm tot} = \frac{64\pi^2(\nu-1)}{45(\nu+2)} \frac{e^4 Q^2 \left\langle \Delta N^2 \right\rangle k_0^{\nu-1}}{c^3 m^2} \left(\frac{v}{\omega_{\rm pe}} \right)^{\nu+1} \frac{vc}{v_T^2}. \qquad (9.239)$$

Comparison of Eq. (9.239) with energy produced at high frequencies (9.224) shows that for particles with $\gamma < c^2/v_T^2$ the RTR produces more power than the standard transition radiation, while for $\gamma > c^2/v_T^2$ bulk of the power is generated at the frequencies $\omega_m \sim \omega_{\rm pe}\gamma > \omega_{\rm pe} c^2/v_T^2$.

If the fast charged particle moves in a gradually nonuniform plasma (with a distribution over plasma frequencies $\Phi(\omega_{\rm pe})$), then the radiation at a given frequency ω is primarily formed by the plasma spatial regions where $\omega_{\rm pe} \approx \omega$. RTR from a small part of such nonuniform sources can be approximated as

$$I^R_\omega = \frac{64\pi^2(\nu-1)}{45(\nu+2)} \frac{e^4 Q^2 \left\langle \Delta N^2 \right\rangle k_0^{\nu-1}}{c^3 m^2} \left(\frac{v}{\omega_{\rm pe}} \right)^{\nu+1} \frac{vc}{v_T^2} \delta(\omega - \omega_{\rm pe}), \qquad (9.240)$$

which yet must be convolved with the function $\Phi(\omega_{\rm pe})$.

The RTR power produced by a fast particle ensemble is obtained by integration of Eq. (9.240) with the particle spectrum. For example, for a power law over momentum modulus with index ξ and $1 < \xi < \nu + 3$ we have

$$P_\omega^R = \frac{2(\nu-1)}{45(\nu+2)} \frac{(\xi-1)\Gamma(\frac{\xi-1}{2})\Gamma\left(\frac{\nu-\xi+3}{2}\right)}{\Gamma\left(\frac{\nu+2}{2}\right)} \frac{e^2}{c} x_0^{\xi-1} N_e \omega_{\rm pe}^2 \frac{\langle \Delta N^2 \rangle}{N^2} \left(\frac{k_{\min} c}{\omega_{\rm pe}}\right)^{\nu-1} \frac{c^2}{v_T^2} \delta(\omega - \omega_{\rm pe}). \tag{9.241}$$

Here the bulk contribution comes from mildly relativistic particles with $E_{kin} \sim mc^2$.

Note that the presence of even a relatively weak magnetic field in the plasma with $\omega_{\rm Be} \ll \omega_{\rm pe}$ can strongly affect the RTR spectrum because it depends on structure of the plasma resonance and also on the refractive index behavior around the mode cutoff frequency. Since the full consideration of the RTR in magnetic field is very cumbersome and lengthy we give here a brief summary only. Formally, the presence of magnetic field requires a substitution $F(\alpha) \to n_\sigma \Phi(\alpha, \beta)$, where the magnetic field effect is described by the refractive index and new parameter $\beta = (\omega_{\rm Be}^2/3\omega_{\rm pe}^2)(v/v_T)^2$ (must not be mixed with dimensionless velocity β used elsewhere). The corresponding spectra are given in Fig. 9.17; one can see that the magnetic field gives rise to a significant suppression of the RTR, which leads to a reduction of the total radiated energy compared with Eq. (9.240). On top of that, the emission can be now strongly polarized in the sense of O-mode. The total (integrated over the peak) RTR power per unit solid angle in O-mode is

$$I_{\mathbf{n}}^o = \frac{\pi^2(\nu-1)}{2(\nu+2)} \frac{(1+\cos^2\theta)}{2^{3/2} \cdot 3^{1/4}} \frac{e^4 Q^2 \langle \Delta N^2 \rangle k_0^{\nu-1}}{c^3 m^2} \left(\frac{v}{\omega_{\rm pe}}\right)^{\nu+1} \left(\frac{c}{v_T}\right)^{1/2} \frac{\omega_{\rm pe}}{\omega_{\rm Be}}, \tag{9.242}$$

if $2\sqrt{3} v_T/c < \beta < 1$ and

$$I_{\mathbf{n}}^o = \frac{2^{1/2}\pi^2(\nu-1)}{(\nu+2)} \frac{(1+\cos^2\theta)}{9 \cdot 3^{1/2}} \frac{e^4 Q^2 \langle \Delta N^2 \rangle k_0^{\nu-1}}{c^3 m^2} \left(\frac{v}{\omega_{\rm pe}}\right)^{\nu+1} \left(\frac{\omega_{\rm pe}}{\omega_{\rm Be}}\right)^{1/2} \left(\frac{cv}{v_T^2}\right)^{1/2} \tag{9.243}$$

if $\beta > 1$ ($\omega_{\rm Be}/\omega_{\rm pe} > \sqrt{3} v_T/v$). For the extraordinary mode the total intensity $I_{\mathbf{n}}^x$ is defined by Eq. (9.242) if $\beta > 2\sqrt{3} v_T/c$ and additionally $v > v_T\sqrt{3\omega_{\rm pe}/\omega_{\rm Be}}$; RTR is weakly polarized in this case. Alternatively, if $\beta < 2\sqrt{3} v_T/c$ or $v < v_T\sqrt{3\omega_{\rm pe}/\omega_{\rm Be}}$, the X-mode intensity is strongly suppressed and emission is highly polarized in the sense of O-mode. Presented equations are sufficient to estimate RTR from a gradually nonuniform magnetized plasmas by using the following approximate expression for the RTR spectrum:

$$I_{\mathbf{n},\omega}^{R,\sigma} = I_{\mathbf{n}}^\sigma \delta(\omega - \omega_*), \tag{9.244}$$

where ω_* corresponds to a local spectrum peak, which is slightly above the local plasma frequency.

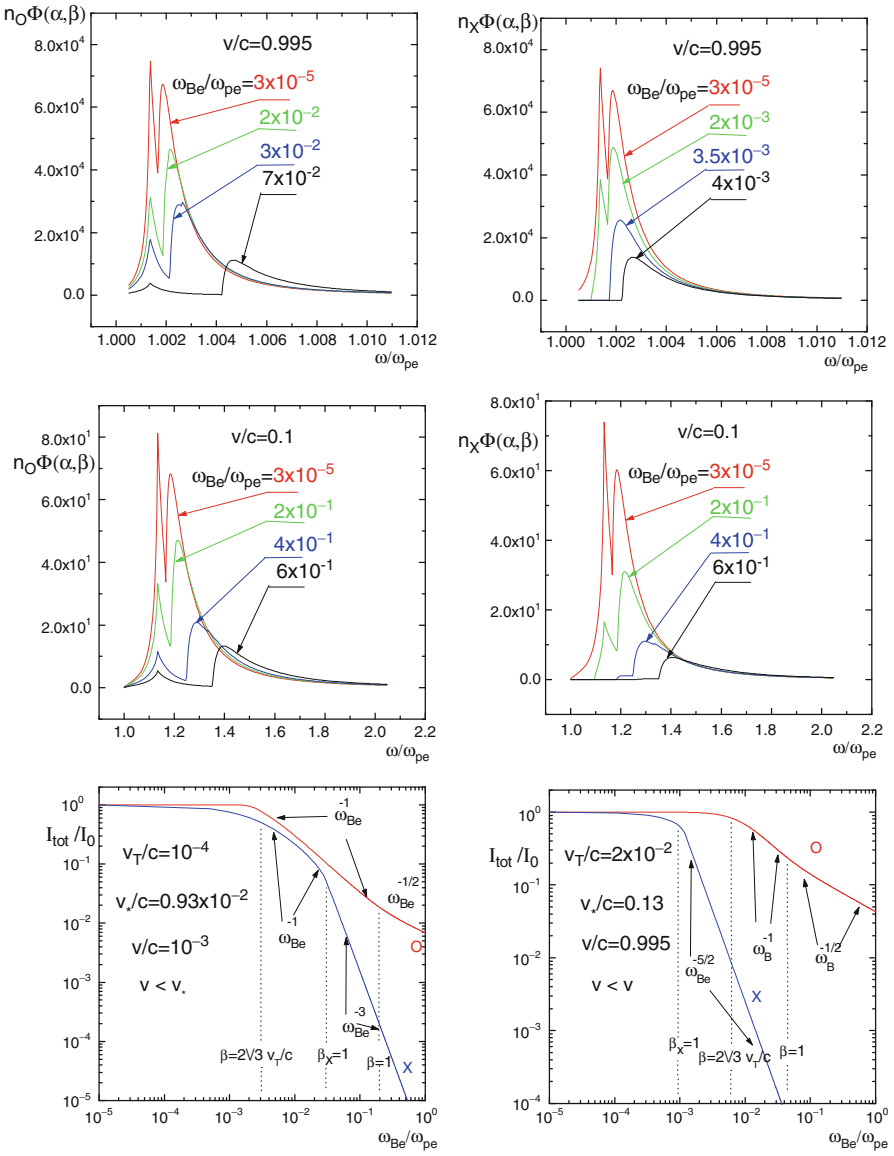

Figure 9.17: Spectra of RTR of O- and X-wave modes in a magnetized plasma with $v_T/c = 0.0315$. For relatively faster emitting particles (*upper panels*) the magnetic field increase results initially in suppression of X-mode radiation and only later to a suppression (and shift to the right) of the peak in the O-mode spectrum. For slower particles (*middle panels*) the spectra are originally broader and the O and X spectra are more similar to each other than in case of faster particles, although the suppression of X-wave radiation is still stronger than that of O-mode. The *lower panels* show how the total (integrated over all frequencies) radiation intensity changes with the magnetic field for a "slow" (*left*) and "fast" (*right*) particles. I_0 is the total intensity in the absence of the magnetic field. At $\beta_x < 1$, the curves for X- and O-modes are similar to each other (the degree of polarization does not exceed 50%), while at $\beta_x > 1$ the X-mode intensity drops rapidly so the radiation becomes almost fully (100%) polarized.

9.6.4 RTR in Astrophysics

As we have seen the transition radiation including the RTR requires fast particle interactions with a turbulent plasma having random inhomogeneities of either plasma density or/and magnetic field—the situation highly typical for many astrophysical sources. For this radiation to be observed from Earth, however, requires additionally that the plasma density at the source is sufficiently large for the corresponding plasma frequency (defining the emission frequency) to occur at a spectral domain observable from either Earth or space. This implies that the RTR can be expected from solar/stellar coronae, interplanetary space, and planetary magnetospheres and ionospheres (Platonov and Fleishman 2002; Fleishman 2008).

Here we give only one example of RTR produced in a continuum burst of decimeter radio emission from a solar flare (Nita et al. 2005). Figure 9.18, upper panel, presents dynamic spectra of the 2001 April 06 solar radio burst in intensity (top) and circular polarization (bottom), observed with OVSA. The RTR occurs at a restricted range of time and frequency shown by the bright red region in the polarization panel, which represents highly right-hand circularly polarized (RCP) emission. Two other panels of Fig. 9.18 present spatial association of the RTR radio source with (1) the accompanying gyrosynchrotron source (see Sect. 10.2 for greater detail on the GS bursts), (2) a dense soft X-ray loop, and (3) the underlying magnetic field structure, confirming the presence of all expected relationships between RTR and other data.

Indeed, as seen in Fig. 9.18, top, the RTR forms a distinct, low-frequency spectral component relative to the higher-frequency gyrosynchrotron component. Both spectral components are smooth in time and frequency, with comparable timescales, with the main difference being that the gyrosynchrotron component is delayed with respect to the RTR component, as expected for emissions produced by high-energy and low-energy electrons, respectively.

Both the RTR (2 GHz) and gyrosynchrotron (7.4 GHz) sources arise in or near a very dense loop. The brightness temperatures (see Sect. 10.1.5 for the definitions) derived from the radio maps, averaged over the pixels lying inside the 85% 2 GHz contour, are 1.5×10^9 K, at 2 GHz, and 4×10^8 K, at 7.4 GHz. The electron temperature inferred from SXT data (Fig. 9.18, right), averaged over the same region, is 2×10^7 K, while the average emission measure corresponding to one pixel (2.5×2.5 arcsec) is 5.6×10^{48} cm^{-3}. Assuming a line of sight length of about 25 arcsec, which roughly equals the projected loop width, we obtain an estimate for the plasma density in the region of interest as 3×10^{11} cm^{-3}. This value directly confirms the existence of a high plasma density in the flaring region, which agrees with indications of the Razin effect (see Sect. 9.4.2), found independently from the microwave GS spectral component. The RTR peak frequency of 2 GHz implies, from the electron plasma frequency $f_{\rm pe} = 9 \times 10^3 \sqrt{n}$ Hz, an electron density of 5×10^{10} cm^{-3} that is small compared with 3×10^{11} cm^{-3} derived above for the underlying soft X-ray loop. Note that the X-ray-derived density demonstrates the presence

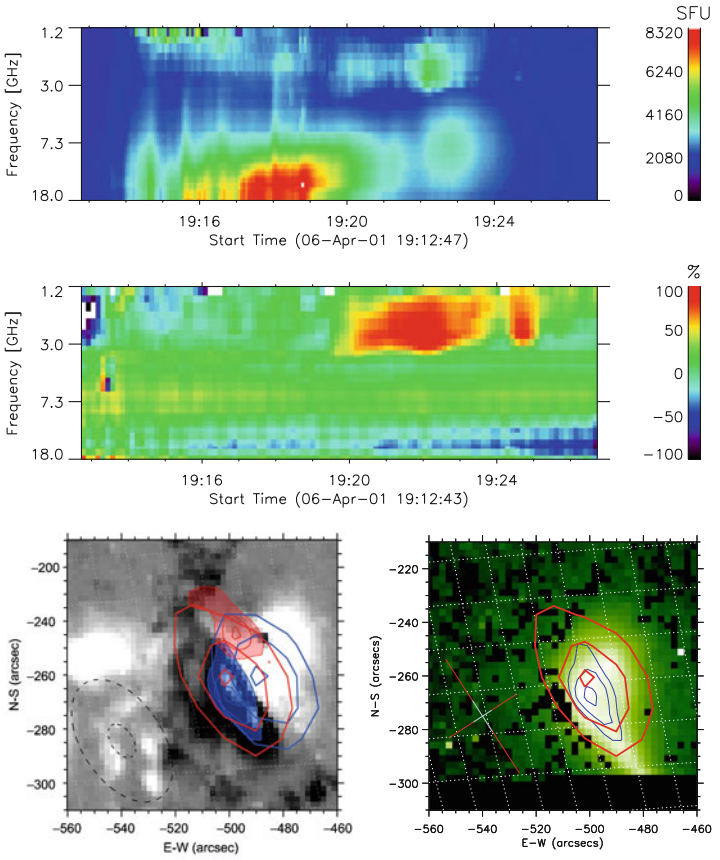

Figure 9.18: 2001 April 06 after 19:12 UT. Total power (*top*) and polarization (*second panel*) dynamic spectra recorded by OVSA with 4 s and 8 s time resolution, respectively, at 40 frequencies in the [1.2–18] GHz range. The period of RTR is the highly polarized (*red*) emission in the *second panel*. Two spectral components are visible in the *upper panel* during this time: the low-frequency RTR component, which peaks at 19:22:11 UT (3700 sfu at 2 GHz), and the delayed high-frequency GS component, which peaks at 19:22:51 UT (2300 sfu at 7.4 GHz). *Bottom panel:* OVSA radio maps (19:22:03 UT) overlaid on the SOHO/MDI magnetogram (19:22:02 UT). The radio contours, representing 55, 75, and 95% of the maximum intensity, are scaled separately for each frequency and polarization: the RCP (*red contours*) and LCP (*blue contours*) at 2 GHz (*unfilled contours*) and 7.4 GHz (*filled contours*). Within the instrumental resolution (see the corresponding beam sizes shown by *dashed ovals*), the 2 GHz RCP source (*red, unfilled contour*) is colocated with the 7.4 GHz LCP GS source (*blue, filled contour*) in the negative magnetic field region. Thus, both low- and high-frequency emissions are likely produced by the same population of electrons traveling along the same magnetic loop. Remarkably, for both frequencies, the *intrinsic* degrees of polarization implied by the radio maps are noticeably larger than those suggested by the unresolved polarization spectrum presented in the *second panel*. *Right bottom panel:* OVSA radio maps of the dominant polarization (19:22:03 UT) as in the *left bottom panel*, overlaid on the emission

of high densities in the region, while the lower radio-derived density (presumably, from higher coronal levels) is expected since the 2 GHz radio emission will come primarily from overlying, less-dense regions due to significant free–free absorption in the higher-density regions.

Figure 9.18, bottom, shows that the RTR and gyrosynchrotron sources are co-spatial. This co-spatiality is highly conclusive in favor of RTR, since having truly separate spectral components requires either completely different source locations or different mechanisms or both. Distinct spectral components having the *same source location* are a strong indicator that each component is produced by *a different emission mechanism* and the RTR is one of very few known emission mechanisms capable of producing a low-frequency (compared with GSR) diffuse emission.

Figure 9.18 shows that the RTR emission is strongly polarized in the sense of the O-mode, as required (see Sect. 9.6.3), while the gyrosynchrotron emission is X-mode. Indeed, the radio maps at 7.4 GHz in Fig. 9.18, middle, (filled contours) reveal RCP (red) overlying positive (white) magnetic polarity and LCP (blue) overlying negative (black) polarity, located on opposite sides of the neutral line. This clearly shows a relatively high degree of X-mode polarization of both 7.4 GHz radio sources. At 2 GHz (unfilled contours), exactly the opposite spatial correspondence is seen, with RCP (red) overlying negative magnetic polarity and LCP (blue) overlying positive polarity. This clearly shows a high degree of O-mode polarization for the RTR spectral component.

The importance of the RTR detection from a cosmic source is several fold. First, RTR is confirmed as another continuum emission mechanism in astrophysical plasmas, among only a small number of others: gyrosynchrotron/synchrotron emission, DSR, bremsstrahlung, and inverse Compton emission. Second, with new radio facilities in development that are capable of simultaneous spatial and spectral measurements of solar bursts (e.g., at the time of writing Expanded VLA, Expanded OVSA, and planned Frequency Agile Solar Radiotelescope, FASR), RTR can be routinely recognized and used as a diagnostic of the plasma density, the low energy part of the electron energy distribution, and of the presence and quantitative level of microturbulence: in this event, for example, the level of inhomogeneities derived from the RTR flux, which can be estimated with equations given in Sect. 9.6.3, is $\langle \Delta n^2 \rangle / n^2 \sim 10^{-5}$.

Figure 9.18: (continued.) measure (EM) map derived from the Yohkoh/SXT instrument (19:22:00 UT) using data obtained with two different filters (Be119 and Al12). The EM map reveals the existence of a magnetic loop or arcade of loops filled with hot and dense plasma, which is consistent with the magnetic and radio topology presented in the *left bottom panel*. The 2 GHz RCP radio source and the 7.4 GHz LCP kernel are well aligned with the most dense section of the loop (Nita et al. 2005). Reproduced by permission of the AAS.

Problems

9.1 Derive expressions for radiated energy produced by a single charged particle moving along a given trajectory using Eqs. (9.46), (9.47), and (9.49).

9.2 Calculate spectral and angular distribution of the VCR energy produced by a charged particle moving rectilinearly in an anisotropic and gyrotropic medium with a given dielectric tensor $\varepsilon_{\alpha\beta}$. Consider different eigenmodes including longitudinal modes and hot plasma modes.

9.3 Calculate DSR spectrum produced by a nonrelativistic particle moving in a random magnetic field.

9.4 Calculate bremsstrahlung spectrum produced by a nonrelativistic particle moving in a fully ionized hydrogen plasma in a weak magnetic field, $\omega_{\mathrm{Be}} \ll \omega_{\mathrm{pe}}$.

9.5 Calculate RTR produced due to random magnetic inhomogeneities.

Answers and Solutions

9.1 Hint: Use electric current produced by a single particle, described by Eq. (9.51). For example, substitution of Eq. (9.51) into Eq. (9.46) yields

$$\mathcal{E}^{\sigma}_{\mathbf{n},\omega} = \frac{Q^2\omega^2 n_\sigma(\omega)}{4\pi^2 c^3} Re \int\limits_{-T}^{T} \mathrm{d}t \int\limits_{0}^{\infty} \mathrm{d}\tau e^{i\omega\tau} e^{-i\mathbf{k}[\mathbf{r}(t+\tau)-\mathbf{r}(t)]} (\boldsymbol{e}^*_\sigma \cdot \boldsymbol{v}(t+\tau))(\boldsymbol{e}_\sigma \cdot \boldsymbol{v}(t)), \tag{9.245}$$

while into Eq. (9.49) yields

$$\mathcal{E}_{\mathbf{n},\omega} = \frac{Q^2\omega^2 n(\omega)}{4\pi^2 c^3} Re \int\limits_{-T}^{T} \mathrm{d}t \int\limits_{0}^{\infty} \mathrm{d}\tau e^{i\omega\tau} e^{-i\mathbf{k}[\mathbf{r}(t+\tau)-\mathbf{r}(t)]} [\boldsymbol{n} \times \boldsymbol{v}(t+\tau)] \cdot [\boldsymbol{n} \times \boldsymbol{v}(t)]. \tag{9.246}$$

9.3 In the nonrelativistic case $v/c \ll 1$ ($\gamma \equiv \sqrt{1 - v^2/c^2} \approx 1$) and $\omega' \approx \omega$, Eq. (9.66) can be written in the form

$$\mathcal{E}_{\mathbf{n},\omega} = \sqrt{\varepsilon} \frac{Q^2}{c^3} \left| [\boldsymbol{n} \times \boldsymbol{w}_\omega] \right|^2, \tag{9.247}$$

where Q is the particle charge and $\boldsymbol{n}$ is the unit wave vector of the radiation. Equation (9.247) shows that the radiation in a given direction $\boldsymbol{n}$ is defined by the acceleration component $|\boldsymbol{w}_{\omega\perp}|^2 = |[\boldsymbol{n} \times \boldsymbol{w}_\omega]|^2$ transverse to $\boldsymbol{n}$, which,

similarly to the derivation in ultrarelativistic case, Sect. 9.2.3, can be expressed via temporal and spatial Fourier transform of the external Lorentz force, $F^{\alpha}_{q_0,\mathbf{q}}$:

$$\mid \boldsymbol{w}_{\omega\perp} \mid^2 = \frac{(2\pi)^3}{M^2 V} \int \mathrm{d}q_0 \mathrm{d}\boldsymbol{q} \delta(\omega - q_0 + \boldsymbol{q}\boldsymbol{v})(\delta_{\alpha\beta} - n_\alpha n_\beta) F^{\alpha}_{q_0,\mathbf{q}} F^{\beta *}_{q_0,\mathbf{q}}, \quad (9.248)$$

where M is the mass of emitting particle and V is the source volume.

For electric component of the Lorentz force $\boldsymbol{F} = Q\boldsymbol{E}$ we have

$$(\delta_{\alpha\beta} - n_\alpha n_\beta) F^{\alpha}_{q_0,\mathbf{q}} F^{\beta *}_{q_0,\mathbf{q}} = Q^2 (\delta_{\alpha\beta} - n_\alpha n_\beta) E^{\alpha}_{q_0,\mathbf{q}} E^{\beta *}_{q_0,\mathbf{q}}, \quad (9.249)$$

where

$$E^{\alpha}_{q_0,\mathbf{q}} E^{\beta *}_{q_0,\mathbf{q}} = \frac{TV}{(2\pi)^4} K_{\alpha\beta}(q_0, \boldsymbol{q}), \quad (9.250)$$

$K_{\alpha\beta}(q_0, \boldsymbol{q})$ is the correlation tensor of the random electric field, such as $\int \mathrm{d}q_0 \mathrm{d}\boldsymbol{q} K_{\alpha\alpha}(q_0, \boldsymbol{q}) = \left\langle E^2_{st} \right\rangle$ (Sect. 7.4).

For magnetic component of the Lorentz force the corresponding expression is different:

$$\begin{aligned} (\delta_{\alpha\beta} - n_\alpha n_\beta) F^{\alpha}_{q_0,\mathbf{q}} F^{\beta *}_{q_0,\mathbf{q}} &= \frac{Q^2}{c^2} \left(v^2 \delta_{\alpha\beta} - v_\alpha v_\beta - [\boldsymbol{n} \times \boldsymbol{v}]_\alpha [\boldsymbol{n} \times \boldsymbol{v}]_\beta \right) B^{\alpha}_{q_0,\mathbf{q}} B^{\beta *}_{q_0,\mathbf{q}} \\ &= Q^2 \frac{v^2}{c^2} \left(n_\alpha n_\beta + \frac{(\boldsymbol{n}\boldsymbol{v})^2}{v^2} \delta_{\alpha\beta} - (\boldsymbol{n}\boldsymbol{v}) \frac{v_\alpha n_\beta + n_\alpha v_\beta}{v^2} \right) B^{\alpha}_{q_0,\mathbf{q}} B^{\beta *}_{q_0,\mathbf{q}}, \end{aligned} \quad (9.251)$$

where the correlation tensor defined by Eq. (9.89) can be used, which yields the DSR intensity, $I_{\mathbf{n},\omega} = \mathcal{E}_{\mathbf{n},\omega}/T$, of a nonrelativistic particle in the presence of random magnetic field:

$$I_{\mathbf{n},\omega} = \sqrt{\varepsilon} \frac{Q^4 v^2}{2\pi M^2 c^5} \int \mathrm{d}q_0 \mathrm{d}\boldsymbol{q} \delta(\omega - q_0 + \boldsymbol{q}\boldsymbol{v}) \left(n_\alpha n_\beta + \frac{(\boldsymbol{n}\boldsymbol{v})^2}{v^2} \delta_{\alpha\beta} - (\boldsymbol{n}\boldsymbol{v}) \frac{v_\alpha n_\beta + n_\alpha v_\beta}{v^2} \right) T_{\alpha\beta}(q_0, \boldsymbol{q}). \quad (9.252)$$

This expression is valid for arbitrary spectrum of magnetic turbulence including anisotropic distributions.

We consider here the DSR produced by accelerated nonrelativistic electrons interacting with the MHD turbulence. In MHD waves $E \sim (v_\mathrm{A}/c)B$, where v_A is the Alfvén speed, Eq. (2.53); therefore the magnetic part of the Lorentz force is larger than the electric part for all electrons with $v > v_\mathrm{A}$. Assuming this condition to be fulfilled, we calculate only the DSR related to the magnetic field of the MHD turbulence; inclusion of electric field effect will further increase the DSR intensity.

Since we are interested in overall spectral shapes and flux level of the DSR, rather than model-dependent details of the emission, we consider here the simplest case of the isotropic MHD turbulence:

$$T_{\alpha\beta} = \frac{1}{2} \left(\delta_{\alpha\beta} - \frac{q_\alpha q_\beta}{q^2} \right) T(\boldsymbol{q}) \delta(q_0 - q_0(\boldsymbol{q})). \quad (9.253)$$

As we assumed $v > v_{\rm A}$, i.e., the electrons move faster than the waves, we can adopt the MHD turbulence to be quasi-static, $q_0(\mathbf{q}) = 0$. When the MHD turbulence is isotropic, the accelerated electrons are isotropic as well, and so the radiation produced is also isotropic. Thus, we consider further the radiation produced into the full solid angle:

$$I_\omega = \int I_{\mathbf{n},\omega} \mathrm{d}\Omega = \sqrt{\varepsilon} \frac{8Q^2}{3\pi c} \cdot q(\omega), \tag{9.254}$$

where, like in the ultrarelativistic case, Sect. 9.2.3, we introduce the scattering rate of the nonrelativistic particle by MHD turbulence $q(\omega)$:

$$q(\omega) = \frac{\pi}{4} \left(\frac{Q}{Mc} \right)^2 \frac{v^2}{c^2} \int T(\boldsymbol{q}) \delta(\omega + \boldsymbol{q}\boldsymbol{v}) \, \mathrm{d}\boldsymbol{q}, \tag{9.255}$$

which contains a small factor v^2/c^2 compared with Eq. (9.176).

To proceed further we adopt the turbulence spectrum to have a single power law down to the smallest (resonant to thermal electrons) scales, Eq. (9.177). Then, substituting Eq. (9.177) into Eq. (9.255), integrating over $\mathrm{d}\boldsymbol{q}$,

$$\begin{aligned} \int \mathrm{d}\boldsymbol{q} T(\boldsymbol{q}) \delta(\omega + \boldsymbol{q}\boldsymbol{v}) &= 2\pi \int \mathrm{d}\cos\theta \cdot \mathrm{d}q \frac{A_\nu}{q^\nu} \delta(\omega + qv\cos\theta) = \frac{2\pi A_\nu}{v} \int\limits_{\omega/v}^{\omega_{pe}/v_{Te}} \frac{\mathrm{d}q}{q^{\nu+1}} \\ &= \frac{2\pi}{\nu} \frac{A_\nu}{v} \left(\frac{v}{\omega} \right)^\nu \left(1 - \left(\frac{\omega v_{Te}}{\omega_{pe} v} \right)^\nu \right) \Theta \left(\frac{\omega_{pe}}{v_{Te}} - \frac{\omega}{v} \right) \end{aligned} \tag{9.256}$$

where

$$v_{Te} = 6.74 \times 10^5 \sqrt{T_e[\mathrm{K}]} \ [\mathrm{cm/s}] \tag{9.257}$$

is the thermal velocity of the plasma electrons, $\Theta(x)$ is the step function, and using the electron charge e and mass m for Q and M, we find

$$q(\omega) = \frac{\pi^2 A_\nu}{2\nu} \frac{e^2 v}{m^2 c^4} \left(\frac{v}{\omega} \right)^\nu \left(1 - \left(\frac{\omega v_{Te}}{\omega_{pe} v} \right)^\nu \right) \Theta \left(\frac{\omega_{pe}}{v_{Te}} - \frac{\omega}{v} \right), \tag{9.258}$$

so the DSR spectrum produced by accelerated nonrelativistic electrons reads

$$I_\omega = \frac{8e^2}{3\pi c} \sqrt{\varepsilon} \cdot q(\omega). \tag{9.259}$$

The DSR power from N electrons with a spectrum $N(E)$ has the form

$$P_\omega = \int\limits_{E_0}^{\infty} I_\omega N(E) \, \mathrm{d}E. \tag{9.260}$$

As an example, let us calculate the radio flux observed at the Earth from a source located at the Sun. We change the variable $\omega = 2\pi f$, so that $I_f = 2\pi I_\omega$, and employ known distance to the source, so

$$F_f = \frac{2\pi P_\omega V}{4\pi \mathcal{R}^2} = \frac{P_\omega L^3}{2\mathcal{R}^2} \times 10^{19}\,\mathrm{sfu}, \tag{9.261}$$

where $\mathcal{R} = 1\,\mathrm{au} = 1.49 \times 10^{13}\,\mathrm{cm}$ is the distance from the Earth to the Sun.

9.4 We use Eqs. (9.247)–(9.249) from the previous solution and express the electric field via the scalar potential, $E^{\alpha}_{q_0,\mathbf{q}} E^{\beta *}_{q_0,\mathbf{q}} = q_\alpha q_\beta |\varphi_{q_0,\mathbf{q}}|^2$, which yields

$$\mathcal{E}_{\mathbf{n},\omega} = \sqrt{\varepsilon}\frac{Q^2}{c^3}\frac{(2\pi)^3}{M^2 V}\int \mathrm{d}q_0 \mathrm{d}\boldsymbol{q}\delta(\omega - q_0 + \boldsymbol{q}\boldsymbol{v})[\boldsymbol{n}\times\boldsymbol{q}]^2 |\varphi_{q_0,\mathbf{q}}|^2. \tag{9.262}$$

The potential of randomly distributed Coulomb centers is described by Eq. (9.127); dividing Eq. (9.262) by the emission time T and taking trivial integral over $\mathrm{d}q_0 \mathrm{d}q_\parallel$ with the use of δ-functions, we obtain the spectral and angular distribution of emission per unit time

$$I_{\mathbf{n},\omega} = \sqrt{\varepsilon}\frac{Q^4 z^2 e^2 n_i}{\pi v M^2 c^3}\int\limits_0^{q_{\perp\max}} \mathrm{d}q_\perp^2 \frac{\left(\frac{\omega}{v}\right)^2 \sin^2\theta + \frac{q_\perp^2}{2}(1+\cos^2\theta)}{\left(q_\perp^2 + \left(\frac{\omega}{v}\right)^2 + R_d^{-2}\right)^2}. \tag{9.263}$$

Then, taking integrals over $\mathrm{d}q_\perp^2$ we finally obtain:

$$I_{\mathbf{n},\omega} = \sqrt{\varepsilon}\frac{Q^4 z^2 e^2 n_i}{\pi v M^2 c^3}\left\{(1+\cos^2\theta)\left[\ln\frac{q_{\perp\max} v}{\omega\sqrt{1+(\omega_{\mathrm{pe}} v/\omega v_T)^2}} - \frac{1}{2}\right] + \frac{\sin^2\theta}{1+(\omega_{\mathrm{pe}} v/\omega v_T)^2}\right\}. \tag{9.264}$$

The upper limit of the integration $q_{\perp\max}$ is specified by smallest of the two values: the radiating charge momentum Mv or $q_{\max} = 2\pi/r_{\min}$, where $r_{\min}$ is the minimal impact parameter of the collision compatible with the classical treatment of the particle motion; its exact finding requires quantum consideration. Total bremsstrahlung power radiated into the full solid angle is easy to find by integration of Eq. (9.264) over $\mathrm{d}\Omega$:

$$I_\omega = \sqrt{\varepsilon}\frac{16 Q^4 z^2 e^2 n_i}{3 v M^2 c^3}\ln\Lambda_C, \tag{9.265}$$

$$\ln\Lambda_C = \ln\frac{q_{\perp\max} v}{\omega\sqrt{1+(\omega_{\mathrm{pe}} v/\omega v_T)^2}} - \frac{(\omega_{\mathrm{pe}} v)^2}{2(\omega v_T)^2(1+(\omega_{\mathrm{pe}} v/\omega v_T)^2)}. \tag{9.266}$$

In the case of weakly magnetized plasma we have to consider emission of two eigenmodes σ (X and O). To do so we have to divide Eq. (9.264) or Eq. (9.265) by 2 and replace $\sqrt{\varepsilon}$ by n_σ. Then, considering radiation produced by electron ($Q = e$) in a hydrogen plasma ($z = 1$) we obtain for any of the eigenmodes:

$$I^\sigma_\omega = n_\sigma \frac{8 e^6 n_i}{3 v m_e^2 c^3}\ln\Lambda_C. \tag{9.267}$$

9.5 Take into account that the plasma response current in the presence of magnetic inhomogeneities is described by Eq. (9.210), which yields

$$I_{\omega}^{R} = \frac{64\pi^2(\nu-1)}{3(\nu+2)} \frac{e^6 N_0^2 Q^2}{v\omega^2 m^4 c^5} k_{\min}^{\nu-1} \left\langle \Delta B^2 \right\rangle \left(\frac{v}{\omega}\right)^{\nu+2} F(\alpha). \tag{9.268}$$

Chapter 10

Radiation Transfer

While propagating through a medium the electromagnetic radiation changes due to emission, absorption, scattering, and nonlinear wave transformations; thus, the radiation intensity, spectral distribution, polarization, and directivity can all vary in space and time. The theory of radiation transfer represents a broad field of the physics with numerous astrophysical applications (Chandrasekhar 1961; Mihalas 1978; Dolginov et al. 1979; Ginzburg 1987; Nagirner 2007a), including radiation transfer in stellar interiors, Faraday rotation in intergalactic and interstellar media, group delay in solar corona, and many more. This chapter considers the most fundamental elements of the radiation transfer theory and gives a few examples of its application to the space plasma.

10.1 Absorption of Radiation and Equation of Radiation Transfer

Let us consider radiation of an eigenmode σ leaving a source with a volume V at a given direction. In a general case the solution depends on boundary conditions; in particular, there can be a partial or full reflection of the radiation, its absorption, polarization transformation etc. To avoid explicit consideration of the boundary we can think either of radiation incident onto the inner source boundary or adopt that the refractive index does not change at the source boundary, while the absorption and scattering of the radiation are entirely unimportant outside the source.

Adopt that the emissivity (i.e., the radiation intensity from a unit volume to a given direction) is $j^{\sigma}_{\mathbf{n},\omega}(\boldsymbol{r},t)$, where dependence on $\boldsymbol{r}$ and t describes possible gradual (compared with the wavelength) and slow (compared with the wave period) variations of the emissivity, while the absorption coefficient of this radiation per unit ray path is $\varkappa^{\sigma}_{\mathbf{n},\omega}(\boldsymbol{r},t)$. Apparently, if other processes

G.D. Fleishman and I.N. Toptygin, *Cosmic Electrodynamics*, Astrophysics and Space Science Library 388, DOI 10.1007/978-1-4614-5782-4_10,

such as wave scattering and mode coupling are inessential, then the radiation intensity $J^{\sigma}_{\mathbf{n},\omega}(\boldsymbol{r},t)$ satisfies the balance equation:

$$\frac{\mathrm{d}J^{\sigma}_{\mathbf{n},\omega}(\boldsymbol{r},t)}{v_g \mathrm{d}t} = j^{\sigma}_{\mathbf{n},\omega}(\boldsymbol{r},t) - \varkappa^{\sigma}_{\mathbf{n},\omega}(\boldsymbol{r},t) J^{\sigma}_{\mathbf{n},\omega}(\boldsymbol{r},t), \tag{10.1}$$

where $\frac{\mathrm{d}}{\mathrm{d}t} = \frac{\partial}{\partial t} + \boldsymbol{v}_g \frac{\partial}{\partial \boldsymbol{r}}$ is the full derivative over time and $\boldsymbol{v}_g = \partial\omega/\partial\boldsymbol{k}$ is the group velocity of the eigenmode.

10.1.1 Equilibrium Radiation

First of all, consider a radiation in a *thermodynamic* equilibrium with a medium. In this case the radiation intensity does not depend on $\boldsymbol{r}$ or t, so the time derivative in the lhs of Eq. (10.1) vanishes, and the radiation intensity is specified according to a familiar Plank formula by the photon gas temperature only. In this case we immediately obtain **Kirchhoff's law** directly from Eq. (10.1):

$$\begin{aligned} \frac{j^{\sigma}_{\mathbf{n},\omega}}{\varkappa^{\sigma}_{\mathbf{n},\omega}} = J^{\sigma}_{\mathbf{n},\omega} = J^{0}_{\mathbf{n},\omega} &= \frac{n_\sigma^2 \hbar\omega^3}{(2\pi)^3 c^2 |\cos\theta|} \frac{1}{e^{\frac{\hbar\omega}{k_\mathrm{B}T}} - 1} \\ &= \begin{cases} \frac{n_\sigma^2 \omega^2}{(2\pi)^3 c^2 |\cos\theta|} k_\mathrm{B} T, & \text{for} \quad \hbar\omega \ll k_\mathrm{B}T \\ \\ \frac{\hbar\omega^3}{(2\pi)^3 c^2} e^{-\frac{\hbar\omega}{k_\mathrm{B}T}}, & \text{for} \quad \hbar\omega \gg k_\mathrm{B}T \end{cases}, \end{aligned} \tag{10.2}$$

where $|\cos\theta| = \frac{c}{v_g} |\frac{\partial(\omega n_\sigma)}{\partial\omega}|^{-1}$, θ is the angle between the wave vector and group velocity $\boldsymbol{v}_g$ vector; the effect of plasma dispersion (factors n_σ^2 and $|\cos\theta|$) can be essential at low frequencies (in the **Rayleigh–Jeans regime**), while at the high-frequency asymptote (the **Wien regime**) we neglected this effect entirely. This equation allows to draw a highly important conclusion: since the rhs does not depend on the medium properties then the lhs does not depend either. Stated another way, although the emissivities and the absorption coefficients along are different for different substances, their ratio is a universal function for any *thermodynamically equilibrium* medium having same temperature.

Let us consider as an example the emission and absorption coefficients of the **free–free emission**, i.e., of Bremsstrahlung produced by a nonrelativistic thermal electron population described by the Maxwellian distribution function $f_e(\boldsymbol{p})$ given by Eq. (1.64) with $\boldsymbol{u}^{(b)} = 0$ and $T(\boldsymbol{r},t) = \mathrm{const}$, or, equivalently, Eq. (3.58) for $f_e(\boldsymbol{v})$. Then, the emissivity is determined by integration of the bremsstrahlung spectral and angular distribution with the Maxwellian distribution:

$$j^{\sigma}_{f,\mathrm{ff}} = 2\pi j^{\sigma}_{\omega,\mathrm{ff}} = 2\pi \int I^{\sigma}_{\mathbf{n},\omega} f_e(\boldsymbol{p}) \mathrm{d}\boldsymbol{p}, \tag{10.3}$$

where $I^{\sigma}_{\mathbf{n},\omega}$ is given by Eq. (9.264) divided by 2 (for one eigenmode), where n_σ is used for $\sqrt{\varepsilon}$. Neglecting weak dependence of the Coulomb logarithm $\ln\Lambda_C$ on the electron velocity, while taking into account the main functional dependence $I^{\sigma}_{\mathbf{n},\omega} \propto v^{-1}$, the integration in Eq. (10.3) is extremely simple: $\int \exp(-p^2/(2m_eT))p\mathrm{d}p = m_eT$, which yields

$$j^{\sigma}_{f,\mathrm{ff}} = \frac{8n_\sigma z^2 e^6 n_i n_e}{3(2\pi)^{3/2} m^{3/2} (k_\mathrm{B}T)^{1/2} c^3} \ln\Lambda_C, \tag{10.4}$$

where we express the plasma temperature in K; k_B is the Boltzmann constant. Now, it is straightforward to find the corresponding absorption coefficient using Kirchhoff's law and Eq. (10.2) and making transformation to usual frequency $f = \omega/2\pi$ (we also adopt $|\cos\theta| = 1$ assuming the magnetic field is weak; see, however, Problem 10.1):

$$\varkappa^{\sigma}_{\mathrm{ff}} = \frac{8}{3(2\pi)^{1/2}} \frac{z^2 e^6 n_i n_e}{n_\sigma c f^2 (m k_\mathrm{B} T)^{3/2}} \ln\Lambda_C, \tag{10.5}$$

where

$$\ln\Lambda_C = \begin{cases} 18.2 + \ln(T^{3/2}/f), & T < 2\times 10^5\,\mathrm{K} \\ 24.5 + \ln(T/f), & T > 2\times 10^5\,\mathrm{K} \end{cases} \tag{10.6}$$

and f is measured in Hz. It is easy to check that absorption coefficient Eq. (10.6) coincides with that determined in Sect. 3.4, Eq. (3.97), from the dielectric tensor of collisional plasma.

Note that if we redefine $j^{\sigma}_{\mathbf{n},\omega}$ to describe a *surface* (rather than *volume*) emissivity and accordingly $\varkappa^{\sigma}_{\mathbf{n},\omega}$ to describe the absorption coefficient by this *surface*, then for $\varkappa^{\sigma}_{\mathbf{n},\omega} = 1$ Eq. (10.2) yields the blackbody radiation law:

$$j^{\sigma}_{\mathbf{n},\omega} = J^{0}_{\mathbf{n},\omega}, \tag{10.7}$$

i.e., the blackbody emissivity is specified by the universal function $J^{0}_{\mathbf{n},\omega}$, which depends on one measure of this black body only—its temperature T and on the frequency ω. The fact that Kirchhoff's law has been comprehensively proved experimentally implies that thermodynamic equilibrium between medium and radiation is, in principle, accessible.

10.1.2 Eddington Luminosity

The idea of the equilibrium, stationary radiation implies a *mechanical* equilibrium along with the explicitly considered above thermodynamic equilibrium. As we will see, the requirement of the mechanical equilibrium puts an upper bound on the energy density of the electromagnetic field, which can be formulated in terms of a critical luminosity. To be specific, consider how the radiation produced by a compact object (e.g., a star) affects its atmosphere.

Adopt for simplicity that the stellar atmosphere is a fully ionized hydrogen plasma. To study the mechanical stability of the atmosphere we have to calculate the force with which an electromagnetic wave acts on an electron. This force is specified by the wave momentum transferred to the electron per unit time; it is directed along the wave propagation, $\boldsymbol{n} = \boldsymbol{k}/k$, and equal to the difference, projected onto $\boldsymbol{n}$, between the original wave momentum and momentum of all scattered waves per unit time, whose intensity is specified only by the original wave and the scattering cross section; an asymmetry introduced by slow motion of the nonrelativistic electrons is small as $v/c \ll 1$. Thus, the force averaged over the wave period is

$$\boldsymbol{\mathcal{F}} = c\overline{\boldsymbol{g}} \int (1 - \cos\theta) \frac{\mathrm{d}\sigma(\theta, \alpha)}{\mathrm{d}\Omega} \mathrm{d}\Omega, \tag{10.8}$$

where $\boldsymbol{g} = \frac{1}{4\pi c}\boldsymbol{E} \times \boldsymbol{B}$ is the density of the wave momentum flux along $\boldsymbol{n}$.

Although differential cross section of the scattering depends on the wave polarization according to Eqs. (9.102) and (9.103), the force does not depend on polarization, so integration in Eq. (10.8) yields a rather simple formula

$$\boldsymbol{\mathcal{F}} = w\sigma_T \boldsymbol{n}, \tag{10.9}$$

containing the energy density $w = (1/8\pi)|\boldsymbol{E}|^2$ of the original wave field and the total Thomson cross section σ_T.

Now we apply this result to estimate the critical **Eddington luminosity** L_c of a star, i.e., a highest luminosity whose radiative pressure force on the stellar atmosphere can still be balanced by the gravitational force. The radiation energy density is reciprocal to the square of the distance from the star center, $w(r) = L/4\pi c r^2$. The radiation pressure force acting on a single electron is defined by Eq. (10.9) and, thus, has the form

$$\mathcal{F}_r = \sigma_T w(r) = \frac{2e^2 L}{3m_e^2 c^5 r^2}. \tag{10.10}$$

The radiative force acting on a proton is smaller than that given by Eq. (10.10) by the factor of $(m_e/m_p)^2$. However, the gravitation force acts mainly on the protons and scales with the distance from the star center in exactly same way as Eq. (10.10):

$$\mathcal{F}_g = \frac{GMm_p}{r^2}, \qquad G = 6.67 \times 10^{-8}\ \mathrm{cm^3 g^{-1} s^{-2}}, \tag{10.11}$$

where M is the mass of the star. Because the electron and ion plasma components are coupled due to Coulomb interaction, both radiative and gravitational forces act on the entire (quasineutral) plasma as a whole. Thus, equating these two forces, we find the critical luminosity:

$$L_c = \frac{4\pi c G m_p M}{\sigma_T} \approx 3.2 \times 10^4 \frac{M}{M_\odot} L_\odot \approx 10^{38} \frac{M}{M_\odot}\ \mathrm{erg/s}, \tag{10.12}$$

where $M_\odot \approx 2 \times 10^{33}$ g is the **solar mass** and $L_\odot \approx 3.86 \times 10^{33}$ erg/s is the **solar luminosity**. Note that the Sun has luminosity much lower than its corresponding Eddington luminosity.

The importance of the Eddington luminosity is that for $L > L_c$ the star cannot have a mechanical equilibrium because the radiation pressure sweeps the stellar plasma atmosphere out. In addition, the critical luminosity controls the possibility of gas accretion onto a compact object: if $L < L_c$ then the gravitation is stronger than the radiative force and accretion from a companion (e.g., in a binary system) is possible; in the opposite case, $L > L_c$, no accretion takes place.

The estimated above critical Eddington luminosity must not be misinterpreted as the largest ever possible luminosity of radiating objects. First, the estimate will change if one accounts for heavier ions, radiation transfer in atomic or ion lines, Compton scattering in case of relativistic plasma, etc. And second, even for a more exact estimate of the critical luminosity, it remains an upper bound of an equilibrium state; however, nonstationary (e.g., exploding) objects, including gamma-ray burst sources, novae, and supernovae, can produce a luminosity orders of magnitude larger than the critical one, although during a short time period, when the strong, super-Eddington luminosity is accompanied by a very strong mass loss rate.

10.1.3 Stationary Radiation and Amplification

In the case of relatively weak, sub-Eddington, radiation pressure force, solution of radiation transfer equation (10.1) is easy to write down for a uniform stationary (though not necessarily equilibrium) source with a linear scale L along the $\boldsymbol{v}_g$ direction:

$$J^\sigma_{\mathbf{n},\omega} = \frac{j^\sigma_{\mathbf{n},\omega}}{\varkappa^\sigma_{\mathbf{n},\omega}} \left(1 - e^{-\tau^\sigma_{\mathbf{n},\omega}}\right), \tag{10.13}$$

where $\tau^\sigma_{\mathbf{n},\omega} = \varkappa^\sigma_{\mathbf{n},\omega} L$ is the optical depth of the source at a given frequency. If the optical depth is large, $\tau^\sigma_{\mathbf{n},\omega} \gg 1$, then the second term in the brackets can be discarded, so in the *optically thick* regime the radiation intensity

$$J^\sigma_{\mathbf{n},\omega} \simeq J^{\sigma,\mathrm{thick}}_{\mathbf{n},\omega} = \frac{j^\sigma_{\mathbf{n},\omega}}{\varkappa^\sigma_{\mathbf{n},\omega}} \tag{10.14}$$

is determined by the **source function** $S^\sigma_{\mathbf{n},\omega} \equiv j^\sigma_{\mathbf{n},\omega}/\varkappa^\sigma_{\mathbf{n},\omega}$ and so does not depend on the source size (most of the observed emission is collected from the ray path of the order of $1/\varkappa^\sigma_{\mathbf{n},\omega} \ll L$). In the opposite case, $\tau^\sigma_{\mathbf{n},\omega} \ll 1$, we can make an expansion $e^{-\tau^\sigma_{\mathbf{n},\omega}} \approx 1 - \tau^\sigma_{\mathbf{n},\omega}$, so the radiation intensity from an *optically thin* source

$$J^\sigma_{\mathbf{n},\omega} \simeq J^{\sigma,\mathrm{thin}}_{\mathbf{n},\omega} = j^\sigma_{\mathbf{n},\omega} L \tag{10.15}$$

is proportional to its length L.

Note that $j^{\sigma}_{\mathbf{n},\omega}$ and $J^{\sigma}_{\mathbf{n},\omega}$ are positively defined values. Therefore, the absorption coefficient of a thermodynamically equilibrium medium is a positive function as well; thus, the radiation intensity always decreases along the ray path. However, in nonequilibrium conditions, the absorption coefficient is not necessarily positive for all frequencies ω and directions $\boldsymbol{n}$. If in some range of ω and $\boldsymbol{n}$ the absorption coefficient is negative, the corresponding radiation experiences amplification instead of damping. Indeed, for $\varkappa^{\sigma}_{\mathbf{n},\omega} < 0$, we have $\varkappa^{\sigma}_{\mathbf{n},\omega} = -|\varkappa^{\sigma}_{\mathbf{n},\omega}|$, $\tau^{\sigma}_{\mathbf{n},\omega} = -|\tau^{\sigma}_{\mathbf{n},\omega}|$, and from Eq. (10.13) for $|\tau^{\sigma}_{\mathbf{n},\omega}| \gg 1$ we obtain

$$J^{\sigma}_{\mathbf{n},\omega} = \frac{j^{\sigma}_{\mathbf{n},\omega}}{|\varkappa^{\sigma}_{\mathbf{n},\omega}|} e^{|\tau^{\sigma}_{\mathbf{n},\omega}|}, \tag{10.16}$$

which describes an exponential growth of the radiation intensity.

Apparently, solution (10.16) has a limited applicability region because the radiation cannot gain arbitrarily large amount of energy; at least it cannot accumulate energy exceeding the free energy of the charge particles generating this radiation. In case of relatively compact source when only a small fraction of the available energy goes to radiation over the source size, solution (10.16) can still be correct, which is indicative of an *unsaturated regime* of the wave amplification. In the opposite case the radiation amplification is dynamically important; it affects strongly the distribution function of the charged particles and, eventually, the absorption and scattering coefficients specified by this distribution function; thus, the linear radiative transfer equation is insufficient any longer to consistently describe the radiation. Depending on situation (see Chap. 4), nonlinear wave–wave interactions or quasilinear wave–particle interactions can dominate. In the latter case the high radiation level affects the particle distribution in such a way that the absorption coefficient becomes eventually positive at all ω and $\boldsymbol{n}$, so the wave amplification seizes and turns to the true absorption. Calculation of the absorption coefficient $\varkappa^{\sigma}_{\mathbf{n},\omega}$ (positive or negative) is one of the central problems within the radiation transfer theory.

10.1.4 Einstein Coefficients

In the astrophysical sources the number density of fast nonthermal electrons is often much smaller than that of the thermal electrons. In this case the dispersion and polarization of the eigenmodes are primarily defined by the background particles, while the fast electrons can provide a major contribution to the absorption coefficient alternating the entire picture of the radiation transfer compared with the no fast particle case.

There are a number of approaches to calculate the absorption coefficients. A general classical method is based on finding the complex dielectric tensor of the given multicomponent plasma using kinetic equations, which is commonly used in the plasma physics. On the other hand, one can use a quantum

approach based on the Einstein coefficient. It turns that the quantum method is often simpler than the classical one, so it is widely used to analyze even purely classical problems.

Let us consider the Einstein coefficient method in more detail. To do so we introduce a probability of spontaneous transition (of a radiating agent—atom, ion, or a free particle) from an initial state m to a final state n with emission of a photon with a polarization σ and frequency belonging to the interval from ω to $\omega + \mathrm{d}\omega$ into element $\mathrm{d}\Omega$ of the solid angle:

$$\mathrm{d}W^{\sigma,s}_{\mathbf{n},\omega} = A^n_m \mathrm{d}\omega \mathrm{d}\Omega. \tag{10.17}$$

Likewise, we write the probability of the induced (stimulated by the external radiation field) radiation per unit time

$$\mathrm{d}W^{\sigma,i}_{\mathbf{n},\omega} = B^n_m \rho^\sigma_{\mathbf{n},\omega} \mathrm{d}\omega \mathrm{d}\Omega \tag{10.18}$$

and the probability of the photon absorption during the inverse transition from state n to state m:

$$\mathrm{d}W^{\sigma,a}_{\mathbf{n},\omega} = B^m_n \rho^\sigma_{\mathbf{n},\omega} \mathrm{d}\omega \mathrm{d}\Omega, \tag{10.19}$$

where the energy density $\rho^\sigma_{\mathbf{n},\omega}$ of the electromagnetic field[1] can be expressed via the power flux (i.e., the radiation intensity crossing a unit area per unit time per unit frequency range per unit solid angle):

$$\rho^\sigma_{\mathbf{n},\omega} = \frac{J^\sigma_{\mathbf{n},\omega}}{v_g}. \tag{10.20}$$

The quantities A^n_m, B^n_m, and B^m_n are called the Einstein coefficients. They are widely used because they are linked by universal relations derived from very fundamental considerations.

Consider a state of full thermodynamic equilibrium. The number of particles at a state i is specified by a canonic distribution $n_i \propto e^{-E_i/T}$, where E_i is the particle energy in the state i, and T is the temperature in units of energy. Apparently, in the equilibrium state, the number of photons absorbed per unit time is compensated by the same number of created photons, therefore, the balance equation must be fulfilled:

$$e^{-E_n/T} B^m_n \rho^\sigma_{\mathbf{n},\omega} = e^{-E_m/T} \left[B^n_m \rho^\sigma_{\mathbf{n},\omega} + A^n_m \right]. \tag{10.21}$$

Since for the temperature increase, $T \to \infty$, the radiation energy density raises infinitely, while both exponential factors go to unity, we obtain

$$B^m_n = B^n_m. \tag{10.22}$$

[1] We use here ρ, rather than W, for the wave energy density because W is commonly used for the probabilities defined above within the Einstein coefficient problem.

Noting that $E_m - E_n = \hbar\omega$, we find

$$\rho^{\sigma}_{\mathbf{n},\omega} = \frac{A^n_m}{B^n_m}\frac{1}{e^{\frac{\hbar\omega}{T}} - 1}. \tag{10.23}$$

Then, the ratio A^n_m/B^n_m can easily be determined from the limiting transition in Eq. (10.23) to low frequencies where the energy density of the equilibrium radiation is described by the familiar Rayleigh–Jeans formulae. Taking into account the wave dispersion in the plasma we obtain:

$$B^n_m = \frac{8\pi^3 c^3}{n^2_\sigma \hbar\omega^3 \left|\frac{\partial(\omega n_\sigma)}{\partial\omega}\right|} A^n_m. \tag{10.24}$$

It should be emphasized that the introduced Einstein coefficients are relevant for a given plasma eigenmode σ, not for the total intensity or Stokes parameters. Thus, the total power radiated into the full solid angle 4π can be found by multiplying Eq. (10.23) by 8π and taking into account Eq. (10.24) (the additional factor of 2 accounts for two available eigenmodes):

$$\rho_\omega = \frac{\hbar\omega^3}{\pi^2 c^3}\frac{1}{e^{\frac{\hbar\omega}{T}} - 1}, \tag{10.25}$$

where we adopted $n_\sigma = 1$ for simplicity.

Let us now derive the absorption coefficient $\varkappa^{\sigma}_{\mathbf{n},\omega}$ of the eigenmode σ. To do so we note that the radiation intensity varies (at a unit ray path) due to two competing processes—true absorption and stimulated emission. Accordingly, the amount of radiation power absorbed over the unit ray path is specified by the imbalance of these two processes:

$$\mathrm{d}w^{\sigma}_{\mathbf{n},\omega} = \hbar\omega\left[N_n \mathrm{d}W^{\sigma,a}_{\mathbf{n},\omega} - N_m \mathrm{d}W^{\sigma,i}_{\mathbf{n},\omega}\right] = \hbar\omega\left[N_n B^m_n - N_m B^n_m\right]\rho^{\sigma}_{\mathbf{n},\omega}\mathrm{d}\omega\mathrm{d}\Omega, \tag{10.26}$$

where $N_{n,m}$ are the number densities of particles at the states n and m, respectively, and the absorption coefficient per unit length is specified by the ratio of Eq. (10.26) to the radiation density flux $\mathrm{d}J^{\sigma}_{\mathbf{n},\omega} = |v_g|\rho^{\sigma}_{\mathbf{n},\omega}\mathrm{d}\omega\mathrm{d}\Omega$:

$$\varkappa^{\sigma}_{\mathbf{n},\omega} = \frac{\hbar\omega\left[N_n B^m_n - N_m B^n_m\right]}{|v_g|}. \tag{10.27}$$

Taking into account the relations between Einstein coefficients Eqs. (10.22) and (10.24), we express the absorption coefficient $\varkappa^{\sigma}_{\mathbf{n},\omega}$ via the probability of the spontaneous emission A^n_m:

$$\varkappa^{\sigma}_{\mathbf{n},\omega} = \frac{8\pi^3 c^3}{n^2_\sigma \omega^2 \left|v_g \frac{\partial(\omega n_\sigma)}{\partial\omega}\right|}\sum A^n_m (N_n - N_m), \tag{10.28}$$

where the summation is assumed over all pairs of states $(n,\ m)$, which transitions give rise to emission or absorption of quanta with a given polarization σ, frequency ω, and direction $\boldsymbol{n}$. Equation (10.28) shows that a necessary condition to maintain the wave amplification is a **population inversion** of the system states, $N_m > N_n$, when the number of particles N_m with higher energy exceeds the number of particles N_n with lower energy.

In a practically important case of ionized plasma, where the electrons are in the states of quasi-continuum spectrum, they can be described by a distribution function. Here the sum entering Eq. (10.28) can be expressed by integration of this distribution function $f(\boldsymbol{p})$, which is assumed to include both background and fast electrons:

$$\sum A_m^n (N_n - N_m) = \int A^{\sigma}_{\mathbf{n},\omega} \left(f(\boldsymbol{p} - \hbar\boldsymbol{k}) - f(\boldsymbol{p})\right) \frac{\mathrm{d}\boldsymbol{p}}{(2\pi)^3} = -\int A^{\sigma}_{\mathbf{n},\omega}(\boldsymbol{p}) \left(\hbar\boldsymbol{k}\frac{\partial f(\boldsymbol{p})}{\partial \boldsymbol{p}}\right) \frac{\mathrm{d}\boldsymbol{p}}{(2\pi)^3}, \tag{10.29}$$

where $A^{\sigma}_{\mathbf{n},\omega}(\boldsymbol{p})$ is the probability of spontaneous emission of a photon with polarization σ, frequency ω, and direction $\boldsymbol{n}$ by a particle with the momentum $\boldsymbol{p}$; the electron distribution function $f(\boldsymbol{p})$ is normalized by the condition

$$\int f(\boldsymbol{p}) \frac{\mathrm{d}\boldsymbol{p}}{(2\pi)^3} = N, \tag{10.30}$$

where N is the electron number density. The quantity $A^{\sigma}_{\mathbf{n},\omega}(\boldsymbol{p})$ can straightforwardly be expressed via spectral and angular radiation intensity by a single electron $I^{\sigma}_{\mathbf{n},\omega}$ (since the radiation intensity is a product of the photon energy and probability of its generation):

$$A^{\sigma}_{\mathbf{n},\omega} = \frac{I^{\sigma}_{\mathbf{n},\omega}}{\hbar\omega}. \tag{10.31}$$

Substituting Eq. (10.31) into Eq. (10.29) and then Eq. (10.29) into Eq. (10.28), we obtain the final expression for the absorption coefficient $\varkappa^{\sigma}_{\mathbf{n},\omega}$ by an ensemble of classical particles (electrons or positrons):

$$\varkappa^{\sigma}_{\mathbf{n},\omega} = -\frac{8\pi^3 c^3}{n_{\sigma}^2 \omega^3 \left| v_g \frac{\partial(\omega n_{\sigma})}{\partial\omega} \right|} \int I^{\sigma}_{\mathbf{n},\omega} \left(\boldsymbol{k}\frac{\partial f(\boldsymbol{p})}{\partial \boldsymbol{p}}\right) \frac{\mathrm{d}\boldsymbol{p}}{(2\pi)^3}. \tag{10.32}$$

The particle angular distribution can be anisotropic, for example, due to the presence of magnetic field. In this case, it could be convenient to rewrite the dot product $(\boldsymbol{k}\partial f(\boldsymbol{p})/\partial \boldsymbol{p})$ in the cylindrical or spherical coordinate system with the z-axes directed along the magnetic field $\boldsymbol{B}$.

10.1.5 Brightness Temperature

Equation of radiation transfer Eq. (10.1) can be reformulated in terms of so-called **brightness temperature** T_b, which is often used at the radio domain where Rayleigh–Jeans law, Eq. (10.2), takes place. We define T_b according to Eq. (10.2) but via frequency $f = \omega/2\pi$ practically used in the radio astronomy:

$$J^\sigma_{\mathbf{n},f} = \frac{n_\sigma^2 f^2}{c^2|\cos\theta|} k_\mathrm{B} T_\mathrm{b} \approx \frac{f^2}{c^2} k_\mathrm{B} T_\mathrm{b} \quad [\mathrm{erg\,cm^{-2}\,s^{-1}\,Hz^{-1}\,Ster^{-1}}], \tag{10.33}$$

where the second (approximate) definition is valid when $n_\sigma \approx 1$ and $|\cos\theta| \approx 1$, i.e., at the frequencies large compared with the plasma resonance frequencies. Likewise, we introduce an **effective temperature** T_eff linked to the source function

$$S^\sigma_{\mathbf{n},f} = \frac{n_\sigma^2 f^2}{c^2|\cos\theta|} k_\mathrm{B} T_\mathrm{eff} \approx \frac{f^2}{c^2} k_\mathrm{B} T_\mathrm{eff}. \tag{10.34}$$

Accordingly, Fig. 10.1, we can rewrite radiation transfer equation (10.1) using the introduced brightness and effective temperatures in the form

$$\frac{\mathrm{d}T_\mathrm{b}}{\mathrm{d}\tau} = -T_\mathrm{b} + T_\mathrm{eff} \tag{10.35}$$

or, equivalently, in the integral form

$$T_\mathrm{b} = \int\limits_0^\tau T_\mathrm{eff} \exp(-t)\mathrm{d}t + T_{b0} \exp(-\tau). \tag{10.36}$$

The usefulness of the introduced temperatures becomes transparent when we consider a uniform stand-alone source with a simple solution of Eq. (10.36):

$$T_\mathrm{b} = T_\mathrm{eff}[1 - \exp(-\tau)] = \begin{cases} T_\mathrm{eff} & \text{for} \quad \tau \gg 1 \\ \\ T_\mathrm{eff}\tau \ll T_\mathrm{eff} & \text{for} \quad \tau \ll 1 \end{cases}. \tag{10.37}$$

This equation demonstrates that in the optically thick case, $\tau \gg 1$, the brightness temperature of *each of two normal modes* is equal to the corresponding effective temperature. In particular, for a Maxwellian plasma with temperature T, we have $T_\mathrm{eff} = T$ and so $T_\mathrm{b} = T$ for each normal mode. We emphasize, that the brightness temperature is defined here as a non-extensive measure, i.e., in this example with equilibrium Maxwellian plasma, we have $T_I = T_O = T_X$, where T_I is the brightness temperature for the total intensity (Stokes I), while T_O and T_X are the brightness temperatures of the ordinary and extraordinary modes, respectively. Stated another way, an

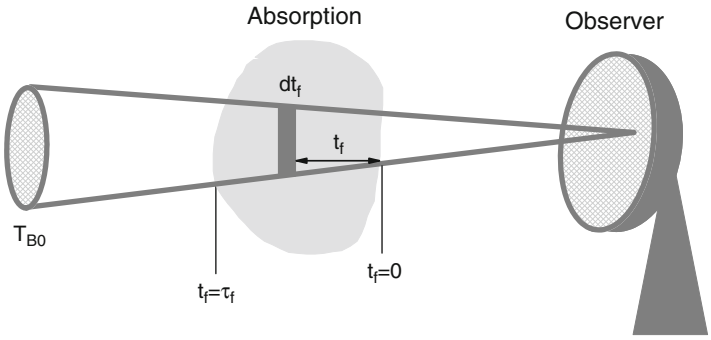

Figure 10.1: Geometry and definitions to equation of radiation transfer and brightness temperature.

additional factor of 2 must be added to the rhs of Eq. (10.33) in case of the Stokes I. Accordingly, in a general case of non-Maxwellian plasma, we have[2] $T_I = (T_O + T_X)/2$.

In a general case of a nonequilibrium electron distribution, the effective and brightness temperatures do not correspond to the plasma kinetic temperature; in contrast, they depend on both frequency and the viewing angle. Nevertheless, even in this case, these temperatures are helpful as they quantify an effective mean energy of the electrons giving the bulk contribution to the emission at a given frequency in case of an incoherent emission process. In contrast, for a coherent emission process, the brightness temperature can greatly exceed the typical energy of the radiating electrons. Thus, measuring the brightness temperature alone can greatly advise our ability to observationally distinguish incoherent and coherent emission processes.

10.1.6 Transfer of Polarization

Equations of radiation transfer in form of Eqs. (10.1) or Eq. (10.35) are written for a given propagating electromagnetic eigenmode and so implicitly adopt that the eigenmode propagates independently of the other eigenmode and its polarization properties do not change during the transfer. Apparently, this is not necessarily the case: in reality the polarization of radiation often changes during its transfer due to the mode coupling (linear or nonlinear), absorption, scattering, or spatial nonuniformity. Thus, in a general case, we have to consider a set of coupled equations for these wave modes accounting, in addition to the amplitudes, also the wave phase evolution. This is convenient to formulate in terms of polarization transfer. In a most general case evolution of radiation propagating in a given direction depends on radiation

[2]Note that many radio observatories use "extensive" definition of the brightness temperature, $T_I = T_O + T_X$, i.e., with additional factor of 2 in the rhs of Eq. (10.33) for any polarization mode.

propagating in all other directions because the wave scattering can change the wave vector direction and so the corresponding balance equation must include all the radiation field with all $\boldsymbol{k}$. Below we consider a simplified case when the wave scattering can be discarded and the 3D problem reduces to 1D problem of radiation transfer in a given direction. Broadly speaking, for the 1D approximation to be valid, one more assumption is needed: the ray paths of both extraordinary and ordinary waves must coincide, which is well justified at high frequencies although can break down close to the wave mode cut-off frequencies. Nevertheless, within the cold plasma approximation the ray paths of the two eigenmodes remain very close to each other so we are not considering any deviation from 1D geometry of the polarization transfer problem.

In this 1D case it is convenient to consider a reference system with the axes z directed along the wave vector $\boldsymbol{k}$, while the magnetic field direction is quantified by the polar angle θ between $\boldsymbol{k}$ and $\boldsymbol{B}$ and azimuth angle ψ between projection of $\boldsymbol{B}$ onto the xy-plane and the x-axes, measured in the anticlockwise direction. In this system the polarization vector, Eq. (3.50), of an eigenmode receives the form (for notations see Sect. 3.2.3):

$$\boldsymbol{e}_\sigma = \frac{(T_\sigma \cos\psi - i\sin\psi, T_\sigma \sin\psi + i\cos\psi, -L_\sigma)}{\sqrt{1+T_\sigma^2+L_\sigma^2}}. \tag{10.38}$$

Note that the longitudinal component of the polarization vector is often small, e.g., it is always small at high frequencies, so in such cases, it becomes a 2D vector in xy-plane:

$$\boldsymbol{e}_\sigma \simeq \frac{(T_\sigma \cos\psi - i\sin\psi, T_\sigma \sin\psi + i\cos\psi)}{\sqrt{1+T_\sigma^2}}. \tag{10.39}$$

An arbitrary radiation field can be represented as a superposition of the two propagating eigenmodes with various frequencies whose overall polarization state can be characterized by a so-called **polarization tensor**

$$I_{\alpha\beta} = \overline{E_\alpha E_\beta^*}, \tag{10.40}$$

where the averaging is performed over the wave period. It is often convenient to introduce another set of four values, the **Stokes parameters** I, Q, U, and V, which form a one-column matrix $\mathfrak{S}$:

$$\mathfrak{S} = \begin{pmatrix} I \\ Q \\ U \\ V \end{pmatrix}. \tag{10.41}$$

The Stokes parameters are defined via the polarization tensor $I_{\alpha\beta}$ components as follows:

$$\begin{aligned} I &= I_{xx} + I_{yy}, \\ Q &= I_{xx} - I_{yy}, \\ U &= I_{yx} + I_{xy}, \\ V &= i(I_{yx} - I_{xy}). \end{aligned} \tag{10.42}$$

In particular, the use of Eqs. (10.39), (10.40), and (10.42) yields the Stokes parameters for an eigenmode σ:

$$\mathfrak{S}_\sigma = I\mathfrak{s}_\sigma = I \begin{pmatrix} 1 \\ \dfrac{T_\sigma^2 - 1}{T_\sigma^2 + 1} \cos 2\psi \\ \dfrac{T_\sigma^2 - 1}{T_\sigma^2 + 1} \sin 2\psi \\ -\dfrac{2T_\sigma}{T_\sigma^2 + 1} \end{pmatrix} \tag{10.43}$$

with the intensity I, which also defines the matrix column $\mathfrak{s}_\sigma$. Apparently, the wave is elliptically polarized in a general case. The shape of the polarization ellipse, for given frequency and plasma parameters, depends on the direction of the wave propagation relative to magnetic field. The components (10.43) satisfy the condition $I^2 = Q^2 + U^2 + V^2$, which is an indication of that obvious fact that the eigenmode is fully polarized.

Discarding any nonlinear wave interaction and wave scattering, it is easy to formulate equation of the polarization transfer in the form:

$$\frac{d\mathfrak{S}}{dz} = \mathbf{S} + \mathsf{R}\mathfrak{S} - \mathsf{K}\mathfrak{S}, \tag{10.44}$$

where the term $\mathbf{S}$ describes the Stokes parameter evolution due to spontaneous emission in the source volume, the matrix R describes the polarization modification due to mode coupling, and matrix K accounts for the wave absorption during the transfer.

The column matrix $\mathbf{S}$ is straightforward to find noting that the spontaneous emission produces the eigenmodes only; thus

$$\mathbf{S} = \mathfrak{s}_X j_X + \mathfrak{s}_O j_O = \begin{pmatrix} j \\ \mu_Q \Delta j \\ \mu_U \Delta j \\ \mu_V \Delta j \end{pmatrix}, \tag{10.45}$$

where j_X and j_O are the plasma volume emissivities of the extraordinary and ordinary wave modes, respectively, and new coefficients μ_Q, μ_U, and μ_V

are defined using Eq. (10.43) and taking the equivalence $T_X T_O = -1$ into account as follows:

$$\mu_Q = \frac{T_X^2 - 1}{T_X^2 + 1} \cos 2\psi, \quad \mu_U = \frac{T_X^2 - 1}{T_X^2 + 1} \sin 2\psi, \quad \mu_V = -\frac{2T_X}{T_X^2 + 1}, \tag{10.46}$$

and

$$j = j_X + j_O, \quad \Delta j = j_X - j_O. \tag{10.47}$$

The parameter $T_X^2 - 1$ is small for a quasiparallel wave propagation; it is determined from Eq. (3.51) as

$$T_X^2 - 1 = -\frac{2u \sin^2 \theta}{u \sin^2 \theta + \sqrt{\mathcal{D}}}. \tag{10.48}$$

Now, expanding an arbitrary radiation as a combination of the eigenmodes and using Eqs. (10.44) and (10.1), we find the mode-coupling matrix

$$\mathsf{R} = \begin{pmatrix} 0 & 0 & 0 & 0 \\ 0 & 0 & -\mu_V \Delta k & \mu_U \Delta k \\ 0 & \mu_V \Delta k & 0 & -\mu_Q \Delta k \\ 0 & -\mu_U \Delta k & \mu_Q \Delta k & 0 \end{pmatrix}, \tag{10.49}$$

where

$$\Delta k = k_X - k_O = \frac{\omega}{c}(n_X - n_O), \tag{10.50}$$

k_X and k_O are the wave numbers of the eigenmodes, and $n_\sigma = k_\sigma c/\omega$ is the refraction index, Eq. (3.48) (see Sect. 3.2.3). The small difference between the refraction indices $n_X - n_O$ is calculated using Eq. (3.48) as

$$n_X - n_O = -\frac{v\sqrt{\mathcal{D}}}{(n_X + n_O)(1 - u - v + uv \cos^2 \theta)}. \tag{10.51}$$

Accordingly, the absorption matrix has the form

$$\mathsf{K} = \begin{pmatrix} \varkappa & \mu_Q \Delta\varkappa & \mu_U \Delta\varkappa & \mu_V \Delta\varkappa \\ \mu_Q \Delta\varkappa & \varkappa & 0 & 0 \\ \mu_U \Delta\varkappa & 0 & \varkappa & 0 \\ \mu_V \Delta\varkappa & 0 & 0 & \varkappa \end{pmatrix}, \tag{10.52}$$

where

$$\varkappa = \frac{\varkappa_X + \varkappa_O}{2}, \quad \Delta\varkappa = \frac{\varkappa_X - \varkappa_O}{2}, \tag{10.53}$$

$\varkappa_X$ and $\varkappa_O$ are the absorption coefficients of the extraordinary and ordinary waves, respectively.

As can be learnt in more detail from problems to this chapter, the polarization of radiation changes in various ways during its propagation through the plasma. In particular, a highly important is the **Faraday effect**, which represents a rotation of the polarization direction of original linearly polarized radiation during its propagation through a plasma by the angle

$$\chi = \lambda^2 \mathrm{RM}, \qquad \mathrm{RM} = \frac{e^3}{2\pi m_e^2 c^4} \int\limits_0^L n_e B_\parallel \mathrm{d}l \approx 0.81 \overline{n_e B}_\parallel L, \tag{10.54}$$

where RM is the **rotation measure** specified by the averaged product $\overline{n_e B}_\parallel$ along the line of sight; in the most right equality the rotation measure is expressed in rad/m^2, the number density in cm^{-3}, the magnetic field in μG, and the scale L in pc. This formula is obtained assuming the radiation frequency to be much larger than the plasma and gyrofrequency at the line of sight, so the propagating ordinary and extraordinary waves are almost circularly polarized (so called, quasiparallel propagation regime). This simple dependence on the plasma density and longitudinal magnetic field component offers a nice way of estimating cosmic magnetic fields via observed Faraday rotation. In practice, this method uses radio emission (the radio domain is preferable because this effect increases with the wavelength) at a few different frequencies from polarized compact sources (e.g., pulsars or quasars) in combination with measurement of the **dispersion measure**, see Problem 10.2, giving a mean number density $\overline{n_e}$ along the same line of sight. Eventually, making use of many compact sources seen from different directions and located at different distances from the Earth, a highly detailed information on the magnetic field value, direction, and spatial structure in the galaxy, diffuse sources, and extragalactic medium is obtained. In particular, the observational estimates of the astrophysical magnetic fields used above throughout the book are largely based on the Faraday rotation measurements. Note that here the radiation is produced somewhere as having a linearly polarized component and then propagates through the cosmic plasma outside the radiation source. This kind of the Faraday effect is called **external Faraday effect**.

Consider now an **internal Faraday effect** occurring in an extended quasi-uniform source of radio emission with a total depth L. Emission produced at various depths z will have accordingly different Faraday rotation angles, $\chi(z) \approx \lambda^2 \mathrm{RM}_L \cdot (z/L)$, where RM_L is the total rotation measure of the radiation source. Thus, if the angle $\chi(L) \gg 1$, i.e., if the Faraday rotation inside the source is strong it results in significant depolarization of the escaping radiation. The depolarization effect is further enhanced by the dependence on the wavelength, $\chi \propto \lambda^2$. Indeed, any real radio receiver records radio emission at a finite bandwidth, $\Delta\lambda$, so integration of the rotation angle over this bandwidth will result in additional depolarization if $\chi(L) \gg 1$.

We found that the linear polarization from a plasma with large rotation measure is supposed to be very low. It is important to note, however, that this

conclusion is not always valid. Indeed, in our consideration, we implied that the linearly polarized radiation can be represented as a sum of two coherent circularly polarized eigenmodes, which independently propagate through the plasma and then, leaving the plasma, add up into a new linearly polarized wave with a rotated polarization direction. In a more general case (e.g., in stellar coronae, where the radio frequencies are somehow comparable with the plasma and gyrofrequencies), the deviation of the polarization ellipse from a circle can be essential. Consider propagation of a certain eigenmode (X or O) with a given polarization ellipse through a uniform plasma. Apparently, the polarization state of this wave will not change during propagation. However, the adopted elliptical polarization contains a fraction of circular polarization (described by the Stokes V parameter) and a fraction of linear polarization (described by the Stokes Q and U parameters), which means that the corresponding linear polarization will fully survive during the wave propagation, so no Faraday rotation affects the linear component of the eigenmode polarization.

Similarly, no Faraday effect takes place if the radiation is composed of two *incoherent*, ordinary and extraordinary, eigenmodes. Nevertheless, despite the fact that linear polarization can survive during propagation through a plasma with large rotation measure, most of polarized radio emission leaving the stellar/solar coronae is almost entirely circularly polarized, while the fraction of the linear polarization is negligible (unmeasurable). However, this happens not because of the Faraday effect, while due to another effect of the polarization modification in a nonuniform plasma—the **limiting polarization**. Consider a wave (X or O) propagating with some original polarization ellipse from some coronal source outward from the stellar corona. Apparently, the thermal plasma density and the magnetic field both decrease along the ray path. Accordingly, the polarization ellipse of the eigenwave will become more and more similar to the circle and, within the geometry optics propagation regime, the polarization of the propagating radiation will evolve from the elliptical to the circular one. We emphasize that, assuming the direction of the magnetic field projection onto the xy-plane does not change along the ray path, the ellipse orientation does not change during formation of the limiting polarization, so no rotation of the linear polarization direction happens. Stated another way, the limiting polarization formation must not be misinterpreted as a *depolarization*, while it is a transformation of the linear polarization to the circular one in such a way that

$$V^2 = Q_0^2 + U_0^2 + V_0^2, \tag{10.55}$$

where Q_0, U_0, and V_0 are the initial Stokes parameters of the propagating wave, so the total *degree of polarization* remains constant. Accordingly, a linearly polarized radiation from stellar/solar coronae can only be observed in some special favorable conditions; detection of the linear polarization is, thus, a very sensitive tool of probing such special conditions in the coronae.

10.2 Gyrosynchrotron Radiation Transfer

Radiation produced by charged particles moving in magnetic fields (magnetobremsstrahlung) plays an exceptionally important role in astrophysics making dominant contribution to radio emission in most of the astrophysical objects, major contribution to gamma-ray and X-ray emission (in compact objects, supernova remnants, and gamma-ray burst sources), and important contribution to the IR/optical/UV (in active galactic nuclei or extragalactic jets), which implies necessity of its calculation in highly diverse conditions specific to the object or phenomenon under study.

Exact equations for the GS emissivity and absorption coefficient for an eigenmode σ in a magnetized plasma are calculated from the GS intensity produced by a single electron, Eq. (9.148) (see Sect. 9.4.1) by integration over electron ensemble distribution function with Eqs. (9.168) and (10.32):

$$\begin{aligned} j_f^\sigma &= \frac{2\pi e^2}{c}\frac{n_\sigma f^2}{1+T_\sigma^2} \\ &\times \sum_{s=-\infty}^{\infty}\int\left[\frac{T_\sigma(\cos\theta - n_\sigma\beta\mu)+L_\sigma\sin\theta}{n_\sigma\sin\theta}J_s(\lambda)+J_s'(\lambda)\beta\sqrt{1-\mu^2}\right]^2 \\ &\times F(\boldsymbol{p})\delta\left[f(1-n_\sigma\beta\mu\cos\theta)-\frac{sf_{\mathrm{Be}}}{\gamma}\right]\mathrm{d}^3\boldsymbol{p}, \end{aligned} \tag{10.56a}$$

$$\begin{aligned} \varkappa^\sigma &= -\frac{2\pi e^2}{n_\sigma(1+T_\sigma^2)} \\ &\times \sum_{s=-\infty}^{\infty}\int\left[\frac{T_\sigma(\cos\theta - n_\sigma\beta\mu)+L_\sigma\sin\theta}{n_\sigma\sin\theta}J_s(\lambda)+J_s'(\lambda)\beta\sqrt{1-\mu^2}\right]^2 \\ &\times \frac{1}{\beta}\left[\frac{\partial F(\boldsymbol{p})}{\partial p}+\frac{n_\sigma\beta\cos\theta-\mu}{p}\frac{\partial F(\boldsymbol{p})}{\partial\mu}\right]\delta\left[f(1-n_\sigma\beta\mu\cos\theta)-\frac{sf_{\mathrm{Be}}}{\gamma}\right]\mathrm{d}^3\boldsymbol{p}, \end{aligned} \tag{10.56b}$$

where the derivative over momentum vector is taken in spherical coordinates linked to the magnetic field direction. The electron distribution function $F(\boldsymbol{p})$ is normalized as follows (we assume that it is azimuthally symmetric, which results in 2π factor):

$$\int F(\boldsymbol{p})\mathrm{d}^3\boldsymbol{p} = 2\pi\int_{p_1}^{p_2}p^2\mathrm{d}p\int_{-1}^{1}F(p,\mu)\mathrm{d}\mu = n_{\mathrm{e}}, \tag{10.57}$$

where n_{e} is the number density of electrons with momentum between p_1 and p_2.

10.2.1 Model Dependencies

Because the gyrosynchrotron (GS) emission depends in a complicated nonlinear way on many involved parameters, it is useful to elucidate the main dependences of the radio spectrum on various parameters of interest for a homogeneous source before turning to a more sophisticated 3D modeling. For such a homogeneous source, the radiation flux at a given frequency is apparently computed as (see Dulk 1985 and Bastian et al. 1998)

$$S(f, B, \theta, T, n_{th}, E_{\min}, E_{\max}, n_{rl}, \delta) = \frac{j_T}{\varkappa_T} \frac{A}{\mathcal{R}^2} [1 - \exp(\varkappa_T L)], \qquad (10.58)$$

where $j_T = j_{\rm ff}(f, T, n_{\rm th}) + j_{gs}(f, B, \theta, n_{\rm th}, n_{rl}, E_{\min}, E_{\max}, \delta)$ is the total emissivity due to the free–free (see Sect. 10.1.1) and gyrosynchrotron mechanisms, $\varkappa_T = \varkappa_{\rm ff}(f, T, n_{\rm th}) + \varkappa_{gs}(f, B, \theta, n_{rl}, E_{\min}, E_{\max}, \delta)$ is the total absorption coefficient, $A/\mathcal{R}^2$ is the solid angle subtended by the source with visible area A, and $\mathcal{R}$ is the distance from the observer to the source ($1\,\mathrm{AU} = 1.496 \times 10^{13}\,\mathrm{cm}$ in case of a source located at the Sun).

The thermal free–free emission and absorption coefficients used for the computation of the source function are readily calculated, Eqs. (10.4) and (10.5); those for gyrosynchrotron emission and absorption, Eq. (10.56), are cumbersome and their calculation is computationally intensive in their original form. A breakthrough in the GS computations is achieved by using Fleishman–Kuznetsov fast and precise gyrosynchrotron code (Fleishman and Kuznetsov 2010), which includes the plasma effects of Razin suppression, pitch-angle anisotropy, and correctly describes the low-frequency harmonic structure in contrast to previous versions of fast GS codes.

Figure 10.2 shows model spectra calculated for various (still highly incomplete) sets of parameters, computed by a continuous version of the fast code, which produces emission averaged over harmonics and so does not produce any local peak at the gyroharmonics. This corresponds to averaging of the emission over some range of the magnetic field values in a realistically nonuniform source. All four panels show a reference spectrum (solid line) due to gyrosynchrotron emission from electrons *in vacuo* ($n_{\rm th} = 0$). The parameters used for the reference spectrum are: $B = 150\,\mathrm{G}$, $\theta = 60^\circ$, $n_{rl} = 5 \times 10^6\,\mathrm{cm}^{-3}$, $E_{\min} = 0.1\,\mathrm{MeV}$, $E_{\max} = 2.5\,\mathrm{MeV}$, $\delta = 3$, $A = 2 \times 10^{18}\,\mathrm{cm}^2$, and $L = 9 \times 10^8\,\mathrm{cm}$. This is a single-peak spectrum, whose spectral peak frequency $f_{\rm peak}$ is determined by the condition $\tau \approx 1$; thus it demarcates the optically thick (low-frequency) and thin (high-frequency) parts of the spectrum. Since GS absorption coefficient Eq. (10.56) increases with the magnetic field value or the number density of emitting electrons, this peak frequency $f_{\rm peak}$ also increases with B, N_e, and L, which is, however, not always the case in the presence of thermal plasma as shown below.

In Fig. 10.2a the dashed lines indicate spectra where the source parameters are identical to those used to compute the reference spectrum except that an ambient thermal plasma is present in the source. The ambient plasma has

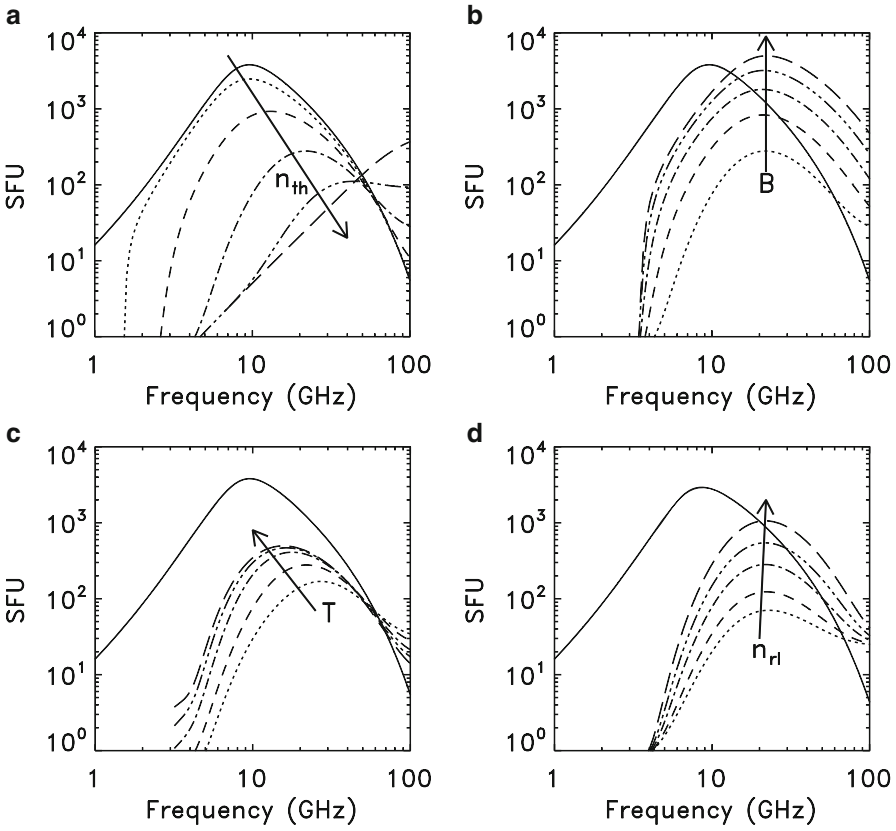

Figure 10.2: Computed GS spectra illustrating the parameter dependencies (Bastian et al. 2007). In all panels, the *solid line* represents GS emission from electrons *in vacuo* for parameters given in the text. (**a**) variation of the spectrum when a background thermal plasma with a temperature $T = 2 \times 10^6$ K is present: *dotted line*: $n_{\rm th} = 2 \times 10^{10}\,{\rm cm}^{-3}$; *dashed line*: $n_{\rm th} = 5 \times 10^{10}\,{\rm cm}^{-3}$; *dot–dash*: $n_{\rm th} = 2 \times 10^{11}\,{\rm cm}^{-3}$; *dot–dot–dot–dash*: $n_{\rm th} = 2 \times 10^{11}\,{\rm cm}^{-3}$; *long-dash*: $n_{\rm th} = 5 \times 10^{11}\,{\rm cm}^{-3}$; (**b**) same, except $n_{\rm th} = 10^{11}\,{\rm cm}^{-3}$, and $B = 150, 200, 250, 300$, and 350 G, respectively; (**c**) same as (b) except $B = 150$ G and $T = 10^6, 2 \times 10^6, 5 \times 10^6, 10^7$, and 2×10^7 K, respectively; (**d**) same as (c) except $T = 2 \times 10^6$ and $n_{rl} = 10^6, 2 \times 10^6, 5 \times 10^6, 10^7$, and $2 \times 10^7\,{\rm cm}^{-3}$, respectively. Reproduced by permission of the AAS.

a temperature of 2×10^6 K and its density varies from $n_{\rm th} = 2 \times 10^{10}\,{\rm cm}^{-3}$ to $5 \times 10^{11}\,{\rm cm}^{-3}$. The combined action of free–free absorption and Razin suppression strongly reduces the radio emission below 10–20 GHz for values of $n_{\rm th} > 5 \times 10^{10}\,{\rm cm}^{-3}$. Moreover, as the density increases, the high-frequency emission is enhanced. This enhancement is entirely due to the thermal free–free contribution.

In Fig. 10.2b, the temperature is again $T = 2 \times 10^6$ K, and the ambient density is held fixed at $n_{\rm th} = 10^{11}\,{\rm cm}^{-3}$, while the magnetic field strength is

allowed to vary. Note that, in contrast to gyrosynchrotron emission in which Razin suppression (Sect. 9.4.2) plays no role (which would be the case for even greater magnetic fields other parameters being the same) and the free-free absorption is insignificant, the spectral maximum is insensitive to B although the peak flux increases with B.

In Fig. 10.2c, the density is again held fixed at $n_{\rm th} = 10^{11}\,{\rm cm}^{-3}$ and $B = 150\,{\rm G}$, but the plasma temperature now varies from $T = 10^6$ to $2\times10^7\,{\rm K}$. For a cooler plasma, the combination of Razin suppression and thermal absorption strongly reduces the microwave emission. As the temperature of the ambient plasma increases, all other parameters held fixed, the microwave emission increases at lower frequencies because the free–free absorption drops as the temperature increases but decreases at the highest frequencies owing to the corresponding decrease of the optically thin free–free opacity, and the spectral maximum moves toward lower frequencies. At high enough temperatures the plasma becomes optically thin to free–free absorption ($\sim10^7\,{\rm K}$ in this example) and the spectrum becomes insensitive to further increases in temperature except the extreme low-frequency end of the spectrum where the emission is due to optically thick thermal radiation of the plasma and is proportional to its temperature.

Finally, in Fig. 10.2d, the thermal plasma density, temperature, and magnetic field are held fixed ($n_{\rm th} = 10^{11}\,{\rm cm}^{-3}$, $T = 2\times10^6\,{\rm K}$, $B = 150\,{\rm G}$), while the number of energetic electrons n_{rl} between $E_{\rm min}$ and $E_{\rm max}$, varies from 10^6 to $2\times10^7\,{\rm cm}^{-3}$. The microwave flux varies with n_{rl}, but the spectral maximum is insensitive to variations in n_{rl}. The optically thin slope steepens with increasing n_{rl} as the influence of the dense thermal plasma becomes relatively less important. At low values of n_{rl} the contribution of free–free emission is significant and acts to flatten the spectrum. We conclude that even for the simple uniform source model there is a wide variety of spectral shapes which becomes even wider when spatial inhomogeneity (and/or evolution) of the relevant source parameters is taken into account.

10.2.2 3D Modeling

A realistic 3D modeling of the microwave emission is highly important because the gyrosynchrotron (GS) emission depends, as said, in a complicated nonlinear way on many involved parameters and source geometry including spatial inhomogeneity and angular anisotropy. The detailed realistic modeling has, therefore, to establish a clear quantitative picture of how the involved physics (i.e., source properties and parameter regimes) affects the emission produced, e.g., what changes in the emission can be expected from variation of a given parameter.

Apparently, there is no hope to derive an analytical solution comprehensively describing spatially resolved radiation from 3D nonuniform evolving sources. On the other hand, given a large number of physical parameters involved and nonlinear dependences on some of them, differing geometry and

source morphology, it is unlikely to create a comprehensive table of models using standard numerical modeling approach. To overcome the mentioned complications, an entirely new, *post-numerical* approach to the 3D solution obtaining has been proposed. The idea is to have a simulation tool capable of smoothly changing all the involved source parameters and quickly compute and return the solution in the form of datacubes describing the microwave emission produced. This approach fully explore the modern computation power and optimized fast codes to calculate the emission while recovering the ability of smoothly changing all the involved parameters, which is typical to general analytical solutions with many free parameters. There are very few such tools at the time of writing, but they start to appear and seem to be one of main streams in developing sophisticated 3D simulations in astrophysics.

As an example, Fig. 10.3 displays an interface of a powerful tool, called the GX Simulator (gyrosynchrotron/X-ray simulator), which shows a graphical user interface (GUI) of the tool. The area on the left is the display area, in which various selectable aspects of the model can be displayed and manipulated, such as magnetic field components, field lines, flux tubes, thermal and nonthermal density, nonthermal energy distribution parameters (e.g., power-law index, pitch angle, high- and low-energy cutoffs). The tool imports a magnetic model in a form of 3D datacube, which can be either fully numerical (i.e., for the solar case—computed from nonlinear force-free field extrapolation from the photosphere boundary) or derived from an analytical model (e.g., a dipole field). Alternatively, it is capable of producing its own magnetic datacube from potential field or linear FFF extrapolation of a "base" magnetic map.

Then, the functional form and parameters governing the distributions are set using the tools shown in the right side of the GUI in Fig. 10.3. The models can be viewed from any perspective and, when complete, can be oriented to the target line of sight view and the emission calculated. The routines for calculating emission may either be external (e.g., C++ or FORTRAN) libraries or IDL routines: the callable emission routines return frequency- or energy-dependent fluxes which are then displayed as images or spectra within the tool, and can be saved as image cubes for further analysis (e.g., for folding through instrument response functions and comparing with observations). To be specific, below we discuss some modeling results obtained using a single dipole magnetic loop.

We consider a simple case of a symmetric dipole magnetic loop produced by a magnetic dipole with moment $\boldsymbol{\mu}$ that makes an adjustable angle $\pi/2-\varphi_0$ with its corresponding solar radius and located below the solar surface at a depth D. The flaring loop is constructed around a central field line that is chosen to lie in the plane defined by the magnetic dipole vector and the local solar radius. The adopted geometry (visualized via a few reference magnetic field lines demarcating the surface of the magnetic loop) for two different loop orientations is shown in Fig. 10.4. Dependence of the magnetic field strength

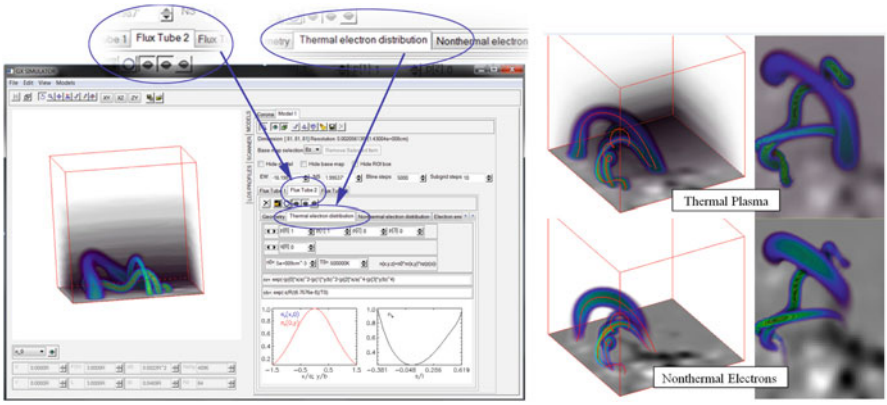

Figure 10.3: *Left panel*: The GX Simulator graphical user interface, showing a model with three flux tubes defined. One can draw any number of field lines by selecting points in the magnetic field model (either with the mouse on the lower surface, or by specifying x, y, z locations numerically) and the program calculates the field lines through those points. Regions around selected reference field lines can be designated as flux tubes, which can be filled with thermal plasma and nonthermal particles. In this example, flux tube 2's thermal electron distribution is being modified with distributions across and along the central field line as shown in the plots in the *lower right*. *Right panel*: Example usage of the GX Simulator, showing a perspective view (*left panels*) and a top view (*right panels*) of an NLFFF extrapolation model with three field lines selected (*red lines* in *left panels*) as the centerline of flux tubes. The three flux tubes are then individually populated with thermal plasma (*upper panels*) and nonthermal populations of electrons (*lower panels*), using the tools available in the GUI. The flux tubes are embedded in a background hydrostatic equilibrium density model visible in the *upper left panel*. The entire view can be manipulated interactively with simple mouse movements (courtesy by Drs. Gelu Nita & Dale Gary).

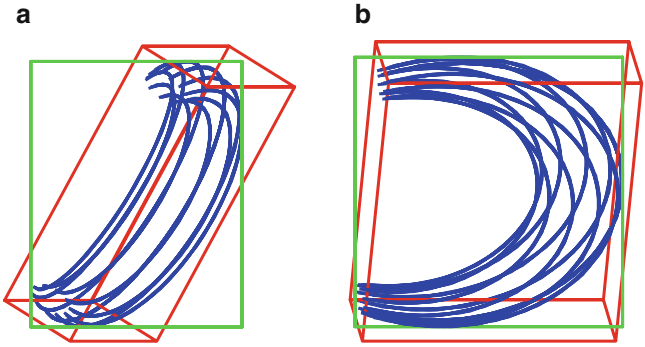

Figure 10.4: The magnetic field model used in the simulations. The *red box* inscribes the portion of the magnetic loop situated above the solar surface, while the *green solid rectangle* represents the top view of an inscribing box that is perpendicular to the observer's line of sight. The two panels shows two different orientations of the same model corresponding to a loop located near the center of the solar disk (**a**) and a loop located near the solar limb (**b**) (Kuznetsov et al. 2011). Reproduced by permission of the AAS.

at the loop axis on the distance from the looptop along the field line is shown in Fig. 10.5a. We assume that the density and temperature of the thermal plasma component within the loop are constant (since the plasma in flaring loops is often heated up to the temperatures of $\gtrsim 10^7$ K, the corresponding barometric scale heights far exceed the loop heights, so the density variations with height can be neglected). Parameters of the energetic electrons can either be constant or vary with the distance from the looptop (see below).

By using the above assumptions, we construct a 3D model of the flaring loop, which is observed at a given direction. The radio brightness map (i.e., the observed emission intensity as a function of 2D coordinates x and y) at a given frequency f is calculated by numerical integration of radiation transfer (10.1) along all selected lines of sight. This equation is solved separately for J_L and J_R, which are the spectral intensities of the left- and right-polarized emission components, respectively, j_L and j_R are the corresponding emissivities, while $\varkappa_\mathrm{L}$ and $\varkappa_\mathrm{R}$ are the absorption coefficients. Left-polarized emission corresponds to either ordinary or extraordinary magnetoionic mode, depending on the magnetic field direction; accordingly the right-polarized emission corresponds to the opposite mode. The plasma emissivities $j_{\mathrm{O,X}}$ and absorption coefficients $\varkappa_{\mathrm{O,X}}$ for the ordinary and extraordinary modes accounting for both GS and free–free contributions at each voxel are computed using Fleishman–Kuznetsov fast gyrosynchrotron codes (Fleishman and Kuznetsov 2010). Outside the flaring loop, the emission propagates like in a vacuum. We adopt the loop to be located at the solar equator; in this case, the loop orientation is characterized by the angle ψ between the magnetic dipole and the equatorial plane and by the longitude λ.

The energetic electrons are described by the distribution function F in a factorized form: $F(E,\mu) = u(E)g(\mu)$, where E is the electron kinetic energy, $\mu = \cos\alpha$, and α is the electron pitch angle (the angle between the particle velocity and the local magnetic field vectors). We assume that the electrons have a power-law energy spectrum $u(E) \propto E^{-\delta}$ in the energy range $E_\mathrm{min} < E < E_\mathrm{max}$. The pitch-angle distribution can be either isotropic or a loss cone described by the model function

$$g(\mu) \sim \begin{cases} 1, & \text{for } |\mu| < \mu_\mathrm{c}, \\ \exp\left[-\dfrac{(|\mu| - \mu_\mathrm{c})^2}{\Delta\mu^2}\right], & \text{for } |\mu| \geq \mu_\mathrm{c}, \end{cases} \tag{10.59}$$

where $\mu_\mathrm{c} = \cos\alpha_\mathrm{c}$, α_c is the loss-cone boundary, and the parameter $\Delta\mu$ determines the sharpness of this boundary. The loss-cone boundary is adopted to exactly follow transverse adiabatic invariant (1.46), i.e., $\sin^2\alpha_\mathrm{c} = B/B_\mathrm{f}$, where B and B_f are the magnetic fields at a given point and at the loop footpoint, respectively. Dependence of the loss-cone boundary on the coordinate along the loop is shown in Fig. 10.5b; this parameter equals 90° at the footpoint and decreases with height, so that the distribution becomes closer to the isotropic one higher in the corona.

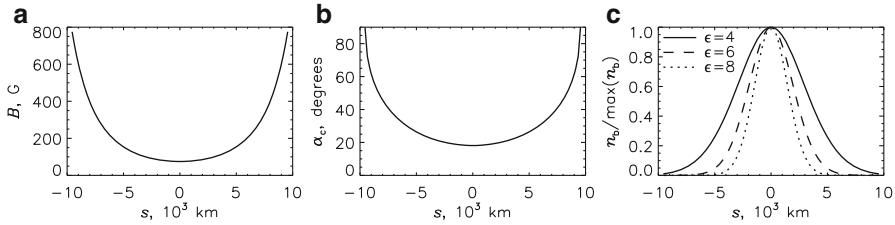

Figure 10.5: Magnetic field strength (**a**), loss-cone boundary (**b**), and relative density of the energetic electrons (**c**) vs coordinate along the loop. All the values correspond to the loop axis (Kuznetsov et al. 2011). Reproduced by permission of the AAS.

We consider both the homogeneous spatial distribution of the energetic electrons (when their number density n_e is constant) and the case when the energetic electrons are accumulated at the looptop. The inhomogeneous distribution of the particles along the loop is described by the following model function:

$$n_e \sim \exp\left[-\epsilon^2(\varphi - \pi/2)^2\right], \tag{10.60}$$

where φ is the magnetic latitude (or the angle between the dipole axis and the vector drawn from the dipole center to a given point) and the parameter ϵ determines the inhomogeneity degree ($\epsilon = 0$ corresponds to the homogeneous case). Density profiles of the energetic electrons along the loop for the different values of ϵ are shown in Fig. 10.5c.

In the simulations, we use the following parameters of the flaring loop: height $H = 10{,}000\,\mathrm{km}$, dipole depth below the photosphere $D = 6{,}000\,\mathrm{km}$ (so that the distance between the footpoints $\Delta \simeq 11,500\,\mathrm{km}$), radius at the top $R_t = 2{,}000\,\mathrm{km}$, and magnetic field at the top $B_t = 75\,\mathrm{G}$ (that results in the footpoint magnetic field of $B_f \simeq 800\,\mathrm{G}$). Two loop orientations are considered: $\psi = 60°$, $\lambda = 20°$ (a loop near the center of the solar disk, Fig. 10.4a) and $\psi = 60°$, $\lambda = 80°$ (a loop at the limb, Fig. 10.4b). The thermal plasma density and temperature are $n_0 = 10^{10}\,\mathrm{cm}^{-3}$ and $T_0 = 2 \times 10^7\,\mathrm{K}$, respectively. The energetic electrons have the power-law index $\delta = 4$, cutoff energies $E_{min} = 100\,\mathrm{keV}$ and $E_{max} = 10\,\mathrm{MeV}$, and the loss-cone boundary width $\Delta\mu = 0.2$. Thus, in each loop orientation, the variable parameters are: type of the pitch-angle distribution (isotropic or loss cone), the number density of the energetic electrons n_e, and the inhomogeneity parameter ϵ.

A direct way of radiation visualization is via the radio images at various frequencies. Without going to the details implied by the plots, we note that the images presented in Fig. 10.6 differ for various distributions of the fast electrons related to various transport regimes of the electrons described in Sect. 7.5.3. For example, the weak diffusion regime implies a loss-cone angular distribution and progressive electron accumulation at the looptop, i.e., an anisotropic and either uniform or nonuniform spatial distribution; the moderate diffusion regime implies more isotropic and uniform distribution

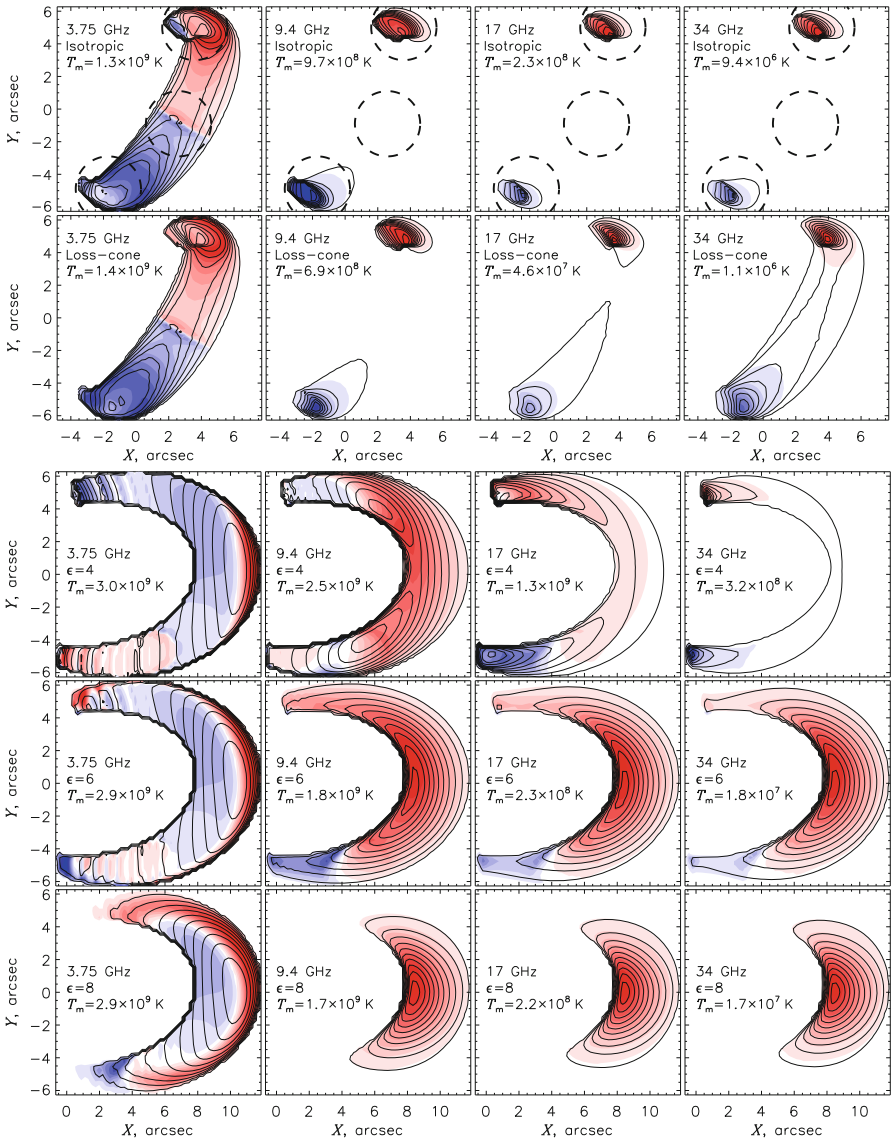

Figure 10.6: Radio brightness maps for a loop located near the center of the solar disk, for the isotropic distribution (*top row*) and loss-cone distribution (*all other rows*); the *north* is up and the *west* is to the right. The number density of the accelerated electrons is assumed to be constant along the loop at two *top rows*, while nonuniform as explained in the text in three *bottom rows*. *Solid lines* are the intensity contours which are evenly distributed between zero and the maximum brightness temperature $T_{\rm m}$ (the corresponding temperatures are given in each panel). *Color shades* represent the circular polarization (Stokes V normalized by the absolute value of V peak); *red and blue* correspond to the *right and left* circular polarizations, respectively (Kuznetsov et al. 2011). Reproduced by permission of the AAS.

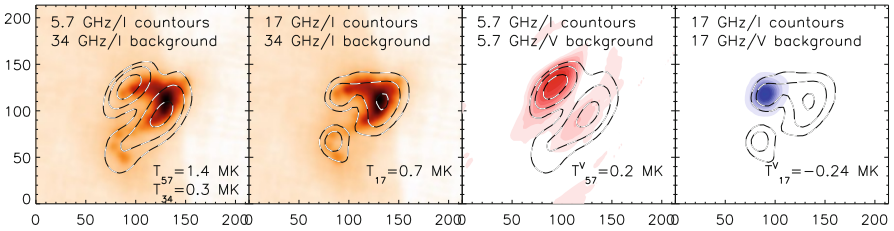

Figure 10.7: Example of observed microwave images (taken around 03:35:30 UT) from a solar flare 13 July 2005 observed by NoRH at 17 GHz and 34 GHz and by SSRT at 5.7 GHz in intensity (Stokes I) and polarization (Stokes V). In two right images the intensity of *blue* (*red*) show LCP (RCP) polarization. Overall agreement between images is evident; however, images at different frequencies clearly display dissimilar morphologies. A sharp jump in the background image intensity at two *left panels* indicates the western solar limb, which is clearly seen at 34 GHz (courtesy by Dr. Alexander Altyntsev).

of the fast electrons over the loop, while the strong diffusion regime implies a spatially nonuniform and isotropic electron distribution. Figure 10.6 offers a representative set of images highlighting main image properties related to these transport regimes; cf. an observed example shown in Fig. 10.7.

A complementary way of thinking of the emission is via the spatially resolved spectra (Fig. 10.7). Figure 10.8 shows that the radiation spectra, polarization, and spectral index all vary with the position along the source. In particular, the spectrum peak frequency increases with the magnetic field strength at the given source region, which implies a way of estimating the magnetic field from spatially resolved microwave spectra observed from solar flares. Let us consider the total (spatially integrated) emission from the flaring loop, which makes sense for both distant astrophysical objects including other stars and also to analyze historically accumulated databases and corresponding statistical studies performed mainly based on the total power observations. The total power data are simpler manageable as they can be easily visualized by dynamic spectra, see an example in Fig. 9.18, and characterized by only a few simple numbers, such as spectral indices, rise and decay times, peak flux, and frequency. In particular, the corresponding high-frequency spectral index is widely used to evaluate the fast electron energy spectral index, which is especially helpful when ultrarelativistic electrons produce synchrotron radiation, e.g., in the Galaxy, SNRs, radio galaxies, and jets etc (see Sect. 9.4.3).

The measures characterizing the total emission are shown in the right column in Fig. 10.8. Considering the right top panel in Fig. 10.8, one can easily isolate three distinct regions of the spectra—low-frequency part (region I), middle-frequency part (region II), and high-frequency part (region III). Visual comparison of these total power spectra with the spatially resolved spectra from the footpoints and looptop in Fig. 10.8 suggests that the low-frequency

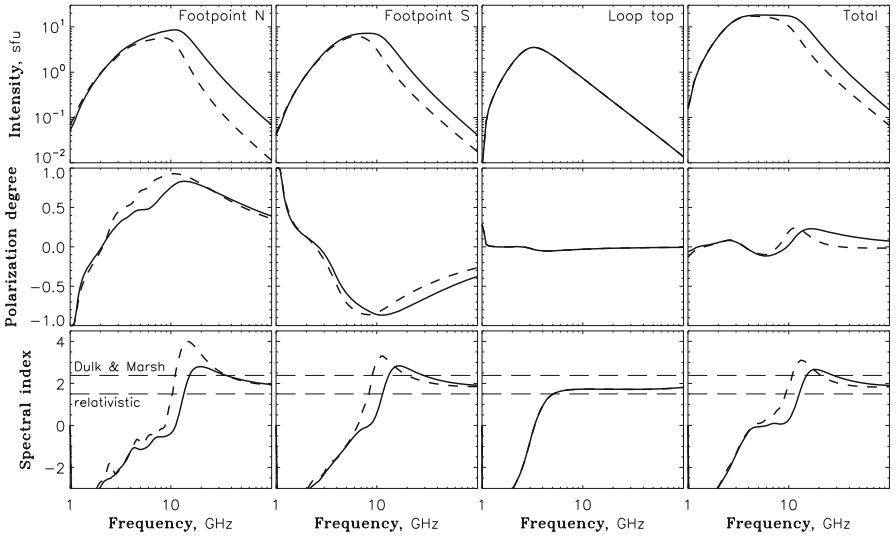

Figure 10.8: Emission intensity, degree of polarization, and spectral index vs. frequency for the loop shown in Fig. 10.6, *top*. The columns (from *left to right*) correspond to the following: *northern* footpoint source, *southern* footpoint source, looptop source, and the emission from the entire loop (spatially integrated). *Solid lines*: isotropic distribution; *dashed lines*: loss-cone distribution. The regions taken to calculate the spatially resolved spectra are indicated in Fig. 10.6 by *thick dashed circles* (Kuznetsov et al. 2011). Reproduced by permission of the AAS.

part is formed primarily at the looptop region with low magnetic field, the high-frequency part in the footpoints where the magnetic field is large, while the middle-frequency part by the entire loop and so related to the magnetic field nonuniformity.

The low-frequency part is known (Sect. 10.2.1) to be formed by the effect of the GS optical thickness and/or the Razin effect, i.e., suppression of the GS emission in a dense background plasma, possibly accompanied by the free–free absorption in the dense plasma; the slope of the spectrum can here be quantified by the index of −2 or less (see the right bottom panel in Fig. 10.8). The high-frequency part is mainly determined by the distribution of fast electrons including the energy spectrum and pitch-angle anisotropy; note the anisotropy-related difference between the solid (isotropic) and dashed (loss-cone) curves in this panel.

The middle-frequency part is clearly seen in Fig. 10.8 as it is almost flat (the spectral index is around zero). Solar microwave bursts with flat spectra have been observed for decades. Our modeling confirms that the electrons trapped in a large dipole magnetic loop can produce the flat radio spectra due to the source nonuniformity in certain parameter regimes. Generally, this middle-frequency part is not always flat but can have either negative

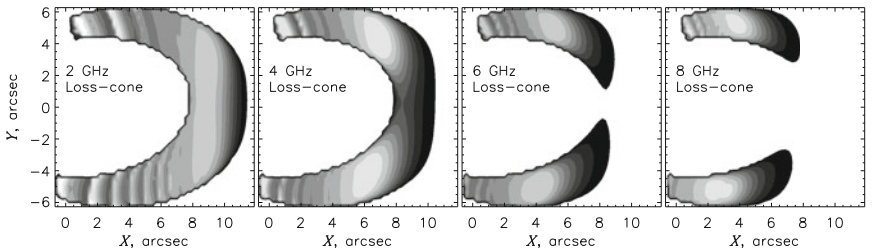

Figure 10.9: Radio brightness maps (emission intensity) for a loop located near the solar limb. *Brighter areas* correspond to higher intensity. Number density of the accelerated electrons is constant and their pitch-angle distribution is of the loss-cone type. *Stripes* in the images originate from the gyroharmonics; positions of the stripes change with frequency following the local resonance conditions (Kuznetsov et al. 2011). Reproduced by permission of the AAS.

or positive spectral index, which can be misinterpreted as either region I or III in observations with a limited spectral coverage. In fact, observations (Nita et al. 2004) reveal that the histograms of both low- and high-frequency spectral indices extend to zero implying that both low- and high-frequency spectra can be much flatter than those determined by optical thickness effect or electron energy index, respectively. For practical application, this means that having the spectrum falling with the frequency does not guarantee that its slope is formed by either energetic or angular properties of the electron distribution function but can instead be related to the source non-uniformity.

Not surprisingly, nonuniform spatial distribution of fast electrons significantly affects region II of the spectrum. In fact, with an inhomogeneous nonthermal electron spatial distribution (with their concentration at the looptop), the radio spectrum begins to resemble emission from a roughly uniform looptop source (see Fig. 10.8). The reason for this to happen for an *inhomogeneous* source is very simple: with the adopted inhomogeneous electron distribution most of them reside at the looptop, where the spatial variation of the magnetic field and the viewing angle are minor, so we have a situation similar to a uniform source.

The gyrosynchrotron emission from a homogeneous source can demonstrate an oscillatory spectral structure in the low-frequency range ($f/f_B \lesssim 10$), when the emission intensity increases at a narrow spectral region near the harmonics (small integer multiples) of the electron cyclotron frequency. In an inhomogeneous source, however, this harmonic structure can be hidden because of natural smoothing: the resonance giving rise to a gyroharmonics at a given location will vary with frequency due to the spatially dependent resonant condition in the spatially nonuniform magnetic field. Thus, even if a spectrum from a single pixel contains harmonics, they often disappear

after integration over even a relatively small part of the source. This is why no harmonic structure is present in either footpoint or looptop spectra in Fig. 10.8.

In the simplest case of a uniform GS source, the harmonic structure is more prominently pronounced for the source viewed at a quasitransverse direction relative to the source magnetic field. Note that for the magnetic model adopted here, the harmonic structure is only expected from the footpoint and leg regions, but not from the looptop where the magnetic field is too weak for the gyroharmonics to be produced at the considered parameter regime; thus, the limb location of the loop is most favorable to produce distinct gyroharmonics, which is evident from Fig. 10.9: the images contain a number of bright stripes highlighting the isolines of the magnetic field strength corresponding to the gyroresonance conditions at a given frequency. If one were gradually increasing the frequency, for which the image has been computed, each stripe would demonstrate an apparent down motion (i.e., toward x coordinate decreases) because same harmonic number requires proportionally larger magnetic field for a higher frequency. Accordingly, at higher frequency images, the stripes are shifted toward the footpoints, and their contrast (or amplitude of the intensity oscillations) decreases.

Apparently, having these stripes detected in real observations would offer a highly efficient way of model-independent quantitative measurement of the coronal magnetic field. These stripes become more pronounced for anisotropic distribution of the fast electrons. Moreover, in the anisotropic case, an amplification due to negative gyrosynchrotron absorption can give rise to a so-called electron cyclotron maser (ECM) coherent emission considered in the next section in more detail.

10.3 Electron Cyclotron Maser Emission from a Source with Random Inhomogeneities

10.3.1 Negative Absorption

As has been noted in Sect. 10.1 the absorption coefficient is not positively defined. Apparently, having a negative absorption coefficient requires a substantial departure of the particle distribution from an equilibrium one, because the absorption coefficient is positive in the equilibrium. Moreover, an arbitrary departure from the equilibrium will not necessarily result in the negative absorption: a distribution with some sort of inverse population is needed (see Sect. 10.1).

In case of gyrosynchrotron radiation produced by free plasma electrons the absorption coefficient is described by Eq. (10.56b), whose sign depends on brackets containing the distribution function derivatives over the momentum and pitch angle. For isotropic particle distributions the necessary condition for the ECM instability is a region with positive derivative of the distribution function over momentum modulus, e.g., a “ring” distribution detected

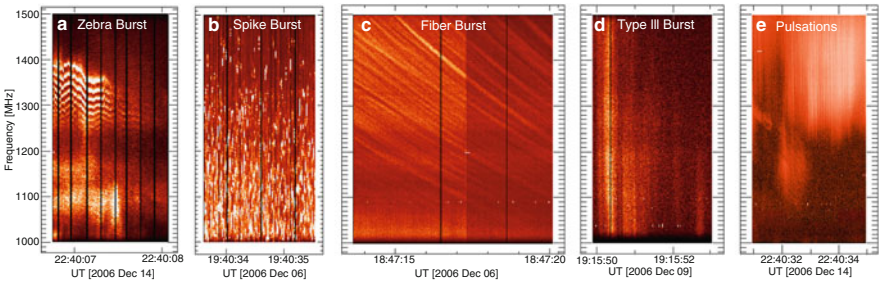

Figure 10.10: Examples of solar radio bursts highly structured in temporal and spectral domains produced by coherent emission mechanisms recorded by FST during strongest on record solar flares occurred on December, 2006: **(a)** zebra burst; **(b)** spike burst; **(c)** fiber burst; **(d)** type III burst; and **(e)** pulsating burst. Areas with a more diffuse continua-like emissions are also present in panels (a) and (e) (courtesy by Dr. Dale Gary).

in planet magnetospheres (Delory et al. 1998; Ergun et al. 2000; Strangeway et al. 2001; Lamy et al. 2010) and implied in cool "brown dwarf" stars (Kuznetsov et al. 2012), although it is not required for anisotropic electron distributions.

For most of the practically interesting cases the instability occurs at one or a few narrow frequency regions around the gyrofrequency or small-integer multiples of it. These narrow windows of instability are specified by favorable resonance conditions when the positive contribution along the integration path (which can be formulated in terms of a "resonance ellipse" (Treumann 2006) because the integrations over $\mathrm{d}p$ and $\mathrm{d}\mu$ are linked to each other by the resonant condition described by the δ-function) overcomes a more usual negative contribution.

It is highly important to realize that to correctly take into account the true resonance conditions one must retain the full relativistic form of the δ-function argument even for nonrelativistic radiating electrons because for a narrow instability window even a small change in the resonance condition can significantly change the whole picture or even quench the instability. This means that the ECM properties are highly sensitive to (otherwise minor) details of the emission source. In particular, the specific results differ substantially depending on the functional form of the electron distribution function and on global source properties including temperature, density, and magnetic field. This implies that any detailed ECM treatment should be performed specifically for each kind of the astrophysical objects where the ECM generation is expected.

Currently, the ECM is believed to be responsible for many kinds of radiation from space plasma and astrophysical objects including planetary magnetospheres (e.g., terrestrial, Jovian, and Saturnian), brown dwarfs, solar and stellar coronae, or even from blazar jets. Among many possible parameter regimes and phenomena of interest we concentrate on only one type of sporadic coherent solar radio emission (Fig. 10.10), the *narrowband mi-*

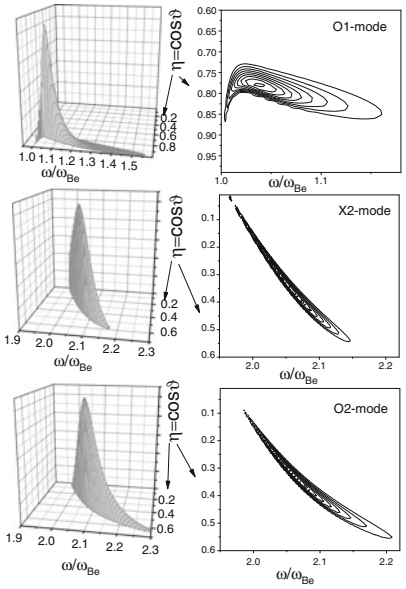

Figure 10.11: 3D (*left column*) and contour (*right column*) plots of the spatial growth rates of O1 (*top*), X2- (*middle*), and O2 (*bottom*) modes for the parameters: $Y = 1$, $\theta_c = 45\,^\circ$, $\Delta\mu = 0.15$, $p_0/mc = 0.2$, $p_{\rm br}/mc = 3$, and the spectral index of the electron distribution over momentum modulus $\gamma = 6$. Note that the instability region covers a rather broad spectral range, although the spectral bandwidth is small for each selected η value.

crowave spikes, likely to be generated by the ECM mechanism in solar coronal (flaring) loops (Fleishman and Melnikov 1998). In a dynamic spectrum, e.g., Fig. 10.10b, the spikes appear as apparently randomly distributed isolated peaks of radio emission. These peaks are characterized by the narrowest spectral bandwidth, shortest duration, strongest brightness temperature, and highest degree of circular polarization among all kinds of the solar emission.

The solar coronal magnetic loops are characterized by the plasma frequency to gyrofrequency ratio $Y = \omega_{\rm pe}/\omega_{\rm Be} \sim 1$ of the order of unity. The fast electrons accelerated in flares are mildly relativistic, $E \gtrsim 10\,{\rm keV}$ with a broad, e.g., power-law, energy spectrum, and the mean angular distribution can be approximated by a loss cone (with a deficit of electrons streaming along the magnetic field lines). Examples of the spatial growth rates of the ordinary wave mode around the fundamental and second harmonics of the gyrofrequency (O1 and O2 modes) and the extraordinary wave mode around the second harmonics (X2 mode) are given in Fig. 10.11 in the 3D perspective view (left) and in projection to the plane of ω and $\eta = \cos\theta$ (right). Figure 10.12 displays how the maximum (over each corresponding peak in the ω–η plane, Fig. 10.11) growth rate changes as the plasma parameter Y

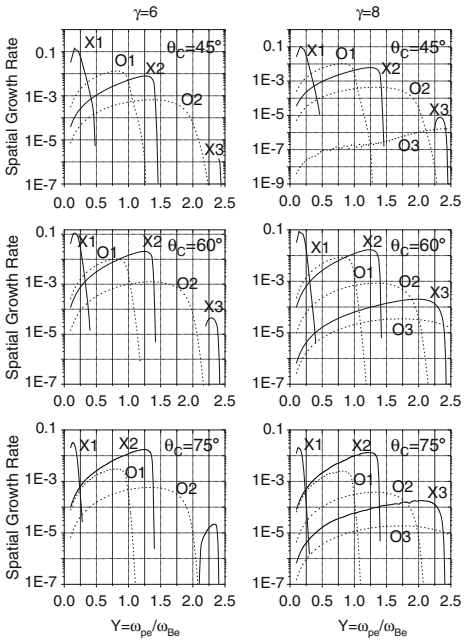

Figure 10.12: Spatial growth rates for three first harmonics of the gyrofrequency for various parameters: $\gamma = 6$ (*left column*) and $\gamma = 8$ (*right column*); $\theta_c = 45\,^\circ$ (*top*), $\theta_c = 60\,^\circ$ (*middle*), and $\theta_c = 75^\circ$ (*bottom*). Set of basic parameters is used: $\Delta\mu = 0.15$, $p_0/mc = 0.2$, and $p_{\rm br}/mc = 3$.

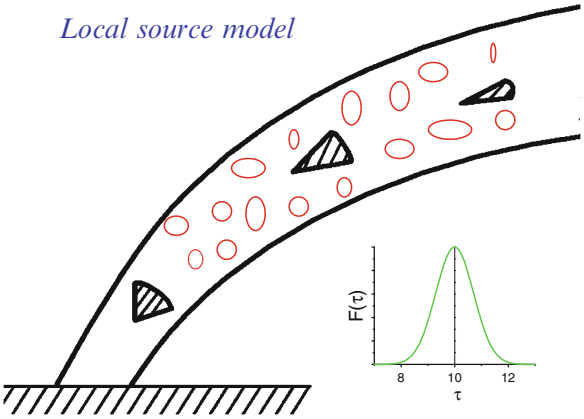

Figure 10.13: Sketch for the local trap model of spike generation. *Red ovals* show local traps in which the pitch-angle anisotropy of the fast electron distribution is enhanced due to fluctuations of the magnetic field provided by magnetic turbulence in the large-scale trap. The *inset* displays the adopted symmetric (gaussian) distribution of the local spike sources over the ECM optical depth τ with a mean value of $\tau = 10$ and a dispersion of $\sigma = 1$ (Rozhansky et al. 2008). Reproduced by permission of the AAS.

changes. One can see that each wave mode can only dominate within a very limited range of Y value, so for moderately large Y no ECM instability is possible.

A most realistic available model of a radio spike source assumes that fast electrons (perhaps, accelerated due to a flare energy release) are trapped in a magnetic loop and maintain a loss-cone distribution not far from a marginal stability state. The model postulates presence of a magnetic turbulence in this loop. This turbulence modulates the angular distribution of the fast electrons in such a way that the ECM instability condition is satisfied at a number of locations in the loop, so each of these locations acts as a local source (see Fig. 10.13) producing a single spike with the properties (e.g., central frequency and spectral bandwidth) set up by the local conditions. In a gradually nonuniform magnetic loop the frequencies of various spikes are different from each other (as they are specified by the local gyrofrequency); having the ECM conditions randomly set up at various locations at differing time because of random nature of the turbulent field, this model offers a consistent qualitative interpretation of the spike cluster phenomenon.

We anticipate that if the radio spikes are generated in a randomly inhomogeneous turbulent plasma the spike properties must inherit some imprints of the turbulence. Intuitively, it is reasonable to expect that the random inhomogeneity will primarily affect the ECM resonance conditions and, thus, the spectral properties of the radio spikes. Below we consider the role of the random inhomogeneity of the magnetic field in the spike source and determine the distribution of spikes over their bandwidth within the "local traps' model."

10.3.2 Approximate Expressions for the Spatial Growth Rates

After a few e-folding amplification lengths the radiation intensity will have a spectral peak at the frequency f_0, where[3] $\varkappa(f, \boldsymbol{r})$ has a local maximum vs frequency. Now, expanding $\varkappa(f, \boldsymbol{r})$ in a series around f_0 (f_0 depends apparently on $\boldsymbol{r}$) to the second-order accuracy terms, provided that the ECM growth rates are smooth functions of frequency (see Fig. 10.11 as an example), we obtain the radiation spectral line in the form of a composition of local gaussian peaks:

$$J = \int \mathrm{d}\boldsymbol{r} S(\boldsymbol{r}) \exp\left(2 \int^{z} \mathrm{d}z \left(\varkappa(f_0, \boldsymbol{r}) - \frac{\partial^2 \varkappa(\boldsymbol{r})}{\partial f_0^2}(f - f_0(\boldsymbol{r}))^2\right)\right). \quad (10.61)$$

In case of random functions $\varkappa(\boldsymbol{r})$ and $f_0(\boldsymbol{r})$, expression (10.61) has yet to be averaged over ensemble of the inhomogeneities. Thus, the account of the magnetic and density inhomogeneities requires finding the spatial dependences

[3] Here, unlike Sect. 10.1, the absorption coefficient is $-\varkappa(f, \boldsymbol{r})$; thus, $\varkappa(f, \boldsymbol{r})$ is the amplification coefficient.

of the quantities entering Eq. (10.61) and further averaging and integrating Eq. (10.61) over the source volume.

Let us present the parabolic approximation of the exponent index in Eq. (10.61) in the form

$$\varkappa_\sigma \simeq \varkappa_\sigma^m (1 - \alpha(s - s_0)^2), \tag{10.62}$$

where $\varkappa_\sigma^m$ is the maximum spatial growth rate for a given parameter set including the viewing angle, $s = f/f_{\rm Be}$, $s_0 = f_0/f_{\rm Be}$, $f_{\rm Be}$ is the gyrofrequency. The coefficient $\varkappa_\sigma^m$ does not depend on frequency, although proportional to the gyrofrequency $f_{\rm Be}$, depends on the plasma parameter $Y = \omega_{\rm pe}/\omega_{\rm Be} = f_{\rm pe}/f_{\rm Be}$ (all these dependences are specific for a given eigenmode σ and harmonic number s_0; see Fig. 10.12) and proportional to the fast to background electron number density ratio (n_b/n_0). The parabolic parameter α (that eventually specifies the natural bandwidth of the ECM spectrum) depends primarily on the functional shape and parameters of the fast electron distribution function (anisotropy, energy spectral index, characteristic electron energy, etc.) and on the viewing angle, while displays only a very weak dependence on Y (Fleishman 2004b). We note that in case of a narrow ECM line the parameter α is much larger than one; we adopt

$$\alpha = \text{const} \gg 1. \tag{10.63}$$

Dependence of the spatial growth rate $\varkappa$ on magnetic field includes both explicit dependence $\varkappa_\sigma^m(f_{\rm Be})$ and $s(f_{\rm Be}) = f/f_{\rm Be}$ and implicit dependence if the plasma parameter Y changes in the source along with the magnetic field. Consider small variations of B in the source

$$\delta B/B \ll 1, \tag{10.64}$$

and approximate the dependences $Y(B)$, $\varkappa_\sigma^m(B)$, and $s_0(B)$ by power-law functions with various indices

$$\varkappa_\sigma^m(\delta B) = \varkappa_\sigma^m(0)\left(1 + \frac{\delta B}{B}\right)^\lambda, \tag{10.65a}$$

$$s_0(\delta B) = s_0(0)(1 + \delta B/B)^\epsilon, \tag{10.65b}$$

where $\varkappa_\sigma^m(0)$, λ, and ϵ are constant parameters; for example, if $Y = \text{const}(B)$, then $\lambda = 1$ and $\epsilon = 0$; B is the mean value of the magnetic field at the source, $s_0 = f_0/f_{\rm Be}$ is the peak frequency of the ECM radiation in the uniform field B, $f_{\rm Be}$ is the corresponding gyrofrequency, and $\delta B(\boldsymbol{r})$ is the variation of the magnetic field in the source. The dimensionless frequency s has obviously the form

$$s(\delta B) = \frac{f}{f_{\rm Be}(1 + \delta B/B)}. \tag{10.66}$$

Note that this approach is not limited to the magnetic inhomogeneities only; the density variations can also be consistently accounted via corresponding variations of the Y parameter. Indeed, the Y variation is produced by variations of both density and magnetic fluctuations:

$$\frac{\delta Y}{Y} = \frac{\delta N}{2N} - \frac{\delta B}{B}. \tag{10.67}$$

Adopt that the density fluctuations are proportional to the magnetic fluctuations (which is exactly valid for the magnetosonic waves, for example):

$$\frac{\delta N}{2N} = a\frac{\delta B}{B}; \tag{10.68}$$

thus

$$\frac{\delta Y}{Y} = (a-1)\frac{\delta B}{B}. \tag{10.69}$$

We see, therefore, that the model parameters λ and ϵ depend on a and, thus, on the density inhomogeneities.

Substituting Eqs. (10.65)–(10.66) into Eq. (10.62), we can safely truncate the expansion of $\varkappa_\sigma$ at the second-order terms over $(\delta B/B)$; discarding small terms we obtain

$$\varkappa_\sigma = \varkappa_\sigma^m(0)\left\{A_0 + A_1\frac{\delta B}{B} + A_2\left(\frac{\delta B}{B}\right)^2\right\}, \tag{10.70}$$

where

$$A_0 = (1-\alpha(s-s_0)^2), \tag{10.71a}$$

$$A_1 = \lambda + 2\alpha s_0(1+\epsilon)(s-s_0) + 2\alpha(2-\lambda)(s-s_0)^2, \tag{10.71b}$$

$$A_2 = -\alpha s_0^2(1+\epsilon)^2 + \alpha s_0(1+\epsilon)(\epsilon - 2(2-\lambda))(s-s_0). \tag{10.71c}$$

Here s_0 is used for $s_0(0)$ (see Eq. (10.65b)). Note that presence of the linear term over $(s-s_0)$ gives rise to a shift of the spectral peak due to magnetic inhomogeneity along with the spectral broadening.

10.3.3 ECM Peak Broadening in a Weak Random Magnetic Field

Let $\delta B/B$ be a random function with zero mean. Then the ECM radiation intensity is a statistical mean (over ensemble) of Eq. (10.61), where we can safely neglect spatial variations of the source function $S(\boldsymbol{r})$ and take it out of the integral:

$$J = J_0\left\langle\int \mathrm{d}\boldsymbol{r}_\perp \exp\left(\int \mathrm{d}z\varkappa_\sigma(\boldsymbol{r})\right)\right\rangle, \tag{10.72}$$

where J_0 is a new constant. We consider here only linear terms over $\delta B/B$ in $\varkappa(\boldsymbol{r})$ expansion Eqs. (10.70)–(10.71b):

$$J = J_0 \int \mathrm{d}\boldsymbol{r}_\perp \Bigg\langle \exp\Bigg(\varkappa_\sigma^m L(1-\alpha(s-s_0)^2) + \varkappa_\sigma^m \Big[\lambda + \alpha(2-\lambda)(s-s_0)^2 + 2\alpha(s-s_0)s_0(1+\epsilon)\Big] \int_{-L/2}^{L/2} \mathrm{d}z \frac{\delta B(\boldsymbol{r})}{B}\Bigg)\Bigg\rangle. \tag{10.73}$$

Assuming the random field to be a gaussian random process we make use of the expression

$$\langle \exp(AX)\rangle = \exp\left(A^2 \left\langle X^2\right\rangle /2\right), \tag{10.74}$$

so the ECM intensity receives the form

$$\begin{aligned} J = {} & J_0 \int \mathrm{d}\boldsymbol{r}_\perp \exp\left\{\varkappa_\sigma^m L\left(1-\alpha(s-s_0)^2\right)\right\} \\ & \times \exp\left\{\left((\varkappa_\sigma^m)^2/2\right)\left[\lambda+\alpha(2-\lambda)(s-s_0)^2+2\alpha(s-s_0)s_0(1+\epsilon)\right]^2\right. \\ & \left. \times \int_{-L/2}^{L/2} \mathrm{d}z \int_{-L/2}^{L/2} \mathrm{d}z' \frac{\langle \delta B(\boldsymbol{r})\delta B(\boldsymbol{r}')\rangle}{B^2}\right\}. \end{aligned} \tag{10.75}$$

Thus, the ECM intensity is expressed via a double integral over the longitudinal coordinate from the pair correlator of the amplitudes of the random magnetic field $\langle \delta B(\boldsymbol{r})\delta B(\boldsymbol{r}')\rangle$.

The averaging in the exponent is convenient to perform by two steps. The first step is averaging of $\langle \delta B(\boldsymbol{r})\delta B(\boldsymbol{r}')\rangle_\phi$ over the random phases of the spatial waves composing the random magnetic field $\delta B(\boldsymbol{r})$. Since there are no reliable data on the turbulence properties in the ECM sources we adopt a simple model of statistically uniform and isotropic magnetic inhomogeneities. In this case,

$$\langle \delta B(\boldsymbol{r})\delta B(\boldsymbol{r}')\rangle_\phi = \int |\delta B|^2_{\mathbf{k}} e^{i\mathbf{k}(\mathbf{r}-\mathbf{r}')}\mathrm{d}\boldsymbol{k} = \left\langle \delta B^2\right\rangle T(|\boldsymbol{r}-\boldsymbol{r}'|), \tag{10.76}$$

where $|\delta B|^2_{\mathbf{k}} = \left\langle \delta B^2\right\rangle T(\boldsymbol{k})$ is the spectrum of random field (cf. Sect. 9.5)

$$\int |\delta B|^2_{\mathbf{k}} \mathrm{d}\boldsymbol{k} = \left\langle \delta B^2\right\rangle, \tag{10.77}$$

$\left\langle \delta B^2\right\rangle$ is the mean square of the random magnetic field and $T(|\boldsymbol{r}-\boldsymbol{r}'|)$ is the spatial pair correlator of the random field normalized by the condition

$$\frac{1}{V_c}\int T(r)\mathrm{d}\boldsymbol{r} = 1, \tag{10.78}$$

where V_c is the correlation volume of the random field, $V_c = L_c^3$, and L_c is the corresponding correlation length.

The second step is, evidently, the averaging over the source volume V_s. To perform this averaging we note that the random phase approximation used at the first step can only be valid for relatively small-scale inhomogeneities with the correlation length L_c much smaller than the source size. Thus, we can safely adopt

$$\frac{1}{V_c}\int_{V_s} T(r)\mathrm{d}\boldsymbol{r} \simeq 1, \tag{10.79}$$

i.e.,

$$\langle \delta B(\boldsymbol{r})\delta B(\boldsymbol{r}')\rangle = \left\langle \delta B^2 \right\rangle. \tag{10.80}$$

Then, taking the remaining integrals in the exponent gives a factor of L^2, so

$$\begin{aligned} J &= J_0 S \exp\left(\varkappa_\sigma^m L(1-\alpha(s-s_0)^2)\right) \\ &\quad \times \exp\left[\frac{(\varkappa_\sigma^m)^2}{2}\left(\lambda+\alpha(2-\lambda)(s-s_0)^2+2\alpha(s-s_0)s_0(1+\epsilon)\right)^2 L^2 \frac{\left\langle \Delta B^2\right\rangle}{B^2}\right], \end{aligned} \tag{10.81}$$

where S is the projected source area. Let us expand the square of the parentheses in the latter exponent retaining the terms up to the order of $(s-s_0)^2$. The higher-order terms describe the spectrum asymmetry and can easily be obtained from Eq. (10.81) if needed. Introducing the optical depth of the corresponding uniform source $\tau_0 = \varkappa_\sigma^m L$ and discarding some small terms (when $\alpha \gg 1$), we obtain

$$J=J_m \exp\left(-\tau_0\alpha\left[\left(1-2(1+\epsilon)^2 s_0^2\alpha\tau_0\frac{\left\langle \Delta B^2\right\rangle}{B^2}\right)(s-s_0)^2-2\lambda(1+\epsilon)s_0\tau_0\frac{\left\langle \Delta B^2\right\rangle}{B^2}(s-s_0)\right]\right), \tag{10.82}$$

where

$$J_m = J_0 S \exp\left(\tau_0\left(1+\lambda^2\tau_0\frac{\left\langle \Delta B^2\right\rangle}{B^2}\right)\right) \tag{10.83}$$

is the ECM peak intensity, which is in most cases set up by quasilinear saturation, Sect. 4.2, or, in some rare cases, by nonlinear wave–wave interactions, Sect. 4.3; see also estimates below in Sect. 10.4.1. Isolating a perfect square in the exponent of Eq. (10.82) we finally obtain

$$J = J_m \exp\left\{-(1-\Delta_{\mathrm{st}})\frac{(s-s_0-\Delta s_0)^2}{2\Gamma_0^2}\right\}, \tag{10.84}$$

where

$$\Gamma_0 = 1/\sqrt{2\alpha\tau_0} \tag{10.85}$$

is the ECM natural spectral bandwidth,

$$\Delta_{\rm st} = 2(1+\epsilon)^2 s_0^2 \alpha \tau_0 \frac{\langle \delta B^2 \rangle}{B^2}, \tag{10.86a}$$

$$\Delta s_0 = \frac{\lambda(1+\epsilon) s_0 \tau_0 (\langle \delta B^2 \rangle / B^2)}{1-\Delta_{\rm st}}. \tag{10.86b}$$

Expression for J (10.84) is derived assuming $\delta B/B \ll 1$. However, the obtained value $\Delta_{\rm st}$ is not necessarily small compared with unity since $\alpha \gg 1$ and $\tau_0 \gg 1$. Nevertheless, for $(1-\Delta_{\rm st}) > 0,\ \Delta s_0 \ll s_0$ the spectral line still has a gaussian shape (Fig. 10.14), with the bandwidth

$$\Gamma = \frac{\Gamma_0}{\sqrt{1-\Delta_{\rm st}}} \approx \Gamma_0 (1 + \Delta_{\rm st}/2). \tag{10.87}$$

In contrast, for $(1-\Delta_{\rm st}) < 0,\ \Delta s_0 \ll s_0$, the coefficient at $(s-s_0)^2$ turns positive, so at $s \approx s_0$ the spectrum has a minimum rather than a peak. This could have meant that in a medium with relatively high magnetic inhomogeneities the original gaussian spectrum breaks onto two (or more) peaks, i.e., a spectral line splitting takes place.

To quantitatively describe the splitting effect we need more statistical information on the random field than contained in second-order correlator (10.76). We do not consider the splitting problem here while addressing the problem of the peak broadening in greater detail.

10.3.4 Theory of Strong Broadening of the ECM Spectrum

As has been found, even in the presence of otherwise weak magnetic inhomogeneities, $\delta B/B \ll 1$, the correction to the natural bandwidth $\Delta_{\rm st}$ is not necessarily small compared with unity. Apparently, expression (10.84) can only be valid if $\Delta_{\rm st} < (\ll) 1$. Otherwise, Eq. (10.84) implies an infinitely large radiated energy, i.e., it could only be applicable at a small vicinity of the frequency $s_0 \pm \Delta s_0$, which is, however, irrelevant to the problem of spectral broadening: for $\Delta_{\rm st} > 1$, Eq. (10.84) describes a minimum of the emission rather than its spectral peak.

Thus, a more accurate way of the ECM spectral peak treatment is called for when $\delta B/B \ll 1$, while $\Delta_{\rm st} \gtrsim 1$. To develop a theory of a strong ECM spectral broadening we use a renormalization approach similar to that developed in Chap. 7 for the charged particle transport.

Specifically, we adopt the random field to consist of statistically independent Fourier components with a broad distribution over spatial scales, Fig. 10.15. In this case the entire inhomogeneity spectrum can be split up

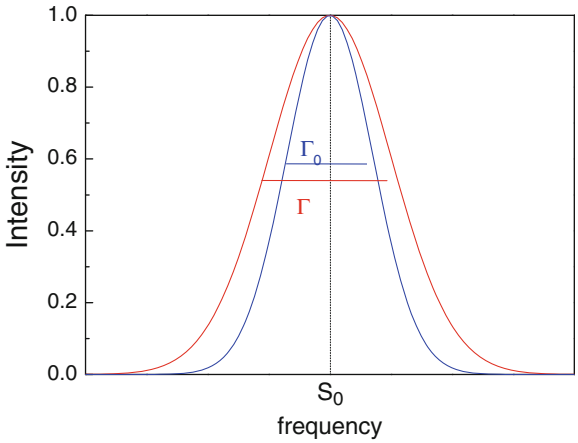

Figure 10.14: ECM emission peaks in uniform and nonuniform magnetic fields normalized to one.

onto many independent regions as shown in Fig. 10.15 in such a way that each of them contains only a small fraction of the random field energy density:

$$\int_{k_i}^{k_{i+1}} |\delta B|^2_{\mathbf{k}} \mathrm{d}\boldsymbol{k} = \delta B_i^2, \tag{10.88a}$$

$$\sum_{i=1}^{N} \delta B_i^2 = \delta B^2, \quad \delta B_i^2 \ll \delta B^2 \text{ if } N \gg 1. \tag{10.88b}$$

Assume that the number of such regions N is so large that the ECM spectrum broadening provided by each of them is small, $\Delta_{st,i} \ll 1$ (here the value $\Delta_{st,i}$ is specified by Eq. (10.86a) in which δB_i^2 is substituted).

Making use of statistical independency of the random field components we can repeat the averaging of Eq. (10.72) N times over each random field component independently. Eventually, the ECM spectrum peak receives the shape:

$$J = J_m \exp\left\{-\frac{(s - s_0 - \Delta s_p)^2}{2\Gamma_0^2} \prod_{i=1}^{N}(1 - \Delta_{st,i})\right\}. \tag{10.89}$$

With no loss of generality we can use such splitting of the random field spatial spectrum over N regions that

$$\Delta_{st,i} = \frac{\Delta_{\mathrm{st}}}{N} \tag{10.90}$$

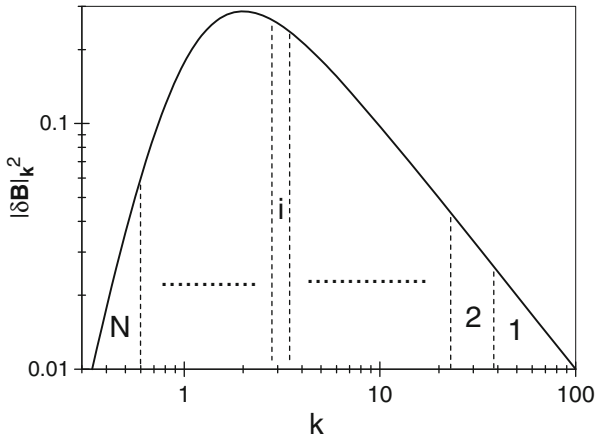

Figure 10.15: Example of the broad spectrum of a random magnetic field. The spectral function of the random field is split onto N statistically independent components. Each component contains a small fraction of magnetic energy and can be taken into account within perturbation theory (Fleishman 2004a). Reproduced by permission of the AAS.

and use limiting transition to the case of large N:

$$\lim_{N\to\infty}\prod_{i=1}^{N}\left(1-\frac{\Delta_{\rm st}}{N}\right)=\lim_{N\to\infty}\left(1-\frac{\Delta_{\rm st}}{N}\right)^{N}=\exp(-\Delta_{\rm st}). \tag{10.91}$$

This yields a *renormalized* gaussian spectral peak:

$$J=J_m\exp\left\{-e^{-\Delta_{\rm st}}\ \frac{(s-s_0-\Delta s_p)^2}{2\Gamma_0^2}\right\}, \tag{10.92}$$

where

$$\Delta s_p=\lambda(1+\epsilon)s_0\tau_0\frac{\langle\delta B^2\rangle}{B^2}. \tag{10.93}$$

Apparently, Eq. (10.92) yields Eq. (10.84) for $\Delta_{\rm st}\ll 1$.

Renormalized spectrum Eq. (10.92) maintains a gaussian shape with the renormalized bandwidth

$$\Gamma=\Gamma_0 e^{\Delta_{\rm st}/2} \tag{10.94}$$

and is valid for relatively large magnetic inhomogeneities. In particular, for $\Delta_{\rm st}\sim 1$, the natural spectral line broadens in 3–10 times. Therefore, the effect of the turbulent magnetic inhomogeneities on the ECM spectrum is rather significant, namely, the small-scale inhomogeneities with a broad spectrum give rise to a large spectrum broadening compared with the ECM "natural" bandwidth.

Nevertheless, the applicability of the renormalized theory is restricted by a requirement that the resulting spectrum bandwidth remains much smaller than one. Indeed, for $\Delta_{st} \gg 1$, the predicted spectral bandwidth is very broad, which implies a broad spectral range occupied by the ECM emission. However, the adopted approximations and simplifications may not be applicable for very large $\Delta_{st} \gg 1$, since the parabolic approximation of growth rates (10.62) fails far from the spectral peak and higher-order terms as $(s - s_0)^3$ and $(s - s_0)^4$ in the exponent may become important, which can give rise to a departure of the spectrum shape from the gaussian. In addition, higher-order moments of the random field may play a role in this case; in particular, they can give rise to the spectral line splitting onto two or more subpeaks.

10.3.5 Local Trap Model

As has already been noted, most of the spike properties are consistent with the local trap model. This model adopts that a spike cluster is produced at a significant portion of a magnetic trap (Fig. 10.13), where a loss-cone distribution of the trapped fast particles is formed due to emptying the loss cone as a result of the electron precipitation into the footpoints. The overall pitch-angle anisotropy is moderate on average provided that the mean fast electron distribution is at about the marginal stability state in respect to ECM generation. An important ingredient of the local trap model is a magnetic turbulence, which gives rise to local variation of the fast electron distribution anisotropy. Under favorable conditions, this turbulence will increase the anisotropy to the extent sufficient for the ECM instability to develop at some local places inside the large-scale magnetic trap. Such favorable places represent those local spike sources, quasi-randomly distributed over the trap.

As a byproduct of the key role of the magnetic turbulence in forming the spike local sources, the model suggests that the small-scale tail of the magnetic turbulence spectrum persists in each local spike source. Therefore, the spikes are formed in a source, where random magnetic inhomogeneities are superimposed on the mean magnetic field of the source. The bandwidth of a single ECM peak described by Eq. (10.94) is convenient to express as

$$\Gamma = \Gamma_0 \exp\left(\frac{a}{2\Gamma_0^2}\right), \tag{10.95}$$

where Γ_0 is the "natural" bandwidth of the ECM peak in the uniform source with the optical depth τ at the spectral peak,

$$a = \frac{s_0^2}{2}\frac{\langle \delta B^2 \rangle}{B^2} \tag{10.96}$$

is a "turbulence parameter," defined by the ECM harmonic number s_0 and the magnetic turbulence energy density $\langle \delta B^2 \rangle / 8\pi$ normalized by the magnetic energy density $B^2/8\pi$. We note that the magnetic inhomogeneities give rise to quite a strong ECM broadening when $a \gtrsim \Gamma_0^2$. Since $\Gamma_0^2 \ll 1$, rather weak random inhomogeneities of the magnetic field provide large ECM broadening.

To simulate the spike bandwidth distribution we consider a simple model based of the ECM emission within the local source model. Specifically, we adopt that the natural spike bandwidth is about 0.1–0.3 % in agreement with calculations of the ECM natural spectral bandwidth (Fleishman 2004b). We postulate a symmetric gaussian distribution of the natural bandwidth over the spike local sources. Then, we adopt that the turbulent parameter a has another gaussian distribution, not correlated with the natural bandwidth distribution.

Random combinations of the pairs of Γ_0 and a taken from those two parent distributions generate artificial sets of spikes. Properties of these artificial spike distributions are specified by the parameters of the adopted gaussian distributions, i.e., mean values and dispersions of Γ_0 and a. In the discussed modeling (Rozhansky et al. 2008) the mean Γ_0 value was kept constant at 0.2 % level, while the a value varied to study dependence of the distribution moments on a. The dispersion of both values was taken to be about 15 %. An example of the distribution produced by the model is given in Fig. 10.16. Eventually, 50 sets with 3,000 artificial spikes in each set were generated and four first moments of this distributions were calculated, which are plotted in Fig. 10.17. The asymmetry of the distribution is characterized by the skewness (the third moment):

$$S = \frac{\left\langle (f - f_0)^3 \right\rangle}{\sigma^3}, \tag{10.97}$$

which is zero for the normal distribution. The deviation from the normal distribution (in terms of distribution peak flatness) is estimated by the forth moment, kurtosis, defined as

$$K = \frac{\left\langle (f - f_0)^4 \right\rangle}{\sigma^4}, \tag{10.98}$$

which is $K_{\mathrm{norm}} = 3$ for the normal distribution.

Figure 10.16 displays a representative example of the model bandwidth distribution, whose most evident feature is a clear asymmetry: the distribution has a sharp cutoff toward narrow spectral lines, while contains a long "tail" toward the broad lines. Remarkably, this *asymmetry* appears in a model with large number of sources with all the relevant parameters adopted to obey *symmetric* gaussian distributions. Therefore, the obtained asymmetry is a model-independent intrinsic property of renormalized ECM spectrum bandwidth Eq. (10.94).

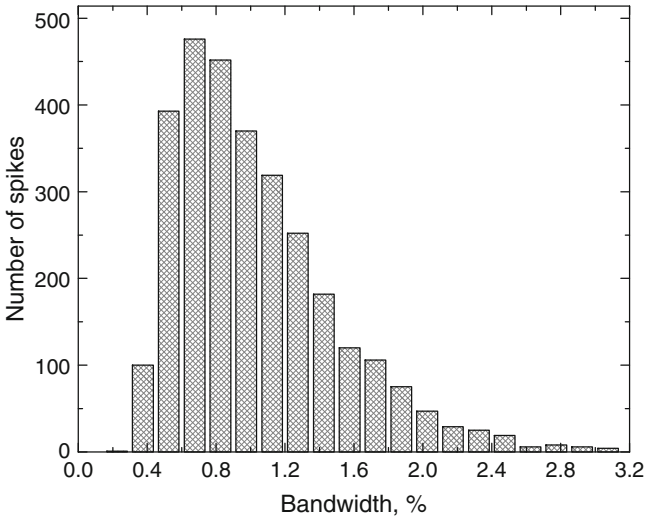

Figure 10.16: Spike bandwidth distribution obtained from the local trap model (Rozhansky et al. 2008). Reproduced by permission of the AAS.

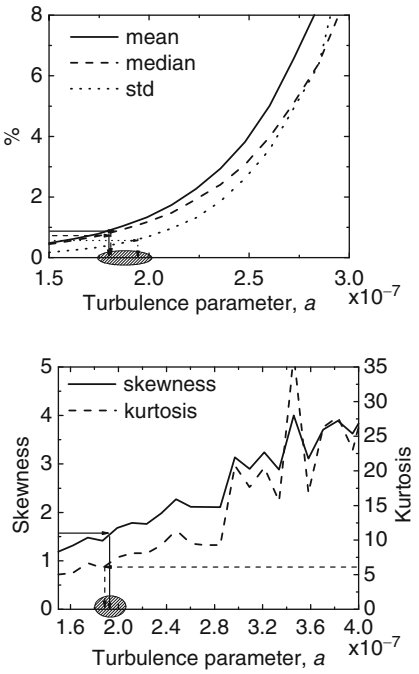

Figure 10.17: Dependences of the spike bandwidth distribution parameters on turbulence parameter a obtained from the local trap model described in the text (Rozhansky et al. 2008). Reproduced by permission of the AAS.

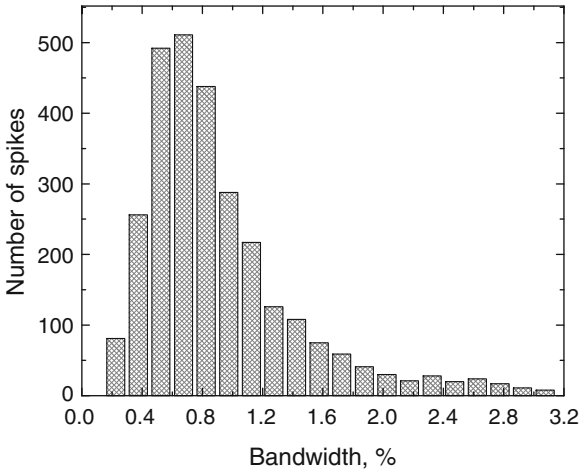

Figure 10.18: Bandwidth distribution of the extracted spikes. The bin size is taken to be 0.15 % to avoid any coincidence with the spectral resolution of the instrument. Note prominent asymmetry of the distribution (Rozhansky et al. 2008). Reproduced by permission of the AAS.

10.3.6 Spectral Bandwidth of Solar Radio Spikes

Solar radio spikes are very narrowband with a typical bandwidth of the order of 1 % and minimal bandwidth less than 0.1 %. The bandwidth was found to change significantly within any single event and even greater from one event to another. In particular, no clear correlation between the bandwidth and the observing frequency was noted. Thus, the bandwidth seems to be more characteristics of the event rather than function of frequency.

Then, no unique correlation between the bandwidth and radio flux of the spikes was found: there were uncorrelated cases, as well as correlated and anti-correlated cases. These observational results imply that the observed spike bandwidth is formed mainly by source inhomogeneity rather than natural bandwidth of the underlying emission process.

Curiously, the observed spike bandwidth distributions demonstrate more or less asymmetric shapes in the sense implied by Fig. 10.16; however, the number of individual spikes used for the analysis is typically too small to derive the higher moments of the distribution reliably, which is needed to make a meaningful comparison with the model presented in Sect. 10.3.5. Here we use one of very few cases with a statistically significant number of the individual spikes analyzed: a dense cluster of solar radio spikes registered from 05:18:03 to 05:18:09 UT on April 10, 2001, at 4.5–6 GHz by the Purple Mountain Observatory spectrometer (Nanjing, China) operating in the 4.5–7.5 GHz range with the temporal resolution of 5 ms. The cluster occurred during a X2.3 flare on April 10, 2001, NOAA region 9415, located close to

the center of the solar disk (S23W06-08). The flare was associated with a halo CME, meter-wavelength types II and IV bursts, and strong microwave continuum burst. The spike cluster occurred during a local impulsive peak of strong long microwave burst with the absolute peak value in excess of 6,000 sfu around 9.4 GHz. Highly polarized coherent emissions were recorded (LCP at 2 GHz and RCP at 3.75 GHz) around the time of the spike cluster.

Using a specially developed technique of overlapping spike decomposition onto individual gaussian peaks, more than 3,000 individual spikes have been identified. Each spike i is characterized by its amplitude A_i, mean frequency f_{0i}, and the bandwidth Γ_i; the entire spike cluster is, accordingly, characterized by distributions of these three measures and correlations between them. Here we discuss only one of these distributions, namely, the distribution of the spike relative bandwidths. This commonly used dimensionless parameter is defined as spike width at half-maximum divided by the central frequency of the spike.

The distribution of the spike relative bandwidths appears to be remarkably asymmetric. It has a skew shape with rapid increase at low values of the relative bandwidth followed by maximum at 0.6 % and smooth tail approaching zero at approximately 3 % (Fig. 10.18) with the mean value of 0.91 ± 0.02, the median value of 0.77 ± 0.01, and standard deviation 0.55 ± 0.04. For the spike cluster under study the overall skewness is about 1.6 ± 0.2, while the kurtosis is $K \approx 6 \pm 0.6$, in contrast to that of the normal distribution, $K_{\mathrm{norm}} = 3$. Rather weak correlation is found between amplitude and spike relative bandwidth; the appropriate rank correlation coefficient is only $r \approx -0.2$. No correlation is observed between mean frequency and relative bandwidth of the spikes (the appropriate rank correlation coefficient is $r \approx 0.04$).

Figure 10.17 displays the obtained values of the observed distribution moments on top of the corresponding model curves. Remarkably, all the observed moments are consistent with corresponding model moments for a single value of the turbulent parameter $a \approx 2 \times 10^{-7}$, which is especially important because the model employs only one free parameter to yield correct values of all four moments together. Stated another way, the simulated spike distribution is remarkably similar to the observed one for this particular event, which is a strong point of evidence in favor of the ECM mechanism of the spike generation within the local trap model with magnetic turbulence. Thus, the demonstrated agreement between the model and observations offers, through the comparison of the observed and model moments, an efficient tool for studying weak magnetic inhomogeneities in the spike sources as a function of time and position for relatively long-lasting spike clusters observed with high spatial resolution, respectively. The spatially resolved observations will also help to determine the ECM harmonic number and thus decouple it from the random magnetic field level in Eq. (10.96). We note that the method is highly sensitive to the magnetic irregularities and capable of detecting the turbulence with remarkably low level $\left\langle \delta B^2 \right\rangle / B^2 \sim 10^{-7}$ or even less.

10.4 Nonlinear Processes

General treatment developed in Sect. 4.3 for nonlinear wave interactions applies, in particular, to the propagating electromagnetic (free-space) modes. Here we consider both stimulated scattering of the transverse waves on thermal ions and also coalescence processes giving rise to conversion of the plasma wave energy to the electromagnetic wave energy.

10.4.1 Stimulated Scattering of Transverse Waves on Thermal Ions

Variation of wave mode σ spectrum due to its nonlinear scattering on thermal ions is given by general equation (4.60), where the corresponding polarization vector components and wave dispersion must be substituted. Using $W_\sigma(\omega, \boldsymbol{n})$ instead of $W(\boldsymbol{k})$, we obtain

$$\frac{d^{(s)}}{\mathrm{d}t} W_\sigma(\omega, \boldsymbol{n}) = 2\gamma_s W_\sigma(\omega, \boldsymbol{n}) = -\frac{16\pi^2 e^2}{m^2\omega^3} W_\sigma(\omega, \boldsymbol{n}) R_\sigma(\boldsymbol{k}) \sum_{\sigma'=\pm\sigma} \mathrm{Re} \int_0^\infty \mathrm{d}\omega' \int_{-1}^{1} \mathrm{d}\eta' k''^2 M_{\sigma\sigma'} W_{\sigma'}(\omega', \boldsymbol{n}') R_{\sigma'}(\boldsymbol{k}') \frac{\delta\varepsilon_e'^2(\omega'', \boldsymbol{k}'')\delta\varepsilon_i''(\omega'', \boldsymbol{k}'')}{|\varepsilon^l(\omega'', \boldsymbol{k}'')|^2}, \tag{10.99}$$

where $\eta' = \boldsymbol{n}' \cdot \boldsymbol{B}/B$ and

$$M_{\sigma\sigma'} = \frac{\omega^4}{\omega_{\mathrm{pe}}^4} \left[(1 - n_\sigma^2)(\boldsymbol{e}^{*\sigma} \cdot \boldsymbol{e}^{\sigma'}) + n_\sigma^2 \frac{(\boldsymbol{k} \cdot \boldsymbol{e}^{*\sigma})(\boldsymbol{k} \cdot \boldsymbol{e}^{\sigma'})}{k^2} \right]^2. \tag{10.100}$$

Note, that because the waves participating in the scattering process have different frequencies and propagation directions, their polarization vectors are not strictly orthogonal to each other. Also, the polarization vectors contain, in a general case, a nonzero longitudinal component. Thus, the rate of nonlinear scattering of the ordinary wave mode to the extraordinary and vice versa is nonzero. Nevertheless, it is much smaller than the scattering without change of the sense of polarization (given that $k'' \ll k, k'$ and $\omega'' \ll \omega, \omega'$). It seems that the cross scattering can only be noticeable as a "leakage" of a dominant polarization into the secondary one in case of original powerful 100 % radiation. Below we make an estimate of the dominant nonlinear process assuming $\sigma' = \sigma$.

Substitution of the required dielectric permeabilities into Eq. (10.99) yields

$$\gamma_s = -\frac{2\pi^2 e^2}{m^2\omega^3} R_\sigma(\boldsymbol{k}) \int_0^\infty \mathrm{d}\omega' \int_{-1}^{1} \mathrm{d}\eta' M_{\sigma\sigma} W_\sigma(\omega', \boldsymbol{n}') R_\sigma(\boldsymbol{k}') \sqrt{\frac{\pi}{2}} \frac{\omega''}{|k_z''| v_{Ti}} \frac{\omega_{\mathrm{pe}}^2}{v_{Te}^2}$$
$$\times \exp\left[-\frac{1}{2}\left(\frac{\omega''}{k_z'' v_{Ti}}\right)^2\right]. \tag{10.101}$$

Now, adopt that the bandwidth of the original emission spectrum, $\Delta\omega_r$ is much broader than the width of the integral core, $\omega'' \sim \Delta\omega = 2\omega n_\sigma \eta v_{Ti}/c$, which allows using expansion of the wave energy density, $W_\sigma(\omega') \approx W_\sigma(\omega) + \omega'' \partial W_\sigma(\omega)/\partial\omega$. The first term of the expansion makes zero contribution as it is integrated with an odd term ω'', while the second term makes a nonzero contribution, so the scattering rate receives the form

$$\gamma_s = -\frac{2\pi^2 e^2}{m^2\omega^3} \sqrt{\frac{\pi}{2}} \frac{\omega_{\mathrm{pe}}^2}{v_{Te}^2} (\Delta\omega)^2 R_\sigma^2(\boldsymbol{k}) M_{\sigma\sigma} \frac{\partial W_\sigma(\omega, \eta)}{\partial\omega}. \tag{10.102}$$

For definiteness, let us consider ECM emission of extraordinary wave mode at the second gyroharmonics, which is believed to be responsible for generation of narrowband microwave solar spikes and a number of other planetary and stellar emission types. Equation (10.100) at $\omega \approx 2\omega_{\mathrm{Be}}$ yields $M_{\sigma\sigma'} \sim$ 1–4 depending on the angle and $\omega_{\mathrm{Be}}/\omega_{\mathrm{pe}}$ ratio; then taking into account $\Delta\omega \sim \omega_{\mathrm{Be}} v_{Ti}/c$ and $|\partial W_\sigma(\omega, \eta)/\partial\omega| \sim W_\sigma(\omega, \eta)/\Delta\omega_r$ and introducing the brightness temperature (Sect. 10.1.5)

$$W_\sigma(\omega, \eta) = T_{\mathrm{b}}^\sigma(\omega, \eta) \frac{\omega^2 n_\sigma^2}{(2\pi)^3 c^3} \frac{\partial\omega n_\sigma}{\partial\omega}, \tag{10.103}$$

we find

$$\gamma_s \approx -\frac{(1-4)\pi^2 e^2 \omega_{\mathrm{pe}}^2}{2mc^3} \sqrt{\frac{\pi}{2}} \left(\frac{v_{Ti}}{c}\right)^2 \left(\frac{2\omega_{\mathrm{Be}}}{\Delta\omega_r}\right) \frac{T_{\mathrm{b}}^\sigma}{T_e}, \tag{10.104}$$

where T_e is the electron plasma temperature.

The natural ECM bandwidth, $\Delta\omega_r/2\omega_{\mathrm{Be}}$, is about 0.2 %; see Sect. 10.3.6. Adopting then $T_e \sim T_i = 10^7$ K and $\omega_{\mathrm{Be}} = 10^{10}\,\mathrm{s}^{-1}$ we obtain an estimate

$$|\gamma_s| \sim 10^{-15} \omega_{\mathrm{Be}} \frac{T_{\mathrm{b}}^\sigma}{T_e}. \tag{10.105}$$

Apparently, for the nonlinear process to be efficient in a source of ECM emission, the nonlinear scattering rate must be comparable with the ECM growth rate, which is about $(10^{-6} - 10^{-7})\omega_{\mathrm{Be}}$; thus, the stimulated scattering of the ECM emission on the thermal ions becomes essential for a rather high brightness temperature of this emission,

$$\frac{T_{\mathrm{b}}^\sigma}{T_e} \gtrsim 10^8\text{–}10^9, \tag{10.106}$$

or $T_{\rm b}^{\sigma} \gtrsim 10^{15}$–$10^{16}\,{\rm K}$. Typically, estimated brightness temperatures of the solar radio spikes are smaller than $10^{15}\,{\rm K}$, so the nonlinear transformations of the solar ECM are inessential. In contrast, some **stellar coherent radio bursts** display large brightness temperature in excess of $10^{16}\,{\rm K}$ (Bastian et al. 1990; Osten and Bastian 2008) for which the nonlinear processes play likely an important role. We note that likewise the case considered in Sect. 4.3.2, equation for the transverse wave energy density can be in certain cases reduced to Lotka–Volterra Eqs. (4.69) resulting in oscillatory solutions for the wave energy density. Here, the coefficient of nonlinear wave coupling is estimated as $\zeta \sim 5 \times 10^{-3}\omega/n_e k_{\rm B} T$. For $\gamma \sim 10^{-8}\omega_{\rm Be}$, Eq. (4.75) yields for the oscillation period $\tau \sim 0.2\,{\rm s}$, while the wave energy density is of the order of $W/n_e k_{\rm B} T \sim \gamma/\zeta \sim 10^{-6}$, which implies the brightness temperature of the order of $3 \times 10^{13}\,{\rm K}$. Remarkably, 100 % polarized oscillations of microwave emission from flaring stars do display periods of a fraction of second, 0.3–0.7 s, which might be interpreted as the self-organizing oscillations of the ECM emission like those described by the Lotka–Volterra equations.

10.4.2 Nonlinear Conversion of Plasma Waves into Transverse Waves

Stimulated scattering of waves on thermal ions is a rather universal process, in which the initial and final waves are different from each other in a general case. Among many possible processes, scattering of longitudinal plasma waves (Langmuir, hybrid, Bernstein, etc.) into transverse electromagnetic waves is of particular importance because such kind of the mode conversion represents a distinct mechanism of electromagnetic (radio) emission that can be detected by a distant observer. To derive an equation describing conversion of the plasma waves into radio waves we must take into account, along with the nonlinear stimulated scattering, the usual (linear) scattering of the plasma waves into electromagnetic waves with small variation of frequency, which will represent the volume emissivity of the considered process, i.e.,

$$\frac{{\rm d}W_{\sigma}(\omega,\boldsymbol{n},t)}{{\rm d}t} = S_{\sigma}(\omega,\boldsymbol{n},t) + 2\gamma_{(l+i\Rightarrow t)} W_{\sigma}(\omega,\boldsymbol{n},t), \tag{10.107}$$

where $S_{\sigma}(\omega,\boldsymbol{n},t)$ is a source term describing the spontaneous (Rayleigh) scattering of the plasma waves into the transverse waves, and

$$\gamma_{(l+i\Rightarrow t)} = -\frac{4\pi e^2\omega}{m^2\omega_{\rm pe}^4} R_{\sigma}(\boldsymbol{k}) \sum_{\rm all\ } \int k''^2 {\rm d}\boldsymbol{k}' W_l(\boldsymbol{k}',t) R_l(\boldsymbol{k}') |(\boldsymbol{e}^{\sigma}\cdot\boldsymbol{\kappa}')|^2 \frac{\delta\varepsilon_e'^2(\omega'',\boldsymbol{k}'')\delta\varepsilon_i''(\omega'',\boldsymbol{k}'')}{|\varepsilon^l(\omega'',\boldsymbol{k}'')|^2} \tag{10.108}$$

is the stimulated scattering contribution derived from Eq. (4.60), where $\boldsymbol{\kappa} = \boldsymbol{k}/k$. Since this scattering process goes with a very small frequency variation,

only those plasma waves which have a frequency higher than the plasma frequency can be converted to the radio emission, i.e., the upper-hybrid waves or high-frequency Bernstein waves in a magnetized plasma or Langmuir waves in a free plasma; lower-hybrid waves cannot scatter into the radio waves except a very narrow parameter region (e.g., $\omega_{\rm Be} \gg \omega_{\rm pe}$ and $\theta \approx 0$).

To estimate an order of magnitude of this effect (Zaitsev and Stepanov 1983) let us consider an isotropic distribution of the plasma waves in a free plasma and replace the energy density by the brightness temperature using Eq. (10.103) [cf. Eqs. (10.1) and (10.35)],

$$\frac{{\rm d}T_{\rm b}(\boldsymbol{r},t)}{v_g {\rm d}t} = a_{(l+i\Rightarrow t)} - (\varkappa_{\rm ff} + \varkappa_{(l+i\Rightarrow t)})T_{\rm b}, \tag{10.109}$$

where

$$a_{(l+i\Rightarrow t)} = \frac{\pi}{36}\frac{\omega_{\rm pe}^3 W_k}{v_g n_e v_{Te}^2 k}, \qquad W_k = 4\pi k^2 W_l(\boldsymbol{k},t), \tag{10.110}$$

$W = \int W_k {\rm d}k$ is the energy density of the plasma waves, $v_g = c\sqrt{1-\omega_{\rm pe}^2/\omega^2}$ is the group velocity of the radio waves,

$$\varkappa_{(l+i\Rightarrow t)} = -\frac{\pi}{108}\frac{m\omega_{\rm pe}^3}{v_g M_i}\frac{1}{n_e v_{Te}^2 T_e}\frac{\partial(kW_k)}{k\partial k}. \tag{10.111}$$

The free–free absorption coefficient, $\varkappa_{\rm ff} = \omega_{\rm pe}^2\nu_{\rm ei}/(\omega^2 v_g)$, is given by either Eq. (3.97) or Eq. (10.5) or solution to Problem 10.1.

For a finite source with a linear size L along the line of sight, the radio emission described by Eq. (10.109) is generated in either optically thin or thick regime depending on whether the optical depth $|\tau| = |(\varkappa_{\rm ff}+\varkappa_{(l+i\Rightarrow t)})|L$ is smaller or larger than 1. If $|\tau| \ll 1$, then $T_{\rm b} = a_{(l+i\Rightarrow t)}L \propto W_k$, i.e., the radio brightness temperature is linearly proportional to the plasma wave energy density. The optically thick regime will differ depending on what process, the free–free absorption or the stimulated scattering, dominates. Indeed, if $|\tau| > 1$ and $\varkappa_{\rm ff} \gg |\varkappa_{(l+i\Rightarrow t)}|$ then we can neglect the stimulated scattering, which yields $T_{\rm b} = a_{(l+i\Rightarrow t)}/\varkappa_{\rm ff}$ again $\propto W_k$. However, at some high level of the plasma wave energy density, we will have $\varkappa_{\rm ff} = |\varkappa_{(l+i\Rightarrow t)}|$ and then $\varkappa_{\rm ff} \ll |\varkappa_{(l+i\Rightarrow t)}|$, so the radio wave absorption will be mediated by the nonlinear process—stimulated scattering of the plasma waves on ions. The result of this nonlinear absorption process depends crucially on the emission frequency. At higher frequencies produced by a falling, higher k, part of the plasma wave spectrum, where $\partial(kW_k)/\partial k < 0$, the radio brightness temperature is saturated at the level of $T_{\rm b} \sim (3M_i/m)T_e$ and does not rise with W_k any longer provided that the plasma wave spectrum shape does not change, $W_k/(\partial(kW_k)/\partial k) = {\rm const}$.

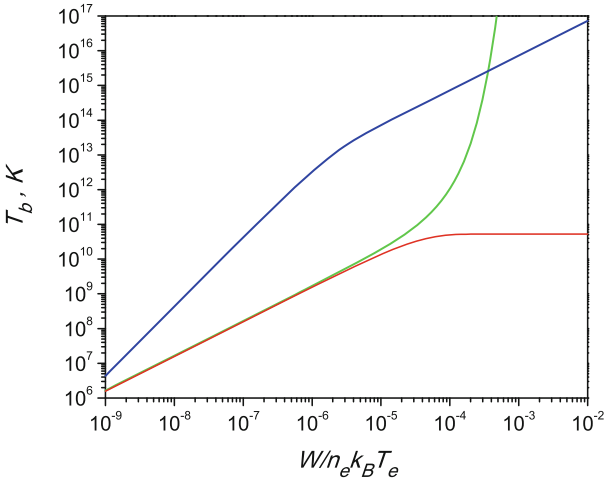

Figure 10.19: Brightness temperature of the plasma radiation at the fundamental (*red and green curves*) and double (*blue curve*) plasma frequency as a function of the plasma wave energy density. Parameters: $n_e = 2.5{\times}10^{10}$ cm^{-3}, $T_e = 10^7$ K, and $L = 3{\times}10^7$ cm.

In contrast, at lower frequencies produced by a raising, lower k, part of the plasma wave spectrum, where $\partial(kW_k)/\partial k > 0$, the absorption coefficient turns negative implying radio wave amplification instead of true absorption:

$$\begin{aligned} T_\mathrm{b} &= \frac{a_{(l+i\Rightarrow t)}}{|\varkappa_{(l+i\Rightarrow t)}|}[\exp(|\varkappa_{(l+i\Rightarrow t)}|L) - 1] \\ &\approx \frac{3M_i}{m} T_e[\exp(|\varkappa_{(l+i\Rightarrow t)}|L) - 1], \end{aligned} \tag{10.112}$$

where the radio brightness temperature increases exponentially with the plasma wave energy density.

Let us estimate the processes involved for conditions typical for coronal sources of coherent solar radio bursts. For the thermal number density $n_e = 2.5 \times 10^{10}\,\mathrm{cm}^{-3}$ ($f_\mathrm{pe} \approx 1.4\,\mathrm{GHz}$) and $T_e = 10^7\,\mathrm{K}$ at a frequency $f = 1.1 f_\mathrm{pe}$ we have $\varkappa_\mathrm{ff} \sim 0.65 \times 10^{-8}\,\mathrm{cm}^{-1}$. Therefore, for the source size smaller than a few $\times 10^8$ cm, the free–free absorption is negligible; it can become important for a denser or/and cooler plasma, however. Then, an estimate of the nonlinear absorption for the same parameters and a mean wave number of the plasma wave spectrum $k \sim 3\omega_\mathrm{pe}/c$ yields $|\varkappa_{(l+i\Rightarrow t)}| \sim 10^{-3}(W/n_e k_\mathrm{B} T_e)$; thus for a source of a few hundred km the radio wave amplification due to stimulated scattering on ions becomes important for $(W/n_e k_\mathrm{B} T_e) \gtrsim 3 \times 10^{-5}$. This amplification takes place at low frequencies, lower that the spectral peak of the plasma waves. Accordingly, the brightness temperature of the radio emission increases exponentially with the energy density of the plasma waves at these low frequencies (see green curve in Fig. 10.19). In contrast, the higher

frequency radio emission (still around the plasma frequency) saturates at some universal level, which depends only on the electron temperature at the source, red curve in Fig. 10.19. This means that at the higher frequencies the stimulated scattering of waves on ions transfers energy from radio waves to the plasma waves, which results in radio wave absorption that saturates the radio emission level, while at the lower frequencies the energy is transferred from plasma waves to the radio waves and the efficiency of this stimulated process increases with the wave energy, which results in the exponential growth shown by the green curve in Fig. 10.19.

Consider now a coalescence of two plasma waves into an electromagnetic wave based on Eq. (4.61), which for this particular process reduces to

$$\begin{aligned}\frac{d^{(l+l'\Rightarrow t)}}{\mathrm{d}t}W_\sigma(\omega,\boldsymbol{n}) &= 4\pi^2\omega(\boldsymbol{k})\sum_{l,l'}\int \mathrm{d}\boldsymbol{k}' Q_{llt}\delta(\omega(\boldsymbol{k})\pm\omega_l(\boldsymbol{k}')\pm\omega_{l'}(\boldsymbol{k}''))\\ &\times\Bigg[\omega(\boldsymbol{k})\frac{(\omega n_\sigma)^2}{c^3}\frac{\partial\omega n_\sigma}{\partial\omega}sign\gamma_\sigma(\omega,\boldsymbol{k})W_l(\boldsymbol{k}')W_{l'}(\boldsymbol{k}'')\\ &-\omega_{l'}(\boldsymbol{k}'')sign\varepsilon''(\omega'',\boldsymbol{k}'')W_\sigma(\omega,\boldsymbol{n})W_l(\boldsymbol{k}')\\ &-\omega_l(\boldsymbol{k}')sign\varepsilon''(\omega',\boldsymbol{k}')W_\sigma(\omega,\boldsymbol{n})W_{l'}(\boldsymbol{k}'')\Bigg], \quad (10.113)\end{aligned}$$

where the core Q_{llt} with the use of Eqs. (4.62) and (4.63) receives the form

$$\begin{aligned}Q_{llt} &\equiv \frac{e^2R(\boldsymbol{k})R(\boldsymbol{k}')R(\boldsymbol{k}'')}{k'^2k''^2m^2\omega_{\mathrm{pe}}^4}\left|(\boldsymbol{k}'\boldsymbol{k}'')(\boldsymbol{k}\boldsymbol{e}^*)-\frac{\omega''}{\omega}(\boldsymbol{k}\boldsymbol{k}')(\boldsymbol{k}''\boldsymbol{e}^*)-\frac{\omega'}{\omega}(\boldsymbol{k}'\boldsymbol{k}'')(\boldsymbol{k}'\boldsymbol{e}^*)\right|^2\\ &= \frac{e^2R(\boldsymbol{k})R(\boldsymbol{k}')R(\boldsymbol{k}'')}{k'^2k''^2m^2\omega_{\mathrm{pe}}^4}\left|(\boldsymbol{k}\boldsymbol{k}')(\boldsymbol{k}'\boldsymbol{e}^*)+\frac{\omega'}{\omega}(\boldsymbol{k}\boldsymbol{k}')(\boldsymbol{k}\boldsymbol{e}^*)-k'^2(\boldsymbol{k}\boldsymbol{e}^*)-\frac{\omega'}{\omega}k^2(\boldsymbol{k}'\boldsymbol{e}^*)\right|^2,\end{aligned} \quad (10.114)$$

which must be multiplied by 1/2 if two merging waves belong to the same wave mode. Note that Eq. (10.113) contains summation over all possible plasma wave modes and all possible combinations of the coupling mode frequencies, $\omega=\omega_l\pm\omega_{l'}$. For example, there can be coalescence of two lower- or upper-hybrid waves into a transverse wave with roughly double frequency $\omega=\omega_\pm+\omega_\pm$ or a decay process when an upper-hybrid wave decays into a lower-hybrid and a radio wave, $\omega=\omega_+-\omega_-$. For example, in a highly magnetized plasma, $\omega_{\mathrm{Be}}\gg\omega_{\mathrm{pe}}$, the radio waves produced at the double lower-hybrid frequency, $2\omega_-$, occupy a region between ω_{pe} and $2\omega_{\mathrm{pe}}$ (see dispersion laws of the plasma waves in Sect. 3.2.2 and Problem 3.1), while those at the double upper-hybrid frequency, $2\omega_+$, occupy a narrow region above the second gyroharmonics. The radio waves from the coupling or decay $\omega=\omega_+\pm\omega_-$ form a doublet around the gyrofrequency. Bandwidth of the corresponding radio emission spectra depends strongly on the gyrofrequency to plasma frequency ratio and also on the lower- and upper-hybrid wave turbulence spectra including the anisotropy. Apparently, in a hot plasma, the

amount of possible coalescence or decay processes is much larger because the number of eigenmodes is accordingly larger. The plethora of plasma emission processes is in qualitative agreement with the observed diversity of solar coherent emissions (see Fig. 10.10).

Consider now in more detail the case of a relatively dense $\omega_{\rm Be} \ll \omega_{\rm pe}$, cold plasma, where only one, the upper-hybrid or Langmuir, wave contributes to Eq. (10.113). Apparently, it has a standard form of the radiation transfer equation, where the contribution arising from the first term in the square brackets, which does not contain $W_\sigma(\omega, \boldsymbol{n})$, describes the (spontaneous) volume emissivity due to the plasma wave coupling, while two remaining terms, proportional to $W_\sigma(\omega, \boldsymbol{n})$, describe the radio wave absorption due to its decay into two plasma waves. In a general case, the free–free absorption must also be added to this equation. Accordingly, replacing again the energy density of the radio waves by the corresponding brightness temperature we obtain

$$\frac{{\rm d}T_{\rm b}(\boldsymbol{r},t)}{v_g {\rm d}t} = a_{(l+l\Rightarrow t)} - (\varkappa_{\rm ff} + \varkappa_{(l+l\Rightarrow t)})T_{\rm b}. \tag{10.115}$$

The coefficients of this equation can be straightforwardly derived from Eq. (10.113) for any given plasma parameters and the turbulence spectra. Below, we make estimates assuming that the Langmuir wave spectrum is isotropic and uniform, $W_l(\boldsymbol{k}') = W/(\Delta k)^3$, where $W = \int {\rm d}\boldsymbol{k} W_l(\boldsymbol{k}')$ is the total energy density of the plasma waves. The actual bandwidth of the plasma wave spectrum is convenient to parameterize as $(\Delta k)^3 = \xi(\omega_{\rm pe}/c)^3$, where the dimensionless parameter ξ can be straightforwardly estimated from its definition given above; in most of the practical cases $\xi = 20$–500. For this case Eq. (10.113) yields (Zaitsev and Stepanov 1983)

$$a_{(l+l\Rightarrow t)} \approx \frac{(2\pi)^5}{15\sqrt{3}} \frac{c^3}{\omega_{\rm pe}^2 \langle v_{\rm ph}\rangle} \frac{w^2}{\xi^2} n_e T_e, \tag{10.116a}$$

$$\varkappa_{(l+l\Rightarrow t)} \approx \frac{(2\pi)^2}{5\sqrt{3}} \frac{\omega_{\rm pe}}{\langle v_{\rm ph}\rangle} \frac{w}{\xi}, \tag{10.116b}$$

where $\langle v_{\rm ph}\rangle = \langle \omega_{\rm pe}/k\rangle$ is the mean phase velocity of the involved plasma waves.

For the condition typical for decimeter radio emission of solar bursts, outlined after Eq. (10.112), the free–free absorption is not important, so the solution of radiation transfer equation (10.115) is only specified by the plasma turbulence and the source size:

$$\begin{aligned} T_{\rm b}(\boldsymbol{r},t) &= \frac{a_{(l+l\Rightarrow t)}}{\varkappa_{(l+l\Rightarrow t)}} \left(1 - \exp[\varkappa_{(l+l\Rightarrow t)} L]\right) \\ &\approx (2\pi)^3 \frac{c^3}{\omega_{\rm pe}^3} \frac{w}{\xi} n_e T_e \left(1 - \exp[\varkappa_{(l+l\Rightarrow t)} L]\right), \end{aligned} \tag{10.117}$$

so the brightness temperature of radio emission produced by the plasma wave coalescence depends on whether the source is optically thin or thick for this process. Adopting for the estimate $n_e = 2.5 \times 10^{10}\,\mathrm{cm}^{-3}$, $\langle v_{\rm ph}\rangle = 10^{10}\,\mathrm{cm/s}$, $\xi = 400$, and $L = 3\times10^7\,\mathrm{cm}$, we obtain $\tau_{(l+l\Rightarrow t)} = \varkappa_{(l+l\Rightarrow t)}L \sim 3\times10^5 w$; thus, the source is optically thin for $w < 3\times10^{-6}$ and the brightness temperature $T_{\rm b} \approx a_{(l+l\Rightarrow t)}L \propto w^2$ increases quadratically with the plasma wave energy density. For a higher energy density of the plasma waves, $w > 3\times10^{-6}$, sufficient to form the optical depth larger than one, the decay of the radio waves into the plasma waves becomes essential, so the brightness temperature $T_{\rm b} \approx a_{(l+l\Rightarrow t)}/\varkappa_{(l+l\Rightarrow t)} \propto w$ increases linearly with the plasma wave energy density (see blue curve in Fig. 10.19).

10.4.3 Coherent Plasma Radiation from Solar Corona

Radio emission produced from plasma wave conversion can, apparently, be expected from sources whose characteristic plasma frequency corresponds to the radio domain, e.g., from stellar and solar coronae. Having in mind primarily application to the solar case, let us introduce the characteristic radio flux in the solar flux units, $1\,\mathrm{sfu} = 10^{-19}\,\mathrm{erg/(s\,cm^2\,Hz)}$

$$F_{\rm sfu} \approx 7\times10^{-11} T_{\rm b} f_9^2 L_8^2, \tag{10.118}$$

where f_9 is radio frequency in GHz, $L_8^2 = (L_\perp/10^8\,\mathrm{cm})^2$ is the source area, and $T_{\rm b}$ is the brightness temperature in K. Adopting the same parameters as before and $w \sim 10^{-5}$ for which $\tau_{(l+l\Rightarrow t)} \sim 1$, we obtain $T_{\rm b} \sim 10^{15}\,\mathrm{K}$ and $F_{\rm sfu,\,cr} \approx 10^3\,\mathrm{sfu}$, i.e., the corresponding coherent radio bursts occur in the optically thin regime for $F_{\rm sfu} < F_{\rm sfu,\,cr}$, while in the thick regime for $F_{\rm sfu} > F_{\rm sfu,\,cr}$.

There is a variety of solar radio emission types that are produced by a coherent emission mechanism (e.g., Fig. 10.10), in particular, by a conversion of plasma waves into radio waves, commonly called **plasma mechanisms of radio emission**. In some cases the presence of a coherent process is unavoidable. For example, if a radio emission peak lasts around 30 ms, which implies that its size does not exceed 10^9 cm and reaches a level of 1,000 sfu at $f = 1\,\mathrm{GHz}$, then Eq. (10.118) requires $T_{\rm b} > 10^{11}\,\mathrm{K}$, which cannot be produced by available non- or mildly relativistic particles via an incoherent emission process. We note that for coherent decimetric bursts the assumed level of 1,000 sfu is quite modest: the radio flux reaches some 10^6 sfu in record radio bursts.

The plasma mechanisms require a source of the free energy capable of exciting the plasma waves to be available. In most cases these plasma waves are excited by nonequilibrium unstable distributions of fast electrons (Sect. 4.1). For example, collimated beams of the fast electrons can generate plasma waves via beaming instability, while fast electrons trapped in a nonuniform magnetic loop can build up a loss-cone angular distribution due to loss of

electrons with small pitch angles, which gives rise to a loss-cone instability. Observable signatures will be different in these two cases. Indeed, an electron beam moving through inhomogeneous solar corona will excite plasma waves along its path with varying plasma frequency (because of varying electron density); thus, the radio waves produced by such plasma waves will display a frequency drift reflecting variation of local plasma density along the beam path. Such drifting bursts (Fig. 10.10d), frequently in large groups, are often observed at decimeter and meter spectral bands and commonly interpreted as signatures of the electron beams. Many other kinds of coherent bursts, such as zebra and fiber bursts (Fig. 10.10a,c) and quasiperiodic pulsations (Fig. 10.10e) can be consistently interpreted in terms of a plasma mechanism driven by a loss-cone instability.

Although we obviously cannot give a comprehensive picture of the solar radio burst, we, nevertheless, consider in some detail one case where the interpretation of radio emission as due to coalescence of plasma waves at the second harmonic looks unavoidable and being combined with accompanying observed effects gives rise to a reliable detailed plasma diagnostics. Specifically, we present here an event recorded during the rise phase of a continuum microwave burst on 2 November 1997 at frequencies $f = 2.81$–$2.89\,\mathrm{GHz}$ from 03:02:17 UT to 03:02:21 UT by spectropolarimeter of the Beijing Astronomical Observatory operated at 2.6–3.8 GHz with 8 ms time resolution and 10 MHz frequency resolution; see event overview in Fig. 10.20. This event displays quasiperiodic pulsations of both left (L or LCP) and right (R or RCP) polarized intensity components and the degree of polarization. A selected fragment of the records in Fig. 10.21 displays clearly that the L and R pulsations are shifted in respect to each other by a considerable part of the period.

No emission mechanism is currently known to produce such oscillatory behavior of the degree of polarization over that short period. In contrast, we show below that this oscillatory behavior is a result of propagation of originally weakly polarized radio emission through the magnetized coronal plasma, or, more specifically, the result of the birefringence effect that reveals itself in *different group velocities* of ordinary and extraordinary waves.

Apparently, the most suitable math tool for oscillation study is the Fourier analysis, which fully characterizes the pulsations by providing their oscillation frequency, phase, and amplitude at all available radio frequencies. For this event, the radio light curves at all "pulsating" radio frequencies demonstrate oscillation period $\tau_p = 40 \pm 1\,\mathrm{ms}$; the Fourier amplitudes of this oscillation vs radio frequency are shown in Fig. 10.22, left. The *time delays* between the light curves at different radio frequencies, calculated as a product of Fourier *phase difference* (between these two frequencies) and the oscillation period, *separately* for L and R waves (auto-delays, for short) are plotted in Fig. 10.22 (right), remarkably, that L and R waves demonstrate opposite trends with frequency. The time delay *between* L and R radio components (cross delay) at a *given* frequency is calculated in a similar

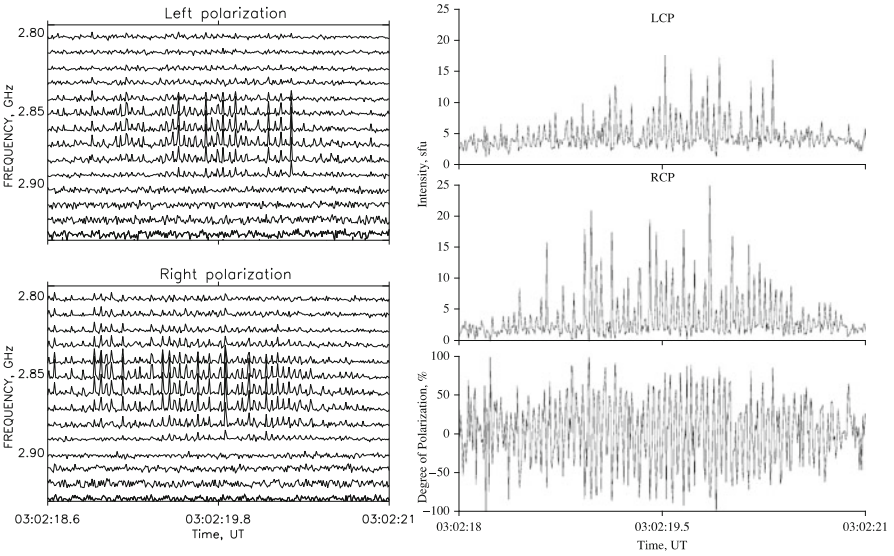

Figure 10.20: 2 November 1997 event. *Left*: Dynamic spectra displaying pulsations in the LCP and RCP channels. A narrowband pulsating emission is clearly seen around 2.85 GHz. *Right*: Time profiles of the LCP and RCP intensities and the degree of polarization at $f = 2.85$ GHz. A puzzling feature is oscillations of the degree of polarization with a very short period, ~ 40 ms (Melnikov et al. 2002a).

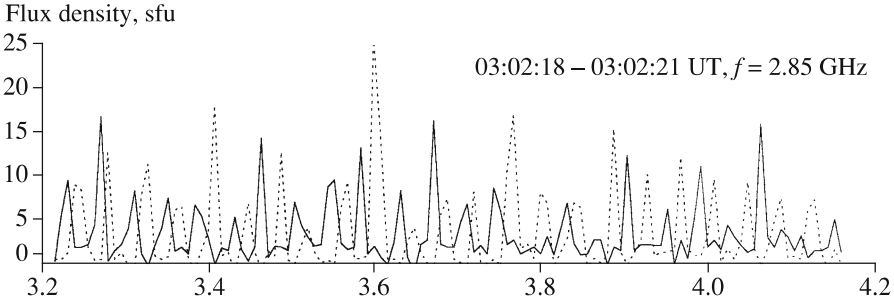

Figure 10.21: Selected fragments of the RCP (*solid curve*) and LCP (*dashed curve*) light curves at $f = 2.85$ GHz. The time delay (shift) between the components is apparent (Melnikov et al. 2002a).

way, which gives $\Delta t = 18$–21 ms depending on frequency. Figure 10.23, left, displays that the cross delay systematically decreases with frequency as a power law, $\Delta t \propto f^{-3.5}$.

Let us outline a consistent interpretation of these remarkable observations. As has been said, no emission mechanism is capable of producing radio emission with so rapidly alternating degree of polarization, while the radio wave propagation through a magnetized coronal plasma can easily make the

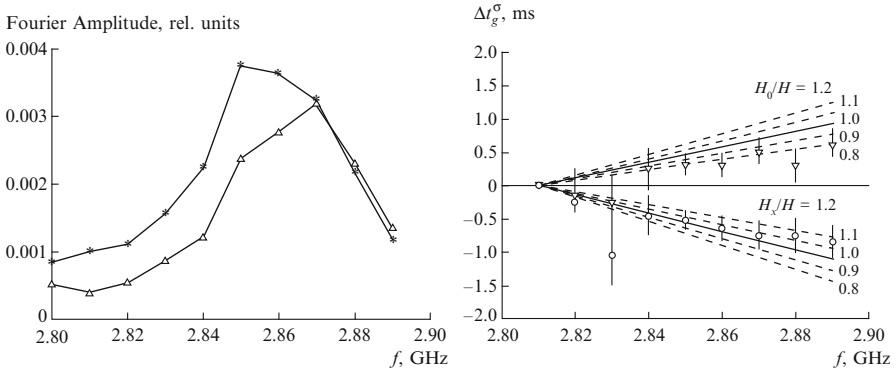

Figure 10.22: *Left*: Fourier amplitudes of the pulsations as a function of frequency for the RCP (*asterisks*) and LCP (*triangles*) components. *Right*: Delays of the wave arrival relative to the waves (with the same polarization) at a reference frequency $f = 2.81$ GHz (auto delays) for the RCP (*triangles*) and LCP (*circles*) components. The *lines* show the model curves obtained for various ratios of the effective scales (see below); the *solid lines* correspond to identical values of all involved effective scales (Melnikov et al. 2002a).

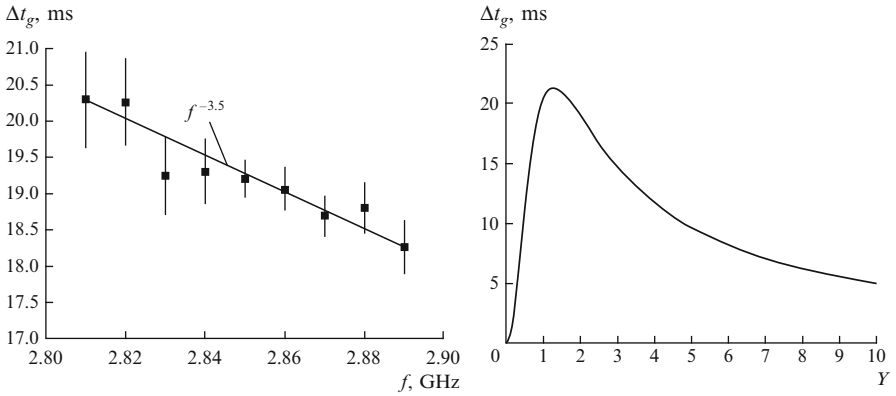

Figure 10.23: *Left*: Frequency dependence of the delay between the RCP and LCP components of the pulsation (*filled squares* with error bars). The *line* shows the theoretical relation obtained using exact formulas for the group velocities of the transverse waves and taking into account the inhomogeneity of the source ($\propto f^{-3.5}$). *Right*: Group delay for waves emitted at the double hybrid frequency in a uniform magnetized plasma with a linear size of 4.5×10^9 cm as a function of the ratio of the plasma frequency to the gyrofrequency $Y = f_{\rm pe}/f_{\rm Be}$.

polarization to oscillate due to **birefringent** properties of the magnetized plasma—a fundamental effect giving rise, in particular, to the **Faraday rotation** of the linear polarization plane (see Sect. 10.1.6) and to the **group delays** between oppositely polarized waves. Indeed, consider a relatively compact source generating a pulsating radio emission with a short period and a

low degree of circular polarization, i.e., with comparable intensities of the ordinary (O) and extraordinary (X) modes. When the radio emission leaves the source, these waves (O and X) propagate in the magnetized corona with different group velocities so that the temporal peaks of the LCP and RCP signals arrive at the Earth with a time delay specified by the plasma density and magnetic field along the emission path. Thus, the LCP signal dominates during one part of the period, while the RCP signal during the other part, leading to especially prominent oscillations of the degree of circular polarization when the time delay is about half of the oscillation period, which is the case for the event under study.

Let us estimate the frequency dependence of the group time delay. For a compact (point-like) source and $f \gg f_{\rm Be}, f_{\rm pe}$, we can write (see Sect. 3.2.3 and Problem 3.2e)

$$\frac{c}{v_{X,O}} \approx 1 + \frac{\omega_{\rm pe}^2}{2\omega^2} - \sigma \frac{\omega_{\rm pe}^2 \omega_{\rm Be} \cos\theta}{\omega^3}, \tag{10.119}$$

where, as usual, $\sigma = 1$ for O waves and $\sigma = -1$ for X waves, $\cos\theta$ is the angle between the wave vector and the magnetic field, $\omega_{\rm Be}^{\parallel} = \omega_{\rm Be}\cos\theta$. The group time delay between simultaneously emitted O and X waves is given by the integral along the radiation path:

$$\Delta t_g = \int_0^\infty \left(\frac{1}{v_X} - \frac{1}{v_O} \right) {\rm d}z = \frac{2}{c\omega^3} \int_0^\infty \omega_{\rm pe}(z) \omega_{\rm Be}^{\parallel}(z) {\rm d}z = \frac{2}{c} \frac{\omega_{ps}^2 \omega_{Bs||}}{\omega^3} H \tag{10.120}$$

where ω_{ps} and ω_{Bs} are the plasma and gyrofrequencies at the source and

$$H = \int_0^\infty \frac{\omega_{pe}^2(z)\omega_{Be||}(z)}{\omega_{ps}^2 \omega_{Bs||}} {\rm d}z = \int_0^\infty \frac{n(z) B_{||}(z)}{n_s B_{s||}} {\rm d}z \tag{10.121}$$

is the effective scale of the coronal inhomogeneity. Note that the integral in the rhs of Eq. (10.120) is directly proportional to the rotation measure, RM, introduced by Eq. (10.54) in connection with the Faraday rotation effect. Accordingly, we have

$$\Delta t_g \propto {\rm RM} \cdot f^{-3}. \tag{10.122}$$

In a similar way, using Eq. (10.119) we can estimate the group auto-delays between $f_0 = 2.81\,{\rm GHz}$ and $f = 2.89\,{\rm GHz}$ for either O or X waves:

$$\delta t_g \approx \Delta t_g \frac{3\Delta f}{f_0} \sim 1.7\ {\rm ms} \tag{10.123}$$

in rough agreement with absolute values of the auto-delays given in Fig. 10.22, right.

Now, let us consider a possible emission mechanism producing the radio burst. Based on either time variability or rather narrow bandwidth of the radio spectrum we can conclude that the source of emission is rather compact, $L < 10^8$ cm; thus, Eq. (10.118) implies $T_b > 5 \times 10^{10}$ K, which requires a coherent emission mechanism to be involved. We note that many coherent mechanisms, including ECM emission and plasma radiation around the fundamental plasma frequency, produce a strongly polarized radiation and so can be eliminated from consideration as we deal with the radiation weakly polarized at the source. This implies that a coalescence of the plasma waves resulting in emission at the second harmonic of the plasma wave frequency must be responsible for the observed radio emission. Remind that gyroabsorption in the solar corona is typically significant up to the third gyroharmonics (see Sect. 3.3.3); thus, the observed frequency range must fall above the third local gyroharmonic, which means that the only suitable plasma wave mode is the upper-hybrid mode; the lower-hybrid mode would generate emission below the second gyrolayer and will be absorbed, while the Bernstein modes would produce many similar pulsating "islands" in the dynamic spectrum in contradiction with the fact that there is only one such region. Thus, we firmly conclude that the radiation is produced by plasma mechanism at the second harmonic of the upper-hybrid wave.

Importantly, as has been shown in Sect. 4.3.2, the energy density of the upper-hybrid waves can oscillate due to nonlinear effects, e.g., stimulated scattering of the waves on thermal ions, and that the energy density of the upper hybrid waves displays either nonperiodic pulsations or quasiperiodic oscillations, depending on the size and shape of the instability region of the upper hybrid waves provided by a given distribution of fast electrons. Quasiperiodic solutions appear for relatively narrow (in the wave-vector plane) regions of instability, while nonperiodic pulsations arise for more extended regions. In the considered case the pulsations are quasiperiodic indicative of a narrow spectral domain of the underlying, presumably loss cone, instability.

Note that narrow regions of instability are more easily formed if the instability operates in a weakly above-threshold regime (with the threshold determined, e.g., by the collisional wave damping). In this case, we expect that the conditions for instability are fulfilled only in a small part of a nonuniform coronal trap, which seems to be a natural reason for that narrow spectral band occupied by the pulsations.

For a loss-cone instability the upper-hybrid waves are generated at quasitransverse directions to the magnetic field (see Fig. 4.2b), i.e., $\omega \approx 2\omega_{UH} \approx 2\sqrt{\omega_{pe}^2 + \omega_{Be}^2}$. Using this relation we can study how the expected group delay depends on the plasma parameter $Y = \omega_{pe}/\omega_{Be}$. Indeed, for the double upper-hybrid frequency, Eq. (10.120) yields

$$\Delta t_g = \frac{H}{4c}\left(\frac{2f_{\rm UH}}{f}\right)^3 \frac{Y^2}{(1+Y^2)^{3/2}} \tag{10.124}$$

where $2f_{\rm UH}/f \approx 1$; the corresponding dependence $\Delta t_g(Y)$ is shown in Fig. 10.23, right. This plot shows that there is a relatively narrow range of Y where the group delay around 20 ms is possible: $Y_{\rm opt} \approx 1.5$, which allows to roughly estimate both plasma and gyrofrequencies provided $f_{\rm UH} \approx 1.4$ GHz. Interestingly, the magnetic field at the source can be estimated precisely from the analysis of the Fourier spectra of the pulsations (Fig. 10.22, right). Indeed, the ratio of the spectra of the LCP and RCP components drastically changes for a minor frequency change of only 0.3 %, at the transition from 2.86 GHz to 2.87 GHz: in the high-frequency part of the spectrum ($f \geq 2.87$ GHz) the Fourier amplitudes for the LCP and RCP signals coincide, whereas in the low-frequency part ($f \leq 2.86$ GHz) the Fourier amplitudes of the LCP signal are systematically lower than for the RCP signal. Such a sharp, stepwise change is indicative of a system transition through some threshold. Given that typically the first three gyrolayers are thick for the X-mode waves, it is natural to suppose that this threshold is the fourth gyrolayer, which is transparent for O-mode, while can be partially opaque for the X-mode; therefore

$$4f_{\rm Be} = 2.865 \pm 0.005\,{\rm GHz}. \tag{10.125}$$

Thus, from Eq. (10.125), we find

$$B = 255.7 \pm 0.5\,{\rm G}, \tag{10.126}$$

which along with Eq. (3.109) yields for the plasma number density

$$n = (1.9 \pm 0.1) \times 10^{10}\,{\rm cm}^{-3}. \tag{10.127}$$

Note that the accuracy of n estimate is lower than that of B because we do not know the angle of the generated upper-hybrid waves relative to the magnetic field.

Combining Eqs. (10.126) and (10.127) we obtain the plasma parameter Y at the source:

$$Y = 1.7. \tag{10.128}$$

The estimated Y value is indeed close to optimal one ($Y_{\rm opt} \approx 1.5$) producing the largest group delay all other conditions being equal. Using Eq. (10.124) with Eq. (10.128) we estimate the effective coronal inhomogeneity scale as

$$H \approx 5 \times 10^9\,{\rm cm}. \tag{10.129}$$

So far, we have considered fundamental effects of plasma birefringence and gyroabsorption to determine the main physical parameters of the problem: the magnetic field, the electron number density, and the coronal inhomo-

geneity scale. Now we turn to analysis of the plasma turbulence and related properties. Since the total spectral width of the radio emission is

$$\Delta f/f \approx 3\,\%, \tag{10.130}$$

we can, to the first approximation (i.e., within an accuracy of 3 %), consider the radio source to be homogeneous; effects produced by the source inhomogeneity, which are also important in the case under study, are considered in Problem 10.6 to this chapter.

In a general case the bandwidth of the radio emission consists of the intrinsic width arising in a homogeneous source and the contribution of the inhomogeneity of the real source. Apparently, the theoretically predicted "natural" width of the plasma waves must not exceed the observed width of the pulsations. From this perspective it is conclusive to recall that the upper-hybrid frequency depends on the wave angle to the magnetic field roughly as $\omega_{\rm UH} \approx \omega_{\rm pe}(1+\sin^2\theta/2Y^2)$ (see Problem 3.1). Thus, if the upper-hybrid waves were distributed isotropically, then, the corresponding natural bandwidth would correspond to the entire range of the angle variation, $0 \le \sin\theta \le 1$, which, for $Y \sim 1.7$ would be

$$\frac{\Delta\omega}{\omega} \sim 10\text{–}20\,\% \tag{10.131}$$

in apparent conflict with observed bandwidth (10.130) suggesting a narrower, anisotropic angular distribution of the upper-hybrid turbulence.

Indeed, numerical studies of the nonlinear plasma wave pulsations (Sect. 4.3.2) suggest that in the case of narrow instability region required to produce quasiperiodic pulsation regime, the upper-hybrid turbulence remains anisotropic and confined within a narrow region of the k-plane comparable to the original instability region with the following typical values and their scatter:

$$kd_e \sim 0.1, \tag{10.132a}$$

$$\theta \sim 80^\circ, \tag{10.132b}$$

$$\Delta kd_e \sim 0.1, \tag{10.132c}$$

$$\Delta\theta \le 20^\circ, \tag{10.132d}$$

implying $\Delta k \sim k$, and, accordingly

$$\frac{\Delta\omega}{\omega} \sim 1\text{–}3\,\%, \tag{10.133}$$

which means that the contribution of the source inhomogeneity to the total spectral width of the observed radio pulsations may be comparable to the natural spectral bandwidth of the emission mechanism.

Let us estimate the relevant plasma wave growth and damping rates in this event. Note that like in numeric simulations in Sect. 4.3.2, the timescales of the radio pulsations' growth and decay are comparable to each other; thus, the maximum growth rate for the wave amplification is of the same order as the effective wave damping rate $\bar{\gamma} \sim \tilde{\gamma}$. The observed pulsation period is specified by the maximum growth rate according to Eq. (4.75) which yields the growth rate estimate:

$$\bar{\gamma} \approx 2.7 \times 10^2\,\mathrm{s}^{-1} \approx 3 \times 10^{-8}\omega_{\mathrm{pe}}. \tag{10.134}$$

Using approximate formula $\bar{\gamma} \sim 10^{-1}(n_b/n_e)\omega_{\mathrm{pe}}$ (see Fig. 4.2c) and the growth rate value from Eq. (10.134) we can estimate the number density of unstable fast electrons driven the loss-cone instability of the upper-hybrid turbulence:

$$n_b \sim 10^4\,\mathrm{cm}^{-3}. \tag{10.135}$$

On the other hand, the effective damping rate $\tilde{\gamma}$ has the same order of magnitude as $\bar{\gamma}$. The damping rate consists of the collisional absorption (ν_{ei}) and contribution from the fast electrons, i.e.,

$$\tilde{\gamma} \geq \nu_{\mathrm{ei}} \approx 60\ nT^{-3/2}. \tag{10.136}$$

Since the plasma number density has been determined by Eq. (10.127), we can find a lower bound of the plasma electron temperature

$$T \geq 3 \times 10^6\,\mathrm{K}. \tag{10.137}$$

Furthermore, we can now estimate energy density of the upper-hybrid turbulence noting that the mean level of the oscillations is defined by the stationary solution $W \approx \bar{\gamma}/\zeta$ and taking into account Eq. (4.70):

$$w = \frac{W}{n_e k_{\mathrm{B}} T} \sim \frac{50}{f\tau} \sim 10^{-6}. \tag{10.138}$$

As has been shown in Sect. 10.4.2, for this relatively low level of the plasma turbulence, the radio waves are generated in the optically thin regime; therefore, $T_{\mathrm{b}} \approx a_{(l+l\Rightarrow t)} L_{\parallel}$, where $L_{\parallel}$ is the source size along the line of sight and $a_{(l+l\Rightarrow t)}$ is defined by Eq. (10.116a), where $\xi \approx 30$ must be used according to Eq. (10.132a). On the other hand the brightness temperature can be calculated from the observed flux ($F \sim 20\,\mathrm{sfu}$) using Eq. (10.118), which contains the transverse size of the source. We know all the entries to these equations, rather than the sizes; however, we can assume the sizes to be comparable to each other and estimate them from the condition that both equations provide the same brightness temperature, which yields both the brightness temperature

$$T_{\mathrm{b}} \sim 5 \times 10^{12}\,\mathrm{K} \tag{10.139}$$

and the source size

$$L_{||} \sim L_{\perp} \sim L \sim 10^7\,\mathrm{cm}. \tag{10.140}$$

Herewith, we have outlined a coherent picture of this pulsating radio bursts, which consistently explains all the observed properties, except positive auto-delays of the RCP emission, which cannot be reconciled within a homogeneous source model and so requires an explicit account of the source inhomogeneity (see Problem 10.6 to this chapter).

Problems

10.1 Calculate the free–free emission and absorption coefficient of O- and X-modes of magnetized plasma using expressions for the corresponding refractive indices (see Problem 3.9) and Kirchhoff's law.

10.2 A short broadband pulsar signal is being recorded by two narrowband receivers at different frequencies ω_1 and ω_2. Each of them is tuned to a narrow bandwidth $\Delta\omega \ll \omega_1,\ \omega_2$. The propagation time of a narrowband signal is specified by the distance to the pulsar and signal group velocity, which is a function of frequency. Thus, simultaneously launched pulsar signals will arrive at the receivers at different times, with a delay of $\Delta t = t_1 - t_2$.

Determine dependence between the delay Δt and **dispersion measure** $DM = \int_0^L n_e \mathrm{d}l = \overline{n}_e L$. Here, n_e is the electron number density and L is the distance between the pulsar and the receiver; the integration is required to account for a nonuniform distribution of the thermal plasma along the line of sight. Adopt that the electron plasma frequency $\omega_{\mathrm{pe}} = \sqrt{4\pi n_e e^2/m_e}$ is small compared with the signal frequencies, ω_1 and ω_2.

10.3 Consider transfer of radiation polarization through a nonabsorbing and non-emitting plasma. Obtain formulae of the Faraday and Cotton–Mouton effects from general solution. Find conditions in which the Faraday rotation does not take place.

10.4 Solve the polarization transfer equation in a radiation source adopting the rotation measure is strong inside the source; no external radiation incident on the radiation source is present.

10.5 Analyze GS images presented in Sect. 10.2.2. Formulate what observational signataries are expected from (i) different lines of sight, (ii) pitch-angle anisotropy, and (iii) spatial inhomogeneity.

10.6 In the solar corona, the plasma density and magnetic field strength, decrease with increasing distance from the solar surface. This means that, on average, the higher frequency emission (of each mode) is generated in deeper layers of the corona and travels a longer distance to the observer than the

lower-frequency emission. If these signals had identical group velocities, this effect would result in a delay of the arrival of the high-frequency signal relative to the low-frequency signal. In fact, however, because of plasma dispersion, the group velocity increases with frequency, asymptotically approaching the velocity of light at high frequencies. Thus, high-frequency waves propagate faster than low-frequency waves, i.e., the effects of wave dispersion and source inhomogeneity are counter directed; thus, under real conditions, high-frequency waves can either lead or lag low-frequency waves, depending on parameters.

Determine the auto- and cross delays taking into account both plasma dispersion and source inhomogeneity. Use data in Fig. 10.22, right, to derive the corresponding parameters of the inhomogeneous model, such as local scale of inhomogeneity and total source size.

Answers and Solutions

10.1 The absorption coefficient $\varkappa_{\rm ff}^{\sigma}$ is defined by the dimensionless absorption index η_σ, Eq. (3.114):

$$\varkappa_{\rm ff}^{\sigma} = \frac{2\omega\eta_\sigma}{c} = \frac{2\omega\nu v}{n_\sigma c}\,\frac{u^2\sin^4\theta - \sigma\sqrt{\mathcal{D}}\left[u\sin^2\theta + 2(1-v)^2\right]}{\sigma\sqrt{\mathcal{D}}\left[2(1-v) - u\sin^2\theta + \sigma\sqrt{\mathcal{D}}\right]^2}. \tag{10.141}$$

Accordingly, the free–free emissivity of the magnetized plasma is specified by Eq. (10.141) and Kirchhoff's law (10.2):

$$j_{\mathbf{n},\omega}^{\sigma} = \frac{n_\sigma^2\omega^2\varkappa_{\rm ff}^{\sigma}}{(2\pi)^3c^2}\left|\frac{v_g\partial(\omega n_\sigma)}{c\,\partial\omega}\right| k_{\rm B}T, \quad \text{for} \quad \hbar\omega \ll k_{\rm B}T, \tag{10.142}$$

and for the practically used emissivity $j_{\mathbf{n},f}^{\sigma}$ related to usual frequency $f = \omega/2\pi$, we obtain:

$$j_{\mathbf{n},f}^{\sigma} = 2\pi j_{\mathbf{n},\omega}^{\sigma} = \frac{n_\sigma^2 f^2\varkappa_{\rm ff}^{\sigma}}{c^2}\left|\frac{v_g\partial(\omega n_\sigma)}{c\,\partial\omega}\right| k_{\rm B}T. \tag{10.143}$$

10.2 The dispersion relation of the transverse waves in a plasma at high frequencies has the form $\omega(k) = \sqrt{\omega_{pe}^2 + (ck)^2}$, while the group speed can be calculated as $v_g = {\rm d}\omega/{\rm d}k$. Some straightforward manipulations yield

$$\Delta t = \int_0^L \left[\frac{1}{v_{g1}} - \frac{1}{v_{g2}}\right]{\rm d}l = \frac{e^2(\lambda_1^2 - \lambda_2^2)}{2\pi m_e c^3}DM \approx 4.6(\lambda_1^2 - \lambda_2^2)DM\,\mu{\rm s}.$$

In the latter equality the delay is expressed in microseconds, the wavelength λ in cm, and DM in pc/cm^3. The relation obtained offers an elegant way of probing the ISM and deriving the mean (over the line of sight) electron number density if the distance to the pulsar is independently known.

10.3 No emission means $j_X = j_O = 0$; thus, $\mathbf{S} = 0$. Accordingly, no absorption means $\varkappa_X = \varkappa_O = 0$; thus $\mathsf{K} = 0$. Then, taking into account the equivalence $\mu_Q^2 + \mu_U^2 + \mu_V^2 = 1$, a solution of Eq. (10.44) is easy to find:

$$I(z) = I_0, \tag{10.144a}$$

$$\begin{aligned} Q(z) &= \mu_Q(\mu_Q Q_0 + \mu_U U_0 + \mu_V V_0) \\ &\quad +[(\mu_U^2 + \mu_V^2)Q_0 - \mu_Q(\mu_U U_0 + \mu_V V_0)]\cos\Delta kz \\ &\quad +(\mu_U V_0 - \mu_V U_0)\sin\Delta kz, \end{aligned} \tag{10.144b}$$

$$\begin{aligned} U(z) &= \mu_U(\mu_Q Q_0 + \mu_U U_0 + \mu_V V_0) \\ &\quad +[(\mu_Q^2 + \mu_V^2)U_0 - \mu_U(\mu_Q Q_0 + \mu_V V_0)]\cos\Delta kz \\ &\quad +(\mu_V Q_0 - \mu_Q V_0)\sin\Delta kz, \end{aligned} \tag{10.144c}$$

$$\begin{aligned} V(z) &= \mu_V(\mu_Q Q_0 + \mu_U U_0 + \mu_V V_0) \\ &\quad +[(\mu_Q^2 + \mu_U^2)V_0 - \mu_V(\mu_Q Q_0 + \mu_U U_0)]\cos\Delta kz \\ &\quad +(\mu_Q U_0 - \mu_U Q_0)\sin\Delta kz, \end{aligned} \tag{10.144d}$$

where I_0, Q_0, U_0, and V_0 are the initial (incident at $z = 0$) values of the Stokes parameters. Apparently, the radiation intensity (Stokes I) does not change when neither emission nor absorption are present. Other Stokes parameters contain oscillating component describing, in particular, the Faraday and Cotton–Mouton effects. The intensity of polarized component, $Q^2 + U^2 + V^2$, and, accordingly, the degree of polarization remain constant.

Consider propagation of originally linearly polarized wave ($Q_0 = I_0$, $U_0 = 0$, and $V_0 = 0$) at a given angle to the magnetic field; Eqs. (10.144) reduce to

$$Q(z) = Q_0 - (\mu_U^2 + \mu_V^2)Q_0(1 - \cos\Delta kz), \tag{10.145a}$$

$$U(z) = \mu_U\mu_Q Q_0(1 - \cos\Delta kz) + \mu_V Q_0 \sin\Delta kz, \tag{10.145b}$$

$$V(z) = \mu_V\mu_Q Q_0(1 - \cos\Delta kz) - \mu_U Q_0 \sin\Delta kz. \tag{10.145c}$$

We see that in a general case, the original linearly polarized radiation experiences a rotation of the polarization plane and, on top of that, it produces a nonzero circular polarization component, Eq. (10.145c). According to Eq. (10.48), in a quasilongitudinal propagation regime at high frequencies, $\mu_Q \sim \mu_U \propto \sqrt{u}\sin^2\theta \ll 1$ and $\mu_V \approx 1$. Thus, the degree of circular polarization remains small compared with the degree of linear polarization, $V \sim \sqrt{\omega_{\mathrm{Be}}/\omega}Q_0$; nevertheless, precise measurements of this secondary circular polarization are potentially highly valuable for the magnetic field diagnostics. In the case of transverse propagation, we have $\mu_Q = -\cos 2\psi$,

$\mu_U = -\sin 2\psi$, and $\mu_V = 0$, which yields the Cotton–Mouton effect; to obtain the correct functional dependence of the rotation angle on the wavelength one yet has to calculate and substitute Δk for the transverse propagation resulting in $\psi \propto \lambda^3$.

To obtain the pure Faraday effect let us consider propagation along the magnetic field. In this case the eigenmodes are precisely circularly polarized, $T_X = 1$ and $T_O = -1$, so $\mu_U = \mu_Q = 0$ and $\mu_V = 1$; thus, Eq. (10.145) yields $Q(z) = Q_0 \cos \Delta k z$, $U(z) = Q_0 \sin \Delta k z$, and $V(z) = 0$, which describes rotation of the linear polarization direction (Faraday effect).

Using Eq. (3.42) we find the polarization plane rotation angle $\delta = \Delta k L$ at the distance L, expressed via the wavelength $\lambda = 2\pi/k$:

$$\delta = \frac{\lambda^2 e^3}{2\pi (m_e c^2)^2} n_e B L.$$

The relative rotation angle of two waves with different frequencies is

$$\Delta\chi = \delta_1 - \delta_2 = (\lambda_1^2 - \lambda_2^2)\mathrm{RM}, \quad \text{where} \quad \mathrm{RM} = \frac{e^3}{2\pi (m_e c^2)^2} n_e B L$$

is the rotation measure.

If the magnetic field makes an angle with the line of sight and, perhaps, nonuniform like the electron distribution in Problem 10.2, then the combination $n_e B L$ must be replaced by the corresponding integral

$$\mathrm{RM} = \frac{e^3}{2\pi (m_e c^2)^2} \int_0^L n_e B_\parallel \mathrm{d}l = 0.81 \overline{n_e B}_\parallel L.$$

Here $B_\parallel$ is the parallel (to the line of sight) magnetic field component in μG, n_e is the thermal electron number density in cm^{-3}, L is the distance in pc, and RM is the rotation measure in radian per square meter. Simultaneous measurements of the dispersion measure and rotation measure complemented by the emission measure offers an efficient way of studying the thermal electron and magnetic field distributions in ISM.

Let us define the conditions when no polarization rotation happens, i.e., solve where the coefficients before the sine and cosine functions turn zeros. Although there are six such equations, they are not independent; they are satisfied all at once if

$$\frac{Q_0}{\mu_Q} = \frac{U_0}{\mu_U} = \frac{V_0}{\mu_V}. \tag{10.146}$$

Thus, when Eq. (10.146) is fulfilled, the oscillating component in Eq. (10.144) vanishes and all the Stokes parameters remain constant during the propagation. This is, in particular, the case when the propagating radiation represents

an *incoherent* combination of the ordinary and extraordinary waves, i.e.,

$$\begin{pmatrix} I_0 \\ Q_0 \\ U_0 \\ V_0 \end{pmatrix} = \mathfrak{s}_X I_X + \mathfrak{s}_O I_O = \begin{bmatrix} I_X + I_O \\ \mu_Q (I_X - I_O) \\ \mu_U (I_X - I_O) \\ \mu_V (I_X - I_O) \end{bmatrix}, \tag{10.147}$$

where I_X and I_O are arbitrary amplitudes of the eigenmodes.

10.4 Plasma particles moving in a magnetized plasma produce *coherent* X- and O-modes, although this coherence is lost quickly if the rotation measure is strong, so we adopt that the propagating radiation consists of *uncorrelated* X and O waves. Then, because there is no radiation incident on the plasma, we have $I = Q = U = V = 0$ at $z = 0$. In this case the solution of radiation transfer equation (10.44) is easy to write

$$I(z) = \frac{j_X}{\varkappa_X}\left(1 - e^{-\varkappa_X z}\right) + \frac{j_O}{\varkappa_O}\left(1 - e^{-\varkappa_O z}\right), \tag{10.148a}$$

$$Q(z) = \mu_Q \left[\frac{j_X}{\varkappa_X}\left(1 - e^{-\varkappa_X z}\right) - \frac{j_O}{\varkappa_O}\left(1 - e^{-\varkappa_O z}\right)\right], \tag{10.148b}$$

$$U(z) = \mu_U \left[\frac{j_X}{\varkappa_X}\left(1 - e^{-\varkappa_X z}\right) - \frac{j_O}{\varkappa_O}\left(1 - e^{-\varkappa_O z}\right)\right], \tag{10.148c}$$

$$V(z) = \mu_V \left[\frac{j_X}{\varkappa_X}\left(1 - e^{-\varkappa_X z}\right) - \frac{j_O}{\varkappa_O}\left(1 - e^{-\varkappa_O z}\right)\right]. \tag{10.148d}$$

Again, no oscillations of the Stokes parameters are present in Eq. (10.148) because for the radiation composed of incoherent eigenmodes conditions (10.146) are fulfilled everywhere along the ray path. The polarization will evolve, however, if the radiation propagates through a nonuniform medium, e.g., in the case of solar corona. In particular, strong modifications of the radio emission polarization can occur when the radiation interacts with layers where the line-of-sight component of the magnetic field changes the orientation (regions of quasitransverse wave propagation), which may happen at the current sheets, where processes of magnetic reconnection and corresponding prompt energy release are likely.

10.6 Let us assume that the spatial center of the low-frequency emission source (e.g., at frequency $f_0 = \omega_0/(2\pi) = 2.81\,\mathrm{GHz}$ in the event under study) is located at $z = 0$ and that the emission at other frequencies is generated at volumes centered at $-z(\omega)$ ($z(\omega)$ is a positive quantity). We can then write for each mode the group auto-delay as a function of frequency and the (already analyzed above) group cross delay between the modes taking into account the source inhomogeneity.

The travel times of a σ wave at the reference frequency ω_0 and arbitrary one ω are

$$t_0^\sigma = \int_0^{\mathcal{R}} \frac{\mathrm{d}z}{v_\sigma(\omega_0)}, \qquad t_\omega^\sigma = \int_{-z(\omega)}^{\mathcal{R}} \frac{\mathrm{d}z}{v_\sigma(\omega)}. \tag{10.149}$$

Accordingly, the delay between them is defined by difference between two expressions in Eq. (10.149):

$$\Delta t_\omega^\sigma = t_\omega^\sigma - t_{\omega_0}^\sigma = \int_{-z(\omega)}^{0} v_\sigma^{-1}(\omega)\mathrm{d}z + \int_0^\infty (v_\sigma^{-1}(\omega) - v_\sigma^{-1}(\omega_0))\mathrm{d}z. \tag{10.150}$$

With this definition, the delay is negative if the high-frequency signal reaches the Earth first and positive if the low-frequency signal arrives first. In the latter integral, the upper limit can obviously be replaced with ∞.

Given that the emission frequency is of the same order as the plasma and gyrofrequencies, in further analysis we use exact expressions of the group velocities while make expansions over the small quantity $\Delta\omega/\omega \sim 3\,\%$. In the second term, this enables us to expand the function $v_\sigma^{-1}(\omega)$ in a series over the frequency with the accuracy $\Delta\omega/\omega_0$. To calculate the first term to the same accuracy, we note that the region of integration for this term is a small quantity of the same order as $\Delta\omega/\omega_0$, $z(\omega)/H_{\text{eff}} \sim \Delta\omega/\omega_0$ where H_{eff} is a characteristic length giving the main contribution to the integration of the second term. The auto-delay then becomes

$$\Delta t_\omega^\sigma = z(\omega)v_\sigma^{-1}(\omega_0) + \frac{\Delta\omega}{\omega_0}\int_0^\infty \left(\omega\frac{\partial v_\sigma^{-1}(\omega)}{\partial\omega}\right)_{\omega=\omega_0} \mathrm{d}z. \tag{10.151}$$

To specify the yet unknown function $z(\omega)$ the sum of the auto-delays in X- and O-modes will be useful:

$$\Delta t_\omega^X + \Delta t_\omega^O = z(\omega)(v_X^{-1}(\omega_0) + v_O^{-1}(\omega_0)) + \frac{\Delta\omega}{\omega_0}\int_0^\infty \omega_0 \left(\frac{\partial v_X^{-1}(\omega)}{\partial\omega} + \frac{\partial v_O^{-1}(\omega)}{\partial\omega}\right)_{\omega=\omega_0} \mathrm{d}z. \tag{10.152}$$

The integral in the second term can be represented as a product of the integrand evaluated at $z = 0$ and the effective integration scale H_{eff}. To a first approximation over $\Delta\omega/\omega_0$, the function $z(\omega)$ can be written as

$$z(\omega) = \chi\frac{\Delta\omega}{\omega_0}H_{\text{eff}}, \tag{10.153}$$

where χ is yet unknown parameter. Then

$$\Delta t_\omega^X + \Delta t_\omega^O = H_{\rm eff}\frac{\Delta\omega}{\omega_0}\left\{\chi(v_X^{-1}(\omega_0)+v_O^{-1}(\omega_0)) + \omega_0\left(\frac{\partial v_X^{-1}(\omega)}{\partial\omega}+\frac{\partial v_O^{-1}(\omega)}{\partial\omega}\right)_{\omega=\omega_0}\right\}. \quad (10.154)$$

Let us introduce for compactness the difference between reciprocal values of the group velocities as follows

$$\Delta v_g^{-1}(\omega) = v_X^{-1}(\omega) - v_O^{-1}(\omega) \quad (10.155)$$

and derive a more precise relation than Eq. (10.120) for the group cross delay Δt_g, taking into account the radio source inhomogeneity. Similar to derivation of Eq. (10.151), we obtain

$$\Delta t_g(\omega) = z(\omega)\Delta v_g^{-1}(\omega_0,0) + \int\limits_0^\infty \Delta v_g^{-1}(\omega_0,z){\rm d}z + \frac{\Delta\omega}{\omega_0}\int\limits_0^\infty\left(\omega\frac{\partial\Delta v_g^{-1}(\omega,z)}{\partial\omega}\right)_{\omega=\omega_0}{\rm d}z. \quad (10.156)$$

Estimating the integrals as

$$\int\limits_0^\infty \Delta v_g^{-1}(\omega_0,z){\rm d}z = \Delta v_g^{-1}(\omega_0,0)H, \quad \int\limits_0^\infty\left(\omega\frac{\partial\Delta v_g^{-1}(\omega,z)}{\partial\omega}\right)_{\omega=\omega_0}{\rm d}z = \left(\omega\frac{\partial\Delta v_g^{-1}(\omega,0)}{\partial\omega}\right)_{\omega=\omega_0}H_1, \quad (10.157)$$

where H, H_1 are the corresponding effective integration scales, and then using Eq. (10.153), obtain

$$\Delta t_g(\omega) = H\Delta v_g^{-1}(\omega_0)\left\{1+\frac{H_1}{H}\frac{\omega_0}{\Delta v_g^{-1}(\omega_0)}\left(\frac{\partial\Delta v_g^{-1}(\omega)}{\partial\omega}\right)_{\omega=\omega_0}\frac{\Delta\omega}{\omega_0}+\chi\frac{H_{\rm eff}}{H}\frac{\Delta\omega}{\omega_0}\right\}.$$

This formula solves the problem of finding the cross delay for the frequencies comparable to the plasma eigenfrequencies with the account of source inhomogeneity. The frequency dependence of Δt_g is described by the second and third terms in the braces. If the emission frequency were much higher than the plasma frequency, we would have $H_1 = H$ and, accordingly,

$$\alpha = \frac{\omega_0}{\Delta v_g^{-1}(\omega_0)}\left(\frac{\partial\Delta v_g^{-1}(\omega)}{\partial\omega}\right)_{\omega=\omega_0} \approx -3 \quad (10.158)$$

in agreement with approximate formula (10.120) that implies $\Delta t_g \propto \omega^{-3} \approx \omega_0^{-3}(1 - 3\Delta\omega/\omega_0)$. In fact, $\alpha(\omega)$ is a function of frequency approaching the value of -3 only asymptotically. Specifically, the $\alpha(\omega)$ dependence for a fixed plasma frequency, which is straightforward to compute based on theory presented in Chap. 3 is given in Fig. 10.24, left. We can see that α can be quite different from -3 near the plasma frequency. In our case, the emission frequency to the plasma frequency ratio is fixed for a given value of Y. Figure 10.24, middle, shows α as a function of Y: α differs appreciably from its asymptotic value (-3) at all values of Y and varies from -3.9 to -3.75 in the Y range of interest. The third term in braces in Eq. (10.158), related to the source inhomogeneity, is positively defined and is determined solely by the constant χ (for a fixed ratio of the effective integration scales $H_{\rm eff}/H$).

Therefore, to determine the cross delay we have yet to find the value of χ. For this purpose, we express this quantity in terms of the sum of auto-delays (10.154):

$$\chi = \frac{\omega_0 \left(\frac{\partial v_X^{-1}(\omega)}{\partial \omega} + \frac{\partial v_O^{-1}(\omega)}{\partial \omega} \right)_{\omega=\omega_0}}{v_X^{-1}(\omega_0) + v_O^{-1}(\omega_0)} + \frac{\omega_0}{\Delta\omega} \frac{(\Delta t_\omega^X + \Delta t_\omega^O)}{H_{\rm eff}(v_X^{-1}(\omega_0) + v_O^{-1}(\omega_0))}. \quad (10.159)$$

The first term in this formula is a function of Y and does not depend on other parameters of the source or on the observational errors. In the second term, the quantity $\omega_0/\Delta\omega$ is known, and the delays Δt_ω^σ are known from the observations (i.e., with some error), whereas the scale $H_{\rm eff}$ is unknown. It will then be convenient to transform the second term using Eq. (10.158). We multiply and divide this term by $\Delta t_g/H$, noting also that at the reference frequency ω_0 we have

$$\Delta t_g/H = \Delta v_g^{-1}(\omega_0). \quad (10.160)$$

Then, Eq. (10.159) receives the form

$$\chi = \frac{\omega_0 \left(\frac{\partial v_X^{-1}(\omega)}{\partial \omega} + \frac{\partial v_O^{-1}(\omega)}{\partial \omega} \right)_{\omega=\omega_0}}{v_X^{-1}(\omega_0) + v_O^{-1}(\omega_0)} + \frac{\omega_0}{\Delta\omega} \frac{\Delta v_g^{-1}(\omega_0)}{v_X^{-1}(\omega_0) + v_O^{-1}(\omega_0)} \frac{\Delta t_\omega^X + \Delta t_\omega^O}{\Delta t_g} \frac{H}{H_{\rm eff}}. \quad (10.161)$$

Advantage of this form is that χ now depends on the ratio of the effective scales $H/H_{\rm eff}$, which is of the order of unity, rather than on the absolute value of $H_{\rm eff}$. The dependence of χ on Y for various values of $H/H_{\rm eff}$ is presented in Fig. 10.24, right. Note that χ is almost independent on either Y or $H/H_{\rm eff}$. This is due to the smallness of the sum of the auto-delays $\Delta t_\omega^X +$

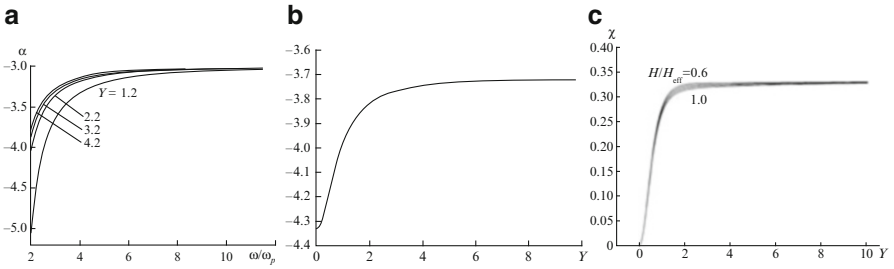

Figure 10.24: *Left*: Index α as a function of frequency for various values of Y (**a**) and as a function of Y for waves at the double hybrid frequency (**b**). *Right*: Inhomogeneity index χ as a function of Y for various values of $H/H_{\rm eff} = 0.6$, 0.7, 0.8, 0.9, and 1.0 (Melnikov et al. 2002a).

Δt_ω^O in the analyzed event. To an accuracy sufficient for the analysis we can adopt

$$\chi = 0.32 = \text{const}(Y, H/H_{\rm eff}), \tag{10.162}$$

which, being substituted into Eq. (10.158) along with $\alpha \approx -3.8$ yields $\Delta t_g(\omega) = \Delta t_g(\omega_0)[1 - 3.5(\Delta\omega/\omega_0)] \propto \omega^{-3.5}$ in agreement with the solid line in Fig. 10.23.

Let us return now to the auto-delays. Substituting expression (10.153) for $z(\omega)$ into Eq. (10.151) and introducing the effective integration scales H_σ ($\sigma = X, O$), we obtain

$$\Delta t_\omega^\sigma = H_{\rm eff}\frac{\Delta\omega}{\omega_0}\left\{\chi v_\sigma^{-1}(\omega_0) + \frac{H_\sigma}{H_{\rm eff}}\left(\omega\frac{\partial v_\sigma^{-1}(\omega)}{\partial\omega}\right)_{\omega=\omega_0}\right\}. \tag{10.163}$$

Figure 10.22, right, shows the theoretical dependences Δt_ω^σ for various values of $H_\sigma/H_{\rm eff}$ taking into account Eq. (10.162), plotted on top of the observational data. Note that the effect of source inhomogeneity is dominant for the ordinary waves (i.e., the low-frequency signal reaches the observer first so that the delays are positive), while the effect of dispersion dominates for the extraordinary waves (i.e., the delays are negative).

Above, estimating various relevant integrals, we introduced five different effective scales having, presumably, the same order of magnitude; however, they are not all independent. Indeed,

$$H_{\rm eff} = \left\{\frac{\frac{\partial v_X^{-1}(\omega)}{\partial\omega}H_X + \frac{\partial v_O^{-1}(\omega)}{\partial\omega}H_O}{\frac{\partial v_X^{-1}(\omega)}{\partial\omega} + \frac{\partial v_O^{-1}(\omega)}{\partial\omega}}\right\}_{\omega=\omega_0}, \tag{10.164a}$$

$$H_1 = \left\{ \frac{\frac{\partial v_X^{-1}(\omega)}{\partial \omega} H_X - \frac{\partial v_O^{-1}(\omega)}{\partial \omega} H_O}{\frac{\partial v_X^{-1}(\omega)}{\partial \omega} - \frac{\partial v_O^{-1}(\omega)}{\partial \omega}} \right\}_{\omega=\omega_0} . \tag{10.164b}$$

In particular, if $H_X = H_O$, then $H_{\rm eff} = H_1 = H_X = H_O$. Generally speaking, a detailed and precise frequency dependence of the delays could allow us to determine the relative values of these effective scales. However, the available data, at least within the observational errors, can be well interpreted assuming all the scales to be identical and equal to H already estimated to be $\sim 5 \times 10^9$ cm in Sect. 10.4.3.

Let us consider the total linear size of the inhomogeneous source $l \approx z(2.89\,\mathrm{GHz})$:

$$l = \chi H_{\rm eff} \frac{\Delta f}{f_o} \approx 4 \times 10^7\,\mathrm{cm}, \tag{10.165}$$

which exceeds by a factor of three the source size found from the radio flux and brightness temperature of the radio emission, Eq. (10.140). This apparent discrepancy appeared because in Sect. 10.4.3 we calculated the size of a *homogeneous* radio source radiating with a *natural* bandwidth, which implies that the effective source size at *each frequency* is ~ 100 km, while the determined source size relates to emission at *all* frequencies. Hence, solving Eq. (10.140) for $\Delta f/f_0$ and substituting $l = 100$ km, we can estimate the natural bandwidth of the emission mechanism to be $\Delta f/f_0 \sim 1\,\%$, or $\Delta f \approx 20$ MHz. The regions radiating at different (though neighboring) radio frequencies are spatially displaced relative to each other because of the inhomogeneity. Note that the value of $\chi H_{\rm eff}$ represents an estimate of the local scale of plasma inhomogeneity at the very source site, which means that the plasma density gradient at the radio source is roughly a factor of three greater than the mean gradient in the corona along the radio emission path. Thus, the instability of the upper hybrid modes arises in a locally more nonuniform site of a magnetic trap.

To summarize the presented rather thorough analysis of this event and emphasize a great potential of the plasma emission for diagnostics of the coronal plasma, we gather below all the parameters determined:

-Background plasma density	$n_e = 1.9 \times 10^{10}\,\mathrm{cm}^{-3}$
-Magnetic field	$B = 256\,\mathrm{G}$
-Kinetic electron temperature	$T_e \geq 3 \times 10^6\,\mathrm{K}$
-Number density of fast electrons	$n_b \sim 10^4\,\mathrm{cm}^{-3}$
-Growth rate of the plasma waves	$\gamma_{\max} \sim 300\,\mathrm{s}^{-1}$
-Spectral bandwidth of the generated plasma waves	$\Delta\omega/\omega \leq 3\,\%$
-Wave number of the generated plasma waves	$kd_e \approx 0.1$
-Scatter of the wave numbers of the generated plasma waves	$c\Delta k/\omega_{\rm pe} \approx 3$ or $\Delta k d_e \approx 0.1$

-Direction of peak amplification of the plasma waves	$\theta \approx 80\,^\circ$
-Angular scatter of the generated plasma waves	$\Delta\theta \approx 30\,^\circ$
-Level of plasma turbulence	$w = W/nT \approx 10^{-6}$
-Brightness temperature of the emission	$T_\mathrm{b} \approx 5 \times 10^{12}\,\mathrm{K}$
-Source size at a given frequency	$L \approx 100\,\mathrm{km}$
-Total source size	$l \approx 400\,\mathrm{km}$
-Plasma parameter in the source	$Y \approx 1.7$
-Natural bandwidth of the spectral line	$\Delta f/f \approx 1\,\%$
-Effective scale of inhomogeneity	
average in the corona	$H \approx 5 \times 10^9\,\mathrm{cm}$
at the radio source	$\chi H \approx 2 \times 10^9\,\mathrm{cm}$

Chapter 11

Particle Acceleration in Astrophysical Media

In the laboratory, the particles with high to very high energy ($\mathcal{E} \gg mc^2$) are obtained by means of extremely sophisticated devices. One of many examples is large Hadron collider (LHC) recently commissioned in Europe. These specially designed accelerating devices are needed because high-energy particles lose their energy very quickly due to interaction with matter and external fields and, thus, become thermally assimilated by the medium.

Nevertheless, there are also natural processes giving rise to particle acceleration up to extremely high energies due to routine interactions with natural media in astrophysics. There are many examples of such sporadic acceleration including particle acceleration in solar and stellar flares, planetary magnetospheres, SNRs, GRBs, etc. Perhaps, the earliest of discovered natural phenomena involving the high-energy particles was the phenomenon of cosmic rays (CRs), which arrive from far far away of the Universe and penetrate the terrestrial atmosphere. CRs have been recorded, over more than century, by both ground-based and spaceborne detectors. The highest detected energy of a single CR particle is about 3×10^{20} eV, i.e., by 7–8 orders of magnitude higher than the highest energy achievable in the modern laboratory accelerators. For comparison, a comparable energy is carried out by a *macroscopic* body with the mass of 1 g moving with the sound speed in air ($\sim$330 m/s).

CRs at moderate energies ($\mathcal{E} < 10^{12}$ eV) consist mainly of protons ($\sim$90%), helium nuclei (α-particles) $\sim$10% by number, and heavier nuclei (less than 1%). Electrons provide around 1% of the total CR flux. In other phenomena, e.g., in solar flares or SNRs, the proportion between various charges can be different; the estimate is complicated by the fact that the ions are much heavier than the electrons (or positrons), so they produce electromagnetic emission much less effectively, thus, it is often difficult to quantitatively derive their relative abundances. Unlike electrons, which are visible throughout the entire electromagnetic spectrum, the ions can mainly

G.D. Fleishman and I.N. Toptygin, *Cosmic Electrodynamics*, Astrophysics and Space Science Library 388, DOI 10.1007/978-1-4614-5782-4_11,

be detected via gamma-ray emission generated in nuclear interactions of the high-energy particles with the background target particles, which requires a reasonably dense target to produce a detectable gamma emission. In case of solar flares, some information of the ion composition (and ionization states) is obtained by in situ measurements in the IPM. These measurements show that the relative abundances of the charged particles vary in very broad limits. For example, there are so-called He^3-rich flares in which the ratio of He^3 to He^4 is much larger than in the thermal plasma $\sim 10^{-4}$ (and sometimes even larger than one).

The problem of the high-energy particle origin has not yet been fully solved. Apparently, an avenue to solve it lies within the physics of highly nonstationary collisionless astrophysical plasma. This plasma, as has been broadly discussed in this book, contains plenty of macroscopic motions and electromagnetic fields including stochastic, turbulent component. Importantly, the plasma number density n can be very low (compared with the terrestrial densities), e.g., $0.1 \lesssim n \lesssim 10\,\mathrm{cm}^{-3}$ outside the stars and $n \sim 10^{10}\,\mathrm{cm}^{-3}$ in stellar coronae.

This nonstationarity is driven by strong energy release which can be supplied by mechanical motion of the celestial bodies, stellar winds and explosions, accreting flows, jets, "annihilation" of magnetic energy, etc. Some of the astrophysical sources, including extragalactic jets, active galactic nuclei, and gamma-ray burst sources, include relativistically moving ejectas (see Chap. 12), which somehow can effectively transfer a part of the expansion energy into the particle acceleration. Thus, the energy releases are followed by a complicated disturbance of the source volume filled by regular and random motions and magnetic fields. A natural outcome of the interaction between these motions and magnetic fields in a highly conducting plasma is generation of electric field, which, in its turn, capable of direct accelerating the charged particles. In addition to the plasma nonstationarity, another important condition required for the efficient acceleration to be possible is availability of free energy capable of transforming to the accelerated particle energy.

A charged particle moving in an electric field over its trajectory from point 1 to point 2, gains energy $\Delta\mathcal{E} = e\int_{(1)}^{(2)} \boldsymbol{E}\cdot\boldsymbol{v}\mathrm{d}t$. If averaging over all allowed trajectories in the acceleration region yields $\langle\boldsymbol{E}\rangle \neq 0$, such acceleration is called **regular** acceleration. If, in contrast, $\langle\boldsymbol{E}\rangle = 0$, i.e., the electric field vector changes its direction repeatedly, an acceleration is still possible. Indeed, the mean work of the electric force on the particle, which is $\langle\int_{(1)}^{(2)} e\boldsymbol{E}\cdot\boldsymbol{v}\mathrm{d}t\rangle$, is nonzero in a general case because the particle velocity $\boldsymbol{v}[\boldsymbol{E}]$ represents a complicated functional form of the electric field; thus, averaging yields terms proportional to $\langle E^2\rangle$, which are apparently positively defined; this kind of acceleration is called **stochastic** acceleration.

For highly conducting plasma the electric field can be expressed via the magnetic field and macroscopic velocity of the plasma using Eq. (2.19). In this case the particle acceleration can be interpreted as a result of their elastic

collisions with moving "magnetic inhomogeneities," which transfer part of their energy to the particles. Here we consider some of many acceleration processes in the nonstationary plasmas capable of producing high-energy particles.

11.1 Regular Change of Particle Energy and Conservation Laws

Apparently, to change energy of a charged particle requires an electric field to be applied to it because the magnetic field does not produce any work, while gravitational field effect is negligible in most of the cases. For example, like in laboratory devices, one can expect a charge acceleration by a potential drop. However, in a highly conducting plasma, it is extremely difficult to support a large-scale DC electric field because rapid charge neutralization—similarly to the situation with neutralizing return currents, considered in Sect. 7.1.3. Below we consider the particle energy change by a regular field or regular plasma motion and formulate a number of general conclusions regarding the particle acceleration in a natural plasma.

11.1.1 Particle Energy Change in Regular Fields

Assume a DC electric field $\boldsymbol{E}$ is applied to a plasma volume and consider immediate consequences of this. Apparently, if this field is somewhat weak, it will stimulate electric current obeying standard Ohm's law. Ohm's law is set up by equality of the electric force and the collisional drag force due to electron-ion friction when the individual particle velocity change between two successive collisions is small compared with the thermal velocity. However, if the velocity change is of the order of the thermal speed, the Coulomb collision cross section decreases and, accordingly, the electron-ion collisions become inefficient to set up a steady electric current, which implies progressive acceleration ("runaway") of all available particles. The critical electric field can be estimated as such a field that doubles the particle (thermal) velocity over one collisional time, which yields for electrons (see Problem 1.13):

$$E_{\mathrm{De}} = \frac{ze \ln \Lambda_{\mathrm{C}}}{r_D^2} = \begin{pmatrix} 2 \times 10^{-8} \\ 0.6 \times 10^{-5} \end{pmatrix} \left(\frac{n_e}{10^9\ \mathrm{cm}^{-3}}\right) \left(\frac{T}{10^7\ \mathrm{K}}\right)^{-1} \left(\frac{\ln \Lambda_{\mathrm{C}}}{20}\right) \begin{pmatrix} \text{statvolt/cm} \\ \text{V/cm} \end{pmatrix} \tag{11.1}$$

and is called the **Dreicer electric field**; here z is the ion charge ($z = 1$ for the hydrogen) and r_D is the Debye length.

It is interesting to address the problem of the **ion Dreicer electric field**, which as we will see depends on both the ion charge and number density. For the estimate we consider a three-component plasma consisting of electrons (e), protons (p), and one more sort of ions (i) with the charge $Z|e|$,

mass m_i, and number density n_i so that $n_e = n_p + Zn_i$, permitted by a sub-Dreicer uniform electric field $\boldsymbol{E}$. To address the question of the runaway ions we have to estimate the value and direction of the component flow velocities in the given plasma. To do so we have to obtain balance conditions between the electric force and forces of the dynamic friction between the plasma components.

The dynamic friction force acting from a plasma component a on a given "test" particle is calculated from the averaged momentum exchange between this plasma component and the test particle (Trubnikov 1965), i.e.,

$$\boldsymbol{\mathcal{F}}_a(\boldsymbol{u}) = -\frac{Z^2 Q}{\mu_a} \int \frac{\boldsymbol{u} - \boldsymbol{v}}{|\boldsymbol{u} - \boldsymbol{v}|^3} f_a(\boldsymbol{v}) \mathrm{d}^3 v, \tag{11.2}$$

where $\boldsymbol{u}$ is the velocity of the test particle, $\mu_a = M m_a/(M + m_a)$ is the reduced mass defined by the test particle mass M and a-component particle mass m_a, $f_a(\boldsymbol{v})$ is the distribution function of the component a, and $Q = 4\pi e^4 \ln \Lambda_{\mathrm{C}}$. Apparently, to find the force acting on a "mean" test particle, we have yet to average force (11.2) over distribution function of the "test" particle component. Both these averagings are convenient to perform assuming $\boldsymbol{u} = \boldsymbol{u}_T + \delta\boldsymbol{u}$ and $\boldsymbol{v} = \boldsymbol{v}_T + \delta\boldsymbol{v}$, where $\boldsymbol{u}_T$ and $\boldsymbol{v}_T$ are the corresponding thermal velocities with zero means (but nonzero rms values), while $\delta\boldsymbol{u}$ and $\delta\boldsymbol{v}$ are flow velocities driven by external electric field. Since we adopted $E/E_{\mathrm{De}} < 1$, the denominators are defined by the thermal velocities, whose contributions to the numerators are zeros, so the numerators are solely determined by the flow velocities.

Accordingly, the balance of forces acting on the electron component yields (we drop δ and use $\boldsymbol{v}$ for all $\delta\boldsymbol{v}$ below for short)

$$-|e|\boldsymbol{E} - \frac{Q n_p}{m_e v_{Te}^3}(\boldsymbol{v}_e - \boldsymbol{v}_p) - \frac{Z^2 Q n_i}{m_e v_{Te}^3}(\boldsymbol{v}_e - \boldsymbol{v}_i) = 0, \tag{11.3}$$

where we took into account that $v_{Te} \gg v_{Tp}$, $v_{Te} \gg v_{Ti}$ and $\mu_a \approx m_e$. Then, in a similar way, we write for protons

$$|e|\boldsymbol{E} - \frac{Q n_e}{m_e v_{Te}^3}(\boldsymbol{v}_p - \boldsymbol{v}_e) - \frac{Z^2 Q n_i}{m_{ip} v_{Tp}^3}(\boldsymbol{v}_p - \boldsymbol{v}_i) = 0, \tag{11.4}$$

where we adopted for simplicity $v_{Tp} \gg v_{Ti}$; this approximation is the least accurate for the Helium ions but even is this case the error is within 30%, which is acceptable for the purpose of the estimate; with the same accuracy we use below the proton mass m_p for the reduced ion-proton masses m_{ip}. Then, we add up Eqs. (11.3) and (11.4) to eliminate the electric field:

$$-\frac{Q Z(Z-1) n_i}{m_e v_{Te}^3}\boldsymbol{v}_e - \frac{Z^2 Q n_i}{m_{ip} v_{Tp}^3}\boldsymbol{v}_p + \frac{Z^2 Q n_i}{m_{ip} v_{Tp}^3}\boldsymbol{v}_i = 0 \tag{11.5}$$

and eliminate the electron velocity using the momentum conservation law $\boldsymbol{v}_e = -(n_p m_p \boldsymbol{v}_p + n_i m_i \boldsymbol{v}_i)/(n_e m_e)$ (provided that the plasma is immobile as a whole in this reference frame):[1]

$$\left[1 + \frac{m_{ip} v_{Tp}^3}{m_e v_{Te}^3} \frac{Z-1}{Z} \frac{n_i m_i}{m_e n_e}\right] \boldsymbol{v}_i = \left[1 - \frac{m_{ip} v_{Tp}^3}{m_e v_{Te}^3} \frac{Z-1}{Z} \frac{n_p m_p}{m_e n_e}\right] \boldsymbol{v}_p. \tag{11.6}$$

This equality demonstrates a remarkable property of the admixture ion behavior in the external electric field: **the admixture ions move in the direction opposite to the main ions** (since the second, negative term dominates the rhs for the natural abundance of the protons), i.e., **the admixture ions move *together* with electrons in the direction *opposite* to the electric vector direction** (Fig. 11.1). This anomalous behavior (see, e.g., Gurevich 1961; Furth and Rutherford 1972; Holman 1995), originates from the fact that the dynamic friction force produced by moving electron component on the ions with $Z > 1$, and so proportional to Z^2, turns out to overcome the electric force, which is proportional to Z. Another remarkable property revealed by Eq. (11.6) is that a significant ion flow velocity can only be achieved for a relatively tiny ion population for which the second term in the lhs brackets can be neglected compared with 1; for some abundant ions including helium and oxygen it is not the case since the second term is larger than or comparable to 1 even though $n_i/n_p \ll 1$ for them.

Let us make estimates of the flow velocity for the Helium isotopes. Consider ^{4}He ($Z = 2$ and $m_i = m_4 = 4m_p$) first and adopt $mv_T^2 \sim T$ for all plasma components, i.e., $v_{Tp}/v_{Te} \approx \sqrt{m_e/m_p}$, then

$$\left[1 + 2\frac{n_4}{n_e}\sqrt{\frac{m_p}{m_e}}\right] \boldsymbol{v}_4 = \left[1 - \frac{n_p}{2n_e}\sqrt{\frac{m_p}{m_e}}\right] \boldsymbol{v}_p. \tag{11.7}$$

Since $n_i/n_e \sim 0.1 \gg \sqrt{m_e/(4m_p)} \approx 1/86 \approx 0.012$, for a rough estimate we can discard the first terms (ones) in both brackets, which simply yields $\boldsymbol{v}_4 \sim -(n_p/4n_i)\boldsymbol{v}_p$. To express the ion flow velocities via the electron flow velocity, however, we have to calculate the ion velocity more accurately, i.e., retain small terms in Eq. (11.7), which yields

$$\boldsymbol{v}_4 \approx -\frac{n_p}{4n_4}\left[1 - \frac{n_e(4n_4 + n_p)}{2n_p n_4}\sqrt{\frac{m_e}{m_p}}\right] \boldsymbol{v}_p. \tag{11.8}$$

Substituting Eq. (11.8) into the component momentum conservation law we find for the protons

$$\boldsymbol{v}_p \approx -\frac{2n_4}{n_p + 4n_4}\sqrt{\frac{m_e}{m_p}}\boldsymbol{v}_e, \tag{11.9}$$

[1] We note that in a purely electron–proton plasma the momentum conservation would imply a very small proton flow velocity $\boldsymbol{v}_p = -(m_e/m_p)\boldsymbol{v}_e$.

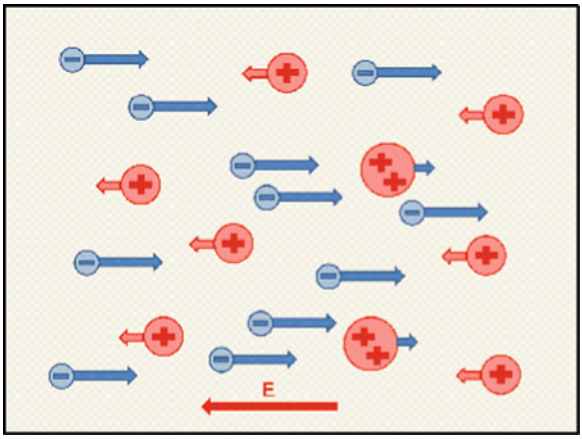

Figure 11.1: Illustration to the origin of the heavy ion velocity directed oppositely to the external electric field due to dynamic friction from moving electrons.

which is noticeably larger than $\boldsymbol{v}_p = -(m_e/m_p)\boldsymbol{v}_e$ in the purely hydrogen plasma. Now, substituting Eq. (11.9) into Eq. (11.8), we find for the ^{4}He ions

$$\boldsymbol{v}_4 \approx \frac{n_p}{2(n_p + 4n_4)}\sqrt{\frac{m_e}{m_p}}\boldsymbol{v}_e. \tag{11.10}$$

A similar analysis for the other helium isotope, ^{3}He ($Z = 2$ and $m_i = m_3 = 3m_p$) gives rise to essentially different result because of much lower ^{3}He number density, $n_3 \approx 1.7 \times 10^{-4} n_4$. For such a low density, we can safely discard the second term in the lhs of Eq. (11.6) (while still discard 1 compared with the second term in the rhs), which eventually yields

$$\boldsymbol{v}_3 \approx \frac{n_p n_4}{n_e(n_p + 4n_4)}\boldsymbol{v}_e, \tag{11.11}$$

roughly one order of magnitude larger than the ^{4}He flow velocity $\boldsymbol{v}_4$, Eq. (11.10).

The results obtained allow estimating effective "Dreicer" fields for various ions, which we define as an electric field needed to form the ion flow velocity equal to the thermal velocity of the same ion. Rewriting Eqs. (11.10) and (11.11) in a compact form $\boldsymbol{v}_i = K_i \boldsymbol{v}_e$ and taking into account that $\boldsymbol{v}_e = -v_{Te}\boldsymbol{E}/E_{\rm De}$ and $v_{Te} = v_{Ti}\sqrt{m_i/m_e}$ (we still assume equal temperatures of all plasma components), we obtain $\boldsymbol{v}_i/v_{Ti} = -K_i\sqrt{m_i/m_e}\boldsymbol{E}/E_{\rm De} \equiv \boldsymbol{E}/E_{Di}$, where the latter equivalence is a definition of the effective ion Dreicer field. Then, using Eqs. (11.10) and (11.11) we find

$$E_{D3} \approx \frac{n_e(n_p + 4n_4)}{n_p n_4}\sqrt{\frac{m_e}{m_3}}E_{\rm De}, \tag{11.12a}$$

$$E_{D4} \approx \frac{n_p + 4n_4}{n_p} E_{\mathrm{De}}. \tag{11.12b}$$

Adopting $n_4 = 0.1n_p$ (i.e., $n_e = 1.2n_p$), we find $E_{D3} \approx 0.23E_{\mathrm{De}}$, while $E_{D4} \approx 1.4E_{\mathrm{De}}$, i.e., $E_{D3} \ll E_{\mathrm{De}} < E_{D4}$.

This remarkable difference in the effective Dreicer fields implies that **a given electric field can be sub-Dreicer for the electrons and ions with large abundance** (e.g., ^{4}He), **while super-Dreicer for ions with small abundance** (e.g., ^{3}He). It is important to make a distinction between runaway electrons and ions in corresponding super-Dreicer fields. Indeed, in case of electron *super-Dreicer* electric field, $E > E_{\mathrm{De}}$, all plasma electrons are being picked up by this electric field and *infinitely* accelerated (until they are affected by this field) because the Coulomb friction force produced by ions is too weak to prevent the acceleration. The runaway admixture ions are driven by the electron drag force (rather than the electric field itself); thus, they start to runaway as soon as their flow velocity becomes comparable to their thermal velocity and the Coulomb friction force produced by other *ions* goes down. Therefore, the ions cannot be *infinitely* accelerated because they cannot achieve a velocity larger than their driver has, i.e., the electron flow velocity. However, in practice this would still mean a highly efficient ion acceleration, up to v_e^2/v_{Ti}^2 times original thermal ion energy.

In the case of the sub-Dreicer electric field, $E < E_D$, some acceleration is still possible in spite of the fact that the drag force is strong enough to prevent acceleration of the particles moving with the thermal velocity. Indeed, the thermal particles are distributed over energy with a tail of particles with large velocities compared with the thermal velocity. Apparently, for the particles with

$$v > v_r = v_{Te} \left(\frac{E_D}{E} \right)^{1/2}, \tag{11.13}$$

where v_r is so-called **runaway velocity**, the Coulomb collisions are too weak to prevent particle acceleration. Nevertheless, acceleration by the sub-Dreicer electric field turns out to have a relatively small efficiency in a typical situation, e.g., in the solar corona. Indeed, even in a reasonably strong sub-Dreicer electric field, $\sim 10^{-6}$ V/cm, an electron has to travel $\sim 10^{10}$ cm to gain energy around 10 keV and $\sim 10^{11}$ cm to gain energy around 100 keV. Having in mind solar flares for which this mechanism has often been applied, we conclude that in the most favorable situation when the electric field is distributed along a big coronal loop with $L \sim 10^{11}$ cm no energy gain above 100 keV is likely.

In the solar flares much stronger, super-Dreicer fields $\sim 1 - 10$ V/cm, are often deduced in localized regions where magnetic reconnection takes place (e.g., Qui et al. 2009), perhaps, in current sheets, which could provide efficient acceleration over much shorter distances, 10^4–10^6 cm. Nevertheless, efficiency of this process was put into question because transverse drifts may remove

electrons from the current sheet much earlier than needed for strong acceleration, with effectively the same upper limit for the energy gain, 100 keV; see Aschwanden (2005) and references therein for greater detail. On the other hand, a modest magnetic field directed along the current sheet can reduce the transverse drifts and allow individual particle to gain high, ultrarelativistic energy (see Somov and Oreshina 2011 and references therein).

11.1.2 Particle Energization in a Collapsing Magnetic Trap

Another kind of regular particle acceleration occurs when a size of the source, where the charged particles are somehow trapped, changes in time. Suppose, for example, that a particle is confined in a 1D source between two walls moving toward each other. If the wall motion is adiabatic, the particle will experience many "head-on" collisions with the walls and will gain energy in each of the collisions. Conservation of the corresponding adiabatic invariant, $pl = \text{const}$, where p is the particle momentum and l is the source size, requires that $p(t)/p(0) = l(0)/l(t)$, which implies rise of the particle momentum reciprocally to the source size, i.e., a corresponding energy gain in a contracting source.

In a reality, a similar kind of particle energization (i.e., acceleration or heating) can happen in magnetic traps with sufficiently large mirror ratio to confine a large number of particles in the trap. Then, suppose the magnetic trap starts to collapse (perhaps, due to strong non-equilibrium magnetic tensions) in such a way that both longitudinal and transverse scales of the trap decrease with time. These contractions will apparently result in corresponding increase of both longitudinal and transverse components of the particle momentum. We note that transverse contraction is associated, because of magnetic flux conservation, with corresponding magnetic field enhancement so the transverse momentum increase can be expressed via the changing magnetic field with the use of the magnetic adiabatic invariant; accordingly, this part of the acceleration in a magnetic trap is called **betatron acceleration**; see Problems 1.5 and 1.6.

Therefore, during the trap collapse the transverse momentum increases as $p_\perp^2(t)/p_\perp^2(0) = B(t)/B(0)$, while the longitudinal momentum as $p_\parallel(t)/p_\parallel(0) = l(0)/l(t)$; thus, for nonrelativistic particles we have $K(t)/K(0) = 2B(t)/B(0) + l^2(0)/l^2(t)$. For a solar coronal loop the loop top value of the magnetic field is typically above a few 10s of G; we adopt 30 G for definiteness. The photospheric values, which can be adopted as a largest possible upper bound for a contracting coronal loop are typically below 3 kG; thus, the largest ever possible change of the magnetic field during the trap collapse is by a factor of 100 or less, which implies, that if we start from particles with energy of a few keV, the highest achievable energy will be a few hundred keV, which is far insufficient to provide bulk acceleration in solar flares up to 10–100 MeV.

In addition, during the trap contraction, the number of accelerated electrons decreases due to particle escape through the loss cone. If we adopt (see, e.g., Somov 2006) that the footpoints of the loop do not move and the magnetic field is fixed there to some value B_m, then the number of particles evolves as[2]

$$N = N_0 \frac{l(t)/l(0)\sqrt{B_m - B(t)}}{\sqrt{B(0) + (B_m - B(0))l^2(t)/l^2(0)}}. \tag{11.14}$$

Note that if the looptop magnetic field reaches the footpoint value B_m, all the particles are lost from the loop via the loss cone. We conclude that even though some acceleration can happen due to magnetic trap collapse, this mechanism is insufficient to provide bulk electron acceleration in solar flares. On the other hand, if this kind of particle energization would repeat many cycles, the overall acceleration could be much more powerful.

11.1.3 Particle Acceleration by Magnetic Pump

In contrast to two previous examples of a *regular* acceleration by regular electric or time-changing magnetic field we envision here how a *stochasticity* of a physical system, if present, can greatly enhance efficiency of the particle energization compared with otherwise the same *regular* system. Specifically, we consider particle acceleration by a magnetic field with a constant direction, while time-oscillating amplitude. We adopt for simplicity that the oscillation period is large compared with periods of the particle gyration in the magnetic field. Although the oscillating magnetic field will necessarily be spatially nonuniform, this nonuniformity will be a small, second-order effect being a product of (1) smallness of the oscillation amplitude and (2) slowness of the oscillation, which allows to discard the field spatial nonuniformity and adopt the uniform field model.

Neglecting all kind of particle angular scattering by either each other or turbulent fields, the longitudinal particle momentum and transverse adiabatic invariant conserve

$$p_\parallel = \text{const}, \qquad \frac{p_\perp^2(t)}{B(t)} = \text{const}; \tag{11.15}$$

see Sect. 1.2. The transverse particle momentum and its energy $\mathcal{E} = \sqrt{m^2c^4 + (p_\parallel^2 + p_\perp^2(t))c^2}$ will oscillate having exactly the same values at the oscillation phases differing by $2\pi n$. Accordingly, the particle distribution function is modulated by oscillations of the external magnetic field. For

[2] More realistic models, e.g., accounting the Coulomb collisions in the trap, are considered by Giuliani et al. (2005), Bogachev and Somov (2009) and Grady and Neukirch (2009).

example, in the case of originally isotropic distribution with mean momentum components obeying

$$\overline{p_x^2} = \overline{p_y^2} = \overline{p_z^2} \quad \text{or} \quad \overline{p_\perp^2} = \overline{p_x^2} + \overline{p_y^2} = 2\overline{p_\parallel^2}, \tag{11.16}$$

the isotropy will break down during either increase or decrease of the magnetic field.

In contrast, in the presence of efficient angular scattering produced, for example, by a small-scale magnetic irregularities, the anisotropy buildup by the oscillating magnetic field will be compensated by isotropization of the distribution due to this efficient angular scattering. Thus, a fraction of "excessive" transverse momentum acquired at the phase of the field growth will be transferred to the longitudinal momentum, which does not directly affected by the magnetic field variations. Apparently, during the phase of the magnetic field decrease, the inverse process of the longitudinal momentum transfer to the transverse one will occur. Remarkably, however, that these two processes will not fully compensate each other and a net effect of systematic increase of the mean particle energy will take place. This in particular means that although the net energy gain of the particles at a single episode of a magnetic loop contraction is relatively small, it can be greatly enhanced due to multiply repeating "contractions" in case of the magnetic field oscillations. This acceleration process can be understood in terms of the system entropy increase that occurs due to growth of the volume in the momentum space occupied by the accelerated particles.

This mechanism of particle acceleration by oscillating magnetic field in the presence of an additional relaxation process (isotropization due to angular scattering) is called a **magnetic pumping** or Alfvén pumping; see Alfven and Fälthammar (1963). Here we consider this effect quantitatively using kinetic equation (7.108) in the drift approximation supplemented by a "collisional" term, Eq. (7.109):

$$\frac{\partial f}{\partial t} + \boldsymbol{v}_c \cdot \frac{\partial f}{\partial \boldsymbol{r}} + \dot{p}_\parallel \frac{\partial f}{\partial p_\parallel} + \dot{p}_\perp \frac{\partial f}{\partial p_\perp} = \widehat{S} f, \qquad \widehat{S} = \frac{\nu_s}{\sin\theta} \frac{\partial}{\partial \theta} \sin\theta \frac{\partial}{\partial \theta} \tag{11.17}$$

where θ is the pitch-angle of the particle; in what follows the scattering rate ν_s is adopted constant for simplicity. Note that the Liouville's theorem implies that

$$\nabla \cdot \boldsymbol{v}_c + \frac{\partial \dot{p}_\parallel}{\partial p_\parallel} + \frac{\partial \dot{p}_\perp}{\partial p_\perp} = 0, \tag{11.18}$$

which will be used below.

The oscillating uniform magnetic field can be written as

$$B(t) = B_0 + b\cos\omega t, \qquad b \ll B_0, \quad \omega = \text{const}. \tag{11.19}$$

Then, from Eqs. (11.15), we find

$$\boldsymbol{v}_c = v_\parallel \boldsymbol{e}_\parallel + \frac{c}{B_0}\boldsymbol{E}\times\boldsymbol{e}_\parallel, \quad \dot{p}_\parallel = 0, \quad \dot{p}_\perp = -p_\perp \frac{b\omega}{2B_0}\sin\omega t, \tag{11.20}$$

where $\boldsymbol{E}$ is the electric field induced by evolving magnetic field. When the amplitude of the magnetic oscillations is small, the distribution function will be almost isotropic and slowly varying with time at a late time $\Delta t \gg \nu_s^{-1},\ \omega^{-1}$ after the process start, while the anisotropic oscillating (with frequency ω) component of the distribution function δf represents a small correction to the main distribution function component:

$$f(p_\parallel, p_\perp, t) = F(p,t) + \delta f(p_\parallel, p_\perp, t), \qquad |\delta f| \ll F, \quad \overline{\delta f} = 0. \tag{11.21}$$

The overline denotes here averaging over period $T = 2\pi/\omega$ of the magnetic field oscillations; any change of the main distribution function $F(p,t)$ over this period can safely be discarded.

Substituting Eq. (11.21) into Eq. (11.17) and isolating the fast oscillating first-order terms, we obtain equation linking the correction δf with the averaged function $F(p,t)$:

$$\frac{\partial \delta f}{\partial t} - \widehat{S}\delta f = -\dot{p}_\perp \frac{\partial F}{\partial p_\perp} = \frac{b\omega}{3B_0} p \frac{\partial F}{\partial p}(1 - P_2(\cos\theta))\sin\omega t. \tag{11.22}$$

The second equality is written for the variables p and θ; $P_2(\cos\theta)$ is the second-order Legendre polynomial. Let us seek a solution in the form:

$$\delta f = f_0(p,t) + f_2(p,t)P_2(\cos\theta); \tag{11.23}$$

for a late time $t \gg \nu_s^{-1}$ we obtain the following solution:

$$\begin{aligned} f_0(p,t) &= -\frac{b}{3B_0} p \frac{\partial F}{\partial p}\cos\omega t, \\ f_2(p,t) &= -\frac{2b\nu_s\omega}{B_0(\omega^2 + (6\nu_s)^2)} p \frac{\partial F}{\partial p}\left[\sin\omega t - \frac{\omega}{6\nu_s}\cos\omega t\right]. \end{aligned} \tag{11.24}$$

In the equation for F we have to retain averaged second-order terms:

$$\frac{\partial F}{\partial t} + \overline{\boldsymbol{v}_c \cdot \frac{\partial \delta f}{\partial \boldsymbol{r}}} + \overline{\dot{p}_\perp \frac{\partial \delta f}{\partial p_\perp}} = 0. \tag{11.25}$$

Then, transform the second term in the lhs using Eq. (11.18):

$$\boldsymbol{v}_c \cdot \frac{\partial \delta f}{\partial \boldsymbol{r}} = \nabla\cdot(\boldsymbol{v}\delta f) + \delta f \frac{\partial}{\partial p_\perp}\dot{p}_\perp. \tag{11.26}$$

The term with ∇ yields higher-order terms upon averaging; thus, substituting Eq. (11.26) into Eq. (11.25), we obtain

$$\frac{\partial F}{\partial t} + \overline{\delta f \frac{\partial}{\partial p_\perp} \dot{p}_\perp} + \overline{\dot{p}_\perp \frac{\partial \delta f}{\partial p_\perp}} = 0. \tag{11.27}$$

After substitution of Eqs. (11.23) and (11.24) into Eq. (11.27) and averaging over the oscillation period, the equation will contain trigonometric functions of θ. Having in mind original weakness of the anisotropy we avoid explicit account of it by averaging coefficients of the equation over all possible values of the pitch-angle, which yields a diffusion-type equation:

$$\frac{\partial F}{\partial t} = \frac{1}{\tau p^2} \frac{\partial}{\partial p} p^4 \frac{\partial F}{\partial p}, \qquad \frac{1}{\tau} = \frac{1}{90} \left(\frac{b}{B_0} \right)^2 \frac{\nu \omega^2}{\omega^2 + \nu^2}, \quad \nu = 6\nu_s. \tag{11.28}$$

Let us normalize the distribution function by the condition $\int_0^\infty F p^2 \mathrm{d}p = n$, where n is the number density of particles with all energies. Equation (11.28) then ensures $n = \text{const}$, in agreement with statement of the problem. Now, we calculate evolution of the mean particle momentum described by $\overline{p} = n^{-1} \int_0^\infty F p^3 \mathrm{d}p$. Integration of Eq. (11.28) yields

$$\frac{\mathrm{d}\overline{p}}{\mathrm{d}t} = \frac{4}{\tau} \overline{p}, \qquad \overline{p}(t) = p_0 e^{4t/\tau}, \tag{11.29}$$

i.e., the mean particle momentum increases exponentially.

For example, for nonrelativistic particles, whose kinetic energy is $K = p^2/2m$, Eq. (11.28) yields

$$\overline{K} = K_0 e^{t/\tau_a}, \qquad \tau_a^{-1} = \frac{1}{9} \left(\frac{b}{B_0} \right)^2 \frac{\nu \omega^2}{\omega^2 + \nu^2}. \tag{11.30}$$

This result is equivalent to that obtained by Schlüter (1957) who used mechanical equation of motion rather than a kinetic equation for the distribution function. To conclude we note that the key element of the considered acceleration mechanism is "mixing" of the particle momentum directions, i.e., efficient angular scattering and isotropization of the particles; we will see below that this is also highly important for many other acceleration mechanisms to efficiently operate. The magnetic pumping works the most efficiently when the angular scattering rate ν and oscillation frequency ω are comparable to each other. In a reality, the acceleration process is supposed to be much more complex: there can be many "slow" magnetic oscillations provided by a large-scale magnetic turbulence (turbulent pulsations), generated self-consistently small-scale turbulence ensuring angular scattering of the particles, particle escape from a finite acceleration region, and other complicating effects and processes, the most important of which will be considered below.

11.1.4 Particle Energy Change by Regular Medium Motion

Let us concentrate on Eq. (7.77) and analyze the electric field effect (included there by means of Eq. (7.59) for the Lorentz force) on the particle energy evolution. If the size of the acceleration region is large enough to isotropize particle distribution due to scattering by random fields then the diffusion approximation can be applied. We substitute Eq. (7.81) into Eq. (7.77), expand the coefficients over powers of u/v, keep the terms $\gtrsim (u/v)^2$, and separate the terms independent on $\boldsymbol{p}/p$ and proportional to this vector. This yields the set of two equations:

$$\frac{\partial N}{\partial t} + \nabla \cdot \boldsymbol{J} = \frac{u^2}{9\kappa_\parallel}\left[p^2\frac{\partial^2 N}{\partial p^2} + \left(1+\frac{v^2}{c^2}\right)p\frac{\partial N}{\partial p}\right] + \frac{\boldsymbol{u}}{3\kappa_\parallel}\left(p\frac{\partial \boldsymbol{J}}{\partial p} + \frac{v^2}{c^2}\boldsymbol{J}\right) + \frac{1}{R_0 v}(\boldsymbol{u}\times\boldsymbol{b}_0)\left[p\frac{\partial \boldsymbol{J}}{\partial p} + \left(1+\frac{v^2}{c^2}\right)\boldsymbol{J}\right] \tag{11.31a}$$

$$\boldsymbol{J} + \frac{\Lambda}{R_0}\boldsymbol{b}_0\times\boldsymbol{J} = -\kappa_\parallel\nabla N - \frac{p}{3}\frac{\partial N}{\partial p}\left(\boldsymbol{u} + \frac{\Lambda}{R_0}\boldsymbol{b}_0\times\boldsymbol{u}\right) - \frac{\Lambda}{v}\frac{\partial \boldsymbol{J}}{\partial t}, \qquad \boldsymbol{b}_0 = \frac{\boldsymbol{B}_0}{B_0}. \tag{11.31b}$$

The terms of the order of $(u/v)^3$ and $(u^2/v^3)J$ are discarded.

The key distinction of Eq. (11.31a) from Eq. (7.83a) is the nonzero rhs in this continuity equation, which is the source (or flux) of the particles with a given energy. The presence of this source implies exchange of the energy between particles and medium, which is mediated by motion of the magnetic inhomogeneities.

Let us simplify Eq. (11.31b). First, the last term in the rhs of Eq. (11.31b) can be omitted at large $t \gg \Lambda/v$. Then, align the coordinate axes along the vectors $\boldsymbol{n}_1 = \boldsymbol{u}\times\boldsymbol{b}_0$, $\boldsymbol{n}_2 = \boldsymbol{b}_0\times\boldsymbol{n}_1$, and $\boldsymbol{n}_3 = \boldsymbol{b}_0$. In this case, Eq. (11.31b) can be solved for $\boldsymbol{J}$:

$$J_\alpha = -\kappa_{\alpha\beta}\nabla_\beta N - \frac{p}{3}\frac{\partial N}{\partial p}u_\alpha, \tag{11.32}$$

where the diffusion tensor $\kappa_{\alpha\beta}$ is expressed by Eqs. (7.84). The second term in Eq. (11.32) describes the convective current due to motion of the medium and magnetic inhomogeneities,

$$\boldsymbol{J}^{(c)}(\boldsymbol{r},p,t) = -\frac{p}{3}\frac{\partial N}{\partial p}\boldsymbol{u} \quad \text{or} \quad \boldsymbol{J}^{(c)}(\boldsymbol{r},K,t) = C(K)N(\boldsymbol{r},K,t)\boldsymbol{u}(\boldsymbol{r}). \tag{11.33}$$

In the first expression quantities $\boldsymbol{J}^{(c)}$ and N are defined per unit volume of momentum space, whereas the second expression contains the differential quantities per unit interval of the kinetic energy $K = \mathcal{E} - mc^2$. Thus,

$$N(\boldsymbol{r},p,t)p^2\mathrm{d}p = N(\boldsymbol{r},K,t)\mathrm{d}K. \tag{11.34}$$

The normalization per unit energy is often used in experimental investigations. The coefficient $C(K)$ is called **Compton–Getting factor**:

$$C(K) = 1 - \frac{1}{3N(K)} \frac{\partial}{\partial K}[\alpha K N(K)], \qquad \alpha = \frac{K + 2mc^2}{K + mc^2}. \tag{11.35}$$

The transport equation is derived by substituting Eq. (11.32) into Eq. (11.31a), which yields

$$\frac{\partial N}{\partial t} = \nabla_\alpha \kappa_{\alpha\beta} \nabla_\beta N - \boldsymbol{u} \cdot \nabla N + \frac{p}{3} \frac{\partial N}{\partial p} \nabla \cdot \boldsymbol{u}. \tag{11.36}$$

Here the terms containing u^2 cancel out. The first term on the rhs describes particle diffusion in an anisotropic medium and the second term describes particle convection due to the motion of scatterers (magnetic inhomogeneities). The last term is responsible for the energy change of the particles interacting with the moving medium.

Transport equation (11.34) can be rewritten in the form of the continuity equation in the phase space (Dorman et al. 1978):

$$\frac{\partial N}{\partial t} + \nabla \cdot \boldsymbol{J} + \frac{1}{p^2} \frac{\partial}{\partial p} p^2 S_p = 0, \tag{11.37}$$

where $\boldsymbol{J}$ is particle current (11.32) in coordinate space and

$$S_p = \frac{1}{3} p \boldsymbol{u} \cdot \nabla N \tag{11.38}$$

is the parallel-to-$\boldsymbol{p}$ component of the particle current in the momentum space. Given the equivalence of transport equations (11.37) and (11.36) we conclude that Eq. (11.36) is compatible, as required, with the particle conservation law.

By integrating Eq. (11.37) over dp, with weight function p^2, we come to the continuity equation in coordinate space,

$$\frac{\partial n}{\partial t} + \nabla \cdot \boldsymbol{j} = 0, \qquad \left\{ \begin{array}{c} n(\boldsymbol{r}, t) \\ \boldsymbol{j}(\boldsymbol{r}, t) \end{array} \right\} = \int_0^\infty p^2 \mathrm{d}p \left\{ \begin{array}{c} N(\boldsymbol{r}, p, t) \\ \boldsymbol{J}(\boldsymbol{r}, p, t) \end{array} \right\}, \tag{11.39}$$

where $n(\boldsymbol{r}, t)$ is the total number density of the particles, and $\boldsymbol{j}(\boldsymbol{r}, t)$ is the total current density.

By integrating Eq. (11.37) over dp with the weight function $K(p)p^2$, it is transformed to the form

$$\frac{\partial w}{\partial t} + \nabla \cdot \boldsymbol{q} = Q(\boldsymbol{r}, t), \tag{11.40}$$

where

$$w(\boldsymbol{r},t)=\int\limits_0^\infty K(p)N(\boldsymbol{r},p,t)p^2\mathrm{d}p=\overline{K}n(\boldsymbol{r},t) \tag{11.41}$$

is the particle kinetic energy density and $\overline{K}$ is the mean kinetic energy defined by Eqs. (11.39) and (11.41). Furthermore,

$$\boldsymbol{q}(\boldsymbol{r},t)=\int\limits_0^\infty \boldsymbol{v}\,K\,F(\boldsymbol{r},\boldsymbol{p},t)\mathrm{d}^3p=\int\limits_0^\infty K\,\boldsymbol{J}(\boldsymbol{r},\boldsymbol{p},t)p^2\mathrm{d}p=\boldsymbol{q}^{(d)}+\boldsymbol{q}^{(c)} \tag{11.42}$$

is the energy flux which consists of the diffusion flux

$$q_\alpha^{(d)}=-\int\limits_0^\infty K\kappa_{\alpha\beta}\nabla_\beta N\,p^2\mathrm{d}p, \tag{11.43}$$

and the convective flux

$$\boldsymbol{q}^{(c)}=(w+P)\boldsymbol{u}. \tag{11.44}$$

The quantity

$$P=\frac{1}{3}\int\limits_0^\infty pvN(\boldsymbol{r},p,t)p^2\mathrm{d}p \tag{11.45}$$

is the pressure of the energetic particle gas equal to $2(\overline{\mathcal{E}}-mc^2)n/3$ and $\overline{\mathcal{E}}n/3$ in the nonrelativistic and ultrarelativistic cases, respectively. The convective energy flux can be rewritten as $\boldsymbol{q}^{(c)}=h(\boldsymbol{r},t)\boldsymbol{u}$, where $h=w+P$ is the specific enthalpy of the energetic particle gas (see the fluid mechanics elements in Chaps. 1 and 2) w is the specific (per unit volume) inner energy of the gas.

The quantity

$$Q(\boldsymbol{r},t)=\frac{1}{3}\int\limits_0^\infty pv\boldsymbol{u}\cdot\nabla Np^2\mathrm{d}p=\boldsymbol{u}\cdot\nabla P \tag{11.46}$$

in the rhs of Eq. (11.40) is the specific energy source. Its sign depends on the gas pressure gradient along the velocity $\boldsymbol{u}$. It is worthwhile to note, however, that the positive sign of Q does not necessarily mean the local particle acceleration, i.e., increase of the average energy per one particle. To illustrate this, adopt $\nabla\cdot\boldsymbol{u}=0$, but $\boldsymbol{u}\neq 0$. For example, this is the case for $\boldsymbol{u}=\mathrm{const}$, $\boldsymbol{u}\propto\boldsymbol{r}/r^3$, and for some other functions. It is evident from Eq. (11.36) that the particle energy remains constant under this conditions; for instance, an initial delta-type energy distribution will remain the same indefinitely long time. On the other hand, generally, the energy production Q is not zero as $u\neq 0$.

In fact, variations of the average particle energy are determined by the sign and magnitude of $\nabla\cdot\boldsymbol{u}$. Let us demonstrate this explicitly neglecting the

spatial diffusion for simplicity. Discarding the diffusion terms in Eqs. (11.39) and (11.40) and using Eqs. (11.41) and (11.44), we obtain

$$\frac{\mathrm{d}}{\mathrm{d}t}\overline{\mathcal{E}} = -\frac{1}{3}\overline{pv}\,\nabla\cdot\boldsymbol{u}, \tag{11.47}$$

where $\overline{pv} = 2(\overline{\mathcal{E}} - mc^2)$ in the nonrelativistic case and $\overline{pv} = \overline{\mathcal{E}}$ in the ultrarelativistic one, and

$$\frac{\mathrm{d}}{\mathrm{d}t}\overline{\mathcal{E}} = \frac{\partial}{\partial t}\overline{\mathcal{E}} + \boldsymbol{u}\cdot\nabla\overline{\mathcal{E}}$$

is the total time derivative. It follows from Eq. (11.47) that the expansion of system ($\nabla\cdot\boldsymbol{u} > 0$) is accompanied by particle deceleration whereas the compression ($\nabla\cdot\boldsymbol{u} < 0$) is accompanied by acceleration. The typical timescale of energy variation, τ_{ad}, is

$$\tau_{\mathrm{ad}}^{-1} = \frac{2}{3}|\nabla\cdot\boldsymbol{u}| \qquad \text{and} \qquad \tau_{\mathrm{ad}}^{-1} = \frac{1}{3}|\nabla\cdot\boldsymbol{u}| \tag{11.48}$$

in the nonrelativistic and ultrarelativistic cases, respectively.

With account of the spatial diffusion the equation describing the average energy change is written as

$$\frac{\mathrm{d}}{\mathrm{d}t}\overline{\mathcal{E}} = -\frac{1}{3}\overline{pv}\nabla\cdot\boldsymbol{u} - \frac{1}{n}\nabla\cdot\boldsymbol{q}^{(d)} + \frac{\overline{\mathcal{E}}}{n}\nabla\cdot\boldsymbol{j}^{(d)}. \tag{11.49}$$

The first term, proportional to $\nabla\cdot\boldsymbol{u}$, describes the energy variations due to motion of the medium. Other terms describe spatial redistribution of particles of various energies due to diffusion in space.

If particles occupy initially a finite volume, the total energy of these particles, $E(t) = \int w(\boldsymbol{r},t)\mathrm{d}^3r$, varies in time according to an equation obtained by integrating (11.40) over space:

$$\frac{\mathrm{d}E}{\mathrm{d}t} = -\int P(\boldsymbol{r},t)(\nabla\cdot\boldsymbol{u})\mathrm{d}^3r. \tag{11.50}$$

In the case of radial plasma outflow with constant velocity, when $\nabla\cdot\boldsymbol{u} = 2ur^{-1} > 0$, particles are adiabatically decelerated, whereas in the case of compression ($\nabla\cdot\boldsymbol{u} < 0$) they are accelerated. Cases of energetic solar proton deceleration (generated initially in solar flares) were widely observed in the interplanetary space. A compression of the interplanetary medium, leading to the particle acceleration, can also occur due to some nonstationary processes on the Sun or in interplanetary space, for instance due to solar coronal mass ejections (CME) or interaction between solar wind streamers having different velocities. Large-scale turbulence also leads to patterns of compression and rarefaction regions and is accompanied by particle acceleration (see below). A strong compression may take place in shocks so that the shocks can also act as effective particle accelerating sources.

11.2 Particle Acceleration by Stochastic Medium Motion: Fermi Mechanism

11.2.1 Diffusion in Momentum Space

The acceleration regimes discussed above are restricted by the assumption that the fluid velocity $\boldsymbol{u}$ in diffusion equations (11.31a) and (11.31b) is a regular and smooth function of the coordinates and time. In a more general situation the realistic fluid motion will often have turbulent stochastic components with various scales; thus, the velocity field can represent a superposition of the regular and random motions:

$$\boldsymbol{u} = \boldsymbol{U} + \Delta\boldsymbol{u}, \qquad \boldsymbol{U} = \langle \boldsymbol{u} \rangle, \qquad \langle \Delta\boldsymbol{u} \rangle = 0, \tag{11.51}$$

where $\boldsymbol{U}$ is a "regular" velocity component with a large characteristic scale, perhaps, of the order of the source size R, while $\Delta\boldsymbol{u}$ varies over much smaller scales, $L \ll R$. The averaging denoted in Eq. (11.51) by the angle brackets is being performed over the small scales L. Note that in diffusion equations (11.31a) and (11.31b) the velocity $\boldsymbol{u}$ is assumed to be a regular function at the scales of the order of the particle mfp; however, it can be a stochastic value at much larger scales, $L \gg \Lambda$, which is still compatible with $L \ll R$. Given that $\Lambda \gg L_c$, we conclude that $L \gg L_c$, where L_c is the correlation length of the random magnetic field (see Sect. 7.4).

Thus, in Eqs. (11.31a) and (11.31b) we now treat $\boldsymbol{u}$ as a stochastic quantity with some known average values $\boldsymbol{U}$ and $\langle u^2 \rangle = U^2 + \langle \Delta\boldsymbol{u}^2 \rangle$, where $\langle \Delta\boldsymbol{u}^2 \rangle = \langle \boldsymbol{u}^2 \rangle - U^2$ is the mean square of the velocity fluctuations. After averaging the equations over $\boldsymbol{u}$, we obtain

$$\begin{aligned} \frac{\partial N}{\partial t} + \nabla \cdot \boldsymbol{J} \;=\; & \frac{\langle u^2 \rangle}{9\kappa_\parallel} \left[p^2 \frac{\partial^2 N}{\partial p^2} + \left(1 + \frac{v^2}{c^2}\right) p \frac{\partial N}{\partial p} \right] + \frac{\boldsymbol{U}}{3\kappa_\parallel} \left(p \frac{\partial \boldsymbol{J}}{\partial p} + \frac{v^2}{c^2} \boldsymbol{J} \right) \\ & + \frac{1}{R_0 v} (\boldsymbol{U} \times \boldsymbol{b}_0) \left[p \frac{\partial \boldsymbol{J}}{\partial p} + \left(1 + \frac{v^2}{c^2}\right) \boldsymbol{J} \right] \end{aligned} \tag{11.52a}$$

$$\boldsymbol{J} + \frac{\Lambda}{R_0} \boldsymbol{b}_0 \times \boldsymbol{J} \;=\; -\kappa_\parallel \nabla N - \frac{p}{3} \frac{\partial N}{\partial p} \left(\boldsymbol{U} + \frac{\Lambda}{R_0} \boldsymbol{b}_0 \times \boldsymbol{U} \right) - \frac{\Lambda}{v} \frac{\partial \boldsymbol{J}}{\partial t}, \qquad \boldsymbol{b}_0 = \frac{\boldsymbol{B}_0}{B_0}. \tag{11.52b}$$

After discarding the term $\partial \boldsymbol{J}/\partial t$, the last equation yields

$$J_\alpha = -\kappa_{\alpha\beta} \nabla_\beta N - \frac{p}{3} \frac{\partial N}{\partial p} U_\alpha. \tag{11.53}$$

Substituting Eq. (11.53) for $\boldsymbol{J}$ into Eq. (11.52a), we arrive at a diffusion equation accounting for the acceleration effect:

$$\frac{\partial N}{\partial t} = \nabla_\alpha \kappa_{\alpha\beta} \nabla_\beta N - \boldsymbol{U} \cdot \nabla N + \frac{p}{3} \frac{\partial N}{\partial p} \nabla \cdot \boldsymbol{U} + \frac{1}{p^2} \frac{\partial}{\partial p} p^2 D(\boldsymbol{r}, p) \frac{\partial N}{\partial p}. \tag{11.54}$$

Here

$$D(\boldsymbol{r},p)=\frac{\langle\Delta\boldsymbol{u}^2\rangle p^2}{3v\Lambda(\boldsymbol{r},p)}=\frac{\langle\Delta\boldsymbol{u}^2\rangle p^2}{9\kappa_{\parallel}} \tag{11.55}$$

is the momentum space diffusion coefficient.

Let us examine the role of the last term in Eq. (11.54). The presence of this term does not violate conservation of the total number of particles. Therefore, integrating Eq. (11.54) over dp with the weight function p^2, we again arrive at Eq. (11.39). Likewise, integrating it over dp with another weight function $p^2\mathcal{E}$, we obtain Eq. (11.40) with a new source term at the rhs:

$$Q(\boldsymbol{r},t)=\boldsymbol{U}\cdot\nabla P+\int\limits_0^\infty \mathrm{d}p\, N\,\frac{\mathrm{d}}{\mathrm{d}p}(p^2vD). \tag{11.56}$$

The integrand is positive,

$$\frac{\mathrm{d}}{\mathrm{d}p}(p^2vD)=\frac{\mathrm{d}}{\mathrm{d}p}\left(\frac{\langle\Delta\boldsymbol{u}^2\rangle p^4}{3\Lambda}\right)>0, \tag{11.57}$$

because the transport mfp can only grow with p as p^2 or slower (see Sect. 7.4). Hence, the last term in Eq. (11.54) describes the particle acceleration due to motions of magnetic inhomogeneities in all physically relevant cases. The acceleration has a diffusive character in the momentum space.

The structure of Eq. (11.54) and the order of magnitude of the acceleration effect can easily be clarified from a simple physical considerations. The velocity dispersion of the magnetic inhomogeneities at a given scale gives rise to induction of a stochastic electric fields with comparable scales. The velocities u of the magnetic structures are bounded according to the inequality $v_{ph}<u\ll v$. Adopt for simplicity of the estimate that the correlation length L is sufficiently small to ensure that the particle energy change over the length L is small compared with the total particle energy. The acceleration effect then will be important at the time intervals much exceeding the isotropization time $\tau_s=\Lambda/v$.

The influence of these chaotic electric fields on a particle results in its diffusion in the momentum space, overall analogous to the diffusion in the real space. The particle momentum changes both its direction and the absolute value, i.e., energy. The operator of momentum diffusion in transport equation is analogous with diffusion operator in usual 3D space and different only in two respects:

1. The variable $\boldsymbol{p}$ is used in momentum space instead of the variable $\boldsymbol{r}$ in the real space.

2. In differential operator we omit all derivatives over vector $\boldsymbol{p}$ angles owing to isotropization of particle distribution function at the acceleration timescale.

As a result, this recipe results in the following acceleration operator:

$$\nabla_\alpha \kappa_{\alpha\beta}(\boldsymbol{r},p)\nabla_\beta N(\boldsymbol{r},p,t) \to \frac{\partial}{\partial \boldsymbol{p}} D(\boldsymbol{r},p)\frac{\partial}{\partial \boldsymbol{p}} N(\boldsymbol{r},p,t) = \frac{1}{p^2}\frac{\partial}{\partial p} p^2 D(\boldsymbol{r},p)\frac{\partial N(\boldsymbol{r},p,t)}{\partial p}, \tag{11.58}$$

having precisely the same form as the one mathematically derived above, Eq. (11.54).

Let us now estimate the acceleration time and diffusion coefficient in the momentum space. Initially, we neglect any regular motion of the medium and adopt $\boldsymbol{u}$ to be a stochastic vector function with $\langle \boldsymbol{u} \rangle = 0$. The effective "collision" frequency of a particle with magnetic inhomogeneities (inverse isotropization time) is $\nu_s = \tau_s^{-1} = v/\Lambda$. This quantity is apparently determined by the stochastic magnetic force $\boldsymbol{\mathcal{F}}_m = (e/c)\boldsymbol{v} \times \boldsymbol{b}$ and is proportional to the square of this force, $\nu_s \propto \langle \boldsymbol{\mathcal{F}}_m^2 \rangle$, because the linear term vanishes after averaging, $\langle \boldsymbol{\mathcal{F}}_m \rangle = 0$.

The stochastic electric force $\boldsymbol{\mathcal{F}}_e = -(e/c)\boldsymbol{u} \times (\boldsymbol{B}_0 + \boldsymbol{b})$ also vanishes after the averaging,[3] $\langle \boldsymbol{\mathcal{F}}_e \rangle = 0$. That is why the acceleration rate (inverse acceleration time) is likewise proportional to the square of $\boldsymbol{\mathcal{F}}_e$, $\nu_a \propto \langle \boldsymbol{\mathcal{F}}_e^2 \rangle$. As a result, we obtain an order of magnitude estimate:

$$\nu_a \approx \nu_s \frac{\langle \boldsymbol{\mathcal{F}}_e^2 \rangle}{\langle \boldsymbol{\mathcal{F}}_m^2 \rangle} \approx \frac{v}{\Lambda}\frac{\langle \boldsymbol{u}^2 \rangle}{v^2}\frac{B_0^2 + b^2}{b^2}. \tag{11.59}$$

Then, in the presence of some overall regular motion, $\langle \boldsymbol{u}^2 \rangle$ here should be replaced by $\langle \Delta \boldsymbol{u}^2 \rangle$. This acceleration rate allows estimating the momentum space diffusion coefficient $D(p)$. According to Eq. (11.54) we have

$$D(p) \sim \frac{p^2}{\tau_a} = \nu_a p^2. \tag{11.60}$$

The obtained simple expressions described by Eqs. (11.59) and (11.60) include a number of qualitatively different while practically important acceleration regimes.

Fermi Mechanism

Consider acceleration of particles by impenetrable magnetic clouds, stochastically moving in a tenuous background fluid with weak magnetic field ($B_0 \ll b$) (Fermi 1949). These magnetic clouds are hypothetic stable structures with a strong magnetic field. In the considered model system, the particle mfp is $\Lambda = (n_{\rm cl}\sigma_{\rm cl})^{-1} = \text{const}$, where $n_{\rm cl}$ and $\sigma_{\rm cl}$ are the number density of

[3] In the end of this section we consider the case of helical turbulence where $\langle \boldsymbol{\mathcal{F}}_e \rangle \neq 0$.

the clouds and the cloud cross section, respectively. From Eq. (11.59) we have $\nu_a \approx \langle \Delta u^2 \rangle / v\Lambda$, which, for relativistic particles with $v \approx c$, yields $\tau_a \approx c\Lambda / \langle \Delta u^2 \rangle = \text{const}$.

In a uniform medium Eq. (11.54) can be written as

$$\frac{\partial N}{\partial t} = \frac{1}{\tau_a p^2} \frac{\partial}{\partial p} p^4 \frac{\partial N}{\partial p}. \tag{11.61}$$

Integrating the last equation over dp with the weight function p^3, we obtain a simple equation for the mean particle momentum $\overline{p}(t) = \int_0^\infty p^3 N(p,t) \mathrm{d}p$:

$$\frac{\mathrm{d}\overline{p}(t)}{\mathrm{d}t} = \frac{4}{\tau_a} \overline{p}(t),$$

with a solution $\overline{p}(t) = p_0 \exp(4t/\tau_a)$. The Fermi model gives a very rapid growth of the particle energy. The obtained unlimited acceleration is an artifact of neglecting any particle energy losses, their escape from the acceleration region and the back reaction of the accelerated particles on the system.

We can qualitatively think of the Fermi acceleration effect in either kinetic or thermodynamic language. The kinetic language involves calculation of particle energy change during head-on and overtaken collisions with clouds ("magnetic mirrors") whose balance forms the frequency of collisions (see Problem 11.2).

The thermodynamic language relies on the effect of temperature equalization after mixing two gases with different temperatures. This is a direct outcome of the entropy increase law, i.e., the second law of thermodynamics. The macroscopic plasma clouds, moving with stochastic velocities, can be considered as a gas of "heavy molecules," having an efficient temperature $T_{\mathrm{cl}} = M_{\mathrm{cl}} u^2/3$. The temperature is very high owing to a large mass of a cloud. Efficient temperature of the particles (their mean energy $\overline{\mathcal{E}}$) increases during collisions with clouds, until collisions are elastic and energy losses are small. The temperature equality between the magnetic cloud gas and the accelerated particle gas would imply that the mean energy of the fast particles is about T_{cl}, which would offer an estimate of the total acceleration power. However, T_{cl} is a poorly defined measure, which is impractical for this estimate.

In a reality, the increase of the particle energy leads to an increase of magnetic clouds transparency for particles. When the particle gyroradius inside the cloud exceeds its size, the particles are not reflected by such clouds any longer, while experience only a weak small-angle scattering; thus, the regime of acceleration changes according to the transport regime considered in Sect. 7.4.2 (small-scale inhomogeneities).

Fermi Mechanism: Transparent Clouds

Now we have to use the transport mfp described by Eq. (7.80) ($\Lambda \propto p^2$) and momentum space coefficient (11.55). This leads to independence of D on the

momentum, $D = \text{const}$. In the uniform medium, Eq. (11.54) receives the form

$$\frac{\partial N}{\partial t} = \frac{D}{p^2}\frac{\partial}{\partial p}p^2\frac{\partial N}{\partial p}. \tag{11.62}$$

Let us adopt the initial condition $N(p,0) = N_0 p_0^{-2}\delta(p-p_0)$ that describes injection of monoenergetic particles into the acceleration process. A familiar solution of diffusion equation (11.62)

$$N(p,t) = \frac{N_0}{pp_0\sqrt{4\pi Dt}}\left\{\exp\left[-\frac{(p-p_0)^2}{4Dt}\right] - \exp\left[-\frac{(p+p_0)^2}{4Dt}\right]\right\} \tag{11.63}$$

yields the time dependent energetic spectrum of the accelerated particles. The mean value of $p(t)$ evaluated for this distribution at $\sqrt{4\pi Dt} \gg p_0$ grows proportionally to the square root of time,

$$\overline{p}(t) = 4\sqrt{Dt/\pi}. \tag{11.64}$$

The particle energy increase is very slow compared with the case $\Lambda = \text{const}$ and $D \propto p^2$; Sect. "Fermi Mechanism" above.

Particle Acceleration by Small-Amplitude MHD Waves

If $b \ll B_0$, the regular magnetic field has an important effect on plasma motion. In this case magnetic disturbances are formed by small-amplitude MHD waves (see Sect. 2.4). For MHD waves, the velocity of plasma motions is of the order of $u \sim v_A b/B_0$, where v_A here is the largest of the Alfven and sound velocities. In this case Eq. (11.59) yields

$$\nu_a \sim v_A^2/v\Lambda, \tag{11.65}$$

which again corresponds to Eq. (11.55) with $\langle \Delta \boldsymbol{u}^2\rangle \sim v_A^2$. More detailed calculations (see, e.g., Toptygin 1985) confirm this result for turbulent spectra with index $\nu \le 2$; for $\nu > 2$, the diffusion coefficients D are different for Alfven and magnetoacoustic waves, so the result becomes "mode dependent." For acceleration of nonrelativistic electrons, some other plasma eigenmodes including the whistler waves (Sect. 7.4.4) may become important in addition to the MHD modes.

Particle Acceleration by Whistler Waves

Consider here electron acceleration by whistler turbulence, which is a by-product of the particle transport by whistler turbulence considered in Sect. 7.4.4. As has been said there, the angular diffusion due to electron scattering by whistler waves occurs faster than the diffusion over energy;

thus, by the time when the acceleration starts to play a role, the angular distribution of the electrons is already almost isotropic. In what follows we fully neglect any anisotropy and adopt the isotropic electron distribution. Then, we note that for an efficient acceleration, the residence time $\tau_e(E)$, Eq. (7.101), at the acceleration region must be much longer than the time of flight, which means that we can safely discard the first term at the rhs of Eq. (7.96); then, the diffusion in the real space can be treated in the residence time approximation by including the escape term, $-f/\tau_e(E)$, in the rhs of Eq. (7.96), which yields

$$\frac{\partial f(E,t)}{\partial t} = -\frac{\partial}{\partial E}[A(E)f(E,t)] + \frac{\partial^2}{\partial E^2}[D(E)f(E,t)] - \frac{f(E,t)}{\tau_e(E)} + S(E,t), \tag{11.66}$$

where, likewise Sect. 7.4.4, we use the dimensionless kinetic energy $E = K/mc^2 = \gamma - 1$. The terms at the rhs are the systematic energy change (gain or loss), the diffusion in the energy space, the particle escape, and the particle source ($S(E,t) = \langle S(E,\vartheta,s,t)\rangle$ averaged over the pitch-angle and source volume, cf. Eq. 7.96), respectively. For a given source term, the acceleration by the whistler turbulence, therefore, is controlled by three energy-dependent coefficients, $A(E)$, $D(E)$, and $\tau_e(E)$. The latter was introduced by Eq. (7.101), while two other coefficients are straightforwardly defined by the electron diffusion coefficient over momentum, Eq. (7.103), and the electron loss rate:

$$D(E) = \frac{\beta^2 \langle D_{pp}\rangle}{m^2c^2}, \tag{11.67}$$

and

$$A(E) = \frac{mc}{p^2}\frac{\partial}{\partial p}[p^2 D(E)/\beta] + \dot{E}_L. \tag{11.68}$$

For power-law spectrum (7.102) of the whistler turbulence the use of Eq. (7.103) yields

$$D(E) = D_w\beta(\gamma\beta)^{q-2}; \qquad A(E) = qD_w(\gamma\beta)^{q-3} - \dot{E}_L, \tag{11.69}$$

where

$$D_w = \frac{\pi(q-1)^2}{2q^2(q-2)^2}\omega_{\rm Be}\left(\frac{m_p}{m}\right)^{3-q}\beta_{\rm A}^{5-q}\left(\frac{8\pi W_{\rm tot}}{B^2}\right)\ [{\rm s}^{-1}], \tag{11.70}$$

and

$$\tau_e(E) = \tau_w\cdot(\gamma\beta)^{q-2}/\beta, \tag{11.71}$$

where

$$\tau_w = \frac{3\pi}{2(q+1)(q+2)}\frac{\omega_{\rm Be}L^2}{c^2}\left(\frac{m_p}{m}\right)^{q-1}\beta_{\rm A}^{1-q}\left(\frac{8\pi W_{\rm tot}}{B^2}\right)\ [{\rm s}], \tag{11.72}$$

and β_A is defined by Eq. (7.99). For conditions typical for solar flares both escape time τ_w and acceleration rate $1/D_w$ can vary from a fraction of second to a few hundred seconds; both regimes, $\tau_w > 1/D_w$ and $\tau_w < 1/D_w$, are possible. Therefore, there can be various regimes of the electron acceleration by whistler turbulence given that various terms in kinetic equation can be comparably important; in addition, Coulomb losses can also be significant at low energies at least, which additionally complicates the whole problem. We will be returning to the electron acceleration in solar flares below in this chapter.

Strong Turbulence Case

Finally, in the case when $b \sim B_0$ and $u \gtrsim v_A$, plasma motions are supersonic; thus, shocks can be formed along with smooth plasma disturbances. This situation will be considered in Sect. 11.5.

To finalize this section we make a number of notes having rather general value for the particle acceleration. If the turbulent pulsations of the plasma have sufficiently large scales to ensure that the collisionless diffusion time $\tau_d \approx L^2/\kappa_\parallel$ (needed for a particle to travel a distance of the order of the main turbulence scale L) exceeds the corresponding advective time $\tau_c \approx L/\langle \Delta u^2 \rangle^{1/2}$, i.e., the Pecklé number is large, then the diffusion coefficient $\chi \approx \langle \Delta u^2 \rangle^{1/2} L$, obtained in Sect. 7.3.2 for large Pecklé number regime should be used for $\kappa_\parallel \approx v\Lambda_\parallel$ in Eq. (11.55) for D (see details in Toptygin 1985; Bykov and Toptygin 1993).

Then, there is a severe constraint of the use of transport equation (11.54) and, accordingly, all further equations derived from it: all these equations do not take into account any particle losses (except adiabatic) such as collisional, Compton, and radiative losses.

Furthermore, all these equations are only applicable to "fast" particles, i.e., particles with energies exceeding at least by a few times the mean (thermal) particle energy. For the higher-energy particles their energy loss in collisions with the background particles is reduced and becomes less and less important for higher and higher energy. Thus, the energy gain due to the described mechanisms overcomes the collisional loss for the fast particles; so, being initially involved in the acceleration, these particles continue to gain energy. The gained energy can exceed the initial particle energy by orders of magnitude. Then, for even higher energies, another kind of the energy losses can come into play, the radiative losses, whose rate is proportional to E^2. Apparently, the radiative losses are much more important for the electrons compared with ions because of large difference in their masses. Recall, the largest CR energy is about 10^{20} eV is indeed much higher than the corresponding thermal energies of (1–100) eV.

In many cases the fraction of particles injected into an acceleration process is very small. In stationary media with Maxwellian distribution the fraction of the particles with energy higher than the thermal one is exponentially

small, which does not favor efficient acceleration. However, in nonstationary media or even in stationary ones with non-Maxwellian (e.g., kappa-) distributions the fraction of the fast suprathermal particles increases; these suprathermal particles form the pool from which an acceleration mechanism picks up and accelerate particles. The process of the particle transfer from the main background population to the population of accelerated nonthermal particles is called **injection**.

It is important to realize that correct treatment of the injection process is extremely complicated; no fully satisfactory injection theory is available, although there are useful analytical or numerical models describing this process under certain assumptions. Apparently, for relatively hard energy spectrum of the accelerated particles, the fraction of injected particles must be very low, say $\lesssim 1\%$, which can be understood based on the energy conservation law. Indeed, for a hard spectrum $\propto E^{-\alpha}$ with $\alpha \leq 2$, the total energy contained in the accelerated particles is defined by the highest energy in the spectrum; thus, the higher the highest energy the smaller the fraction of injected particles for the same amount of the free energy available for acceleration. This consideration is relevant for young SNRs and galactic superbubbles formed by OB associations believed to be the main source of the Galactic CRs. Indeed, the fraction of relativistic ions above 10^9 eV in the Galactic disk is about 10^{-9} of the background ions, which implies a relatively low injection fraction. In contrast, in solar flares the spectra of accelerated electrons are typically much softer; accordingly, the fraction of accelerated electrons is often very large; in some cases almost all available electrons in a volume are being accelerated during the course of a solar flare. Finally, we note that distinct acceleration mechanisms or regimes can dominate over different energy ranges, thus, the entire acceleration can be a multi-step process.

11.2.2 Particle Acceleration by Helical Turbulence

The rate of particle acceleration by a stochastic plasma motion can be greatly enhanced when the turbulence is helical, i.e., when the helicity parameter $\alpha \neq 0$ (see Sect. 8.4). To develop theory of particle acceleration by helical (gyrotropic) turbulence let us make use of Eqs. (7.58) and (7.59). In contrast to consideration of Sect. 7.4, we will treat $\boldsymbol{u}$ as a purely random vector with zero mean value $\langle \boldsymbol{u} \rangle = 0$ and with the correlation tensor given by expression (8.12). It is important, however, that the mean magnetic field is assumed to be different from zero, so that

$$\boldsymbol{B} = \boldsymbol{B}_0 + \boldsymbol{b}, \qquad \langle \boldsymbol{B} \rangle = \boldsymbol{B}_0 \neq 0, \qquad \langle \boldsymbol{b} \rangle = 0. \tag{11.73}$$

Let us average Eq. (7.58) over an ensemble of turbulent motions by the method introduced and discussed in some detail in Sect. 7.4. For analyzing the effect of particle acceleration, we assume that the average distribution function is independent on coordinates:

$$\langle f(\boldsymbol{r}, \boldsymbol{p}, t) \rangle = F(\boldsymbol{p}, t). \tag{11.74}$$

Then, adopt the transport regime mediated by resonant scattering of the particles by small-scale inhomogeneities like in Sect. 7.5.1. After averaging we obtain the equation

$$\frac{\partial F}{\partial t} + \langle \boldsymbol{\mathcal{F}} \rangle \cdot \frac{\partial F}{\partial \boldsymbol{p}} = \frac{v}{2\Lambda(p)} \widehat{\boldsymbol{\mathcal{O}}}^2 F + \widehat{S}_a F, \tag{11.75}$$

where Λ is the transport mfp given by Eq. (7.106), and the operator $\widehat{S}_a$ includes all acceleration effects (addressed already in Sect. 11.2.1) besides that produced by the helical part of the turbulence.

A new effect, qualitatively distinct from what have been analyzed so far, is described by the term proportional to $\langle \boldsymbol{\mathcal{F}} \rangle$. If $\boldsymbol{u}$ and $\boldsymbol{b}$ at the same point are correlated we have

$$\langle \boldsymbol{\mathcal{F}} \rangle = \frac{e}{c} \boldsymbol{v} \times \boldsymbol{B}_0 - \frac{e}{c} \langle \boldsymbol{u} \times \boldsymbol{b} \rangle, \tag{11.76}$$

where the last term represents an electric force $\langle \boldsymbol{\mathcal{F}}_h \rangle$ acting on the particles. This average, representing an effective electric field created by helical turbulence, was calculated in Sect. 8.5.1, Eq. (8.28) and also in Problem 8.3 specifically for the turbulence helicity driven by the force-free field (FFF) nonpotentiality. As a result we find

$$\langle \boldsymbol{\mathcal{F}}_h \rangle = -\frac{e}{c} \langle \boldsymbol{u} \times \boldsymbol{b} \rangle = e \boldsymbol{E}_h = -\frac{e}{c} \alpha \boldsymbol{B}_0, \tag{11.77}$$

Hence, Eq. (11.75) for the particle distribution function receives the form

$$\frac{\partial F}{\partial t} + \frac{ec}{\mathcal{E}} \boldsymbol{B}_0 \cdot \widehat{\boldsymbol{\mathcal{O}}} F - \frac{e\alpha}{c} \boldsymbol{B}_0 \cdot \frac{\partial F}{\partial \boldsymbol{p}} = \frac{v}{2\Lambda(p)} \widehat{\boldsymbol{\mathcal{O}}}^2 F. \tag{11.78}$$

In this equation we have neglected the contribution from the term $\widehat{S}_a F$, assuming that the dominant contribution comes from the large-scale electric field $(-\alpha/c)\boldsymbol{B}_0$.

In a general case kinetic equation (11.78) describes anisotropic particle distributions. However, if the departure from the isotropy is small, which is reasonable to expect because of the efficient angular scattering of the particles by the very same turbulence described by the rhs of Eq. (11.78), this equation can be further simplified if the source size L is much larger than the particle mfp $L \gg \Lambda$. Assuming this to be the case and expanding the distribution function $F(\boldsymbol{p}, t)$ over moments according to Eq. (7.81), we obtain the set of coupled equations

$$\begin{aligned} \frac{\partial N}{\partial t} &= \frac{e\alpha}{cpv} \boldsymbol{B}_0 \cdot \left[\left(1 + \frac{v^2}{c^2} \right) \boldsymbol{J} + p \frac{\partial \boldsymbol{J}}{\partial p} \right], \\ \frac{1}{v} \frac{\partial \boldsymbol{J}}{\partial t} &+ \frac{ec}{v\mathcal{E}} \boldsymbol{B}_0 \times \boldsymbol{J} - \frac{e\alpha}{3c} \frac{\partial N}{\partial p} \boldsymbol{B}_0 = -\frac{1}{\Lambda} \boldsymbol{J} \end{aligned} \tag{11.79}$$

for the isotropic part of the particle distribution function N and the flux density $\boldsymbol{J}$. Note that the direction of the flux density depends on the charge sign, implying opposite flux directions for the protons and electrons, respectively. Let us eliminate $\boldsymbol{J}$ from Eq. (11.79) neglecting the term $(1/v)\partial\boldsymbol{J}/\partial t$. We then arrive at the diffusion equation in the momentum space,

$$\frac{\partial N}{\partial t} = \frac{1}{p^2}\frac{\partial}{\partial p}p^2 D_h \frac{\partial N}{\partial p}, \tag{11.80}$$

where Kichatinov (1983)

$$D_h = \frac{\alpha^2 \Lambda p^2}{3vR_0^2} \tag{11.81}$$

is the diffusion coefficient which describes the particle acceleration by the helical turbulence, and $R_0 = cp/eB_0$ is the Larmor radius.

In spite of the presence of regular electric field along the uniform magnetic field, we have arrived at a diffusive form of equation describing particle acceleration by helical turbulence. This happens because of efficient particle angular scattering by the turbulence, which makes particle motion back and forth relative to the accelerating electric field almost equally probable, although the probability to gain energy remains larger than to lose energy. Accordingly, though the regular electric field enhances explicitly only the parallel particle momentum, the angular scattering transfers it to the transverse momentum, so all momentum components rise proportionally roughly preserving the distribution isotropy.

In fact, the (discarded earlier) Fermi acceleration process does contribute to the right-hand side of Eq. (11.80) in addition to the acceleration due to turbulence helicity. According to Eq. (11.55), the Fermi acceleration coefficient is given by

$$D_F = \frac{\langle \Delta u^2 \rangle p^2}{3v\Lambda}. \tag{11.82}$$

Thus, the helical part of the velocity correlation tensor gives a dominant contribution to the acceleration if

$$\frac{D_h}{D_F} = \frac{\alpha^2}{\langle \Delta u^2 \rangle}\frac{\Lambda^2}{R_0^2} \gg 1. \tag{11.83}$$

For cosmic plasmas, as a rule, $\Lambda \gg R_0$. The helical parameter $\delta = \alpha^2/\langle \Delta u^2 \rangle$ is generally unknown and hard to reliably estimate; however, it seems to be rather small for most of the astrophysical objects.

To get some idea of possible order of magnitude of the helicity parameter α we express it in the form $\alpha = \tau_c \langle h_k \rangle/3$, where h_k is the kinetic helicity density defined as $h_k = \boldsymbol{u}(\boldsymbol{r}, t) \cdot \nabla \times \boldsymbol{u}(\boldsymbol{r}, t)$, cf. Eq. (8.13) One object, where the helicity density can be estimated using helioseismology data is the subphotospheric solar convective zone, which below ARs yields typically

$|h_k| \sim 10^{-6}\,\mathrm{cm\ s^{-2}}$ with $|h_k| < 10^{-5}\,\mathrm{cm\ s^{-2}}$ in all analyzed cases (Maurya et al. 2011). There are also some ways of estimating the helicity density by tracking apparent motions of bright features in ARs on the photosphere. The problem here is that these measurements give only two (u_x and u_y) of three velocity components, which is insufficient to compute the helicity density. Using the transverse velocity components we can only get a very rough estimate of the helicity density, which, nevertheless, offers an idea of the plausible order of magnitude of this value. For example, for AR 10030 (Park, private communication, 2011), the estimate yields $|h_k| \sim 0.3\,\mathrm{cm\ s^{-2}}$. Adopting $\tau_c \sim 1\,\mathrm{min}$, this yields $|h_k|\tau_c \sim 20\,\mathrm{cm/s}$, which is roughly consistent with that from Eq. (8.15), if we take the solar rotation frequency $\Omega \approx 2.8\times10^{-6}\,\mathrm{rad\ s^{-1}}$, the subphotospheric density scale $h \sim 10^9\,\mathrm{cm}$ and the turbulence length scale $l \sim 10^8\,\mathrm{cm}$, which yields $\alpha \sim 30\,\mathrm{cm/s}$. However, both subphotospheric and photospheric plasmas are very dense so the Coulomb collisions are very frequent there, which makes any nonthermal acceleration process highly unlikely.

The charge particle acceleration in solar flares occurs in more tenuous corona, where, however, no direct measurement of the kinetic helicity is available. In the case of the solar corona, we, nevertheless, can reliably estimate the kinetic helicity density using observational data on the current helicity density defined as

$$h_c = \boldsymbol{B}(\boldsymbol{r},t)\cdot\nabla\times\boldsymbol{B}(\boldsymbol{r},t) = \alpha_{\mathrm{FFF}}B^2, \tag{11.84}$$

where the second equality is written for a FFF, see Sect. 2.3.3 and problem 2.5, which implies a direct link between the force-free parameter α_{FFF} and the current helicity h_c for the case when the magnetic field satisfies the force-free conditions. Although none of these two parameters can be directly measured in the corona, we make use of α_{FFF} conservation in the FFF along any given field line ($\boldsymbol{B}\cdot\nabla\alpha_{\mathrm{FFF}} \equiv 0$) and use the photospheric current helicity measurements (or a corresponding nonlinear FFF extrapolation), which implies that we can have a reliable estimate of the current helicity in the corona.

Let us now estimate how the turbulence kinetic helicity is related to the current helicity. For the linear MHD modes, according to Sect. 2.4.2 (see, e.g., Eq. (2.56)), the fluid velocity is proportional to the magnetic field in the waves,

$$\boldsymbol{u} \approx \mp v_{\mathrm{A}}\boldsymbol{b}/B; \tag{11.85}$$

thus, assuming $\rho = \mathrm{const}$ for simplicity, we obtain

$$h_k = \boldsymbol{u}(\boldsymbol{r},t)\cdot\nabla\times\boldsymbol{u}(\boldsymbol{r},t) = \frac{v_{\mathrm{A}}^2}{B^2}\boldsymbol{b}(\boldsymbol{r},t)\cdot\nabla\times\boldsymbol{b}(\boldsymbol{r},t). \tag{11.86}$$

The last needed step is to link the full current helicity h_c, Eq. (11.84), with that related to only the turbulent magnetic field, $\hat{h}_c = \boldsymbol{b}(\boldsymbol{r},t)\cdot\nabla\times\boldsymbol{b}(\boldsymbol{r},t)$.

To obtain this link let us consider an MHD wave as an oscillation of a given field line and take into consideration the $\alpha_{\rm FFF}$ conservation along this new (distorted) field line,

$$(\boldsymbol{B}_0(\boldsymbol{r},t)+\boldsymbol{b}(\boldsymbol{r},t))\cdot\nabla\times(\boldsymbol{B}_0(\boldsymbol{r},t)+\boldsymbol{b}(\boldsymbol{r},t))=\alpha_{\rm FFF}(\boldsymbol{B}_0(\boldsymbol{r},t)+\boldsymbol{b}(\boldsymbol{r},t))^2. \tag{11.87}$$

After averaging Eq. (11.87), all linear over $\boldsymbol{b}$ terms drop out and then, subtracting the original equality $\boldsymbol{B}_0\cdot\nabla\times\boldsymbol{B}_0=\alpha_{\rm FFF}\boldsymbol{B}_0^2$, we obtain

$$\langle\hat{h}_c\rangle\equiv\langle\boldsymbol{b}(\boldsymbol{r},t)\cdot\nabla\times\boldsymbol{b}(\boldsymbol{r},t)\rangle=\alpha_{\rm FFF}\langle b^2\rangle, \tag{11.88}$$

so, in agreement with formal derivation performed in Problem 2.6, the kinetic helicity density takes the form

$$\langle h_k\rangle=\alpha_{\rm FFF}v_{\rm A}^2\frac{\langle b^2\rangle}{B^2}. \tag{11.89}$$

Now, estimating τ_c as $L_c/v_{\rm A}$, where L_c is the main scale of the turbulence, we obtain the required kinetic helicity parameter

$$\alpha=\frac{\tau_c\langle h_k\rangle}{3}=\alpha_{\rm FFF}L_cv_{\rm A}\frac{\langle b^2\rangle}{3B^2}, \tag{11.90}$$

which enables us of estimating relative efficiency of the standard stochastic (Fermi) acceleration and the "helical" acceleration; Eq. (11.83) with the account of Eqs. (11.90) and (11.85) yields

$$\frac{D_h}{D_F}\sim\frac{\alpha_{\rm FFF}^2L_c^2b^2}{B^2}\frac{\Lambda^2}{R_0^2}\sim\alpha_{\rm FFF}^2L_c^2\frac{B^2}{b^2}\left(\frac{L_c}{R_0}\right)^{2(\nu-1)}, \tag{11.91}$$

where in the second equality we use Eq. (7.106) to estimate the particle mfp formed by the same turbulence. It is transparent from here that the helical acceleration is relatively more important for (1) more nonpotential loops (larger $\alpha_{\rm FFF}$), (2) weaker turbulence (smaller b^2/B^2 ratio), and (3) lower energy (smaller Larmor radius R_0).

For example, substituting into Eq. (11.91) some standard values of $\alpha_{\rm FFF}\sim10^{-10}\,{\rm cm}^{-1}$ (Abramenko et al. 1996, 1997; Longcope et al. 1998), $R_0\sim1\,{\rm cm}$, $L_c\sim10^7\,{\rm cm}$, $\nu=1.5$, and $(b/B_0)^2\sim10^{-4}$, we find $D_h/D_F\sim10^5$, i.e., acceleration by helical turbulence can be up to a few orders of magnitude more efficient in the solar corona than the standard stochastic acceleration by turbulence (Fleishman and Toptygin 2013). Note, that the particle Larmor radius grows with energy, so the relative efficiency of the acceleration by helical turbulence drops and the standard stochastic (Fermi) acceleration will dominate at a large energy in case of a reasonably strong MHD turbulence preserving all known advantages of the stochastic acceleration at those high

energies. But on top of that, the particle flux density described by Eq. (11.79) now depends on the particle charge sign, i.e., the accelerated protons and electrons will now preferentially precipitate into the opposite footpoints in agreement with observations, while in contrast to expectations within the standard Fermi acceleration.

As has been noticed, the helical acceleration is efficient at low energies and for a weaker turbulence and so can form a particle seed population from which the particles are then picked up by an acceleration process. Indeed, the turbulence helicity builds up a large-scale regular electric field which can form a runaway particle population. The runaway electrons represent collimated beams, which are supposed to reveal themselves via radio type III bursts (Aschwanden et al. 1990; Vlahos and Raoult 1995), see Fig. 10.10, and via sub-second fluctuations of microwave (Altyntsev et al. 2008) or X-ray (Kiplinger et al. 1983; Aschwanden et al. 1996) emissions. In particular, if the turbulence consists of many turbulent "cells," where the mean magnetic field has different directions relative to the line of sight, then the directions of the electron beams will also be different in agreement with observations in the microwave range (Altyntsev et al. 2007).

Let us estimate how big the regular electric field induced by the helical turbulence can be compared with the electron Dreicer field. Substituting Eq. (11.90) into Eq. (11.77) defining the electric field and using the same parameters as used for estimating Eq. (11.91), with $B = 100$ G and $n_e = 2 \times 10^{10}\,\mathrm{cm}^{-3}$, we obtain

$$E \sim 10^{-9} B \sim 10^{-7}\mathrm{statvolt/cm} \approx 3 \times 10^{-5}\mathrm{V/cm}. \tag{11.92}$$

Therefore, in our example, the induced electric field is slightly sub-Dreicer, although it can exceed the Dreicer field, e.g., for more tenuous plasma and/or for stronger turbulence. The sub-Dreicer field creates beams of the runaway electrons with the velocity exceeding the critical velocity, $v_c \sim v_{Te}\sqrt{E_{\mathrm{De}}/E}$, which can immediately produce the type III radio bursts and then be picked up by the main acceleration process, i.e., the seed electron population is formed by the runaway electrons, whose amount depends on the E/E_{De} ratio. In case of super-Dreicer field, $E/E_{\mathrm{De}} \gtrsim 1$, most of available electrons will "run away" and form the seed population, i.e., almost all these electrons are eventually accelerated in agreement with recent observations of the flare acceleration regions (Krucker et al. 2010; Fleishman et al. 2011). We note that because the powerful turbulence forms particle mean free paths much shorter that the purely collisional transport would imply, the obtained large regular electric field does not produce any problem typical for classical acceleration in DC electric fields; see, e.g., Miller et al. 1997. Thus, we see that the helical component of the turbulence is easily capable of forming a seed population of electrons, which is needed for the mechanism of stochastic acceleration to efficiently work.

Furthermore, we point out that the same electric field can form highly non-even seed populations of various ions because of a remarkable difference in the effective electron and ion Dreicer fields discussed in Sect. 11.1.1, which implies that a given electric field can be sub-Dreicer for the electrons and ions with large abundance (e.g., ^{4}He), while super-Dreicer for ions with small abundance (e.g., ^{3}He). This is in particular the case for the electric field driven by the helical turbulence estimated by Eq. (11.92). Therefore, all available ^{3}He ions can "run away" in the regular electric field present in the helical turbulence, and, thus, all the ^{3}He ions become available for further acceleration by this turbulence, while only a minor fraction of the ^{4}He ions from the corresponding Maxwellian tail will run away in the same electric field, so a much smaller number of the ^{4}He ions are available for acceleration, which offers an efficient mechanism of ^{3}He enrichment in solar flares.

This enrichment mechanism based on the use of Eq. (11.6) can account for the entire ^{3}He enhancement in the ^{3}He-rich events, which have been puzzling since their discovery at early 1970s. Equation (11.6) shows that the ions with $Z > 1$ and a low number density can have relatively small effective Dreicer fields, which is favorable for them to run away and be picked up by the bulk acceleration process. We note that no enrichment is expected for the hydrogen isotopes ^2H and ^3H, because the terms containing $Z - 1$ drop out from Eq. (11.6) for these ions. And indeed, no ^2H or ^3H enrichment has ever been observed from solar flares (Kocharov and Kocharov 1984). On the other hand, high-Z ions can display even stronger enrichment than the ^{3}He ions, because $(Z - 1)/Z \approx 1$ for them in contrast to helium, where $(Z - 1)/Z = 1/2$. In fact, enrichment of ^{3}He-rich events with ultraheavy ions is widely observed (Mason 2007). Note also that a high correlation between the ^{3}He-rich events and radio type III bursts (Mason 2007) also receives a natural interpretation within the proposed enrichment mechanism, because the formation of the ^{3}He seed population happens along with formation of the runaway electrons responsible for the generation of the radio type III bursts. Apparently, whether the electron beam is formed or not is determined by the balance between the runaway electron acceleration by the electric field, which is proportional to $\Lambda \propto B_0^2/\langle b^2 \rangle$ and their angular scattering by the same turbulence, which is reciprocal to Λ. Therefore, for a stronger turbulence, when, e.g., the induced electric field becomes closer to the ^{4}He Dreicer field, Eq. (11.12b), the electron angular scattering can effectively isotropize the electron beams and so quench the type III burst generation in more powerful flares not showing a considerable ^{3}He enrichment (Mason 2007).

Then, in the presence of this electric field, the particle flux direction depends on their electric charge sign; thus, the accelerated electrons and protons are supposed to precipitate into the opposite foots of the same flaring loop or loop system, which offers a consistent explanation of the observed spatial displacement between sources of hard X-ray (HXR) (produced by

electrons) and gamma-ray (produced by ions) emissions (Lin et al. 2003; Hurford et al. 2006). On top of that, the rate of stochastic particle acceleration can be greatly enhanced when the turbulence is helical, i.e., when the helicity parameter $\alpha \neq 0$; see estimates of Eq. (11.91).

Therefore, the acceleration by the helical turbulence is a promising mechanism in the magnetically dominated stellar coronae including the solar flares and eruptions. It is well established that magnetic twists related in particular to the differential rotation of the star plays an important role in the corresponding energy release and particle acceleration; we have argued that the presence of strong magnetic helicity (twists) may imply a correspondingly strong helicity of the turbulence produced by release of the flaring energy stored in the helical magnetic field. It should be noted that this attractive mechanism of particle acceleration by helical turbulence has not yet been analyzed in any detail, so many important aspects of it remain unclear. Realistic self-consistent nonlinear models of particle acceleration by the helical turbulence supplied by (yet nonexistent) nonlinear theory of the helical turbulence are called for to fully assess the role of this acceleration mechanism.

11.2.3 Second-Order Acceleration Effects for Regular Plasma Motions

In Sect. 11.1.4 we consider the first-order particle energy change connected with the compressibility of the medium ($\nabla \cdot \boldsymbol{u} \neq 0$). Then, in Sects. 11.2.1 and 11.2.2, the second-order acceleration effect for stochastic motion of the plasma was analyzed. It should not be overlooked that second-order acceleration is also produced by a regular plasma motion in the presence of any velocity gradient, in particular, when $\nabla \cdot \boldsymbol{u} = 0$. In this case the acceleration is the second-order effect relative to the *velocity gradient* $\partial u_\alpha / \partial x_\beta$, which can be understood as follows.

We can think of the diffusive motion of the particle as of a sequence of successive jumps from collision to collision with a mean distance between the collisions equal to the transport mfp. Then, each collision will take place at a distance of the order of Λ from the previous collision, i.e., in a region where the regular speed of the fluid is somewhat different (roughly by $\sim \partial u / \partial r$) from that at the previous collision location. This leads to Fermi acceleration of second order, because in the first-order approximation in $\boldsymbol{u}$, the energy losses and gains are equally probable.

To analyze the second-order effects let us start from the kinetic equation in the form of Eq. (7.77). Let the regular magnetic field be absent for simplicity. When the size of the system considerably exceeds the transport mfp, the distribution function F is almost isotropic. However, to properly analyze effects of the second-order over $\boldsymbol{u}$, we take into account a small anisotropy of the distribution function, including the first and second spherical harmonics:

$$F = \frac{1}{4\pi}\left[N(\boldsymbol{r},p,t) + \frac{3}{v}n_\alpha J_\alpha(\boldsymbol{r},p,t) + n_\alpha n_\beta f_{\alpha\beta}(\boldsymbol{r},p,t) + \ldots\right], \quad (11.93)$$

where $n_\alpha = p_\alpha/p$ and $f_{\alpha\beta}$ is a traceless tensor, $f_{\alpha\alpha} = 0$.

The further required manipulations are straightforward, while cumbersome, which we path by directly to the main results of the consideration. The inverse particle acceleration time is of the order of

$$\tau_{ag}^{-1} \approx \frac{\kappa}{v^2}\left(\frac{\partial u}{\partial r}\right)^2 \approx \frac{u^2\Lambda}{vL^2}, \quad (11.94)$$

where L is the scale length of hydrodynamic speed. The increase of total energy of accelerated particles with time depends on the type of the MHD flow. For example, for a shear flow with a linear velocity profile, when $\partial u_1/\partial x_2 = \text{const}$ and other derivatives $\partial u_\alpha/\partial x_\beta = 0$ we have

$$\frac{\mathrm{d}E}{\mathrm{d}t} = \frac{1}{3}\int \mathrm{d}^3 r \int_0^\infty \mathrm{d}p\, p^3 N\Lambda \left(\frac{\partial u_1}{\partial x_2}\right)^2 \left(\frac{7}{5} + \frac{2v^2}{3c^2}\right), \quad (11.95)$$

while, in a fluid body rotating with the angular velocity $\boldsymbol{\Omega} = \text{const}$, so that $\boldsymbol{u} = \boldsymbol{\Omega} \times \boldsymbol{r}$, we obtain

$$\frac{\mathrm{d}E}{\mathrm{d}t} = \frac{4}{3}\int \mathrm{d}^3 r \int_0^\infty \mathrm{d}p\, p^3 N\Lambda\Omega^2 \left(1 + \frac{v^2}{3c^2}\right). \quad (11.96)$$

Equations (11.95) and (11.96) allow estimating the second-order effect in the effective particle energy change due to regular fluid motion when the distribution function of accelerated particles is known. The efficiency of the second-order acceleration driven by a regular fluid velocity flow compared with the Fermi acceleration efficiency is

$$\frac{\tau_{ag}^{-1}}{\tau_{aF}^{-1}} \approx \frac{u^2}{\langle \Delta u^2\rangle}\frac{\Lambda^2}{L^2}. \quad (11.97)$$

The considered acceleration effect can be important in regions with large velocity gradients, for instance, at the boundaries of high-speed solar wind streamers or magnetic sectors, interfaces between slow and fast solar wind regions, accretion disks, tangential discontinuities in IPM, and near the Earth's magnetosheath.

11.3 Formation of Accelerated Particle Spectra

Time evolution of particle spectra can be evaluated by solving Eq. (11.54) with corresponding initial and boundary conditions. However, this equation is very complicated because it describes joint effect of particle acceleration, adiabatic loss, real space diffusion, and advective transport. To better highlight the corresponding physics, we address all these effects in a sequential order.

11.3.1 Nonstationary Acceleration in a Uniform System

Neglecting any losses, acceleration in a uniform system is described by equation

$$\frac{\partial N}{\partial t} = \frac{1}{p^2}\frac{\partial}{\partial p}p^2 D(p,t)\frac{\partial N}{\partial p}. \tag{11.98}$$

We assume that the diffusion coefficient in this equation depends on both momentum and time; the time dependence may appear due to turbulence generation, dissipation, or spectral transformation. For protons and other heavy particles, the radiative losses are typically unimportant, so only ionization and adiabatic losses can be essential, which, however, can be discarded if their typical timescales are much larger than the acceleration time.

Since the system is assumed uniform, the total number density of the particles remains constant. This condition is fulfilled, for instance, when accelerated particles are confined in a trap whose size does not change with time, or the boundaries of acceleration region are far and their influence is minor.

Adopt the turbulent acceleration coefficient in the form

$$D(p,t) = D_0(t)(p/p_0)^{\alpha}, \tag{11.99}$$

where p_0 is a constant. Introducing dimensionless variables

$$\tau = p_0^{-2}\int_0^t D_0(t')\mathrm{d}t', \qquad q = p/p_0, \tag{11.100}$$

we rewrite Eq. (11.98) as

$$\frac{\partial N}{\partial \tau} = \frac{1}{q^2}\frac{\partial}{\partial q}q^{2+\alpha}\frac{\partial N}{\partial q}. \tag{11.101}$$

A partial solution to this equation is given by

$$N_\lambda(q,\tau) = f_\lambda(q)\exp(-\lambda^2\tau) \tag{11.102}$$

with an arbitrary λ. Substituting

$$f_\lambda(q) = q^{(2\mu-3)/2}F_\lambda(\xi), \qquad \xi = q^\mu, \qquad \mu = 1-\alpha/2, \tag{11.103}$$

for $\alpha \neq 2$ we reduce Eq. (11.98) to the Bessel equation for $F_\lambda(\xi)$,

$$\xi^2 F_\lambda'' + \xi F_\lambda' + \mu^{-2}\left[\lambda^2\xi^2 - \frac{1}{4}(\alpha+1)^2\right]F_\lambda = 0. \tag{11.104}$$

A partial regular solution to this equation is given by

$$F_\lambda(\xi) = J_\beta(\lambda\xi|\mu|^{-1}), \qquad \beta = \frac{1}{2}(1+\alpha)|\mu|^{-1}. \tag{11.105}$$

The general solution to Eq. (11.98) can be written in the integral form

$$N(q,\tau) = q^{(2\mu-3)/2} \int_0^\infty \psi(\lambda) \exp(-\lambda^2\tau) J_\beta(\lambda q^\mu |\mu|^{-1}) \lambda \mathrm{d}\lambda. \tag{11.106}$$

The expansion coefficient $\psi(\lambda)$ is determined from the initial condition $N(p,0) = N_0(p)$ using the Fourier–Bessel theorem, which yields

$$\psi(\lambda) = |\mu|^{-1} \int_0^\infty N_0(q) q^\mu J_\beta(\lambda q^\mu |\mu|^{-1}) \sqrt{q} \mathrm{d}q. \tag{11.107}$$

Substituting this expression into Eq. (11.106) and integrating over λ, we obtain the solution for any initial condition ($\alpha \neq 2$),

$$N(q,\tau) = (2|\mu|\tau)^{-1} q^{(2\mu-3)/2} \int_0^\infty N_0(q') q'^\mu I_\beta \left(\frac{q^\mu q'^\mu}{2\mu^2\tau} \right) \exp\left(-\frac{q^{2\mu} + q'^{2\mu}}{4\mu^2\tau} \right) \sqrt{q'} \mathrm{d}q', \tag{11.108}$$

$I_\beta(x)$ is the modified Bessel function. The case $\alpha = 2$ is considered in Problem 11.3. If the turbulence disappears during a finite time, then $\tau \to \tau_0$ as $t \to \infty$, and after the turbulence decay the particle spectrum is determined by Eq. (11.108) with $\tau = \tau_0$.

Case $\alpha < 2$. Let the initial particle momentum be much smaller than the mean momentum of the accelerated particles, $q \sim \tau^{1/2\mu}$. Then, for values of q corresponding to the bulk of accelerated particles, the argument of $I_\beta(x)$ is small for $\sqrt{\tau} \gg 1$. Using the relevant asymptote of $I_\beta(x)$, we obtain

$$N(q,\tau_0) = \frac{n_0}{(2-\alpha)^{1+2\beta}\Gamma(1+\beta)\tau_0^{1+\beta}} \exp\left(-\frac{q^{2\mu}}{4\mu^2\tau_0} \right), \tag{11.109}$$

where $n_0 = \int_0^\infty N_0(q) q^2 \mathrm{d}q$ is the total number density of the particles. The mean momentum of the particle distribution (11.109) is given by

$$\overline{q} = (2\mu\sqrt{\tau_0})^{1/\mu} \frac{\Gamma(2/\mu)}{\Gamma(3/2\mu)}. \tag{11.110}$$

The value of $\alpha = 1$ is typical for interplanetary space and corresponds to the energy-independent transport mfp Λ. In this case the exponential over the rigidity spectrum is formed

$$N(q,\tau_0) \sim \exp(-q/\tau_0), \qquad \overline{q} = 3\tau_0. \tag{11.111}$$

Spectra with a similar, quasiexponential, cutoff have been detected in the IPM.

Case $\alpha > 2$. At sufficiently large q and fixed $\tau = \tau_0$ the argument of $I_\beta(x)$ in Eq. (11.108) becomes small provided that $q^{|\mu|}\tau \gg 1$. Then, the particle spectrum is the power law:

$$N(q,\tau) = \frac{n_0}{(2\mu)^{1+2\beta}\Gamma(1+\beta)\tau_0^{1+\beta}(q_0 q)^{1+\alpha}}, \tag{11.112}$$

where q_0 is the initial particle momentum. For nonrelativistic particles, Eq. (11.112) corresponds to the differential spectrum over kinetic energy:

$$N(K) \propto K^{-\alpha/2}. \tag{11.113}$$

The stochastic Fermi acceleration is believed to play a role in solar flares supplying IPM with **solar energetic particles** (SEP). Observations in IPM performed by numerous space missions detect a variety of the SEP spectra, which can be fitted, at least in certain ranges of SEP kinetic energy with quasiexponential, cf. Eq. (11.111),

$$I(K) = A\exp\left[-\left(\frac{K}{K_0}\right)^{1/2}\right] \tag{11.114}$$

or power-law

$$I(K) = A(K_0/K)^\gamma \tag{11.115}$$

functions, where typically $\gamma > 2$. The idealized model considered above does not offer such power-law asymptotes for a typical value of $\alpha \sim 1$, which implies that some important physics is missing from this acceleration regime. In addition, while analyzing real data on the SEP spectra one has to keep in mind that the detected spectrum is supposed to deviate from the original spectrum of particles accelerated at the flare site due to a number of important transport effects including energy-dependent escape time of the SEP from the acceleration region, Coulomb and adiabatic losses, in situ stochastic acceleration by turbulence in IPM, etc.

11.3.2 Stationary Fermi Spectra in a Finite Accelerated Region

Let us consider stationary spectra of the accelerated particles formed by a balance between the stochastic acceleration and particle loss from a finite source. Adopt that in a spatially finite acceleration region there is a source of turbulence forming a constant transport mfp $\Lambda = \text{const}$ of relativistic particles and corresponding diffusion coefficient in the momentum space. Remind that the constant transport mfp can be formed by either rigid magnetic "clouds" or by MHD turbulence with a broad power-law spectrum with index $\nu = 2$ [see Eq. (7.106)].

We assume that a minor fraction of the background particles, being scattered by small-scale macroscopic electric fields, gains suprathermal energies and so is injected into the stochastic acceleration process. Adopt the injection source to be uniform and to have the form $Q(p_0)p_0^2\delta(p-p_0)$ per unit volume per unit time. There is no acceleration outside the acceleration region; the escaped particles never come back.

We start from a simple estimate of the expected acceleration particle spectrum neglecting the spatial nonuniformity in the particle distribution and using the lifetime approximation, i.e., replace the spatial diffusion term by a simpler term N/τ_d, where τ_d is the mean residence time of the fast particle in the acceleration region (that is of the order of diffusion time through the acceleration region $\tau_d \approx L^2/\kappa$). This approximation is often used to approximately solve transport equations. The corresponding stationary equation for the distribution function has the form

$$\frac{1}{p^2}\frac{\mathrm{d}}{\mathrm{d}p}\frac{p^4}{\tau_a}\frac{\mathrm{d}N}{\mathrm{d}p} - \frac{N}{\tau_d} + \frac{Q_0}{p_0^2}\delta(p-p_0) = 0, \tag{11.116}$$

where the diffusion coefficient in the momentum space $D(p) = p^2/\tau_a$ is substituted; $\tau_a = \text{const}$.

The δ-source of the particles can be replaced by corresponding boundary conditions in the momentum space, one of which is derived from the continuity of the distribution function at $p = p_0$:

$$N(p)|_{p=p_0+0} = N(p)|_{p=p_0-0}. \tag{11.117}$$

The other boundary condition can be obtained from integration of Eq. (11.116) over a narrow momentum range around $p{=}p_0$ and taking into account that N is a bounded function:

$$\left.\frac{\mathrm{d}N}{\mathrm{d}p}\right|_{p=p_0+0} - \left.\frac{\mathrm{d}N}{\mathrm{d}p}\right|_{p=p_0-0} = -Q_0\frac{\tau_a}{p_0^4}. \tag{11.118}$$

Then, we can solve homogeneous ($p \neq p_0$) Eq. (11.116), which yields the solution:

$$N(p) = Ap^{-s_1} \qquad \text{for } p > p_0, \qquad N(p) = Bp^{s_2} \qquad \text{for } p < p_0, \tag{11.119}$$

where

$$s_1 = \sqrt{\frac{9}{4} + \frac{\tau_a}{\tau_d}} + \frac{3}{2}, \qquad s_2 = \sqrt{\frac{9}{4} + \frac{\tau_a}{\tau_d}} - \frac{3}{2}. \tag{11.120}$$

Then, the boundary conditions specify the unknown amplitudes A and B, so

$$N(p) = \frac{N_0}{p_0^3}\left(\frac{p_0}{p}\right)^{s_1} \qquad p > p_0, \qquad N_0 = \frac{Q_0\tau_a}{s_1+s_2}. \tag{11.121}$$

The *decelerated* particle spectrum at $p < p_0$ can straightforwardly be written down as well, although this part of the spectrum is often not interesting.

Therefore, we have found that a power-law spectrum of fast particles is formed with a spectral index dependent on the ratio τ_a/τ_d of the characteristic time constants, which can now be easily made consistent with power-law spectra (11.115) in IPM by appropriate choice of the ratio τ_a/τ_d. Let us compare this model spectrum with the observed spectrum of the Galactic CRs. Observations typically deal with a differential particle flux $I(\mathcal{E})$ per unit area, per unit solid angle, per unit time, while solution (11.121) is written for the particle density in the phase space $N(p)$; these measures are related to each other by

$$I(\mathcal{E})\mathrm{d}\mathcal{E} = vN(p)p^2\mathrm{d}p = Np^2\mathrm{d}\mathcal{E}. \tag{11.122}$$

The observed CR spectrum is well fitted by a power law $I(\mathcal{E}) \propto \mathcal{E}^{-\gamma}$, with the spectral index $\gamma \approx 2.7$ in the proton energy range $10 \lesssim \mathcal{E} \lesssim 10^6$ GeV. For the ultrarelativistic particles, $\mathcal{E} \approx cp$, Eq. (11.122) yields

$$I(\mathcal{E})\mathrm{d}\mathcal{E} = cN_0\left(\frac{\mathcal{E}_0}{\mathcal{E}}\right)^{\gamma}\frac{\mathrm{d}\mathcal{E}}{\mathcal{E}_0}, \qquad \gamma = s_1 - 2. \tag{11.123}$$

This implies $\tau_a/\tau_d \approx 8$ for all significant sources of the Galactic CRs, which is extremely hard to justify within any realistic model of the CR origin. At the higher energies ($\approx 3 \times 10^6 \lesssim \mathcal{E} \lesssim 10^{11}$ GeV) the CR spectrum has a number of breaks and cannot be well described by a single power law.

Overall, the smaller the ratio τ_a/τ_d the harder (flatter) the energetic spectrum. In particular, in the limiting case $\tau_a/\tau_d \to 0$ the spectral index $\gamma \to 1$, which can also be obtained from Eq. (11.108) assuming $\tau \to \infty$. This means that the accelerated particle could gain an infinite energy:

$$E = \int_{\mathcal{E}_0}^{\mathcal{E}} I(\mathcal{E})\mathcal{E}\mathrm{d}\mathcal{E} \sim \mathcal{E} \to \infty. \tag{11.124}$$

In fact, this implies that the linear statement of the problem breaks down and one has to take into account the finite power of the turbulence sources and its decay due to energy transfer from turbulence to the accelerated particles. In addition, the acceleration can also be suppressed by the mfp increase with the particle energy $\Lambda \propto p^2$ above some critical energy [see Eq. (7.80)] and corresponding decrease of the particle residence time in the acceleration region resulting in $\tau_a/\tau_d \gg 1$ at some high energies; at this energy range the spectrum has an exponential cutoff according to Eq. (11.63). In contrast, if the condition $\tau_a/\tau_d \gg 1$ is fulfilled just above the injection momentum, then the entire spectrum of accelerated particles is very steep, i.e., most of the particles gain only moderate energies.

An interesting assessment of the lifetime approximation accuracy and applicability can be done based on comparison of the results of this section with a more exact solution given to Problem 11.5 obtained with the account of boundary conditions.

11.3.3 Stochastic Acceleration of Electrons in Solar Flares

Let us return to the problem of resonant electron acceleration in solar flares considered in Sect. 11.2.1. Combining all needed expressions for coefficients entering Eq. (11.66), it can be rewritten in the form (recall, $E = K/mc^2$ is the dimensionless kinetic energy here):

$$\frac{\partial f}{\partial t} = \frac{\partial^2}{\partial E^2}[\beta(\gamma\beta)^{q-2} D_w f] - \frac{\partial}{\partial E}\left[\left(q(\gamma\beta)^{q-3} D_w - \frac{c}{\lambda_0}\beta^{-1}\right) f\right] - \frac{\beta(\gamma\beta)^{2-q}}{\tau_w} f + S(E,t). \tag{11.125}$$

This equation is rather complicated and cannot be solved analytically since neither of the terms in the rhs can be discarded in a general case. To illustrate this, adopt $q = 4$ (Hamilton and Petrosian 1992) and consider the second term in the rhs. The two contributions, turbulent and Coulomb, have dissimilar dependence on the electron velocity, $\propto \beta$ and $\propto \beta^{-1}$, respectively, which implies certain critical velocity β_c where the acceleration rate is equal to the Coulomb loss rate. Figure 11.2 displays a number of accelerated electron

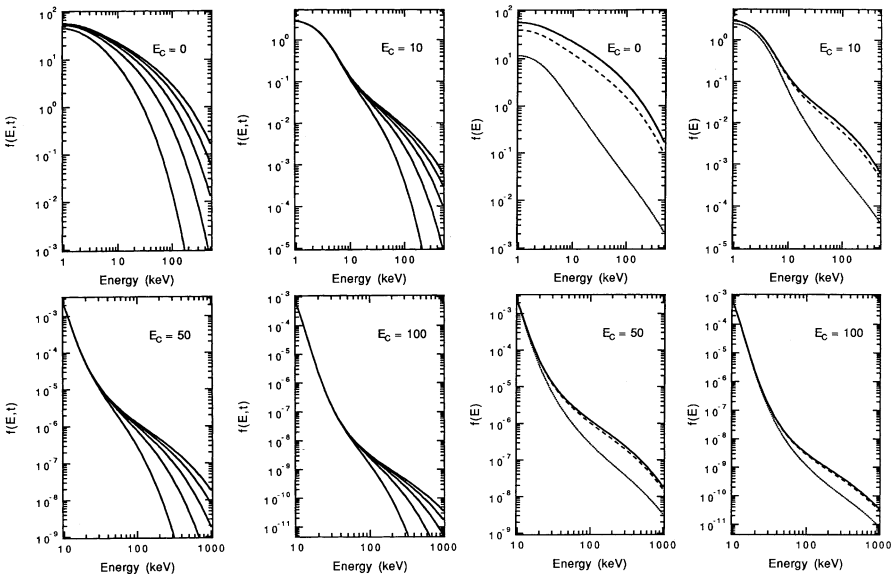

Figure 11.2: *Four left panels*: Time-dependent spectra $f(E,t)$ of electrons stochastically accelerated by resonant whistler-wave turbulence. The adopted parameters are: $D_w\tau_w = \infty$; $E_c = E(\beta_c) = 0,\ 10,\ 50$, and 100 keV; thermal energy $E_T = 1$ keV; plotted for times $D_w t = 0.05,\ 0.1,\ 0.15$, and 0.2. *Four right panels*: the steady-state $D_w t \gg 1$ spectra for different $D_w\tau_w = \infty$ (*thick solid*), $D_w\tau_w = 1$ (*dashed*), and $D_w\tau_w = 0.1$ (*thin solid*) for the same E_c and E_T; from Hamilton and Petrosian (1992). Reproduced by permission of the AAS.

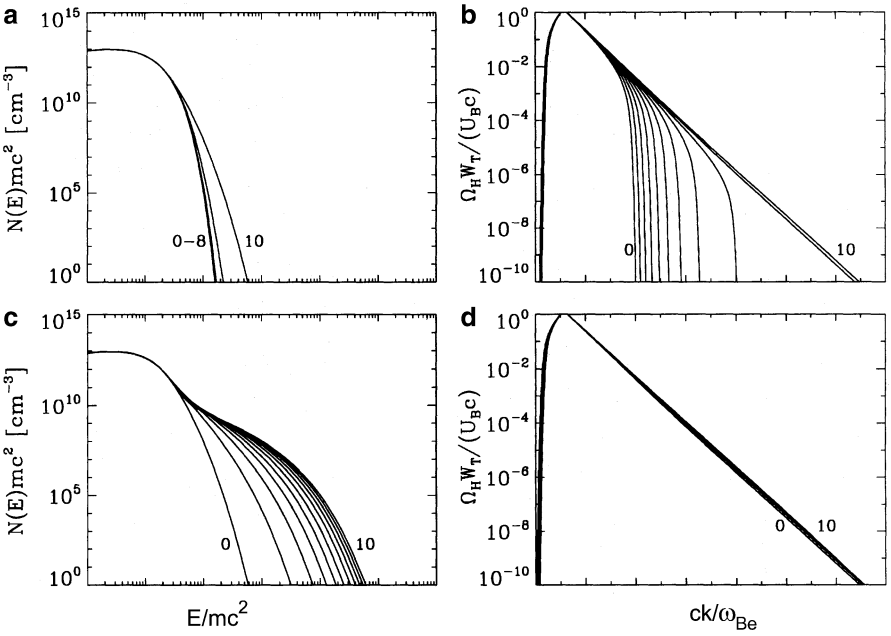

Figure 11.3: Example of self-consistent evolution of the cascading fast mode turbulence and accelerated electrons from Miller et al. (1996). Evolution of electron distribution function (**a** and **c**) and wave spectral density (**b** and **d**) is shown for times $t_n\omega_{\rm Be} = 1.5\times10^6 + 5\times10^4 n$ for $n = 1,\ldots,10$ (**a** and **b**) and $t_n\omega_{\rm Be} = 2\times10^6 + 10^5 n$ for $n = 1,\ldots,10$ (**c** and **d**). Reproduced by permission of the AAS.

spectra obtained from numerical solution of Eq. (11.125) for various parameter combinations. One can see that the spectra differ from each other representing rather complicated curves, which is difficult to describe by a simple analytical (e.g., a power-law) function.

Even though the problem described by Eq. (11.125) is complicated, it is incomplete because it adopts a prescribed level of turbulence without consideration of the turbulence generation and decay. A more complete picture including MHD wave cascading (see Chap. 6), while discarding particle escape from the source, was considered by Miller et al. (1996). They assumed that the primary release of free magnetic energy in a solar flare generates initially a large-scale MHD disturbances, which then cascade toward smaller scales to form a Kolmogorov-like spectrum in a broad range of spatial scales. From Chap. 6 we know that a power-law inertial range of the turbulence spectrum is formed down to a dissipative scale, which can be related to the kinematic viscosity, magnetic diffusivity, or (gyro or Cherenkov) resonant wave–particle interactions. In the latter case the MHD wave damping implies acceleration of the particles absorbing the wave energy.

Figure 11.3 displays an example of such consistent evolution of the cascading fast mode turbulence and its accelerated electrons. Initially, when the cascade develops, we can see how the inertial range grows toward smaller scales, while the electron distribution remains almost unchanged. Later, as soon as sufficiently small-scale fast waves capable of resonantly interacting with slightly suprathermal electrons appear, the fast mode turbulence starts to decay transferring a part of its energy to the particle acceleration. The apparent break of the spectrum around mc^2 is related to transition from nonrelativistic to relativistic regime, while does not imply any particle loss mechanism.

These examples demonstrate that efficient stochastic acceleration by resonant wave–particle interaction with turbulence can happen in conditions implied for solar flares. Moreover, the particle (electron or ion) acceleration can be very strong, so the accelerated particle component accumulate a significant fraction of the system free energy. In such cases of strong acceleration the problem becomes highly nonlinear and the effect of accelerated particles on the turbulence properties must be explicitly taken into account, see Sect. 11.5.4 for greater detail.

11.3.4 Effect of Adiabatic Losses and Acceleration on Transport of Solar Protons

Most of the particles accelerated in a solar flare die collisionally in the chromosphere or dense coronal flaring loops. A minor fraction, however, typically less than 5%, escapes into IPM and can be detected in situ by a spacecraft. Apparently, spectra of detected particles can differ from those escaping from the corona due to different transport effects in the IPM. Consider the spectrum of particles which are emitted from the Sun and evolve during their propagation. The particle energy can vary due either to adiabatic losses or the acceleration in the turbulent solar wind flow. For the sake of simplicity, consider the case of rather strong scattering resulting in a small mfp and so providing that any fast particle is linked to a particular fluid element. Stated another way, this means that the particle diffusion can be neglected compared with the advective transport. This transport regime takes place when $ur/\kappa \gg 1$; in the slow solar wind with $u \sim 400\,\mathrm{km/s}$ for 1 MeV protons the latter inequality implies $\Lambda \ll 0.1\ r$. This condition is only marginally satisfied for the typical parameter values near the Earth orbit but is supposed to better fulfilled for the outer heliosphere.

Within the approximation adopted, the transport equation written for the spherically symmetric, stationary case, including the source term, is given by

$$u\frac{\partial N}{\partial r} = \frac{1}{p^2}\frac{\partial}{\partial p}p^2 D(r,p)\frac{\partial N}{\partial p} + \frac{p}{3}\frac{\partial N}{\partial p}\frac{1}{r^2}\frac{\partial}{\partial r}(r^2 u) + \frac{N_0}{p_0^2}\delta(r-r_0)\delta(p-p_0). \tag{11.126}$$

We seek a general solution valid for arbitrary $u(r)$ and for $D(r,p)$ in the model form

$$D(r,p) = D_0(r)(p/p_0)^\alpha, \tag{11.127}$$

where $D_0(r)$ is an arbitrary function of r. Introducing variables

$$q = \frac{p}{p_0}(r^2 u(r))^{1/3}, \qquad \tau = p_0^{-2}\int\limits_{r_0}^{r} \mathrm{d}r' D_0(r')\left(\frac{r'^{4-2\alpha}}{u^{1+\alpha}}\right)^{1/3}, \tag{11.128}$$

we reduce Eq. (11.126) to Eq. (11.101), which has already been considered above,

$$\frac{\partial N}{\partial \tau} = \frac{1}{q^2}\frac{\partial}{\partial q} q^{2+\alpha}\frac{\partial N}{\partial q} + N_0(q)\delta(\tau). \tag{11.129}$$

In this case

$$N_0(q) = N_0 r_0^{2/3} p_0^{-3} u_0^{-2/3}\delta(q - r_0^{2/3}u_0^{1/3}) \tag{11.130}$$

plays the role of the "initial conditions" at $\tau = 0$ for this equation.

Although, using the solution in general form Eq. (11.108), one can solve Eq. (11.129) for an arbitrary dependence of $N_0(q)$ in the source term, we restrict the analysis to the monoenergetic source case described by Eq. (11.130). Then, we assume that the source is located at small enough r_0 (at the solar atmosphere) so that the argument of $I_\beta(x)$ in Eq. (11.108) is small, $x \ll 1$, so the corresponding asymptote of the modified Bessel function can be used. Under these assumptions

$$N(q,\tau) = \frac{N_0 r_0^2}{(2-\alpha)^{1+2\beta}\Gamma(1+\beta)p_0^3 r^{1+\beta}}\exp\left(-\frac{q^{2\mu}}{4\mu^2\tau}\right), \tag{11.131}$$

where again $\mu = (2-\alpha)/2,\ \beta = (1+\alpha)/|2-\alpha|$. If u and D_0 do not depend on r, the intensity spectrum $I(K) = p^2 N(p)$ is given by

$$I(r,K) = \frac{|2-\alpha|N_0}{\Gamma(1+\beta)p_0 u r^2}\xi^{-1-\beta}\frac{K}{K_0}\exp\left(-\frac{K^\mu}{\xi K_0^\mu}\right), \tag{11.132}$$

where $\xi = 3(2-\alpha)^2 D_0 r/(7-2\alpha)p_0^2 u,\ \alpha \neq 2,\ \alpha < 3.5$. The mean energy for this spectrum is equal to

$$\overline{K} = K_0\Gamma(3/\mu)\Gamma^{-1}(2/\mu)\xi^{1/\mu}. \tag{11.133}$$

Note that $\xi \sim \tau_{\mathrm{ad}}/\tau_a$, where $\tau_{\mathrm{ad}} \sim r/u$ is the adiabatic loss time and $\tau_a \sim p_0^2/D_0$ is the acceleration time. In the case of arbitrary source spectrum Eq. (11.132) is to be integrated over K_0. Far away from the source the

spectrum is determined by the distance r as well as by energy dependence of the ratio p_0^2/D_0.

Let us envision an interesting limiting regime occurring for $\alpha = 1$, $u = \text{const}$, and $p_0^2/D_0 \sim p_0$. The latter proportionality takes place for nonrelativistic particles experiencing "classical" Fermi acceleration (i.e., when the mfp does not depend on energy, $\Lambda = \text{const}$). In this case the initial particle energy K_0 drops out of the exponent, so the spectrum is given by

$$I(r, K) \propto \frac{K}{r^5} \exp\left[-\frac{5\Lambda u^2}{\overline{\Delta u^2} r}\left(\frac{K}{K_*}\right)^{1/2}\right] \tag{11.134}$$

independently of the source spectrum; $K_* = mu^2/2 \approx 1\,\text{keV}$ is the kinetic energy of solar wind particles.

Equation (11.134) shows that particles emitted from the Sun experience strong adiabatic "cooling" at small r for the adopted parameter regime. However, as r increases, the Fermi acceleration wins competition with the adiabatic losses providing that the mean particle energy increases with distance. From Eq. (11.134) we obtain

$$\overline{K} = K_*\left(\frac{2\overline{\Delta u^2} r}{\sqrt{5} u^2 \Lambda}\right)^2. \tag{11.135}$$

Adopting $\Lambda = 0.1\,\text{AU}$, in the most favorable case $\overline{\Delta u^2} \approx u^2$ we have $\overline{K} \approx 100\,\text{keV}$ near the Earth orbit.

Observationally, the effect of the mean energy increase for the ions accelerated in corotating streams was discovered by McDonald et al. (1976): they found that instead of strong adiabatic cooling with the heliocentric distance while traveling between 1 AU and 4 AU, the fluxes of ion with 0.1–1 MeV could raise by more than one order of magnitude implying an efficient particle acceleration between 1 and 4 AU. The theory developed above offers an elegant way of interpreting this observation. Adopt $\alpha = 1$ ($\beta = 2$) and $\overline{\Delta u^2} \approx u^2$ for definiteness and estimate the particle mfp needed to ensure the 1 MeV proton intensity increase by a factor of ∼10 between 1 and 4 AU. As has been said for the solar wind we have $K_* \approx 1\,\text{keV}$, so $K/K_* \approx 10^3$ for the 1 MeV particles. Then, Eq. (11.134) yields the required 10 fold intensity increase at 4 AU if the mfp is $\Lambda \sim 0.1\,\text{AU}$ for the 1 MeV particles, which fully agrees with measurements in IPM. Then, Eq. (11.135) yields the mean fast particle energy of ∼80 keV at the Earth orbit, while ∼1300 keV at 4 AU.

11.4 Acceleration of Charged Particles by MHD Shock Waves

Shock waves are currently believed to represent the main sources of relativistic particles in the Galaxy and in many isolated sources such as SNRs and

GRBs, where a highly powerful particle acceleration occurs. The basic reason for this expectation is easy to understand: a powerful particle acceleration requires a correspondingly large source of the free energy in the accelerating agent, e.g., MHD disturbances in case of the MHD turbulence. As we have seen (see Sect. 5.1.4) strong MHD waves experience nonlinear evolution and can eventually form sharp shock fronts. In this section we consider basic concepts of the particle acceleration by the shock waves. Main ideas and the first conceptual science-transforming results on that were obtained almost simultaneously and independently by several scientists and groups of scientists (Axford et al. 1977; Krymskii 1977; Bell 1978; Blandford and Ostriker 1978). It is a good example of the popular proverb that good ideas are in the air.

11.4.1 Fast Particle Interaction with Shock Front: Acceleration, Reflection, and Crossing

We begin with investigating how single (test) fast particles interact with a shock. Consider a fast shock where the magnetic field jump $\Delta B = B_2 - B_1$ at the front is positive and can have arbitrary magnitude between 0 and $3B_1$ for a classical shock wave, Sect. 5.4.1, in nonrelativistic plasma. Let us adopt the conditions

$$R_{1,2} \gg \delta, \qquad v_\perp \gg u, \tag{11.136}$$

where R is particle Larmor radius, u is the shock velocity relative to the upstream plasma, and δ is the shock front thickness within which the magnetic field varies from the value B_1 to the value $B_2 > B_1$ behind the front. Further, we assume throughout this section that the magnetic field is regular and uniform near the front. Note that in the case opposite to (11.136) when $R \ll \delta$ the adiabatic theory of the particle transport, Sects. 1.2 and 7.5.3, can be used for the assumed here laminar shock structure.

First, consider the case of a purely transverse shock (i.e., the shock front normal is transverse to the magnetic field vector); the plasma moves perpendicular to the front in the front rest frame, Fig. 11.4. In this frame, along with the magnetic fields which are different on both sides of the front, there also exist the electric fields

$$\boldsymbol{E} = -\frac{1}{c}\boldsymbol{u}_1 \times \boldsymbol{B}_1 = -\frac{1}{c}\boldsymbol{u}_2 \times \boldsymbol{B}_2, \tag{11.137}$$

equal to each other on both sides of the front. Fast particles gyrate around magnetic field lines and drift through the front with the plasma stream velocity. Since $v_\perp \gg u$, particles perform many Larmor rotations during their drift. In addition to the drift through the front and trivial motion along magnetic field lines, particles also drift along the front perpendicular to the magnetic field due to the difference of Larmor radii in the upstream and downstream plasmas, Fig. 11.5.

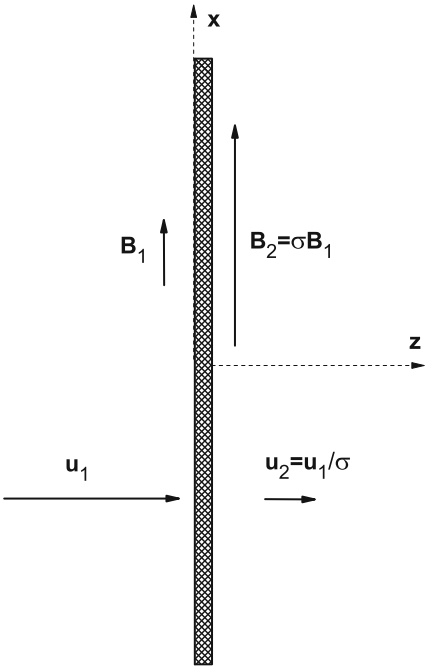

Figure 11.4: Cartoon of a transverse MHD shock.

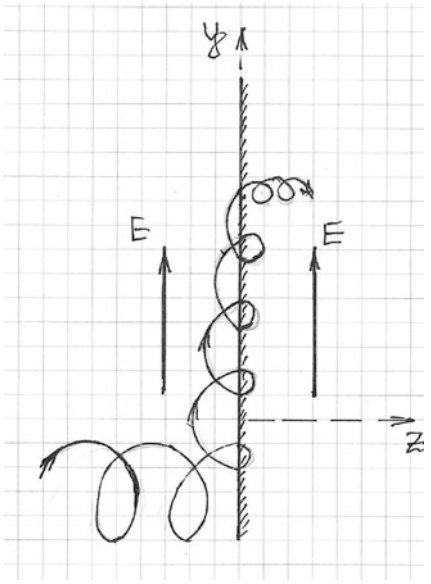

Figure 11.5: Drift acceleration of a particle which crosses the shock front.

The drift through the front is accompanied by acceleration because the energy gained by the particle from the electric field along the fragment of the Larmor circle upstream the front exceeds the energy lost along a complementary fraction behind the front, Fig. 11.5. Direct analysis of a particle trajectory shows that when the particle finally crosses the front its transverse momentum component $p_{\perp 2}$ is related to the initial momentum component $p_{\perp 1}$ before crossing as

$$\frac{p_{\perp 2}^2}{B_2} = \frac{p_{\perp 1}^2}{B_1}, \tag{11.138}$$

while the longitudinal component remains unchanged, $p_{\parallel 2} = p_{\parallel 1}$. The details of calculations are given by Toptygin (1985). Note that Eq. (11.138) cannot be interpreted within usual adiabatic theory (see Sects. 1.2 and 7.5.3), because in the case under consideration, $\delta \ll R$, the adiabatic approximation does not apply. However, Khodzhaev et al. (1981) found that the adiabatic invariant for a particle crossing a transverse shock is conserved for any relation between R and δ. Equation (11.138) appears to be satisfied rather accurately even when $R \sim \delta$.

We see that while crossing the transverse shock, the transverse particle energy increases proportionally to the magnetic field for a nonrelativistic particle or to the square root of the field for an ultrarelativistic one. Therefore, for a strong shock, $B_2/B_1 \approx 4$, the energy of a relativistic particle is doubled, which is a rather weak acceleration efficiency.

Now, consider an oblique shock. In this case interaction of a particle with the front is more complicated, Fig. 11.6: some particles are reflected from the front; others cross it and transit downstream depending on the particle pitch-angle and on the angle of the magnetic field to the front normal. We summarize here briefly the main results referring to the review by Toptygin (1980) for greater detail:

1. If the particle reflects off a shock front or intersect it in any direction, particle energy increases.

2. The maximum energy gain can exceed the initial particle energy by a factor of a few (by one order of magnitude at most). The largest energy gain is possible if the angle α_1 between the magnetic field and the front plane is small, $\alpha_1 \ll u_1/c$. The maximum energy gains during the reflection ($\Delta\mathcal{E}^R$) or intersection ($\Delta\mathcal{E}^C$) of the front by the Larmor circle are

$$\Delta\mathcal{E}^R = 2\mathcal{E}\frac{v^2}{c^2}\left(\frac{B_2}{B_1} - 1\right) \qquad \text{or} \qquad \Delta\mathcal{E}^C = \frac{1}{2}\Delta\mathcal{E}^R, \tag{11.139}$$

respectively. If the angle between the field and the shock plane is large, $\alpha_1 \gg u_1/v$ or $\alpha_1 \sim 1$, the energy increase is a small fraction of the total particle energy:

$$\Delta\mathcal{E} \approx pu_1/\alpha_1 \ll \mathcal{E}. \tag{11.140}$$

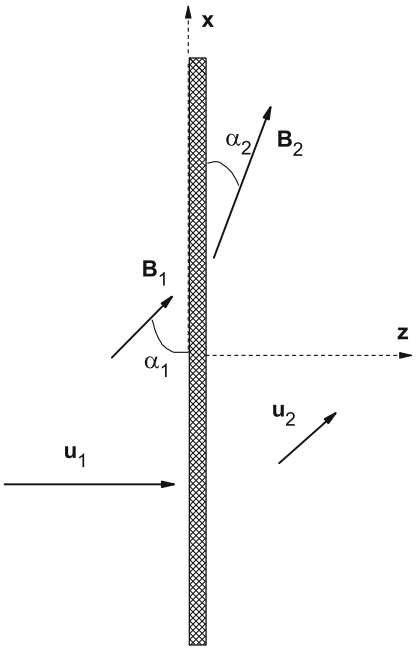

Figure 11.6: MHD shock with arbitrary orientation of magnetic field relative to the front.

3. In the case of purely parallel shock, Fig. 11.7, no electric field is present in the front rest frame, and particle energy is conserved during the front intersection.

11.4.2 Diffusive Particle Acceleration at the Shock Front: Test Particle Approximation

As shown above, a particle energy gain at one shock crossing is quite modest under typical conditions. However, repeating multiple shock crossing by a particle can result in a noticeable energy gain. This multiple crossing can be achieved either by (1) repeating interactions with one shock in a turbulent medium or (2) successive interactions with many shocks. Each of the cases can happen in astrophysical objects. We start here from a relatively simple case of the particle acceleration by single plane boundless stationary shock front in a turbulent medium.

The particle energization at the shock front is supplied by two closely related factors: (1) the presence of turbulent magnetic field (magnetic inhomogeneities) responsible for particle scattering and their random walk and (2) a regular flow of the scatterers that abruptly slows down at the shock front, Fig. 11.8. These two effects emulate the situation similar to the particle

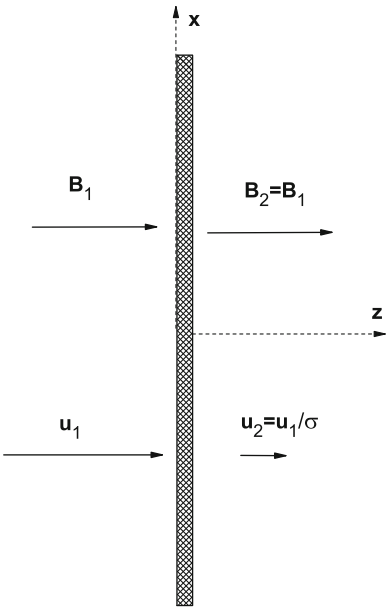

Figure 11.7: Cartoon of a parallel MHD shock.

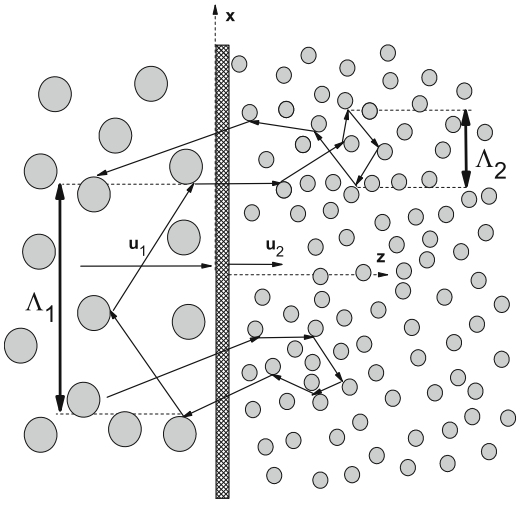

Figure 11.8: Random walk of a particle in turbulent fluid around the shock front.

motion between two walls moving toward each other even though the particle energy is conserved during the very crossing of the front at the parallel shock wave. The walls are emulated by the magnetic inhomogeneity flows and have

the effective thickness of the order of the mfp Λ along the flow direction. The larger the total number of the front crossings the higher the energy it gains in this process from the kinetic energy stored in the shock wave motion. Apparently, each particle is advected far away downstream the front so the energy gain is seized sooner or later.

Let us justify this qualitative picture by balance equation for the particles interacting with a plane front in the turbulent fluid. To do so, integrate Eq. (11.40) with source (11.56) over the entire finite spatial region occupied by the fast particles:

$$\frac{\mathrm{d}E}{\mathrm{d}t} = -\int P(\boldsymbol{r},t)\,\nabla\cdot\boldsymbol{u}\mathrm{d}^3r + \int \mathrm{d}^3r \int\limits_0^\infty N(\boldsymbol{r},p,t)\frac{\mathrm{d}}{\mathrm{d}p}\left(vp^2D(p)\right)\mathrm{d}p. \quad (11.141)$$

Here $E = \int w\mathrm{d}^3r$ is the total energy of accelerated particles. For a 1D case at an infinitely narrow front we have:

$$\nabla\cdot\boldsymbol{u} = \frac{\partial u}{\partial z} = -(u_1-u_2)\delta(z) = -\Delta u\delta(z), \quad (11.142)$$

so the first term in the rhs of Eq. (11.141) yields the particle energy gain proportional to the flow velocity jump at the front:

$$\frac{\mathrm{d}E}{\mathrm{d}t} = \Delta u \int P(x,y,z=0,t)\mathrm{d}x\mathrm{d}y + \int \mathrm{d}^3r \int\limits_0^\infty N(\boldsymbol{r},p,t)\frac{\mathrm{d}}{\mathrm{d}p}\left(vp^2D(p)\right)\mathrm{d}p. \quad (11.143)$$

The second term (stochastic acceleration) is also present (and positive). Since it has already been considered in the previous section we do not specifically consider it here; however, the two corresponding acceleration mechanisms will be compared later based on the obtained solutions.

It should be noted, however, that this picture complicates in the 3D case, e.g., for a shock wave produced by a point-like explosion. In such a case, the fluid compression at the front can be followed by a rarefaction wave, Sect. 5.5.1, where $\nabla\cdot\boldsymbol{u} > 0$. The energy balance takes the form

$$\frac{\mathrm{d}E}{\mathrm{d}t} = \Delta u_n\, P(\boldsymbol{r},t)|_S - \int P(\boldsymbol{r},t)\nabla\cdot\boldsymbol{u}\,\mathrm{d}^3r, \quad (11.144)$$

where the first (positive) term describes acceleration at the front, while the second one arises due to adiabatic cooling (deceleration); the stochastic acceleration is discarded. The net effect is specified by the balance of these two processes. Below, we concentrate on the acceleration effect at the front.

As usual, there is no simple and reliable way of estimating the fraction of particles injected into the shock acceleration process. We can expect that

the main injector is the front itself as the small-scale turbulence capable of resonantly interacting with thermal and slightly supra-thermal particles is supposed to be enhanced there owing to numerous possible wave–particle instabilities, see Chap. 4. Having this in mind, we adopt the particle injection density at the front:

$$Q = Q_0 p_0^2 \delta(p - p_0)\delta(z). \tag{11.145}$$

The injection momentum p_0 is reasonable to adopt around a few times larger than the thermal particle momentum. Apparently, the shock front can also accelerate particles with the momentum above p_0 if they are available in the inflow coming from infinity, which is considered in Problem 11.7.

Return to the 1D problem with all the variables dependent on only one coordinate z, which is parallel to the front normal and write down Eq. (11.36) without stochastic acceleration, while with a source, for two regions: (1) upstream, $z < 0$, and (2) downstream, $z > 0$, Fig. 11.8:

$$\frac{\partial}{\partial z}\kappa(z,p)\frac{\partial N}{\partial z} - u\frac{\partial N}{\partial z} + \frac{p}{3}\frac{\partial N}{\partial p}\frac{\mathrm{d}u}{\mathrm{d}z} + \frac{Q_0}{p_0^2}\delta(z)\delta(p - p_0) = 0. \tag{11.146}$$

Here the fluid velocity profile corresponds to a step-function jumping from $u_1 = \text{const}$ to $u_2 = \text{const}$. The considered linear acceleration regime implies that only a minor fraction of the available shock free energy is being spent for acceleration; thus, the fluid velocity profile does not change. The coefficient of spatial diffusion $\kappa(z,p) \equiv \kappa_{zz}(z,p)$ is defined by the level and spectrum of turbulence and energy of accelerated particles. Again, within the linear theory, it is a given function of its arguments.

Then, we need boundary conditions at the front and infinities. At the front, the distribution function N is continuous

$$N_1 = N_2, \qquad z = 0, \tag{11.147}$$

while the derivatives $\partial N/\partial z$ are bounded everywhere. The second derivatives have a δ-function singularity. To specify the second boundary condition we integrate all terms of Eq. (11.146) over a small distance Δz around the front ($z = 0$). We obtain

$$\kappa_2\frac{\partial N_2}{\partial z} - \kappa_1\frac{\partial N_1}{\partial z} - \frac{p}{3}\frac{\partial N}{\partial p}\Delta u + \frac{Q_0}{p_0^2}\delta(p - p_0) = 0, \qquad z = 0, \tag{11.148}$$

where N denotes the (continuous) value of the distribution function at the front. Without the particle source, the obtained equality reduces to the particle flux conservation condition at the front, Eq. (11.32). With the source, the particle flux has a corresponding discontinuity. At the positive infinity $z \to \infty$ the distribution function is bounded; at the negative one $z \to -\infty$ it goes to zero as all the particles are advected downstream the front by the magnetic irregularities.

Beyond the front, Eq. (11.146) has the form

$$\kappa_{1,2}\frac{\partial^2 N_{1,2}}{\partial z^2} - u_{1,2}\frac{\partial N_{1,2}}{\partial z} = 0 \tag{11.149}$$

whose solution is

$$N_{1,2}(z,p) = A_{1,2}(p)\exp\left(\int\limits_0^z \frac{u_{1,2}\mathrm{d}z'}{\kappa_{1,2}(z',p)}\right) + C_{1,2}(p). \tag{11.150}$$

The undefined functions A and C are determined from the boundary conditions. The conditions at infinities imply

$$N_1(z,p) = A_1(p)\exp\left(\int\limits_0^z \frac{u_1\mathrm{d}z'}{\kappa_1(z',p)}\right), \qquad N_2(p) = C_2(p), \tag{11.151}$$

while from condition (11.148) at the front, which reduces to a simple first-order ordinary differential equation, along with apparent requirement $A_1(p) = C_2(p)$, obtain

$$N_2(p) = \frac{3Q_0}{\Delta u p_0^3}\left(\frac{p_0}{p}\right)^{\alpha}\Theta(p-p_0), \qquad \alpha = \frac{3u_1}{u_1-u_2},$$
$$N_1(z,p) = N_2(p)\exp\left(\int\limits_0^z \frac{u_1\mathrm{d}z'}{\kappa_1(z',p)}\right). \tag{11.152}$$

For the particle flux density $I(K)$ per unit area, unit solid angle and unit kinetic energy range, $K = \mathcal{E} - mc^2$, we use Eq. (11.122):

$$I(K)\mathrm{d}K = vNp^2\mathrm{d}p = Np^2\mathrm{d}K. \tag{11.153}$$

Thus, downstream the front, we have

$$I(K) = \frac{3Q_0}{p_0\Delta u}\left(\frac{K_0^2 + 2mc^2K_0}{K^2 + 2mc^2K}\right)^{\gamma/2}, \quad \text{where } \gamma = \frac{\sigma+2}{\sigma-1} = \alpha - 2, \quad \sigma = \frac{u_1}{u_2} = \frac{\rho_2}{\rho_1}, \tag{11.154}$$

σ is the compression ratio at the shock front.

For ultrarelativistic particles ($K \gg mc^2$, $K_0 \gg mc^2$), the spectrum simplifies to

$$I(\mathcal{E}) = \frac{3Q_0}{p_0\Delta u}\left(\frac{\mathcal{E}_0}{\mathcal{E}}\right)^{\gamma}, \qquad \mathcal{E} \geq \mathcal{E}_0, \tag{11.155}$$

while for nonrelativistic particles ($K, K_0 \ll mc^2$) to

$$I(K) = \frac{3Q_0}{p_0\Delta u}\left(\frac{K_0}{K}\right)^{\gamma/2}, \qquad K \geq K_0. \tag{11.156}$$

Finally, if the injection energy is nonrelativistic ($K_0 \ll mc^2$), while the energy range of interest is relativistic ($K \gg mc^2$), the spectrum receives the form

$$I(\mathcal{E}) = \frac{3Q_0}{p_0 \Delta u} \frac{(2mc^2 K_0)^{\gamma/2}}{\mathcal{E}^{\gamma}}. \tag{11.157}$$

Let us summarize main properties of the diffusive particle acceleration at the shock front and make general assessment of this mechanism applicability:

- Within the 1D model, the spectrum of relativistic accelerated particles has a power law with index γ defined solely by the shock wave strength described by the compression ratio σ of the fluid at the front. For $\sigma = 4$ (that is the largest value for the adiabatic shock wave in nonrelativistic plasma) $\gamma = 2$. The galactic CRs have a power-law spectrum with $\gamma \approx 2.7$ (implying $\sigma \approx 2.8$) within rather broad energy range, $10 \leq \mathcal{E} \leq 10^6$ GeV; for nonrelativistic energies the spectral index is $\gamma/2$. Remarkably, the power-law index does not depend on the detailed turbulence properties around the front.

- The spatial inhomogeneity of the particle distribution is specified by the scale:

$$L = \frac{\kappa_1}{u_1} = \frac{v\Lambda_1}{3u_1}, \tag{11.158}$$

  where Λ_1 is the mfp along the front normal upstream. For fast particles, $v \gg u_1$, this scale L much exceeds the mfp Λ itself. The scale L sets up the distance over which the particles from around the front can travel upstream before returning back to the front by the fluid inflow. The particles occupying the layer with thickness L repeatedly cross the front; the mean number of crossings is about v/u_1.

- Consider energy balance (11.143) and estimate the relative efficiency of diffusive shock acceleration and stochastic acceleration by accompanying turbulence. The first integral in the rhs is estimated as $(u_1 - u_2)P$ as per unit front area, where P is the accelerated particle pressure. To estimate the second integral we use Eq. (11.55) for the diffusion coefficient in which $\langle \Delta u^2 \rangle \equiv \langle \delta u^2 \rangle$ is the mean square of the turbulent velocity. Integration over dz can be replaced by multiplication by the scale of inhomogeneity L upstream the front, Eq. (11.158), which yields the estimate $P\langle \delta u^2 \rangle / u_1$, so the ratio of the two terms is $\langle \delta u^2 \rangle / u_1 \Delta u \ll 1$, if the alfvénic Mach number is large because the turbulent velocity at the prefront region is about the Alfvén speed. It should be noted that the diffusive shock acceleration is linearly proportional to the fluid

velocity jump at the front in contrast to the stochastic acceleration which is proportional to the second power of the turbulent velocity.

- Any real shock front has a finite size and a finite lifetime. The energy range of accelerated particles in which the power law is established depends on the shock wave lifetime, front transverse size, and efficiency of the turbulent diffusion around the front (described by real space diffusion coefficients κ_1 and κ_2). For instance, the acceleration is off for relatively high-energy particles when the mfp Λ_1 reaches the same order as the front size. Available estimates suggest that an isolated shock wave produced by a supernova II explosion can accelerate protons up to 10^4–10^6 GeV, which still has a two order of magnitude uncertainty. Remind that the highest possible acceleration energy of the electrons can be additionally reduced by the radiative (e.g., synchrotron, see Chap. 9) losses.

- As said, the acceleration efficiency is highly dependent on the particle mfp around the front. The smaller the mfp the more efficient the acceleration. Importantly, that the accelerated particles, having a considerable amount of free energy, can themselves enhance the MHD turbulence, which, in its turn, forms the particle mfp. This implies that the detailed solution of the acceleration problem must be consistently linked with a nonlinear self-consistent dynamics of the turbulence generation by the fast particles. On top of that, the electromagnetic radiation, Chap. 9, produced in such a system must take into account the turbulent component of the magnetic field in addition to or instead of the standard synchrotron radiation in a regular magnetic field.

- For an extremely strong shock, $\sigma = 4$, the particle spectral index is $\gamma = 2$ so the energy density of the accelerated particles $w = \int_{\mathcal{E}_0}^{\mathcal{E}_{\max}} \mathcal{E} I(\mathcal{E}) \mathrm{d}\mathcal{E} \sim \ln \mathcal{E}_{\max}$ diverges logarithmically at high-energy limit. This implies that the fraction of the inflow energy transferred to the fast particles can be significant compared with the total available kinetic energy of the flow. In such a case, one more nonlinearity arises: the accelerated particles will affect the front itself, which calls for analysis of this back reaction to the shock front structure including the fluid velocity profile and the pressure and temperature distributions in the fluid flow.

11.4.3 Nonlinear Modification of the Shock Wave Structure by Accelerated Particles

The astrophysical shock waves accelerating particles up to high (ultrarelativistic) energies are typically collisionless. Their front structure (neglecting the fast particle pressure) is specified by the background thermal gas and depends essentially on the prefront magnetic field orientation. In strong quasiparallel shock waves with the alfvénic Mach number above "a few," the thermal front is a narrow transition interface with the thickness of the order of a few ion inertial lengths $c/\omega_{\rm pi}$ (see Sect. 5.4.2), which is filled with strong magnetic field fluctuations $\delta B/B \approx 1$ with frequencies below the ion gyrofrequency. These fluctuations are supplied by a number of kinetic instabilities arising in the counter-streaming flows formed by upstream and downstream particles (see Chap. 4 for some examples) and, likely, play a dominant role for the particle injection into the acceleration process.

As the fast particle pressure grows, an extended region, where the incoming flow gradually decelerates (called the prefront), develops upstream the thermal front. The prefront appears because the accelerated particles take the energy away from the inflow. The fast and background particle interaction is mediated by the turbulence in the form of random magnetic irregularities. This can be either a given "predefined" turbulence or, more importantly, self-generated one by the accelerated particles themselves. This process brings a positive loopback to the system (the more the accelerated particle number, the stronger the turbulence) further facilitating the energy transfer to the accelerated particles.

In the latter case, the turbulence is also fed by the energy of the shock wave, and so the turbulent pulsations represent one of the dynamic ingredients affecting structure of the shock transition. Nevertheless, in a strong shock wave, most of the energy is shared between the fluid flow and accelerated particles, while the dynamic role of the turbulence remains minor, which could imply that the turbulence evolution passively follows the coupled evolution of the flow and fast particle. For this reason, here we consider the turbulence in the vicinity of the shock transition to be specified by an external source and fixed.

The prefront thickness is defined by parameter L, Eq. (11.158), which can exceed the thermal front thickness by orders of magnitude. Therefore, we adopt the thermal front to be infinitely narrow. While the accelerated particle pressure grows, the amplitude of the fluid velocity jump at the thermal front decreases and the hydrodynamics allows its full disappearance in case of plane geometry.

The prefront thickness depends, by means of the diffusion coefficient, on the particle energy: the higher the energy the thicker the prefront. Note that for a given geometry and the turbulence spectrum, the turbulence cannot confine at the front vicinity the particles with energies above some $\mathcal{E}_m$; these particles run away from the front and lose any connection with it. This implies

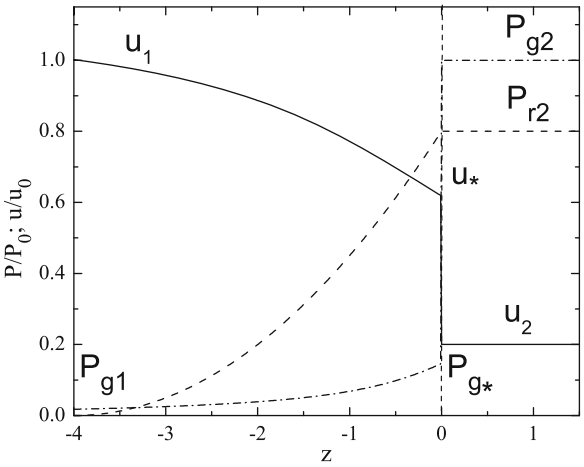

Figure 11.9: Nonlinear modification of a strong shock front by accelerated particles. A thermal jump arises at $z = 0$ with jumps of the fluid velocity $\Delta u = u_* - u_2$ and pressure $\Delta P = P_{g2} - P_{g*}$. The velocity and pressure change smoothly at the prefront region, $z < 0$. The accelerated particle pressure has no jumps; it asymptotically vanishes at the prefront.

that such a shock wave suffers significant additional energy loss related to these runaway particles; thus, the shock wave becomes a nonadiabatic one. Indeed, this kind of energy loss has an effect similar to the radiative losses from the optically thin heated plasma downstream the front, so it gives rise to an increase of the compression ratio at the front: the enhanced compression is provided by a relatively smaller downstream temperature as some of the energy, which would otherwise heat the plasma, is transferred to the runaway particles and so does not contribute to the plasma heating.

Let us quantitatively consider a purely hydrodynamic model (no MHD effect included) of the shock transition with the account of the energetic ions, whose pressure is supposed to be comparable with the dynamic pressure of the background gas forming the shock. Below we use the hydrodynamics of three-component fluid, namely, background electrons and ions and the accelerated ions, whose energy density is comparable with the energy density of the gas flow, while the number density is small compared with the background number density. This simplified approach, avoiding the use of kinetic equations, does not yield any detailed information (e.g., a distribution function) at the shock transition. Nevertheless, it does allow drawing a qualitatively correct flow structure and get important links between a number of macroscopic parameters.

Figure 11.9 outlines the front structure modified by a strong fast particle pressure. Key parameters forming this structure are the overall compression ratio in the flow σ and the fraction η of the dynamic pressure transferred to the fast particle pressure:

$$\sigma = \frac{u_1}{u_2} = \frac{\rho_2}{\rho_1}, \qquad \eta = \frac{P_{r2}}{ju_1}, \tag{11.159}$$

where u_1 and ρ_1 are the fluid velocity and mass density far away upstream; u_2 and ρ_2 are the corresponding parameters downstream; $\rho = \rho_g + \rho_r$, the subscript g denotes the background gas, while r the energetic (relativistic) particles; P_{r2} is their pressure behind the front; and $j = \rho_1 u_1$ is the full flux of the mass through the front. The figure also displays the thermal jump of the fluid velocity at the front $u_* - u_2$ and thermal pressure jump at the front $P_{g2} - P_{g*}$; energetic particles freely cross the front, so their pressure is continuous there.

Let us write down the continuity conditions for the fluxes of the mass j, momentum Π_{zz}, and energy q through the front, analogous to Eqs. (5.61) and (5.62) valid for a shock wave without accelerated particles:

$$j = \rho(z)u(z) = \rho_1 u_1, \tag{11.160a}$$

$$\Pi_{zz} = ju(z) + P_g(z) + P_r(z) = ju_1 + P_{g1}, \tag{11.160b}$$

$$q = \frac{1}{2}ju^2(z) + \frac{\gamma_g}{\gamma_g - 1}u(z)P_g(z) + \frac{\gamma_r}{\gamma_r - 1}u(z)P_r(z) - \frac{\overline{\kappa}(z)}{\gamma_r - 1}\frac{\mathrm{d}P_r}{\mathrm{d}z} + q_m\Psi(z) = \frac{1}{2}ju_1^2 + \frac{\gamma_g}{\gamma_g - 1}u_1 P_{g1}. \tag{11.160c}$$

The magnetic field does not enter here because it is continuous at the front within the considered geometry (parallel shock wave). The energy flux is written with the account of the relation between the energy density and the pressure for the ideal gas familiar from the statistical physics:

$$P_g = (\gamma_g - 1)\epsilon, \qquad P_r = (\gamma_r - 1)w, \tag{11.161}$$

where ϵ and w are the densities of the kinetic energy of the background gas and the fast particles, respectively, γ_g and γ_r are the corresponding indices of the Poisson adiabats (ratios of specific heats). For a gas composed of nonrelativistic particles $\gamma_g = 5/3$, while for the accelerated component $4/3 \le \gamma_r \le 5/3$; the lower bound $\gamma_r = 4/3$ is achieved for photons and other ultrarelativistic particles. If the distribution function of the accelerated particles is known, one can explicitly calculate γ_r from the second of Eqs. (11.161).

To derive Eq. (11.160c) we simplified diffusive flux (11.43) of the energy to the form

$$q_r^{(d)} = -\overline{\kappa}(z)\frac{\mathrm{d}w}{\mathrm{d}z} = -\frac{\overline{\kappa}(z)}{\gamma_r - 1}\frac{\mathrm{d}P_r}{\mathrm{d}z}, \tag{11.162}$$

where $\overline{\kappa}(z)$ denotes the diffusion coefficient averaged over the energetic particle spectrum. Apparently, this flux includes only the particles with energies

$\mathcal{E} < \mathcal{E}_m$ linked to the front by the turbulence effect. The runaway particles with $\mathcal{E} \geq \mathcal{E}_m$ are included in the term $q_m \Psi(z)$, where q_m is the flux density of the runaway particles and $\Psi(z)$ is their normalized spatial distribution. The function $\Psi(z) = 1$ at $z > 0$ while drops to zero outside the prefront, i.e., at $z \to -\infty$.

In the absence of accelerated particles, the velocity varies only within the thin thermal front, and conservation laws (11.160) enable us to express ρ_2, u_2, and P_{g2} behind the front in terms of incoming flux j, u_1, and P_{g1}, although this is not possible any longer when the accelerated particles are present. This important distinction arises because the conservation laws themselves contain no information about the fraction of particles transferred into the accelerated component from the incoming flux or the energy they gain during acceleration. These parameters themselves depend on the global structure of the shock front, including its smooth part.

Applying Eqs. (11.160a) and (11.160b) to the region $z > 0$, excluding P_{g2} from them, and using notations (11.159), we find a relation

$$\eta = \frac{(\gamma_r - 1)(\sigma - 1)}{\gamma_g - \gamma_r + k\sigma(\gamma_g - 1)(\gamma_r - 1)} \left[\frac{(\gamma_g - 1)}{2} - \frac{(\gamma_g + 1)}{2\sigma} + \frac{1}{M^2} \right] \geq 0. \tag{11.163}$$

Here we have introduced the dimensionless parameters $k = q_m / u_1 P_{r2}$ for the energy flux of escaping particles and $M^2 = j u_i / \gamma_g P_{g1}$ for the square of the Mach number of the incoming nonrelativistic plasma flow.

If $\gamma_r = \gamma_g$ (acceleration up to nonrelativistic energies only) and there is no particle escape, $k = 0$, then the denominator turns to zero, therefore, the expression in square brackets must also go to zero to keep η finite, which yields the familiar compression ratio for the hydrodynamic shock waves:

$$\sigma_{\min}^{-1} = \frac{\gamma_g - 1}{\gamma_g + 1} + \frac{2}{M^2(\gamma_g + 1)}. \tag{11.164}$$

Note that even though the numerator and denominator in Eq. (11.163) both turn to zero in this limiting case, the parameter η remains finite according to its definition (11.159). The compression ratio $\sigma_{\min}$ defined by Eq. (11.164) does not exceed 4 for any Mach number in a nonrelativistic plasma with $\gamma_g = 5/3$. However, for $\gamma_r < \gamma_g$ the compression ratio increases accordingly.

Let us obtain now an upper bound of the accelerated particles pressure using Eq. (11.160b). Applying it to the region behind the front $z > 0$, we have

$$P_{r2} = j(u_1 - u_2) + P_{g1} - P_{g2}. \tag{11.165}$$

The ratio P_{g2}/P_{g1} cannot be lower than implied by the Poisson adiabat $P_g \sim \rho_g^{\gamma_g}$, for a given compression σ, i.e., $P_{g2}/P_{g1} \geq \sigma^{\gamma_g}$. The equality corresponds here to a fluid flow without any thermal jump, when the entropy of the thermal component (per particle) does not change. In such a case, the

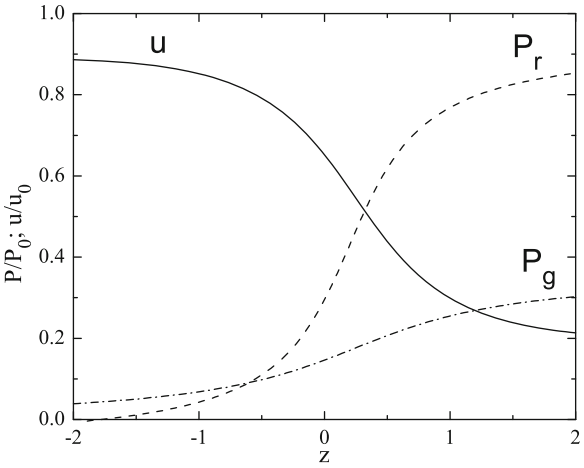

Figure 11.10: Shock front model without the thermal jump, where all the macroscopic parameters vary smoothly. The characteristic spatial scale of the shock "front" is $L \approx \kappa/u_1$, which is controlled by the accelerated particle transport.

total entropy increases at the "shock" transition due only to the particle acceleration. Figure 11.10 displays behavior of the velocity and pressure at the shock transition without the thermal jump. The thickness $L_{\rm sh}$ of the shock front is determined here by the accelerated particle effect. It has the same order of magnitude as thickness of prefront (11.158), $L_{\rm sh} \approx \overline{\kappa}/u_1$. So far, there is no compelling observational case reporting that smooth shock fronts in either laboratory or an astrophysical object; although, this kind of the shock structure must certainly be kept in mind as a theoretically admissible option. Note, however, that an essential requirement for the smooth shock to exit is absence of additional plasma heating in the precursor region. A possible source of the heating is dissipation of the neglected here turbulence generated by the accelerated particles.

From Eq. (11.165) we obtain

$$0 \le \eta \le \eta_m = 1 - \sigma^{-1} + \frac{1 - \sigma^{\gamma_g}}{\gamma_g M^2}, \tag{11.166}$$

which, combined with Eq. (11.163), bounds the range of the involved parameters. The equality in the rhs of Eq. (11.166) defines the dimensionless pressure η_m of the accelerated particles behind the shock transition.

Equation (11.163) and inequality (11.166) specify the allowable range of the compression ratio at the shock wave transition and the energy flux of the escaping runaway particles for a given Mach number. By considering the lower bound put by inequality (11.166) and, accordingly, $k = 0$ implied by $\eta = 0$, we obtain the lower bound of the compression ratio $\sigma_{\rm min}$, Eq. (11.164), i.e., $\sigma > \sigma_{\rm min}$. The upper bound in inequality (11.166) corresponds to the

case when all the excess energy of the incoming flow is transferred to the accelerated particles. Here, there is no thermal jump and, for a given M, the energy of the accelerated particles is highest. Denoting the corresponding compression by $\sigma_{\max}$, we obtain

$$\frac{1}{2}\left(1-\frac{1}{\sigma_{\max}^2}\right)+\frac{1-\sigma_{\max}^{\gamma_g}}{(\gamma_g-1)M^2}=\left[k+\frac{\gamma_r}{\sigma_{\max}(\gamma_r-1)}\right]\left[1-\frac{1}{\sigma_{\max}}+\frac{1-\sigma_{\max}^{\gamma_g}}{\gamma_g M^2}\right]. \tag{11.167}$$

This equation is a generalization of the Hugoniot adiabat to the case of a shock wave with accelerated particles and a smooth front without a sharp thermal jump. It connects four quantities: the Mach number, the energy flux of escaping particles, the compression ratio, and the adiabatic index for accelerated particles. Of them, the Mach number is supposed to be a given externally defined parameter. The quantities γ_r and k can be calculated self-consistently from the corresponding kinetic solution of the problem. The remaining parameter, the maximum compression ratio $\sigma_{\max}$, can be expressed in terms of the other three using Eq. (11.167); it can vary substantially depending on these three other parameters.

Let us consider an important case of strong shock waves, i.e., $M \gg 1$. Neglecting the small terms $(1-\sigma_{\max}^{\gamma_g})/M^2 \to 0$ as $M \to \infty$, Eq. (11.167) yields the compression ratio:

$$\sigma_{\max}=\frac{\gamma_r+1}{(\gamma_r-1)(1-2k)}. \tag{11.168}$$

If nonrelativistic particles predominate among the accelerated particles and the escape effect is small, then $\gamma_r \approx \gamma_g$ and $k \to 0$, so $\sigma_{\max} \approx 4$ that coincides with Eq. (11.164) as $M \to \infty$. Note that although we have assumed that the acceleration leads primarily to nonrelativistic energies, this does not rule out the possibility of the front fuzing. The accelerated nonrelativistic particles have larger transport mfp than the thermal particles, which eventually determines the front thickness when the pressure of the accelerated particles exceeds the pressure of the thermal plasma.

Let us suppose now that relativistic particles dominate the spectrum, $\gamma_r \to 4/3$, and the particle escape occurs with the highest possible rate, i.e., $k \to 1/2$, yielding $\sigma_{\max} \to \infty$ and $\eta_m \to 1$. In this hypothetic case, the gas behind the front would be motionless and infinitely compressed, and all the energy of the incoming plasma flow transferred to escaping particles:

$$q_m = k\,u_1 P_{r2} = k\,\eta_m\, j u_1^2 = j u_1^2/2.$$

Thus, depending on the injection power, acceleration efficiency, and the particle escape conditions, the following range of values is possible for a shock wave with a smooth front:

$$0 < k \le 1/2, \qquad 4 < \sigma_{\max} < \infty; \tag{11.169}$$

these inequalities are, apparently, valid for shock waves with a finite thermal jump as well.

Therefore, for strong shocks with $M \to \infty$, the allowable range of the compression ratio for shock waves with finite thermal jumps and fuzzy fronts:

$$\frac{\gamma_g + 1}{\gamma_g - 1} \le \sigma \le \sigma_{\max} = \frac{\gamma_r + 1}{(\gamma_r - 1)(1 - 2k)}, \tag{11.170}$$

while for finite M this range narrows; it can be found numerically for any given M.

Let us now find the velocity jump u_*/u_1 at the prefront (excluding the thermal front itself) using conservation of the momentum flux. Taking into account that the accelerated particles pass freely through the thermal front, so that their pressure is the same on both sides of it, we find $P_{g2} = P_{g*} + j(u_* - u_2)$. In the region $z < 0$ the fluid velocity varies smoothly, and the pressure of the thermal component follows the Poisson adiabat $P_{g*} = P_{g1} y_*^{-\gamma_g}$, where $y_* = u_*/u_1$. Substituting these relations into Eq. (11.165) and using Eq. (11.163), we find

$$y_* + \frac{1}{\gamma_g M^2 y_*^{\gamma_g}} = 1 + \frac{1}{\gamma_g M^2} - \eta. \tag{11.171}$$

Here the possible values of parameter η are bounded by inequalities (11.166).

From roots of Eq. (11.171) we have to select one providing $y_* \ge \sigma^{-1}$. In the strong shock wave case $M \to \infty$, the range of values (11.170) for the *global* compression ratio σ corresponds to the range $1 \le \sigma_* \le \sigma_{\max}$ for the *local* compression ratio σ_* at the thermal jump. At the upper bound, σ_* coincides with σ, implying no thermal jump in this (unique) case. For $\sigma < \sigma_{\max}$ we always have $\sigma_* \le \sigma$, i.e., the thermal jump is nonzero, although it can be very small for large M.

Equation for the velocity profile $u(z)$ over the smooth segment $-\infty < z < 0$ can be obtained using conservation laws (11.160b,c). Although the corresponding equation is rather complicated, one can use a simplified interpolation equation retaining all essential physics over the entire domain of the variable $0 \ge z > -\infty$

$$\frac{\mathrm{d}y}{\mathrm{d}x} = \frac{2}{1 - y_m}(1 - y)(y - y_m), \tag{11.172}$$

where a new independent variable has been introduced:

$$\mathrm{d}x = \frac{(1 - y_m)u_1}{2\overline{\kappa}(z)} \left\{ 1 + \frac{\gamma_r - 1}{2} \exp\left[-\int_x^0 \frac{u_1 \mathrm{d}z'}{2\overline{\kappa}(z')} \right] \right\} \mathrm{d}z, \qquad x(0) = 0. \tag{11.173}$$

Equation (11.172) has a solution that satisfies the boundary condition $y(0) = y_*$:

$$y(x) = \frac{y_*(\sigma_{\max} - 1) + [2 - y_*(\sigma_{\max} + 1)] \tanh x}{\sigma_{\max} - 1 + (\sigma_{\max} + 1 - 2\sigma_{\max} y_*) \tanh x}, \qquad x \le 0, \quad y_* > y_m. \tag{11.174}$$

Likewise the usual MHD shock wave, the velocity of the plasma is constant downstream the shock transition: $y(x) = u_2/u_1$ for $x > 0$. For $y_* = y_m$ no thermal jump is present, so the shocked boundary washes out entirely:

$$y(x) = \frac{1}{2}(1 + y_m) - \frac{1}{2}(1 - y_m) \tanh x. \tag{11.175}$$

Here we have a simple solution for a smooth transition between two stationary states [see expression Eq. (5.91)].

Although the fluid velocity profile is rather complex, the distribution function of accelerated particles at the thermal front and behind the front is simple:

$$N(p) = (\alpha - 3)\left(1 - \frac{1}{\sigma_{\max}}\right) \frac{u_1^2 n_{g1}}{c v_0 p_0^3} \left(\frac{p_0}{p}\right)^{\alpha}, \quad p \le p_m. \tag{11.176}$$

However, to calculate the spectral index α and the compression parameter $\sigma_{\max}$ requires a self-consistent (numerical) computation (see, e.g., Toptygin 1997). Note, that an increase of global compression ratio σ leads to a decrease of the exponent α in the momentum spectrum. For relativistic index $\gamma_r = 4/3$ neglecting the particles escape, $(k \to 0)$, the largest possible compression ratio from Eq. (11.170) is $\sigma = \sigma_{\max} = 7$. Thus, Eq. (11.152), $\alpha = 3u_1/(u_1 - u_2) = 3\sigma/(\sigma - 1)$, yields $\alpha = 7/2$. If the particle escape is essential, the spectral index $\alpha < 7/2$.

A prominent feature of the considered non-linear problem is the presence of several (one or three) different solutions for the same set of involved parameters. In particular, for a certain range of injection power, there are regimes corresponding to the same injection, while displaying essentially different global compression ratio, velocity profile shape, and spectra of accelerated particles. The presence of several branches of the solution is typical for many highly diverse nonlinear systems. It is indicative of existing unstable states of the shock transition, being in which the system is capable of a spontaneous transition to another state differing strongly from the original one due to a very small change in, e.g., the injection power, which, thus, can lead to a considerable change of the involved parameters such as the global compression ratio and the spectrum of accelerated particles.

It is worthwhile to note that the outlined picture of the shock nonlinear modification is confirmed by numerous numerical simulations. For example, in a model presented by Vladimirov et al. (2009) the upstream velocity $u(z)$ decreases from u_1 at a numeric boundary $z = z_{feb}$ to $u_* < u_1$ at $z = 0$, then

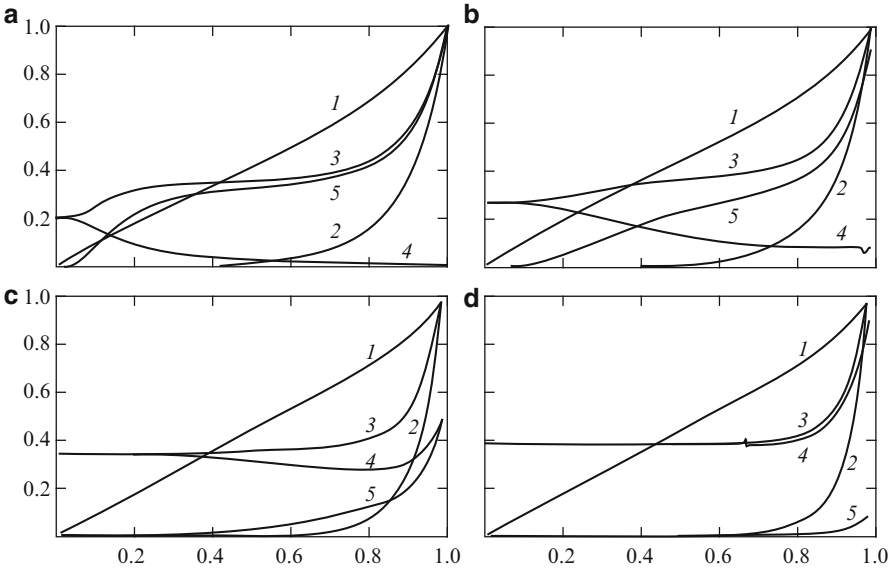

Figure 11.11: The fluid velocity (curves labeled 1), number density (2), and total pressure (3) versus distance from the explosion center in the perturbed (downstream) region, normalized to their values at the inner boundary of the front for various compression ratios: **(a)** $\sigma = 4.01$, **(b)** $\sigma = 4.25$, **(c)** $\sigma = 5.5$, and **(d)** $\sigma = 6.75$. Curves 4 and 5 stand for the relative pressure of either relativistic (4) or nonrelativistic (5) particles normalized to the total pressure at the front.

has a small thermal jump and then, at $z > 0$, reaches a constant downstream value $u_2 < u_*$. The compression ratio was much larger than the classical value of 4: $\sigma = u_1/u_2 = 15$ in a model without the turbulence cascading or $\sigma = 11$ in a model with cascading. Qualitatively, the velocity profile is similar to that shown in Fig. 11.9. The temperature of the background plasma is constant in the prefront in the model without turbulence cascading and experiences strong jump at the thermal jump, while in the model with cascading the temperature increases gradually at the prefront and has a minor jump at the thermal front at $z = 0$.

A plane front with a one-dimensional velocity field considered above does not account a true shape of the shock wave from a strong point explosion. Effect of the accelerated relativistic particles on the spherical shock wave can be analyzed via a generalization of the auto-model Sedov solution for a strong point explosion (Toptygin 2000). Without derivation, Fig. 11.11 shows distributions of the velocity, density, and pressures downstream for various compression ratios. The plots show that as the compression ratio increases, the fluid is "raked up" to the front, so the shell becomes narrower. Distribution of the fluid velocity depends on the compression ratio only weakly, while the full pressure increases greatly. Curiously, the plots imply that the full gas

pressure in the center region of the cavity is dominated by the relativistic particles even if their pressure is small compared with the background gas pressure at the front region.

As has been said, the multiple front crossing by particles needed to ensure an efficient acceleration requires either many shock fronts or an enhanced turbulence level to form a reasonably small particle mfp. We start from the first option, while address the turbulence generation later, in Chap. 12.

11.5 Particle Acceleration by Supersonic Turbulence

11.5.1 Physical Model and Basic Equations

We have already pointed out that the particle acceleration is highly powerful in many astrophysical objects, which implies a correspondingly strong energy release supplying the acceleration. Indeed, the strong energy release gives rise to strong perturbations of the fluid with the stochastic velocities exceeding that of the linear modes of the fluid, i.e., the sound speed c_s and the Alfvén speed v_A. Apparently, these fast fluid motions will either be produced in the form of shock waves or evolve due to nonlinear front sharpening, Sect. 5.1.4, toward formation of the shocks. On top of that, these shock wave ensembles can be superimposed on large-scale contraction and rarefaction waves along with other gradual turbulent structures with a broad spatial and temporal spectra, Sect. 6.10. This rather complicated turbulence is reasonable to be called supersonic and superalfvénic; a simple model of that strong turbulence produced by multiple supernova explosions has been considered in Sect. 6.10.1 without account of the particle acceleration.

Formation of the strong supersonic turbulence is likely inside galactic superbubbles, Sect. 5.6, produced in the OB associations due to cumulative effect of powerful stellar winds from massive stars and supernova explosions occurring at the end of the massive star evolution lasting $\sim 10^6$–10^7 years. A similar turbulence can be present in other galaxies, especially, in the active galactic nuclei, as well as in powerful solar and stellar flares. A distinctive feature of this strong turbulence is its intermittency, revealing itself in the form of sharp discontinuities (basically, shock waves in the plasma dominated by the kinetic energy or tangential discontinuities, called also the current sheets, in the magnetically dominated plasma). The diffusive particle acceleration near the shock fronts results in a corresponding intermittency of the fast particle distribution; the acceleration time of bulk of the particles is short compared with typical time of the acceleration region evolution, so we adopt a stationary turbulence for an initial qualitative consideration of the acceleration effect.

Since efficient acceleration occurs near an MHD shock front, the spatial distribution of the fast particles has an inhomogeneity there with a spatial scale $l \sim \kappa/u \approx v\Lambda/3u$, where u is the front velocity and κ is the local diffusion coefficient along the front normal. This diffusion is caused by macroscopic

small-scale fluctuations of the turbulent fields, while Coulomb collisions are not suitable for that as they imply severe collisional loss of energy. The formation of the mean accelerated particle spectrum depends on both strength of the fronts and on the ratio of the introduced scale l and the mean distance L between the fronts. The latter scale can apparently be identified with the main scale of the supersonic turbulence.

The corresponding ratio, $L/l = uL/\kappa = Pe$, is in fact the Pecklé number introduced in Sect. 7.3, where we demonstrated that the particle diffusion can be described within the perturbation theory for small Pecklé numbers, $Pe \ll 1$. This remains valid in considering the particle acceleration as well. The other case, $Pe = L/l \gg 1$, is more interesting while much more demanding. Now, a strong spatial inhomogeneity of the fast particle distribution with an established power-law spectrum is formed near each front faster that the mean time L/u between front collisions with each other. The spatial scale of the fast particle cloud is small compared with the main scale of the turbulence, thus, the spatial distribution of the fast particles is highly inhomogeneous with strong spatial enhancements around the fronts, which then will spread out in the volume due to turbulent diffusion after shock–shock collisions. Then, a new strong front will again form a strong inhomogeneity of the fast particle distribution and so on. This qualitative picture is a natural outcome of the intermittency of the supersonic turbulence, namely, of the presence of strong discontinuities (shock waves).

To correctly account the (local) shock front contribution to the overall acceleration by the strong turbulence, we are to use the solution for a single front obtained in Sect. 11.4 and average this solution over volumes with scale l near the fronts. This yields an integral operator describing strong acceleration at a single front. Then, we average over larger regions of the order of the main turbulence scale L. Since $Pe = L/l \gg 1$, the perturbation theory does not apply here, so a renormalization of the kinetic coefficients is called for, which is performed by a method described in Sect. 7.3.2. However, the problem addressed here is much more complicated and it requires more information about the turbulence properties complementary to the pair correlators considered earlier in Sect. 7.3.2.

Specifically, we need the distribution of the shock fronts over the Mach number (or, equivalently, over the velocity jumps). Then, in addition to the spectral functions $T(k, \omega)$ and $S(k, \omega)$ of the vortex and potential motions characterizing pair correlator (7.51), we need two more spectral functions. One of them will describe the correlation between the velocity jumps at different fronts, the other one the correlations between the fronts and rarefaction waves characterized by the divergence $\partial u_\alpha / \partial x_\alpha$ between fronts.

The outlined scheme is basically similar to that presented in Chap. 7; however, much more cumbersome for the reasons explained above. Below we present the overall form of the corresponding equations for further use [see the details in a review by Bykov and Toptygin (1993)]:

1. A simpler case, when the particle acceleration is weak over one turbulence correlation scale L, i.e., the absolute change Δp of the particle momentum satisfies the condition $\Delta p \ll p$. Note that the acceleration at fronts can be arbitrarily strong. Then, the distribution function F of the accelerated particles satisfies the integro-differential equation:

$$\frac{\partial F}{\partial t} - \chi \Delta F = \left(\frac{1}{\tau_{\rm sh}} + C\right) \widehat{L} F + \frac{1}{p^2}\frac{\partial}{\partial p} p^4 D \frac{\partial F}{\partial p} + A\widehat{L}^2 F + \frac{2}{3} C \widehat{L} p \frac{\partial F}{\partial p}. \tag{11.177}$$

The integral operator entering the equation

$$\widehat{L} = \frac{1}{3p^2}\frac{\partial}{\partial p} p^{3-\alpha} \int\limits_0^p {\rm d}p' p'^{\alpha} \frac{\partial}{\partial p'}, \qquad \alpha = \frac{3\sigma}{\sigma - 1}, \tag{11.178}$$

describes strong acceleration of the particles at the fronts, where all the fronts are adopted to be equally strong. The constants $\tau_{\rm sh}$, χ, A, C, and D can be expressed via statistical measures of the fronts and turbulence (cf. Eq. (7.53) for χ in the incompressible case):

$$\tau_{\rm sh} \approx \frac{L}{\Delta u_{\rm sh}}, \ \chi = \kappa + \frac{1}{3}\int \frac{{\rm d}^3 k {\rm d}\omega}{(2\pi)^4} \left[\frac{2T(k,\omega) + S(k,\omega)}{i\omega + k^2\chi} - \frac{2k^2 \chi S(k,\omega)}{(i\omega + k^2\chi)^2}\right], \tag{11.179a}$$

$$D = \frac{\chi}{9}\int \frac{{\rm d}^3 k {\rm d}\omega}{(2\pi)^4} \frac{k^4 S(k,\omega)}{\omega^2 + k^4\chi^2}, \quad A = \chi \int \frac{{\rm d}^3 k {\rm d}\omega}{(2\pi)^4} \frac{k^4 \tilde{\phi}(k,\omega)}{\omega^2 + k^4\chi^2},$$
$$C = \chi \int \frac{{\rm d}^3 k {\rm d}\omega}{(2\pi)^4} \frac{k^4 \tilde{\mu}(k,\omega)}{\omega^2 + k^4\chi^2}. \tag{11.179b}$$

They do not depend on the particle momentum until the particle transport is mediated by the turbulent diffusion. Here, like in Sect. 7.3.2, T and S are the transverse and longitudinal components of the turbulent velocity correlation tensor, while $\tilde{\phi}$ and $\tilde{\mu}$ describe shock–shock and shock–rarefaction velocity correlations, respectively, and $\Delta u_{\rm sh}$ is the mean jump of the fluid velocity at fronts.

2. A more complicated is the case of strong acceleration, $\Delta p \gtrsim p$, between the fronts. Here, in addition to the acceleration at the fronts, the acceleration between them is also described by an integral operator. The corresponding equation is easier to formulate using a logarithmic substitution $\eta = \ln(p/p_0)$, where p_0 is an arbitrary constant momentum:

$$\frac{\partial F}{\partial t} = \int\limits_{-\infty}^{\infty} \chi(\eta - \eta')\Delta F(\boldsymbol{r}, \eta', t)\mathrm{d}\eta' + \left(\frac{\partial}{\partial \eta} + 3\right) \int\limits_{-\infty}^{\infty} D(\eta - \eta')F(\boldsymbol{r}, \eta', t)\mathrm{d}\eta'. \tag{11.180}$$

The Fourier transforms of the core χ and D can be calculated from a set of two transcendental equations (not shown here) containing both spectral functions of turbulence and statistical characteristics of the fronts (Bykov and Toptygin 1993).

11.5.2 Evolution of Particles Accelerated by Strong Turbulence

Let us consider formation of the accelerated particle distribution function by solving Eq. (11.177). To do so we replace the real space diffusion term by a model escape term, F/τ_e, replace the source term by a δ-term, $(1/p_0^2)$ $\delta(p-p_0)\delta(t-t')$, and apply the Green function method (Bykov and Fleishman 1992). The Green function is determined using Laplace transformation in time and Fourier transformation over variable $\ln(p/p_0)$ and then back to physical variables. A remarkable property of this Green function is that it does not depend on detailed properties of the turbulence and shock ensemble at large time, $t \gg \tau_{\mathrm{sh}}$, but depends on the acceleration time τ_{sh}. In particular, for the case of sustained, constant in time, injection rate of the particles into the acceleration, the Green function at $t \gg \tau_{\mathrm{sh}}$ has the form

$$G(p,t) = \frac{\tau_{\mathrm{sh}}}{9p_0^3} \begin{cases} \alpha\left[1 - e^{-\sigma(t-t_{p-})}\right]\Theta(t - t_{p-}), & p \le p_0, \\ (\alpha - 3)\left(\frac{p_0}{p}\right)^3\left[1 - e^{-\sigma(t-t_{p+})}\right]\Theta(t - t_{p+}), & p \ge p_0, \end{cases} \tag{11.181}$$

where

$$\sigma = \frac{3}{(2\alpha - 3)\tau_{\mathrm{sh}}}, \qquad t_{p-} = \alpha\tau_{\mathrm{sh}}\ln(p_0/p), \qquad t_{p+} = (\alpha - 3)\tau_{\mathrm{sh}}\ln(p/p_0). \tag{11.182}$$

In reality, the injection spectrum is not monoenergetic, so to obtain a meaningful solution we have yet to integrate the Green function with a realistic injection function over p_0. In the considered physical system involving an ensemble of strong shocks it is reasonable to assume that these shocks are the main injectors of the seed particles into the global acceleration process, i.e., according to Eq. (11.152) describing the accelerated particle spectrum at a single shock wave we have

$$F_i(p_0) = (\alpha - 3)q_i\frac{p_i^{\alpha-3}}{p^\alpha}\Theta(p_0 - p_i). \tag{11.183}$$

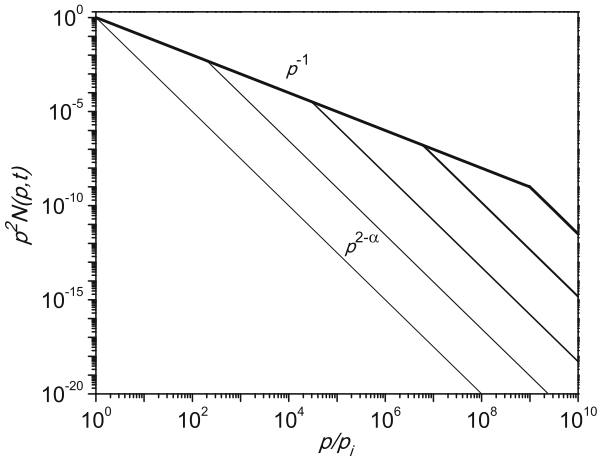

Figure 11.12: A sequence of the accelerated particle spectra described by Eq. (11.184) at $t/\tau_{\rm sh} = 0$, 5, 10, 15, and 20 shown by the lines with correspondingly increasing thickness.

Then, convolution of Eqs. (11.181) and (11.183) yields

$$N(p,t) = \frac{(\alpha-3)q_i\tau_{\rm sh}}{9p_i^3} \begin{cases} \left(\frac{p_i}{p}\right)^3 \left[1 - \frac{e^{-\sigma(t+t_p)}}{1-3\alpha/[(\alpha-3)(2\alpha-3)]}\right], & p_i \le p \le p_*, \\ \left(\frac{p_i}{p}\right)^\alpha \exp(t/\tau_{\rm sh}), & p_* \le p \le p_{\rm max}, \end{cases} \tag{11.184}$$

where $p_* = p_i \exp(t/(\alpha-3)\tau_{\rm sh})$, $t_p = \alpha\tau_{\rm sh}\ln(p/p_i)$, and $p_{\rm max}$ is the maximum possible momentum, which can be set up by applicability of Eq. (11.177), i.e., by a requirement that the advective turbulent transport dominates over the diffusive transport, $\Lambda(p) \ll 3l_*u/v$, or by applicability of the test particle approximation used to obtain solution (11.184). Apparently, solution (11.184) illustrated by Fig. 11.12 describes highly efficient particle acceleration in a form of quickly raising, hard power-law tail with spectral index 3 from original softer tail with spectral index $\alpha \le 4$, which takes only a few $\tau_{\rm sh}$ intervals. Note that the hard spectrum with index 3 recovers the spectral shape obtained in Sect. 11.3.2 for the Fermi acceleration regime with $\tau_a/\tau_d \to 0$.

11.5.3 Particle Acceleration in Galactic Superbubbles

Let us apply solution (11.184) to evaluate particle acceleration in Galactic superbubbles (see Sect. 5.6.2), the objects supplied by strong "mechanical luminosity," $\dot{L}_k \sim 10^{37}$–10^{38} erg/s, formed by mutual action of power stellar winds from massive stars and shock waves generated as these stars start to explode as type II supernovae in 1–3 Myear after formation of the OB association. This strong energy release forms a cavity with radius $R \sim 100$ pc filled

by a hot ($T \sim 10\,\mathrm{MK}$) tenuous ($n \sim 10^{-2}\,\mathrm{cm}^{-3}$) plasma with an ensemble of primary and secondary shocks and accompanying developed turbulence with a broad range of spatial scales. The main scale of the turbulence is reasonable to associate with the mean distance between shock fronts, $l_* \sim 3$–$10\,\mathrm{pc}$, the corresponding plasma velocity fluctuation is about $(1\text{–}3)\times 10^8\,\mathrm{cm/s}$. The original ISM magnetic field is swept out from the volume by the plasma flow, see Sect. 5.5.2; however, the turbulent plasma motions generate a turbulent magnetic field (with the same main scale l_*) with a saturated value of $\delta B \sim 3 \times 10^{-5}\,\mathrm{G}$, see Chap. 8. Here we consider the stage of slow, quasi isotropic expansion of the volume, when the linear scale of it is smaller than the Galactic disk density scale, i.e., before the superbubble blowout into the Galactic halo (Sect. 5.6.2) may come into play.

First of all, as explained in Sect. 11.5.2, we estimate the maximum energy $E_{\max}(p_{\max})$ from the model applicability requirement $3l_* u/(v\Lambda(p_{\max})) = 1$. Using the particle mfp described by Eq. (7.106) for the case when the entire magnetic field is the turbulent field, i.e., $B^2/\langle \widetilde{B}^2 \rangle \sim 1$ and $\nu = 1.7$, we find for protons

$$E_{\max} \sim 10\ \mathrm{GeV}, \tag{11.185}$$

that increases for smaller ν. Thus, for most of the realistic turbulence spectra (Chap. 6) the kinetic equation used is applicable at least up to 10 GeV protons.

The estimate of the test particle approximation applicability is more demanding. To do so we first have to estimate the particle injection rate and then, using solution (11.184), calculate the energy density in the accelerated particle population. As has been said, we assume that the strong shock fronts themselves are the main particle injectors. Thus, the injection rate q_i can formally be written as

$$q_i = \langle \eta n u_{\mathrm{sh}} \Sigma_{\mathrm{sh}} / V_{\mathrm{SB}} \rangle, \tag{11.186}$$

where η is a probability of a background particle interacting with the front to be picked up by the diffusive shock acceleration process, u_{sh} is the front velocity, Σ_{sh} is the shock surface area, V_{SB} is the source volume, the angular brackets denote averaging over the shocks. Observations, modeling, and theoretical considerations suggest the range

$$10^{-5} < \eta < 10^{-1}. \tag{11.187}$$

Now we can use the introduced values to estimate the energy content of the accelerated particles; note that with the hard spectrum, $p^2 N(p) \propto p^{-1}$, the accelerated proton energy density $W_p \sim \int_{p_i}^{p_*} E(p) p^2 N(p) \mathrm{d}p$ is specified by the upper limit, so that $W_p \sim \eta_p n p_* c$. Let us estimate p_m that is the largest p_*, still compatible with the test particle approximation used. Since the kinetic energy density of the large-scale plasma motions is

$$W_k \sim 10^{-10} \left(\frac{u}{10^8\ \mathrm{cm\ s}^{-1}} \right)^2 \left(\frac{n}{10^{-2}\ \mathrm{cm}^{-3}} \right)\ \mathrm{erg\,cm}^{-3}, \tag{11.188}$$

the apparent condition $W_p/W_k < 1$ requires that $p_m/mc < (u/c)^2/\eta_p$, i.e., $E_m \equiv E(p_m) < 1\,\mathrm{GeV}$ for $\eta_p > 10^{-5}$ [Eq. (11.187)] and $u \sim 10^8\,\mathrm{cm/s}$, i.e., well within the applicability range of Eq. (11.177). Within the test particle approximation one can suppose that the particle spectrum evolution described by Eq. (11.184) stops as soon as p_* reaches p_m.

In a reality, however, the accelerated particles become dynamically important and start to modify (i.e., exhaust) the turbulence well before that moment, which calls for much more sophisticated joint analysis of the particle evolution, Eq. (11.177), and the coupled turbulence evolution taking into account the turbulence decay for particle acceleration (Bykov 2001):

$$\frac{\partial S(k,t)}{\partial t} + \frac{\partial \Pi^S(k,t)}{\partial k} = \gamma_{ST} T(k,t) - \gamma_{dS} S(k,t) - \gamma_{CR} S(k,t), \quad (11.189a)$$

$$\frac{\partial T(k,t)}{\partial t} + \frac{\partial \Pi^T(k,t)}{\partial k} = \gamma_{TT} T(k,t) - \gamma_{ST} T(k,t) - \gamma_{dT} T(k,t), \quad (11.189b)$$

where, compared with Eq. (6.133), one more term, $-\gamma_{CR} S(k,t)$, describing the compressible turbulence decay due to particle (CR) acceleration, is added.

Therefore, we arrive at a set of coupled equations, describing generation and nonlinear evolution of the transverse turbulence component, Eq. (11.189b), whose energy density goes partly (term $\gamma_{ST} T(k,t)$) to excite the longitudinal (compressible) component of the turbulence capable of accelerating the charged particles, and the particle evolution, Eq. (11.177). The term $-\gamma_{CR} S(k,t)$ accounts for the energy density balance in such a way that the corresponding decrease of the turbulence energy density is equivalent to the energy gain of the accelerated particles.

Apparently, the obtained set of equations is rather complicated, and so, not surprisingly, no analytical solution to it has been found. Numerical solution of this equation set with monoenergetic injection function (Bykov 2001), whose efficiency is convenient to characterize by the injection energy loading parameter (instead of fraction of electrons η defined by Eq. (11.186))

$$\zeta_\mathrm{i} = \frac{2\int E(p) F_\mathrm{i}(p) p^2 \mathrm{d}p}{D(0)\,\rho\,\langle u^2\rangle} \approx \eta \frac{p_0^2}{m^2\langle u^2\rangle}, \quad (11.190)$$

where $E(p)$ is the particle kinetic energy expressed via its momentum p, reveals a number of interesting features, Fig. 11.13. Initially, the spectrum hardening occurs in agreement with test particle solution (11.184), in particular, the hard spectrum range $p^2 N(p) \propto p^{-1}$ covering about two decades develops by the time of 10^5 years. Soon after that the turbulence power conversion reaches its maximum and the power-law tail growth slows down and stops; afterwards, steeper spectra with breaks up appear. Such spectra are novel compared with the test particle solution; the total energy density in accelerated particles goes down and the distribution function evolves towards a

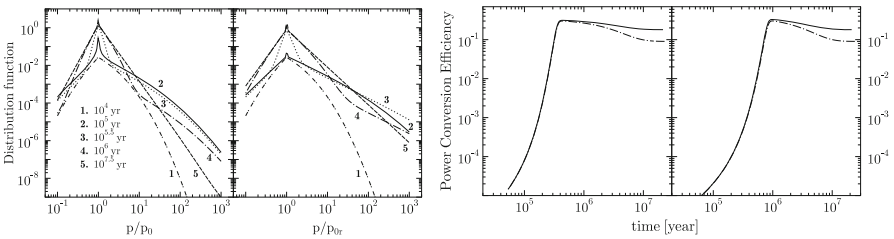

Figure 11.13: *Left double panel* presents time series of accelerated particle spectra ($p^2N(p)$) computed taking into account the accelerated particle back reaction on the turbulence for source scale $R = 220$ pc, monoenergetic injection of 10 keV (*left*) or 10 GeV (*right*), $\zeta = 10^{-3}$. *Right double panel* shows power conversion efficiency for the acceleration patterns shown in the *left double panel*; *dash–dotted* lines display the same measure for a source size of 100 pc; from Bykov (2001).

relatively steep state containing relatively small energy density. Overall, the solution suggests a prominent spectral evolution, which, however, is difficult to directly detect because the timescale of the evolution is long compared to commonly available observation periods.

Details of the distribution function evolution depend on many factors involved. For example, left and right parts of the panels in Fig. 11.13 show evolution for the cases of nonrelativistic (10 keV) and relativistic (10 GeV) injection of protons. Although the spectral patterns are similar, the spectral indices, acceleration times, and final states of the spectra are all different. This behavior is a direct consequence of the nonlinearity of the system under study; in particular, the obtained solutions (even though computed for the monoenergetic source function) do not represent the Green function, i.e., the solution for the case of a more realistic injection function cannot be obtained by integration of the given solution with the source function.

The presented acceleration model shows that the acceleration efficiency by strong supersonic turbulence can be very high, up to ∼30% relative to the accelerating turbulence energy density, although it decreases slightly after reaching the efficiency peak. It is interesting that a similar consideration for even stronger acceleration, described by integral equation (11.180) may result in oscillations of the power conversion efficiency after the peak time (Bykov 1998) instead of monotonic decline in Fig. 11.13, right. It is yet unclear if the equation set considered here can produce similar oscillatory regimes for certain parameter ranges or the monotonic decline represents an intrinsic property of this acceleration process.

11.5.4 Particle Acceleration by Strong Turbulence in Solar Flares

Signatures of particle acceleration in solar flares are obtained from nonthermal radio, X-ray, and gamma radiation (see Chaps. 9 and 10) they generate in

solar corona, from analysis of secondary effects they produce, e.g., on plasma heating or ionization, or from in situ detection of escaping fast particles by specialized spacecrafts in IPM. In particular, modern HXR observations allow investigating spectral evolution during individual subpeaks of the impulsive HXR emission. Often, each such subpeak displays a soft-hard-soft (SHS) evolution; the property, which was earlier established for the impulsive phase as a whole. It is commonly adopted now that the SHS spectrum evolution of the accelerated particle population is an intrinsic property of the acceleration mechanism involved. We note, however, that a fraction of stronger events (typically, the proton reach events) displays a different kind of the spectral evolution, namely, soft-hard-harder (SHH) as well as a gradual phase of the impulsive events.

Another important accomplishment is that a significant fraction (some tens of percent) of the released energy goes into nonthermal accelerated particles. This conclusion is also confirmed by the radio data suggesting that in some cases the total energy of accelerated electrons can be as high as 30% of the estimated magnetic energy of the flaring loop. These findings imply that the back reaction of the fast particles on the accelerating agent (e.g., the turbulence) is essential so this back reaction must be properly taken into account by the acceleration model. Based on the model considered in Sect. 11.5.3 we anticipate that taking into account this back reaction dictated by the large energy content in the accelerated particles will also offer a prominent spectral evolution implied by HXR observations as has been said.

To be specific, we adopt the following scenario (Bykov and Fleishman 2009). A process of flare energy release results in formation of large-scale flows and strong MHD fluctuations in a reasonably tenuous plasma with frozen-in magnetic fields. The turbulence is assumed to be confined in the acceleration region; possible turbulence leakage from the acceleration region is compensated by the adopted sustained source of the transverse component of the large-scale turbulence. Particles, however, can escape from the region through its boundaries because of a large mean free path of the particles outside the region. The distribution function $N(\boldsymbol{r}, p, t)$ of nonthermal particles averaged over an ensemble of turbulent motions satisfies kinetic equation (11.177), which we simplify here in several ways. Firstly, because the model does not include shock fronts and other discontinuities, we neglect all terms containing integral operators from the rhs. And secondly, we replace the real space diffusion by the escape term, which yields

$$\frac{\partial N}{\partial t} + \frac{N}{\tau_e} = \frac{1}{p^2}\,\frac{\partial}{\partial p}\,p^4 D(t)\,\frac{\partial N}{\partial p} + F_i(p), \tag{11.191}$$

where $\tau_e = R^2/4\chi$, R is the characteristic size of the acceleration region, χ is the (renormalized) turbulent diffusion coefficient defined by Eq. (11.179a). The particle source term $F_i(p)$ can differ depending on the dominating injection process of the electrons and nuclei. Although we do not consider

explicitly any injection process, we note that there are many ways, e.g. the resonance wave–particle interactions (Sect. 11.3.3) or acceleration by helical turbulence (Sect. 11.2.2), to inject particles into the stochastic acceleration process by strong turbulence considered here. A continuous injection of mono energetic particles (electrons and protons i = e, p) with some injection energy loading parameters $\zeta_{\rm i}$ was adopted.

The model accounts only for the evolution of large-scale (energy-containing) motions with $k\,\Lambda(p) \ll 1$, where $\Lambda(p)$ is particle mean free path due to scattering by small-scale (resonant and nonresonant) magnetic field fluctuations. Although no evolution of the small-scale fluctuations is considered explicitly, see in Sect. 12.1, a relatively strong level of small-scale scattering is needed to provide $\kappa(p) = v\Lambda(p)/3 < k_0^{-1} \cdot \sqrt{\langle u^2 \rangle}$, which is required for Eq. (11.191) to be valid. Kinetics of particles satisfying this inequality is determined by turbulent advection and so does not depend on the details of the small-scale diffusion coefficient $\kappa(p)$. The energy range, where this inequality holds, does depend on the charged particle mean free path $\Lambda(p)$. The estimates show that it is typically fulfilled for electrons up to a few MeV, where the particle transport is fully driven by the large-scale turbulence and as so it does not depend on the actual momentum dependence of the mean free path $\Lambda(p)$. In fact, this acceleration regime is an advanced version of considered in Sect. 11.1.3 magnetic pumping.

Then, Eqs. (11.189) for the turbulence evolution can also be simplified. In particular, the transverse component of the turbulence $T(k, \omega, t)$ decays slower than the longitudinal component $S(k, \omega, t)$ because only the latter explicitly decays due to particle acceleration; thus, $T(k, \omega, t) \approx$ const over the time interval of interest. Accordingly, the temporal evolution of the spatial diffusion coefficient χ is very slow since in Eq. (11.179a) it is dominated by the transverse component of the turbulence; thus, the escape time τ_e depends on neither time nor particle energy.

Finally, in case of a single scale long-wavelength injection of the turbulent motions (gaussian spectrum with the characteristic wave number k_0) we can safely neglect in Eq. (11.189a) both cascading term in the lhs and direct turbulence damping $\gamma_{dS} = 0$ in the rhs. We, therefore, consider a simplified equation for $S(k, \omega, t)$

$$\frac{\partial S(k, \omega, t)}{\partial t} = \gamma_{ST} T(k, \omega, t) - \gamma_{\rm ap} S(k, \omega, t), \tag{11.192}$$

where the expression for the damping rate of large-scale turbulence due to particle acceleration $\gamma_{\rm ap} = \theta D$. The θ parameter was determined (iteratively) in such a way as to preserve conservation of the total energy in the system of the turbulence and the particles with account for energetic particle escape from the acceleration region. Although this simplified set of equations neglects many of potentially important effects, it, nevertheless, properly takes into

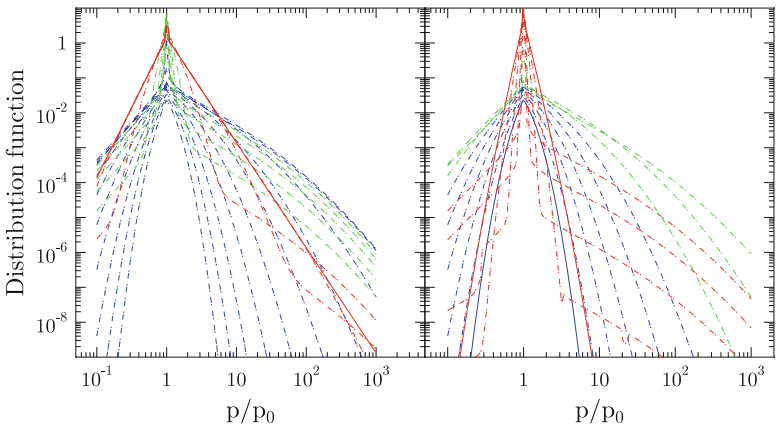

Figure 11.14: Temporal evolution of particle distribution function (sequence of p^2N vs p/p_0 plots, where p/p_0 is the dimensionless particle momentum normalized by the injection momentum p_0) simulated within a flare acceleration region of the scale size $R = 14\pi/k_0$ for the particle injection energy loading parameters $\zeta_e = 10^{-3}$ (*left panel*) and $\zeta_e = 0.1$ (*right panel*). Particle spectra are shown in 20 logarithmically distributed consequent time frames measured in $t\,D(0)$ starting from 0.01 to 30. For some typical parameters, e.g., $R = 2 \times 10^9$ cm, B=300 G, $n = 10^9 - 10^{11}$ cm^{-3}, we have $v_A \simeq 2.2 \times (10^8 - 10^9)$ cm/s, and the characteristic acceleration time $\tau_{acc} \equiv 1/D(0) \simeq 1$–10 s in agreement with HXR (Grigis and Benz 2006) and radio (Bastian et al. 2007) observations (Bykov and Fleishman 2009). Reproduced by permission of the AAS.

account the nonlinear coupling between accelerated particles and accelerating compressible turbulence.

Figure 11.14 shows the particle distribution function ($\propto p^2N$) computed within the model for $\zeta_e = 10^{-3}$ (left panel) and $\zeta_e = 0.1$ (right panel). Although there are apparent differences in particle spectra for different ζ_e, all of them display clearly SHS behavior of the spectra of accelerated particles. The origin of this spectral evolution is easy to understand within the proposed model. Initial phase of the acceleration occurs in the linear regime (test particle approximation is still valid at this stage), which results in effective particle acceleration by the longitudinal large-scale turbulent motions and spectral hardening. Then, the fast particles accumulate a considerable fraction of the turbulent energy by the end of the linear stage and start to exhaust the turbulence, thus, the efficiency of the acceleration decreases, which first affects higher-energy particles resulting in the spectrum softening. Remarkably, the slope of the spectrum at the late decay phase (red solid curves) depends strongly on the injection efficiency ζ_e. In fact, the final spectrum is much steeper in case of strong injection compared with weak injection. Besides the general SHS evolution, we should note that in agreement with previous studies of the stochastic acceleration, e.g., Sect. 11.3.3, these spectra do not obey power laws exactly: breakups and breakdowns are evident from the plots.

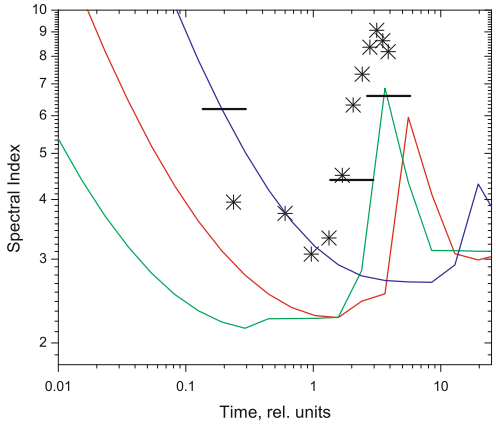

Figure 11.15: HXR spectral index evolution for theoretically calculated spectra with various ratios of the escape time to the acceleration time, $T_{esc}/\tau_{acc} = 5$ (*green curve*), 1 (*red curve*), and 0.2 (*blue curve*) and observed from the 04 December 2002 flare, *asterisks*, and from the occulted 06 September 2002 flare, *horizontal dashes* (E. Kontar, private communication) Bykov and Fleishman (2009). Reproduced by permission of the AAS.

11.5.5 Observational Evidence for Stochastic Particle Acceleration in Solar Flares

Observationally, the conclusion of the SHS spectral evolution of the fast electron spectra in impulsive flares came from analysis of HXR data. Therefore, to address the question if the considered acceleration regime and corresponding spectral softening on the flare decay phase are consistent with observations, the HXR spectral evolution must be computed based on the electron spectra presented above. Since it is reasonable to expect that the coronal thin-target HXR emission is closer related to the accelerated electron spectra than the footpoint thick-target emission, Bykov and Fleishman (2009) computed the evolution of the thin-target HXR emission generated by the evolving ensemble of the accelerated electrons (as in Fig. 11.14) and then derived the evolution of the HXR spectral index at $E = 35$ keV to compare with observations of the coronal HXR sources. The model dependences of the HXR spectral index on time are shown in Fig. 11.15 by three curves computed for various ratios of the acceleration time to the escape time. The asterisks in the same plot show the evolution of the HXR spectral index observed for the coronal source in the December, 04, 2002 event (Battaglia and Benz 2006).

The spectral index analysis of the coronal source can in principle be biased by much stronger footpoint contribution; thus, a more reliable way of the thin-target HXR analysis could be the study of the occulted X-ray flares. An example of the corresponding spectral index evolution in an occulted 06 September 2002 flare is shown by three long horizontal dashes in Fig. 11.15.

Even though no theoretical curve is the exact fit to the data, one can clearly note remarkable similarities between theoretical curves and observations including the main SHS behavior and some hardening at the later stage in both model curves and the December 04, 2002 event.

In spite of overall consistency of the model and observed SHS spectral evolution, there are also apparent differences between them. However, dissimilarities between the theory and observations are comparable to the dissimilarities between the spectra observed from different events. Thus, we can ascribe these differences to the effects discarded from the model, e.g., the varying geometry of the source and/or to different regimes of the turbulence generation, cascading, damping, resonant stochastic acceleration of electrons, and various injection regimes. Note that all these mentioned effects will influence the linear stage of the particle acceleration, where we do see the most obvious departure of the model curves from the data; in contrast, during the decay (softening) phase the model and observed curves behaves highly consistently, which confirms that the nonlinearity originated from the fast particle–turbulence coupling does represent the main physical effect controlling the spectrum evolution at the late phase of stochastic acceleration.

Moreover, the considered model offers a consistent way of interpreting the SHH evolution in a subclass of HXR flares. Indeed, the final spectrum in the right panel of Fig. 11.15 is so steep that it is perhaps undistinguishable against background thermal particle distribution (not explicitly included in the model). This means that the sequence of the (dash–dotted) spectra of accelerated electrons in the right panel will reveal itself as SHH evolution of the HXR spectrum. This conclusion is consistent with the fact that the SHH evolution is observed in stronger, often proton reach, events, where enhanced injection of the charged particles (including protons) is likely, and with a recent finding of gradual transitions between SHS and SHH evolution fragments (Grigis and Benz 2008), which requires a common acceleration mechanism for both SHS and SHH evolution patterns. Overall, we conclude that taking into account the nonlinearity, which is unavoidable ingredient in a system where efficient acceleration by strong turbulence occurs, offers a plausible way of interpreting both kinds of the characteristic spectrum evolution, SHS and SHH, observed from solar flares.

A by-product of the adopted here model of the turbulent electron transport is the energy independent, constant in escape time from the acceleration region, which implies that electrons with different energies leave the acceleration site simultaneously: the property required by measurements of the HXR fine structure timing, see Sect. 7.1.1. Furthermore, the decay time of microwave light curves is often independent on the radio frequency, i.e., on corresponding energy of radio-emitting electrons, see an example in Sect. 7.4.4. The electron diffusion due to resonant scattering on turbulent waves can be consistent with this property; however, as shown in Sect. 7.4.4, this requires a certain fine tuning of the model parameters. In contrast, the considered here

turbulent transport regime intrinsically results in an energy-independent residence/escape time. On the other hand, the decay phase, even if mediated by turbulence, is a post-acceleration phase, so the parameters derived from the electron transport at this stage are not directly relevant to the acceleration region. From this perspective it would be valuable to derive the required parameters directly from the acceleration region analysis.

However, detection of X-ray and radio emission from the acceleration region is difficult. The detection of X-rays from the acceleration site is challenging due to (i) a relatively low density of the surrounding coronal plasma and (ii) the presence of competing emissions, i.e., emission from hot coronal flare plasma and trapped electron populations. In addition, as HXR flux is proportional to the plasma density, the bulk of HXRs is emitted in the dense plasma of the chromosphere (HXR footpoints) biasing the X-ray imaging of tenuous coronal emission. Studies of flares with footpoints occulted by the solar disk (Krucker and Lin 2008; Krucker et al. 2010) provide direct imaging of the looptop X-ray emission but are hampered because essential information on the flare energy release contained in the precipitating electrons becomes unavailable. What is needed is to cleanly separate the acceleration and precipitation regions while retaining observations of both. Stated another way, having both radio and X-ray observations of a flare without significant plasma heating and without noticeable magnetic trapping would provide the needed information on both components to make characterization of the acceleration region possible. Below we consider one (at the time of writing—unique) event whose observed microwave GS emission is produced directly in the acceleration region of a flare, and hence, parameters derived from the microwave spectrum pertain to the directly accelerated electron population and the acceleration region (Fleishman et al. 2011).

X-ray image (Fig. 11.16) clearly shows that the flare has two well-defined footpoints, which are well visible over the entire range of the X-ray spectrum 6–80 keV. The imaging below or around 10 keV does not demonstrate any thermal component in a separate location as is often seen at the top of a loop in flares (see, e.g., Fig. 9.18, right), so all the detectable X-ray emission down to the lowest energy ∼6 keV comes from the footpoints. The flare occurred at the extreme eastern edge of the active region with the weaker X-ray source projected onto the photosphere in a region of strong positive magnetic field, while the stronger X-ray source projects onto a small region of weaker negative magnetic field, as has commonly been observed from asymmetric flaring loops.

Both the number of accelerated electrons and the spectral index demonstrate typical SHS behavior like that considered above. The hardest electron

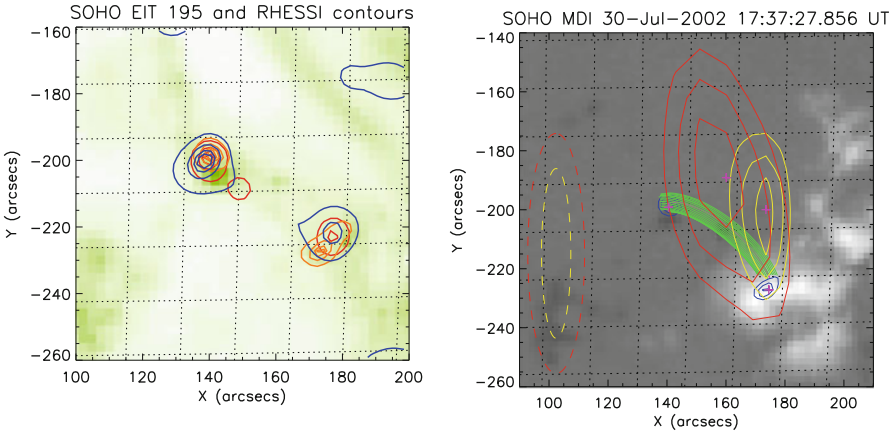

Figure 11.16: *Left panel*: Spatial distribution of X-ray emission (contours at 30, 50, 70, and 90% levels) from July 30, 2002, flares at 9–15 keV (*red*), 15–30 keV (*orange*), and 30–100 keV (*blue*). Time accumulation interval for RHESSI images is 17:37–17:38 UT. Background image is SoHO EIT 195 Å taken just before the flare at 17 : 36 UT. *Right panel*: theclose-up view of the active region and a potential extrapolated flux tube (*green*) connecting two X-ray footpoints (*blue contours*), 2.6–3.2 GHz radio image (*red contours*) and 4.2–8.2 GHz radio image (*yellow contours*). *Magenta plus signs* mark the spatial peaks of the HXR and radio sources. *Dashed ellipses* display the sizes of the synthesized beams (Fleishman et al. 2011). Reproduced by permission of the AAS.

spectra $\delta_x \sim 3.5$ are reached around 17 : 37 : 40 UT. At the same time, the electron acceleration rate has its maximum of $F_{e\,\max}(> 10\ \mathrm{keV}) \simeq 10^{35}$ electrons per second.

Radio imaging performed in two separate bands, 2.6–3.2 GHz and 4.2–8.2 GHz, reveals that the corresponding radio images (Fig. 11.16) are located between the X-ray footpoints although with an offset from their connecting line, which is consistent with the radio sources placement in a coronal part of a magnetic loop connecting the X-ray footpoints. The higher-frequency radio source is displaced compared with the lower-frequency one toward the stronger magnetic field (weaker X-ray) footpoint. No spatial displacement with time is detected for either of the radio sources. Based on the source separation, implied magnetic topology, and the northern HXR source size, the sizes of the radio sources can be estimated as $10''$(transverse the loop)$\times 15''$(along the loop), and the depth of $10''$ for the lower-frequency radio source, which suggests the radio source volume of $V_{\mathrm{radio}} \sim 6 \times 10^{26}\ \mathrm{cm}^3$, and roughly half of that for transverse sizes of the higher-frequency source.

Generally, GS continuum radio emission (see Chap. 10 for more detail) can be produced by any of (1) a magnetically trapped component, Sect. 7.5.3, or (2) a precipitating component, Sect. 7.1.1, or (3) the primary component within the acceleration region, Sects. 11.2.2, and 11.5.4. Remarkably, these three populations of fast electrons produce radio emission with distinctly

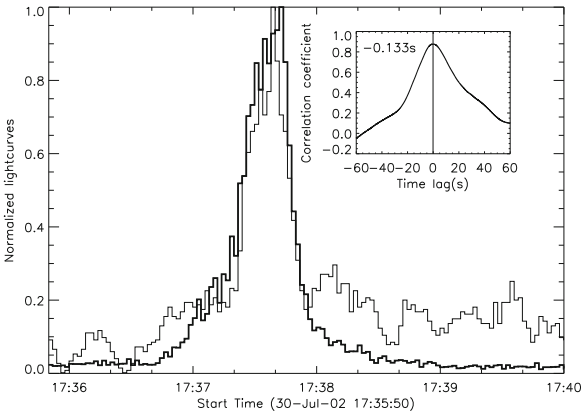

Figure 11.17: RHESSI 30–100 keV (*thick line*) and Phoenix-2 3.2–3.6 GHz (*thin line*) lightcurves of July 30, 2002 flare with 2 s time resolution both. The light curves are highly correlated; no significant delay is present: the lag correlation plot is given in the insert; negative delay means the radio emission comes first (Fleishman et al. 2011). Reproduced by permission of the AAS.

different characteristics. Indeed, (1) in the case of magnetic trapping the electrons are accumulated at the looptop (Melnikov et al. 2002b), and the radio light curves are delayed by roughly the trapping time $\tau_{\rm trap}$ relative to accelerator/X-ray light curves. (2) In the case of free electron propagation, Sect. 7.1, untrapped precipitating electrons are more evenly distributed in a tenuous loop, and no delay longer than L/v is expected. However, even with a roughly uniform electron distribution, most of the radio emission comes from loop regions with the strongest magnetic field. Spectral indices of the radio- and X-ray- producing fast electrons differ here by 1/2 from each other, because $L/v \propto E^{-1/2}$. (3) In the case of radio emission from the acceleration region, even though the residence time (τ_e) that fast electrons spend in the acceleration region can be relatively long, the radio and X-ray light curves are proportional to each other simply because the flux of the X-ray producing electrons is equivalent to the electron loss rate from the acceleration region, $F_e(t) = N_r(t)/\tau_e$.

To address the timing, needed for analysis of the radio data, it is reasonable to compare the radio and HXR light curves. The cross-correlation (Fig. 11.17) displays clearly that the radio and HXR light curves are very similar to each other and there is no delay in the radio component. In fact, the cross-correlation is consistent with the radio emission peaking ∼130 ms earlier. The lack of noticeable delay between the radio and X-ray light curves is further confirmed for all available radio frequencies. Therefore, the magnetically trapped electron component appears to be absent, and the radio emission is formed by either (ii) precipitating electrons or (iii) electrons in the acceleration region or both.

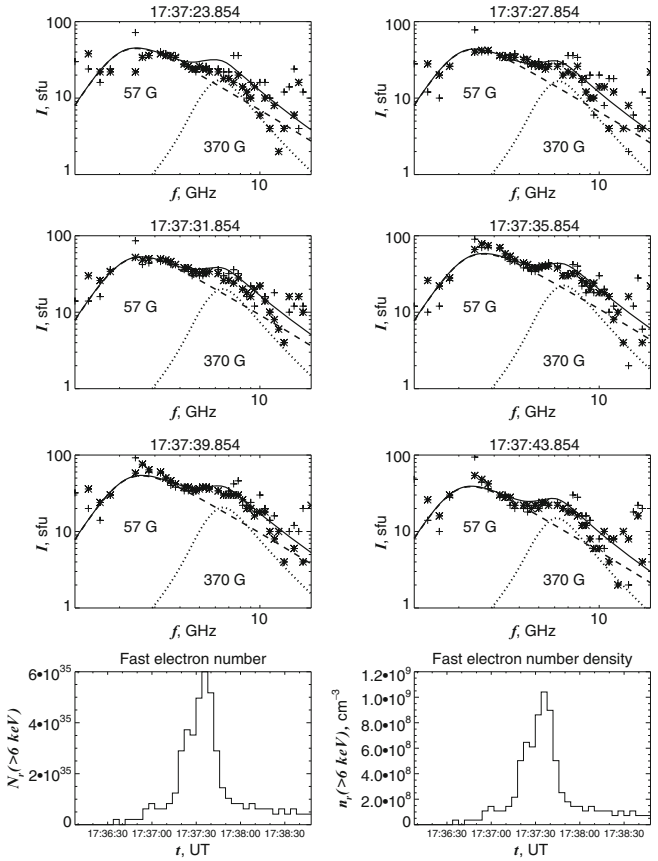

Figure 11.18: OVSA radio spectra obtained by two small antennas (*pluses and asterisks*; differences between them offer an idea about the data scatter vs. frequency) and model GS emission from the acceleration region (*dashed lines*), precipitating electrons (*dotted lines*), and sum of these components (*solid line*). Total number and number density of the fast electrons at the radio source as derived from the OVSA radio spectrum are shown in two *bottom panels* (Fleishman et al. 2011). Reproduced by permission of the AAS.

With the spectrum of energetic electrons from HXR data, it is easy to estimate the radio emission produced by the precipitating electron component. Taking the electron flux, the spectral index of the radio-producing electrons $\delta_r \approx \delta_x + 1/2$, and the electron lifetime at the loop L/v (the time of flight, Sect. 7.1.1), one can vary the magnetic field at the source in an attempt to match the spectrum shape and flux level. However, if we match the spectrum peak position, we strongly underestimate the radio flux, while if we match the flux level at the peak frequency or at an optically thin frequency, we overestimate the spectrum peak frequency; examples of such spectra are given in Fig. 11.18 by the dotted curves.

We conclude that precipitating electrons only [option (ii)] cannot make a dominant contribution to the observed radio spectrum. Indeed, having the spectrum peak at the observed low frequency requires a low magnetic field, see 3D GS modeling in Sect. 10.2.2; however, in a low magnetic field the observed radio flux density requires a relatively large number density of radio-emitting electrons, which, for the given injection rate determined from the HXR data implies a relatively long residence time of the fast electrons in the low-frequency radio source, $\tau_e \gg L/v$. On the other hand, this residence time must be shorter than the radio light curve decay time, $\sim$10 s; otherwise, the decay of the radio emission would be longer than observed. Thus, a reasonable estimate of this lifetime is somewhere between those two extremes $\tau_e \sim 3$ s.

Figure 11.18 displays a sequence of meaningful radio spectrum fits adopting the following parametric dependences and available constraints obtained from the data: $N_{r\,\max}(> 6\ \mathrm{keV}) = \tau_e F_{e\,\max}(>6\ \mathrm{keV})$ with a value of $F_{e\,\max}(>6\ \mathrm{keV}) = 2 \times 10^{35}$ electrons/s and $\tau_e = 3$ s, and the time evolution of $N_r(>6\ \mathrm{keV})$ is assumed proportional to an optically thin gyrosynchrotron light curve. The total lifetime of the electrons in the flaring loop is a sum of the residence time at the radio source and the time of flight between the radio source and the footpoints. As we adopted a constant, energy-independent, electron lifetime τ_e to be much larger than the time of flight $\sim L/v$ we have to accept for consistency that the spectral index of the radio-emitting fast electrons is roughly the same as the spectral index of HXR emitting fast electrons determined above, $\delta_r = 3.5$. The radio source sizes are taken as estimated above based on the flare imaging. The thermal electron number density is adopted to be $n_{\mathrm{th}} = 1.5 \times 10^9\ \mathrm{cm}^{-3}$: the GS spectra are insensitive to this parameter until $n_{\mathrm{th}} \lesssim 2 \times 10^9\ \mathrm{cm}^{-3}$, while at least $n_{\mathrm{th}} = 10^9\ \mathrm{cm}^{-3}$ is needed to supply the observed acceleration rate. The remaining radio source parameter, not constrained by other observations, is the magnetic field B, which is determined by comparing the observed (symbols) microwave and calculated (dashed curves) GS spectra (Fleishman and Kuznetsov 2010) in Fig. 11.18.

Remarkably, that the whole time sequence of the radio spectra is reasonably fitted with a single magnetic field strength of $B \approx 60$ G; the only source parameter changing with time is the instantaneous number of the fast electrons, see Fig. 11.18. The microwave spectra, however, deviate from the model-dashed curves by the presence of a higher-frequency bump at $f \sim 4-8$ GHz. Nevertheless, adding the contribution produced by precipitating electrons (dotted curves) at a larger magnetic field strength B_{leg} peaking somewhere at the western leg (60 G$< B_{\mathrm{leg}} <$1000 G) of the loop as directly follows from the radio imaging, Fig. 11.16, offers a nice, consistent overall fit (solid curves) to the spectra. We conclude that the radio spectrum is dominated by the GS emission from the electron acceleration region with a distinct weaker contribution from the precipitating electrons.

In order to complete the model for this event let us address the 3D structure of the flaring loop. As a zero-order approximation a potential field extrapolation based on the line-of-sight magnetogram is utilized. Figure 11.16 shows that there is a flux tube connecting the two X-ray footpoints, which confirms existence of the required magnetic connectivity. This magnetic loop is highly asymmetric with the magnetic field reaching its minimum value (around 130 G) at the northern footpoint (stronger X-ray source). The length of the central field line is about 4×10^9 cm. We know, however, that the flare phenomenon requires a source of free energy to be released, i.e., a nonpotential magnetic structure. We, therefore, propose that the true flaring loop, connecting two HXR footpoints and two coronal radio sources, is higher and the length of the central field line is somewhat longer; for the estimate we adopt $L \sim 7 \times 10^9$ cm that yields the loop volume $V_{\rm loop} \sim 4 \times 10^{27}\,{\rm cm}^3$ roughly 5 times larger than the radio source volume.

Let us proceed now to the energy release and plasma heating efficiency. The energy release rate $\mathrm{d}W/\mathrm{d}t$ is estimated as the product of the minimum energy (6 keV) and the acceleration rate $F_e(> 6$ keV), which yields $\sim 2 \times 10^{27}$ ergs/s at the flare peak time. Being evenly distributed over the loop volume this corresponds to the averaged density of the energy release of $\sim 0.5\,{\rm erg\,cm^{-3}s^{-1}}$ and, being multiplied by the effective duration $t_{1/2}$, the energy density deposition of $w \sim 12\,{\rm erg\,cm^{-3}}$. Most of this energy is produced in the form of accelerated electrons around 10 keV. During the time of flight in the loop (with density $1.5 \times 10^9\,{\rm cm^{-3}}$ and half length $\sim 3 \times 10^9$ cm) these electrons lose about $\Delta \simeq 15\%$ of their initial energy. Thus, we can estimate the plasma heating by the accelerated electrons up to $T \simeq w/(1.5 k_{\rm B} n_{\rm th}) \times \Delta \sim 5$ MK, where $k_{\rm B}$ is the Boltzmann constant. Combined with a relatively low emission measure of this tenuous loop, this heating is undetectable by X-ray spacecrafts (GOES and RHESSI), even though the acceleration efficiency is extremely high.

The observed properties of the acceleration region allow to narrow the range of possible acceleration mechanisms in this event: indeed neither DC field acceleration (inconsistent with the long residence time of fast electrons) nor acceleration in collapsing magnetic traps (inconsistent with constancy of the magnetic field at the source and with constancy of its spatial location) is relevant for this case, while they are fully consistent with the stochastic acceleration in a magnetic loop, when a standard, relatively narrowband, GS emission is produced at a given volume (permitted with a loop magnetic field) by the electrons accelerated there by a turbulence, whose side effect is to enhance the electron trapping ("strong diffusion transport regime," Sect. 7.5.3) and so increase, as observed, their residence time at the acceleration region. The electron acceleration efficiency is very high in the flare, so almost all available thermal electrons are eventually accelerated. Some sort of stochastic acceleration process is, therefore, needed to account for an approximately energy-independent lifetime of about 3 s for the electrons in

the acceleration region. All these discovered properties of the acceleration region, in particular, high acceleration efficiency, SHS evolution, and constant residence time independent on either electron energy or time, are naturally consistent with the considered above nonresonant electron acceleration by strong turbulence. We conclude that detection of GS radio emission from a region of the electron stochastic acceleration by strong turbulence is likely in this event.

Let us summarize the physical parameters of the detected acceleration region in this solar flare: the apparent source area is $10'' \times 15''$; the source volume is $V \sim 6 \times 10^{26}\,\mathrm{cm}^3$; $F_{e\,\max}(>6\ \mathrm{keV}) = 2 \times 10^{35}\,\mathrm{electrons/s}$; $\tau_e = 3\,\mathrm{s}$; $N_{r\,\max}(>6\ \mathrm{keV}) = 6 \times 10^{35}\,\mathrm{electrons}$; magnetic field $B \sim 60\,\mathrm{G}$; $n_{\mathrm{th}} \sim 1.5 \times 10^9\,\mathrm{cm}^{-3}$; duration $\sim$30 s. Based on these acceleration region parameters we can estimate some properties of the MHD turbulence needed to provide the residence time of the order of 3 s. Indeed, for a strong while smooth turbulent motions, $u \sim v_{\mathrm{A}} \approx 3 \times 10^8\,\mathrm{cm/s}$ for the obtained magnetic field and thermal density. Then, the escape time is $\tau_e \sim L^2/4\chi \approx L^2/(4v_{\mathrm{A}}l_*)$. Substituting the observed values of v_{A}, $L \sim 10^9$ cm, and τ_e, we can estimate the main scale of the MHD turbulence to be $l_* \sim 2 \times 10^8$ cm, which is in full agreement with the idea of acceleration by large-scale turbulence (l_* is much smaller than the source size L as needed). We conclude that the nonlinear acceleration of electrons by strong large-scale MHD turbulence is a plausible mechanism capable of driving the bulk particle acceleration in solar flares compared with other logical possibilities, some of which (runaway electrons in DC electric fields, in reconnecting current sheets, or particle energization in collapsing traps) have been considered in this chapter, whose role seems more local.

Problems

11.1 Particles accelerated at the Sun propagate in the radial solar wind that has a speed $u = \mathrm{const}$ and suffer the adiabatic cooling. The transport mfp is small, so one can neglect the diffusion term in Eq. (11.36). Calculate dependence of average (over the spectrum) particle energy on the distance from the Sun.

11.2 Heavy rigid magnetic clouds (magnetic mirrors) move one dimensionally with the same nonrelativistic velocity $u \ll c$ in the observer's reference frame; the number of the clouds moving in each direction (back and forth along Ox axes) is the same on average. Calculate the change of relativistic particle energy due to a head-on or tail-on collision. Demonstrate that the particle energy increases exponentially with time and determine the characteristic time τ_a of the e-folding energy increase. Adopt the mean collision frequency of the particles with clouds ν to be known.

11.3 Obtain fast particle distribution function from Eq. (11.61) with the initial condition $N(p,0) = N_0 p_0^{-2}\delta(p-p_0)$ (i.e., consider the Fermi acceleration for a constant transport mfp $\Lambda = \text{const}$).

11.4 Assume that in the case considered in the previous problem, the acceleration is off in a finite time due to the turbulence decay. This process can be described by Eq. (11.61) adopting the acceleration time $\tau_a(t)$ to depend on time in such a way that $\tau_a \to \infty$ at $t \to \infty$. Determine the accelerated particle spectrum after the turbulence decay.

11.5 Consider the problem of the particle acceleration similar to that considered in Sect. 11.3.2, but for a spherical region with the radius a and with the account of boundary conditions. The diffusion coefficient in the momentum space $D(p) = p^2/\tau_a$ is only nonzero inside the sphere. The spatial diffusion coefficient $\kappa = \text{const}$ is constant and same in and out the sphere. Particles with a momentum p_0 are injected into the acceleration process uniformly inside the sphere.

11.6 For conditions of Fermi acceleration modified by the adiabatic losses studied in Sect. 11.3.4 consider limiting cases such as: (a) no adiabatic loss is present, $u = 0$, and (b) no acceleration is present, $D = 0$.

11.7 Adopt that a plane front considered in Sect. 11.4.2 does not inject particles, while there are fast particles with a distribution over momentum $N_0(q)$ (in the range $q_{\min} \le q \le q_{\max}$) in the inflow. Assume that $q_{\min}$ exceeds the minimal injection momentum p_0 needed for the diffusive shock acceleration to operate. Calculate the accelerated particle spectrum at the front.

11.8 ⋆ Consider the particle acceleration by a stationary spherically symmetric termination shock formed at the transition from a supersonic to subsonic flow in a stellar wind. Adopt the following stellar wind model:

$$\kappa = \kappa_1 = \text{const}, \quad u = u_1 = \text{const} \quad \text{at} \quad r < r_0;$$
$$\kappa = \kappa_2(r), \quad u = u_2 \left(\frac{r_0}{r}\right)^2 \quad \text{at} \quad r > r_0.$$

The shock front is located at $r = r_0$ and has a velocity jump $\Delta u = u_1 - u_2 > 0$. In the subsonic region, $r > r_0$, the fluid velocity decreases as r^{-2}, which implies expansion with a constant density. Adopt the injected particle population in the form $Q(r,p) = (Q_0/4\pi r_0^2 p_0^2)\delta(p-p_0)\delta(r-r_0)$. Calculate the accelerated particle spectrum over momentum and their spatial distribution.[4]

[4] Recall, Sect. 2.5, most of active stars have a stellar wind with $u_1 \approx (2\text{–}3) \times 10^8$ cm/s, $r_0 \approx 3\text{–}10$ pc $\approx 10^{19} - 3 \times 10^{20}$ cm. The solar wind has much more modest parameters: $u_1 \approx 4 \times 10^7$ cm/s, $r_0 \approx 90$ au $\approx 1.4 \times 10^{15}$ cm, see Sect. 2.5.1 .

Answers and Solutions

11.1 Use Eq. (11.47). By definition we have $\nabla \cdot \boldsymbol{u} = 2u/r$. The particles with small mfp propagate with the solar wind velocity, thus, $\mathrm{d}t = \mathrm{d}r/u$. Integrating Eq. (11.47), we find $\overline{K} = \overline{K}_0(r_0/r)^{4/3}$ in the nonrelativistic case, where $K = \mathcal{E} - mc^2$ is the particle kinetic energy and r_0 is the inner radius of the solar wind region. The solar wind temperature will drop with the same law if no heating source is available. In the ultrarelativistic case we have $\overline{\mathcal{E}} = \overline{\mathcal{E}}_0(r_0/r)^{2/3}$.

11.2 At the head-on collision the particle gains energy $\Delta\mathcal{E}_+ \approx 2\mathcal{E}u(v + u)/c^2$, while at the tail-on collision it loses energy $\Delta\mathcal{E}_- \approx -2\mathcal{E}u(v-u)/c^2$. So, if the collisions were equally frequent, then the result of *two collisions* would be $\Delta\mathcal{E}_\pm \approx 4\mathcal{E}u^2/c^2$ on average, or $\Delta\mathcal{E}_\pm \approx 2\mathcal{E}u^2/c^2$ *per one collision*. On top of that, we have to take into account that the head-on and tail-on collisions have uneven rates, so they must be added with their corresponding statistical weights proportional to the relative velocities[5] of the colliding agents: $w_\pm = (v \pm u)/2v$. Account of these nonequal weights further doubles the energy change $\Delta\mathcal{E}_\pm \approx 4\mathcal{E}u^2/c^2$ per one collision; thus, per unit time we have: $\mathrm{d}\mathcal{E}/\mathrm{d}t = \nu(w_+\Delta\mathcal{E}_+ + w_-\Delta\mathcal{E}_-) = 4\nu(u/c)^2\mathcal{E}$. This yields exponential energy growth $\mathcal{E}(t) = \mathcal{E}_0 \exp(t/\tau_a)$ with the e-folding time constant $\tau_a = c^2/4u^2\nu$.

11.3 The equation is reduced to the diffusion equation by the variable substitution

$$x = \ln(p/p_0),\ \tau = t/\tau_a,\ \tau_a = p^2/D(p) = \mathrm{const}$$

and factorizing the unknown function as follows:

$$N(p,t) = N_0(pp_0)^{-3/2}e^{-9\tau/4}f(x,t).$$

The function f represents a solution of the 1D diffusion equation

$$f(x,t) = \frac{1}{(4\pi\tau)^{1/2}}\exp\left(-\frac{x^2}{4\tau}\right), \qquad \overline{p} = p_0 e^{4\tau/\tau_a}.$$

This acceleration regime yields a very hard spectrum with a lot of high-energy particles, while energy of each single particle grows exponentially. It must be noted, however, that any real magnetic cloud becomes more and more transparent for particles with higher and higher energy, which reduces the acceleration rate. In addition, acceleration region has always a finite size, which implies finite acceleration time. Eventually, any acceleration occurs only up to a finite energy.

[5] We note here that the relative velocity of two bodies can exceed the speed of light c in some inertial reference frame.

11.4 This problem is reduced to the previous one by introducing a dimensionless time: $\tau = \int_0^t \mathrm{d}t'/\tau_a(t')$. The spectrum is described by the previous solution where the dimensionless time τ is replaced by a finite value $\tau_0 = \int_0^\infty \mathrm{d}t/\tau_a(t)$, where $\tau_a(t) = p^2/D(p,t)$. The diffusion coefficient must decay faster than t^{-1} at $t \to \infty$.

11.5 In Eq. (11.116) replace the term N/τ_d by original isotropic diffusive term

$$\frac{\kappa}{r^2}\frac{\partial}{\partial r}r^2\frac{\partial N}{\partial r},$$

while the source term by

$$(Q_0/p_0^2)\delta(p-p_0)\Theta(a-r).$$

Given the symmetry, we look for a solution dependent on the scalars r and p only. The variables in the equation separate, $N(r,p) = R(r)P(p)$; the radial one obeys the equation

$$\frac{1}{r^2}\frac{\mathrm{d}}{\mathrm{d}r}r^2\frac{\mathrm{d}R}{\mathrm{d}r} = -\frac{\lambda}{\kappa}R,$$

where λ is the separation parameter, which is an eigenvalue of both operators. In the inner part a bounded solution has the form $R(r) = (A/r)\sin kr$, where $k = \sqrt{\lambda/\kappa}$. In the outer region the symmetric solution is $R(r) = B/r$, where A and B are constants.

Matching the radial functions R and the particle fluxes $\kappa \mathrm{d}R/\mathrm{d}r$ at $r = a$ yields k values: $k_n = (\pi/2a)(2n+1),\ n = 0, 1, \ldots$ Therefore, we determine an infinite set of the relaxation times:

$$\tau_{dn} = \frac{1}{\lambda_n} = \frac{\tau_{d0}}{(2n+1)^2}, \qquad \text{where } \tau_{d0} = \frac{4a^2}{\pi^2\kappa}$$

is the longest relaxation time denoted as τ_d in Eq. (11.116).

The function $P_n(p)$ is determined in a way used to solve Eq. (11.116) and has the same form. However, each n value generates now its own spectral index s_{1n}, increasing as n increases. Thus, the distribution function is expressed as an infinite sum

$$N(r,p) = \sum_{n=0}^{\infty} A_n R_n(r) P_n(p).$$

At high energies, $p \gg p_0$, the term with $n = 0$ dominates. The coefficients A_n are defined by expansion of the radial distribution in a series over the orthogonal set of the functions $R_n(r)$ with the weight r^2, taking into account the radial dependence of the particle source function. The approximate solution

with only one lifetime in Sect. 11.3.2 ignores all the terms with large spectral indices, which may not be essential if we are interested in a high-energy tail of the distribution. On top of that, it yields incorrect spatial distribution of the particle in the acceleration region, which might be essential if, e.g., we analyze spatially resolved observation of the acceleration region.

11.7

$$z<0,\quad N_1(z,p)=\alpha\exp\left(\int\limits_0^z\frac{u_1\mathrm{d}z'}{\kappa_1(z',p)}\right)\int\limits_{q_{\min}}^p N_0(q)\left(\frac{q}{p}\right)^\alpha\frac{\mathrm{d}q}{q}$$
$$+N_0(p)\left(1-\exp\left(\int\limits_0^z\frac{u_1\mathrm{d}z'}{\kappa_1(z',p)}\right)\right);$$

$$z>0,\quad N_2(z,p)=\alpha\int\limits_{q_{\min}}^p N_0(q)\left(\frac{q}{p}\right)^\alpha\frac{\mathrm{d}q}{q},\qquad \alpha=\frac{3u_1}{\Delta u}.$$

The second term describes the particles that have not yet interacted with the front. The function $N_0(q)$ has a sharp cutoff at $q>q_{\max}$, where $q_{\max}$ is the largest momentum of the original particle population. Thus, at $p>q_{\max}$ the second term goes to zero, while the distribution behind the front is $N_2(z,p)\sim p^{-\alpha}$. The function N_2 does not depend on z. If the accelerated particles are monoenergetic far away upstream the front, then

$$N_2(p)=\frac{\alpha N_0}{p_0^3}\left(\frac{p_0}{p}\right)^\alpha.$$

11.8 The boundary conditions are

$$N_2(r,p)\to 0\quad\text{at}\quad r\to\infty;$$
$$N_1=N_2,\quad \kappa_2\frac{\partial N_2}{\partial r}-\kappa_1\frac{\partial N_1}{\partial r}=\frac{p}{3}\frac{\partial N_1}{\partial p}\Delta u-\frac{Q_0}{4\pi r_0^2p_0^2}\delta(p-p_0)\quad\text{at}\quad r=r_0. \tag{1}$$

Apparently, both functions must be bounded everywhere.

The problem is convenient to solve using the Mellin transformation over p:

$$\overline{N}(r,s)=\int\limits_0^\infty N(r,p)p^{s-1}\mathrm{d}p. \tag{2}$$

The transport equation for the Mellin transform has the form

$$r\frac{\mathrm{d}^2\overline{N}_1}{\mathrm{d}r^2}+\left(2-\frac{u}{\kappa}r\right)\frac{\mathrm{d}\overline{N}_1}{\mathrm{d}r}-\frac{2us}{3\kappa}\overline{N}_1=0 \tag{3}$$

in the inner part. Its solution can be expressed via the degenerate hypergeometric function (see, e.g., Abramowitz and Stegun 1964):

$$\overline{N}_1(r,s) = A(s)\Phi\left(\frac{2s}{3}, 2, \frac{ur}{\kappa}\right). \tag{4}$$

In the outer region the equation takes the form

$$\frac{1}{r^2}\frac{\mathrm{d}}{\mathrm{d}r}r^2\kappa_2(r)\frac{\mathrm{d}\overline{N}_2}{\mathrm{d}r} - u_2\frac{r_0^2}{r^2}\frac{\mathrm{d}\overline{N}_2}{\mathrm{d}r} = 0 \tag{5}$$

that has a solution

$$\overline{N}_2(r,s) = B(s)\left\{1 - \exp\left[-\int\limits_r^\infty \frac{u_2 r_0^2}{\kappa_2(r)r^2}\,\mathrm{d}r\right]\right\}. \tag{6}$$

Matching them both using the boundary conditions, we obtain

$$\overline{N}_1(r,s) = \frac{Q_0 p_0^{s-3}(e^{k_2}-1)}{4\pi r_0^2 u_2}\frac{\Phi(2s/3,2,u_1 r/\kappa_1)}{\Psi(s,\Delta u,k_1,k_2)},\quad k_1 = \frac{u_1 r_0}{\kappa_1},\quad k_2 = \int\limits_{r_0}^\infty \frac{u_2 r_0^2}{\kappa_2(r)r^2}\,\mathrm{d}r\,, \tag{7}$$

$$\Psi = \left[1 - (e^{k_2}-1)\frac{s\Delta u}{3u_2}\right]\Phi(2s/3,2,k_1) + \frac{u_1}{u_2}(e^{k_2}-1)\Phi'(2s/3,2,k_1)\,, \tag{8}$$

where the prime denotes the derivative of the degenerate hypergeometric function over its last argument. To perform the inverse Mellin transform we have to integrate the direct Mellin transform in the complex plane s over the straight line contour parallel to the imaginary axes:

$$N(r,p) = \frac{1}{2\pi i}\int\limits_{\beta-i\infty}^{\beta+i\infty}\overline{N}(r,s)p^{-s}\mathrm{d}s. \tag{9}$$

To do so one has to find zeros of the function Ψ over the variable s. Using recurrent formulae for the degenerate hypergeometric function we transform equation $\Psi = 0$ to the form

$$s = \frac{3u_1}{\Delta u}\left\{1 - \frac{1}{k_1} + \frac{\Phi(2s/3-1,1,k_1)}{k_1\Phi(2s/3,2,k_1)}\right\} + \frac{3u_2}{\Delta u(e^{k_2}-1)}\,. \tag{10}$$

We are primarily interested in the smallest absolute root of Eq. (10), which yields the main asymptote at $p \gg p_0$. For $k_1 \to \infty$ and $k_2 \to \infty$ Eq. (10) yields $s_0 = 3u_1/\Delta u$, which corresponds to the particle acceleration by a

plane front (see Sect. 11.4.2). Then, for finite while large k_1 and k_2, we use an asymptote of Φ to obtain a larger root

$$s_0 = \frac{3u_1}{\Delta u}\left[1 + \frac{2u_2}{k_1 \Delta u}\right] + \frac{3u_2}{\Delta u(e^{k_2} - 1)} > \frac{3u_1}{\Delta u}. \tag{11}$$

Taking the inverse Mellin transform, we obtain

$$N_1(r,p) = \frac{3Q_0}{4\pi r_0^2 \Delta u p_0^3} \frac{\Phi(2s_0/3, 2, u_1 r/\kappa_1)}{\Phi(2s_0/3, 2, k_1)} \left(\frac{p_0}{p}\right)^{s_0}, \tag{12}$$

$$N_2(r,p) = \frac{3Q_0}{4\pi r_0^2 \Delta u p_0^3 (1 - e^{-k_2})} \left\{1 - \exp\left[-\int_r^\infty \frac{u_2 r_0^2}{\kappa_2(r) r^2}\, \mathrm{d}r\right]\right\} \left(\frac{p_0}{p}\right)^{s_0}. \tag{13}$$

Compared with the plane front, the spectrum is steeper, i.e., the number of high-energy particles is smaller. This change is related to two effects: (1) the particle faster escapes from the spherical front than from an infinite plane front and (2) the particles suffer adiabatic cooling in the supersonic region, $r < r_0$, $\nabla \cdot \boldsymbol{u}_1 = 2u_1/r > 0$, where the fluid expands.

Chapter 12

Ultrarelativistic Component of Astrophysical Plasmas

We have already noted in many places throughout the book that the very dynamics of astrophysical plasma often results in production of an ultrarelativistic plasma component on top of nonrelativistic background plasma or drives the entire plasma to an ultrarelativistic state. A vivid example of the first option is the galactic and extragalactic (ultra-high-energy) cosmic rays (CRs), while the latter one includes ultrarelativistic pulsar winds or jets and shock waves in active galactic nuclei (AGN) and GRBs. Physics of such ultrarelativistic plasmas represents an extremely broad, highly dynamic, and rapidly developing field of the modern astrophysics, which is hardly possible to comprehensively describe within a textbook format. Nevertheless, below we attempt to present some basic ideas and selected results having in mind to (1) introduce current concepts related to the ultrarelativistic plasma components and (2) demonstrate that the general theoretical framework developed within the cosmic electrodynamics is fully applicable here as well as to traditional nonrelativistic cases.

Study of the ultrarelativistic plasma component has already acquired a long history. An extraterrestrial air-ionizing radiation was discovered a century ago by Victor Hess during a solar eclipse on April 12, 1912, in balloon experiments when he flight at about 5 km above the Earth surface. Long years of experimental and theoretical studies have passed until the nature of this radiation, CRs—charged particles with energy up to 10^{20} eV—has been basically clarified and a consistent (although yet incomplete) theory of the CR origin has been proposed.

By now a large body of observational data on the CR spectra, nuclear composition, and anisotropy has been accumulated, which must all be eventually accommodated within a self-consistent theoretical picture. Let us summarize the very basic observational data on the CRs gathered by numerous ground- and space-based experiments.

G.D. Fleishman and I.N. Toptygin, *Cosmic Electrodynamics*, Astrophysics and Space Science Library 388, DOI 10.1007/978-1-4614-5782-4_12,

The energy spectrum of the nuclear CR component recorded at the Earth orbit is very broad and conventionally subdivided onto three roughly power-law regions. At relatively low energies, $\mathcal{E} \gtrsim 10^{10}\,\mathrm{eV}$, $N_{CR}(\mathcal{E}) \propto \mathcal{E}^{-2.7}$. This power-law region extends up to a so-called "**knee energy**" $\mathcal{E}_{\mathrm{kn}} \sim 3 \cdot 10^{15}\,\mathrm{eV}$ above which the spectrum steepens to $N_{CR}(\mathcal{E}) \propto \mathcal{E}^{-3}$. At a higher energy, $\sim 3 \cdot 10^{18}\,\mathrm{eV}$, the spectrum flattens again to form an "**ankle region**"; no CR particle has yet been detected above $10^{21}\,\mathrm{eV}$. It is interesting that the CRs are dominated by protons at relatively low energies $\mathcal{E} \ll \mathcal{E}_{\mathrm{kn}}$, while by iron nuclei at and above $\mathcal{E}_{\mathrm{kn}}$. The angular CR distribution is almost isotropic within accuracy $\sim 10^{-3}$. The integrated CR energy density is about $1\,\mathrm{eV/cm^3}$. The electron component of the CRs at the Earth orbit composes only about 1% of the integrated particle flux density. Most of the observed CR spectrum is produced at the Galaxy, although the very high energy (VHE) tail at $\mathcal{E} \gtrsim 10^{18}\,\mathrm{eV}$ has an extragalactic origin.

We emphasize that the theory plays an unusually important role in the astrophysics of CRs. Indeed, unlike the electromagnetic radiation that propagates almost rectilinearly from its source, the CRs possess an electric charge so their propagation is controlled by electromagnetic fields. The energetic particles have Larmor radii up to $R_L \sim 1\,\mathrm{pc}$ and mfp $\Lambda_{\parallel} \gtrsim R_L$; thus, they diffuse in the turbulent ISM filling more or less uniformly the galactic disk and, perhaps, a more extended quasispherical galactic halo. Therefore, the charged particles detected at the Earth orbit gained their energy somewhere very far away from the solar system and their arrival direction carries no information about the corresponding source location.

The main sources of the free energy supplying the CR energy are supernova explosions (as there is no other kind of objects capable of depositing energy at the required rate) described in Sect. 5.5. The rate of SN explosions in the Galaxy is estimated as one explosion over 30 years although most of them remain unobserved due to strong absorption of the light by dust in the galactic plane. Roughly 10% of the explosion kinetic energy must transfer to the CRs to supply their energy density at the observed level of $1\,\mathrm{eV/cm^3}$. Even though the free energy input provided by SNe is sufficient to supply the observed CR level, the theory has yet to sort out how and where exactly the CRs are accelerated—(1) during the prompt stage of the SN explosion, (2) at the shock wave formed by expanding SN ejecta, or (3) at the compact remnants—neutron stars.

Recall that in Sect. 11.5.3 we have considered a model of particle acceleration in galactic superbubbles in which the SN explosions and corresponding shock wave ensemble play an important role. Even though the model takes into account a lot of essential physics including turbulent particle transport and back reaction of the accelerated particles on the turbulence spectrum and capable of reproducing some essential features of the CR spectrum, it still contains many postulated model parameters self-consistent calculation of which remains an open question. Stated another way, it is still a long way

from the simplified models (like that considered in Sect. 11.5.3) to a fully self-consistent comprehensive solution of the CR origin problem. Although it seems established that the main accelerating element is a strong shock wave from a SN explosion, many important details have yet to be work out. Theoretically, most of the problems needed to be solved here are highly nonlinear. In particular, it is highly difficult to quantitatively obtain the required energy density and the spectrum shape of the turbulence forming the charged particle transport in real astrophysical conditions.

In this chapter we derive and discuss some selected results confirming that the relevant sophisticated problems are becoming better understood based on new detailed observations and deep theoretical study. In particular, we show that the nuclear component of the galactic CRs and a significant fraction of the electron component are produced at extended SNRs; a fraction of CR electrons and positrons is generated by neutron stars (pulsars) whose atmosphere contains relativistic electron–positron plasma and by pulsar nebulae, while ultra-high-energy extragalactic CRs are likely to be generated by sources of cosmological GRBs.

12.1 Galactic Cosmic Rays and Supernova Remnants

The main foundation of the theory of CR origin was formulated in monograph (Ginzburg and Syrovatskii 1964) in half a century after the Hess CR discovery.[1] Remarkably, the developed concept relied essentially on accumulated by the time data on CR composition, energy spectrum, intensity, and anisotropy of the particle flux complemented by science-transforming radio astronomy results. Indeed, a hypothesis [proposed by Alfvén and Herlofson (1950), Kiepenheuer (1950) and actively promoted by Vitaly Ginzburg] of synchrotron origin of the radio emission from many sources became widely accepted during 1950s. It has been established that the radio waves are produced by ultrarelativistic electrons with $\mathcal{E} \gg m_e c^2$ moving through magnetic fields of the cosmic objects. These achievements confirmed that charged particle acceleration up to very high energies is a universal astrophysical phenomenon taking place in and out the Galaxy: even though the radio astronomy is only sensitive to the electron CR component (radiation produced by a proton with same Lorentz factor is roughly one million times weaker), there were no doubts that nuclear CR component must have been generated along with electron component.

[1] By now many fundamental monographs and review articles on the CR origin have been published including Hayakawa (1974), Longair (1981), Ginzburg (1987), Berezinskii et al. (1990) and Murzin (2007).

12.1.1 Generation of MHD Oscillations by Accelerated Particles Ahead of the Shock Front

As has been shown in Sect. 11.4 the most attractive property of the diffusive shock acceleration mechanism is its ability to form a broad energy spectrum of accelerated particles obeying roughly a power law with an index close to that observed in the CR spectrum. Within the concept of CR generation by SNRs one has to consider formation of accelerated particle spectrum by spherical SNR shock waves having a finite size and living a finite time. A question that immediately arises is if the required CR spectrum can in fact be formed over a limited phase when a strong shock from SN explosion is still available. One can easily estimate that for a standard ISM magnetic field $\sim 3 \cdot 10^{-6}$G the Larmor radius R_L of a proton with an energy comparable with the knee energy $3 \cdot 10^{15}$ eV ($\gamma \approx 3 \cdot 10^6$) is about the SNR radius (see Sect. 5.5.3). Therefore, the high-energy particles cannot be confined at the shock wave by the ISM magnetic field so they must escape from the remnant making particle acceleration at the front up to the knee energy problematic. The problem of the CR escape becomes even more severe if we recall that the transport mfp $\Lambda_\parallel$ along the field is formed by particle scattering by MHD turbulence and $\Lambda_\parallel \gg R_L$ if the turbulence energy density is smaller than the regular magnetic field energy density. These simple estimates unavoidably imply that in order to ensure efficient CR acceleration at the SNR shock waves up to the knee energy the level of MHD turbulence up front the shock must be strongly enhanced.

Indeed, a plasma with a population of relativistic particles is often unstable (see Sect. 4.1); MHD waves with the wavelength of the order of the Larmor radius of the accelerated particles experience amplification and in their turn scatter the particles and so form their mfp needed for them to be Fermi accelerated. However, the *resonant* self-generation of the MHD waves at the front by accelerated particles[2] turns out to be too weak to support the required acceleration efficiency (Lagage and Cesarsky 1983; Fedorenko and Fleishman 1988).

However, in Sect. 4.1, we have already established that a *nonresonant* instability can be much more powerful than the *resonant* one in case of high-frequency waves. Complementarilly, below we are going to demonstrate that a *nonresonant MHD wave generation* can make additional contribution to the wave generation by accelerated particles at a level exceeding that of the resonant generation resulting in a strong turbulence regime potentially sufficient to facilitate the CR acceleration at the SNR shocks up to the knee

[2]The problem of MHD wave generation by relativistics particle is under active discussion in the astrophysics context since (Wentzel 1968). More recent analytical and numerical studies on the topics are done by Bell and Lucek (2001), Bell (2004), Bykov and Toptygin (2007), Zirakashvili et al. (2008) and Bykov et al. (2011) etc.

energy at least. The entire problem is highly nonlinear and so complicated; therefore, we restrict the consideration to calculation of the linear growth rates and some simplified estimates of the strong turbulence nonlinear regime.

12.1.2 Statement of the Problem

Although the general approach developed in Chap. 3 is fully applicable to analyzing the eigenmodes in a plasma with relativistic particles, a number of important distinctions must here be taken into account, which include (1) breaking of the background plasma quasineutrality, which is especially essential at low frequencies (see Sect. 3.2.2, Fig. 3.2); (2) fluid motion in the prefront region; and (3) need of kinetic treatment of the relativistic component (though the background plasma component can still be described hydrodynamically). For what follows it is highly important that the distribution function of the accelerated particles determined in Sect. 11.4.2 within the test particle approximation is spatially nonuniform and anisotropic. Moreover, distribution function (11.152) depends on the corresponding upstream diffusion coefficient that, in its turn, is defined by the upstream turbulence level, which implies that properties of the eigenmodes we are going to specify will depend on the preexistent turbulence level and spectrum and, therefore, are supposed to differ from "standard" linear MHD modes. Stated another way, we are looking here for the dispersion and damping/amplification rate of the waves created on top of already available, perhaps, strong turbulence.

Let us consider the problem in the front frame (i.e., the shock front is immobile). Adopt the upstream plasma to contain three components—a spatially uniform fully ionized cold background plasma with the number densities n_i and n_e and a relativistic nuclear component with the number density N_0 at the front. The total plasma quasineutrality requires that $n_e = n_i + N_0$. Accuracy of this condition in low-frequency processes is very high (see Sect. 7.6.1). However, the background plasma alone is not quasineutral, while dominated by the electrons. The fluid moves toward the front with a constant velocity $u = \text{const}$. The external magnetic field $\boldsymbol{B}_0$ is normal to the front as well. Apparently, we consider here a simplified picture of the phenomenon; in particular, we do not take into account the shock front modification considered in Sect. 11.4.3. This simplification seems to be appropriate until only a relatively small fraction of the flow energy is being spent onto the particle acceleration and wave generation; we will conventionally adopt the upper bound of $\leq 10\%$ in the energy densities.

To find the wave dispersion we have to form the dielectric tensor or conductivity tensor, which requires finding electric currents associated with all available plasma components created in response to small electromagnetic perturbation. Let us start from calculating electric current stimulated in the background plasma component by a weak plane monochromatic wave with

the electric and magnetic vectors $\boldsymbol{E}$ and $\boldsymbol{b}$ proportional to $\exp(i\boldsymbol{k}\cdot\boldsymbol{r}-i\omega t)$. Let us introduce the macroscopic velocities of the electron and ion components as

$$\boldsymbol{u}_{i,e} = \boldsymbol{u} + \boldsymbol{v}_{i,e}, \qquad \boldsymbol{v}_{i,e} \sim \exp(i\boldsymbol{k}\cdot\boldsymbol{r} - i\omega t) \tag{12.1}$$

and write down corresponding linearized equations similar to Eq. (3.38)

$$\frac{\partial \boldsymbol{v}_{i,e}}{\partial t} + (\boldsymbol{u}\cdot\nabla)\boldsymbol{v}_{i,e} = \pm\frac{e}{m_{i,e}}\left[\boldsymbol{E} + \frac{1}{c}\boldsymbol{v}_{i,e}\times\boldsymbol{B}_0 + \frac{1}{c}\boldsymbol{u}\times\boldsymbol{b}\right]. \tag{12.2}$$

To further simplify the problem we only consider the wave propagating along the external magnetic field, $\boldsymbol{k} \parallel \boldsymbol{B}_0 \parallel \boldsymbol{u}$. Maxwell's equations in the Fourier domain yield

$$\boldsymbol{k}\times\boldsymbol{b} = -i\frac{4\pi}{c}\boldsymbol{j}, \qquad \boldsymbol{b} = \frac{c}{\omega}\boldsymbol{k}\times\boldsymbol{E}, \qquad \boldsymbol{k}\cdot\boldsymbol{E} = 0, \tag{12.3}$$

where $\boldsymbol{j}$ is the total current density associated with the field perturbations $\boldsymbol{E}$ and $\boldsymbol{b}$. The latter equality is a result of zero macroscopic electric charge density in any large-scale fluid perturbations. Using Eq. (12.3) it is easy to find

$$\boldsymbol{E} + \frac{1}{c}\boldsymbol{u}\times\boldsymbol{b} = \frac{\omega'}{\omega}\boldsymbol{E}, \qquad \omega' = \omega - \boldsymbol{k}\cdot\boldsymbol{u}; \tag{12.4}$$

then, Eq. (12.2) yield the plasma component velocities

$$\boldsymbol{v}_{i,e} = \pm\frac{e\omega'[i\omega'\boldsymbol{E} \pm \omega_{Bi,e}\boldsymbol{e}_\parallel\times\boldsymbol{E}]}{m_{i,e}\omega(\omega'^2 - \omega_{Bi,e}^2)}. \tag{12.5}$$

Here ω is the frequency in the front frame, while ω' is the corresponding proper frequency in the upstream frame, which is different due to the **Doppler effect**.

Thus, the electric current $\boldsymbol{j}_{\rm pl}$ of the background plasma components associated with the MHD perturbation receives the form

$$\begin{aligned}\boldsymbol{j}_{\rm pl} = en_i\boldsymbol{v}_i - en_e\boldsymbol{v}_e \quad = \quad & \frac{i}{4\pi\omega}\left\{\left[\frac{\omega_{\rm pi}^2\omega'^2}{\omega'^2-\omega_{Bi}^2} + \frac{\omega_{\rm pe}^2\omega'^2}{\omega'^2-\omega_{Be}^2}\right]\boldsymbol{E}\right. \\ & \left. -i\left[\frac{\omega_{\rm pi}^2\omega_{Bi}\omega'}{\omega'^2-\omega_{Bi}^2} - \frac{\omega_{\rm pe}^2\omega_{Be}\omega'}{\omega'^2-\omega_{Be}^2}\right]\boldsymbol{e}_\parallel\times\boldsymbol{E}\right\},\end{aligned} \tag{12.6}$$

which greatly simplifies in the range of low frequencies $\omega' \ll \omega_{Bi} \ll \omega_{Be}$. Using definitions of the gyro- and plasma frequencies, we obtain

$$\boldsymbol{j}_{\rm pl} = -i\frac{c^2\omega'^2}{4\pi v_A^2\omega}\boldsymbol{E} + \frac{\omega_{\rm pr}^2\omega'}{4\pi\omega_{Bi}\omega}\boldsymbol{e}_\parallel\times\boldsymbol{E}. \tag{12.7}$$

The first term at the rhs contains the ion current only; the omitted electron current is m_e/m_i smaller. The second term describes the background plasma gyrotropy, which does not go to zero (as $\omega \to 0$) here as it would in a quasineutral plasma, cf. Sect. 3.2.2, and so contains the square of the plasma frequency

$$\omega_{\rm pr}^2 = \frac{4\pi e^2 N_0}{m_i}, \qquad N_0 = n_e - n_i, \tag{12.8}$$

related to the ions transited from the background to accelerated component.

Coefficient at the vector components E_β in the rhs of Eq. (12.7) represents the components of the corresponding complex conductivity tensor $\sigma_{\alpha\beta}$. In its turn, this tensor specifies the plasma dielectric permittivity tensor according to Eq. (3.9). To obtain the total conductivity tensor, we have yet to take into account a contribution made by relativistic particles.

12.1.3 Accelerated Particle Current Driven by a Weak MHD Wave

We turn now to calculating the accelerated particle current in the plane prefront of a nonrelativistic shock wave propagating through a fully ionized turbulent plasma. This problem is highly sophisticated as it is essentially nonlinear and requires a self-consistent calculation of the absolute number, spatial distribution, and spectrum of accelerated particles along with the spectrum, spatial distribution, and intensity of MHD turbulence which determines the diffusion coefficient and thereby the efficiency and rate of particle acceleration, as well as the shock front structure.

No self-consistent analytical solution has yet been found for the full problem, although there are some numeric models highlighting one or another side of the whole problem. The problem can be simplified, however, by adopting a reasonably strong turbulence upstream such as it ensures more or less effective diffusive shock acceleration, while not too strong to modify the accelerated particle distribution and anisotropy upstream, so test particle solution (11.152) for the distribution function remains valid. Accordingly, the accelerated particles in the turbulent prefront posses a weakly anisotropic distribution function which can be written down in form (7.81), (11.32) with distribution function (11.152) valid for 1D case:

$$f_0(z, \boldsymbol{p}) = \frac{1}{4\pi}\left[N(z,p) + \frac{3}{pv} p_z J_z(z,p)\right], \; J \ll vN, \tag{12.9}$$

where

$$N(z,p) = \frac{3Q_0}{\Delta u p_0^3}\left(\frac{p_0}{p}\right)^{\alpha}\Theta(p-p_0)\mathrm{e}^{uz/\kappa_\parallel}, \quad z \le 0,\ p_0 \le p \le p_m, \quad (12.10a)$$

$$J_z = -\kappa_\parallel \frac{\partial N}{\partial z} - \frac{p}{3}\frac{\partial N}{\partial p}u = \frac{1}{3}(\alpha-3)u\left[N(z,p) - N_0 p_0^{-2}\delta(p-p_0)\mathrm{e}^{uz/\kappa_\parallel}\right]. \quad (12.10b)$$

Here Q_0 is the source power at the front, $N_0 = 3Q_0/(\alpha-3)\Delta u$ is the number density of relativistic ions, $\alpha = 3u/\Delta u$ is the index of the momentum spectrum, and $\Delta u > 0$ is the velocity jump at the front.

Solution (12.10a) is valid when only a small fraction of the shock energy is spent to the particle acceleration and the upstream velocity is approximately constant: $u = \text{const}$. For a moderately strong front, the exponent $\alpha > 4$, while for a strong shock wave $\alpha \le 4$ (see estimates in Sect. 11.4.3). The actual value of α depends on both the Mach number of the shock wave and also the rate of the particle injection into acceleration process. Apparently, for $\alpha < 4$, the bulk of the energy belongs to the highest energy particles with $\mathcal{E} \lesssim \mathcal{E}_m = cp_m$, so a large fraction, up to a few dozen percents of the total shock energy, is transferred to the accelerated particles.

We, therefore, restrict our consideration to the case of efficient acceleration up to the highest particle momentum $p_m \gg p_0 \approx m_i c$ with values $\alpha \ge 4$ and assume a moderate acceleration rate where the total kinetic energy of accelerated particles remains within 10% of the total energy of the system compatible with the test particle solution. For $\alpha = 4$ the total energy of accelerated particles at the front ($z = 0$) depends on p_m logarithmically:

$$w_r \approx \int_{p_0}^{p_m} cpN(p,0)p^2\mathrm{d}p = N_0 m_i c^2 \ln(p_m/p_0). \quad (12.11)$$

As no consistent turbulence theory in the upstream region is currently available we analyze two extremes motivated by the demanded high efficiency of the diffusive shock acceleration.

Case 1. The transport mfp and the longitudinal diffusion coefficient are constant in the energy range of interest:

$$\Lambda_\parallel = \text{const}, \qquad \kappa_\parallel = \frac{c\Lambda_\parallel}{3} = \text{const}, \qquad p_0 \le p \le p_m. \quad (12.12)$$

This requires a magnetic turbulence with the spectrum $\langle b^2\rangle_k \sim k^{-2}$ (see Sect. 7.5.1). Assuming the turbulent field at the largest scale to be comparable with the regular field, the transport mfp is estimated as the Larmor radius of the highest energy particles: $\Lambda_\parallel \approx r_g(p_m)$. The smaller-scale harmonics of

the turbulent magnetic field are weak, which results in a strongly anisotropic diffusion with a constant longitudinal mean free path $\Lambda_{\parallel} \approx r_g(p_m) = \text{const}$ for particles with $p \ll p_m$.

Case 2. Strong turbulence with the diffusion coefficient approaching the **Bohm limit**, i.e., the transport mean free path $\Lambda(p)$ of a particle is of the order of its Larmor radius:

$$\Lambda(p) \approx \Lambda_{\parallel} \approx r_g(p) = \frac{cp}{eB}, \qquad \kappa_{\parallel} = \frac{c\Lambda}{3}, \qquad p_0 \le p \le p_m, \tag{12.13}$$

where the case $p_m \gg p_0$ is of particular interest. The turbulent and regular fields must be comparable to each other $B \approx B_0$. It must be noted that this is not in conflict with the assumption of a weak energy transfer to the accelerated particles: in a strong SNR shock wave the mechanical energy density is by several orders of magnitude higher than the energy density of the ISM magnetic field; this is also valid for most of the astrophysical shocks.

The accelerated particle distribution function $f(\boldsymbol{r}, p, \theta, \phi, t)$ perturbed by the same as in Sect. 12.1.2 external small-amplitude wave field satisfies the kinetic equation

$$\frac{\partial f}{\partial t} + \boldsymbol{v} \cdot \frac{\partial f}{\partial \boldsymbol{r}} + \frac{e}{m}\boldsymbol{E} \cdot \frac{\partial f}{\partial \boldsymbol{r}} - \frac{ec}{\mathcal{E}}(\boldsymbol{b} + \boldsymbol{B}_0) \cdot \boldsymbol{\mathcal{O}} f = \left(\frac{\partial f}{\partial t}\right)_{col}, \ \boldsymbol{\mathcal{O}} = \boldsymbol{p} \times \frac{\partial}{\partial \boldsymbol{p}}, \tag{12.14}$$

where $\boldsymbol{\mathcal{O}}$ is the momentum rotation operator, and $\boldsymbol{E}$, $\boldsymbol{b}$ are the external electromagnetic field vectors of the MHD wave.

Let us linearize kinetic equation (12.14) by adopting $f = f_0 + \delta f$, where the small correction δf is proportional to the field:

$$\frac{\partial \delta f}{\partial t} + \boldsymbol{v} \cdot \frac{\partial \delta f}{\partial \boldsymbol{r}} - \frac{ec}{\mathcal{E}}\boldsymbol{B}_0 \cdot \boldsymbol{\mathcal{O}} \delta f = -\frac{e}{m}\boldsymbol{E} \cdot \frac{\partial f_0}{\partial \boldsymbol{p}} + \frac{ec}{\mathcal{E}}\boldsymbol{b} \cdot \boldsymbol{\mathcal{O}} f_0 + \left(\frac{\partial \delta f}{\partial t}\right)_{col}. \tag{12.15}$$

The last term in Eq. (12.15) takes into account relaxation of the distribution function δf due to particle interaction with the preexisting magnetic turbulence. We simplify this term within the "relaxation frequency" approximation:

$$\left(\frac{\partial \delta f}{\partial t}\right)_{col} \approx -\nu \delta f, \qquad \nu \approx v/\Lambda_{\parallel}, \tag{12.16}$$

and separately analyze the cases of weak (12.12) and strong (12.13) turbulence to estimate the relaxation frequency. Below we employ Maxwell's equation (12.3) with a real wave vector $\boldsymbol{k}$ and a complex frequency ω.

We can make further simplifications while solving Eq. (12.15). Although the correction δf contains the same nonuniform exponential factor as unperturbed function (12.10a), $\delta f \sim \exp(uz/\kappa_\parallel)$, it can be discarded. Indeed, this factor results in the frequency correction $\nu' = v_\parallel u/\kappa_\parallel = 3u/\Lambda_\parallel$, which is small $\nu' \ll \nu$ for relativistic particles if $3u \ll v$.

Within the assumptions made, Eq. (12.15) implies that the coordinate and time dependence of the distribution function perturbation is the same as for the test wave field. The equation can therefore be written in the form

$$\frac{\partial \delta f}{\partial \phi} - a\delta f = Q(\phi), \qquad a = \frac{1}{\Omega}(\nu - i\omega + ik_\parallel v_\parallel), \tag{12.17}$$

where ϕ is the azimuth angle of relativistic particle momentum counted around the regular magnetic field, so that

$$\boldsymbol{B}_0 \cdot \boldsymbol{\mathcal{O}}\delta f = B_0 \frac{\partial \delta f}{\partial \phi}, \qquad \Omega = \frac{ceB_0}{\mathcal{E}},$$

while the rhs of Eq. (12.17) contains only known quantities:

$$Q(\phi) = \left(\frac{e\boldsymbol{E}}{\Omega} - \frac{ec}{\mathcal{E}\Omega} \boldsymbol{b} \times \boldsymbol{p} \right) \cdot \frac{\partial f_0}{\partial \boldsymbol{p}}. \tag{12.18}$$

In what follows we assume all accelerated particles to be strongly relativistic protons, i.e., $v \approx c$, $\mathcal{E} \approx cp$ and $p_0 \approx m_p c$.

A solution to Eq. (12.17) can be written in the form

$$\delta f = \int\limits_{-\infty}^{\phi} Q(\phi') \mathrm{e}^{a(\phi - \phi')} \mathrm{d}\phi'. \tag{12.19}$$

Explicit calculation of the quantity $Q(\phi)$ yields

$$Q(\phi) = \frac{e}{\Omega}(\boldsymbol{e}_\perp \cdot \boldsymbol{E}) \left(\sin\theta \frac{\partial f_0}{\partial p} + \cos\theta \frac{\partial f_0}{\partial \theta} - \frac{ck_\parallel}{\omega p} \frac{\partial f_0}{\partial \theta} \right). \tag{12.20}$$

Here $\boldsymbol{e}_\perp = \boldsymbol{p}_\perp / p_\perp$ is a unit vector perpendicular to $\boldsymbol{B}_0$; other values entering here can be calculated from Eqs. (12.9) and (12.10).

The correction δf to the relativistic particle distribution function is straightforward to calculate from Eqs. (12.19) and (12.20):

$$\delta f = -e \left(\sin\theta \frac{\partial f_0}{\partial p} + \cos\theta \frac{\partial f_0}{\partial \theta} - \frac{ck_\parallel}{\omega p} \frac{\partial f_0}{\partial \theta} \right) \frac{(\boldsymbol{e}_\phi \cdot \boldsymbol{E}) + a(\boldsymbol{e}_\perp \cdot \boldsymbol{E})}{\Omega(1 + a^2)}, \tag{12.21}$$

where $\boldsymbol{e}_\phi = \boldsymbol{e}_\parallel \times \boldsymbol{e}_\perp$ and the variable a is defined above by Eq. (12.17). Electric current driven by accelerated particles is now calculated by familiar formula (3.2) written for the relativistic particle component

$$\boldsymbol{j}_r = \int e\boldsymbol{v}\delta f(p, \theta, \phi) p^2 \mathrm{d}p \sin\theta \mathrm{d}\theta \mathrm{d}\phi. \tag{12.22}$$

Substituting the distribution function correction δf and integrating over $d\phi$ we obtain

$$\boldsymbol{j}_r = \pi e^2 c \int p^2 \mathrm{d}p \int \sin^2\theta \mathrm{d}\theta \left(\sin\theta \frac{\partial f_0}{\partial p} + \cos\theta \frac{\partial f_0}{\partial \theta} - \frac{ck_\parallel}{\omega p} \frac{\partial f_0}{\partial \theta} \right) \frac{(\boldsymbol{e}_\parallel \times \boldsymbol{E}) - a\boldsymbol{E}}{\Omega(1+a^2)}. \tag{12.23}$$

To calculate the remaining integrals, we expand the denominator of the integrand onto the simple fractions:

$$\begin{aligned} \frac{1}{\Omega(a^2+1)} &= \frac{1}{2\Omega} \left[\frac{1}{1+ia} + \frac{1}{1-ia} \right] \\ &= \frac{1}{2} \left[\frac{1}{\Omega + \omega - k_\parallel cx + i\nu} + \frac{1}{\Omega - \omega + k_\parallel cx - i\nu} \right], \end{aligned} \tag{12.24}$$

where $x = \cos\theta$. The main contribution to the integral over momentum comes from a region at the lower limit, $p \approx p_0 = m_i c$; therefore, for the estimate, we can accept $\Omega \approx \omega_{Bi}$. Within the weak turbulence regime, Eqs. (12.12) and (12.16) imply that the relaxation frequency is small: $\nu \sim \omega_{Bi} m_p c/p_m \ll \omega_{Bi}$. Therefore, one can adopt $\nu \to 0$, take into account that $\omega \ll \omega_{Bi}$, and apply the Sokhotsky formula, which in agreement with quasilinear approximation considered in Sect. 4.2 yields

$$\frac{1}{\Omega(1+a^2)} = \frac{1}{2ck_\parallel} \left[\frac{\mathcal{P}}{x+\xi} - \frac{\mathcal{P}}{x-\xi} + i\pi[\delta(x+\xi) - \delta(x-\xi)] \right], \tag{12.25a}$$

$$\frac{a}{\Omega(1+a^2)} = -\frac{i}{2ck_\parallel} \left[\frac{\mathcal{P}}{x+\xi} + \frac{\mathcal{P}}{x-\xi} + i\pi[\delta(x+\xi) + \delta(x-\xi)] \right]. \tag{12.25b}$$

Here, we introduced a new dimensionless parameter $\xi = \Omega/ck_\parallel$; the symbol $\mathcal{P}$ stands for the principal value. The terms containing δ-functions describe wave–particle resonances as they contain the resonant conditions $\Omega \pm \omega \mp k_\parallel v_\parallel = 0$, cf. Eqs. (3.62) and (4.38). Accordingly, the terms with the principle values are nonresonant.

Using Eq. (12.25) we can write down the relativistic proton current in the form

$$\boldsymbol{j}_r = (\sigma'_\perp + i\sigma''_\perp)\boldsymbol{E} - (g' + ig'')\boldsymbol{e}_\parallel \times \boldsymbol{E}, \tag{12.26}$$

where the kinetic coefficients are given by

$$\sigma'_\perp = \left(1 - \frac{\pi A c k_\parallel}{4\omega}\right)\frac{\omega_{\rm pr}^2}{16\omega_{Bi}^2}ck_\parallel, \quad \sigma''_\perp = \frac{A\ln(\xi_0/3.4)\omega_{\rm pr}^2}{12\omega_{Bi}^2}ck_\parallel,$$
$$g' = \frac{\omega_{\rm pr}^2}{4\pi\omega_{Bi}}, \quad g'' = -\frac{A\omega_{\rm pr}^2}{24\omega_{Bi}^2}ck_\parallel. \tag{12.27}$$

Here $\xi_0 = \omega_{Bi}/ck$; we use notation (12.8) for $\omega_{\rm pr}^2$ and a new notation $A = u/c$ for the anisotropy parameter of relativistic particles. Finally, we assume $\alpha = 4$ for the momentum spectral index and use approximations

$$\mathcal{P}\int\limits_{-1}^{1}\frac{(1-x^2)x}{x+\xi}{\rm d}x = -\frac{4}{15\xi^2}, \qquad \mathcal{P}\int\limits_{-1}^{1}\frac{1-x^2}{x+\xi}{\rm d}x = \frac{4}{3\xi}$$

valid for $|\xi| \gg 1$.

12.1.4 Linear Growth Rate

Now we can calculate eigenmodes in the plasma containing accelerated relativistic particles and address the question of wave amplification in such plasmas. From Maxwell's equation (12.3) we find

$$\boldsymbol{E} = i\frac{4\pi\omega}{(ck_\parallel)^2}(\boldsymbol{j}_{\rm pl} + \boldsymbol{j}_r), \tag{12.28}$$

where the rhs includes the total electric current formed by background plasma (12.7) and relativistic particles (12.26). Let us write down Eq. (12.28) in the form

$$C_1\boldsymbol{E} - iC_2\boldsymbol{e}_\parallel \times \boldsymbol{E} = 0, \tag{12.29}$$

where

$$C_1 = \omega'^2 - (v_A k_\parallel)^2 - \frac{Av_A\ln(\xi_0/3.4)}{3c}\frac{(\omega' + \boldsymbol{u}\cdot\boldsymbol{k})\omega_{\rm pr}^2}{\omega_{Bi}^2}v_A k_\parallel$$
$$+ i\frac{\pi\omega_{\rm pr}^2}{4\omega_{Bi}^2}\left[\frac{\omega' + \boldsymbol{u}\cdot\boldsymbol{k}}{ck_\parallel} - \frac{\pi A}{4}\right](v_A k_\parallel)^2, \tag{12.30a}$$

$$C_2 = -\frac{\omega_{\rm pr}^2 v_A^2}{\omega_{Bi}c^2}\boldsymbol{u}\cdot\boldsymbol{k} - i\frac{\pi A\omega_{\rm pr}^2 v_A}{6\omega_{Bi}^2 c}(\omega' + \boldsymbol{u}\cdot\boldsymbol{k})v_A k_\parallel. \tag{12.30b}$$

Cross product of $\boldsymbol{e}_\parallel$ and Eq. (12.29) yields another equation:

$$iC_2\boldsymbol{E} + C_1\boldsymbol{e}_\parallel \times \boldsymbol{E} = 0. \tag{12.31}$$

The compatibility condition for either Eqs. (12.29) or (12.31) can apparently be written in the form of two equalities

$$C_1 \pm C_2 = 0, \tag{12.32}$$

which, in combination with Eq. (12.29), shows that the eigenmodes are circularly polarized.

The dispersion relation receives the form

$$\omega'^2 - (v_A k_\parallel)^2 + i4\pi\left(\frac{v_A}{c}\right)^2 \omega(\sigma'_\perp + i\sigma''_\perp) \pm i4\pi\left(\frac{v_A}{c}\right)^2 (g' + ig'') \mp \frac{\omega_{\rm pr}^2 v_A^2}{\omega_{Bi} c^2 \omega'} = 0. \tag{12.33}$$

The obtained dispersion equation contains small terms of different orders. To sort them out one can note that conditions $v_A \ll u \ll c$ are often fulfilled. Then, the terms from the accelerated particles are small proportionally to the relativistic particles number density. In the absence of relativistic particles, the dispersion relation reads

$$\omega'^2 - (v_A k_\parallel)^2 = 0, \qquad \omega' = \pm v_A k = \pm\omega_A, \tag{12.34}$$

and describes equal frequencies of standard MHD Alfven and magnetosonic modes, which, for the longitudinal propagation adopted in our treatment, degenerate.

Account of the accelerated particle current gives rise to new effect via the imaginary terms in dispersion relation (12.33), which can have different signs. This implies that growing and damping wave modes appear. Their growth (damping) rates γ and corrections ω_1 to the real parts of the frequencies, $\omega' = \pm\omega_A + \omega_1 + i\gamma$, can easily be found provided that they are small:

$$\gamma = \pm\frac{\pi(4-\pi)A\omega_{\rm pr}^2}{32\omega_{Bi}^2}\omega_A, \qquad \omega_1 = \pm\frac{\omega_{\rm pr}^2 u}{2\omega_{Bi} c}. \tag{12.35}$$

Here all the terms of the order of v_A/u or $(u/c)^2$ have been omitted.

Let us estimate now the order of magnitude of the effect obtained. A critical parameter in Eq. (12.35) is apparently the number density of accelerated particles N_0. In the ISM of the galactic disk it is very small, $N_0/(n_i + n_a) \approx 10^{-9}$ on the average. At the CR source, however, during the particle acceleration at the SNR shock front, this ratio depends heavily on the spectrum shape (i.e., the spectral index) and the highest energy up to which the acceleration occurs. Based on the energy conservation law we can write the following relationship:

$$\eta\frac{m_p u^2}{2} n_0 u = \overline{K} N_0 u', \tag{12.36}$$

where η is the fraction of the primary energy flux transferred to the accelerated particles, u and u' are the velocities of the fluid ahead and behind the front, n_0 is the average proton number density ahead the front (including the neutral component if present), and $\overline{K}$ is the average kinetic energy of the accelerated particles. For a power-law spectrum with index $\alpha = 4$ we obtain from Eq. (12.11) $\overline{K} = m_p c^2 \ln(p_m/p_0)$. With a moderate fraction $\eta \approx 0.1$ of the energy flux transferred to the accelerated particles and with $\mathcal{E}_m = cp_m \approx 3 \times 10^6\,\mathrm{GeV}$ (the knee energy of the galactic CR spectrum), Eq. (12.36) yields

$$\frac{N_0}{n_0} \approx \frac{0.2}{\ln(p_m/p_0)} \left(\frac{u}{c}\right)^2 \approx 1.4 \times 10^{-2} \left(\frac{u}{c}\right)^2 . \tag{12.37}$$

We can now calculate the growth rate to Alfvén frequency ratio from Eq. (12.35) using $A = u/c$ and introducing the proton plasma frequency defined from $\omega_{\mathrm{pt}}^2 = 4\pi n_0 e^2/m_p$ where the total background proton number density n_0 (with the account of neutrals if available[3]) enters, as

$$\frac{\gamma}{\omega_A} \approx 5 \times 10^{-3} \frac{\omega_{\mathrm{pt}}^2}{\omega_{Bi}^2} \left(\frac{u}{c}\right)^3 . \tag{12.38}$$

Considering as an example SN explosion in the warm galactic gas we adopt $B_0 \approx 3 \times 10^{-6}\,\mathrm{G}$, $n_0 \approx 0.2\,\mathrm{cm}^{-3}$ (see Table 1.1) and obtain $\omega_{\mathrm{pt}}^2/\omega_{Bi}^2 \approx 4 \times 10^8$, which yields

$$\frac{\gamma}{\omega_A} \approx 2 \times 10^5 \left(\frac{u}{c}\right)^3 . \tag{12.39}$$

SN type II explosions produce strong shocks with $u \approx 3 \times 10^8\,\mathrm{cm/s}$ at the Sedov stage, Sect. 5.5.3. We, thus, obtain a rather promising estimate of $\gamma/\omega_A \approx 0.2$ implying a highly efficient turbulence generation. Moreover, at the initial (free expansion) SNR stage characterized by $u \sim 10^9\,\mathrm{cm/s}$, the amplification rate can even exceed the wave frequency resulting in a rapid aperiodic regime of the instability with the growth rate $\gamma/\omega_A \sim 5$. Apparently, the considered linear theory is not capable of predicting the limit of turbulence growth or the final saturated state of the system.

12.1.5 Strong Turbulence Regime

We have to emphasize that the method developed accounts both resonant and nonresonant interactions within single unified consistent approach. In agreement with theory developed in Sects. 3.3 and 4.2 in the weak turbulence regime ($\nu \to 0$, Sect. 12.1.3), the resonances are accounted in Eq. (12.25)

[3] If the shock wave propagates through warm ISM gas containing neutrals, they become ionized at the shock so the total proton number must be used in estimating the Alfvén speed.

by the δ-functions, while the fractions with principal values describe the nonresonant contributions. Although this separation onto resonance and nonresonance processes is well justified for the weak turbulence case, it fails in the strong turbulence case when the resonances become very broad and the quasilinear theory relying on well-defined resonances becomes invalid. Remarkably, the general approach developed in Sect. 12.1.3 remains applicable in this case as it is more general than the conventual quasilinear method.

As we have established above, in the regime of (arbitrary) weak turbulence, the MHD wave growth rate remains positive and so will drive the system toward a state of strong turbulence characterized by Eq. (12.13). Let us consider if the wave growth stops or continues in the strong turbulence regime. Importantly, we cannot adopt $\nu \to 0$ any longer in Eq. (12.16); instead, in the strong turbulence regime, it becomes equal to the relativistic gyrofrequency of accelerated proton:

$$\nu \approx v/\Lambda_{\parallel} \approx \Omega. \tag{12.40}$$

Instead of Eq. (12.25) we now have

$$\begin{aligned} \frac{1}{\Omega(1+a^2)} &= \frac{1}{2ck_{\parallel}}\left[\frac{1}{x+\xi(1-i)} - \frac{1}{x-\xi(1+i)}\right], \\ \frac{a}{\Omega(1+a^2)} &= \frac{-i}{2ck_{\parallel}}\left[\frac{1}{x-\xi(1+i)} + \frac{1}{x+\xi(1-i)}\right]. \end{aligned} \tag{12.41}$$

Taking the integrals within the same approximation as in Sect. 12.1.3 yields the accelerated particle current in the form of Eq. (12.26), with, however, different kinetic coefficients:

$$\sigma'_{\perp} = g' = \frac{\omega_{\rm pr}^2}{4\pi\omega_{Bi}}, \qquad \sigma''_{\perp} = 0, \qquad g'' = -\frac{\omega_{\rm pr}^2 ck_{\parallel}}{120\pi\omega_{Bi}^2} A(\ln\xi_0 - 1). \tag{12.42}$$

Accordingly, the complex frequency ω' obeys the equation

$$\omega'^2 - (v_A k_{\parallel})^2 + i\frac{\omega_{\rm pr}^2 v_A^2 (uk_{\parallel} + \omega')}{\omega_{Bi} c^2} = 0. \tag{12.43}$$

Although it is straightforward to exactly solve this equation, we analyze below its approximate solutions valid for the limiting cases of relatively small-scale and large-scale waves adopting $\omega' \ll uk_{\parallel}$. The demarcating scale $\lambda_c = 2\pi/k_c$ is reasonable to calculate from the condition that the absolute values of the second and third terms at the rhs of Eq. (12.43) are equal to each other, which yields $k_c = \omega_{\rm pr}^2 u/\omega_{Bi} c^2$.

For $k \gg k_c$ the imaginary term in the equation is small, so rewriting $\omega'^2 \approx (v_A k_{\parallel})^2 \pm 2i\gamma v_A k$, we find the imaginary part of the frequency

$$\gamma \approx \pm\frac{\omega_{\rm pr}^2 u v_A}{2\omega_{Bi} c^2}. \tag{12.44}$$

Thus, in the small-scale region of the spectrum, there is a growing mode whose growth rate is proportional to the number density N_0 and anisotropy u/c of the relativistic particles.

For the long waves, $k \ll k_c$, we can discard the quadratic over k term in Eq. (12.43), which yields the complex wave frequency in the form

$$\omega' \approx \pm(1-i)\sqrt{\frac{\omega_{\rm pr}^2 v_A^2}{2\omega_{Bi}c^2}uk} \sim \sqrt{k}. \tag{12.45}$$

This perturbation grows rapidly with the growth rate equal to the wave frequency; the growth rate is reciprocal to the square root of the corresponding wavelength in contrast to the case of the weak turbulence described by Eq. (12.35). Therefore, the considered instability is capable of generating large-scale irregularities of the magnetic field needed to efficiently accelerate high-energy particles. It is highly remarkable that even in the strong turbulence regime the instability does not quench and the growing mode still exist. This implies that excitation of such a strong turbulence by the relativistic particles in the upstream region is likely; to quench the instability one has to take into consideration the explicit effect of the strong turbulence ensemble on the spatial and angular distribution of the accelerated particles in the prefront region.

Let us estimate the effects obtained. Using Eq. (12.37) and employing definitions of frequencies $\omega_{\rm pr}$ and ω_{Bi} we obtain $k_c \approx 5.6 \times 10^{-6}(u/c)^3\,{\rm cm}^{-1}$ for the warm ISM phase. Then, for $u/c = 10^{-2}$, we find $\lambda_c = 2\pi/k_c \approx 10^{12}\,{\rm cm}$, which is comparable with the Larmor radius of moderately relativistic proton, $r_g = m_p c^2/eB = c/\omega_{Bi} \approx 10^{12}\,{\rm cm}$. Thus, Eq. (12.45) applies for all relativistic protons. For example, at the scale two orders of magnitude larger than the critical one, $\lambda = 10^2\lambda_c \approx 10^{14}\,{\rm cm}$, we estimate the growth rate as $\gamma \approx 10^{-6}\,{\rm s}^{-1}$; thus, the amplification time is $\Delta t \approx 10^6\,{\rm s}$, which is very short compared with all available SNR time scales including the free expansion and Sedov phase durations. The corresponding amplification time for the protons having the knee energy is about 10 years, which is still acceptable to support the efficient particle acceleration at the SNR shock waves and encouraging for developing acceleration models with self-generated strong turbulence.

Although the developed theory includes a nonlinearity over the turbulent wave ensemble (in the relaxation frequency approximation) it remains linear over the distribution function perturbations. We have to emphasize once again that this linearity of the theory preclude reliable analysis of the instability saturation level and saturated turbulence spectrum. A more advanced theory must take into account the modification of the particle distribution by the strong turbulence, as well as prefront nonuniformity and finite size of the quasispherical SNR shock front. Apparently, our plane front model can only be valid for perturbations with the scale small compared with the SNR radius and if the prefront thickness is small compared with the front size.

12.1.6 Spatial Distribution of Accelerated Particles Upstream

As we have seen the growth rate of the instability is proportional to the local number density of accelerated particles (with all energies). Test particle distribution function (12.10) used in our analysis is nonuniform in the prefront region; if $u \approx u_0 = \text{const}$ then the accelerated particles reside mainly in a finite layer with a thickness of $l(p) \approx \kappa_\parallel(p)/u_0$ dependent on the particle energy. Below we calculate the spatial distribution $N(z) = \int_{p_0}^{p_m} N(z,p)p^2\mathrm{d}p$ of the accelerated particles integrated over energy. The layer where $N(z)$ is reasonably large will also represent a region where the turbulence is efficiently generated. We again consider two cases—of either weak or strong turbulence.

1. **Weak Turbulence.** We employ a turbulence spectrum $\langle b^2\rangle_k \sim k^{-2}$ at a range of $k_0 \le k \le k_m$, Sect. 12.1.3, where the diffusion coefficient of relativistic particles is given by Eq. (12.12) with the longitudinal mfp $\Lambda_\parallel \approx r_g(p_m)$ comparable with the Larmor radius of the most energetic protons, which in its turn is comparable with the scale $L_0 = 2\pi/k_0$ of the largest-scale magnetic inhomogeneities.

   For constant $\kappa_\parallel$ and $u = u_0$ integration of $N(z,p)$ over entire momentum range yields

$$N(z) = \int_{p_0}^{p_m} N(z,p)p^2\mathrm{d}p = N_0 \exp\left(\frac{z}{l_m}\right), \qquad l_m = \frac{c}{3u_0}\Lambda_\parallel = \text{const}. \tag{12.46}$$

   Thus, the prefront thickness is specified by the scale l_m that depends on the mfp of largest energy particles, while does not depend on the accelerated particle spectrum.

2. **Strong Turbulence.** According to Sect. 12.1.3, the mfp of a particle is comparable with its Larmor radius (the smallest possible value, the Bohm mfp) (see Eq. (12.13)). Integrating distribution function (12.10a) with account of momentum dependence $\kappa_\parallel(p) \sim p$ we obtain adopting the spectral index $\alpha = 4$,

$$N(z) = N_0\zeta_0^{-1}[\Gamma(1,\zeta_m) - \Gamma(1,\zeta_0)], \tag{12.47}$$

   where $\Gamma(1,\zeta)$ the incomplete gamma function (Abramowitz and Stegun 1964)

$$\zeta_0(z) = \frac{3eu_0}{c^2p_0}\int_z^0 B(z')\mathrm{d}z' \quad (z \le 0) \tag{12.48}$$

   is a dimensionless scale, while ζ_m is similar to ζ_0 but with p_m instead of p_0.

The incomplete gamma-function asymptotes are

$$\Gamma(1,\zeta) \approx \begin{cases} 1-\zeta, & \zeta \ll 1, \\ \exp(-\zeta), & \zeta \gg 1. \end{cases} \tag{12.49}$$

Using these asymptotes we obtain $N(z) \approx N_0$ at small distance from the front, $\zeta_0 \ll 1$ and $\zeta_m \ll 1$, while

$$N(z) \approx N_0 \frac{p_0}{p_m} \frac{\exp(-\zeta_m)}{\zeta_m} \tag{12.50}$$

at large distance from the front, $\zeta_0 \gg \zeta_m \gg 1$. In the intermediate range of distances where $\zeta_0 \gg 1$, while $\zeta_m \ll 1$ we obtain

$$N(z) \approx N_0 \zeta_0^{-1} = \frac{N_0 c^2 p_0}{3u_0 e \int\limits_z^0 B(z')\mathrm{d}z'}. \tag{12.51}$$

Thus, for a moderate acceleration efficiency ($\lesssim 10$)% at a strong shock ($\alpha \approx 4$) and if the magnetic field is constant upstream, the number density decreases slowly with distance from the front,[4] as $N(z) \sim |z|^{-1}$. However, if the magnetic field itself decreases with the distance from the front, which is reasonable to expect if the strong turbulence is produced by particles accelerated at the front, the number density will decrease even slower than $N(z) \sim |z|^{-1}$. To summarize, the accelerated particle number density is roughly constant within a layer with thickness $l_0 \approx cr_g(p_0)/3u_0$ and then decreases slower than $1/|z|$ in the layer bounded by l_0 and $l_m \approx cr_g(p_m)/3u_0 \gg l_0$. At even larger distance $|z| \gg l_m$ the number density decreases exponentially. Thus, the total prefront thickness is again specified by the particles with largest available energy.

12.1.7 On Numerical Simulations of Strong Turbulence Generation at Shocks

Apparently, the considered above analytical model is built on many simplifying assumptions since it is difficult to analytically account such important ingredients of the system as strong multi-scale inhomogeneity and consistently obtain nonlinear evolution and saturated levels of the turbulence and particles in the anticipated regime of strong turbulence generation and powerful particle acceleration. Not surprisingly, a huge amount of (nonlinear self-consistent)

[4]Note that quasilinear solution for the particle and resonant self-generated turbulence distributions (Lee 1983; Lagage and Cesarsky 1983; Fedorenko and Fleishman 1988) contains a similar spatial dependence, $\sim|z|^{-1}$, for particles with a *given energy*, while here it is only valid for the particle number density. The difference originates because the quasilinear models consider saturated state of the resonant streaming instability, while here a preexisting turbulence level is postulated and further wave generation on top of it studied.

numerical models addressing different aspects of the collisional shock wave physics have been developed (e.g., Zirakashvili and Ptuskin 2008; Vladimirov et al. 2009; Reville and Bell 2012). In particular, we have already noted in Sect. 11.4.3 that a numerical model of (Vladimirov et al. 2009) yields the inflow velocity profile and the compression ratio range fully consistent with the simplified analytical model developed in Sect. 11.4.3.

The situation with strong turbulence generation and formation of its broad-band spectrum is more complicated. For example, there can appear a variety of instabilities capable of generating magnetic field at different scales: from very small-scale Weibel/filamentation instability (see Sect. 4.1.2) to very large-scale nonresonant instability considered above in this section. To correctly account the entire range of the scales the numerical model must correctly describe all these scales over many orders of magnitude, which is a highly demanding computational task. Then, the results of the computer simulations are highly sensitive to nonlinear cascading regime of the generated turbulence. A simplified model of isotropic cascading may not be necessarily applicable, since we saw in Sect. 6.9.3 that the turbulence cascades anisotropically within the strong turbulence regime. On the other hand, in the regime of very strong turbulence generation, the role of the anisotropy induced by original (weak) regular magnetic field can be minor; all these considerations produce huge uncertainty in the turbulence cascade modeling.

Taking all these uncertainties into account, we mention the most general (model independent) results of these numeric simulations. A highly efficient generation of the turbulent magnetic field does take place. Mean (turbulent large-scale) magnetic field increases gradually at the upstream region from the ISM values of $\sim 3\,\mu$G to 0.1–1 mG, i.e., the rms magnetic field value experiences 30–300-fold enhancement. The spectrum of generated turbulence is, however, highly sensitive to the model assumptions: overall, almost any spectrum can be obtained—from almost flat to highly structured multi-peak spectrum indicative that the problem of the turbulent generation upstream is far from its final solution. The particle distribution functions in most cases display highly efficient acceleration expected in the regime of strong magnetic turbulence amplification. To summarize, we can conclude that the analytical treatment given above and in Sect. 11.4.3 offers a correct physical picture of main physical phenomena occurring in the vicinity of a strong collisionless shock front, although many important details have yet to be clarified and worked out.

12.1.8 Evidence of Efficient Particle Acceleration at SNRs

Ample observational evidence confirming highly efficient electron and ion acceleration at the SNR shocks has been accumulated. In particular, the electrons accelerated at a strong shock front, Sect. 11.4.2, have energy spec-

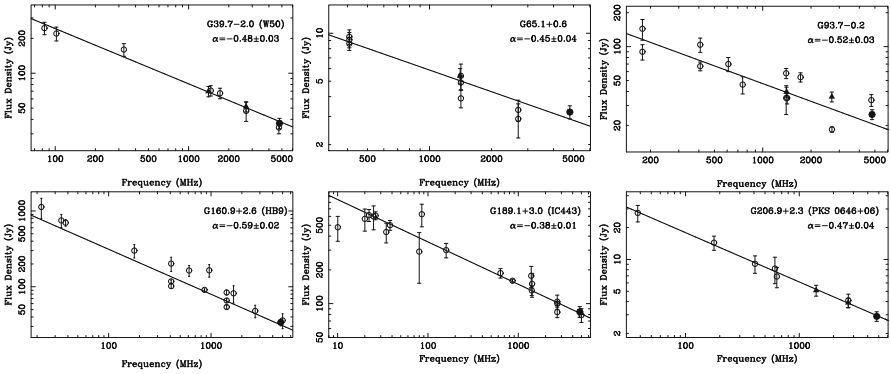

Figure 12.1: Examples of observed radio spectra from a few galactic SNRs. The spectral indices are grouped around 0.5, which is expected value for particle acceleration at a strong shock; however, the scatter of the indices is noticeable including values significantly smaller than the nominal value 0.5, which is indicative of effects of nonlinear shock modification considered in Chap. 11. Credit: (Gao et al. 2011). Reproduced with permission © ESO.

tral index $\xi \approx 2$ in Eq. (9.169) and so must produce synchrotron radiation with spectral index $\alpha_{\rm nth} \approx 0.5$. Indeed, radio spectra with such indices (see Fig. 12.1) are commonly observed from shell-type SNRs where a quasispherical shock wave is formed at the supernova explosion and then expands into the ISM as has been described in Sect. 5.5.

Note that the statistically significant deviations of the observed radio spectral indices from the nominal value of 0.5 imply (though indirectly) a key role of the CRs: the indices $\alpha < 0.5$ might be indicative of the compression ratio increase due to non-negligible CR pressure, while the indices $\alpha > 0.5$ are likely produced at a thermal jump of a shock whose structure is nonlinearly modified by the CR effect considered in Sect. 11.4.3. The observations of the power-law radio spectra from SNRs, however, directly confirm acceleration of electrons only and up to a moderate energies only, typically, $\lesssim 10\,$GeV, much smaller than the knee energy, while the electrons approaching the knee energy would produce X-ray emission (see Sect. 9.4.3).

Thus, not surprisingly, key evidence of the efficient particle acceleration at the SNR shocks came from X-ray and gamma astronomy as soon as they become mature to record the emissions with high spectral and spatial resolution, high sensitivity, and reliable absolute calibration. For example, in case of young SNR 1006, Allen et al. (2008) demonstrated that the spatially resolved radio-to-X-ray spectra obtained for all the square boxes in Fig. 12.2, left, have a concave shape, which implies that the electron energy spectrum flattens with the electron energy having $\xi \approx 2.2$ at the GeV range, while $\xi \approx 2.0$ at the TeV range. This finding was reasonably interpreted in terms of the nonlinear modification of the shock wave profile by the CR pressure: high-energy X-ray-producing particles "see" the total compression of the en-

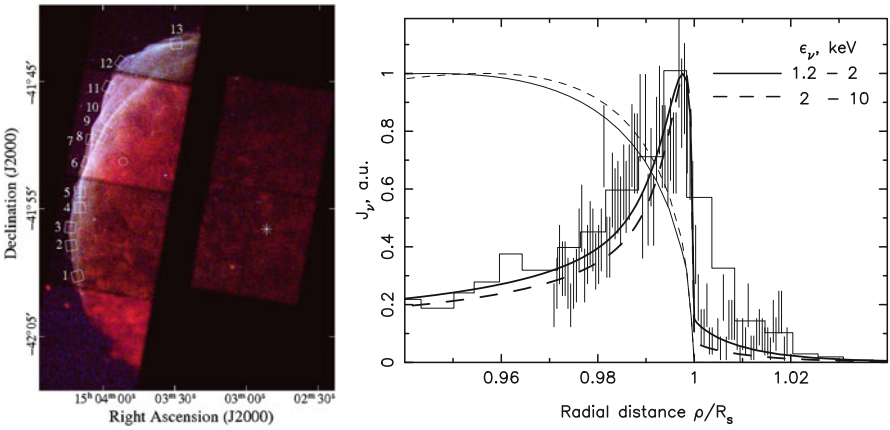

Figure 12.2: *Left*: composite X-ray image of SNR 1006 with a number of spatial boxes used for the spectral shape study by Allen et al. (2008). Reproduced by permission of the AAS. *Right*: radial distribution of X-ray brightness at the SNR and two model distributions—with and without significant magnetic field amplification (Berezhko et al. 2003). Reproduced with permission © ESO. Apparently, the observations support the model with significant magnetic field amplification.

tire shock transition region including the sharp thermal jump and a more gradual prefront region (see Sect. 11.4.3), while lower-energy radio-producing particles having smaller mfp experience acceleration by a fraction of the total fluid compression at the thermal jump only, which results in a steeper spectrum.

Furthermore, the radial distribution of the observed X-ray intensity offers a highly conclusive diagnostics. Indeed, this distribution (see Fig. 12.2, right, as an example) displays a prominent peak at the apparent shock front location. However, if one adopts the downstream magnetic field to be just shock-compressed ISM value, $\sim 10\,\mu$G, the radial distribution would be very broad provided that the quasiuniform magnetic field does not significantly decay downstream, while the particle distribution is more or less uniform there unless an efficient mechanism of the particle energy loss is on. For a relatively tenuous ISM plasma the electron Coulomb losses are negligible, while the radiative (synchrotron) losses, whose characteristic time scale is

$$\tau_s \approx 2 \cdot 10^4 \left(\frac{10^{-5}\mathrm{G}}{B}\right)^2 \left(\frac{10^7}{\gamma}\right) \text{ years}, \tag{12.52}$$

where γ is the electron Lorentz factor, may become essential.

Nevertheless, for typical ISM magnetic field values, the synchrotron losses are too weak to form the observed narrow filaments even if the particle diffuse

in the Bohm regime (i.e., their diffusion rate down from the front is slowest possible). Thus, we must unavoidably conclude that the magnetic field amplitude at the front must be greatly enhanced, which increases the synchrotron loss rate and also enhances the particle diffusion confining electrons near the front. To fit the data consistently (see Fig. 12.2) right, requires a model with a highly efficient, by more than 10 times, magnetic field amplification, $B \gtrsim 100\,\mu$G. This enhanced magnetic field, as we have seen above, can only be generated by the accelerated particles themselves in the form of strong magnetic turbulence.

This conclusion has a number of particularly important consequences. First, the self-generated turbulent magnetic field strongly exceeds the initial regular magnetic field, which implies that the accelerated particles do diffuse in the Bohm regime or very close to it. Second, one can easily estimate that the relativistic electron energy content needed to produce the absolute radio and X-ray fluxes in the derived magnetic field of $B \gtrsim 100\,\mu$G is a minor fraction, about 10^{-3}, compared with the shock wave kinetic energy. Therefore, the accelerated electrons are dynamically negligible and so they cannot produce either shock structure modification or magnetic field generation. Thus, a much more powerful acceleration of the nuclear component is needed to modify the shock dynamics as observed. And third, given that the turbulent (random) magnetic field dominates in the radiation source, one must consistently take this into account while computing the radiation spectra, spatial distribution, and the radiative losses, which was considered in great detail in Sect. 9.5. In particular, as can be noted (see Fig. 12.6), the electron radiative losses are reduced if the magnetic field is random instead of regular. This further implies that to have the same radiative losses at the level needed to form the narrow filaments as observed requires even stronger turbulent magnetic field to be produced by accelerated particles.

Nevertheless, all the presented evidence and considerations remain indirect, so it would be desirable to detect a radiation produced by the nuclear CR component itself. One of very few radiation windows in which the nuclear component can make a dominant contribution is the gamma-ray range, where the nucleon collisions of CRs with background nuclei produce neutral pions π^0 decaying, in their turn, into gamma quanta with $\mathcal{E} \gtrsim 50\,$MeV and up to VHE quanta of $> 100\,$TeV produced by the particles with the knee energy. Although detection of these VHE quanta is very difficult observationally, there are VHE data on a few SNRs. Figure 12.3 displays an example of a very broadband SNR spectrum including the VHE range. Remarkably that the inverse Compton contribution calculated based on the relativistic electron spectrum and magnetic field derived from the synchrotron data underestimates the observed VHE emission level substantially, while the nuclear π^0 contribution calculated based on nonlinear shock acceleration model with strong self-generated turbulence where about 10% of the fluid flow energy is

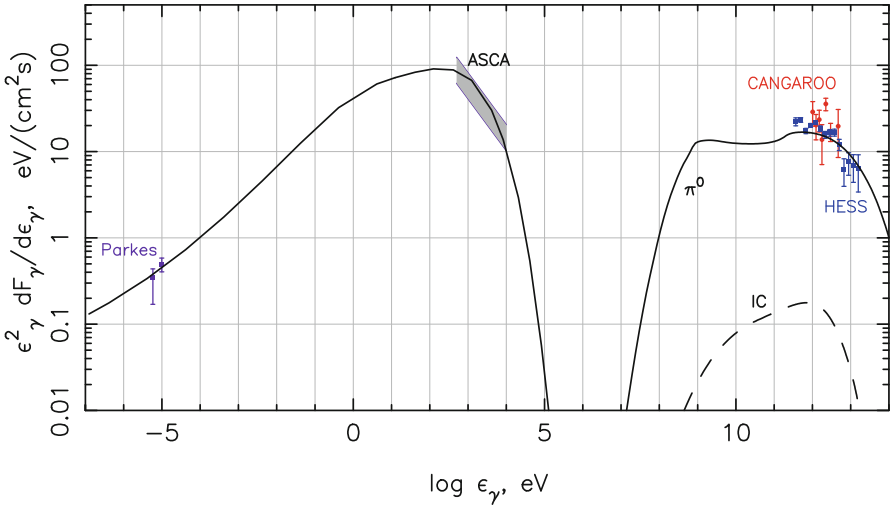

Figure 12.3: Calculated broadband spectral energy distribution of SNR RX J0852.0-4622 versus photon energy ϵ_γ. The synchrotron part of the spectrum is calculated for an enhanced magnetic field of $\sim 100\,\mu$G needed to account the spatial morphology of the remnant including observed narrow filaments. Having the same radiation level with an enhanced magnetic field implies a correspondingly reduced electron energy spectrum, resulting in a very weak level of the inverse Compton radiation (*dashed line*) compared with the observed VHE gamma-ray emission indicative of the VHE gamma rays to be hadronically dominated (*solid curve* displays the gamma-ray emission produced via π^0-decay). Credit: (Berezhko et al. 2009). Reproduced with permission © ESO.

spent to the CR acceleration offers a nice consistent fit to the data. Thus, this observation of the VHE radiation yields a firm direct evidence in favor of the CR acceleration at the SNR shocks up to at least the knee energy.

Although we presented only a few particular results and discussed explicitly a very limited number of objects, we emphasize that similar observations are available for many other young SNRs, so the picture outlined is currently adopted as a standard acceleration scenario at the SNR shocks. We conclude that recent progress of the multiwave astronomical observations in radio, X-ray, and gamma-ray ranges has provided us with firm evidence in favor of turbulence generation and strong particle acceleration at least up to the knee energy at the SNR shocks with the efficiency sufficient to account the phenomenon of galactic CRs and also shed new light on the dynamics of the SNRs themselves (see Ptuskin 2010; Vink 2012 and references therein for greater detail).

12.2 Neutron Stars and Particle Acceleration in Their Magnetospheres

We have already addressed in Sect. 8.7.3 a key property of the neutron starts—their superstrong magnetic fields reaching likely very high values of 10^{14}–10^{15} G. This and other extreme properties of the neutron stars, e.g., their very high density, put them in the very top of the list of the most intriguing and peculiar objects in the Universe. Indeed, for a modest stellar mass of $M \approx 1.4 M_\odot \approx 2.8 \times 10^{33}$ g, while a very small radius $a \approx 10$ km, the mean density of a neutron star is about $\overline{\rho} = 3M/4\pi a^3 \approx 7 \times 10^{14}\,\mathrm{g/cm^3} \approx (2$–$3)\rho_0$, where $\rho_0 \approx 2.8 \times 10^{14}\,\mathrm{g/cm^3}$ is the density inside usual heavy nuclei; the corresponding gravitational energy is $E_g \approx GM^2/a \approx 5 \times 10^{53}$ erg$\approx 0.2Mc^2$. For comparison, the Sun having roughly the same mass has a radius of $R_\odot \approx 7 \times 10^5$ km$\approx 7 \times 10^4 a$, the density of $\rho_\odot \approx 1.4\,\mathrm{g/cm^3} \approx 2 \times 10^{-15}\overline{\rho}$, and the gravitational energy of $E_{\odot g} \approx 1.5 \times 10^{-5} E_g \approx 10^{-5} M_\odot c^2$. Neutron stars are very powerful and peculiar emitters of electromagnetic energy—from radio waves to TeV gamma rays.

The neutron stars were discovered as **radio pulsars**; this term was proposed to highlight the main observational property specific to this type of objects—their ability to produce a pulsating radio emission with highly stable periods. Remarkably, that identification of discovered in 1967 radio pulsars with neutron stars happened very quick, during a few first years of pulsar study. The uniqueness of the neutron stars and their impact on the global picture of the Universe were boldly summarized by outstanding American scientists Freeman Dyson (1970):

> I myself find that the most exciting part of physics at the present moment lies on the astronomical frontier, where we have just had an unparalleled piece of luck in discovering the pulsars. Pulsars turn out to be laboratories in which the properties of matter and radiation can be studied under conditions millions of times more extreme than we had previously had available to us. We do not yet understand how pulsars work, but there are good reasons to believe that they are the accelerators in which God makes CRs. Besides providing CRs for the particle physicists, the pulsars will, during the next 30 years, provide crucial tests of theory in many parts of physics ranging from superfluidity to general relativity.

The cited Dyson's words imply that a deep study of the neutron stars requires usage of almost all kinds of physical science. Below we give a very brief description of some most fundamental observable physical phenomena occurring in the neutron star magnetospheres.

12.2.1 Basic Observational Data

A first guess that there can be stars having densities comparable with the nuclear density was made by Lev Landau (1932) even before the very neutron was discovered by James Chadwick in 1932: "...the density of matter becomes so great that atomic nuclei come in close contact, forming one gigantic nucleus." Then, after the neutron discovery, Baade and Zwicky (1934) proposed that neutron stars can be produced by supernova explosions. But observationally, the neutron stars had to await the discovery of pulsating radio sources, pulsars, by Cambridge University scientists Jocelyn Bell and Antony Hewish in 1967. Detailed reviews of the topic were published by ter Haar (1972) and then by Manchester and Taylor (1977), Shapiro and Teukolsky (1983), Beskin et al. (1993), Haensel et al. (2007), Istomin (2008) and Potekhin (2010).

The most fundamental properties of the pulsar radio emission are:

1. The periods of pulse repetition P belong to the range from $\sim$1 ms to a few seconds.

2. The accuracy of the pulse periodicity is very high. Some of the pulsars have periods with 13 meaningful digits, i.e, they represent highly precise clocks.

3. The pulsar periods are gradually declining; no *gradual* increase of the period was ever detected. However, *abrupt* increases of the period are observed sometimes, which have been interpreted as "starquakes" resulted in a fast star restructurization. The gradual period decline is characterized by its derivative $\dot{P}$. Typically, $\dot{P} \approx 10^{-15}$; the ratio $P/\dot{P}$ characterizing the pulsar age is $\approx 10^6$–10^7 years; it never exceeds 10^9 years.

Intensity of the pulsar radio emission varies significantly; sometimes the emission switches off entirely (switching-off or periodically active pulsars). The light curve of a single pulse has a complex structure with a few sub-pulses. The radio emission contains linearly and circularly polarized components. A single pulse lasts only a tiny fraction of the period. The pulsar radio emission is broadband occupying a spectral range at least from 10 MHz to 5 GHz. Some of the pulsars also display pulsations in the infrared, visual, X-ray, and gamma-ray ranges (e.g., TeV gamma emission was recorded from Vela pulsar). Then, there are X-ray pulsars that do not produce radio pulsations (radio quiet pulsars; we discussed a possible interpretation for that in Sect. 8.7.3). It should be noted that the brightness temperatures (see Chap. 10 for definition) are strongly different depending on the emission wavelength: the radio emission has a very high brightness temperature up to 10^{21} K indicative of a coherent emission process, while both optical and X-ray emissions have brightness temperatures below 10^9 K. More than 1,500 pulsars have been detected by the time of writing (2012).

Almost half a century of intensive pulsar study resulted in a classification of the known neutron stars into distinct subclasses. In particular, a neutron star can emit either a steady X-ray (gamma-ray) flux or a pulsating emission resembling the radio pulsar phenomenon. Then, if a neutron star enters a binary system, the companion star can supply it with an accreting material. This accretion reveals itself via sporadically occurring strong X-ray flashes and gamma-ray bursts (GRBs) releasing up to 20% of the accreting plasma rest energy. Of particular interest is a population of the neutron stars with superstrong magnetic field reaching 10^{14}–10^{15} G, called **magnetars**, which, compared with the radio pulsars, are characterized by (1) relatively slow star rotation, $P = 5$–10 c; (2) fast spin-down deceleration, $\dot{P} = 10^{-10}$–10^{-12}; (3) strong X-ray and gamma-ray flashes; and (4) dominance of the magnetic energy over the rotational kinetic energy.

Let us show the latter explicitly. The magnetic energy in the star volume is $E_{\rm magn} \approx (B^2/8\pi)(4\pi a^3/3) \approx 1.5 \times 10^{47}$ erg for $B = 10^{15}$ G (we adopted the same magnetic field at the surface and inside the star) and $a = 10$ km. The rotational kinetic energy is $E_{\rm rot} = J\Omega^2/2 \approx 2 \times 10^{44}$ erg for $J = 10^{45}$ g cm^2 and $P = 10$ s. The mentioned above deceleration rate implies the loss of rotational energy with the rate $\dot{E}_{\rm rot} = J\Omega\dot{\Omega} \approx 4 \times (10^{32} - 10^{30})$ erg/s, while the observed X-ray luminosity of a magnetar is $L = 10^{35}$–10^{36} erg/s. Therefore, the kinetic energy of the star is insufficient to supply the observed X-ray luminosity, which, thus, must be taken largely from the magnetic energy.

Perhaps, the most studied neutron star is the pulsar PSR 0532 in the Crab Nebula, which has been produced by a supernova explosion observed by Chinese astronomers in 1054. The Crab Nebula is located roughly 2 kpc from the solar system. The Crab pulsar has been thoroughly observed throughout the electromagnetic spectrum from 10 MHz up to 100 MeV including infrared, optical, and X-ray ranges. These emission pulses arrive with a frequency-dependent delay defined by the dependence of the wave group velocity on frequency (see Problem 10.2). The Crab pulsar has a relatively short period, $P = 0.033$ s and large spin-down deceleration, $\dot{P} = 4.2 \times 10^{-13}$. The full luminosity of the nebula is estimated as $L \approx 10^{38}$ erg/s, with roughly 12% in the radio domain.

The common hypothesis of the neutron star origin is core-collapse supernova explosions of heavy stars with $M \gtrsim 8M_\odot$. A considerable fraction of this mass is ejected into ISM to form a nebula, while a compact central remnant with a mass of $M \lesssim 1.4M_\odot$ forms a neutron star. The exact upper bound of the neutron stars depends on yet unknown equation of state of the superdense substance. The heaviest ever detected neutron star in a binary system PSR J1614 2230 has a mass of $M = (1.97 \pm 0.04)M_\odot$. This hypothesis agrees well with spatial distribution of the pulsars in the Galaxy that is similar to the distribution of their progenitors—OB stars and supernovae. In particular, most of the pulsars are located in the galactic disk.

Nevertheless, a direct identification of the pulsars with given supernovae has only been performed for a very limited number of the cases. One of these lucky cases is the Crab pulsar, while most of the pulsars are lacking any identification with a supernova. This can partly happen because of supernova explosion asymmetry resulting in a large runaway velocity of the neutron star that can be in excess of 100 km/s. If so the star can run dozens of parsecs from the explosion site over million years of its evolution. Another possible cause of the pulsar runaway is an asymmetry of the emitted radiation (see the next section) back reaction, which is possible if the magnetic dipole axes is displaced from the star rotation axes.

In what follows, unless explicitly stated a different, we use for estimates the following "mean" parameters of the neutron star: $M \approx M_\odot$ is of the order of the solar mass, the radius $a \approx 10^6\,\mathrm{cm} = 10\,\mathrm{km}$, the inertia moment $J \approx 10^{45}\,\mathrm{g{\cdot}cm^2}$, the rotation period $P \approx 1\,\mathrm{s}$, spin-down deceleration rate $\dot{P} \approx 10^{-15}$, and the magnetic field at the surface of rigid crust $B_{\max} \approx 10^{12}\,\mathrm{G}$.

12.2.2 Magnetic Dipole Radiation and Particle Acceleration

Perhaps, a simplest model capable of explaining the most basic pulsar properties is the oblique magnetic rotator in vacuum. A conducting filled sphere with a magnetic moment $\boldsymbol{m}$ rotates in the vacuum with the angular velocity $\boldsymbol{\Omega}$ ($\Omega = 2\pi/P$); the vectors $\boldsymbol{m}$ and $\boldsymbol{\Omega}$ are not parallel to each other while making an angle $\varphi \neq 0$. In the system rotating along with the sphere there exists a static dipole magnetic field, whose peak values $B_{\max}$ are located at the magnetic poles of the sphere and can easily be calculated for a given magnetic dipole model:

$$m = B_{\max} a^3/2. \tag{12.53}$$

In the laboratory (observer's) system the rotating magnetic moment produces the magnetic dipole radiation, whose intensity [similarly to the electric dipole radiation described by Eqs. (9.66) and (9.100)] is described by

$$\frac{\mathrm{d}I}{\mathrm{d}\Omega_{\mathbf{n}}} = \frac{1}{4\pi c^3}|\boldsymbol{n} \times \ddot{\boldsymbol{m}}|^2, \tag{12.54}$$

where $d\Omega_{\mathbf{n}}$ is the solid angle element and $\boldsymbol{n}$ is the unit wave vector of radiation. From the equation of steady rotation $\dot{\boldsymbol{m}} = \boldsymbol{\Omega} \times \boldsymbol{m}$ of the magnetic moment we find

$$\frac{\mathrm{d}I}{\mathrm{d}\Omega_{\mathbf{n}}} = \frac{\Omega^4 m_\perp^2}{4\pi c^2}[1 - \sin^2\vartheta \cos^2(\Omega t' - \alpha)]. \tag{12.55}$$

Here $t' = t - r/c$ is the retarded time, $\boldsymbol{m}_\perp$ is component transverse to the rotation axes; ϑ is the polar angle relative to the rotation axes; $\Omega t'$ and α are the azimuth angles of vectors $\boldsymbol{m}_\perp$ and $\boldsymbol{n}$ in the plane transverse to $\boldsymbol{\Omega}$.

The equation obtained (for $\sin^2\vartheta \neq 0$) is fully consistent with the observed constancy of emission period specified by the angular velocity Ω of the star rotation, which is highly stable due to angular momentum conservation. Apparently, Eq. (12.55) does not and cannot explain either shape or duration of the radio pulses or their spectra. Emission (12.55) is monochromatic at the frequency Ω, while the observed radiation has a broadband spectrum. The pulse duration is only a few percent of the period P; the shape of the light curve is complicated and not unique. The short duration of the pulses suggests a high directivity of the emission in contrast to angular distribution described by Eq. (12.55).

After averaging over time and integration over the full solid angle we find the full radiated power:

$$\overline{\frac{\mathrm{d}I}{\mathrm{d}\Omega_{\mathbf{n}}}} = \frac{\Omega^4 m^2 \sin^2\varphi}{8\pi c^3}(1+\cos^2\vartheta), \qquad \overline{I} = \frac{2\Omega^4 m^2 \sin^2\varphi}{3c^3}. \tag{12.56}$$

Assuming that the energy losses due to the magneto-dipole radiation are the main cause of the star spin down ($\dot{\Omega} < 0$ or $\dot{P} > 0$), we can estimate the star magnetic field via observed values of P and $\dot{P}$ and theoretically well-determined inertia moment J and radius a of the neutron star.

The rotational kinetic energy of the star is $\mathcal{E}_{\mathrm{rot}} = J\Omega^2/2$; for its loss rate we can apparently write

$$\dot{\mathcal{E}}_{\mathrm{rot}} = J\Omega\dot{\Omega} = -(2\pi)^2 J\dot{P}/P^3. \tag{12.57}$$

Equating this loss rate to the radiated power, Eq. (12.56), using Eq. (12.53), and adopting $\sin^2\varphi = 1$ we obtain

$$B_{\max} = \left(\frac{3c^3 JP\dot{P}}{2\pi^2 a^6}\right)^{1/2}. \tag{12.58}$$

Equation (12.58) offers an observational estimate for the magnetic field regardless its origin. Adopting the "standard" parameters of a neutron star given at the end of Sect. 12.2.1, we obtain $B_{\max} \approx 1.4 \times 10^{12}$ G. Apparently, this estimate gives only a very rough idea of the global magnetic field magnitude at a neutron star surface. As we have noticed in Sect. 8.7.3, local magnetic fields derived from cyclotron X-ray lines can be much larger than this global field.

On the other hand if the pulsar magnetic field is independently known then the derived simple equations allow estimating another important parameter of the pulsar—its age if we additionally adopt approximate constancy of the magnetic field over the star lifetime. The latter assumption is reasonable because the star body contains many free charges and so represents a highly conducting medium. The magnetic field dissipation time, according to results of Sect. 2.3.1, is:

$$\tau_d \approx \frac{a^2}{4\pi\nu_m} = \frac{a^2\sigma}{c^2}, \tag{12.59}$$

where σ describes some effective "mean" conductivity of the star substance.

It is, however, difficult to reliably estimate this effective conductivity because the neutron star is highly inhomogeneous in the composition, density, temperature, and, eventually, the conductivity. On top of that, superfluidity and superconductivity are likely to be present in the star core (Yakovlev et al. 1999; Haensel et al. 2007; Potekhin 2010). Accordingly, estimates of the global field dissipation time differ by orders of magnitude ranging from a few million years to longer than the Universe age. However, even the minimum estimate of a few million years allows neglecting the magnetic field dissipation over the pulsar lifetime. For a constant field (and constant star radius and inertia moment) Eqs. (12.56) and (12.57) yield a simple law of the star angular velocity variation:

$$\frac{\mathrm{d}\Omega}{\mathrm{d}t} = -C\Omega^3, \quad \text{where} \quad C = \frac{B_{\max}^2 a^6 \sin^2\varphi}{6c^3 J} = \text{const}. \tag{12.60}$$

Integration of this equation yields the pulsar lifetime:

$$\Delta t = \frac{1}{2C}\left(\frac{1}{\Omega^2} - \frac{1}{\Omega_0^2}\right), \tag{12.61}$$

where $\Omega_0 > \Omega$ is the original star angular velocity at the time the neutron star was born. For old stars with noticeable angular deceleration, $\Omega \ll \Omega_0$, we obtain a simple expression of the pulsar age via its period P and magnetic field:

$$\Delta t = \frac{3c^3 J}{4\pi^2 B_{\max}^2 a^6 \sin^2\varphi} P^2, \tag{12.62}$$

which is two times smaller than $|P/\dot{P}|$, i.e., both rough estimates agree with each other to the order of magnitude.

This simple model of radiating magnetic dipole in vacuum does not include other important deceleration mechanisms such as gravitational radiation and numerous plasma effects. For example, the gravitational radiation is possible when the star shape deviates from the ideal spherical shape while represents an ellipsoid due to rotation and anisotropy induced by the magnetic field. Shapiro and Teukolsky (1983) estimated that the gravitational radiation can dominate the star spin down at an early stage of the pulsar evolution. Higher multipoles can further contribute to electromagnetic radiation and corresponding losses; the plasma effects will be considered in the next section.

Phenomenologically, the cumulative effect of all deceleration mechanisms is taken into account by introducing a so-called **breaking index** n:

$$\dot{\Omega} = \text{const} \cdot \Omega^n. \tag{12.63}$$

Comparison of this form with Eq. (12.60) shows that for the magnetodipole case $n = 3$. Other braking mechanisms are characterized by different dependencies of $\dot{\Omega}$ on the angular velocity Ω. For example, if the gravitational radiation dominates, then $n = 5$, while for multipole electromagnetic radiation $n \geqslant 5$. Furthermore, n can deviate from the canonic value $n = 3$ due to any asymmetry: if the magnetic poles wander over the star surface or the rotation axes deviates from one of the star principal axes.

Observationally, the braking index can be determined from the rotation period and its two first derivative. Indeed, taking the time derivative of Eq. (12.63) and solving for n, we obtain $n = \Omega\ddot{\Omega}/\dot{\Omega}^2$. Apparently, precise measurements of the derivatives is a highly challenging task that was addressed for some of the pulsars. For example, for one of the best studied Crab pulsar, the braking index is found to be $n = 2.515 \pm 0.005$.

Rotation of the neutron star magnetic moment induces a strong variable electric field in the ambient space, which can accelerate charged particles. Let us estimate expected energy of the accelerated particles within the considered simple vacuum model. Below we use equation of motion

$$m\dot{\boldsymbol{v}} = e\left(\boldsymbol{E} + \frac{1}{c}\boldsymbol{v} \times \boldsymbol{B}\right) \tag{12.64}$$

for nonrelativistic particles and equation of energy balance

$$\dot{\mathcal{E}} = e\boldsymbol{v} \cdot \boldsymbol{E} \tag{12.65}$$

for relativistic particles. In the vacuum case the electric field in the near field zone, $r \lesssim \lambda = 2\pi c/\Omega = cP$, is small because $\boldsymbol{E} = -i(c/\Omega)\nabla \times \boldsymbol{B}$, while $\nabla \times \boldsymbol{B} \approx 0$ there. The electric field approaches by value the magnetic field in the wave zone only, $r \gtrsim \kappa\lambda \gg a$, where $\kappa > 1$ is a constant. We expect, therefore, that the particle acceleration region is located in a closest to the star part of the wave zone.

Let us estimate the energy gain of a nonrelativistic particle over half of the wave period using Eq. (12.64):

$$\Delta v \approx \frac{1}{2}P\dot{v} = \frac{eP}{2m_{e,p}}E. \tag{12.66}$$

Here we retain only the electric field that is capable of explicitly changing the absolute value of the particle velocity. This electric field is then calculated using formulae for the magneto-dipole radiation:

$$\boldsymbol{E} = -\frac{1}{c}\frac{\partial \boldsymbol{A}}{\partial t} = \frac{1}{c^2 r}\boldsymbol{n} \times \ddot{\boldsymbol{m}}. \tag{12.67}$$

Equations (12.67) and (12.53) along with equation of the magnetic moment motion yield

$$\Delta v \approx \frac{e\Omega^2 B_{\max} a^3}{4\kappa m_{e,p} c^3} \approx \frac{1}{\kappa P^2}\left\{\begin{array}{c} 10^{17} \\ 10^{14} \end{array}\right\} \text{cm/s}. \tag{12.68}$$

This implies that both electrons and protons became ultrarelativistic over a very short time compared with the field period; thus, the energy gain must be calculated using Eq. (12.65) adopting $v \approx c$:

$$\Delta\mathcal{E} = ec \int_{t_0}^{\infty} E \, \mathrm{d}t. \tag{12.69}$$

The particles are picked up toward wave propagation so we can integrate over $\mathrm{d}r = c\mathrm{d}t$, where $\kappa\lambda \leq r < \infty$. The field depends on r as $r^{-1}\exp(i\Omega r/c)$. Making estimate like in Eq. (12.68) we obtain

$$\Delta\mathcal{E} \approx \frac{2\pi e B_{\max} a^3}{\kappa c^2 P^2}. \tag{12.70}$$

Note that the rhs does not contain the particle mass.

Parameter $2\pi/\kappa$ is about one. The accelerated particle energy is proportional to the pulsar magnetic field and reciprocal to the period squared. Substituting $a^3 \approx 10^{18}\,\mathrm{cm}^3$, we obtain

$$\Delta\mathcal{E} \approx \frac{0.5 B_{\max}}{P^2}\ eV. \tag{12.71}$$

For most of the pulsars $B_{\max} \approx 10^{11}$–$10^{12}\,\mathrm{G}$ and the rotation period $\sim$1 s or less. This gives a moderate energy of the accelerated particles, $\mathcal{E} \approx 10^{11}$–$10^{12}\,\mathrm{eV}$. However, much higher energies are well possible. Indeed, for the Crab pulsar (PSR 0532), we have $B_{\max} \approx 10^{12}\,\mathrm{G}$ and $P \approx 0.033\,\mathrm{s}$, which yields $\mathcal{E} \approx 10^{15}\,\mathrm{eV}$. For the Vela pulsar (PSR 0833) $B_{\max} \approx 10^{12}\,\mathrm{G}$ and $P \approx 0.1\,\mathrm{s}$; thus, $\mathcal{E} \approx 10^{14}\,\mathrm{eV}$. Overall, in terms of the plausible conditions for the particle acceleration the most promising are the youngest pulsars having the shortest pulsation periods of the order of 1 ms. For the standard field $10^{12}\,\mathrm{G}$ they can ensure particle acceleration up to $\sim 10^{18}\,\mathrm{eV}$.

12.2.3 Structure of Pulsar's Magnetosphere

Let us now consider if the above assumption that the vacuum immediately surrounds the solid surface of the star is plausible and what is a more realistic structure of the stellar atmosphere. We first try to establish an analogy between atmospheres of the neutron star and the Earth because both these celestial bodies have solid crusts. The terrestrial atmosphere is confined by the Earth gravitation that controls distributions of its density and pressure, which for a isothermal atmosphere model results in a well-known barometric distribution.

Given the pulsar temperature is high, $\gtrsim 10^6\,\mathrm{K}$, the matter in the magnetosphere is supposed to be almost fully ionized. The charged particles are affected by both gravitational and electromagnetic forces, whose role we estimate below. Adopt a to be the radius of the solid body of the star, then, at

$r > a$, the density of the pulsar atmosphere obeys the Boltzman distribution:

$$n(r) = A \exp\left(-\frac{U(r)}{T}\right), \quad \text{where} \quad U(r) = -\frac{GmM}{r}, \; r > a \tag{12.72}$$

is the potential energy of a particle with mass m in the gravitational field of the star with mass M, G is the gravitational constant, T is the temperature expressed in energy units, and A is a normalization constant. At large heights, $z \ll a$, we can substitute $r = a + z$ to obtain the barometric formula:

$$n(z) = n_0 \mathrm{e}^{-z/h}, \qquad h = \frac{Ta^2}{GmM}, \tag{12.73}$$

where h is the effective atmosphere height. Adopting $T \approx 100\,\mathrm{eV}$, $a = 10^6\,\mathrm{cm}$, and $M = M_\odot$, we arrive at $h_p \approx 1\,\mathrm{cm}$ for a proton and $h_e \approx 10\,\mathrm{m}$ for an electron. The smallness of these heights compared with the star radius could imply applicability of the vacuum model. However, account of the strong magnetic field supplemented by the star rotation entirely breaks down this expectation because the electromagnetic rather than gravitational field plays a dominant role in this case.

Let us consider a neutron star as a highly conducting sphere rotating with the angular velocity $\boldsymbol{\Omega}$. Electric field $\boldsymbol{E}'$ in a system "temporarily" comoving with a given element of the star body is approximately zero, $\boldsymbol{E}' = 0$. Expressing this field via vectors $\boldsymbol{E}$ and $\boldsymbol{B}$ in the observer's system and linear velocity of star rotation, $\boldsymbol{u} = \boldsymbol{\Omega} \times \boldsymbol{r}$, we obtain for $u \ll c$

$$\boldsymbol{E}' = \boldsymbol{E} + \frac{1}{c}(\boldsymbol{\Omega} \times \boldsymbol{r}) \times \boldsymbol{B} = 0, \tag{12.74}$$

which implies that the field vectors are perpendicular to each other $\boldsymbol{E} \cdot \boldsymbol{B} = 0$. The nonzero electric field in the observer's system means that in the rotating conducting star a macroscopic volume charge $\rho_e = \nabla \cdot \boldsymbol{E}/4\pi$ and a surface charge can be present, which necessarily will produce electric field outside the star. Below, following Goldreich and Julian (1969), we calculate the external electric field for a simplified case of "coaxial" rotation, which allows more detailed treatment at the expense of evanescent magneto-dipole radiation.

Initially, we adopt a vacuum outside the star and match internal field inside the star with the external field. The external magnetic field is the static field of the magnetic dipole. The external electric field must be matched with the internal field: tangential component is continuous, while the radial one has a jump if a surface charge is present. In the external region there is no charge (there is vacuum according to our assumption) the electrostatic potential $\varphi(r, \vartheta)$ obeys the Laplace equation and so can be expanded onto static multipole moments. The electric charge and the dipole moment are apparently zeros because of electric neutrality and spherical symmetry of the star. Thus, the electrostatic potential can only depend on the quadruple and higher moments.

Taking into account symmetry of the star, we write the quadruple moment in the form

$$\varphi(r,\vartheta) = \frac{C}{r^3} P_2(\cos\vartheta), \quad \text{where} \quad P_2 = \frac{1}{2}(3\cos^2\vartheta - 1) \tag{12.75}$$

is the second-order Legendre polynomial and C is a constant. In the subsurface area Eq. (12.74) yields $E_\vartheta = -(B_{\max}\Omega a/c)\sin\vartheta\cos\vartheta$, while above the surface $E_\vartheta = -(3C/a^4)\sin\vartheta\cos\vartheta$. Equating them we determine the constant C and then write

$$\varphi(r,\vartheta) = -\frac{B_{\max}\Omega a^5}{6cr^3}(3\cos^2\vartheta - 1). \tag{12.76}$$

The normal electric field component experiences a discontinuity, which implies a surface charge with the following density:

$$\sigma = \frac{1}{4\pi}[E_r(r,\vartheta)|_{r=a+0} - E_r(r,\vartheta)|_{r=a-0}] = -\frac{B_{\max}\Omega a}{4\pi c}\cos^2\vartheta \le 0. \tag{12.77}$$

The electric force F_e acting on an immobile particle just above the star surface is

$$F_e = 2\pi e\sigma = \frac{B_{\max}\Omega a}{2c}\cos^2\vartheta. \tag{12.78}$$

Comparison of the electric and gravitational forces results in

$$\frac{F_e}{F_g} = \frac{eB_{\max}\Omega a^3}{GmMc} \approx 10^9 \tag{12.79}$$

for a proton. Thus, the gravitation has almost no effect on the structure of the neutron star magnetosphere. Then, let us compare this electric force, Eq. (12.78), with the attraction force between nuclei and electrons in a normal substance, e.g., in a hydrogen atom we have $F_H = e^2/a_B^2$, where $a_B \approx 0.5 \times 10^{-8}$ cm is the Bohr radius. Their ratio is

$$\frac{F_e}{F_H} = \frac{B_{\max}\Omega a a_B^2}{2ec} \approx 5. \tag{12.80}$$

This, almost an order of magnitude, excess of the force is, apparently, sufficient to pull an electron out from the neutron star crust to the magnetosphere. In addition, the particle emission from the star surface is further facilitated by its high temperature, $T > 10^6$ K, and chemical composition: heavy ions with lower work function because the light elements have been burned out during

supernova progenitor evolution. Therefore, the stability of the star surface breaks down and emission of the charged particles from the star surface fills the surrounding space by a plasma.

This plasma has high electric conductivity; thus, the magnetic field must be frozen in this plasma. Stated another way, the magnetospheric plasma is rigidly linked to the magnetic field lines and rotates along with them. Therefore, the magnetospheric magnetic and electric fields are connected to each other by the same equation (12.74) as they are inside the star. Let us now estimate the lower bound of the plasma density in the magnetosphere via the electric charge density. If the magnetic moment of the star is directed along its rotation axes, then the magnetic field in the magnetosphere is static and obeys the condition $\nabla \times \boldsymbol{B} = 0$. The number density of elementary charges is

$$n_e = \frac{1}{4\pi e}\nabla \cdot \boldsymbol{E} = -\frac{\boldsymbol{B}\cdot\boldsymbol{\Omega}}{2\pi ce} \approx \frac{B_{\max}\Omega}{2\pi ce} \gtrsim 10^{10}\ \mathrm{cm}^{-3}, \tag{12.81}$$

above the surface. Apparently, the magnetic field is nonuniform in the magnetosphere, so it contains region dominated by either positive or negative charges.

The corotation of the magnetosphere with the star cannot happen up to arbitrarily long distance from the star. The linear velocity of the plasma rotation $\boldsymbol{u} = \boldsymbol{\Omega} \times \boldsymbol{r}$ reaches the limiting speed of light value c at the distance

$$R_c = \frac{c}{\Omega} = \frac{cP}{2\pi} \tag{12.82}$$

from the rotation axes. The cylinder with the radius R_c and the axes coinciding with the star rotation axes is called the **light cylinder**. The corotation will necessarily break down at some distance inside the light cylinder. Note that the radius of the light cylinder is 2π times shorter than the vacuum wavelength emitted by the rotating magnetic moment.

This dense magnetosphere with the light cylinder bounding the plasma corotation region significantly complicates physical processes in the circumstellar space. In particular, plasma behavior differs substantially in the regions of the closed and opened field lines, respectively, Fig. 12.4. The plasma linked to the closed field lines, located inside the light cylinder, corotates having the linear velocity below the speed of light c. Since the plasma motion transverse to the field lines is limited, it does not, presumably, escape from this magnetic trap.

The field lines reaching the light cylinder are the open field lines. They deflect back (relative to the star rotation) to form a toroidal magnetic field far away from the star. Charged particles moving along such open field lines can escape from the magnetosphere. The particle escape from the star along the open field line can result in charged particle depletion in the corresponding regions of the magnetosphere. In this case Eq. (12.74) breaks down and

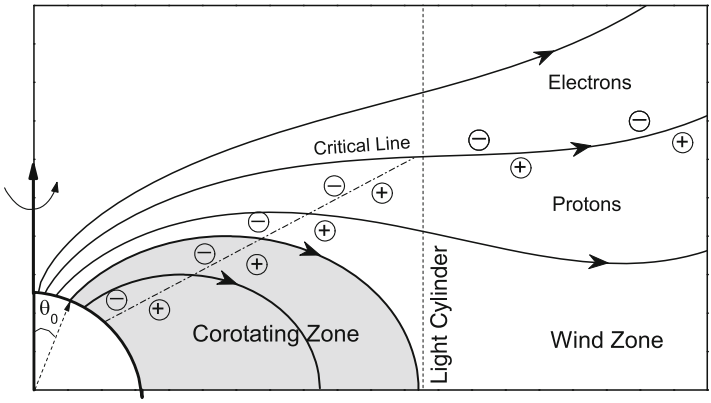

Figure 12.4: Cartoon of the magnetosphere of a neutron star.

so the plasma is no longer freezing in the magnetic field, so a noticeable component of the electric field along the magnetic field $\boldsymbol{B}$ arises, which can drive the particle acceleration. Now we address the efficiency of this particle acceleration process.

We adopt that the magnetic field is dipole around the star so the field lines are described by the following equation in the spherical coordinates:

$$r = C \sin^2 \vartheta, \qquad C = \text{const}. \tag{12.83}$$

The last closed field line, Fig. 12.4, must touch the light cylinder, whose equation is $r = R_c = c/\Omega$, at $\sin\vartheta = 1$. This condition yields the constant $C = R_c$ and the angle ϑ_p, which this field line makes with the polar axes at the star surface: $\sin^2 \vartheta_p = a/R_c \ll 1$. This angle determines the radius of **polar cusp**, which hosts the bunch of the open field lines:

$$R_p = a \sin \vartheta_p = a(a\Omega/c)^{1/2}. \tag{12.84}$$

Typically, the polar cusp radius is about $10^{-2}a$. If $\boldsymbol{m} \cdot \boldsymbol{\Omega} > 0$, as has been adopted for calculating electric potential (12.76), it turns out to be positive at the equatorial zone and negative in polar regions, in particular, in the polar cusps. Therefore, negatively charged electrons can escape from there to ISM.

However, the use of vacuum expression (12.76) is controversial. Indeed, conservation of the full charge requires that the electron escape must be compensated by a corresponding escape of positive charges, e.g., ions. But the region of positive potential described by Eq. (12.76) hosts only the closed field lines which does not allow the positive charges to leave the star farther that the light cylinder radius.

Users of the Goldreich and Julian (1969) model [including Goldreich and Julian themselves as well as Manchester and Taylor (1977) and Shapiro and

Teukolsky (1983)] overcome this difficulty by postulating a modified angular dependence of the potential compared with Eq. (12.76) in such a way to place the critical field lines, those with zero value of the potential coinciding with that in ISM, inside the polar cusp, i.e., at some $\vartheta = \vartheta_{\rm crit} < \vartheta_p \approx 10^{-2}$. For comparison, vacuum formula (12.76) gives the critical angle of $\vartheta_{\rm crit} = \arccos(1/\sqrt{3}) \approx 0.95$, i.e., roughly 100 times larger. With this modification of the electrostatic potential the central part of the polar cusp emits electrons, while a ring bounded by the angles ϑ_p and $\vartheta_{\rm crit}$ emits ions; the value of $\vartheta_{\rm crit}$ is selected to provide the net zero current from the polar cusp.

It is obvious that vacuum potential (12.76) deviates from the true potential in the magnetosphere due to presence of macroscopic volume charge. Because no exact solution is available, a simple modification of the vacuum solution that account for the most fundamental properties of the physical system such as charge conservation, rotation, and strong magnetic field is commonly employed. Adopting this described modification we can estimate the energy gained by the particles escaping from the polar cusp along the open field lines. Assuming that a particle gets roughly half of the potential drop of the polar cusp we obtain

$$\Delta\varphi = \varphi(a, \vartheta_p) - \varphi(a, 0) \approx \frac{1}{2}(a\Omega/c)^2 a B_{\rm max}, \tag{12.85}$$

which gives the particle energy

$$\mathcal{E} = \frac{e}{2}\Delta\varphi \approx 3 B_{\rm max} P^{-2}\, eV. \tag{12.86}$$

Here B is measured in G and P in seconds; no energy loss by the particle is taken into account. The losses can be essential especially for the electrons that effectively lose their energy for radiation in various energy domains including the gamma-ray emission (see the next section). Note finally that estimate (12.86) is derived from Eq. (12.85) that contains a small factor $(a\Omega/c)^2 \approx 10^{-4}$. This factor originates from the selected small value of the critical angle $\vartheta_{\rm crit} \lesssim 10^{-2}$ for the latitude where the potential has zero value. If we use the vacuum potential described by Eq. (12.76) and adopt $\vartheta_{\rm crit} \approx 1$ then the estimate of the particle energy would increase by roughly four orders of magnitude compared with Eq. (12.86).

12.2.4 Emission of Hard Quanta and Generation of Electron–Positron Plasma in Pulsar's Magnetosphere

Equation (12.86) with $B_{\rm max} \approx 10^{12}\ G$ implies electron acceleration up to the Lorentz factor of $\gamma \approx 3 \times 10^6 P^{-2}$. These, highly energetic, electrons quickly lose their transverse (relative to the magnetic field) energy due to radiative losses in this magnetic field and, thus, move along a given field

line being at the bottom (zeroth) transverse Landau level. Given that the dipole field lines has a finite curvature, a particle moving along such a curved field line experiences an acceleration alternating its direction of motion. As a result, this particle generates a so-called **curvature radiation**, which has a lot in common with the synchrotron radiation considered in Sect. 9.4.2. Accordingly, a broad spectrum is emitted with a peak at the frequency $\omega = 0.29\omega_c$, where

$$\omega_c = \frac{3eB}{2mc}\gamma^2 = \frac{3c}{2r_g}\gamma^3, \tag{12.87}$$

r_g is radius of the circle along which the particle is moving. Remind that this result is obtained in Sect. 9.4.2 within classical consideration, which will not be valid if so calculated energy $\hbar\omega_c$ of the emitted quantum is comparable or exceeds the particle kinetic energy. In such (quantum) case the radiation spectrum vanishes at and above the largest frequency marginally consistent with the energy conservation.

The radiation spectrum produced by an ultrarelativistic particle is formed over a finite fraction of its path with the length about ρ/γ. This allows us to easily obtain the spectrum of the curvature radiation based on the theory of the synchrotron radiation given in Sect. 9.4.2. Indeed, identifying the circle radius r_g with the curvature radius ρ of the magnetic field line we can easily estimate the characteristic frequency of the curvature radiation from Eq. (12.87). Then, the corresponding substitution, $\omega_c = c\gamma^3/\rho$, to synchrotron radiation spectrum Eq. (9.158) yields the curvature radiation spectrum

$$\mathrm{d}I = \frac{\sqrt{3}}{2\pi}\frac{e^2\gamma}{\rho}F_s\left(\frac{\omega}{\omega_c}\right)\mathrm{d}\omega, \tag{12.88}$$

where the function $F_s(z)$ is defined by Eq. (9.159).

In spite of significant similarity between the synchrotron and curvature radiations we emphasize an essential distinction between them: the synchrotron radiation is produced due to particle gyration *transverse* to the magnetic field along a circle with a radius proportional to the particle energy, while the curvature radiation is produced as the particle moves *along* a curved field line; thus, the radius of the particle trajectory does not depend on the particle energy. Therefore, both the characteristic frequency and the spectrum have dissimilar dependencies on the particle Lorentz factor.

Let us estimate a typical energy of the curvature quanta produced by electrons in the polar region of the pulsar magnetosphere. The radius of the dipole field line curvature is easy to calculate; at the edge of the polar cusp it is estimated as $\rho \approx (8acP/\pi)^{1/2}$. The characteristic energy of accelerated electrons is given by Eq. (12.86); thus, the energy of the curvature quanta is

$$\hbar\omega_c \approx \frac{\hbar c\gamma^3}{\rho} \approx 1.4\times 10^{-29}\frac{B_{\max}^3}{P^{6.5}}\ \ \mathrm{eV}. \tag{12.89}$$

We see that the frequency/energy of the curvature radiation depends strongly on two main characteristics of the neutron star—its magnetic field and rotation period. Since both these values differ from star to star we make estimates for a few selected pulsars.

1. Pulsar PSR 0833 (Vela): $P = 0.089\,\mathrm{s}$, $B_{\max} \approx 1.1 \times 10^{12}\,\mathrm{G}$. Energy of radiating electrons is $\mathcal{E} \approx 3 \times 10^{14}\,\mathrm{eV}$; energy of curvature quanta is $\hbar\omega_c \approx 7.5 \times 10^{12}\,\mathrm{eV}$.

2. Pulsar PSR 0532 (Crab): $P = 0.033\,\mathrm{s}$, $B_{\max} \approx 1 \times 10^{12}\,\mathrm{G}$. Energy of radiating electrons is $\mathcal{E} \approx 3 \times 10^{15}\,\mathrm{eV}$; energy of curvature quanta calculated from Eq. (12.89) is $\hbar\omega_c \approx \times 10^{16}\,\mathrm{eV}$, which exceeds the particle energy. Therefore, quanta with $\hbar\omega \lesssim 10^{15}\,\mathrm{eV}$ will be produced.

3. Pulsar PSR 1133, $P = 1.19\,\mathrm{s}$, $B_{\max} \approx 6 \times 10^{11}\,\mathrm{G}$. Energy of radiating electrons is $\mathcal{E} \approx 3 \times 10^{14}\,\mathrm{eV}$; energy of curvature quanta is $\hbar\omega_c \approx 1.5 \times 10^{5}\,\mathrm{eV}$.

These examples suggest that rapidly rotating neutron stars with strong magnetic field can generate gamma rays with energies $\hbar\omega_c > 10^6\,\mathrm{eV}$, which are sufficient to produce electron–positron pairs. In the laboratory a e^+e^- pair can be produced by either a single photon in the presence of electric field of a heavy ion or collision of two energetic charged particles or "collision" of two photons. In the strong magnetic field of a neutron star a single photon can produce the e^+e^- pair (the magnetic field substitutes here the nuclear electric field present in the laboratory experiments), although two-photon process involving a soft X-ray photon and a hard curvature photon is also relevant if the star has a high X-ray luminosity (see, e.g., Takata et al. (2006)). Below we briefly consider the process of single-photon process of the pair production in a strong magnetic field.

The field is adopted to be strong if the distance between the transverse Landau levels in this field B_c is comparable with the electron rest mass, $mc^2 = \hbar e B_c/mc$, i.e.,

$$B_c = m^2c^3/e\hbar \approx 4.4 \times 10^{13}\ \mathrm{G}. \tag{12.90}$$

The full probability W of the pair creation per unit time valid for ultrarelativistic energies and integrated over energy and angles of the created particles is well known; we take it from the Landau and Lifshitz course (Berestetskii et al. 1982):

$$W = \frac{3^{3/2}}{2^{9/2}} \frac{mc^2}{\hbar} \frac{e^2}{\hbar c} \frac{B \sin\beta}{B_c} \exp\left(-\frac{8B_c}{3B} \frac{mc^2}{\hbar\omega \sin\beta}\right). \tag{12.91}$$

This probability contains dimensional values; it is valid for

$$\kappa = \frac{B\hbar\omega \sin\beta}{B_c mc^2} \ll 1, \tag{12.92}$$

where $\hbar\omega$ is the quantum energy, β is the angle between the wave vector and the magnetic field $\boldsymbol{B}$, and m is the electron mass. In the opposite case the probability takes the form

$$W = 0.38\frac{mc^2}{\hbar}\frac{e^2}{\hbar c}\frac{B\sin\beta}{B_c}\kappa^{-1/3}, \quad \kappa \gg 1. \tag{12.93}$$

Maximum of the probability corresponds to $\kappa \approx 11$. A threshold value above which the pair creation becomes possible is specified by conservation of energy and longitudinal momentum:

$$\hbar\omega\sin\beta > 2mc^2. \tag{12.94}$$

From here as well as from Eq. (12.91) it is transparent that a photon moving along the magnetic field, ($\beta = 0$), does not produce pairs. Such a photon moving in a nonuniform magnetic field must first accumulate a noticeable transverse momentum (i.e., $\beta \neq 0$). Nevertheless, if the magnetic field is not far from the critical one and the quantum is reasonably hard, $\hbar\omega \gg 2mc^2$, the pair creation happens very fast because pre-exponential factor in Eq. (12.91) is very large, e.g., $mc^2/\hbar \approx 10^{21}\,\mathrm{s}^{-1}$. This implies that a cascading process in which newly born ultrarelativistic particles generate new curvature quanta and those quanta, in their turn, produce next generation of electrons and positrons. An additional generation of quanta is also possible due to transition between the Landau levels.

These numerous mechanisms of pair production result, in some of the neutron stars, in creation of ultrarelativistic electron–positron plasma, which expands in the ISM in a form of ultrarelativistic "pulsar wind." Such winds then form pulsar wind nebulae (PWNe) around some of the pulsars including the Crab pulsar (see Figs. 1.6 and 1.7).

12.3 Pulsar Wind Nebulae

SNRs containing in their volume a pulsar created by the same SN explosion are often highly different from the shell-type SNRs considered in Sect. 12.1.8 in the morphology, evolution, and spectral energy distribution. Not surprisingly, a primary driver of these dissimilarities is the pulsar supplying the nebula volume with energy in the form of plasma flows including magnetic field. In Sect. 12.2 we found that electrodynamics of the pulsar magnetosphere naturally results in a highly relativistic corpuscular emission from the neutron star surface, which can form an ultrarelativistic "pulsar wind" outside the corresponding light cylinder. In this section we briefly outline essentials and main implications of the pulsar wind for the corresponding nebular physics.

12.3.1 Simplified MHD Flow Model

Observations of PWNe reveal a lot of spatial inhomogeneity, structures, and anisotropy (see jet, torus, and wisps in Figs. 1.6 and 1.7 as vivid examples). Apparently, to fully describe such a complicated evolving morphology requires a highly detailed (presumably, numerical) model taking into account all essential (inhomogeneous, anisotropic, and time-dependent) physics, which is not yet fully developed. As a zero-order approximation, in what follows we mainly employ a highly simplified isotropic model of the PWNe developed by Kennel and Coroniti (1984b): this model is fully analytical and so relatively simple and manageable, while nevertheless is capable of reproducing the most essential properties of the PWNe (Fig. 12.5).

The model adopts that the free energy released from the pulsar spin-down luminosity L ($= 5 \cdot 10^{38}$ erg/s in case of Crab pulsar) is somehow divided between the leptonic flow and the magnetic field:

$$L = 4\pi n \gamma u r_s^2 m c^3 (1 + \sigma), \tag{12.95}$$

where n is the proper number density of the flow, γ is the Lorentz factor, u is the radial four speed of the flow so that $\gamma^2 = 1 + u^2$, r_s is the radius of the flow termination shock from the pulsar position, m is the electron mass, c is the speed of light, and σ is the fraction of the electromagnetic energy flux relative to the corpuscular energy flux:

$$\sigma = \frac{B^2}{4\pi n u \gamma m c^2}, \tag{12.96}$$

B is the magnetic field in the observer's frame, which is supposed to be fully toroidal (azimuthal) as it is typical for stellar winds (Sect. 2.5.3).

For the shock with the magnetic field directed along the front and ultrarelativistic upstream flow the conservation laws can be written as (cf. Sect. 5.3 and Problem 5.8):

$$n_1 u_1 = n_2 u_2, \tag{12.97a}$$

$$E = \frac{u_1 B_1}{\gamma_1} = \frac{u_2 B_2}{\gamma_2}, \tag{12.97b}$$

$$\gamma_1 \mu_1 + \frac{E B_1}{4\pi n_1 u_1} = \gamma_2 \mu_2 + \frac{E B_2}{4\pi n_1 u_1}, \tag{12.97c}$$

$$\mu_1 u_1 + \frac{P_1}{n_1 u_1} + \frac{B_1^2}{8\pi n_1 u_1} = \mu_2 u_2 + \frac{P_2}{n_1 u_1} + \frac{B_2^2}{8\pi n_1 u_1}. \tag{12.97d}$$

Particle flux conservation (12.97a) has already been applied to Eqs. (12.97c,d) of the energy and momentum flux conservation. Subscripts 1 and 2 are used for upstream and downstream values (regions II and III, respectively); B, E, and $N = \gamma n$ are the shock frame electric and magnetic fields and number

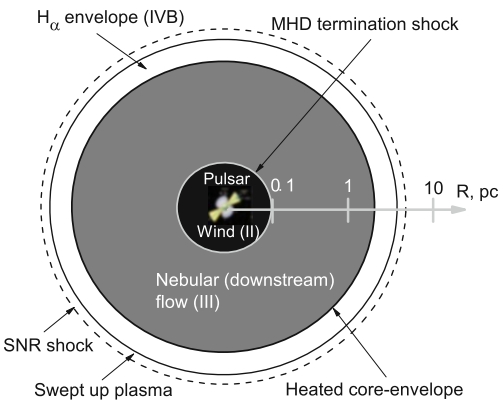

Figure 12.5: Model structure of a PWN inside a SNR (Kennel and Coroniti 1984a). Region I (not marked up) is the rotating central neutron star producing ultrarelativistic leptonic pulsar wind. Region II is the pulsar wind (*upstream*) region bounded by a termination spherical shock front. Region III is *downstream* region representing the PWN itself, where most of the observed radiation is produced. Outer regions are formed due to interaction of the nebular flow with the expanding SNR shell.

density; μ is the specific enthalpy, which for the ideal gas with adiabatic index Γ (small γ is used to denote the Lorentz factors here):

$$\mu = mc^2 + \frac{\Gamma}{\Gamma - 1}\frac{P}{n}; \tag{12.98}$$

the compression ratio Y is defined as

$$Y = \frac{B_2}{B_1} = \frac{N_2}{N_1} = \frac{\gamma_2 u_1}{\gamma_1 u_2}. \tag{12.99}$$

Now to derive the Rankine–Hugoniot relations we assume $\Gamma_2 = 4/3$ provided that the plasma is relativistic downstream, $P_2/(n_2 mc^2) \gg 1$, solve Eq. (12.97c) and insert the solution into Eq. (12.97d), which yields

$$Y^2 - Y\left[\frac{2}{\gamma_2 u_2}\left(u_2^2 + \frac{1}{4}\right)\frac{u_1}{\gamma_1}\right] + \left[\frac{2}{\gamma_2 u_2}\left(u_2^2 + \frac{1}{4}\right)\left(\frac{4\pi n_1 \mu_1 \gamma_1^2}{B_1^2} + \frac{u_1}{\gamma_1}\right)\right]$$

$$-\frac{2\pi n_1 mc^2}{B_1^2}\frac{u_2}{u_1} - \left(1 + \frac{8\pi n_1 \mu_1 u_1^2 + P_1}{B_1^2}\right) = 0. \tag{12.100}$$

We consider an ultrarelativistic pulsar wind with $\gamma_1 \approx u_1 \gg 1$, although "cold," i.e., $P_1/(n_1 mc^2) \ll 1$, which implies $\mu_1 \approx mc^2$. Assuming the termination shock is strong, we also accept $u_2/u_1 \ll 1$; $\gamma_2^2 = 1 + u_2^2$. Discarding corresponding small terms and using definition (12.96) of σ parameter after some algebra we obtain

$$u_2^2\left(u_2^2 + \frac{1}{4}\right)^2 = (1 + u_2^2)\left(u_2^2 - \frac{\sigma}{4(1+\sigma)}\right)^2, \tag{12.101}$$

whose meaningful solution has the form

$$u_2^2 = \frac{8\sigma^2 + 10\sigma + 1 + \sqrt{64\sigma^2(\sigma+1)^2 + 20\sigma(\sigma+1) + 1}}{16(\sigma+1)}. \tag{12.102}$$

Then, from Eq. (12.97c) in the adopted parameter regime, we obtain the downstream pressure P_2:

$$\frac{P_2}{n_1 u_1^2 mc^2} = \frac{1}{4u_2\gamma_2}\left[1 + \sigma\left(1 - \frac{\gamma_2}{u_2}\right)\right], \tag{12.103}$$

and, accordingly, the downstream temperature T_2 (in ergs):

$$\frac{T_2}{u_1 mc^2} = \frac{P_2}{n_2 u_1 mc^2} = \frac{1}{4\gamma_2}\left[1 + \sigma\left(1 - \frac{\gamma_2}{u_2}\right)\right]. \tag{12.104}$$

It is remarkable that according to Eqs. (12.101), (12.103), and (12.104), the key downstream parameters, the flow velocity, the pressure, and the temperature all depend on the magnetization parameter σ only in the strong shock regime. We note that having strong energization of the corpuscular component downstream needed to support strong radiation efficiency of the nebula requires the magnetization parameter to be small, $\sigma \lesssim 0.1$. Accordingly, in the small-σ limiting case, the above equations yield

$$u_2^2 = \frac{1 + 9\sigma}{8}, \tag{12.105a}$$

$$\gamma_2^2 = \frac{9 + 9\sigma}{8}, \tag{12.105b}$$

$$\frac{T_2}{u_1 mc^2} = \frac{1}{\sqrt{18}}(1 - 2\sigma), \tag{12.105c}$$

$$\frac{B_2}{B_1} = \frac{N_2}{N_1} = 3(1 - 4\sigma). \tag{12.105d}$$

It is important to realize that the solution obtained depends on only one free parameter and this dependence is very weak; in particular, all parameters defined by Eq. (12.105) become constant when $\sigma \to 0$ including $u_2^2 \to 1/8$ and $\gamma_2^2 \to 9/8$ implying the flow three velocity to be $c(u_2/\gamma_2) \approx c/3$. Stated another way, a "minimum" set of assumptions, namely, (1) the upstream flow is ultrarelativistic with a small temperature and (2) formation of a *strong* termination shock with a high pressure downstream, has lead us to a *unique* solution, whose properties depend on the magnetization parameter σ and the product of the number density and the four speed of the upstream flow, which is straightforwardly defined by the pulsar spin-down luminosity and radius of the termination shock according to Eq. (12.95).

12.3.2 Downstream Particle Distribution and PWN Broadband Spectrum

The mean particle energy downstream, T_2, defined by Eq. (12.105c) is ultra-relativistic provided that $u_1 \approx \gamma_1 \gg 1$: $T_2/(mc^2) \approx \gamma_1/\sqrt{18}$. However, one can hardly expect that the particle distribution downstream is thermal. In fact, as we have comprehensively demonstrated in Sects. 11.4 and 12.1, the particles interacting with a strong shock acquire a broad power-law spectrum starting from a minimum "injection" energy and up to a high energy specified by the acceleration time, particle escape, or particle energy losses. Therefore, it is reasonable to adopt that the particle distribution function downstream obeys Eq. (9.169) with $\gamma_{\rm min} \sim \gamma_1/\sqrt{18}$ and $\gamma_{\rm max} \gg \gamma_{\rm min}$, which is capable of generating a broadband electromagnetic spectrum via interaction with the nebular magnetic fields.

In fact to compute the radiation from a PWN in some detail one has yet to find the spatial distributions of the particles and magnetic field. Indeed, the magnetic field is supposed to decline in the 3D nebular flow, while the particles to experience adiabatic cooling and radiative energy losses (see Kennel and Coroniti 1984b for greater detail). In particular, for the highest energy electrons with $\mathcal{E} \sim mc^2\gamma_{\rm max}$, the radiative losses are severe, so these electrons cannot reach the nebula border without a significant energy decrease; as a result, the observed PWN size decreases with the increase of photon energy in which the observation is being made. Having these remarks in mind as well as many idealizations adopted in this simplified model, we will not perform the corresponding calculations in any detail; instead, we make an estimate of the PWN spectral shape assuming some averaged PWN parameters implied by the obtained flow solution.

Let us assume that the electromagnetic radiation is produced by the specified above power-law particle spectrum in the nebular magnetic field, which we adopt to be regular for now. The corresponding synchrotron spectrum has been discussed in detail in Sects. 9.4.2 and 9.4.3. For $\gamma_1 \sim 3 \cdot 10^6$ of the pulsar wind flow[5] we have $\gamma_{\rm min} \sim 10^6$ and adopting $B \sim 1\,{\rm mG}$ we obtain $f_{\rm Be}\gamma_{\rm min}^2 \sim 10^{15}\,{\rm Hz}$, which corresponds to the optical range. Therefore, the "standard" nonthermal power-law spectral range described by Eq. (9.170) is expected at the optical to the X-ray range in agreement with observation. In contrast, at lower frequencies down to the radio band, the synchrotron spectrum has a shape $\propto f^{1/3}$ (see dash-dotted spectrum in Fig. 12.6) which is in a strong conflict with radio observations of PWN spectra, $\propto f^{-\alpha_{\rm r}}$ with $\alpha_{\rm r} = 0.2 \pm 0.2$. To remedy the situation it has been suggested that there are in fact two distributions of electrons: the one mentioned above, called the *nebular* electrons, and a second distribution to fit the radio observations,

[5] A pulsar wind with that relativistic factor is required to ensure the observed high efficiency, ∼10–20%, of the pulsar spin-down luminosity into the PWN luminosity (Kennel and Coroniti 1984b).

called *radio* electrons. The postulated radio electrons have a relatively flat spectrum at $\gamma \ll 10^6$; however, it is entirely unclearly how these postulated radio electrons could be created in the nebula.

In particular in the case of the Crab Nebula, which is the best studied PWN, a standing shock (where a power-law energy spectrum of nebular electrons, which produce the bulk of the nebula's synchrotron emission, is generated) forms in the pulsar wind at a distance of ∼0.1 pc from the pulsar. Highly mobile features, called wisps (see Fig. 1.7), which have been associated with this shock, are observed in optical and X-ray emission (Hester et al. 1996; Mori et al. 2002). The observation of the wisps also in the radio (Bietenholz et al. 2001, 2004) suggests that the radio electrons are accelerated in the same region (rather than, e.g., injected once at some early stage of the nebula evolution) as the higher-energy nebular ones. The origin and production mechanism of these radio electrons, however, are unclear since it is extremely difficult to produce them from a pulsar wind with high γ (Arons 2002; Atoyan 1999). It would, therefore, be highly desirable to interpret the whole PWN spectrum with the single *nebular* electron population, rather than requiring a separate population of radio electrons.

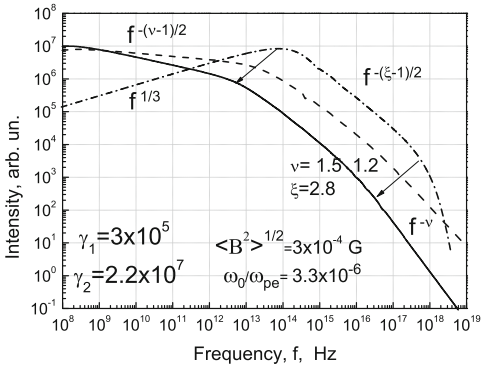

Figure 12.6: DSR radiation spectra for a power-law magnetic field spectrum characterized by different spectral indices, ν. The *dashed curve* is $\nu = 1.2$ and the *solid curve* is $\nu = 1.5$. In addition, the *dash-dotted curve* shows the standard synchrotron spectrum for the same power-law electron distribution and the same magnetic field energy density. *Arrows* indicate the changes of the break frequencies which separate various spectral asymptotes. A region with the standard nonthermal spectrum, $P_\omega \propto \omega^{-\alpha_{\rm nth}}$, is present in all cases, although at differing frequency ranges and at different levels. Beyond this region, the spectra differ significantly from each other.

12.3.3 DSR Model of PWN Spectrum

To reconcile the obtained energy spectrum of the nebular electrons with the observed broadband radio to X-ray PWN spectra, we employ the results obtained above, e.g., in Sects. 4.1.2 and 12.1, that the magnetic fields are produced at the shock front vicinity in a form of strong magnetic turbulence, which implies that the magnetic fields are random rather than regular. Therefore, the DSR theory developed in Sect. 9.5 rather than the standard synchrotron theory must be used to calculate the PWN electromagnetic spectrum (Fleishman and Bietenholz 2007).

To do so, let us proceed to the DSR spectra produced by a power-law distribution of relativistic electrons, Eq. (9.169). The bulk of the DSR energy, Sect. 9.5.2, produced by a single particle is emitted at frequencies $\omega \sim \omega_{\rm lsc}\gamma^2$ (if $\nu < 3$). Accordingly, it is easy to estimate that in the region of "intermediate" frequencies

$$\omega_{\rm lsc}\gamma_{\rm min}^2 \ll \omega \ll \omega_{\rm lsc}\gamma_{\rm max}^2, \tag{12.106}$$

the standard well-known nonthermal (synchrotron-like) spectrum $P_\omega \propto \omega^{-\alpha_{\rm nth}}$ is formed (see Fig. 9.15 and 12.6). However, the DSR spectrum will deviate significantly from the standard synchrotron spectrum at high ($\omega > \omega_{\rm lsc}\gamma_{\rm max}^2$) and low ($\omega < \omega_{\rm lsc}\gamma_{\rm min}^2$) frequencies, where it will reproduce the single-particle spectra, $P_\omega \propto \omega^{-\nu}$ (in place of the exponential synchrotron cut-off) and $P_\omega \propto \omega^{-(\nu-1)/2}$ (in place of $P_\omega \propto \omega^{1/3}$), respectively. Therefore, differences in the shape of the radiation spectrum between DSR and standard synchrotron theory will occur when a particular spectral region is formed primarily by electrons from near *either end* of the electron distribution ($\gamma_{\rm min}$ or $\gamma_{\rm max}$) (see an example of the DSR spectrum in Fig. 9.15).

Thus, the DSR mechanism, namely the low-frequency asymptote $P_\omega \propto \omega^{-(\nu-1)/2}$, indeed suggests a simple and straightforward interpretation of the observed wideband PWN spectra with only a single population of electrons. Within the DSR model, the flat radio spectrum (with spectral indices $\alpha_{\rm r} = 0.2 \pm 0.2$) should be associated with this low-frequency (non-perturbative) DSR asymptote $P_\omega \propto \omega^{-(\nu-1)/2}$. The required spectral index of the random magnetic field is, therefore, in the range ν =1–1.8, which is in remarkable agreement with available turbulence models, Chap. 6.

The optical emission (and possibly also down to the millimeter or infrared and/or up to X-ray emission) then is produced by the inner part of the electron distribution, Eq. (9.169), and has the standard form $P_\omega \propto \omega^{-\alpha_{\rm nth}}$. Finally, at the frequencies $\omega \gg \omega_{\rm lsc}\gamma_{\rm max}^2$, which can occur in the X-ray or

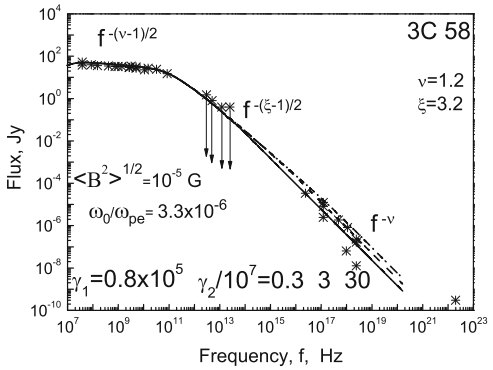

Figure 12.7: The model DSR spectra and observed broadband spectrum of 3C 58. The values adopted for the energy index of the power-law electron distribution, ξ, and the mean square of the random magnetic field $\langle B_{\rm st}^2 \rangle$ are indicated in the figure.

gamma-ray range depending on the actual value of $\gamma_{\max}$, which is also a decreasing function of the distance from the pulsar due to significant radiative losses at these high energies, the DSR model predicts a spectrum $P_\omega \propto \omega^{-\nu}$, resembling the spectrum of relatively small-scale magnetic inhomogeneities. The DSR spectrum given in Fig. 9.15 nicely matches the observed wideband spectrum from the Crab Nebula. One more example of excellent broadband DSR fit to the spectrum observed from another PWN, 3C 58, from the radio to X-ray domain is shown in Fig. 12.7. These findings suggest that highly efficient electron acceleration and magnetic turbulence generation indeed take place in the PWNe driven by power pulsar winds.

12.4 Some Remarks on Other Relativistic Sources

Modern astrophysics deals with many objects that either move relativistically, or contain a relativistically hot plasma or both. In many cases such objects originate from a strong explosion or gas accretion onto a massive central object, presumably, a **black hole**. In particular, this includes galactic microquasars/X-ray binaries produced by accretion from a normal star onto a compact stellar mass object (black hole or neutron star). The accretion forms an accretion disk whose interaction with the central object produces somehow a single or pair of oppositely directed highly collimated relativistic jets (Beskin 2009b). These jets produce most of the observed radio emission and contribute essentially to emission at other wavelength ranges.

A similar but much more powerful phenomenon is AGN. Here the central object is a supermassive black hole (up to $\sim 10^8 M_\odot$); the AGN structure is essentially anisotropic (see Fig. 12.8, left): the central object is surrounded by

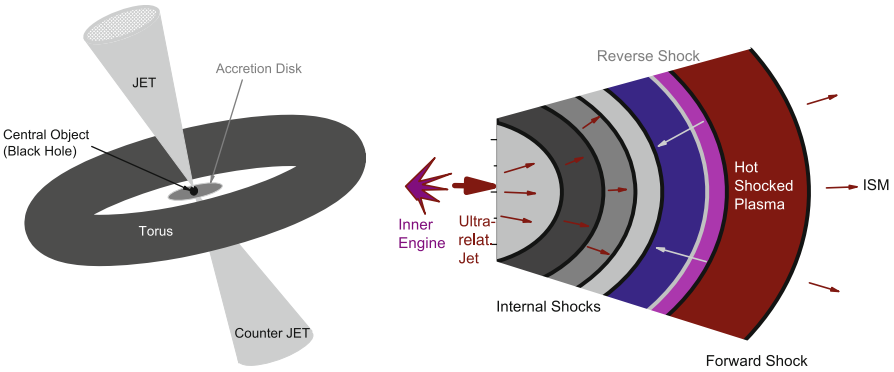

Figure 12.8: *Left*: a cartoon illustrating anisotropic AGN structure involving a central black hole with an accretion disk surrounded by a torus of absorbing material. Two counter jets are ejected relativistically transverse to the accretion disk plane. *Right*: a schematic structure of a collimated ultrarelativistic jet in a cosmological source of prompt gamma-ray burst emission produced by an asymmetric explosion of an inner engine. The jet is a highly nonlinear structure, which includes a forward and reverse shocks, as well as (perhaps, numerous) internal shocks, which produce strong gamma-ray flashes at each shock–shock collision. Each such collision is believed to generate strong random magnetic and electric fields and efficiently accelerate particles.

an accretion disk, which provides a sustained flux of mass and energy toward the central object where two jets can be launched (in yet unidentified physical process) in the directions transverse to the accretion disk plane. The central object and the accretion disk are surrounded by a relatively dense and cool torus, whose gas is capable of absorbing emission produced in some vicinity of the central object and disk. This anisotropic source structure implies that the AGN will look highly differently depending on the observer's line of sight. Historically, those differently viewed AGNs were named differently: the radio galaxies and Seyfert II galaxies are, in fact, the AGNs viewed roughly at 90° to the jet axes (the accretion disk is occulted by the torus); quasars and Seyfert I galaxies are AGNs viewed by an oblique angle to the jet axes (the region of the accretion disk is seen), while the blazars including BL Lac and optically violent variable (OVV) quasars are viewed almost along the jet axes. In the latter case effects of relativistic jet expansion are largely responsible for most of the observed radiation properties including the strong variability. These jets are the sites where most of the nonthermal radiation is produced throughout the entire electromagnetic range (see Fig. 12.9 as a vivid example) which implies a highly efficient particle acceleration and magnetic field generation in this relativistically expanding collimated flows. However, it seems premature to discuss the jet models in the textbook since the physics of the jets (in spite of considerable progress of corresponding

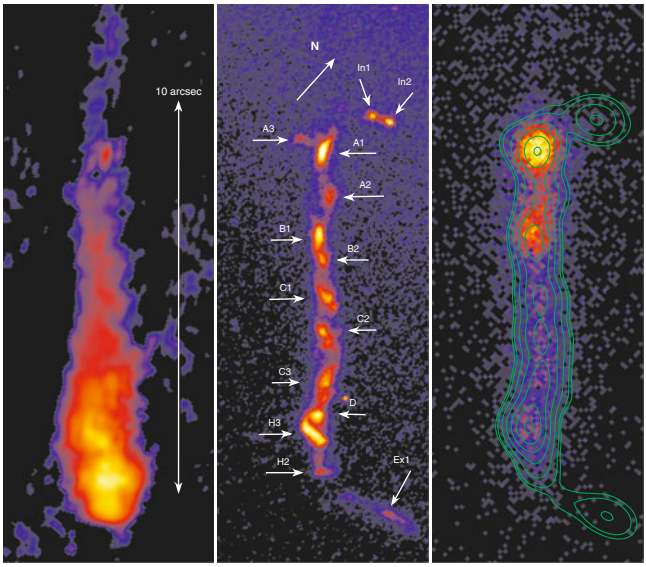

Figure 12.9: Images of the jet in quasar 3C 273 in radio 1.647 GHz (MERLIN array data), *left*; optical (Hubble Space Telescope data), *middle*; and X-ray (Chandra data), *right*, with smoothed optical contours overlaid. Note highly inhomogeneous structure with many labeled bright knots and significant dissimilarities in the detailed structure between the images. Credit: (Marshall et al. 2001). Reproduced by permission of the AAS.

numerical models) remains highly uncertain; in particular, it is yet unclear if the jets are pressure dominated or Poynting flux dominated (see Sect. 2.3.3 for the definition).

Another type of objects where the ultrarelativistic jets are likely present is the cosmological GRBs (see a cartoon in Fig. 12.8, right). A common currently accepted "fireball model" of the prompt GRB emission suggests that a strong anisotropic explosion of a central engine (presumably, a special regime of a core-collapse SN, called hypernova) produces an ultrarelativistic jets with a sequence of strong nonlinear perturbations of the flow structure (so-called "internal shocks"). These shocks interact with each other to produce highly variable X-ray and gamma-ray emission at the time scale of the order of seconds.

Physics of GRBs represents today so broad and so rapidly growing field of astrophysics that there is no hope to describe it in any sufficient detail here. We make only a few very general remarks on the subject, since the GRB cannot be fully ignored in the chapter discussing ultrarelativistic astrophysical plasma. Observationally, the GRBs represent sporadic flashes of X-ray to gamma-ray emission (in the range from a few keV to tens MeV) with

a duration of $\sim$ 1–100 s. It was established (based on their highly isotropic distribution over the sky, afterglow, and redshift detections) that the GRB sources are located at cosmological distances from the Earth, which requires that they generate enormously large luminosity of the observed high-energy radiation with the energy release of at least 10^{51} erg.[6]

Assuming any source model relying on a nonrelativistic plasma motion results immediately in a conclusion that the photon density is so high that the source must be strongly optically thick for the photon–photon scattering, which is in strong conflict with falling with energy radiation spectra implying an optically thin radiation regime. An elegant solution of this apparent contradiction is that the radiation source moves, as a whole, ultrarelativistically, which, eventually, greatly reduces the optical thickness. A possible source model comes from comparison with a SN explosion, which has a comparable energy release of $\sim 10^{51}$ erg, while much lower, nonrelativistic ejecta velocity: apparently, to have much larger expansion velocity requires that proportionally much smaller mass is being ejected.

Here, formation of *propagating* ultrarelativistic shocks is likely in the jet outflow, which results in a very strong energization of the downstream particles producing electromagnetic emission similarly to the case considered above for PWNe (again, with $\gamma_{\min} \gg 1$). In the case of propagating ultrarelativistic shock, however, new important effects come into play. In particular, the radiation spectrum formed in the co-moving frame is boosted by the bulk Lorentz factor Γ_B of the expanding shell, and, because of the relativistic kinematics, the distant observer can only see a fraction $\theta \sim 1/\Gamma_B$ of the expanding shell.

The outlined source model is complete enough to allow computing the prompt GRB radiation spectra produced by different emission mechanisms considered in Chap. 9. Models of the GBR spectra based on the standard synchrotron theory suffer from inconsistencies similar to that in case of the PWN spectra: the corresponding low-energy spectrum range (occurring now in X-ray rather than radio range because of the relativistic boosting and stronger source magnetic fields) is on average flatter than expected from the synchrotron theory, while the corresponding spectral index distribution contains values higher than 1/3, which is impossible to reconcile with the synchrotron theory irrespectively of the parameter regime.

Remarkably, a most plausible solution of this problem is exactly the same as in case of PWNe: one must explicitly take into account that the magnetic field in the GRB source is random, not regular, and apply the DSR theory to compute the corresponding spectra. As an example, Fig. 12.10 displays a comparison between the observed and model DSR histograms of the GRB

[6] This estimate assumes a highly collimated explosion with a jet occupying only 10^{-3} of the full solid angle; isotropic explosion would require a release of $\sim 10^{54}$ erg, which looks unrealistic for a star explosion.

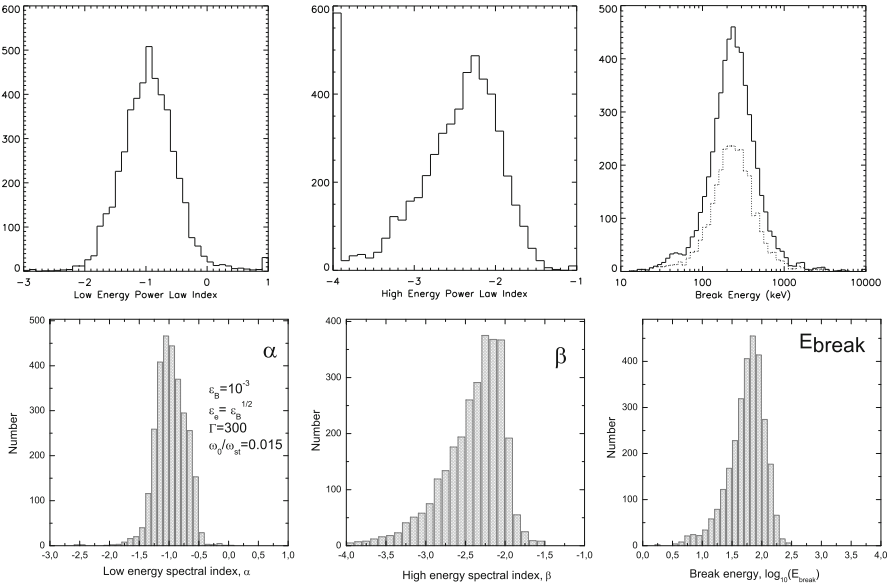

Figure 12.10: Observed (Preece et al. 2000) (*top*; reproduced by permission of the AAS) and modeled (*bottom*) histograms of the band function parameters α, β, and $E_{\rm br}$.

spectral parameters. To obtain the model histograms a few thousand of GRB parameter combinations were randomly generated from the corresponding parent distributions taking into account physical links between the parameters involved in the way similar to, but much more sophisticated than, the modeling described in Sect. 10.3.5. The magnetic field was adopted to be strong and composed of random waves whose wave vectors are isotropically distributed. The model DSR histograms closely resemble the observed ones, while it is not possible to reach a comparable level of agreement within a standard synchrotron model with a regular (rather than random) magnetic field. This implies that similar (to the PWN case) physical phenomena of efficient particle acceleration and magnetic turbulence generation take place in essentially different class of astrophysical objects—GRBs, which confirms an universal character and exceedingly wide applicability of the corresponding dynamic processes considered throughout the book.

Problems

12.1 Using consideration in Sect. 12.2.2, estimate the magnetic field of the pulsar *PSR 0532* in the Crab Nebula making use of the observational data $P \approx 0.033\,\mathrm{s}$ and $\dot{P}/P \approx 1.3 \times 10^{-11}\,\mathrm{s}^{-1}$ and using the inertia moment of $J \approx 10^{45}\,\mathrm{g\,cm}^2$, which corresponds to the inertia moment of a uniform

spherical body with the mass $M = 1.4M_{\odot}$ and radius $R = 10^6$ cm. In addition, estimate the pulsar magneto-dipole luminosity and compare it with the solar bolometric luminosity, $L_{\odot} \approx 4 \times 10^{33}$ erg/s.

Answers and Solutions

12.1 $B \approx 8 \times 10^{12}$ G; $\quad L_{PSR} \approx 4 \times 10^{38}$ erg/s $\approx 10^5 L_{\odot}$.

References

V.I. Abramenko, V. Carbone, V. Yurchyshyn, P.R. Goode, R.F. Stein, F. Lepreti, V. Capparelli, A. Vecchio, Turbulent diffusion in the photosphere as derived from photospheric bright point motion. ApJ **743**, 133 (2011)

V.I. Abramenko, T. Wang, V.B. Yurchishin, Analysis of electric current helicity in active regions on the basis of vector magnetograms. Solar Phys. **168**, 75–89 (1996)

V.I. Abramenko, T. Wang, V.B. Yurchishin, Electric current helicity in 40 active regions in the maximum of solar cycle 22. Solar Phys. **174**, 291–296 (1997)

M. Abramowitz, I.A. Stegun, in *Handbook of Mathematical Functions with Formulas, Graphs, and Mathematical Tables*, 9th dover printing, 10th gpo printing edn. (Dover, New York, 1964)

F. Aharonian et al., Discovery of two candidate pulsar wind nebulae in very-high-energy gamma rays. A&A **472**, 489–495 (2007)

S.I. Akasofu, S. Chapman, *Solar-Terrestrial Physics*, Part 1 (Clarendon Press, Oxford, 1974)

S.I. Akasofu, S. Chapman, *Solar-Terrestrial Physics*. II (Clarendon Press, Oxford, 1975)

A.I. Akhiezer, I.A. Akhiezer, R.V. Polovin, A.G. Sitenko, K.N. Stepanov, Plasma Electrodynamics. Volume 1-Linear Theory, Volume 2-Non-Linear Theory and Fluctuations (Pergamon Press, Oxford, 1975)

A.I. Akhiezer, Y.B. Fainberg, Dokl. Akad. Nauk. SSSR **69**, 555 (1949)

A.I. Akhiezer, Y.B. Fainberg, Uspekhi Fiz. Nauk **44**, 321 (1951)

G.D. Fleishman and I.N. Toptygin, *Cosmic Electrodynamics*, Astrophysics and Space Science Library 388, DOI 10.1007/978-1-4614-5782-4,

A.F. Aleksandrov, L.S. Bogdankevich, A.A. Rukhadze, in Principles of Plasma Electrodynamics (Osnovy elektrodinamiki plazmy, Moscow, Izdatel'stvo Vysshaia Shkola, 1978) Berlin and New York, Springer (Springer Series in Electrophysics. vol. 9, p. 506). Translation. Previously cited in issue 13, p. 2444, Accession no. A80-32901, vol. 9, p. 2444 (1984)

H. Alfvén, Existence of electromagnetic-hydrodynamic waves. Nature **150**, 405–406 (1942)

H. Alfven, *Cosmical Electrodynamics* (Clarendon Press, Oxford, 1950)

H. Alfven, C.G. Fälthammar, *Cosmical Electrodynamics. Fundamental Principles* (Clarendon Press, Oxford, 1963)

H. Alfvén, N. Herlofson, Cosmic radiation and radio stars. Phys. Rev. **78**, 616–616 (1950)

C.W. Allen, *Astrophysical Quantities* (Athlone Press, New York, 1976)

G.E. Allen, J.C. Houck, S.J. Sturner, Evidence of a curved synchrotron spectrum in the supernova remnant SN 1006. ApJ **683**, 773–785 (2008)

A.T. Altyntsev, G.D. Fleishman, G.L. Huang, V.F. Melnikov, A broadband microwave burst produced by electron beams. ApJ **677**, 1367–1377 (2008)

A.T. Altyntsev, V.V. Grechnev, N.S. Meshalkina, Y. Yan, Microwave type III-like bursts as possible signatures of magnetic reconnection. Solar Phys. **242**, 111–123 (2007)

J. Arons, Theory of pulsar winds, in *ASP Conference Series 271: Neutron Stars in Supernova Remnants*, p. 71 (2002)

M.J. Aschwanden, *Physics of the Solar Corona. An Introduction with Problems and Solutions*, 2nd edn. (Springer, Berlin, 2005)

M.J. Aschwanden, A.O. Benz, S.R. Kane, Correlation of solar radio pulsations with hard X-ray emission. A&A **229**, 206–215 (1990)

M.J. Aschwanden, M.J. Wills, H.S. Hudson, T. Kosugi, R.A. Schwartz, Electron time-of-flight distances and flare loop geometries compared from CGRO and YOHKOH observations. ApJ **468**, 398 (1996)

A.M. Atoyan, Radio spectrum of the crab nebula as an evidence for fast initial spin of its pulsar. A&A **346**, L49–L52 (1999)

W.I. Axford, E. Leer, G. Skadron, The acceleration of cosmic rays by shock waves, in International Cosmic Ray Conference, vol. 11, pp. 132–137 (1977)

W. Baade, F. Zwicky, Phys. Rev. **45**, 138 (1934)

S.A. Balbus, Enhanced angular momentum transport in accretion disks. ARA&A **41**, 555–597 (2003)

S.A. Balbus, J.F. Hawley, A powerful local shear instability in weakly magnetized disks. I - Linear analysis. II - Nonlinear evolution. ApJ **376**, 214–233 (1991)

V.B. Baranov, K.V. Krasnobaev, *Hydrodynamic theory of a cosmic plasma* [in Russian]. (Moscow Izdatel Nauka, Moscow, 1977)

T.S. Bastian, A.O. Benz, D.E. Gary, Radio emission from solar flares. ARA&A **36**, 131–188 (1998)

T.S. Bastian, J. Bookbinder, G.A. Dulk, M. Davis, Dynamic spectra of radio bursts from flare stars. ApJ **353**, 265–273 (1990)

T.S. Bastian, G.D. Fleishman, D.E. Gary, Radio spectral evolution of an X-Ray-poor impulsive solar flare: implications for plasma heating and electron acceleration. ApJ **666**, 1256–1267 (2007)

M. Battaglia, A.O. Benz, Relations between concurrent hard X-ray sources in solar flares. A&A **456**, 751–760 (2006)

V.A. Bazylev, N.K. Zhevago, *Emission from Fast Particles in Matter and in External Fields* [in Russian] (Izdatelstvo Nauka, Moscow, 1987)

R. Beck, Galactic and extragalactic magnetic fields. Space Science Rev. **99**, 243–260 (2001)

R. Beck, Magnetism in Galaxies - Observational Overview and Next Generation Radio Telescopes, ed. by A. Bonanno, E. de Gouveia Dal Pino, A.G. Kosovichev. IAU Symposium, vol. 274, pp. 325–332 (2011)

A.R. Bell, The acceleration of cosmic rays in shock fronts. I. MNRAS **182**, 147–156 (1978)

A.R. Bell, Turbulent amplification of magnetic field and diffusive shock acceleration of cosmic rays. MNRAS **353**, 550–558 (2004)

A.R. Bell, S.G. Lucek, Cosmic ray acceleration to very high energy through the non-linear amplification by cosmic rays of the seed magnetic field. MNRAS **321**, 433–438 (2001)

A. Benz (ed.), *Plasma astrophysics*, 2nd edn., Astrophysics and Space Science Library, vol. 279 (Kluwer, Dordrecht, 2002)

V.B. Berestetskii, E.M. Lifshits, L.P. Pitaevskii, *Quantum Electrodynamics*, vol. 4 (Pergamon Press, Oxford, 1982)

E.G. Berezhko, L.T. Ksenofontov, H.J. Völk, Confirmation of strong magnetic field amplification and nuclear cosmic ray acceleration in SN 1006. A&A **412**, L11–L14 (2003)

E.G. Berezhko, G. Pühlhofer, H.J. Völk, Theory of cosmic ray and γ-ray production in the supernova remnant RX J0852.0-4622. A&A **505**, 641–654 (2009)

V.S. Berezinskii, S.V. Bulanov, V.A. Dogiel, V.S. Ptuskin, *Astrophysics of Cosmic Rays* (North-Holland, Amsterdam, 1990)

I.B. Bernstein, Waves in a plasma in a magnetic field. Phys. Rev. **109**, 10–21 (1958)

V.S. Beskin, *Gravitatsiya i Astrofizika* [in Russian] (Fizmatlit, Moscow, 2009a)

V.S. Beskin, *MHD Flows in Compact Astrophysical Objects: Accretion, Winds and Jets* (Springer, Berlin, 2009b)

V.S. Beskin, A.V. Gurevich, Y.N. Istomin, *Physics of the Pulsar Magnetosphere* (Cambridge University Press, Cambridge, 1993)

P.L. Bhatnagar, E.P. Gross, M. Krook, A model for collision processes in gases. I. Small amplitude processes in charged and neutral one-component systems. Phys. Rev. **94**, 511–525 (1954)

L. Biermann, Kometenschweife und solare Korpuskularstrahlung. Z. Astrophys. **29**, 274 (1951)

L. Biermann, Über den Schweif des Kometen Halley im Jahre 1910. Zeitschrift Naturforschung Teil A **7**, 127 (1952)

M.F. Bietenholz, D.A. Frail, J.J. Hester, The crab nebula's moving wisps in radio. ApJ **560**, 254–260 (2001)

M.F. Bietenholz, J.J. Hester, D.A. Frail, N. Bartel, The crab nebula's wisps in radio and optical. ApJ **615**, 794–804 (2004)

G.S. Bisnovatyi-Kogan, S.A. Silich, Shock-wave propagation in the nonuniform interstellar medium. Rev. Mod. Phys. **67**, 661–712 (1995)

E.G. Blackman, G.B. Field, New dynamical mean-field dynamo theory and closure approach. Phys. Rev. Lett. **89**(26), 265007 (2002)

R.D. Blandford, C.F. McKee, Fluid dynamics of relativistic blast waves. Phys. Fluids **19**, 1130–1138 (1976)

R.D. Blandford, J.P. Ostriker, Particle acceleration by astrophysical shocks. ApJ **221**, L29–L32 (1978)

S.I. Blinnikov, V.S. Imshennik, V.P. Utrobin, The cygnus superbubble as the remnant of a peculiar supernova. Soviet Astron. Lett. **8**, 361–365 (1982)

S.A. Bogachev, B.V. Somov, Effect of coulomb collisions on the particle acceleration in collapsing magnetic traps. Astron. Lett. **35**, 57–69 (2009)

N.N. Bogoliubov, *Problems of Dynamical Theory in Statistical Physics* [in Russian] (Gostechizdat, Moscow, 1946)

N.N. Bogoliubov, Y.A. Mitropolski, *Asymptotic Methods in the Theory of Non-Linear Oscillations* (Gordon and Breach, New York, 1961)

D. Bohm, E.P. Gross, Theory of plasma oscillations. A. Origin of medium-like behavior. Phys. Rev. **75**, 1851–1864 (1949a)

D. Bohm, E.P. Gross, Theory of plasma oscillations. B. Excitation and damping of oscillations. Phys. Rev. **75**, 1864–1876 (1949b)

A. Bonanno, V. Urpin, G. Belvedere, Protoneutron star dynamos and pulsar magnetism. A&A **440**, 199–205 (2005)

M. Born, E. Wolf, *Principles of Optics* (Cambridge University Press, Cambridge, 1999)

S.I. Braginskii, Transport processes in a plasma. Rev. Plasma Phys. **1**, 205 (1965)

A. Brandenburg, Advances in theory and simulations of large-scale dynamos. Space Science Rev. **144**, 87–104 (2009)

A. Brandenburg, in Simulations of Astrophysical Dynamos, ed. by A. Bonanno, E. de Gouveia Dal Pino, A.G. Kosovichev. IAU Symposium, vol. 274, pp. 402–409 (2011)

A. Brandenburg, K. Subramanian, Astrophysical magnetic fields and nonlinear dynamo theory. Phys. Rep. **417**, 1–209 (2005)

J.C. Brandt, *Emissions from the Sun. Introduction to the Solar Wind* (W. H. Freeman, San Francisco, 1970)

J.C. Brandt, S.R. Harrington, R.G. Roosen, Interplanetary gas. XIX. Observational evidence for a meridional solar-wind flow diverging from the plane of the solar equator. ApJ **184**, 27–32 (1973)

A. Bruzek, C.J. Durrant (eds.), Illustrated glossary for solar and solar-terrestrial physics, *Astrophysics and Space Science Library*, vol. 69 (D. Reidel, Dordrecht, 1977)

O. Buneman, Instability, turbulence, and conductivity in current-carrying plasma. Phys. Rev. Lett. **1**, 8–9 (1958)

A. Bykov, in *Non-Thermal Electron Acceleration and GRB Spectral Evolution*, ed. by J. Paul, T. Montmerle, E. Aubourg. 19th Texas Symposium on Relativistic Astrophysics and Cosmology (1998)

A.M. Bykov, Particle acceleration and nonthermal phenomena in superbubbles. Space Sci. Rev. **99**, 317–326 (2001)

A.M. Bykov, G.D. Fleishman, On non-thermal particle generation in superbubbles. MNRAS **255**, 269–275 (1992)

A.M. Bykov, G.D. Fleishman, Particle acceleration by strong turbulence in solar flares: theory of spectrum evolution. ApJ **692**, L45–L49 (2009)

A.M. Bykov, S.M. Osipov, D.C. Ellison, Cosmic ray current driven turbulence in shocks with efficient particle acceleration: the oblique, long-wavelength mode instability. MNRAS **410**, 39–52 (2011)

A.M. Bykov, I. Toptygin, Reviews of topical problems: particle kinetics in highly turbulent plasmas (renormalization and self-consistent field methods). Physics Uspekhi **36**, 1020–1052 (1993)

A.M. Bykov, I. Toptygin, Reviews of topical problems: instabilities of a multicomponent plasma with accelerated particles and magnetic field generation in astrophysical objects. Physics Uspekhi **50**, 141–174 (2007)

S. Chandrasekhar, *Hydrodynamic and Hydromagnetic Stability* (Clarendon Press, Oxford, 1961)

F.F. Chen, *Introduction to Plasma Physics and Controlled Fusion* (Plenum Press, New York, 1984)

G.F. Chew, M.L. Goldberger, F.E. Low, The Boltzmann equation and the one-fluid hydromagnetic equations in the absence of particle collisions. R. Soc. London Proc. Series A **236**, 112–118 (1956)

J. Cho, A. Lazarian, E.T. Vishniac, New regime of magnetohydrodynamic turbulence: cascade below the viscous cutoff. ApJ **566**, L49–L52 (2002)

L.L. Cowie, A. Songaila, High-resolution optical and ultraviolet absorption-line studies of interstellar gas. ARA&A **24**, 499–535 (1986)

T.G. Cowling, *Magnetohydrodynamics* (Interscience, London, 1957)

G.T. Delory, R.E. Ergun, C.W. Carlson, L. Muschietti, C.C. Chaston, W. Peria, J.P. McFadden, R. Strangeway, FAST observations of electron distributions within AKR source regions. Geophys. Res. Lett. **25**, 2069–2072 (1998)

A.Z. Dolginov, Reviews of topical problems: origin of the magnetic fields of the earth and celestial bodies. Soviet Phys. Uspekhi **30**, 475–493 (1987)

A.Z. Dolginov, Y.N. Gnedin, N.A. Silant'ev, *Propagation and Polarization of Radiation Through Cosmic Medium* (Nauka, Moskva, 1979)

A.Z. Dolginov, I.N. Toptygin, Galactic magnetic field generation by the electric current of cosmic rays. A&A **416**, 411–422 (2004)

L.I. Dorman, M.E. Kats, Y.I. Fedorov, B.A. Shakhov, Energy balance of cosmic rays in multiple scattering in a randomly inhomogeneous magnetic field. Soviet J. Exp. Theor. Phys. Lett. **27**, 353 (1978)

P. Drude, Zur Elektronentheorie der Metalle. Annalen der Physik **306**, 566–613 (1900a)

P. Drude, Zur Elektronentheorie der Metalle; II. Teil. Galvanomagnetische und thermomagnetische Effecte. Annalen der Physik **308**, 369–402 (1900b)

G.A. Dulk, Radio emission from the sun and stars. ARA&A **23**, 169–224 (1985)

F. Dyson, Physics Today, **23**(9) (1970)

V.Y. Eidman. Soviet Phys.–JETP **7**, 91 (1958)

V.Y. Eidman. Soviet Phys.–JETP **9**, 947 (1959)

W.M. Elsasser, The hydromagnetic equations. Phys. Rev. **79**, 183–183 (1950)

R.E. Ergun, C.W. Carlson, J.P. McFadden, G.T. Delory, R.J. Strangeway, P.L. Pritchett, Electron-cyclotron maser driven by charged-particle acceleration from magnetic field-aligned electric fields. ApJ **538**, 456–466 (2000)

V.N. Fedorenko, G.D. Fleishman, Enhancement of hydromagnetic turbulence near a shock wave front and the limiting energies of particles accelerated in supernova remnants. Soviet Astron. **32**, 398 (1988)

E. Fermi, Phys. Rev. **75** 1169

A.V. Filippenko, Optical spectra of supernovae. ARA&A **35**, 309–355 (1997)

G.D. Fleishman, Effect of random inhomogeneities on electron cyclotron maser emission. ApJ **601**, 559–564 (2004a)

G.D. Fleishman, Natural spectral bandwidth of electron cyclotron maser emission. Astron. Lett. **30**, 603–614 (2004b)

G.D. Fleishman, Generation of emissions by fast particles in stochastic media. ArXiv Astrophysics e-prints, astro-ph/0510317 (2005)

G.D. Fleishman, Diffusive synchrotron radiation from relativistic shocks in gamma-ray burst sources. ApJ **638**, 348–353 (2006)

G.D. Fleishman, *Stokhasticheskaya Teoriya Izlucheniya* [in Russian] (IKI, Moscow–Izhevsk, 2008)

G.D. Fleishman, M.F. Bietenholz, Diffusive synchrotron radiation from pulsar wind nebulae. MNRAS **376**, 625–633 (2007)

G.D. Fleishman, E.P. Kontar, Sub-THz radiation mechanisms in solar flares. ApJ **709**, L127–L132 (2010)

G.D. Fleishman, E.P. Kontar, G.M. Nita, D.E. Gary, A cold, tenuous solar flare: acceleration without heating. ApJ **731**, L19 (2011)

G.D. Fleishman, A.A. Kuznetsov, Fast gyrosynchrotron codes. ApJ **721**, 1127–1141 (2010)

G.D. Fleishman, V.F. Melnikov, Millisecond solar radio spikes. Uspekhi Fizicheskikh Nauk **41**, 1157–1189 (1998)

G.D. Fleishman, I.N. Toptygin, Stochastic particle acceleration by helical turbulence in solar flares, Provided by the SAO/NASA Astrophysics Data System, p. 447 (2013). doi 10.1093/mnras/sts518. http://adsabs.harvard.edu/abs/2013MNRAS.tmp..447F

P.G. Frick, *Turbulentnost': Podkhody i Modeli* [in Russian] (IKI, Moscow–Izhevsk, 2003)

B.D. Fried, Mechanism for instability of transverse plasma waves. Phys. Fluids **2**, 337 (1959). doi 10.1063/1.1705933. http://adsabs.harvard.edu/abs/1959PhFl....2..337F. Provided by the SAO/NASA Astrophysics Data System

A. Friedman, Z. Physik **10**, 377 (1922)

U. Frisch, *Turbulence. The legacy of A. N. Kolmogorov* (Cambridge University Press, Cambridge, 1995)

H.P. Furth, P.H. Rutherford, Ion runaway in tokamak discharges. Phys. Rev. Lett. **28**, 545–548 (1972)

A. Gailitis, O. Lielausis, E. Platacis, G. Gerbeth, F. Stefani, Colloquium: laboratory experiments on hydromagnetic dynamos. Rev. Mod. Phys. **74**, 973–990 (2002)

X.Y. Gao, J.L. Han, W. Reich, P. Reich, X.H. Sun, L. Xiao, A Sino-German $\lambda 6$ cm polarization survey of the galactic plane. V. Large supernova remnants. A&A **529**, A159 (2011)

D.E. Gary, C.U. Keller (eds.), Solar and space weather radiophysics - current status and future developments, *Astrophysics and Space Science Library*, vol. 314 (Kluwer, Dordrecht, 2004)

V.L. Ginzburg, *Theoretical Physics and Astrophysics*, 3rd revised and enlarged edn. [in Russian] (Izdatel Nauka, Moscow, 1987)

V.L. Ginzburg, A.A. Rukhadze, *Waves in Magnetoactive Plasma* /2nd Revised edn. [in Russian] (Nauka, Moscow, 1975)

V.L. Ginzburg, S.I. Syrovatskii, *The Origin of Cosmic Rays* (Macmillan, New York, 1964)

V.L. Ginzburg, S.I. Syrovatskii, Cosmic magnetobremsstrahlung (synchrotron radiation). ARA&A **3**, 297–+ (1965)

V.L. Ginzburg, V.N. Tsytovich, *Transition Radiation and Transition Scattering* (Hilger, Bristol, 1990)

P. Giuliani, T. Neukirch, P. Wood, Particle motion in collapsing magnetic traps in solar flares. I. Kinematic theory of collapsing magnetic traps. ApJ **635**, 636–646 (2005)

P. Goldreich, W.H. Julian, Pulsar electrodynamics. ApJ **157**, 869 (1969)

P. Goldreich, S. Sridhar, Toward a theory of interstellar turbulence. 2: Strong alfvenic turbulence. ApJ **438**, 763–775 (1995)

G.S. Golitsyn, Fluctuations of the magnetic field and current density in a turbulent flow of a weakly conducting fluid. Soviet Phys. Dokl. **5**, 536 (1960)

G.S. Golitsyn, Dissipation fluctuations in locally isotropic turbulent flow. Soviet Phys. Dokl. **7**, 380 (1962)

K.J. Grady, T. Neukirch, An extension of the theory of kinematic MHD models of collapsing magnetic traps to 2.5D with shear flow and to 3D. ARA&A **508**, 1461–1468 (2009)

P.C. Grigis, A.O. Benz, Electron acceleration in solar flares: theory of spectral evolution. ARA&A **458**, 641–651 (2006)

P.C. Grigis, A.O. Benz, Spectral hardening in large solar flares. arXiv eprint 0708.2472. ApJ **683**, 1180–1191 (2008). doi 10.1086/589826. http://adsabs.harvard.edu/abs/2008ApJ...683.1180G. Provided by the SAO/NASA Astrophysics Data System

E.P. Gross, Plasma oscillations in a static magnetic field. Phys. Rev. **82**, 232–242 (1951)

E.P. Gross, M. Krook, Model for collision processes in gases: small-amplitude oscillations of charged two-component systems. Phys. Rev. **102**, 593–604 (1956)

S.N. Gurbatov, A.I. Saichev, I.G. Iakushkin, Nonlinear waves and one-dimensional turbulence in nondispersive media. Soviet Phys. Uspekhi **141**, 221–255 (1983)

A.V. Gurevich. Sov. Phys. JETP **13**, 1282 (1961)

A.V. Gurevich, L.P. Pitaevskii, Decay of initial discontinuity in the Korteweg-de Vries equation. Soviet J. Exp. Theor. Phys. Lett. **17**, 193 (1973)

A.V. Gurevich, L.P. Pitaevskii, An averaged description of waves in the Kortweg-de Vries-Burgers equation. Zhurnal Eksperimental noi i Teoreticheskoi Fiziki **93**, 871–880 (1987)

P. Haensel, A.Y. Potekhin, D.G. Yakovlev (eds.), Neutron stars 1 : equation of state and structure. *Astrophysics and Space Science Library*, vol. 326 (Springer, New York, 2007)

R.J. Hamilton, V. Petrosian, Stochastic acceleration of electrons. I - Effects of collisions in solar flares. ApJ **398**, 350–358 (1992)

A. Hasegawa, K. Mima, M. Duong-van, Plasma distribution function in a superthermal radiation field. Phys. Rev. Lett. **54**, 2608–2610 (1985)

H. Hasegawa, Nonextensive aspects of small-world networks. Physica A Stat. Mech. Appl. **365**, 383–401 (2006)

S. Hayakawa, *Cosmic Ray Physics*. Part_2. Astrophysical Aspects (Mir, Moskva, 1974)

C.V. Heer, *Statistical Mechanics, Kinetic Theory, and Stochastic Processes* (Academic, NYC, 1972)

J.J. Hester, J.M. Stone, P.A. Scowen, B. Jun, J.S. Gallagher, M.L. Norman, G.E. Ballester, C.J. Burrows, S. Casertano, J.T. Clarke, D. Crisp, R.E. Griffiths, J.G. Hoessel, J.A. Holtzman, J. Krist, J.R. Mould, R. Sankrit, K.R. Stapelfeldt, J.T. Trauger, A. Watson, J.A. Westphal, WFPC2 studies of the crab nebula. III. Magnetic Rayleigh-Taylor instabilities and the origin of the filaments. ApJ **456**, 225 (1996)

A. Herzenberg, Phil. Trans. Roy. Soc. **A250**, 543–585 (1958)

G.D. Holman, DC electric field acceleration of ions in solar flares. ApJ **452**, 451–+ (1995)

E. Hubble, Proc. Nat. Acad. Sci. Wash. **15**, 168 (1929)

A.J. Hundhausen, *Coronal Expansion and Solar Wind* (Springer, Berlin, 1972)

G.J. Hurford, S. Krucker, R.P. Lin, R.A. Schwartz, G.H. Share, D.M. Smith, Gamma-ray imaging of the 2003 October/November solar flares. ApJ **644**, L93–L96 (2006)

V.S. Imshennik, N.A. Bobrova, Dynamics of Collision Plasmas [in Russian] (Energoatomizdat, Moscow, 1997)

V.S. Imshennik, D.K. Nadezhin, *Supernova 1987A in the Large Magellanic Cloud: Observations and Theory* (Harwood Academic Publishers, Amsterdam, 1989)

M.B. Isichenko, Percolation, statistical topography, and transport in random media. Rev. Mod. Phys. **64**, 961–1043 (1992)

Y.N. Istomin, Conferences and symposia: electron-positron plasma generation in the magnetospheres of neutron stars. Physics Uspekhi **51**, 844–848 (2008)

S. Jester, H.J. Röser, K. Meisenheimer, R. Perley, The radio-ultraviolet spectral energy distribution of the jet in 3C 273. A&A **431**, 477–502 (2005)

C.A. Jones, M.J. Thompson, S.M. Tobias, The solar dynamo. Space Science Rev. **152**, 591–616 (2010)

S.A. Kaplan, S.B. Pikel'ner, *The Physics of the Interstellar Medium* [in Russian] (Izdatelstvo Nauka, Moscow, 1979)

S.A. Kaplan, S.B. Pikel'ner, V.N. Tsytovich, *Plasma Physics of the Solar Atmosphere* [in Russian] (Izdatel'stvo Nauka, Moscow, 1977)

P. Kaufmann, G. Trottet, C.G. Giménez de Castro, J.P. Raulin, S. Krucker, A.Y. Shih, H. Levato, Sub-terahertz, microwaves and high energy emissions during the 6 December 2006 Flare, at 18:40 UT. Solar Phys. **255**, 131–142 (2009)

W.C. Keel, The optical continua of extragalactic radio jets. ApJ **329**, 532–550 (1988)

C.F. Kennel, F.V. Coroniti, Confinement of the crab pulsar's wind by its supernova remnant. ApJ **283**, 694–709 (1984a)

C.F. Kennel, F.V. Coroniti, Magnetohydrodynamic model of crab nebula radiation. ApJ **283**, 710–730 (1984b)

K.S. Khodzhaev, A.G. Chirkov, S.D. Shatalov, Motion of a charged particle in crossed fields when the magnetic field is strongly inhomogeneous. J. Appl. Mech. Tech. Phys. **22**, 439–442 (1981)

L.L. Kichatinov, New mechanism for acceleration of cosmic particles in the presence of reflectively noninvariant turbulence. Sov. Phys. JETP Lett. **37**, 51 (1983)

K.O. Kiepenheuer, Cosmic rays as the source of general galactic radio emission. Phys. Rev. **79**, 738–739 (1950)

A.L. Kiplinger, B.R. Dennis, K.J. Frost, L.E. Orwig, A.G. Emslie. Millisecond time variations in hard X-ray solar flares. ApJ **265**, L99–L104 (1983)

R. Kippenhahn, A. Schlüter, Eine Theorie der solaren Filamente. Mit 7 Textabbildungen. Z. Astrophys. **43**, 36 (1957)

Y.L. Klimontovich, *Statisticheskaya Fizika* [in Russian] (Nauka, Moscow, 1972)

L.G. Kocharov, G.E. Kocharov, He-3-rich solar flares. Space Science Rev. **38**, 89–141 (1984)

M.N. Kogan, *Dinamika Razrezhennogo Gaza. Kineticheskaya Teoriya* [in Russian] (Nauka, Moscow, 1967)

A. Kolmogorov, The local structure of turbulence in incompressible viscous fluid for very large Reynolds' numbers. Akademiia Nauk SSSR Dokl. **30**, 301–305 (1941)

A.S. Kompaneets, A point explosion in an inhomogeneous atmosphere. Soviet Phys. Dokl. **5**, 46 (1960)

V.P. Korobeinikov, Problem of strong point explosion in a gas with zero temperature gradient. Dokl. Akad. Nauk SSSR **109**, 271–273 (1956)

V.B. Korsakov, G.D. Fleishman, Periodic and irregular modes of the nonlinear plasma radio emission mechanism. Radiophys. Quantum Electron. **41**, 28–38 (1998)

D.J. Korteweg, G. de Vries, On the change of form of long waves advancing in a rectangular channel, and on a new type of long stationary waves. Phil. Mag. **39**, 422–443 (1895)

L.S. Kovasznay, The spectrum of locally isotropic turbulence. Phys. Rev. **73**, 1115–1116 (1948)

F. Krause, K.H. Rädler, *Mean-Field Magnetohydrodynamics and Dynamo Theory* (Pergamon Press, Oxford, 1980)

S. Krucker, H.S. Hudson, L. Glesener, S.M. White, S. Masuda, J.P. Wuelser, R.P. Lin, Measurements of the coronal acceleration region of a solar flare. ApJ **714**, 1108–1119 (2010)

S. Krucker, R.P. Lin, Hard X-Ray emissions from partially occulted solar flares. ApJ **673**, 1181–1187 (2008)

G.F. Krymskii, A regular mechanism for the acceleration of charged particles on the front of a shock wave. Soviet Phys. Dokl. **22**, 327 (1977)

R.M. Kulsrud, MHD Description of Plasma, ed. by A.A. Galeev, R.N. Sudan, Basic Plasma Physics: Selected Chapters, in *Handbook of Plasma Physics*, vol. 1, pp. 1 (1983)

R.M. Kulsrud, *Plasma Physics for Astrophysics* (Princeton University Press, Princeton, 2005)

A.A. Kuznetsov, J.G. Doyle, S. Yu, G. Hallinan, A. Antonova, A. Golden, Comparative analysis of two formation scenarios of bursty radio emission from ultracool dwarfs. ApJ **746**, 99 (2012)

A.A. Kuznetsov, G.M. Nita, G.D. Fleishman, Three-dimensional simulations of gyrosynchrotron emission from mildly anisotropic nonuniform electron distributions in symmetric magnetic loops. arXiv eprint 1108.5150. ApJ, vol. 742, pp. 87 (2011). doi 10.1088/0004-637X/742/2/87. http://adsabs.harvard.edu/abs/2011ApJ...742...87K. Provided by the SAO/NASA Astrophysics Data System

A.A. Kuznetsov, V.G. Vlasov, Kinetic simulation of the electron-cyclotron maser instability: effect of a finite source size. arXiv eprint 1202.0926. A&A vol. 539, pp. A141 (2012). doi 10.1051/0004-6361/201118716. http://adsabs.harvard.edu/abs/2012A%26A...539A.141K . Provided by the SAO/NASA Astrophysics Data System

P.O. Lagage, C.J. Cesarsky, The maximum energy of cosmic rays accelerated by supernova shocks. A&A **125**, 249–257 (1983)

L. Lamy, P. Schippers, P. Zarka, B. Cecconi, C.S. Arridge, M.K. Dougherty, P. Louarn, N. André, W.S. Kurth, R.L. Mutel, D.A. Gurnett, A.J. Coates, Properties of Saturn kilometric radiation measured within its source region. Geophys. Res. Lett. **371**, 12104 (2010)

L. Landau, Phys. Z. Sowjetunion Band 1, s. **285** (1932)

L.D. Landau, E.M. Lifshits, *The electrodynamics of continuous media* (2nd revised and enlarged edn.) Teoreticheskaia Fizika, 8 (Moscow Izdatel Nauka, 1982)

L.D. Landau, E.M. Lifshitz, *Electrodynamics of Continuous Media* (Pergamon Press, Oxford, 1960)

L.D. Landau, E.M. Lifshitz, *Hydrodynamik* (Akademie-Verlag, Berlin, 1966)

L.D. Landau, E.M. Lifshitz, *Mechanics* (Pergamon Press, Oxford, 1969)

L.D. Landau, E.M. Lifshitz, The classical theory of fields, *Course of Theoretical Physics - Pergamon International Library of Science, Technology, Engineering and Social Studies*, 3rd revised, English edn. (Pergamon Press, Oxford, 1971)

M.A. Lee, Coupled hydromagnetic wave excitation and ion acceleration at interplanetary traveling shocks. Journ. Geo. Res. **88**, 6109–6119 (1983)

M.P. Leubner, Fundamental issues on kappa-distributions in space plasmas and interplanetary proton distributions. Phys. Plasmas **11**, 1308–1316 (2004)

E.M. Lifshitz, L.P. Pitaevskii, *Physical Kinetics* (Pergamon Press, Oxford, 1981)

R.P. Lin, S. Krucker, G.J. Hurford, D.M. Smith, H.S. Hudson, G.D. Holman, R.A. Schwartz, B.R. Dennis, G.H. Share, R.J. Murphy, A.G. Emslie, C. Johns-Krull, N. Vilmer, RHESSI observations of particle acceleration and energy release in an intense solar gamma-ray line flare. ApJ **595**, L69–L76 (2003)

J.G. Lominadze, Development of the Theory of Instabilities of Differentially Rotating Plasma with Astrophysical Applications, ed. by A. Bonanno, E. de Gouveia Dal Pino, A.G. Kosovichev. IAU Symposium, vol. 274, pp. 318–324 (2011)

M.S. Longair, *High Energy Astrophysics* (Cambridge University Press, Cambridge, 1981)

D.W. Longcope, G.H. Fisher, A.A. Pevtsov, Flux-tube twist resulting from helical turbulence: the sigma-effect. ApJ **507**, 417–432 (1998)

F.J. Lowes, I. Wilkinson, Geomagnetic dynamo: a laboratory model. Nature **198**, 1158–1160 (1963)

F.J. Lowes, I. Wilkinson, Geomagnetic dynamo: an improved laboratory model. Nature **219**, 717–718 (1968)

T.A. Lozinskaya, *Supernovae and Stellar Wind in the Interstellar Medium* (American Institute of Physics, New York, 1992)

M.M. Mac Low, R. McCray, Superbubbles in disk galaxies. ApJ **324**, 776–785 (1988)

M.M. Mac Low, R. McCray, M.L. Norman, Superbubble blowout dynamics. ApJ **337**, 141–154 (1989)

R.N. Manchester, J.H. Taylor, *Pulsars* (W. H. Freeman, San Francisco, 1977)

L.S. Marochnik, A.A. Suchkov, *Galactika* [in Russian] (Nauka, Moscow, 1984)

E. Marsch, H. Rosenbauer, R. Schwenn, K.H. Muehlhaeuser, F.M. Neubauer, Solar wind helium ions - observations of the HELIOS solar probes between 0.3 and 1 AU. Journ. Geo. Res. **87**, 35–51 (1982a)

E. Marsch, R. Schwenn, H. Rosenbauer, K.H. Muehlhaeuser, W. Pilipp, F.M. Neubauer, Solar wind protons - three-dimensional velocity distributions and derived plasma parameters measured between 0.3 and 1 AU. Journ. Geo. Res. **87**, 52–72 (1982b)

H.L. Marshall, D.E. Harris, J.P. Grimes, J.J. Drake, A. Fruscione, M. Juda, R.P. Kraft, S. Mathur, S.S. Murray, P.M. Ogle, D.O. Pease, D.A. Schwartz, A.L. Siemiginowska, S.D. Vrtilek, B.J. Wargelin, Structure of the X-ray emission from the Jet of 3C 273. ApJ **549**, L167–L171 (2001)

H.L. Marshall, B.P. Miller, D.S. Davis, E.S. Perlman, M. Wise, C.R. Canizares, D.E. Harris, A high-resolution X-ray image of the Jet in M87. ApJ **564**, 683–687 (2002)

G.M. Mason, ^{3}He-rich solar energetic particle events. Space Science Rev. **130**, 231–242 (2007)

R.A. Maurya, A. Ambastha, V. Reddy, Kinetic and magnetic helicities in solar active regions. J. Phys. Con. Series **271**(1), 012003 (2011)

F.B. McDonald, B.J. Teegarden, J.H. Trainor, T.T. von Rosenvinge, W.R. Webber, The interplanetary acceleration of energetic nucleons. ApJ **203**, L149–L154 (1976)

V.F. Melnikov, G.D. Fleishman, Q.J. Fu, G.L. Huang, Flare-plasma diagnostics from millisecond pulsations of the solar radio emission. Astron. Rep. **46**, 497–514 (2002a)

V.F. Melnikov, K. Shibasaki, V.E. Reznikova, Loop-top nonthermal microwave source in extended solar flaring loops. ApJ **580**, L185–L188 (2002b)

D.B. Melrose, The emission and absorption of waves by charged particles in magnetized plasmas. Astrophys. Space. Sci. **2**, 171–235 (1968)

D.B. Melrose, *Plasma astrohysics. Nonthermal processes in diffuse magnetized plasmas - vol.1: The emission, absorption and transfer of waves in plasmas; vol.2: Astrophysical applications* (Gordon and Breach, New York, 1980)

D.B. Melrose, J.C. Brown, Precipitation in trap models for solar hard X-ray bursts. MNRAS **176**, 15–30 (1976)

A.B. Migdal, Bremsstrahlung and pair production in condensed media at high energies. Phys. Rev. **103**, 1811–1820 (1956)

D. Mihalas, Stellar atmospheres /2nd edition/. San Francisco, W. H. Freeman and Co., 1978. 650 p., Provided by the SAO/NASA Astrophysics Data System, p. 650 (1978). http://adsabs.harvard.edu/abs/1978stat.book.....M

A.B. Mikhailovskii, J.G. Lominadze, A.P. Churikov, V.D. Pustovitov. Progress in theory of instabilities in a rotating plasma. Plasma Phys. Rep. **35**, 273–314 (2009)

J.A. Miller, P.J. Cargill, A.G. Emslie, G.D. Holman, B.R. Dennis, T.N. LaRosa, R.M. Winglee, S.G. Benka, S. Tsuneta, Critical issues for understanding particle acceleration in impulsive solar flares. Journ. Geo. Res. **102**, 14631–14660 (1997)

J.A. Miller, T.N. Larosa, R.L. Moore, Stochastic electron acceleration by cascading fast mode waves in impulsive solar flares. ApJ **461**, 445–+ (1996)

H.K. Moffatt, *Magnetic Field Generation in Electrically Conducting Fluids* (Cambridge University Press, Cambridge, 1978)

H.K. Moffatt, Some developments in the theory of turbulence. J. Fluid Mech. **106**, 27–47 (1981)

S.A. Molchanov, A.A. Ruzmaikin, D.D. Sokolov, Reviews of topical problems: kinematic dynamo in random flow. Soviet Physics Uspekhi **28**, 307–327 (1985)

A.S. Monin, A.M. Yaglom, *Statistical Hydromechanics* (Nauka, Moscow, 1965)

K. Mori, J.J. Hester, D.N. Burrows, G.G. Pavlov, H. Tsunemi, Chandra Reveals the Dynamic Structure of the Inner Crab Nebula, in *ASP Conference Series 271: Neutron Stars in Supernova Remnants*, p. 157 (2002)

P.M. Morse, H. Feshbach, *Methods of Theoretical Physics* (McGraw-Hill, New York, 1953)

V.S. Murzin, *Astrofizika Kosmicheskikh Luchei* [in Russian] (Logos, Moscow, 2007)

D.K. Nadyozhin, V.S. Imshennik, Physics of supernovae. Int. J. Mod. Phys. A **20**, 6597–6611 (2005)

D.I. Nagirner, *Lektsii po Teorii Perenosa Izlucheniya* [in Russian] (SPb University, St. Petersburg, 2007a)

D.I. Nagirner, *Radiatsionnye Mekhanizmy v Astrofizike* [in Russian] (SPb University, St. Petersburg, 2007b)

I.A. Nikolaev, V.N. Tsytovich, The power law spectra of relativistic electrons in a plasma in a random magnetic field. Phys. Scripta **20**, 665–668 (1979)

G.M. Nita, D.E. Gary, G.D. Fleishman, Spatial evidence for transition radiation in a solar radio burst. ApJ **629**, L65–L68 (2005)

G.M. Nita, D.E. Gary, J. Lee, Statistical study of two years of solar flare radio spectra obtained with the Owens valley solar array. ApJ **605**, 528–545 (2004)

V.N. Obridko, *Sunspots and Activity Complexes* (Izdatelstvo Nauka, Moscow, 1985)

A.M. Obukhov, On spectral energy distribution in a turbulent flow. Izvestiya AN SSSR: Seria Geography & Geophysics **5**, 453–466 (1941)

R.A. Osten, T.S. Bastian, Ultrahigh time resolution observations of radio bursts on AD Leonis. ApJ **674**, 1078–1085 (2008)

E. Parker, Extension of the solar corona into interplanetary space. Journ. Geo. Res. **64**, 1675–1681 (1959)

E.N. Parker, *Interplanetary Dynamical Processes* (Interscience, New York, 1963)

E.N. Parker, *Cosmical Magnetic Fields: Their Origin and Their Activity* (Clarendon Press, Oxford, Oxford University Press, New York, 1979)

E.S. Perlman, J.A. Biretta, W.B. Sparks, F.D. Macchetto, J.P. Leahy, The optical-near-infrared spectrum of the M87 Jet from Hubble space telescope observations. ApJ **551**, 206–222 (2001)

R. Phythian, W.D. Curtis, The effective long-time diffusivity for a passive scalar in a Gaussian model fluid flow. J. Fluid Mech. **89**, 241–250 (1978)

J.H. Piddington, Electromagnetic field equations for a moving medium with hall conductivity. MNRAS **114**, 638 (1954)

S.B. Pikel'ner, *Foundations of Cosmical Electrodynamics* [in Russian] (Nauka, Moscow, 1966)

K.Y. Platonov, G.D. Fleishman, Transition radiation in media with random inhomogeneities. Uspekhi Fizicheskikh Nauk **45**, 235–291 (2002)

A.Y. Potekhin, The physics of neutron stars. Physics Uspekhi **53**, 1235–1256 (2010)

R.D. Preece, M.S. Briggs, R.S. Mallozzi, G.N. Pendleton, W.S. Paciesas, D.L. Band, The BATSE gamma-ray burst spectral catalog. I. High time resolution spectroscopy of bright bursts using high energy resolution data. ApJS **126**, 19–36 (2000)

E. Priest, T. Forbes, *Magnetic Reconnection* (Cambridge University Press, Cambridge, 2000)

V.S. Ptuskin, Conferences and symposia the origin of cosmic rays. Physics Uspekhi **53**, 958–961 (2010)

V.V. Pustovalov, V.P. Silin, Nelineinye processy v plazme (in Russian). Trudy FIAN **61**, 42 (1972)

Qiu, J. and Gary, D. E. and Fleishman, G. D., Evaluating Mean Magnetic Field in Flare Loops, *solphys* Provided by the SAO/NASA Astrophysics Data System, **255**, pp. 107–118 (2009) doi: 10.1007/s11207-009-9316-y. http://adsabs.harvard.edu/abs/2009SoPh..255..107Q

R. Ramaty, Gyrosynchrotron emission and absorption in a magnetoactive plasma. ApJ **158**, 753 (1969)

A.B. Rechester, M.N. Rosenbluth, Electron heat transport in a Tokamak with destroyed magnetic surfaces. Phys. Rev. Lett. **40**, 38–41 (1978)

Y. Rephaeli, Comptonization of the cosmic microwave background: the Sunyaev-Zeldovich effect. ARA&A **33**, 541–580 (1995)

B. Reville, A.R. Bell, A filamentation instability for streaming cosmic rays. MNRAS **419**, 2433–2440 (2012)

G.H. Rieke, W.Z. Wisniewski, M.J. Lebofsky, Abrupt cutoffs in the optical-infrared spectra of nonthermal sources. ApJ **263**, 73–78 (1982)

K. Rohlfs (ed.), Lectures on density wave theory, in *Lecture Notes in Physics*, vol. 69 (Springer, Berlin, 1977)

M. Rowan-Robinson, *Cosmology* (Clarendon Press, Oxford, 2004)

I.V. Rozhansky, G.D. Fleishman, G.L. Huang, Millisecond microwave spikes: statistical study and application for plasma diagnostics. ApJ **681**, 1688–1697 (2008)

A.A. Ruzmaikin, D.D. Sokolov, A.M. Shukurov (eds.), Magnetic fields of galaxies. *Astrophysics and Space Science Library*, vol. 133 (Kluwer, Dordrecht, 1988)

G.B. Rybicki, A.P. Lightman, *Radiative Processes in Astrophysics* (Wiley, New York, 1986)

R.Z. Sagdeev, Cooperative phenomena and shock waves in collisionless plasmas. Rev. Plasma Phys. **4**, 23 (1966)

R.Z. Sagdeev, D.A. Usikov, G.M. Zaslavsky, *Nonlinear Physics. From the Pendulum to Turbulence and Chaos* (Harwood Academic, New York, 1988)

J.I. Sakai, Y. Ohsawa, Particle acceleration by magnetic reconnection and shocks during current loop coalescence in solar flares. Space Science Rev. **46**, 113–198 (1987)

A.A. Schekochihin, S.C. Cowley, *Turbulence and Magnetic Fields in Astrophysical Plasmas*, p. 85 (Springer, Berlin, 2007)

A.Z. Schluter, Naturforschung, 12a, 822 und 855

L.I. Sedov, DAN SSSR **42**, 1, (1946); L.I. Sedov, Prikladnaya matematika i mechanika **10**, 2 (1946)

L.I. Sedov, *Metody Podobiya i Razmernosti v Mekhanike* [in Russian] (Nauka, Moscow, 1987)

S.L. Shapiro, S.A. Teukolsky, *Black Holes, White Dwarfs, and Neutron Stars: The Physics of Compact Objects* (Wiley-Interscience, New York, 1983)

J.V. Shebalin, W.H. Matthaeus, D. Montgomery, Anisotropy in MHD turbulence due to a mean magnetic field. J. Plasma Phys. **29**, 525–547 (1983)

I.S. Shklovskij, *Supernovae and Problems Connected With Them* [in Russian] (Nauka, Moskva, 1976)

V.P. Silin, *Vvedenie v Kineticheskuyu Teoriyu Gazov* [in Russian] (Nauka, Moscow, 1971)

D.V. Sivukhin, Motion of charged particles in electromagnetic fields in the drift approximation. Rev. Plasma Phys. **1**, 1 (1965)

S.J. Smartt, Progenitors of core-collapse supernovae. ARA&A **47**, 63–106 (2009)

A. Solinger, J. Buff, S. Rappaport, Isothermal blast wave model of supernova remnants. ApJ **201**, 381–386 (1975)

B.V. Somov, *Plasma Astrophysics, Part I: Fundamentals and Practice* (Springer, New York, 2006)

B.V. Somov, *Plasma Astrophysics, Part II: Reconnection and Flares* (Springer, Berlin, 2007)

B.V. Somov, A.V. Oreshina, Magnetic reconnection and acceleration of particles on the sun. Bulletin of the Russian Academy of Science, Phys. **75**, 735–737 (2011)

L. Spitzer, *Physics of Fully Ionized Gases* (Interscience, New York, 1962)

L. Spitzer Jr., *Physical Processes in the Interstellar Medium* (Mir, Moskva, 1981)

H.C. Spruit, A. Nordlund, A.M. Title, Solar convection. ARA&A **28**, 263–301 (1990)

S. Sridhar, P. Goldreich, Toward a theory of interstellar turbulence. 1: Weak Alfvenic turbulence. ApJ **432**, 612–621 (1994)

M. Steenbeck, I.M. Kirko, A. Gailitis, A.P. Klyavinya, F. Krause, I.Y. Laumanis, O.A. Lielausis, Experimental discovery of the electromotive force along the external magnetic field induced by a flow of liquid metal (α-effect). Soviet Phys. Dokl. **13**, 443 (1968)

A.V. Stepanov, Determination of energetic particle sources using radio emission from solar magnetic traps. Issl. Geomagn. Aeron. and Sol. Phys. **54**, 141–148 (1980)

R.J. Strangeway, R.E. Ergun, C.W. Carlson, J.P. McFadden, G.T. Delory, E.L. Pritchett. Accelerated electrons as the source of auroral kilometric radiation. Phys. Chemistry of the Earth C **26**, 145–149 (2001)

S.I. Syrovatskii, Zhur. Exper. Teor. Fiz. **27**, 121 (1953)

S.I. Syrovatskii, Magnetohydrodynamik. Fortschritte der Physik **6**, 437–503 (1958)

S.I. Syrovatskii, Pinch sheets and reconnection in astrophysics. ARA&A **19**, 163–229 (1981)

J. Takata, S. Shibata, K. Hirotani, H—K. Chang, MNRAS, **366**, 1310 (2006)

G.I. Taylor, Experiments with rotating fluids. Royal Society of London Proceedings Series A **100**, 114–121 (1921)

D. ter Haar, Pulsars. Phys. Rep. **3** (1972)

M.L. Ter-Mikhaelyan, Reviews of topical problems: high energy electromagnetic processes in amorphous and inhomogeneous media. Physics Uspekhi **46**, 1231–1252 (2003)

I.N. Toptygin, Acceleration of particles by shocks in a cosmic plasma. Space Science Rev. **26**, 157–213 (1980)

I.N. Toptygin, *Cosmic Rays in Interplanetary Magnetic Fields* (D. Reidel, Dordrecht, 1985)

I.N. Toptygin, Structure of a collisionless shock front with relativistically accelerated particles. Soviet J. Exp. Theor. Phys. **85**, 862–872 (1997)

I.N. Toptygin, A self-similar solution for a supernova explosion with allowance for accelerated relativistic particles. Astron. Lett. **26**, 356–361 (2000)

I.N. Toptygin, Influence of accelerated particles on the large-scale magnetic field in young supernova remnants. Astron. Lett. **30**, 393–403 (2004)

I.N. Toptygin, *Modern Electrodynamics* [in Russian] (IKI, Moscow-Izhevsk, 2005)

I.N. Toptygin, G.D. Fleishman, A role of cosmic rays in generation of radio and optical radiation by plasma mechanics. Astrophys. Space. Sci. **132**, 213–248 (1987)

I.N. Toptygin, G.D. Fleishman, Methodological notes: eigenmode generation by a given current in anisotropic and gyrotropic media. Physics Uspekhi **51**, 363–374 (2008)

R.A. Treumann, The electron-cyclotron maser for astrophysical application. A&AR **13**, 229–315 (2006)

R.A. Treumann, C.H. Jaroschek, Gibbsian theory of power-law distributions. Phys. Rev. Lett. **100**(15), 155005 (2008)

B.A. Trubnikov, Plasma radiation in a magnetic field. Soviet Phys. Dokl. **3**, 136 (1958)

B.A. Trubnikov, Particle interactions in a fully ionized plasma. Rev. Plasma Phys. **1**, 105 (1965)

C. Tsallis, Nonextensive statistics: theoretical, experimental and computational evidences and connections. Brazilian J. Phys. **29**, 1 (1999)

C. Tsallis, Nonadditive entropy: the concept and its use. European Phys. J. A **40**, 257–266 (2009)

V.N. Tsytovich, *Nonlinear Effects in Plasma* (Plenum Press, New York, 1970)

S.I. Vainshtein, *Magnetic Fields in Space* (Izdatelstvo Nauka, Moscow, 1983)

S.I. Vainshtein, A.M. Bykov, I.N. Toptygin, *Turbulence, Current Sheets, and Shocks in Cosmic Plasma* (Gordon and Breach Science Publishers, New York, 1993)

S.I. Vainshtein, I.B. Zeldovich, A.A. Ruzmaikin, *The Turbulent Dynamo in Astrophysics* (Nauka, Moskva, 1980)

S.I. Vainshtein, Y.B. Zel'dovich, Reviews of topical problems: origin of magnetic fields in astrophysics (turbulent "dynamo" mechanisms). Soviet Phys. Uspekhi **15**, 159–172 (1972)

J.P. Vallée, Astral magnetic fields as observed in starforming nurseries, in stars, and in the solar system. New Astron. **47**, 85–168 (2003)

J.P. Vallée, Cosmic magnetic fields - as observed in the Universe, in galactic dynamos, and in the milky way. New Astron. **48**, 763–841 (2004)

G.H.J. van den Oord, The electrodynamics of beam/return current systems in the solar corona. A&A **234**, 496–518 (1990)

J. Vink, Supernova remnants: the X-ray perspective. ArXiv e-print 1112.0576. AAPR vol. 20, pp. 49 (2012). doi 10.1007/s00159-011-0049-1. http://adsabs.harvard.edu/abs/2012A%26ARv..20...49V . Provided by the SAO/NASA Astrophysics Data System

I.I. Vitinskii, *Solnechnaia aktivnost'* [in Russian] (Nauka, Moskva, 1983)

A.E. Vladimirov, A.M. Bykov, D.C. Ellison, Spectra of magnetic fluctuations and relativistic particles produced by a nonresonant wave instability in supernova remnant shocks. ApJ **703**, L29–L32 (2009)

L. Vlahos, A. Raoult, Beam fragmentation and type III bursts. A&A **296**, 844 (1995)

C.Z. Waters, S.E. Zepf, Ultraviolet hubble space telescope observations of the Jet in M87. ApJ **624**, 656–660 (2005)

S. Weinberg, *Gravitation and Cosmology: Principles and Applications of the General Theory of Relativity* (Wiley, New York, 1972)

N.O. Weiss, M.J. Thompson, The solar dynamo. Space Science Rev. **144**, 53–66 (2009)

D.G. Wentzel, Hydromagnetic waves excited by slowly streaming cosmic rays. ApJ **152**, 987 (1968)

K.C. Westfold, The polarization of synchrotron radiation. ApJ **130**, 241 (1959)

G.B. Whitham, *Linear and Nonlinear Waves* (Wiley, New York, 1974)

S.E. Woosley, J.S. Bloom, The supernova gamma-ray burst connection. ARA&A **44**, 507–556 (2006)

D.G. Yakovlev, K.P. Levenfish, Y.A. Shibanov, Reviews of topical problems: cooling of neutron stars and superfluidity in their cores. Physics Uspekhi **42**, 737–778 (1999)

V.V. Zaitsev, A.V. Stepanov, Nature of type IV solar radiation pulsations. Pulsating regime of the beam and loss-cone instabilities. Issl. Geomagn. Aeron., and Sol. Phys. **37**, 11–18 (1975)

V.V. Zaitsev, A.V. Stepanov, The plasma radiation of flare kernels. Solar Phys. **88**, 297–313 (1983)

A.V. Zasov, K.A. Postnov, *Obshchaya Astrophysika* [in Russian] (Vek 2, Fryasino, 2006)

Y.B. Zel'dovich, I.D. Novikov, *Theory of Gravitation and the Evolution of Stars* [in Russian] (Nauka, Moskva, 1971)

Y.B. Zeldovich, R.A. Sunyaev, The interaction of matter and radiation in a hot-model universe. Astrophys. Space. Sci. **4**, 301–316 (1969)

L.M. Zelenyi, A.V. Milovanov, Reviews of topical problems: fractal topology and strange kinetics: from percolation theory to problems in cosmic electrodynamics. Physics Uspekhi **47**, 1 (2004)

V.N. Zirakashvili, D. Breitschwerdt, V.S. Ptuskin, H.J. Voelk, Magnetohydrodynamic wind driven by cosmic rays in a rotating galaxy. mechanism for the acceleration of charged **311**, 113–126 (1996)

V.N. Zirakashvili, V.S. Ptuskin, Diffusive shock acceleration with magnetic amplification by nonresonant streaming instability in supernova remnants. ApJ **678**, 939–949 (2008)

V.N. Zirakashvili, V.S. Ptuskin, H.J. Völk, Modeling Bell's nonresonant cosmic-ray instability. ApJ **678**, 255–261 (2008)

Author Index

G.D. Fleishman and I.N. Toptygin, *Cosmic Electrodynamics*, Astrophysics and Space Science Library 388, DOI 10.1007/978-1-4614-5782-4,

Subject Index

G.D. Fleishman and I.N. Toptygin, *Cosmic Electrodynamics*, Astrophysics and Space Science Library 388, DOI 10.1007/978-1-4614-5782-4,

T